SCHOLARLY PUBLICATIONS

A CURRENT AWARENESS BULLETIN
OF RESEARCH OUTPUT

@DTU

(63rd Edition)

MARCH, 2018

BY: CENTRAL LIBRARY

DELHI TECHNOLOGICAL UNIVERSITY
(FORMERLY *DELHI COLLEGE OF ENGINEERING)*
GOVT. OF N.C.T. OF DELHI
SHAHBAD DAULATPUR, MAIN BAWANA ROAD
DELHI 110042

PREFACE

This is the **Sixty Third** Issue of Current Awareness Bulletin started by Delhi Technological University, Central Library. The aim of the bulletin is to compile, preserve and disseminate information published by the faculty, students and alumni for mutual benefits. The bulletin also aims to propagate the intellectual contribution of Delhi Technological University (DTU) as a whole to the academia.

The bulletin contains information resources available in the internet in the form of articles, reports, presentations published in international journals, websites, etc. by the faculty and students of DTU. The publications of faculty and student which are not covered in this bulletin may be because of the reason that the full text either was not accessible or could not be searched by the search engine used by the library for this purpose.

The learned faculty and students are requested to provide their uncovered publications to the library either through email or in CD, etc. to make the bulletin more comprehensive.

This issue contains the information published during **March, 2018**. The arrangement of the contents is alphabetical. The full text of the article which is either subscribed by the university or available in the web is provided in this bulletin.

Central Library

CONTENTS

1. A DESIGN AND IMPLEMENTATION OF HIGH SPEED IEEE-754 DOUBLE PRECISION FLOATING POINT UNIT BASED ON VEDIC TECHNIQUES, ***8.RAHUL KUMAR AGRAWAL***, ***8.RHYTHM TYAGI*** and ***3.MADAN MOHAN TRIPATHI***, Electrical, DTU

2. AGRICULTURAL TECHNOLOGY ADOPTION AND ITS DETERMINANTS IN ETHIOPIA: A REVIEWED PAPER, ***6.Aynalem Shita***, ***3.Nand Kumar*** & ***3.Seema Singh***, Economics, DTU

3. An Aggregative Machine Learning Approach for Output Power Prediction of Wind Turbines, Solomon Netsanet, Jianhua Zhang, Dehua Zheng, ***8.Rahul Kumar Agrawal***[1] and ***6.Frankle Muchahary***[2], Electrical[1] and Applied Chemistry[2], DTU

4. An Experimental Study and Analysis of the Mechanical Properties of Titanium Dioxide Reinforced Aluminum (AA 5051) Composite, Surabhi Lata, Ankur Pandey, Labhansh, Ankit Sharma, Kuldeep Meena, ***6.Ramakant Rana*** and ***3.Roop Lal***, MECHANICAL, DTU

5. An FPGA based floating point Gauss-Seidel iterative solver, Ramakant Joshi, Aman Raghuvanshi, Yatin Gilhotra, Shivani Sharma, Suyash Sharma, Preyesh Dalmia and Neeta Pandey, Electronics and Communication, DTU

6. Application of Regression in the Analysis of Cutting Parameters for Surface Roughness in Turning, Ankit Tyagi, Yashwant Koli and Sumit Kumar, Mechanical, DTU

7. ARD-PRED: an in silico tool for predicting age-related-disorder-associated proteins, ***6.Kirti Bhadhadhara*** and ***3.Yasha Hasija***, Biotechnology, DTU

8. Automatic Static and Cyclic Shear Testing Machine under Constant Normal Stiffness Boundary Conditions, S. M. Mahdi Niktabar, K. Seshagiri Rao, and ***3.Amit Kumar Shrivastava***, Civil, DTU

9. Autonomous Pathfinding in Simulated 3D Environment, Sidharth Raja, Tanuj Bhatia, ***6.Akshat Mishra***, ***8.1.Sanket Kashyap*** and ***6.Om Prakash Verma***, CSE, DTU

10. ClusFuDE: Forecasting low dimensional numerical data using an improved method based on automatic clustering, fuzzy relationships and differential evolution, Charu Gupta, Amita Jain, Devendra Kumar Tayal and Oscar Castillo, CSE, DTU

11. Comparative Study of PID and Fuzzy Logic Controller for Steam Temperature Control in Thermal Power Plant, ***6.Ajendra Singh*** and ***3.J N Rai***, Electrical, DTU

12. Decreasing of Agricultural Costs for The Indian Farmer by using Jatropha Easters, ***3.Raghvendra Gautam***, Mechanical, DTU

13. Development and Investigation of Hybrid Electric Discharge Machining Electrode Process, ***6.Ramakant Rana***, ***3.R. S. Walia*** and Surabhi Lata, Mechanical, DTU

14. Electroforming Defects During Metal Deposition on Plastic Substrate Produced by Additive Manufacturing, Gurpreet Singh Phull, Sanjeev Kumar and ***3.Ravinderjit Singh Walia***, Mechanical, DTU

15. Epoxy-glass Microballoon Syntactic Foams for Blast Mitigating Applications, ***6.A.V. Ullas***, P.K. Sharma, P. Chandel, P. Sharma, D. Kumar, ***3.D. Kumar*** and P.K. Roy, Applied Chemistry and Polymer Technology, DTU

16. Evidence of circular Rydberg states in beam-foil experiments: Role of the surface wake field, ***6.Gaurav Sharma***, ***3.Nitin K. Puri***, Pravin Kumar and T. Nandi, A Physics, DTU

17. Fast Combinational Architecture for a Vedic Divider, ***6.Preyesh Dalmia***, ***6.Abhinav Parashar***, ***6.Gaurav Aggarwal***, ***6.Radhika Dang*** and ***3.Neeta Pandey***, ECE, DTU

18. Fourth Industrial Revolution, Indian Labour Market and Continuing Engineering Education, ***3.Dr. Seema Singh***, ***6.Kritika Sarkar***, and ***6.Nitya Bahl***, Economics, ELECTRICAL AND ELECTRONICS, DTU

19. Grid interfaced solar photovoltaic system using ZA-LMS based control algorithm, Manoj Badonia, ***3.Alka Singh***, Vijay P. Singh and Ravi Nath Tripathi, Electrical, DTU

20. Hybrid control approach for PV/FC fed voltage source converter tied to grid, ***6.Priyanka Chaudhary*** and ***3.M. Rizwan***, Electrical, DTU

21. Hydrogeochemical characterization and suitability appraisal of groundwater around stone quarries in Mahendragarh, India, ***7.Chitrakshi*** and ***3.A. K. Haritash***, Environmental, DTU

22. Influence of Nano-particle on the Wear behaviour of Thin Film Coatings A Review, Shailesh Kumar Singh, Somnath Chattopadhyaya, A. Pramanik, Sanjeev Kumar and ***6.Navendu Gupta***, Mechanical, DTU

23. Investigation of Chip-Tool Interface Temperature: Effect of Machining Parameters and Tool Material on Ferrous and Non-Ferrous Metal, Surabhi Lata, ***6.Ramakant Rana*** and Hitesh, Mechanical, DTU

24. Long Term Load Forecasting with Hourly Predictions based on Long-Short-Term-Memory Networks, Rahul Kumar Agrawal, Frankle Muchahary and ***3.Madan Mohan Tripathi***, Electrical and Chemistry, DTU

25. Matrix games with 2-tuple linguistic information, ***6.Anjali Singh***, ***3.Anjana Gupta*** and Aparna Mehra, Applied Mathematics, DTU

26. Measure of Entropy for Past Lifetime and k-Record Statistics, ***6.Ritu Goel***, ***3.H.C. Taneja*** and Vikas Kumar, Applied Mathematics, DTU

27. Moderating effects of age, income and internet usage on Online Brand Community (OBC)-induced purchase intention, ***6.Anurag Tiruwa***, ***3.Rajan Yadav*** and ***3.Pradeep Kumar Suri***, DSM, DTU

28. Multiwalled Carbon Nanotube Modified Microfluidic-Based Biosensor Chip for Nucleic Acid Detection, Aditya Sharma Ghrera, ***6.Chandra Mouli Pandey***[1] and ***3.Bansi Dhar Malhotra***[2]***,*** 1.Chemistry and 2.Biotechnology, DTU

29. Novel High speed Vedic Multiplier proposal incorporating Adder based on Quaternary Signed Digit number system, ***6.Preyesh Dalmia***, ***6.Vikas***, ***6.Abhinav Parashar***, ***6.Akshi Tomar*** and ***3.Dr. Neeta Pandey***, ECE, DTU

30. Optimization to the parameters of abrasive flow machining by Taguchi method, ***3.Ravi Butola***, ***6.Rishabh Jain***, ***6.Priyesh Bhangadia***, ***6.Ashwani Bandhu***, ***3.R.S Walia*** and Qasim Murtaza, Mechanical, DTU

31. Pr3+ ions doped single alkali and mixed alkali fluoro tungsten tellurite glasses for visible red luminescent devices, Ch.B Annapurna Devi, Sk. Mahamuda, K. Swapna, M. Venkateswarlu, ***3.A. Srinivasa Rao*** and G. Vijaya Prakash, Physics, DTU

32. Predicting Crowdfunding Success with Optimally Weighted Random Forests, Fahad Sarfaraz Ahmad, ***8.Devank Tyagi*** and ***8.Simran Kaur***, Computer, DTU

33. Spectroscopic study of Pr3þ ions doped Zinc Lead Tungsten Tellurite glasses for visible photonic device applications, ***6.Ritu Sharma***, ***3.A.S. Rao***, ***6.Nisha Deopa***, M. Venkateswarlu, ***3.M. Jayasimhadri***, D. Haranath and G. Vijaya Prakash, Applied Physics, DTU

34. STRESS INDUCED MAGNETIC FIELD INHOMOGENEITY IN A 1.5 T SUPERCONDUCTING MRI MAGNET, S. R. Thekkethil, S. Kar, M. Kumar, V. Soni, N. K. Suman, R.G. Sharma, ***3.V. Rastogi*** and T. S. Datta, Mechanical, DTU

35. Structural, optical absorption and photoluminescence spectral studies of Sm3þ ions in Alkaline-Earth Boro Tellurite glasses, K. Siva Rama Krishna Reddy, K. Swapna, Sk. Mahamuda, M. Venkateswarlu, M.V.V.K. Srinivas Prasad, ***3.A.S. Rao*** and G. Vijaya Prakash, Applied Physics, DTU

36. Swelling and drug release kinetics of composite wound dressing, ***6.Anuja Agrawal*** and ***3.Roli Purwar***, Chemistry and Polymer Technology, DTU

37. Synthesis of Iminolactones through Iodocyclization of Functionally Substituted Alkynes, ***3.Saurabh Mehta***, Applied Chemistry, DTU

38. Thermodynamic (energy-exergy) analysis of combined cycle power plant for improving thermal energetic and exergetic efficiencies by integration of organic Rankine cycle (ORC), ***6.Yunis Khan*** and ***3.R.S. Mishra***, Mechanical, DTU

39. Thermodynamic Analysis of Irreversible Regenerative Gas Turbine Cycle, ***6.Shabir Grover*** and S.S.Bhatti, Mechanical, DTU

40. Validation of various cryogenics systems using exergy analysis, ***3.R.S. Mishra*** and ***6.Devender Kumar***, Mechanical, DTU

41. Viscous cosmology in new holographic dark energy model and the cosmic acceleration, ***3.C. P. Singh*** and ***6.Milan Srivastava***, Mathematics, DTU

1. *Chancellor*

2. *Pro Vice Chancellor*	***2.1.*** *Ex Pro Vice Chancellor*
3. *Faculty*	***3.1.*** *Ex Faculty*
4. *Teaching-cum-Research Fellow*	***4.1.****Asst. Librarian*
5. *Alumni*	
6. *Research Scholar*	***6.1.*** *Ex Research Scholar*
7. *PG Scholar*	***7.1.*** *Ex PG Scholar*
8. *Undergraduate Student*	***8.1.*** *Ex Undergraduate Student*

ResearchGate

See discussions, stats, and author profiles for this publication at: https://www.researchgate.net/publication/323241410

A Design and Implementation of High Speed Ieee-754 Double Precision Floating Point Unit Based on Vedic Tech....

Article · September 2017

DOI: 10.26634/jele.8.1.13836

CITATIONS
0

READS
6

3 authors, including:



Rahul Kumar Agrawal
Delhi Technological University
4 PUBLICATIONS **0** CITATIONS

SEE PROFILE

All content following this page was uploaded by Rahul Kumar Agrawal on 18 March 2018.

The user has requested enhancement of the downloaded file.

A DESIGN AND IMPLEMENTATION OF HIGH SPEED IEEE-754 DOUBLE PRECISION FLOATING POINT UNIT BASED ON VEDIC TECHNIQUES

By

RAHUL KUMAR AGRAWAL * RHYTHM TYAGI ** MADAN MOHAN TRIPATHI ***

*-** UG Scholar, Department of Electrical Engineering, Delhi Technological University, India.
*** Professor, Department of Electrical Engineering, Delhi Technological University, India.

Date Received: ..... Date Revised: ..... Date Accepted: .....

ABSTRACT

In this paper, a high speed 64-bit double precision Floating Point Unit (FPU) using Vedic mathematics is proposed. In a general processor, the multiplication and division architectures play a crucial role in deciding the overall speed of the system. However, the standard algorithms are sequential units and reduce the performance of the processor. Vedic Mathematics on the other hand offers a new holistic approach of realizing these operations in a combinational unit. In the proposed architecture, the multiplication operation has been implemented using a 54-bit Vedic multiplier based on Urdhva Tiryagbhyam Algorithm while an optimized binary division architecture using Nikhilam Sutra is realized. The proposed method is coded in Verilog High Description Language (HDL), synthesized for Spartan 6 Field-Programmable Gate Array (FPGA) board and simulated using Xilinx Vivado Design Suite. An operating frequency of 205.08 MHz has been attained which is 92.61% faster than the conventional implementation of a 64-bit floating point unit. The number of slice registers required for the overall realization of the FPU has also been reduced significantly by 94.3% and hence reducing the area requirement of the FPU in a general processor.

Keywords: Floating Point Unit, Vedic Mathematics, Verilog, Double Precision, FPGA.

INTRODUCTION

Floating point unit is a part of a processor specifically designed to perform operations on floating point or real numbers. An IEEE 754 double precision floating point format has been used for the representation of floating point numbers [3]. A floating point unit is widely used in the design of processors used in Automatic Control, Digital signal processing, Information processing and application specific systems. Applications involving higher speed, accuracy and precision necessitate the use of double precision floating point operations. Floating point representation has better resolution and accuracy as compared to fixed point number representation.

The performance of any processor is defined by its power consumption, clock speed and area requirement. For performing operations on floating point numbers, it is essential to have time and space competent techniques. Vedic mathematics offers a combinational method to implement multiplication and division operations as opposed to the conventional techniques which are sequential [7]. Vedic mathematics is primarily established on sixteen sutras [5]. Among these sixteen sutras, Urdhva Tiryagbhyam algorithm is used to perform multiplication and Nikhilam sutra is used to perform division [2], [10]. By employing Vedic methodology, the operating speed of a floating point unit can be increased drastically. As the number of registers are also reduced, the area requirement of the processor overall is decreased.Hence the performance of a floating point unit and in turn a general processor is improved significantly due to the use of Vedic techniques.

The existing works on floating point unit have adapted the conventional methodologies for the arithmetic operations where division is performed through multiple

subtractions [4]. As the partial results have to be stored in registers, a sequential circuit is realized. A logarithmic approach for performing the arithmetic operations on floating point numbers has been described in [9]. Although this approach reduces the complexity of computation and simplifies the overall data-path of the FPU, its memory occupancies lead to the latency in the model. In [6], the floating-point multiply-add units have been embedded in an island style FPGA. Using this technique has helped reduce the area and also improved the clock speed. But significant silicon wastage has also resulted from these embedded units in non-floating-point applications [6]. In this paper, the mantissa parts of the operands have been multiplied or divided using Vedic architectures and hence offer a dramatic improvement in clock rate.

This paper has been divided into five sections. The paper first briefly describes the IEEE-754 format for representation of double precision floating point numbers in Section II. The standard floating point operations and their algorithms have also been explained in Section II. The Vedic techniques for implementation of multiplication and division operations on 54-bit numbers are illustrated in Section III.The simulation of the proposed architecture and itsperformance comparison is carried out in Section IV.Finally, conclusions are drawn in Section V.

1. IEEE-754 Format and Floating Point Operations

For floating point computations, IEEE developed a standard format known as IEEE-754 [3]. The double precision format consists of 64 bits and is divided into three parts; 1 sign bit, exponential (11 bits) and mantissa (52 bits) as shown in Figure 1. The sign bit defines whether the number is positive or negative, 0 for positive and 1 for negative. The exponent value is offset by 1023. The mantissa also consists of a leading 1 for all double precision floating point numbers with exponential magnitude greater than 0. This leading 1 is not included in the 52 bits of mantissa.

The IEEE-754 standard also defines five exceptions; Invalid, division by zero, overflow, underflow and inexact. In the proposed floating point unit, these exceptions are indicated by output flag signals.

Sign	Exponent	Mantissa
63	62....52 bits	51....0 bits

Figure 1. IEEE-754 Format for Double Precision Floating Point Numbers

If the addition operation is selected and the operands are opposite in sign, the floating point unit computes the operation as subtraction. Similarly, if the subtraction operation is selected and the operands are opposite in sign, the floating point unit performs addition on the operands. The sign bit is computed in accordance with the magnitude of the operands.

1.1 Addition

In addition of two 64-bits double precision floating point numbers; we broadly consider two cases- numbers with unequal exponents and numbers with equal exponents.

Case I:

First two numbers A and B with unequal exponents are considered. After separation of the numbers A and B into their corresponding mantissas and exponents, four values man_A, exp_A, man_Bandexp_Bare obtained. Next the exponents of the two are compared to get exp_large and exp_small. By the comparison of exponents, man_large and man_smallare obtained. If the exponents are equal, man_large might have the smaller mantissa as only the exponent values is considered in assigning the small and large values. But in the next case, after obtaining the four values man_large, man_small, exp_large, and exp_small, shifting of the mantissa is performed.

Let the difference between the values of exp_large and exp_smallbe'd'. The mantissa of smaller exponent i.eman_small is shifted by d bits to the right. Let the new mantissa obtained be denoted by man_new_small. Then it is added to the mantissa of the other number (man_large). This addition is performed after including a leading 1 to both the 52 bits mantissas for normalization. The man1_small is 53 bits of d bits right shifted man_small (including a leading 1) and man1_large is 53 bits of the mantissa of the number with larger exponent (including a leading 1). Resultant mantissa is res_man= man1_small + man1_large and resultant exponent is rs_exp=



Figure 2. Flowchart for Addition/ Subtraction

exp_large.

Case II:

If the exponents of the two numbers are equal, a leading 1 is included in front of each mantissa and an extra 0 in front of the 1 in case the addition overflows. Because when an overflow occurs, the exponent must be increased by 1. The resultant mantissa is res_man= man_1+man_2 which is 54 bits (including the leading 0 and 1). After the addition, the 54th bit gets shifted out of the result and can be used for rounding purposes later. The leftmost 1 can become the leading 1 of the resulting mantissa.

1.2 Subtraction

Similar to addition, two numbers with unequal exponents are considered. After separation of the numbers A and B into their corresponding mantissas and exponents, four values man_A, exp_A, man_B and exp_Bare obtained. Next the exponents of the two are compared to get exp_large and exp_small. By the comparison of exponents, man_large and man_smallis also obtained. If the exponents are equal, man_large might have the smaller mantissa as only the exponent values is considered in assigning the small and large values. After obtaining the four values man_large, man_small, exp_largeandexp_small, shifting of the mantissa is performed. Let the difference between the values of exp_large and exp_smallbe 'd'. The mantissa of smaller exponent i.eman_small is shifted by d bits to the right. Let the new mantissa obtained be denoted by man_new_small. In case the exponents are equal, the mantissas are subtracted without any right shift of the

mantissa.

The resultant mantissa after the subtraction is denoted by 'diff'. The number of 0s in diff before the leftmost 1 is counted, let the number of zeros be num. Now, the exponent of the larger operand is reduced by num and the result is left shifted by num number of bits to obtain the mantissa of the answer. The leftmost 1 of diff becomes the leading 1 of the resulting mantissa.

1.3 Multiplication

The sign of the result is obtained by XORing the sign bits of the two operands. Next, the exponents are added and 1023 is subtracted from the result to obtain the resultant exponent. A leading 1 is added to both the mantissas to obtain 53 bit man_A and man_B which are multiplied using the 54-bit Vedic multiplication module based on Urdhva Tiryagbhyam Algorithm as explained in the next section. Hence we obtain a 106 bit product.

For normalization, if 105th bit of result is 1, mantissa is normalized to 52 bit by taking 104th to 53th bit position number and exponent is increased by decimal value one. If 105th bit of result is 0, mantissa is normalized to 52 bit by taking 103th to 52th bit position number and there is no increment in the exponent value.

1.4 Division

Firstly, a leading 1 is added to mantissas of both the operands to obtain a 53 bit divisor and a 53 bit dividend. The two mantissas with leading 1 are divided using a 54-bit Vedic divider module based on Nikhilam Sutra as explained in the next section. The resulting mantissa is normalized to 52 bits.

A 54 bit quotient is obtained from the 54 bit Vedic Divider Module. If the most significant bit of the quotient is 1, mantissa is normalized to 52 bit by taking 52th to 1st bit position number and exponent is increased by decimal value one. If 53th bit of result is 0, mantissa is normalized to 52 bit by taking 51th to 0 bit position number and there is no increment in the exponent value.

To obtain the resultant exponent, we subtract the exp_small from exp_large and add 1023 to the result to obtain result_exp. If the result_exp is less than 0, the quotient will be right shifted by the magnitude. The sign bit is obtained by XORing the sign bits of the two operands.

1.5 Rounding and Exceptions

In this paper, all the four rounding modes specified by the IEEE 754 standard have been defined. The user has the liberty to choose the desired rounding mode. The four rounding modes are:

- Round to Nearest
- Round towards zero
- Round towards positive Infinity
- Round towards negative Infinity

The output signals of underflow, overflow, inexact, exception, and invalid arein accordance with the IEEE 754 standard. The special cases have been described in

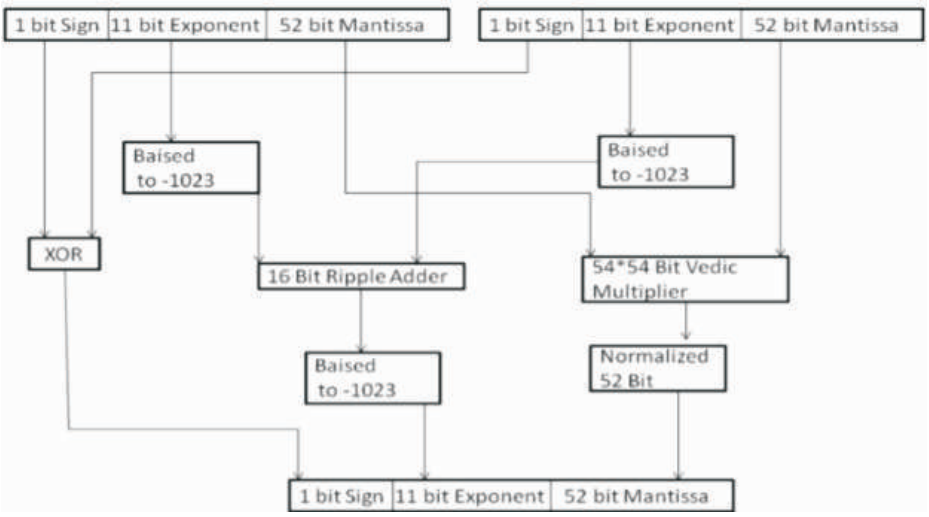


Figure 3. Architecture for Floating Point Multiplication

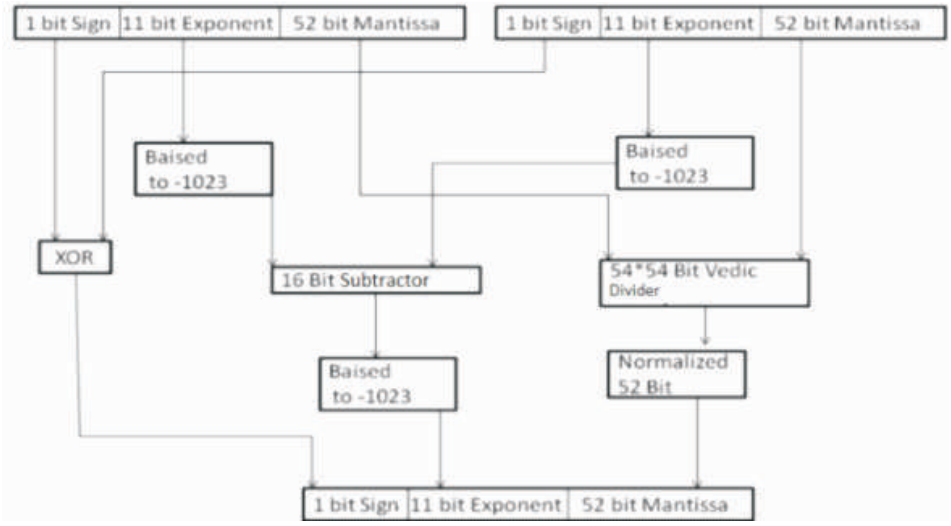


Figure 4. Architecture for Floating Point Division

Table 1. If any of the below cases occur, exception signal is asserted.

2. Vedic Techniques for Arithmetic Operations

2.1 Urdhva Tiryagbhyam Sutra for Vedic Multiplication

The Vedic technique for multiplication of two 54 bit unsigned numbers using Urdhva Tiryagbhyam sutra has been demonstrated in this section. The mantissa part of a double precision floating point number along with its leading 1 constitutes 53 bits. The mantissa parts of the two operands need to be multiplied using an unsigned multiplier. The word Urdhva Tiryagbhyam signifies vertical and crosswise [6]. This methodology is implemented by computing partial products and subsequent addition. The delay and area of the architecture of a Vedic multiplier increases gradually with the number of bits of the operands in comparison to conventional multipliers.

Case	Result	Flag Asserted
Divide by 0	Infinity	
0/0	Signaling Not a Number (sNaN)	Invalid
Infinity/Infinity	Signaling Not a Number (sNaN)	Invalid
Divide by infinity	Zero	Underflow
Overflow	Infinity	Overflow
Underflow	Zero	Underflow
Positive Infinity+Negative Infinity	Signaling Not a Number (sNaN)	Invalid
Positive Infinity-positive Infinity	Signaling Not a Number (sNaN)	Invalid
Negative Infinity-Negative Infinity	Signaling Not a Number (sNaN)	Invalid
Input is Quiet Not a Number (qNaN)	qNaN	Invalid
Input is sNaN	qNaN	Invalid

Table 1. Cases for Exception Signals

A 3-bit Vedic multiplier is used as a fundamental block for the 54-bit multiplier. For multiplication of 3-bit binary numbers, consider two operands x and y. x can be denoted as x2x1x0 and y as y2y1y0. As shown in Figure 5, x0 and y0 are multiplied and stored as s0=x0y0. For cross multiplication, x0 is multiplied with y1 and y0 is multiplied with x1. The partial results are added together and stored as c1s1=x1y0 + y0x1. Similarly, c2s2= c2+ x2y0+ x1y1+x0y2; c3s3=c2+x1y2+x2y1 and c4s4=c3+x2y2. The final product is computed as c4s4s3s2s1s0. Using the

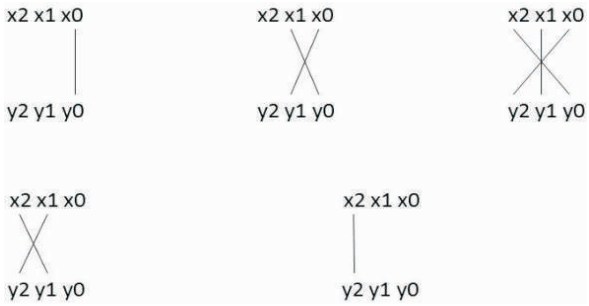


Figure 5. Vedic Multiplication of two 3-bit Numbers

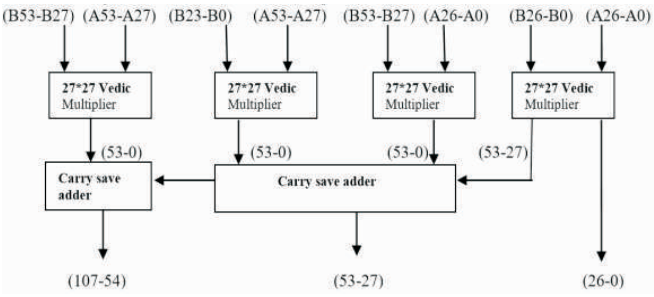


Figure 6. Vedic Multiplication Architecture for 54-bit Binary Numbers

3-bit Vedic multiplier as a fundamental block, a 54*54 Vedic multiplier is implemented. The architecture of the proposed 54-bit multiplier is shown in Figure 6. Carry save adder is used for the summation of partial products. The final product is of 108 bits which is normalized to a 52 bit mantissa using the normalization procedure explained in the section above.

Table 2 compares the combinational time delay between an array multiplier and a Vedic multiplier for 2, 4 and 8 bits [1]. As can be observed from the table, vedic multiplier is faster than array multiplier for all the three cases. The difference in the time delay between the two multipliers increases as the number of bits is increased.

2.2 Nikhilam Sutra for Vedic Division

The Nikhilam NavatascaramamDasatah sutra literally means 'all from 9 and the last from 10' [8]. Division algorithm using Nikhilam Sutra utilizes only addition and complement operations. The mantissas of the two operands are divided using a 54 bit Vedic divider based on Nikhilam Sutra.

Proposed architecture for 54-bit divider using Nikhilam sutra has been shown in Figure 7. Consider A as dividend and B as divisor. B is fed as input to the circuit of two's complement operation. The two's complement of B is

	Combinational Time Delay (ns)	
Bits	Array Multiplier	Vedic Multiplier
2*2	9.073	5.132
4*4	18.057	9.944
8*8	32.261	15.396

Table 2. Delay Comparision of Vedic Multipler [9]

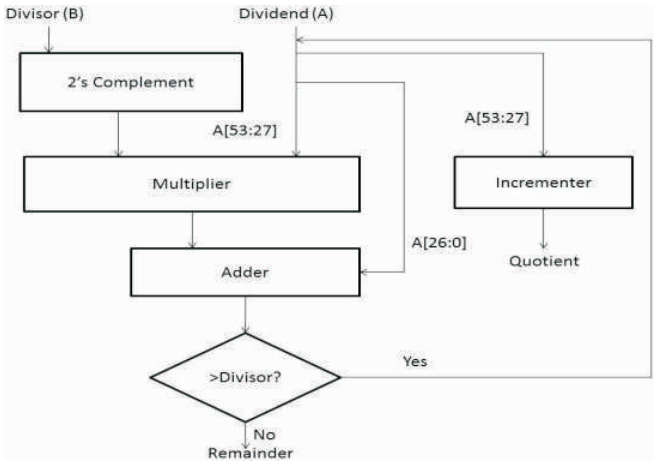


Figure 7. Flowchart for Nikhilam Sutra

multiplied with the most significant 27 bits of A. The same 27 bits of A are also given as input to an incrementer initialized by 0. The product of multiplication is summed with the 27 LSB of A. If the sum is greater than B, the sum is again fed as input to the multiplier replacing A [54:27]. The operation is reiterated until the sum is less than the divisor B. The result of the incrementer is the quotient of the division. The quotient is normalized to 52 bits and forms the mantissa of the final output.

3. Simulation Section

The architectural schematic of 64 bit double precision floating point unit using Vedic mathematics was synthesized using Xilinx Vivado Design Suite for Spartan 6 FPGA board. Vivado Design Suite is a software suite developed by Xilinx for synthesis and analysis of HDL designs. Verilog HDL has been used for the design of the proposed floating point unit. Spartan 6 was specifically chosen as to compare the performance of the FPU based on speed and area with the existing work [6] under the same conditions. The maximum frequency achievable by a clock in an FPGA board is defined by its speed grade. The speed grade of Spartan 6 FPGA board chosen is -3. The design has been verified by simulation using ISIM Simulator. The synthesized Register-transfer level (RTL) schematic has been shown in Fig. 8. The synthesis report generated by Xilinx Vivado provides information on the maximum clock frequency, minimum clock period and the number of slice Registers as tabulated in Table 2.

This section verifies the operation of the FPU for four mathematical operations; addition, subtraction, multiplication and division. Signals a andb are the 64 bit operands and a two bit signalop_code selects the desired operation. The result is stored in the 64 bit signal result. As shown in Figure 8, error signals exception, inexact, invalid, overflow and underflow are also generated in accordance with IEEE-754 standard.

As tabulated in Table 3, the performance of the proposed architecture has been compared with the conventional implementation of a 64 bit floating point unit [4]. The existing work does not integrate the use of Vedic mathematics in its operations. The results show the

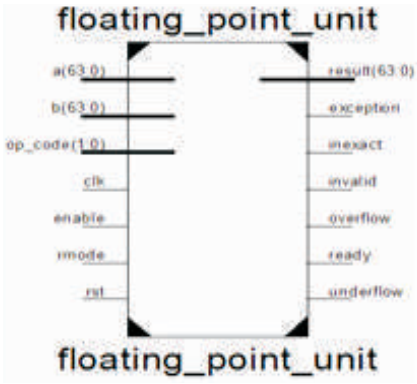


Figure 8. RTL Schematic of FPU

maximum clock frequency achieved is 205.08 MHz which is 92.61% faster than its conventional counterpart. This increase in speed can be attributed to the use of Vedic techniques for multiplication and division operations. As the Vedic architecture is purely combinational as opposed to the conventional methods of multiplication and division which are sequential units, the number of slice registers essential for the implementation of floating point unit has been significantly reduced by 94.3%. The area requirement of the floating point unit has thus been

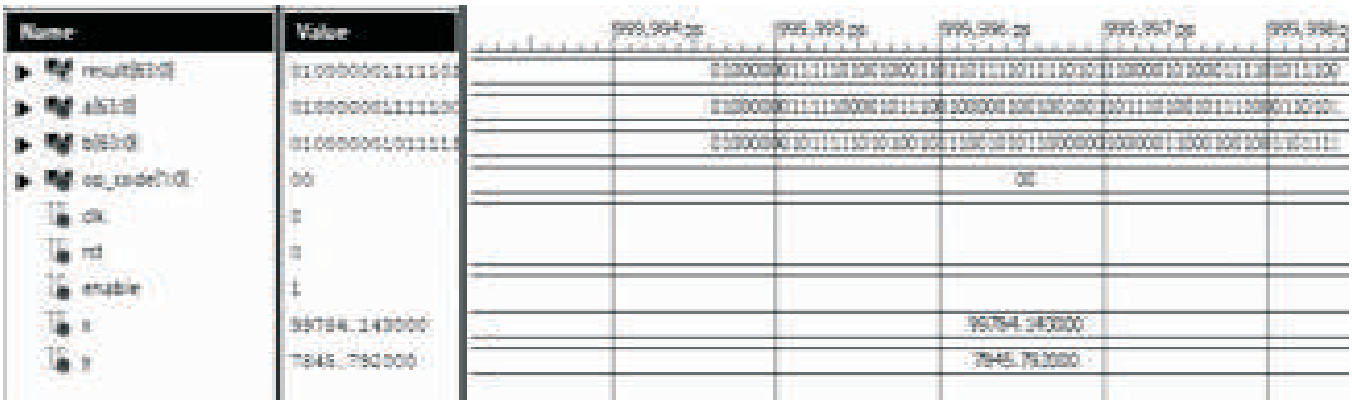


Figure 9. Simulation of 64-bit Addition

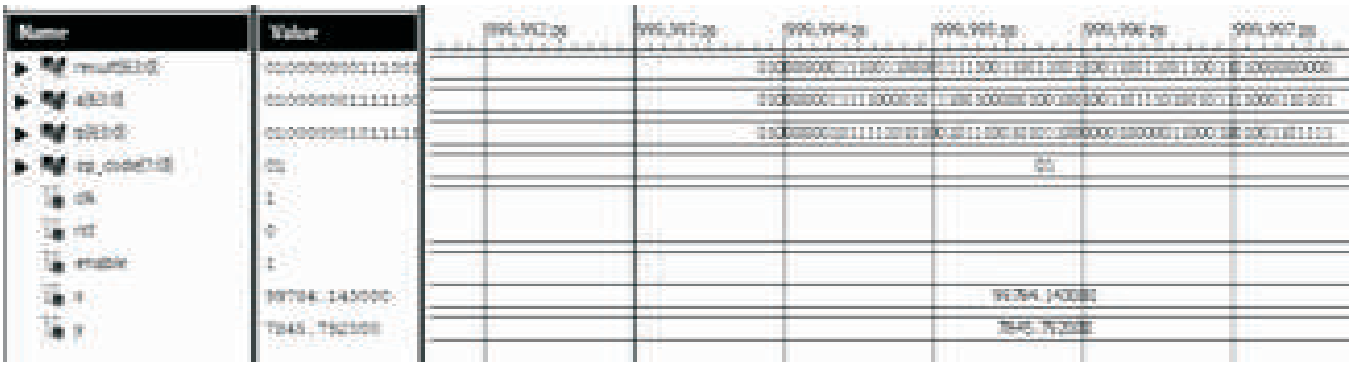


Figure 10. Simulation of 64-bit Subtraction

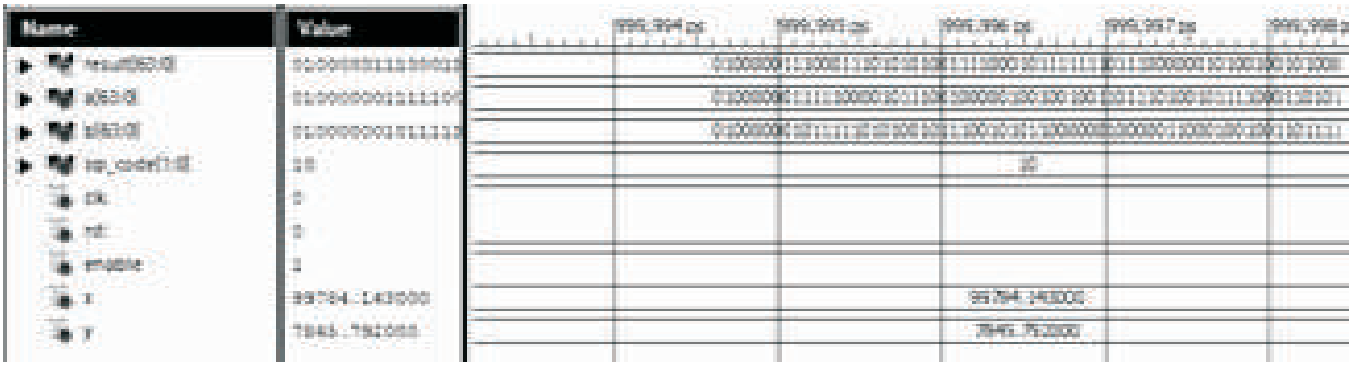


Figure 11. Simulation of 64-bit Multiplication

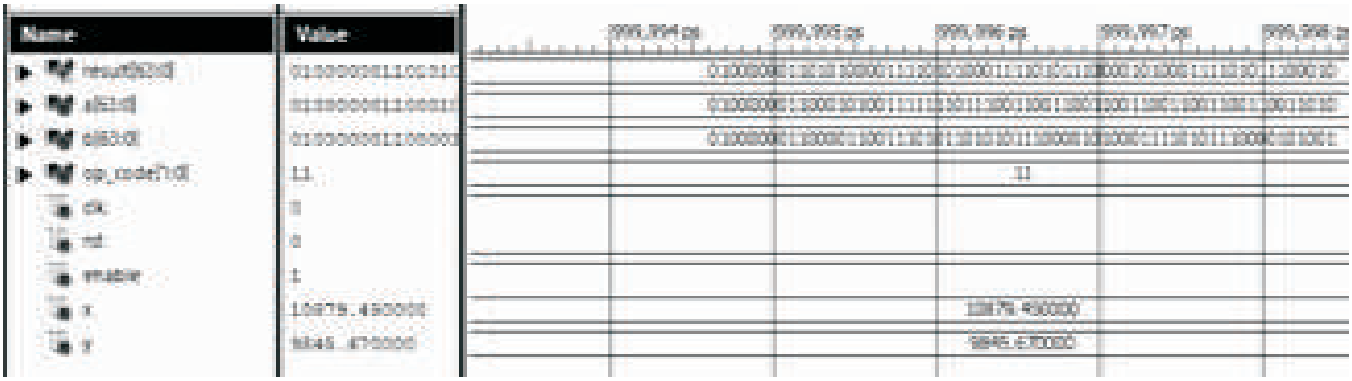


Figure 12. Simulation of 64-bit Division

Performance Parameter	Existing Work [6]	Proposed Architecture	Improvement (%)
Device	Spartan 6	Spartan 6	
Minimum clock period (ns)	9.392	4.876	48.08%
Maximum clock frequency (MHz)	106.474	205.080	92.61%
Number of Slice Registers	4710	265	94.3%

Table 3. Performance Comparison

condensed which makes it more economical.

Conclusion

In this paper, a more efficient IEEE-754 double precision Floating point unit based on Vedic techniques is proposed. The multiplication operation is realized using 54-bit Vedic multiplier based on Urdhva Tiryagbhyam Algorithm and the division operation is based on Nikhilam Sutra. The unit has been coded in Verilog HDL, synthesized for the Spartan 6 FPGA board using Xilinx Vivado Design Suite. The proposed architecture outperforms its counterpart in terms of clock speed by 92.61%. Accredited to the use of Vedic Sutras, the proposed work is improved with respect to speed, area and accuracy. The design attained a maximum clock frequency of 205.08 MHz. The synthesized design can be further implemented on an FPGA board to confirm its operation and analyze its performance in terms of power dissipation.

References

[1]. Gadakh, S.N., and Khade, A.S. (2016). "FPGA Implementation of High Speed Vedic Multiplier", *International Conference and Workshop on Electronics and Telecommunication Engineering (ICWET)*, pp. 184-187, 2016, DOI: 10.1049/cp.2016.1144.

[2]. Gupta, A., Malviya, U., & Kapse, V. (2012). A novel approach to design high speed arithmetic logic unit based on ancient vedic multiplication technique. *International Journal of Modern Engineering Research (IJMER)*, 2(4), 2695-2698.

[3]. IEEE Computer Society (1985). IEEE Standard for Binary Floating-Point Arithmetic, IEEE Std 754,1985.

[4]. Kshirsagar, C.A., and Palsodkar, P.M. (2014). "An FPGA Implementation of IEEE - 754 Double Precision Floating Point Unit Using Verilog", *International Journal of Electrical, Electronics and Data Communication*, Vol. 2, Issue 6, pp. 1-3, June-2014.

[5]. Maharaja, J.S.S.B.K.T, (1994). Vedic Mathematics, MotilalBanarsidass, New Delhi, India, 1994.

[6]. Pramod, P., Nisha, C.K., Saranya, M.K., Nithya, K., and Chithra, S. (2015). "Design of Fast Multipliers using Vedic Mathematics", *International Journal of Electrical, Electronics and Computer Systems (IJEECS)*, Vol. 3, Issue 2, 2015.

[7]. Saha, P., Banerjee, A., Bhattacharyya, P., & Dandapat, A. (2011, December). Vedic divider: Novel architecture (ASIC) for high speed VLSI applications. In *Electronic System Design (ISED), 2011 International Symposium on* (pp. 67-71). IEEE.

[8]. Senapati, R., Bhoi, B. K., & Pradhan, M. (2013, April). Novel binary divider architecture for high speed VLSI

applications. In *Information & Communication Technologies (ICT), 2013 IEEE Conference on* (pp. 675-679). IEEE.

[9]. Swathi, G.R. and Veena, R. (2014). "Design of IEEE-754 Double Precision Floating Point Unit Using Verilog", *International Journal of Engineering Research & Technology (IJERT)*, ISSN: 2278-0181, Vol. 3, Issue 4, pp. 1136-1139, April – 2014.

[10]. Tej, S. B. (2013, December). Vedic divider-A high performance computing algorithm for VLSI applications. In *Circuits, Controls and Communications (CCUBE), 2013 International conference on* (pp. 1-5). IEEE.

ABOUT THE AUTHORS

Rahul Kumar Agrawal is a final year undergraduate from Delhi Technological University doing his majors in Electrical and Electronics. Some of the research areas of his interest include VLSI, Analog & Digital Design, Image Processing and Computer Architecture.



Rhythm Tyagi is a final year undergraduate from Delhi Technological University doing her majors in Electrical and Electronics. Some of the research areas of her interest include VLSI, Analog & Digital Design, Embedded Systems and Computer Architecture.



Dr. Madan Mohan Tripathi is a professor at Delhi Technological University in the Department of Electrical Engineering. His research interests include Restructured Power Systems, Artificial Intelligence and Embedded Systems.



View publication stats

ResearchGate

See discussions, stats, and author profiles for this publication at: https://www.researchgate.net/publication/323539891

AGRICULTURAL TECHNOLOGY ADOPTION AND ITS DETERMINANTS IN ETHIOPIA: A REVIEWED PAPER

Article · February 2018

CITATIONS
0

READS
24

3 authors, including:



Nand Kumar
Delhi Technological University
34 PUBLICATIONS **41** CITATIONS
SEE PROFILE



Seema Singh
Delhi Technological University
31 PUBLICATIONS **17** CITATIONS
SEE PROFILE

Some of the authors of this publication are also working on these related projects:



AICTE sponsored project on Indian Continuing Engineering Education System in context of Globalisation
View project



Women in Engineering Education in Ethiopia View project

All content following this page was uploaded by Seema Singh on 03 March 2018.

The user has requested enhancement of the downloaded file.

Asia Pacific Journal of Research

ISSN (Print): 2320-5504
ISSN (Online): 2347-4793

Asia Pacific Journal of Research
A peer reviewed international Journal
IMPACT FACTOR : 6.58
Print -ISSN -2320 - 5504
Online-E-ISSN - 2347 - 4793
University Grants Commission
Approved Journal S.N.45797

AGRICULTURAL TECHNOLOGY ADOPTION AND ITS DETERMINANTS IN ETHIOPIA: A REVIEWED PAPER

Aynalem Shita[1], Nand Kumar[2] & Seema Singh[3]

ABSTRACT

The main objective of this paper is to review recent research works studied on agricultural technology adoption and its determinants in Ethiopia. In this paper, therefore, empirical studies done on the area were reviewed in terms of their publication year, the sources of data, methodology they employed and the results they obtained. Moreover, this paper has tried to assess secondary data collected from Central Statistical Agency (CSA) in order to get a more insight on the application rate of agricultural technologies by farm households. In Ethiopia, even though improvements have been seen over time, the use of agricultural technologies is found at its low level. Even though the results of studies conducted on the determinants of agricultural technology adoption were varied based on their study area and the type of technology they studied, variables such as accessibility of credit, farm size, distance from market, oxen ownership, and education were found to be the most common significant factors influencing adoption of agricultural technology in Ethiopia. .

Key words: Ethiopia, Agriculture, Technology, Determinant, Adoption rate.

1. Introduction

Technology can be described as the integration of people, knowledge, tools and systems with the objective to improve people's lives (Porter, 1985). According to Betz (1998), technology is always the means of creating new tools serving humans and their environment. Technology adoption refers to a decision to make full application of an innovation as the best course of action (Rogers, 2003)

Agricultural Transformation in many developing countries that led to a significant increase in agricultural productivity resulted from programmes of agricultural research, extension and infrastructural development occurred in the late 1960s, and this revolution was known as Green Revolution. According to Andersen and Hazell (1985) Green Revolution refers to a rapid increase in wheat and rice productivity resulted from the adoption of improved seed varieties, fertilizers and pesticides.

Technological change in agriculture comprises of introduction of high yielding variety of seeds, fertilizers, plant protection measures and irrigation. These changes in agricultural sector enhance the productivity per unit of land and bring about rapid increase in production.

Ethiopia is a country situated at the Eastern part of Africa with a population of more than 100 million (CSA, 2017). Agriculture is the backbone of the Ethiopian economy, playing a vital role in the country's economic development. The sector accounts for 36.7% of the GDP and generates 88.8% of export earnings. However, the Ethiopian agriculture is a rain feed which its growth depends on favorable climate among others things. For example, the agricultural sector exhibited the lower growth rate of 2.3% in 2015/16 largely on account of Elino effect (NBE, 2016).

[1] *Research Scholar in Economics, Department of Humanities, Delhi Technological University*

[2] *Assistant Professor in Economics, Department of Humanities, Delhi Technological University*

[3] *Associate Professor in Economics, Department of Humanities, Delhi Technological University*

ISSN (Print): 2320-5504
ISSN (Online): 2347-4793

Out of the total crops produced in the country, grain crops took the lion share both in terms of the total area of land coverage and output production. From the total area of land 89.5% of it was covered by grains crops (cereals, pulses and oilseeds) which not only constituted the major food crops for the majority of the country's population but also served as a source of income at household level and a contributor for the country's foreign currency earnings, among others. Out of the total grain crop area, 79.88% hectare of land was covered by cereals where Teff, maize, sorghum and wheat took up 22.95%, 16.91%, 14.85 % and 13.33% of the grain crop area respectively. In terms of production, cereals constituted 86.68% grain production in which Maize, teff, wheat and sorghum 26.80%, 16.76%, 15.81% and 16.20% of the grain production respectively (CSA, 2017).

Since more than 80% of the population lives in the rural area where agriculture is the source of their livelihood, its growth is a major driver of poverty reduction in rural Ethiopia. As a result the government of Ethiopia has planned to increase agricultural productivity through the adoption of agricultural technologies among other strategies.

Even though the supply of improved seeds and fertilizer that help increase agricultural production and productivity has increased overtime, but still falls short of the target set in order to transform smallholder agriculture (MoFED, 2016).

The main objective of this paper is to review recent empirical research works on the rate of agricultural technology adoption and its determinants in Ethiopia. Moreover, this paper has tried to review the application of agricultural technologies based on secondary data collected from CSA Ethiopia.

2. Agricultural Technology Adoption In Ethiopia

The application of fertilizer to crop fields in Ethiopia is gathering momentum. The area covered by fertilizer used and the extent of area covered as a share of the total crop area has shown increment from 6.74 million hectare (50.48%) to 8.18 (57.06%) from 2010/11 to 2014/15. From the total fertilizers applied in Ethiopia, the area of land covered by both UREA and DAP took the largest share followed by DAP which constitutes 28.06% and 15.10 % in 2014/15.
Improved seeds are another important input that contributes to an increase in agricultural productivity. Even though its application has increased from 5.58% to 8.55% in terms of the area

Table 1 Agricultural Technologies Applied in Ethiopia from 2010/11-2014/15

Types of Agricultural Technologies	2010/11		2011/12		2012/13		2013/14		2014/15	
	Applied area in million hectare	Covered Area (%)	Applied area in million hectare	Covered Area (%)	Applied area in million hectare	Covered Area (%)	Applied area in million hectare	Covered Area (%)	Applied area in million hectare	Covered Area (%)
Fertilizer	6.74	50.48	6.80	49.70	7.44	53.41	7.43	52.56	8.18	57.06
Growth (% Change)	-	-	0.88	-1.55	9.42	7.46	-0.15	-1.59	9.98	8.57
Dap	2.11	15.78	20.48	14.96	2.27	16.25	2.03	14.38	2.16	15.10
Growth (% Change)	-	-	-2.86	-5.21	10.61	8.63	-10.22	-11.52	6.35	0.97
Urea	0.30	2.26	0.35	2.55	0.41	2.91	0.37	2.64	0.42	2.93
Growth (% Change)	-	-	15.75	12.95	16.34	14.25	-7.95	-9.28	12.49	11.05
Both Dap and Urea	2.43	18.16	2.56	18.68	3.10	22.23	3.40	24.03	4.02	28.06
Growth (% Change)	-	-	5.45	2.91	21.15	18.99	9.66	8.08	18.32	16.81
Natural	1.91	14.28	1.85	13.50	1.67	12.01	1.63	11.51	1.57	10.96
Growth (% Change)	-	-	-3.14	-5.48	-9.44	-11.06	-2.77	-4.17	-3.49	-4.72
Improved	0.75	5.58	0.86	6.29	0.83	5.97	1.04	7.33	1.23	8.55
Growth (% Change)	-	-	15.40	12.61	-3.27	-5.00	24.59	22.79	18.10	16.59
Pesticide	2.24	16.79	2.27	16.59	2.77	19.89	2.76	19.53	3.20	22.32
Growth (% Change)	-	-	1.20	-1.24	22.08	19.89	-0.34	-1.78	15.76	14.28
Irrigation	0.18	1.36	0.17	1.21	0.15	1.09	0.17	1.18	0.18	1.25
Growth (% Change)	-	-	-9.08	-11.28	-8.43	-10.07	9.72	8.14	7.52	6.15

Source: Own computation based on CSA

ISSN (Print): 2320-5504
ISSN (Online): 2347-4793

covered on improved seeds between 2010/11 to 2014/15, still it is found at a very low level. When extensive pests and weeds damage crops the use of pesticides is indispensable. The total pesticide applied area reached 3.2 million hectares (22.32%) in 2014/15 which has increased over time. Even though irrigation enables to increase the frequency of crop production and alleviates water shortage caused by poor rains /dry seasons, the use of irrigation in Ethiopia is very low. In 2014/15 irrigation was practiced in only 0.18 million hectares (1.25%). Moreover, its application did not show a significant increment over time.

Now let us review recent studies done in Ethiopia which tried to assess the adoption rate of agricultural technologies by farm households based on survey data collected from different parts of Ethiopia.

As it is shown by table 2, most of the studies conducted in Ethiopia were concentrating on the adoption of fertilizer and improved seed varieties. However, regarding to the type of crops studied, while some of them tried to study the adoption of agricultural technologies on selected crops such as chickpea and maize (Asfaw et al. , 2011; Zeng et al., 2015; Verkaart et al., 2017; Tigist, 2017) other studies considered the adoption of technologies in either of the crops grown by farmers (Beshir et al., 2012; Berihun et.al, 2014; Gebregziabher et al., 2014; Abate et al., 2016; Husen et al., 2017) .

Studies indicated that the adoption status of households for improved agricultural technologies has shown tremendous change. In this regard Verkaart et.al (2017), found that the percentage of improved chickpea adopters in Ethiopia has increased over time. According to this study, there were only 31.2% adopters in 2006/07 while this rate has been increased to 63.0% and 79.0% in 2009/10 and 2013/14 respectively. In line with the above result, Asfaw et al. (2011) revealed that 32% of the farm households adopt improved seed variety of Chickpea.

From the existing studies done in Ethiopia, the adoption of fertilizers by farmers has increased over time. For instance, Beshir et al. (2012) and Berihun et al. (2014) have found the adoption rate at fertilizers at 17.8% and 26.67% respectively where as more recent studies such as Husen et al. (2017) and Tigist (2017) have got the adoption rate of 56.8% and 63% respectively.

Table 2 Summary of studies conducted on the rate of Agricultural Technology Adoption in Ethiopia

Author /s	Study Area	Type of adopted technology	Rate of Adoption
Asfaw et al. (2011)	Central highlands of the Ethiopia	improved Seed varieties of Chickpea	32%
Beshir et al. (2012)	North East Ethiopia	Fertilizer adoption in at least one of the crops	17.8%
Berihun et.al (2014)	Northern Ethiopia	Fertilizer adoption in at least one of the crops	26.67%
		Improved seed varieties in at least one of the crops	34.44%
Gebregziabher et al. (2014)	Four major Regions (Amhara, Oromia, SNNP and Tigray)	Motor Pumps adoption in at least one of the crops	33.5%
Zeng et al. (2015)	Four major Regions (Amhara, Oromia, SNNP and Tigray)	improved seed varieties of Maize	46.3%
Abate et al. (2016)	It covered all areas of Ethiopia	Fertilizer in at least one of the crops	85.5%
		Improved seed varieties in at least one of the crops	51.7%
Husen et al. (2017)	SNNP	fertilizers or improved seed varieties in at least one of the crops	56.8%
Verkaart et.al (2017)	Central highlands of the Ethiopia	Improved Seed varieties of Chickpea	79.0%
Tigist (2017)	Four Regions (Amhara, Oromia, SNNP and Tigray	Improved seed varieties of Wheat, Maize, Teff, Sorghum, and Barley	18%
		Fertilizer adoption in Wheat, Maize, Teff, Sorghum, and Barley	63%

ISSN (Print): 2320-5504
ISSN (Online): 2347-4793

3. Determinants of Agricultural Technology Adoption in Ethiopia

The adoption of agricultural technologies depends on different demographic and socio-economic factors. In this section recent studies conducted on factors influencing adoption of agricultural technologies in Ethiopia are reviewed. Hence, the data they used, their method of estimation and results obtained are presented. For the purpose of convenience, the reviewed studies are presented chronologically.

Croppenstedt et al. (2003) studied on determinants of fertilizer adoption in Ethiopia based on a survey covered 6147 cereal households from four regions. By applying double-hurdle model, they found that access of fertilizer, availability of credit, household size; formal education and value-to-cost ratio are the major factors that affect households' decision for fertilizer adoption.

Dadi et al. (2004) studied on the duration analysis of technological adoption in Ethiopian Agriculture by using accelerated lifetime model. The estimated models suggest that economic incentives such as prices are appear to be the most important determinants for the speed of adopting new technologies followed by oxen ownership and infrastructural factors.

Admassie and Ayele (2010) conducted a study on adoption of improved technology in Ethiopia based on 1920 farm household heads drawn from four national regional states. The results of the logit and probit model identified that farm size and extension service affects technology adoption positively where as distance to market and age of the household head affects it negatively. Moreover, they employed tobit model to analyze factors influencing the intensity of fertilizer use and found that while farm size, family size, literacy and extension contact affect positively, age and distance affects intensity of fertilizer use negatively and significantly.

Yesuf and Kohlin (2008) employed probit model to examine the effect of market and institutional imperfections on technology adoption (fertilizer use and soil conservation) in Ethiopia based on survey data collected from 202 farm households in five districts of Amhara region. The study found that while household's decision to adopt fertilizer depends negatively on whether the same household adopts soil conservation, the reverse was not found significant. Moreover, access to credit, plot size, risk considerations, and rates-of-time preference, were significant factors influencing technology adoption decision.

Asfaw et al. (2011) examined the determinants of agricultural technology adoption and their impact on farmers' integration into output market in Ethiopia based on cross-section sample of 700 farmers. The Double-Hurdle model results show that knowledge of existing varieties, perception about the attributes of improved varieties, household wealth (livestock and land) and availability of active labor force are major determinants for adoption of improved technologies.

Beshir et al. (2012), by employing Double hurdle approach studied determinants of chemical fertilizer technology adoption in north eastern highlands of Ethiopia. The study found that distance from farmers' home to markets, Distance to input supply, Extension service access and credit supply affects the adoption of inorganic fertilizer.

A study by Berihun et al. (2014) has employed both probit model and OLS to identify factors influencing technology adoption and their impact on Farm Income based on cross-sectional study in Southern Tigray Zone of Northern Ethiopia. The result stated that sex, irrigation use, off-farm income, plot distance and distance to market affects adoption of chemical fertilizer whereas age, irrigation use, access to credit and distance to market were found as determinants of high yield variety in Ethiopia. Moreover, the OLS result revealed that agricultural technology adoption has a positive and significant effect on farm income by which adopters are better-offs than non-adopters.

Gebregziabher et al. (2014), using probit model found that gender, age, oxen ownership, access to extension, access to surface & ground water, social capital and region of residence influence farmers' decision of motor pump adoption in Ethiopia.

Zeng et al. (2015) studied the impacts of improved maize varieties on poverty in rural Ethiopia by using propensity score matching (PSM) and revealed that improved maize varieties have led to a 0.8–1.3 percentage drop of poverty headcount ratio and relative reductions of poverty depth and severity.

Abate et al. (2016) estimated the effect of Rural Finance on agricultural technology adoption in Ethiopia using 817 household survey data and a propensity-score-matching technique. The results suggest that access to institutional finance has a significant positive impact on both the adoption and extent of technology use. It revealed that in the absence of financial institutions, both adoption and application rates of fertilizer and modern seeds would have been significantly lower by 11% and 32%, respectively.

A study by Verkaart et al. (2017) done on welfare impacts of improved chickpea adoption in Ethiopia based on three years panel data from 606 randomly selected households by using double-hurdle model. The study reported that improved chickpea adoption significantly increases household income and reducing household poverty.

ISSN (Print): 2320-5504
ISSN (Online): 2347-4793

Tigist (2017) studied productivity and welfare impact of technology adoption in Ethiopia based on survey data collected from 1500 rural households drawn from four regions. The estimation of endogenous treatment effect model indicate that there is positive and significant effect of improved technology adoption (HYVs and inorganic fertilizer) on the rural households' crop productivity and welfare (Real per capita consumption expenditure) in Ethiopia.

A study by Husen et al. (2017), employed probit model to analyzed the impact of social capital on Agricultural Technology Adoption among Ethiopian Farmers using socio-economic data of 398 farming households. The estimated probit model revealed that being members of *Jarsumma* (informal conflict resolution) increased the likelihood of soil and water conservation practices and productivity enhancing technologies such as fertilizers and improved high yielding seed varieties adoption by 12.87% and 17.8%, respectively. It also found that while members of *Iddir* (informal funeral group) were 18.2% more likely to adopt soil and water conservation practices, *Iddir* members were 12.8% less likely to adopt productivity enhancing technologies.

4. Conclusion

Literatures on the area observed the significant impact of modern agricultural technologies such as fertilizers, improved seeds, pesticides and irrigation for the growth of the agricultural productivity. This paper reviewed the rate of agricultural technology adoption and its determinants in Ethiopia based on secondary data collected from CSA and empirical studies conducted in the area. In Ethiopia, even though improvements have been observed, the use of agricultural technologies is appeared to be low. From the total crop area, on average nearly 50% and 20% of the land is covered by fertilizers and pesticides where as the area covered by improved seed and irrigation is less than 10% and nearly 1% respectively. Empirical studies on adoption of agricultural technologies in Ethiopia were concentrating on the adoption of fertilizer and improved seed varieties. However, the adoption rate of technologies by farm household is varied based on the type of technology and the time of study. Reviewed studies revealed that farm households were adopt more of chemical fertilizers than improved seeds and their adoption rate increases for more recent studies. Studies conducted on the determinants of agricultural technology adoption identified different variables depending on their study area and the type of technology they studied. However, in most of the studies variables such as accessibility of credit, farm size, distance from market, oxen ownership, and level education were found to be significant determinants for agricultural technology adoption in Ethiopia.

References

1. Abate G.T., Rashid, S., Borzaga, C. and Getnet, K. (2016). Rural Finance and Agricultural Technology Adoption in Ethiopia: Does the Institutional Design of Lending Organizations Matter? *World Development, 84*, 235–253.
2. Admassie A. and Ayele G. (2010). Adoption of Improved Technology in Ethiopia. *Ethiopian Journal of Economics, 19*(1), 155-180
3. Anderson, P.P. and P.B.R. Hazell (1985) The Impact of the Green Revolution and Prospects for the Future. Washington, D.C. *(*Reprinted from *Food Reviews International).*
4. Asfaw, S., Shiferaw, B., Simtowe, F., and Haile, M.G., (2011). Agricultural technology adoption, seed access constraints and commercialization in Ethiopia. *Journal of Development and Agricultural Economics, 3*(9), 436-447.
5. Berihun K., Bihon K., and Kibrom A., (2014). Adoption and Impact of Agricultural Technologies on Farm Income: Evidence from Southern Tigray, Northern Ethiopia. *International Journal of Food and Agricultural Economics, 2*(4), 91-106
6. Beshir, H., Emana, B., Kassa, B., and Jema Haji, J., (2012). Determinants of chemical fertilizer technology adoption in North eastern highlands of Ethiopia: the double hurdle approach. *Journal of Research in Economics and International Finance, 1*(2), 39-49
7. Betz, F. (1998). Managing technological innovation: Competitive advantage from change New York: John Wiley & Sons, Inc.
8. Croppenstedt,A., Demeke,M., and Meschi, M., (2003). Technology Adoption in the Presence of Constraints: the Case of Fertilizer Demand in Ethiopia. *Review of Development Economics, 7*(1), 58–70.
9. CSA (2017). Agricultural Sample Survey: Report on Area and Production of Major Crops. Addis Ababa, Ethiopia.
10. Dadi, L., Burton M., and Ozanne, A., (2004). Duration Analysis of Technological Adoption in Ethiopian Agriculture. *Journal of Agricultural Economics, 55*, 613-631
11. Gebregziabher, G., Giordano, M., Langan J. and Namara R, (2014). Economic Analysis of Factors Influencing Adoption of Motor Pumps in Ethiopia. *Journal of Development and Agricultural Economics, 6*(12), 490-500.
12. Husen, N.A., Loos,T.K. and Siddig K. H. (2017). Social Capital and Agricultural Technology Adoption among Ethiopian Farmers. *American Journal of Rural Development*, 5(3), 65-72.
13. MoFED, (2016). Growth and Transformation Plan II (2015/16-2019/20). National Planning Commission, Addis Ababa, Ethiopia

ISSN (Print): 2320-5504
ISSN (Online): 2347-4793

14. NBE (2016). Annual Report of National Bank of Ethiopia. Addis Ababa, Ethiopia.
15. Porter, M. E. (1985). Competitive Advantage. Cambridge: Harvard University Press.
16. Rogers, E. M. (2003). Diffusion of Innovation, 5th ed. New York: The Free Press.
17. Tigist M., (2017). Productivity and household welfare impact of technology adoption: Micro-level evidence from rural Ethiopia, United Nations University working paper (007).
18. Verkaart, S., Munyua, B., Mausch, K. and Michler, J., (2017). Welfare impacts of improved chickpea adoption: A pathway for rural development in Ethiopia. *Food Policy 66*, 50–61.
19. Yesuf, M. and Kohlin G. (2008), Market Imperfections and Farm Technology Adoption Decisions; A Case Study from the Highlands of Ethiopia. *Environment for Development, Discussion Paper Series, 08-04.*
20. Zeng, D., J. Alwang, G.W. Norton, B. Shiferaw, M. Jaleta and C. Yirga, (2015). Ex-Post Impacts of Improved Maize Varieties on Poverty in Rural Ethiopia. *Agricultural Economics 46* (4), 515-526.

View publication stats

An Aggregative Machine Learning Approach for Output Power Prediction of Wind Turbines

Solomon Netsanet[1,2], Jianhua Zhang[1], Dehua Zheng[2], Rahul Kumar Agrawal[3], Frankle Muchahary[4]
[1]School of Electrical & Electronic Engineering
North China Electric Power University
Beijing, China
[2]Goldwind Sc. & Tech. Co. Ltd.
Beijing, China
[3]Department of Electrical Engineering
Delhi Technological University
New Delhi, India
[4]Department of Applied Chemistry
Delhi Technological University
New Delhi, India

Abstract— **Accurately forecasting power output of renewable sources is a necessity in operation of today's grid in order to achieve optimal energy utilization and carbon-free ecosystem. This study devises a stable, effective and accurate model for dayahead prediction of wind turbine power output through use of an aggregative approach. The method involves two types of Artificial Neural Network (Radial Basis and Conventional Feedforward Networks), Adaptive Neuro-Fuzzy Inference System (ANFIS) and Support Vector Machine (SVM) techniques. It is targeted at comparing the prediction models for their individual performances and finally coming upon an aggregative approach which outperforms the individual models through a strategic combination of them. Three techniques of combining (Simple Averaging, Regression and Outperformance) were tested. Though the individual models showed satisfactory performance by themselves, the combination techniques were able to outperform the individual models. Regression technique of combining was seen to be the most effective of all. The predicted output power through this technique was seen to greatly fit with the measured data with an NMSE of 1.03% for the test year. The combination techniques have also demonstrated more stable performance than the individual models while tested with the extreme cases of windy and less windy weeks.**

Keywords—ANFIS, BPNN, Prediction, RBNN, SVM

I. INTRODUCTION

The energy generation mixture has been mostly dominated by fuel based conventional sources until recently. The worrying signs of climate change and a huge number of scientific findings relating the change to use of such energy sources have forced the international community to appreciate the treats and look for options. Renewable sources of different types have started to gain considerable attention. Wind power is one of the most widely applied of those renewable sources accounting the largest share of new installations in recent years. The intermittent nature of most of renewable sources has however caused eyebrows to be raised over security of renewables-led transformation of the power sector. Improved methods of forecasting would improve power security as well as enable efficient utilization of the sources.

This study focuses on predicting the power output from a wind turbine based on weather parameters such as wind speed and air density and power output of the previous hour. It may be suggested that applying the turbine manufacturer's power curve should be good enough. The manufacturer's power curve, however, offers an idealized power output as a function of wind speed by assuming specific air density conditions and a minimal amount of turbulence and wind shear across the blade span [1]. The issue of inertia which enables a spinning turbine to produce power at a lower wind speed than a turbine starting from a standstill is also another factor. Those factors make it impossible to draw a simple one-to-one relationship between wind speed and power outputs. Hence, power output of a turbine can often deviate substantially from the manufacturer's power curve, which can lead to significant forecasted power error.

There is a wide range of perdition techniques employed for renewables' power output prediction. They can grossly be classified as statistical and physical models. The comparatively less complex and older statistical techniques are autoregressive moving average (ARMA/ ARIMA) models. They, however, lack the required level of accuracy in most cases and hence are being replaced by machine learning techniques such as neural networks, Fuzzy systems and support vector machines which employ different mechanisms to learn the pattern and relation of parameters.

Different literatures are available on the applicability and success stories of machine learning approaches in wind power prediction. Artificial Neural Network is the most widely used of the techniques and it has been reported to be an effective tool by [2] [3] while [4] utilized it in combination with SVM and [5] hybridized it with evolutionary algorithms such as GA claiming to find improved forecasts. There were favorable results reported in achieving higher forecast accuracy through use of

978-1-5386-1006-0/18/$31.00 ©2018 IEEE

wavelet, SVM [6] [7] and ANFIS [8] as well. Ref. [9] compared Artificial Neural Network (ANN) with SVM based techniques and other approaches and emphasized the need for a large set of training data as an important factor for effectiveness of ANN.

A lot of research works had been carried out with the objective of searching for a better technique. Despite the continued effort for a better forecasting model, it had not been possible to come up with a forecasting method that is always best or even better than another for every period and time horizon [10]. That is where the idea of combining multiple approaches with a satisfactory individual performance gets a good ground. The most common and simple way of combining is simple averaging. This technique is employed in wind power forecasting as well [11] [12]. Unlike its simplicity, it has been reported to have an impressive performance. There have been various attempts to discover more advanced and highly effective approaches especially in the other fields. Some of the methods applied in different studies include simple average, outperformance, optimal, regression and others [13]. Ref. [14] can be referred for a detailed review of literatures on the theory of combining forecasts.

The studies in wind power prediction did not usually go farther than a weighted average approach, which is just a slight modification from simple averaging as in [11] and using additional network to combine intermediate forecasts as in [4] and [7].

The motivation of this study is the thought of devising a stable, effective and accurate day-ahead prediction model through use of an aggregative approach which combines machine learning techniques. The method used in this study is based on two types of ANN (Radial Basis Network - RBN and Conventional Feedforward Network - CFFN), ANFIS and SVM. An aggregative approach which outperforms the individual models through a strategic combination of them is devised. Regression and outperformance techniques of aggregating models are tested in this paper and compared with the individual models and their simple average. The approach is tested using recorded data of an operational 2.5 MW Permanent Magnet Direct Driven (PMDD) wind turbine in Goldwind Smart Microgrid in Beijing, China.

The remainder of this paper is organized as follows. Section II summarizes some of the existing machine learning based prediction models used in short term wind power forecasting. The next section continues with discussing some of the techniques that can be used for combining an ensemble of forecasts. Though there exist a wide range of such techniques, it specifically focuses on the three approaches investigated in this paper. Section IV presents detailed description of the proposed aggregative approach for wind power prediction. The data employed for the study is also briefly explained in this section. Section V briefly introduces the metrics used to evaluate the performance of the individual models as well as the aggregative approach. The results of the study are shown and discussed in Section VI while the last section sets forth a brief conclusion.

II. MACHINE LEARNING APPROACHES IN WIND POWER PREEDICTION

Machine learning is a wide pool of techniques in programing that employ nonlinear models for learning relationship between two or more parameters or recognizing some pattern. Some of the most familiar machine learning approaches are ANN, Fuzzy systems, Wavelets and evolutionary algorithms. The use of such approaches individually or in combination with each other or others is one of the trend practices in wind power prediction application. The techniques investigated in this study are discussed shortly in this section.

A. ANN

Artificial Neural network is the most popular of the machine learning techniques employed in forecasting studies. A neural network is made of simple elements called neurons operating in parallel in a similar way that biological nervous system works. This network can be trained to learn a specific relation between its inputs and output by adjusting the weights of the connections between its elements and biases. Though this operating logic is common to all, there are different types of ANN with varying architectures and training mechanisms.

1) Conventional Feedforward Network

A Conventional Feedforward Network is one type of neural network which is composed of a series of layers with each subsequent layer connected to the previous layer. The network input is given to the first layer while the final layer produces the network's output. It is the most commonly used network for different types of input to output mapping.

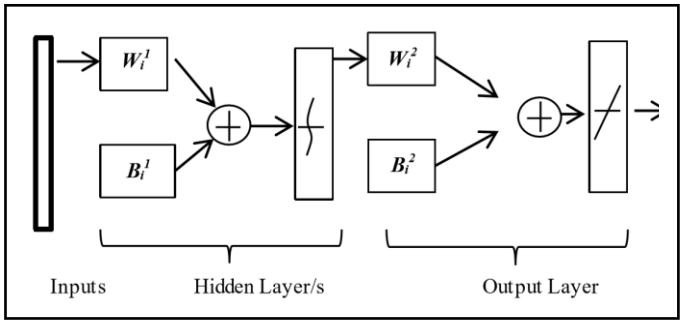


Fig. 1. Structure of Conventional Feedforward Network

The multiple layers hidden of a Feedforward network mostly made of sigmoid neurons (as it is the case in this study) allow the network to learn nonlinear relationships between input and output vectors. Networks for function fitting (or nonlinear regression) problems usually consist of linear output layer [15].

2) Radial Basis Network

Radial basis network is a type of artificial neural network which consist of two layers: a hidden radial basis layer and an output linear layer. Its activation function is a single univariate function (the radial basis function). The net input to the transfer function of the radbas neuron is the vector distance between the input vector and its weight vector multiplied by the bias.

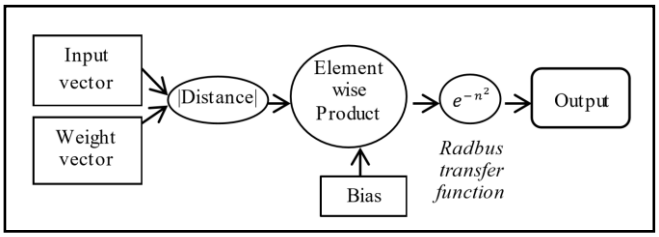


Fig. 2. Operation Principle of First Layer of Radial Basis Network

Radial basis networks are different from the conventional feed forward neural networks in that they require more neurons while they can be trained faster. They are more efficient when many training vectors are available.

B. ANFIS

ANFIS is a machine learning tool that integrates features of Neural Network with Fuzzy systems. Its architecture resembles a multilayer feed-forward network consisting of nodes and directional links. Each node performs a particular function on incoming signals and has adaptive nature so that the input-output relation can be modified by the learning rules [16]. The five layers which form the basic structure of ANFIS are described in Table I.

C. SVM

SVM is a popular machine learning tool characterized by the capacity control of the decision function and the use of kernel functions which is also why the method is considered as a nonparametric technique. SVM estimates regression using a set of linear functions by defining the regression estimation as the problem of risk minimization where the risk function is defined as a combination of the empirical error and a regularization term.

TABLE I. TABLE STYLESNODE FUNCTIONS AND DESCRIPTION OG LAYERS OF ANFIS

Layer 1	$O_{1,j} = \mu_{P_i}(x)$ (1) $O_{1,j} = \mu_{Q_{j-2}}(y)$ (2) $\mu(x) = exp\left\{-\frac{1}{2}\left(\frac{(x-c)^2}{\sigma}\right)\right\}$ (3)	maps the input parameters using membership functions.
Layer 2	$O_{2,k} = \mu_{P_k}(x) * \mu_{Q_k}(y) = w_k$ (4)	performs "AND" operation to determine the firing strength, wk.
Layer 3	$O_{3,k} = \frac{w_k}{\sum w_k} = \bar{w}_k$ (5)	perform normalization
Layer 4	$O_{4,k} = \bar{w}_k Z_k$ (6)	the node is adaptive with output
Layer 5	$O_{5,k} = \sum_{k=1}^{3} \bar{w}_k (\alpha_k + \beta_k x + \gamma_k y)$ (7)	gives weighted average of all rule outputs

Given a set of data points $G = \{(x_i, y_i)\}_i^n$ where x_i is the input vector of weather parameters record, y_i is the desired value, which in this case is the power output of the wind turbine, SVMs approximate the function as:

$$y' = f(x) = w\varphi(x) + b \tag{8}$$

Where $\varphi(x)$ is the high dimensional feature space which is nonlinearly mapped from the input space x. The coefficients w and b are estimated by minimizing the risk function consisting of the empirical error E_e and regularization term $0.5\|w\|^2$.

$$R = E_e + {}^1/_2 \|w\|^2 \tag{9}$$

Where $E_e = C\frac{1}{n}\sum_{i=1}^{n} L_\varepsilon(y_i', y_i)$ (10)

$$L_\varepsilon(y_i', y_i) = \begin{cases} |y_i' - y_i| - \varepsilon, & |y_i' - y_i| \geq \varepsilon \\ 0, & |y_i' - y_i| < \varepsilon \end{cases} \tag{11}$$

III. METHODS OF AGGREGATING ENSEMBLE OF APPROACHES

This study looks into the possibility of employing a combination of techniques in an effort to get the maximum possible forecast accuracy. The combining techniques examined in this paper are: Simple averaging, Regression and Outperformance.

A. Simple Averaging

This is the simplest method of combining where all combination members are treated impartially with equal weights. The final combination is simply an arithmetic mean of the alternative forecasts. It has been reported to be a very popular choice in many researches, especially in business forecasting [14]. One major downside of this method is its high sensitiveness to extreme values.

B. Regression

Though statistical averaging techniques such as simple average are easy to implement and interpret, the fact that they assign predefined weights to individual forecasts regardless of their relative performances is a downside. Hence, there are various other technics of linear combination which are more sophisticated and take into consideration the forecasting performance of the individual models. Regression is one of such techniques which assign optimal weights to component forecasts by minimizing the combined forecast's sum of squared errors (SSE). This way it will ensure that a model with larger forecasting error gets less weight and vice versa. In regression method of combination, the time series observations are considered to be the dependent variables while forecasts of individual models are the explanatory variables [17].

For a series to be forecasted using combinations of k forecasts fj, the solution for the problem to determine the weight vector w so as to minimize the SSE of forecasts can be written as:

$$F^T(y - Fw) = 0 \qquad \text{or} \qquad w' = (F^T F)^{-1} F^T \text{y} \tag{12}$$

where $y=(y_1,y_2, \ldots y_n)^T$ is a n x 1 vector of values of y to be forecast and $F = (f_1,f_2, \ldots , f_k)$ is an n x k matrix of forecast values. The combined forecast is:

$$y'_A=Fw'=F(F^TF)^{-1}F^Ty \quad (13)$$

and the attained minimum SSE is:

$$Q_A=(y-y'_A)^T(y-y'_A)= y^Ty-y^TFw' \quad (14)$$

This procedure is equivalent to regressing the parameter to be forecasted y against the forecasts of individual models f_1, f_2, . . ., fk while QA is simply the sum of squared residuals available in the regression.

C. Outperformance

This is a method that weights the component forecast models in proportion to their relative past performance measured in terms of a squared loss function [18]. A Bayesian probabilistic framework was adopted by Bunn [18] to decide the weight assignation in combining forecast models based on the number of times an individual model outperforms all others as measured by the absolute error in the past forecasting trials. The outperformance probability P_j (j=1, 2, … k) after n trials is calculated as:

$$P_j= \frac{O_j}{n} \quad (15)$$

where O_j … is the number of times the jth model exhibited the lowest MAE of all. This method has the advantages of being robust, nonparametric and easy to implement.

IV. The Devised Aggregative Approach

It would have been simpler and straight forward to choose a single method which consistently performs best if such a model exists. However, it is often the case that different models perform differently for different inputs. There is also the challenge of selecting optimal learning parameters in the application of those soft computing techniques. The selection is usually made relying on human experience and repeated trial and errors while the parameters are highly influential in deciding the forecasting accuracy. Therefore, a composite forecast model that combines individual forecasts is devised. This aggregative approach of forecasting is shown in Fig. 3.

The methodology employs forecasts of weather parameters (wind speed and air density) to predict the hourly power output from a wind turbine. The wind turbine upon which the recommended approach in this study was tested and compared is a 2.5 MW PMDD turbine operating in the Goldwind smart microgrid in Beijing, China.

The first stage involves training four types of soft computing models for prediction of the output power of a wind turbine based on the forecasted wind speed and air density and the power output of the turbine during the previous hour. Not necessarily all inputs are used for each model though. The decision on which inputs to use for which model was rather made by repeated trials depending on the relative performance and suitability of each model for lower or larger size of input variables. After the best individual performance was achieved by each scheme, the next procedure was combining them in such a way that a more accurate and stable forecast can be achieved. Three techniques of combining forecasts were tested in this study and their performance is evaluated relative to each other and the individual models.

The historical records of weather data for the period of 4/21/2015 - 4/19/2017 from a numerical weather prediction model called Weather Research and Forecasting (WRF) and power output of the wind turbine for the same period from the aforementioned microgrid's SCADA were utilized for training and testing the individual models and their combination. Half of the data was used to train the individual forecast models and evaluate the weights for their combination in the in the later stage of combining the forecasts. The other half was divided into three sections for testing the effectiveness of the devised approach. The seasonal variation in wind speed does not seem to be consistent. Hence, it is decided to intentionally pick a less windy week of July and a windy week of May to test the performance of the approach in both extreme scenarios.

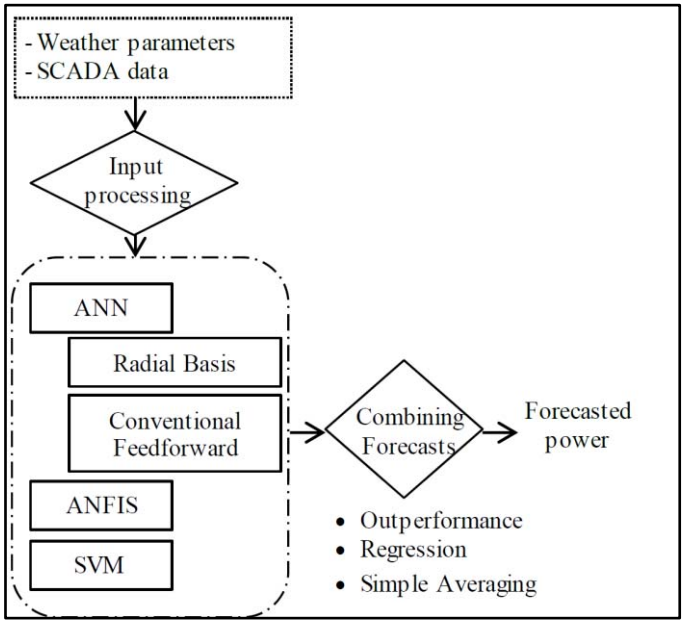


Fig. 3. Devised Aggregative Approach

V. Performance Metrics

The prediction performance of the individual forecast models as well as the devised aggregative approach is evaluated and compared with each other using the statistical metrics: Mean Absolute Error (MAE) and Normalized Mean Squared Error (NMSE).

For a predicted variable y of n data points and its corresponding forecast f, MAE and NMSE are defined by (16) and (17).

$$MAE= \frac{1}{n} \sum_{i=1}^{n} |y_i-f_i| \quad (16)$$

$$NMSE = \frac{1}{\delta^2 n} \sum_{i=1}^{n} (y_i - f_i)^2 \times 100\% \quad (17)$$

$$\delta^2 = \frac{1}{n-1} \sum_{i=1}^{n} (y_i - \bar{y})^2 \quad (18)$$

Both NMSE and MAE measure how much the forecasts deviate from the actual measurements. NMSE gives a more general picture of the accuracy of the forecast as it is a scale-free entity.

VI. Results and Discussion

This paper has addresses the issue of stable performance and accuracy in wind turbine output power prediction models. In the first stage of the study two types of ANN, SVM and ANFIS techniques were utilized. During the initial stages of developing the best individual models, it was observed that the effectiveness of the SVM and Radial Basis network declines as the size of the input parameter increases. A special observation was the significantly lower performance of radial basis network when the 'power output of the previous hour' was added to the input matrix suggesting lower effectiveness of the approach in time series forecasting. SVM regression was also seen to deteriorate in terms of prediction accuracy when more input parameters than wind speed are considered. Hence, a decision was made to use only wind speed for the SVM model and avoid the 'power output of the previous hour' for the radial basis NN.

TABLE II. Performance Measurement of Forecasts

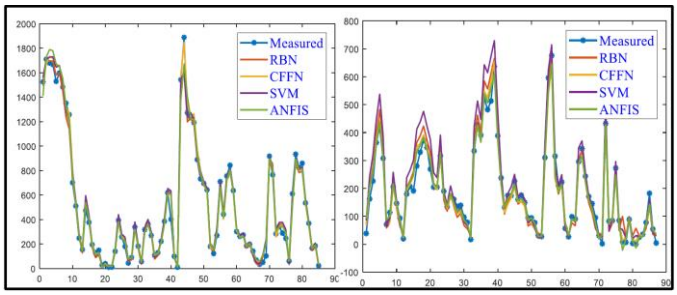
Method	Test year		Less Windy Test Week		Windy Test Week	
	MAE	*NMSE (%)*	*MAE*	*NMSE (%)*	*MAE*	*NMSE (%)*
RBN	40.25	2.53	28.53	5.16	33.84	1.10
CFFN	34.53	1.65	23.72	3.49	31.41	0.98
SVM	43.59	3.17	38.82	12.29	37.32	1.34
ANFIS	32.97	1.65	21.94	3.41	35.86	1.29
Simple Averaging	32.97	1.58	22.69	3.45	30.96	0.93
Outperformance	31.55	1.46	21.58	3.38	30.85	0.91
Regression	28.31	1.03	17.19	2.19	30.86	0.90

The individual models are compared with each other and their combinations as shown in Table II. The performance of the models does not seem to follow a common trend as they are applied for different seasons. ANFIS showed the best performance in all cases compared to the other individual models. The Conventional Feedforward Network which appeared to performer reasonably well being the second best while verified with the test year data.

The combination techniques of simple averaging, regression and outperformance were also tested. While the simple averaging technique assumes identical weights, the other two approaches assign weights based on performance based analysis as shown in (19) and (20). The weights given to the component forecasts somehow reflect the relative individual performance discussed earlier.

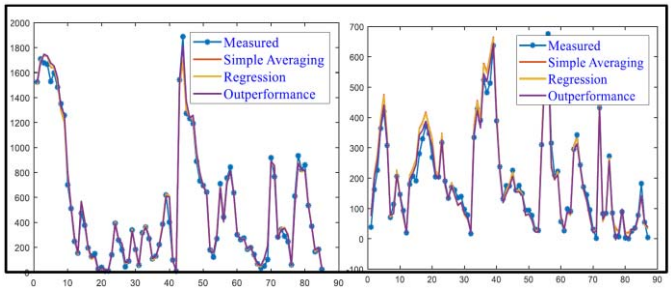
$$F_{outper} = 0.199F_{RB} + 0.301F_{CFF} + 0.22F_{SVM} + 0.28F_{ANF} \quad (19)$$

$$R_{Regress} = -0.108F_{RB} + 0.814F_{CFF} + 0.031F_{SVM} + 0.261F_{ANF} \quad (20)$$



a) Windy test week *b) Less windy test week*

Fig. 4. Forecasts by Individual Machine Learning Models



a) Windy test week *b) Less windy test week*

Fig. 5. Combination of Forecasts

The regression technique resulted in the best accuracy of all with a very slim 1.03% NMSE and MAE of 28.31. The approach showed a great deal of stability being the best performer under the test year and both extreme cases. Simple averaging has also shown an acceptable performance bettering the individual models in most cases. Though this method is most utilized and popular for its simplicity, its major downside is that it does not consider the relative performances of the individual models and is mainly suitable when the component forecasts have comparable accuracies.

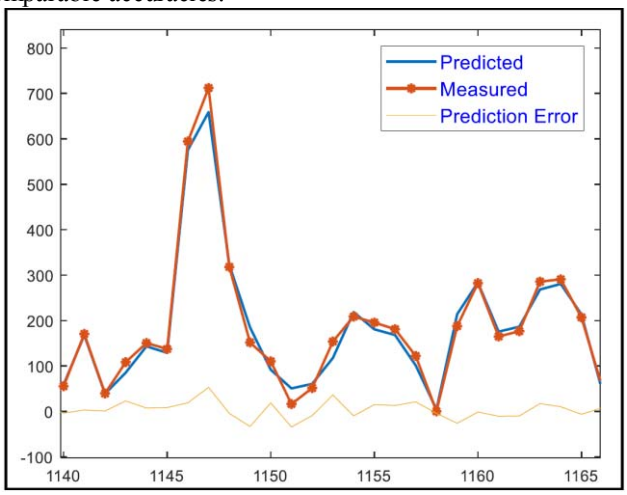


Fig. 6. The best performing Regression Combination model for a random day

VII. CONCLUSIONS

In this study the use of soft computing approaches in predicting the power output from a wind turbine was investigated and a strategic approach of combining the forecasts from individual models was devised.

The regression method of combining forecasts showed the best performance by outperforming the other combining options as well as the best performing individual model. The aggregative approach exhibited not only better accuracy under specific conditions but also showed stable performances under extreme cases of windy and less windy periods.

Though the individual models performed with a satisfactory forecast performance, the addition of the combining step resolved the difficulty to identify a single best forecast model. The aggregative approach alleviated issues of state-dependent performance of individual models and their systematic errors.

REFERENCES

[1] W. P. Mahoney et al., "A Wind Power Forecasting System to Optimize Grid Integration," in IEEE Transactions on Sustainable Energy, vol. 3, no. 4, pp. 670-682, Oct. 2012. doi: 10.1109/TSTE.2012.2201758

[2] Ali N. Celik, Mohan Kolhe, Generalized feed-forward based method for wind energy prediction, In Applied Energy, Volume 101, 2013, Pages 582-588, ISSN 0306-2619, https://doi.org/10.1016/j.apenergy.2012.06.040

[3] Shetty, Rashmi & Alangar, Sathyabhama & Pai, P & Rai, Adarsh. (2016). Optimized Radial Basis Function Neural Network model for wind power prediction. 1-6. 10.1109/CCIP.2016.7802846

[4] S. Buhan and I. Çadırcı, "Multistage Wind-Electric Power Forecast by Using a Combination of Advanced Statistical Methods," in IEEE Transactions on Industrial Informatics, vol. 11, no. 5, pp. 1231-1242, Oct. 2015. doi: 10.1109/TII.2015.2431642

[5] A. T. Eseye, J. Zhang, D. Zheng, H. Ma and G. Jingfu, "Short-term wind power forecasting using a double-stage hierarchical hybrid GA-ANN approach," *2017 IEEE 2nd International Conference on Big Data Analysis (ICBDA)*, Beijing, 2017, pp. 552-556. doi: 10.1109/ICBDA.2017.8078695

[6] J. Zeng and W. Qiao, "Short-Term Wind Power Prediction Using a Wavelet Support Vector Machine," in IEEE Transactions on Sustainable Energy, vol. 3, no. 2, pp. 255-264, April 2012. doi: 10.1109/TSTE.2011.2180029

[7] Y. Liu, J. Shi, Y. Yang and W. J. Lee, "Short-Term Wind-Power Prediction Based on Wavelet Transform–Support Vector Machine and Statistic-Characteristics Analysis," in IEEE Transactions on Industry Applications, vol. 48, no. 4, pp. 1136-1141, July-Aug. 2012. doi: 10.1109/TIA.2012.2199449

[8] Y. Kassa, J. H. Zhang, D. H. Zheng and Dan Wei, "Short term wind power prediction using ANFIS," 2016 IEEE International Conference on Power and Renewable Energy (ICPRE), Shanghai, 2016, pp. 388-393. doi: 10.1109/ICPRE.2016.7871238

[9] M. B. Ozkan and P. Karagoz, "A Novel Wind Power Forecast Model: Statistical Hybrid Wind Power Forecast Technique (SHWIP)," in IEEE Transactions on Industrial Informatics, vol. 11, no. 2, pp. 375-387, April 2015. doi: 10.1109/TII.2015.2396011

[10] Benito E. FloresEdna M. White, "A framework for the combination of forecasts," Journal of the Academy of Marketing Science, September 1988, Volume 16, Issue 3 –4, pp 95–103 doi: https://doi.org/10.1007/BF02723365

[11] S. Lu et al., "Machine learning based multi-physical-model blending for enhancing renewable energy forecast – improvement via situation dependent error correction," 2015 European Control Conference (ECC), Linz, 2015, pp. 283 -290. doi: 10.1109/ECC.2015.7330558

[12] D. Chen, P. Li, X. Li, C. Xu, Y. Xiao and B. Lei, "Short –term wind speed forecasting considering heteroscedasticity," 2011 International Conference on Advanced Power System Automation and Protection, Beijing, 2011, pp. 884 -888. doi: 10.1109/APAP.2011.6180720

[13] Lilian M de Menezes, Derek W. Bunn, James W Taylor, Review of guidelines for the use of combined forecasts, In European Journal of Operational Research, Volume 120, Issue 1, 2000, Pages 190-204, ISSN 0377-2217, https://doi.org/10.1016/S0377-2217(98)00380-4.

[14] T. Clemen, Robert. (1989). Combining forecasts: A review and annotated bibliography. International Journal of Forecasting. 5. 559-583. 10.1016/0169-2070(89)90012-5.

[15] Mark Beale, Martin T. Hagan, Howard Demuth, "Neural Network Toolbox: For Use with MAT LAB", The MathWorks, Inc.3 Apple Hill Drive Natick, MA 01760 -2098, Sep 2012

[16] Salman Zaferanlouei, Dariush Rostamifard, Saeed Setayeshi, Prediction of critical heat flux using ANFIS, In Annals of Nuclear Energy, Volume 37, Issue 6, 2010, Pages 813-821, ISSN 0306-4549, https://doi.org/10.1016/j.anucene.2010.02.019 .

[17] W. J. Granger, Clive & Ramanathan, Ramu. (1984). Improved Methods of Combining Forecasts. Journal of Forecasting. 3. 197 - 204. 10.1002/for.3980030207.

[18] W. Bunn, D. (1975). A Bayesian Approach to the Linear Combination of Forecasts. Operational Research Quarterly (1970-1977). 26. 10.1057/jors.1975.67.

Available online at www.sciencedirect.com

ScienceDirect

Materials Today: Proceedings 5 (2018) 6090–6097

materialstoday: PROCEEDINGS

www.materialstoday.com/proceedings

ICMPC 2017

An Experimental Study and Analysis of the Mechanical Properties of Titanium Dioxide Reinforced Aluminum (AA 5051) Composite

Surabhi Lata[a,*], Ankur Pandey[b], Labhansh[b], Ankit Sharma[b], Kuldeep Meena[b], Ramakant Rana[c], Roop Lal[d]

[a,b] *Maharaja Agrasen Institute of Technology,Rohini, Delhi-110085, India*
[c,d] *Delhi Technological University, Delhi-110042, India*

Abstract

The research work investigates the mechanical properties of aluminium reinforced with titanium dioxide particles which is fabricated through casting process. A comparative study has been conducted by varying the percentage of the reinforcement in the base metal matrix. The composite was casted and the samples were prepared, by simple turning and milling processes, for performing various mechanical tests. The reinforcement i.e. titanium dioxide weight percent of 5 %, 10 % and 15 % resulted in increasing ultimate tensile strength, impact strength, average hardness and density with increasing concentration of titanium dioxide particles, while the compressive strength decreases with increase in the concentration of titanium dioxide reinforcement. Hence, it can be concluded that as the percentage of titanium dioxide increases the properties show enhancement due to the development of strong bonding between the particles of reinforcement and the base matrix and also due to the wettability property of the reinforcement in the base metal matrix.
© 2017 Elsevier Ltd. All rights reserved.
Selection and/or Peer-review under responsibility of 7th International Conference of Materials Processing and Characterization.

Keywords: Titanium dioxide particle; metal matrix composite; reinforcement; aluminium; mechanical property

1. Introduction

Composites are materials consisting of at least two constituents bonded together along the interface in the composite, each originating from a separate ingredient material which pre-exists the composite. Metal matrix composites (MMCs) are materials in which one constituent is a metal or alloy forming at least one percolating

* Corresponding author. Tel.: +91 9210055994.
E-mail address: surabhilata.delhi@gmail.com

2214-7853© 2017 Elsevier Ltd. All rights reserved.
Selection and/or Peer-review under responsibility of 7th International Conference of Materials Processing and Characterization.

Nomenclature

AMC	Amuminium matrix composite
KN	Kilo-Newton
MMC	Metal matrix composite

network. The other constituent is embedded in this metal matrix and usually serves as reinforcement [1].Aluminium metal matrix composites (Al MMCs) are being considered as a group of new advanced materials for its light weight, high strength, high specific modulus, low co-efficient of thermal expansion and good wear resistance properties. The primary function of the reinforcement in metal matrix composites is to carry most of the applied load, where the matrix binds the reinforcements together, and transmits and distributes the external loads to the individual reinforcement. Metal–matrix composites (MMCs) are most promising materials in achieving enhanced mechanical properties such as: hardness, Young's modulus, yield strength and ultimate tensile strength due to the presence of micro-sized reinforcement particles into the matrix [2]. Most research works on Al based matrix composites found in literature have been based on the 2XXX and 6XXX series. The 6XXX series of Al-Mg- Si alloys are widely used as medium strength structural alloys which have the advantages of good weldability, corrosion resistance, and immunity to stress corrosion cracking .However, very little has been reported on the use of Al (6063) alloy as metal matrix [3]. Common matrix materials are aluminium, magnesium and titanium while the typical reinforcing ceramics are SiC, B_4C, Al_2O_3, TiC, WC and ZrO_2 either in a continuous, discontinuous or particulate form**.** Hybrid aluminium matrix composites are used for high performance "ceramic" brake disks as it can withstand extreme temperatures [3].

Metal matrix Composites have proved to be an important class of materials, with the potential to replace a number of conventional materials being used in automotive, aerospace, defence and leisure industries, where the demand for lightweight &higher strength is increasing day by day [4]. Furthermore Aluminum Metal Matrix Composites are mostly used for producing porous parts like bearings because of its porous structure and it is suitable to serve as self-lubricated bearings [5].Behaviours of TiO_2 in the alumina carbothermic reduction and chlorination process in vacuum at different temperatures were investigated experimentally by means of XRD, SEM and EDS. In the preparation of materials, the molar ratio of Al_2O_3 to C was 1:4, and 10% TiO_2 and excess $AlCl_3$ were added. The results show that TiC is produced by the reaction between C and TiO_2 after which TiO_2 transforms from anatase into rutile gradually. The purity of aluminum reaches 98.35%, and TiO_2 does not participate in alumina carbothermic reduction process and chlorination process in vacuum [6]. The stir casting process and high pressure die casting technique was employed for the fabrication of AA6061/titanium oxide metal matrix composites by varying the titanium oxide (TiO_2) volume fractions of 10%, 20% and 30%. Two unit cell models consisting of circular TiO_2 nanoparticles modelled to obtain composites with and without clustering and porosity using finite element methods. Several techniques have been used to quantify clustering of particles in a composite [7]. The aluminum 2024/ TiO_2 metal matrix composite is prepared by stir casting method by varying the amount of TiO_2 particles. The different experiments are carried out on the fabricated aluminum 2024/ TiO_2 metal matrix composite as per ASTM standard. The experimental results showed that on increasing the TiO_2 content in the aluminum metal matrix composite results in increase in tensile strength, hardness and Impact strength of the composite. The uniform distribution of TiO_2 particles and strong bonding with aluminum matrix are the causes for increase in tensile strength, hardness and Impact strength of the material [8].The ultimate tensile strength of the AMCs is enhanced with increased weight percentage of TiO_2 particles content in the AA6082 matrix. The higher variation in the coefficient of thermal expansion develops a mismatch between AA6082 aluminum alloy and titanium oxide which encourages more amount of dislocation in the composites. At higher dislocation density, dislocations interact with each other which ultimately develop the strength of the fabricated composite materials. If the bonding between the AA6082 matrix and the TiO_2 reinforcement is instead solid enough, the ultimate tensile strength of the produced composite can be greater than that of the matrix materials. The gradual development in ultimate tensile strength of the produced composite reveals that the stresses are effectively shifted through interface [9].The effect of titanium dioxide content on the compressive strength of the composites is analyzed as TiO_2 content is increased from 0 to 6 per cent, the compressive strength increases monotonically by about 22 per cent.The toughness (as quantified by the impact

strength) of the composite decreases monotonically by about 35 per cent as the content of the titanium dioxide in the composite is increased from 0 to 6 per cent. These effects of the titanium dioxide particles are also believed to be mechanical in nature, formed under the influence of tensile loads probably undergoing limited growth, leading to the failure of the composite matrix. Researchers studying deformation and failure mechanisms of the composites have observed that they fail by the progressive fracture of the reinforcing particles present in the microstructure, and the final fracture of the composite results from the crack propagation through the matrix material between the particles [10]. As the wt-% of reinforcement increases, there is an increase in hardness value of the material from base alloy, due to presence of Al_2O_3 and SiC. It can also be identified that Al_2O_3 and SiC particles have higher hardness than LM25 alloy. The matrix deforms plastically to accommodate the volume expansion due to incorporation of hard reinforcement particles. With increasing reinforcement content, the dislocation density increases further, causing the hardness values to increase [11]. The addition of 2.5 weight percentage of TiO_2 increases the hardness while addition of 4 weight percentage of graphite to the Al+2.5%TiO_2 composite decreases the hardness. The formability stress index increases with the addition of 2.5 weight percentage of TiO_2 and 2 and 4 weight percentage of Gr reinforcements in pure Al matrix during cold upsetting[12].

2. Experimental Details

The series of aluminum selected as base matrix is AA 5051 while titanium dioxide (TiO_2) with particulate size of 0.2-0.3 microns in diameter as reinforcement. TiO_2 was considered in 5%, 10%, and 15% on mass fraction as reinforcing material in the base matrix.

2.1. Fabrication of aluminum based composite

The fabrication of aluminium metal matrix composite is carried out by casting process. AA5051 alloy ingots were melted in a crucible kept in electric resistance furnace at 1200˚C.The crucible was then taken out and the calculated amount of the preheated reinforcement particles of TiO_2 was added slowly into the melt. The mixture was manually stirred for about 8-10minutes. Further, the mixed melt was poured into the sand mould of 22mm diameter and 300mm length (for tensile and compressive specimen) and 15mm size square cross section and 300mm length (for charpy and izod specimen) respectively. The molten metal was then allowed to solidify and later the casting was removed from the mould.

2.2. Preparation of Test Specimen

The casted composites were cut into pieces of required dimension which were then taken for machining operations to prepare the final specimens for the tensile, compressive, izod, charpy and brinell hardness tests. A minimum of three specimens were prepared to conduct three runs of following tests:

1. Tensile Test Specimen
2. Compressive Test Specimen
3. Charpy Test Specimen
4. Izod Test Specimen
5. Brinell Hardness Test

2.2.1. Tensile Test Specimen

The procedure initiated with the sectioning of cylindrical shaped piece (D=22 mm, L=260 mm) from the casted composite. The final dimensions were obtained as 250 mm length and 16 mm diameter through simple facing and turning operations. Further, the gauge length of 50 mm was generated with the diameter dimension as 9 mm. Lastly, taper turning operation was performed to produce the final desired shape as shown in the Fig. 1.

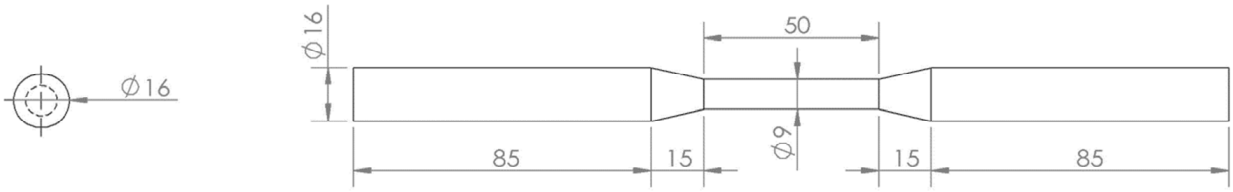


Fig. 1. Dimension of Tensile Test Specimen.

2.2.2. Compressive Test Specimen

The cylindrical shaped piece (D=22mm, L=30mm) from the casted composite was sectioned and was turned and faced to obtain the final dimension as 25 mm length and 15 mm diameter as shown Fig 2.



Fig. 2. Dimension of Compression Test Specimen.

2.2.3. Charpy Test Specimen

The square cross-sectioned casted composite was sectioned whose initial dimension was A=15*15 mm^2 and L=60mm. With the help of milling operation the workpiece was reduced to 10*10 mm^2 and length as 55 mm with the sawing operation. The required V-notch was created using sawing and filing processes as shown in below Fig 3.

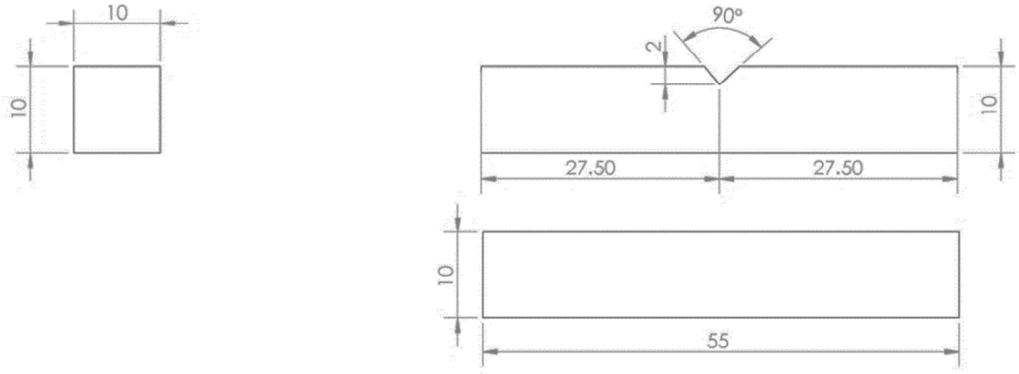


Fig. 3. Dimension of Charpy Test Specimen

2.2.4. Izod Test Specimen

The square cross-sectioned casted composite was sectioned whose initial dimension was A=15*15 mm^2 and L=80 mm. Similar to Charpy test specimen, Izod test specimen was also prepared with the help of milling operation. The workpiece was reduced to 10*10 mm^2 and length to 55 mm with the sawing operation. The required V-notch was made with the help of sawing and filing processes as shown in below Fig 4 and Fig 5 and Table 1, Table 2.

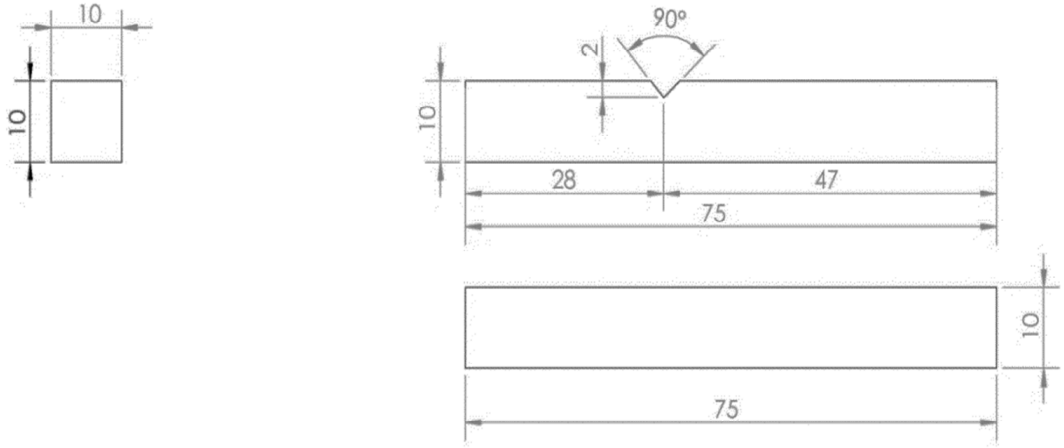


Fig. 4. Dimension of Izod Test Specimen

3. Result and Discussion

3.1.1. Tensile test

Table 1: 5% Composition of TiO2 in aluminium (Cross-sectional area of specimen=66.47 mm^2)

Load(KN)5%	Gauge length (mm)	Engg. Stress (MPa)	Engg. Strain
0	50	0	0
7.84	51	117.6	1
9.81	52	147.14	2
10.60	53	159.00	3
11.77	54	176.54	4
14.12	55	211.78	5
16.08	56	241.18	6
19.62	57	294.28	7
21.58	58	323.68	8
21.97	59	329.53	9

Table 2: 10% Composition of TiO2 in aluminium (Cross-sectional area of specimen Area=65.99 mm^2)

Load(KN)10%	Gauge length (mm)	Engg. Stress (MPa)	Engg. Strain
0	50	0	0
2	51	30.34	1
4.4	52	66.76	2
5.5	53	83.45	3
11.78	54	178.75	4
12.17	55	184.67	5

Table 3. 15% Composition of TiO2 in aluminium (Cross-sectional area of specimen Area=60.95 mm^2)

Load(KN)15%	Gauge length (mm)	Engg. Stress (MPa)	Engg. Strain
0	50	0	0
8.24	51	135.19	1
10.20	52	167.35	2
12.55	53	205.90	3
14.51	54	238.06	4
16.48	55	270.38	5
21.97	56	360.45	6
27.46	57	450.53	7

The tensile tests were performed in three runs for all the three compositions of aluminium matrix composites. For the same stress-strain curves were generated which defined mearly linear curve beyond which the specimens experienced fracture. As the load is increased the stress and strain increases at a gradual rate. It is observed that the tensile strength of composite increases with increase in concentration of TiO2 upto 5% followed by decrease in strength upto 10% and beyond 10% the strength keeps on increasing till its ultimate failure.

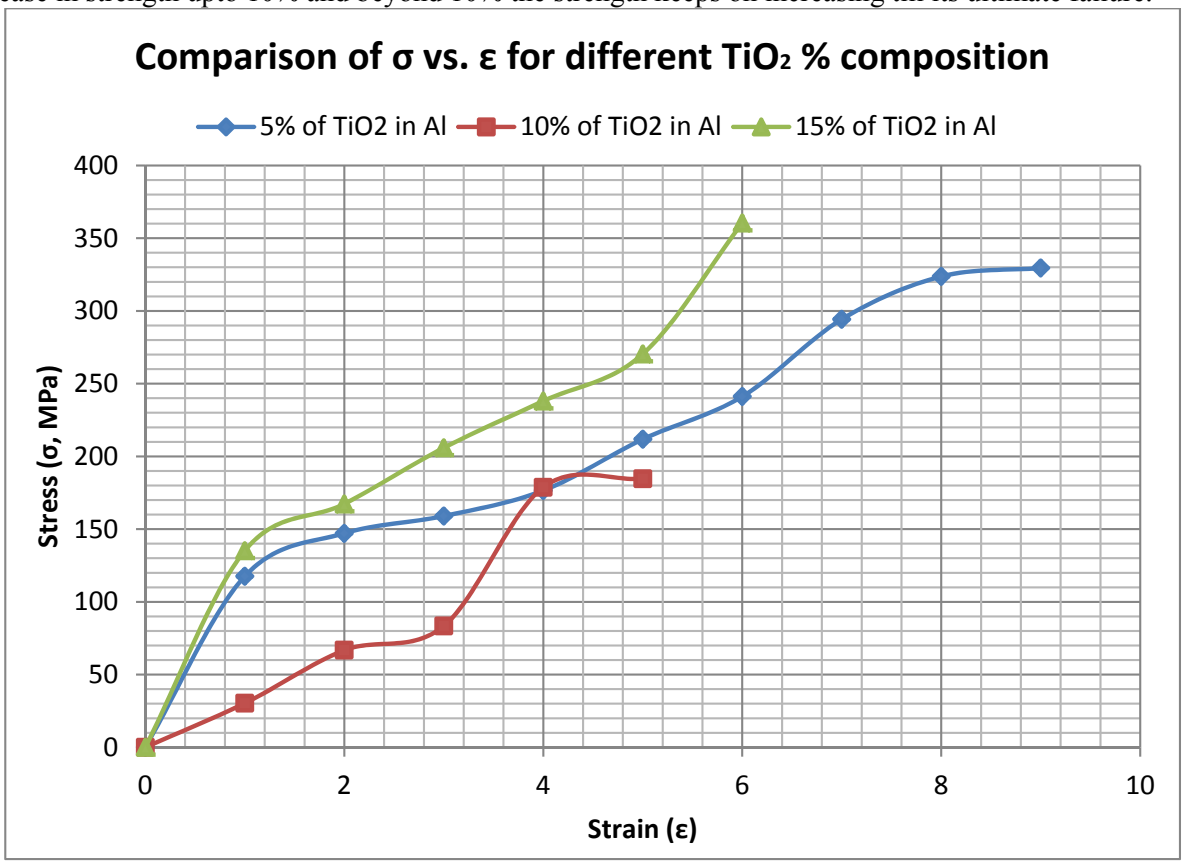


Fig. 5. Stress-Strain Curve for Aluminium Composite with 5%. 10%, & 15% TiO_2

3.1.2. Compression test

Table 4: Compression Test (5%, 10% &15%) of TiO2 in Aluminium

TiO_2 Percentage (%)	Load (KN)	Reduction in length of work piece
5%	176.58	15mm
10%	176.58	11mm
15%	176.58	10mm

3.1.3. Charpy test and Izod test

Table 5: Charpy & Izod Test (5%, 10% &15%) of TiO2 in Aluminium.

TiO_2 Percentage (%)	Charpy Test	Izod Test
	Required energy for fracture (Joule)	Required energy for fracture (Joule)
5%	24	0
10%	50	2
15%	112	4

Among all the three variations of the aluminium matrix composites, it was observed that compressive strength decreases with increase in the concentration of TiO_2 reinforcement. This is due to the brittle nature imparted by the reinforcement to the base matrix. The impact strength increases with the increase in concentration of TiO_2 in the base matrix. This happens due to the uniform distribution of the reinforcement in the metal matrix ad the strong bonding of the TiO_2 particles with aluminium acting as matrix as shown in above Table 3 , Table 4 and Table 5.

3.1.4. Brinell hardness test

Table 6: Brinell Hardness Test (5%, 10% &15%) of TiO_2 in Aluminium.

TiO_2 Percentage (%)	Hardness(kg/mm^2)
5%	42.20
10%	83.11
15%	70.64

It is observed that the hardness of the composite initially increases but later decreases with increase in concentration of TiO_2beyond 10%. This is due to the amalgamation of reinforcement particles and decreased wettability in the base matrix shown in Above Table 6.

4. Conclusion

Every engineering field is treading the path of technology in search of new smart materials possessing the best of all properties needed by the today's manufacturing world. This paper conducted a research in fabricating an aluminium based composite where AA 5051 was used as matrix alloy and titanium dioxide (TiO_2) was the reinforcing material. Three compositions were made with three different percentages of TiO_2 particles viz. 5%, 10% and 15%. The composite was successfully manufactured through casting technique. The investigation after the number of tests conducted concluded that the strength and hardness of the composite increases with the introduction of reinforcement i.e. TiO_2 in comparison to the pure base matrix. The tests also revealed that there exist an optimized percentage of reinforcement which enhances mechanical properties. This is the percentage beyond which the properties showa decrease in their values. The optimized percentage of the reinforcement i.e. TiO2 in the AA 5051 base matrix has been inferred as 15%. This composite can effectively serve as the promising material for the automobile, manufacturing, architectural buildings and aerospace industries.

References

[1] Roussos G. Papagiannakis, Fabrication of hybrid (Al+Tio2+Gr) metal matrix composites- An Experimental Study; Vol. 37, No. 2, 33 - 36, 2014.

[2] Ganesh Raja, Daniel Lawrence, Jayabal, and Rajmohan;Prediction of mechanical characteristics on aluminium based reinforcement with SiC and TiO_2; International Journal of Applied Engineering Research, ISSN 0973-4562 Vol. 10 No.51 (2015).

[3] Swamy and Chandru; Characterization of Aluminum Alloy Particulate Reinforced Metal Matrix Composite; International journal of Advances in Scientific Research and Engineering, Volume.1 Issue.1 July 2015.

[4] K. K. Alaneme and M. O. Bodunrin;Corrosion Behavior of Alumina Reinforced Aluminium (6063) Metal Matrix Composites;Journal of Minerals & Materials *Characterization & Engineering*, Vol. 10, No.12, pp.1153-1165, 2011.

[5] Manickam Ravichandrana, Abdullah Naveen Saita, Veeramani Anandakrishnanb*;*Study on Mechanical Properties of Hot Extruded Al (Mg)-TiO_2 Composites DOI: http://dx.doi.org/10.1590/1516-1439.258713*Materials Research*. 2014; 17(6): 1489-1496.

[6] M.Ravichandran and S.Dineshkumar; Synthesis of Al-TiO_2 Composites through Liquid Powder Metallurgy Route; SSRG International Journal of Mechanical Engineering (SSRG-IJME), Volume 1 Issue 1, Feb 2014.

[7] A. Chennakesava Reddy; Effect of Clustering Induced Porosity on Micromechanical Properties of AA6061/Titanium Oxide Particulate Metal matrix Composites;Materials and Characterization.

[8] Siddesha S., T. D. Jagannath, Punith T. R., Punith T. R.;Effects of Fabrication of Aluminium 2024/ TiO_2 Metal Matrix Composite; International Journal of Innovative Research & Development; ISSN 2278 – 0211.

[9] K. Yoganandam, K. Raja and K. Lingadurai;Mechanical and Micro Structural Characterization of Al6082-TiO_2 Metal Matrix Composites produced via Compo Casting Method; DOI:10.17485/ijst/2016/v9i41/101975, November 2016, ISSN (Print): 0974-6846ISSN (Online) : 0974-5645.

An FPGA based floating point Gauss-Seidel iterative solver

Ramakant Joshi, Aman Raghuvanshi, Yatin Gilhotra*,
Shivani Sharma, Suyash Sharma, Preyesh Dalmia, Neeta Pandeyˆ
Dept. of Electronics and Communication Engineering
Delhi Technological University
New Delhi, India
Email: yatingilhotra_2k14@dtu.ac.in*,
neetapandey@dce.ac.inˆ

***Abstract*—In this paper, an FPGA-based single precision floating point hybrid iterative architecture for solving a linear system of equations is proposed. The novel architecture implements Gauss-Seidel method using a Jacobi method based building block. The design takes advantage of the fast convergence of Gauss-Seidel Method conflated with parallel, pipelined architecture of Jacobi Iterative solver resulting in a much efficient architecture with acceptable hardware augmentation. The whole design has been implemented in Verilog HDL, having Virtex 7 XCV2000T as targeted device. Other design optimizations include using modified high-speed radix 4 multiplier and optimized high-speed 2's complementer. The efficacy of the design is tested and implemented in solving nonsingular, exactly determined and strictly diagonally dominant coefficient matrix based dense and sparse linear system of equations with different number of variables. The design results in reduced number of iterations and equivalent speedups are presented, which are calculated factoring in, the increased delay effects.**

***Index Terms*—Jacobi method; Gauss-Seidel method; diagonally dominant matrix; direct methods; iterative methods.**

I. Introduction

Partial Differential Equations (PDEs) possess radical importance in defining and modeling physical phenomenon. Complex problems from a multitude of domains such as electrical and mechanical engineering, materials science, fluid dynamics, quantum mechanics, etc, all converge down to solving different types of PDEs. They can be discretized and linearized into an approximate system of equations with a finite number of unknowns that can be computed and processed. This system of equation can be represented by the vector equation

$$Ax = B \tag{1}$$

where A and B are known coefficient matrices and x is an unknown vector.

Other than PDEs, many scientific models and problems such as network modeling, assignment problems[11], etc. can be disintegrated into a problem of solving linear system of equations. Though, mathematically trivial, computing this kind of system can prove to be severely complex. Hence, solving this crucial form of system has been a topic of research for the whole past century. The classical methods which can solve this linear system of equations can be broadly classified into two categories, namely direct and iterative methods. Direct methods such as Gaussian Elimination method are the traditional methods for solving sparse linear systems but these methods compromise with the accuracy of the solutions in the form of round-off errors[1], which propagate through a number of arithmetic operations to give inaccurate results and they use prohibitively large storage[12]. Hence, in order to solve systems with higher dimensions, iterative methods were introduced, which tend to be computationally less expensive because of their repeating nature.

Jacobi and Gauss-Seidel iterative methods are two of the most prominent methods used in solving linear systems of equations of the form $Ax = B$ and are used in many specific implementations[5],[11],[13],[15],[16]. Now, one of the major concerns with using iterative methods is their speed of finding accurate solutions which can be measured by their convergence rate. Convergence rate is a highly sensitive issue because these solvers are used in high-speed scientific computing and massively parallel computing architectures. Other than being stand-alone solvers, these classic iterative methods, these days, are also used as preconditioners, conflated with more sophisticated methods such as Krylov Subspace accelerator techniques[2]-[5] or Multigrid methods to create a multilevel solving system. Using multilevel solving systems may drastically increase the speed of finding the solution.

Preconditioning aims at bringing an implicit or explicit modification to the ill-conditioned, original linear system for sophisticated solvers creating a multilevel procedure. Preconditioners can be considered as subsidiary approximate solvers, whose outputs, when worked upon by outer iterative solvers, give enhanced accuracy of the solutions and facilitate the fast convergence.

Talking about these two classical iterative methods, Gauss-Seidel method usually converges much faster than the Jacobi method[14]. The reason lies in the fact that the Gauss-Seidel method uses the newly computed approximation

of a solution component as soon as it is available. However, as a consequence, the Gauss-Seidel method is inherently sequential, and does not possess natural parallelism[13]. The architectural implementation of the Gauss-Seidel method designed to exhibit parallelism would take prohibitively large area and high computation cost. In this paper we explore a novel hardware implementation of the Gauss Seidel method, which uses Jacobi architecture[7] with some hardware augmentation and propose a new hybrid architecture, which conflates the advantages of the two, i.e. the parallelism of the Jacobi and the convergence rate of Gauss Seidel method.

The rest of the paper is organized as follows. The fundamentals and functioning of the two iterative methods are discussed in Section II. The proposed architecture is a consequence of a mathematical manipulation discussed under Section III. In this paper, the Gauss Seidel method is implemented for equation set with a maximum size of 5×5. The hardware design and various blocks are discussed in section IV. The critical path delay and the speed up of the proposed architecture with respect to Jacobi is discussed in Section V and the overall results are shown. Finally, the paper is concluded in Section VI and references are presented.

II. Method Analysis

The fundamental idea behind iterative methods is to produce a sequence of approximate solutions $x^{(\delta)}$ that refine themselves with each iteration to finally converge to the actual value.

$$x = \lim_{\delta \to \infty} x^{(\delta)} \tag{2}$$

This equation represents the concept of convergence, where x is the exact solution and $x^{(\delta)}$ is the approximate solution after δ number of iterations. Theoretically, it takes infinite iterations to reach the exact solution, but practically, the solution is obtained when it reaches a certain region of tolerance. The iterative process is terminated such that $\left\|x^{(\delta)} - x\right\| \leq \epsilon$, at the minimum value of δ , where $\|.\|$ is the vector norm and ϵ is the tolerance. Jacobi and Gauss-Seidel Iterative methods both have their own advantages. In this section, we discuss these two methods and study their convergence analysis. The analysis and proposed design is specifically presented for nonsingular, exactly determined and strictly diagonally dominant coefficient matrices.

A. Jacobi Method

Let us represent the equation (1) in the matrix form as,

$$\begin{pmatrix} a_{11} & a_{12} & \dots & a_{1n} \\ a_{21} & a_{22} & \dots & a_{2n} \\ \vdots & \vdots & \ddots & \vdots \\ a_{n1} & a_{n2} & \dots & a_{nn} \end{pmatrix} \times \begin{pmatrix} x_1 \\ x_2 \\ \vdots \\ x_n \end{pmatrix} = \begin{pmatrix} b_1 \\ b_2 \\ \vdots \\ b_n \end{pmatrix} \tag{3}$$

Where A, the coefficient matrix, with coefficients represented as a_{ij}, B, the constant matrix with coefficients represented as b_i, x be the variable vector with unknowns represented as x_i. If $B = 0$, the system is called homogeneous system, else it is called heterogeneous system. Jacobi method considers the following assumptions for solving the system.

1) The coefficient matrix is a nonsingular matrix, i.e. $|A| \neq 0$.
2) The system has a unique solution.
3) The coefficient matrix has no zeros on its main diagonal i.e. $a_{ii} \neq 0$.

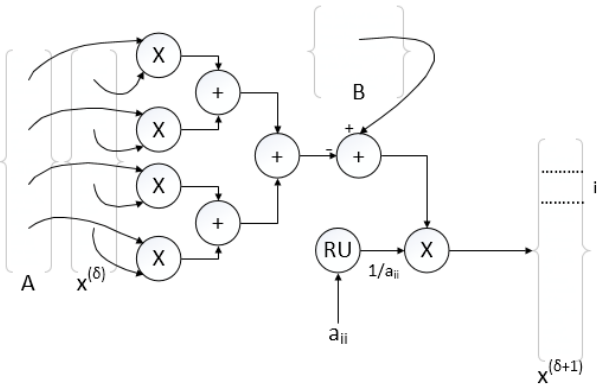


Fig. 1: Jacobi Iterative Architecture

Let A matrix presented in equation (3) be decomposed according to the equation,

$$A = L + U + D \tag{4}$$

where L is the strictly lower triangular matrix, U is the strictly upper triangular matrix and D is the diagonal matrix. Solving for $x^{(\delta+1)}$ using equations (3) and (4) yield,

$$x^{(\delta+1)} \Leftarrow D^{-1}[B - (L+U)x^{(\delta)}] \tag{5}$$

The same iteration in the point form can be expressed as presented in [7] and the architecture is shown in Fig. 1.

$$x_i^{(\delta+1)} \Leftarrow \frac{1}{a_{ii}}\left[b_i - \sum_{j=1, j\neq i}^{j=n} a_{ij} x_j^{(\delta)}\right] \forall \;\; i = 1, 2 \dots n. \tag{6}$$

Where, $x_i^{(\delta+1)}$ is the iteratively approximated value of x_i, after $\delta+1$ iterations. In Jacobi method, the values $x_i^{(\delta)}$ remain unchanged until the $(\delta+1)th$ iteration occurs. In equation (5), let $Y = D^{-1}(L+U)$. The necessary and sufficient condition for the Jacobi iterative method to converge is $\rho(Y) < 1$, where $\rho(Y)$ represents the spectral radius of Y as discussed in [6].

B. Gauss Seidel

In Jacobi method, the $x_i^{(\delta)}$ values remain unchanged until the $(\delta+1)th$ iteration occurs and the entire next iteration values get calculated, but in Gauss-Seidel method, the values of $x_i^{(\delta+1)}$ get updated and are used in the calculation of next variables as soon as they are calculated. The assumptions taken into account before are same as Jacobi method. The solution can be presented in vector form as,

$$(L+D)x^{(\delta+1)} \Leftarrow [B - Ux^{(\delta)}] \tag{7}$$

$$\Rightarrow (x)^{(\delta+1)} \Leftarrow (L+D)^{-1}[B - x^{(\delta)}] \tag{8}$$

The necessary and sufficient condition for the Gauss-Seidel method to be convergent is $\rho((D+L)^{-1}U) < 1$ [6]. This condition ensures that the coefficient matrix is convergent with the Gauss-Seidel method. The Gauss-Seidel iteration can be represented in the point form as:

$$x_i^{(\delta+1)} \Leftarrow \frac{1}{a_{ii}}\left[b_i - \sum_{j=i+1}^{j=n} a_{ij}x_j^{(\delta)} - \sum_{j=1}^{j=i-1} a_{ij}x_j^{(\delta+1)}\right] \quad \forall\ i = 1, 2 \ldots n. \tag{9}$$

III. Proposed Method

The proposed architecture is the consequence of a mathematical manipulation on equation (9). Here, we demonstrate the manipulation with an example on an equation set of 5 variables and then generalize the result. By specifying the equation (9) for x_2, we get,

$$x_2^{(\delta+1)} = \frac{1}{a_{22}}\big[b_2 - a_{21}x_1^{(\delta+1)} - a_{23}x_3^{(\delta)} - a_{24}x_4^{(\delta)} - a_{25}x_5^{(\delta)}\big] \tag{10}$$

A scaled term $a_{21}x_1^{(\delta)}$ is added and subtracted from the equation, shown in parenthesis, to give,

$$x_2^{(\delta+1)} = \frac{1}{a_{22}}\big[b_2 - a_{21}x_1^{(\delta+1)} - a_{23}x_3^{(\delta)} - a_{24}x_4^{(\delta)} - a_{25}x_5^{(\delta)} + (a_{21}x_1^{(\delta)} - a_{21}x_1^{(\delta)})\big] \tag{11}$$

which can be rearranged as:

$$x_2^{(\delta+1)} = \frac{1}{a_{22}}\big[(b_2 - a_{21}x_1^{(\delta)} - a_{23}x_3^{(\delta)} - a_{24}x_4^{(\delta)} - a_{25}x_5^{(\delta)})(\mathbf{I}) + (a_{21}x_1^{(\delta)} - a_{21}x_1^{(\delta+1)})(\mathbf{II})\big] \tag{12}$$

The first part **(I)**, of this equation is a manifestation of (6), which can be implemented by the Jacobi architecture as presented in Fig. 1. The second part **(II)** can be implemented using synchronized, combinational hardware additional to the Jacobi architecture to give the proposed architecture as shown in Fig. 2. The proposed design in Fig. 2, like the equations above, is an illustrious design for solving a linear system of equations with 5 variables. The general, point form of the proposed approach can be represented as:

$$x_i^{(\delta+1)} = \frac{1}{a_{ii}}\left(\left[b_i - \sum_{j=1, j\neq i}^{j=n} a_{ij}x_j^{(\delta)}\right](\mathbf{I}) - \left[\sum_{j=1}^{j=i-1} a_{ij}(x_j^{(\delta)} - x_j^{(\delta+1)})\right](\mathbf{II})\right) \forall\ i = 1, 2 \ldots n. \tag{13}$$

Adding the parallel, multiplier-adder tree architecture, the critical path delay increases a bit; by the delay of an adder in comparison to the Jacobi architecture. But the improved convergence rates of the Gauss-Seidel method massively overshadow this increased delay when implemented for systems of higher dimensions resulting in overall speed efficient circuit with acceptable hardware augmentation, discussed further in the Section V.

IV. Hardware Design

The designed hardware is a 32-bit floating point architecture implemented in Verilog using Xilinx ISE design suite, having Virtex 7 XCV2000T as the target device. The proposed architecture requires a synchronized augmented hardware, which uses a multiplexer as a selector circuit to select the coefficients required in the current cycle for computations. The coefficients are selected by the 5X1 multiplexer according to Table I and fed into the system.

TABLE I: Cycle number Vs Matrix Coefficient

Cycle Number	Coefficients		
	Select Lines (s_1, s_2, s_3)	A	C(c_1, c_2, c_3, c_4)
1	000	$a_{12}a_{13}a_{14}a_{15}$	0000
2	001	$a_{21}a_{23}a_{24}a_{25}$	$a_{21}000$
3	010	$a_{31}a_{32}a_{34}a_{35}$	$a_{31}a_{32}00$
4	011	$a_{41}a_{42}a_{43}a_{45}$	$a_{41}a_{42}a_{43}0$
5	100	$a_{51}a_{52}a_{53}a_{54}$	$a_{51}a_{52}a_{53}a_{54}$

A. Functioning of proposed architecture

Coefficients of the A matrix are stored in a lookup table to access in each cycle. The unknowns are initialized as a zero vector ($x^{(0)} = [0, 0, 0....0]$). For instance, in the first cycle, the value of $x_1^{(\delta+1)}$ is computed using the initialized vector. The coefficients $a_{12} - a_{15}$ are read from the lookup table and given as input to the first stage of the multiplier-adder tree to the left of the highlighted adder along with the unknowns evaluated in the previous iteration. Simultaneously, the element a_{11} is fed to the reciprocal unit. The elements in C are taken to be zero for the first cycle. These elements vary in each cycle as described in Table I and appropriate values are selected by the synchronized multiplexer. The newly computed value of $x_1^{(\delta+1)}$ is stored in a register. Next cycle involves the computation of $x_2^{(\delta+1)}$. Coefficients $a_{21} - a_{25}$ are read from the lookup table and fed to the multiplier-adder tree and a_{22} to the reciprocal unit. The coefficient c_1 of the C matrix in the augmented multiplier adder tree is selected to be a_{21} using the

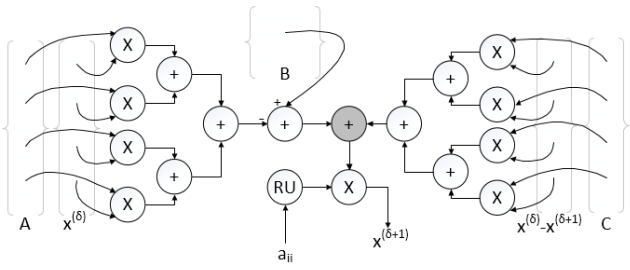


Fig. 2: Proposed Design

multiplexer while the other coefficients $c_2 - c_4$, are forced to 0. The stored value of $x_1^{(\delta)}$ along with the newly computed $x_1^{(\delta+1)}$ is also fed to this block while the values not required in the current cycle are forced to zero. This gives the newly computed value $x_2^{(\delta+1)}$ which is stored for use in the next cycle. These cycles are repeated to obtain the values of $x_3^{(\delta+1)}$, $x_4^{(\delta+1)}$ and $x_5^{(\delta+1)}$ with the required coefficients of A and C matrix as described in the proposed equations and given in Table I. The other newly computed values, $x_1^{(\delta+1)} - x_4^{(\delta+1)}$, are used in successive cycles as per (II) of equation (13). Computing all 5 unknowns once completes one iteration. These values are stored for use in the next iteration and this cycle goes on till the unknowns converge to an approximate solution with desired tolerance. The architecture can be broken down into building blocks which are designed and optimized for best performance, as discussed below.

B. Multiplier

Instead of a conventional multiplier, a 32-bit floating point multiplier which uses a 24-bit Radix-4 Booth Encoded multiplier to multiply mantissas of the numbers is designed. The study in [8] shows that Radix-4 Booth Encoded multiplier is the most speed efficient and area efficient among other higher radix Booth Encoded multipliers. The partial products required for computation are significantly reduced compared to the traditional multipliers. These partial products are added using a Dadda tree structure and the final summation is carried out using a Koggestone adder. The Dadda tree structure is used over Wallace because it is relatively speed efficient and possesses less complexity as shown in [9]. The Koggestone adder was chosen among Carry-Save adder, Carry-Select adder etc. after simulation and testing for speed to get as low combinational delay as possible. The proposed design is presented in the Fig. 3.

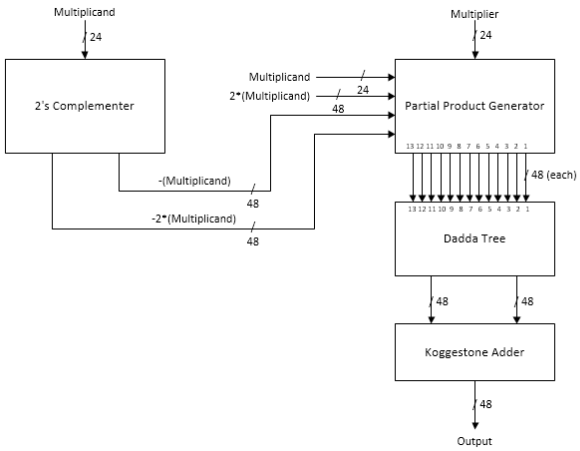


Fig. 3: Proposed Radix 4 Multiplier

C. 2's Complementer

An improved 2's complementer unit is designed for generating the partial products of the radix 4 multiplier. Unlike the conventional method of complement and add we propose a parallel complementer unit whose logic delay remains the same for an arbitrary input size. The proposed design as shown in Fig. 4 works as following:

1) Starts from the right of the number and forms a quadruple of bits. Repeats this process and forms non overlapping quadruples. Adds additional 0's towards the end if no more bits are left.
2) Logical OR these sets of 4 bits to generate signals $o_0^{'}, o_1^{'}, o_2^{'}.....o_n^{'}$ where $o_0^{'}$, is the signal from the right-most 4 bits.
3) Uses the above signals to generate $o_0 = o_0^{'}, o_1 = (o_0^{'} + o_2^{'}), o_2 = (o_0^{'} + o_1^{'} + o_2^{'})$ and so on.
4) Passes the 4 bits: unchanged, complemented or in 2's complement form based on the combination $o_i o_{i-1}$, take $o_{-1} = 0$, as given in Table II.
5) The output thus obtained is the 2's complement of the original number.

TABLE II: Multiplexer Output

o_i, o_{i-1}	4 Bit Output
00	Pass Bits Unchanged
01	0000∗(this case never occurs)
10	2's Complement Form
11	Complemented Form

D. Reciprocal Unit(RU)

Instead of using a conventional full divider architecture, the reciprocal unit is based on a compact iterative architecture using Newton-Raphson method as described in [10]. The architecture proposed in [10] is designed to compute the reciprocal $1/x$ for $x \in (0.5, 1]$, but our design is optimized to compute the reciprocal for $x \in (0, \infty]$. Hence, reciprocal of any diagonal coefficient $a_{ii} \in R$(Set of Real numbers) can be computed by normalizing the coefficient by 2^p to first bring the coefficient into the working range of the reciprocal unit i.e. $(0.5, 1]$, which actually corresponds to p number of arithmetic left or right shifts depending on whether the number lies in the

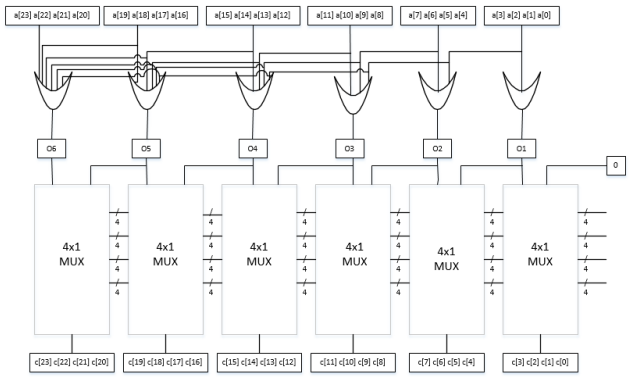


Fig. 4: Proposed 2's Complementer

range $(0, 0.5]$ or $(1, \infty)$ respectively. After the computations, p number of arithmetic shifts in the complementary direction yield the true result. The circuit approximates the reciprocal of a number in just 3 iterations and the architecture effectively uses same hardware to compute the initializing value and the reciprocal resulting in compact, fast implementation of the reciprocal unit.

V. Results

The proposed architecture has been synthesized, using Xilinx design tools. The combinational delay of each building block, the maximum operating frequency of the proposed hardware, the area and the percentage resources utilized of the target FPGA are presented in Table III.

TABLE III: Hardware Summary

Module	Combinational Delay(ns) (Δ)	f_{max} (MHz)	Area (Sliced Used)	%age Resources Utilized
adder_32_bit	20.64	-	444	0.03
adder_64_bit	33.56	-	1036	0.08
2's complementer	3.69	-	28	0
multiplier_64_bit	17.65		1205	0.09
reciprocal_64_bit	-	25.76	7344	0.06
Jacobi Block	127.15	25.98	18126	1.48
Proposed Design(GS)	162.17	25.18	29761	2.43

It can be manifested from the Table III that the proposed method has larger critical path in comparison to the Jacobi architecture. The increased value in delay corresponds to the 64-bit adder used to combine the results of the Jacobi architecture and the extended hardware as discussed in Section III. However, the fast convergence rate of the proposed method, which is by virtue of the Gauss-Seidel method, massively overshadows the increased critical path delay. This can be manifested from Table IV which presents the comparison of Jacobi method and the proposed architecture. The architectures are tested for equation sets, chosen randomly, of various dimensions of two types: Dense and Sparse coefficient matrix(A). In order to test the efficacy of the system, 10 trials were performed for each type of equation presented in Table IV and their averaged results are shown.

Here, speed up is a figure of merit, which demonstrates the relative speed of the proposed architecture to the Jacobi architecture. The Speed Up is introduced as:

$$S = \frac{N_J}{N_{GS}} * \frac{\Delta_J}{\Delta_{GS}} \tag{14}$$

Where N_J is the number of iterations required to converge by Jacobi method, N_{GS} is the number of iterations required to converge the Proposed Gauss-Seidel architecture, and Δ_J and Δ_{GS} are respectively the critical path delays of Jacobi architecture and the Gauss-Seidel architecture respectively, which are in this case 127.15ns and 162.17ns respectively.

TABLE IV: Gauss Seidel Vs Jacobi Iterative Solver

Type of matrix	N_J (Jacobi)	N_{GS} (Gauss-Seidel)	Speed Up(S)
Dense 5×5	19	10	1.48
Sparse 5×5	9	5	1.41
Dense 4×4	14	8	1.36
Sparse 4×4	8	5	1.24
Dense 3×3	10	6	1.31
Sparse 3×3	5	3	1.30
Dense 2×2	7	5	1.09
Sparse 2×2	2	2	0.78

Here we emphasize on the system of dimension 5×5, as it is the highest dimensional system tested in this paper. The mean error percentage of the computed, converged solutions and the theoretical solutions is presented in Table V, averaged over 10 different test equation sets, chosen randomly. It can be observed from Table IV that the speed up value increases as we go from a lower to a higher dimension linear system of equations. Following this trend, it is safe to conclude that system would perform even better at solving larger dimensional systems.

TABLE V: Mean Error Percentage

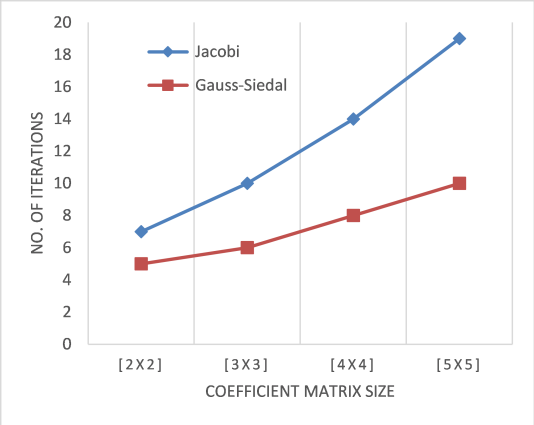
Type of Matrix	Error Percentage
Dense 5×5	0.00002097782
Sparse 5×5	0.00003614089

VI. Conclusion

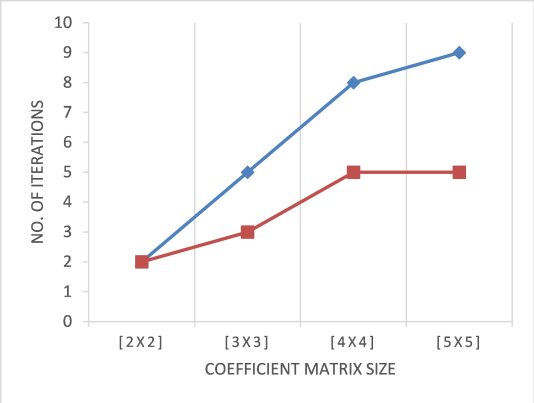
This paper introduces a novel implementation of an existing iterative method used to solve linear system of equations, viz. the Gauss-Seidel method. The proposed design uses the basic Jacobi architecture and optimized adders and multipliers to implement the Gauss-Seidel method which offers better convergence rates than the conventional Jacobi method to solve the linear system of equations especially with large dimensions. The proposed method can be employed to solve higher dimension system of equations and is expected to deliver larger speedup(S) as the system gets larger(following the trend in Fig. 5). This speed efficiency comes conflated with an acceptable increase in hardware with respect to the Jacobi architecture but reduced hardware requirement relative to the Gauss-Seidel implementation designed to exhibit parallelism. The data to compare our design with other hardware implementations of Gauss-Seidel is not readily available in literature to the best of our knowledge. Hence, our future aim is to test and compare this architecture with other existing Gauss-Seidel implementations used in specific applications [5],[11],[13],[15],[16] for speed, area, hardware cost, etc.

Acknowledgement

The authors would like to thank anonymous reviewers for their constructive comments and scrutiny.



(a) Dense Matrices.



(b) Sparse Matrices

Fig. 5: No. of iterations used by the Jacobi and Gauss-Seidel(Proposed) method in solving dense and sparse matrices

REFERENCES

[1] Larson,Ron. Numerical methods in Elementary Linear Algebra, 6th edition, Brooks/Cole,Cengage Learning, 2009.

[2] Reusken, Arnold. "Convergence analysis of the Gauss-Seidel preconditioner for discretized one dimensional Euler equations." SIAM journal on numerical analysis 41.4 (2003): 1388-1405.

[3] Liu, Qingbing, Guoliang Chen, and Jing Cai. "Convergence analysis of the preconditioned GaussSeidel method for H-matrices." Computers & Mathematics with Applications 56.8 (2008): 2048-2053.

[4] Adams, Mark, et al. "Parallel multigrid smoothing: polynomial versus GaussSeidel." Journal of Computational Physics 188.2 (2003): 593-610.

[5] Dziekonski, Adam, Adam Lamecki, and Michal Mrozowski. "Jacobi and Gauss-Seidel preconditioned complex conjugate gradient method with GPU acceleration for finite element method." Microwave Conference (EuMC), 2010 European. IEEE, 2010.

[6] Liu, Hongxia, and Tianxiang Feng. "Study on the Convergence of Solving Linear Equations by Gauss-Seidel and Jacobi Method." Computational Intelligence and Security (CIS), 2015 11th International Conference on. IEEE, 2015.

[7] Morris, Gerald R., and Viktor K. Prasanna. "An FPGA-based floating-point Jacobi iterative solver." Parallel Architectures, Algorithms and Networks, 2005. ISPAN 2005. Proceedings. 8th International Symposium on. IEEE, 2005.

[8] Swee, Kelly Liew Suet, and Lo Hai Hiung. "Performance comparison review of radix-based multiplier designs." Intelligent and Advanced Systems (ICIAS), 2012 4th International Conference on. Vol. 2. IEEE, 2012.

[9] Townsend, Whitney J., Earl E. Swartzlander, and Jacob A. Abraham. "A comparison of Dadda and Wallace multiplier delays." Proc. SPIE, Advanced Signal Processing Algorithms, Architectures, and Implementations 13 (2003): 552-560.

[10] Habegger, Andreas, et al. "An efficient hardware implementation for a reciprocal unit." Electronic Design, Test and Application, 2010. DELTA'10. Fifth IEEE International Symposium on. IEEE, 2010.

[11] Zhu, Pengfei, et al. "An FPGA-based acceleration platform for auction algorithm." Circuits and Systems (ISCAS), 2012 IEEE International Symposium on. IEEE, 2012.

[12] Saad, Yousef, and Henk A. Van Der Vorst. "Iterative solution of linear systems in the 20th century." Journal of Computational and Applied Mathematics 123.1 (2000): 1-33.

[13] Bylina, Jaroslaw, and Beata Bylina. "Merging Jacobi and Gauss-Seidel methods for solving Markov chains on computer clusters." Computer Science and Information Technology, 2008. IMCSIT 2008. International Multiconference on. IEEE, 2008.

[14] Bahi, Jacques Mohcine, Sylvain Contassot-Vivier, and Raphael Couturier. Parallel iterative algorithms: from sequential to grid computing. CRC Press, 2007.

[15] Chassin, David P., et al. "Gauss-Seidel accelerated: implementing flow solvers on field programmable gate arrays." Power Engineering Society General Meeting, 2006. IEEE. IEEE, 2006.

[16] Wu, Zhizhen, et al. "Efficient architecture for soft-output massive MIMO detection with Gauss-Seidel method." Circuits and Systems (ISCAS), 2016 IEEE International Symposium on. IEEE, 2016.

ResearchGate

See discussions, stats, and author profiles for this publication at: https://www.researchgate.net/publication/323656295

Application of Regression in the Analysis of Cutting Parameters for Surface Roughness in Turning

Article · March 2018

CITATIONS
0

READS
8

1 author:



Ankit Tyagi
Delhi Technological University
5 PUBLICATIONS **0** CITATIONS

SEE PROFILE

Some of the authors of this publication are also working on these related projects:



Fabrication & Mechanical Testing of AA6082/Si3N4 Composites View project



Studies on AA6082-Si 3 N 4 & AA7075-Si 3 N 4 Composites View project

All content following this page was uploaded by Ankit Tyagi on 09 March 2018.

The user has requested enhancement of the downloaded file.

International Journal of Emerging Technology and Advanced Engineering
Website: www.ijetae.com (ISSN 2250-2459, ISO 9001:2008 Certified Journal, Volume 8, Issue 2, February 2018)

Application of Regression in the Analysis of Cutting Parameters for Surface Roughness in Turning

Ankit Tyagi[1], Yashwant Koli[2], Sumit Kumar[3]
[1,2]*Department of Mechanical Engineering, Delhi Technological University, Delhi110042, India*
[3]*Department of Mechanical Engineering, NIT Kurukshetra, Haryana, India*

Abstract: **This paper focuses on analysis of cutting parameters using regression analysis which is a set of statistical processes for estimating the relationships among variables, is used to analyse surface roughness (SR). A full factorial 27 experiment is engaged to scrutinize the cutting characteristics of mild steel bars using carbide cutting tool. The key objective is to analyze the effect of cutting speed, feed and depth of cut on SR of mild steel in turning operation using carbide tool. The specimen was turned under different level of constraints and the SR was established using a Taylor Hobson's Surtronic 3+. From the result, it is concluded that higher cutting speed and lower feed produce better surface finish. The optimum cutting constraints were 119.380m/min, 0.04mm/rev and 0.6mm, which produced minimum surface roughness of 1.33µm. According to the non-linear regression equation, the optimum surface Roughness comes out to be 1.35µm which gives the error of 1.5%.**

Keywords: **Surface roughness (SR), Regression Analysis and Taylor Hobson's Surtronic 3+.**

I. INTRODUCTION

In manufacturing industries, surface finish of a product is vital in defining the quality. Suitable surface finish not only guarantees superiority, but also eases manufacturing cost. Surface finish is vital in terms of tolerances, it eases assembly time and evades the requirement for secondary operation, thus diminishes operation time and leads to overall cost reduction. CNC lathes are capable to produce fast, precision cuts, usually by indexable tools and drills in comparison to normal lathe. They are predominantly effective for complex programs intended to produce parts that would be infeasible to make on normal lathes.

CNC lathes usually have two axes (X and Z), but fresher models have more axes, letting for more innovative jobs to be machined by frequent interpretation of G-code as well as the manufacturer's exclusive programming language. CNC's are extremely versatile and allow you to cut an array of different types of product and materials. The exact capacities of a machine will vary with size, inflexibility and power. CNC machines offer many advantages in manufacturing like higher flexibility, increased productivity, improved quality, reduced scrap rate, reliable and safe operation.

SR also affects numerous functional qualities of parts, such as wearing, heat transmission, and facility of sustaining a lubricant, coating and resisting fatigue. Commonly known model to establish the SR is $Ra = f^2/32r$, where f is the feed rate and r is the nose radius. Undoubtedly, feed rate and nose radius influence SR the most [1][2].

There were two purposes of this research. First was to exhibit an organized method of operating Taguchi parameter design. The second was to exhibit a use of the Taguchi parameter design in order to recognize the optimum SR performance with a certain grouping of cutting parameters in a turning operation.

II. LITERATURE REVIEW

Davim.J et al. [3] worked on surface roughness prediction models using artificial neural network (ANN) are developed to investigate the effects of cutting conditions during turning of free machining steel, 9SMnPb28k(DIN). I.A. Choudhury et al. [4] worked on the development of surface roughness prediction models for turning EN 24T steel (290 BHN) utilizing response surface methodology. W.H. Yang et al. [5] An orthogonal array, the signal-to-noise (S:N) ratio, and the analysis of variance (ANOVA) are employed to investigate the cutting characteristics of S45C steel bars using tungsten carbide cutting tools. M. Nalbant et al. [6] The orthogonal array, the signal-to-noise ratio, and analysis of variance are employed to study the performance characteristics in turning operations of AISI 1030 steel bars using TiN coated tools. IlhanAsilturk et al. [7] focuses on optimizing turning parameters based on the Taguchi method to minimize surface roughness (Ra and Rz). [8] the effects of cutting speed, feed rate, workpiece hardness and depth of cut on surface roughness and cutting force components in the hard turning were experimentally investigated. Ramesh et al. [9] studies the effect of cutting parameters on the surface roughness in turning of titanium alloy has been investigated using response surface methodology.

International Journal of Emerging Technology and Advanced Engineering
Website: www.ijetae.com (ISSN 2250-2459, ISO 9001:2008 Certified Journal, Volume 8, Issue 2, February 2018)

Günay.M et al. [10], focused on optimizing the cutting conditions for the average surface roughness (Ra) obtained in machining of high-alloy white cast iron (Ni-Hard) at two different hardness levels (50 HRC and 62 HRC). N.R. Abburi et al. [11] develops a knowledge-based system for the prediction of surface roughness in turning process. Janez Kopac et al. [12] focuses on optimising the turning of raw workpieces of low-carbon steel with low cold pre-deformation to achieve acceptable surface roughness.

P.V.S. Suresh et al. [13], The experimentation was carried out with TiN-coated tungsten carbide (CNMG) cutting tools, for machining mild steel work-pieces covering a wide range of machining conditions. W.S. Lin et al. [14], an abductive network is adopted to construct a prediction model for surface roughness and cutting force. M.Y. Noordin et al. [15], The performance of a multilayer tungsten carbide tool was described using response surface methodology (RSM) when turning AISI 1045 steel. D.I. Lalwani et al. [16], In the present study, an attempt has been made to investigate the effect of cutting parameters (cutting speed, feed rate and depth of cut) on cutting forces (feed force, thrust force and cutting force) and surface roughness in finish hard turning of MDN250 steel [equivalent to 18Ni(250) maraging steel] using coated ceramic tool. Davim. J et al. [17], presents a study of the influence of cutting parameters on surface roughness in turning of glass-fibre-reinforced plastics (GFRPs). Dilbag Singh et al. [18], An experimental investigation was conducted to determine the effects of cutting conditions and tool geometry on the surface roughness in the finish hard turning of the bearing steel (AISI 52100). Ahmet Hasçalhk et al. [19], the effect and optimization of machining parameters on surface roughness and tool life in a turning operation was investigated by using the Taguchi method. The experimental studies were conducted under varying cutting speeds, feed rates, and depths of cut. An orthogonal array, the signal-to-noise (S/N) ratio, and the analysis of variance (ANOVA) were employed to the study the performance characteristics in the turning of commercial Ti-6Al-4V alloy using CNMG 120408-883 insert cutting tools.

Vishal S. Sharma et al. [20], machining variables such as cutting forces and surface roughness are measured during turning at different cutting parameters such as approaching angle, speed, feed and depth of cut. Hardeep Singh et al. [21], an experimental study to investigate the effects of cutting parameters like spindle speed, feed and depth of cut on surface finish and material removal rate on EN-8. Thomas M. et al. [22], focus of this study is the collection and analysis of surface roughness and tool vibration data generated by lathe dry turning of mild carbon steel samples at different levels of speed, feed, depth of cut, tool nose radius, tool length and workpiece length. Ranganath M.S. et al. [23], investigates the parameters affecting the roughness of surfaces produced during the turning process for the material Aluminium 6061. Ranganath M.S. et al. [24], MOTIF-method is a system for the evaluation of the primary profile and based on the envelope system and is suitable as an alternative to the mean line system. The specimen was turned under different levels and R, Rx and Ar values were analysed.

III. Experimental Procedure

Experiment was conducted on a LL20TL3 CNC lathe with work piece of 38 mm diameter and 300 mm long mounted between 3-jaw chuck and tailstock. Initially rough turning is done on CNC to remove scaling that is present on the surface of mild steel. The full factorial 27 experiments were performed according to the Taguchi Design of experiment and surface is gauged by using instrument Surtronic 3+.With the aid of Minitab software, Regression Analysis is applied and results are obtained.

3.1 Surface Roughness Measuring Instrument

The Surtronic 3+ is a movable, self-contained for the measurement of surface texture and is appropriate for use in both the workshop and laboratory. Parameters accessible for surface texture evaluation are: Ra, Rq, Rz (DIN), Ry and Sm. The instrument is normally powered by an alkaline non-rechargeable battery. If preferred, a Ni-Cad rechargeable battery can be used [15].

International Journal of Emerging Technology and Advanced Engineering
Website: www.ijetae.com (ISSN 2250-2459, ISO 9001:2008 Certified Journal, Volume 8, Issue 2, February 2018)

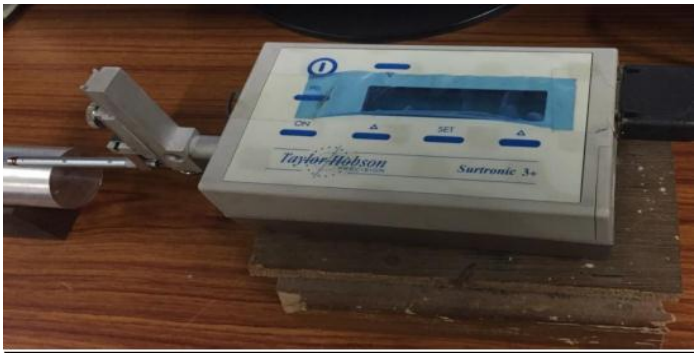


Fig: 1 Surface roughness measurement apparatus

Table 1.
Cutting Parameters and their levels

Symbol	Cutting Parameters	Units	Level 1	Level 2	Level 3
A	Speed (s)	m min-1	71.628	95.504	119.380
B	Feed (f)	mm rev-1	0.04	0.14	0.24
C	Depth of Cut (d)	mm	0.2	0.4	0.6

IV. Analysis And Discussion

Table 2.
Regression Analysis for Surface Roughness

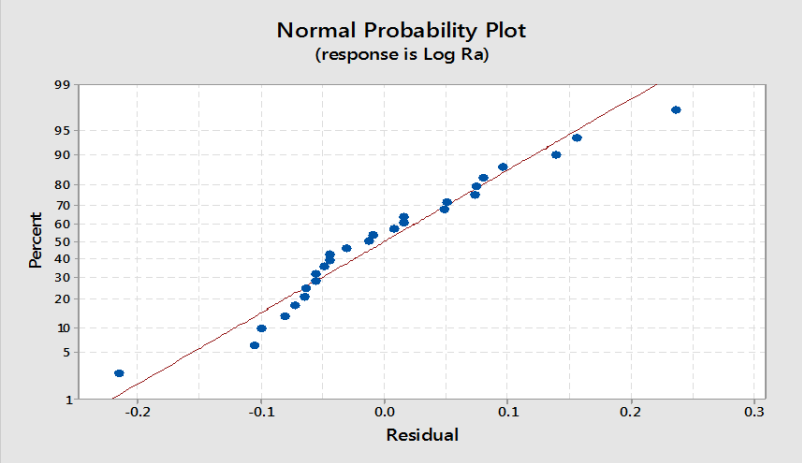
S.No.	Log S	Log d	Log f	Log Ra	Residual	Fits
1.	1.855082825	-0.698970004	-1.397940009	0.232996	-0.063812	0.296808
2.	1.855082825	-0.698970004	-0.853871964	0.690196	0.074377	0.615819
3.	1.855082825	-0.698970004	-0.619788758	0.769377	0.016305	0.753072
4.	1.855082825	-0.397940009	-1.397940009	0.161368	-0.099211	0.260579
5.	1.855082825	-0.397940009	-0.853871964	0.499687	-0.079902	0.579589
6.	1.855082825	-0.397940009	-0.619788758	0.686636	-0.030206	0.716842
7.	1.855082825	-0.22184875	-1.397940009	0.290035	0.050649	0.239386
8.	1.855082825	-0.22184875	-0.853871964	0.698101	0.139704	0.558396
9.	1.855082825	-0.22184875	-0.619788758	0.640481	-0.055168	0.695649
10.	1.980021562	-0.698970004	-1.397940009	0.181844	-0.055161	0.237005
11.	1.980021562	-0.698970004	-0.853871964	0.636488	0.080473	0.556015
12.	1.980021562	-0.698970004	-0.619788758	0.681241	-0.012027	0.693268
13.	1.980021562	-0.397940009	-1.397940009	-0.01457	-0.215348	0.200775
14.	1.980021562	-0.397940009	-0.853871964	0.756636	0.236851	0.519785

International Journal of Emerging Technology and Advanced Engineering
Website: www.ijetae.com (ISSN 2250-2459, ISO 9001:2008 Certified Journal, Volume 8, Issue 2, February 2018)

15.	1.980021562	-0.397940009	-0.619788758	0.665581	0.008543	0.657038
16.	1.980021562	-0.22184875	-1.397940009	0.33646	0.156878	0.179582
17.	1.980021562	-0.22184875	-0.853871964	0.450249	-0.048343	0.498592
18.	1.980021562	-0.22184875	-0.619788758	0.592177	-0.043669	0.635845
19.	2.076931575	-0.698970004	-1.397940009	0.206826	0.016209	0.190617
20.	2.076931575	-0.698970004	-0.853871964	0.606381	0.096754	0.509628
21.	2.076931575	-0.698970004	-0.619788758	0.541579	-0.105301	0.646881
22.	2.076931575	-0.397940009	-1.397940009	0.227887	0.073499	0.154387
23.	2.076931575	-0.397940009	-0.853871964	0.522444	0.049046	0.473398
24.	2.076931575	-0.397940009	-0.619788758	0.537819	-0.072832	0.610651
25.	2.076931575	-0.22184875	-1.397940009	0.123852	-0.009343	0.133194
26.	2.076931575	-0.22184875	-0.853871964	0.38739	-0.064815	0.452205
27.	2.076931575	-0.22184875	-0.619788758	0.545307	-0.044151	0.589458

4.1 Graphs from MiniTab for Regression Analysis

i. Normal probability plot of Residuals for Log Ra



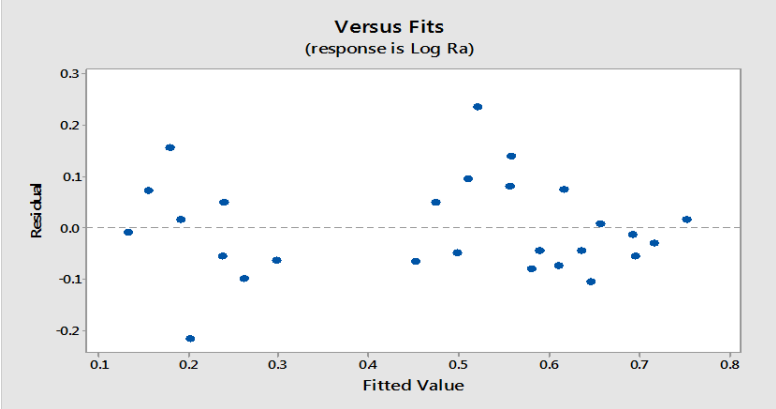
The points in this plot generally form a straight line if the residuals are normally distributed. If the points on the plot depart from a straight line, the normality assumption may be invalid. As in this project work data have less than 50 observations, the plot may show bend in the tails even if the residuals are normally distributed. As the number of observations drops, the probability plot may show substantial difference and nonlinearity even if the residuals are normally distributed.

ii. Residuals vs Fits for Log Ra

This plot displays a random pattern of residuals on both sides of 0. If a point lies distant from the majority of points, it may be an outlier. Also, there should not be any familiar patterns in the residual plot. The following may show error that is not random:

- a series of increasing or decreasing points
- a majority of positive residuals, or a majority of negative residuals
- patterns, such as increasing residuals with increasing fits

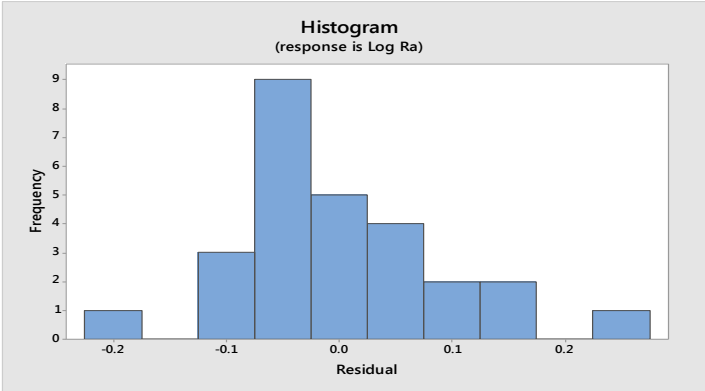
International Journal of Emerging Technology and Advanced Engineering
Website: www.ijetae.com (ISSN 2250-2459, ISO 9001:2008 Certified Journal, Volume 8, Issue 2, February 2018)



It can be concluded that all the values are within the control range, indicating that there is no obvious pattern and unusual structure.

iii. Residual Histogram for Log Ra

Long tails in the plot may indicate skewness in the data. If one or two bars are far from the others, those points may be outliers because the appearance of the histogram changes depending on the number of intervals used to group the data.

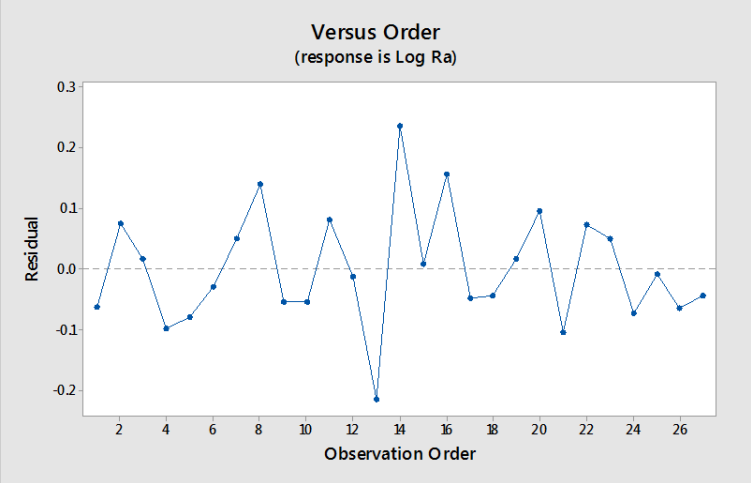


iv. Residuals vs Order for Log Ra

This is a plot of all residuals in the order that the data was collected and can be used to find non-random error, especially of time-related effects.

A positive correlation is indicated by a clustering of residuals with the same sign and a negative correlation is indicated by rapid changes in the signs of consecutive residuals.

International Journal of Emerging Technology and Advanced Engineering
Website: www.ijetae.com (ISSN 2250-2459, ISO 9001:2008 Certified Journal, Volume 8, Issue 2, February 2018)



From above graphs, it can be concluded that all the values are within the control range, indicating that there is no obvious pattern and unusual structure and also the residual analysis does not indicate any model inadequacy. Hence these values yield better results in future predictions.

4.2 Non-Linear Regression Equation

Log Ra = 1.920 - 0.479 Log S - 0.1204 Log d + 0.5863 Log f

$$Ra = 83.1763 \frac{f^{0.5863}}{s^{0.479} d^{0.1204}}$$

International Journal of Emerging Technology and Advanced Engineering
Website: www.ijetae.com (ISSN 2250-2459, ISO 9001:2008 Certified Journal, Volume 8, Issue 2, February 2018)

Table 3.
Calculated Surface Roughness from Regression Equation

S.No.	S (m/min)	d mm	f (mm/rev)	Ra (µm)	Calculated Ra (µm)	Error (%)
1.	71.628	0.20	0.04	1.71	1.98	15.78947
2.	71.628	0.20	0.14	4.90	4.12	-15.9184
3.	71.628	0.20	0.24	5.88	5.65	-3.91156
4.	71.628	0.40	0.04	1.45	1.82	25.51724
5.	71.628	0.40	0.14	3.16	3.79	19.93671
6.	71.628	0.40	0.24	4.86	5.20	6.995885
7.	71.628	0.60	0.04	1.95	1.73	-11.2821
8.	71.628	0.60	0.14	4.99	3.60	-27.8557
9.	71.628	0.60	0.24	4.37	4.95	13.27231
10.	95.504	0.20	0.04	1.52	1.72	13.15789
11.	95.504	0.20	0.14	4.33	3.59	-17.0901
12.	95.504	0.20	0.24	4.80	4.92	2.5
13.	95.504	0.40	0.04	0.97	1.58	62.8866
14.	95.504	0.40	0.14	5.71	3.30	-42.2067
15.	95.504	0.40	0.24	4.63	4.53	-2.15983
16.	95.504	0.60	0.04	2.17	1.50	-30.8756
17.	95.504	0.60	0.14	2.82	3.14	11.34752
18.	95.504	0.60	0.24	3.91	4.31	10.23018
19.	119.380	0.20	0.04	1.61	1.55	-3.72671
20.	119.380	0.20	0.14	4.04	3.23	-20.0495
21.	119.380	0.20	0.24	3.48	4.42	27.01149
22.	119.380	0.40	0.04	1.69	1.42	-15.9763
23.	119.380	0.40	0.14	3.33	2.97	-10.8108
24.	119.380	0.40	0.24	3.45	4.07	17.97101
25.	119.380	0.60	0.04	1.33	1.35	1.503759
26.	119.380	0.60	0.14	2.44	2.83	15.98361
27.	119.380	0.60	0.24	3.51	3.88	10.54131

International Journal of Emerging Technology and Advanced Engineering
Website: www.ijetae.com (ISSN 2250-2459, ISO 9001:2008 Certified Journal, Volume 8, Issue 2, February 2018)

From Table 3, it can be concluded that the optimum combination process parameters for minimum SR is obtained at speed 119.380m/min (1000rpm), feed 0.04mm/rev and depth of cut 0.6mm which gives 1.33µm surface roughness.

V. CONCLUSION

The following conclusions can be drawn based on the experimental results:

- From the help of non-linear regression equation it can be stated that, at lower value of speed and depth of cut the surface roughness value increases, whereas at lower value of feed rate the surface roughness decreases.
- In turning, use of higher speed (119.380 m/min), low feed rate (0.04 mm/rev) and high depth of cut (0.6 mm) are proposed to attain superior surface roughness for the particular test range.
- According to the non-linear regression equation, the optimum surface Roughness comes out to be 1.35µm at speed (119.380m/min), feed (0.04mm/rev) and depth of cut (0.6mm) which gives the error of 1.5%.

REFERENCES

[1] Upadhyay.V, P.K. Jain, N.K. Mehta; (2013) In-process estimate of roughness in turning of Ti–6Al–4V alloy using cutting constraints and vibration signals: Measurement 46 pp.154–160.

[2] Tugrul Ozel, Yigit Karpat; (2005) Extrapolative modeling of roughness and tool wear in hard turning using regression and neural networks: International Journal of Machine Tools & Manufacture 45 pp.467–479.

[3] Davim. J , V.N. Gaitonde, S.R. Karnik; (2008) Inquiries into the effect of cutting circumstances on roughness in turning of free machining steel by ANN models: journal of materials administering technology 2 0 5 pp.16–23.

[4] I.A. Choudhury, M.A. EI-Baradie; (1997) Rroughness estimate in the turning of high-strength steel by factorial design of tests: Journal of Materials Processing Technology 67 pp.55-61.

[5] W.H. Yang, Y.S. Tarng; (1998) Strategy optimization of cutting constraints for turning operations based on the Taguchi method: Journal of Materials Processing Technology 84 pp.122–129.

[6] M. Nalbant, H. Gokkaya, G. Sur; (2007) Presentation of Taguchi hmetod in the optimization of cutting parameters for roughness in turning: Materials and Design 28 pp.1379–1385.

[7] Ilhan Asilturk, Harun Akkus; (2011) Determining the effect of cutting constraint on roughness in hard turning using the Taguchi method: Measurement 44 pp.1697–1704.

[8] Hamdi Aouici, Mohamed Athmane Yallese, Kamel Chaoui, Tarek Mabrouki, Jean-François Rigal; (2012) Exploration of roughness and cutting force elements in hard turning with CBN tool: Prediction model and cutting conditions optimization: Measurement 45 pp.344–353.

[9] S. Ramesh, L. Karunamoorthy, K. Palanikumar; (2012) Dimension and investigation of roughness in turning of aerospace titanium alloy (gr5): Measurement 45 pp.1266–1276.

[10] Günay.M, Emre Yücel; (2013) Usage of Taguchi method for determining ideal roughness in turning of high-alloy white cast iron: Measurement 46 pp.913–919

[11] N.R. Abburi, U.S. Dixit; (2006) A data -based system for the calculation of surface roughness in turning operation: Robotics and Computer-Integrated Manufacturing 22 pp.363–372.

[12] Janez Kopac, Marko Bahor, Mirko Sokovic ; (2002) Finest machining constraints for attaining the desired roughness in fine turning of cold pre-formed steel workpieces: International Journal of Machine Tools & Manufacture 42 pp.707–716.

[13] P.V.S. Suresh e, P. Venkateswara Rao, S.G. Deshmukh; (2002) A genetic algorithmic method for optimization of surface roughness estimate model: International Journal of Machine Tools & Manufacture 42 pp.675–680.

[14] W.S. Lin, B.Y. Lee, and C.L. Wu; (2001) demonstrating the roughness and cutting force for turning: Journal of Materials Processing Technology 108 pp.286-293.

[15] M.Y. Noordin, V.C. Venkatesh, S. Sharif, S. Elting, A. Abdullah; (2004) predicted the performance of coated carbide tools when turning of AISI 1045 steel: Journal of Materials Processing Technology 145 pp.46–58.

[16] D.I. Lalwani, N.K. Mehta, P.K. Jain; (2008) Experimental investigations of and influence on cutting forces and roughness in finish hard turning of MDN250 steel: journal of materials processing technology 2 0 6 pp.167–179.

[17] Davim. J, Francisco Mata; (2004) Impact of cutting constraints on roughness in turning glass-fiber- strengthened plastics using geometric analysis: Industrial Lubrication and Tribology Volume 56 Number 5 pp. 270–274.

[18] Dilbag Singh, P. Venkateswara Rao; (2007) A roughness evaluation model for hard turning process: Int J Adv Manuf Technol 32: pp.1115–1124.

[19] Ahmet Hasçahk, Ulaş Çaydaş; (2008) Optimization of turning constraints for roughness and tool life centered on the Taguchi method: Int J Adv Manuf Technol 38: pp.896–903.

[20] Vishal S. Sharma , Suresh Dhiman, Rakesh Sehgal, S. K. Sharma; (2008) Assessment of cutting forces and roughness for hard turning using neural networks: J Intell Manuf 19: pp.473–483.

[21] Hardeep Singh, Rajesh Khanna, M.P. Garg; (2011) Consequence of Cutting Constraints on MRR and Roughness in Turning EN-8: Current Developments in Engineering Research Vol.1, No.1.

[22] Thomas M., Beauchamp Y., Youssef A.Y., Masounave J; (1996) Consequence of tool shakings on roughness during lathe dry turning process: Computers ind. Engng, Vol 31, No. 3/4, pp. 637 – 644.

[23] Ranganath M. S., Vipin, R. S. Mishra, Prateek; (2015) Optimization of surface roughness in CNC turning of Aluminium 6061 using Taguchi Techniqques: International Journal of Modern Engineering Research (IJMER): vol 5; pp. 1-9.

[24] Ranganath M.S., Vipin, Lalit Kumar, Jitender Kumar; (2014) Surface Texture Analysis in Turning of Mild Steel Using Carbide Inserts: International Journal of Advance Research and Innovation: volume 2, Issue 3; pp.601-606.

View publication stats

Soft Computing
https://doi.org/10.1007/s00500-018-3154-5

METHODOLOGIES AND APPLICATION

ARD-PRED: an *in silico* tool for predicting age-related-disorder-associated proteins

Kirti Bhadhadhara[1] · **Yasha Hasija**[1]

© Springer-Verlag GmbH Germany, part of Springer Nature 2018

Abstract
Interactions among various proteins largely govern cellular processes, and this leads to numerous efforts toward extraction of information related to the proteins, their interactions and the function which is determined by these interactions. The main concern of the study is to present interface analysis of age-related-disorder (ARD)-related proteins to shed light on details of the interactions. It also emphasizes on the importance of using structures in network studies. A major goal in the post-genomic era is to identify and characterize disease susceptibility of genes and to apply this knowledge to disease prevention and treatment. Attempts have been made to integrate biological knowledge of Gene Ontology and Kyoto Encyclopedia of Genes and Genomes pathways into the genomics field. Many gene set analysis methods have been used to detect disease-related risk pathways. The present study combines the network-centered approach with three-dimensional structures to comprehend the biology behind ARDs. Interface properties of the interacting complexes have been used as descriptors to classify age-related-disorder-associated proteins and non-age-related-disorder-associated proteins. Machine learning has been used to generate a classifier which is used to predict potential age-related proteins. The ARD-PRED tool achieved an overall accuracy in terms of precision score 81.5, recall score 81.2, accuracy value 79 and ROC Area score 89.6, F-measure 81.1. The tool has been made online at http://genomeinformatics.dtu.ac.in/ARD-PRED/. The present work would comprehend ongoing research in the field of ARDs and would also significantly improvise the understanding of the molecular mechanism of age-related diseases.

Keywords Interface properties · Age-related disorder · Machine learning · 3-Dimensional structure · Network analysis

1 Introduction

The major risk factors associated with ARD include advancing age, genetic predisposition, gender and ethnicity, with aging being the major risk factor. Despite numerous studies on the age-related disorders, many questions pertaining to their causation and genetic predisposition remain unanswered. A number of longevity genes and related pathways identified in model organisms have been evaluated for their role in ARDs (Srivastava et al. 2017). The association between genes and diseases is well studied in the past and has been well documented in various databases as in DisGENET (http://www.disgenet.org), Online Mendelian Inheritance in Man (http://omim.org), Genetic Association Database and Disease Ontology (Bauer-Mehren et al. 2010). These databases not only provide genes related with the disorders but also provide an insight about the common or essential genes which are involved in pathways of multiple disorders. The human disease gene network has established a link between genetic disorders and the genes. A significant conclusion derived from these networks is that genes associated with similar disorders show higher likelihood of physical interactions between their products, thus forming hubs of essential genes and the products (Goh et al. 2007).

Documentation of genes with the associated disease is not enough to understand the biological details of pathogenesis and disease development. It is important to identify various molecules and mechanisms which help in triggering, participating and controlling the biological processes. The understanding of molecular mechanisms is a complex process since not much is known about them (Gonzalez and Kann 2012). With increase in human interaction data, it is important to understand how biological functions are exerted

Communicated by V. Loia.

✉ Yasha Hasija
yashahasija@gmail.com

[1] Department of Biotechnology, Delhi Technological University, Main Bawana Road, Shahbad Daulatpur, Delhi 110042, India

Published online: 22 March 2018

over the body and this can be made possible only by the inclusion of structural details in the network.

Undoubtedly, sequence-based annotation is important in sorting out encoded information but knowing finer details of the mechanism within the cell is possible only with structural statistics.

Protein structures provide a higher resolution of information and a more sensitive approach for identifying similarities among proteins by including details about structures of interacting proteins in the networks, protein hubs and protein interfaces. Structural outline of the proteins provides opportunities in understanding the cellular and molecular functioning in terms of structural scaffolds which facilitate the molecular events. Moreover, the protein's structure is more conserved than its sequence (Choura and Rebai 2011).

Protein–protein interaction network is a way of representing how two or more proteins interact with each other in a cell (Zhang and Ouellette 2011). They control the flow of information both within and between the cells. Network is the representation where proteins are nodes and interactions are edges. These are useful indicators of biological processes (Choura and Rebai 2011). It is well known that proteins are main agents of biological function, which is based on their interactions with other proteins and biomolecules such as DNA and RNA. They, thus, mediate cellular processes, metabolic and signaling pathways. Protein interactions do not necessarily mean physical association but can also be metabolic interactions where proteins are involved in similar pathways and genetic interactions presenting co-expressed and co-regulated proteins (Gonzalez and Kann 2012). The protein does not act alone but as stated above interacts with other proteins to carry out a definite function. This pair of interacting proteins forms protein complexes. The protein fragments within the complex actually come together and interact to form a special region called protein interface (Aung 2006). Protein interaction networks are useful resources to gain knowledge about different systems in which they are evolved.

Alteration in this network can possibly lead to various disorders which are often caused by alteration in the binding sites of the protein (Zhang and Ouellette 2011). In protein–protein interaction network, most proteins have lesser interactions, whereas some proteins have multiple interactions. These proteins are significant for the stability as well as normal functioning of the proteins in the network. As examples, p53, p27, BRCA1, p21 ubiquitin and calmodulin are involved in different types of cancer, and the product of these genes forms a hub protein. Deletion of these hub proteins is fatal to the organism. Hence, it can be concluded that these proteins are encoded by essential genes and are targets for molecular as well as structural studies (Choura and Rebai 2011). In some cases, during the binding process, interactions between two proteins may involve order–disorder transitions in partial disordered regions of the interacting proteins. These disordered regions have been found to be involved in many mechanisms of the disease. For instance, the cancer suppressor gene BRCA1 has shown to contain disordered regions through which it binds to several other proteins (Kann 2007). Other than the interferences in the protein–protein interaction network, several diseases are caused due to disorders in protein–DNA interactions, protein folding mechanisms, protein–RNA disruptions, pathogen–host protein interactions and new undesired protein interactions (Gonzalez and Kann 2012).

Protein interactions are facilitated by specific recognition of multiple binding regions on the surface of interacting proteins. This recognition should be of good affinity to effectively bind fragments of proteins. This is decided by specificities such as interfaces. The interface properties and topology of protein complexes involved play an important role in deciphering the function in the network. Various studies have been carried out to integrate PPI (protein–protein interaction) network with the structural properties. A significant work in this regard has been done in the field of cancer biology. These cancer genes were mapped with human PPI network, and the network was studied with respect to structural features as interface properties and study demonstrates successful results in classifying cancer and non-cancer proteins (Kar et al. 2009). A process was developed to find network-based signatures by incorporating PPI networks and gene expression profiles to classify the metastatic and non-metastatic tumors (Chuang et al. 2007). Studies have shown that molecular mechanisms leading to diseases are dependent on interlinked proteins and networks, but we are far from sorting out differences in molecular interactions between healthy and diseased organisms. The mechanism of genetic malfunctioning, which may lead to one or diseases, can be stated when the molecular level of protein interactions is known. Understanding these interactions and hence, binding between proteins is critical for the rational design of new therapeutic agents targeted to disorder the interactions that cause several disorders (Gonzalez and Kann 2012). PPIs not only predict disease-associated interacting proteins but also predict the potential disease-associated gene candidates (genes coding for interactive proteins are putative disease-causing genes). This theory has been used in the present work where all the proteins associated with ARDs have been retrieved and different classifiers using machine learning algorithms are used to identify potential proteins associated with ARDs. These classifiers are based on interface properties of interacting complexes to differentiate between ARD-related proteins from non-ARD associated proteins (Jain et al. 2015).

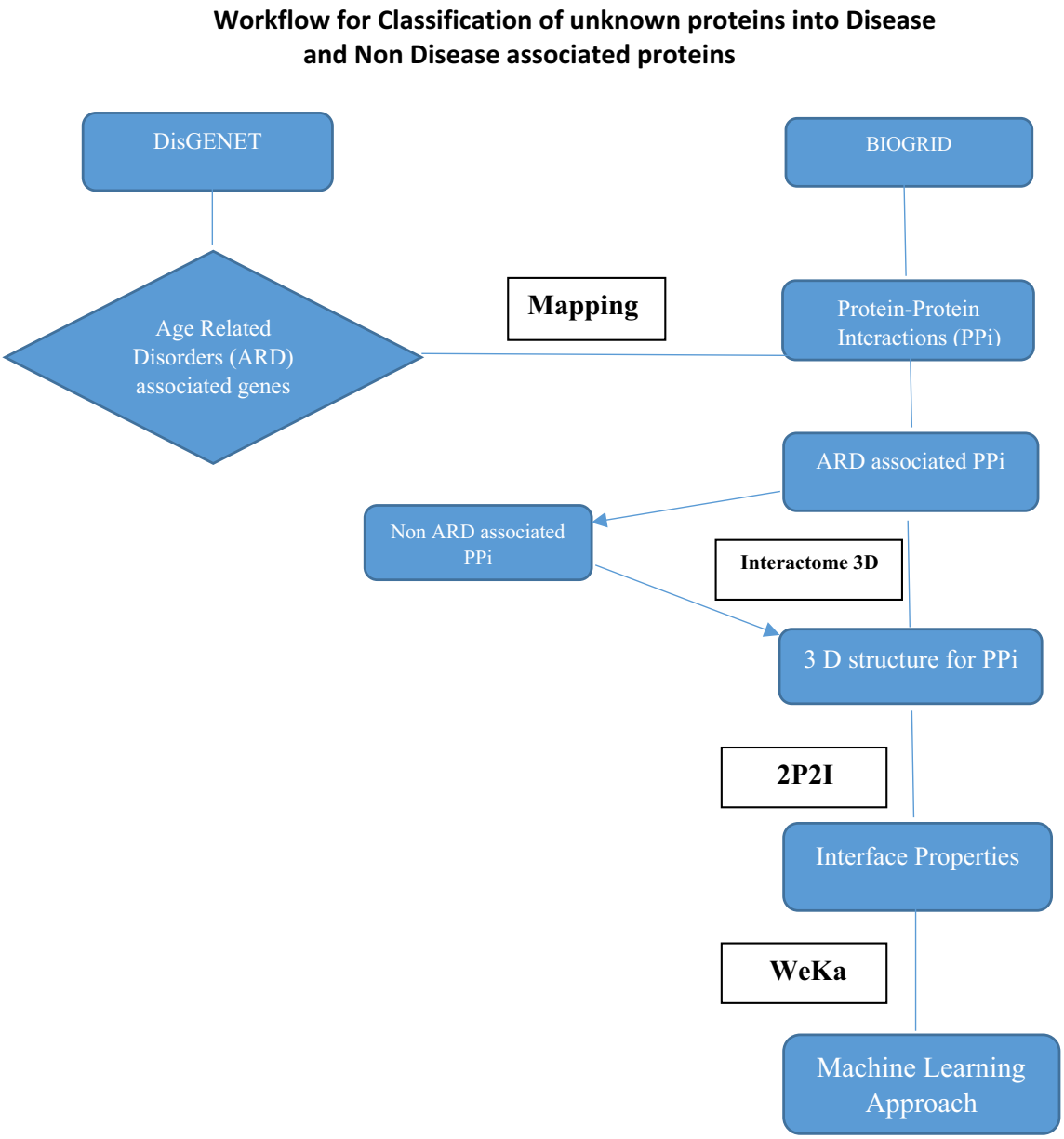


Fig. 1 Methodology carried out in the development of tool

2 Materials and methods

The detailed procedure for the study has been mentioned below and is depicted as a flow chart in Fig. 1.

2.1 Building datasets

BIOGRID was used to obtain all human protein–protein interactions, and DisGeNET was used to retrieve all ARD-related genes (Stark et al. 2006). The interactions in BIOGRID were mapped to UniProt IDs and subsequently to complex PDB structures using INTERACTOME 3D (http://interactome3d.irbbarcelona.org/) (Mosca et al. 2013). The complex PDB IDs were then mapped to ARDs. The interface properties were extracted using 2P2I Inspector. 2P2I Inspector (protein–protein interface analysis) invokes layers such as VMD, NACCESS and SURFNET (Hamon et al. 2013). It is a complete tool which computes the interaction properties from 3D structure of interacting complexes. Descriptors provided by this tool include the (ASA) accessible surface area, gap volume, percentage charged residues, secondary structure contributions, number of hydrogen bonds, number of salt bridges and number of disulfide bonds. All these parameters are useful in determining the specificity and the strength of the interface. OMIM's Morbid Map is used for attaining training samples and test samples. The training sample con-

sisted of two subsets: one subset consisting of all proteins associated with the age-related disorders and the other set consisting of all proteins, associated with diseases other than ARDs. In the present study, proteins were retrieved from UniProt (Magrane 2011).

2.2 Retrieval of interacting proteins

Wang discovered high-quality binary PPI along with the atomic resolution interface. They pooled reliable literature-curated binary interactions and verified yeast two-hybrid interactions to produce the human's PPI network (Wang et al. 2012). Then, they structurally resolved the interfaces of the interactions using layers—iPfam and 3did using homology modeling approaches. This resulted in a human structural interaction network (hSIN). The information is stored in the database with the gene-ID and the Pfam-ID. hSIN was used to determine structurally related interactions to the proteins involved in age-related interactions. Gene IDs for the disease-associated proteins were retrieved from NCBI (National Centre for Biotechnology Information). The interacting partners with reliable structures were retrieved from NCBI and were obtained from the hSIN.

2.3 Structural interaction network

After structurally interacting components were attained, a structure interaction network was formed using Interactome3D. It is a web-based service for the structural annotation of protein–protein interaction networks and pathways (Mosca et al. 2013). PDB codes with interacting chains between the proteins were retrieved.

2.4 Interface property analysis

For interface analysis, 2P2I Inspector (a protein–protein interface analysis tool) that invokes NACCESS, VMD, SURFNET was used. It is a complete tool that computes interaction properties from the 3D structure of interacting complexes. Various descriptors provided by the tool include accessible surface area (ASA), gap volume, percentage charged residue, secondary structure contributions, number of hydrogen bonds, number of disulfide bonds and number of salt bridges. All these parameters are important in defining the specificity and strength of the interface. The input can be a PDB code or PDB file along with chains involved in the complex structure (Basse et al. 2013).

2.5 Balancing and building random training dataset

Prior to running the Weka tool (Hall et al. 2009), Cygwin (DLL) tool was used, which is a popular GNU development tool for Microsoft Windows operating system. With Cygwin, it is possible to easily port different UNIX programs without the need for extensive changes insource code. With Cygwin, a series of random files were created by combining the positive data set and negative data set. These files were then used in Weka tool for classifying and predicting the prediction probability of the test dataset.

2.6 Classification analysis: the algorithm and its analysis

Comparison between proteins involved in ARDs and those which are not known to be involved in these diseases was prepared using interface features which depicts the protein complexes. By using machine learning algorithm, automatic classifiers capable of identifying genes more likely to be involved in ARDs based on the interfacial patterns were made. Different algorithms (classifiers) were tested and parameters such as true positive, false positive, true negative, false negative scores, precision, recall and accuracy were used to determine the best algorithm for the study. Random Forest, J48, Naïve Bayes, Bayesian Network classifiers with iteration 30 were used to generate the model for prediction. Ten runs of tenfold cross-validation were performed on the different classifiers used. The model generated was evaluated and used to predict the probability of polymorphic proteins associated with the ARDs.

2.7 Development of graphical user interface

For the likelihood of involvement of unknown proteins in ARD-PRED, user friendly web interface is developed. XHTML and CSS were used for creating presentation layer of the ARD-PRED. The web server used was Apache/2.4.4 (Win 32) Open SSL/0.9.8.y PHP/5.4.19. For backhand, database server version number 5.5.32 My SQL community server (GPL) was used. It is hosted at http://genomeinformatics.dtu.ac.in/ARD-PRED/. Screenshots from the tool are shown in Figs. 2, 3, 4 and 5.

3 Results

3.1 Proteins associated with the age-related disorders

A network with the PDB structures mapped with interacting proteins was obtained from Interactome 3D.

This network was generated separately for both training set and test set. A complete analysis of network helped in interpreting individual structures of proteins as well as the protein structures of interacting complexes. Beside the structures, this tool provides a description of chains from both the

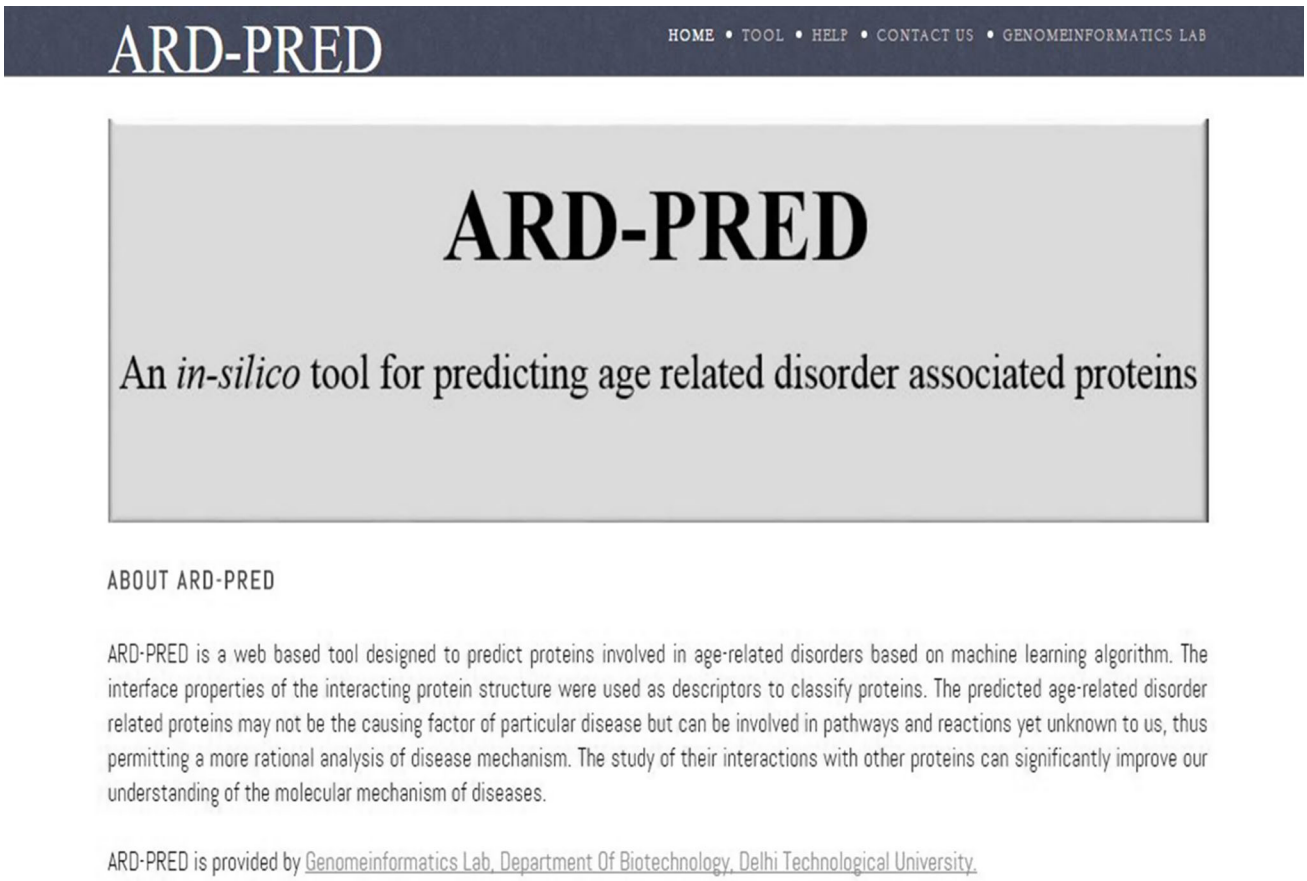


Fig. 2 Overview of home page of ARD-PRED tool

proteins responsible for the complex formation. This forms an important part of our study.

A total of eight descriptors were obtained from 2P2I Inspector, i.e., accessible surface area, gap volume index, gap volume, percentage charged residues, number of salt bridges, number of hydrogen bridges, number of disulfide bonds and secondary structure at interface. Parameters of interfaces for analyzing interactions in the present study are as follows:

Accessible surface area (ASA) is the mean ASA buried by each domain of the complexes.

Complementarity of the interface *gap volume* provides a measure of complementarity or closeness of packing of the interface among the two interacting proteins by measuring the volume of empty spaces in them (Kar et al. 2009).

Gap volume index Gap volume index between two protein domains is calculated as the ratio of gap volume to interface area. It evaluates the volume enclosed between any two molecules, delimiting boundary by defining a maximum allowed distance of both interfaces (Kar et al. 2009).

Planarity The planarity of interfaces analyzes shape of the interface. It is defined as root-mean-squared deviation of the interface atoms from the least-squares plane fitted with through all interface atoms (Kar et al. 2009).

Hydrogen bonding The hydrogen bonds play a key role in specificity of interactions between the two proteins. Average number of hydrogen bonds present is proportional to the area of subunit surfaces, i.e., ASA: one bond for each 100-200 Angstrom (Moreira et al. 2007).

Number of salt bridges More the number of salt bridges, the more will be electrostatic interactions leading to tighter packing within the residues.

Precision Fraction of retrieved instances that are relevant (Davis and Goadrich 2006).

$$\text{Precision} = \text{True Positives}/(\text{True Positives} + \text{False Positives})$$

Recall Fraction of relevant instances that are retrieved. Both precision and recall are therefore based on an understanding and measure of relevance (Davis and Goadrich 2006).

Area under ROC curve It is a measure of accuracy and is a plot of specificity versus sensitivity at various cutoff values (Davis and Goadrich 2006).

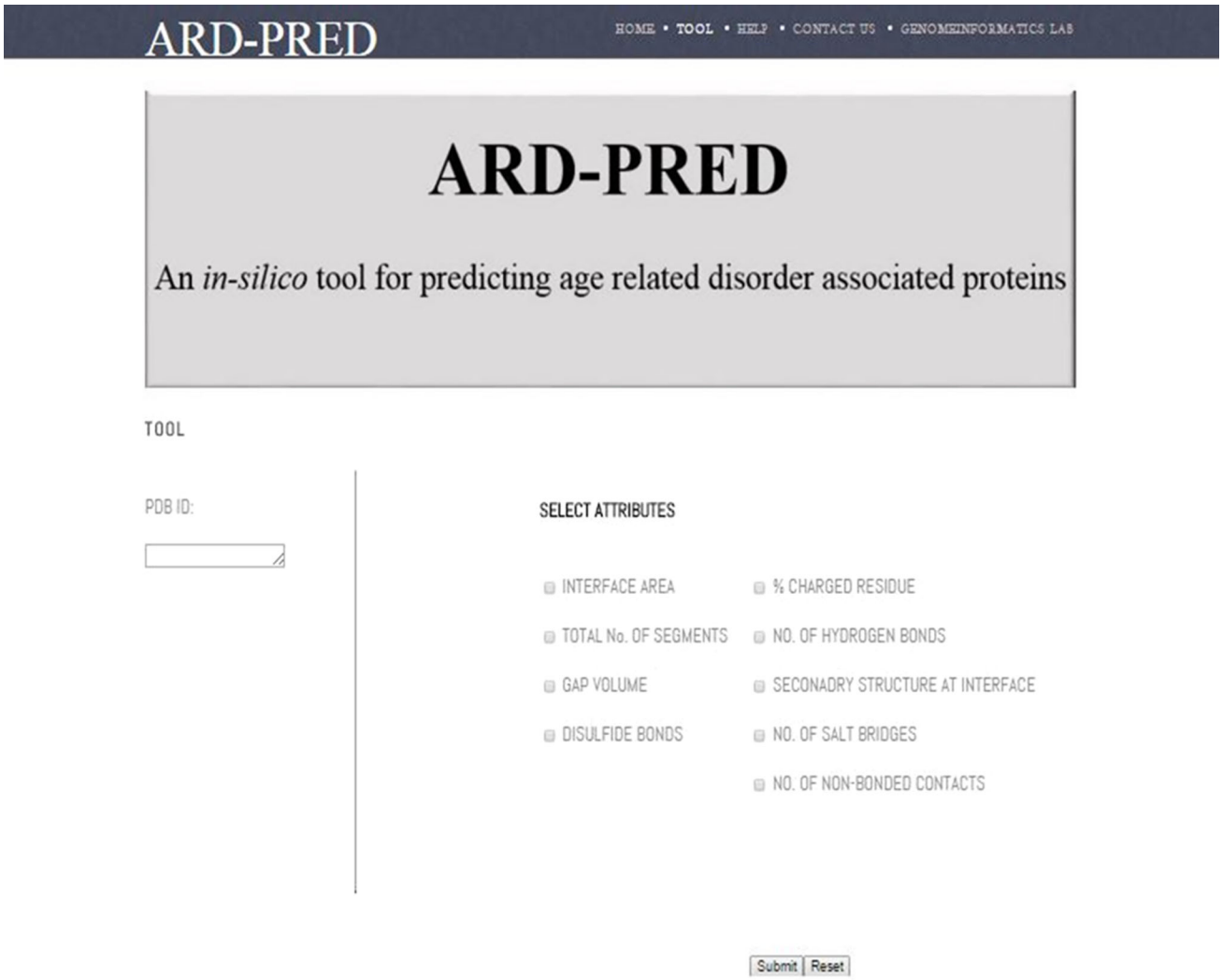


Fig. 3 Tool page of ARD-PRED representing the attributes—interface area, percentage charged residue, gap volume index, number of hydrogen bonds, gap volume, secondary structure interface, disulfide bonds, number of salt bridges

F-measure It is harmonic mean of precision and recall, which reflects average effect of precision and recall (Davis and Goadrich 2006).

Based on the highest value of precision, recall, area under ROC curve, F-measure, the classifier Random Forest was found to perform well and was used to build the final model for predictions. These descriptors were used to form the training and test sample. These files were used as inputs in Weka tool.

3.2 Classification and the prediction analysis

A set of famous algorithms such as Naïve Bayes, Random Forest, J48, Bayesian Network Classifier with iteration 30, bagging with Multilayer Perceptron were run on the dataset, and comparisons were done between them. Various statistical values mentioned above were used to determine the optimum classifier for our training sample. The true positive rate, true negative rate, precision, recall and accuracy—all these scores were highest for Random Forest with iterations 30. In the columns of false positive and in false negative, Random Forest_30 scored the least. Thus, Random Forest was found to be the best classifier in our dataset for model building.

3.3 Prediction probability for the test set

Predictions were made using the test sample to predict all the possible potential ARD-related proteins from a subset of polymorphic proteins. Advanced research of these proteins may provide understanding of molecular mechanisms of various ARDs that are still unknown. List of all the experimented polymorphic proteins along with the prediction probability was obtained. The predicted proteins are not directly involved

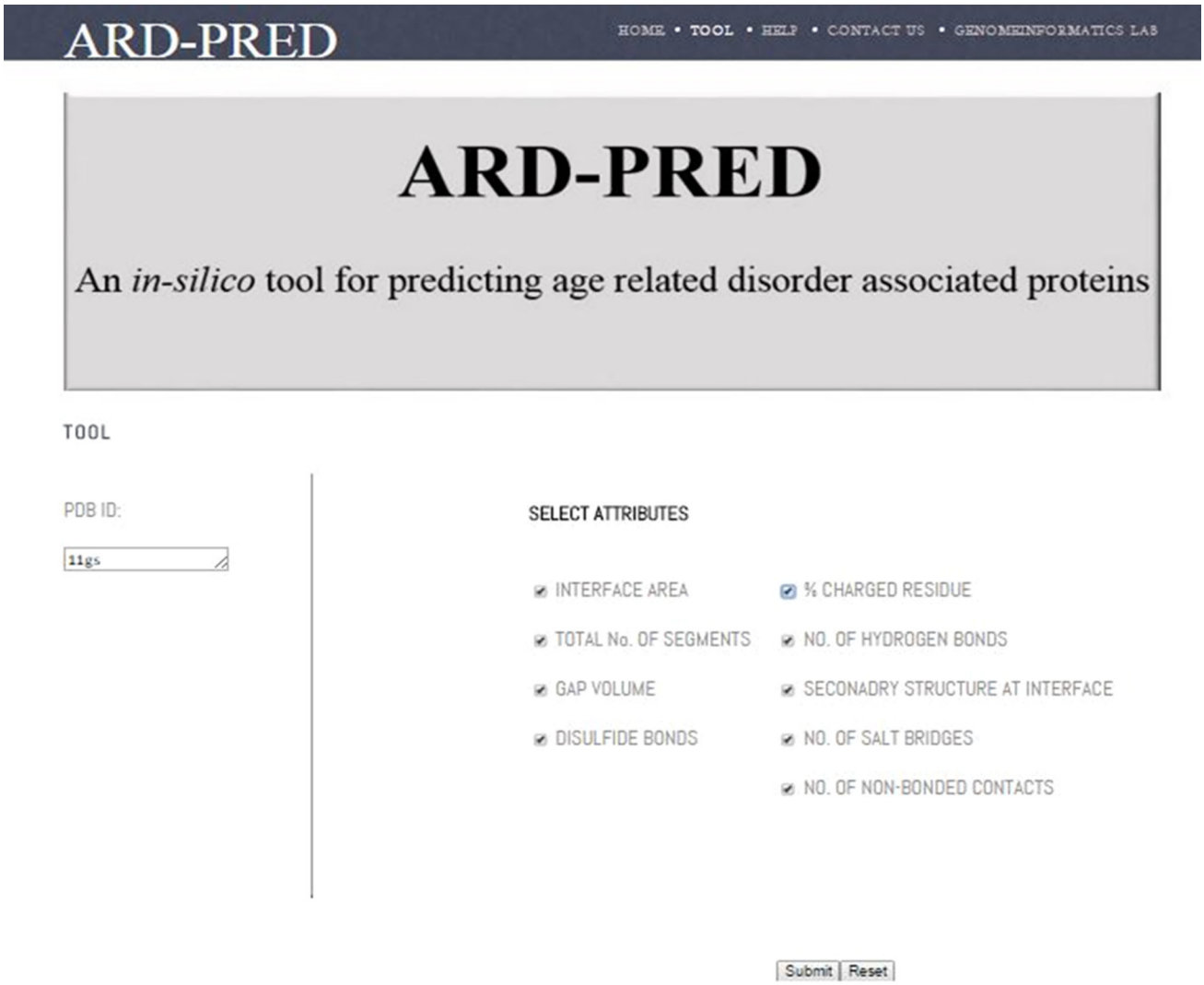


Fig. 4 Example: using PDB-id "11gs" and selecting different attributes to be displayed

in causing ARDs but might be involved in various pathways and mechanisms associated with them.

4 Discussion

The main concern of the study was to present an interface analysis of ARD-related proteins and to shed light on the details of interactions and to emphasize on the importance of using structures in network studies (Kar et al. 2009). These results obtained revealed that the interface properties can be used as descriptors for classifying purposes; be it two different diseases, set of disease having the same phenotypic effect from other set of disease with different phenotypic effect, or for all the known hereditary diseases. The study provided insights into the usage of adequate structural details in disorders related to the age-related system. A further exploration of this study can be utilized to study whether the classifiers would work with equal efficiency when used for classifying all the inherited diseases.

These results can be used as data when searching for candidate gene in predefined disease loci and also for predictions to predict novel genes involved in the mechanisms. Studies have been carried out where sequence features such as cDNA, number of exons and protein size were investigated between a set of genes known to be involved in hereditary disease and those which are not (Lopez-Bigas and Ouzounis 2004; Adie et al. 2006). Functional annotation shared between known disease genes has also been used to design a classifier. The classification based on genomic sequences has drawbacks associated with them. This is because algorithms based on functional annotations are inherently biased toward a particular known set of genes. This present study utilized human PPI network with structural properties to compare genes involved

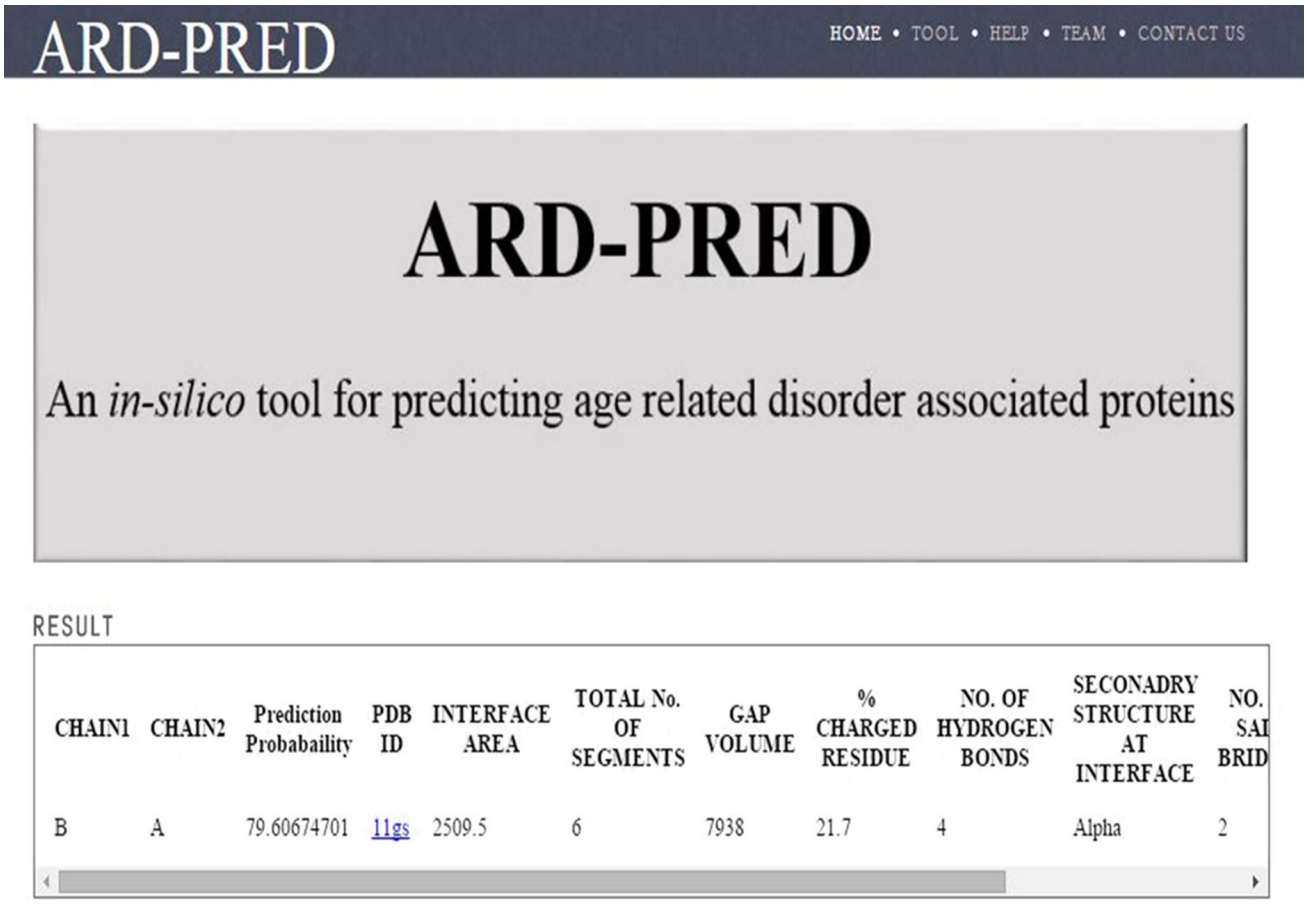


Fig. 5 Result page showing output for PDB-id "11gs" with all mentioned attributes

in genes. It is assumed that structural properties provide a much wider coverage of the understanding of mechanisms of diseases than its sequence analysis. A promising approach for disease gene discovery is to merge all the information available such as PPIs, structures, sequences, transcriptional expression and functional annotations to make a classifier that would possibly predict accurately without any ambiguities (Calvo et al. 2006).

Protein–protein interaction network delivers a vast area of study in which different criteria, and different features can be utilized to devise new diagnostic tools and to understand novel mechanisms. Further, new predictive tools can be made by identification of pathways or disease networks that get activated only in diseases states. For instance, a recent study integrated protein–protein interaction networks with a cancer expression profile and well-identified pathways that get activated during tumor progression. These pathways discriminate metastasis more efficiently than previously studied markers (Gonzalez and Kann 2012). Drug target identification as well as drug design techniques can be made more comprehensive by including disease networks and protein structural details. As an example, structural information on allosteric site or binding site can be used to design the potential drug to affect protein function. Further, it can be used for rebuilding of different interaction networks such as metabolic signaling. Predictions about hub protein can be made which are involved in various pathways for proper functioning of the cell. This information can be used during designing of drugs, i.e., whether to target hub proteins or not. The prediction of ARD-associated genes is of great importance to understand the mechanism behind PPI. Intensive research efforts have been dedicated to classifying proteins, either as disease associated or not associated with a disease. Several bioinformatics approaches have been explored to develop an efficient model for the classification. Machine learning techniques have been applied using different classifiers and various kinds of features/attributes based on protein sequence, structure and binding affinities. All such approaches in machine learning were used to develop the optimal model by exploring the contribution of all attributes for interaction. The precision, recall, accuracy and ROC—all were highest for Random Forest with iterations 30 (the number of trees were increased from 10 to 30) as shown in Table 1 and Fig. 6.

Table 1 The performance parameters of machine learning algorithms

Classifier	Precision	Recall	Accuracy	ROC area	F-measure	True positive	False positive
Naïve Bayes	57.6	57	36	57.4	52.9	57	47
Random Forest	81.5	81.2	79	89.6	81.1	81.2	19.7
Random tree	72.6	72.5	71	72.4	72.5	72.5	27.7
J48	74	74	71	76.6	73.9	74	26.7

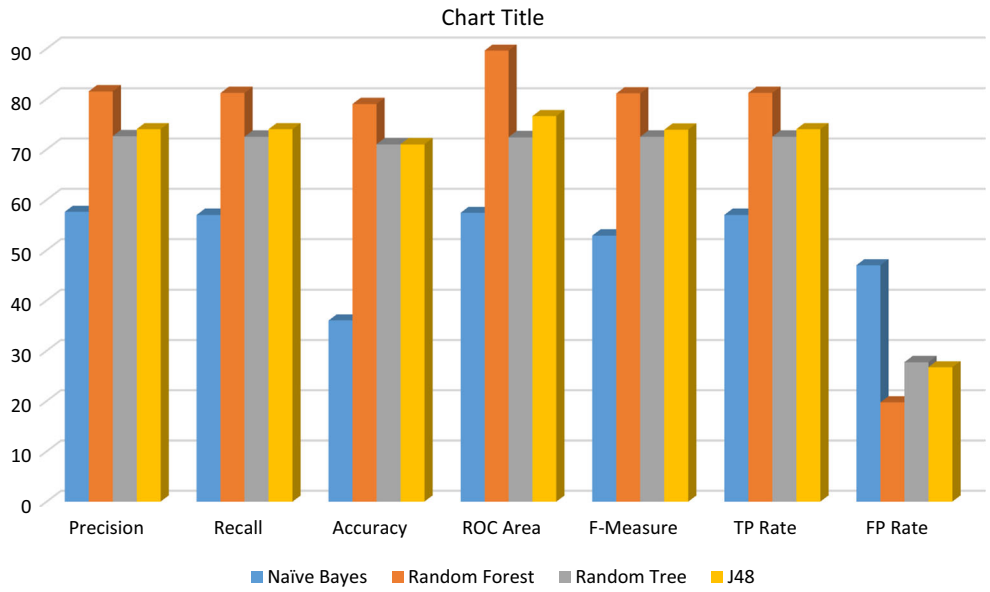


Fig. 6 Bar graph with different classifiers and the statistical values

5 Performance comparison with known disease-protein/gene prediction tool

To compare the performance of the ARD-PRED tool with other machine learning tools for disease-protein/gene prediction, the performance was predicted and compared with one of the known machine learning-based tool AGP tool (Srivastava et al. 2016) for predicting age-related-disorder-associated proteins. Using the training set containing 8729 positive set entries, 10025 negative set entries and employing tenfold cross-validation, we measured the performance of ARD-PRED tool and AGP tool to predict the proteins associated with particular class of age-related disorder in terms of F-measure. Our tool achieved 81.1% F-measure which is 7.5% better than the AGP tool (73.6%).

6 Conclusion

The present study aimed at identifying and differentiating proteins as ARD associated and ARD non-associated based on the interface parameters of the structure involved. It started with genes associated with disease to the structures associated with diseases. The classifier using Random Forest with 30 iterations was used to train based on the training set which included interface properties of proteins associated with ARDs and proteins (with their interacting partners) associated with the diseases other than ARDs. To the best of our web knowledge, there are no prediction servers which are accessible based on interface properties of protein for predicting ARD-associated proteins. In the present study, classifier: Random Forest-based method was used for prediction of ARD-associated proteins with the precision score 81.5, recall score of 81.2, accuracy of 79%, ROC Area score 89.6, F-measure 81.1. The predicted proteins/genes may not be the causing factor of the disease but can be involved in various pathways and mechanisms still unknown to us. Study of these interactions with other proteins can significantly increase our understanding in the molecular mechanism of diseases. Mostly, mutations in proteins affect the structure of proteins. Thus, it became significant to shift the focus from genetic studies to molecular studies. The classifying method has been implemented to develop a web-based tool, ARD-PRED, which is available online at http://genomeinformatics.dtu.ac.in/ARD-PRED/.

Acknowledgements Authors acknowledge Pooja Khurana, Nitin Thukral, Lokesh Kumar Gahlot and Isha Srivastava for their scientific contributions.

Compliance with ethical standards

Conflict of interest The authors declare that they have no conflict of interest.

Ethical approval This article does not contain any studies with human participants or animals performed by any of the authors.

References

Adie EA, Adams RR, Evans KL, Porteous DJ, Pickard BS (2006) SUSPECTS: enabling fast and effective prioritization of positional candidates. Bioinformatics 22(6):773–774. https://doi.org/10.1093/bioinformatics/btk031

Aung Z (2006) Computational analysis of 3D protein structures. Doctoral dissertation, School of Computing, National Institute of Singapore

Basse MJ, Betzi S, Bourgeas R, Bouzidi S, Chetrit B, Hamon V, Morelli X, Roche P (2013) 2P2Idb: a structural database dedicated to orthosteric modulation of protein–protein interactions. Nucleic Acids Res 41:D824–D827. https://doi.org/10.1093/nar/gks1002

Bauer-Mehren Anna, Rautschka Michael, Sanz Ferran, Furlong Laura I (2010) DisGeNET: a cytoscape plugin to visualize, integrate, search and analyze gene-disease networks. Bioinformatics 26(22):2924–6. https://doi.org/10.1093/bioinformatics/btq538

Calvo S, Jain M, Xie X, Sheth SA, Chang B, Goldberger OA, Spinazzola A, Zeviani M, Carr SA, Mootha VK (2006) Systematic identification of human mitochondrial disease genes through integrative genomics. Nat Genet 38(5):576–582. https://doi.org/10.1038/ng1776

Choura M, Rebai A (2011) Structural analysis of hubs in human NRRTK network. Biol Direct 6:49. https://doi.org/10.1186/1745-6150-6-49

Chuang HY, Lee E, Liu YT, Lee D, Ideker T (2007) Network-based classification of breast cancer metastasis. Mol Syst Biol 3:140. https://doi.org/10.1038/msb4100180

Davis J, Goadrich M (2006) The relationship between precision-recall and ROC curves. In: Proceedings of the 23rd international conference on machine learning, Pennsylvania, USA, 2006. ACM, New York, NY

Goh KI, Cusick ME, Valle D, Childs B, Vidal M, Baraba'si AL (2007) The human disease network. Proc Natl Acad Sci 104(21):8685–8690. https://doi.org/10.1073/pnas.0701361104

Gonzalez MW, Kann MG (2012) Protein interactions and disease. PLoS Comput Biol 8(12):e1002819. https://doi.org/10.1371/journal.pcbi.1002819

Hall M, Frank E, Holmes G, Pfahringer B, Reutemann P, Witten IH (2009) The WEKA data mining software: an update SIGKDD explorations. ACM SIGKDD Explor Newsl. https://doi.org/10.1145/1656274.1656278

Hamon V, Brunel JM, Combes S, Basse MJ, Roche P, Morelli X (2013) 2P2Ichem: focused chemical libraries dedicated to orthosteric modulation of protein–protein interactions. MedChemComm 4(5):797–809. https://doi.org/10.1039/C3MD00018D

Jain P, Thukral N, Gahlot LK, Hasija Y (2015) CARDIO-PRED: an *in silico* tool for predicting cardiovascular-disorder associated proteins. Syst Synth Biol 9(1–2):55–66. https://doi.org/10.1007/s11693-015-9164-z

Kann MG (2007) Protein interactions and disease: computational approaches to uncover the etiology of diseases. Brief Bioinf 8(5):333–346. https://doi.org/10.1093/bib/bbm031

Kar G, Gursoy A, Keskin O (2009) Human cancer protein–protein interaction network: a structural perspective. PLoS Comput Biol 5(12):e1000601. https://doi.org/10.1371/journal.pcbi.1000601

Lopez-Bigas N, Ouzounis CA (2004) Genome-wide identification of genes likely to be involved in human genetic disease. Nucleic Acids Res 32(10):3108–3114. https://doi.org/10.1093/nar/gkh605

Magrane M, The UniProt consortium (2011) UniProt knowledgebase: a hub of integrated protein data. Database (Oxford) 2011:bar009. https://doi.org/10.1093/database/bar009

Moreira IS, Fernandes PA, Ramos MJ (2007) Hot spots—a review of the protein–protein interface determinant amino-acid residues. Proteins 68(4):803–812. https://doi.org/10.1002/prot.21396

Mosca R, Ce'ol A, Aloy P (2013) Interactome3D: adding structural details to protein networks. Nat Methods 10(1):47–53. https://doi.org/10.1038/nmeth.2289

Srivastava I, Gahlot LK, Khurana P, Hasija Y (2016) dbAARD and AGP: a computational pipeline for the prediction of genes associated with age related disorders. J Biomed Inf 60:153–61. https://doi.org/10.1016/j.jbi.2016.01.004

Srivastava I, Khurana P, Yadav M, Hasija Y (2017) An integrative system biology approach to unravel potential drug candidates for multiple age related disorders. Biochimica et Biophys Acta (BBA) Proteins Proteomics 1865(12):1729–1738. doi: 10.1016/j.bbapap.2017.07.016

Stark C, Breitkreutz BJ, Reguly T, Boucher L, Breitkreutz A, Tyers M (2006) BioGRID: a general repository for interaction datasets. Nucleic Acids Res 34(suppl 1):D535–D539. https://doi.org/10.1093/nar/gkj109

Wang X, Wei X, Thijssen B, Das J, Lipkin SM, Yu H (2012) Three dimensional reconstruction of protein networks provides insight into human genetic disease. Nat Biotechnol 30(2):159–164. https://doi.org/10.1038/nbt.2106

Zhang KX, Ouellette BF (2011) CAERUS: predicting cancer outcomes using relationship between protein structural information, protein networks, gene expression data, and mutation data. PLoS Comput Biol. https://doi.org/10.1371/journal.pcbi.1001114

ASTM INTERNATIONAL

Geotechnical Testing Journal

S. M. Mahdi Niktabar,[1] K. Seshagiri Rao,[2] and Amit Kumar Shrivastava[3]

DOI: 10.1520/GTJ20170083

Automatic Static and Cyclic Shear Testing Machine under Constant Normal Stiffness Boundary Conditions

Copyright by ASTM Int'l (all rights reserved); Mon Mar 19 00:45:37 EDT 2018
Downloaded/printed by
Delhi College Of Engineering (Delhi College Of Engineering) pursuant to License Agreement. No further reproductions authorized.

Geotechnical Testing Journal

doi:10.1520/GTJ20170083 available online at www.astm.org

S. M. Mahdi Niktabar,[1] K. Seshagiri Rao,[2] and Amit Kumar Shrivastava[3]

Automatic Static and Cyclic Shear Testing Machine under Constant Normal Stiffness Boundary Conditions

Reference

Niktabar, S. M. M., Rao, K. S., and Shrivastava, A. K., "Automatic Static and Cyclic Shear Testing Machine under Constant Normal Stiffness Boundary Conditions," *Geotechnical Testing Journal* https://doi.org/10.1520/GTJ20170083. ISSN 0149-6115

ABSTRACT

Dynamic loads, including earthquake, blasting, and vibration loads, induce cyclic shear loads along the joints in rock masses; hence, the risk of failure increases on the joints due to changing shear resistance. On the other hand, joints are under different boundary conditions: constant normal load (CNL) and constant normal stiffness (CNS). Normal stiffness increases on the joints with increasing depth, and it can affect shear resistance. For an accurate assessment of joint shear resistance under varying normal stiffness and number of cycles, advanced laboratory shear apparatus is essential for the shear test. Conventional direct shear apparatuses have limitations such as boundary conditions, working under monotonic (static) shear loads only, or cyclic shear loads with no change of frequency and amplitude of shear loads. Therefore, a new large-scale servo-controlled direct shear testing machine was developed to conduct cyclic shear test (as well as monotonic shear test) under CNL and CNS boundary conditions with varying normal stiffness at different frequencies and amplitudes of shear loads. In the present study, the cyclic shear tests were conducted on nonplanar joints under varying normal stiffness. Moreover, the effects of different frequencies and amplitudes of shear loads were investigated. The test results indicate that peak shear stress increases with increasing normal stiffness at the first cycle, but the influence of normal stiffness decreases with an increase in the number of shear cycles. The frequency of shear load influences peak shear stress, i.e., peak shear stress increases with increasing frequency. The number of cycles does not affect peak shear stress on the joints at low shear amplitude, but peak shear stress decreases with higher amplitude.

Keywords

shear behavior, shear apparatus, cyclic loads, constant normal stiffness, regular and irregular joints, frequency, amplitude, joint dilation

Manuscript received March 15, 2017; accepted for publication September 22, 2017; published online March 15, 2018.

[1] Department of Civil Engineering, Indian Institute of Technology, Outer Ring Road, Hauz Khas, New Delhi, Delhi 110016, India (Corresponding author), e-mail: mehdiniktabar@yahoo.com, https://orcid.org/0000-0002-1723-3375

[2] Department of Civil Engineering, Indian Institute of Technology, Outer Ring Road, Hauz Khas, New Delhi, Delhi 110016, India

[3] Department of Civil Engineering, Delhi Technological University, Bawana Road, Delhi 110042, India

Copyright by ASTM Int'l (all rights reserved); Mon Mar 19 00:45:37 EDT 2018
Copyright © 2018 by ASTM International, 100 Barr Harbor Drive, PO Box C700, West Conshohocken, PA 19428-2959
Downloaded/printed by
Delhi College Of Engineering (Delhi College Of Engineering) pursuant to License Agreement. No further reproductions authorized.

Need of Study

Rock masses and rock structures are often subjected to expected and unexpected seismic and dynamic loads. Examples of these loads are earthquakes, blasting, vibrations, and traffic loads, which are very necessary for a study on the joints. These loads can be simulated as cyclic shear loads along the joint.

The shear behavior of the joints can be studied under two boundary conditions: constant normal load (CNL), in which the normal load is kept constant, and constant normal stiffness (CNS), in which normal stiffness is kept constant (normal load changes). The suitability of each depends upon the joint roughness and joint dilation condition. The CNS condition is more realistic in simulating field conditions for underground structures and reinforced rock slopes, as compared to the CNL condition. Based on this concept, direct shear equipment has been developed by several researchers. The recent shear apparatuses presented by Indraratna, Haque, and Aziz (1998); Jiang et al. (2004); Kim, Chun, and Yang (2006); and Shrivastava and Rao (2013) are under monotonic shear load and CNS condition. However, a few reports have been presented for the cyclic shear test under CNS condition, such as Homand-Etienne et al. (1999) and Mirzaghorbanali, Nemcik, and Aziz (2014).

Direct shear apparatuses under CNS and monotonic load with the small size of shear box were developed by Obert, Brady, and Schmechel (1976) and Ooi and Carter (1987). Normal stiffness was provided by rods or beams for the apparatuses. The first large-scale direct shear equipment under CNS condition was used by Indraratna, Haque, and Aziz (1998). A set of springs between the sample and normal load provides the CNS condition on the joints, i.e., stiffness of surrounding rock mass simulated by the stiffness of springs. Jiang et al. (2004) and Kim, Chun, and Yang (2006) developed servo-controlled direct shear apparatuses under CNS conditions for the monotonic shear load. The normal load fluctuation is obtained by variation of joint normal displacement and feedback from the servo valve for the equipment presented by Jiang et al. (2004). The second apparatus used by Kim, Chun, and Yang (2006) has limitations for the CNS condition. It can operate under the lowest and highest boundaries of the CNS condition, i.e., $K_n = 0$ and $K_n = \infty$ (infinity). Shrivastava and Rao (2013) developed a direct shear testing machine under the CNS condition. The apparatus is servo controlled, and normal load is changed based on time intervals, dilation, and normal stiffness of surrounding rock joint with prismatic asperity, which was entered as input data.

Most of the shear apparatuses used by researchers for cyclic shear loads were under CNL condition, supervised by Hutson and Dowding (1990), Huang et al. (1993), Lee et al. (2001), and Jafari et al. (2003). Few studies have been carried out under CNS and cyclic shear loads. Homand-Etienne et al. (1999) conducted cyclic shear test under CNL and CNS conditions. The apparatus is not large scale, and amplitude and frequency are presented as constants. Mirzaghorbanali (2013) utilized a cyclic shear apparatus that was an embedded set of springs for stiffness on the joints, the same as shear equipment presented by Indraratna, Haque, and Aziz (1998) for static shear loads under CNS condition. Conducting shear test under varying normal stiffness is required to make springs with specific stiffness and changing springs between normal loads and samples. Moreover, calibration is needed for each spring, separately.

Most direct shear equipment for the cyclic condition has limitations as described: it either works only under CNL or has difficulty conducting a test under varying normal stiffness, frequency, and amplitude of shear loads.

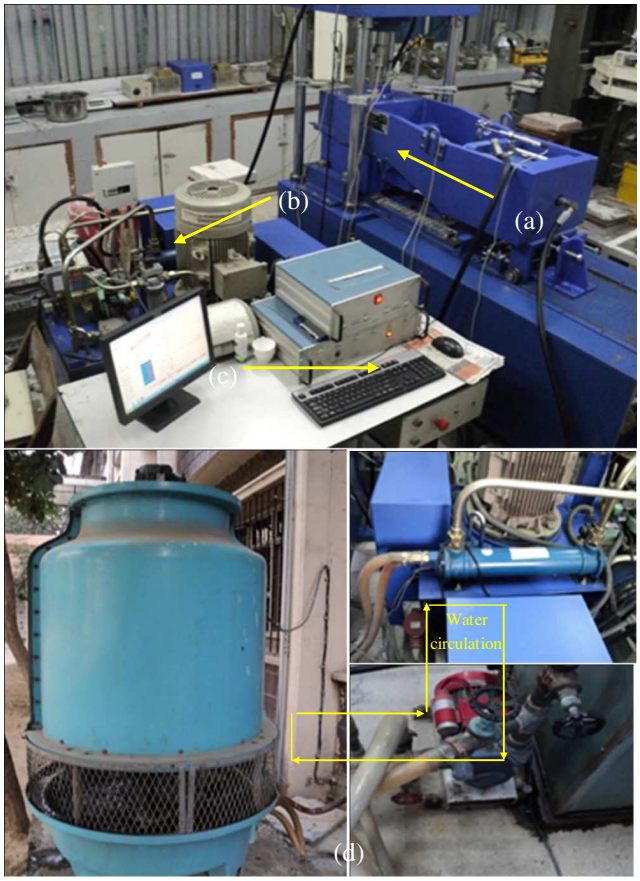
To remove limitations from shear equipment and to achieve simulation of loads and joint conditions, it is essential to develop equipment to conduct cyclic shear tests on jointed rocks under varying normal stiffness, frequency, and amplitude of shear loads. A precise evaluation of shear strength, normal stress, and monitoring of joint deformation during testing will be of immense utility in the analysis, design, and safety of structures in rocks.

Development of Shear Testing Machine for Static and Cyclic Loads

An existing servo-controlled direct shear testing machine designed by Shrivastava and Rao (2013) was modified to conduct monotonic and cyclic shear tests under CNL and CNS boundary conditions. It can work under varying normal stiffness, frequency, and amplitude of cyclic shear loads. The apparatus presented by Shrivastava and Rao (2013) can operate under monotonic shear test, i.e., only one peak stress–strain along the joint can be investigated under these unidirectional or monotonic (static) shear loads. The apparatus is composed of the following three main units: (1) frame and loading unit, (2) data acquisition and controlling unit, and (3) hydraulic power pack with servo valve. The piston as the horizontal transducer can move the lower part of the shear box in the forward direction only. No connection is provided between the head of the horizontal transducer and the shear box for backward movement. Software and other hardware parts of the shear testing machine are also designed or selected for monotonic shear loads, and the results are valuable only for static loads under CNL and CNS conditions. Due to seismic and dynamic loads, the rock joints will be subjected to loading and unloading. Hence, the existing equipment is required to be upgraded to remove the above limitations. Each of three components is removed for a new design and modification. All components of the testing machine are reassembled subsequently and the cooling unit is added to the existing equipment to conduct tests under

Copyright by ASTM Int'l (all rights reserved); Mon Mar 19 00:45:37 EDT 2018
Downloaded/printed by
Delhi College Of Engineering (Delhi College Of Engineering) pursuant to License Agreement. No further reproductions authorized.

FIG. 1 Photograph of shear testing machine. (a) Loading unit, (b) hydraulic power pack with servo valve, (c) data acquisition and controlling unit, and (d) cooling unit (water circulation).



both cyclic and static conditions, as presented in **Fig. 1**. Detailed development of the shear apparatus is explained below.

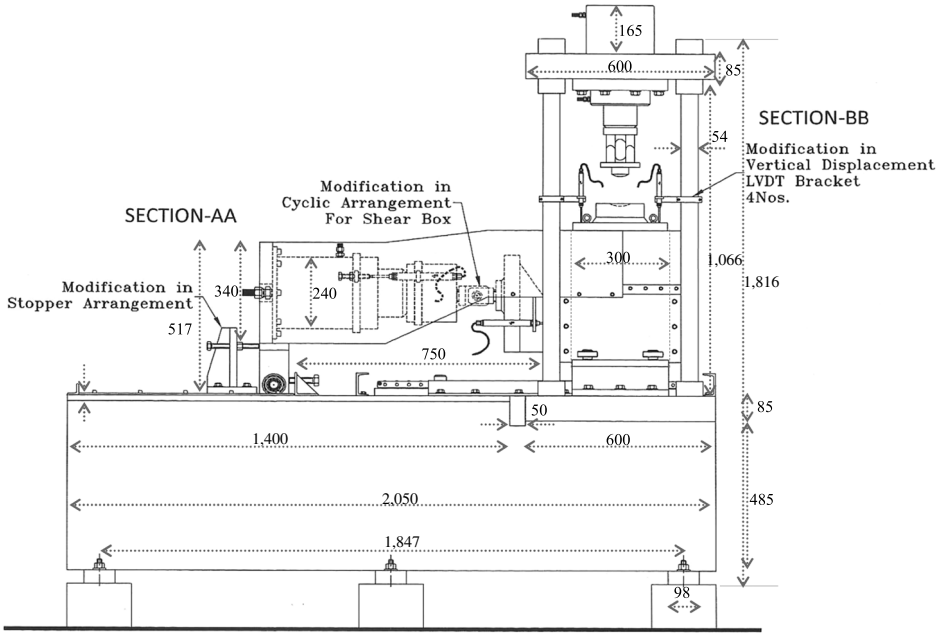
Frame and Loading Unit

This unit consists of upper and lower shear boxes, shear and normal load cells, horizontal and normal displacement measurements, two spacer plates, bottom plates, spherical seating platen, and the hydraulic ram (for loads and unloads the samples), which was already described in detail by Shrivastava and Rao (2013). The modification of this section is presented below and depicted in **Fig. 2**.

CONNECTIONS BETWEEN BOX AND HORIZONTAL TRANSDUCER

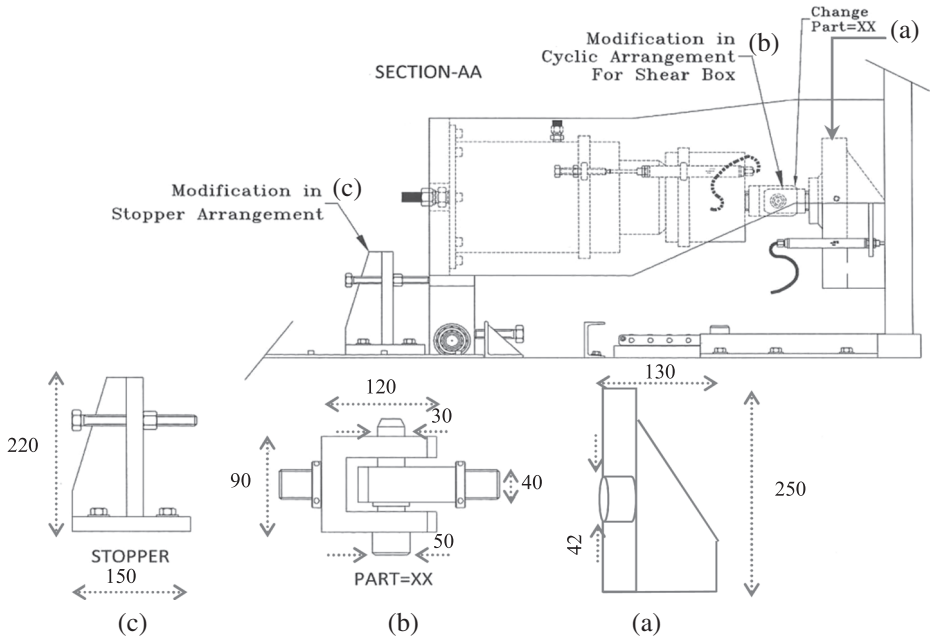
An L-shaped frame in the existing apparatus, which is connected to the lower shear box (due to the piston inserting horizontal pressure and the lower shear box moving in the forward direction only), is removed from the box, and a new frame (**Fig. 3a**) is embedded with the proper horizontal hole on the center of the frame, as shown in **Fig. 3**. A permanent connection between the piston and the lower shear box is designed and made (**Fig. 3b**) subsequently. The upper shear box is fixed, and the lower shear box is placed on two bearings that can move horizontally both forwards and backwards without any vertical displacement. Due to the prevention of any movement of the horizontal frame and disturbing deformation of linear variation displacement transducers (LVDTs), a stopper (**Fig. 3c**) is designed and

FIG. 2
Schematic diagram of loading unit (all dimensions are mm).



Copyright by ASTM Int'l (all rights reserved); Mon Mar 19 00:45:37 EDT 2018
Downloaded/printed by
Delhi College Of Engineering (Delhi College Of Engineering) pursuant to License Agreement. No further reproductions authorized.

FIG. 3
Section AA from horizontal load (all dimensions are mm).

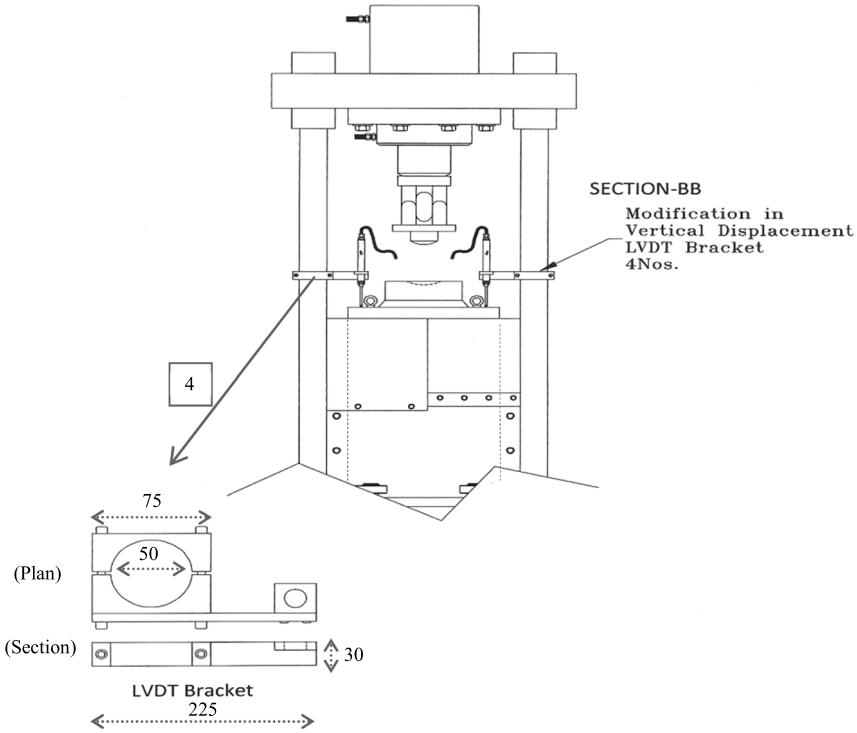


fabricated to keep the frame fixed during cyclic shear test, as illustrated in **Fig. 3**. This stopper is fixed by the bolts during the shear test, and it can be removed while unloading samples from the shear box.

LOAD CELLS AND LVDTs

The apparatus consists of two separate actuator cells: normal load and shear load. The normal load cell is kept without modification, whereas the shear load cell is developed to move under both static

FIG. 4
Section BB from vertical load (all dimensions are mm).



Copyright by ASTM Int'l (all rights reserved); Mon Mar 19 00:45:37 EDT 2018
Downloaded/printed by
Delhi College Of Engineering (Delhi College Of Engineering) pursuant to License Agreement. No further reproductions authorized.

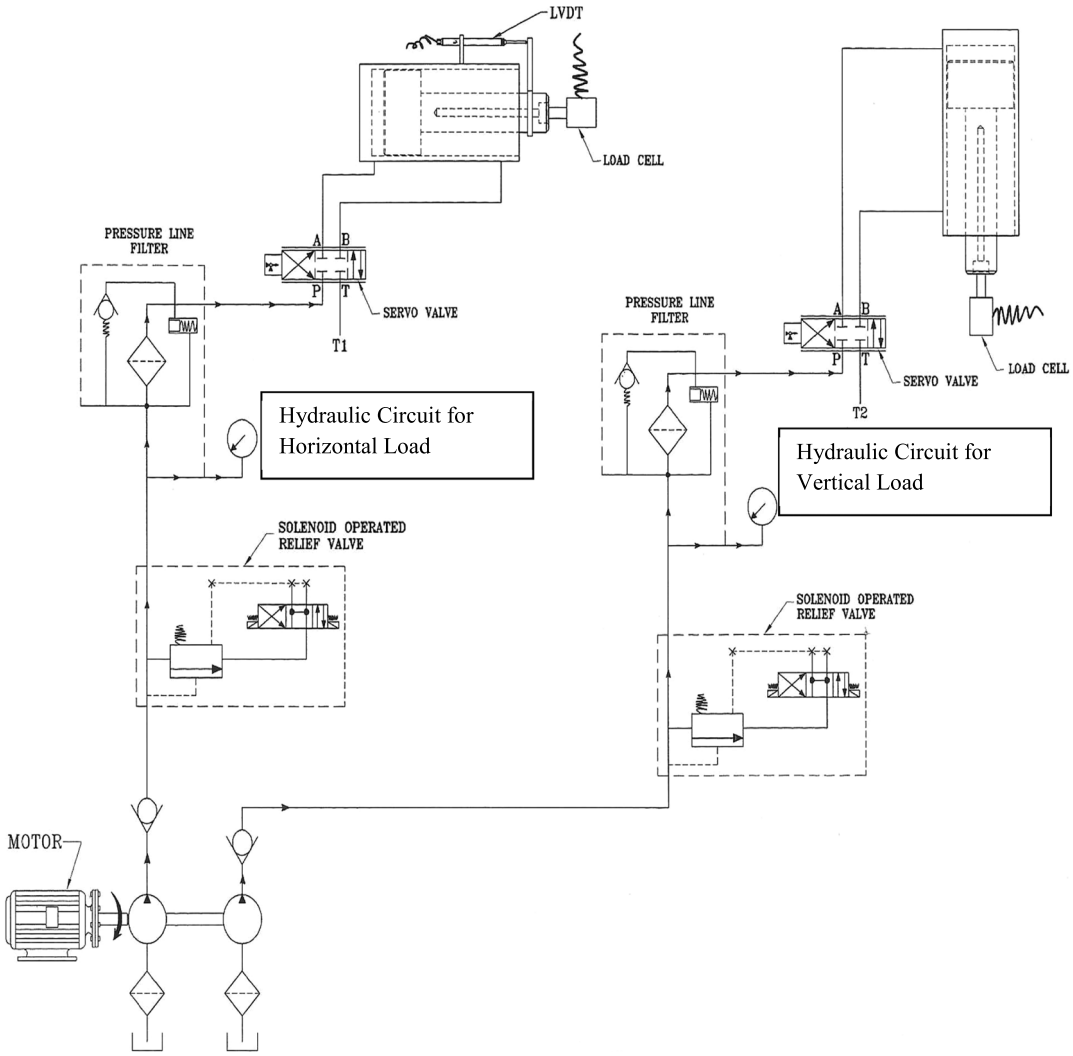
and cyclic conditions. Maximum capacity of normal and horizontal load cells is 500 kN and 1,000 kN, respectively. Actuators of the direct shear system can be active on either a stress or strain basis.

Joint deformations can be measured by six LVDTs. Horizontal and normal displacements are monitored and captured through LVDTs. Two LVDTs are used to measure the displacement of shear load (forward or backward movements). One LVDT is for measuring horizontal piston movement, and the other is used for shear box displacement. Four LVDTs are appropriate for measuring normal displacement. Dilation and compression of joints can be measured by these types of LVDTs. The position of LVDTs due to modification of the shear testing machine and the sensitivity of this device is changed and embedded into vertical columns of normal load (4), i.e., new frames are designed and fabricated for normal LVDT attachment, as indicated in **Fig. 4**.

Hydraulic Power Pack with Electrohydraulic Servo Valve

The hydraulic power pack supplies sufficient flow and pressure of oil from the oil tank for the activation of the actuators. The double vane–type pump is powered by a three-phase motor. The electrohydraulic servo valve is the significant part, and it is an electrically operated valve that controls the flow of the hydraulic fluid to the actuator. A new electrohydraulic servo valve (G761 Series with a flow of 20 LPM) is embedded on the hydraulic power pack to provide sufficient flow and pressure of the horizontal load under cyclic or dynamic conditions. In order to select the appropriate servo valve, particular selection application and criteria, which are flow and dynamic responses, are required. The servo-control valve is a throttle valve for four-way applications. It is a two-stage valve that is suitable to a pressure drop of 1,000 psi (70 kg/cm^2). The output stage is a

FIG. 5 Hydraulic circuit diagram for servo-controlled direct shear apparatus under cyclic/static loads.



Copyright by ASTM Int'l (all rights reserved); Mon Mar 19 00:45:37 EDT 2018
Downloaded/printed by
Delhi College Of Engineering (Delhi College Of Engineering) pursuant to License Agreement. No further reproductions authorized.

closed center with a four-way sliding spool. This valve enjoys high performance and high speed and is extensively used in cyclic applications. The servo-hydraulic cyclic/static actuator is based on the servo-hydraulic closed loop principle, and it is extensively used for applying cyclic/static loads or displacements for different applications. A map of the hydraulic circuit of the shear testing machine for horizontal and vertical loads is presented in **Fig. 5**.

Data Acquisition and Controlling Unit

The central processing unit (CPU) was replaced, and a new CPU, which is a high-speed processor, is connected to a shear apparatus; the new software is installed on the processor. The software has two modes of shearing: static (monotonic) and cyclic shearing. Based on the mode of shearing, parameters are different. In the static shear mode, the parameters are inserted as input data into the direct shear software, such as the rate of loading, initial normal load, and normal stiffness of the surrounding rock mass. In the cyclic mode, the parameters as input data are wave type, frequency, amplitude, base, number of cycles, normal stiffness, and initial normal load. For both static and cyclic conditions, all LVDTs and the shear load must initially be zero. The software also has the facility to collect data automatically during shearing. The control mode is defined under a stress or strain basis. It consists of two dedicated servo-controller cards that give the desired processed signal through the two different proportional integral derivative controllers to the servo valve to operate in stress or strain mode. It also sends the signal to the computer and accepts the command from the software to operate in the desired manner. A wave generator and data acquisition cards are connected to the CPU to control the machine and acquire data through various sensors. The wave generator card can generate sine, triangular, and square waveforms along with the ramp signal. The software is Windows based and programmable under both static and cyclic conditions. The programming facility is given to operate the horizontal actuator in a static mode at the programmed rate of loading in both load and displacement controls. In the cyclic mode, the horizontal transducer can operate in a range of frequencies from 0.01 to 5 Hz under varying amplitudes (from ±1 mm to ±20 mm). Input data such as normal load, waveforms, normal stiffness, frequency, amplitude, and number of cycles can also be fed through computer software based on the capability of the testing machine, as presented in **Table 1**. This software works with the online display of readings such as shear load, normal load, and horizontal load as well as the online display graph of shearing load versus horizontal displacement (or versus time) during the shear test.

Eqs 1 and 2 are programmed into the direct shear software to conduct the shear test under different boundary conditions.

$$\text{If } \Delta Y > 0, \text{ then} \quad P_n = P_i + K_n(\Delta Y) \tag{1}$$

$$\text{otherwise } (\Delta Y \le 0), \quad P_n = P_i \tag{2}$$

where:

P_n = normal stress,
P_i = initial normal stress,
K_n = normal stiffness, and
ΔY = dilation resisted by surrounding rock mass.

If dilation ($\Delta Y > 0$) occurs during shear, normal stress can change based on Eq 1 under CNS; otherwise, compression is dominant ($\Delta Y \le 0$), and normal stress is equal to initial normal stress, i.e., $P_n = P_i$ (because overburden is constant on the joint, normal stress will be equal to at least the initial normal stress).

Cooling Unit

The large-scale direct shear testing machine provides loads for static and cyclic tests from the hydraulic power pack. The complex testing unit produces a high temperature during the testing. To avoid damaging the testing machine, a cutoff temperature is set at 50°C. The cooling system is designed to reduce the heat of the hydraulic power pack, as indicated in **Fig. 6**. It maintains the temperature lower than 50°C. It is very effective for the cyclic condition due to having many cycles and a long time period. The oil

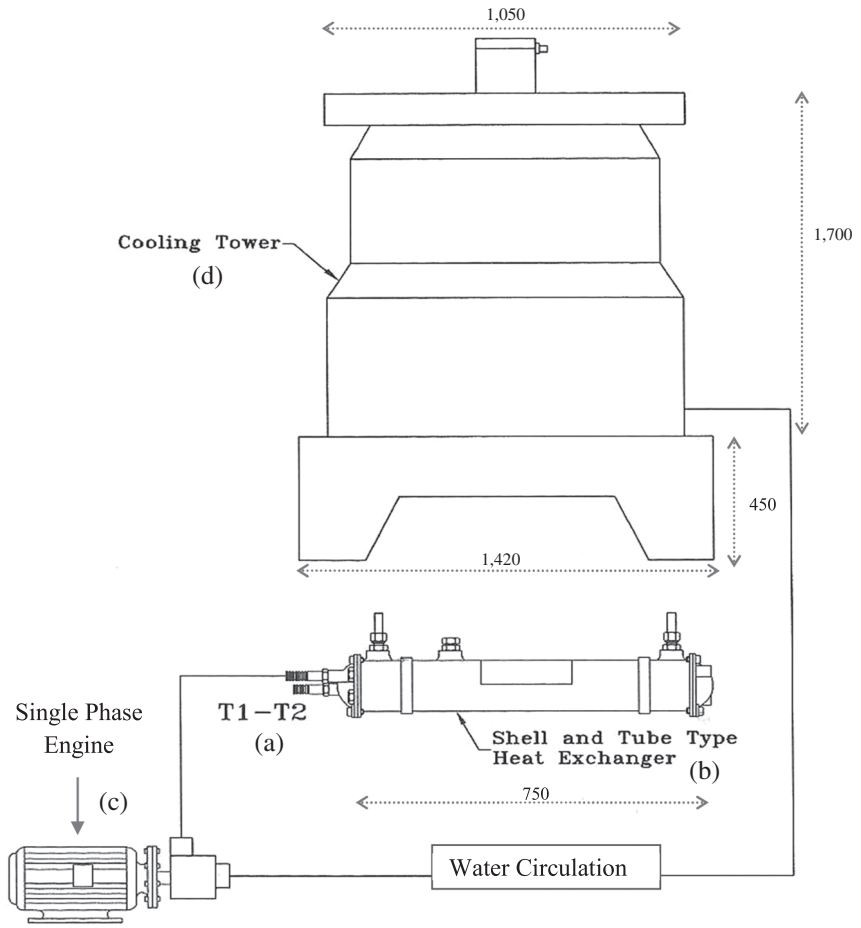
TABLE 1 Capability of shear testing machine under static and cyclic loads.

No.	Parameter	Minimum	Maximum	Unit
1	Initial Normal Load	0	500	kN
2	Horizontal Load	0	1,000	kN
3	Size of Shear Box	300 by 300 by 125	300 by 300 by 448	mm
4	Frequency	0.01	5	Hz
5	Amplitude	±1	±20	mm
6	Normal Stiffness	0	500	kN/mm
7	Wave Form	–	four wave*	–
8	Number of cycle	1	1,000	–

Note: *Including sine, triangular, and square waveforms and ramp signal.

Copyright by ASTM Int'l (all rights reserved); Mon Mar 19 00:45:37 EDT 2018
Downloaded/printed by
Delhi College Of Engineering (Delhi College Of Engineering) pursuant to License Agreement. No further reproductions authorized.

FIG. 6
Schematic diagram of cooling unit (all dimensions are mm).



gets heated during operation, and the cooling system can provide cooling to the oil and keep it below 50°C to avoid damaging the servo valves and electronic parts fitted in the hydraulic power pack.

Water circulation is selected to reduce the heat. Two pipes (**Fig. 6a**) and one single phase pump engine (**Fig. 6c**) circulate water into the hydraulic power pack (shell and tube type heat exchanger [**Fig. 6b**]) and decrease the heat. The hot water flows into the cooling tower. The cooling tower (**Fig. 6d**), as shown in **Fig. 6**, is separate equipment for decreasing the temperature of returned hot water from the hydraulic power pack. This system has a mechanical rotary sprinkler placed above the cooling tower. The water pressure rotates the sprinkler and disperses water over the fill media. During operations, the fan attached to the single phase motor takes the heat away from the water by an induced draft mechanism. Finally, the cold water is collected at the collection sump, and it is recirculated into the hydraulic power pack.

Calibration

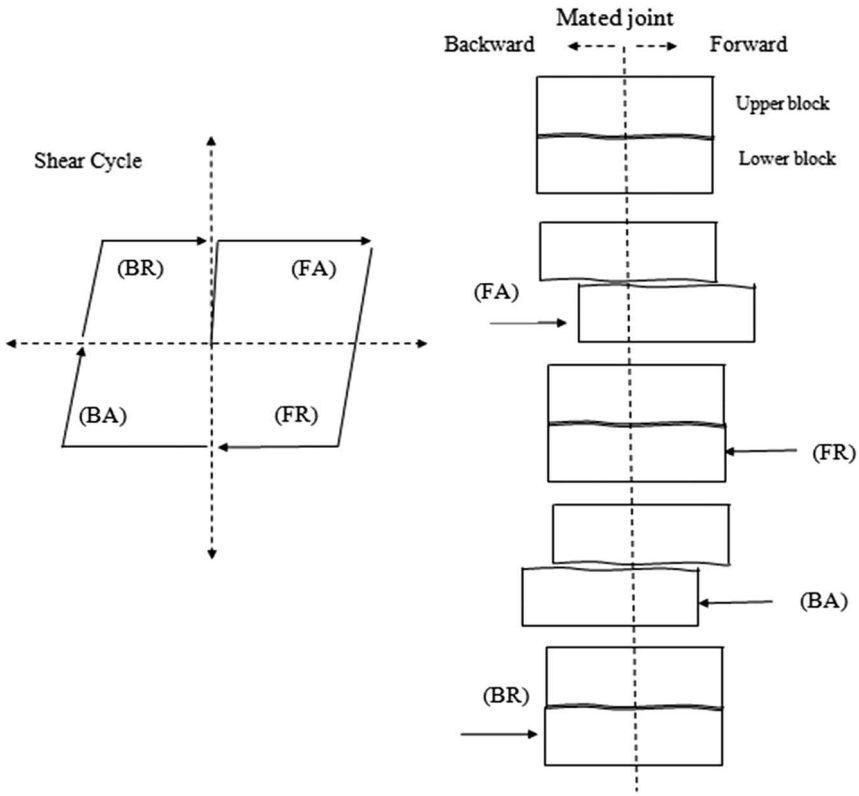
The horizontal load is modified in such a way that it can move under cyclic load with the following four stages: forward advance (FA), forward return (FR), backward advance (BA), and backward return (BR), as shown in **Fig. 7**. The static and cyclic shear testing machine is calibrated before the start of the experiment. Calibrations are done for all load cells and LVDTs. Shear and normal load cells are calibrated by proving rings, as per Indian Standard IS 1828 (Part 1) (2005), *Metallic Materials—Verification of Static Uniaxial Testing Machines, Tension/Compression Testing Machines—Verification and Calibration of the Force-Measuring System*, and the percentage error was found within permissible limits; also, six LVDTs are calibrated separately by external micrometer, and the percentage error was within permissible limits. In addition, the calibration of the horizontal load cell is cross checked by conducting a cyclic shear test on the planar joint, and it is found that forward and backward loads are the same.

Selection Model Material

Preparation of large-scale natural jointed rocks with the same joint roughness is very difficult; hence, plaster of paris was selected as the material, so as to have reproducibility and same-jointed samples. Moreover, it is desired for casting and making jointed samples with any asperity shape.

Copyright by ASTM Int'l (all rights reserved); Mon Mar 19 00:45:37 EDT 2018
Downloaded/printed by
Delhi College Of Engineering (Delhi College Of Engineering) pursuant to License Agreement. No further reproductions authorized.

FIG. 7
Load directions and joint movements under shear cyclic condition. FA, forward advance; FR, forward return; BA, backward advance; BR, backward return.



To prepare intact samples, several types of plaster of paris with different powder and water ratios were tested, and finally, the selected 0.6 ratio was based on the strength to simulate soft rock and have better workability of the paste. Mechanical properties of the model material are presented in **Table 1**. As per ISRM (International Society for Rock Mechanics) (1981), it can be classified as weak rock, like chalk, claystone, potash, marl, siltstone, shale, and rock salt. A cylindrical mold with 76-mm height and 38-mm diameter was utilized. Plaster of paris and water with prescribed ratios were mixed and poured into the mold, and vibration for a few seconds removed any trapped air from the paste. The samples could be removed from the mold after 40 min and cured in free space at room temperature. Length/diameter ratio of the removed specimen is 2, which is appropriate for an unconfined compressive strength test after 2 weeks. Mechanical properties of the model material are useful for the interpretation of test results.

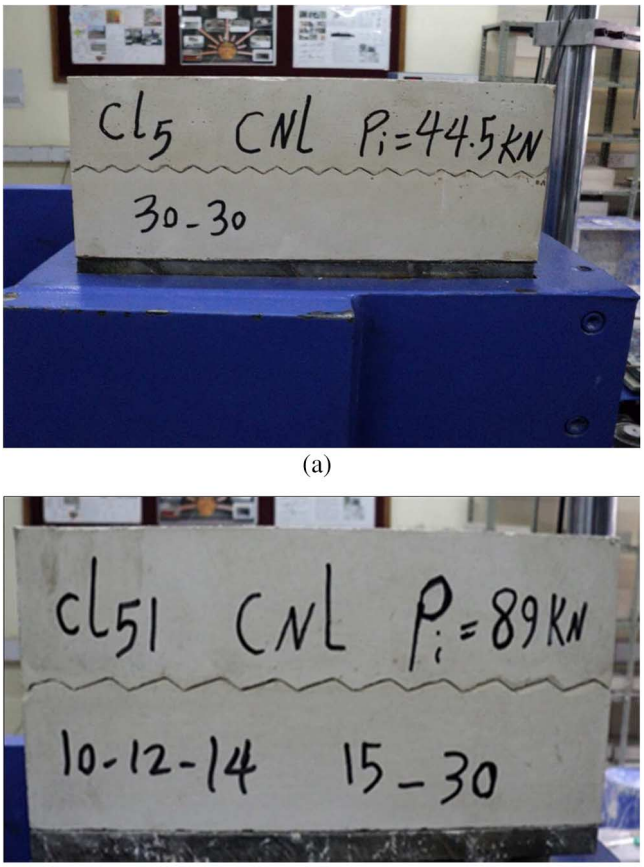
Preparation of Specimens

One pair of the mold is arranged, and one deserved set of asperity plate was put inside the mold in such a way that asperities were placed upward; the mold was kept on the vibration table by bolts. Thus, one jointed sample or both lower and upper parts of the sample could be fabricated simultaneously. The process of sample preparation is the same for regular and irregular joints; only different asperity plates are used to prepare joints with different roughness.

The liquid release chemical is applied on both of the molds and asperity plates to remove the sample without breakage of asperities. The water-to-powder ratio is kept constant for all of the samples, and they were mixed properly by the mixer. To remove air bubbles trapped in the paste, they were vibrated for 30 s. Final setting time of the plaster of paris with 0.6 water-to-powder ratio was 50 min. Two parts of the sample were removed from the molds and placed separately in proper conditions in such a way that the asperities were in an upward position. Regular (30°–30° joint asperity) and irregular (15°–30° joint asperity) samples were prepared as demonstrated in **Fig. 8**. The samples were kept at room temperature for at least 14 days for air curing. In the present work, a few natural rock specimens were prepared by tensile splitting from a huge slab of Jodhpur sandstone. This type of rock joint is represented in **Fig. 9**. The size of the samples is 299 by 299 by 125 mm (length by width by thickness), and the ratio between length and thickness was kept in accordance with the guidelines of ASTM D5607-02, *Standard Test Method for Performing Laboratory Direct Shear Strength Tests of Rock Specimens under Constant Normal Force*.

Copyright by ASTM Int'l (all rights reserved); Mon Mar 19 00:45:37 EDT 2018
Downloaded/printed by
Delhi College Of Engineering (Delhi College Of Engineering) pursuant to License Agreement. No further reproductions authorized.

FIG. 8 Photograph of (a) regular and (b) irregular jointed samples.



(a)

(b)

FIG. 9 Photograph of natural jointed rock.



Experimental Results

The developed shear testing machine has the extensive capability for varying shear tests (static and cyclic), as presented in **Table 1**. Static or monotonic shear tests were conducted on large, intact samples (model material) by the shear testing machine, and the results are depicted in **Fig. 10**. The machine is useful for the calculation of some mechanical parameters (C and $\emptyset$) of the model material, as represented in **Table 2**. The other parameters were measured based on ISRM (1979). In the present study, the influence of the number of cycles and boundary conditions (CNL and CNS) were investigated on the shear behavior of rock joints with regular and irregular asperities; moreover, the effects of frequency and amplitude of shear loads are discussed. The effect of increasing normal stress (P_i) on the joints was studied by Niktabar, Rao, and Shrivastava (2015, 2016a, 2016b). In the present study, cyclic shear tests were conducted on the joints under varying normal stiffness ($K_n = 0$, 32, and 64 kN/mm). To study the effect of normal stiffness, low initial normal stresses were selected (0.1 and 0.5 MPa), i.e., there is no difference between CNL and CNS at high initial normal stress, as described by Shrivastava (2012) and Shrivastava and Rao (2013). This is due to the lack of dilation on the joints. The frequency and amplitude of shear loads were set to constant values, 0.01 Hz and ±8 mm, respectively, for the tests. Each specimen was tested on 30 shear cycles with sinusoidal waveform.

Cyclic Behavior of Joints under Different Normal Stiffness

In order to conduct the cyclic shear test, input data such as the value of normal stiffness, initial normal load, waveform, number of cycles, frequency, and amplitude of loads were fed into the software. The sample was loaded into the shear box and the horizontal frame was fixed properly by the stopper. Six LVDTs were installed, and the cooling unit was operated. The shear testing machine and software run consecutively. Data were saved automatically during the test, and the apparatus stopped after finishing the number of cycles. In cyclic shear tests, shear stress, dilation, and normal stress variation are discussed in detail. Joints in underground structures and reinforced slopes are under CNS boundary condition. With increasing the depth, the normal stiffness of the joints increases, according to Jiang et al. (2009). In order to observe the effect of normal stiffness under cyclic loads, laboratory cyclic shear tests are conducted on regular and irregular joints for different normal stiffness. The behavior of the joints under CNL and CNS is studied in the following part.

SHEAR BEHAVIOR OF REGULAR JOINT (30°–30° JOINT ASPERITY)

The test results are plotted for 30°–30° joint asperity. Shear stress of the joint versus horizontal displacement at different normal stiffness values, $K_n = 0$ (CNL) and $K_n = 64$ kN/mm (CNS), are presented in **Fig. 11a** and **11c**, and **Fig. 12a** and **12c**, respectively. Peak shear stress decreased with increasing the number of shear cycles. This is because of a decrease in the asperity angle or

Copyright by ASTM Int'l (all rights reserved); Mon Mar 19 00:45:37 EDT 2018
Downloaded/printed by
Delhi College Of Engineering (Delhi College Of Engineering) pursuant to License Agreement. No further reproductions authorized.

FIG. 10 Shear stress versus horizontal displacement (a, b, c) and normal displacement versus horizontal displacement (d, e, f) for intact samples at three different normal stresses, 0.1, 0.5, and 1 MPa, respectively, under CNL and static load.

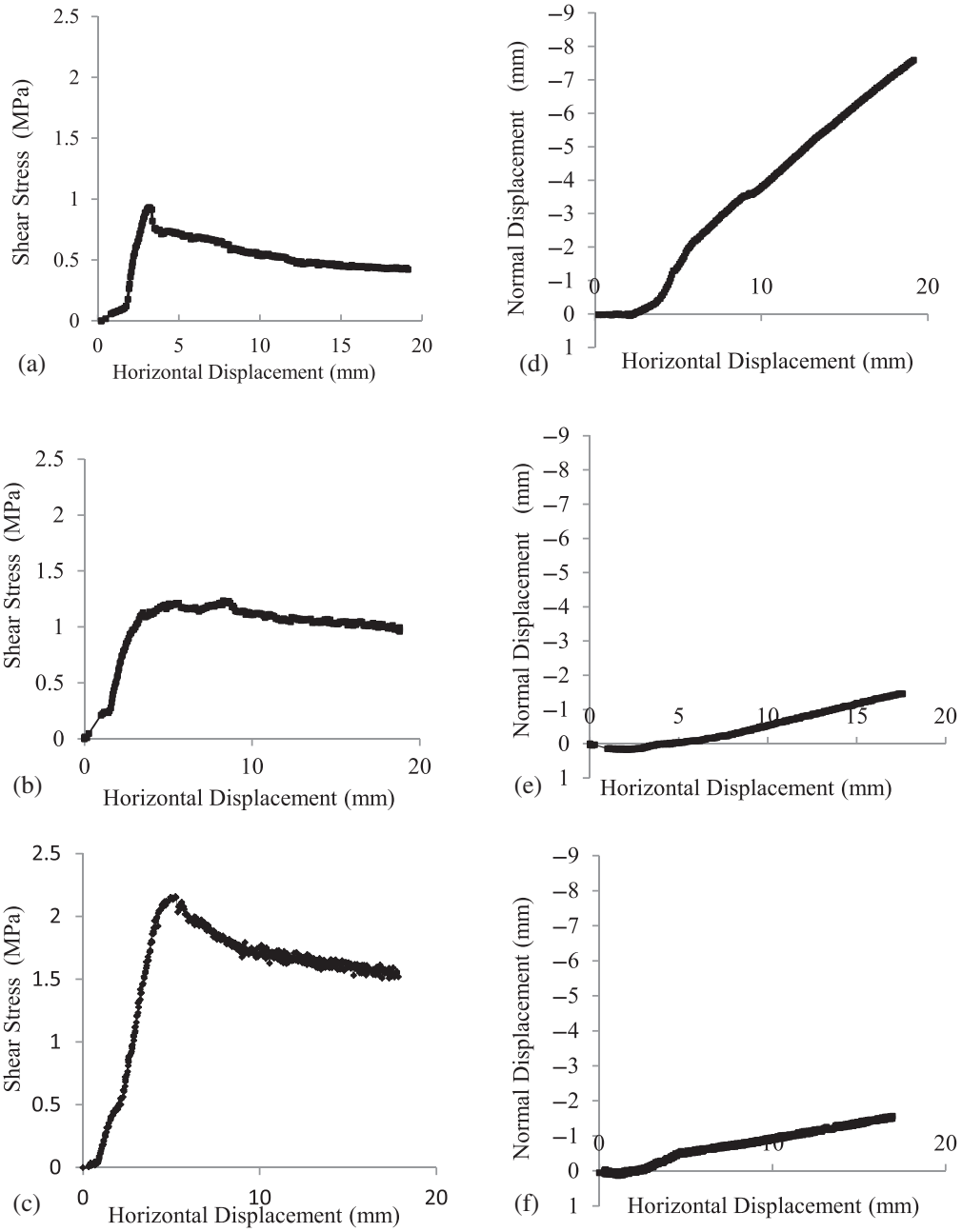


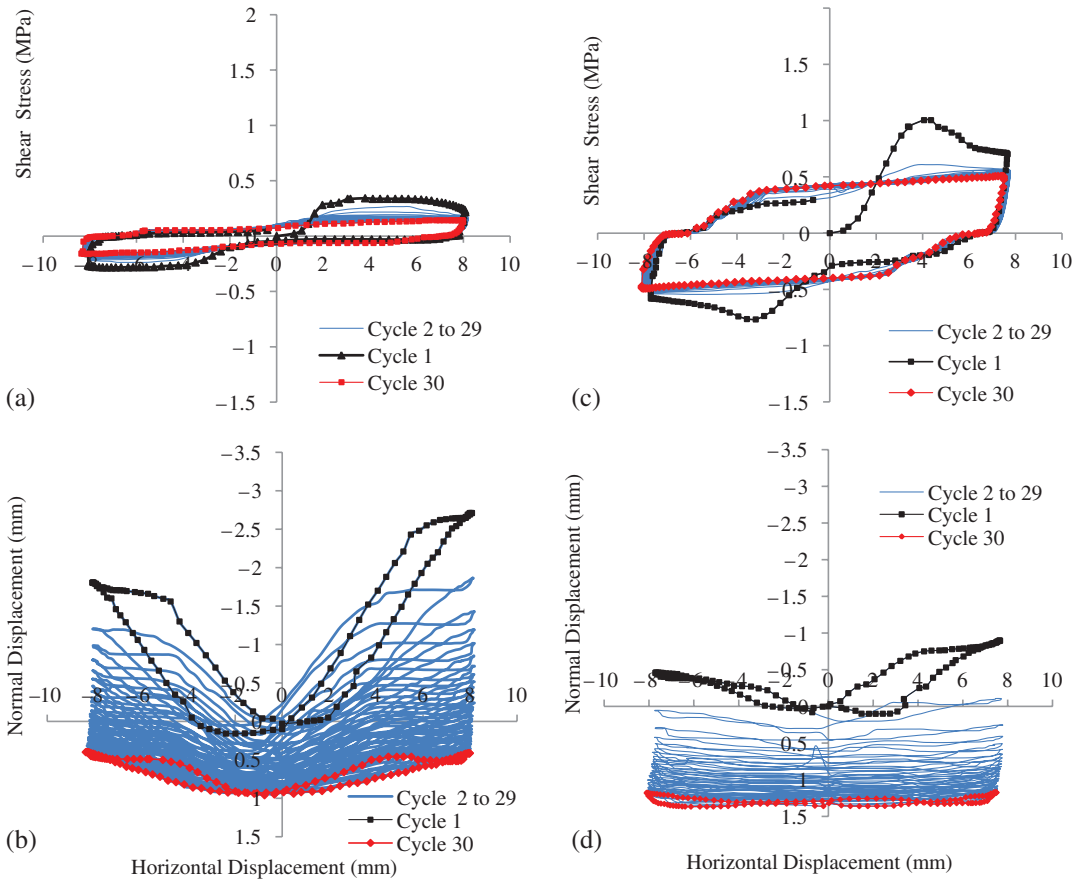
TABLE 2 Mechanical properties of the model material (plaster of paris).

No.	Parameter of Intact Sample	(Value)
1	uniaxial compressive strength (MPa)	6
2	tangent modulus, E_{t50} (MPa)	2,447.2
3	Poisson ratio	0.23
4	cohesion, C (MPa)	0.72
5	internal friction, Ø	51.3

diminishing of asperities (because dilation angle decreased with increasing the number of shear cycles, as presented in **Fig. 11b** and **11d**, this can show the joint degradation). As the normal stiffness (K_n) or initial normal stress (P_i) increases, the difference of peak shear stress between the first cycle and the subsequent cycles is increased significantly, which is clear by comparing **Fig. 11a** and **Fig. 12a** or **Fig. 11a** and **Fig. 11c**. The shear stress behavior is changed from elastoplastic to increasing gradually when normal stiffness value increases from $k_n = 0$ kN/mm to $k_n = 64$ kN/mm for initial

Copyright by ASTM Int'l (all rights reserved); Mon Mar 19 00:45:37 EDT 2018
Downloaded/printed by
Delhi College Of Engineering (Delhi College Of Engineering) pursuant to License Agreement. No further reproductions authorized.

FIG. 11 Shear stress and normal displacement versus horizontal displacement on 30°–30° asperity joint at 0.1 MPa (a, b) and 0.5 MPa (c, d), respectively, under CNL (K_n = 0) and cyclic shear load.



shear cycles. First, peak shear stress of the joint increases with raising normal stiffness; it is 206 % for $k_n = 64$ kN/mm (**Fig. 12a**) as compared to $k_n = 0$ kN/mm (**Fig. 11a**) under the same P_i. With increasing the number of cycles, the difference of peak shear stress between CNL and CNS decreases, as presented in **Table 3**.

DILATION AND NORMAL STRESS BEHAVIORS OF REGULAR JOINT (30°–30° JOINT ASPERITY)

Normal displacement of the joint versus horizontal displacement at different normal stiffness values or $K_n = 0$ and 64 kN/mm are presented in **Fig. 11b** and **11d**, and **Fig. 12b** and **12d**, respectively. The dilation angle (slope of normal displacement versus horizontal displacement curve) and the peak dilation of the joint have decreased gradually with increasing the number of cycles, as demonstrated in **Figs. 11b**, **11d**, **12b**, and **12e**. Normal stress is kept constant by shear testing machine during shear cycles under CNL ($K_n = 0$ kN/mm) boundary condition, whereas normal stress is changed under CNS condition. Normal stress versus horizontal displacement under CNS ($K_n = 64$ kN/mm) is indicated in **Fig. 12c** and **12f**. With increasing normal stiffness, normal stress increases at initial cycles. The first peak normal stress is multiplied six times over under CNS condition ($K_n = 64$ kN/mm) with respect to initial normal load or $P_i = 0.1$ MPa (**Fig. 12c**). However, the peak normal stress is multiplied almost two times over only for $P_i = 0.5$ MPa, as shown in **Fig. 12f**. Due to the increase in normal stress under CNS condition, peak shear stress increases with respect to CNL condition. This phenomenon was observed in few cycles or at initial cycles, and normal stress remained constant or equal to P_i for subsequent cycles (there was no difference between CNL and CNS for normal stress after several shear cycles). Normal stress for the number of shear tests was observed less than P_i after a few cycles in the studies of Mirzaghorbanali (2013) and Mirzaghorbanali, Nemcik, and Aziz (2014). The minimum normal stress must be equal to P_i, because overburden is constant (it is equal to P_i in the present study). There are no data or graph provided for the variation of normal stress under CNS condition in the study of Homand-Etienne et al. (1999). This might be due to the lack of a measurement device for capturing variation of normal stress in the shear apparatus.

Copyright by ASTM Int'l (all rights reserved); Mon Mar 19 00:45:37 EDT 2018
Downloaded/printed by
Delhi College Of Engineering (Delhi College Of Engineering) pursuant to License Agreement. No further reproductions authorized.

FIG. 12 Shear stress, normal displacement, and normal stress versus horizontal displacement of joint asperity 30°–30° at P_i = 0.1 MPa (a, b, c) and P_i = 0.5 MPa (d, e, f), respectively, under CNS, with K_n = 64 kN/mm and cyclic shear load.

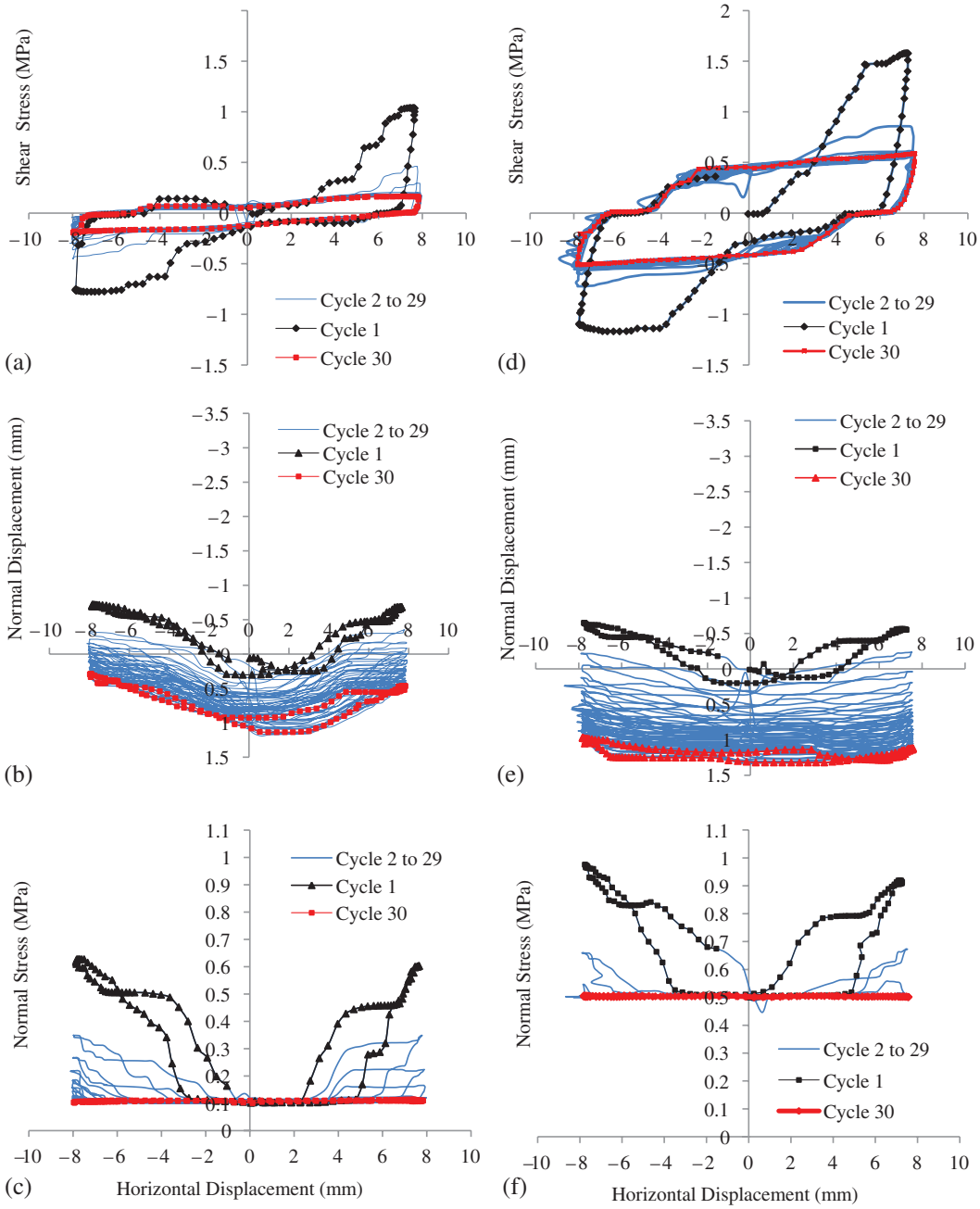


TABLE 3 Peak shear stress under CNL (K_n = 0 kN/mm) and CNS (K_n = 64 kN/mm) conditions at the same initial normal stress (P_i = 0.1 MPa) for the joint with 30°–30° asperity at different cycles.

N	τ_p CNS, MPa	τ_p CNL, MPa	Increase in Shear Strength (CNS–CNL)/CNL, %
1	1.04	0.34	206
2	0.46	0.27	70
3	0.29	0.22	32
29	0.16	0.16	0
30	0.16	0.16	0

Note: CNL, constant normal load; CNS; constant normal stiffness; N, number of cycles; τ_p, peak shear stress.

Copyright by ASTM Int'l (all rights reserved); Mon Mar 19 00:45:37 EDT 2018
Downloaded/printed by
Delhi College Of Engineering (Delhi College Of Engineering) pursuant to License Agreement. No further reproductions authorized.

SHEAR BEHAVIOR OF IRREGULAR JOINT (15°–30° JOINT ASPERITY)

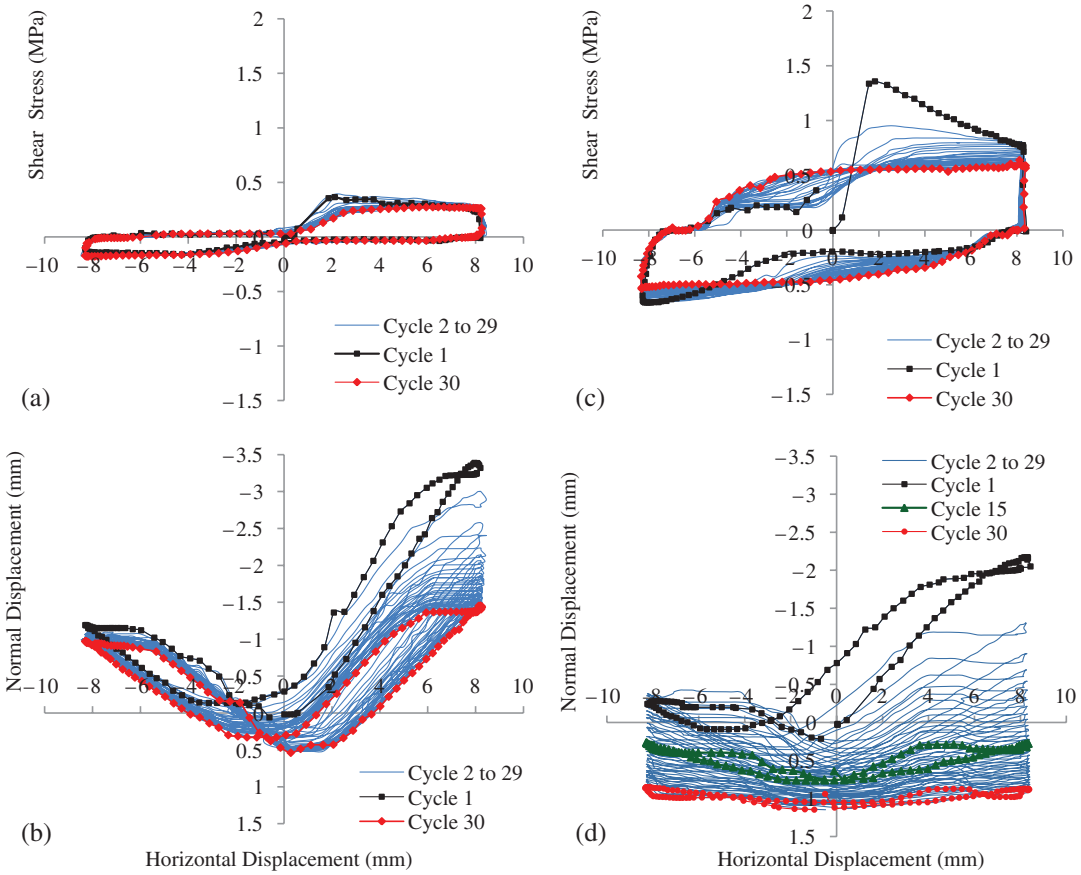
Irregular joint shear behavior is different from the regular joint. Shear strength of irregular joints is largely influenced by the direction of shearing, but it is the same for the regular joint, i.e., shear strength is independent of shear direction for regular joints. The shear behavior of irregular joint with asperity 15°–30° was investigated under different normal stiffness values (CNL and CNS), as presented in **Fig. 13**. The shear strength of the irregular joint (15°–30° asperity) was more than the regular joint (30°–30° asperity), as compared between **Figs. 13a** and **11a** or **Figs. 13c** and **11c** under CNL condition and **Figs. 14a** and **12a** or **Figs. 14d** and **12d** under CNS condition. Peak shear stress on the slope of 30° decreased and reached a constant level at $P_i = 0.1$ MPa and 0.5 MPa after several shear cycles, whereas peak shear stress was constant during 30 shear cycles for the slope of 15°, as shown in **Fig. 13a** and **Fig. 13c**. The shear strength or absolute value of peak shear stress in FAs and BAs was significantly different due to different angles of slopes on asperity. This is because of the shearing mechanism, which changed from sliding with low asperity angle (15°) to shearing or diminishing of asperities with high angle (30°). This phenomenon was not observed on the joint with normal stiffness or $K_n = 64$ kN/mm under CNS condition, as indicated in **Fig. 14a** and **14d**, due to the increase in normal stress and degradation of slopes of asperities on the joint.

DILATION AND NORMAL STRESS BEHAVIORS OF IRREGULAR JOINT (15°–30° JOINT ASPERITY)

In this type of joint, dilation and dilation angle of the joint from the slope of 30° on irregular joint is reduced gradually during cyclic loads, but it was constant for the slope of 15° at $P_i = 0.1$ MPa, as represented in **Fig. 13b**, i.e., only asperity sliding occurred in this part of asperities or 15° slopes, and degradation was observed for slopes of 30°. Hence, joint degradation was predominant on the slope of asperity with higher angles on irregular joints until two angles of asperity became equal under shear cycles; at that point, the joint started behaving like the regular joints, as illustrated in **Fig. 13d**.

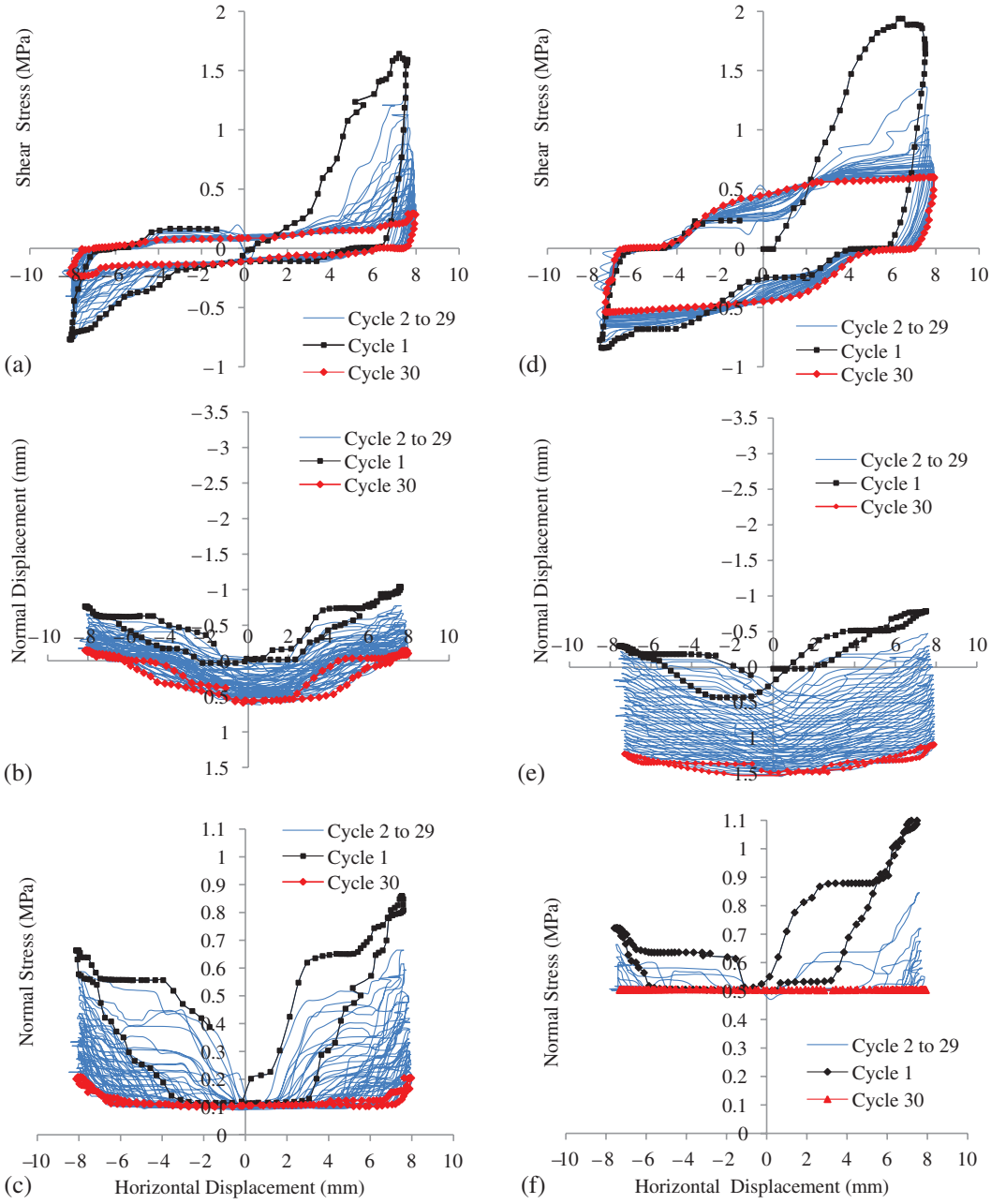
Peak dilation on the joint decreased with the increase in P_i under cyclic load. Dilation behavior was converted to compression behavior after several cycles (**Figs. 13d** and **14e**). Decreasing dilation or dilation angle with increasing the number of cycles

FIG. 13 Shear stress and normal displacement versus horizontal displacement on 15°–30° asperity joint at 0.1 MPa (a, b) and 0.5 MPa (c, d), respectively, under CNL and cyclic shear load.



Copyright by ASTM Int'l (all rights reserved); Mon Mar 19 00:45:37 EDT 2018
Downloaded/printed by
Delhi College Of Engineering (Delhi College Of Engineering) pursuant to License Agreement. No further reproductions authorized.

FIG. 14 Shear stress, normal displacement, and normal stress versus horizontal displacement of joint asperity 15°–30° at P_i = 0.1 MPa (a, b, c) and P_i = 0.5 MPa (d, e, f), respectively, under CNS, with K_n = 64 kN/mm and cyclic shear load.



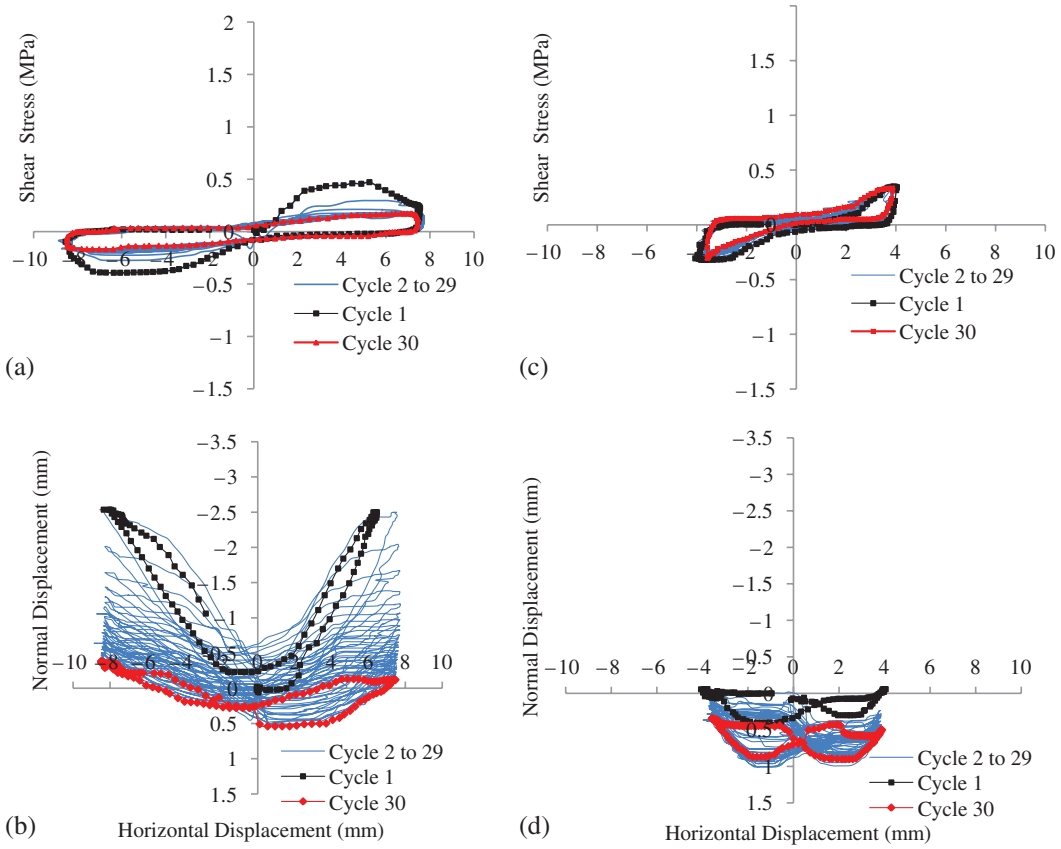
indicates asperities degradation on the joint. Increasing normal stress was more predominant at low P_i under CNS condition, which is clear by comparing **Fig. 14c** and **14f**.

BEHAVIOR OF THE JOINTS UNDER DIFFERENT FREQUENCY AND AMPLITUDE

Influence of dynamic parameters, such as frequency and amplitude of shear loads on regular joints, were investigated in this section. The study of joints under different frequencies and amplitudes of shear loads is very important, due to seismic events with different magnitudes. In order to study the effects of frequency and amplitude of shear load on shear strength, a regular joint with 30°–30° asperity was selected, and cyclic shear tests were conducted on the joints with 0.1-Hz frequency (higher frequency, keeping ±8 mm amplitude constant) and ±4 mm amplitude (lower amplitude, keeping frequency 0.01 Hz constant), as shown in **Fig. 15a** and **15b**, and **Fig. 15c** and **15d**, respectively, under similar conditions at P_i = 0.1 MPa.

Copyright by ASTM Int'l (all rights reserved); Mon Mar 19 00:45:37 EDT 2018
Downloaded/printed by
Delhi College Of Engineering (Delhi College Of Engineering) pursuant to License Agreement. No further reproductions authorized.

FIG. 15 Shear stress and normal displacement versus horizontal displacement of joint asperity 30°–30° for different frequency and amplitude (0.1 Hz and 8 mm in [a] and [b] and 0.01 Hz and 4 mm in [c] and [d]), respectively, at P_i = 0.1 MPa under CNL and cyclic shear load.



The test results (**Fig. 15**) were compared with cyclic shear test under 0.01-Hz frequency and ±8-mm amplitude, as represented in **Fig. 11a–c**. With increasing the frequency from 0.01 to 0.1 Hz, shear strength increased from 0.33 to 0.5 MPa, as compared between **Figs. 11a** and **15a**. It was also observed that the difference of peak dilation between forward and backward directions decreased with raising the frequency (0.1 Hz), and this is almost the same as illustrated in **Fig. 15b**.

Peak shear stress was constant with increasing the number of shear cycles at low amplitude or ±4 mm, i.e., no significant change was observed in shear strength or peak shear stress with increasing the number of cycles, as indicated in **Fig. 15c**. With increasing the amplitude of shear load to ±8 mm, the peak shear stress decreased with increasing the number of shear cycles (**Fig. 11a**). Compression (positive normal displacement) was observed on the joint at low amplitude or ±4 mm (**Fig. 15d**), and this is due to asperity deformation for the small amount of horizontal displacement, whereas dilation (negative normal displacement) was dominant on the joint with increasing amplitude (±8 mm), as demonstrated in **Fig. 15d** under cyclic shear load, i.e., the increase (dilation) and the decrease (compression) in volumes of the sample during initial cycles for high and low amplitudes were observed, respectively. This can simulate swelling and subsidence of the ground in seismic events.

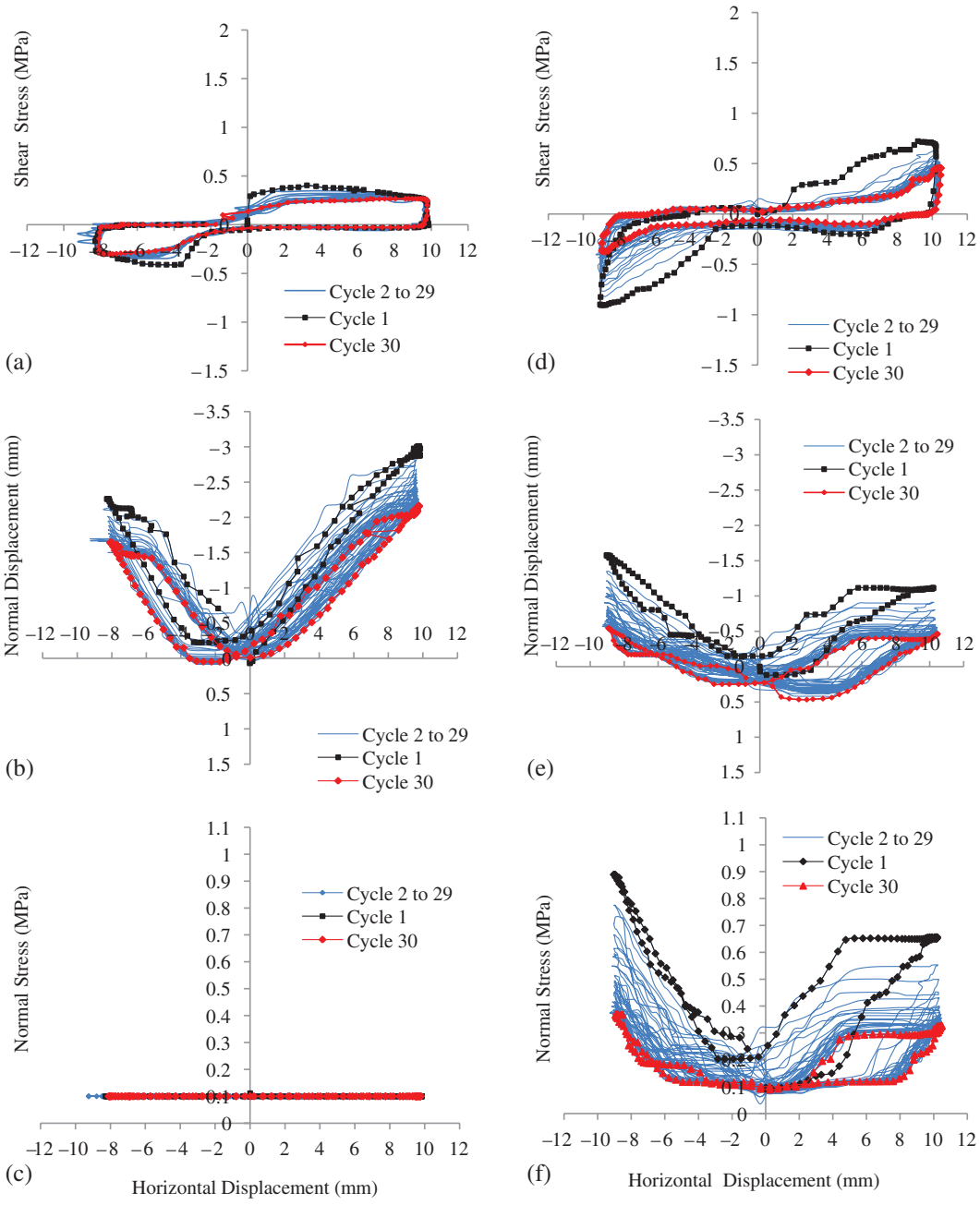
SHEAR BEHAVIOR OF NATURAL JOINT

The developed shear testing machine has the ability to perform a cyclic shear test on any natural jointed rock. Shear tests were conducted on two joints under CNL (CNS with $K_n = 0$ kN/mm) and CNS with $K_n = 32$ kN/mm at low initial normal stress ($P_i = 0.1$ MPa), as is represented in **Fig. 16**. Two rough joints were selected with the same joint roughness coefficient (JRC), which was measured based on Barton (1982). This is a graphical method based on maximum amplitude (highest asperity) and the length of the sample. The maximum amplitude and the length of the samples for both joints were 13 mm and 26.5 cm, and 12.5 mm and 25 cm. According to the chart presented by Barton (1982), JRC values for both of the joints were 20. Frequency and amplitude of shear loads were kept constant, 0.01 Hz and ±10 mm, respectively.

Elastoplastic shear stress behavior was dominant on the joint at low $P_i = 0.1$ MPa under CNL conditions (**Fig. 16a**). However, this behavior was not observed on the joint under CNS with normal stiffness, $K_n = 32$ kN/mm, at the same $P_i = 0.1$ MPa (after first

Copyright by ASTM Int'l (all rights reserved); Mon Mar 19 00:45:37 EDT 2018
Downloaded/printed by
Delhi College Of Engineering (Delhi College Of Engineering) pursuant to License Agreement. No further reproductions authorized.

FIG. 16 Shear stress, normal displacement, and normal stress versus horizontal displacement of rough joints, respectively, under CNL or K_n = 0 (a, b, c) and CNS with K_n = 32 kN/mm (d, e, f) at P_i = 0.1 MPA.



cycle), as represented in **Fig. 16d**. The first peak shear stress under CNS (K_n = 32 kN/mm) increased 100 % with respect to CNL (K_n = 0 kN/mm), due to the increase in normal stress, as indicated in **Fig. 16f**.

DILATION AND NORMAL STRESS BEHAVIOR OF NATURAL JOINT

Significant dilation was observed on the joint under CNL condition, as the first peak dilation was 3 mm (**Fig. 16b**), but it was observed as only 1.5 mm (**Fig. 16e**) for the joint under CNS condition at the first cycle. Dilation is dominant on both natural rock joints (CNL and CNS) during 30 shear cycles, and no compression is observed due to hard natural rock. Normal stress is constant under CNL, but it changed under CNS condition during shear cycles, as illustrated in **Fig. 16f**. Normal stress increased and peak normal stress reached 0.9 MPa (9 times P_i = 0.1 MPa) under CNS with K_n = 32 kN/mm at the first cycle, but it decreased to 0.3 MPa on the last cycle. The influence of CNS boundary

Copyright by ASTM Int'l (all rights reserved); Mon Mar 19 00:45:37 EDT 2018
Downloaded/printed by
Delhi College Of Engineering (Delhi College Of Engineering) pursuant to License Agreement. No further reproductions authorized.

condition decreased with increasing the number of shear cycles, because some parts of asperities were sheared at initial cycles.

Conclusions

(1) An automatic servo-controlled static and cyclic shear testing machine was developed to study the shear behavior of rocks and rock joints under CNL and CNS boundary conditions. A new design, which has been presented by Shrivastava and Rao (2013), was carried out on three main units of the equipment, including (i) frame and loading unit, (ii) data acquisition and controlling unit, and (iii) hydraulic power pack with servo valve. The cooling unit was added to the shear testing machine in the present study. The developed shear testing machine can work with varying normal stiffness values (0 to 500 kN/mm), frequencies (0.01 to 5 Hz), and amplitudes of shear loads (±1 mm to ±20 mm).

(2) Static shear tests were conducted on large-scale intact samples, and cyclic shear tests were performed on regular and irregular jointed samples by the developed shear testing machine.

(3) Peak shear stress increased 206 % with increasing normal stiffness (from 0 to 64 kN/mm at the same $P_i = 0.1$ MPa) on the joints with 30°–30° asperity at the first shear cycle, but the effect of stiffness decreased with the increase in the number of cycles. Similar behavior was observed on natural rock joint.

(4) Peak shear stress of the irregular joint was more than the regular joint, and the irregular joint behaved like the regular joint after several shear cycles.

(5) The number of cycles was not effective on the peak shear stress on the joints at low shear amplitude (±4 mm), but the peak shear stress decreased at higher amplitudes (±8 mm). The frequency of shear loads affected the peak shear stress, i.e., shear strength increased with increasing the frequency under the same P_i.

ACKNOWLEDGMENTS

We are thankful to Mr. Jattinder Singh, managing director, Hydraulic Engineering and Instrument Company, New Delhi, for extending help during the modification and fabrication of the direct shear testing machine.

References

ASTM D5607-02, 2006, *Standard Test Method for Performing Laboratory Direct Shear Strength Tests of Rock Specimens under Constant Normal Force*, ASTM International, West Conshohocken, PA, www.astm.org

Barton, N., 1982, "Shear Strength Investigations for Surface Mining," presented at the *Third International Conference on Stability in Surface Mining*, Vancouver, Canada, Society of Mining Engineers of AIME, New York, pp. 171–196.

Homand-Etienne, F., Lefèvre, F., Belem, T., and Souley, M., 1999, "Rock Joints Behavior under Cyclic Direct Shear Tests," *Proceedings of the 37th U.S. Rock Mechanics Symposium*, B. Amadei, R. L. Kranz, G. A. Scott, and P. H. Smeallie, Eds., Balkema, Rotterdam, pp. 399–406.

Huang, X., Haimson, B. C., Plesha, M. E., and Qiu, X., 1993, "An Investigation of the Mechanics of Rock Joints—Part I. Laboratory Investigation," *Int. J. Rock Mech. Min. Sci. Geomech. Abstr.*, Vol. 30, No. 3, pp. 257–269, https://doi.org/10.1016/0148-9062(93)92729-A

Hutson, R. W. and Dowding, C. H., 1990, "Joint Asperity Degradation during Cyclic Shear," *Int. J. Rock Mech. Min. Sci. Geomech. Abstr.*, Vol. 27, No. 2, pp. 109–119, https://doi.org/10.1016/0148-9062(90)94859-R

IS 1828 (Part I), 2005, *Metallic Materials—Verification of Static Uniaxial Testing Machines. Tension/Compression Testing Machines—Verification and Calibration of the Force-Measuring System*, Bureau of Indian Standards, New Delhi, India, www.bis.gov.in

Indraratna, B., Haque, A., and Aziz, N., 1998, "Laboratory Modelling of Shear Behaviour of Soft Joints under Constant Normal Stiffness Conditions," *J. Geotech. Geol. Eng.*, Vol. 16, No. 1, pp. 17–44, https://doi.org/10.1023/A:1008880112926

ISRM, 1979, "Suggested Method for Determining the Uniaxial Compressive Strength and Deformability of Rock Materials," International Society for Rock Mechanics, Lisbon, Portugal.

ISRM, 1981, "Suggested Methods for Rock Characterization, Testing and Monitoring," Pergamon Press, Oxford, United Kingdom.

Jafari, M. K., Amini Hosseini, K., Pellet, F., Boulon, M., and Buzzi, O., 2003, "Evaluation of Shear Strength of Rock Joints Subjected to Cyclic Loading," *J. Soil Dyn. Earthquake Eng.*, Vol. 23, No. 7, pp. 619–630, https://doi.org/10.1016/S0267-7261(03)00063-0

Jiang, Y., Xiao, J., Tanabashi, Y., and Mizokami, T., 2004, "Development of an Automated Servo- Controlled Direct Shear Apparatus Applying a Constant Normal Stiffness Condition," *Int. J. Rock Mech. Min. Sci.*, Vol. 41, No. 2, pp. 275–286, https://doi.org/10.1016/j.ijrmms.2003.08.004

Jiang, X.-W., Wan, L., Wang, X.-S., Liang, S.-H., and Hu, B. X., 2009, "Estimation of Fracture Normal Stiffness Using a Transmissivity-Depth Correlation," *Int. J. Rock Mech. Min. Sci.*, Vol. 46, No. 1, pp. 51–58, https://doi.org/10.1016/j.ijrmms.2008.03.007

Kim, D., Chun, B., and Yang, J., 2006, "Development of a Direct Shear Apparatus with Rock Joints and Its Verification Tests," *Geotech. Test. J.*, Vol. 29, No. 5, pp. 365–373, https://doi.org/10.1520/GTJ12553

Lee, H. S., Park, Y. J., Cho, T. F., and You, K. H., 2001, "Influence of Asperity Degradation on the Mechanical Behavior of Rough Rock Joints under Cyclic Shear Loading," *Int. J. Rock Mech. Min. Sci.*, Vol. 38, No. 7, pp. 967–980, https://doi.org/10.1016/S1365-1609(01)00060-0

Mirzaghorbanali, A., Nemcik, J., and Aziz, N., 2014, "Effects of Shear Rate on Cyclic Loading Shear Behaviour of Rock Joints under Constant Normal Stiffness Conditions," *Int. J. Rock Mech. Rock Eng.*, Vol. 47, No. 5, pp. 1931–1938, https://doi.org/10.1007/s00603-013-0453-0

Copyright by ASTM Int'l (all rights reserved); Mon Mar 19 00:45:37 EDT 2018
Downloaded/printed by
Delhi College Of Engineering (Delhi College Of Engineering) pursuant to License Agreement. No further reproductions authorized.

Mirzaghorbanali, A., 2013, "Shear Behaviour of Rock Joints under Cyclic Loading and Constant Normal Stiffness Conditions," Ph.D. thesis, University of Wollongong, Australia.

Niktabar, S. M. M., Rao, K. S., and Shrivastava, A. K., 2015, "Shear Behaviour of Rock Joints under Cyclic Condition," *J. Eng. Geol.*, Special Publication, Indian Society of Engineering Geology, pp. 277–286, ISSN 0970-5317.

Niktabar, S. M. M., Rao, K. S., and Shrivastava, A. K., 2016a, "Shear Behaviour of Infilled Joints under Cyclic Loads and Constant Normal Stiffness Boundary Condition," presented at the *Seventh International Symposium on In-Situ Rock Stress*, Tampere, Finland, International Society for Rock Mechanics and Rock Engineering, pp. 558–567.

Niktabar, S. M. M., Rao, K. S., and Shrivastava, A. K., 2016b, "Shear Behaviour of Regular and Irregular Rock Joints under Cyclic Conditions," presented at the *Third International Symposium on Mine Safety Science and Engineering*, McGill University, Montreal, Canada, pp. 193–198.

Obert, L., Brady, B. T., and Schmechel, F. W., 1976, "The Effect of Normal Stiffness on the Shear Resistance of Rock," *Rock Mech.*, Vol. 8, No. 2, pp. 57–72, https://doi.org/10.1007/BF01239760

Ooi, L. H. and Carter, J. P., 1987, "A Constant Normal Stiffness Direct Shear Device for Static and Cyclic Loading," *Geotech. Test. J.*, Vol. 10, No. 1, pp. 3–12, https://doi.org/10.1520/GTJ10132J

Shrivastava, A. K., 2012, "Physical and Numerical Modelling of Shear Behaviour of Jointed Rocks under CNL and CNS Boundary Conditions," Ph.D. thesis, Indian Institute of Technology Delhi, India.

Shrivastava, A. K. and Rao, K. S., 2013, "Development of a Large-Scale Direct Shear Testing Machine for Unfilled and Infilled Rock Joints under Constant Normal Stiffness Conditions," *Geotech. Test. J.*, Vol. 36, No. 5, pp. 670–679, https://doi.org/10.1520/GTJ20120155, https://doi.org/10.1520/GTJ20120155

Copyright by ASTM Int'l (all rights reserved); Mon Mar 19 00:45:37 EDT 2018
Downloaded/printed by
Delhi College Of Engineering (Delhi College Of Engineering) pursuant to License Agreement. No further reproductions authorized.

Autonomous Pathfinding in Simulated 3D Environment

Sidharth Raja
Delhi Technological University
New Delhi, India
sidharth15.raja@gmail.com

Tanuj Bhatia
Delhi Technological University
New Delhi, India
tanuj.bhatia95@gmail.com

Akshat Mishra
Delhi Technological University
New Delhi, India
one.akshat@gmail.com

Sanket Kashyap
Delhi Technological University
New Delhi, India
sanket.dtu@gmail.com

Om Prakash Verma
Delhi Technological University
New Delhi, India
opverma@dce.ac.in

ABSTRACT
This paper presents an approach for navigating an autonomous agent in a simulated room environment with multiple obstacles. It presents a technique for depth map estimation using stereoscopic images - a vital intermediate technique for autonomous navigation and pathfinding. It also proposes a path planner interfaced with the depth map for locally planning a sequence of steps to the desired location. A single RGB camera does not contain sufficient information to estimate depth with satisfactory accuracy. Depth cameras are significantly more expensive than RGB cameras, and hence would not be suited for projects requiring lower budget constraints. Hence a middle ground is required which requires depth calculation from limited available input. Depth estimation is accomplished with a convolutional neural network trained on synthetic randomly generated stereo image data. The path planner comprises a short-term path planner for obstacle avoidance, and a long-term path planner for approaching the destination co-ordinates. The results show that this approach yields a factor of approximately 1.8 times the steps of human performance on the same task.

CCS Concepts
•Computing methodologies → Robotic planning •Computing methodologies →Vision for robotics

Keywords
Computer vision; Simulation; Path finding; Neural Network; Artificial Intelligence; Convolutional Neural Network; Depth map; Stereo images; Autonomous agents;

Permission to make digital or hard copies of all or part of this work for personal or classroom use is granted without fee provided that copies are not made or distributed for profit or commercial advantage and that copies bear this notice and the full citation on the first page. Copyrights for components of this work owned by others than ACM must be honored. Abstracting with credit is permitted. To copy otherwise, or republish, to post on servers or to redistribute to lists, requires prior specific permission and/or a fee. Request permissions from Permissions@acm.org.
ICRAI 2017, December 29–31, 2017, Shanghai, China
© 2017 Association for Computing Machinery.
ACM ISBN 978-1-4503-5358-8/17/12…$15.00
DOI: https://doi.org/10.1145/3175603.3175621

1. INTRODUCTION
The path planning problem for mobile robots can be defined as the search for a path which a robot (with specified geometry) has to follow in a described environment, in order to reach a particular position and orientation B, given an initial position and orientation A. [1]. Path planning can be divided into two categories - global and local planning. If the knowledge of the environment is known beforehand, the global path can be planned before the robot starts to move. If there exists no prior knowledge about the environment, the path must be computed online and the agent must avoid obstacles in real-time [2]. In the past year, neural network based models have shown remarkable results in a sensory role for obtaining depth information from standard RGB camera images [3], which motivated our inquiry for the use of neural networks to enhance the sensory data used by agents. This paper describes an approach for an agent to navigate from source coordinates to destination coordinates while avoiding obstacles that may appear in its path. Through this project, we also introduce an autonomous control policy to govern agents.

2. RELATED WORK
Synthetically generated imagery is a useful tool in computer vision as it allows the generation of a large number of arbitrary examples in various positions and orientations. This would allow a more precise sample set than would ordinarily be possible with real world data. It also provides us with precise groundtruth data such as depth information which might not be trivial to collect from real data. Synthetically generated data has been used in several instances in the past to augment performance. Taylor et al. present a system called Object Video Virtual Video (OVVV) [4] based on Half-life for evaluation of tracking in surveillance systems. Peng et al. [5] use synthetic CAD generated images models to fine-tune on the object detection task and significantly outperform previous methods with this approach. Lim et al. [6], and Aubry et al. use CAD models for detection and object alignment in the image. Aubry and Russell use synthetic RGB images rendered from CAD models to analyze the response pattern and the behavior of neurons in the commonly used deep convolutional networks. There has recently been increased interest in using video game data to train computer vision models [7]. Although video games generate images from a finite set of textures, there is variation in viewpoint, illumination, weather, and level of detail which could provide valuable augmentation of the data. Nikolaus Mayer et al. [8] present a method for visual scene

generation using an open source 3D modeling software Blender3D which includes stereo color images and ground truth for bidirectional disparity, bidirectional optical flow and disparity change, motion boundaries, and object segmentation. Existing methods for disparity map estimation include semi global matching (SGM) proposed by Hirschmuller [9] and MC-CNN, proposed by Zbontar and LeCunn, a convolutional neural network which compares image patches to initialize the stereo matching cost [10]. Mayer et. al. also propose a convolutional neural network, DispNet, in their work which they evaluate against the before mentioned approaches. They find that DispNet outperforms the other two in various datasets [8]. The neural network architecture mentioned in our approach is based on DispNet. There has been historical prior work in localized path planning, where the mobile robot aims to use local sensory information in a reactive fashion [11].

Ziegler et al. present a mechanism for depth sensor based detection of a target object and for generation of trajectories for a robot-aided scanning process for inspection and verification processes. [12].

3. METHOD

3.1 Depth Map Estimation

A blender script was created to generate randomized 3D situations for analysis. This stochastic approach generates a large number of 3D scene environments and their associated depth maps. Through this training, we aim to obtain a neural network that takes input as stereo images and output the depth parity. This depth parity would later used as part of the short-term path planner in the control policy. Shapenet [13], an annotated, large-scale dataset of 3D shapes was used as obstacles in the training phase of the CNN for depth parity estimation, and as the obstacles for the agent to circumnavigate in the test phase. A dataset of 20,000 training examples was generated using 3D models from the Shapenet dataset. For each example, 8-10 models were chosen at random and placed in the scene. The placement and rotation of each model is random, and 3 scenes are rendered as depicted in Figure 1.

1. Left Camera stereo image
2. Right Camera stereo image
3. Depth Map

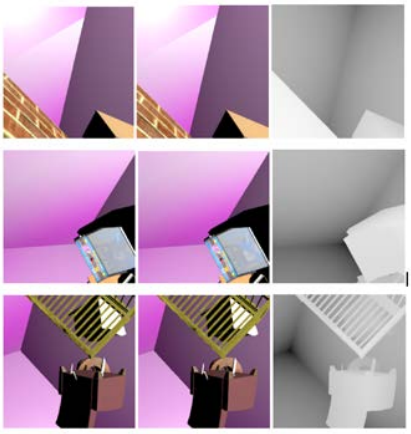


Figure 1. Left Stereo RGB image(left), Right Stereo RGB Image(center), Ground Truth Depth Map (right).

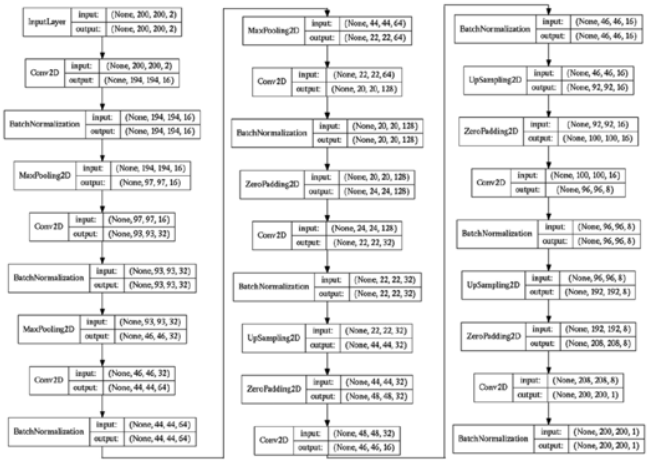


Figure 2. Network architecture for depth map estimation.

This dataset of 20,000 images was normalized along each pixel to aid the training process. A Convolutional Neural Network for estimating depth maps using a stereo image pair was trained. The network accepts as input 2 grayscale images and produces an estimate of the depth map corresponding to the images [8] [14]. The network architecture is shown in Figure 2.

A loss function of mean squared error was used to as the objective. The network was trained using an Adam Optimizer [15], with learning rate 0.01. Hold out validation with split 10% was performed i.e 18,000 training examples were used as the training set and 2000 as the validation set.

The validation loss and training loss at each epoch were recorded. The training was halted once validation loss did not improve significantly. Loss function used:

$$L(x_n, y_n) = \sum_{i=0}^{200} \sum_{j=0}^{200} (y_{ij} - x_{ij})^2$$

3.2 Simulated Environment

The agent was placed inside a simulated 3D room environment containing multiple point light sources for illumination. The environment contains various real life room obstacles from the Shapenet Dataset. We measure the performance of our algorithm using a fitness function that determines the step count to the destination. We compare the results of this to human results on the same problem, and the observations are mentioned in table in the subsequent chapter.

Room structures were created using Blender 3D, an open source 3D modelling software. The overall room environment was then imported as .egg files into Panda3D.

The simulated environment, and the different camera views are represented in Figure 3.

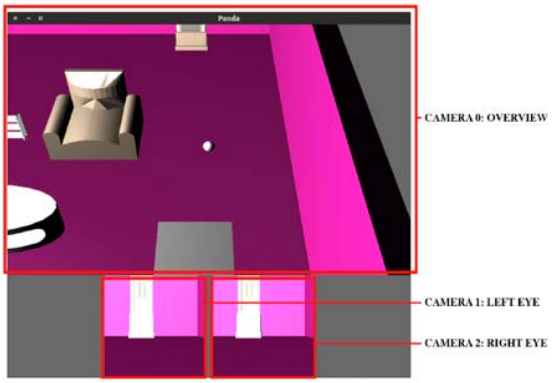


Figure 3. Simulated Environment in Panda3D.

We set up 3 cameras in Panda3D while conducting the experiment.

C**amera 0:** Overview for the observer to view the whole system.

Camera 1: Left Camera component of the stereo vision system

Camera 2: Right Camera component of the stereo vision system

Camera 1 and Camera 2 send buffered streams to the robotic agent

Camera 0 is not viewed by the agent, and is simply for observational purposes.[1]

3.3 Path Planning

The entire 3 dimensional environment is divided into unit volume cubes, centred at integer coordinates. A heuristic aided search algorithm is used as the basis for path planning. It is augmented by the depth map discussed in the previous section. The interfacing between the algorithm and the generated depth map will be discussed in the subsequent section.

The following implicit data structures and objects are maintained by the agent controller object:

set_visited A set of previously visited nodes
set_prospects Currently available prospects for immediate motion
stack_active A stack of nodes on the currently active path
to_cube The highest priority cube in the immediate surroundings on the path to destination

Two types of step movement policies were examined for this control policy:

1. 4-connected policy
2. 8-connected policy

Two distance heuristics were compared in the experiment:

1. Manhattan distance
2. Euclidean Distance

3.4 Interfacing Depth Map with Path Planner

The entire 3 dimensional environment is divided into virtual unit volume cubes, centred at integer coordinates. There are 8 immediately neighbouring cubes to which the agent can move. The path planner locally generates the next cube towards which it intends to move based on the heuristic. Figure 4 represents a high level flowchart depicting the same.

The agent receives two 200×200 input image streams from the left and right cameras based on which it must plan it's short term path and avoid obstacles. The agent step rotates and faces the heuristic selection. The agent uses the trained CNN to generate a single 200 x 200 pixel depth map from the stereo image camera stream.

Algorithm 1 Path planning experiment staging

1. Import Blender model, and obstacles from the Shapenet database
2. Initialize neural network and load CNN model weights
3. Two cubes are selected (src_cube or dest_cube)
4. Ensure there is no collision with src_cube or dest_cube
5. Initialize agent controller with these initial values
6. Interface agent controller with left and right camera stream
7. Start game and log the step counts
8. End log when destination reached

This depth map is filtered and cropped to focus on the target window W for the agent, and mean intensity statistics are computed. If the agent evaluates the mean intensity to be above a threshold T, it decides that the heuristic generated next-cube isn't safe for traversal and directs it to present an alternate option. This process continues until the heuristic selects a subsequent neighbouring cube with no detected obstacles.

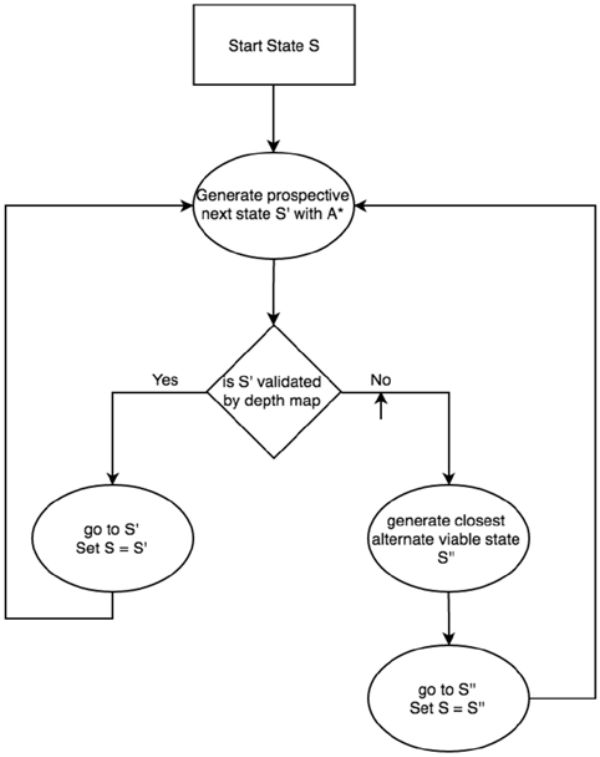


Figure 4. Flowchart for interfacing depth map to path planner.

4. RESULT

The neural network was able to accurately estimate the depth parity given 2 input stereo images. The validation loss was calculated by comparing the ground truth depth map generated using Blender against the predicted depth map obtained from the Neural Network. Validation loss was determined to be in the order of 10−3. The performance of the algorithm with different heuristics is given in Table 1 and the loss in each epoch is shown in Figure 5. Sample comparisons between the ground truth and predicted depth map are shown in Figure 6.

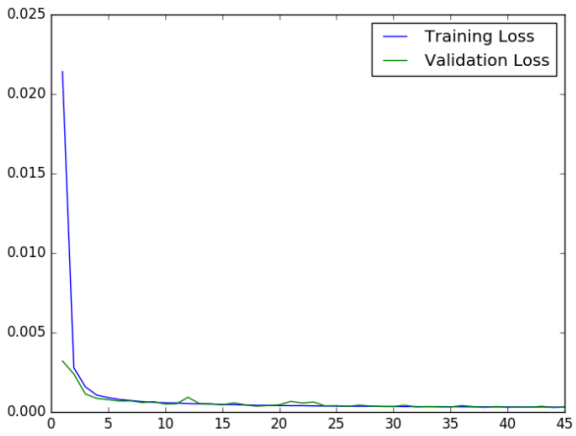


Figure 5. Training and validation loss for depth estimation.

Table 1. Performance Metrics

S.No.	Human Baseline	M_{Man}	M_{Euc}	R_{Man}	R_{Euc}
1	179	330	241	1.84	1.35
2	209	472	472	2.26	2.26
3	276	556	520	2.01	1.88
4	269	252	551	0.93	2.05
5	167	401	401	2.40	2.40
6	197	462	361	2.35	1.83
7	123	114	114	0.93	0.93
Median	-	-	-	2.01	1.88
Average	-	-	-	1.81	1.80

SNo. : Scenario number, each having different source and destination

Human Baseline: Step count of a human performing the experiment

$\mathbf{M_{Man}}$: Step count using Manhattan distance as base distance heuristic.

$\mathbf{M_{Euc}}$: Step count using Euclidean distance as base distance heuristic.

$\mathbf{R_{Man}}$: Ratio of Manhattan to Baseline performance (Lower is Better)

$\mathbf{R_{Euc}}$: Ratio of Euclidean to Baseline performance (Lower is Better)

The average relative performance of the Manhattan and Euclidean based heuristic was found to be 1.81 and 1.80 respectively. The median relative performance of the Manhattan and Euclidean based heuristic was found to be 2.01 and 1.88 respectively. The average metric is susceptible to outliers in observations and is hence a less reliable metric for evaluation. The median metric is able to circumvent this problem, and is thus a better measure of the relative performances of the heuristics in this situation. The Euclidean heuristic equaled or outperformed the Manhattan heuristic on 85.71% of the experiments, and is hence a better heuristic for evaluation. The performances can be visualized in Figure 7.

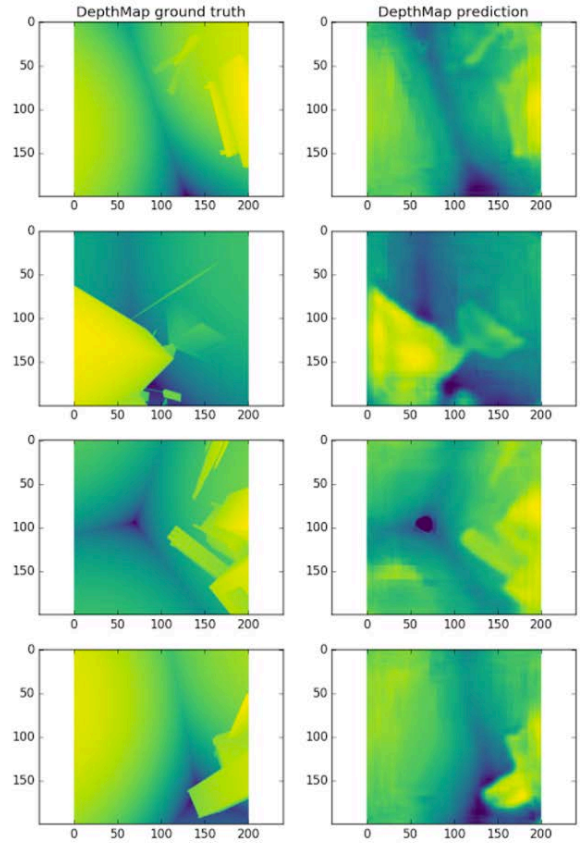


Figure 6. Ground Truth depth map (left), Predicted depth map from stereo images (right).

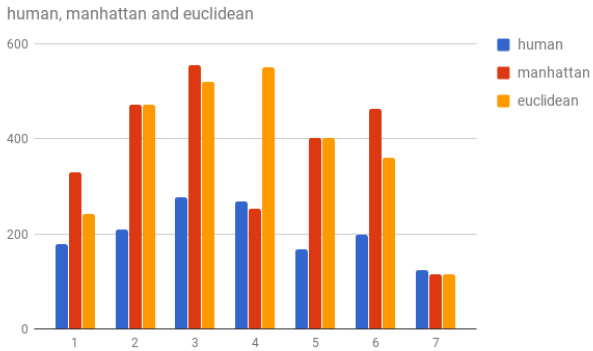


Figure 7. Visualization of the path heuristic performance and human baselines for each test experiment.

5. FUTURE WORK

The heuristic could be further improved by adding penalties for changes in direction as currently, a lot of energy of the agent is involved in continuously checking other directions for a marginally better path. The long term path planning algorithm is not effective with complex maze patterns. The inability of the agent to have awareness about large obstacles like walls leads to inefficient path planning. Simultaneous Localization and Mapping (SLAM) using the depth map can be performed, in order to obtain better relative performance and more awareness about the surroundings.

6. REFERENCES

[1] S. N. Buniyamin N. W. N. W. and M. Z. A simple local path planning algorithm for autonomous mobile robots. In *INTERNATIONAL JOURNAL OF SYSTEMS APPLICATIONS, ENGINEERING and DEVELOPMENT*, June 2011.

[2] N. B. NOHAIDDA BINTI SARIFF. Ant colony system for robot path planning in global static environment. In *SELECTED TOPICS in SYSTEM SCIENCE and SIMULATION in ENGINEERING*, 2010.

[3] F. Liu, C. Shen, and G. Lin. Deep convolutional neural fields for depth estimation from a single image. In *The IEEE Conference on Computer Vision and Pattern Recognition (CVPR)*, June 2015.

[4] G. R. Taylor, A. J. Chosak, and P. C. Brewer. Ovvv: using virtual worlds to design and evaluate surveillance systems. In *2007 IEEE Conference on Computer Vision and Pattern Recognition*, pages 1–8, June 2007. DOI: 10.1109/CVPR.2007.383518.

[5] X. Peng, B. Sun, K. Ali, and K. Saenko. Exploring invariances in deep convolutional neural networks using synthetic images. *CoRR*, abs/1412.7122, 2014. URL: http://arxiv.org/abs/1412.7122.

[6] J. J. Lim, H. Pirsiavash, and A. Torralba. Parsing ikea objects: fine pose estimation. In *2013 IEEE Interna- tional Conference on Computer Vision*, pages 2992– 2999, Dec. 2013. DOI: 10.1109/ICCV.2013.372.

[7] A. Shafaei, J. J. Little, and M. Schmidt. Play and learn: using video games to train computer vision models. *CoRR*, abs/1608.01745, 2016. URL: http://arxiv.org/abs/1608.01745.

[8] N. Mayer, E. Ilg, P. Ha¨usser, P. Fischer, D. Cremers, A. Dosovitskiy, and T. Brox. A large dataset to train convolutional networks for disparity, optical flow, and scene flow estimation. *CoRR*, abs/1512.02134, 2015. URL: http://arxiv.org/abs/1512.02134.

[9] H. Hirschmuller. Stereo processing by semiglobal matching and mutual information. *IEEE Trans. Pattern Anal. Mach. Intell.*, 30(2):328–341, Feb. 2008. ISSN: 0162-8828. DOI: 10.1109/TPAMI.2007.1166. URL: http://dx.doi.org/10.1109/TPAMI.2007.1166.

[10] J. Zbontar and Y. LeCun. Stereo matching by training a convolutional neural network to compare image patches. *CoRR*, abs/1510.05970, 2015. URL: http://arxiv.org/abs/1510.05970.

[11] E. Rimon, I. Kamon, and J. F. Canny. *Local and global planning in sensor based navigation of mobile robots*. In *Robotics Research: The Eighth International Symposium*. Y. Shirai and S. Hirose, editors. Springer London, London, 1998, pages 112–123. ISBN: 978-1- 4471-1580-9. DOI: 10.1007/978-1-4471-1580-9 11. URL: https://doi.org/10.1007/978-1-4471-1580-9 11.

[12] J. Ziegler, H. Gattringer, D. Kaserer, and A. Mu¨ller. *Automated, depth sensor based object detection and path planning for robot-aided 3d scanning*. In *Advances in Service and Industrial Robotics: Proceedings of the 26th International Conference on Robotics in Alpe- Adria-Danube Region, RAAD 2017*. C. Ferraresi and G. Quaglia, editors. Springer International Publishing, Cham, 2018, pages 336–343. ISBN: 978-3-319-61276- 8. DOI: 10.1007/978-3-319-61276-8 37. URL: https: //doi.org/10.1007/978-3-319-61276-8 37.

[13] A. X. Chang, T. Funkhouser, L. Guibas, P. Hanrahan, Q. Huang, Z. Li, S. Savarese, M. Savva, S. Song, H. Su, J. Xiao, L. Yi, and F. Yu. ShapeNet: An Information-Rich 3D Model Repository. Technical re- port arXiv:1512.03012 [cs.GR], Stanford University — Princeton University — Toyota Technological Institute at Chicago, 2015.

[14] L. Foucard. Stereoconvnet, Mar. 2016. URL: https : / / github.com/LouisFoucard/StereoConvNet.

[15] D. P. Kingma and J. Ba. Adam: A method for stochastic optimization. *CoRR*, abs/1412.6980, 2014. URL: http: //arxiv.org/abs/1412.6980.

Engineering Applications of Artificial Intelligence 71 (2018) 175–189

Contents lists available at ScienceDirect

Engineering Applications of Artificial Intelligence

journal homepage: www.elsevier.com/locate/engappai

ClusFuDE: Forecasting low dimensional numerical data using an improved method based on automatic clustering, fuzzy relationships and differential evolution

Charu Gupta [a], Amita Jain [b], Devendra Kumar Tayal [c], Oscar Castillo [d,*]

[a] Computer Science & Engineering Department, Bhagwan Parshuram Institute of Technology, Delhi, India
[b] Computer Science & Engineering Department, Ambedkar Institute of Advanced Communication Technologies and Research, Delhi, India
[c] Computer Science & Eng. Department, Indira Gandhi Delhi Technological University for Women, Kashmere Gate, New Delhi, India
[d] Tijuana Institute of Technology, Calzada Tecnologico s/n, CP 22379, Tijuana, Mexico

ARTICLE INFO

Keywords:
Automatic clustering
Differential evolution
Evolutionary computation
Fuzzy logical relationships
Forecasting
University enrollment

ABSTRACT

In this paper, a novel hybrid model for forecasting low dimensional numerical data is proposed which is named as *ClusFuDE*. The proposed method uses an improved automatic clustering approach for clustering the historical numerical data. Further fuzzy logical relationships are used to forecast the approximate values which are then defuzzified to calculate the exact forecasted values of the data. The fuzzy logical relationships are useful in modelling the fuzzy relations and help in forecasting the fuzzy time series data in a very simplified manner. The forecasted sub-optimal candidate solutions are optimized using Differential Evolution. The Differential Evolution method uses a dynamic differential crossover rate (Cr_i) for the ith solution, for identifying and discarding suboptimal candidate solutions in early stages of the iterative run. This makes the method more suitable for iterative modification of candidate solutions by using differential mutation and crossover, and suitable for global search. The proposed method is applied for forecasting, the year wise enrollments of the University of Alabama, Lahi (crop) production, monthly amount of outpatients visit in a hospital, inventory demand and population of India from years 1930–2000 and the results are consistent. We have compared our method with the recent forecasting methods available in literature and the proposed method outperforms all the existing methods in the literature. The accuracy of the proposed method is computed by calculating the Mean square error (MSE) and Mean Absolute percentage error (MAPE). The proposed method provides the lowest MSE and MAPE when compared to all other methods available in the literature.

1. Introduction

Forecasting is helpful in predicting changes in the time series. These changes when monitored over a period of time help the decision makers to survive and grow in a dynamic and uncertain world. Forecasting is useful in decision making process in various real-world applications which helps in analysing the future requirements. Song and Chissom (1993) understood the importance of time series data and designed a model for forecasting the academic enrollments of a university using fuzzy set operations. Since then, forecasting of fuzzy time series data has become an active area of research.

Many researchers have worked on real world applications of fuzzy time series data to understand and analyse the effectiveness of their forecasting models. Applications like Stock prediction (Yu, 2005; Chen and Wang, 2010; Chen and Chen, 2010a), temperature prediction (Chen and Hwang, 2000; Lee et al., 2006; Zarandi et al., 2009), estimating agriculture production (Singh, 2008, 2007), earthquake prediction (Aydin et al., 2009), foreign exchange daily price estimation (Lai et al., 2006), forecasting water temperature (Meng et al., 2015), forecasting tourist travels in Taiwan (Sakhuja et al., 2016) are some of the well-known examples of numerical data forecasting. These applications are of good use in various decision making scenarios. The use of numerical data helps in understanding easily the shortcomings with the fuzzy time series.

In Tanuwijaya and Chen (2009), and Chen et al. (2009), the forecasting of numerical data is done with the use of unsupervised learning. These unsupervised learning techniques provide a stable platform to capture the hidden patterns/associations in the data. There are hidden uncertainties in time series data which affect forecasting accuracy.

* Corresponding author.
E-mail address: ocastillo@tectijuana.mx (O. Castillo).

https://doi.org/10.1016/j.engappai.2018.02.015
Received 24 August 2017; Received in revised form 28 December 2017; Accepted 19 February 2018
0952-1976/© 2018 Elsevier Ltd. All rights reserved.

These uncertainties can arise due to changes in trend, use of linguistic information, observational changes, and other miscellaneous stagnant conditions.

To deal with this uncertainty, fuzzy logical relationships with unsupervised learning techniques are used (Chen et al., 2009; Qiu et al., 2015). Fuzzy logical relationships are a simplified version of fuzzy sets proposed by Chen (1996) for easy formulation and understanding of the problem. In fuzzy time series data, the establishment of relationships, among the data values helps in *conceptual capture of vagueness*. The vagueness is due to the linguistic information available in the historical data. Fuzzy logical relationships help the decision makers in determining fuzzy relations in a simplified and easy manner. The vagueness, if not dealt properly with the data, affects the performance of the forecasting model. An effort in developing a robust and reliable forecasting model is required for modelling complex problems.

To enhance the performance of the forecasting model, optimization techniques like Genetic algorithms (Chen and Chung, 2006; Wazan et al., 2014), swarm intelligence (Chen et al., 2013; Chen and Kau, 2013), harmony search algorithm (Shahraki and Ebrahimi, 2015), simulated annealing (Radmehr and Gharneh, 2012) have been used. Finding of appropriate length of the interval is a major consideration. These artificial intelligence techniques help in dynamic formation of intervals instead of fixed length intervals (Chen and Chung, 2006; Chen et al., 2013; Chen and Kau, 2013). In Bas et al. (2014) Differential Evolution is used for forecasting yearly enrollments using a modified mutation operator. Differential Evolution (Storn and Price, 1997), is a population based stochastic method developed by Storn and Price. It consists of two control parameters — Mutation and Crossover. Mutation operator helps in influential scaling of the selected pairs of solution and crossover influences the offspring from the parent and diversifies the population. It has been tested that parameter tuning (either for mutation or crossover) in Differential Evolution has varied impact on the outcome in low dimensional datasets (Vesterstrom and Thomsen, 2004).

The control parameters which can adapt in response to the evolved results enhance the efficiency of Differential Evolution. In Qin and Suganthan (2005), and Tvrdik (2007), it is tested that self-adaptive control parameters in evolutionary algorithms are better than deterministic control parameters. Using the strengths of Differential Evolution, this paper presents a hybrid method, to forecast low dimensional data, which comprises an improved automatic clustering technique, fuzzy logical relationships and Differential Evolution algorithm. The hybrid method is called as ClusFuDE.

The improved automatic clustering algorithm clusters the historical data into intervals (with the proposed modification in clustering, it is easy to handle the primary cluster with large data points, which was not possible in the earlier approach (Chen et al., 2009)). Based on the intervals, the data is then fuzzified into fuzzy sets and fuzzy logical relationships are formed. Clustering with fuzzy logical relationships helps in establishing relations in historical data, instead of forming membership functions for each datum. These formed relationships with the obtained intervals are, then used to compute the forecasted values. The candidate solutions, under effective interval length, are optimized using the Differential Evolution algorithm. The robustness and use of self-adaptive (dynamic) control parameters in Differential Evolution for numerical optimization is studied in this work.

The main contribution of the paper is the use of dynamic differential crossover to optimize numerical data. It helps in creating diversity in the trial offspring. For enhancing diversity in the population, the proposed method uses a dynamic crossover rate Cr_i for the ith candidate solution for iteration k. The experimental results reveal that the proposed crossover parameter performs better in locating a global minimum of the test function. The test function is the objective function. In forecasting, with numerical data, the objective function minimizes the forecasting error.

In the proposed ClusFuDE, Differential Evolution with fuzzy logical relationships helps in minimizing the objective function much better than the procedures in the literature, which involve gradient methods. The sub-optimal solutions in forecasting are iteratively modified using dynamic differential crossover. The dynamic crossover helps in partitioning of the universe of discourse into appropriate intervals, necessary for good forecasting results in fuzzy time series data. In crossover settings, the value is varied in the interval (0, 1); but in separable functions and in parameter independence conditions, the settings do not work properly. For promoting better space search, dynamic crossover is a good option. It adapts easily to the problem (after initial parameter settings) for offspring evolution from the parent.

Further, the proposed method is tested on low dimensional numerical data, of enrollments of the University of Alabama (Song and Chissom, 1993), Lahi production (Singh, 2007), outpatients visit (Cheng et al., 2008), inventory demand (Chen and Chen, 2010a), population of India from year 1930–2000 (Lahmeyer, 2003). The need for such a forecasting system arises in order to improve the management of resources in an organization/institution for reducing overheads and delays. It helps in gaining a better knowledge of the upcoming situation for risk analysis.

The datasets for forecasting using ClusFuDE, are selected to analyse the future demands of the society which can help the decision makers to go ahead with the planning of a real world situation. For instance, if the number of students taking admission in a university in a year is estimated beforehand then, the resources (for effective learning) can be managed. Similarly, if the authorities know the possible number of outpatients in a hospital, then arrangements for handling patients can be done properly. Also, every business viz. small or large scale uses inventory analysis. This motivates the use of low dimensional data, which besides being numerical in nature has an effective role in various applications as well.

The rest of this paper has been organized as follows: In Section 2, the motivation behind the proposed work is discussed. Related work to the proposed model is presented in Section 3. Section 4 is divided into Sections 4.1 and 4.2. Section 4.1, discusses the automatic clustering method and fuzzy logical relationships. It explains the modification proposed by us in the clustering process. It also presents the evolutionary computational model used in developing the proposed methodology. In Section 4.2, the proposed method for forecasting numerical data is explained with a flowchart. In Section 5, we experiment, evaluate, compare and analyse the proposed ClusFuDE method with the previously available forecasting methods in the literature. Section 6 is devoted to the conclusion of the results and future work.

2. Motivation

Forecasting low dimensional numerical data has been a well-studied problem in the literature. It has been dealt in literature using various novel methods of high order fuzzy time series (Chen, 2002; Chen and Hsu, 2008), and multi-order fuzzy time series (Ye et al., 2016). An advantage of working with fuzzy time series on numerical data is the ease of understanding the data. Also, fuzzy time series can work with small datasets as well. The two major considerations with time series data are — determination of appropriate intervals and computation of effective interval length. The current deterministic analysis models exhibit inherent vagueness in determining the interval length. So there is a need to develop a robust soft computing method to deal with these problems of uncertainty.

This motivated the authors to explore and exploit the use of an evolutionary method with fuzzy logical relationships for low dimensional numerical data. Genetic algorithms (Chen and Chung, 2006) have been used on these problems. The use of Differential Evolution, an evolutionary strategy, has given better results by evolving the alleles (candidates) over an effective interval length (Huarng, 2001). Besides interval length, choosing optimal parameters in self-adaptive Differential Evolution is also a relatively unexplored area. This idea encouraged us to optimize the interval length for candidate solutions and the use of dynamic crossover for optimizing forecasted low dimensional numerical data.

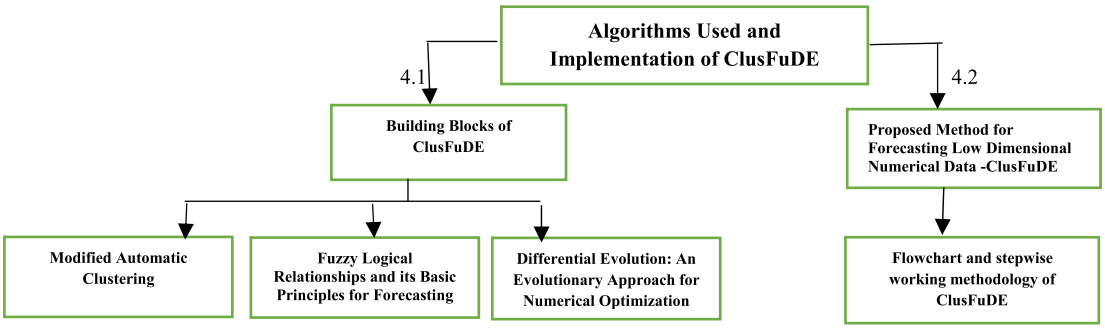


Fig. 1. Structural organization details of Section 4.

3. Related work

From the late 20th century, researchers have focused on forecasting activities and the use of fuzzy time series for forecasting (Chen and Hwang, 2000; Lee et al., 2006; Zarandi et al., 2009). The properties of fuzzy time series are defined in Song and Chissom (1993), and Sullivan and Woodall (1994). Over the years, experts and researchers have focused on the forecasting of educational enrollments. The work in forecasting the University enrollments has been done using both the time variant and time invariant fuzzy time series (Song and Chissom, 1993). Different approaches, such as the use of the time-invariant Markov model (Sullivan and Woodall, 1994), use of arithmetic operations (Chen, 1996; Hwang et al., 1998), determining effective length of intervals with distribution-and average-length based methods (Chen, 2002; Huarng, 2001), first order and time variant methods (Chen and Hsu, 2008, 2004), ratio based interval length (Huarng and Yu, 2006), high order fuzzy time series (Tanuwijaya and Chen, 2009; Xihao and Yimin, 2008) have been studied in literature. The basic concepts of fuzzy sets, fuzzy reasoning and fuzzy linguistics are based on (Zadeh, 1975, 1965; Wu, 1986). Forecasting is studied using statistical techniques and high order fuzzy logical relationships (Chen et al., 2009). Furthermore, the educational enrollment forecasting was dealt with fuzzy interval length and weight age factor (Rajaram and Sakthisree, 2010). The historical enrollments at the University of Alabama were used to illustrate the process of forecasting (Song and Chissom, 1993). According to Tayal et al. (2011), a disadvantage with time series analysis is that the time series should be converted to stationary and periodic series in order to analyse it.

For numeric prediction on continuous values, techniques such as clustering, and fuzzy logic have been used for exploring the area of forecasting. Different Researchers have used clustering for forecasting using time series data (Tanuwijaya and Chen, 2009; Chen and Hsu, 2004; Chen and Hsiao, 2005). Data clustering and fuzzy logical relationships have also proven to be efficient for forecasting purposes, which do not necessarily use the time series principles. The method presented in Chen et al. (2009) is a statistical method that clusters historical data into variable sized intervals and performs fuzzification for forecasting using fuzzy logical relationships. The approach maps the historical data to intervals and then places the data into appropriate fuzzy sets. In addition to this, the field of evolutionary computation has also been associated with cluster analysis, like in Paterlini and Minerva (2003). The first pioneering study on evolutionary computation was presented in Holland (1975). The concept of evolutionary algorithms (EA) is to adapt ideas from the theory of natural selection to explore large search spaces (Holland, 1975). Heuristics deal effectively with the problem of EAs "getting stuck" in local optimum. In studies like in Storn and Price (1997), Qin and Suganthan (2005), and Aladag et al. (2012), the understanding of new search strategies, such as Particle Swarm Optimization and Differential Evolution for numerical optimization outside the search heuristics has been a useful exploration. In Das et al. (2008a) an improved Differential Evolution for clustering has been proposed. These methods offer an insight into an approach where EA can produce effective results for clustering. Although there are other evolutionary computation or swarm intelligence techniques, such as Particle Swarm Optimization, Simulated Annealing, Random Search that have also been studied, according to the studies in Das et al. (2008b), and Paterlini and Krink (2006) Differential Evolution (DE) has proven to be an effective optimization technique for time series prediction problems and in other areas. This is due to its robust character of the scaling factor, the use of a lower number of control parameters and ease of implementation.

4. Algorithms used in the implementation of ClusFuDE

This section is divided into two parts — Sections 4.1 and 4.2. First, Section 4.1 discusses three building blocks used in developing ClusFuDE — Automatic Clustering, Fuzzy Logical Relationships and Differential Evolution. The proposed modifications in the clustering algorithm and Differential Evolution are also explained in this section. Section 4.2 gives the implementation of the proposed ClusFuDE on real world datasets of academic enrollment of University of Alabama, Lahi production, outpatients visit and inventory demand. This section is long in terms of details, so for the ease of understanding, Fig. 1 clearly depicts the structure of this section.

4.1. Building blocks of ClusFuDE

In this section, the building blocks of the proposed ClusFuDE are discussed. The proposed modifications in automatic clustering principal and dynamic differential crossover are presented. Section 4.1.1 discusses the adjoining basics of clustering and the proposed modification in the automatic clustering technique is presented. Section 4.1.2 explains the use of fuzzy logical relationships (with adjoining principles) for forecasting. Section 4.1.3 explains the stochastic population based Differential Evolution algorithm steps with the proposed dynamic differential crossover on the predicted optimization outcomes.

4.1.1. Modified automatic clustering

Cluster analysis is a data analysis tool that sorts different data items into groups in a way that the association degree between two objects in the same cluster is maximal and minimal otherwise. Clustering has been applied in a number of research fields such as medicine, psychiatry, archaeology etc. In short, whenever we have a plethora of information that we want to classify into meaningful piles, data clustering is of great utility. A representative overview of clustering techniques and their applications can be found in Jain et al. (1999). The use of clustering for forecasting has also been studied (Chen and Wang, 2010; Tanuwijaya and Chen, 2009; Chen et al., 2009; Chen and Hsiao, 2005; Mitchell, 2003). In Chen et al. (2009) a statistical method of clustering numerical data and transforming the clustered data into intervals is presented. The method does not require a priori knowledge of the number of clusters, but this proposed method fails to address the

Sort the data in ascending sequence
Compute average difference (average_diff) using:

$$average_diff = \frac{\sum_{i=1}^{n-1}(d_{i+1} - d_i)}{n-1} \quad \text{(i)}$$

Where, "*average_diff*" denotes the average of the differences between every pair of data in ascending data sequence.

Put the smallest datum in the ascending sequence in the first cluster (current cluster)

IF current cluster != first cluster

$d_1, \{..d_i\}, d_j \ldots,..d_n$
d_j is the adjacent datum and d_i is the largest datum in antecedent cluster
begin
Compute current cluster count, K_c
PRINCIPLE 1
if K_c =1 /* element count in current cluster*/
if ($d_j - d_i$<= average_diff)
then put d_j into current cluster
else create new cluster for d_j
PRINCIPLE 2
if K_c !=1
if($d_j - d_i$<= average_diff) and ($d_j - d_i$<= cluster_diff)

$$/* cluster_diff = \frac{\sum_{i=1}^{n-1}(c_{i+1} - c_i}{n-1} */ \quad \text{(ii)}$$

then put d_j into current cluster
else create new cluster for d_j
end

IF current cluster = first cluster

$\{d_i\}, d_j, d_k, \ldots\ d_n$
d_i is the current cluster datum and d_j is the adjacent datum
begin
Computer cluster count K_c
PRINCIPLE 3
if K_c = 1 /* element count in current cluster*/
if ($d_j - d_i$<= average_diff)
then put d_j into current cluster
else create new cluster for d_j
PRINCIPLE 4
/* **PROPOSED MODIFICATION***/
if K_c =1
if ($d_j - d_i$<= average_diff) and ($d_j - d_i$<= cluster_diff)
then put d_j into current cluster
else create new cluster for d_j
end

Fig. 2. Modified Automatic Clustering Algorithm.

issue of clustering more than one data point in the primary cluster. In the present work, we propose a modification to this clustering algorithm for forecasting university enrollments and then transform the clustered data into intervals of varied lengths. This method relies on the fact that only homogeneous clusters are created and any inhomogeneous clusters are broken apart. The principle of homogeneity is based on the distance metric used in the approach that acts as a decisive factor.

The improved clustering algorithm is used to cluster & transform numerical data into intervals as shown in Fig. 2. The working of the improved clustering algorithm is explained, where the algorithm clusters historical data (low dimensional data) and transforms it into contiguous intervals. The principles to transform clustered data into intervals of varied lengths is presented in Fig. 3, where, first, the contents of the clusters are adjusted in such a manner that it contains *at most* two data points and second, the clusters are transformed into contiguous intervals. Automatic clustering is used for the analysis of low dimensional data because data points under consideration (dataset) have overlapping boundaries. Automatic clustering provides a very elegant way of clearly separating out the homogeneous points. The intra cluster similarity also helps in defeating formation of outliers (as explained earlier).

4.1.2. Fuzzy logical relationships and its basic principles for forecasting

Fuzzy Logic (Zadeh, 1965) has an interesting feature for predicting data under uncertainty. Low dimensional data is aptly modelled by a rich collection of fuzzy sets and their operations. Fuzzy logic is a multivalued logic that allows modelling of imprecise concepts & imprecise dependencies (Ross, 1995). This imprecision is represented by a fuzzy set, which has a smooth boundary. The fuzzy set is associated with a degree of membership. For forecasting of academic enrollments, a fuzzy time series is used. In this work, for comparing forecasting results with other methods in the literature, the forecasting of enrollments of the University of Alabama is considered. The fuzzy time series model in forecasting can be defined as follows:

Let $Y(t)\,(t = \ldots, 0, 1, 2 \ldots)$ a subset of R^1,

be the universe of discourse on which fuzzy sets $f_i(t)\,(i = 1, 2, \ldots.)$ are defined and,

$F(t)$ is the collection of $f_i(t)\,(i = 1, 2, \ldots)$,

then $F(t)$ is called the fuzzy time series on $Y(t)\,(t = \ldots, 0, 1, 2 \ldots)$

Where, $F(t) \rightarrow$ linguistic variable; a function of time

$f_i(t)\,(i = 1, 2, \ldots.) \rightarrow$ possible linguistic values of $F(t)$

Content Adjustment

Based on the clustering results obtained , adjust the contents of the clusters:
Principle 1: If a cluster has more than two datum
Then keep the largest and the smallest datum
Principle 2: If cluster has exactly two data
Then leave cluster unchanged
Principle 3: If cluster has only one datum *X*,
compute '*X- average_difference*'
If ('*X- average_difference*'<Y) /*Y= Largest value in the antecedent cluster */
Then leave it unchanged
else put'*X+average_diff*" and '*X- average_difference*' in the cluster and remove *X*

Transformation into intervals

$\{d_1,d_2\};\{d_3,d_4\}\ldots\ldots\ldots;\{d_m,d_n\}$ /* Clusters after content adjustment*/
$d_1,d_2,\ldots,d_n$ are data in respective clusters

begin
for cluster $\{d_1,d_2\}$ /* First cluster forms the first interval*/
form interval $[d_1,d_2)$
endfor

for current interval $[d_i,d_j)$ and current cluster $\{d_k,d_l\}$ /* current cluster $\{d_k,d_l\}$ and current interval $[d_i,d_j)$ */
if $d_k \leq d_j$
then transform current cluster into interval $[d_j,d_l)$
/* Let current interval = $[d_j,d_l)$ and next cluster = $\{d_m,d_n\}$*/

else transform current cluster $\{d_k,d_l\}$ into interval $[d_k,d_l)$ and create new interval $[d_j,d_k)$
if current interval $[d_i,d_j)$ and current cluster is $\{d_k\}$
then transform current interval$[d_i,d_j)$ into $[d_i,d_k)$
/* Let $[d_i,d_k)$ be the current interval and next cluster be the current cluster*/
endif

/*Repeatedly check the current interval and current cluster till all the clusters are transformed into intervals*/
endfor
/* Calculate midpoints for each obtained interval*/
end

Fig. 3. Cluster Transformation into intervals.

The use of fuzzy logical relationships for forecasting numerical data is studied in Chen and Wang (2010), and Chen and Chen (2010b). A novel method for forecasting, using low order fuzzy logical relationships, is studied in Chen et al. (2009), which uses the principle that the variation in a current year is related to the trend in the previous year. The method uses the approach of establishing fuzzy logical relationships, where the data,

$$d_1, d_2, d_3 \ldots d_n$$

are fuzzified into fuzzy sets $A_1, A_2 \ldots A_n$ based on the formed contiguous intervals. For instance, if the fuzzified data of year i and $i+1$ are A_r and A_s respectively, then we can construct a fuzzy logical relationship "$A_r \rightarrow A_s$" where "A_r" and "A_s" are the current state and the next state respectively. The forecasting method is then defined as follows:

Apply the clustering algorithm to cluster the data into intervals (Figs. 1 and 2) and calculate the midpoint values of the intervals. For n intervals u_1, $u_2 \ldots$ and u_n, define the fuzzy set A_i and fuzzify data into the corresponding fuzzy set. The principles of forecasting are given as follows:

Principle 1: If the fuzzy logical relationship (FLR) in the fuzzy logical relationship group is "$A_r \rightarrow A_s$" where A_r, A_s are the fuzzified data of years t and $t+1$, then the forecasted data value of year $t+1$ is m_s, where m_s is the midpoint of the interval u_s.

Principle 2: If there is a fuzzy logical relationship group whose current state is A_r,"$A_r \rightarrow A_{k1}(x_1), A_{k2}(x_2) \ldots A_{kp}(x_{kp})$", then the forecasted data for year $t+1$ is calculated as given below in (1):

$$x_1 * m_{k1} + x_2 * m_{k2} + \cdots + x_p * m_{kp} / x_1 + x_2 + \cdots + x_p \quad (1)$$

where, x_i denotes the number of fuzzy logical relationships "$A_r \rightarrow A_{ki}$" in the fuzzy logical relationship group, $1 \leq i \leq p; m_{k1}, m_{k2}, \ldots,$ and m_{kp} are the midpoints of intervals $u_{k1}, u_{k2}, \ldots,$ and u_{kp} respectively. For the sake of brevity, the details of the method are not presented here and further description can be found in Chen et al. (2009).

4.1.3. Differential evolution: an evolutionary approach for numerical optimization

Evolutionary algorithms have found huge number of applications in both supervised and unsupervised learning scenarios (Katari et al., 2007). Differential Evolution is an evolutionary meta-heuristic, which optimizes a problem by improving a candidate solution iteratively with respect to an objective function. The method is fairly fast and robust. The method can handle non-differentiable, nonlinear and multimodal objective functions. In an n-dimensional search space, vectors are randomly chosen, which are evolved over time in order to efficiently search the space and to find the minimum value of objective function. The basic functional components of the algorithm are: (i) Initialization (ii) Mutation (iii) Crossover and (iv) Selection. The algorithm initializes a set of vectors in the form of a chromosome. The structure of a chromosome is depicted in Fig. 4. In the literature, these vectors are called chromosomes or genomes.

Different methods for obtaining crossover and mutation have been proposed in the literature (Das et al., 2008a, b; Tvrdik, 2007; Das et al., 2005; Zaharie, 2007). The Differential Evolution method used for optimizing the results of forecasted data is defined as follows:

Step 1 : Initialize ith individual vector, at time step t generation g, with initial lower and upper bounds. For jth component of ith member, (using

...	$X_{1,g}$	$X_{2,g}$	$X_{3,g}$	...	...	...	$X_{n-1,g}$	$X_{n,g}$	...

Fig. 4. Structure of the Chromosome.

Eq. (2))

$$x(i,j) = x\left(Lower_j\right) + rand\,(0,1).\{x\left(Upper_j\right) - x\left(Lower_j\right)\} \quad (2)$$

Where, rand (0, 1) is a uniformly distributed random number between 0 and 1. The generation number refers to the iteration of the algorithm, which generates a mutant vector.

Step 2: Apply Mutation and generate the mutant vector using Eq. (3). The basic variant of Differential Evolution, DE/best/1 is used. The scale factor *f*, generates the vector as follows:

$$\overbrace{X_{best,n(t)} + f(X_{i,n(t)} - X_j, n(t))}^{X_{off}}, \quad (3)$$

where, X_{off} is the trial vector, X_{best} is the best value from the candidate population, f is the scale factor. The scale factor is varied in a basic form as in Eq. (4):

$$f = 0.5 * \{rand\,(0,1)\} \quad (4)$$

Step 3: For diversity in the population, the *proposed crossover (Cr)* is performed as given in Eq. (5). Crossover enables to diversify the population and leads to a better selection of trial vector.

$$Cr_i = 0.5 * \left[f_{av} - f_i + rand(0,1)\right] \quad (5)$$

where, f_{av} is the mean value of scale factor, f_i is the value of scale factor for *i*th candidate solution. If the adaptive crossover rate of the *i*th solution is close to minimum value of Cr ($Cr_{min} = 0.5$) then Cr_i tends to be a small value and if it is close to C_{rmax} ($Cr_{max} = 1.0$) then Cr_i tends to be large (Zaharie, 2007).

The dynamic nature of Differential Evolution influences retaining of individuals with lower errors. Their selection in the next generation encourages the production of offsprings with better quantitative value. The vector is selected based on a minimization objective function, which reduces the error rate between the optimized value and actual value. For more details on Differential Evolution the readers can look into (Zaharie, 2007).

4.2. Proposed method for forecasting low dimensional numerical data — ClusFuDE

In this sub-section, the implementation of the proposed ClusFuDE approach for optimizing low dimensional numerical data using clustering, fuzzy logical relationships and Differential Evolution is presented. The historical data (low dimensional) is clustered using an improved automatic clustering technique and fuzzy logical relationships are applied to the clustered data for forecasting. The forecasted values (candidate solutions) are subjected to initialization in the Differential Evolution. The essence of Differential Evolution is in the operation of the control parameters — Mutation and crossover. Mutation and crossover operators are used to diversify the population. Then, in subsequent iterations, the solution (trial vector: minimizing the objective function) is selected otherwise the parent is retained. In forecasting time series data, the objective function is a minimization function. The trial vector is admitted to the next generation only if it minimizes the mean square error.

The block diagram depicting the steps of the proposed method is illustrated in Fig. 5. The detailed explanation of the experimentation is made available for the University enrollments dataset. The stepwise working of the proposed method is given to obtain the optimized values of low dimensional enrollment data. The historical enrollments of University of Alabama (Song and Chissom, 1993) are presented in

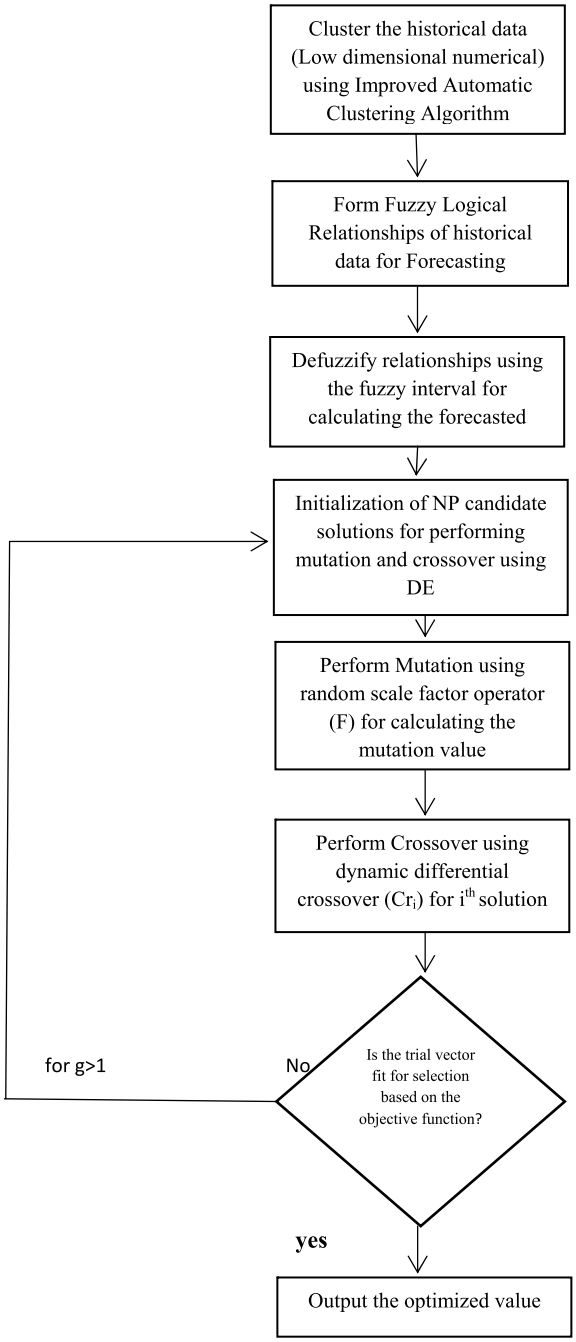


Fig. 5. Flowchart of the Proposed System: ClusFuDE.

Table 1. First, we cluster the historical data as explained in Section 4.1, and then we establish fuzzy logical relationships (FLRs) for forecasting and optimizing the intervals using Differential Evolution.

Step 1: *Apply the improved automatic clustering algorithm (Fig. 2) to cluster the historical enrollments into distinct clusters* $c_1, c_2 \ldots c_n$. [Section 4.1]

Step 1.1: If the current cluster is not the first cluster and has only one datum in it, then perform clustering using

Table 1
Year-wise enrollments of University of Alabama from 1971 to 1992.

Year	Actual enrollment	Year	Actual enrollment
1971	13055	1982	15433
1972	13563	1983	15497
1973	13867	1984	15145
1974	14696	1985	15163
1975	15460	1986	15984
1976	15311	1987	16859
1977	15603	1988	18150
1978	15861	1989	18970
1979	16807	1990	19328
1980	16919	1991	19337
1981	16388	1992	18876

principle 1 and if it has more than one datum in it then use ***principle 2*** as shown in Fig. 2.

Step 1.2 If the current cluster is the first cluster and has only one datum in it, then perform clustering using ***principle 3*** and if it has more than one datum then use the ***proposed principle 4*** as shown in Fig. 2. Repeatedly perform *steps 1.1* and *1.2* on the sorted data sequence to automatically cluster the historical enrollments.

Step 2: *Transform the clustered data into intervals* u_1, $u_2 \ldots u_n$ *of varied lengths (shown in Table 2).*

Step 3: *Define each fuzzy set* A_i *based on the intervals and fuzzify the data where fuzzy set* A_i *denotes the linguistic value of the enrollment data represented by a fuzzy set (as shown in Table 3).*

Step 4: *Establish fuzzy logical relationships (FLRs) based on the fuzzified data where the FLRs "*$A_i A_j$*" denotes that if fuzzified data of year 'i' is* A_i *then the fuzzified data of year 'j' is* A_j *(shown in Table 4)*

Step 5: *Forecast values based on fuzzy logical relationship groups (FLRGs)[Section 4.1.2]*
/ This acts as a candidate solution for Differential Evolution */*

Step 6: *Optimize the forecasted results using Differential Evolution [*Section 4.1.3*]*
/ ClusFuDE */*

Using the above proposed forecasting method, the forecasted enrollments of the University of Alabama are presented in Table 5. Forecasted results from Tables 5 and 6 serve as candidate solutions for Differential Evolution. The objective function is a minimization function which minimizes the forecasting error (Mean Square Error).

The methodology is tested on numerical data of Lahi (crop) production (Singh, 2007), monthly amount of outpatients visit in a hospital (Cheng et al., 2008), inventory demand (Chen and Chen, 2010a) and population of India from years 1930–2000 (Lahmeyer, 2003). The method gives the lowest error of forecasting, i.e. good accuracy of the optimized data. These results can be correlated from Section 5.

5. Experimentation, evaluations, comparison and analysis

In Section 5.1, the experimental details are presented, then 5.2 gives the evaluation metrics used for dispersion analysis, 5.3 presents the counterpart comparison with the methods in the literature and finally in Section 5.4, the convergence and analysis of the proposed method is discussed.

5.1. Experimentation

In the following section, the proposed algorithm is tested with well-known real world datasets of historical enrollments of the University of Alabama (Song and Chissom, 1993), Lahi crop production (Singh, 2007), monthly amount of outpatients' visit (Cheng et al., 2008) in a hospital, inventory demand (Chen and Chen, 2010a) and population of India from years 1930–2000 (Lahmeyer, 2003). The first dataset consists on

Table 2
Fuzzy intervals for enrollment dataset.

Intervals		Midpoint value (for forecasting)
u_1 =	[13055, 13354)	13205
u_2 =	[13354, 13862)	13608
u_3 =	[13862, 14166)	14014
u_4 =	[14166, 14397)	14282
u_5 =	[14397, 14995)	14696
u_6 =	[14995, 15145)	15070
u_7 =	[15145, 15163)	15154
u_8 =	[15163, 15311)	15237
u_9 =	[15311, 15497)	15404
u_{10} =	[15497, 15603)	15550
u_{11} =	[15603, 15861)	15732
u_{12} =	[15861, 15984)	15923
u_{13} =	[15984, 16089)	16037
u_{14} =	[16089, 16687)	16388
u_{15} =	[16687, 16807)	16747
u_{16} =	[16807, 16859)	16833
u_{17} =	[16859, 16919)	16889
u_{18} =	[16919, 17851)	17385
u_{19} =	[17851, 18449)	18150
u_{20} =	[18449, 18876)	18663
u_{21} =	[18876, 18970)	18923
u_{22} =	[18970, 19328)	19149
u_{23} =	[19328, 19337]	19333

Table 3
Fuzzy logical relationships for forecasting enrollment dataset.

Year	Actual enrollments	Fuzzified enrollments
1971	13055	A1
1972	13563	A2
1973	13867	A3
1974	14696	A5
1975	15460	A9
1976	15311	A9
1977	15603	A11
1978	15861	A12
1979	16807	A16
1980	16919	A18
1981	16388	A14
1982	15433	A9
1983	15497	A10
1984	15145	A7
1985	15163	A8
1986	15984	A13
1987	16859	A17
1988	18150	A19
1989	18970	A22
1990	19328	A23
1991	19337	A23
1992	18876	A21

Table 4
Fuzzy logical relationships for enrollment dataset.

Group1	A1->A2
Group2	A2->A3
Group3	A3->A5
Group4	A5->A9
Group5	A7->A8
Group6	A8->A13
Group7	A9->A9(1); A10(1); A11(1)
Group8	A10->A7
Group9	A11->A12
Group10	A12->A16
Group11	A13->A17
Group12	A14->A9
Group13	A16->A18
Group14	A17->A19
Group15	A18->A14
Group16	A19->A22
Group17	A21->#
Group18	A22->A23
Group19	A23->A21(1), A23(1)

Table 5
Forecasted enrollment values and optimized enrollment values using differential evolution ($G = 50$).

Year	Actual enrollments	Forecasted enrollments Candidate Solution	Population At $G = 0$		Optimized enrollments At $G = 50$
1971					
1972	13608	13608	X1(0) =	[13608]	13560
1973	13865	14014	X2(0) =	[14014]	13800
1974	14695	14696	X3(0) =	[14696]	14545
1975	15456	15404	X4(0) =	[15404]	15001
1976	15309	15562	X5(0) =	[15562]	15111
1977	15603	15562	X6(0) =	[15562]	15862
1978	15863	15923	X7(0) =	[15923]	15213
1979	16805	16833	X8(0) =	[16833]	16218
1980	16920	17385	X9(0) =	[17385]	16900
1981	16387	16388	X10(0) =	[16388]	16767
1982	15435	15404	X11(0) =	[15404]	15897
1983	15497	15562	X12(0) =	[15562]	15465
1984	15147	15154	X13(0) =	[15154]	15837
1985	15163	15237	X14(0) =	[15237]	15485
1986	15988	16037	X15(0) =	[16037]	15968
1987	16857	16889	X16(0) =	[16889]	16855
1988	18155	18150	X17(0) =	[18150]	18875
1989	18971	19149	X18(0) =	[19149]	18475
1990	19322	19333	X19(0) =	[19333]	19867
1991	19337	19128	X20(0) =	[19128]	19857
1992	18873	19128	X21(0) =	[19128]	18879

Table 6
Final optimized results obtained by ClusFuDE for year wise enrollments of University of Alabama ($G = 100$).

Year	Forecasted enrollments (candidate solution)	Optimized enrollments (Using ClusFuDE) ($G = 100$)	Year	Forecasted enrollments (candidate solution)	Optimized enrollments (Using ClusFuDE) ($G = 100$)
1971	–	–	1982	15404	15435
1972	13608	13608	1983	15562	15497
1973	14014	13865	1984	15154	15147
1974	14696	14695	1985	15237	15163
1975	15404	15456	1986	16037	15988
1976	15562	15309	1987	16889	16857
1977	15562	15603	1988	18150	18155
1978	15923	15863	1989	19149	18971
1979	16833	16805	1990	19333	19322
1980	17385	16920	1991	19128	19337
1981	16388	16387	1992	19128	18873

values of enrollments from years 1971–1992. The data is characterized by the value of enrollment in a particular year. Similarly, the Lahi crop data is in terms of productivity in kilogram per hectare (kg/ha) from 1981–2003, the number of outpatients visit (monthly) from the department of internal medicine in a hospital, the inventory demand dataset from time 1 to time 24. The population of India from years 1930–2002 was accessed online from Lahmeyer (2003). The file contains the historical, demographical and statistical overview of the population of all the countries in the world, their administrative divisions and their important cities. The construction and lay-out of this site was set up in April 1999; in January 2002 the compiler (*Jan Lahmeyer*) completed the first input of all files and is still continuing the work. The population data for India is chosen such that it has the specific information of the historical demographic development of the whole country.

Settings in Training Phase

The automatic clustering algorithm and the fuzzy logical relationships do not require any parameter settings. In DE, the parameters such as population size NP, is almost twice the number of dimensions for any particular application. The number of iterations initially set to 50 and extended up to 100 with different interval values. The population values (representing different chromosomes) in different intervals are shown in Table 7. Further, the scale factor f and the dynamic crossover rate Cr are varied in a random manner as explained previously. The average value of scale factor f_{av}, 0.48 is taken (random iterations), ith scale factor value f_i, is determined for every solution using Eq. (4). The X_{best} vector is perturbed by scaling the difference of two random vectors. The training data for all datasets are as follows: academic enrollment of University of Alabama, the enrollments from 1971 to 1992, for Lahi crop, production count from 1981–2003, outpatient's visit from January–December 2005, inventory demand from 1 to 24 time units.

The application was built in C# with Microsoft VisualStudio.NET 2017 for the Differential Evolution. For executing the forecasting queries, scripts are written in Microsoft SQL Server 2012. The experiment was run on Windows 7 on a DELL latitude PC (64 bit operating system) with Intel(R) core i5 CPU at 2.67 GHz processor with 4 GB installed memory.

Settings in Testing Phase:

In the experiment, the enrollment from 1990–92, Lahi production from 2001–2003, outpatient visit from October–December, inventory from 20–24 time units are used for testing. Tables 8 to 11 show the performance comparison of the data with other existing methods. The evaluation of the results is done using evaluation metrics (as explained in Section 5.2). Since, the method works on numerical optimization, it is fairly easy to omit the complex chromosome structure representation of the solutions. The results are validated in real numbers.

5.2. Evaluation criteria

The proposed statistical approach studies the quantitative data. This section presents the evaluation criteria for ClusFuDE with other existing methodologies in the literature. The comparison is given for the year-wise enrollments of the University of Alabama. The dispersion is studied

Table 7
The population values (chromosomes) in different intervals.

Year	Actual enrollments	2	4	5[a]	6	7[a]	8	9	10[a]
1972	13563	13560	13561	13565	13565	13558	13564	13564	13608
1973	13867	13863	13865	13869	13871	13862	13868	13872	13865
1974	14696	14692	14691	14692	14693	14693	14695	14695	14695
1975	15460	15458	15456	15457	15457	15458	15459	15456	15456
1976	15311	15307	15308	15311	15310	15307	15306	15307	15309
1977	15603	15600	15602	15601	15600	15600	15599	15598	15603
1978	15861	15860	15857	15859	15856	15858	15858	15856	15863
1979	16807	16806	16805	16805	16803	16805	16804	16806	16805
1980	16919	16914	16919	16917	16917	16915	16919	16915	16920
1981	16388	16384	16388	16384	16386	16385	16385	16386	16387
1982	15433	15430	15430	15428	15429	15431	15428	15429	15435
1983	15497	15493	15493	15499	15496	15497	15501	15501	15497
1984	15145	15148	15140	15148	15148	15143	15147	15145	15147
1985	15163	15163	15163	15161	15167	15158	15160	15162	15163
1986	15984	15988	15983	15987	15982	15981	15982	15988	15988
1987	16859	16859	16859	16863	16860	16861	16856	16857	16857
1988	18150	18147	18147	18149	18146	18149	18148	18147	18155
1989	18970	18969	18967	18967	18967	18968	18968	18966	18971
1990	19328	19325	19327	19325	19324	19327	19327	19325	19322
1991	19337	19334	19335	19333	19336	19333	19337	19334	19337
1992	18876	18881	18877	18878	18875	18879	18879	18876	18873

[a] Best performance values are taken.

very easily using descriptive measures like the mean square error that quantifies the error rate in the proposed approach.

For performance comparison of the proposed ClusFuDE, we calculate the Mean Square Error (MSE) and the Mean Absolute Percentage Error (MAPE) and the values are compared with the results of the previous methods in the literature. The MSE and MAPE are given by Eqs. (6), and (7) where, O_i denotes the optimized value & A_i denotes the actual value of data (i.e. the parent value) (i),

$$MSE = \frac{\sum_{i=1}^{n}(O_i - A_i)^2}{n} \tag{6}$$

$$MAPE = \frac{I}{N}\sum \|(O_i - A_i)/\|A_i * 100\% \tag{7}$$

These evaluation metrics (MSE and MAPE) are widely used for time series analysis. MSE is scale dependent and MAPE offers an easy interpretation of the results in percentages. This is useful for comparing accuracy across time series analysis.

5.3. Counterpart comparison

In Table 3, a comparison of the results obtained from the proposed ClusFuDE method is done with that of Chen et al.'s method (Chen et al., 2009), Rajaram & Sakthisree's method (Rajaram and Sakthisree, 2010), Huang's Method (Huang et al., 2011), Aladag's Method (Aladag et al., 2012), Radmehr's Method (Radmehr and Gharneh, 2012), Jasim's Method (Jasim and Salim, 2012), Wazan's Method (Wazan et al., 2014), Qiu's Method (Qiu et al., 2015), Bisht's Method (Bisht and Kumar, 2016), and Jiang's Method (Jiang et al., 2017). The proposed method exhibits the smallest Mean Square Error and the smallest Mean Absolute Percentage Error as compared to other methods of forecasting as shown in Table 8. That is, the proposed method gets a higher forecasting accuracy rate for forecasting university enrollments than the previous existing methods (Chen et al., 2009; Rajaram and Sakthisree, 2010; Huang et al., 2011; Aladag et al., 2012; Radmehr and Gharneh, 2012; Jasim and Salim, 2012; Wazan et al., 2014; Qiu et al., 2015; Bisht and Kumar, 2016; Jiang et al., 2017).

Table 9 shows the superiority of the proposed model over the Singh's (Singh, 2008) model with seven and twenty intervals and Chen's (Chen and Hwang, 2000) model for the forecast of Lahi crop production. For the forecast of monthly amount of outpatients visit in a hospital, Table 10 shows that the proposed method forecasts better than Hadavandi et al. (2012) method and Cheng's method (Zarandi et al., 2009). For the optimized forecast of inventory demand from Table 11, we can note that the proposed method gets a higher forecasting accuracy than the Huarng and Yu's method (Huarng and Yu, 2006), the AR(1) model and AR(2) model (Chen and Wang, 2010), and the Chen's method (Chen and Chen, 2010a).

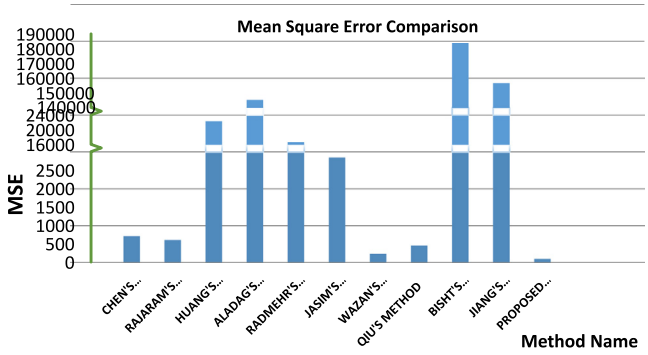


Fig. 6. Comparison of Mean Square Errors.

The proposed method is able to forecast the university enrollments with higher forecasting accuracy rate than all of the existing methods (please refer to Figs. 6 and 7). The proposed methodology has also been applied on the real world dataset of Lahi (crop) production (Aydin et al., 2009), monthly amount of outpatients visit in a hospital (Chen et al., 2013), inventory demand (Yu, 2005) and population of India from years 1930–2000. In all these cases the proposed method also achieves a lower Mean Square Error as compared to other approaches (Please refer to Tables 8–12). The overlapping graphs in Figs. 8–12 clearly indicate the optimized performance of the proposed method ClusFuDE.

5.4. Analysis

The idea behind the proposed descriptive statistical model for low dimensional numerical data is twofold: first, to analyse fuzzy logical relationships for low dimensional data. Second, to use a self-adaptive dynamic crossover parameter with fuzzy logical relationships for optimizing the uncertainty with predicted outcomes.

Table 8
Comparison of ClusFuDE and other existing forecasting methods for enrollments of University of Alabama.

Year	Actual enrollment	2009 Chen's Method (Chen et al., 2009)	2010 Rajaram's Method (Rajaram and Sakthisree, 2010)	2011 Huang's Method (Huang et al., 2011)	2012 Aladag's Method (Aladag et al., 2012)	2012 Radmehr's Method (Radmehr and Gharneh, 2012)	2012 Jasim's Method (Jasim and Salim, 2012)	2014 Wazan's Method (Wazan et al., 2014)	2015 Qiu's Method (Qiu et al., 2015)	2016 Bisht's Method (Bisht and Kumar, 2016)	2017 Jiang's Method (Jiang et al., 2017)	Proposed ClusFuDE 2017
	13055	–	–									–
1972	13563	13608	13537	13527	13480	13706	13350	13568	13566	13596		13608
1973	13867	13892	13815	13928	13480	13706	13850	13869	13887	13815		13865
1974	14696	14696	14705	14680	14781	14749	14650	14686	14646	14930		14695
1975	15460	15467	15465	15305	15474	15341	15450	15463	15481	15541	15679	15456
1976	15311	15314	15314	15477	15524	15346	15317	15297	15299	15541	15838	15309
1977	15603	15629	15569	15477	15610	15346	15650	15626	15624	15541	16290	15603
1978	15861	15873	15827	15891	15563	15923	15825	15849	15871	15541	15921	15863
1979	16807	16818	16808	16655	16752	16839	16850	16796	16816	16255	16862	16805
1980	16919	17012	16922	17143	16838	17046	16950	16953	16910	17040	17066	16920
1981	16388	16388	16395	16655	16838	16400	16350	16395	16338	17040	16811	16387
1982	15433	15413	15391	15649	15902	15455	15450	15416	15433	16255	15362	15435
1983	15497	15521	15443	15477	15525	15346	15450	15498	15481	15541	15524	15497
1984	15145	15147	15148	15305	15527	15346	15150	15125	15147	15541	15275	15147
1985	15163	15180	15171	15114	15493	15341	15150	15160	15162	15541	14821	15163
1986	15984	15995	15989	15649	15571	15923	15975	15988	15993	15541	16168	15988
1987	16859	16863	16863	16655	16907	16839	16850	16859	16854	16255	17154	16857
1988	18150	18150	18144	18023	16838	18007	18150	18130	18100	17040	18678	18155
1989	18970	19006	18952	18932	19144	19059	18975	18958	18962	18902	19298	18971
1990	19328	19329	19292	19307	19144	19197	19350	19306	19329	19357	20266	19322
1991	19337	19336	19344	19307	19144	19197	19350	19356	19336	19169	19653	19337
1992	18876	18885		18932	19144	19059	18850	18903	18884	19169	19310	18873
MSE		718.24	618.25	22340	145399	16660.29	2851.29	246	461.62	183749	156653	**102.8095**
MAPE		0.104	0.11386	0.7348	1.5829	0.684437	0.20458	0.0754	0.0909	1.9403	1.8606	**0.027204**

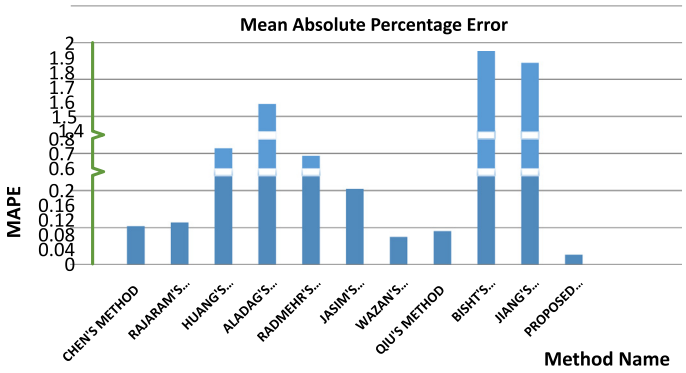


Fig. 7. Mean Absolute Percentage Error Comparison.

Table 9
Comparison of optimized forecasted results of Lahi production with existing methods.

Year	Actual production	Chen and Hwang (2000)	Singh's Method — 2007	Singh (2008) (Int' 7; 2008)	Singh (2007) (Int' 20; 2008)	Proposed ClusFuDE
1981	–	–	–	–	–	–
1982	**1030**	783.33	–	–	–	
1983	**704**	800	–	–	–	**1004.5**
1984	**453**	783.33	850	850	837.5	**470.92**
1985	**507**	725	450	450	452.5	**439.5**
1986	**785**	650	559.75	541.42	491.8	**502.29**
1987	**482**	800	750	750	767.5	**774.3**
1988	**798**	725	450	450	452.5	**765.02**
1989	**988**	650	750	750	802.5	**795.1**
1990	**380**	725	950	950	977.5	**369**
1991	**761**	800	750	750	732.5	**734**
1992	**988**	725	669.5	658.33	631.7	**834.5**
1993	**380**	950	950	974	977.5	**392.7**
1994	**761**	800	746	746	754.7	**758.5**
1995	**772**	725	851.33	851.33	877.5	**781.8**
1996	**501**	725	550	550	592.5	**599.6**
1997	**595**	800	444.5	444.5	487.5	**499**
1998	**887**	650	570.5	553.92	591.7	**889.5**
1999	**772**	800	950	950	907.5	**911.1**
2000	**772**	800	850	858.72	872.5	**862.2**
2001	**1061**	725	850	833.33	804.3	**1001.18**
2002	**944**	725	1050	1050	1082.5	**1065.8**
2003	**944**	783.33	957.25	957.25	907.5	**916.7**
	MSE	60026.4	71898.66	75063.09	77350.62	**18528.75**
	MAPE	34.03664	36.66202	37.37959	38.2991	**14.01996**

Table 10
Comparison of optimized forecasted results of Lahi production with existing methods.

Month	Outpatients Visit	Cheng et al. (2008)	Hadavandi et al. (2012)	Proposed
2005/01	5920	5982	5803	
2005/02	5512	5012	5623	5512
2005/03	6548	6555	5536	6545
2005/04	5987	6897	5721	5986
2005/05	5638	5633	5746	5640
2005/06	5851	5876	5593	5848
2005/07	5514	4356	5670	5509
2005/08	5395	4675	5534	5358
2005/09	5598	5588	5480	5595
2005/10	5284	5245	5501	5281
2005/11	4545	4587	5361	4539
2005/12	4624	4523	4624	4644
	MSE	246299.4	164138.7	**170.0909**
	MAPE	5.359393	4.982277	**0.145515**

5.4.1. The hybrid idea

The idea of fuzzy logical relationships with dynamic Differential Evolution fostered because of the independent advantages of both concepts. Fuzzy logical relationships offer a simplified way of modelling the relationships between data for forecasting. They minimize the complicated computations of fuzzy relational matrices and provide a suitable defuzzification process for better accuracy of the forecasted values. They are critical to the success of the process because they generate linguistic relationships between the data.

Differential Evolution enables easy use of control parameters (scale factor, crossover). The control parameters do not use any probability distribution rather diversify the population by scaling the random differences of selected vectors. The self-adaptive control parameters have a different impact on the outcome. The proposed method presents

Table 11
Comparison of optimized inventory demand (Test Data) with existing methods.

Time	Actual Demand	Huarng (2001)	Huarng and Yu (2006)	AR(1) Chen and Wang (2010)	AR(2) Chen and Wang (2010)	Chen and Chen (2010a)	Proposed ClusFuDE
20	**227**	208	206	209	192	210	**222**
21	**223**	228	228	232	242	224	**224**
22	**242**	228	228	228	221	224	**238**
23	**239**	244	244	247	255	234	**235**
24	**266**	236	244	244	237	244	**265**
	MSE	301.4	234.2	229.8	624.8	224.6	**11.8**
	MAPE	5.953513	5.528221	5.873694	10.04264	5.147632	**1.270709**

Table 12
Computed Mean Square Error (MSE) for population of India (1930–2000).

Year	Population of India	Optimized population (India)	Year	Population of India	Optimized population (India)
1930	277175	–	1967	504345	**504326**
1931	279115	**279133**	1968	515601	**515581**
1932	284102	**284084**	1969	527177	**527153**
1933	287902	**287871**	1970	539075	**539052**
1934	291753	**291801**	1971	547900	**547882**
1935	295666	**295619**	1972	563530	**563577**
1936	299614	**299597**	1973	575887	**575916**
1937	303626	**303653**	1974	588299	**588324**
1938	307694	**307684**	1975	600763	**600774**
1939	311820	**311772**	1976	613273	**613250**
1940	316004	**316015**	1977	630200	**630185**
1941	318826	**318791**	1978	644330	**644354**
1942	324180	**324157**	1979	658730	**658741**
1943	328255	**328293**	1980	688956	**688982**
1944	332332	**332363**	1981	685200	**685179**
1945	336562	**336568**	1982	703570	**703598**
1946	340796	**340788**	1983	719090	**719064**
1947	345085	**345078**	1984	734870	**734853**
1948	349430	**349440**	1985	749184	**749224**
1949	353832	**353862**	1986	767200	**767201**
1950	350445	**350478**	1987	783730	**783734**
1951	363211	**363235**	1988	797526	**797569**
1952	369231	**369199**	1989	817490	**817449**
1953	375633	**375617**	1990	833929	**833917**
1954	382438	**382477**	1991	843931	**843980**
1955	395096	**395086**	1992	883473	**883452**
1956	397334	**397322**	1993	900453	**900487**
1957	405450	**405428**	1994	918570	**918541**
1958	414021	**414059**	1995	934228	**934256**
1959	423053	**423061**	1996	945121	**945158**
1960	431463	**431498**	1997	962378	**962359**
1961	438800	**438799**	1998	979673	**979677**
1962	452378	**452365**	1999	997515	**997541**
1963	462196	**462246**	2000	1014003	**1014002**
1964	472305	**472342**			
1965	482706	**482673**		**MSE**	**740.91429**
1966	493389	**493375**		**MAPE**	**0.0051746**

encouraging results for self-adaptive control of differential parameters. It selects the fittest individual for the next iteration (minimizing the difference between the expected and actual outcome).

There are two major advantages of dynamic crossover with fuzzy logical relationships. *First*, it helps in handling sub-optimal forecasted candidate solutions. Take for example, the values which are close to each other, during the formation of fuzzy logical relationships, map to the same interval value. This results in the same forecasted value for different time periods. The dynamic differential crossover significantly improves the interval values thus, reducing the chances of overlapping for the values. *Second*, it controls how much the parent influences the solution (offspring) which is admitted to the next generation. In the proposed ClusFuDE method, the crossover also considers the influence of the solution pairs which are helpful in selecting the mutation score.

5.4.2. Constraints

Differential Evolution is a fast and robust population based scheme. Along with its advantages, parameter tuning is necessary for good results. For some values of the parameters, the algorithm may not guarantee optimum results. It works on a trial-and-error mechanism. The optimal crossover and mutation values (in a genetic process) may vary with the problem in consideration. The influence of control parameters can be gauged based on the solution's quality. Furthermore, there are many variants of Differential Evolution. The appropriate selection of the variant is also important. The variants differ in the formation of the solution, so a hit-and-trial mechanism needs to be employed.

5.4.3. Convergence

In Brest et al. (2006), it is studied that the convergence in dynamic Differential Evolution is not straightforward because of random changes in control parameters. The convergence measures for Differential Evolution are studied in Feoktistov (2006). One of the measures is discussed here which depicts the convergence of the algorithm.

P-measure (Population Measure) accounts for the clustering of individuals around the optimum. The higher is the density, the better is the convergence. *P*-measure is the distance between the centre of the formed solutions and the solution farthest from it. The centre is

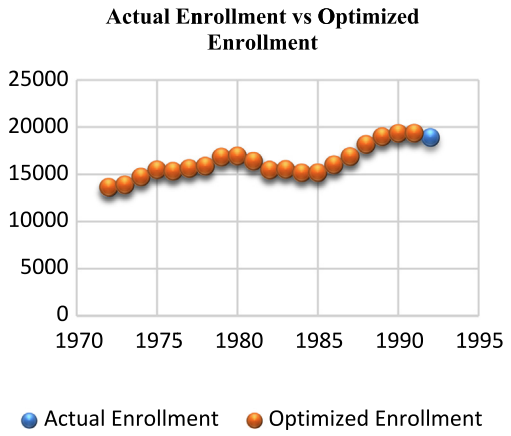


Fig. 8. Actual vs. Optimized Enrollments.

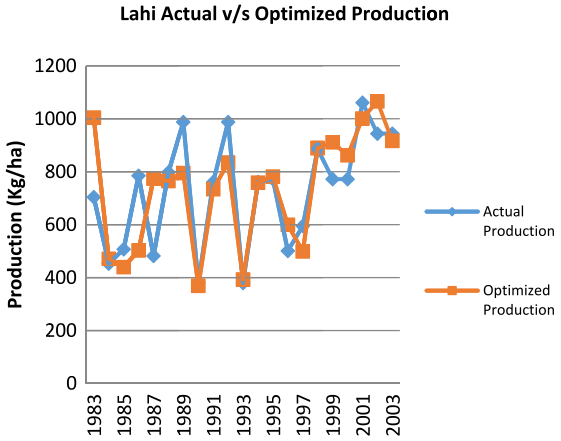


Fig. 9. Actual vs. Optimized Lahi Production.

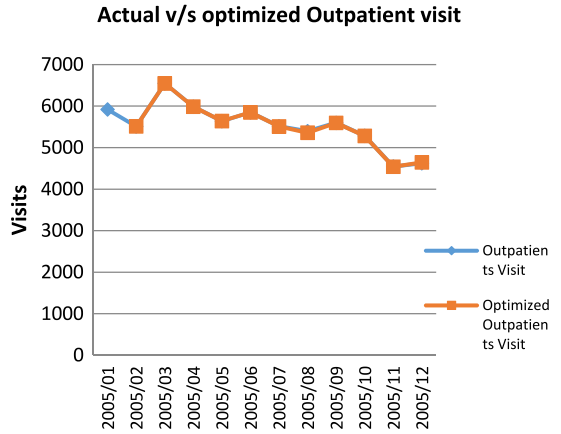


Fig. 10. Actual vs. Optimized Outpatient Visit.

calculated as the average of all solutions given by:

$$C_s = \sum_{j=1}^{NP} \frac{I_j}{NP} \tag{8}$$

$$P_m = \max \left|\left| I_j - C_s \right|\right|_E \tag{9}$$

where, NP is the population size, I_j is the jth individual, and $j = 1 \ldots \ldots$ NP. The population convergence measures the rate of convergence of

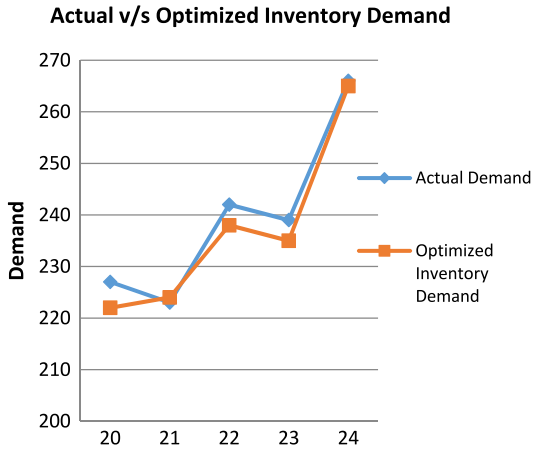


Fig. 11. Actual vs. Optimized Inventory Demand.

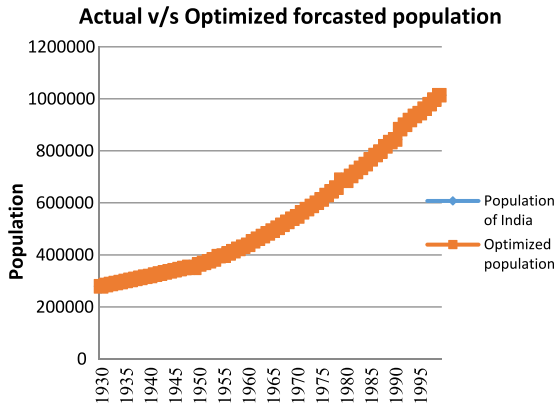


Fig. 12. Population of India.

the solutions with respect to the functional dependence measure (of generations).

This section summarizes the advantage of proposed hybrid method, the constraints involved and the convergence of the solution. Results from section 4, encourage the workaround of the behaviour of fuzzy time series data with Differential Evolution in multi-dimensional problems. Some future aspects are discussed in Section 6.

6. Conclusion and future work

In this research, a hybrid model for forecasting low dimensional numerical data called ClusFuDE is proposed. The methodology demonstrates that improved clustering with fuzzy logical relationships help to easily form the membership functions for each datum, which improves the *forecasting* of numerical data. It is experimentally observed that because of the use of Differential Evolution with an adaptive nature, the *accuracy of forecasting* has been significantly improved in, ClusFuDE.

Unlike other evolutionary algorithms, Differential Evolution has tremendous impact on the candidate solutions. The behaviour and efficiency of Differential Evolution control parameters (crossover rate and scale factor) is well studied with the proposed method. The variation in the control parameters influence the character of optimization, which is validated by performing experiments on University Enrollment, Lahi Production, Outpatient Visit in a hospital, Inventory demand and population of India from years 1930–2000.

It is also observed that minor changes in the control parameters drastically change the optimization performance. So a fine tuning of

the control variables significantly helps to automatically adapt, to the problem domain i.e. optimization of numerical data.

The MSE and MAPE value pair in ClusFuDE for Enrollment forecasting, Lahi production, Outpatient's visit, Inventory demand and Population dataset comes out to be (102.8 and 0.02%), (18528 and 14.01%), (170.09 and 0.14%), (11.8 and 1.27%), (740.9 and 0.005%) respectively and hence, the results obtained from ClusFuDE outperform other popular methods in the literature with higher accuracy rate of forecasting. This further validates that the use of Differential Evolution for forecasting numerical data is very effective.

Further, since Differential Evolution requires only a few robust control variables which can be drawn from a well-defined numerical interval, hence its vector generation and the variation in control parameters can lead to faster convergence and this can be investigated more deeply. In the present work, we have focused only on low dimensional numerical data and did not consider the multi-dimensional view of the data, which can be useful in understanding the nature of data in real world scenarios more effectively. In the future, it would be interesting to analyse the performance of Differential Evolution to other multi-dimensional datasets where the variation in control parameters can be further validated. Additionally, the behaviour of self-adaptive Differential Evolution control parameters can be investigated with Type-2 fuzzy sets, hesitant fuzzy sets and intuitionistic fuzzy sets to better handle uncertainty in the control process.

Appendix A. Supplementary data

Supplementary material related to this article can be found online at https://doi.org/10.1016/j.engappai.2018.02.015.

References

Aladag, C.H., Yolcu, U., Egrioglu, E., Dalar, A.Z., 2012. A new time invariant fuzzy time series forecasting method based on particle swarm optimization. Appl. Soft Comput. 12 (10), 3291–3299.

Aydin, I., Karakose, M., Akin, E., 2009. The prediction algorithm based on fuzzy logic using time series data mining model. World Acad. Sci. Eng. Technol. 51.

Bas, E., Uslu, V.R., Yolcu, U., Egrioglu, E., 2014. A modified genetic algorithm for forecasting fuzzy time series. Appl. Intell. 41 (2), 453–463.

Bisht, K., Kumar, S., 2016. Fuzzy time series forecasting method based on hesitant fuzzy sets. Expert Syst. Appl. 64, 557–568.

Brest, J., Greiner, S., Boskovic, B., Mernik, M., Zumer, V., 2006. Self-adapting control parameters in differential evolution: A comparative study on numerical benchmark problems. IEEE Trans. Evol. Comput. 10 (6), 646–657.

Chen, S.M., 1996. Forecasting enrollments based on fuzzy time series. Fuzzy Sets and Systems 81 (3), 311–319.

Chen, S.M., 2002. Forecasting enrollments based on high-order fuzzy time series. Cybern. Syst. 33 (1), 1–16.

Chen, S.M., Chen, C.D., 2010a. Handling forecasting problems based on high-order fuzzy logical relationships. Expert Syst. Appl. 38 (4), 3857–3864.

Chen, S.M., Chen, C.D., 2010b. Handling forecasting problems based on high-order fuzzy logical relationships. Expert Syst. Appl. 38 (4), 3857–3864.

Chen, S.M., Chung, N., 2006. Forecasting enrollments using high order fuzzy time series and genetic algorithms. Int. J. Intell. Syst. 21 (5), 485–501.

Chen, S.M., Hsiao, H.R., 2005. A new method to estimate null values in relational database systems based on automatic clustering techniques. Inform. Sci. 169 (1–2), 47–69.

Chen, S.M., Hsu, C.C., 2004. A new method to forecast enrollments using fuzzy time series. Int. J. Appl. Sci. Eng. 2 (3), 234–244.

Chen, S.M., Hsu, C.C., 2008. A new approach for handling forecasting problems using high order fuzzy time series. Intell. Autom. Soft Comput. 14 (1), 29–43.

Chen, S.M., Hwang, J.R., 2000. Temperature prediction using fuzzy time series. IEEE Trans. Syst. Man Cybern. B 30 (2), 263–275.

Chen, S.M., Kau, P.Y., 2013. TAIEX forecasting based on fuzzy time series, particle swarm optimization techniques and support vector machines. Inform. Sci. 247, 62–71.

Chen, S.M., Manalu, G.M.T., Pan, J.S., Liu, H.C., 2013. Fuzzy forecasting based on two factor second order fuzzy trend logical relationship group and particle swarm optimization. IEEE Trans. Cybern. 43 (3), 1102–1117.

Chen, S.M., Wang, N.Y., 2010. Fuzzy forecasting based on fuzzy-trend logical relationship groups. IEEE Trans. Syst. Man Cybern. B 40 (5).

Chen, S.M., Wang, N.Y., Pan, J.S., 2009. Forecasting enrollments using automatic clustering techniques and fuzzy logical relationships. Expert Syst. Appl. 36 (8).

Cheng, C.H., Wang, J.W., Li, C.H., 2008. Forecasting the number of outpatient visits using a new fuzzy time series based on weighted-transitional matrix. Expert Syst. Appl. 34, 2568–2575.

Das, S., Abraham, A., Konar, A., 2008a. Automatic clustering using an improved differential evolution algorithm. IEEE Trans. Syst. Man Cybern. A 38 (1).

Das, S., Abraham, A., Konar, A., 2008b. Particle swarm optimization and differential evolution algorithms: technical analysis, applications and hybridization perspective. Stud. Comput. Intell. 116, 1–38.

Das, S., Konar, A., Chakraborty, U.K., 2005. Two improved differential evolution schemes for faster global search. In Proceedings of ACM-SIGEVO GECCO, Washington, DC, pp. 991–998.

Feoktistov, V., 2006. Differential Evolution: In Search of Solutions. Springer.

Hadavandi, E., Shavandi, H., Ghanbari, A., Abbasian-Naghneh, S., 2012. Developing a hybrid artificial intelligence model for outpatient visits forecasting in hospitals. Appl. Soft Comput. 12 (2), 700–711.

Holland, J.H., 1975. Adaptation in Natural and Artificial Systems. University of Michigan Press, Ann Arbor, MI.

Huang, Y.L., Horng, S.J., Kao, T.W., Run, R.S., Lai, J.L., Chen, R.J., et al., 2011. An improved forecasting model based on the weighted fuzzy relationship matrix combined with a pso adaptation for enrollments. Int. J. Innov. Comput. Inf. Control 7 (7A), 4027–4046.

Huarng, K., 2001. Effective length of intervals to improve forecasting in fuzzy time series. Fuzzy Sets and Systems 123 (3), 387–394.

Huarng, K., Yu, H.K., 2006. Ratio-based lengths of intervals to improve fuzzy time series forecasting. IEEE Trans. Syst. Man Cybern. B 36 (2), 328–340.

Hwang, J.R., Chen, S.M., Lee, C.H., 1998. Handling forecasting problems using fuzzy time series. Fuzzy Sets and Systems 100 (2), 217–228.

Jain, A.K., Murty, M.N., Flynn, P.J., 1999. Data clustering: A review. ACM Comput. Surv. 31 (3).

Jasim, H.T., Salim, A.G.J., 2012. A novel algorithm to forecast enrollment based on fuzzy time series. Int. J. Appl. Appl. Math. 7 (1), 385–397.

Jiang, P., Dong, Q., Li, P., Lian, L., 2017. A novel high-order weighted fuzzy time series model and its application in nonlinear time series prediction. Appl. Soft Comput. 55, 44–62.

Katari, V., Satapathy, S.C., Murthy, J.V.R, Reddy, P.V.G.D., 2007. Hybridized improved genetic algorithm with variable length chromosome for image clustering. Int. J. Comput. Sci. Netw. Secur. 7 (11), 121–131.

Lahmeyer, J.J., 2003. India, Historical Demographical data of the whole country. [Online] Available at: http://www.populstat.info/. [Accessed August 2016].

Lai, K.K., Yu, L., Wang, S., Huang, W., 2006. Hybridizing exponential smoothing and neural network for financial time series predication. Comput. Sci. 493–500.

Lee, L.W., Wang, L.H., Chen, S.M., Leu, Y.H., 2006. A new method for handing forecasting problems based on two-factors high-order fuzzy time series. In: Proceedings of 9th International Conference on the Application of Artificial Intelligence, Taipei, Taiwan.

Meng, H., Wang, G., Zhang, X., Deng, W., Yan, H., Jia, R., 2015. Water quality prediction based on a novel fuzzy time series model and automatic clustering technique. In: Ciucci, D., Wang, G., Mitra, S., Wu, W.Z. (Eds.), Rough Sets and Knowledge Technology. In: Lecture Notes in Computer Science, vol. 9436, Springer.

Mitchell, R.J., 2003. Forecasting electricity demand using clustering. In: Proceedings of the 21st IASTED international conference on applied informatics, Innsbruck, Austria, pp. 225–230.

Paterlini, S., Krink, T., 2006. Differential evolution and particle swarm optimization. Comput. Statist. Data Anal. 1220–1247.

Paterlini, S., Minerva, T., 2003. Evolutionary approaches for cluster analysis. In: Bonarini, A., Masulli, F., Pasi, G. (Eds.), Soft Computing Applications. Springer-Verlag, Berlin, Germany, pp. 167–178.

Qin, A.K., Suganthan, P.N., 2005. Self- adaptive differential evolution algorithm for numerical optimization. In: Evolutionary Computation. IEEE, pp. 1785–1791.

Qiu, W., Zhang, P., Wang, Y., 2015. Fuzzy time series forecasting model based on automatic clustering techniques and generalized fuzzy logical relationship. Mathematical Problems in Engineering.

Radmehr, F., Gharneh, N.S., 2012. Forecasting method based on high order fuzzy time series and simulated annealing technique: case study. South Afr. J. Ind. Eng. 23 (2), 176–190.

Rajaram, S., Sakthisree, P., 2010. Forecasting enrollments using interval length, Weightage factor and fuzzy logical relationships. Int. J. Stat. Syst. 5 (2), 173–182.

Ross, T.J., 1995. Fuzzy Logic with Engineering Applications. McGraw-Hill, New York.

Sakhuja, S., Jain, V., Kumar, S., Chandra, C., Ghildayal, S.K., 2016. Genetic algorithm based fuzzy time series tourism demand forecast model. Ind. Manag. Data Syst. 116 (3), 483–507.

Shahraki, A., Ebrahimi, S.B., 2015. A new approach for forecasting enrollments using harmony search algorithm. J. Intell. Fuzzy. Syst. 28 (1), 279–290.

Singh, S.R., 2007. A simple method of forecasting based on fuzzy time series. Appl. Math. Comput. 186, 330–339.

Singh, S.R., 2008. A computational method of forecasting based on fuzzy time series. Math. Comput. Simulation 79, 539–554.

Song, Q., Chissom, B.S., 1993. Forecasting enrollments with fuzzy time series—Part I. Fuzzy Sets and Systems 54 (1), 1–9.

Storn, R., Price, K., 1997. A simple and efficient heuristic for global optimization over continuous space. J. Global Optim. 34, 1–359.

Sullivan, J., Woodall, W.H., 1994. A comparison of fuzzy forecasting and Markov modeling. Fuzzy Sets and Systems 64 (3), 279–293.

Tanuwijaya, K., Chen, S.M., 2009. A new method to forecast enrollments using fuzzy time series and clustering techniques. In: proceedings of 8th International Conference on Machine learning and Cybernetics, Baoding, China.

Tayal, D., Ansari, G., Sonawani, S., Gupta, C., 2011. Fuzzy time series forecasting of low dimensional numerical data. Int. Jr. Eng. Res. Appl. 2 (1), 132–135.

Tvrdik, J., 2007. Differential evolution with competitive setting of control parameters. Task Quart. 11 (1–2), 169–179.

Vesterstrom, J., Thomsen, R., 2004. A comparative study of differential evolution, particle swarm optimization, and evolutionary algorithms on numerical benchmark problems. In: Evolutionary Computation, 2004. CEC2004. Congress on, vol. 2. IEEE, pp. 1980–1987.

Wazan, H.A., Ibraheem, K., Salim, A.J., 2014. A hybrid algorithm to forecast enrolment based on genetic algorithms and fuzzy time series. Int. Arab J. Inf. Technol. 11 (3), 250–257.

Wu, W., 1986. Fuzzy reasoning and fuzzy relation equations. Fuzzy Sets Syst. 20, 67–68.

Xihao, S., Yimin, L., 2008. Average-based fuzzy time series models for forecasting shanghai compound index. World J. Model. Simul. 4 (2), 104–111.

Ye, F., Zhang, L., Zhang, D., Fujita, H., Gong, Z., 2016. A novel forecasting method based on multi-order fuzzy time series and technical analysis. Inform. Sci. 367, 41–57.

Yu, H.K., 2005. Weighted fuzzy time series models for TAIEX forecasting. Physica A 349, 609–624.

Zadeh, L.A., 1965. Fuzzy sets. Inf. Control 8, 338–353.

Zadeh, L.A., 1975. The concept of linguistic variable and its application to an approximate reasoning. Inform. Sci. 8, 199–249.

Zaharie, D., 2007. A comparative analysis of crossover variants in differential evolution. In: Proceedings of the International Multi-conference on Computer Science and Information Technology, pp. 171–181.

Zarandi, M.H.F., Molladavoudi, A., Beigi Ali, M.H., 2009. A new method for temperature prediction and the TAIFEX Forecasting based on fuzzy logical relationship and double interval division. Ind. Eng. Eng. Manag. IEEM 1, 1543–1547.

1st International Conference on New Frontiers in Engineering, Science & Technology NFEST-2018

Comparative Study of PID and Fuzzy Logic Controller for Steam Temperature Control in Thermal Power Plant

Ajendra Singh[1], J N Rai[2]

[1] Research scholar, Department of Electrical Engineering, Delhi Technological University, India
E-mail:ajendrasingh25@gmail.com

[2]Professor, Department of Electrical Engineering, Delhi Technological University, India
E-mail:jnrai@dce.ac.in

Abstract

The precision control of superheated steam fed to turbines for the generation of electrical power has been a challenging task for control engineers for a long time. There are several limitations that are associated with conventional control philosophies used for this purpose. The modern control techniques are being preferred due to their inherent merits over the conventional control techniques in thermal steam temperature control in particular. These days, fuzzy logic control concept is one of the intelligent control techniques which has been the revolutionary applications in power system operation and control. In this paper, an attempt has been made to design fuzzy logic based PID controllers for super heater temperature control of a boiler. The PID controllers based on ZEIGLER-NICHOLS are also designed. Considering a small change in inlet temperature as the disturbance, the PID controllers designed in the study are implemented and the dynamic response plots are obtained. Standard SIMULINK Software is used on MATLAB platform to get the results. The investigations of simulation studies demonstrate the superiority of fuzzy logic based controllers over the conventional PID controllers designed using ZEIGLER-NICHOLS tuning technique.

*Keywords***:** Superheated Steam, Super Heater; Intelligent techniques; PID controller; Ziegler-Nichols tuning Technique; Fuzzy logic controller

1. INTRODUCTION

The electrical energy consumption has been considered as a prime index to determine the trend of development of a country. Therefore, for overall development of a country, availability of electric energy is one of the important requirements. As far as our country is concerned, there is always a gap exists between requirement of energy and its availability. Major part of electrical power generation in India comes from fossil fuel fired power plants. The fossil reserves are depleting rapidly, In order to conserve fossil reserves, the power plant should run more efficiently. In the chain of thermal cycle, since boiler is the front end requirement, its role plays a major importance in the overall reliability and efficiency of a thermal power plant. In turn the efficiency of the boiler depends on several operating parameters, and superheated steam temperature is one amongst them, which is very important.

The efficiency of boiler mainly depends on superheated steam temperature. With the development of advanced control systems in the conventional controllers are getting replaced for superheated steam temperature control. In power boilers the temperatures of superheated steam depends on the amount of fuel input, angle of the flame burner, load etc. Spray water which is a manipulating variable is used to control the temperature of the superheated steam. The overall cycle efficiency is very sensitive to this parameter and a tight control of this parameter would also ensure a better life of boiler components. For example, a one percent fall in thermal efficiency of a 500 MW unit would amount to burning an extra coal of about 10,000 tons per annum. Therefore, it becomes very important to increase the efficiency of thermal turbines by implementing properly designed regulators for the turbine outputs. The temperature control of superheated steam should be considered as an important parameter as a first step in this regard.

In the past few years there has been tremendous increase in the popularity of PID controllers [5]. The test of the evolution of the PID is that, actually most of the classical industrial controllers have procedure to automate its parameters. Then, if we can get a good model of the process, given by analytic linear equation, direct technique of control are the simplest and least cost alternatives. The classical PID controller provides an accurate and efficient solution to linear control problems. But the involved process are in general complex, time variant, with delays and non-linearity's and very often, with a poorly-defined dynamics. When the processes are too complex to be described by analytic models, they are hardly controlled by drastic approaches that simplifies them but do not get the required efficiency. To circumvent, some of these problems, modern control techniques have emerged for their applications in power systems. However, optimal control technique based on full state vector feedback has its limitations for practical applications due to its requirement of availability of all system states for their measurement.

The evolution of intelligent control concepts like, artificial Neural Network, Fuzzy logic, Genetic Algorithm and Neuro- Fuzzy control system has changed the whole scenario of control systems as far the design and implantation of controllers for practical systems are concerned. Fuzzy logic control concept (FLC) [1-4] is one of the fittest tools to counter the vagueness associated in defining/describing the physical systems. The parts of physical power system are having various parameters which cannot be modelled accurately. The mathematical modelling of super heater used for cheat the steam available is done with some assumptions to simplify the mathematical manipulations. Therefore, investigations carried out with these approximated models do not serve the purpose of providing accurate and realistic results. With the application of fuzzy logic control concept in the design of controllers for superheated steam temperature, more realistic studies can be carried out. In this work, FLC is considered as one of the intelligent control concepts for application to superheated steam temperature control.

2.DESIGN PARAMETERS OF SUPERHEATING SYSTEM

For the present study, a superheated steam turbine is considered for the investigation. The block diagram of the system is shown in Fig. I. A brief description of designing parameters of various parts of the system is given in the ensuing paragraphs.

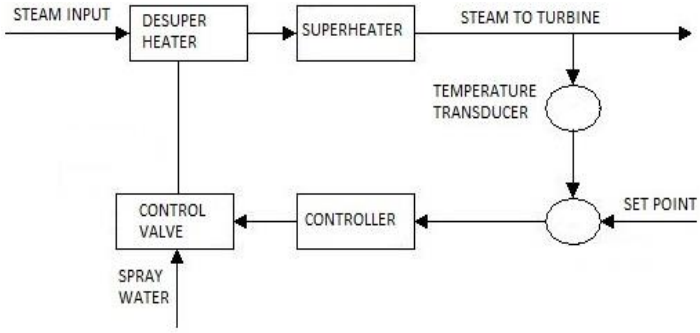


Figure 1. Control system with Single Controller

De super heater: The response of outlet temperature to the changes in spray water is instantaneous. Hence, there is no dynamics involved in the coefficient connecting the spray change to change in outlet temperature at 100% load has been derived.

Super heater: In this system, the inlet temperature of the super heater is increased by a factor of 1.3882 at 100% load for a 500 MW boiler because of heat input from the furnace.

Transducer: It measures the outlet temperature of the superheated steam whose time constant is of the order of 10 sec. this time delay is added on to the delay of the superheating system for simulation purpose.

Control valve: The time constant of control valve is different for opening and closing. This value is of the order

of 10 seconds for closing and 5 seconds for openings per data provided by the manufacturers. The overall steady state coefficient for control valve and de super heater is found to be 0.556 relating the change at the superheated outlet temperature to the change in the controller design.

3. DESIGN OF PID CONTROLLER

The design of controller consists of the following two steps:

(1) Selection of the mode of the controller and their combination i.e. proportional (P), integral (I), derivative (D) and PID.
(2) Specification of the value of the parameters associated with the selected control mode (Kp, Ki, and Kd).

The above two steps are to be executed by properly designing Kp, Ki, and Kd of in order to meet the specification of the closed-loop system such as overshoot/undershoot, decay ratio, settling time, rise time, etc. in time domain(or) gain margin, phase margin, bandwidth, etc. in frequency domain.

A. Tuning of conventional controllers

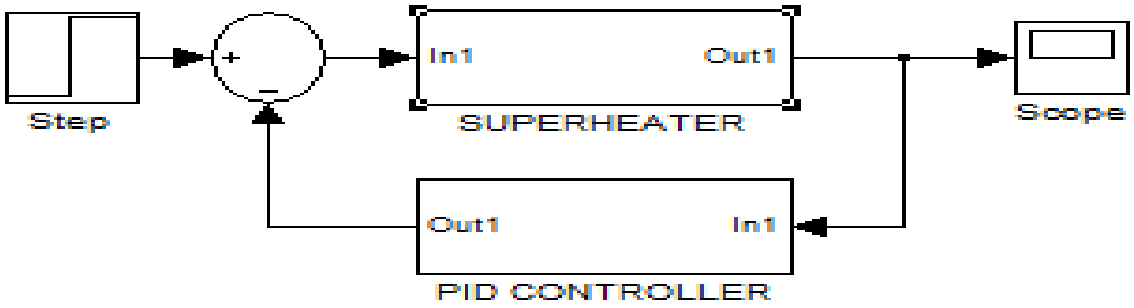
The conventional PID controllers may be tuned [6] using well known Zeigler-Nichols Technique as:

Zeigler-Nichols Technique [10]

- Increase the proportional gain until the system oscillates; that gain is the ultimate gain Ku.
- Read the time between peaks Tcr at this setting.
- Table-I gives approximate values for the controller gains.

Controller	Gain K	Integration time Ti	Derivation time Td
P	0.5Kcr	0	0
PI	0.5Kcr	0.85Tcr	0
PID	0.6Kcr	0.5Tcr	0.125Tcr

TABLE 1. ZEIGLER-NICHOLAS RULES



The Simulink model of PID controller implementation on super heater is shown in Figure 2.

4. DESIGN OF FUZZY LOGIC CONTROLLER

FLC is mainly used for the systems whose mathematical models are difficult to derive from first principle [7]. The heart of the FLC is to form knowledge base which can be obtained from the experts in that field. In power boilers, the temperature of superheated steam depends upon the amount of fuel input, angle of the flame burner, load etc. spray water which is manipulating variable, is used to control the temperature with spray water. This time constant varies inversely with load.
Block diagram of this control system with a single FLC controller is given in Figure 3.

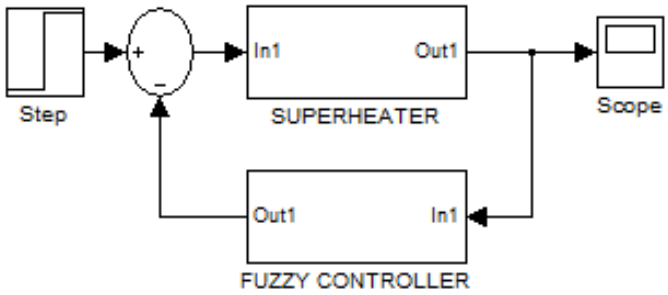


Figure 3. Simulink model of heater with Fuzzy logic controller

The FLC contains two input variables (error and error rate) and one output variable. At every time instant FLC computes the change of output and adds to the previous output to get the current value. The membership functions and their ranges for all the input and output variables are as detailed below: [11-12]

A. Mamdani Model

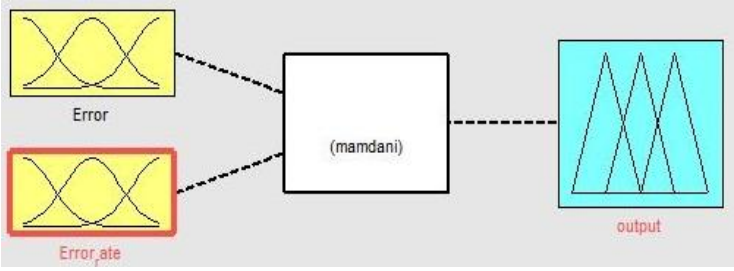


Figure 4. Mamdani Model

B. Membership Function

No. of membership functions: 3

Labels are small, medium and HIGH.

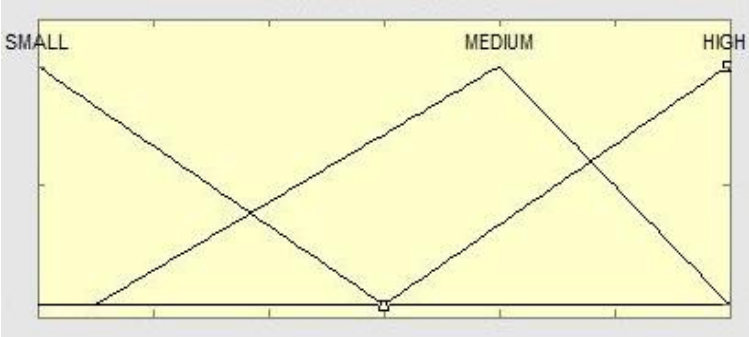


Figure 5. Error

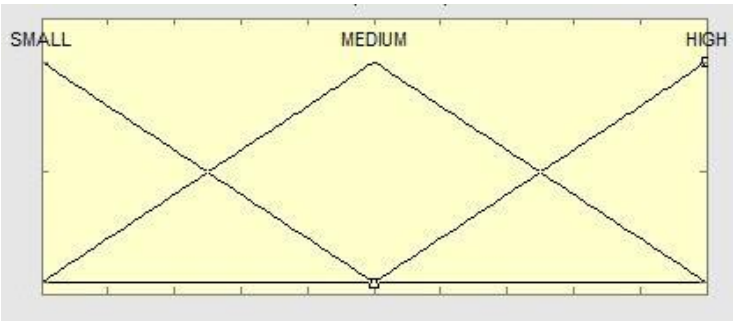


Figure 6. Error rate

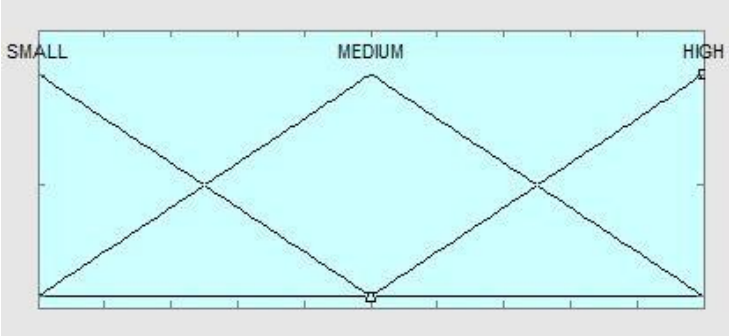


Figure 7. Output

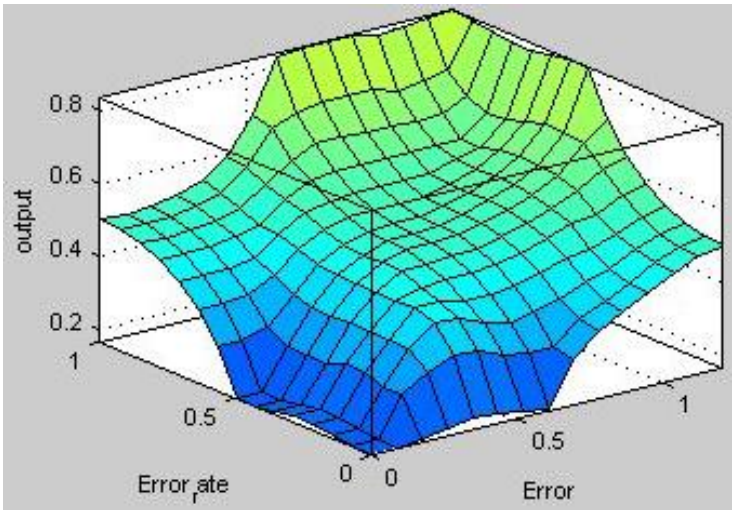


Figure 8. Control Surface

C. Expert Rules

The following 9 rules [8-9] are applicable for this controller:

(1) If (ERROR is SMALL) and (ERROR RATE is SMALL) then (CONTROL is small).
(2) If (ERROR) is SMALL) and (ERROR RATE is MEDIUM) then (CONTROL is SMALL).
(3) If (ERROR is SMALL) and (ERROR RATE is HIGH) then (CONTROL is MEDIUM.
(4) If (ERROR is MEDIUM) and (ERROR RATE is SMALL) then (CONTROL is SMALL)
(5) If (ERROR is MEDIUM) and (ERROR RATE is MEDIUM) then (CONTROL is MEDIUM)
(6) If (ERROR is MEDIUM) and (ERROR RATE is HIGH) then (CONTROL is HIGH)
(7) If (ERROR is HIGH) and (ERROR RATE is SMALL) then (CONTROL is MEDIUM).
(8) If (ERROR is HIGH) and (ERROR RATE is MEDIUM) then (CONTROL is HIGH)
(9) If (ERROR is HIGH) and ERROR RATE is (HIGH) then (CONTROL is HIGH).

5. SIMULATION RESULTS

This paper presents design of PID controller using Ziegler-Nichols (ZN) technique for the system under consideration. A fuzzy logic controller using simple approach and smaller number of set of rules is proposed. Simulation results are obtained with a step change as disturbance in the system. The dynamic performance is achieved with the implementation of conventional PID and fuzzy logic based system controllers. Figure 9 shows the natural response of the super heater system while the controlled outputs are shown in Figures 9&10. The dynamic performance obtained with these controllers is compared. The investigations carried out show the fuzzy logic based controller offers less overshoot and settling time as compared to that of conventional PID controller.

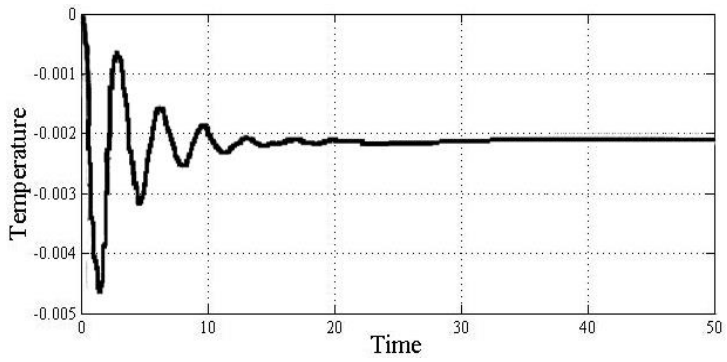


Figure 9. Natural response of super heater with 50c step change (in input)

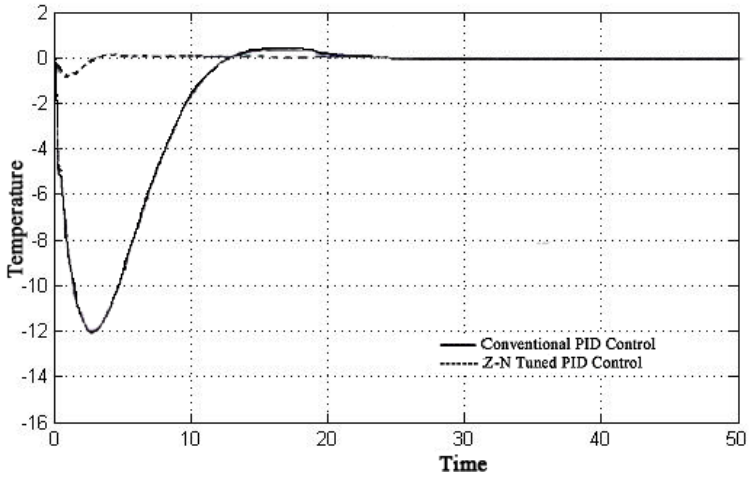


Figure 10. Controlled output superheated using PID controller.

Time

.

The FLC contains two input variables (error and error rate) and one output variable. At every time instant FLC computes the change of output and adds to the previous output to get the current value. The membership functions and their ranges for all the input and output variables are as detailed below: [11-12]

REFERENCES

[1.] H. Ying, Fuzzy Control & Modelling: Analytical foundations and applications. New York, IEEE Press, 2000.
[2.] Fuzzy logic toolbox for use with MATLAB, user's guide,rev.2(1995)
[3.] J. Zhang, N. Wang and S. Wang, "A developed method of tuning PID controllers with fuzzy rules for integrating process," Proceedings of the American Control Conference, Boston, 2004, pp. 1109-1114.
[4.] D.M Ang Wlberg, fuzzy logic and control.schaum's outline series. Mc-Graw-Hill.New York, NY2007.
[5.] K.H. Ang, G. Chong and Y. Li,"PID control system analysis, design and technology," IEEE transaction on Control System Technology, Vol.13, No4, 2005, pp. 559-576.
[6.] P. Cominos and N. Munro. "PID controllers:recent tuning methods and design to specification," IEEE proceedings, Control Theory and Application, 2002, pp.46-53.

[7.] L.A. Zadeh and C. A. fuzzy logic and state functons: A static space approach. Mc Hraw. New York, 1990.
[8.] S. Chopra, R. Mitra and V. kumar, "Fuzzy controller: Choosing an appropriate & smallest rule set," International Journal of Computational Cognition, Vol.3, No. 4, 2005, pp. 73-78.
[9.] S.R. Vaishnav, Z.J. Khan, Design and Performance of PID and Fuzzy Logic Controller with smaller rule set for Higher Order System," WCECS 2007, October 24-26,2007, San Francisco, USA.
K.Astrom, T. Hagglund, PID controllers: Theory, design and tuning. 2nd ed., The Instrumentation, Systems and Automation Society (ISA), 1995
[10] Y.Yongquan, H.Ying and Z.Bi, "The dynamic fuzzy method to tune weight factors of Neural fuzzy PID controller," IEEE,2004, pp.2397-2402
[11] Z.Y Zhao, M. Tomizuka and S. Isaka, "Fuzzy Gain scheduling of PID controllers, "IEEE transactions on Systems, Man and Cybernetics, Vol.23, No.5, 1993, pp.1392-1398

International journal of basic and applied research
www.pragatipublication.com
ISSN 2249-3352 (P) 2278-0505 (E)

Decreasing of Agricultural Costs for The Indian Farmer by using Jatropha Easters

Raghvendra Gautam
Department of Mechanical Engineering
Delhi Technological University
Delhi

Abstract: Agriculture farms are the pillar of the Indian economy which contributes the largest part but the rising expenditures in the form of cultivation costs are making it less and less profitable day by day. The use of artificial insecticides and pesticides along with fertilizers is not only expensive for the average Indian farmer but it also causes environmental pollution. The use of diesel in tractors also adds to the bill in agriculture, Use of Jatropha curcus as a fencing crop for the protection of food crops offers a solution to all these problems as it can shield the crops, can be used as an organic manure and the biodiesel derived from Jatropha can drastically reduce costs.

Key words: Jatropha, cultivation, cost , crops, Fence.

1.EXPENDITURES IN CROP CULTIVATION IN INDIA

85.8% and 70.8% ofIndian farm households undertook cultivation in the Kharif and Rabi seasons in 2012-13. Out of these, only 59% and 68% households were able to access irrigation facilities. The average land cultivated in Kharif and Rabi was 0.944hectares and 0.785 hectares respectively which points out effectively that the majority of Indian farmers have small size land-holdings. (Aachen, W. et al 2010). The average irrigated and unirrigated land in Kharif season was 0.469and 0.468 hectares area respectively while the same was 0.622 and 0.161 hectares area in Rabi season respectively.

• Irrigation costs (191%), electricity costs (143%), diesel costs (126%), machine hiring costs (120%) and lease rent (106%) were greater for farmers cultivating in Rabi season as compared to Kharif by percentages indicated in brackets and take a toll on the cultivator. (Basili, M., and Fontini, F. 2010). Similarly, animal labour and humanlabour costs in Rabi were 49% and 80% of the same in Kharif which are again significant as shown in figure 1

2. CROP LOSSES TO PESTS

The efficiency of crop protection was higher in cash crops than in food crops. Weed control can be managed mechanical or chemical means, as a result worldwide efficacy was substantiallygreater than for the control of animal pests or diseases, which is dependent on the use of synthetic chemicals. In spite of a clear increase in

Received: 5 February Revised: 13 February Accepted: 22 February
Index in Cosmos
March 2018 Volume 8 Number 3
UGC APPROVED

International journal of basic and applied research
www.pragatipublication.com
ISSN 2249-3352 (P) 2278-0505 (E)

the use of pesticides, the decrease in crop losses has not been noteworthykeeping track of the last 40 years.(Gexsi 2008)Though, pesticide use has enabled farmers to modify production systems and to increase crop productivity without sustaining the higher losses likely to occur from an increased susceptibility to the damaging effect of pests but that comes at the cost of the environment. The concept of integrated pest or crop management includes a proven concept for the application of pest control measures and reduction in the amount and frequency of pesticides applied to an economically and ecologically acceptable level. InIndia Jatropha curcus can be used to effectively protect the crops and reduce the amount of pesticides applied.

Pests, weeds and pathogens have been the adversaries of crop production for human consumption since ancient times. Crop losses in yield and value due to these factors are significant and can be reduced or even prevented with the help of crop protection measures. The overall global potential losses due to pests differ in various crops grown worldwide which have been tabulated in table 1.

As can be seen, a substantial part is lost to pets in all the major crops grown. Altogether,the potential loss due to weeds was the greatest ie. 34% with pathogens and pests being comparatively less significant (losses of 16% and 18%). The efficiency of crop protection was higher in cash crops than in food crops. Weed control can be managed mechanical or chemical means, as a result worldwide efficacy was substantially greater than for the control of animal pests or diseases, which is dependent on the use of synthetic chemicals. In spite of a clear increase in the use of pesticides, the decrease in crop losses has not been noteworthy keeping track of the last 40 years. Though, pesticide use has enabled farmers to modify production systems and to increase crop productivity without sustaining the higher losses likely to occur from an increased susceptibility to the damaging effect of pests but that comes at the cost of the environment. The concept of integrated pest or crop management includes a proven concept for the application of pest control measures and reduction in the amount and frequency of pesticides applied to an economically and ecologically acceptable level. In India Jatropha curcus can be used to effectively protect the crops and reduce the amount of pesticides applied.

3.JATROPHA CURCAS L.

KNOWING THE SPECIES

(a) Habitat and History

Euphorbiaceae is the family to which Jatropha curcas belongs and is closely related to someother important cultivated plants like rubber tree and castor etc.W.A. Talbot in his book "The Forest Flora of the Bombay Presidency"describesJatropha curcas (Euphorbiaceae) as a soft wooded shrub, 3 to 4 metres high. It is believed to be indigenous in Mexico and a few African nations and wasspread to other continents of theworld by the Portuguese settlers. It can grow in most tropical parts of the Indian subcontinent, commonly in hedges, in a cultivated or naturalized form. Since ancient times, Arabs have been using Jatropha for medicinal purposes. Today it propagates in almost all the tropical and sub-tropical regions of the worldand is known by

Received: 5 February Revised: 13 February Accepted: 22 February
Index in Cosmos
March 2018 Volume 8 Number 3
UGC APPROVED

International journal of basic and applied research
www.pragatipublication.com
ISSN 2249-3352 (P) 2278-0505 (E)

nearly 200 different names, which is an evidence of its significance. Also, the variouspossibilities of its use is an exciting feature, chiefly extraction of oil from its seeds reportedly being the most sought after use.

(b) Distribution in India

Jatropha curcas grows in almost all the Indian states which comprise of a collection of various climates highlighting its rugged nature.It is generally popular for its use as a livefence for protection of agricultural fields against damage by livestock as it is unpalatable to cattleand goats.Jatropha curcas in India is found in semi-wild conditions in the proximity of villages. It can be easilypropagated by seeds or cuttings, has a short germination span, is capable of enduring drought and is not grazed on by animals.It may be lopped at any desired height and is very convenient to be grown in form of a hedgerow.

(c) Plant biology

Jatropha curcas can adapt to a wide range of climates and soils which is a source of attraction. It can grow almost on anytype of soil whether gravelly, sandy or saline and burgeons. Cases of Jatropha thriving even on the poorest stony soils androck crevices have also been registered. In this plant, supply of Phosphates is ensured byutilizing the symbiosis with a root fungiknown as Mycorrhiz. The leaves which are shed in winter months form a mulch around the plant base andorganic matter from there enhances earthworm populations around the root-zone of theplants, thus increasing the soil fertility.

The productivity of Jatropha curcas is better in the regions of tropics and sub-tropics which have warm climates, althoughit does well even in slightly cool conditions and can withstand a high frost. The amount of water needed to sustain is extremely low and it withstands long periods of drought by shedding itsleaves to decrease losses due to transpiration. The organic mulch around the base of the plant formedby the fallen leaves also greatlylessens water loss from surface evaporation. Thespecies is hence well adapted to arid conditions, showing remarkable survival instincts.Jatropha curcas is also well suited for improving soil in degraded areas and stabilization ofshifting sand dunes due to its ability to thrive on sandy soils too.(Ndong, R. et al 2009). Therefore, it can beintroduced on wastelands to great effect as a first step towardstheir successful rehabilitation. Because of the hardy nature of this species and the fact that it can bepropagated easily by branch cuttings or direct seed sowing, it is ideal for theecological and economic rehabilitation of wastelands in the country. In India, its flowering period is from September to December. The fruits mature two to four monthsafter flowering, turning yellow when mature. Jatropha can be grown over a wide range of aridor semi-arid climatic conditions and soils.(Gautam R. & Kumar N. 20106) A hot and humid climate like most of the Indian mainland helps in the early germination ofseeds.

(d) As a Plantation Tree/Shrub About 75 million hectares of wastelands exist in India which urgently need revegetation. As we have seen, Jatropha curcasis a wild growing hardy plant and can acclimatize to extreme conditions of soil. Seeds as well as branch cuttings can be used for Jatropha's propagations which makes

Received: 5 February Revised: 13 February Accepted: 22 February
Index in Cosmos
March 2018 Volume 8 Number 3
UGC APPROVED

International journal of basic and applied research
www.pragatipublication.com
ISSN 2249-3352 (P) 2278-0505 (E)

thespecies the best bet for afforestation of degraded sites economically. Jatrophacurcas moreover can also be profitably grown as a perennial non-edible oil crop on irrigatedand partially irrigated lands.Jatropha curcas oil has a wide number of implications and can be used profitably in industries on a large scale. Progressive research forsystematic cultivation; detoxification of oil for edible purposes and development of a suitabletechnology for its use as a fuel for engines are integral for India to fully advantage of Jatropha.

UTILIZATION OF THE SPECIES

(a) Use as a live fence

Jatropha curcas can be maintained as a hedge and is commonly grown as a live fencearound agricultural fields. It can be cut or lopped at any desired height and sheltersagricultural crops from damaging winds while not causing adverse competition at the same time. Its useas a hedge plant for field embankments needs to be familiarized as a technique to the Indian farmers. Jatropha curcas mayalso be used as a bio-fence around pasturesand plantation areas due to it being unpalatable and in rehabilitating areas where the soil has been extensively eroded.

(b) Potential oil producingcrop

On analysis of Jatropha curcas seed , the following chemical composition is found: moisture6.62%; protein 18.2%; fat 38.0%; carbohydrates17.30%; fibre 15.50%; and ash 4.5%. The oil contentis 35 to 40% of seed weight and 50 to 60% of the kernel which is the reason of its popularity as a potential biodiesel producing plant. The oil has 21% saturated fattyacids and 79% unsaturated fatty acids. The presence of a pernicious chemical withpurgative properties renders Jatropha oil unfit for human consumption settling the food vs fuel debate for it upto some extent. Thoughtechnologies arenow available, whereby Jatropha oil could be detoxified for use as an edible oil. A non-toxic species of Jatropha has been reported from Brazil

(c) Industrialraw material

Jatropha oil has a very high saponification value and is extensively used in India and othercountries for soap manufacturing. In the present Indian scenario,Jatropha curcas oil is imported to meet the demand ofcosmetic industry. The Chinese prepare a varnish by boiling the oil with iron oxide and the English use the oil for wool spinning. In various other nation especially in rural areas,the oil is used as an illuminant as it burnswithout emitting smoke.The oil is also a lubricant, hydraulic oil and useful for making likecandle castor oil.This can be exploited by the Indian farmers particularly in the process of achieving a self-sustainable village community by the use of Jatropha oil. Also,the proteins in the Jatropha oil cake could be used as raw material formaking plastics and synthetic fibres, thus providing more impetus to the local industries.

Received: 5 February Revised: 13 February Accepted: 22 February
Index in Cosmos
March 2018 Volume 8 Number 3
UGC APPROVED

International journal of basic and applied research
www.pragatipublication.com
ISSN 2249-3352 (P) 2278-0505 (E)

(d) Use as fuel

Jatropha oil is environment friendly, economical and a renewable source of non-conventionalenergy.It is a promising substitute for diesel, kerosene and other fuel oils.Jatropha oil is an alternative source of energy with a promise as it can be manufactured on a large scale within the country providing relief from the enormous bill of importing crude oil. Moreover, cultivation of Jatropha, as an agroforestry businessventure can not only generate millions of jobs in rural India but also invite more investment in economically backward regions . More than 30million people in Asia and Pacific region face fuelwood shortage. Receding of forestsfrom human habitations is taking placeat an alarming rate and finding fuelwood for domestic use is also becoming an uphill task with each passing day. The increasing gap between demand and supply of fuelwood is the main cause ofrapidly depleting forest cover which, has proved to have catastrophic consequences, leading tofloods, soil erosion and drought. To bridge thegap between demand and supply, 34 million hectares of land area is required to beplantedwith fuelwood crops in the coming years .High density plantations of this species can also be an ideal way of harnessing maximum solarenergy over a short gestation period as Jatropha curcas is fast growing and can be grownsuccessfully on all kinds of barren and unproductive wastelands. Also, it does not competewith food crops for land area. Conversely, the rich organic manure obtained fromJatropha can enrich the soils for increased food production to feed a gigantic population that continues to grow.Jatropha curcas has a productive life of nearly forty to fifty years without calling for replantingor retending unlike with fuelwood crops.

(e) Use for rehabilitating wastelands

Jatropha curcas can be used to successfully revegetate all barren and denuded areas. Animals do not eat or damage Jatropha plants. In many regions of the country Jatropha is therefore being extensively used as a live fence along the peripheryofagricultural fields which perhaps is the best way to utilize it currently from India's perspective.Use of Jatropha oil cake as organic fertilizer can curtail dependence on chemical fertilizers , (Abdalbasit A . et al. 2017). prevent the entry of chemicals into the food chainand also reduce under-ground water pollution significantly.(Vaibhav A . et al 2014)
From the total land area of 328 million hectare about162 million hectare. i.e. 51 % is agricultural land, 4% is pasture land , 21 % is forest land and 24 % is waste land as shown in figure 2.

4.CASE STUDIES IN AFRICA FOR USE OF JATROPHA OIL FOR DOMESTIC USE

• A group of Zambian women with the support from German Technical Cooperation (GTZ) was involved in a soap making enterprise from Jatropha oil. The National Oilseeds Development Programme under the Ministry of Agriculture and Cooperatives of Zambia, carried out demonstrations on the various uses of jatropha oil through national agricultural and commercial shows to increase awareness among the masses during 2001-2003.

Received: 5 February Revised: 13 February Accepted: 22 February
Index in Cosmos
March 2018 Volume 8 Number 3
UGC APPROVED

International journal of basic and applied research
www.pragatipublication.com
ISSN 2249-3352 (P) 2278-0505 (E)

• A project by the name "Fuel Fences and Biodiesel" has planted jatropha trees for biodiesel production in Gorongosa, Nhamatanda, and Chimoio Districts in Mozambique. The project has successfully demonstrated the use of liquid biofuel to combat deforestation and provide a sustainable source of fuel for rural communities. Plantation of Jatropha was done on deteriorated land along roads and around community farms in rural Mozambique. Making communities capable to produce biodiesel, the project lays the groundwork for activities that have the potential to be upscaled and invite private sector participation.

• In Ghana, two demonstration liquid biofuel projects are underway namely "Production and Utilization of Jatropha Oil in the West Mamprusi District of the Northern Region," and "Cultivation of the Physic Nut to Produce Biodiesel and Mitigate the Threat to Climate Change" for the purpose of capacity building, awareness raising, networking, and policy dialogueIn the first project ,women's groups have been engaged in rural areas to process jatropha oil into soap for rural bio-enterprises and biodiesel for the operation of lamps and mills. In the second project works was done with 2,000 farmers to produce jatropha biodiesel on a larger scale. The two projects have successfully attracted the interest of policy makers and a Ghanaian National Biofuel Policy Committee has been formed to draft and later implement the national policy.

5.CONCLUSION

The cultivation of jatropha in India comes with its own set of challenges as the plant can grow in degraded soils without offering much production costs but its yield can be increased only by fertilizers and irrigation which makes it compete against the food crops who have to feed andever-growing population.So,an adaptation of jatropha as a fencing crop in most of the regions of India can be made and production of biodiesel from it can make community life self-sustaining by using Jatropha oil for domestic use such as for lamps, in stoves and in place of diesel. This can bring down costs for farmers by providing organic fertilizers and protection to crops against predators and pests along with drastic reduction of diesel expenses.As can be seen from the African case studies, biodiesel can provide self-sustaining community life and by engaging women's groups,can emerge as a powerful tool for empowering women.

REFRENCES

1. Achten, W. M. J., Almeida, J., Fobelets, V., Bolle, E., Mathijs, E., Singh, V. P., Tiwari, D. N., and Muys, B. 2010. Life cycle assessment of *Jatropha* biodiesel as transportation fuel in rural India. *Appl. Energy* 87:3652–3660.
2. Basili, M., and Fontini, F. 2010. *Biofuel from* Jatropha curcas*: Environmental Sustainability and Option Value*. Available at: www.unisi.it
3. GEXSI. 2008. *Global Market Study on* Jatropha – *Final Report*. Berlin, Germany: GEXSI LLP. Available at: www.tinyurl.com

Received: 5 February Revised: 13 February Accepted: 22 February
Index in Cosmos
March 2018 Volume 8 Number 3
UGC APPROVED

International journal of basic and applied research
www.pragatipublication.com
ISSN 2249-3352 (P) 2278-0505 (E)

4. Ndong, R., Montrejaud-Vignoles, M., Girons, O. S., Gabrielle, B., Pirot, R., Domergue, M., and Sablayrolles, C. 2009. Life cycle assessment of biofuels from *Jatropha curcas* in West Africa: A field study. *Global Biol. Bioenergy* 1:197–210.
5. Raghvendra Gautam & Naveen Kumar (2016) Effect of ethanol addition on the properties of Jatropha ethyl ester, Energy Sources, Part A: Recovery, Utilization, and Environmental Effects, 38:23, 3464-3469, DOI: 10.1080/15567036.2016.1145766
6. Abdalbasit A. Mariod, Mohammed Salaheldeen. 2017. Oilseed crops and biodiesel production. Oilseed Crops, pages 52-79
7. Vaibhav A. Mantri, D.R. Parmar, P. Nageswara Rao, Arup Ghosh. (2014) Observations on ecosystem services in *Jatropha curcas* plantations established in degraded lands in India. *International Journal of Environmental Studies* 71:2, pages 209-214.

Received: 5 February Revised: 13 February Accepted: 22 February
Index in Cosmos
March 2018 Volume 8 Number 3
UGC APPROVED

Available online at www.sciencedirect.com

ScienceDirect

Materials Today: Proceedings 5 (2018) 3936–3942

materialstoday: PROCEEDINGS

www.materialstoday.com/proceedings

ICMPC 2017

Development and Investigation of Hybrid Electric Discharge Machining Electrode Process

Ramakant Rana[a], R. S. Walia[b], Surabhi Lata[c,*]

[a]*Delhi Technological University, Delhi-110042, India*
[b]*Delhi Technological University, Delhi-110042, India*
[c]*Maharaja Agrasen Institute of Technology, Rohini, Delhi-110085, India*

Abstract

Hybrid Electric Discharge Machining Electrode (HEDME) process is developed by comprising the features of Electric Discharge Machining (EDM) and traditional grinding which occurs alternatively in place of their simultaneous effect as Electric Discharge Grinding (EDG) process. This paper reports the experimental study of HEDME during machining of High Carbon Alloy Steel for material removal rate (MRR), tool wear (TW) and surface roughness (SR). The experiments were carried out on an indigenously developed HEDME attachment on Sparkonix EDM. The effects of main machining parameters such as type of tool, current and machining time have been studied. The effect of the machining on the workpiece surface machined by HEDME has been optimized using Taguchi L_9 orthogonal array and results are reported. Experimental study shows that the TW is found to be the least with third design of the electrode and it decrease with the decreasing value of current, also surface finish increases with decrease in current. Moreover, the third design of electrode gives the lowest SR and highest MRR.
© 2017 Elsevier Ltd. All rights reserved.
Selection and/or Peer-review under responsibility of 7th International Conference of Materials Processing and Characterization.

*Keywords:*HEDME; EDM; Grinding; MRR; TW; Surface Roughness.

1. Introduction

In today's fast growing technological world, machining of hard-to-machine metals have been a challenge for the manufacturing firms. The ergonomic value of the finished product has always been the market need and to meet it, continuous improvement is mandatory. The refinement of quality of product largely depends on efficiency and productivity of the process involved. Various machining processes have been evolved as the product design and

* Corresponding author. Tel.:+91 9210055994.
*E-mail address:*surabhilata.delhi@gmail.com

2214-7853© 2017 Elsevier Ltd. All rights reserved.
Selection and/or Peer-review under responsibility of 7th International Conference of Materials Processing and Characterization.

Nomenclature

EDG	Electric discharge grinding
EDM	Electric discharge machining
GA	Genetic algorithm
HEDME	Hybrid electric discharge machining electrode
HMP	Hybrid machining processes
MRR	Metal removal rate
SR	Surface roughness
TWR	Tool wear rate

demand changed. To meet the growing demands, manufacturing industries have by passed the unconventional machining processes and found their solution in the hybrid machining processes (HMPs). These processes are combination of one or more machining processes to incorporate the advantages of both. The development of such processes have revolutionised the machining of very complex geometries on difficult-to-machine metals without compromising the surface finish. These unconventional machining processes have helped achieve high precision and high dimensional accuracy even for the most complex profile at a reasonable cost. The HMPs can be grouped into collaborative and cooperative process based on their involvement in material removal process. They usually club unconventional machining process with the abrasive grinding process in order to enhance the performance and efficiency of the process.

2. Literature Review

Today's industries aim at meeting the everyday challenges faced by them. This includes the most prominent factor of machining of difficult-to-machine metals along with the need of automation, high dimensional accuracy and precision. To accomplish the aims of the market new researches and experiments are being conducted all-round the globe. Quality requirements of desired product should be met effectively and economically by the machining process. Hence, to make the process compatible with changing product demand and design, it would be worthy to increase the efficiency of the process [Shan (2005)]. The principle of EDM is analogous to the principle of EDG. Both the processes are being extensively researched to explore the new findings. Machining of the difficult to machine electrical conductive advance engineering materials is accomplished by the EDM process, an efficient and effective alternative without compromising its performance due to the workpiece mechanical properties [Jain (2004), Benedict (1987)]. Similarly grinding is used to machine advance engineering materials but its use is limited due to generation of surface cracks on ground surface and high specific energy [Kopac et al. (2006), Hegeman et al. (2002)]. Like grinding, EDM restricts its applicability due to the generation of residual stresses, low machining rate and formation of recast layer. Researchers initially substituted the stationary electrode with rotating disk wheel made of electrically conductive materials. This developed process is known as electrical discharge grinding (EDG) [Jain (2004), Benedict (1987)]. [Wei et al. (1995)] studied EDDG process under the name of Abrasive Electro-Discharge Grinding (AEDG) and tested its performance during machining of tungsten carbide and poly crystalline diamond through a comparison between the hybrid and constituent processes concluding MRR to be significantly improved along with high quality surface. [Kozak (2002)] researched the machining of the polycrystalline diamond (PCD), aluminium silicon carbide (Al/SiC) composite and polycrystalline cubic boron nitride (PCBN) with copper bonded diamond wheel in cut-off grinding mode. [Koshy et al. (1996, 1997)] investigated the mechanism of material removal and effect of process parameters of EDDG process during machining high speed steel and cemented carbide

with bronze bonded diamond wheel concluding that electrical discharge enhanced the grinding performance. [Yadav et al. (2008, 2010)] investigated the effect of process parameters on MRR in the EDDG process of HSS with copper bonded and bronze bonded diamond wheel during cut-off grinding mode resulting in increased MRR with increase in process parameters. In the recent researches, the optimization techniques being used includes ANN and GA techniques for modeling of the complex manufacturing processes due to their ability to approximate the nonlinear and complex relation between multiple input and output parameters [Joshi et al. (2009)]. [Bagci et al. (2006)] works revealed that in use of design of experiment, the Taguchi method was a powerful approach. The Taguchi method's parameter design can optimize the machining characteristics through the settings of process parameter and reduce the sensitivity of the system performance to sources of variation. This paper presents the mechanism of material removal in Hybrid Electric Discharge Machining Electrode (HEDME) process developed by combination of EDM and traditional grinding process. HEDME is captivating for machining electrically conducting difficult-to-machine advanced materials. Various researchers support this study [Koshy (1996), Choudhury et al. (1999), Kozak (2002), Kumar (2007), Yadav et al. (2008, 2010)] and substituted the metallic wheel utilized in EDG process with metal bonded diamond wheel and called it as electrical discharge diamond grinding (EDDG) concluding it advantageous for machining of the heat treated alloys, carbides alloys, super alloys, ceramics and composites. In lieu of the potential applications of EDDG process in modern manufacturing, this process as well endures with several problems such as continuous loss of diamond abrasives, trammeling of the debris particles with workpiece and bond materials [P. Koshy (1996), J. Kozak (2002)]. To forefend the above problems, HEDME process has been proposed followed by its fabrication and implementation. In this investigation, Design of Experiments was utilized to plan the experiments and further determine the significant machining parameters and to obtain the optimal combination levels of machining parameters for MRR, TW and SR.

3. Experimental Details

The mechanism of material removal of the HEDME process is shown in Fig. 1 (a). The process is marked by the use of special attachment for the EDM machine where the attachment holds and rotates the electrode while machining shown in Fig. 1 (b). The developed electrode holder is made in two sections as shown in Fig. 1 (c).

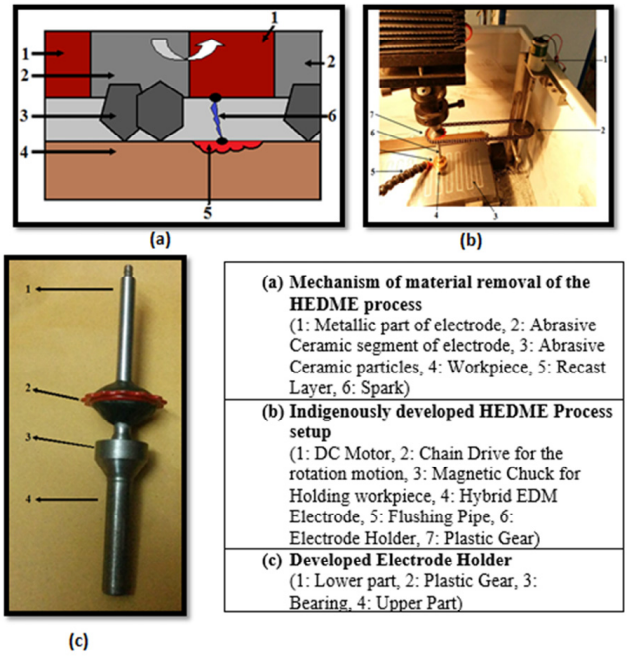


Fig. 1. HEDME Process and its Electrode Holder

In HEDME process, the metallic electrode used during EDG process has been replaced with segmented electrode whose cavity is completely filled with vitrified bond abrasive ceramic slab that takes a uniform circular shape due to the rotation of the hybrid electrode. In this process, the material is removed in two phases. In initial phase, the spark is generated between workpiece and metallic portion of the electrode during Pulse-on state. Due to

the spark generation the material is melted, softened below the melt zone and removed during the pulse off-time. This phenomenon is repeated for the complete metallic portion of the hybrid electrode. In the second phase, the material is removed due to the abrasive action of the abrasive ceramic particles. Hence, material removal process is completed by the individual effect of spark erosion and abrasion process.

Figure 2 shows all the three profile designs of developed Hybrid Electric Discharge Machining Electrode (HEDME).The EN-31 High Carbon Alloy Steel was selected as test workpieces with the diameter as 50 mm. The workpiece is machined for a predetermined time and then cleaned with acetone followed by the measurement of amount of material removed through an electronic balance and measurement of surface roughness by The Mahr Federal surface tester at different locations on the workpieces surface.

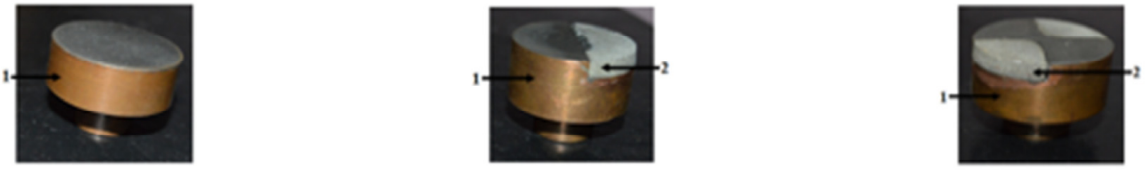


Fig. 2. Various design of developed Hybrid Electric Discharge Machining Electrode
(1: Copper Part, 2: Abrasive Ceramic particles Slab)

4. Process Parameters of HEDME Process

The various process variables selected that may affect the material removal rate (MRR) tool wear (TW) and surface roughness (SR) of the HEDME process are as follows:

1. Machine-based parameters: Current, Voltage, Pulse-on Time, Pulse-off Time, Polarity, Flushing method, machining time, Duty cycle.
2. Tool-based parameters: Type of Tool, abrasive material, and abrasive grain size and shape of tool.
3. Workpiece-based parameters: material of workpiece, workpiece diameter, shape and geometry.

Out of these parameters the following are kept constant to limit the volume of work involved in the investigation: Work Material, Workpiece Diameter, Polarity, Flushing Pressure.

This article reports the optimization of the selected significant parameters that affect the material removal rate, tool wear and surface roughness. The workable range of the parameters is decided on the basis of the results of the experiments conducted by varying one parameter at a time approach [Montgomery (2001)] considering the limitations imposed by the experimental setup. In the present work, among the three tools selected (Figure 2), the pure copper tool is used to compare the responses with the rotational EDM process. Among the various types of abrasive particles, such as silicon carbide, boron carbide, aluminium oxide, diamond, etc., the boron carbide abrasive was selected because of its easy availability. The range of current is 2, 6, and 10 A. The process parameters, their designated symbols and ranges are given in Table 1.

Table 1: Workable Range of the Selected Process Parameters

Process Parameters Designation	Process Parameters	Level 1	Level 2	Level 3
A	Type of Tool	S_1 (0%)	S_2 (40%)	S_3 (60%)
B	Current (Ampere)	2	6	10
C	Time (minutes)	30	40	50

Work Material: EN-31 High Carbon Alloy Steel, Workpiece Diameter : 50 mm, Electrode (Tool): Copper and Abrasive particles (Diameter 36mm, Abrasive particle Height 5mm, Total Height 18mm), Polarity: Positive, Dielectric Fluid: EDM Oil (LL 21), Flushing Pressure: Normal Submerged (1kg/cm^2): Temperature: 32±2^{o}C.

5. GA based Optimization

Any optimization process involves two phases namely development of a mathematical model comprising of formulation of objective function along with constraints and bounds of the variables; and search for the optimal solution under all defined limitations. In this research work the objective function is to minimize the tool wear and surface roughness while maximize the material removal rate possessing direct relations with machining time, current and the area of the abrasive used in the electrode. The formulated objective functions were tool wear (TW) = φ (A, I, t), surface roughness (SR) = φ (A, I, t) and material removal rate (MRR) = φ (A, I, t) which are optimized by using GA toolbox in MATLAB. As there are no nonlinear constraints, the transformed equations for tool wear, material removal rate and surface roughness were analysed within the bounds of variables.

6. Results and Discussion

The modern optimization technique i.e. genetic algorithm was utilised to generate the result at optimum level. The optimization was run through the MATLAB software for the material removal rate, tool wear and surface roughness at various predefined parameters.

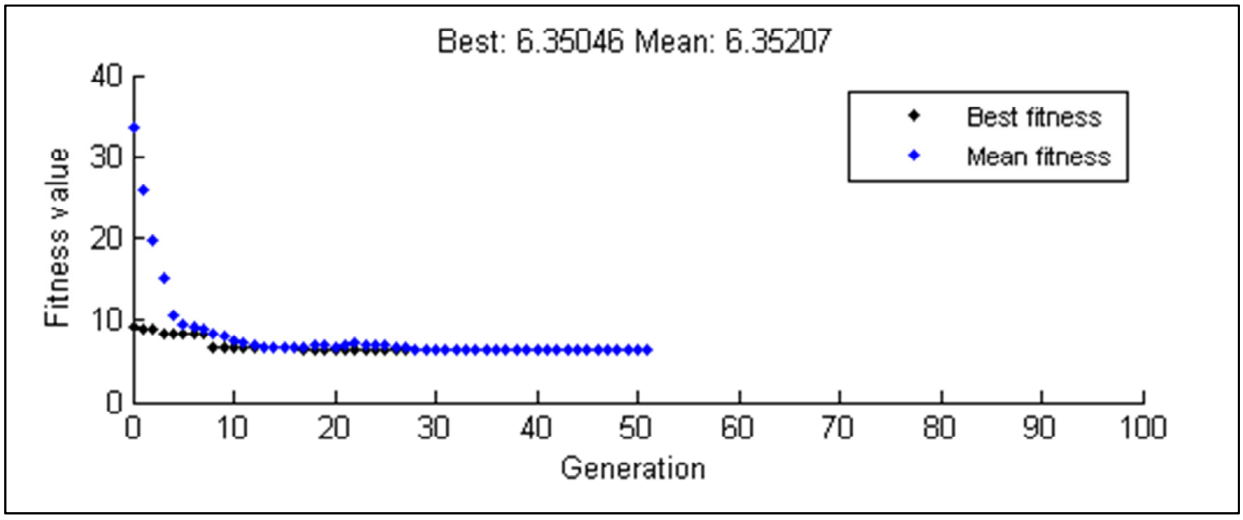


Fig. 3. Generation of Fitness value of MRR

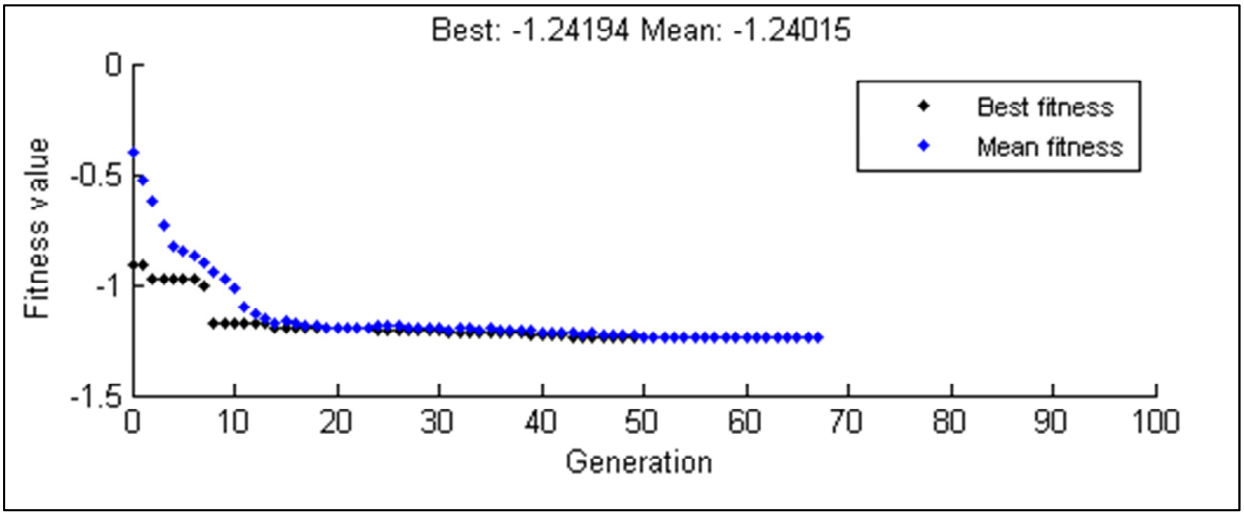


Fig. 4: Generation of Fitness value of TWR

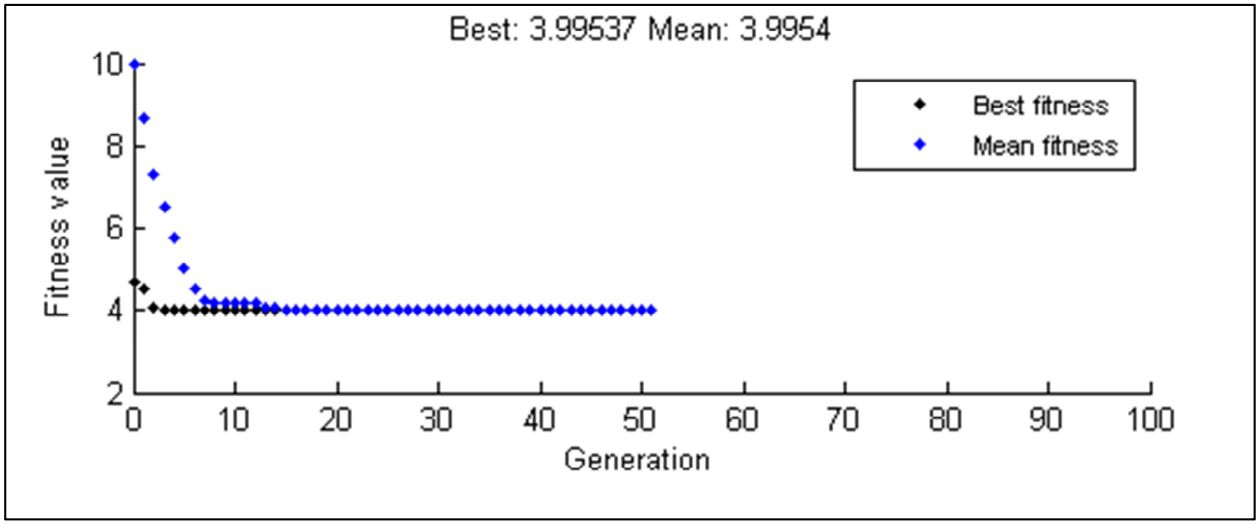


Fig. 5. Generation of Fitness value of SR

When the optimization process was terminated, the optimized value of the objective function satisfying the constraint equations were found to be:
MRR_{max} = 6.3504 mg at area of copper as 40.003%, current as 2.006 A and machining time as 41.006 mins.
TWR_{min} = -1.241936 mg at an area of copper as 99.904%, current as 9.999 A and machining time as 49.997 mins.
SR_{min} = 3.99537 µm at an area of copper as 40 .007%, current as 2.003 A and machining time as 42.329 mins.
The population size, generations and initial population have been changed, but the approximately same results have been obtained in all cases as shown in above Fig (3) (4) and (5)

7. Confirmation Experiments

To check the optimised results, a set of confirmatory experiments were performed. The defined parameters were set at the optimum level and the output variables were analysed. It was inferred that the material removal rate and surface roughness were optimum when the tool surface comprised of 60% of abrasive at low current and medium machining time while tool wear was minimum when the tool was completely made of copper. The tool wear was recorded minimum at high current density and high machining time. The results obtained were in accordance to the reulst obtained through the designed GA model and was within the tolerance limits.

8. Conclusion

The following results reported in this article are for Hybrid Electric Discharge Machining Electrode (HEDME) process and which can be considered as one of the important processes for machining of rotating EDM. Within the range of test conditions used, the following conclusions can be drawn:

1. The use of abrasive material in the EDM tool (electrode) increased the rate of material removal thereby reducing the machining time.
2. The Type of Tool, Current and Time showed significant effect on the selected output parameters i.e. material removal, surface roughness and tool removal rate. However, the surface roughness was least affected by the machining or processing time.

The results obtained from the genetic algorithm were confirmed through the confirmatory experiments performed. This paper shows the possibilities of using genetic algorithms for solving various machining problems. Material Removal Rate, Tool Wear Rate and Surface Roughness in machining process, depending on are of abrasive, current and machining time were successfully optimized. Hence it may be concluded that GA is a modern optimization method for finding the optimal values of functions with many variables, such as those modelling the machining process.

References

[1] Bagci, E., Ozcelik, B., Int. J. Adv. Manuf. Technol, 2006, 29, 629–636.
[2] Benedict G.F., Non-traditional manufacturing processes, Marcel Dekker, New York, 1987.
[3] Choudhury S.K., Jain V.K. and Gupta M., Machining Science and Technology, 1999, Vol. 3(1), pp. 91-105.
[4] Hegeman J.B.J.W., J.T.M.G. Hosson and G. With, Wear, 2002, Vol. 248(1-2), pp. 187-196.
[5] Jain V.K., Advanced machining processes, Allied Publishers, New Delhi, 2004.
[6] Joshi S N, Pande S S., International Journal of Advanced Manufacturing Technology, 2009, 45(3-4): 300–317
[7] Kopac J. and Krajnik P., Journal of Materials Processing Technology, 2006, Vol. 175(1-3), pp. 278 - 284.
[8] Koshy P, Jain V K, Lal G K., Journal of Materials Processing Technology, 1997, 72(1): 61–68
[9] Koshy P., Jain V.K., Lal G.K., Int. J. Mach. Tools Manuf., 1996, Vol. 36 (10), pp. 1173-1185.
[10] Kozak J., Achieve of Civil and Mechanical Engineering, 2002, Vol. 2(1-2), pp. 83-101.
[11] Liao, Y.S., Huang, J.T., Su, H.C., J. Mater. Process. Technol, 1997, 71, 487–493.
[12] Lin, Y.C., Yan, B.H., Huang, F.Y., Int. J. Adv. Manuf. Technol., 2001b, 18, 673–682.
[13] Montgomery D., Design and Analysis of Experiments, John Wiely and Sons, New York, 2001.
[14] Rana Ramakant, M.Tech thesis, Delhi Technological University, Delhi, India, 2014.
[15] Ravindra Nath Yadav, Vinod Yadava, G.K. Singh, Frontiers of Mechanical Engineering, 2013, 8(3): 319–332.
[16] Rhoades, L.J. “Abrasive flow machining”, Manuf. Eng., 1998, Nov., 75–78.
[17] Ross P.J., Taguchi Techniques for Quality Engineering, McGraw-Hill Book Company, New York, 1988.
[18] Roy R.K., A Primer on Taguchi Method, Van Nostrand Reinhold, New York, 1990.
[19] Shan, H.S. Advanced Manufacturing Methods; Tata McGraw-Hill: New Delhi, India, 2005.
[20] Walia R.S., Shan H.S. & Kumar Pradeep, Materials and Manufacturing Processes, 2006, Vol. 21, pp. 375–382.
[21] Wei B, Rajurkar K P, Proc. 1st Int. Mach. Grind. Conf. Dearborn, Michigan, 1995, 188–196.
[22] Yadav S K S, Yadava V, Narayana V L., International Journal of Advanced Manufacturing Technology, 2008, 36(1-2): 34–42.
[23] Yadav S K S, Yadava V. International Journal of Manufacturing Technology and Industrial Engineering, 2010, 1: 193–198
[24] Yang, W.H., Tarng, Y.S., 1998. J. Mater. Process. Technol. 84, 122–129.

© 2018 IJSRST | Volume 4 | Issue 2 | Print ISSN: 2395-6011 | Online ISSN: 2395-602X
Themed Section: Science and Technology

Electroforming Defects During Metal Deposition on Plastic Substrate Produced by Additive Manufacturing

Gurpreet Singh Phull*[1], Sanjeev Kumar[2], Ravinderjit Singh Walia[3]

[1]PhD Research Scholar, Department of Production and Industrial Engineering PEC University of Technology, Chandigarh, India

[2]Professor, Department of Mechanical Engineering PEC University of Technology, Chandigarh, India

[3]Professor,Department of Mechanical Engineering Delhi Technological University, Delhi, India

ABSTRACT

Additive manufacturing is evolving as an important process in the product and tooling development as direct or indirect process in the recent decade. The hybrid processes are being experimented by using additive manufacturing for the development of a component, assembly, EDM electrode, inserts or moulds etc. The investigated work in this paper highlights the possible manufacturing defects surfaced during metal deposition on fused deposition produced modelling. The study is the compilation of the observations during the experimentation of deposition of nickel and copper on the plastic substrate for process parameters of electroforming. The challenges of the depositions are categorized in two parts (i) Problems due to the Process (ii) Problems due to the Design. The main process parameter influenced the quality of the deposition found are activation of the nonconductive plastic, current density, solution concentration and agitation of the bath. The design of the components to be plated requires special attention about sharp corners, edges, hidden area and vertical walls.

Keywords: Electroforming; Fused Deposition Modeling; Additive Manufacturing; Nickle Plating

I. INTRODUCTION

Electroplating is the process of deposition of thin metal coating on various materials. Since the invention of the electroplating in 1805 by the Italian inventor Luigi V. Brugnatelli and commercialization during 1840s, it has evolved as a mature technology and widely being used in various products. Other important uses of electroplating is called electroforming, which is the deposition of thick layer on the substrate of more than 300 microns to 400 microns. Electroforming is deposition of metal on to a master of substantial thickness, so as to extract the shell after removal of the master. The shell produced must be of desired shape, surface finish and accurate dimensions so as to be used for producing the replicas of the master (Ron P). The electroforming has wide acceptance and usage as an additive manufacturing process for making molds, mandrels or components.

Electroforming of the ABS components produced by Fused Deposition Modeling (FDM) for the use in rapid tooling is one of the areas of interest in recent years. The tools produced by this method can be used for injection molding, sheet metal dies or investment casting molds (Sadegh et al., 2009). Rennie et al. (2001) used electroforming of Rapid Prototyping (RP) mandrels for producing electric discharge machining electrodes in fairly reasonable timescales. Hsu et al. (2008) used stereolithography to produce gypsum powder electrode and electrode-less plating with electroforming to produce EDM electrodes. Jetley et al.

(2006) presented a study to make injection molding insert using a low melting point metal casting alloy. A small insert of simple geometry was made by casting a tin-bismuth alloy over a plastic core. The insert was then used in injection molding process. Monzon et al. (2006) analyzed electroforming as a procedure to make cores for plastics injection molds. Shells were obtained from models manufactured through rapid prototyping using the FDM system. The main objective was to analyze the mechanical features of electroformed nickel shells, studying different aspects related to their metallographic structure, hardness, internal stresses and possible failures, by relating these features to the parameters of production of the shells with electroforming equipment. Finally a core was tested in an injection mold.

II. BACKGROUND

2.1 Electroforming

There are different ways to define electroforming, but ASTM B 832-93 describes it simply and concisely as follows: "Electroforming is the production or reproduction of articles by electrodeposition upon a mandrel or mould that is subsequently separated from the deposit." In the electroforming the main part is electrolytic cell in which current is passes through a bath containing electrolyte, the anode and the cathode. The deposition of a metallic coating onto an object is achieved by putting a negative charge on the object to be coated and immersing it into a solution containing a salt of the metal to be deposited. The metallic ions of the salt carry a positive charge and are thus attracted to the object. When they reach the negatively charged object, it provides electrons to reduce positively charged ions to metallic form (Helen H. L, 2006)

The deposition rate for electroforming process is controlled by current density, voltage, and electrolytic concentration of the electrolyte. The properties such as hardness, ductility, strength and internal stress can be varied significantly by changing electrolyte composition and operating condition.

B. Stein (1996) discussed about the nature of the stresses induced during the electroforming process, with an elaboration about measuring and controlling the stresses within the process window. It was emphasized to create a bath stress profile and process window for the better stress control. McGeough et al. (2001) described the process principles and mechanisms of electroforming, outlining its advantages and limitations. The review work established that electroforming can be successfully done with metals such as copper, nickel, and iron with thickness up to 16 mm. Xiang el al. (2006) suggested a process for direct electroplating on ABS plastics. They referred that although electroless copper plating on nonconductive plastics is very effective and economical method, but it is not environment friendly. The deposition rate presented in the study was 0.07 mm/s. The deposits were uniform and their difference of thickness was less than 0.1 micron meter. Hsu et al. (2008) performed electroless plating on the 3DP produced gypsum powdered electrode prototype. The electroless nickel plating was followed by electroforming of copper of up to 1mm thickness. The surface to be electroplated were made rough using corrosive compound of potassium dichromate, sulfuric acid and water. The optimization also done for the corrosion time, which was 3 minute in this study.

III. METHODS

3.1 Electroforming process

The setup for electroforming is made up of stainless steel tank with provisions for agitation of the salt solution and mounting of the electrodes and the samples to be plated. The main setup remains same whether the substrate is of plastic or metallic nature. The nonconductive materials are required to be made conductive before final deposition. Two options are primarily used to make the surface of a nonconductive

material to conductive surface, (i) the use of chemicals to activate the surface through electroless plating and (ii) application of the conductive paint on the surface using a spray gun or brush. Once the components are made conductive after that the process of the electroforming remains almost similar for both metallic and nonmetallic surfaces.

The parameters affecting the nickel deposition based on their influence as referred by the various literatures, are pH level, current density, concentration of the solution and temperature. The setting s used in this experiments are taken as per the studies conducted by the author and published (Gurpreet et al., 2017) . The response parameters such as deposition thickness, deposition rate or surface roughness have a contribution from each control factors like voltage, temperature, time, pH level, solution concentrations or current density. These optimum parameters obtained in the experiments is represented in Table 1 for copper electroforming and Table 2 for nickel electroforming.

Table 1. Optimum Settings for Copper Electroforming

Process arameter	Level of Factor	Response Parameter	Best Value Attained	Significant
Voltage	4 V	Deposition	0.18 mm/hr	Yes
CSS Conc.	200 g/L			Yes
Time	8 Hrs			No
Voltage	2V	Surface Roughness	1.81 μm	No
CSS Conc.	190 g/L			Yes
Time	6 Hrs			No

Table 2. Optimum Settings for Nickel Electroforming

Process Parameter	Level of Factor	Response Parameter	Best Value Attained	Significant
pH	4 pH	Deposition	0.086 mm/hr	Yes
Temperature	50 ^{0}C			No
Nickel Sulphate Conc.	270 g/L			No
Nickel Chloride Conc.	64.5 g/L			No
Current Density	6 A/dm^2			Yes
pH	4 pH	Surface Roughness	0.57 μm	Yes
Temperature	50 ^{0}C			No
Nickel Sulphate Conc.	300 g/L			No
Nickel Chloride Conc.	90 g/L			No
Current Density	1 A/dm^2			Yes

During the experimentation various process settings were tested for the above parameters to achieve the best parameters for the good quality product. The non-desired results obtained during these experimentation are discussed in the next section in detail

IV. CHALLENGED OF THE PROCESS

The challenges which have surfaced for during the deposition of the metal were found to be both due to the process and design.

4.1 Problems due to the Process

The process problem which affected the final electrode position can be due to the FDM process, activation process or electroforming control parameters. The following points are the compilation of few such observations. The poor quality of FDM product due to process parameters or poor machine leads to the porosity in the components, which create the problem during the activation process particularly for electroless nickel plating. This results uneven covering on the surface and some part of it remains without plating. Figure 1 shows the improper plating on the poor quality FDM part



Figure 1. Poor Quality FDM Part with Improper Deposition

Error in cleaning and pre-processing before activation leads to the conductivity problems, sometimes partial part is conductive and in some cases the whole part is not activated for plating.



Figure 2. Uncover Area due to Poor Conductivity

Figure 2 shows the part which remained non-conductive on some portion due to pre-processing. The higher rate of currents leads to the burning of the plating Figure 3.



Figure 3. Burnt Samples Due to High Current Density during Nickel Deposition

Due to poor activation the adhesion of the deposition with the substrate surface is not proper and the deposition start to peel off. Figure 4 shows such component.

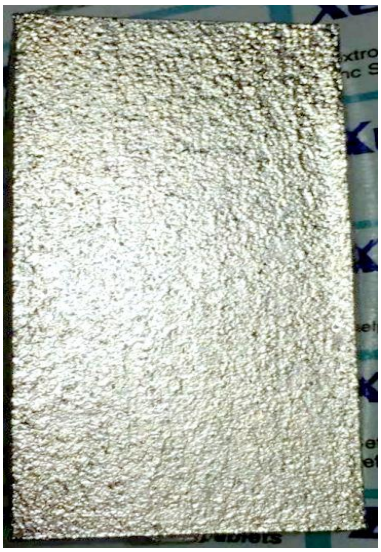


Figure 4. Sample with Poor Adhesion

The poor agitation also leads to the drops in the efficiency of the plating bath after some time, hence slow down the rate of reaction. The formation of the lumps is another area of concerns owing to the different current density zones. The figure 5 shows a component with the lumps formed at some high current density zones.

4.2 Problems due to the Design

As such there is no constraint of fabricating any part using additive manufacturing, but the designing of the part to be done taking in to consideration the limitation of the electrodeposition process. Following discussion highlights a few of the observation found during the process. The sharp corners or edges to be avoided, as sharp corners depleted the plating and sharp edges increase the sensitivity of the part as high current density point. Figure 6 (a) and (b) show the components having the flaws in the electrodeposition.

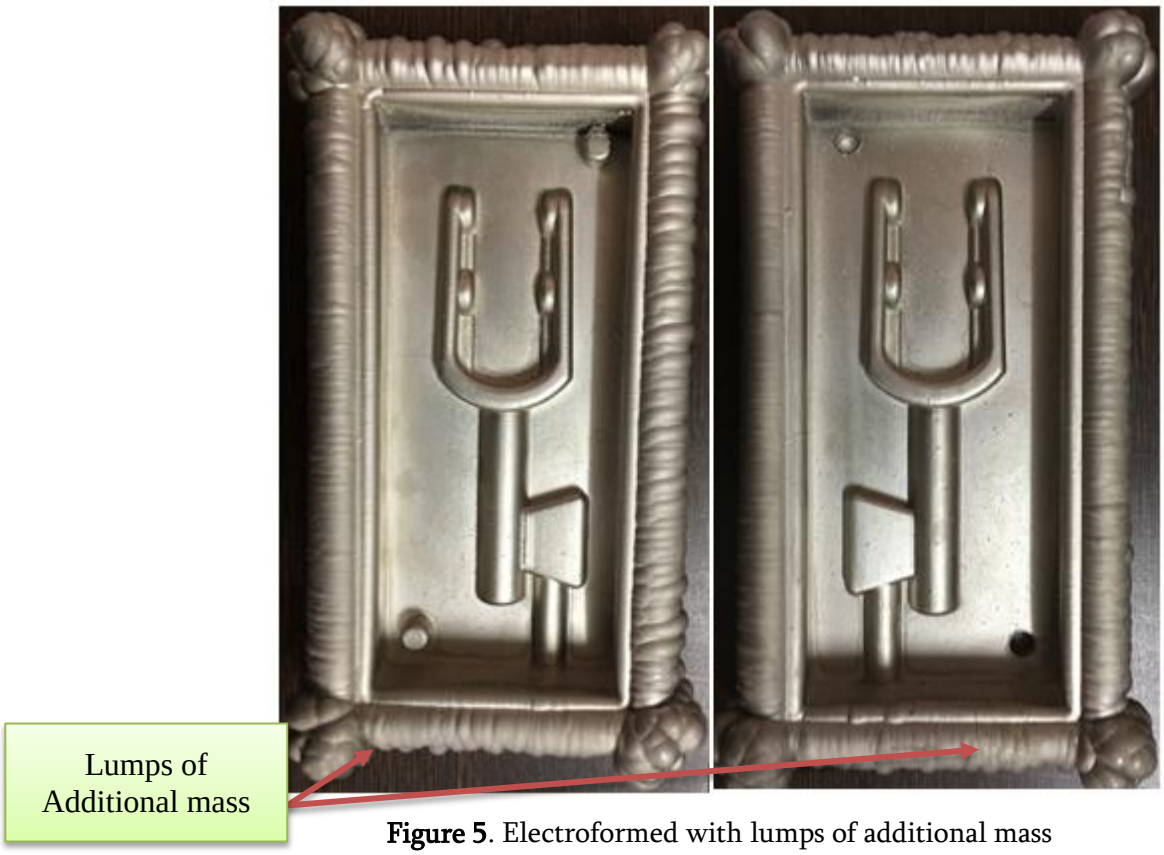


Figure 5. Electroformed with lumps of additional mass

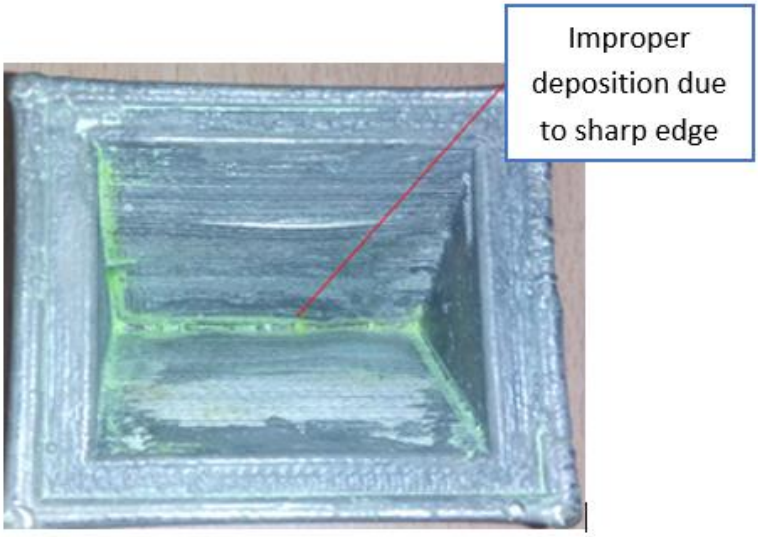


Figure 6 (a). Poor Deposition due to the Sharp Corner

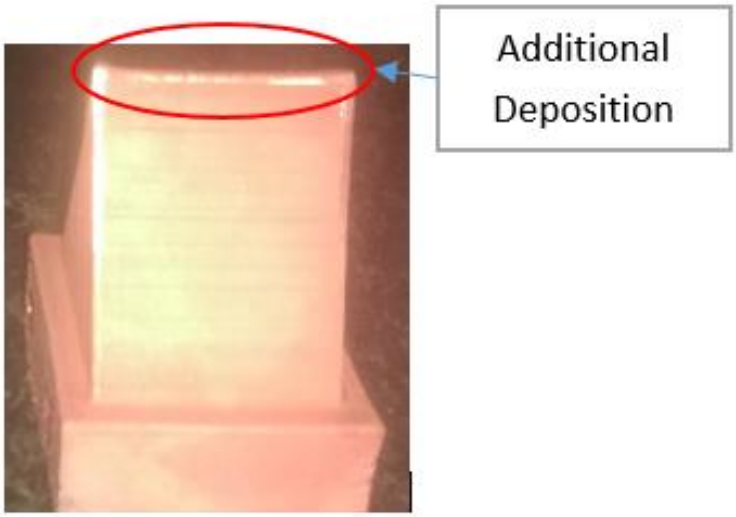


Figure 6 (b). Excessive Deposition due to the Sharp Edge as High Current Density Area

The area to be plated has to be exposed as an open surface to the solution, the plating in the undercover portions of the part does not yield sound results. Figure shows the component with improper plating at the hidden surfaces.

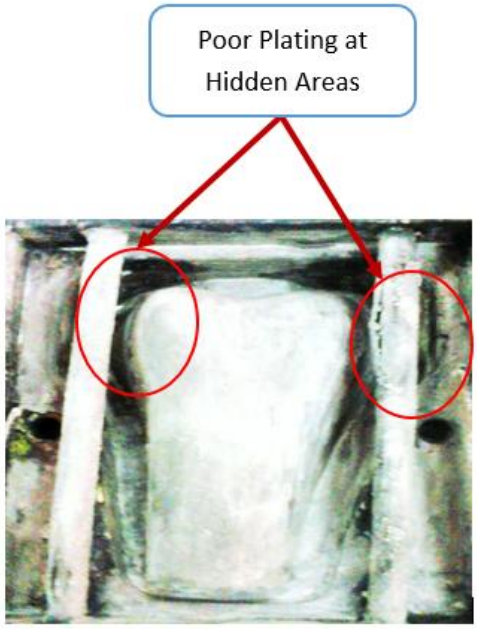


Figure 7. Poor Deposition on the Hidden Surfaces

Vertical walls to the solution also not result in the proper plating, some draft angle will help in improving the quality of the plating. Figure 8 represents the point made in this discussion.



Figure 8. Poor Deposition on the Vertical Surfaces

4.3 Microstructure Analysis

In order to analyze any flaw or critical observation at micro level the SEM image of the microstructure of the deposited copper was obtained. The observation clearly suggest as depicted in Figure 9, the grain size changes as the deposition thickness increases. The variation in the grain size is owing to the change in the thermal conductivity of the metal as its growth increases, resulting in to better heat dissipation. So the variation in the grain structure can be minimized with better heat dissipation arrangments.

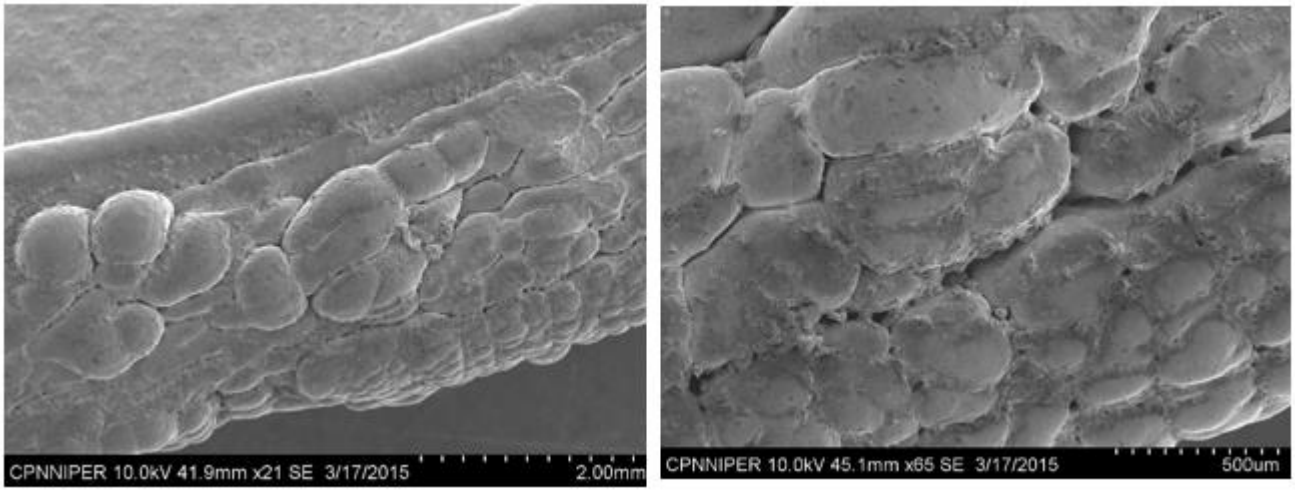


Figure 9. Microstructure of deposited metal

V. CONCLUSIONS

In this study the experiment was conducted by considering variable parameters namely pH, solution concentration, temperature and current density. The objective was to find the deposition rate and surface roughness to study the effects of the variable parameters on these characteristics, but during the process some critical observations came to the surface which should be taken care to avoid the production of bad quality noncompliance product. The following conclusions are drawn:

- ✓ The pre plating surface preparation treatment has to be done with utmost care to avoid any nonconductive zone generation.
- ✓ Temperature has least contribution for the metal deposition rate and surface finish.

- ✓ The ph value is the major contributor to improve the surface finish in comparison to current density and temperature.
- ✓ Higher current rates and lower boric acid shows the burning of the deposit.
- ✓ It was observed that after some time, the deposition of material does not remain uniform throughout the surface being plated due to the formation of high and low current density zones, hence retarding the overall thickness deposition rate on the complete profile.
- ✓ The initial plating of copper also affects nickel electroforming process. Higher copper plating coverage, better will be nickel electroforming. When copper plating was done after applying the conductive paint on ABS components, the coating was not good at the sharp edges. This problem may be circumvented by providing rounds or fillets at the corners during the design stage.
- ✓ The proper bath agitation system ensures the mixing of the solution and dissipation of the heat for better surface finish and uniform grain size.

VI. REFERENCES

[1]. B. Stein, 1996. A Practical Guide to Understanding, Measuring and controlling stress in Electroformed Metals. AESF Electroforming Symposium, Las Vegas.

[2]. Galantucci L.M., Lavecchia F., Percoco G., 2009. Experimental study aiming to enhance the surface finish of fused deposition modeled parts. CIRP Annals - Manufacturing Technology, 58, 189–192.

[3]. Garga Ashu, Bhattacharya Anirban & Batish Ajay, 2016. On Surface Finish and Dimensional Accuracy of FDM Parts after Cold Vapor Treatment. Materials and Manufacturing Processes, 31,522-529.

[4]. Gurpreet Singh Phull, Sanjeev Kumar & Ravinderjit Singh Walia, 2017. Nickel Deposition Optimization on Plastic Substrate Produced by Additive Manufacturing. International Journal of Manufacturing Science and Engineering, 8(2), 119-125.

[5]. Hsu C. Y., Chen D. Y., Lai M. Y. , Tzou G. J., 2008. EDM electrode manufacturing using RP combining electro less plating with electroforming. Int J Adv Manuf Technol. 38, 915–924.

[6]. Helen H. L, 2006. Electroplating. Encyclopedia of Chemical Processing DOI: 10.1081/E-ECHP-120007747, Taylor & Francis.

[7]. Jetley S and Daniel K. L, 2006. A Rapid Tooling Technique Using a Low Melting Point Metal Alloy for Plastic Injection Molding. Journal of Industrial Technology, 22, 3.

[8]. Kurth J.P, M.C.Leu and T nakagawa, 1998. Progress in additive Manufacturing and rapid prototyping. Keynote paper, Annals of the CIRP, 47,525-540.

[9]. McGeough J.A., Leu M.C., Rajurkar K.P., De Siliva A.K.M. and Liu Q., 2001. Electroforming Process and Application to Micro/Macro Manufacturing. CIRP Annals - Manufacturing Technology,50,499-514.

[10]. Monzon M D., Marrero M. D, A. Nizardo B, Pedro M. H, Cardenes J. F, 2006. A technical note on the characterization of electroformed nickel shells for their application to injection molds. Journal of Materials Processing Technology, 176, 273-277.

[11]. Prasad K.D.V Yarlagadda, Ismet P. Ilyas, Periklis Christodoulou, 2001. Development of rapid tooling for sheet metal drawing using nickel electroforming and stereo lithography process. Journal of Materials Processing Technology, 111, 286-294.

[12]. Prasad K.D.V. Yarlagadda, Periklis Christodoulou, Vijay S. Subramanian, 1999. Feasibilities studies on the production of electro

discharge machining electrodes with rapid prototyping and the electroforming process. Journal of Materials Processing Technology, 89-90,231-237.

[13]. Rennie A. E.W., Bocking C. E., Bennett G. R., 2001. Electroforming of rapid prototyping mandrels for electro-discharge machining electrodes. Journal of Materials Processing Technology.110, 186-196.

[14]. Ron P. Electroforming-a unique metal fabrication process. Nickel Development Institute Technical Series N 10 084.

[15]. Sadegh R, Rezaei M R, Akbari J, 2009. Design and Manufacturing of a wax injection tool for investment casting using rapid tooling. Tsinghua Science and technology,14, 108-115.

[16]. Sood A.K., Odhar R.K., Mahapatra S.S., 2009. Improving dimensional accuracy of fused deposition modelling processed part using grey Taguchi method. Materials and design, 30, 4243-4252.

[17]. S.Watson,Reprinted from transaction of the institute of Metal Finishing,NiDi Publication no.14005.

[18]. Stratasys inc, Fused deposision modeling for fast, safe plastic models, 12 th Annual conference on computer graphics, Chicago, April 1991, pp326-332.

[19]. Vidhata Mehta et al, Qualitative comparison of activation of ABS plastic component for Electroplating, International Journal of Science, Technology & Management, Volume No 04, Special Issue No. 01, March 2015 ISSN (online): 2394-1537.

[20]. J.A. Mc Geough, "Electroforming Process and Application to Micro/Macro Manufacturing", School of Mechanical Engineering, Edinburgh, UK.

[21]. Xiang Gui Wang, Ning Li, Hui-Li Hu and Chun yuan Yu, 2006. Process of direct copper plating on ABS plastics. Applied Surface science, 253, 480-484.

Defence Science Journal, Vol. 68, No. 2, March 2018, pp. 210-217, DOI : 10.14429/dsj.68.12048
© 2018, DESIDOC

Epoxy-glass Microballoon Syntactic Foams for Blast Mitigating Applications

A.V. Ullas[!,@], P.K. Sharma[!], P. Chandel[#], P. Sharma[#], D. Kumar[#], D. Kumar[@], and P.K. Roy[!,*]

[!]*DRDO-Centre for Fire, Explosive and Environment Safety, Delhi -110 054, India*
[@]*Department of Applied Chemistry and Polymer Technology, Delhi Technological University, Delhi -110 042, India*
[#]*DRDO-Terminal Ballistic Research Laboratory, Chandigarh - 160 003, India*
[*]*E-mail: pk_roy2000@yahoo.com*

ABSTRACT

Polymeric syntactic foams refer to a class of cellular material created using preformed hollow spheres bound together with a polymeric matrix. These cellular materials possess exceptional ability to respond against high impact dynamic loads. This paper is an attempt to fabricate polymeric syntactic foams of epoxy containing hollow glass microballoon at varying loading (40 % - 60 %) and explore their potential towards blast mitigation. The tensile, compressive and flexural strength were found to be inversely proportional to the microballoon loading in the quasi-static regime. The strain rate sensitivity of the foams was confirmed by performing high strain rate studies using split hopkinson pressure bar. The flow stress of these foams was found to increase with increasing strain rates. The syntactic foams were subjected to controlled transient blast loadings using a shock tube. The samples remained intact and no strain was observed on the strain gauge, even under a blast load of ~ 90 psi, which clearly highlight their potential as core materials for blast mitigating applications.

Keywords: Syntactic foams; High strain rate; Blast load; Shock tube

1. INTRODUCTION

Syntactic foams belong to a subclass of composite cellular materials prepared by dispersing hollow micro balloons in a matrix of polymer, ceramic or metal[1,2]. The presence of a large proportion of gaseous phase in these composites lead to significant weight reduction, and impart special mechanical properties which vastly differs from the bulk materials. These cellular composites are finding diverse applications ranging from deep sea to space vehicles[3] especially as energy absorbing core materials in sandwiched structures[4]. The presence of soft condensed matter helps reduce the damage arising from impact and other transient loads[5]. Although, both open and closed cell foams have been effectively utilised in their ability to resist blast/dynamic loads[6,7], the latter owing to the presence of entrapped air, forbears additional deformation at high strain rates and increase the compressive strength and energy absorbing ability of the foams[8].

Glass microballoons have been extensively used for syntactic foam manufacturing because of their high strength and low density[9]. Additionally, these microspheres act as independent energy absorbing loci on being subjected to compressive loads. Potential applications of syntactic foams as core materials, utilising their ability to act as energy absorbers, include them being used in the underbelly of tanks to attenuate the blast effects arising out from anti tank mines or other such applications where the ability to mitigate the effects of explosion are vital. Sandwich cores have found place in the literature[8,10], most important of them being balsa and foam cores in various naval applications such as surface ship deck structures and in boat hulls[11,12].

Rigid polymeric foams, usually prepared by the chemical reaction of isocyanates with polyols, are not strong enough to withstand blast loads and therefore mandate reinforcement[13]. Also, the processing of polymer-based foams is an involved process with interfacial phenomena and fluid dynamics being very critical[14,15]. In the field of defence technologies, in view of their excellent mechanical properties syntactic foams have been reported to withstand dynamic loads[16]. It is worth mentioning that blast effects, fall into the category of high impact dynamic loading which are characterised by the occurrence of high amplitude and high frequency waves which act on the structures for a very short period of time[17].

The aim of this study is to develop epoxy based syntactic foams and evaluate their behaviour both at quasi static and high strain rates using a Split Hopkinson pressure bar. Further, their response on being subjected to controlled transient loading has been studied on a shock tube facility. The aim is to explore the potential of these syntactic foams as core materials for energy absorbing applications.

2. EXPERIMENTAL

2.1 Materials and Methods

Cycloaliphatic epoxy resin (Ciba Geigy, Araldite CY 230; epoxy equivalent 200 eq g^{-1}), hardener (HY 951; amine content 24 eq kg^{-1}) and Hollow glass microballoons (K46, 3M) were used for the preparation of syntactic foams. The HGMs used have a true particle density of 0.46 g/cm^3, mean diameter of 40 μm (wall thickness 1.29 μm) and isostatic

Received : 05 October 2017, Revised : 07 December 2017
Accepted : 11 December 2018, Online published : 13 March 2018

crushing strength of 6000 psi.

2.2 Preparation of Syntactic Foams

Epoxy syntactic foams containing varying loadings of hollow glass balloons (40 %v/v, 50 %v/v, and 60 %v/v) were prepared as per the procedure reported previously[3]. In brief, theoretically calculated amounts of HGM was added to the epoxy resin and the contents were mechanically mixed and degassed followed by introduction of calculated amounts of triethylene tetramine. The viscous slurry hence obtained was transferred to silicone moulds and cured for 48 h at room temperature to prepare specimens for mechanical testing.

The mass of HGM to be added was calculated as follows:

$$\frac{Mass\ of\ HGM}{Mass\ of\ Syntactic\ foam} = \frac{\rho_{HGM} \times \Phi_{HGM}}{\rho_{HGM} \times \Phi_{HGM} + \rho_m \times \Phi_m}$$

where ρ and Φ refer to the density and volume fraction of the constituent respectively, and the subscripts *HGM*, and *m* refer to microballoons and epoxy respectively. For the purpose of calculation, density of HGM and epoxy have been assumed to be 0.46 g cc^{-1} and 1.17 g cc^{-1}[3], respectively. The syntactic foams were designated as *Sx*, where *x* refers to the microballoon loading (%v/v). For example, S40 refers to a formulation containing 40 % HGM and 60 % epoxy. The air-void porosity trapped within the foam was determined as the ratio of the difference in the theoretical (ρ_{th}) and experimental densities (ρ_{ex}) to theoretical density[2], as per the standard procedure.

$$\text{Void volume (\%)} = \frac{\rho_{th} - \rho_{ex}}{\rho_{th}} \times 100$$

The theoretical density was calculated using the standard rule of mixtures.

$$\rho_{th} = \rho_{HGM} \times \Phi_{HGM} + \rho_m \times \Phi_m$$

The experimental density (ρ_{ex}) was determined experimentally by averaging the mass : volume ratio of five specimens per sample as per the standard method ASTM D1622–98.

2.3 Characterisation

The thermal behaviour was investigated using Perkin Elmer Diamond STG-DTA under N_2 atmosphere in the temperature range 50-600 °C. A heating rate of 10 °C/min and sample mass of 5.0 ± 0.5 mg was used for each experiment. Rheological studies were performed for HGM-epoxy formulations using an Anton Paar Rheometer (MCR 102) using 25 mm disposable aluminium parallel plates. Shear rate sensitivity studies were performed, while varying the same over 0.1 s^{-1} to 1 s^{-1} under isothermal conditions (30 °C). The morphology of fractured surface was studied using a scanning electron microscope (Zeiss EVO MA15) under an acceleration voltage of 1 kV. Samples were mounted on aluminium stubs and sputter-coated with gold and palladium (10 nm) using a sputter coater (Quorum SC7620) operating at 10-12 mA for 120 s.

2.4 Mechanical Testing

Mechanical testing was carried out using Universal Testing Machine (International Equipment) at ambient temperature. For compression testing, standard cylindrical specimens (12mm diameter, 6 mm thick) were compressed at a rate of 1.3 mm min^{-1}. Five specimens of each composition were tested and the load-displacement data obtained from the tests was used to obtain stress-strain curves for calculation of compressive strength. Toughness, which refers to the area under compression stress-strain curve, was quantified as an index of the amount of energy absorbed by the foams[18].

$$\text{Energy absorption} = \frac{1(\rho_c \times \in_c)}{2} + (\rho_c \times \varepsilon_c)$$

where ρ_c and ε_c refer to the compression yield strength and crushing strain of the foam, respectively.

Flexural testing of the samples was performed under three point bending mode as per ASTM D790. For this purpose, specimens of standard dimensions (127 mm length x 12.5 mm width x 3.5 mm thickness) were prepared and subjected to a deformation rate of 2 mm min^{-1} while maintaining a span length of 60 mm.

The tensile properties were determined as per ASTM method D638 using a Universal Testing System (International equipments) at ambient temperature. The dumb bell shaped specimens used for tensile testing were 165 mm long, 3 mm thick, and 13 mm wide along the centre of the casting for syntactic foams. The samples were subjected to a cross head speed of 10 mm min^{-1}.

2.5 High Strain Rate Testing

The mechanical response of the samples under high strain rates was investigated using a Split Hopkinson Pressure bar. The basic principle of SHPB is based on one-dimensional wave propagation in elastic bars, and since it is not possible in practice, the theory is adopted with certain approximations. The setup at Terminal Ballistic Research Laboratory (TBRL), Chandigarh comprises of two high strength maraging steel with yield strength 1750 MPa, diameter 20 mm and length 2000 mm. A projectile (300 mm length, 20 mm dia) is made to hit the cylindrical foam sample sandwiched between the two bars to produce different strain rates varying between 1376 s^{-1} - 2574 s^{-1}. Strain gauges of 120 Ω, 90° tee rosette precision strain gauges designated as EA-06-125TM-120 were used. For wave shaping a 1.5 mm OFHC copper wave shaper was used.

In all the experiments, cylindrical specimens with length to diameter (L/D) ratio of 0.5 were used, with the diameter of the specimen being 12 mm. This ensures the impact on full cross-section of the specimen and also permits the specimen to expand along radial direction within the cross-sectional area of the bars after the compressive load is applied.

2.6 Shock Tube Test

The dynamic response of the syntactic foams was evaluated by subjecting disc shaped specimens to controlled blast loadings on a shock tube. A shock tube assembly essentially comprises of a long rigid cylinder, sub-divided into a high-pressure driver section and a low pressure driven section, which are separated by a mylar diaphragm. The shock tube, used for the present study has an overall length of 8.7m;

divided into 1.7 m driver and 7 m driven sections. A cylindrical disc of syntactic foam specimen (12 cm diameter, thickness 1 cm) was sandwiched between two aluminium sheets (0.25 mm thickness), held under simply supported boundary conditions in front of the driven section. Pressurised air is used as the driver gas, the driven gas being ambient air. The rapid release of gas due to diaphragm rupture results in the creation of a shock wave, which travels down the driven tube to impart dynamic blast loadings. A circular region of 10 cm diameter was effectively subjected to blast loading, as pictorially shown in Fig. 1. Pressure sensor (113B21, PCB make), placed at a distance of 11.3 cm from the sample was used to monitor the pressure profile during the testing. Strain gauge (HBM:K-LY4-1-11-120-3-2) was affixed on the blast–opposing face of syntactic foam specimen to measure sample deflections.

The signal recorded on the strain gauge installed on the opposite face of the blast is indicative of the extent of deformation in the syntactic foam sample due to blast loading. A control set of experiments was also performed, which comprised of two aluminium sheets with no foam between.

3. RESULTS AND DISCUSSION

3.1 Rheological Studies

The effect of introducing glass micro balloons on the rheological behaviour of the resin is of particular interest for processing of the foams. The shear rate dependence of the formulation is presented in Fig. 2. Unfilled epoxy resin exhibits a viscosity of ~ 1000 mPa.s at 30 °C (shear rate =0.1 s^{-1}) and inclusion of microballoons lead to a considerable increase in its viscosity, the extent of which is proportional to microballoon loading(~10^5 mPa.s, 40 per cent microballoon loading). The viscosity-shear rate profiles of all the formulations are clearly indicative of the shear thinning nature of the composition.

3.2 Void age in Syntactic Foams

The ratio of experimental and theoretical densities was used to quantify the void age in each sample, and the results are presented in Table 1. As expected, an increase in the microballoon loading lead to a decrease in the density of the foams.

3.3 Thermal Properties

TG-DTG traces (under inert atmosphere) of syntactic foams are presented in Fig. 3. The profile associated with the degradation of epoxy was found to remain unaltered, except for the substantial increase in the char content, due to the presence of hollow microballoons. The thermogravimetric trace of neat

Table 1. Experimental and theoretical densities of syntactic foams

Sample designation	Density (kg/m³)		Voids (% v/v)
	Experimental	Theoretical	
S40	859.3 ± 7	886	3.0
S50	775.3 ± 4	815	4.8
S60	712.7 ± 5	744	4.2

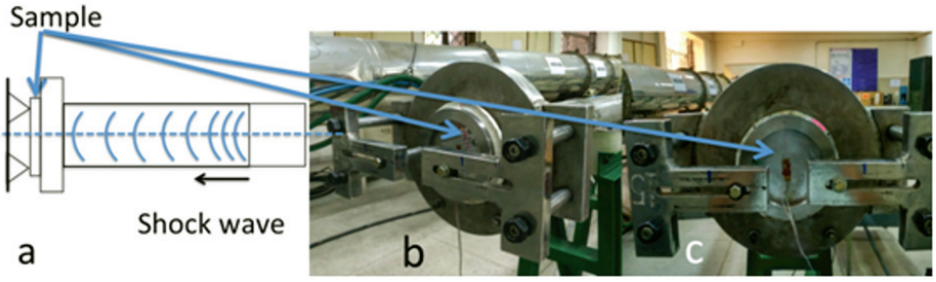


Figure 1. (a) Representation of the specimen loading on shock tube, (b) Specimen placement, and (c) Front view.

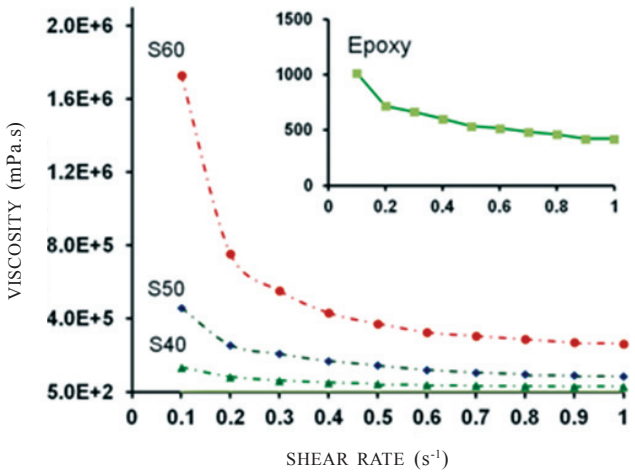


Figure 2. Effect of increasing shear rate on viscosity of syntactic foam formulations.

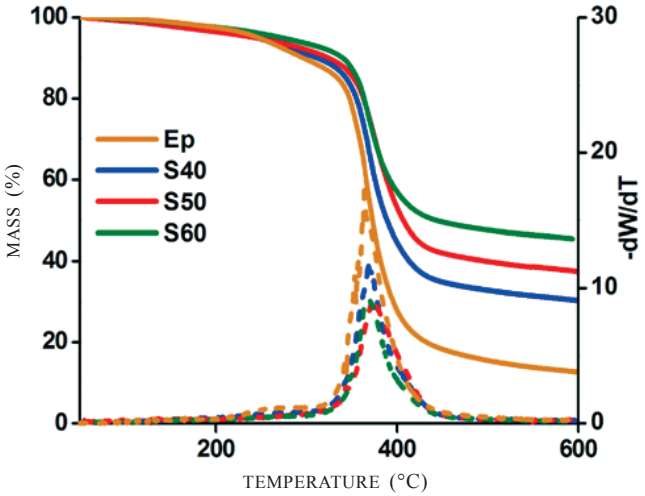


Figure 3. TG-DTG traces of syntactic foams with varying microballoon loading.

epoxy is also included in the figure for ready reference. For syntactic foams with 40 per cent microballoon loading, a char content of 29 per cent was observed (at 600 °C), a major fraction (~21%), being the incombustible glass microballoons.

3.4 Mechanical Properties

3.4.1 Quasi-static Testing

The effect of increasing microballoon content (40% v/v - 60 % v/v) on the mechanical properties of syntactic foams under quasi-static conditions is presented in Fig. 4. The stress-strain curves (compressive mode) are also included (Fig. 4(a)). In general, the lower compressive strength of microballoons (41 MPa) in comparison to neat epoxy (138 MPa)[19] is expected to result in a reduction of compressive strength, which is very well evidenced from our studies (Fig. 4(b)). It is to be noted that under low microballoon loading, the hollow constituents are well embedded within the resin. During compression, substantial energy is absorbed by the matrix as well as the microballoon-epoxy interface prior to the fracture of microspheres[20]. With increasing microballoon loading, the contact between the microballoons increases due to the reduction of resin content, leading to localised aggregation which leads to further reduction in the compressive properties.

Mechanical response was also determined in tensile and flexural mode, the results of which are included in Fig. 4(c). The precipitous drop in stress after the end of elastic region was indicative of the brittle failure in the sample. Flexural strength was also found to be inversely proportional to the microballoon loading. However, it is to be noted that under flexure, failure occurs primarily due to matrix fracture and is less dependent on failure of microballoons[21]. The tensile properties, which depend primarily on the response of the matrix rather than on the filler i.e. glass microballoons[2], are presented in Fig. 4(d). It can be seen that the tensile properties are also inversely proportional to the microballoon loading[22]. It is to be noted that the properties of syntactic foams are strongly dependant on the wetting and interfacial bonding between microballoon and the resin[23]. Further improvement is possible by surface treatment of the glass microballoons[24,25].

The microstructure of syntactic foams was studied using a scanning electron microscope. The SEM image of syntactic foam specimen (S40) post quasi-static testing (both compressive and tensile) is presented in Fig. 5. Embedded hollow glass microballoons are observed in the image. During compression, glass microballoons undergo extensive crushing which results in the failure of the foams (Fig. 5(a)). On the other hand, tensile failure is brought about by the failure of matrix (Fig. 5(b)). Flexural failure occurs due to a combination of tensile and compressive forces and results in microballoons debonding as well as matrix failure.

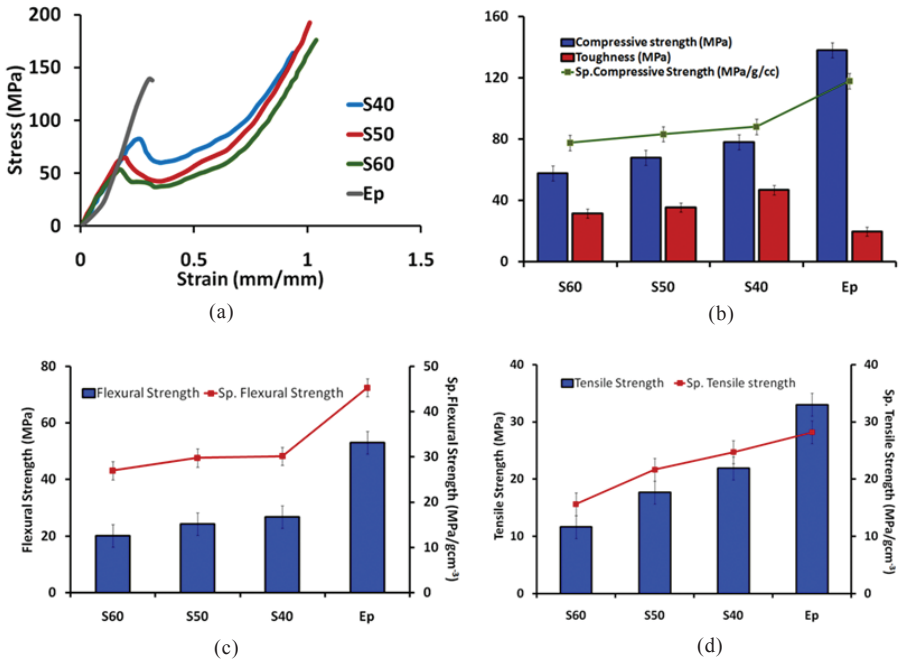


Figure 4. (a) Stress-strain curves (Compressive mode), b) variation of compressive, (c) flexural and (d) tensile properties of syntactic foams as a function of microcapsule loading.

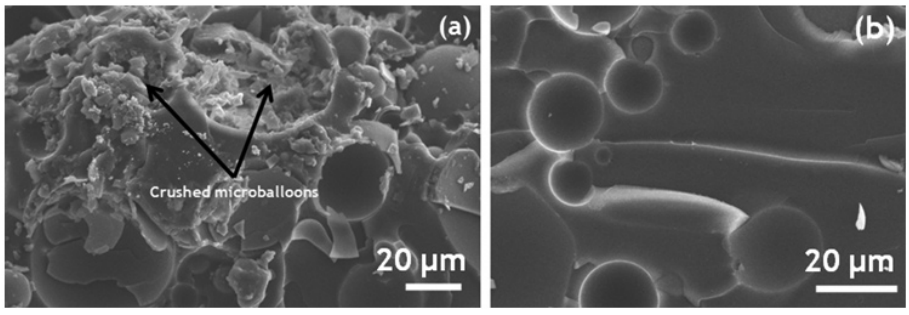


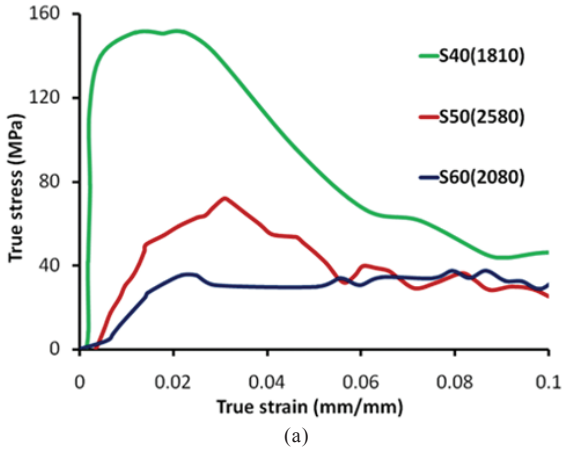
Figure 5. (a) Compressive and (b) tensile fracture features of epoxy syntactic foam.

3.4.2 High Strain-rate Studies

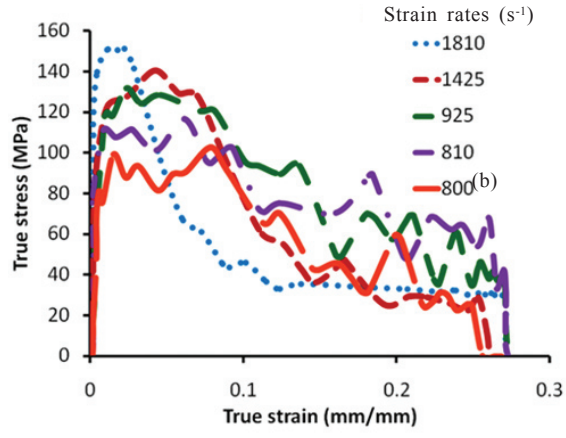
The effect of increasing strain rates on the compressive behaviour of syntactic foam was quantified using Split Hopkinson Pressure bar setup, which consists of input and output bar sandwiching a short specimen[26,27]. The details of the setup are presented in the published paper[19]. Pressurised air propels a projectile, which strikes at one end of the input bar. A compressive stress wave is generated, which upon hitting the specimen, is partially transmitted and reaches the output bar while a part of it is reflected back to the input bar. In the present case, this propagation of the compressive wave leads to an irreversible plastic deformation in the specimen. The reflected pulse propagates as a tension wave, while the transmitted pulse remains in compression. The wave signal responses are quantified using

strain gauges attached on the input and output bars. The stress – strain profile obtained for different samples are presented in Fig. 6. Representative curve for each loading is presented for the sake of comparison of the results. It is to be noted that under high strain compressive testing, the strain rate rapidly increases during the initial stages of loading; therefore it was not attempted to estimate the Young's modulus from the strain gauge data. As in the case of quasi-static testing, the flow stress (maxima) decreased with increasing microballoon loading (38MPa S60 (ε =2080 s^{-1}), 71 MPa, S50 (ε =2580s^{-1})and 151 MPa, S40, (ε =1810s^{-1}).

The mechanical response of the specimens under high strain rate was found to follow the same order as under quasi-static testing, however a distinct difference in terms of the absence of a stress plateau was clearly evidenced. In line with the quasi-static tests, decrease in microcapsule loading leads to a proportional increase in the maximum flow stress. The strain rate sensitivity of a representative formulation (S40) is presented in Fig. 6(b). In line with previous studies[28], the flow stress was found to increase proportionally with increasing strain rates. The fracture mechanics of syntactic foams has been extensively studied, wherein significant dependence of the compressive failure upon the strain rate has been reported[28].



(a)



(b)

Figure 6. (a) Stress-strain profile of syntactic foams under high strain rates (~1380-2580 s^{-1}) and (b) effect of increasing strain rate on a representative syntactic formulation (S40).

The failure has been reported to occur via varied mechanisms. At low strain rates, the foams have been reported to undergo shear cracking due to crushing of the microballoons whereas at higher strain rates, the failure occurs primarily due to crack propagation in the direction of compression.

3.4.3 Shock Tube Studies

The dynamic response of the syntactic foams was evaluated by subjecting circular disc shaped specimens to controlled transient loadings on a shock tube. The pressure profile along with the peak pressure, impulse as well as the response of the syntactic foam in terms of strain deformation is presented in Table 2.

It can be seen that the control set (aluminium sheets) undergo extensive deformation due to blast loadings (35.5 psi). In comparison, the syntactic foam specimens do not undergo any deformation even when subjected to larger over pressure. A photograph of the S40 specimen post-blast loading (~89.6MPa) is presented in Fig. 7. It can be seen that the sample is intact, which clearly highlights the potential of syntactic foams, as core material in sandwich configuration for blast mitigating applications.

S40 syntactic foams were repeatedly subjected to blast pressures of ~90 psi. The post-blast visual of the sample exposed to 5 repetitive shock loadings is presented in Fig. 8. It can be seen that the sample underwent chipping, with no visual evidence of microballoon crushing.

4. CONCLUSIONS

Polymeric syntactic foams were prepared by introducing

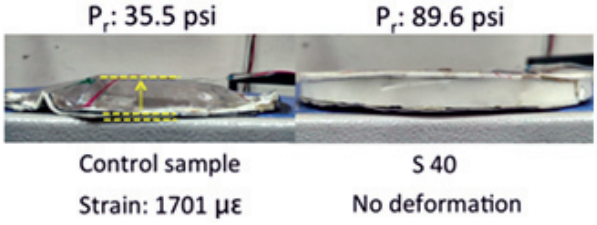
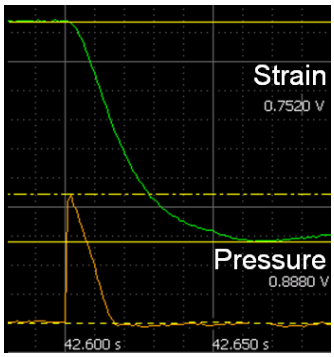
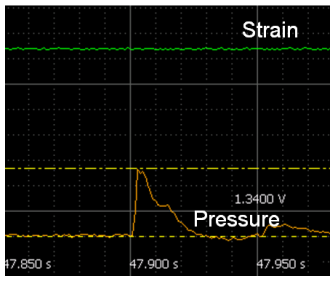
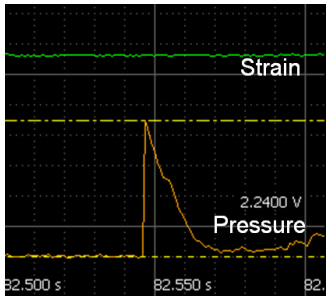


Figure 7. Post-blast visuals of control and S40 syntactic foam.



Figure 8. Post-blast visuals of S40 syntactic foam after 5 repeated blast loadings (P_r~90psi).

Table 2. Response of syntactic foam under blast loading conditions

Sample	ΔP (Driver pressure-driven pressure)	Pressure/ strain profile	Peak pressure (psi)	Sample response
Control 2 Aluminium sheets	2		35.5	Extensive deformation observed. Strain: 1701 με
S40 (1cm) sandwiched between 2 Aluminium sheets	5		53.6	No strain observed. Sample intact post-blast
S40 (1 cm) sandwiched between 2 Aluminium sheets	15		89.6	No strain observed. Sample intact post-blast

K46 hollow glass microballoons at varied loading (40 %v/v - 60 %v/v) into a cycloaliphatic epoxy resin. Rheological studies were performed to establish the dependence of viscosity on increasing shear rates. Increasing the loading of glass microballoons led to a proportional increase in the viscosity of the formulation, however all the formulations exhibited a shear thinning behaviour. The zero shear viscosity increased from ~ 10^3 MPa.s to 10^5 MPa.s at 30 °C as the microballoon loading was increased to 40 %v/v. Mechanical properties of the foamed composites was evaluated both at quasi-static (tensile, compressive and flexure) and high strain rates. The difference in the crushing strength of glass microballoons (41 MPa) and cured epoxy (138 MPa) reflected in terms of a proportional decrease in the mechanical properties with increasing filler loading. The strain rate sensitivity of the foams was confirmed by high strain rate studies using a split Hopkinson pressure bar. In line with quasi-static tests, the flow stress (maxima in stress strain curve) for compositions containing 40 per cent loading was substantially higher 151 MPa as compared to 38 MPa (60 per cent loading). Syntactic foams (S40) were subjected to controlled transient blast loadings on a shock tube, the intensity of which was varied by varying the pressure gradient between the driver and driven sections. Specimens with 40 per cent microballoon loading were found to withstand blast loads of the order of ~90 psi, while control samples underwent extensive deformation (1701 με at ~36 psi),which clearly highlight the potential of the syntactic foams as a blast mitigating material, especially as a core material in sandwich configuration.

ACKNOWLEDGEMENTS

The authors gratefully acknowledge Director, CFEES, DRDO for providing logistic support to perform this work. A.V.U is pleased to acknowledge DTU for providing financial support. All the authors acknowledge DRDO for funding this research work through the grant ST/14-15/CFE-1311. Thanks are also due to Sh. Rajan, CFEES for assistance during shock tube testing.

REFERENCES

1. John, B. & Reghunadhan Nair, C.P. In *Handbook of Thermoset Plastics (Third Edition)*; Dodiuk, H., Goodman, S. H., Eds.; William Andrew Publishing: Boston, 2014, p 511-554.
doi: 10.1016/B978-1-4557-3107-7.00013-0:
2. Colloca, M.; Gupta, N. & Porfiri, M. Tensile properties of carbon nanofiber reinforced multiscale syntactic foams. *Compos Part B,* 2013, **44**, 584-591.
3. Ullas, A.V.; Qayyum, B.; Kumar, D. & Roy, P.K.

Electrospun polyamide nanofiber-reinforced hybrid syntactic foams. *Polym. Plast. Technol. Eng.,* 2016, **55**, 1797-1806.
doi: 10.1080/03602559.2016.1163590

4. Asif, A.; Rao, V.L. & Ninan, K.N. Nanoclay reinforced thermoplastic toughened epoxy hybrid syntactic foam: Surface morphology, mechanical and thermo mechanical properties. *Mater. Sci. Eng. A,* 2010, **527**, 6184-6192.
doi: 10.1016/j.msea.2010.06.058
5. Vitali, N.F. Shock (Blast) Mitigation by 'soft' condensed matter. *MRS Symp. Proc,* 2003, **759**, 4.3.1- 4.3.12.
6. Tan, P.J.; Reid, S.R. & Harrigan, J.J. On the dynamic mechanical properties of open-cell metal foams – A re-assessment of the 'simple-shock theory'. *Int. J. Solids Struct.,* 2012, **49**, 2744-2753.
doi: 10.1016/j.ijsolstr.2012.03.026
7. Gupta, N. & Maharsia, R. Enhancement of energy absorption in syntactic foams by nanoclay incorporation for sandwich core applications. *Appl. Compos. Mater.,* 2005*,* **12**, 247-261.
doi: 10.1007/s10443-005-1130-6
8. Chakravarty, U.K. An investigation on the dynamic response of polymeric, metallic, and biomaterial foams. *Compos. Struct.,* 2010, **92**, 2339-2344.
doi: 10.1016/j.compstruct.2010.02.013
9. Panteghini, A. & Bardella, L. On the compressive strength of glass microballoons-based syntactic foams. *Mech. Mater.,* 2015, **82**, 63-77.
doi: 10.1016/j.mechmat.2014.12.005
10. Abrate, S. Impulsive response of sandwich structures. *Procedia Eng.,* 2014, **88**, 62-68.
doi: 10.1016/j.proeng.2014.11.127
11. Daniel, I.M.; Cho, J.-M. & Werner, B.T. Characterisation and modeling of stain-rate-dependent behaviour of polymeric foams. *Compos. Part A Appl. Sci. Manuf.,* 2013, **45**, 70-78.
doi: 10.1016/j.compositesa.2012.10.003:
12. Atas, C. & Sevim, C. On the impact response of sandwich composites with cores of balsa wood and PVC foam. *Compos. Struct.,* 2010, **93**, 40-48.
doi: 10.1016/j.compstruct.2010.06.018
13. Mostafa, H. E.; El-Dakhakhni, W. W. & Mekky, W.F. Use of reinforced rigid polyurethane foam for blast hazard mitigation. *J. Reinf. Plast. Compos.,* 2010, **29**, 3048-3057.
doi: 10.1177/0731684410363184
14. Verdejo, R.; Tapiador, F. J.; Helfen, L.; Bernal, M. M.; Bitinis, N. & Lopez-Manchado, M. A. Fluid dynamics of evolving foams. *Phys. Chem. Chem. Phys.,* 2009, **11**, 10860-10866.
doi: 10.1039/b913262g
15. Kalpathy, S. & Ravi Shreyes, A. Thermodiffusion as a means to manipulate liquid film dynamics on chemically patterned surfaces. 2017, **146**.
doi: 10.1063/1.4984610:
16. Jahsman, W. E. *In* Mechanical Behavior of Materials under Dynamic Loads: Symposium Held in San Antonio, Texas, September 6-8, 1967; Lindholm, U.S., Ed.; Springer Berlin Heidelberg: Berlin, Heidelberg, 1968, p 365-387.
doi: 10.1007/978-3-642-87445-1_18
17. Irshidat, M.; Al-Ostaz, A.; Cheng, A. H. D.; Mullen, C.; 41171 ed.; Ames, D., Droessler, T. L., Hoit, M., Eds.; ASCE: Las Vegas, NV, 2011, **401**, 185-185.
18. Raghu, P.; Kunigal, S. & Larry, R. *In* 48th AIAA/ASME/ASCE/AHS/ASC Structures, Structural Dynamics, and Materials Conference; American Institute of Aeronautics and Astronautics: 2007.
doi:10.2514/6.2007-2336
19. Chaudhary, S.; Iqbal, N.; Mangla, V.; Kumar, D. & Roy, P.K. Strain rate sensitivity of toughened epoxy. *Iran Polym. J.,* 2015, **24**, 871-881.
doi: 10.1007/s13726-015-0375-7:
20. Dimchev, M.; Caeti, R. & Gupta, N. Effect of carbon nanofibers on tensile and compressive characteristics of hollow particle filled composites. *Mater. Des.,* 2010, **31**, 1332-1337.
21. Zhang, L. & Ma, J. Effect of carbon nanofiber reinforcement on mechanical properties of syntactic foam. *Mater. Sci. Eng. A,* 2013, **574**, 191-196.
doi: 10.1016/j.msea.2013.03.028
22. Gupta, N. & Nagorny, R. Tensile properties of glass microballoon-epoxy resin syntactic foams. *J. Appl. Polym. Sci.,* 2006, ***102***, 1254-1261. 10.1002/app.23548
23. Marur, P.R. Influence of imperfect interface on the elastic moduli of syntactic foams. *Comput. Mater. Sci.,* 2009, **46**, 327-332.
doi: 10.1016/j.commatsci.2009.03.010
24. Bharath Kumar, B.R.; Zeltmann, S.E.; Doddamani, M.; Gupta, N.; Uzma; Gurupadu, S. & Sailaja, R.R.N. Effect of cenosphere surface treatment and blending method on the tensile properties of thermoplastic matrix syntactic foams. *J. Appl. Polym. Sci.,* 2016, **133**.
doi: 10.1002/app.43881
25. Bharath Kumar, B.R.; Doddamani, M.; Zeltmann, S.E.; Gupta, N.; Uzma; Gurupadu, S. & Sailaja, R.R.N. Effect of particle surface treatment and blending method on flexural properties of injection-molded cenosphere/HDPE syntactic foams. *J. Mater. Sci.,* 2016, ***51***, 3793-3805.
doi: 10.1007/s10853-015-9697-2:
26. Naik, N.K.; Shankar, P.J.; Kavala, V.R.; Ravikumar, G.; Pothnis, J.R. & Arya, H. High strain rate mechanical behavior of epoxy under compressive loading: Experimental and modeling studies. *Mater. Sci. Eng. A,* 2011, **528**, 846-854.
doi: 10.1016/j.msea.2010.10.099
27. Shim, J. & Mohr, D. Using split Hopkinson pressure bars to perform large strain compression tests on polyurea at low, intermediate and high strain rates. *Int. J. Impact Eng.,* 2009, **36**, 1116-1127.
doi: 10.1016/j.ijimpeng.2008.12.010
28. Gupta, N. & Shunmugasamy, V.C. High strain rate compressive response of syntactic foams: Trends in mechanical properties and failure mechanisms. *Mater. Sci. Eng. A,* 2011, **528**, 7596-7605.
doi: 10.1016/j.msea.2011.06.073

CONTRIBUTORS

Mr A.V. Ullas is a doctoral research fellow in Department of Applied Chemistry & Polymer Technology, Delhi Technological University. His research interests include development of polymeric syntactic foams for blast mitigating applications. He has been involved in the Preparation and testing of syntactic foam specimens.

Prof. D. Kumar is presently heading the Biotechnology department in DTU. He has vast research experience in the field of conducting polymers, polymer composites, etc. Dr. D.Kumar has to his credit over 170 research papers in elite journals. He has provided technical guidance on the research paper

Dr Prasun Kumar Roy joined DRDO in the year 2000 and is presently working as Scientist 'F' in CFEES. His areas of research include development of polymeric coatings, syntactic foams and degradable polymers. He has been involved in planning the experimentsfordevelopment of syntactic foams.

Mr Pankaj Sharma joined DIAT, Pune in the year 2002. He is presently working as Scientist 'E' in CFEES, DRDO. He is involved in the shock tube testing of syntactic foam samples.

Mr Prince Sharma is working as Scientist 'E' in Terminal Ballistic research laboratory, Chandigarh, DRDO. He has contributed in high strain rate testing of syntactic foam samples.

Mr Prince Chandel is working as Scientist 'E' in Terminal Ballistic research laboratory, DRDO. He has contributed in high strain rate testing of syntactic foam samples.

Mr Devendra Kumar is working as Scientist 'C' in Terminal Ballistic research laboratory, DRDO. He has contributed in high strain rate testing of syntactic foam samples.

A LETTERS JOURNAL EXPLORING THE FRONTIERS OF PHYSICS

Società Italiana di Fisica

sciences IOP Institute of Physics

LETTER

Evidence of circular Rydberg states in beam-foil experiments: Role of the surface wake field

To cite this article: Gaurav Sharma *et al* 2017 *EPL* **120** 63002

View the article online for updates and enhancements.

Related content

- Experimental confirmation of circular Rydberg states with projectile-like ions
  T Nandi
- Measurement of wakefield intensity
  T Nandi and B P Mohanty
- A New Method for Producing Circular Rydberg States
  D. Delande and J. C. Gay

This content was downloaded from IP address 14.139.251.107 on 13/03/2018 at 10:39

A Letters Journal Exploring the Frontiers of Physics

December 2017

EPL, **120** (2017) 63002
doi: 10.1209/0295-5075/120/63002

www.epljournal.org

Evidence of circular Rydberg states in beam-foil experiments: Role of the surface wake field

Gaurav Sharma[1], Nitin K. Puri[1], Pravin Kumar[2] and T. Nandi[2(a)]

[1] *Department of Applied Physics, Delhi Technological University - Bawana road, New Delhi 110042, India*
[2] *Inter University Accelerator Centre - Aruna Asaf Ali Marg, New Delhi 110067, India*

received 20 December 2017; accepted in final form 13 February 2018
published online 1 March 2018

PACS 34.35.+a – Interactions of atoms and molecules with surfaces
PACS 34.90.+q – Other topics in atomic and molecular collision processes and interactions
PACS 34.50.Fa – Electronic excitation and ionization of atoms (including beam-foil excitation and ionization)

Abstract – We have employed the concept of the surface wake field to model the formation of the circular Rydberg states in the beam-foil experiments. The experimental studies of atomic excitation processes show the formation of circular Rydberg states either in the bulk of the foil or at the exit surface, and the mechanism is explained by several controversial theories. The present model is based on the interesting fact that the charge state fraction as well as the surface wake field depend on the foil thickness and it resolves a long-standing discrepancy on the mechanism of the formation of circular Rydberg states. The influence of exit layers is twofold. Initially, the high angular momentum Rydberg states are produced in the last layers of the foil by the Stark switching due to the bulk wake field and finally, they are transferred to the circular Rydberg states as a single multiphoton process due to the influence of the surface wake field.

Copyright © EPLA, 2018

Introduction. – The electronic states of excited ions, atoms or molecules are classified into two broad categories, *viz.* penetrating and non-penetrating. These two classes differ from each other concerning the penetration of the excited electron through the effective charge region of the inner electronic core and the nucleus. The electrons orbiting with the maximum angular momentum ($l_{max} = n - 1$) and the maximum magnetic quantum number ($|m| = n - 1$), are not allowed to penetrate the core due to high centrifugal barrier $l_{max}\,(l_{max} + 1)/r^2$ and, therefore, the electrons are almost in an isolated state from the core resulting in the reduced perturbation and increased lifetime of the excited states [1]. The electrons in such high l states are much less perturbed by the nuclear charge and, therefore, decay according to the selection rules for $E1$ transitions, *i.e.*, $\Delta l = \pm 1$ (with negligible configuration interaction). The penetration to the core of these states is small, and the quantum defects are usually less than 0.1 [2]. For such states, "l" is a good quantum number for describing the properties of an electron which is forced to follow a circular path and thereby, are called circular Rydberg states (CRS) [3]. The nuclear size correction is almost negligible for the high l states and zero for the CRS, which provides us with precise measurement of the Rydberg constant and energy levels. Besides, the quantum electrodynamic effects [4], fundamental constants such as nuclear mass [5], and predictive power of a theory [6] can also be deduced with high accuracy.

A lot of theoretical studies and many experimental approaches were employed for populating the electrons in the CRS. Freemen and Kleppner [7] proposed a Stark switching method to transfer the electrons to the high angular momentum states. Koch and Martin [8] used laser excitation of the collisionally excited Rydberg atoms. Hullet and Kleppner [9] proposed and used the adiabatic rapid passages of the time varying microwave fields. Afterward, an RF-optical technique was suggested for the formation of the CRS [10], which has not been realized yet. Later, Delande and Gay [11] proposed a new theoretical scheme, which was based on the application of crossed weak magnetic and electric (time varying) fields [12]. Liang *et al.* [13] and Cheret *et al.* [14] used this crossfields method for the formation of CRS up to $n = 30$. Brecha *et al.* [15] detected the CRS around $n = 67$. In 1994, the CRS were produced by the incidence of a circularly polarized microwave field [16] on Na atoms.

(a) E-mail: nanditapan@gmail.com

All above-mentioned methods were applied only to the neutral atoms, where the electrons were forced into the CRS. However, the formation of such states was never observed in the beam-foil experiments worldwide. Nevertheless, Nandi [17] recently observed these states in the H-like projectile ions and thereafter confirmed the same in the projectile-like ions [18] using the beam-foil technique. Later, Nedeljković *et al.* [19,20] explained these results using the two-state vector model (TVM). Mishra *et al.* [21] also presented the above experimental results using the summing method of Curtis [22].

The CRS decays through a yrast chain following the electric dipole selection rules. The $2p$ state, the last candidate of the chain from where the Ly-α emission takes place in the H-like heavy ions, is populated very late. Each delayed Ly-α transition, originating from a certain CRS, appears as a hump at a particular delay. Therefore, it is possible to find the origin of the CRS by summing the lifetime of the upper CRS levels in the decaying yrast chain. This method has been applied recently in the lifetime measurements for the H-like Fe and Ni projectile ions [17]. Besides, the projectile-like ions having atomic number and mass number close to the projectile ions can also be produced if the beam energy supersedes the Coulomb barrier energies for a chosen target-projectile combination. The detection of such projectile-like ions can be employed in lifetime measurement studies as reported elsewhere [18]. In contrast, the lifetime measurements carried out in the earlier studies [23,24] have not observed the signature of the CRS. In the experimental methods [23,24], either the data had been taken only for the small flight times or the consecutive steps in the lifetime measurements were too large to notice the hump-like structures [17,18], which are the characteristics of the CRS in the lifetime decay curves. Though both types of the Rydberg states (circular and non-circular) were populated in the beam-foil experiments, the decay curves following the power law (the characteristics of the penetrating Rydberg states) were only realized. It is worth noting here that the H-like ions are the best candidate to study the CRS using the beam-foil spectroscopy. The He-like ions could be used to some extent, but the Li-like ions or the higher multi-electron systems do not allow to form the CRS because of the autoionization process. The projectile ion energy should be high enough to yield its high charge states during the beam-foil interactions. Subsequent high inner shell vacancy production at this condition gives rise to substantial x-ray production. The multiply excited states containing two or more electrons decay fast through the auto-ionization before attaining the CRS [25].

The excitation mechanism leading to the formation of CRS using two different approaches is illustrated in the literature. As per theoretical model and experimental studies, these states are either formed inside the bulk of the foil [26–28] or at the exit layer [29–33]. According to Burgdörfer [34], the collective electronic response in ion-solid and ion-surface collisions effectively modifies the ionic and atomic potentials leading to dynamic screening and wake effects. The dynamic screening and wake effects of the ion-solid and ion-surface collisions support the origin of CRS in the bulk of the foil and at the exit surface, respectively. The latter is in agreement with the idea of Day and Ebel [29] proposed in the late seventies. They suggested that the wake-bound electrons can be captured at the exit of the foil by a hydrogenic bound circular orbit of the traversing ion. The experiment carried out by Schiwietz *et al.* [33] using the 140 MeV Ne beam on the carbon foil is in good agreement with the classical-trajectory Monte Carlo calculations of the independent-particle model. The quantum-state populations for the ions interacting with gas as well as the foil target indicate that the last-layer electron capture is responsible for populating the Rydberg states. Further, Mirković *et al.* [35] has proposed a model for explaining the high l population at the exit surface of the foil. Nedeljković *et al.* [20] applied the TVM for the high n and the high l states to get the resonance like structures, which are in good agreement with the experimental observations [17,18]. In contrast, the experimental study by Betz *et al.* [28] shows the signature of the bulk effect on the formation of CRS. To resolve this discrepancy, we have reanalysed the data sets given in this paper for the Ly-α ($2p\,^2P_{1/2,3/2}$-$1s\,^2S_{1/2}$) and the Ly-β ($3p\,^2P_{1/2,3/2}$-$1s\,^2S_{1/2}$) x-ray cross-sections as a function of the foil thickness. Interestingly, the present analysis not only reveals the effect of the surface layers but also explores the possibility of an unusual and important mechanism for the formation of the CRS in the beam-foil experiments.

Experiment, analysis, and discussion. – To study the thickness dependence of the Rydberg state formation, the ion beams of either S^{15+} or S^{16+} at 125 MeV energy were allowed to pass through 2–200 μg/cm^2 carbon targets placed at a certain distance from the detector [28]. The Ly-α and the Ly-β x-rays of the H-like S ions were recorded at 90° to the beam axis using the Si (Li) detector with a resolution of 150 eV at 5.9 keV. The data were recorded at four different distances, *viz.*, 2, 4, 6 and 200 cm. The variations in the yields of the Ly-α and the Ly-β as a function of the foil thickness showed that the Rydberg states are formed in the bulk of the foil. We re-examine the data with a different perspective.

The passage of the ion beam through any solid medium leads to its charge state distribution due to the various physical processes [36,37]. Even if S^{15+} or S^{16+} ions are incident on the target foil, many other charge states are also likely to be produced. Since only the Ly-α and the Ly-β x-ray lines of the H-like S are detected, the original states belonging to only S^{15+} need careful attention. The theories [29–31] and the experiments [32,33] support the formation of the Rydberg states right at the last layers (∼50 layers [33]) of the exit surface. Therefore, the high Rydberg states (HRS) can be produced either from S^{15+} by various excitation processes near the surface or from

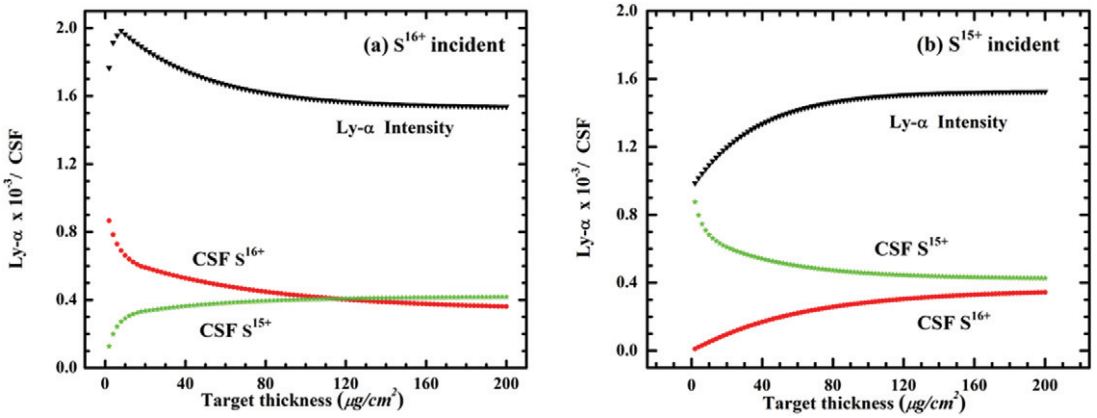


Fig. 1: (Colour online) Ly-α yield and CSF *vs.* foil thickness plot: absolute Ly-α intensities (black) and CSF of the projectile ions (a) S^{16+} and (b) S^{15+} as a function of the carbon foil thickness. The targets were kept 2 cm away from the Si (Li) detector. CSF are calculated from the ETACHA code.

S^{16+} by capturing the electrons directly in such states at the surface. Irrespective of the charge state of the incident ion, both S^{15+} and S^{16+} ionic states, in either case, contribute to the formation of the HRS in the H-like ions. Very recently, a thorough study of the charge state fraction (CSF) distribution right at the bulk of the foil has been carried out using the x-ray spectroscopy [38]. It reveals that the calculated CSF from the ETACHA code [39] is in good agreement with the measured CSF distributions for beam energies above 2 MeV/u. The code shows that the CSF of sulfur ions of 125 MeV energy incident on thin foils dominates in the incident charge state, whereas a certain equilibrium charge state is attained with increasing foil thickness. For instance, the CSF of S^{15+} and S^{16+} become comparable as the thickness of the foil increases.

Betz *et al.* [28] have measured both the Ly-α ($2p\ ^2P_{1/2,3/2} \rightarrow 1s\ ^2S_{1/2}$) and the Ly-$\beta$ ($3p\ ^2P_{1/2,3/2} \rightarrow 1s\ ^2S_{1/2}$) transitions with S^{16+} as an incident ion and only the Ly-α transition with the S^{15+}. Since the Ly-α transition is measured with both the incident ions, therefore the present discussion is focussed only on the Ly-α measurements. The $2p\ ^2P_{1/2,3/2}$ state can be fed by both the elliptic ($l < l_{max}$) and the circular states. The feeding due to the elliptic states follows the power law decay [24], whereas that due to the circular states gives rise to a hump-like structure in the tail of the decay curves [17,18,40]. Since the Ly-α lines are detected at 20 mm distance or ∼700 ps delay, the power law dependence of the decay is highly ineffective [40]. Hence, the Ly-α lines detected at such a long distance from the detector must be originating from the circular state ($n = 12, l_{max} = 11$) and the hump-like structure in the decay curve is likely to appear at around 725 ps. Thereby, we discuss only the mechanism of the CRS formation.

In fig. 1(a) and (b), the Ly-α yields for the incident ions S^{16+} and S^{15+} as a function of the foil thickness are compared with the CSF of S^{15+} and S^{16+} as obtained from the ETACHA code. Two figures are classified with the irradiation of S^{15+} and S^{16+}. In the case of the low foil thickness and incidence of the S^{16+} ions, the CSF of S^{16+} and S^{15+} are about 90% and 10%, respectively. For S^{15+} as incident ions, the CSF of S^{16+} and S^{15+} are about 10% and 90%, respectively. This clearly indicates that the incident ions do not undergo large charge exchange for the low foil thickness, which is very far from the equilibrium thickness [41]. Figure 1(a) shows that the variation in the Ly-α yield and the CSF of S^{16+} follows the same trend as expected with the effect of the bulk. The nature of the two curves is quite similar for the thickness beyond 20 μg/cm^2. In the case of the incident S^{15+} ions, the variation in the Ly-α yield and CSF of the S^{16+} ions again follows the same trend at the higher thickness. This pattern implies that even though the formation of the Rydberg state is the last layer effect, the foil thickness is still a crucial parameter for physical phenomena, the electron capture and the excitation process. The thickness of these last layers which are responsible for the formation of the CRS must be less than the mean free path [42] of the collision system. The collisional mean free path is given by $\lambda = 1/n\sigma$; where n is the number of the atoms per unit volume (∼10^{23} atoms/cc for carbon foil), and σ is the collisional cross-section (∼4×10^{-18} cm^2) [42].

The size of the orbit formed in the bulk must be less than the interplanar spacing of the amorphous carbon target, which is about 0.34 nm [43]. It implies that $n \leq 10$ orbits are only possible to be formed at the bulk of the amorphous carbon target. Nevertheless, the K x-rays are detected by placing the detector at a distance of 2, 4, 6, and 200 cm from the target foil, which corresponds to the delay (T_d) of 728, 1456, 2184, 72850 ps, respectively. These delays are required for certain CRS of H-like S decaying to the ground state through the yrast chain, and the last member of the chain emits the K x-rays. The time taken by the decay chain (T_c) can be calculated with the procedure given in [17]. If $T_c \sim T_d$, then the corresponding CRS ($n, l = n - 1$) becomes responsible for the detection of the x-rays at a particular distance. Accordingly, we see that the CRS of (12,11), (13,12), (14,13) and

(26,25) are responsible for the x-rays detected at 2, 4, 6, 200 cm, respectively. Thus, the above CRS detected under the present experimental conditions must have been populated at the exit surface.

Surface wake field model. – The laser excitation of the Rydberg states is now a well-established fact. The atom-laser interaction region which extends up to only a few Bohr radii around the atomic nucleus results in the excitations of the Rydberg states [44]. Thereby, the electrons are excited to the Rydberg states through the electromagnetic waves. A recent study has revealed that a finite electric field exists at the exit surface of the foil during the passage of the ion beam [45]. This electric field probably plays some role in producing the Rydberg states. Further, this study clearly indicates the thickness dependence of the surface wake field (SWF), which increases with increasing the foil thickness and attains a saturation level at a certain thickness. Therefore, assuming the effect of the variation of the SWF with the foil thickness on the formation of the CRS in the last layers of the exit surface, we present a possible mechanism.

The energy loss in the bulk of the foil produces a strong electric field [46]. Vernhet *et al.* [47–49] have made a thorough study on the Stark-mixing between np and ns states for n up to 5 due to the wake field in the bulk of the foil. The SWF-induced Stark mixing between np and ns states is reported in the previous works [21,50]. The mixing takes place between a short-lived p state and a long-lived s state. Nevertheless, the Stark mixing will make only a minor difference in the formation of the CRS as both the participating levels are long-lived. The measurement of the surface energy loss shows that the positively charged ions lose a certain energy due to the SWF [45]. The field resulting from both, the bulk and the surface wake (fig. 1 of [51]) attracts the ions towards the foil surface and repels the electrons away from it.

We consider the formation of the CRS in the last exit layers via two steps. Firstly as the ions exit from the foil, many of the electronic states are in the HRS with $l = l_{max}$ but $|m|$ is not high [35] and secondly, the high Rydberg states are transferred to the CRS during the passage of the ions through the SWF. The proposed model for the excitation mechanism of the CRS is illustrated in fig. 2. The stage I represents a high Rydberg state (HRS) formed in the H-like ions in the last layers when the bulk wake field (BWF) is still on from Stark switch low l-states to l_{max} states [7] and the SWF is off, *i.e.*, the electrons are moving in the orbits nlm ($l = l_{max}$, but $|m| < n - 1$) and the circular orbits remain vacant. The circular orbits shown correspond to a CRS $nl'm$ such that $l' = |m| = n - 1$. As soon as the SWF is switched on, the electrons in the HRS are transferred to the CRS as illustrated in stage II. By this time, the ions reach to the field-free region and the electrons will remain in that orbit according to their lifetimes. It is illustrated in stage III of fig. 2. The range of the SWF is of the order of 5 nm [45] and the time taken by

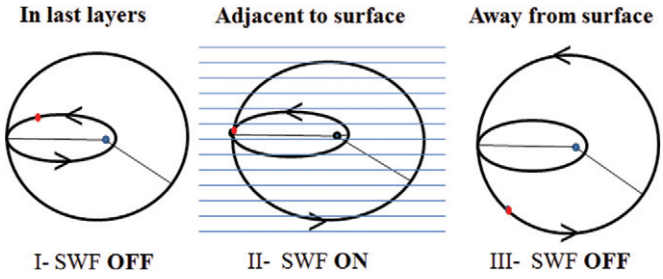


Fig. 2: (Colour online) Excitation model for CRS at the foil surface: I) HRS is formed at the foil surface in the absence of SWF and in the presence of BWF; II) HRS is promoted to CRS in the presence of SWF only; and III) CRS lasts as per its mean lifetime in the field-free regions. The red dot indicates the orbiting electron and the black dot the nucleus of the ion. The electron will remain in the circular state as the ion exits the SWF.

the ions to traverse the field region is less than the period of the orbiting electrons. The strength of the SWF is of the order of 10^7 V/cm [50], which decreases with increasing distance from the foil [29]. Hullet and Kleppner [9] have created the HRS by the laser-atom interaction in the presence of the strong electric field and passing them in a time varying electric field to transfer the low $|m|$ states to high $|m|$ states. The CRS population is done very successfully with nearly 100% efficiency either by a series of adiabatic rapid passage processes or by a single multiphoton process. When the microwave power is increased, interference effects enable that more than two levels get significantly populated simultaneously. In the limit of a very strong field, all the states have been excited at the same time, and the process can be viewed as a single multiphoton process [9]. The nature of the surface wake potential can be seen in fig. 1 of [29]. Since the strong SWF is decreased very fast, the population is transferred from low $|m|$ to high $|m|$ states in the present experiments as a single multiphoton process.

According to the TVM model [19,20], the state of a single active electron of the ion-surface system is described by the two state vectors $\psi_1(t)$ and $\psi_2(t)$. Here $\psi_1(t)$ evolves from the initial parabolic state towards the future, while $\psi_2(t)$ proceeds towards the final state. The state $\psi_1(t)$ represents an electron state in the field of the solid distorted by the presence of the ion. In contrast, the state $\psi_2(t)$ is a moving, atomic-like state, weakly distorted by the presence of the solid. Though the time evolutions of the states $\psi_1(t)$ and $\psi_2(t)$ are governed by two different Hamiltonians, both the states describe simultaneously one and the same representative electron. This implies that the dynamics of the system cannot be viewed in two steps as the present model. As a result, these two wave functions in TVM model contribute to the quantum description of the final HRS formation, and not of the CRS. In the present case, HRS are formed in the first step by Stark switching in the last layers (so that they will not be destroyed

by further collisions) and in the second step the HRS are transferred to the CRS by the single multiphoton process due the SWF.

As seen in fig. 1, the CSF of S^{15+} and S^{16+} ions are comparable for the foil thickness $\geq 75\,\mu g/cm^2$. Contrary to the incidence of the S^{16+} ions, the contribution of S^{15+} and S^{16+} ions to the total CSF changes significantly (almost inverted) in the case of the S^{15+} ion irradiation. The capture of an electron to the S^{16+} in high n states at the surface layers leads to the formation of the Rydberg states in the H-like S. Similarly, the excitation of the electron remaining with the S^{15+} in the Rydberg states may also be possible at the surface layers. Consequently, both the charge states, *i.e.*, the sum of the CSF of S^{15+} and S^{16+}, may equally be responsible for producing the Rydberg states in the H-like ions irrespective of the specific incident charge state used. However, the CSF varies with the foil thickness and we need to exclude the variation of the charge state from the target-thickness–dependent x-ray photon yield. To do that we define a parameter R:

$$R = \frac{\text{Ly-}\alpha\text{ yield}}{\text{CSF}\left(S^{15+} + S^{16+}\right)}.$$

This quantity represents the relative CRS formation probability. Thus, the ratios so obtained with S^{16+} and S^{15+} as the incident ions are plotted as a function of the foil thickness and are shown in fig. 3(a) and (b), respectively. The Ly-α yield shown in fig. 1 is attributed to the effect of the SWF as already discussed. For the incidence of both the ions, the R saturates only after a certain foil thickness as indicated with green lines in fig. 3. In fig. 3(a), R overshoots the saturation level marked by the red lines at a particular foil thickness. The saturation in the value of R in the case of the S^{16+} ion incident is relatively faster (about $32\,\mu g/cm^2$) than that in the case of the S^{15+} ion incidence (about $55\,\mu g/cm^2$). It is known that the contribution of the self-wake [52] in the SWF [45] is significant in addition to the collective plasmon excitations. The data given in table 1 of [45] clearly indicate that the SWF varies with the foil thickness. Further, the self-wake depends on the charge state of the incident ions [52] and thus, the saturation is achieved with lower foil thickness for the S^{16+} ion incidence. The transfer probability of having the CRS from the HRS depends on the magnitude of the SWF. As the SWF is smaller for the lower foil thickness than for the higher foil thickness, the probability of having the CRS from the HRS is expected to be smaller for the lower foil thickness than that for the higher foil thickness. Thus, we observe the lower yield of the Ly-α x-ray for the lower foil thickness as seen in fig. 1.

Conclusion. – We have re-analyzed the Ly-α yield *vs.* the foil thickness data [28] in the light of the fact that the ETACHA code represents the charge state distribution of the projectile ions in the bulk of the target foil, and presented a surface wake field model for the formation of circular Rydberg states in beam foil experiments. Though

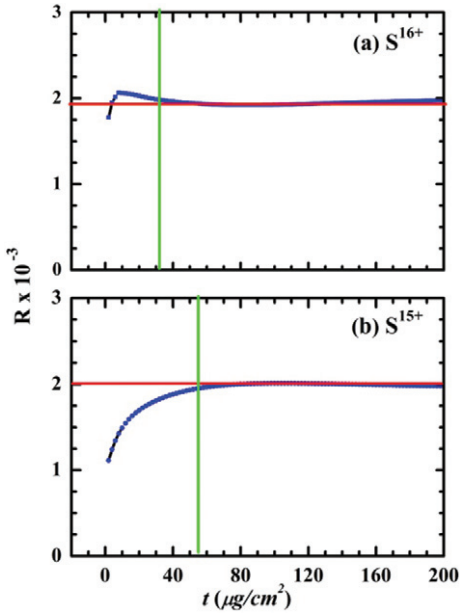


Fig. 3: (Colour online) Relative CRS formation probability: the ratio R, as defined in the text, is plotted as a function of carbon foil thickness (t) for incident ions S^{16+} (a) and S^{15+} (b). Red lines represent the saturated value of R and green lines represent the thickness where the saturation is reached.

the Rydberg states in the fast-ion foil collisions are formed in the last layers at the exit surface, the production of the projectile Rydberg states in the H-like ions exhibits a pronounced target thickness dependence because of the variation in SWF with the foil thickness [45]. As per the present model, the HRS are formed by the Stark switching process in the last layers with low $|m|$, and the HRS states so formed are transformed into the CRS by the single multiphoton process while passing through the SWF. In the present study, this transformation occurs with a probability higher than that seen in other methods [9].

The target foil thickness provides the bulk as well as the last layers (about 50 monolayers) effect [33]. In the bulk, the ion energy loss is large and, thus, the wake-induced Stark field is too strong, which can even admix odd- and even-parity states fully [46]. As a result, raising a low angular momentum state to a high angular momentum state through the $E2$ selections rules is not possible. In contrast, the Stark field at the last layers is weak [50] and converts low angular momentum states into high angular momentum states. Hence, the dynamic screening and wake effects due to ion-solid collisions do not play any role in the CRS formation, but those due to the ion-surface collisions do. High angular momentum states so formed are transferred to the circular Rydberg states by a single multiphoton process due to the influence of the surface wake field while moving out of the SWF. The present findings provide an important connection between atomic physics and condensed-matter physics. Further, an interesting role of the solid-state effects [47] such as the SWF [45] on populating the CRS is evidenced.

* * *

GS acknowledges the University Grant Commission for financial support and IUAC for all other support. The authors highly appreciate the useful discussions with A. P. Mishra. We also acknowledge DST for funding the project No. SP/S2/LOP-0006/2011.

REFERENCES

[1] Marxer H. and Spruch L., *Phys. Rev. A*, **43** (1991) 1268.
[2] Theodosiou C. E., *J. Phys. B: At. Mol. Phys.*, **16** (1983) L309.
[3] Tan J. N., Brewer S. M. and Guise N. D., *Phys. Scr.*, **T144** (2011) 14009.
[4] Jentschura U. D., Le Bigot E.-O., Evers J., Mohr P. J. and Keitel C. H., *J. Phys. B: At. Mol. Opt. Phys.*, **38** (2005) S97.
[5] Wundt B. J. and Jentschura U. D., *J. Phys. B: At. Mol. Opt. Phys.*, **43** (2010) 115002.
[6] Jentschura U., Mohr P. J., Tan J. N. and Wundt B. J., *Phys. Rev. Lett.*, **100** (2008) 160404.
[7] Freeman R. R. and Kleppner D., *Phys. Rev. A*, **14** (1976) 1614.
[8] Koch P. M. and Mariani D. R., *J. Phys. B: At. Mol. Phys.*, **13** (1980) L645.
[9] Hullet R. G. and Kleppner D., *Phys. Rev. Lett.*, **51** (1983) 1430.
[10] Molander W. A., Stroud C. R. jr. and Yeazell J. A., *J. Phys. B: At. Mol. Phys.*, **19** (1986) L461.
[11] Delande D. and Gay J. C., *Europhys. Lett.*, **5** (1988) 303.
[12] Nussenzveig P., Bernardot F., Brune M., Hare J., Raimond J. M., Haroche S. and Gawlik W., *Phys. Rev. A*, **48** (1993) 3991.
[13] Liang J., Gross M., Goy P. and Haroche S., *Phys. Rev. A*, **33** (1986) 4437.
[14] Chen L., Cheret M., Roussel F. and Spiess G., *J. Phys. B: At. Mol. Opt. Phys.*, **26** (1993) L437.
[15] Brecha R. J., Raithel G., Wagner C. and Walther H., *Opt. Commun.*, **102** (1993) 257.
[16] Cheng C. H., Lee C. Y. and Gallagher T. F., *Phys. Rev. Lett.*, **73** (1994) 3078.
[17] Nandi T., *J. Astrophys.*, **673** (2008) L103.
[18] Nandi T., *J. Phys. B: At. Mol. Opt. Phys.*, **42** (2009) 125201.
[19] Nedeljković N. N., Nedeljković L. D. and Mirković M. A., *Phys. Rev. A*, **68** (2003) 12721.
[20] Nedeljković N. N., Galijaš S. M. D. and Mirković M. A., *J. Quant. Spectrosc. Radiat. Transfer*, **134** (2014) 46.
[21] Kumar Y., Mishra A. P. and Nandi T., *J. Quant. Spectrosc. Radiat. Transfer*, **148** (2014) 22.
[22] Curtis L. J., *Am. J. Phys.*, **36** (1968) 1123.
[23] Armourt I. A., Silver J. D. and Traberti E., *J. Phys. B: At. Mol. Phys.*, **14** (1981) 3563.
[24] Can C., Maurer R. J., Bandong B. and Watson R. L., *Phys. Rev. A*, **35** (1987) 3244.
[25] Madsen L. B., *J. Phys. B: At. Mol. Opt. Phys.*, **36** (2003) R223.
[26] Burgdorfer J. and Bottcher C., *Phys. Rev. Lett.*, **61** (1988) 2917.
[27] Kemmler J., Burgdörfer J. and Reinhold C. O., *Phys. Rev. A*, **44** (1991) 2993.
[28] Betz H.-D., Roschenthaler D. and Rothermel J., *Phys. Rev. Lett.*, **50** (1983) 34.
[29] Day M. and Ebel M., *Phys. Rev. B*, **19** (1979) 3434.
[30] Garcia J. D., *Nucl. Instrum. Methods*, **90** (1970) 295.
[31] Lennard W. N. and Cocke C. L., *Nucl. Instrum. Methods A*, **110** (1973) 137.
[32] Bashkin S., Oona H. and Veje E., *Phys. Rev. A*, **25** (1982) 417.
[33] Schiwietz G., Schneider D. and Tanis J., *Phys. Rev. Lett.*, **59** (1987) 1561.
[34] Burgdörfer J., *Nucl. Instrum. Methods B*, **67** (1992) 1.
[35] Mirković M. A., Nedeljković N. N. and Božanić D. K., *J. Phys.: Conf. Ser.*, **257** (2010) 12010.
[36] MacAdam K. B., Martin N. L. S., Smith D. B., Rolfes R. G. and Richards D., *Phys. Rev. A*, **34** (1986) 4661.
[37] Thorsen J., *XXVIII. Electron Capture and Loss by Heavy Ions Penetrating through Matter: (With Jens Lindhard),* in *The Penetration of Charged Particles through Matter (1912–1954)*, edited by Thorsen J., *Niels Bohr Collected Works*, Vol. **8** (Elsevier) 1987, pp. 593–625.
[38] Sharma P. and Nandi T., *Phys. Lett. A*, **380** (2016) 182.
[39] Rozet J. P., Stephan C. and Vemhet D., *Nucl. Instrum. Methods B*, **107** (1996) 67.
[40] Mishra A. P., Nandi T. and Jagatap B. N., *J. Quant. Spectrosc. Radiat. Transfer*, **120** (2013) 114.
[41] Imai M., Sataka M., Kawatsura K., Takahiro K., Komaki K., Shibata H., Sugai H. and Nishio K., *Nucl. Instrum. Methods B*, **267** (2009) 2675.
[42] McGuire J. H., Land D. J., Brennan J. G. and Basbas G., *Phys. Rev. A*, **19** (1979) 2180.
[43] Dash R., Chmiola J., Yushin G., Gogotsi Y. and Laudisio G., *Carbon*, **44** (2006) 2489.
[44] Alber G., *Phys. Rev. A*, **40** (1989) 1321.
[45] Nandi T., Haris K., Singh G., Kumar P., Kumar R., Saini S., Khan S., Jhingan A., Verma P., Tauheed A., Mehta D. and Berry H. G., *Phys. Rev. Lett.*, **110** (2013) 163203.
[46] Dunford R. W., Berry H. G., Church D. A., Hass M., Liu C. J., Raphaelian M. L. A., Zabransky B. J., Curtis L. J. and Livingston A. E., *Phys. Rev. A*, **48** (1993) 2729.
[47] Reinhold C. O., Arbó D. G., Burgdorfer J., Gervais B., Lamour E., Rozet J. P. and Vernhet D., *J. Phys. B: At. Mol. Phys.*, **33** (2000) L111.
[48] Vernhet D., Rozet J. P., Lamour E., Gervais B., Fourment C. and Dube L. J., *Phys. Scr.*, **T80** (1999) 83.
[49] Vernhet D., Fourment C., Lamour E., Rozet J. P., Gervais B., Dube L. J., Martin F., Minami T., Reinhold C. O., Seliger M. and Burgdorfer J., *Phys. Scr.*, **T92** (2001) 233.
[50] Nandi T. and Mohanty B. P., *J. Phys. B: At. Mol. Opt. Phys.*, **42** (2009) 225402.
[51] Nordlander P. and Dunning F. B., *Phys. Rev. B*, **53** (1996) 8083.
[52] Echenique P. M., Brandt W. and Ritchie R. H., *Phys. Rev. B*, **33** (1977) 43.

Fast Combinational Architecture for a Vedic Divider

Preyesh Dalmia, Abhinav Parashar, Gaurav Aggarwal, Radhika Dang, Neeta Pandey
Dept. of Electronics and Communication Engineering
Delhi Technological University
New Delhi, India
preyeshdalmia@gmail.com, abhinavparashar.1810@gmail.com, gauravagg.1996@gmail.com, radhika_bt2k14@dtu.ac.in, neetapandey@dce.ac.in

***Abstract*—This paper proposes a fast, purely combinational implementation of a divider, based on the Dhwajanka Sutra of Vedic mathematics. Vedic mathematics offers algorithms that are computationally efficient over conventional arithmetic algorithms. Dhwajanka Sutra has been chosen as it is an algorithm efficient for all possible cases, unlike other sutras for division (Nikhilam and Paravartya) which are case specific. The simplicity of the Vedic algorithm implemented in combinational form has reduced computation time significantly The proposed design is compared with existing divider architectures implemented on an FPGA namely Non-restoring Algorithm based Divider, Vedic Divider (Paravartya Algorithm), Vedic Divider (Nikhilam Algorithm), Decimal Divider based on Newton Raphson algorithm, Decimal Divider based on SRT algorithm and Combination divider algorithms. The proposed vedic divider shows a maximum of 273.72% speed improvement while the minimum is 99.95%. The results have been validated using the Xilinx ISE Design Suite 14.7, on the Virtex5 (xc5vlx20T-2ff323) FPGA Target Technology and the design has been implemented in Verilog.**

Keywords— Vedic division; Dhwajanka Sutra; Combinational Divider

I. INTRODUCTION

With the ever-increasing number of computer and signal processing applications. The need for High speed computation has only spiked over the years. Higher throughput arithmetic operations are very important to achieve high performance in a lot of real-time signal and image processing applications where high quality graphics are processed for e.g. a GPU. Division operation is the most resource consuming algorithm in the arithmetic unit of a processor. As, Division operation is perennially a sequential type of operation it is costlier in terms of computational complexity, latency, and area compared with other mathematical operations. Division is also widely used in radar technology, communication, industrial control systems and linear predictive coding (LPC) algorithms in speech processing making. Thus, the development of fast division circuit has been a key topic of research for a long time.

Many recursive techniques have so far been proposed in literature to implement the high-speed divider [1]-[11], such as digit recurrence implementation methodology [12] (restoring [7]-[9], [11], non-restoring [4]-[6], [11]), division by convergence method (Newton-Raphson method [11]), division by series expansion (Goldschmidt algorithm [10]). Due to the large number of iterations the cost in terms of area and computational complexity of digit recurrence algorithms [4]-[9], [11] is low but, the propagation delay becomes high as a affect. Some iterative architectures, like Goldschmidt's [10] and Newton-Raphson utilized multiplication techniques along with the series expansion, wherein per iteration, the amount of quotient digits obtained is doubled. The drawback of these methods is the need of normalization of the operand before operation and the remainder is also not obtained directly [13]. Vedic Mathematics [14] comprises of 16 sutras which offer unique methods for calculations. There are certain sutras which are particularly useful for division, such as Nikhilam Navatascaramam Dasatah, Paravartya Yojayet, and Dhwajanka. Dhwajanka Sutra, however, is well suited for all kinds of numbers, unlike Nikhilam Navatascaramam Dasatah, Paravartya Yojayet, which are more efficient if the divisor is close to a power of 10 or just greater than a power of 10, respectively.

The Dhwajanka sutra follows a flag and pole method which enables to breakdown a complex division problem into smaller parts which can then be realized using a combinational circuit. This will enable to counter major drawback of the dividers mentioned above that the speed of computation is dependent on a clock, which not only decreases the computation speed but also leads to higher power consumptions, even in modern microprocessors the clock cycles required for integer division are even more than the double precision floating-point division [15]. Also, most models proposed for division are directed towards 2N/N-bit IEEE floating point division.

Typically, these iterative algorithms are implemented sequentially and many optimization techniques can be used to reduce the number of division cycles required. However, many DSP implementations in literature, where signals are represented with fixed width integers, make use of N/N divisions that are realized as combinational logic. Therefore, optimization techniques for sequential implementations of division are not applicable.

A combinational architecture is also proposed in [3], though it is based on binary division, hence limiting the efficiency of the design. To improve the computation time, an algorithm which promotes parallel computation needs to be used. In this paper, a

high speed combinational divider has been implemented using the Dhwajanka Sutra on a virtex-5 FPGA as the proposed solutions use small lookup tables, they match well with the hardware resources of an FPGA

In this paper, a high speed combinational divider has been implemented using the Dhwajanka Sutra, elaborated in section II, while section III discusses the design proposed in this paper. Finally, section IV states the results obtained and the derived conclusions.

II. VEDIC MATHEMATICS AND ASSOCIATED TERMINOLOGIES

A. *Vedic mathematics*

Vedic Mathematics is a system of mathematics reconstructed from Ancient Sanskrit texts by Sri Bharati Krishna Tirthaji during the years 1911-1918. The word Vedic has been derived from Vedas, which are a large body of knowledge texts originating in the ancient Indian subcontinent written in Vedic Sanskrit. It elaborates on 16 sutras, or word formulae, which can be used to define mathematics for easy mental calculations. It also mentions upa sutras or corollaries derived from the Sutras [14] which are increasingly being used to devise computationally efficient algebraic algorithms. Of the originally available sutras, Nikhilam Navatascaramam Dasatah, Dhwajanka and Paravartya Yojayet are the sutras which mainly focus on division. This paper uses a technique based on the Dhwajanka sutra for division.

B. *Dhwajanka and related terms*

This method is extremely useful for division operations where the divisor is of 3 digits or less. Dhwajanka has been derived from the Sanskrit word Dhwaja, which means 'flag'. In this method, the divisor is split into two parts – the least significant digit (LSD) is called the Flag and the rest of the divisor ((n-1) MSDs for an n digit divisor) is the Working Divisor (WD). The division process has been explained below:

Step 1: Divide the MSD of dividend with the WD using regular arithmetic division/ repeated subtraction. Note the quotient and remainder at this stage as the first Intermediate Quotient (IQ1) and Intermediate Remainder (IR1).

Step 2: Concatenate IR1 with the next most significant digit of the original dividend and subtract the product of IQ1 and Flag from this number. This is the dividend for the next stage.

Step 3: Continue the same process for each subsequent stage till the LSD of the original dividend is reached. At the final stage, the difference as obtained in step two with respect to this stage is the final remainder and the final quotient is obtained by concatenating intermediate quotients at all stages.

The following example will make the procedure clear:

Division of 38982 by 73

Using the above steps, WD = 7, Flag = 3. Dividing 38 by 7, we get IQ1= 5, IR1 = 3.

For the dividend at the next stage, IR1 is clubbed with the next digit of the dividend, i.e. 9 to get 39, and the product IQ1*Flag = 5*3 = 15 is subtracted from it to get 24.

On dividing 24 by 7, IQ2 = 3, IR2 = 3, and the next dividend is 38 – 3*3 = 29.

The next stage gives IQ3 = 4, IR3=1. Finally, clubbing IR3 with last digit of dividend, Remainder = 12 – 4*3 = 0; and Quotient = 534.

III. PROPOSED DESIGN

The Proposed design based on Dhwajanka sutra of Vedic mathematics has two inputs a 5-digit BCD dividend and a 3-digit BCD divisor. According to the algorithm, the intermediate dividend at each stage is divided by the 2 Most Significant Digits (MSD) and the quotient digit are repeatedly multiplied by the Least Significant Digit (LSD) of the divisor. In order to improve the efficacy of the design and to keep a purely combinational approach, a LUT based approach has been followed. For every set of two inputs we create two LUTs in parallel as part of the initial computation. The Architecture for the proposed design is given in fig. 1. Some of the elements that have been devised as part of the architecture have been described below.

A. *Look Up Table*

There are three LUTs in the proposed design. The first LUT consist of 0-10 multiples of 2-MSD of divisor and is used for division of intermediate dividend. The second LUT consist of 0-9 multiples of LSD of divisor and is used for multiplication of quotient with LSD of divisor. The third LUT consist of 0-10 decimal numbers for selection of quotient. The first two LUTs are initialized using independent adders for each number and thus providing the results as fast as possible while the third is initialized as a fixed memory in the circuit. Only one of the elements can be read from these LUTs at once. The selection is done using a buffer.

B. *Look Ahead 9*

A combinational logic circuit is used in the BCD addition of two 4 bit numbers to determine whether their sum will exceed 9 in parallel with the addition process. This helps in generating a carry for the next stage and reduces the carry propagation delay of the circuit. This also helps in generating a signal for decimal adjust of the sum for these numbers.

C. *BCD doubler*

A combinational logic circuit is used for constructing LUTs which take 3 digit BCD number i.e., a 12-bit number as input and generates it's double as an output. The shifting method is used for the circuit but an extra care is required for the decimal adjusting of the number. This circuit is faster than the BCD adder for two numbers of 3 decimal digit and hence is used to generate even multiples for LUT-1 and LUT-2.

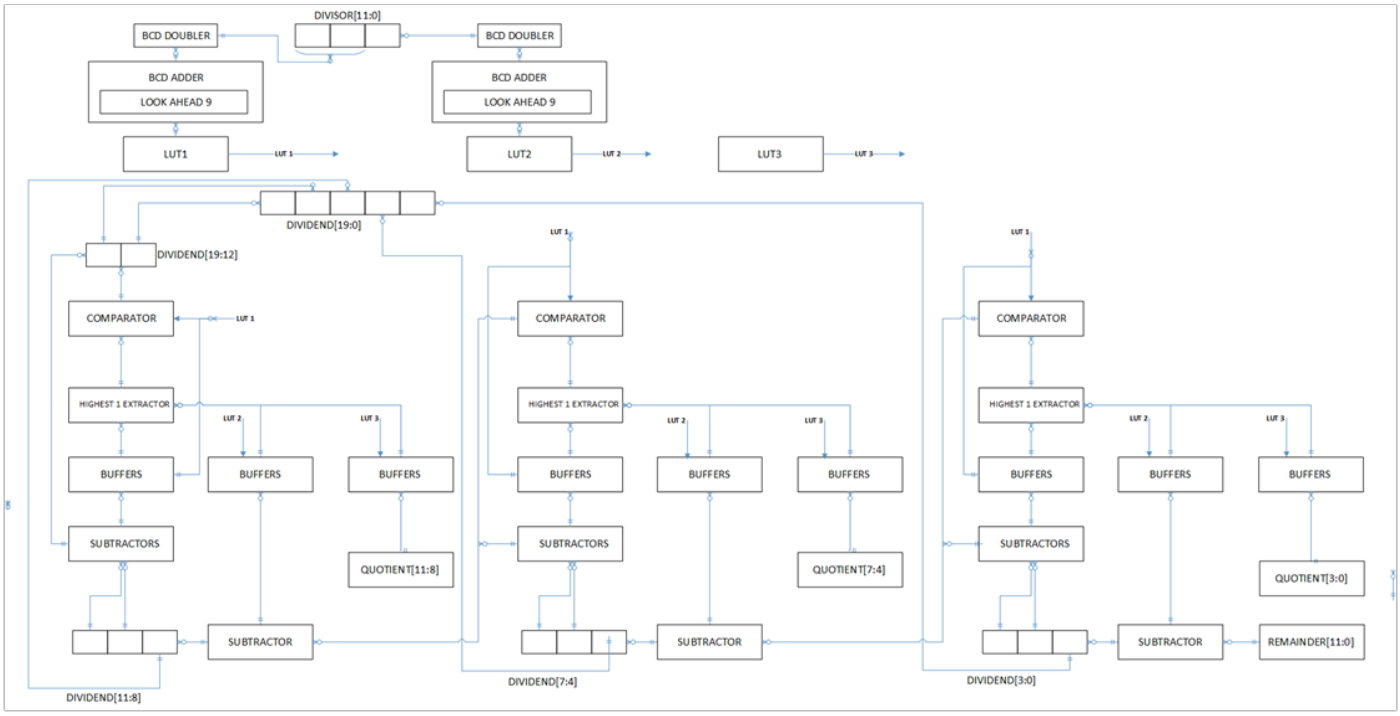


Fig.1. Proposed Design Block Diagram

IV. PROCESS FLOW

The proposed design is combinational in nature and hence is independent of clock signal. The complete flow is illustrated in the form of RTL statements.

Firstly, Look Up Tables (LUTs) are constructed using independent adders. As explained above, only two LUTs are dynamic in nature, that is, depend on the input divisor and thus needs adders for evaluation. While the third LUT consisting of 0-9 fixed decimal numbers does not require any additional combinational logic. The intermediate dividend is then compared with the numbers stored in the first LUT to compare with the dividend. If dividend is found to be less than the value in LUT, a corresponding 1 is stored in the control string or else a 0. Thus, the control string consists of continuous 0s and 1s.

CS[i] = (DIVIDEND>LUT1[i])

The highest set (most significant) 1 is extracted from the string using an array of NOT-AND gates.

BC[0] = CS[0]

BC[n] = ~CS[n-1].CS[n] ; n = 1, 2,3...10

Now, the string obtained works as the control signals for enabling the required buffer and thus select only one number from the LUT-1, LUT-2 and LUT-3. The selected number from LUT-1 is the highest multiple which is less than intermediate dividend and hence its subtraction yields the intermediate remainder.

REM = DIVIDEND - LUT1[enabled_buffer]

The number selected from the LUT-3 is the quotient digit of that stage.

QUOTIENT = LUT3[buffer]

TABLE I. PROPOSED DESIGN FLOW

INPUTS	**DIVIDEND = 39814**	**DIVISOR = 314**
INITIAL MEMORY	LUT1	{0,31,62,93,124,155,186,217,248,279,310}
	LUT2	{0,4,8,12,16,20,24,28,32,36,40}
	LUT3	{0,1,2,3,4,5,6,7,8,9}
STAGE 1	Intermediate Dividend Part(IDP)	39
	LUT1,LUT2,LUT3(data extracted)	31,4,1
	REM,QUOTIENT,INT	8(IDP – LUT1 data), 1, 4(LUT2 data)
STAGE 2	Intermediate Dividend Part(IDP)	84(REM cascaded with Dividend next digit – INT)
	LUT1,LUT2,LUT3(data extracted)	62,8,2
	REM,QUOTIENT,INT	22(IDP – LUT1 data), 2, 8(LUT2 data)
STAGE 3	Intermediate Dividend Part(IDP)	213(REM cascaded with Dividend next digit – INT)
	LUT1,LUT2,LUT3(data extracted)	186,24,6
	REM,QUOTIENT,INT	27(IDP – LUT1 data), 6, 24(LUT2 data)
Final Result	REM, QUOTIENT	250((REM cascaded with Dividend next digit – INT)),126(100 + 20 + 6)

The selected number from LUT-2 is the product of LSD and quotient of that stage.

INT = LUT2[buffer]

After this, the new intermediate dividend is formed by appending the next digit of the input dividend to the intermediate remainder and subtracting the selected quotient from the LUT-2.

{SIGN, ND} = {REM, DIVIDEND[n+1]} – INT

Since there is a possibility of negative result in this step, it is important to store the sign of the intermediate dividend in a sign register. This sign register is required for addition/subtraction of the intermediate quotient at the last stage for successful computation of the final quotient. The example in Table I offers more clarity on the design.

V. Implementation Results

The Design simulations and synthesis have been carried out using Xilinx ISE Design Suite 14.7, on the Virtex5 (xc5vlx20T-2ff323)) FPGA Target Technology. The proposed design is compared with existing divider architectures implemented on an FPGA namely Non-restoring Algorithm based Divider, Vedic Divider (Paravartya Algorithm), Vedic Divider (Nikhilam Algorithm), Decimal Divider based on Newton Raphson algorithm, Decimal Divider based on SRT algorithm and Combination divider algorithms given in [5]-[6]. Some existing designs gave implementation results for smaller/larger input bit sizes. The area and LUT count of these designs are scaled up/down proportionally according to bit size, to be compared with the proposed design which implements a 17/10 bit division. The authors will like to acknowledge that the scaled results only provide an approximate conversion, and the real performance of the circuits may vary. Delay and Area Analysis Table depicts that the proposed design has made significant amelioration in terms of speed over the mentioned existing designs proposed design is 273.72% faster than Non-restoring Algorithm, 161.22% faster than Vedic Divider based Nikhilam Algorithm, 99.95% faster Vedic Divider based on Paravartya Algorithm, 208.77% faster than Combinational Divider [5], 156.55% faster than Combinational Divider [6], 197.81% faster than Newton Raphson Algorithm and 191.97% faster than SRT Algorithm.

As shown in table II, LUT count of the proposed design is lesser than existing sequential divider architectures based on Newton Raphson, SRT and Non-Restoring algorithm where its biggest improvement is 21% lesser area than [20]. However, its LUT count is more than both Vedic implementations of Nikhilam and Parvartya. This is expected as Dhwajanka algorithm is a more generalized division method. Thus, it will give similar propagation delay for higher range of input values whereas Nikhilam and parvartya are more efficient only if the divisor is close to a power of 10 or just greater than a power of 10, respectively but that results in an area overhead

VI. Conclusion

An ALU is the heart of almost every digital design may it be a processor, DSP filter or MAC/division units. The prime focus of this design is to make a fast and completely clock independent Integer divider architecture because division often forms the bottleneck when it comes to speed of arithmetic ALU. Also, with extensive use of FPGAs to accelerate classical DSP algorithms, optimization efforts have concentrated on multiplication, addition, and multiply-add units. High-speed Integer division, which is relevant for novel applications such as convex solvers or model-predictive control, has received less attention.

The proposed design implements a fast-combinational divider based on dhwajanka sutra that uses elementary hardware elements such as look up tables complementing the FPGA architecture. Also, it performs simple arithmetic operations like addition and multiplication instead of complex predictive techniques used in iterative methods such as Newton Raphson method. This requires evaluation of a function and its derivative. The design being combinational in nature also eliminates the issues such as clock skew, and power consumption due to the presence of clock.

The Implementation area for the design is expected to increase over non-multiplicative division as the higher performance of multiplicative division methods usually comes at the expense of an increased area, which may become acceptable with growing FPGA capacities. Also, the parallelism introduced in the design both at the time of LUT computation and LUT comparison with intermediate dividend. Requires augmented hardware, But the substantial advantages gained in speed justifies the augmented hardware.

TABLE II. Comparison of Propsed design with other designs

Type of Divider	Target Device	Delay (ns)	Frequency (MHz)	Area (LUT Utilization)
Non-Restoring Algorithm [19]	Virtex4 (SX3512)	128.67	60	991
Vedic Divider-Nikhilam Algorithm [21]	Virtex5 (xc5vlx20T-2ff323)	89.468	100	558
Vedic Divider-Paravartya Algorithm [21]	Virtex5 (xc5vlx20T-2ff323)	68.483	100	235
Combinational Divider [16]	Spartan 3e (xc3s200-4)	105.755	N.A.	1005
Combinational Divider [17]	Spartan 3e (xc3s200-4)	87.867	N.A.	437
Newton Raphson Algorithm [20]	Virtex-4 SX35- 12 FPGA	102	294.11	1256
SRT Algorithm [19]	Virtex4 (SX3512)	100	60	1267
Proposed Design	Virtex5 (xc5vlx20T-2ff323)	34.25	N.A.	943

References

[1] R. Hagglund, P. Lowenborg, M. Vesterbacka and “, “A polynomial-based division algorithm,” in IEEE Int..Symp. on Circuits and Systems, May 26-29, 2002.

[2] P. Saha, A. Banerjee, P. Bhattacharyya and A. Dandapat, “Vedic Divider: Novel Architecture (ASIC) for High Speed VLSI Applications,” IEEE Int. Sym on Electronic System Design (ISED), pp. 67-71, 2011.

[3] M. Langhammer, “Improved subtractive division algorithm,” in Proceedings Eleventh Annual IEEE International ASIC Conference (Cat. No.98TH8372), Rochester, NY, 1998, pp. 343-347.

[4] N. Burgess, “A fast division algorithm for VLSI,” in [1991 Proceedings] IEEE International Conference on Computer Design: VLSI in Computers and Processors, Cambridge, MA, 1991, pp. 560-563..

[5] S.-G. Chen and C.-C. Li, “An efficient division algorithm and its architecture,” in IEEE Int. Computer, Communication, Control and Power Engineering Conf., Beijing , China, Oct. 19-21, 1993.

[6] W. Marnane, S. Bellis and P. Larsson-Edefors, “Bit-serial interleaved high speed division,” Electronics Letter, vol. 33, no. 13, pp. 1124-1125, June-1997..

[7] H. T. Vergos, “An Efficient BIST Scheme for Non-Restoring Array Dividers,” in IEEE 10th Euromicro Conf. on Digital System Design Architectures, Methods and Tools, Lubeck, Aug. 29-31,2007.

[8] J. Andersen, A. Nielsen and O. Olsen, “A Systolic ON-LINE Non-restoring Division Scheme,” in IEEE Twenty-Seventh Hawaii Int. Conf. on System Sciences, Wailea, USA, Jan. 4-7, 1994.

[9] N. Aggarwal, K. Asooja, S. Verma and S. Negi, “An Improvement in the Restoring Division Algorithm (Needy Restoring Division Algorithm),” in IEEE Int. Conf. Computer Science and Information Technology, Beijing, Aug. 8-11, 2009.

[10] P. Nair, D. Kudithipudi and E. John, “Design and Implementation of a CMOS Non-Restoring Divider,” in Proc. IEEE Int. Region 5 Conf, San Antonio, USA , April 7-9, 2006.

[11] C. Senthilpari, S. Kavitha and J. Joseph, “Lower delay and area efficient non-restoring array divider by using Shannon based adder technique,” in Proc. IEEE Int. Conf. on Semiconductor Electronics, Melaka, June 28-30, 2010.

[12] S. Oberman and M. Flynn, “Division Algorithms and Implementations,” IEEE Trans. on Comp., vol. 46, no. 8, pp. 833-854, Aug. 1997.

[13] J. Robertson and T. M. Carter, “Radix-16 signed-digit division,” IEEE, Trans. Computers, Vols. C-39, no. 12, pp. 1424-1433, Dec. 1990.

[14] J. Maharaja, Vedic Mathematics, Delhi: Motilal Banarsidass Publishers Pvt. Ltd., 2001.

[15] N. Takagi, S. Kadowaki and K. Takagi, “A hardware algorithm for integer division,” 17th IEEE Symposium on Computer Arithmetic (ARITH'05), pp. 140-146, 2005.

[16] J. Kolouch, “Combinational Divider in FPGA,” in 17th International Conference Radioelektronika, Brno, 2007.

[17] Z. Fedra and J. Kolouch, “VHDL procedure for combinational divider,” in 34th International Conference on Telecommunications and Signal Processing (TSP), Budapest, 2011.

[18] R. D. Blanton and J. P. Hayes , “Design of a fast, easily testable ALU,” in Proceedings of 14th VLSI Test Symposium, Princeton, NJ, USA, 1996.

[19] P. Krishnamoorthy and R. Tekumalla, “Quotient prediction for low power division,,” in IEEE International SOC Conference, Erlangen, 2013.

[20] J.-P. Deschamps, G. Bioul and G. Sutter, Synthesis of Arithmetic Circuits, FPGA, ASIC and Embedded System,publication, John Wiley & Sons, Inc., 2006.

[21] R. Senapati, B. K. Bhoi and M. Pradhan, “Novel Binary divider architecture for high speed VLSI applications,” in Conference on Information and Communication Technologies, 2013.

[22] P. Nair, D. Kudithipudi and E. John, “Design and Implementation of a CMOS Non-Restoring Divider,” in IEEE Int. Region 5 Conf, San Antonio, USA, April 7-9, 2006. J. Clerk Maxwell, A Treatise on Electricity and Magnetism, 3rd ed., vol. 2. Oxford: Clarendon, 1892, pp.68–73.

Fourth Industrial Revolution, Indian Labour Market and Continuing Engineering Education

Dr. Seema Singh[1], Kritika Sarkar[2], and Nitya Bahl[3]
[1](Associate Professor of Economics, Delhi Technological University, Delhi, India)
[2](Student, Electrical Engineering, Delhi Technological University, Delhi, India)
[3](Student, Electronics & Communication Engineering, Delhi Technological University, Delhi, India)

Abstract: *The fourth industrial revolution is characterized by the fusion and amplification of emerging technology due to breakthroughs in artificial intelligence, automation and robotics multiplied by the far-reaching connectivity between billions of people with mobile devices with unprecedented access to data and knowledge (World Economic Forum,2016; UNESCO-KEDI,2017) which would be the root of industrial success in the years to come. This paper summarizes some of the important characteristics of the Fourth Industrial Revolution (4th IR) and the history leading to the 4th IR. Over the technologies or the disruption that will come with this new revolution, being an exogenous force, no particular person or group of people has control. If it is going to be cost-effective, is enviable. Thus, India, as a country and all the stakeholders should thus, grasp the opportunity and power to shape the 4th IR so that we can direct it towards a better future that reflects our common objectives and values. The paper discusses its impact on the Indian production system and the labour market. Critically analysis has been done regarding the issue of preparedness of the Indian workforce to reap the demographic dividend and challenges before the Indian continuing engineering education. The paper also provides the suggestion for the Indian CEE to equip for the 4th IR.*

Keyword: *Fourth Industrial Revolution, Artificial Intelligence, Engineering Education, Robots, Employment*

I. INTRODUCTION

The Fourth Industrial Revolution (4th IR) is characterized by the fusion and amplification of emerging technology breakthroughs in artificial intelligence, automation and robotics, multiplied by the far-reaching connectivity between billions of people with mobile devices with unprecedented access to data and knowledge (World Economic Forum, 2016; Schwab 2016; UNESCO-KEDI,2017). It has grown at the background of globalization and the advancements in the digital economy coupled with biotechnology, nanotechnology and similar other technologies which target to meet individual customer needs more accurately in the production and supply area. Though evolution is gradual, but 4th IR came to the center stage of discussion when Professor Klaus Schwab, Founder and Executive Chairman of the World Economic Forum discussed it in his address at the forum in 2016. He was convinced of the beginning of a revolution that is going to fundamentally change the way we live, work and relate to one another (Schwab, 2016). In this background, the paper has tried to discuss fourth Industrial revolution and its implication for the Indian labour market. One thing is very clear that the 4th IR will be highly technology intensive. Thus, the status and challenges before the continuing engineering education (CEE) have also been discussed in the paper to upgrade the knowledge of large stock of engineering manpower. Though there is a paucity of literature on the topic whatever is available has been reviewed in the second section. The objective of the paper has been discussed in the third section. The fourth section provides the analysis part of the paper. The analysis on Indian Continuing Engineering Education has been done under two groups i.e. i. Programs for Engineers and ii. Programs for workers who will work on highly technical platforms. The last section provides conclusion and provides suggestions for the Continuing Engineering Education to gear up to meet the challenges of the 4th IR.

II. LITERATURE REVIEW

Literature has been reviewed under following five groups:

Fourth Industrial Revolution- What is it?

The first industrial revolution was steam-powered, the second electrical; the birth of the computer age marked beginning of the third revolution and the fourth – which some argue is just a continuation of the third – is the era of wearable gadgets, 3D printing, machine intelligence and networked devices such as street lights full of electronic sensors, or smart fridges that order eggs when you've run out (Schwab, 2016).In a nutshell, according to a statement by Malcolm Frank in 2017, the Executive Vice-President of Cognizant Technology

This work is licensed under a Creative Commons Attribution 4.0 International License

Solutions, Artificial Intelligence (AI) is the new engine that is going to launch the fourth industrial revolution after loom, steam engine and assembly line. Tailor-made products or services have always been criticized, now personalized products through artificial intelligence are available. The operational machine world has become more human. Sensors are more entrenched in that field which has helped the IT world to integrate the domains of operations to add value. What to talk of human-machine interaction there is increasing Machine-to-Machine (M2M) interaction (Bloem, 2014). Not specific products or services but systems will be transformed. Cyber-physical systems will emerge which will combine communication, IT, data and physical elements. The digitalization of products, big data and cloud computing will make it easier to understand and develop products for an individual (Moavenzadeh, 2015). Equipping everything on the factory floor and everything that leaves the factory with sensors and Internet connections brings benefits to the user and, of course, to the underlying industry. And when the Internet connection is lacking, the telecom providers, in particular, dive directly into the market of m2m services with their SIM cards: covering everything from postal packages to hospital beds (Bloem, 2014).

AI and machine learning systems will likely create many new jobs across all sectors, and ultimately, three scenarios could emerge in future:

i) Machines will replace humans

There is a fear that things like more machines, automation and AI could lead to layoffs, and companies will restructure. Though data suggests that nearly 12 percent jobs could be replaced and nearly three-quarters of all jobs will be 'cobots' (collaborative robot) with AI as a partner (The Hindu, 2017; Baweja ,2016). If automation of machines takes over more of manufacturing in high-income countries; the demand for such work in emerging markets will decrease. In such scenario, the world economy will need to create some 600 million new jobs in the next 15 years—most of them in Asia and Sub-Saharan Africa (*World Development Report 2013*). A recent report by the International Labour Organization estimates that automation will replace the jobs of 137 million people in Southeast Asia within the next 20 years (ILO, 2017).

ii) Enhance and make people better at what they are doing

The top five global companies in terms of market value are digital companies, and either Apple or Amazon could be a $1 trillion company in next 12-18 months. Most of the jobs of these companies will be in occupations that already exist, although the task requirements could change considerably. There is also the potential that entire categories of new jobswill emerge as suggested in a recent global study by Accenture (Wilson et al. 2017)

iii) Invent entirely new jobs

The more conservative estimate takes into account specific job tasks within occupations that, even when not automated, will go through significant changes. Moreover, the skill sets required to perform today's jobs will be wholly new by 2020 (World Economic Forum, 2017.a).

What will be its impact on the labour markets of developing countries with special reference to India?

Economic growth is defined as a positive change in the level of goods and services produced by a country over a certain period of time. Important factors that affect the economic growth of a country are Human Resource, Natural Resources, Technological Development, Social and Political Factors (Nitisha, 2017) However, gradually technology has become most important factors among them. In the process, countries that get it right will have strong GDP growth. The difference in technological endowment between developed and developing countries will play a major role in changing the production and division of wealth. The competitive disadvantage of a developed economy (lower availability of low-cost labour) is some ways mitigated by the consequences of extreme automation and connectivity. On the other hand, the competitive advantage of the developing economies (abundance of low skilled labour) is becoming more of a relative liability in the context of the changes that the 4^{th} IR is expected to bring (World Economic Forum, 2016). Ferrari has discussed that how graphic design and industrial design would become a major role player in the coming 4^{th} Industrial Revolution. He correlates computer (a function of three paradigms) and software revolution via various journal theories. Finally, the author concludes 4^{th} revolution will bring significant changes in design practices (Ferrari, 2017). According to Stewart et al. (2015), management consultants, business analysts and information technology managers have been among the fastest-growing occupations in England and Wales since the early 1990s. Second, technological innovations propel new industries and help develop new products, often meeting previously unfulfilled human needs and generating additional employment. Third, technological innovation and automation positively impact productivity, driving down costs and prices. This is likely to raise demand, thus increasing production and employment. Fourth, productivity gains lead to an overall increase in economic growth and income, thus creating higher demand for both new and existing products and services. For example, rising incomes have boosted expenditures on activities related to leisure, such as travel or dining, and on health care, generating more jobs in these industries (Frontier issue, 2017).

India and China alone will have about a half billion young people joining the workforce in the next 15 years, and 11 million young Africans are expected to join the labour market every year for the next decade. As the relationship between capital and labour is shifting so that we are using more capital per worker, then

This work is licensed under a Creative Commons Attribution 4.0 International License

productivity would increase (Anders Borg, 2016). However, there will be a loss of a number of jobs. Sector-wise, machinery manufacturing is one of the largest and most competitive sectors of the manufacturing economy contributing vastly to the economy and the GDP growth. The expected declines in "Manufacturing and Production", employment will be driven by technologies that can substitute human labour. (Tanmoy Ray, 2017; Baweja, 2016;Patti S., 2016). Another biggest employment declines are expected in the "Office and Administrative" job family, due to such change drivers as mobile internet, cloud technology, and workplace flexibility (World Economic Forum, 2016; Baweja, 2016).

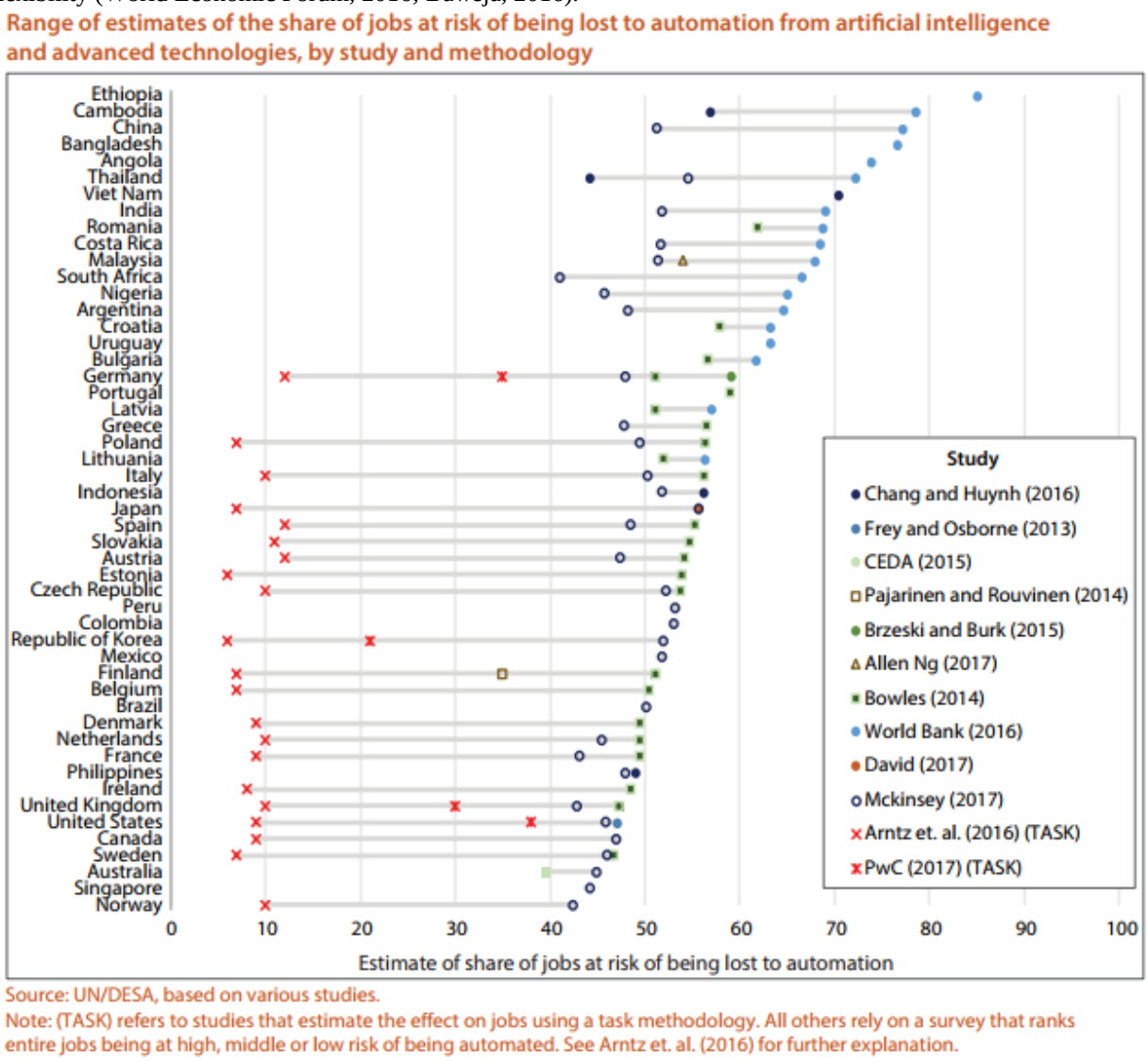


Figure1: Range of estimates of the share of jobs which are at risk

Source: Frontier Issues (2017), pp. 29.

Figure-1 provides extent of jobs which are at a risk of being lost to automation from artificial intelligence and advanced technologies by study and methodology and it shows up to forty percent in Norway to more than 80 percent in Ethiopia. The impact of the Fourth Industrial Revolution on jobs is determined by a person's skill level. Some studies predict that lower-skilled jobs will be affected the most, while others predict that middle-skill jobs will be most impacted. Most studies tend to agree that high-skilled workers would be least affected, which is a scenario that could result in rising inequality. Based on a study of the labour force in 46 countries, McKinsey Global Institute concludes that almost half of work activities globally have the potential to be automated. In India, it would be 50-70 percent (figure-1). Helping workers to acquire new skills is crucial (Mckinsey Report, 2014). However, according to a recent study by Bessen (2016), only one out of the 270 occupations listed in the 1950 US Census had been eliminated by 2010 due to automation: the elevator operator has been eliminated from the list of occupations. Through the introduction of new tools and techniques, technological progress at times alters the tasks an occupation requires. The role of bookkeepers, for example, has been rapidly changing with the use of computers and specialized software. Instead of mainly tracking and

This work is licensed under a Creative Commons Attribution 4.0 International License

recording financial transactions, they increasingly serve as data managers and advisors for clients. Bessen has characterized the automation witnessed over the past half-century as 'partial automation' (Bessen; 2016).

So, technology and globalization are significantly shifting business models in all sectors, increasing the pace of change in job destruction and job creation—including new forms of work— as well as skills churn within existing jobs. While some estimates have put the risk of automation as high as half of the current jobs, other research forecasts indicate a risk at a considerably lower value of 9% of today's occupations. (World Economic Forum, 2017.b).

What will be its impact on the Indian Labour Market?

The breakthroughs in science and technology are having a profound effect on business, labour markets, and ultimately, education systems. Indian is a labour surplus economy which has experienced an exponential growth in engineering education and thus, a significant stock of engineers (Singh, 2010). India has also reaped the benefit and many foreign and MNCs were coming to India for its large-scale English speaking engineers (Singh, 2005). However, lack of employability and unemployment among engineers has also been emerged as a question to ponder over (Bloem, 2011). About 29.4% of India's population is below fourteen years and 34.8% is between the ages of 15-30 years (Census, 2011; GoI, 2017) who will require continuous retraining to remain employable. There would be major implications due to 4IR on the Indian economy. After all, the issues which will transform the industry are:

- Skills Mismatch:Changes in technology and commerce challenge the development of skills and capabilities
- Complexity of Innovation:Adapting to the increasing complexity of innovation
- Industrial Policy:Using industrial policy to affect producers or consumers in line with socio-economic and political goals
- Infrastructure Gap: The provision of infrastructure supporting manufacturing sectors
- Value Chain Shifts:Value creation is shifting with technological, regulatory and market disruptions
- Socio-economic Changes:Fostering manufacturing relies on consumption patterns, market conditions and societal inclusiveness
- Capital Intensity:Increase in capital intensiveness as manufacturing moves towards further automation (Moavenzadeh, 2015; World Economic Forum, 2016)

Indian Education System with special reference to Continuing Engineering Education

The World Economic Forum predicts net job growth overall, with as many as four new roles emerging for each role lost. Without bold reforms and clear policies to guide us through, many people will lack the necessary skills to fill these new positions in economies and societies that are anticipated to be fundamentally different. Businesses and governments in the Asia Pacific region will then confront a unique challenge — growth in employment opportunities and a shortage of potential employees with the skills to occupy both new and existing roles (World Economic Forum, 2016). The most obvious way for policy-makers to meet technological disruptions is to increase investments in education and re-education. Technological change also has implications for income distribution, and this reinforces the upwards pressure on government expenditures. Job disruption can undermine earnings of low-income groups.

However, the education and training systems, have remained largely static and under-invested in for decades, are largely inadequate for these new needs. Some studies suggest that 65% of children entering primary school today will have jobs that do not yet exist and for which their education will fail to prepare them, exacerbating skills gaps and unemployment in the future workforce. In addition, poorly developed adult training and skilling systems in most economies delay the speed of adjustment to the new context for the currently active workforce (World Economic Forum, 2017.a).

First and foremost, countries will need to address the issue of continued and improved training in science, technology, engineering, and mathematics (STEM) subjects, as well as investment in Information and Communications Technologies (ICTs). Many countries have taken the initiative to expand and focus on these areas over the past several years, and continued efforts will be needed to expand existing facilities, as well as improve human resource capacity. However, less clear is the vital role that liberal arts and social sciences will have in the coming years. For instance, creative problem-solving, people management, and social intelligence remain significant bottlenecks to machine learning and artificial intelligence. This means that 'soft' skills (i.e. transversal competencies or 21st-century skills) will increase in value as these fields mature. Therefore, for policymakers, by bridging critical thinking and problem-solving with entrepreneurship and design, liberal arts programs may be positioned to generate the kinds of intuitive thinkers that understand the future (UNESCO-KEDI, 2017).

Indian government realized significance of continuing engineering education and the Jawaharlal Nehru Technological University, Hyderabad started the Continuing Engineering Education (CEE) programme at degree level (B.E./B.Tech.) in 1983 with courses in civil, electrical, electronics & communication ,and mechanical engineering. Since, then many institutions came forward and started continuing engineering

This work is licensed under a Creative Commons Attribution 4.0 International License

education at diploma, degree and at Postgraduate level for the working professional through 'Face-to-Face' mode part-time program as well as distance mode (Kumar, 2004). In short, the program was developed to acquire higher knowledge and qualification for linear career progression. However, globalization and advent of Information Technology (IT) has provided engineers a multi-pronged development path which they can acquire outside the 'face-to-face' method at the time of their convenience. (Singh, 2012). Now with the advent of 4th IR, the problem in the future could not be the lack of employment, but the shortage of skills that the new jobs will demand (World Economic Forum, 2017.b). Naude in his study of the 4th IR for African (re-) industrialization has suggested to promote the (i) development of business schools and technical vocational colleges with a strong link to the commercial sector; (ii) raising of investment in technical and STEM skills; (iii) shifting of learning towards acquisition of complex, problem-solving skills; (iv) creation of a nurturing environment for human capital to better protect Africa's knowledge base from conflict and disease; (v) underpinning of investments in the knowledge base and entrepreneurial ecosystem with better social protection and insurance; and that (vi) promotes the efficiency of financial markets and access to finance, given that education is costly and subject to fixed costs (Naude, 2017)- 'To optimize flow inside talent pipeline, an organization must continually review talent management activities and ensure they are aligned with corporate strategy. What's more, that the talent community—the employees—needs to feel a sense of control over its development and destiny. Investment in re-skilling and up skilling of the workforce and to create opportunities for experiential learning has been emphasized (Maria Ho, 2015; Moavenzadeh, 2015). During the World Engineering Education Forum 2015, Professor Sabina Jeschke from RWTH Aachen University said "the complexity of the systems developed to meet the demands of the fourth industrial revolution necessitate interdisciplinary and collaboration as a precondition for innovation" (AbuMezied, 2016).

Objective

The main objective of the paper is to discuss expected changes in the Indian labour market for engineers as well as the less skilled and marginalized labour due to the 4th Industrial Revolution. The paper has also tried to discuss the challenges before the Indian continuing engineering education to train and retrain engineers and less skilled labour regarding the emerging skill needs.

III. ANALYSIS

One will agree, accept or not, the 4th IR has arrived and will affect every aspect of the production system but here, its impact on the labour market and the education system have been discussed as follows:

Impact of the Fourth Industrial Revolution on the Indian Labour Market

India, being a young and labour surplus economy has reaped the benefit of the Third Industrial Revolution powered & provided by Information Technology through reaping the benefit of the virtual platform. However, the story will not be the same during the 4th IR. The impact will be highly non-linear and complex. The machine-to-machine interface will replace human-to-machine interface even at the start and end points of any production system, which will ultimately lead to a complete automation of the production cycle. These are often achieved by substituting capital for labour, with new machines performing tasks that were previously carried out by humans. As capital component of the production system will increase in the production system, the labour productivity of engaged labours will increase but labour employment will decrease. The low-end and repetitive work will be automated and will be done by robots. The tractor, the combine harvester, the forklift and desktop publishing software are prominent examples of labour-saving technologies. In the past, new technologies substitute workers only in specific tasks, but do not necessarily eliminate entire occupations, for instance farm workers, warehousemen and typesetters. Again the Information Technology has made internet connectivity quite cost-effective and the AI automation will make the things more accessible further but as the large Indian population is illiterate or less educated, they are not aware of the repercussions, like we have very often read about fraudulent in e-banking and cybercrimes. So, along with bringing changes in the education system for current students, adults also need to be given skill development courses and there should be continuous learning and re-skilling in order to help the low-skill and middle-skill level workers that will be the most affected in this revolution.

Continuing Indian Engineering Education

The change brought by the Fourth Industrial Revolution is inevitable, not optional. The possible rewards are staggering. The 4th IR will have very high level and new technological inputs. Thus, not only the existing large-scale engineering manpower of India will be required to upgrade their knowledge but the non-engineering manpower will also need to learn the basics of the upgraded technology to be able to work on the same platform.

Programs for Engineers

To enhance the knowledge base of the stock of engineering manpower the CEE needs to bring about courses and practical education with respect to these technologies and that also very soon. At the same time, it should get rid of the courses and subjects that are no longer relevant, have become stagnant or need up gradation in their syllabus. The MOOCs help reducing the barriers of space and time, reach remote areas and also bring

This work is licensed under a Creative Commons Attribution 4.0 International License

advanced research topics' lectures from professors around the world to the developing areas. However, the real challenge may be to develop MOOCs and make them accessible to all at the fastest rate as this is an AI-driven revolution and engineers are the ones who can bring that technological edge to any business around the world. Engineers will need to expand their knowledge not only regarding emerging technology but also beyond the knowledge of engineering subjects. Many CEOs today are reinventing their businesses by innovating and advancing their product technology and financial models with the help of data scientists and other such researchers.

For the development of 'Business models' with many stakeholders, engineers can play a very important role by acting as an anchor. The CEE thus, trains engineers not only in engineering area but in other related areas also. During the 4th IR, engineers will have Big Data which they will have to analyse for taking business decisions. So, the CEE should especially target the related subjects as Econometrics, Data mining Fuzzy Logic, machine learning, MATLAB etc. It should focus not only on the upgraded engineering and technology but on innovation and entrepreneurship also.

Programs for Workers who will work at highly technical platforms

Due to the enhancement of capital intensity in the production process, workers who are not engineers will also have to deal with advanced machines. Risks to privacy and security is another issue. Under the 4IR, everything is available on a virtual platform, such as online banking, online shopping, registration & verification of official documents online and much more. All this poses a huge threat to cyber security as all our data is present on the online platform and not taking the required measures to protect our personal data can lead to its grave misuse by illegal hackers. Thus, people need to be trained for the upcoming AI and digitization. CEE should initiate short-term courses to train people, especially from non-engineering and economically weaker backgrounds to make them computer-literate at an advanced level. Such training will help them face the 4th as an advantage rather than a nightmare. Collaboration, integration and aligning security process are keywords for scaling CEE efforts and bringing sustainability.

IV. CONCLUSION

The 4th IR is going to be an era of AI enabled wearable gadgets, 3D printing, machine intelligence and networked devices such as street lights full of electronic sensors. The change brought by the 4th IR is inevitable, not optional which will have high technological intensity. The products and services will be very individualized so as a customer, we can feel happy. What remains in store for a labour surplus country like India is still not completely definite. As India has one of the largest numbers of English speaking Engineers, it should design its development strategy as it reaped the benefit during the Third Industrial Revolution. However, the shelf life of technology is small so, the onus comes on the CEE to train them about the latest technology. It should focus not only on the upgraded engineering and technology but on innovation and entrepreneurship as well. At the same time, a large-scale of the Indian workforce is not capable of working with advanced technology. The CEE should also start short-term programmes for such workers dealing with the various technical aspects, human-machine interface and issues related to cyber security.

V. REFERENCES

[1] *Agha, A.,(2017). Does Your Talent Pipeline Flow Without a Flaw? Retrieved from https://www.td.org/insights/ on 13/1/2018.*

[2] *Andreas, B. & Saeki, H. (2011). Employability and Skill Set of Newly Graduated Engineers in India. World Bank Policy Research Working Paper no. 5640, retrieved from https://papers.ssrn.com/sol3/papers.cfm?abstract_id=1822959 on 21/01/2018.*

[3] *Bhanu, B., Donovan, P., Haefele, M., Siddiqi, L. &Smiles, S. (2016).Extreme automation and connectivity: The global, regional, and investment implications of the Fourth Industrial Revolution. UBS White Paper for the World Economic Forum 2016 Annual Meeting, January retrieved from http://www.tadviser.ru/images/b/b7/Extreme_automation_and_connectivity_The_global%2C_regional%2C_and_investment_implications_of_the_Fourth_Industrial_Revolution.pdf on 28/12/2017.*

[4] *Borg, A.(2016, January)How will the Fourth Industrial Revolution affect economic policy? Retrieved on from https://www.weforum.org/agenda/ on 29/12/2017.*

[5] *Census (2011).Census 2011. Government of India. Retrieved from http://www.censusindia.gov.in/vital_statistics/srs_report/9chap%202%20-%202011.pdf on 05/01/2018.*

[6] *Choi, J.(2017). The Future of Jobs and the Fourth Industrial Revolution: Business as Usual for Unusual Business. Retrieved from http://blogs.worldbank.org. on 21/12/2017.*

[7] *Daniel ,A. & Lamb ,C. (2017,April). Surfing the 4th Industrial Revolution: Artificial intelligence and the liberal arts. Brookings Institute: Brown Center Chalkboard. Retrieved from https://www.brookings.edu*

[8] *Ferrari, T.G.(2017,April.). Design and the fourth Industrial Revolution, Dangers and opportunities for a mutating discipline. 12th EAD Conference at Sapienza University, Rome.*

[9] *Frontier Issues (2017).The impact of the technological revolution on labour markets and income distribution. Department of Economic & Social Affairs, Retrieved from https://mail.google.com/mail/u/1/#inbox/1611797e43f9da00?projector=1&messagePartId=0.1 accessed on 12.1.2018.*

[10] *Garcia, F.T.(2017).Design and the Fourth Industrial Revolution: Dangers and opportunities for a mutating discipline. The Design Journal, pp. s2625-s2633. Retrieved from http://www.tandfonline.com/doi/abs/10.1080/14606925.2017.1352774 on 29/12/2017.*

This work is licensed under a Creative Commons Attribution 4.0 International License

[11] *GoI (2017).Youth in India Government of India publication. Retrieved from http://mospi.nic.in/sites/default/files/publication_reports/Youth_in_India-2017.pdfon 06/01/2018.*
[12] *ILO(2016). ASEAN in Transformation: How Technology is Changing Jobs and Enterprises. Geneva, International Labour Organisation, Geneva. Retrieved from http://www.ilo.org/public/english/dialogue/actemp/downloads/publications/2016/asean_in_transf_2016_r1_techn.pdf on 08/01/2018.*
[13] *James M., Michael C., Jacques B., Jonathan W., Parul B., Ryan Ko , Saurabh S. (McKinsey & Company,2017) Jobs Lost, Jobs Gained: Workforce Transitions In A Time Of Automation , retrieved from https://www.mckinsey.com/~/media/McKinsey/Global%20Themes/Future%20of%20Organizations/What%20the%20future%20of%20work%20will%20mean%20for%20jobs%20skills%20and%20wages/MGI-Jobs-Lost-Jobs-Gained-Report-December-6-2017.ashx on 21/12/2017.*
[14] *Moavenzadeh, J.(2015, October). The 4th Industrial Revolution: Reshaping the Future of Production. World Economic Forum, DHL Global Engineering & Manufacturing Summit, October, Amsterdam. Retrieved from https://www.eiseverywhere.com/file_uploads/fe238270f05e2dbf187e2a60cbcdd68e_2_Keynote_John_Moavenzadeh_World_Economic_Forum.pdf on 17/12/2017.*
[15] *Marco, N.(2017). The (unknown) Impact of the fourth Industrial Revolution in Education. Scientix: Europe. Retrieved from http://blog.scientix.eu/2017/07/the-unknown-impact-of-the-fourth-industrial-revolution-in-education/ on17/01/2018.*
[16] *Mazeid, A.(2016).What role will education play in the Fourth Industrial Revolution? Retrieved from https://www.weforum.org/agenda/2016/01/what-role-will-education-play-in-the-fourth-industrial-revolution/ on 21/01/2018.*
[17] *Kumar, A (2004). Continuing Engineering Education in India: An overview.9th World Conference on Continuing Engineering Education, Tokyo, May 15-20.*
[18] *Mckinsey & Company(2014).Offline and falling behind: Barriers to Internet adoption .Retrieved fromhttps://www.mckinsey.com/industries/high-tech/our-insights/offline-and-falling-behind-barriers-to-internet-adoption on 22/01/2018.*
[19] *Maria, H.(2015). Are we prepared for the learners of the future?Retrieved from https://www.td.org/insights/are-we-prepared-for-the-learners-of-the-futureon 23/01/2018.*
[20] *NaudeWim (2017,June).Entrepreneurship, Education and the Fourth Industrial Revolution in Africa. IZA – Institute of Labor Economics (IZA DP No. 10855). Retrieved from http://ftp.iza.org/dp10855.pdf on 05/1/2018.*
[21] *Nitisha (2017).5 Factors that Affect the Economic Growth of a Country", Economic Discussion. Retrieved fromhttp://www.economicsdiscussion.net/economic-growth/5-factors-that-affect-the-economic-growth-of-a-country/4199 on 12/01/2018.*
[22] *Patti, S. (2016).The Fourth Industrial Revolution: What Happens with Employment? Retrieved from https://www.td.org/insights/the-fourth-industrial-revolution-what-happens-with-employmenton 25/01/2018.*
[23] *Price Waterhouse Cooper. (2017). Managing man and machine.20th CEO survey. Retrieved from https://www.pwc.com/gx/en/ceo-agenda/ceosurvey/2017/gx/talent.htmlon 12/01/2018.*
[24] *Schwab Klaus, (2016).The Fourth Industrial Revolution. Retrieved from https://www.weforum.org/about/the-fourth-industrial-revolution-by-klaus-schwab on 12/01/2018.*
[25] *Singh, S. (2012,May). A Study on Emerging Trends in Indian Continuing Engineering Education System. Presented at WCCEE, Valencia, Spain, May, 17- 19.*
[26] *Tanmoy, R. (2017), Future of Jobs Employment Post Fourth Industrial Revolution. Retrieved from https://www.linkedin.com/pulse/future-jobs-employment-post-fourth-industrial-revolution-tanmoy-ray on 20/12/2018.*
[27] *The Hindu Correspondent (2017). Artificial Intelligence is the engine of the fourth industrial revolution. The Hindu: Business Line. Retrieved from http://www.thehindubusinessline.com on 22/12/2017.*
[28] *The World Bank,(2013).The World Development Report 2013. Retrieved from http://econ.worldbank.org/external/default/main?contentMDK=23044836&theSitePK=8258025&piPK=8258412&pagePK=8258258 on 15/01/2018.*
[29] *Taap, B., Doorn, M.V., Duivestein, S., Excoffier, D., Maas, R. & Ommeren, E.V. (2014). The Fourth Industrial Revolution: Things to Tighten the link between IT and OT. Sogeti VINT. Retrieved from https://www.fr.sogeti.com/globalassets/global/downloads/reports/vint-research-3-the-fourth-industrial-revolutionon 24/01/2018.*
[30] *UNESCO- Kedi(2017).Educatingfor the 4th Industrial Revolution. Asia-Pacific Regional Policy Seminar. United Nations Educational,Scientific and Cultural Organisation- Kedi Retrieved from https://teams.unesco.org/ORG/fu/bangkok/public_events/Shared%20Documents/IQE/2017/09-KEDI/docs/unesco-kedi-policy-seminar-2017-concept-note.pdfon 26/01/2018.*

[31] *Wilson H. James, Paul R. Daugherty, and Nicola Morini-Bianzino (2017) The jobs that artificial intelligence will create. Published in MIT Sloan Management Review:Summer 2017 issue. Retrieved fromhttps://sloanreview.mit.edu/article/will-ai-create-as-many-jobs-as-it-eliminates/on 22/12/2017.*
[32] *World Economic Forum (2016). The Future of Jobs: Employment, Skills and Workforce Strategy for the Fourth Industrial Revolution. Global Challenge Insight Report, Geneva. Retrieved from http://reports.weforum.org/future-of-jobs-2016/ on 21/12/2017.*
[33] *World Economic Forum (2017.a, January). Realizing Human Potential in the Fourth Industrial Revolution-An Agenda for Leaders to Shape the Future of Education, Gender and Work is a White Paper retrieved from https://youtheconomicopportunities.org/resource/8510/realizing-human-potential-fourth-industrial-revolution-agenda-leaders-shape-future on 02/1/2018.*
[34] *World Economic Forum (2017.b, November). ASEAN 4.0: What does the Fourth Industrial Revolution mean for regional economic integration? White paper retrieved from https://www.adb.org/sites/default/files/publication/379401/asean-fourth-industrial-revolution-rci.pdf on 28/12/2017.*
[35] *Zahidi, S. (2016,May). "The Next Industrial Revolution is Coming to Southeast Asia", retrieved from http://time.com/4347339/asean-world-economic-forum/on 213/1/2018.*

This work is licensed under a Creative Commons Attribution 4.0 International License

Electric Power Systems Research 160 (2018) 261–272

Contents lists available at ScienceDirect

Electric Power Systems Research

journal homepage: www.elsevier.com/locate/epsr

Grid interfaced solar photovoltaic system using ZA-LMS based control algorithm

Manoj Badoni [a], Alka Singh [b,*], Vijay P. Singh [c], Ravi Nath Tripathi [d]

[a] Department of Electrical & Instrumentation Engineering, Thapar Institute of Engineering and Technology, Patiala, India
[b] Department of Electrical Engineering, Delhi Technological University, Delhi, India
[c] Department of Electrical Engineering, Government Engineering College, Sonbhadara, UP, India
[d] Next Generation Power Electronics Research Center, Kyushu Institute of Technology, Japan

ARTICLE INFO

Article history:
Received 18 September 2017
Received in revised form 7 February 2018
Accepted 1 March 2018

Keywords:
Renewable energy sources
Solar photovoltaic
ZA-LMS
Power quality

ABSTRACT

Renewable energy sources such as solar photovoltaic can meet increasing energy demand in countries where there is sufficient availability of sun light. Intermittent nature of this kind of renewable energy sources demands a control which can handle fast dynamics of the system. This paper presents a grid coupled solar photovoltaic (SPV) system which includes solar photovoltaic array, incremental conductance based MPPT and boost converter. Grid integration of SPV array is performed using three phase voltage source converter (VSC) controlled with a fast and robust control algorithm. A Zero Attracting Least Mean Square (ZA-LMS) based controller is proposed to generate reference grid currents. These currents are compared along with sensed grid currents to generate switching pulses for three phase VSC. The proposed system is used to feed real power demand of load along with power quality refinement features such as suppression of harmonics, maintaining grid current at unity power factor and balancing of loads. Performance of the ZA-LMS controller is compared with conventional controllers such as normalized least mean square (NLMS) and dq0 frame theory. These controllers are compared for various characteristics concerning weight convergence, mathematical complexity, computational burden on real time controller and harmonic compensation. Proposed controller is implemented using dSPACE 1104 and tested on developed laboratory prototype of grid connected VSC working as shunt active power filter. Performance of the controller is observed and verified for steady state and dynamic load conditions.

© 2018 Elsevier B.V. All rights reserved.

1. Introduction

Nowadays power sector industries are concerned about utilizing renewable energy sources (RESs), because energy demand is increasing and the fossil fuels are depleting. In near future, emphasis will be on the use of clean and green energy by the use of RESs. Sources like Photovoltaic, wind, biomass, biofuels etc. in the form of DG (Distributed Generation) are gaining increased importance [1,2]. Among these, RESs based photovoltaic is an emerging energy source especially in the tropical countries where there is sufficient availability of sun light. The characteristics of SPV system are exponential in nature and depend upon the weather conditions.

The SPV is required to track the maximum power point to improve the efficiency of SPV system [3]. The aim of maximum power point tracking (MPPT) is to achieve SPV array operation always at a specified value of output voltage and current. Therefore, MPPT is required to adjust the SPV array output voltage and current to appropriate values to provide maximum power to the grid. The tracking of maximum power point (MPP) requires implementation of suitable MPPT algorithm along with a DC–DC boost converter [4]. A number of MPPT algorithms [5–9] are proposed in the literature for maximum power point tracking (MPPT) such as incremental conductance (InC), perturb and observe (P&O), fractional open circuit voltage, fractional short circuit current, fuzzy logic, ripple correlation control etc. Small units of solar photovoltaic can be installed locally to augment conventional generation. However, due to intermittent nature of RESs and different voltage and power level, these sources cannot be integrated to the grid directly [10,11]. Power electronic converters are required to interface these to the utility grid. These electronic converters are mainly voltage

* Corresponding author.
E-mail address: alkasingh@dce.ac.in (A. Singh).

https://doi.org/10.1016/j.epsr.2018.03.001
0378-7796/© 2018 Elsevier B.V. All rights reserved.

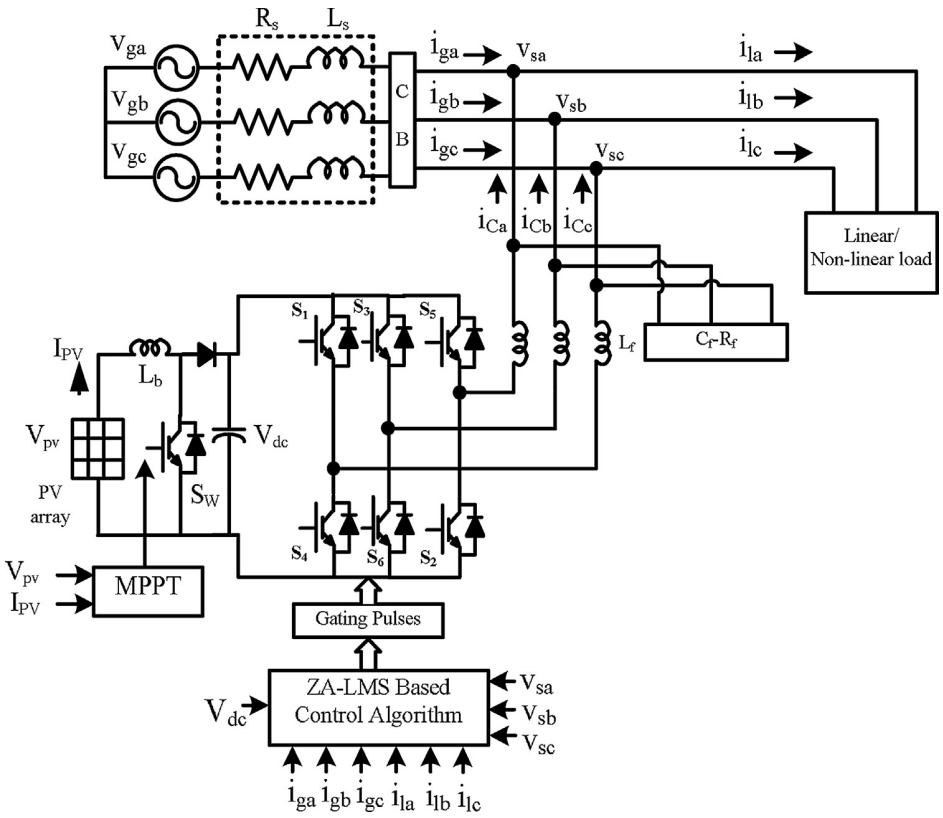


Fig. 1. Schematic diagram of grid integrated SPV system.

source converters (VSC) which can be controlled for real power transfer from SPV array. Additionally, these can be controlled to improve power quality features such as maintaining grid current at unity power factor, suppression of harmonics and load balancing [12].

Numerous standards (by IEEE and IEC) are in existence to stipulate the limit of total harmonic distortions (THDs) of the grid voltages and currents [13]. The behavior of VSC used in SPV system mainly depends upon type of control algorithm used. A grid coupled solar photovoltaic power generating system is developed using current synchronous detection controller along with power quality refinement features in paper [14]. Single stage three phase SPV system using Improved Linear Sinusoidal Tracer (ILST) based control is used to feed electric power evacuated from solar PV into the grid along with enhanced power quality features at distribution level [15]. Several other control algorithms such as power balance theory [16], leaky least mean square forth (LLMF) [17], adaptive neuro fuzzy inference system-least mean square (ANFIS-LMS) [18], Comprehensive synchronous reference frame (dq0) [19], recursive least square [20] sliding mode control [21] have been reported in the literature and some of these have been realized for the control of SPV.

This paper presents the design and development of solar photovoltaic (SPV) feeding linear as well as nonlinear loads. The SPV source is interconnected at the DC side of the voltage source converter. Modeling of photovoltaic (PV) array with boost converter and incremental conductance based maximum power point tracking (MPPT) is performed. The control of VSC is developed using Zero Attracting Least Mean Square (ZA-LMS) algorithm. Steady state performance is improved with ZA-LMS algorithm vis. a vis. standard LMS technique especially in highly distorted environment because this algorithm incorporates cost function L_1 differently. This gives a modified LMS update with zero attractor, hence the name the Zero-Attracting LMS (ZA-LMS). The main advantage of ZA-LMS is that its computational complexity is comparatively less than conventional LMS, NLMS adaptive filters [22–25].

A complete evacuation of SPV array is expected during day time and in the night time VSC can be used as shunt active power filter. Real power demand of the load along with power quality compensation features such as maintaining grid at unity power factor, harmonics suppression, and retaining grid stability in case of unbalanced load are performed with the proposed ZA-LMS based control algorithm. Performance of the proposed control algorithm is compared with normalized least mean square (NLMS) [25], and dq0 frame based controller to demonstrate fast and accurate operation of the SPV system.

2. System configuration

Fig. 1 illustrates the diagram of the system whose system parameters are indicated in Appendix A. Linear/nonlinear load is connected with small line impedance (connected in series as feeder impedance, R_s-L_s) to the utility grid of 415 V, 50 Hz. Voltage source converter (VSC) is coupled at the PCC with series inductor at the AC side of VSC. Solar photovoltaic (SPV) array representing renewable energy source (RES) is interfaced to the DC side of the VSC. The SPV system actually comprises SPV array, boost converter and power semiconductor devices (such as IGBTs) based three leg VSC. Each leg of VSC incorporates two IGBT switches with diode connected in reverse. The SPV converter is connected to the grid through an L_f-C_f filter where R_f is introduced to provide damping. Moreover, the values of these parameters are chosen to avoid resonance. Value of R_f is selected to be small (<1 Ω), so that power losses can be minimized. This system is developed using Matlab/Simulink and Sim Power System (SPS) tool box.

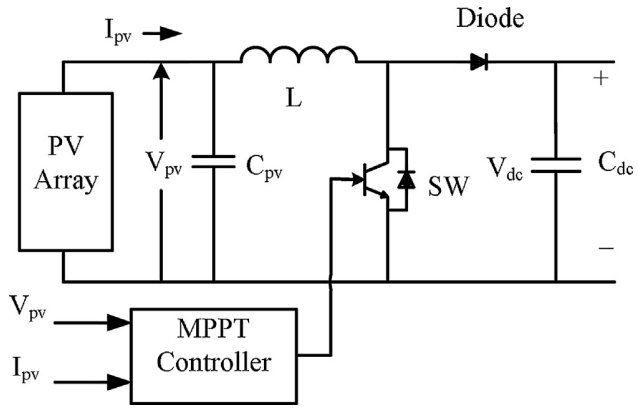


Fig. 2. Schematic diagram of DC–DC boost converter.

3. Maximum power point tracking (MPPT) and DC–DC boost converter

An incremental conductance (InC) based MPPT algorithm is developed here for generation of reference SPV array voltage. This method computes the maximum power point by comparing the incremental conductance and the array conductance. When these two quantities appear to be same then the output voltage is termed as the maximum power point voltage. This algorithm possesses advantage in terms of improved dynamic response under varying weather conditions. Development and flow chart of InC based control algorithm MPPT algorithm is mentioned in Ref. [6]. The reference PV array voltage (V_{ref}), is determined by the InC MPPT algorithm. This reference voltage along with DC bus voltage (V_{dc}) of VSC is used to estimate the reference duty ratio for the boost converter, which is given as,

$$d(n) = 1 - \left\{ V_{ref}(n)/V_{dc}(n) \right\} \tag{1}$$

This reference duty ratio is compared with saw-tooth waveform of 10 kHz, to generate gating pulse for the switch used in DC–DC boost converter. This converter converts SPV voltage to a constant DC voltage level thus providing a regulated output [26,27]. Fig. 2 shows schematic diagram of DC–DC boost converter. The value of inductor used in this circuit is calculated based on the maximum allowed ripple current (Δi_1) for minimum duty cycle (D), at maximum input voltage (V_{pv}) given as,

$$L = \frac{V_{pv} D}{2 \Delta i_1 f_{sb}} \tag{2}$$

where duty cycle (D) is calculated as, $D = 1 - \frac{V_{in}}{V_b} = 1 - \frac{680}{800} = 0.15$. The case considered in this paper for SPV is having maximum possible output voltage of 680 V. Therefore the duty cycle of boost converter for this condition corresponds to minimum value of D according to the duty cycle calculation for boost converter given in Ref. [26].

The MPPT implemented through boost converter has minimum value of D limiter so that the algorithm needs not to go through the duty cycle calculation below the specified minimum value of D. And, duty cycle of boost converter will be adjusted according to MPPT algorithm for the output voltage of PV system corresponding to tracked peak power during the real-time operating condition. The converter is designed to boost $V_{pv} = V_{in} = 680$ V to $V_b = 800$ V. Thus, the calculated value of duty cycle (D) is around 0.15. The current Δi_1 is the output current ripple and the value of ripple current is considered to be 10% of the input current, which is obtained around 30.5 A. The value of Δi_1 is calculated to be 3.05 A, switching frequency (f_{sb}) is selected 10 kHz and from the above calculated parameters, the value of inductor is selected as 1.67 mH for simulation purpose.

4. Control algorithm

Fig. 3 shows block diagram of Zero Attracting Least Mean Square (ZA-LMS) based control algorithm. This algorithm combines the LMS framework and l_1-norm regularization, which generates a zero attractor in LMS iteration to filter out distortions in the load current. The l_1-norm is also known as least absolute deviation and it is used to minimize sum of the absolute difference between the target value and the estimated values [24]. Purpose of ZA-LMS controller proposed in this paper is to estimate the reference grid currents from the distorted load current. These reference grid currents are then used for the production of gating pulses for the converter. Voltages at PCC (v_{sa}, v_{sb} and v_{sc}), grid currents (i_{ga}, i_{gb} and i_{gc}), load currents (i_{la}, i_{lb} and i_{lc}) and DC bus voltage (V_{dc}) are inputs to the control algorithm and fundamental active (w_{pa}, w_{pb} and w_{pc}) as well as reactive (w_{qa}, w_{qb} and w_{qc}) power components are outputs computed using the control algorithm. These inputs and outputs in the control algorithm block diagram are encircled by dashed rectangles. A detailed mathematical formulation of the control algorithm is given as follows.

4.1. Fundamental weight extraction by Zero Attracting-LMS (ZA-LMS)

The problem with the standard LMS algorithm is the slow rate of convergence; therefore to get rid of this problem, an adaptive algorithm using the unknown system sparsity is employed in the proposed system to improve the performance of the system.

The estimated error signal of the ZA–LMS algorithm is calculated as,

$$e(n) = d(n) - x^T(n) w(n) \tag{3}$$

where $x(n) = [x(n), x(n-1), \ldots, x(n-N+1)]^T$ are input vectors. In the modeling of ZA-LMS control for VSC these vectors are represented as unit inphase vectors (u_{pa}, u_{pb} and u_{pc}) and unit quadrature vectors (u_{qa}, u_{qb} and u_{qc}), which are used to generate reference active and reactive grid currents. The desired response d(n) is modeled as, $d(n) = w_o^T x(n) + v(n)$ here w_0 is optimal weight vector of length N and v(n) is the source of noise. Term $x^T(n) w(n)$ denotes the estimated output for given input x(n) and weight value w(n).

The cost function $L_1(n)$ of ZA-LMS control is defined by incorporating the instantaneous square error with the l_1-norm of the coefficient vector

$$L_1(n) = \frac{1}{2} e^2(n) + \gamma \|w(n)\|_1 \tag{4}$$

where e(n) estimated error signal, w(n) weight value and γ is a positive constant.

The ZA-LMS weight equation (using gradient descent updating) is given as [23],

$$w(n+1) = w(n) - \mu \frac{\delta L_1(n)}{\delta w(n)} \tag{5}$$

$$w(n+1) = w(n) + \mu e(n) x(n) - Q \operatorname{sgn}(w(n)) \tag{6}$$

where μ is the step size and sgn(w(n)) is the component wise sign function given as,

$$\operatorname{sgn}(w(n)) = \begin{cases} \dfrac{w(n)}{|w(n)|}, & \text{if} \quad w(n) \neq 0 \\ 0, & \text{if} \quad w(n) = 0 \end{cases} \tag{7}$$

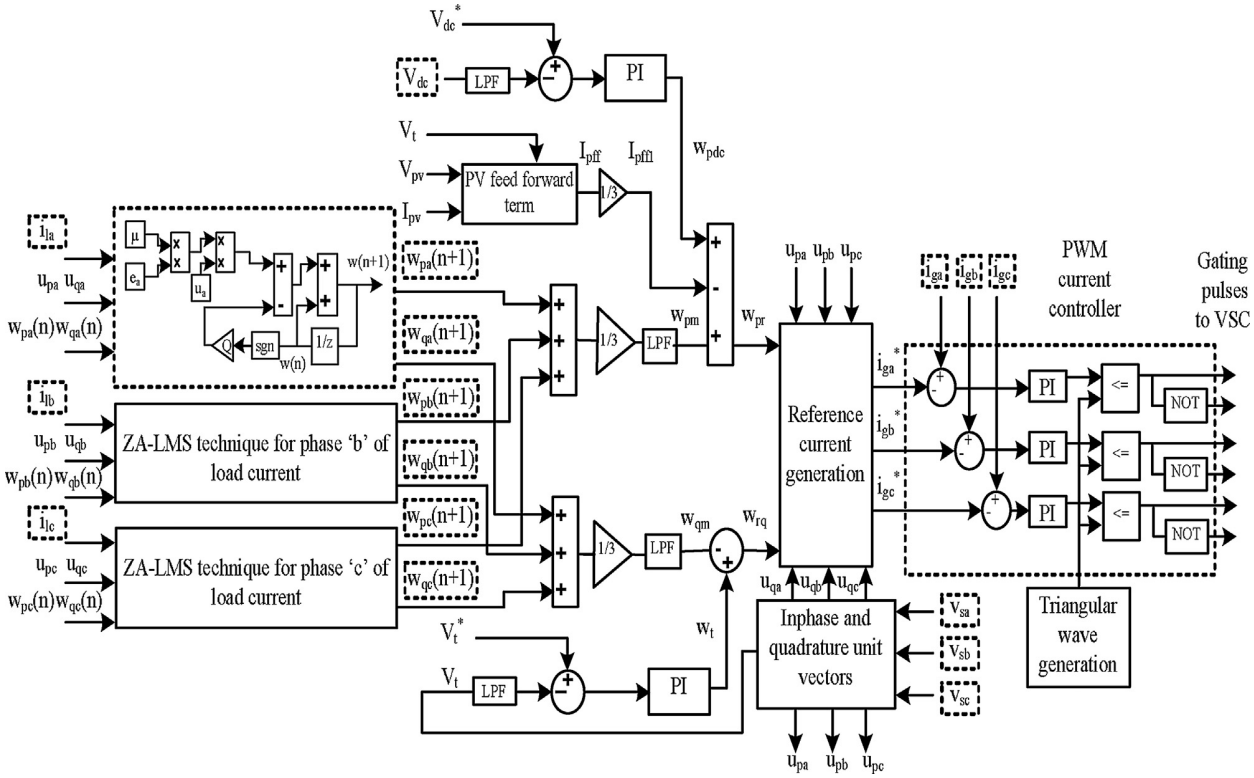


Fig. 3. Block diagram of ZA-LMS based control algorithm.

and Q is the zero attractor controller which decide the strength of attraction.

Eq. (6) represents an additional term $-Q\mathrm{sgn}(w(n))$ which always attracts the coefficients of weighted value to zero. This is named as zero attractor, whose strength is controlled by *Q*. This zero attractor term contributes to the increased speed of convergence in highly distorted environment. The values of μ and Q are taken empirically like all other intelligent algorithms.

Fundamental active power components (w_{pa}, w_{pb} and w_{pc}) of load currents (i_{la}, i_{lb} and i_{lc}) are extracted by computing updated weights using Eq. (6), which are rewritten for the three phases as,

$$w_{pa}(n+1) = w_{pa}(n) + \mu e_a(n) u_{pa} - Q\mathrm{sgn}\left(w_{pa}(n)\right) \quad (8)$$

$$w_{pb}(n+1) = w_{pb}(n) + \mu e_b(n) u_{pb} - Q\mathrm{sgn}\left(w_{pb}(n)\right) \quad (9)$$

$$w_{pc}(n+1) = w_{pc}(n) + \mu e_c(n) u_{pc} - Q\mathrm{sgn}\left(w_{pc}(n)\right) \quad (10)$$

Fundamental reactive (w_{qa}, w_{qb} and w_{qc}) power components of load currents are extracted with the help of ZA-LMS equation (Eq. (6)), which are computed as,

$$w_{qa}(n+1) = w_{qa}(n) + \mu e_a(n) u_{qa} - Q\mathrm{sgn}\left(w_{qa}(n)\right) \quad (11)$$

$$w_{qb}(n+1) = w_{qb}(n) + \mu e_b(n) u_{qb} - Q\mathrm{sgn}\left(w_{qb}(n)\right) \quad (12)$$

$$w_{qc}(n+1) = w_{qc}(n) + \mu e_c(n) u_{qc} - Q\mathrm{sgn}\left(w_{qc}(n)\right) \quad (13)$$

Average weights (w_{pm} and w_{qm}) corresponding to fundamental active (w_{pa}, w_{pb} and w_{pc}) and reactive (w_{qa}, w_{qb} and w_{qc}) power components are computed as,

$$w_{pm} = \left(w_{pa} + w_{pb} + w_{pc}\right)/3 \quad (14)$$

$$w_{qm} = \left(w_{qa} + w_{qb} + w_{qc}\right)/3 \quad (15)$$

The average weights obtained from ZA-LMS control are used to generate reference supply currents, which is presented in sub sections given below.

4.2. Generation of reference grid currents corresponding to active power components

Fig. 3 presents the block sketch of ZA-LMS controller. The amplitude of PCC voltage (V_t) is computed using instantaneous PCC phase voltages (v_{sa}, v_{sb} and v_{sc}) as,

$$V_t = \sqrt{2\left(v_{sa}^2 + v_{sb}^2 + v_{sc}^2\right)/3} \quad (16)$$

The amplitude of PCC voltage (V_t) along with instantaneous PCC phase voltages (v_{sa}, v_{sb} and v_{sc}) is used to compute unit in-phase vectors (u_{pa}, u_{pb} and u_{pc}) given below as,

$$u_{pa} = v_{sa}/V_t;\ u_{pb} = v_{sb}/V_t;\ \text{and}\ u_{pc} = v_{sc}/V_t \quad (17)$$

Unit in phase vectors are further used to compute reference active currents.

Voltage is sensed at DC bus (V_{dc}) of VSC and compared with reference DC bus voltage (V_{dc}^*). This way error (v_{de}) is generated and forwarded across PI (proportional integrator) controller. The outcome of DC bus PI (w_{pdc}) is computed as [28],

$$w_{pdc}(n) = w_{pdc}(n-1) + k_{pd}\left\{v_{de}(n) - v_{de}(n-1)\right\} + k_{id}\left\{v_{de}(n)\right\} \quad (18)$$

where k_{pd} is proportional gain and k_{id} is integral gain of DC bus PI.

The SPV instantaneous feed forward compensation term (I_{pff}) for all three phases is computed from SPV power (P_{pv}) and magnitude of PCC voltage (V_t) as [15],

$$I_{pff} = \frac{2P_{pv}}{V_t} \quad (19)$$

In a three phase system, this term is divided by three and effective SPV instantaneous feed forward compensation term (I_{pff1}) is computed.

Reference active power weight (w_{pr}) is computed by adding average active power weight (w_{pm}) along with output of PI controller (w_{pdc}) and subtracting feed forward compensation term (I_{pff}) as [17],

$$w_{pr} = w_{pm} + w_{pdc} - I_{pff} \tag{20}$$

Fundamental active power component of reference grid currents are generated from unit inphase templates (u_{pa}, u_{pb} and u_{pc}) and reference active power weight (w_{pr}) as,

$$i^*_{pa} = w_{pr}u_{pa},\ i^*_{pb} = w_{pr}u_{pb} \text{ and } i^*_{pc} = w_{pr}u_{pc} \tag{21}$$

These reference active currents are added to the reference reactive currents (computed below) to generate reference grid currents.

4.3. Generation of reference reactive current components

The following Eqs. (22)–(24) show computation of quadrature vectors (with unit magnitude) by using unit in-phase vectors as [15],

$$u_{qa} = -u_{pb}/\sqrt{3} + u_{pc}/\sqrt{3} \tag{22}$$

$$u_{qb} = \sqrt{3}u_{pa}/2 + \left(u_{pb} - u_{pc}\right)/2\sqrt{3} \tag{23}$$

$$u_{qc} = -\sqrt{3}u_{pa}/2 + \left(u_{pb} - u_{pc}\right)/2\sqrt{3} \tag{24}$$

The unit quadrature vectors are used to compute reference reactive currents. Voltage regulation at PCC is performed with a second PI controller. To achieve voltage regulation at PCC, the amplitude (V_t) is computed by Eq. (16) and compared with the reference amplitude of PCC (V_t^*). Thus an error signal (v_{te}) is generated and propagated through PI controller. Output of the PI is formulated as [28],

$$w_t(n) = w_t(n-1) + k_{pq}\left\{v_{te}(n) - v_{te}(n-1)\right\} + k_{iq}\left\{v_{te}(n)\right\} \tag{25}$$

where k_{pq} is proportional gain and k_{iq} is integral gain of AC bus PI.

The reference weight (w_{qr}) corresponding to reactive power is computed by subtracting output of AC bus PI (w_t) from the average reactive power weight value (w_{qm}) as,

$$w_{qr} = w_t - w_{qm} \tag{26}$$

Now, reference currents correspond to reactive power are generated by unit quadrature vectors (u_{qa}, u_{qb} and u_{qc}) and reference weight (w_{qr}) as,

$$i^*_{qa} = w_{qr}u_{qa},\ i^*_{qb} = w_{qr}u_{qb} \text{ and } i^*_{qc} = w_{qr}u_{qc} \tag{27}$$

These reference reactive currents are used along with reference active currents to compute reference grid current shown below.

4.4. Generation of gating pulses for three phase VSC

The reference grid currents (i_{ga}^*, i_{gb}^* and i_{gc}^*) are estimated by addition of reference active (i_{pa}^*, i_{pb}^* and i_{pc}^*) and reactive (i_{qa}^*, i_{qb}^* and i_{qc}^*) components of grid currents as,

$$i^*_{ga} = i^*_{pa} + i^*_{qa},\ i^*_{gb} = i^*_{pb} + i^*_{qb} \text{ and } i^*_{gc} = i^*_{pc} + i^*_{qc} \tag{28}$$

Grid currents (i_{ga}, i_{gb} and i_{gc}) are sensed and compared with reference currents (i_{ga}^*, $i_{gb}^*$and i_{gc}^*). Thus, the generated current errors (i_{gae}, i_{gbe} and i_{gce}) are processed through PWM current controller. The PWM current controller consists of PI controllers to amplify the above computed current errors. Signals after PI controllers are compared with triangular waveform to generate gating pulses for IGBTs of three phase VSC. Values of PI controllers used in control block diagram have been calculated using loop shaping methods. Prior to using this method, mathematical model has been developed where each loop has been calculated separately and the values of PI parameters are computed. Thereafter, simulation models are run and values of PI controllers are further improved/modified. The final tuned parameters of DC bus, AC bus and PWM PI controllers have been added in Appendix A.

5. Results and discussion

Results are presented for three phase SPV using ZA-LMS under linear and nonlinear loads. Results under linear load show evacuation of solar power and reactive power compensation along with load balancing considering different irradiance level. Results under nonlinear load present harmonic compensation and load balancing with changing irradiance level in PFC and VR modes.

5.1. Performance of SPV system under linear load

Fig. 4 shows the dynamic performance of the system in PFC mode with a 20 kV A and 0.8 linear lagging pf load. The waveforms of PCC voltages (v_s), grid currents (i_g), load currents (i_{la}, i_{lb} and i_{lc}), converter currents (i_{Ca}, i_{Cb} and i_{Cc}) and DC bus voltage (V_{dc}) are shown in this figure. Phase 'a', 'b' and 'c' of PCC voltages (V_s) and grid currents (i_g) are represented by blue, green and red colors respectively. The grid currents are observed to be balanced and sinusoidal in steady state (before t = 0.3 s) condition. Unbalancing in load is created, when phase 'c' is removed. During unbalancing (t = 0.3 s to t = 0.4 s), grid currents can be observed perfectly balanced sinusoidal. The active power demand along with load balancing during unbalance load condition of load is fulfilled by SPV system. The surplus power generated by the system is fed to the utility grid. The grid voltages and currents are observed to be in phase with each other. Solar irradiance is decreased at t = 0.5 s to value of 500 W/m^2, which causes power generation from SPV system to decrease. Load active power demand is now partially supplied by the AC mains. The DC bus voltage of VSC is maintained to its reference value 800 V under varying load conditions.

5.2. Performance of SPV system for reactive power compensation under linear load

Fig. 5 shows the generation and evacuation of active and reactive powers by SPV system. The waveforms of SPV voltage (V_{pv}), SPV current (I_{pv}), SPV output power (P_{pv}), load real power (P_l), grid real power (P_s), and SPV real power (P_C), load reactive power (Q_l), grid reactive power (Q_s) and SPV reactive power (Q_C) are shown in these results. Under steady state condition (before t = 0.3 s) the output voltage of SPV system is 680 V and current is around 30.5 A, which gives output power around 20 kW. The load active power demand is approximately 16 kW, which is fed by SPV system and the excess power is transferred to the AC mains as observed in Fig. 5. Moreover, the load reactive power demand is around 12 kVAR which is fed completely by VSC and there is almost negligible reactive power burden on the AC mains.

The effect of unbalancing is presented by removing one phase (phase 'c') of load. During unbalancing (t = 0.3–0.4 s), the output power of SPV system is unaffected. The active power demand of load is fulfilled by SPV system and there is negligible reactive power burden on the grid side. The SPV system power is reduced (after t = 0.5) due to change in irradiance level from 1000 W/m^2 to 500 W/m^2. During this time, the active power demand of the load which is around 10 kW is fed by AC mains, whereas reactive power demand of the load (12 kVAR) is completely fed by SPV system. The action of PI controller regulates the DC link voltage to a reference level of 800 V.

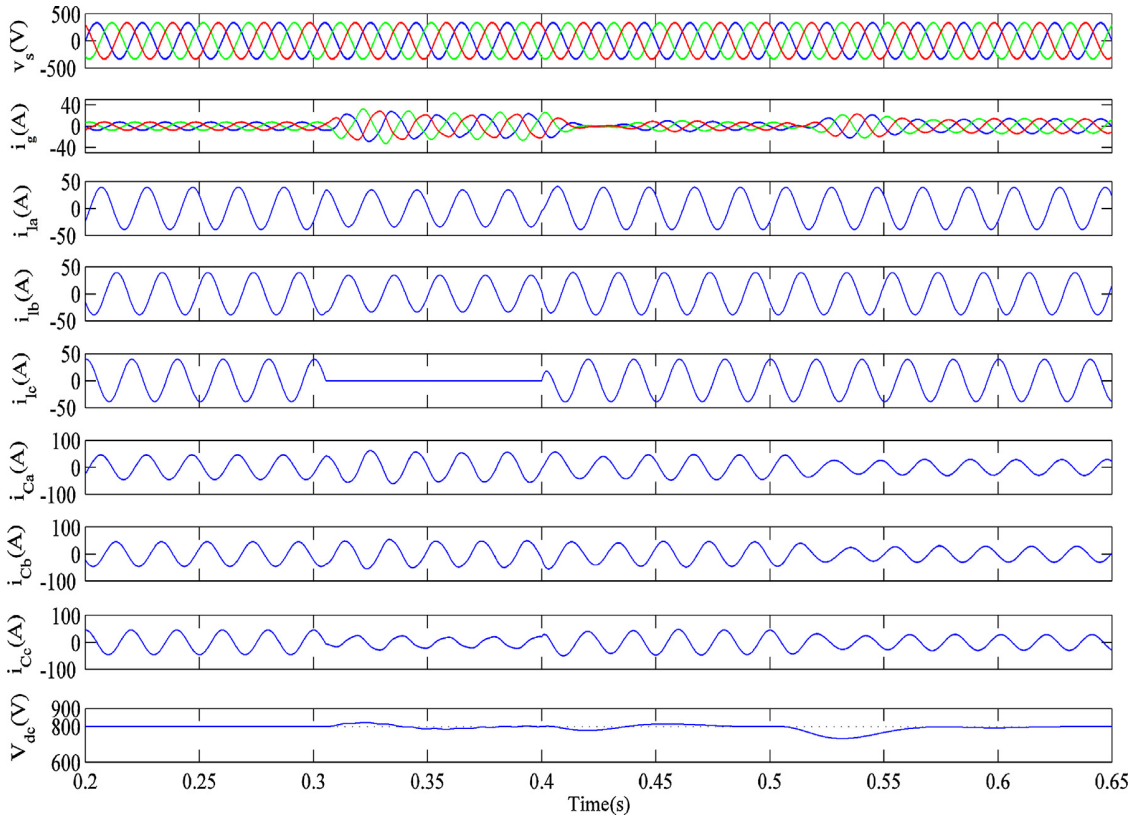


Fig. 4. Performance of SPV system in PFC mode under linear load.

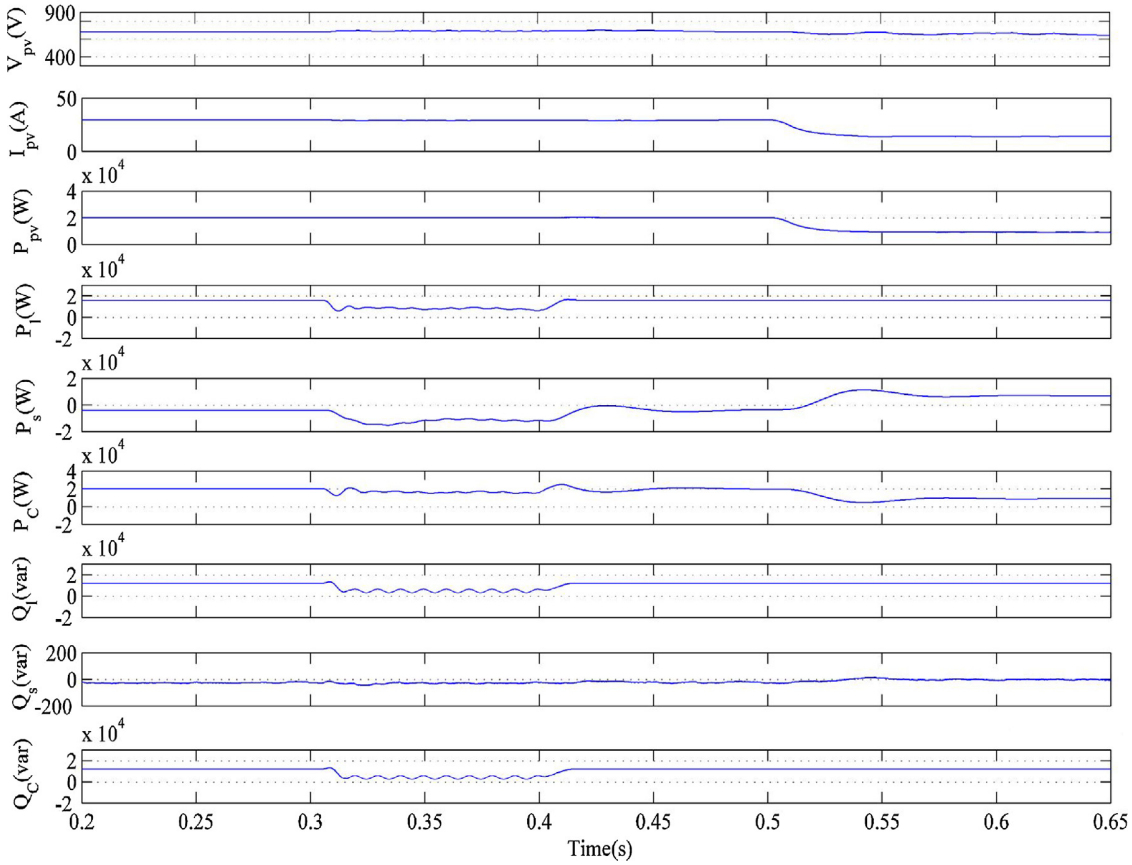


Fig. 5. Performance and powers of SPV array under linear load.

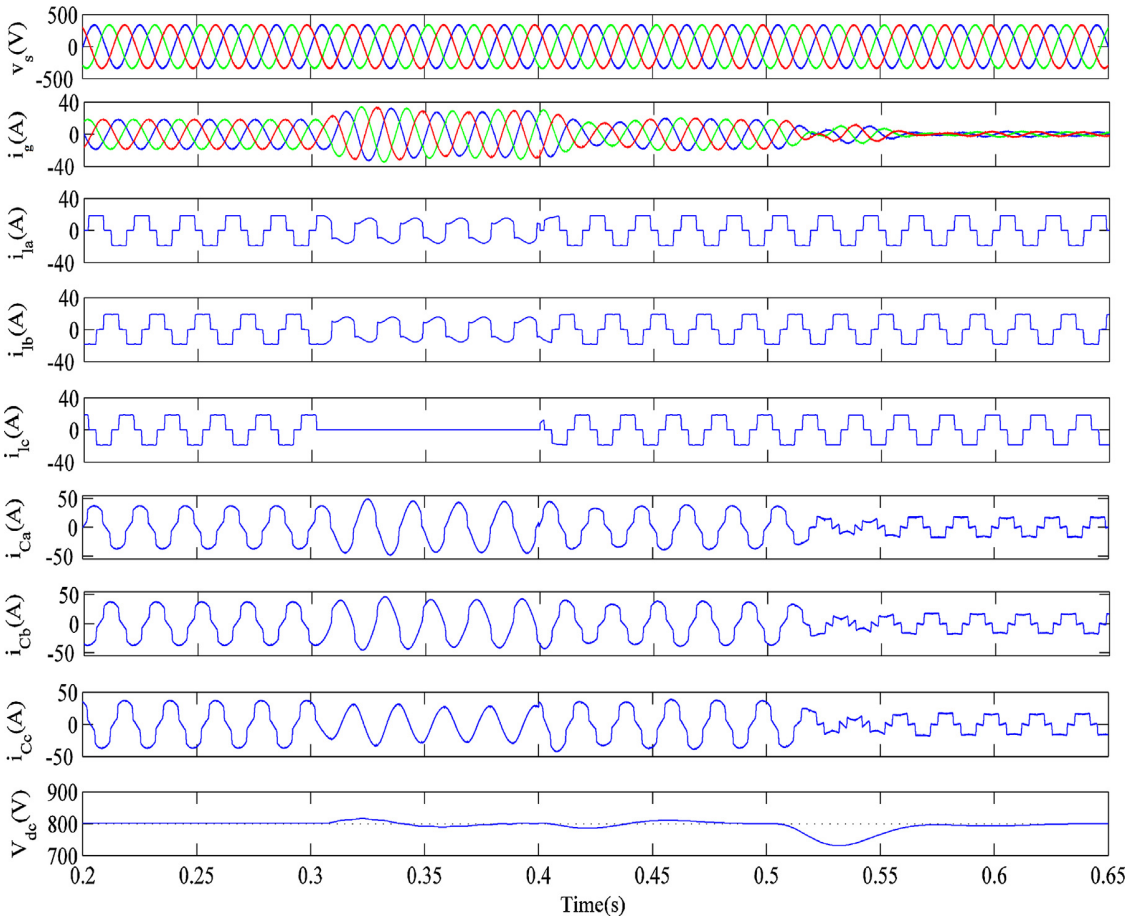


Fig. 6. Performance of SPV array in PFC mode.

5.3. Performance of the SPV system for correction of power factor under nonlinear load

Fig. 6 presents the behavior of the SPV with ZA-LMS based control algorithm for correcting power factor under nonlinear load. The waveforms of PCC voltages (v_s), grid currents (i_g), load currents (i_{la}, i_{lb} and i_{lc}), converter currents (i_{Ca}, i_{Cb} and i_{Cc}) and DC bus voltage (V_{dc}) are shown in this result. Phase 'a', 'b' and 'c' of PCC voltages (V_s) and grid currents (i_g) are represented by blue, green and red colors respectively. The grid currents are observed balanced and sinusoidal in steady state (before t = 0.3 s) condition. Unbalanced load is created by removing on phase (phase 'c'). During unbalancing (t = 0.3–0.4 s), grid currents are also balanced and sinusoidal with the action of SPV system. The active power demand along with load balancing during unbalance load condition of load is fulfilled by SPV system. The excess power generated by the system is fed to the AC mains. Solar irradiance decrease at t = 0.5 s, which causes power generation from SPV system to decrease. Load active power demand is now partially supplied by the AC mains. The DC bus voltage of VSC is maintained to its reference value 800 V, with all load and SPV conditions.

Fig. 7 shows harmonic spectra of PCC voltage (v_{sa}), grid current (i_{ga}) and load current (i_{la}) (all phase 'a'). These results present 1.38%, 1.95% and 27.87% THD in PCC voltage, grid current and load current respectively. The THD in grid current is achieved as 1.95%, whereas there is 27.87% THD in load current. These results show the adequate working of the SPV system in harmonic removal and load balancing in PFC mode.

5.4. Performance of SPV system in voltage regulation (VR) mode

Fig. 8 shows the performance of SPV system in voltage regulation mode under nonlinear load. This result shows waveform of PCC voltages (v_s), grid currents (i_g), load currents (i_{la}, i_{lb} and i_{lc}), converter currents (i_{Ca}, i_{Cb} and i_{Cc}), DC bus voltage (V_{dc}) and PCC voltage amplitude (V_t). Phase 'a', 'b' and 'c' of PCC voltages (V_s) and grid currents (i_g) are represented by blue, green and red colors respectively. The grid currents are observed to be balanced and sinusoidal in steady state (before t = 0.3 s) condition. Unbalancing is created by removing one phase of load. During unbalancing (t = 0.3 s to t = 0.4 s), grid currents are also balanced and sinusoidal with the action of SPV system. The active power demand along with load balancing during unbalance load condition of load is fulfilled by SPV system. The excess power generated by the SPV system is fed into the AC mains. Solar irradiance decreases at t = 0.5 s, which causes power generation from SPV system to decrease. Load active power demand is now partially supplied by the AC mains. The DC bus and AC bus voltages are maintained at their reference value 800 V and 339 V respectively in all load and SPV varying conditions.

Fig. 9 shows the harmonic spectra of PCC voltage (v_{sa}), grid current (i_{ga}) and load current (i_{la}) (all phase 'a'). These results present 1.83%, 2.1% and 27.95% THD in PCC voltage, grid current and load current. The results present improved THD in grid current 2.1%, however load current contains harmonic distortion around 27.95%. The THDs of PCC voltage and grid current are within the limit stated by IEEE-519 standard.

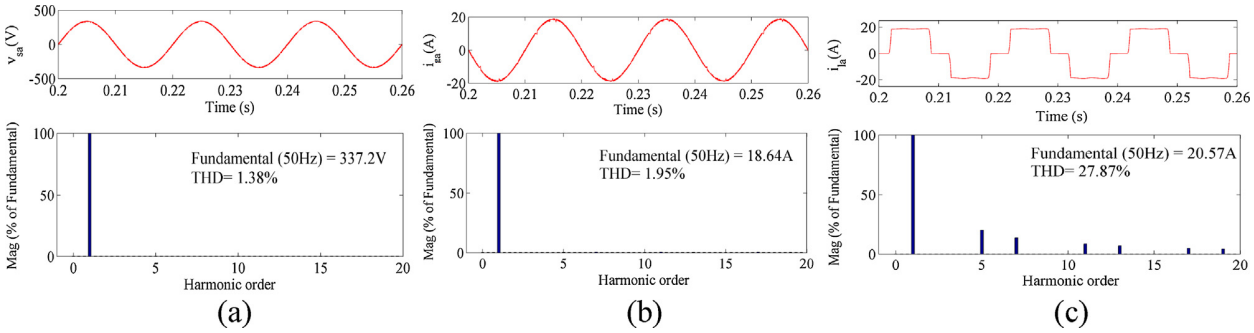


Fig. 7. Harmonic spectra of phase 'a' of (a) PCC voltage, v_{sa}, (b) grid current, i_{ga}, (c) load current, i_{la} in PFC mode.

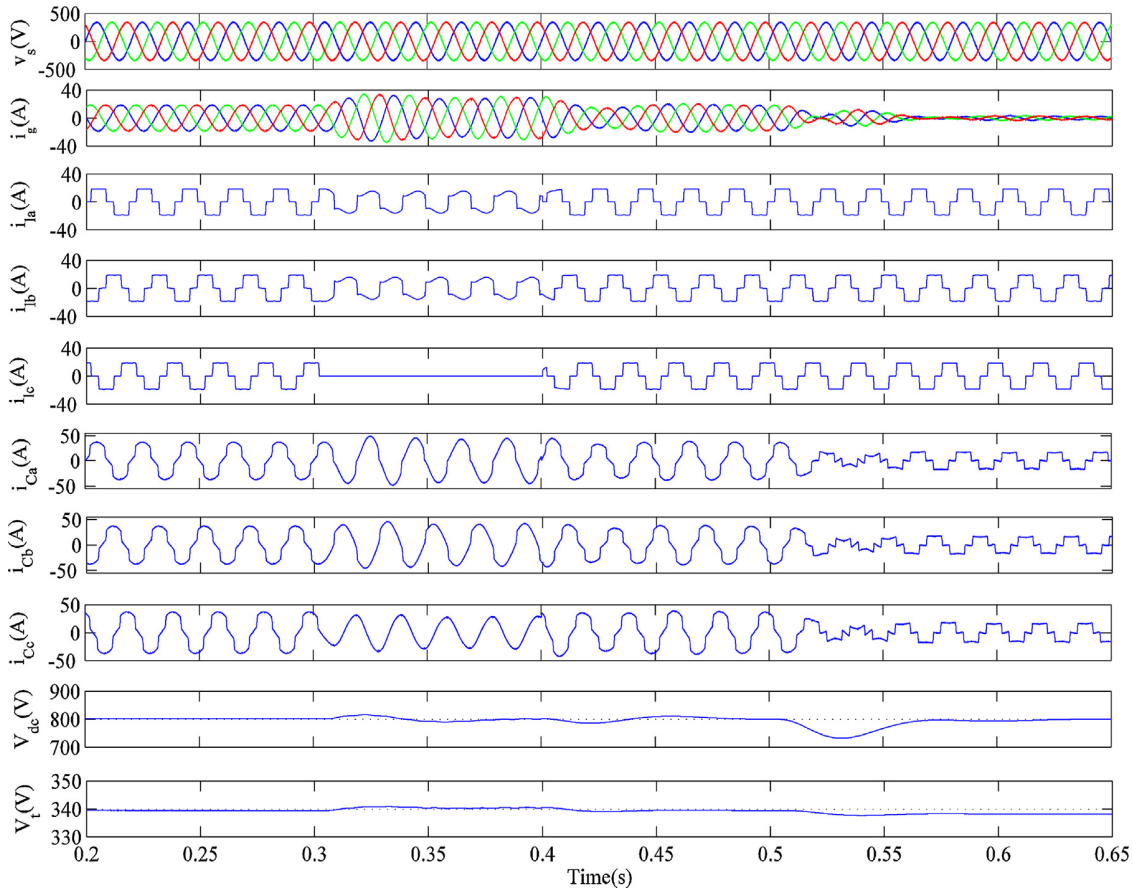


Fig. 8. Performance of SPV system in VR mode.

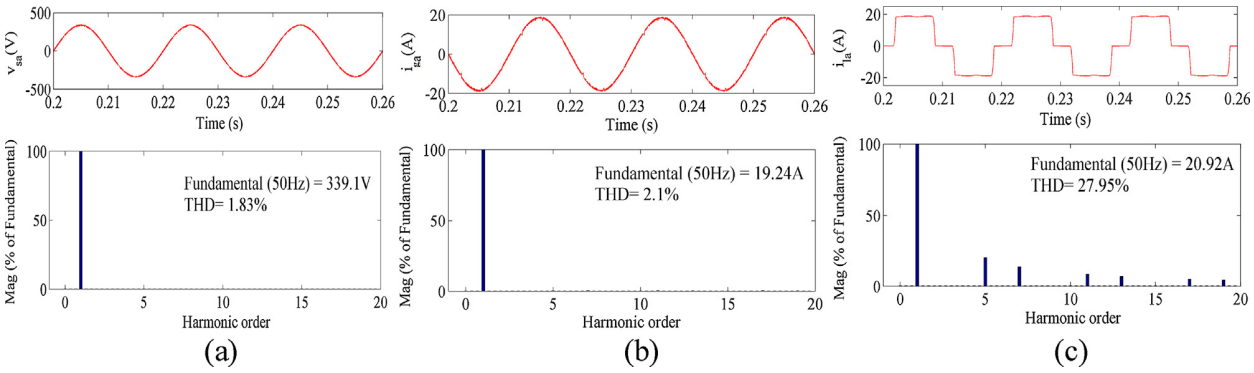


Fig. 9. Harmonic spectra of phase 'a' of (a) PCC voltage, v_{sa}, (b) grid current, i_{ga}, (c) load current, i_{la} in VR mode.

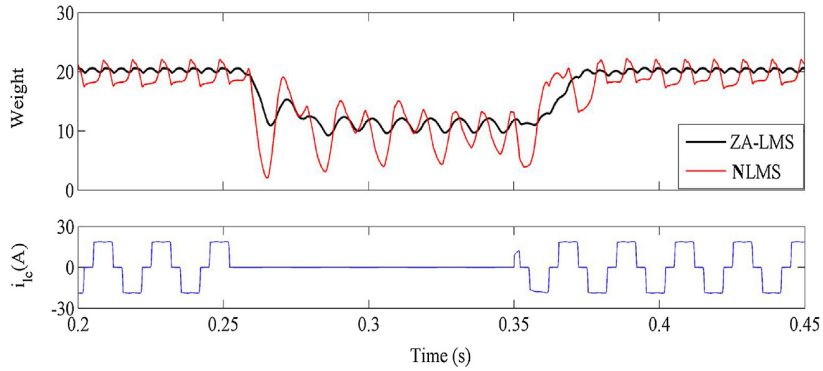


Fig. 10. Weight convergence with ZA-LMS and NLMS controller in steady state and dynamic load conditions.

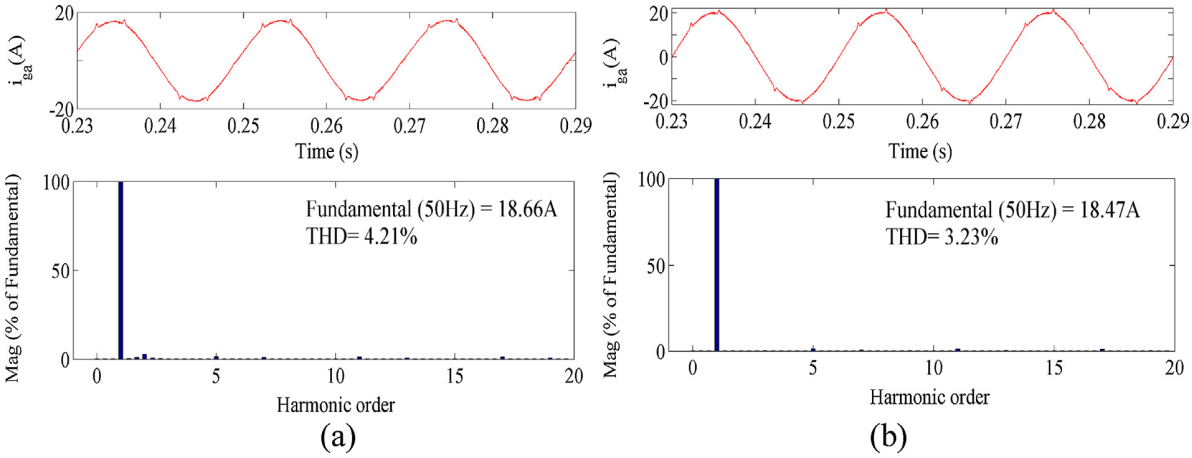


Fig. 11. Harmonic spectra of grid current using (a) NLMS and (b) dq0 frame.

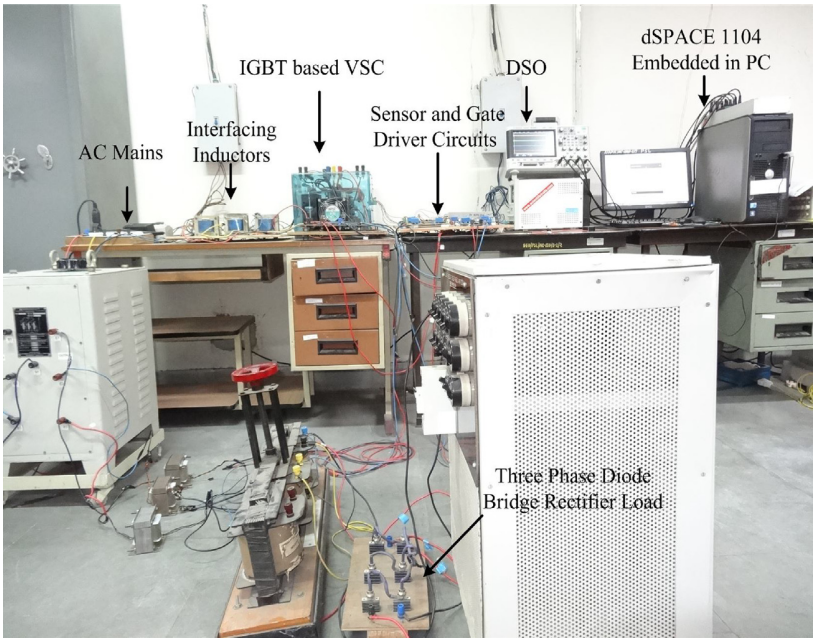


Fig. 12. Experimental setup.

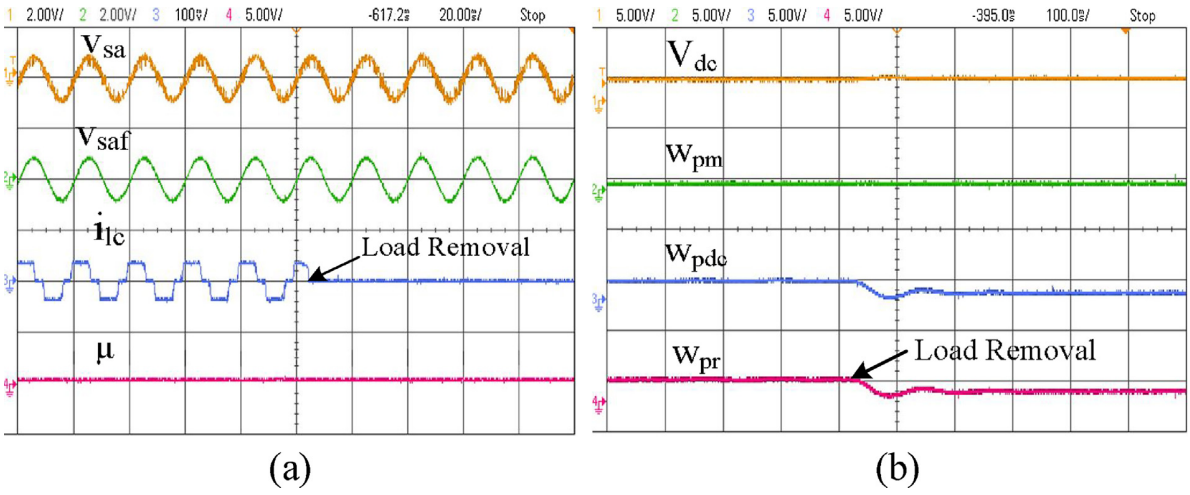


Fig. 13. Performance of ZA-LMS controller on grid connected converter (a) v_{sa}, v_{saf}, i_{lc} and step size (b) V_{dc}, w_{pm}, w_{pdc} and w_{pr}.

5.5. Comparative behavior of the ZA-LMS controller with NLMS and dq0 frame controller

The ZA-LMS based controller is compared with conventional controllers such as NLMS and dq0 frame. Fig. 10 depicts convergence of weighted value of load current (phase 'a') with ZA-LMS and NLMS based control in steady state and unbalanced load conditions. The maximum and minimum value of weight is dependent upon load current variations. For the SPV considered in the paper, the range of values of these fundamental active and reactive currents not only depends upon load considered but also solar irradiance, DC and AC bus PI controllers output. From Fig. 10, the value of fundamental active weight can be seen around 20 ± 0.3 A (as weights are obtained from currents, therefore their unit is in Ampere) in steady state load condition with ZA-LMS controller. Convergence of weight with ZA-LMS control offers fast response along with less steady state oscillations, whereas large oscillations are observed with NLMS control for various load conditions. Fundamental weight values are extracted from load currents (for the three phases) and averaged to compute fundamental active component (w_{pm}) as given in Eq. (14) using ZA-LMS controller. For balanced three phase system the value of w_{pm} is around 20 ± 0.3 A depending on the load considered. Fig. 11(a) and (b) presents harmonic spectra of grid current with NLMS and dq0 frame based controllers. It is observed from these spectra that grid current possess 4.21% and 3.23% THD with NLMS and dq0 controls, whereas THD of grid current obtained with ZA-LMS control is only 1.95%. Significant improvements in convergence speed, harmonic compensation, complexity of algorithm and computation burden on real time controller are observed with ZA-LMS based control over conventional controllers (summarized in Table 1).

6. Experimental results

Performance of ZA-LMS based controller is tested on implemented laboratory prototype of grid connected VSC working as a shunt active power filter. Fig. 12 presents the photograph of the experimental prototype developed in the laboratory. This system is implemented using a IGBTs based VSC, Hall effect voltage and current sensors, interfacing inductor, nonlinear loads and dSPACE 1104 R&D controller board. The proposed control algorithm is implemented on dSPACE 1104 controller using voltage and current sensors and their associated circuitry. Gating pulses are generated for VSC, after execution of the controller in dSPACE 1104. This system is tested at lower voltage of 110 V, 50 Hz due to laboratory equipment constraints and results are presented for steady state and dynamic operations. Parameters of the setup are specified in Appendix B.

6.1. Behavior of ZA-LMS based control algorithm on grid connected VSC

Fig. 13 depicts behavior of ZA-LMS controller on developed experimental prototype of grid connected VSC as shunt filter. Fig. 13(a) represent wave shapes of PCC voltage (v_{sa}), voltage after passing through band pass filter (v_{saf}), load current (i_{la}) and step size parameter (μ). Fig. 13(b) shows wave shapes of DC bus voltage (V_{dc}), average active power weight (w_{pm}), DC bus PI controller output (w_{pdc}) and reference active power weight (w_{pr}) in steady state and dynamic load conditions. These intermediate signals present satisfactory behavior of the controller which works well to extract weights under variety of loading conditions.

Table 1
Comparative performance of ZA-LMS based controller with NLMS and dq0.

Operations		ZA-LMS	NLMS	dq0
Type		Adaptive filter	Adaptive filter	Parks transformation
PLL requirement		Not required	Not required	Required
Complexity		Less	More	More
Convergence of weights	Steady state condition	Fast with less oscillations	Slower with oscillations	Not weight based
	Dynamic condition	Fast with less oscillations	Slower with large oscillations	Not weight based
Steady state error		Less	More	Less than NLMS
Harmonic compensation	Grid current, i_{ga}	18.64 A, THD 1.95%	18.66 A, THD 4.21%	18.47 A, THD 3.23%
	Load current, i_{la}	20.57 A, THD 27.87%	20.57 A, THD 27.87%	20.57 A, THD 27.87%
Sample time, T_s		50 μs	65 μs	70 μs

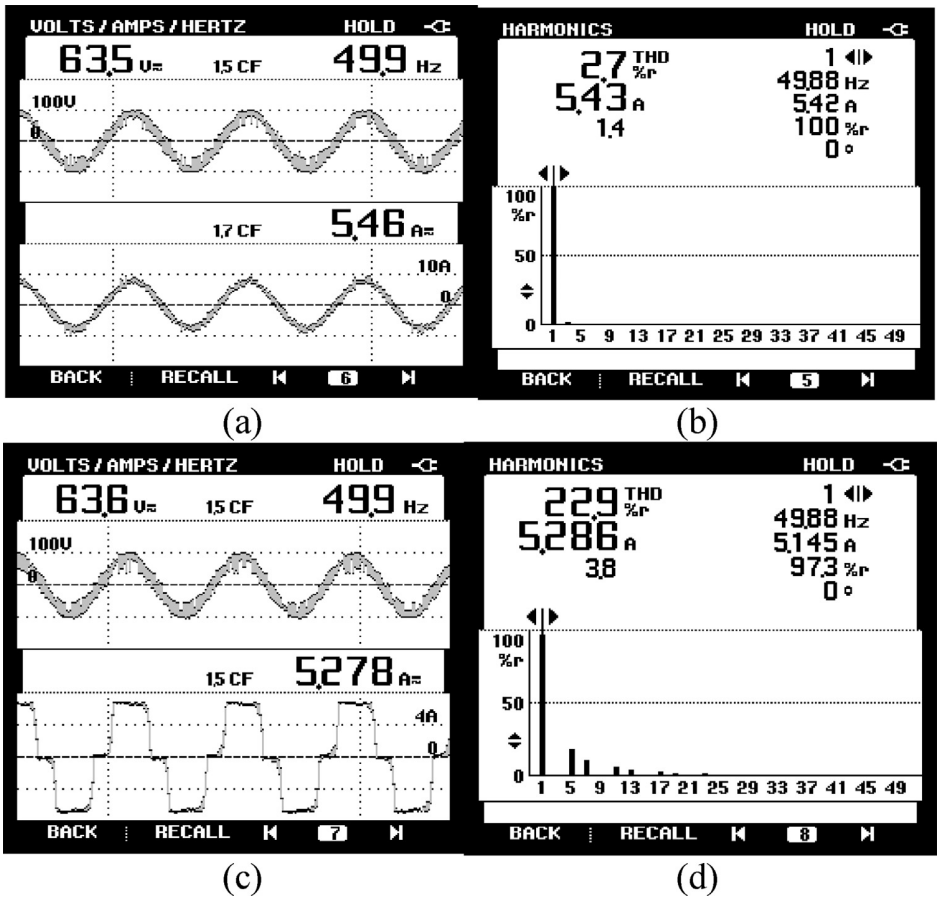


Fig. 14. Steady state performance of ZA-LMS controlled on developed shunt filter (a) v_{sa}, i_{ga} (b) harmonic spectrum of i_{ga} (c) v_{sa}, i_{la} (d) Harmonic spectrum of i_{la}.

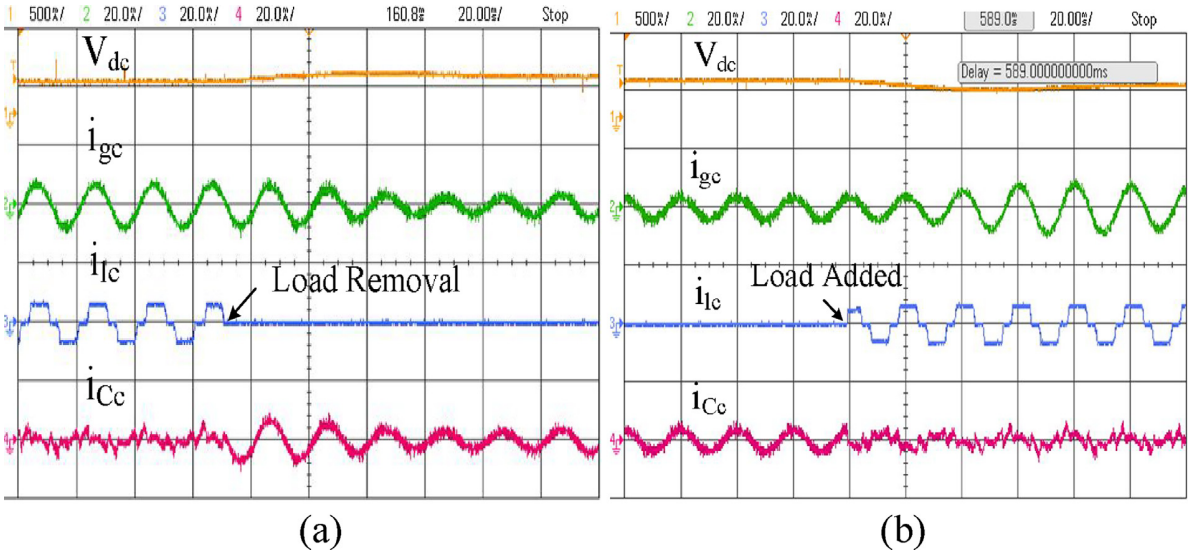


Fig. 15. Dynamic behavior of shunt filter using ZA-LMS controller (a) V_{dc}, i_{gc}, i_{lc} and i_{Cc} with load removal (b) V_{dc}, i_{gc}, i_{lc} and i_{Cc} with load added.

6.2. Behavior of controller in steady state and dynamic load conditions

Fig. 14 presents steady state behavior of controller for achieving shunt filtering. Fig. 14(a) and (b) depicts grid current (i_{ga}) with PCC voltage (v_{sa}) and harmonic spectrum of grid current. This spectrum shows 2.7% THD in load current. Fig. 14(c) and (d) shows load current (i_{la}) with PCC voltage (v_{sa}) and harmonic spectra of load current. This shows 22.9% THD in load current. Therefore, it can be concluded from these results that due to controller action, the grid current meets THD less than limit (<5%) specified in international standards.

Behavior of ZA-LMS based control algorithm with dynamic load condition is shown in Fig. 15(a) and (b), when phase 'c' of load is switched off. These results present wave patterns of DC bus voltage (V_{dc}), grid current (i_{gc}), load current (i_{lc}) and converter current (i_{Cc}) under load removal and increased load respectively. It can be concluded from these results that grid current has been maintained balanced and sinusoidal even with removal of one phase of load and DC bus voltage is well regulated to maintain reference voltage in dynamic load condition.

7. Conclusions

A grid connected solar photovoltaic system (SPV) has been designed and controlled using a new algorithm. A 20 kW SPV array has been modeled with DC–DC boost converter and MPPT for feeding load connected at the PCC. The SPV array has been integrated to the grid with three phase voltage source converter (VSC) having self-sustained DC bus and interfacing inductors. A control algorithm based on ZA-LMS technique has been developed for generation of reference grid currents and gating pulses for three phase VSC. The behavior of the ZA-LMS control for SPV system has been verified under linear as well as nonlinear loads. This system with ZA-LMS based control has demonstrated satisfactory operation for feeding load real power demand along with power quality compensation features such as maintaining grid at unity power factor, harmonics elimination, and load unbalancing. This system operation is observed in both the PFC and VR modes. Grid current THD is achieved to be 1.95% and 2.1% in both the PFC and VR modes respectively in simulation. Performance of the proposed controller has been compared with conventional controllers NLMS and dq0 frame. Better performance of ZA-LMS controller has been observed over other controllers for various characteristics such as weight convergence, mathematical complexity, computational burden on real time controller and harmonic compensation. This designed controller has been tested on developed laboratory prototype of grid connected converter working as a shunt active power filter. Controller has been implemented using dSPACE 1104 and its performance has been verified for various load conditions. Harmonic spectrum in the experimental results shows 2.7% THD in grid current which has been within the limit specified by international standards. Experimental results have also been presented for dynamic load condition, which shows satisfactory performance of the controller for balancing the load and achieving load compensation features.

Acknowledgement

The authors are thankful to the Department of Science and Technology, Government of India for the Sponsored Project (EMR/2016/001874).

Appendix A.

AC grid: 415 V (L–L), 50 Hz; feeder impedance $L_s = 1.5$ mH, $R_s = 0.07\ \Omega$; non-linear load: three phase full bridge diode rectifier with 15 Ω and 100 mH; linear load: 20 kV A with 0.8 lagging pf, C_{dc}: 1650 μF; DC bus voltage, V_{dc}: 800 V; DC bus PI gains: $k_{pd} = 0.3$, $k_{id} = 8$; AC bus PI gains: $k_{pq} = 0.012$, $k_{iq} = 0.011$; PWM current controller PI gains: $k_{p(iga)} = 0.11$, $k_{p(igb)} = 0.11$, $k_{p(igc)} = 0.11$; $L_f = 3$mH, $C_f = 5$ μF.

Appendix B.

AC grid: 110 V (L–L), 50 Hz; feeder impedance $L_s = 1$ mH, $R_s = 0.3\ \Omega$; non-linear load: three phase full bridge diode rectifier with 15 Ω and 100 mH; C_{dc}: 1650 μF; DC bus voltage V_{dc}: DC bus PI 200 V; $L_f = 2.3$mH.

References

[1] N. Hamrouni, M. Jraidi, A. Dhouib, A. Cherif, Design of a command scheme for grid connected PV systems using classical controllers, Electr. Power Syst. Res. 143 (2017) 503–512.
[2] C. Jain, B. Singh, A three-phase grid tied SPV system with adaptive DC link voltage for CPI voltage variations, IEEE Trans. Sustain. Energy 7 (2016) 337–344.
[3] S. D'Souza, Luiz A.C. Lopes, XueJun Liu, Comparative study of variable size perturbation and observation maximum power point trackers for PV systems, Electr. Power Syst. Res. 80 (2010) 296–305.
[4] T. Esram, P.L. Chapman, Compression of photovoltaic array maximum power point tracking technique, IEEE Trans. Energy Convers. 22 (2007) 439–449.
[5] N. Ponkarthik, K.K. Murugavel, Performance enhancement of solar photovoltaic system using novel Maximum Power Point Tracking, Int. J. Electr. Power Energy Syst. 60 (2014) 1–5.
[6] N.E. Zakzouk, M.A. Elsaharty, A.K. Abdelsalam, A.A. Helal, B.W. Williams, Improved performance low-cost incremental conductance PV MPPT technique, IET Renew. Power Gener. 10 (2016) 561–574.
[7] Ö. Çelik, Ahmet Teke, A hybrid MPPT method for grid connected photovoltaic systems under rapidly changing atmospheric conditions, Electr. Power Syst. Res. 152 (2017) 194–210.
[8] J. Ahmed, Z. Salam, An improved perturb and observe (P&O) maximum power point tracking (MPPT) algorithm for higher efficiency, Appl. Energy 150 (2015) 97–108.
[9] C.B. Salah, M. Ouali, Comparison of fuzzy logic and neural network in maximum power point tracker for PV systems, Electr. Power Syst. Res. 81 (2011) 43–50.
[10] G. Tsengenes, G. Adamidis, Investigation of the behavior of a three phase grid-connected photovoltaic system to control active and reactive power, Electr. Power Syst. Res. 81 (2011) 177–184.
[11] S. Mishra, Y. Mishra, Decoupled controller for single-phase grid connected rooftop PV systems to improve voltage profile in residential distribution systems, IET Renew. Power Gener. 11 (2017) 370–377.
[12] L.B.G. Campanhol, S.A.O. da Silva, A.A. de Oliveira, V.D. Bacon, Single-stage three-phase grid-tied PV system with universal filtering capability applied to DG systems and AC microgrids, IEEE Trans. Power Electron. 32 (2017) 9131–9142.
[13] IEEE Recommended Practice and Requirements for Harmonic Control in Electric Power Systems, IEEE Std. 519, 1992.
[14] A.K. Verma, B. Singh, D.T. Shahani, Current synchronous detection based control of grid interfaced solar photovoltaic power generating system, 2013 Annual IEEE India Conference (INDICON) (2013) 1–6.
[15] B. Singh, C. Jain, S. Goel, ILST control algorithm of single-stage dual purpose grid connected solar PV system, IEEE Trans. Power Electron. 29 (2014) 5347–5357.
[16] R.N. Tripathi, A. Singh, T. Hanamoto, Design and control of LCL filter interfaced grid connected solar photovoltaic (SPV) system using power balance theory, Int. J. Electr. Power Energy Syst. 69 (2015) 264–272.
[17] R. Agarwal, I. Hussain, B. Singh, Three-phase grid-tied single-stage solar energy conversion system using LLMS control algorithm, IET Renew. Power Gener. 10 (2016) 1638–1646.
[18] M. Badoni, A. Singh, B. Singh, Adaptive neurofuzzy inference system least-mean-square-based control algorithm for DSTATCOM, IEEE Trans. Ind. Inform. 12 (2016) 483–492.
[19] Pedro M. Almeida, Pedro G. Barbosa, Jorge L. Duarte, Paulo F. Ribeiro, Comprehensive synchronous reference frame discrete-time modeling of a grid-connected PV for fast DC-side voltage control, Electr. Power Syst. Res. 150 (2017) 162–168.
[20] M. Badoni, A. Singh, B. Singh, Variable forgetting factor recursive least square control algorithm for DSTATCOM, IEEE Trans. Power Deliv. 30 (2015) 2353–2361.
[21] S. Rokade, B. Bandyopadhyay, V. Agarwal, S. Mishra, Control of single-stage grid-connected three-phase solar photovoltaic system using sliding mode control, in: IECON 2015—41st Annual Conference of the IEEE Industrial Electronics Society, Yokohama, 2015, pp. 3749–3754.
[22] S. Haykin, Adaptive Filter Theory, 4th ed., Pearson Education, New Delhi, India, 2005.
[23] J. Chen, C. Richard, Y. Song, D. Brie, Transient performance analysis of zero-attracting LMS, IEEE Signal Process. Lett. 23 (2016) 1786–1790.
[24] Y. Chen, Y. Gu, A.O. Hero, Sparse LMS for system identification, in: 2009 IEEE International Conference on Acoustics, Speech and Signal Processing, Taipei, 2009, pp. 3125–3128.
[25] W. Zhao, S.C. Chan, Design and implementation of a variable step-size transform domain NLMS adaptive filter, in: 2015 IEEE Region 10 Conference (TENCON), Macao, 2015, pp. 1–3.
[26] N. Mohan, T.M. Undeland, W.P. Robbins, Power Electronics: Converters, Applications, and Design, 3rd ed., Wiley India Pvt. Ltd., New Delhi, India, 2002.
[27] R.N. Tripathi, A. Singh, M. Badoni, A MATLAB-simulink-based solar photovoltaic array (SPVA) module with MPPT, in: 2013 International Conference on Emerging Trends in Communication, Control, Signal Processing and Computing Applications (C2SPCA), Bangalore, 2013, pp. 1–6.
[28] R. Poley, Control Theory Fundamentals, 3rd ed., CreateSpace, 2015.

INTERNATIONAL JOURNAL OF HYDROGEN ENERGY XXX (2018) 1–16



Available online at www.sciencedirect.com

ScienceDirect

journal homepage: www.elsevier.com/locate/he



Hybrid control approach for PV/FC fed voltage source converter tied to grid

Priyanka Chaudhary[*], *M. Rizwan*

Department of Electrical Engineering, Delhi Technological University, Delhi, 110042, India

ARTICLE INFO

Article history:
Received 31 August 2017
Received in revised form
30 January 2018
Accepted 19 February 2018
Available online xxx

Keywords:
Grid integrated PV systems
Voltage source converter
Incremental conductance MPPT
Gradient descent back propagation neural network
Power quality

ABSTRACT

A hybrid and adaptive control approach for solar photovoltaic system and fuel cell fed voltage source converter (VSC) is presented in this work. Further maximum power from solar photovoltaic array is extracted by using incremental conductance (INC) based maximum power point tracking approach. This hybrid approach combines $I \cos \phi$ technique and gradient descent back propagation learning (GDBP) neural network (NN) to extract fundamental components from load current for efficient harmonics compensation and provides power quality improvement and support the three-phase AC grid by supplying power to the grid and as well as connected loads. The proposed system includes photovoltaic (PV) array, a voltage source converter (VSC), ripple filter and combination of linear and non-linear loads. The proposed control approach provides a fast response during dynamic conditions as well. Results of the proposed control technique also compared with the other available control techniques for its superiority analysis. The developed control technique is demonstrated by using MATLAB/SIMULINK platform.

© 2018 Hydrogen Energy Publications LLC. Published by Elsevier Ltd. All rights reserved.

Introduction

Electrical energy is the foundation for basic day to day needs of humans. Depleting fossil fuels and the environment concerns lead to set the alternative energy sources such as solar, hydrogen fuel cell as a replacement to the traditional options for electricity generation [1]. Solar Photovoltaic systems (PV) and hydrogen fuel cells (FC) are most widely used renewable energy sources (RES) because of various advantages such as high efficiency and minimal environmental impact [2–6]. Modern power systems are witnessing the significant impact of PV systems as distributed generation (DG) to motivate the clean, pollution-free and decentralized electricity generation units. Integration of RES based power generation systems at the utility grid level increase the power generation as well as create some negative impacts such as voltage limit violation at the point of common coupling (PCC), frequency variations, grid stability issues, etc. because of intermittent nature of PV systems. Grid-integrated RES must follow the grid codes and regulations which has been defined by the authorities to accommodate the RES based generation systems. IEEE 1547, IEC 61727 and VDE-AR-N4105 are major standards for RES integration as a distribution generator (DG) in low voltage (LV) distribution systems [7]. DC/AC converter (Voltage source converter) is used converts the DC obtained from PV systems into AC to supply power to the AC loads and connect to the grid [8–11]. Control of voltage source converter (VSC) in a grid integrated system plays a vital role to control and synchronize the system with the grid. VSC control is used the estimation of active, reactive current components as a basic unit of control architecture. Further, the VSC control efficient performance

* *Corresponding author*. Department of Electrical Engineering, Delhi Technological University, Bawana Road, Delhi, 110042, India.
E-mail address: priyankach.iilm@gmail.com (P. Chaudhary).

https://doi.org/10.1016/j.ijhydene.2018.02.131

0360-3199/© 2018 Hydrogen Energy Publications LLC. Published by Elsevier Ltd. All rights reserved.

Please cite this article in press as: Chaudhary P, Rizwan M, Hybrid control approach for PV/FC fed voltage source converter tied to grid, International Journal of Hydrogen Energy (2018), https://doi.org/10.1016/j.ijhydene.2018.02.131

Nomenclature

A	Diode ideality factor
C	DC link capacitor (μF)
D	Duty cycle
E_{fc}	Reversible open circuit voltage (Volts)
E^0	Standard reversible cell voltage (Volts)
f_{max}	Maximum switching frequency (kHz)
f_{sw}	Switching frequency (kHz)
h	Current ripple
i_{fc}	Output current of fuel cell (Ampere)
I_{in}	Input current (Ampere)
i_{La}, i_{Lb}, i_{Lc}	Load currents of phase 'a', 'b' and 'c' respectively (Ampere)
I_{Lp}	Fundamental active current component
I_{Lq}	Fundamental reactive current component
I_{MPP}	PV current at maximum power point (Ampere)
i_{psa}	Active reference component of grid current
I_{PV}	PV array output current (Ampere)
i_{qsa}	Reactive reference component of grid current
I_{rs}	Reverse saturation current of diode (Ampere)
i_{sa}, i_{sb}, i_{sc}	Grid currents of phase 'a', 'b' and 'c' respectively (Ampere)
i^*_{sa}, i^*_{sb}, i^*_{sc}	Reference currents of phase 'a', 'b' and 'c' respectively (Ampere)
I_{sc}	Photocurrent (Ampere)
k	Boltzman constant ($1.38 \times 10\text{-}^{23}$ JK^{-1})
K	Polarization constant
k_i	Short circuit current/temperature coefficient
K_i	Integral gain of PI controller
K_p	Proportional gain of PI controller
L_b	Input inductor of boost converter (mH)
L_f	Interfacing inductor (mH)
N	Number of cells in stack
N_p	Number of cells connected in parallel in PV module
N_s	Number of cells connected in series in PV module
P_i	Mole fraction of species
P_{pv}	PV power (W)
q	Electric charge (1.602×10^{-19} C)
R	Universal gas constant (JK/Kmol)
R_{fc}	Equivalent resistance of fuel cell (Ohms)
R_p	Shunt resistance (Ω)
R_s	Series resistance (Ω)
S	Solar irradiance (W/m^2)
T	Cell temperature (Kelvin)
T_k	Actual temperature (Kelvin)
T_{ref}	Reference temperature (Kelvin)
u_{pa}, u_{pb}, u_{pc}	In phase unit templates of phase voltages
u_{qa}, u_{qb}, u_{qc}	Quadrature unit templates of phase voltages
V_a, V_b, V_c	Phase voltage of utility grid (Volts)
v_{ab}, v_{bc}, v_{ca}	Line voltage of utility grid (Volts)
V_{act}	Activation overvoltage (Volts)
V_{con}	Concentration overvoltage (Volts)
V_{dc}	DC link voltage (Volts)
V^*_{dc}	Reference DC link voltage (Volts)
V_{fc}	Output voltage of fuel cell (Volts)
V_{MPP}	PV voltage at maximum power point (Ampere)
V_{ohm}	Ohm voltage (Volts)
V_{pv}	PV output voltage (Volts)
V_t	Voltage at point of common coupling (Volts)
V^*_t	Reference voltage at point of common coupling (Volts)
V_{te}	Error between sensed and reference voltage at point of common coupling (Volts)
w_{pdc}	Active current component
w_{qt}	Function of reactive loss current component
w_{pv}	Feed forward weight function of solar power
w_{ap}, w_{bp}, w_{cp}	Updated weights for hidden layer of active components
w_{aq}, w_{bq}, w_{cq}	Updated weights for hidden layer of reactive components
w_{Lp}	Mean active component of load current
w_{Lq}	Mean reactive component of load current

Greek Symbols

α	Learning rate
μ	Micro
Ω	Ohm
ϕ	Phase

depends on algorithm utilized to generate the reference currents which will further use to generate the gate pulses IGBT switches. Utilization of RES based systems (PV and FC) as a DG makes essential to deploy efficient and coordinated control measures for the integration and measurement issues. These control approaches are useful in accommodating and facilitating the integration of RES systems into distribution grid with numerous advantages.

PV and FC power generation systems are utilized to meet the load demand and supplying the excessive generation to the grid as well to mitigate numerous challenges related to power quality. Single stage and two stage system topologies are being used by researchers to integrate the PV systems to the grid and reported in the literature [12]. In literature, various control techniques are widely available for effective integration of DG systems with reactive power compensation and harmonics elimination capabilities to the distribution grid at PCC [13–31]. As per available literature, broadly classified as conventional, intelligent and adaptive techniques. Some of the conventional control techniques are Synchronous Reference Frame theory (SRFT), Enhanced phase locked loop based approaches, Instantaneous Reactive Power (IRP) theory, power balance theory based approach, conductance fryze, etc. Control techniques based on conventional approaches for VSC grid synchronization are not much successful for nonlinearities associated with RES based systems as these approaches possess overshoots and long settling time in response. Intelligent and adaptive approaches are key solutions to these issues which results in better accuracy and very fast dynamic response.

Please cite this article in press as: Chaudhary P, Rizwan M, Hybrid control approach for PV/FC fed voltage source converter tied to grid, International Journal of Hydrogen Energy (2018), https://doi.org/10.1016/j.ijhydene.2018.02.131

Moreover, Jain et al. [32] presented PV power generation system with an adjustable DC link voltage for voltage variations at PCC utilizing two-stage based circuit topology with interweaved DFSOGI (Double Frequency Second Order Generalized Integrator) based control technique to control multifunctional VSC for dynamic loads at PCC. Kannan et al. [33] developed I cos Φ based synchronization algorithm for DSTATCOM which gives far better source harmonic reduction, reactive power compensation and load compensation using Fuzzy Logic Controller (FLC) in comparison with the conventional Proportional Integral (PI) controller. A control scheme based on power conditioner unit (PCU) placed in parallel with the plant and works in a feed-forward mode to compensate the PV plant's output current distortion to reduce the current harmonics from PV system is presented in [34]. Singh et al. [33] developed grid integrated PV power generation system using a ANN based control algorithm which uses LMS (least mean-square) algorithm and known as Adaline (adaptive linear element). A hybrid control algorithm is proposed in [35] and called as gradient descent back propagation (GDBP)-based I cos ϕ for a distribution static compensator (DSTATCOM) to avail harmonic mitigation, power factor correction (PFC) mode under non-linear reactive loads. Artificial neural network based algorithms have complexity in learning needs large computational time. A substantial research is being carried out by the researchers for improving the performance of PV-DSTATCOM system with the help of various control algorithms to reduce computation time, provided more reliability and less complexity [36]. Various control approaches based on artificial neural networks (ANN) are available in the literature for various applications [37–47] but rarely available for PV fed VSC. Control algorithms, based on neural network techniques have many specific advantages such as feed forward, supervised, self-organization principles and reinforcement training etc. ANN has multilayer perceptron is a feasible solution to analyze the non-linearity in distribution system's load behavior. Moreover, fuel cells are being utilized for power generation for domestic and industry level applications. PV power generation combines with FC provides an attractive and efficient solution for increasing power generation. A typical fuel cell power generating system includes fuel cell stacks, a fuel processor, power conditioning unit (PCU) etc. FCs are high current and low voltage devices, so AC application of FC needs voltage boost before conversion to 220 V, 50 Hz AC. Samaiah et al. [48] investigated and compared the mitigation of low frequency (LF) current ripples by using cascaded converter with conventional push-pull converters for FC applications. A single stage, single phase FC for grid connected as well as standalone mode is proposed based on boost inverter by Jang et al. [49]. Bensmail et al. [50] presented modelling of a hybrid PV/FC system, which utilized a power conditioning unit (PCU) for effective management. Akin et al. [51] proposed a soft-switched space vector PWM controlled parallel resonant DC link based inverter for fuel cell applications. Further, authors used the proposed converter with an induction motor to evaluate the results of a controller. Behavior of PEM fuel cells has been investigated by authors in [52] for grid connected mode. Further, this study has been extended from practical conditions to material degradation during grid connected mode. However, multilevel inverters can serve effective practical solution for supplying increased power demand and less harmonics. Seyezhai et al. [53] investigated the use of single phase hybrid cascaded multilevel inverter (HCMLI) with a PEMFC. The proposed inverter controlled using a novel hybrid modulation technique which combines fundamental frequency switching scheme and variable frequency inverted sin pulse with modulation (FISPWM) technique. A hybrid power generating system consisting PV and FC was proposed by Bayrak et al. [54].

Further, to enhance more efficiency of PV systems, the maximum power point tracking (MPPT) of PV array is significantly important too. MPPT tracking is very complex because of non-linarites associated with PV system due to varying meteorological parameters. So many MPPT techniques have been developed and reported in literature by various researchers includes perturb and observe, incremental conductance, constant voltage, open circuit voltage, short circuit current, extremum seeking control and hybrid etc. [55–60], and other techniques based on artificial neural networks, fuzzy logic, genetic algorithms [61–64]. An INC based MPPT algorithm is used in this work to track the maximum power point of PV system to achieve fast response and convergence.

The main contributions of the present work are: A hybrid algorithm is proposed combining I cos ϕ technique and gradient descent back propagation learning (GDBP) neural network for PV/FC fed VSC to provide reactive power compensation and mitigation of power quality issues. The proposed system feed active power to the connected loads, provide reactive power compensation and support the grid. The feed forward back propagation technique has been chosen to deal the complex non-linear problems associated with the proposed system. However, performance of back propagation learning algorithm for multilayer feed forward NN highly depends on the learning rate and the complexity of the given problem to be modelled [65]. To speed up the convergence process with BPNN many algorithms were developed. These algorithms can be broadly classified into two types: heuristic techniques and standard numerical optimization technique. Heuristic techniques consist approaches such as gradient descent adaptive learning rate, gradient descent with momentum etc. Standard numerical optimization techniques includes conjugate gradient back propagation (CGBP) learning algorithm, quasi-newton back propagation (QNBP), resilient back propagation (RBP), etc. Learning rate for these methods is fixed and very difficult to find the optimal value. GDBP based NN is easy to implement for complex system and provides fast convergence in comparison with other algorithms. The proposed system exhibits very less static error and fast convergence, robustness, adaptive for dynamic loads, provides harmonics compensation, power factor correction, load balancing, etc. In this application, all the power quality related issues are achieved successfully by using the proposed control technique under both balanced and unbalanced linear/non-linear loading conditions. Maximum power from PV array is extracted using INC MPPT method with variations in solar irradiations. The performance of the developed system is validated through simulations carried out in MATLAB/Simulink platform.

Please cite this article in press as: Chaudhary P, Rizwan M, Hybrid control approach for PV/FC fed voltage source converter tied to grid, International Journal of Hydrogen Energy (2018), https://doi.org/10.1016/j.ijhydene.2018.02.131

System configuration

In the proposed system single stage circuit configuration is considered to integrate a 10 kW solar PV power generating system with the utility grid. Further, the developed system constitute a Solar PV array, VSC, ripple filter to remove the excessive fluctuations from the output of VSC, loads and grid which is shown in Fig. 1. The proposed system has been implemented in MATLAB/Simulink with an INC based MPPT algorithm to extract maximum power from PV array for various meteorological parameters. Hybrid approach using *I* cos ϕ technique GDBP neural network has been implemented to control the switching of VSC. System parameters are given in Table 1.

Table 1 – The developed system design specifications.

S. No.	Components of the test system model	Specifications
1.	AC Grid specifications	3 ϕ, 415 V, 50 Hz,
2.	PV array voltage (V_{MPP})	700 V
3.	PV array current (I_{MPP})	13.5 A
4.	PV array power (P_{MPP})	10 kW
5.	Interfacing inductor ($L_{fa} = L_{fb} = L_{fc}$)	2.6 mH
6.	DC bus capacitor (C_{DC})	10mf
7.	DC bus voltage (V_{DC})	700 V
8.	Ripple Filter (R_f) and (C_f)	5 Ω, 10 μ F
9.	Gains for DC link controller K_{pd} and K_{id}	0.25 and 0.28
10.	Gains for AC bus controller K_{pt} and K_{it}	0.75 and 0.67

Modelling of fuel cell

A fuel cell works on the electrochemical process and converts fuel (hydrogen) energy into form of electricity. It works on principal of chemical reaction between oxidant and the fuel for producing electrical energy with heat and water byproducts [48,66–71]. The equivalent circuit of a solid oxide fuel cell (SOFC) is shown in Fig. 2.

Tafel equation is used to calculate the output voltage of a fuel cell.

$$V_{fc} = E_{fc} - V_{act} - V_{con} - V_{ohm} \quad (1)$$

where, E_{fc} denotes the reversible open circuit voltage, V_{act} is activation overvoltage, V_{con} shows the concentration

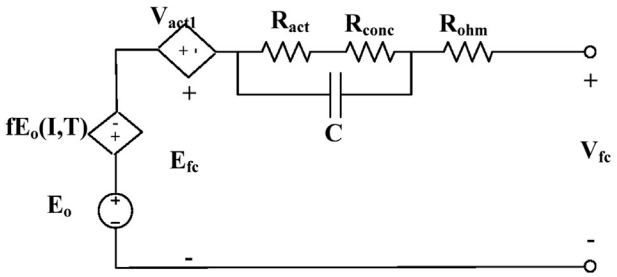


Fig. 2 – Equivalent circuit of a solid oxide fuel cell (SOFC.).

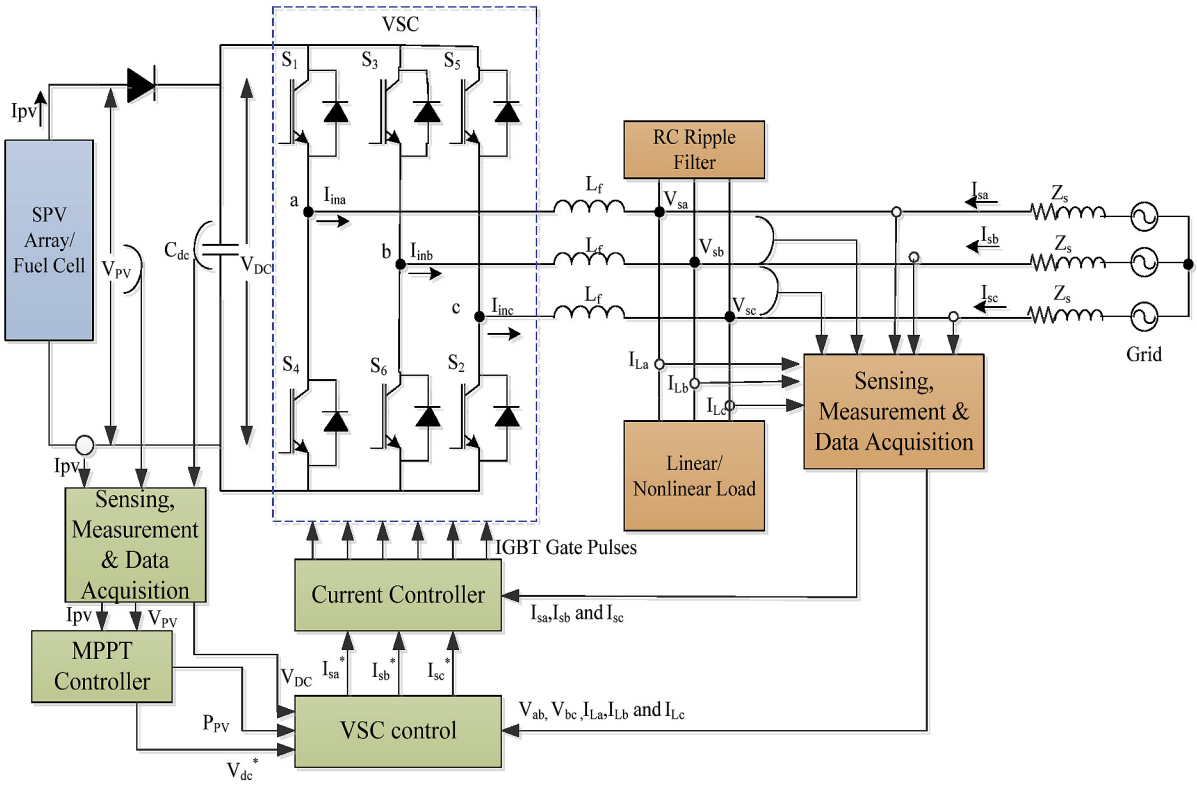


Fig. 1 – Test system schematic.

Please cite this article in press as: Chaudhary P, Rizwan M, Hybrid control approach for PV/FC fed voltage source converter tied to grid, International Journal of Hydrogen Energy (2018), https://doi.org/10.1016/j.ijhydene.2018.02.131

overvoltage and V_{ohm} is the ohm voltage. Value of the reversible open circuit voltage (E_{fc}) can be found using Nernst equation:

$$E_{fc} = N\left\{E^0 + \frac{RT}{2F}\ln\left(\frac{PH_2}{PH_{20}}(PO_2)^{0.5}\right)\right\} \quad (2)$$

where, E^0 is standard reversible cell voltage, R denote universal gas constant (JK/kmol), T shows the stack temperature in Kelvin, N is the number of cells in stack and $P_i$is mole fraction of species. Ohmic voltage in Eq. (1) is because of electrical resistance of electrodes and the resistance offered due to flow of ions in the electrolyte and can be computed using Ohm's law:

$$V_{ohm} = i_{fc}{*}R_{fc} \quad (3)$$

V_{act} is the voltage due to cell current and hydrogen concentration and can be written as:

$$V_{act} = -A\ln i_{fc} \quad (4)$$

Constant A depends on the type of cell used, Concentration voltage $V_{conc}$is ignored by considering the operation in linear region and hydrogen, oxygen flow constant. Fuel cells possesses several advantages over other renewable energy resources such as high efficiency, high power quality, less or no moving parts which results in lesser noise, low maintenance and fuel flexibility. Efficiency of fuel cells varies 40–60% and in cogeneration applications can be further improve up to 90%. Cost is also lesser now a days due to high temperature operation which removes the requirement of precious metal catalysts.

Modelling of solar PV array

A PV array combines various PV modules in series and parallel configuration as per requirements of the end user. A PV cell, basic unit of PV module works as an active transducer and directly converts the photon energy of sunlight directly into electricity after being exposed to sunlight or any other high intensity light source. The present section deals with the mathematical modelling of PV array which can be model by considering a single PV cell as a basic unit [72,73].

The output current equation can be written for a single diode model as:

$$I_{PV} = I_{sc}N_p - N_sI_o\left[\exp\left\{\frac{q(V_{PV} + I_{PV}Rs)}{N_sAkT}\right\} - 1\right]V_{PV} + \frac{I_{PV}Rs}{Rp} \quad (5)$$

In Eq. (5) k is the Boltzmann constant (1.38×10^{-23} J K^{-1}), q depicts the electronic charge (1.602×10^{-19} C), T shows the cell temperature (K); A is known as diode ideality factor, R_s and R_p are known as series resistance (Ω) and shunt resistance (Ω) respectively. N_S and N_p are number of cells connected in series and parallel respectively. I_{sc} is the photocurrent in amperes produced at the standard condition (25 °C and 1000 W/m^2) and is given as:

$$I_{sc} = \left[I_{scref} + K_i\left(T_k - T_{ref}\right)\right]{*}I_r/1000 \quad (6)$$

K_i shows the short-circuit current/temperature coefficient at I_{scref} (0.00065 A/K), T_k and T_{ref} are the actual and reference temperature in Kelvin respectively, I_r shows the actual solar irradiance which incident at the surface of device and 1000 W/m^2 at standard reference conditions. The saturation current (I_o) is a function of ambient temperature and which can be expressed as;

$$I_o = I_{rs}\left[\frac{\left(\frac{T}{T_{ref}}\right)^3 e^{qCg}}{Ak}{*}\left(\frac{1}{T_{ref}} - \frac{1}{T}\right)\right] \quad (7)$$

Reverse saturation current I_{rs} of diode can be written as:

$$I_{rs} = I_{scref} + \left[\exp\left(\frac{qVoc}{NskAT}\right) - 1\right] \quad (8)$$

V_{oc} is the open-circuit voltage output of solar PV cell. A Vikram Solar ELDORA 270 of 270.66 W_p solar PV module has been consider to obtain a 10 KW_p PV system. PV and IV characteristics of system is presented in Fig. 3 for different solar irradiances conditions.

VSI parameters

A three phase voltage source converter (VSC) of 10 kV A, 415 V is used to convert DC voltage to AC voltage. The VSC consists

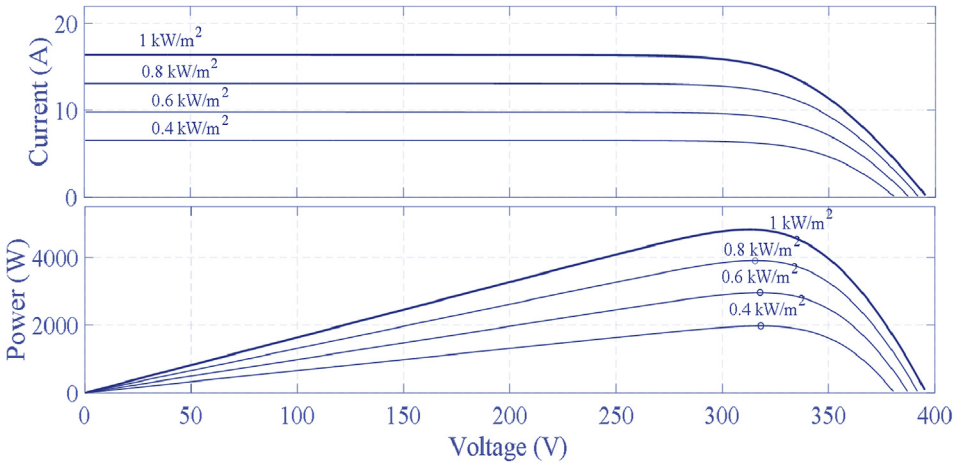


Fig. 3 – PV-IV characteristics at different solar irradiances PV system.

Please cite this article in press as: Chaudhary P, Rizwan M, Hybrid control approach for PV/FC fed voltage source converter tied to grid, International Journal of Hydrogen Energy (2018), https://doi.org/10.1016/j.ijhydene.2018.02.131

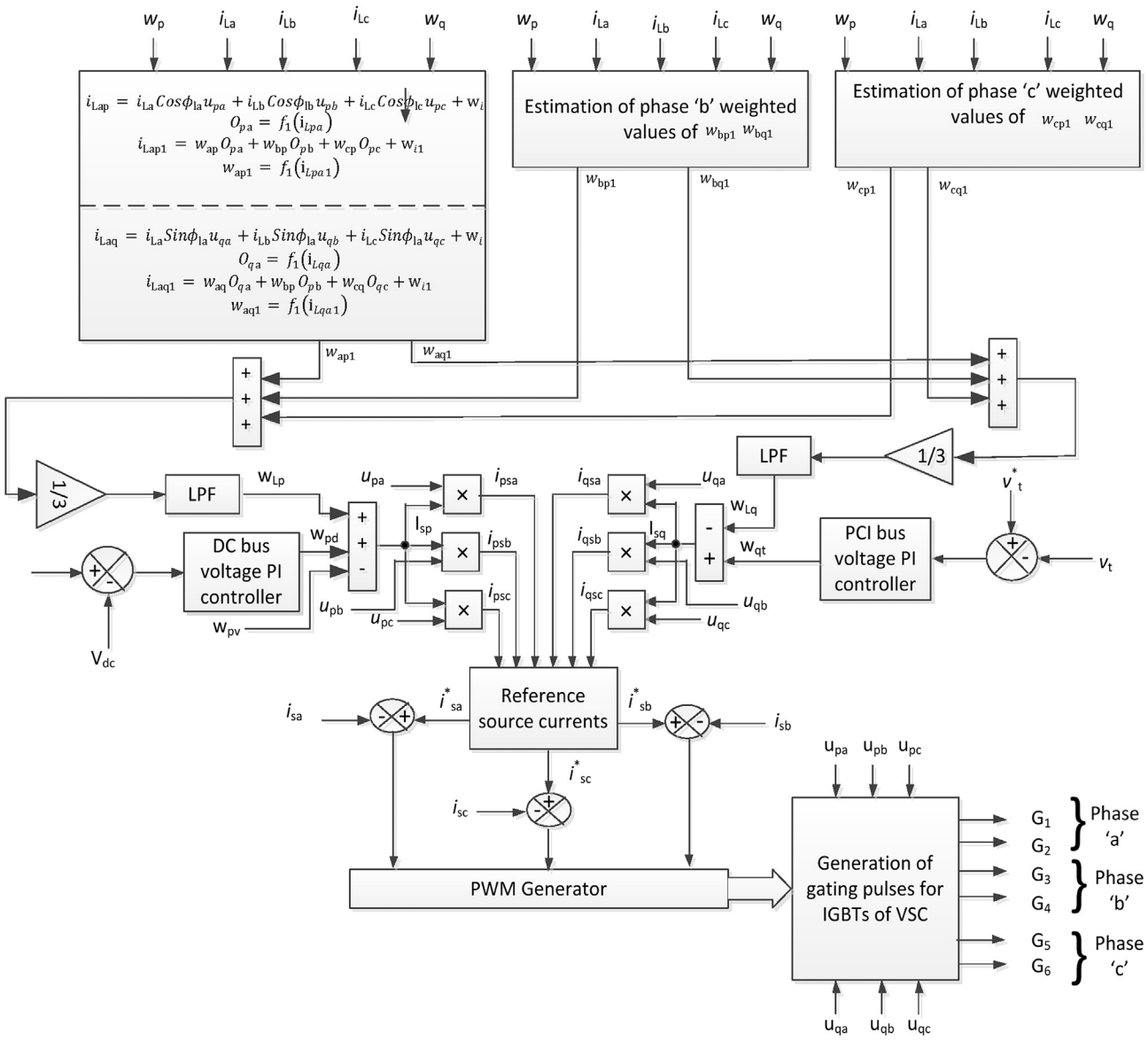


Fig. 4 – Detailed schematic of the proposed VSC control algorithm.

of six IGBTs and other design specifications are provided in Table 1. DC link Capacitors (C)

$$C = \frac{I_{in}D}{\Delta v f_{sw}} \tag{9}$$

Interfacing Inductor Design (L_f): The interfacing inductors for VSC is very important part and accuracy of tracking given reference current is highly affected by the design. The design value of L_f can be computed from the given equation:

$$L_f = \frac{V_{dc}}{4hf_{max}} \tag{10}$$

Here, 2 h depicts the maximum current ripple and f_{max} denotes the maximum frequency of the control approach for switching purpose. A Passive RC filter is design by series combination of resistance and capacitances.

Control strategy

Maximum power point tracking (MPPT) control

Incremental conductance (INC) method has been used in this work which is found better in comparison to the other control techniques [74]. INC method works on the fact that the slope of the PV module output PV curve is zero at maximum power point (MPP). Slope of this curve is positive for the values which are lesser then MPP and negative for more than MPP. PV maximum output power can be achieved by using the derivative of PV power output w.r.t voltage and equating to zero.

$$\frac{dP}{dV} = I + v\frac{dI}{dV} = 0 \tag{11}$$

Please cite this article in press as: Chaudhary P, Rizwan M, Hybrid control approach for PV/FC fed voltage source converter tied to grid, International Journal of Hydrogen Energy (2018), https://doi.org/10.1016/j.ijhydene.2018.02.131

Further by using Eq. (11) expressions can be obtained:

$$\frac{dI}{dV} \cong \frac{\Delta I}{\Delta V} = -\frac{I_{MPP}}{V_{MPP}} \tag{12}$$

$$\frac{dP}{dV} = 0 \quad \frac{\Delta I}{\Delta V} = -\frac{I}{V} \quad \text{at MPP}$$

$$\frac{dP}{dV} > 0 \quad \frac{\Delta I}{\Delta V} > -\frac{I}{V} \quad \text{left side of MPP}$$

$$\frac{dP}{dV} < 0 \quad \frac{\Delta I}{\Delta V} < -\frac{I}{V} \quad \text{right side of MPP}$$

VSC control

The present section deals with the detail modelling of hybrid control approach for VSC which combines GDBP base neural network and *i* cos ϕ control technique Fig. 4. This algorithm is very robust and provides fast response and convergence. The algorithm is used to compute weighted value of fundamental components of active currents (w_{ap}, w_{bp} and w_{cp}) and fundamental components of active currents (w_{aq}, w_{bq} and w_{cq}) from load currents. The weight training includes three stages such as input signals, error signal calculations and weights correction. Weights of the network is initialized for analyzing the value of corresponding neurons. The detail analysis of the proposed control technique is explained in a systematic procedure without requirement of any particular learning process. The detailed algorithm responsible for generation of switching signal patterns are provided in 3.2.1 to 3.2.4.

Calculation of amplitude of terminal voltage and unit templates
Sensed line voltages (v_{ab}, v_{bc}, v_{ca}) at PCC is used to calculate phase voltages, the amplitude of phase voltages (V_a, V_bandV_c) are calculated as Eq. (13):

$$v_a = \frac{2v_{ab} + v_{bc}}{3}, v_b = \frac{-v_{ab} + v_{bc}}{3}, v_c = \frac{-v_{ab} - 2v_{bc}}{3} \tag{13}$$

The terminal voltage amplitude (V_t) at PCC can be computed as:

$$V_t = \sqrt{\left[\frac{2\left(v_a^2 + v_b^2 + v_c^2\right)}{3}\right]} \tag{14}$$

The in-phase unit templates ofv_a, v_b and v_c are obtained as:

$$u_{pa} = \frac{v_a}{V_t}, u_{pb} = \frac{v_b}{V_t}, u_{pc} = \frac{v_c}{V_t} \tag{15}$$

Quadrature unit templates can be obtained from in phase unit templates as:

$$u_{qa} = \frac{u_{pc}}{\sqrt{3}} - \frac{u_{pb}}{\sqrt{3}}, u_{qb} = \frac{\sqrt{3}u_{pa}}{2} + \frac{u_{pb} - u_{pc}}{2\sqrt{3}}, u_{qc} = \frac{u_{pb} - u_{pc}}{2\sqrt{3}} - \frac{\sqrt{3}u_{pa}}{2} \tag{16}$$

Estimation of active and reactive loss components
The voltage at dc link capacitor (V_{dc}) is measured and sensed to compare it with the reference dc link voltage (V_{dc}^*) to derive the active loss component.

$$V_{dce}(k) = V_{dc}^*(k) - V_{dc}(k) \tag{17}$$

A PI controller is used to minimize the error (V_{dce}) of reference V_{dc}^* and sensedV_{dc}, output of which gives active current component(w_{pdc}) and regulates the DC link voltage. The controller's output at k^{th} instant is computed as:

$$w_{pd}(k) = w_{pd}(k-1) + k_{pd}\{V_{dce}(k) - V_{dce}(k-1)\} + k_{id}V_{dce}(k) \tag{18}$$

The reactive loss component is calculated by taking error V_{te} between sensed and reference terminal voltage $V_t$and V_t^* respectively at PCC processed through a PI controller. Reactive loss component is responsible to maintain the constant AC terminal voltage.

$$V_{te}(k) = V_t^*(k) - V_t(k) \tag{19}$$

The controller output at k^{th} instant is given as:

$$w_{qt}(k) = w_{qt}(k-1) + k_{pt}\{V_{te}(k) - V_{te}(k-1)\} + k_{it}V_{te}(k) \tag{20}$$

In above equation w_{qt} is a function of the reactive loss current component, k_{pt} and k_{it} are proportional and integral gains respectively.

A feed forward weight can be estimated as a function of solar power (P_{PV}) and AC terminal voltage at PCC (V_t) to achieve fast dynamic response and calculated as:

$$w_{PV}(k) = \frac{2P_{PV}(k)}{3V_t} \tag{21}$$

Estimation of fundamental active and reactive load current
Fundamental active and reactive load current components extraction has been done by considering load currents (i_{La}, i_{Lb}, i_{Lc}) as inputs to the input layer and consideringw$_i$ as initial weight. The three layer GDBP based NN architectures for calculating weighted fundamental active and reactive current components are shown in Appendix A. Weighted values of fundamental active current components for all phases are given by Eq. (22):

$$\left.\begin{aligned} i_{Lap} &= i_{La}Cos\phi_{la}u_{pa} + i_{Lb}Cos\phi_{lb}u_{pb} + i_{Lc}Cos\phi_{lc}u_{pc} + w_i \\ i_{Lbp} &= i_{La}Cos\phi_{la}u_{pa} + i_{Lb}Cos\phi_{lb}u_{pb} + i_{Lc}Cos\phi_{lc}u_{pc} + w_i \\ i_{Lcp} &= i_{La}Cos\phi_{la}u_{pa} + i_{Lb}Cos\phi_{lb}u_{pb} + i_{Lc}Cos\phi_{lc}u_{pc} + w_i \end{aligned}\right\} \tag{22}$$

The above extracted components are processed through a sigmoid activation function. Output can be obtained as O_{pa}, O_{pb}, O_{pc} and calculated as:

$$\left.\begin{aligned} O_{pa} &= f_1(i_{Lpa}) = \frac{1}{1+e^{-i_{Lpa}}} \\ O_{pb} &= f_1(i_{Lpb}) = \frac{1}{1+e^{-i_{Lpb}}} \\ O_{pc} &= f_1(i_{Lpc}) = \frac{1}{1+e^{-i_{Lpc}}} \end{aligned}\right\} \tag{23}$$

The above output values are being input to hidden layer of the neural network considered here with initial weight ofw$_{i1}$. Further the output of this layer can be written as fundamental componenti_{Lap1}, i_{Lbp1} and i_{Lcp1} withw_{ap}, w_{bp} and w_{cp} as updated weighted of respective phase currents active components.

$$\left.\begin{aligned} i_{Lap1} &= w_{ap}O_{pa} + w_{bp}O_{pb} + w_{cp}O_{pc} + w_{i1} \\ i_{Lbp1} &= w_{ap}O_{pa} + w_{bp}O_{pb} + w_{cp}O_{pc} + w_{i1} \\ i_{Lcp1} &= w_{ap}O_{pa} + w_{bp}O_{pb} + w_{cp}O_{pc} + w_{i1} \end{aligned}\right\} \tag{24}$$

Please cite this article in press as: Chaudhary P, Rizwan M, Hybrid control approach for PV/FC fed voltage source converter tied to grid, International Journal of Hydrogen Energy (2018), https://doi.org/10.1016/j.ijhydene.2018.02.131

The updated weights for hidden layer computed as:

$$\left.\begin{array}{l} w_{ap} = w_p + \alpha\{w_p - w_{ap1}\}f'(i_{Lap1})O_{pa} \\ w_{bp} = w_p + \alpha\{w_p - w_{bp1}\}f'(i_{Lbp1})O_{pb} \\ w_{cp} = w_p + \alpha\{w_p - w_{cp1}\}f'(i_{Lcp1})O_{pc} \end{array}\right\} \quad (25)$$

In Eq. (25) expression w_p shows the average weighted value of active current component $f'(i_{Lap1})$and first derivative ofi_{Lap1}. $\alpha$is the learning rate and used to speed up the convergence process.

$$\left.\begin{array}{l} w_{ap1} = f_1(i_{Lpa1}) = \dfrac{1}{1+e^{-i_{Lpa1}}} \\ w_{bp1} = f_1(i_{Lpb1}) = \dfrac{1}{1+e^{-i_{Lpb}1}} \\ w_{cp1} = f_1(i_{Lpc1}) = \dfrac{1}{1+e^{-i_{Lpc1}}} \end{array}\right\} \quad (26)$$

w_{ap1}, w_{bp1} and w_{cp1} as fundamental weighted values of respective phase currents active components. The mean active component of load currents (w_{Lp}) is obtained by averaging the weighted components and given as

$$w_{Lp} = \frac{(w_{ap1} + w_{bp1} + w_{cp1})}{3}. \quad (27)$$

Further, the estimation of fundamental reactive current components for load currents have been calculated in similar way using the developed control. The sensed load currents(i_{La}, i_{Lb}, i_{Lc}).

$$\left.\begin{array}{l} i_{Laq} = i_{La}Sin\phi_{la}u_{qa} + i_{Lb}Sin\phi_{la}u_{qb} + i_{Lc}Sin\phi_{la}u_{qc} + w_i \\ i_{Lbq} = i_{La}Sin\phi_{la}u_{qa} + i_{Lb}Sin\phi_{la}u_{qb} + i_{Lc}Sin\phi_{la}u_{qc} + w_i \\ i_{Lcq} = i_{La}Sin\phi_{la}u_{qa} + i_{Lb}Sin\phi_{la}u_{qb} + i_{Lc}Sin\phi_{la}u_{qc} + w_i \end{array}\right\} \quad (28)$$

Similar to the active components, above extracted components are processed through a sigmoid activation function. Output can be obtained as O_{qa}, O_{qb}, O_{qc} and calculated as:

$$\left.\begin{array}{l} O_{qa} = f_1(i_{Lqa}) = \dfrac{1}{1+e^{-i_{Lqa}}} \\ O_{qb} = f_1(i_{Lqb}) = \dfrac{1}{1+e^{-i_{Lqb}}} \\ O_{qc} = f_1(i_{Lqc}) = \dfrac{1}{1+e^{-i_{Lqc}}} \end{array}\right\} \quad (29)$$

Again output values are being input to hidden layer of the neural network with initial weight ofw_{i1}. Further the output of this layer can be written as fundamental componenti_{Laq1}, i_{Lbq1} and i_{Lcq1} withw_{aq}, w_{bq} and w_{cq} as updated weighted of respective phase currents reactive components.

$$\left.\begin{array}{l} i_{Laq1} = w_{aq}O_{qa} + w_{bq}O_{qb} + w_{cq}O_{qc} + w_{i1} \\ i_{Lbq1} = w_{aq}O_{qa} + w_{bq}O_{qb} + w_{cq}O_{qc} + w_{i1} \\ i_{Lcq1} = w_{aq}O_{qa} + w_{bq}O_{qb} + w_{cq}O_{qc} + w_{i1} \end{array}\right\} \quad (30)$$

The updated weights for hidden layer computed as:

$$\left.\begin{array}{l} w_{aq} = w_q + \alpha\{w_q - w_{aq1}\}f'(i_{Laq1})O_{qa} \\ w_{bq} = w_q + \alpha\{w_q - w_{bq1}\}f'(i_{Lbq1})O_{qb} \\ w_{cq} = w_q + \alpha\{w_q - w_{cq1}\}f'(i_{Lcq1})O_{qc} \end{array}\right\} \quad (31)$$

In above expression w_p shows the average weighted value of reactive current component $f'(i_{Laq1})$and first derivative of i_{Laq1}.

$$\left.\begin{array}{l} w_{aq1} = f_1(i_{Lqa1}) = \dfrac{1}{1+e^{-i_{Lqa1}}} \\ w_{bq1} = f_1(i_{Lqb1}) = \dfrac{1}{1+e^{-i_{Lqb}1}} \\ w_{cq1} = f_1(i_{Lqc1}) = \dfrac{1}{1+e^{-i_{Lqc1}}} \end{array}\right\} \quad (32)$$

w_{aq1}, w_{bq1} and w_{cq1} as fundamental weighted values of respective phase currents reactive components. The mean reactive component of load currents (w_{Lq}) is obtained by averaging the weighted components and given as:

$$w_{Lq} = \frac{(w_{aq1} + w_{bq1} + w_{cq1})}{3}. \quad (33)$$

Reference grid currents and IGBTs switching signals generation
The total fundamental active current component of load current can be defined as:

$$I_{Lp} = w_{pd} + w_{Lp} - w_{PV} \quad (34)$$

The active reference components of grid currents can be obtained as:

$$i_{psa} = I_{Lp}{}^*u_{pa}, i_{psb} = I_{Lp}{}^*u_{pb}, i_{psc} = I_{Lp}{}^*u_{pc} \quad (35)$$

Fundamental reactive current component of load current can be defined in similar manner:

$$I_{Lq} = w_{qt} + w_{Lq} \quad (36)$$

The reactive reference component of grid currents can be obtained as:

$$i_{qsa} = I_{Lq}{}^*u_{qa}, i_{qsb} = I_{Lq}{}^*u_{qb}, i_{qsc} = I_{Lq}{}^*u_{qc} \quad (37)$$

Net fundamental reference grid currents $(i^*_{sa}, i^*_{sb}, i^*_{sc})$ can be obtained as:

$$i^*_{sa} = i_{psa} + i_{qsa}, i^*_{sb} = i_{psb} + i_{qsb}, i^*_{sc} = i_{psc} + i_{qsc} \quad (38)$$

VSC switching signals has been produced by comparing reference $(i^*_{sa}, i^*_{sb}, i^*_{sc})$ and actual (i_{sa}, i_{sb}, i_{sc}) grid currents for individual phase and error is passed through a PI current regulator for minimization.

Results

The proposed system is developed considering MPP rating of 10 kW for PV array. Validation of the proposed control

Table 2 – Performance parameters of the proposed system.

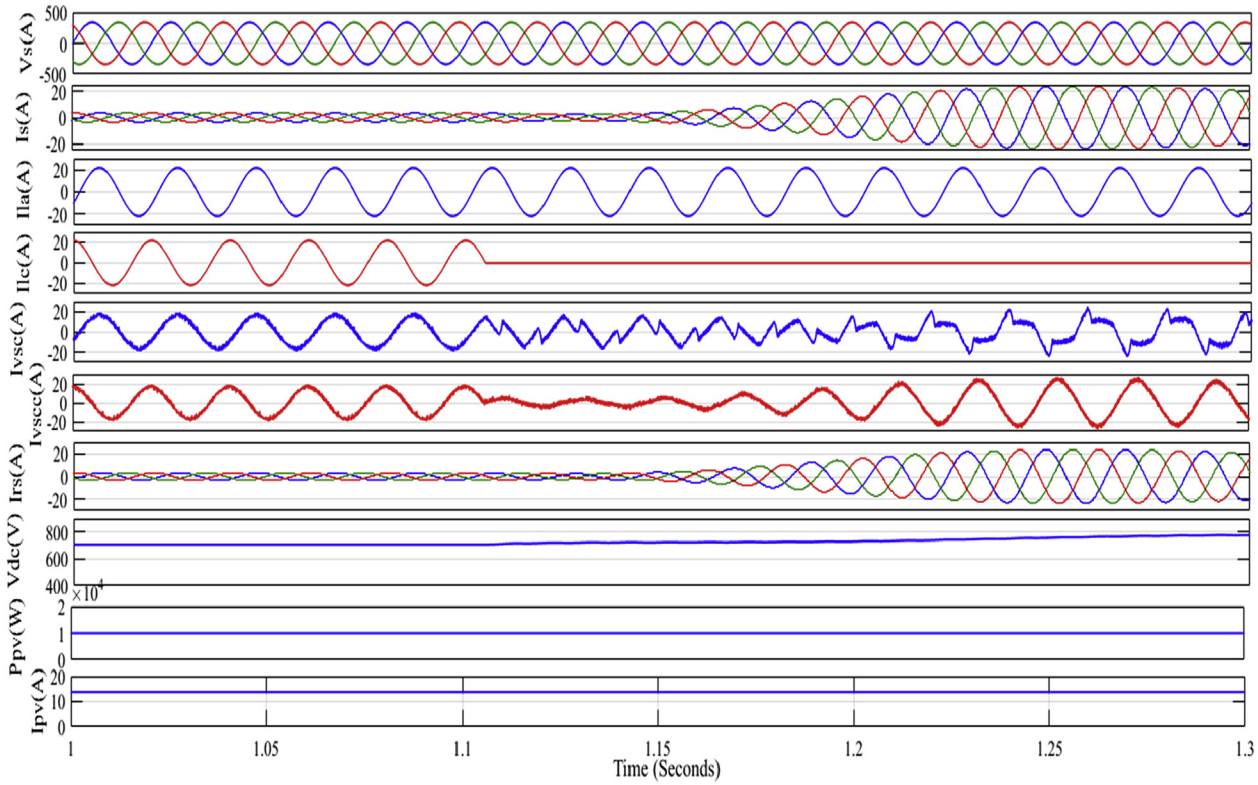
Operating mode	Parameters	*I* cosϕ based control algorithm	*GDBP NN I* cosϕ based control algorithm
ZVR	Grid current (A), %THD at PCC	23.27 A, 4.16%	23.13 A, 1.24%
	Load current (A), %THD at PCC	40.58 A, 41.62%	42.54 A, 40.77%
	V_{dc} (V)	718 V	694 V

Please cite this article in press as: Chaudhary P, Rizwan M, Hybrid control approach for PV/FC fed voltage source converter tied to grid, International Journal of Hydrogen Energy (2018), https://doi.org/10.1016/j.ijhydene.2018.02.131

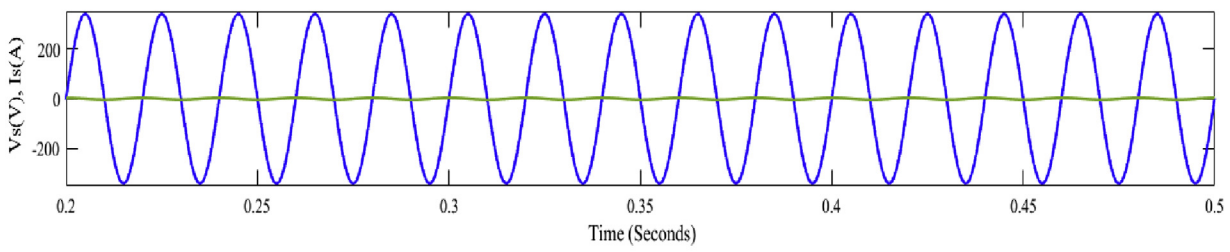
technique for PV/FC fed VSC is done by simulating the developed system using MATLAB/Simulink simulation platform. The specifications for various components are given in appendix (Table 3). Performance of the system is validated under different scenarios such as linear loads with power factor correction (PFC) mode, dynamic linear loads, nonlinear loads with power factor correction (PFC) mode, dynamic nonlinear loads, variable solar irradiance etc.

Table 3 – Comparative analysis of proposed GNN controller with existing ANN based controllers.

Algorithm	Settling Time (sec)	DC link voltage overshoot (V)	DC link voltage undershoot (V)	THD % (Grid current)
SRF	0.096	820	763	5.63
$I\cos\phi$	0.095	850	786	4.16
Conductance fryze	0.11	957	796	5.79
ANN based	0.095	815	774	3.25
ANFIS based	0.094	820	779	2.78
FLC based	0.095	815	780	2.25
Adaptive	0.095	810	770	2.18
GDBP NN $I\cos\phi$	0.093	790	775	1.24



(a)



(b)

Fig. 5 – (a) Performance parameters (b) Waveforms of phase 'a' of source voltage and source current.

Please cite this article in press as: Chaudhary P, Rizwan M, Hybrid control approach for PV/FC fed voltage source converter tied to grid, International Journal of Hydrogen Energy (2018), https://doi.org/10.1016/j.ijhydene.2018.02.131

System performance under linear load for PFC

The performance of the proposed neural network based $I\cos\phi$ algorithm is evaluated for a linear load. The performance of the proposed controller is investigated on the basis of different performance indices such as grid voltage (v_s), grid current (i_s), load current (i_L), VSC current (i_{vsc}), grid real power (P_g), grid reactive power (Q_g), PCC terminal voltage (V_t), PV array power (P_{pv}), PV array current (I_{pv}) and dc-link voltage (V_{dc}) which are shown in Fig. 5(a–b) under steady state linear load (at t = 0.2–0.3 s) conditions. Power factor is observed to be considerably enhanced, and can be identify from the voltage and current waveforms as shown in Fig. 5 (b). The PV system maintains to feed maximum power to the load and grid at unity power factor (UPF) operation.

System performance analysis under dynamic linear load for zero voltage regulation (ZVR)

If load draws reactive power with unbalanced nature then this may lead changes in the terminal voltage (V_t) at PCC. Fig. 6 (a) shows the performance of proposed control for unbalanced linear load in zero voltage regulation (ZVR) case. Phase 'c' of the given load is disconnected at 1.1 s, then also grid currents (i_s) are maintained sinusoidal with the help of VSC controller. The proposed controller takes appropriate action to incorporate the changes in the system. The PCC voltage (V_t) and DC link voltages are observed as 415 V and 700 V, respectively without significant fluctuations. Again in this case also the improvement of power factor can be observed by analyzing the behavior of grid voltage and grid current from Fig. 6 (b).

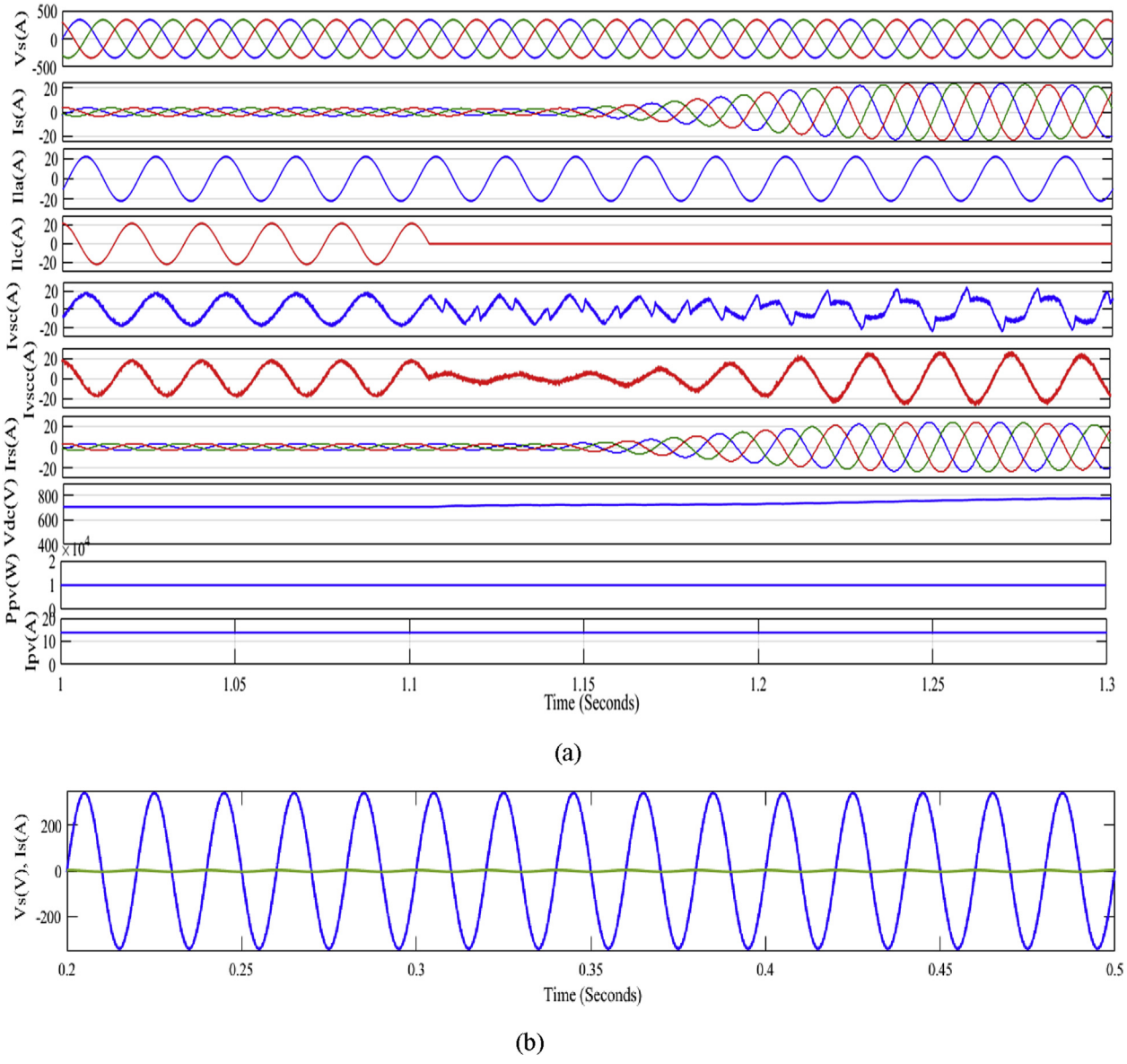


Fig. 6 – (a) Performance parameters (b) Waveforms of phase 'a' of source voltage and source current.

Please cite this article in press as: Chaudhary P, Rizwan M, Hybrid control approach for PV/FC fed voltage source converter tied to grid, International Journal of Hydrogen Energy (2018), https://doi.org/10.1016/j.ijhydene.2018.02.131

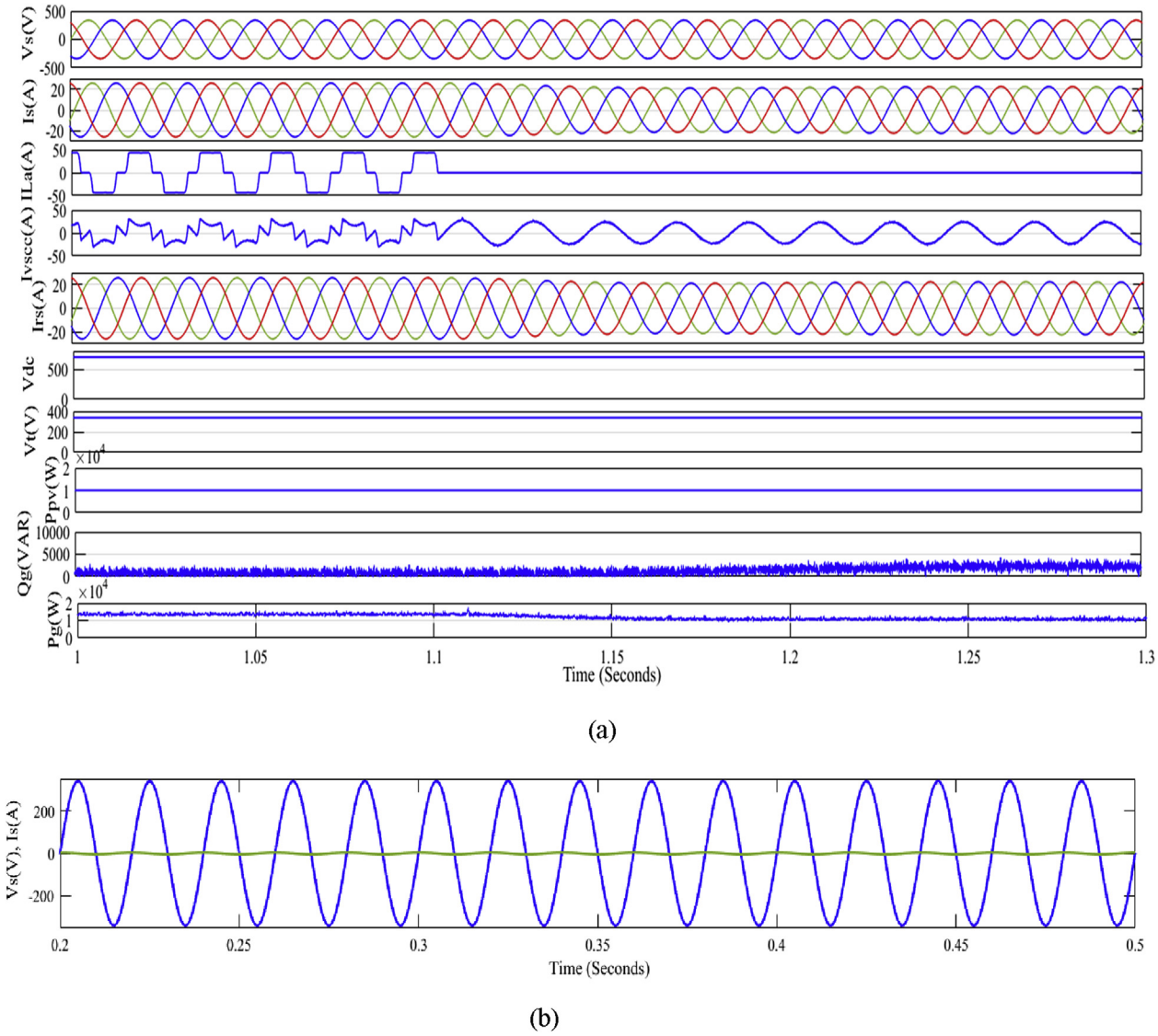


Fig. 7 – (a) Performance indices (b) Waveforms of phase 'a' of source voltage and source current.

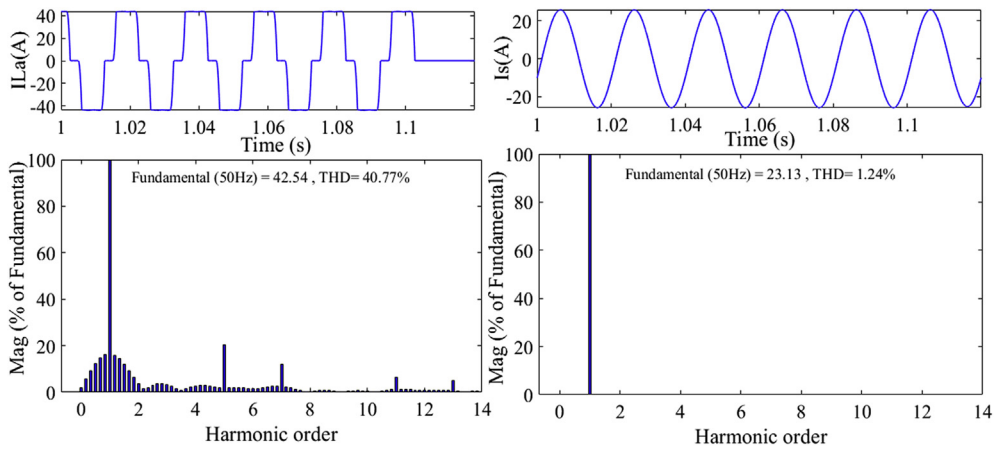


Fig. 8 – THD for (a) load current of phase 'a' (b) grid current.

Please cite this article in press as: Chaudhary P, Rizwan M, Hybrid control approach for PV/FC fed voltage source converter tied to grid, International Journal of Hydrogen Energy (2018), https://doi.org/10.1016/j.ijhydene.2018.02.131

The reactive power (Q_g) feeding by grid is equal to zero, hence the compensation is also done for linear loads which are consuming reactive power.

System performance analysis under non-linear load

Dynamic behavior of proposed controller under unbalanced nonlinear load conditions is shown in Fig. 7 (a) show for zero voltage regulation (ZVR) mode of operation with different performance indices. Phase 'c' of load is disconnected at 1.1 s, grid currents (i_s) are maintained sinusoidal with the help of VSC controller at required values. The PCC voltage (V_t) and DC link voltages are also maintained constant at 415 V and 700 V, respectively. Power factor improvement can be observed from Fig. 7 (b). Fig. 8 (a)-(b) shows the THDs at PCC for phase 'a' of load current, grid current respectively and obtained as 40.77%, 1.24% respectively, which is well within the limits of IEEE 519–2014 standard. Thus, the proposed algorithm effectively carries out the load balancing and harmonic compensation.

Further, the proposed control approach has been tested for FC fed inverter and shown in Fig. 9. This is the case when PV power is unavailable or less then to the threshold value due to less or zero irradiance (e.g. cloudy weather or during night time. Only the FC supplies the load power and support the utility grid. For this case also phase 'c' of load is disconnected at 1.1 s, here also controller works efficiently to maintain grid currents (i_s) sinusoidal and DC link voltage at near to the reference value. The PCC voltage (V_t) and DC link voltages are also maintained constant at 415 V and 700 V, respectively. Active power demand by the load is supplied by the FC in conjunction with the grid for linear and nonlinear loads condition, which can be seen from Fig. 10.

Performance under variable solar irradiance

The solar irradiance (S) is increased to 1000 W/m^2 from 600 W/m^2 at 0.5 s as can be seen in Fig. 11. PV power generation system is meeting the power demand of the load and excess

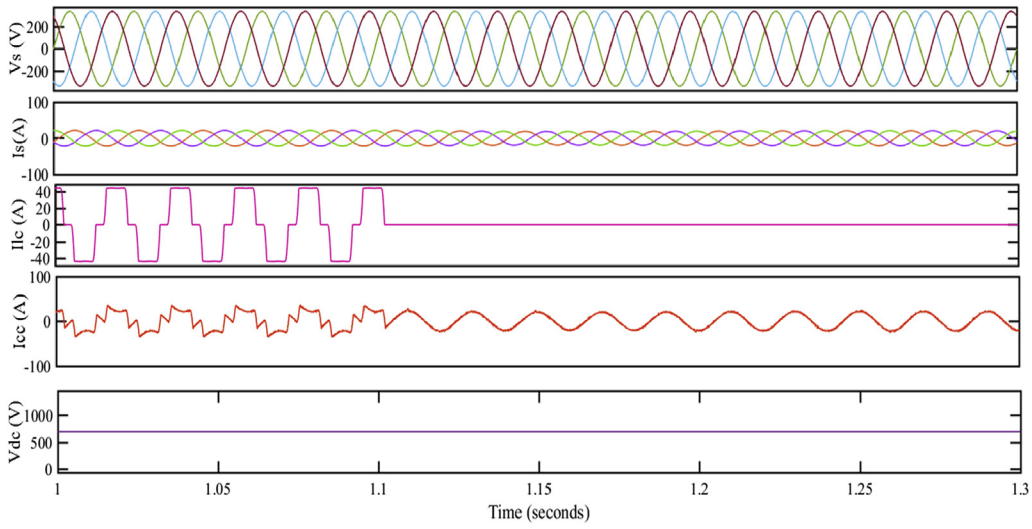


Fig. 9 – Control approach performance for FC fed inverter under nonlinear unbalanced load.

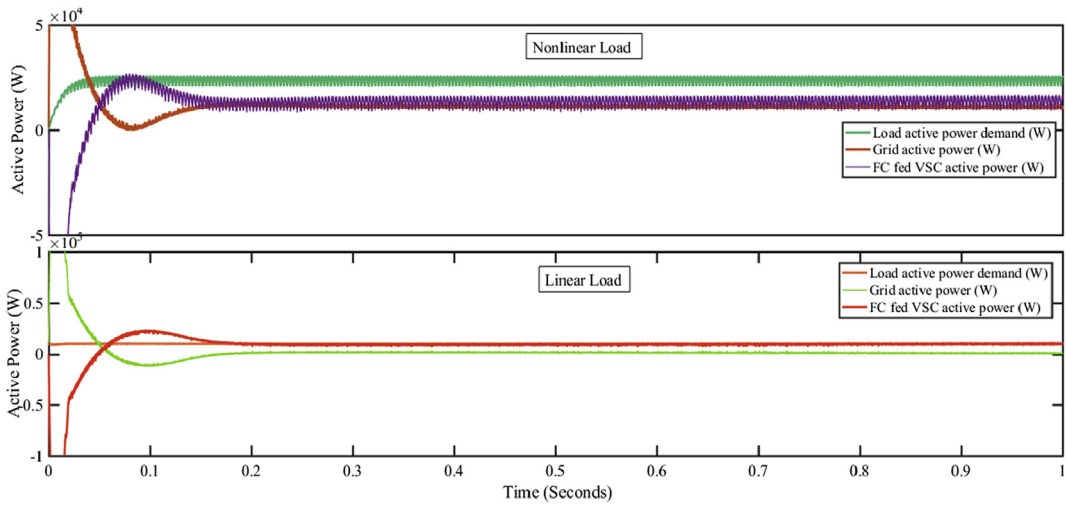


Fig. 10 – Control approach performance for FC fed inverter in terms of active power.

Please cite this article in press as: Chaudhary P, Rizwan M, Hybrid control approach for PV/FC fed voltage source converter tied to grid, International Journal of Hydrogen Energy (2018), https://doi.org/10.1016/j.ijhydene.2018.02.131

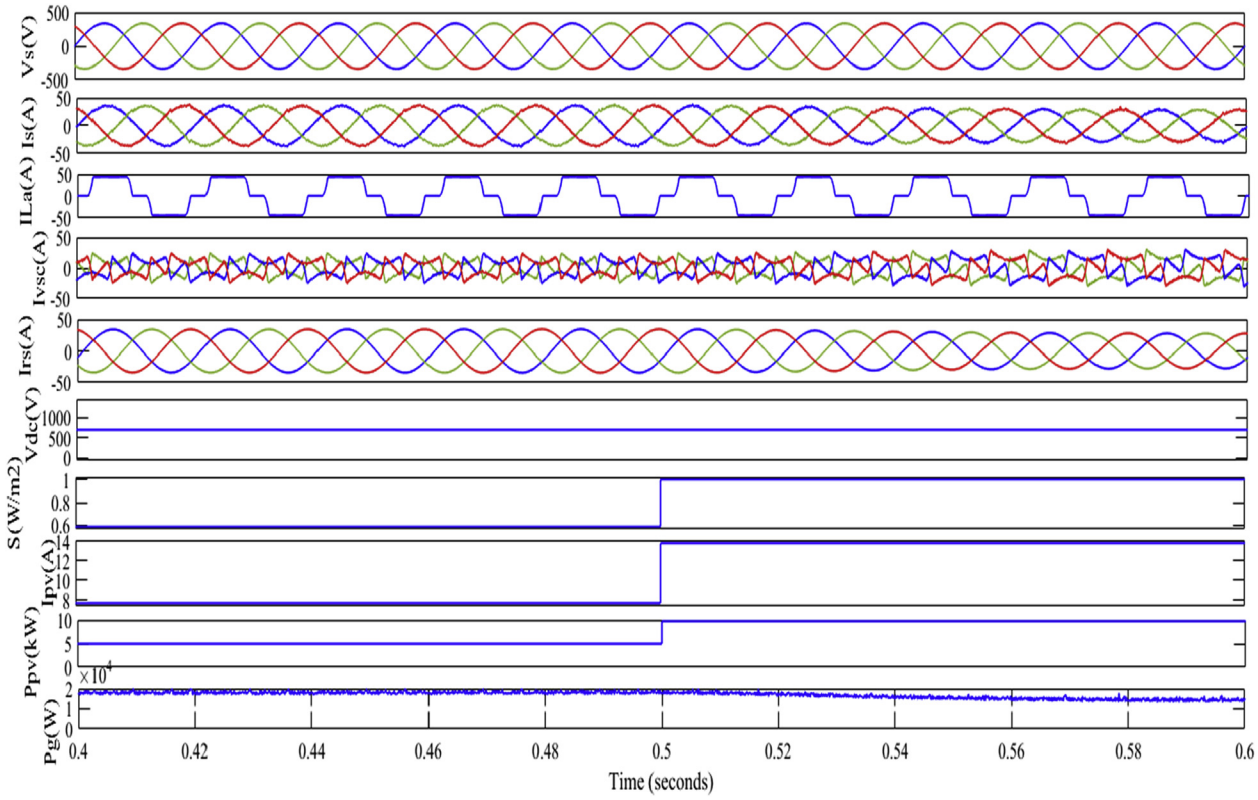


Fig. 11 – Performance parameters under non-linear load conditions for variable solar irradiance.

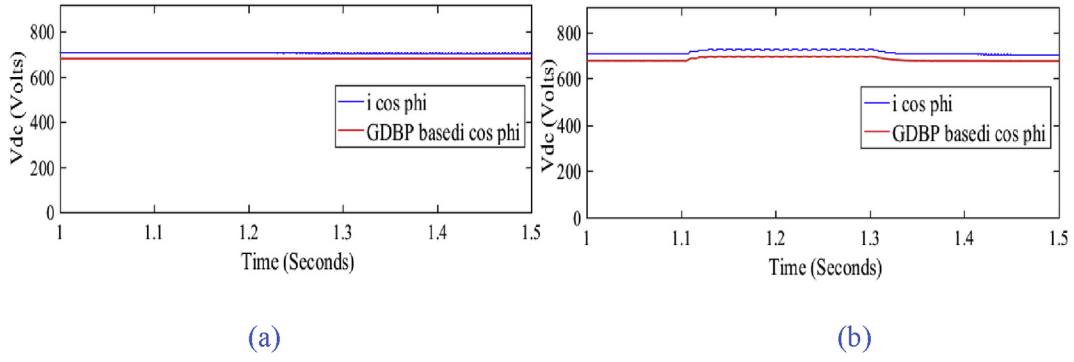


Fig. 12 – Comparison of V_{dc} for nonlinear load (a) balanced conditions (b) unbalanced conditions.

generation is being fed to the grid. Hence, the grid power (P_g) in Fig. 8 reducing after 0.5s when PV power (P_{pv}) is increasing. The system in case of variable solar irradiance keeps continue to extract maximum power from a PV system and operates at unity power factor (UPF). The source current is maintained to be sinusoidal with DC link voltage at its set reference point.

Comparative analysis of proposed algorithm with conventional approaches

The proposed control approach based on GDBP NN *icosϕ* algorithm has been analyzed and found satisfactory for each of the case discussed in the above result section. In present subsection the THD analysis of the proposed algorithm is being compared with the conventional *I* cosϕ based algorithm in Table 2 to show the superiority of the proposed algorithm.

The performance of proposed GDBP-based *I* cos ϕ control approach regarding V_{dc} is compared with *I* cos ϕ and shown in Fig. 12 (a) and (b) respectively for balanced and unbalanced loading conditions. The developed GDBP NN *I* cosϕ based control algorithm is observed as better than other conventional, intelligent and adaptive approaches and comparison is shown in Table 3 for dynamic nonlinear load. Conventional control algorithms such as SRF, *I* cosϕ, and conductance fryze algorithms, intelligent algorithms as ANN based algorithm, ANFIS based approaches, fuzzy logic controller (FLC) based and adaptive algorithm are compared by large undershoot in DC link voltage, overshoot in DC link voltage, settling time and

Please cite this article in press as: Chaudhary P, Rizwan M, Hybrid control approach for PV/FC fed voltage source converter tied to grid, International Journal of Hydrogen Energy (2018), https://doi.org/10.1016/j.ijhydene.2018.02.131

THD in grid currents, under dynamic load conditions. The proposed algorithm performs smoother and response of given algorithm found better than other approaches.

Conclusions

The system is developed in MATLAB simulation environment and performance of the proposed GDBP NN *icosϕ* based VSC control algorithm is observer for linear and nonlinear load under steady state and dynamic conditions. The control algorithm has successfully enhanced the performance of the developed RES based grid integrated system. The developed system is subjected to load unbalancing and variable solar insolation to validate the performance of the proposed controller and the results show satisfactory performance of the system with continuous operation under UPF mode with providing reactive power compensation, load balancing, maximum power extraction and grid harmonic reduction, gives very fast response. The system has acceptable limits of harmonics in grid currents and voltage fluctuations according to the IEEE-519 and IEEE-1547 standards. This has performed better for the grid current harmonic reduction, power factor improvement, voltage regulation and load balancing than other conventional methods. The developed control strategy shall be advantageous for power system engineers to integrate more RES based generation systems with the utility grid.

Appendix A

The three layer GDBP based NN architecture for calculating weighted fundamental active and reactive current components are shown in Figs. 13 and 14 respectively.

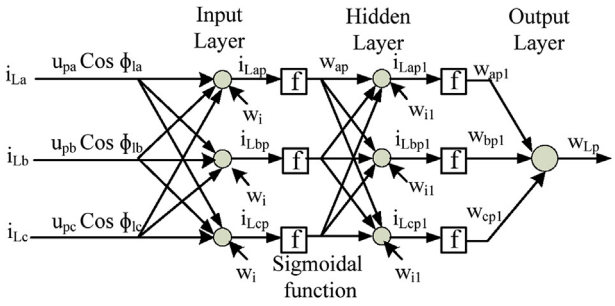


Fig. 13. Proposed GDBP NN structure for calculating weighted fundamental active current components.

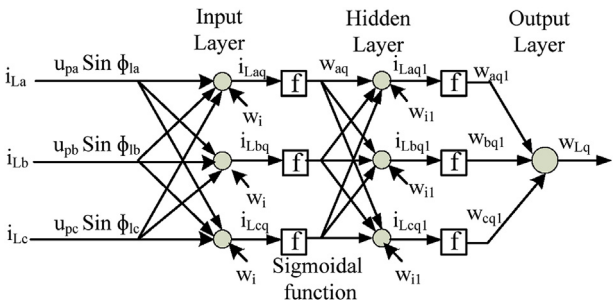


Fig. 14. Proposed GDBP NN structure for calculating weighted fundamental reactive current components.

REFERENCES

[1] Hudson R, Heilscher G. PV grid integration system management issues and utility concerns. Energy Procedia 2012;25:82–91.
[2] Dincer I, Acar C. Review and evaluation of hydrogen production methods for better sustainability. Int J Hydrogen Energy September 2015;40(34):11094–111.
[3] Ellis MW, Von Spakovsky MR, Nelson DJ. Fuel cell systems: efficient, flexible energy conversion for the 21st century. Proc IEEE 2001;39(12):1808–18.
[4] Tourkia LF, Slim A, Anis A. Modeling, control, and simulation of a solar hydrogen/fuel cell hybrid energy system for grid connected applications. Adv Power Electron 2013;9.
[5] Vigneysh T, Kumarappan N. Autonomous operation and control of photovoltaic/solid oxide fuel cell/battery energy storage based microgrid using fuzzy logic controller. Int J Hydrogen Energy 21 January 2016;41(3):1877–91.
[6] Chaudhary P, Rizwan M. Voltage regulation mitigation techniques in distribution system with high PV penetration: a review. Renew Sustain Energy Rev 2018;82:3279–87.
[7] IEEE Recommended practices and requirement for harmonic control on electric power system. IEEE Std 1992;519.
[8] Bouzelata Y, Kurt E, Chenni R, Altın N. Design and simulation of a unified power quality conditioner fed by solar energy. Int J Hydrogen Energy 26 November 2015;40(44):15267–77.
[9] Pacas JM, Molina MG, Santos EC. Design of a robust and efficient power electronic interface for the grid integration of solar photovoltaic generation systems. Int J Hydrogen Energy July 2012;37(13):10076–82.
[10] Molina MG, Espejo EJ. Modelling and simulation of grid connected photovoltaic energy conversion systems. Int J Hydrogen Energy 27 May 2014;39(16):8702–7.
[11] Deveci O, Kasnakoglu C. MIMO nonlinear modelling and robust control of standalone dc photovoltaic systems. Int J Hydrogen Energy April 2017;42(28):18064–80.
[12] Wu T, Chang C, Lin L, Kuo C. Power loss comparison of single and two-stage grid-connected photovoltaic systems. IEEE Trans Energy Convers 2011;26(2):707–15.
[13] Chaudhary P, Rizwan M. Energy management supporting high penetration of solar photovoltaic generation for smart grid using solar forecasts and pumped hydro storage system. Renew Energy 2018;118:928–46.
[14] Arya SR, Niwas R, Bhalla KK, Singh B, Chandra A, Al-Haddad K. Power quality improvement in isolated distributed power generating system using DSTATCOM. IEEE Trans Ind Appl 2015;51(6).
[15] Singh B, Jayaprakash P, Kothari DP, Chandra A, Al Haddad K. Comprehensive study of DSTATCOM configurations. IEEE Trans Ind Inform 2014;10(2):854–70.
[16] Singh B, Solanki J. A comparison of control algorithms for DSTATCOM. IEEE Trans Ind Electron 2009;56(7):2738–45.
[17] Kumar C, Mishra MK. A multifunctional DSTATCOM operating under stiff source. IEEE Trans Ind Elect 2014;61(7):3131–6.
[18] Chaudhary P, Rizwan M. A predictive current control for solar PV fed VSI in distribution system. In: 2017 IEEE International Conference on environment and electrical engineering and 2017 IEEE Industrial and Commercial power systems Europe. Milan: EEEIC/I&CPS Europe; 2017. p. 1–7.
[19] Li YW, He J. Distribution system harmonic compensation methods: an overview of DG-interfacing inverters. IEEE Trans Ind Elect 2014;8(4):18–31.
[20] Chaudhary P, Rizwan MA. Grid synchronization method based on adaptive notch filter for PV system with modified

Please cite this article in press as: Chaudhary P, Rizwan M, Hybrid control approach for PV/FC fed voltage source converter tied to grid, International Journal of Hydrogen Energy (2018), https://doi.org/10.1016/j.ijhydene.2018.02.131

MPPT. World Academy of Science. Eng Technol 2015;9(7):1162–7.
[21] Baran ME, Hooshyar H, Shen Z, Huang A. Accommodating high PV penetration on distribution feeders. IEEE Trans Smart Grid 2012;3(2):1039–46.
[22] He J, Li YW. Hybrid voltage and current control approach for dg-grid interfacing converters with LCL filters. IEEE Trans Ind Elect 2013;60(5):1797–809.
[23] Agarwal RK, Hussain I, Singh B. Implementation of LLMF control algorithm for three-phase grid tied PV-DSTATCOM system. IEEE Trans Ind Electron 2017;9:1. 1.
[24] Agarwal RK, Hussain I, Singh B. Three-phase single-stage grid tied solar PV ECS using PLL-less fast CTF control technique. IET Power Electron 2017;10(2):178–88.
[25] Singh B, Jain C, Goel S, Chandra A, Al-Haddad K. A multifunctional grid-tied solar energy conversion system with ANF-based control approach. IEEE Trans Ind Appl 2016;52(5):3663–72.
[26] Sing B, Jain C, Goel S. ILST control algorithm of single-stage dual purpose grid connected solar PV system. IEEE Trans Power Electron 2014;29(10):5347–57.
[27] Campanhol L, Silva S, Oliveira A, Bacon V. Single-stage three-phase grid-tied PV system with universal filtering capability applied to DG systems and AC Microgrids. IEEE Trans Power Electron Dec. 2017;32(12):9131–42.
[28] Trinh QN, Lee HH. An enhanced grid current compensator for grid-connected distributed generation under nonlinear loads and grid voltage distortions. IEEE Trans Ind Elect 2014;61(12):6528–37.
[29] Jain C, Singh B. An adjustable DC link voltage based control of multifunctional grid interfaced solar PV system. IEEE J Emerg Sel Top Power Electron June 2017;5(2):651–60.
[30] Varma RK, Rahman SA, Vanderheide T. New control of PV solar farm as STATCOM (PV-STATCOM) for increasing grid power transmission limits during night and day. IEEE Trans Power Deli 2015;30(2):755–63.
[31] Arya SR, Singh B, Chandra A, Al-Haddad K. Learning-based Anti-Hebbian algorithm for control of distribution static compensator. IEEE Trans Ind Electron 2014;61(11):6004–12.
[32] Jain C, Singh B. A three-phase grid tied PV system with adaptive DC link voltage for CPI voltage variations. IEEE Trans Sustain Energy 2016;7(1):337–44.
[33] Kannan VK, Rengarajan N. Investigating the performance of photovoltaic based DSTATCOM using I cos Φ algorithm. Elect Power Energy Syst 2014;54:376–86.
[34] Hamid MI, Jusoh A, Anwari M. Photovoltaic plant with reduced output current harmonics using generation-side active power conditioner. IET Renew Power Gener 2014;8(7):817–26.
[35] Singh B, Shahani DT, Verma AK. Neural network controlled grid interfaced solar photovoltaic power generation. IET Power Electron 2013;7(3):614–26.
[36] Kumar AP, Mangaraj M. DSTATCOM employing hybrid neural network control technique for power quality improvement. IET Power Electron 2013;10(4):480–9.
[37] Mazumdar J, Harley RG. Recurrent neural networks trained with back propagation through time algorithm to estimate nonlinear load harmonic currents. IEEE Trans Ind Electron 2008;55(9):3484–91.
[38] Arya SR, Singh B. Neural network based conductance estimation control algorithm for shunt compensation. IEEE Trans Ind Inform 2014;10(1):569–77.
[39] Singh B, Arya SR. Back-Propagation control algorithm for power quality improvement using DSTATCOM. IEEE Trans Ind Electron 2014;61(3):1204–12.
[40] Singh B, Jayaprakash P, Kumar S, Kothari DP. Implementation of neural network controlled three leg VSC and a transformer as three phase four wire DSTATCOM. IEEE Trans Indus Appl 2011;47(4):1892–901.
[41] Jayachandran J, Sachithanandam R. Neural network based control algorithm for DSTATCOM under nonideal source voltage and varying load conditions. Canadian J Elect Comp Eng 2015;38(4):307–17.
[42] Janpong S, Areerak KL, Areerak KN. A literature survey of neural network applications for shunt active power filters. World Acad Sci Eng Tech 2011;60:392–8.
[43] Chaturvedi DK, Malik OP, Kalra PK. Generalised neuron-based adaptive power system stabilizer. IEEE Proc-Gener Transm Distrib 2004;151(2).
[44] Chaturvedi DK, Malik OP, Kalra PK. Experimental studies with a generalized neuron based power system stabilizer. IEEE Trans Power System 2004;19(3):1445–53.
[45] Chaturvedi DK. Soft computing techniques and its applications in electrical engineering. Springer-Berlin Heidelberg; 2008.
[46] Rizwan M, Jamil M, Kothari DP. Generalized neural network approach for global solar energy estimation in India. IEEE Trans Sust Engy 2012;3(3):576–83.
[47] Kulkarni RV, Venayagamoorthy GK. Generalized neuron: feedforward and recurrent architecture. Elsevier Neural Network 2009;22:1011–7.
[48] Samaiah B, Agarwal V, Choudhury SR, Duttagupta SP, Govindan K. Analysis and comparative study of pulsating current of fuel cells by inverter load with different power converter topologies. Int J Hydrogen Energy 2011;36:15018–28.
[49] Jang M, Ciobotaru M, Agelidis VG. A single-phase grid connected fuel cell system based on a boost inverter. IEEE Trans Power Electron 2013;28(1):279–88.
[50] Bensmail S, Reioua D, Azzi H. Study of hybrid photovoltaic/fuel cell system for standalone applications. Int J Hydrogen Energy 2015;40:13820–6.
[51] Akin B, Sarul MH. Soft switched SVPWM controlled PRDCL inverter. Int J Hydrogen Energy 2017;42:17886–94.
[52] Sergi F, Brunaccini G, Stassi A, Blasi AD, Dispenza G, Arico AS, et al. PEM fuel cells analysis for rid connected applications. Int J Hydrogen Energy 2011;36:10908–16.
[53] Seyezhai R, Mathur BL. Modelling and control of a PEM fuel cell based hybrid multilevel inverter. Int J Hydrogen Energy 2011;36:15029–43.
[54] Bayrak G, Gebeci M. Grid connected fuel cell and PV hybrid power generating system design with MATLAB Simulink. Int J Hydrogen Energy 2014;39:8803–12.
[55] Reisi AR, Moradi MH, Jamsab S. Classification and comparison of maximum power point tracking techniques for photovoltaic system: a review. Renew Sustain Energy Rev 2013;19:433. 443.
[56] Deveci O, Kasnakoglu C. Performance improvement of a photovoltaic system using a controller redesign based on numerical modelling. Int J Hydrogen Energy 3 August 2016;41(29):12634–49.
[57] Amrouche B, Belhaouas N, Achachera S, Boukadoum MT. A software tool for testing maximum power point tracking algorithms using real working conditions. Int J Hydrogen Energy 3 August 2016;41(29):12525–34.
[58] Faranda R, Leva S, Maugeri V. MPPT techniques for PV systems: energetic and cost comparison. In: Proceedings of IEEE PES GM; 2008.
[59] Masoum MAS, Dehbonei H, Fuchs EF. Theoretical and experimental analysis of photovoltaic systems with voltage and current based maximum power-point tracking. IEEE Trans Energy Converter 2002;7(4):514–22.
[60] Hussein KH, Muta I, Hoshino T, Osakada M. Maximum photovoltaic power tracking: an algorithm for rapidly changing atmospheric conditions. IEE Proc Generat Transm Distrib 1995;142:59–64.

Please cite this article in press as: Chaudhary P, Rizwan M, Hybrid control approach for PV/FC fed voltage source converter tied to grid, International Journal of Hydrogen Energy (2018), https://doi.org/10.1016/j.ijhydene.2018.02.131

[61] Bahgat AB, Helwab NH, Ahmadb GE, Shenawyb ET. Maximum power point tracking controller for PV systems using neural networks. Renew Energy 2005;30:1257–68.
[62] Simoes MG, Franceschetti NN, Friedhofer MA. Fuzzy logic based photovoltaic peak power tracking control. In: Proceedings IEEE Int. Symp. Ind. Electron; 1998. p. 300–55.
[63] Salah CB, Ouali M. Comparison of fuzzy logic and neural network in maximum power point tracker for PV systems. Elec Power Syst Res 2011;81:43–50.
[64] Hiyam T, Kitabayashi K. Neural network based estimation of maximum power generation from PV module using environmental information. IEEE Trans Energy Convers 1997;12:241–7.
[65] Mathias IM, Zanlorensi Jr LA, Bueno ML. Artificial neural networks simulator with topology multilayer perceptron using the encog framework. IEEE Latin Am Trans 2016;14(1):309–13.
[66] Mekhilef S, Saidur R, Safari A. Comparative study of different fuel cell technologies. Renew Sustain Energy Rev 2012;16:981–9.
[67] Odeim F, Roes J, Wü lbeck L, Heinzel A. Power management optimization of fuel cell/battery hybrid vehicles with experimental validation. J Power Sources 2014;252:333–43.
[68] Somkun S, Sirisamphanwong C, Sukchai S. A DSP-based interleaved boost DCeDC converter for fuel cell applications. Int J Hydrogen Energy 2015;40:6391–404.
[69] Kuo J, Wang C. An integrated simulation model for PEM fuel cell power systems with a buck DC-DC converter. Int J Hydrogen Energy 2011;36:11846–55.
[70] Seyezhai R, Mathur BL. Design and implementation of interleaved boost converter for fuel cell systems. Int J Hydrogen Energy 2012;37:3897–903.
[71] Guilbert D, N'Diaye A, Gaillard A, Djerdir A. Fuel cell systems reliability and availability enhancement by developing a fast and efficient power switch open-circuit fault detection algorithm in interleaved DC/DC boost converter topologies. Int J Hydrogen Energy 2016;41:15505–17.
[72] Pandiarajan N, Ramaprabha R, Ranganath M. Application of circuit model for photovoltaic energy conversion system. Int J Adv Eng Technol 2011;2(4):118–27.
[73] Gow JA, Manning CD. Development of a photovoltaic array model for use in power-electronics simulation studies. IEEE Proc Electric Power Appl 1999;146(2):193–200.
[74] Rizwan M, Chaudhary P, Ahmad T. Performance analysis of maximum power point tracking techniques for photovoltaic systems. Adv Sci Lett 2014;20:1231–47.

Please cite this article in press as: Chaudhary P, Rizwan M, Hybrid control approach for PV/FC fed voltage source converter tied to grid, International Journal of Hydrogen Energy (2018), https://doi.org/10.1016/j.ijhydene.2018.02.131

Environmental Earth Sciences (2018) 77:252
https://doi.org/10.1007/s12665-018-7431-5

ORIGINAL ARTICLE

Hydrogeochemical characterization and suitability appraisal of groundwater around stone quarries in Mahendragarh, India

Chitrakshi[1] · **A. K. Haritash**[1]

Received: 27 September 2017 / Accepted: 19 March 2018
© Springer-Verlag GmbH Germany, part of Springer Nature 2018

Abstract
The present study is the first attempt to assess the impact of stone quarrying on quality of groundwater and its suitability for drinking and irrigation in Mahendragarh region of Haryana State. The suitability for drinking and irrigation was determined by comparing the observed values with prescribed standards and indices. The groundwater was found suitable for drinking for most of the parameters except TDS, total hardness, calcium, magnesium, and nitrate. With respect to suitability in agriculture, the groundwater was classified as good with the only problem of magnesium hazard in few villages located north of mining region. Based on the ratios of different anions and cations, silicate weathering and reverse base exchange were found responsible for regulation of groundwater chemistry. Most of the shallow meteoric genesis groundwater samples were classified as Na–Cl type, and the deep meteoric genesis groundwater was classified as Na–HCO_3 type. Values of base exchange and piper trilinear, too, confirmed that the groundwater belonged to either Na–Cl or Ca–Mg–Cl type. Further, FTIR analysis of crushed mined material and soil around mining area confirmed the presence of calcite and kaolinite, respectively, which confirmed that silicate weathering is regulating groundwater chemistry. The study concluded that there is no significant direct effect of stone quarrying on groundwater in Mahendragarh district.

Keywords Stone quarrying · Mahendragarh · Sodium adsorption ratio (SAR) · Base exchange · Silicate weathering

Introduction

Mining is the second oldest profession of human beings after agriculture. Although it has a fair contribution in economic growth and development, its environmental effects cannot be overseen. Degradation of land, clearing of vegetation, obstruction to natural flow of streams, and ponding in mine pits are commonly observed direct environmental effects (Abdullah et al. 2016). India produces about 87 minerals which chiefly include non-metallic and minor minerals and account for about 2.1% of Indian GDP (Annual Report 2014–2015). Coal, ferrous mineral, and aluminum are the major mineral resources of India. These resources are mainly concentrated in eastern and central parts of India, and extraction of these minerals has associated environmental and social effects in affected regions. There have been number of studies on determination of quality of groundwater (Haritash et al. 2008), surface water (Haritash et al. 2016) or water in coastal regions (Haritash et al. 2017), but the research reports presenting the environmental effects of mining and quarrying (Haritash et al. 2007; Amitshreeya and Panda 2012; Bayram and Onsoy 2015) are limited. Besides water deficit in mining areas, the account of excess extraction of ground water for use of mining operation, presence of toxic anions, heavy metals, radioactivity, and other organic and biological impurities has been reported in discharged mine water (Singh et al. 2012; Wu et al. 2011; Abiye and Shaduka 2017). In other words, it consumes and contaminates the water resources around the region. Compared to mining of coal, metals, radioactive material, etc., quarrying of sandstone has limited or relatively less effects on water resources. Whereas effect of stone mining and crushing on air quality (Amitshreeya and Panda 2012), soil (Haritash et al. 2007), vegetation (Saha and Padhy 2011), and surface water (Bayram and Onsoy 2015) has been attempted in some studies, effects of stone quarrying on ground water quality, particularly in Haryana State of India, have not been reported so far. It becomes even significant to study the effect on quality of ground water since the ground water availability in these regions is very scanty. As per Central

✉ A. K. Haritash
akharitash@dce.ac.in

[1] Department of Environmental Engineering, Delhi Technological University, Bawana Road, Shahbad Daulatpur, Delhi 110042, India

Published online: 23 March 2018

Ground Water Board (CGWB 2013a, b), the net ground water draft available for future is negative particularly in Mahendragarh district. The depth of the water level in the region is around 200 mbgl. The distribution of groundwater depth in Mahendragarh district is given in Fig. 1.

Mahendragarh district is located between 27°47′ to 28°26′N latitude and 75°51′E longitude with geographic area of 1899 km^2. It is dominantly a region of piedmont and aeolian plains located along Aravali ranges comprising of rocks of post-Delhi and Delhi system. The Ajabgarh lithology of Delhi Supergroup in Mahendragarh is rich in garnet and staurolite deposits with crystals of kyanite, deposits of slate, impure calc-silicate rocks, quartzite, calcite, and dolomite. The alluvial has heterogeneity of sand, silt, and calcareous granules. The climate of Mahendragarh is classified as dry and arid with hot summers and cold winters and unevenly distributed annual rainfall of 500 mm during monsoon. The landuse–landcover (LULC) classifies it as an agricultural region with dispersed pockets of stone quarrying (Fig. 2). The district has seven major stone mines, and Bakhrija stone mine is the largest with an area of about 40 hectares. Bakhrija mine is located between 27°55′1″ to 27°54′6″ North latitude and 76°03′28.34″ to 76°03′27.56″ East longitude and is famous for quarrying of calcite, limestone, mica, and garnet as important minerals. Till date, there is no report on effect of mining on surrounding areas of Bakhrija mines. Therefore, the present study was undertaken to study groundwater quality in and around Bakhrija mines and to determine the suitability of water for drinking and irrigation.

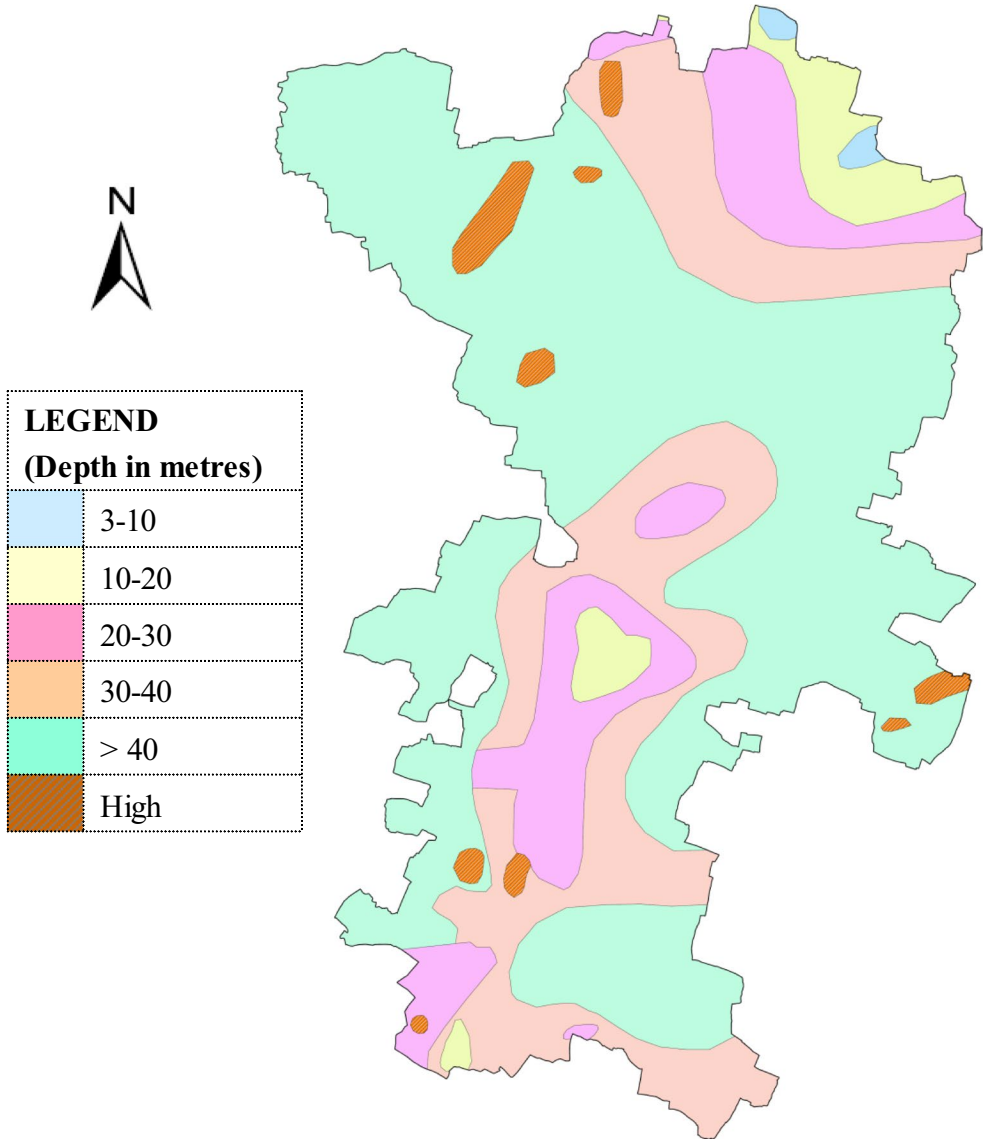


Fig. 1 The groundwater depth (in meters) in Mahendragarh district, Haryana

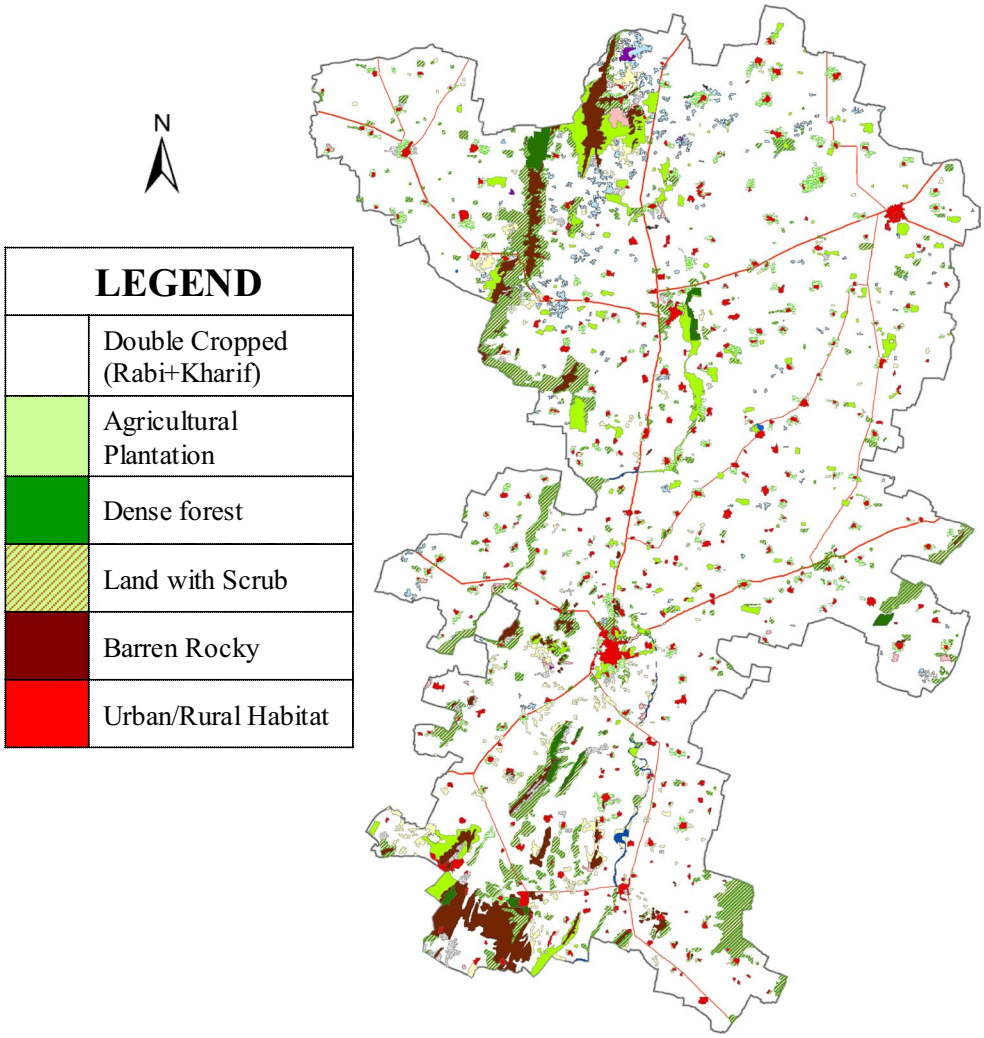


Fig. 2 Details of landuse–landcover (LULC) in Mahendragarh, Haryana

Materials and methods

Study area

Bakhrija mines of Mahendragarh district are famous for its sandstone and interspersed mica deposits. It is located 45 km south from Mahendragarh town and is surrounded by Pavera, Bighopur, Dholera, Meghot Binja, Bakhrija, and Islampura villages. Groundwater samples were collected from the mining area and neighboring villages from identified tube wells. The samples were collected during March 2017 from fifteen (15) locations covering an area of about 25 km^2 around the mining region. The site-specific details are given in Table 1 and Fig. 3. The samples were collected directly from the respective source in pre-rinsed PET bottles of 2 L capacity. Determination of pH, electrical conductivity (EC), total suspended solids (TDS), and salinity was done onsite using Orion (USA) make Star A320 model multi-parameter meter. The so collected samples were stored at low temperature in an ice box during transfer and were analyzed within 24–48 h for rest of the parameters. The characterization of the samples was performed in triplicate following standard prescribed methods (APHA 2005) using analytical grade (AR) chemicals and ultrapure (Type 1) water. The total hardness (TH), total alkalinity (TA), chloride (Cl^-), carbonate (CO_3^{2-}), and bicarbonate (HCO_3^-) were analyzed using volumetric analysis; phosphate (PO_4^{3-}), sulfate (SO_4^{2-}), nitrate (NO_3^-), and iron (Fe) were determined spectrophotometrically on LabIndia make UV3092 model double-beam UV–Vis spectrophotometer. The cations, viz. sodium (Na^+), potassium (K^+), calcium (Ca^{2+}), magnesium (Mg^{2+}) and lithium (Li^+), were analyzed on Systronics make 128 µC model flame photometer. The suitability for drinking was determined by comparing the observed values against the prescribed standards of Bureau of Indian Standards (BIS

Table 1 Site-specific details and metadata of sampling locations

S. no.	Coordinates		Name of village	Source	MOC	Depth (m)	Usage
	Latitude (N)	Longitude (E)					
1	27°56′48.51″	76°01′15.91″	Pavera	Tubewell	Plastic	47	D/BK
2	27°57′00.07″	76°01′8.39″	Pavera	Tubewell	Plastic	305	D/BK
3	27°56′41.50″	76°1′32.92″	Sareli	Tubewell	Plastic	47	D/BK
4	27°56′50.98″	76°3′17.51″	Bighopur	Tubewell	Plastic	200	D/I
5	27°57′01.93″	76°3′13.33″	Bighopur	Tubewell	Plastic	260	D/I
6	27°54′48.27″	76°3′15.68″	Bakhrija	Surface water	Mine pit	30	Mining
7	27°54′45.04″	76°3′49.83″	Meghot	Tubewell	Iron	245	D/I
8	27°54′33.18″	76°3′43.49″	Meghot	Tubewell	Iron	305	D/I
9	27°53′40.82″	76°3′19.64″	Nangal Dargu	Tubewell	Iron	180	D/I
10	27°53′46.63″	76°3′19.71″	Nangal Dargu	Tubewell	Iron	180	I
11	27°53′44.29″	76°2′54.06″	Nangal Dargu	Tubewell	Iron	180	I
12	27°53′58.82″	76°2′33.59″	Bakhrija	Tubewell	Iron	245	D/I
13	27°54′06.85″	76°2′36.43″	Bakhrija	Tubewell	Iron	245	D/I
14	27°54′24.61″	76°2′42.45″	Bakhrija	Tubewell	Iron	230	D
15	27°55′04.37″	76°1′55.31″	Niaz Alipur	Tubewell	Iron	275	D

MOC material of construction, *D* drinking, *BK* Brick Kiln, *I* irrigation

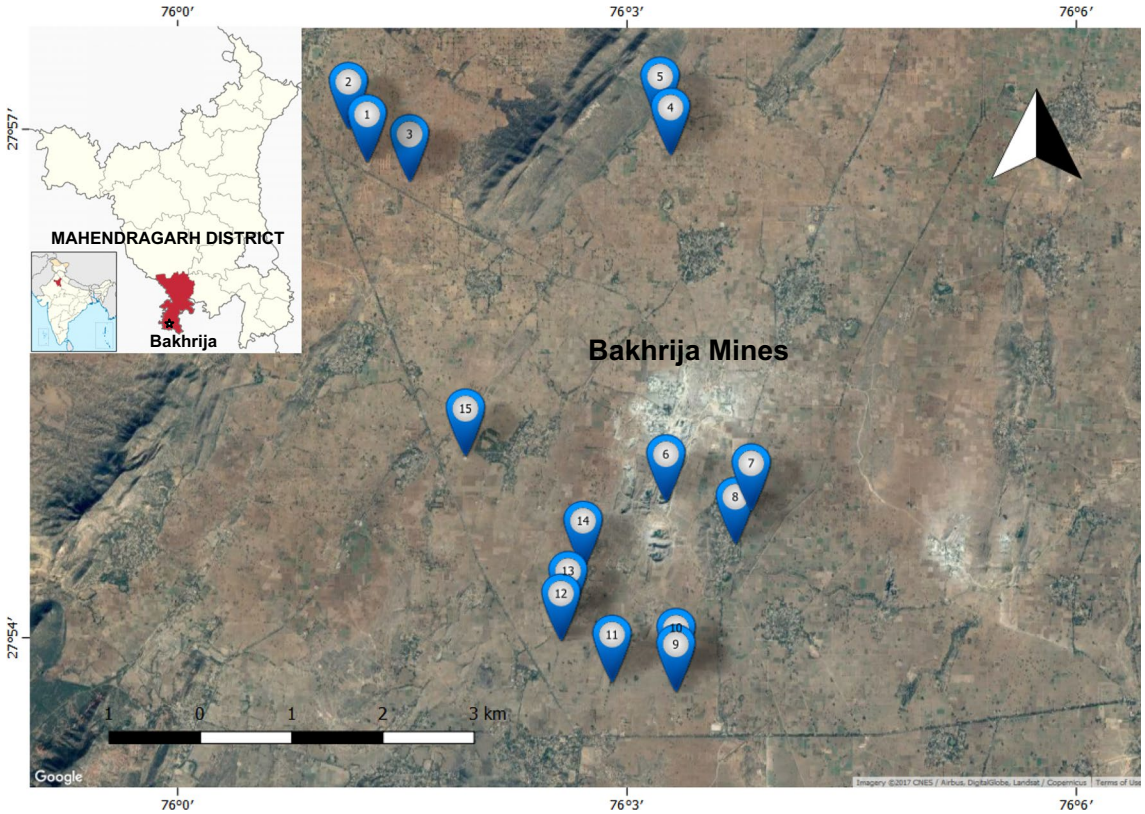


Fig. 3 Location of Bakhrija mines and sampling locations

2012). To assess the suitability for irrigation, the following indices/ratios were calculated. For the determination of chief minerals present in the mined material and soil, one sample each of dust of crushed mine material, and soil (1 km away from Bakhrija mine) was collected; and its mineralogical composition was determined using Fourier transform infrared (FTIR) spectroscopy (PerkinElmer make Spectrum 2 model).

Results and discussion

Based on physicochemical analysis of the groundwater samples, and their classification for drinking and agricultural use, it was observed that there are spatial variations in terms of quality. For comprehensive understanding about suitability of groundwater in domestic and agricultural sector, the observed results were compared with normative values; and/or various ratios and indices were calculated to affirm the suitability for respective sector. The average ionic balance of major cations (Na, K, Ca, Mg) and anions (CO_3, HCO_3, Cl, and SO_4) was 2.7; and EC/TDS ratio of 0.51 confirmed the precision of data.

Weathering profile and geochemical classification

The dissolution of different chemical species from the interacting rock minerals and their relative abundance in groundwater may be used as an indirect inference of the type of weathering and its mechanism which has played a major role in regulating the chemistry of groundwater. The major routes for addition of different anions and cations in water are atmospheric deposition, interaction with rocks and input from human activities (Subramanian 1987). In the present study, atmospheric fallout and anthropogenic processes are ruled out and the interaction with underlying rocks may be inferred using Gibb's classification (Gibbs 1970). Based on Gibb's boomerang plots (Fig. 4a), it is observed that the prominent process controlling groundwater chemistry is rock–water interaction. To further classify the source and the type of weathering, relative ratios of cations and anions were calculated. Average Ca/Na value 1.19; Mg/Na value 1.24; and HCO_3/Na value close to 0.21 suggest that silicate weathering is major weathering type which regulates the groundwater chemistry since water with silicate end member has Ca/Na ratio 0.35 ± 0.15; Mg/Na 0.24 ± 0.12; HCO_3/Na 2 ± 1 (Gaillardet et al. 1999). The observed values are significantly lower than the aquifers draining carbonate lithology (50 for Ca/Na; 10 for Mg/Na; and 120 for HCO_3/Na) (Meybeck 1986). The sodium-normalized calcium and magnesium relationship also suggests that silicate weathering plays the major role in regulating groundwater chemistry. The (Ca + Mg)/(Na + K) value close to 1.0 also confirms that silicate weathering is the dominant process followed by carbonate weathering. Average value of 0.37 for (Na + K)/TZ^+, too, confirms of silicate weathering. The general reaction representing weathering of silicate rocks can be written as (Zaczek and Porowski 2017).

$$2NaAlSi_3O_8 + 2CO_2 + 6H_2O \rightarrow Al_2Si_4O_{10}(OH)_2 + 2Na^+ + HCO_3^- + 2H_4SiO_4$$

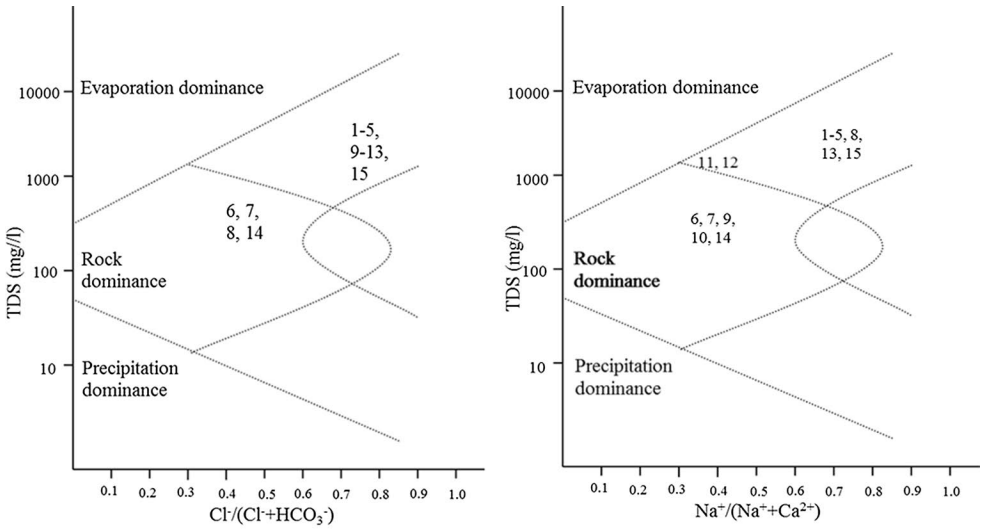
$$2NaAlSi_3O_8 + 2CO_2 + 11H_2O \rightarrow Al_2Si_2O_5(OH)_4 + 2Na^+ + 2HCO_3^- + 4H_2SiO_4$$

Based on the values of CAI–I, groundwater in Bighopur and Nangal Dargu villages is observed to follow direct base exchange indicating that sodium and potassium of groundwater are exchanged with calcium and magnesium of rocks. On the other hand, reverse base exchange governs groundwater chemistry in Pavera, Sareli, Meghot, and Bakhrija villages. Based on normalized percentages of different anions and cations, piper trilinear diagram (Fig. 4b) was plotted to arrive at the hydrochemical facies of groundwater (Piper 1953). It was observed that most of the water samples belonged to Na–Cl or mixed Ca–Mg–Cl type. Further, it was observed that alkaline earth (Ca + Mg) exceeds the alkaline (Na + K); and strong acids (Cl^- and SO_4^{2-}) exceed weak acids (HCO_3^- and CO_3^{2-}). According to the classification of meteoric genesis, groundwater is of two types—deep meteoric water percolation type (Met. gen. < 1) and shallow meteoric water percolation type (Met. gen. > 1). Based on the values of base exchange, values < 1 represent sodium sulfate type water, and values > 1 represent Na–Cl type water. Based on the classification criteria of base exchange and meteoric genesis, the groundwater with shallow meteoric percolation was found to be Na–Cl type, and water with deep meteoric percolation was Na_2–SO_4^{2-} type.

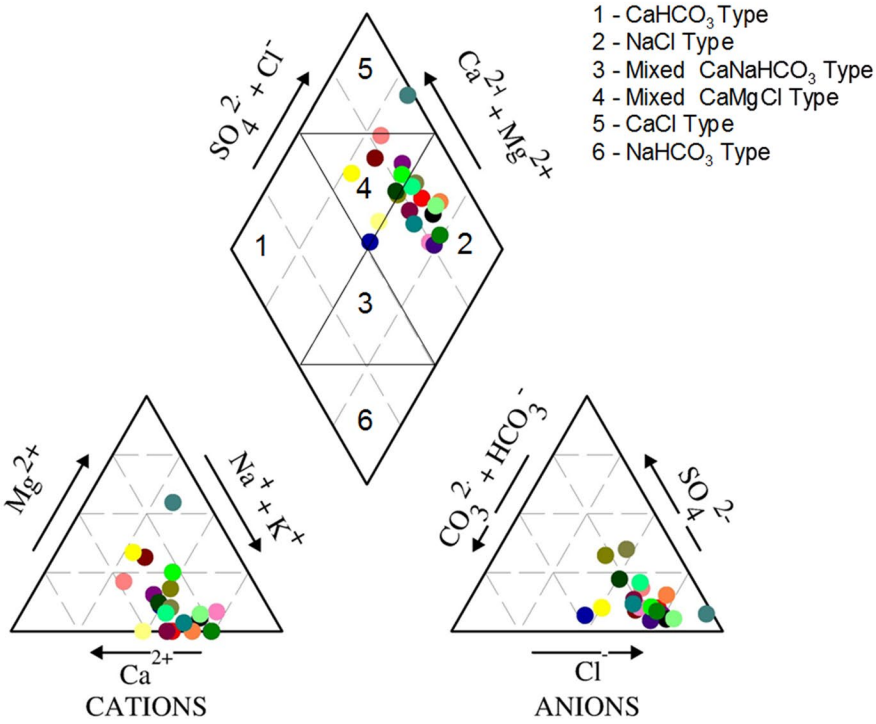
Further, source-specific investigation of mechanisms involved in regulating groundwater chemistry was also done using ratios of cations and anions (Fig. 5). The Cl^- versus Na^+ plot (Fig. 5a) represents points along 1:1 equiline indicating that halite dissolution is one of the sources of Na^+ and Cl^-, whereas some of the samples from Sareli, Bighopur, and Nangal Dargu villages had Cl^- more than Na^+ indicating the contribution of silicate weathering. The depletion of Na ions may also be attributed to base ion exchange. The plot of Na/Cl against EC (Fig. 5b) shows a decreasing Na/Cl ratio with increasing salinity. The Na/Cl ratio close to 1.0 is an indicator of halite dissolution, and in the present study, dominance of Cl ions against Na ions may be attributed to halite dissolution (mean Na/Cl value of 1.08) or base ion exchange which results in depletion of Na ions. Most of the CAI–I are negative which further supports that reverse ion exchange results in addition of Na ions (Meybeck 1987). The plot of (Ca + Mg) against (Na + K) (Fig. 5c) reveals that alkaline earth elements dominate over alkaline species. Excess of Ca and Mg ions may be attributed to direct base ion exchange (Jankowski and Acworth 1997).

$$\frac{1}{2}\text{Ca-clay}_2 + Na^+ \rightarrow \frac{1}{2}Ca^{2+} + \text{Na-clay}$$

Similarly, relatively higher concentration of (Ca + Mg) against ($HCO_3 + SO_4$) (Fig. 5d) reveals that direct base exchange is the major reaction controlling groundwater cations at most of the locations. Further, if the only source of Ca and Mg in groundwater is carbonate or silicate weathering, then (Ca + Mg)/HCO_3 ratio is close to 0.5



(a) Gibb's Boomerang plots



(b) Piper Tri-linear diagram

Fig. 4 **a** Gibbs boomerang plots and **b** piper trilinear diagram for classification of groundwater

(Sami 1992), whereas in the present study m(Ca + Mg)/HCO_3 ratio (Fig. 5e) is fairly above 0.5 indicating that direct base exchange reaction plays a major role controlling groundwater chemistry. A more than 1.0 m(Ca + Mg)/HCO_3 ratio is also suggestive of the absence of fresh recharge of water (Nazzal et al. 2014). The plot of m(Ca + Mg) against m(Cl) (Fig. 5f) represents an increase with increasing salinity, and the plot of m(Na/Cl) against m(Cl) (Fig. 5g) shows decreasing trend indicating that the dissolved Na in groundwater is exchanged by Ca and Mg of interacting rocks (Rajmohan and Elango 2004). Finally, dominance of Ca and Mg ions in groundwater may be contributed by interaction with carbonate rock. The Ca/Mg ratio (Fig. 5h) equal to one indicates dissolution of dolomite rocks, whereas higher ratios indicates dissolution of calcite rocks (Mayo and Loucks 1995); and ratio more than 2 indicates dissolution of silicate minerals (Katz et al. 1997). In the present study, groundwater in Pavera, Bighopur, Meghot, Nangal Dargu, and Islampura indicated interaction with dolomite rocks, whereas groundwater in

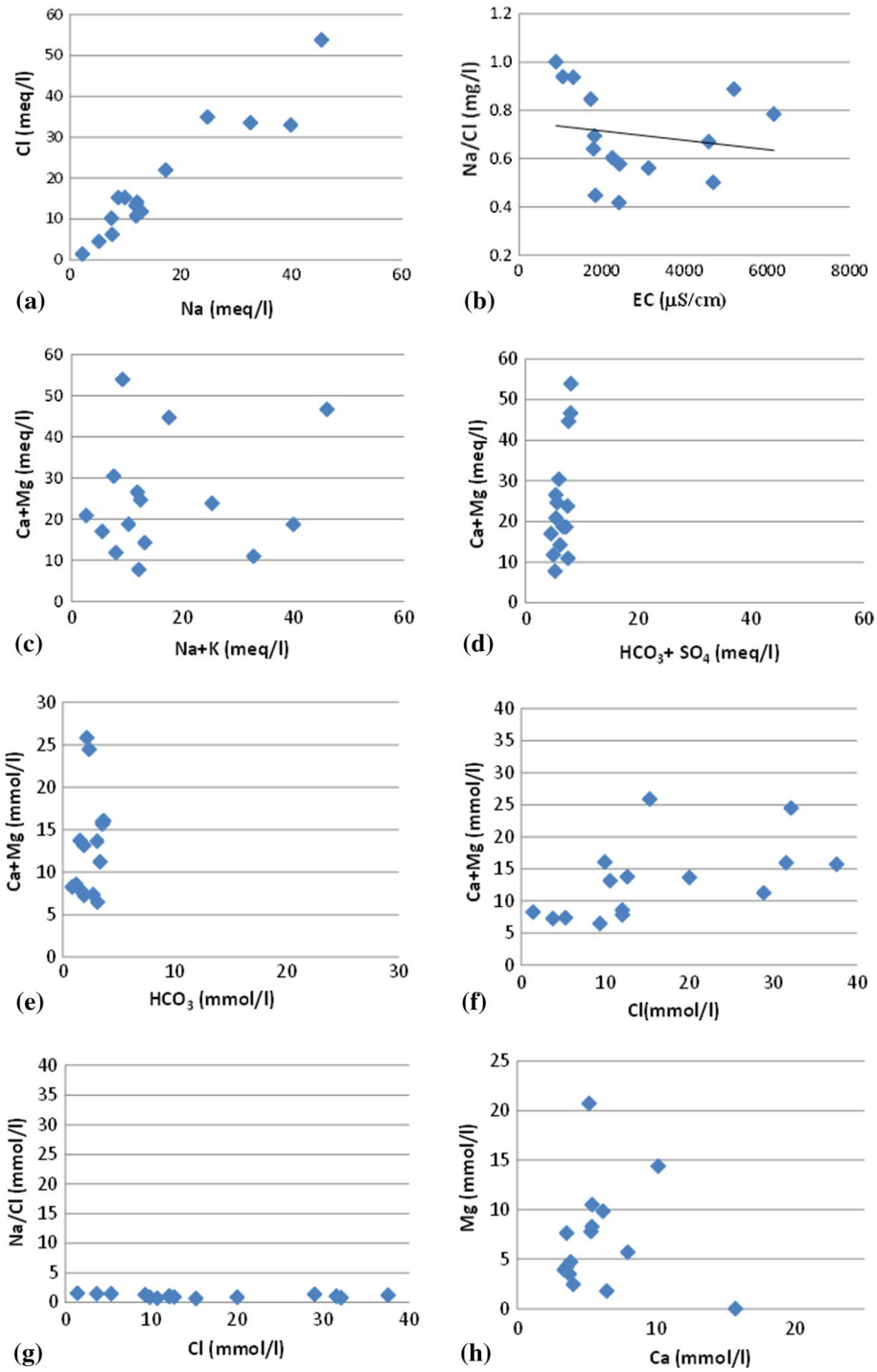


Fig. 5 The plots of ionic ratios to represent rock–water interactions

Bakhrija had interaction with calcite rocks. The only sample from mining area (mine pit) represented dominance of silicate weathering.

Suitability for drinking

The observed physicochemical characteristics of analyzed groundwater samples are given in Table 2. The groundwater was observed to be slightly alkaline in nature with an average pH value of 7.3. The alkalinity may be accounted to dissolution of alkaline/earth minerals. Dissolution of different rock minerals resulted in significantly high EC and TDS in groundwater. The EC ranged from 898 to 6170 µs/cm with an average value of 2762 µs/cm. Similarly, average TDS was 1398 mg/l ranging from 458 to 3110 mg/l. About 93% of the collected groundwater samples exceeded the prescribed

Table 2 Physicochemical characteristics of groundwater around Bakhrija stone mines, Mahendragarh, Haryana (March 2017)

S. no.	pH	EC	TDS	TH	TA	CO_3^{2-}	HCO_3^-	Cl^-	SO_4^{2-}	NO_3^-	PO_4^{3-}	Ca^{2+}	Mg^{2+}	Na^+	K^+	Fe	Li
1	7.1	4580	2500	788	450	18	220	1120	134	103	0.40	217	252	750	18	0.02	0.40
2	7.2	6170	3110	656	420	12	220	1336	148	71	0.01	627	0	1048	17	0.00	0.35
3	7.6	5200	2580	556	460	24	207	1030	124	166	0.05	144	183	914	13	0.00	0.30
4	7.1	3110	1570	676	300	0	183	710	150	8	0.15	317	137	398	17	0.00	0.30
5	7.0	4710	2350	1212	240	0	147	1140	169	1	0.02	403	345	571	17	0.09	0.30
6	7.4	898	458	412	90	0	55	50	153	144	0.02	259	43	50	14	0.01	0.20
7	7.5	1301	650	356	300	6	165	190	79	5	0.07	137	94	178	13	0.08	0.15
8	7.6	1760	877	320	320	0	195	330	124	0	0.06	160	59	279	10	0.11	0.25
9	7.3	2290	1142	680	270	24	92	450	133	84	0.10	218	199	271	11	0.04	0.25
10	7.4	1849	936	652	250	12	116	380	131	89	0.07	214	187	170	8	0.08	0.20
11	6.9	2410	1204	920	370	0	226	350	143	35	1.70	249	236	202	11	0.38	0.25
12	7.8	2420	1213	1276	280	12	134	540	154	90	0.21	205	497	225	14	0.19	0.25
13	7.6	1842	923	388	220	12	98	430	147	0	0.19	144	101	298	16	0.11	0.20
14	7.1	1089	545	360	200	0	122	130	87	134	0.72	150	84	122	8	0.11	0.20
15	7.6	1805	909	424	180	12	73	430	133	0	0.16	154	113	275	11	0.22	0.25
Mean ± SD	7.3 ± 0.3	2762 ± 1631	1398 ± 834	645 ± 301	290 ± 103	8.8 ± 8.7	150 ± 57	574 ± 401	134 ± 24	62 ± 59	0.3 ± 0.4	240 ± 130	169 ± 128	383 ± 300	13 ± 3	0.1 ± 0.1	0.3 ± 0.1
Limit[a]	6.5–8.5	NM	500	200	200	NM	NM	250	200	45	NM	75	30	NM	NM	0.3	NM
Exd.[b] (%)	0	–	93	100	86	–	–	80	0	53	–	100	93	–	–	6	–

All the parameters are expressed in 'mg/l' except pH and EC (µS/cm)

TH total hardness (as $CaCO_3$), *TA* total alkalinity (as $CaCO_3$), *NM* not mentioned

[a]Standard prescribed for drinking (BIS 2012), [b]percentage samples exceeding the limit

limit of 500 mg/l for TDS in drinking water (World Health Organization (WHO) 2006). Some of the water samples were found to be significantly saline in the region in Pavera, Bighopur, and Bakhrija villages. Total hardness (TH) was also observed to be high in these regions. Average value of TH was 645 mg/l ranging from 320 to 1276 mg/l; and none of the sample was found to be within the prescribed limit of 200 mg/l. Total alkalinity (as $CaCO_3$) ranged from 90 to 460 mg/l with an average value of 290 mg/l. More than 85% of the samples exceeded the prescribed limit of alkalinity, which may be attributed to dissolution of alkaline/earth chemical species as explained earlier. Further, it was observed that alkaline earth species (Ca + Mg) exceeded the alkaline species (Na + K), resulting in exceedance of Ca and Mg against the prescribed standards for drinking. Among the anions, chloride dominated with an average value of 574 mg/l, and 80% of the samples exceeded the prescribed limit of 250 mg/l. The levels were observed to be high in Pavera, Bighopur, and Bakhrija regions. Similarly, relatively higher value of sulfate was observed in these regions. Concentration of nitrate exceeded the prescribed standard (45 mg/l) at about 50% of the locations with relatively higher values in Pavera, Sareli, Meghot and Nangal Dargu regions, which is mostly under the land use of agriculture. But, significantly high value in water collected from mine pit indicates that mined material, too, acts as a source of nitrate in groundwater. The concentration of phosphate was significantly low at all the locations except at one location in Nangal Dargu which may be attributed to agriculture as a source. Upon comparison with the prescribed standards for drinking (BIS 2012), the water quality was found to be compromised with respect to hardness, calcium, magnesium, TDS, alkalinity, and chloride which may be attributed to mining; and nitrate from mining/agricultural activities in the region. The comparative analysis of average concentration of parameters relevant for drinking is represented by Schoeller's diagram (Fig. 6).

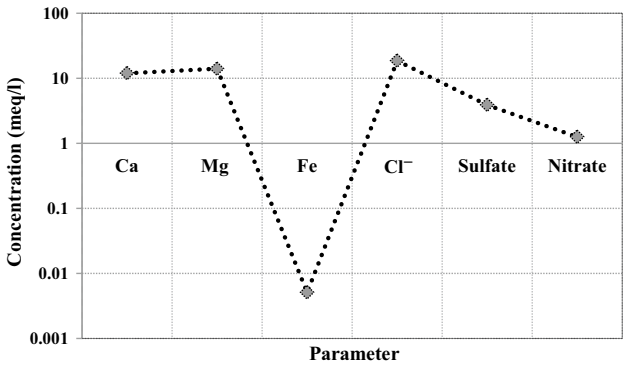


Fig. 6 Schoeller diagram of average drinking water quality

Suitability for irrigation

In order to determine the suitability for agricultural use, various ratios/indices were calculated and sources were classified as per the criteria for classification of quality for irrigation (Table 3). The parameters so used are discussed below. Based on EC, the quality of irrigation water can be classified for its suitability in agriculture as it is an indirect inference of TDS in groundwater. Depending upon the type and nature of chemical species dissolved in groundwater, its suitability for irrigation can be commented upon; nevertheless, excess of dissolved solids in irrigation water leads to deposition of salts on soil, which leads to reduced productivity. The criteria for classification of irrigation water for suitability are discussed in Table 4. In the present study, more than 50% groundwater samples were classified as poor to harmful for use in irrigation. Excess of dissolved solids in groundwater may be an outcome of mining as an activity. Among the dissolved cations, sodium plays an important role in determining productivity, salinity, cation exchange, and permeability of soil. Therefore, percentage of sodium in groundwater is significantly useful to determine its suitability. In the present study, most of the groundwater samples were observed to be good and rest classified as marginal for quality with respect to percent sodium (%Na). Similarly, values of soluble sodium percentage (SSP) varied from 11.6 to 63.9% with an average value of 36.2%, stating that most of the groundwater samples had relatively low contribution of Na among the cations. The values were relatively high in Pavera and Sareli regions, but since the soil is sandy and sufficiently permeable, there would be insignificant effect of long-term irrigation on such soil. Residual sodium carbonate (RSC) is a measure of excess sodium carbonate present in groundwater after all calcium and magnesium have been precipitated with carbonate. Excess sodium carbonate may adsorb over the soil particles and may affect the soil structure leading to interlayer swelling and reduced permeability particularly in case of clays. Values of RSC are negative at all the locations indicating that the water is suitable for irrigation with respect to RSC. Similarly, values of sodium adsorption ratio (SAR) in the present study indicated good to very good quality (Fig. 7) of irrigation water stating that there is relatively less influence of mining on presence of sodium in groundwater. Apart from sodium, magnesium also plays an important role in determining suitability of groundwater for irrigation, and the parameter is designated as magnesium hazard (Mg hazard). Value of Mg hazard represented high concentration of magnesium in the groundwater and it was not suitable for irrigation since it may disturb the cation exchange system of soil particles. On the other hand, based on Kelly's ratio (KR), the groundwater samples were classified as good for irrigation. Permeability index (PI) is another parameter to designate the quality of groundwater for use in agriculture.

Table 3 Suitability of water for irrigation based on different ratios/indices

S. no.	%Na (%)	SSP (%)	RSC (meq/l)	SAR	Mg hazard (%)	KR	PI	CAI-1	PS (meq/l)	BE	MG
1	50.94	50.59	−27.64	8.17	65.93	1.02	53.53	−0.05	32.95	0.38	0.54
2	59.47	59.24	−27.34	11.51	0.00	1.45	61.71	−0.22	39.18	2.57	2.71
3	64.09	63.90	−18.26	11.86	67.93	1.77	66.86	−0.38	30.31	4.15	4.28
4	39.42	38.82	−24.27	4.69	41.87	0.63	42.71	0.11	21.56	−0.86	−0.72
5	34.06	33.67	−46.49	5.02	58.79	0.51	35.78	0.21	33.87	−2.07	−1.95
6	13.28	11.62	−15.63	0.76	21.67	0.13	16.70	−0.80	3.00	0.24	0.35
7	35.47	34.52	−11.78	2.86	53.35	0.53	41.85	−0.51	6.18	1.45	1.65
8	48.95	48.43	−9.72	4.77	38.06	0.94	55.57	−0.33	10.59	1.10	1.20
9	30.51	30.01	−25.18	3.18	60.34	0.43	33.13	0.05	14.06	−0.32	−0.22
10	22.42	21.95	−23.98	2.04	59.29	0.28	26.04	0.29	12.07	−1.21	−1.14
11	22.01	21.47	−28.41	2.19	61.24	0.27	26.18	0.08	11.35	−0.36	−0.27
12	16.41	15.92	−49.07	1.92	80.16	0.19	18.33	0.33	16.82	−1.69	−1.58
13	46.12	45.35	−13.61	4.64	53.90	0.83	49.78	−0.10	13.64	0.28	0.41
14	27.53	26.78	−12.50	1.97	48.28	0.37	33.92	−0.50	4.57	0.91	1.02
15	41.69	41.13	−15.52	4.09	55.01	0.70	44.89	−0.01	13.50	−0.06	0.05

Residual sodium carbonate (RSC) = $(HCO_3^- + CO_3^{2-}) - (Ca^{2+} + Mg^{2+})$ (Eaton 1950)

Soluble sodium percentage (SSP) = $[Na^+/(Ca^{2+} + Mg^{2+} + Na^+)] \times 100$ (Eaton 1950)

Sodium adsorption ratio (SAR) = $Na^+/(Ca^{2+} + Mg^{2+}/2)^{1/2}$ (Richards 1954)

Percent sodium (%Na) = $[(Na^+ + K^+) \times 100]/(Ca^{2+} + Mg^{2+} + K^+)$ (Wilcox 1955)

Permeability index (PI) = $[Na^+ + (HCO_3^-)^{1/2}/(Ca^{2+} + Mg^{2+} + Na^+)] \times 100$ (Doneen 1964)

Kelly's ratio (KR) = $Na^+/(Ca^{2+} + Mg^{2+})$ (Kelly 1963)

Magnesium hazard (Mg hazard) = $(Mg^{2+} \times 100)/(Ca^{2+} + Mg^{2+})$ (Paliwal 1972)

Chlor-alkali index − 1 (CAI − 1) = $[Cl - (Na + K)]/Cl$ (Schoeller 1977)

Potential salinity (PS) = $Cl + 1/2(SO_4)$ (Doneen 1961)

Base exchange (BE) = $(Na^+ - Cl^-)/SO_4^{2-}$ (Matthess 1982)

Meteoric genesis (MG) = $(Na^+ + K^+) - Cl^-/SO_4^{2-}$ (Moneim 1988)

All ionic concentrations are in milliequivalent per liter (meq/l)

Table 4 Criteria for classification of water quality for irrigation

Quality	EC range (µS/cm)		%Na	RSC (meq/l)		KR	SAR	Mg hazard (%)
Very good	250[a]	< 1000[b]	20[a]	< 0[c]	< 1.25[d]	< 1[g]	0–10[e]	< 50%[f]
Good	250–750	1000–2000	20–40	0–2.5			10–18	
Marginal	750–2000	2000–4000	40–60	2.5–5.0	1.25–2.5	1–2	18–26	
Poor	2000–3000	4000–6000	60–80	5.0–7.5	> 2.5	> 2		> 50%
Harmful	3000	> 6000	80	> 7.5			> 26	

[a]Wilcox (1955), [b]Bhumbla and Abrol (1972), [c]Bishnoi et al. (1984), [d]Eaton (1950), [e]Richards (1954), [f]Paliwal (1972), [g]Kelly (1963)

Based on the values of PI observed, all the samples were found to be fit for irrigation (Class I 75% of maximum permeability). Based on potential salinity (PS), 26% of samples were classified as class I, and 37% each of class II and class III for soils with high permeability. It was observed that the suitability of groundwater for agriculture is compromised with respect to EC, magnesium hazard, PI, and KR, particularly in Pavera, Sareli, and Bighopur villages.

Statistical analysis

The data generated in the present study was subjected to statistical analysis to categorize the correlated variables which chiefly regulate the quality of water. The correlation among various parameters analyzed for the collected samples of water is given in Table 5. It was observed that EC and TDS

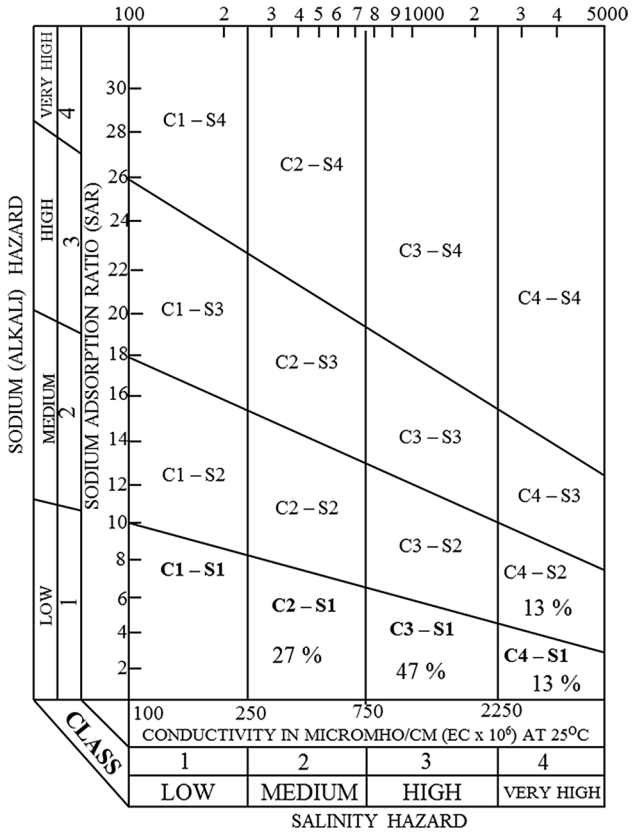


Fig. 7 Classification of groundwater for sodium hazard

had a strong positive correlation with Na^+, Cl^-, Li^+, and HCO_3^- indicating toward a common source of these species which is crustal in origin, since addition of Li^+ to groundwater is considered as crustal. Total hardness had strong correlation with Mg^{2+} and SO_4^{2-} indicating permanent nature of hardness; and total alkalinity had a correlation with HCO_3^-, Na^+, Li^+, and Cl^- which may also be attributed to crustal origin. Coexistence of sodium and lithium chloride may be attributed to saltwater evaporation and formation of Lepidolite which may be the reason for significant positive correlation of Li^+ with potassium (K^+). Similarly, a good positive correlation of Fe and PO_4^{3-} is observed which points to presence of polymorphs of $FePO_4$ as minerals.

Similarly, principal component analysis (PCA) a statistical method which is used to reduce the observed correlated value to smaller set of important independent composite variables was also done. The interrelationships of variables in the present study are explained using component 1 to component 5. The rotated component matrix is shown in Table 6. Component 1 explains 43.25% of the cumulative variance with an *eigen value* of 7.35. It contains variables like EC, TDS, TA, HCO_3^-, Cl^-, Na^+, K^+ and Li^+, respectively. All relationships between variables had positive correlations, indicating that the increase in one variable would also lead to an increase in the other one. Component 2 explains a cumulative variance of 59.24% with an *eigen value* of 2.72. It contains TH, SO_4^{2-} and Mg^{2+}. Component 3 had Fe^{3+} and PO_4^{3-} as important variables with cumulative variance 71.39% and *eigen value* of 2.07.

Table 5 Pearson correlation matrix of physicochemical parameters of groundwater in the study area

Variables	pH	EC	TDS	TH	TA	CO_3^{2-}	HCO_3^-	Cl^-	SO_4^{2-}	NO_3^-	PO_4^{3-}	Ca^{2+}	Mg^{2+}	Na^+	K^+	Fe^{3+}
EC	−0.29															
TDS	−0.30	**1.00**														
TH	−0.26	0.43	0.43													
TA	−0.17	**0.73**	**0.74**	0.23												
CO_3^{2-}	0.36	0.37	0.38	0.04	0.42											
HCO_3^-	−0.36	**0.64**	**0.64**	0.23	**0.91**	0.00										
Cl^-	−0.26	**0.98**	**0.98**	0.47	**0.67**	0.37	**0.57**									
SO_4^{2-}	−0.12	0.39	0.38	**0.61**	−0.06	−0.02	−0.05	0.44								
NO_3^-	0.02	0.13	0.14	−0.01	0.12	0.37	−0.05	0.04	−0.13							
PO_4^{3-}	−0.52	−0.15	−0.15	0.18	0.17	−0.29	0.32	−0.23	−0.09	0.00						
Ca^{2+}	−0.47	**0.66**	**0.65**	0.37	0.23	−0.13	0.32	**0.64**	**0.52**	−0.06	−0.12					
Mg^{2+}	0.03	0.17	0.17	**0.88**	0.14	0.18	0.07	0.23	0.38	0.05	0.15	−0.09				
Na^+	−0.16	**0.96**	**0.96**	0.20	**0.75**	0.45	**0.62**	**0.94**	0.24	0.16	−0.23	**0.56**	−0.02			
K^+	−0.18	**0.61**	**0.63**	0.36	0.29	0.07	0.29	**0.67**	**0.54**	−0.17	−0.26	**0.51**	0.15	**0.58**		
Fe^{3+}	−0.05	−0.35	−0.35	0.25	−0.11	−0.29	0.01	−0.36	0.03	−0.35	**0.75**	−0.25	0.32	−0.44	−0.39	
Li^+	−0.36	**0.85**	**0.87**	0.42	**0.67**	0.30	**0.59**	**0.87**	0.45	0.12	−0.03	**0.53**	0.21	**0.82**	**0.60**	−0.27

Level of significance > 0.05, and > 0.01 (two-tailed) for highlighted values

Table 6 Rotated component matrix representing principal component analysis (PCA) for groundwater around Bakhrija, Mahendragarh

Variables	Components				
	PC 1	PC 2	PC 3	PC 4	PC 5
EC	−0.25	−0.03	−0.32	−0.82	−0.10
TDS	**0.92**	0.23	−0.20	0.14	0.08
TH	**0.93**	0.22	−0.20	0.14	0.09
TA	0.26	**0.91**	0.18	0.12	0.02
CO_3^{2-}	**0.92**	−0.07	0.29	−0.18	0.06
HCO_{3-}	0.39	0.09	−0.21	−0.63	0.42
Cl^-	**0.83**	−0.12	0.42	0.10	−0.13
SO_4^{2-}	**0.89**	0.30	−0.27	0.11	0.01
NO_{3-}	0.14	**0.74**	−0.32	0.30	−0.17
PO_4^{3-}	0.05	−0.02	−0.05	−0.03	**0.96**
Ca^{2+}	−0.03	0.06	**0.90**	0.30	0.05
Mg^{2+}	0.48	0.20	−0.32	**0.65**	−0.08
Na^+	0.07	**0.87**	0.27	−0.26	0.08
K^+	**0.94**	0.02	−0.27	0.03	0.09
Fe^{3+}	**0.53**	0.33	−0.44	0.22	−0.27
Li^+	−0.28	0.28	**0.77**	−0.04	−0.31
EC	**0.83**	0.28	−0.11	0.19	0.09
Eigen value	**7.35**	**2.72**	**2.07**	**1.83**	**1.08**
CV (%)	**43.25**	**59.24**	**71.39**	**82.16**	**88.50**

Values in bold have significance value $p < 0.05$

In order to arrive at the spatial categorization of quality classes of groundwater, hierarchical cluster analysis using centroid linkage was performed using SPSS v20 to highlight the interrelationships among various sites (sampling locations) along with the selected water quality parameters. The dendrogram classified the data into three cluster memberships (Fig. 8). First cluster includes location numbers 1, 2, 3, 4, and 5 which are located North of Bakhrija mines. The second cluster includes sites at 6–15 (excluding location 11), which are located south of Bakhrija. The water quality at locations south of the mines was observed to be close to the one (Location 6) in mining area.

FTIR analysis

Finally, the FTIR analysis of the mined material and soil (1 km away) from the mining area revealed the presence of calcite ($CaCO_3$) and kaolinite ($Al_2Si_2O_5(OH)_4$), respectively, confirming to the fact that apart from reverse ion exchange reactions, silicate weathering is dominantly taking place around the mining region since kaolinite is the end member of silicate weathering profile.

Conclusion

Based on the observed results, the quality of most of the groundwater samples was compromised for drinking on account of TDS, hardness, alkalinity, calcium, magnesium, and nitrate. The suitability for irrigation was good except for relatively high concentration of magnesium. Since the soil is chiefly composed of aeolian sand with good permeability and hydraulic conductivity, long-term

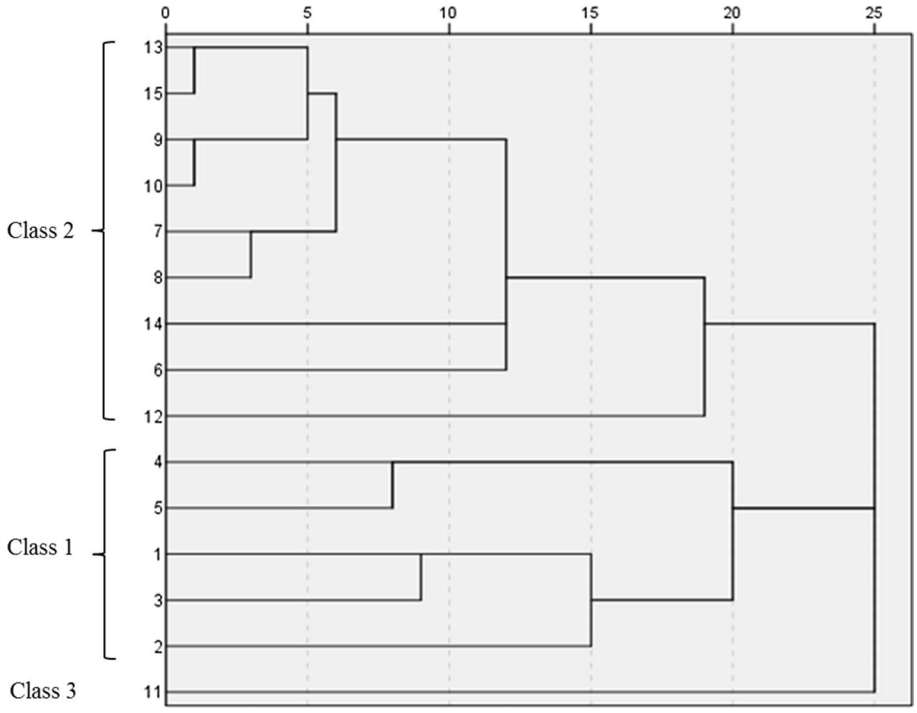


Fig. 8 Dendrogram for cluster analysis of groundwater samples

usage of groundwater in irrigation can be undertaken without affecting the quality of soil and agricultural production. Further, spatial variations in quality of groundwater were observed; and silicate weathering, dissolution of halite, calcite, and dolomite along with direct base exchange primarily governed the groundwater chemistry. The groundwater at most of the locations was classified as Na–Cl type with shallow meteoric percolation. The ratios of cations and anions, and FTIR analysis of soil and mine dust revealed that silicate weathering and halite dissolution have played a key role in regulating quality of groundwater. The study concluded that though stone mining in Mahendragarh district has limited direct effect on groundwater quality, its regular monitoring is imperative since increased intensity of mining in the future may enhance dissolution and dispersion of rock components thereby affecting groundwater.

Acknowledgements The authors acknowledge the help of Mr. Rajesh Sehrawat, Mine Inspector, Mahendragarh, for his help in sample collection and Dr. Ram Singh, Assistant Professor, Department of Chemistry, DTU, for his help in FTIR analysis of soil samples.

References

Abdullah TO, Ali SS, Al-Ansari NA (2016) Groundwater assessment of Halabja Saisadiq Basin, Kurdistan region, NE of Iraq using vulnerability mapping. Arab J Geosci 9:223. https://doi.org/10.1007/s12517-015-2264-y

Abiye T, Shaduka I (2017) Radioactive seepage through groundwater flow from the uranium mines, Namibia. Hydrology 4:11. https://doi.org/10.3390/hydrology4010011

Amitshreeya R, Panda RB (2012) Dust pollution in stone crusher units in and around Balasore, Orissa, India. J Ind Pollut Control 28(1):41–44

Annual Report 2014–2015, Ministry of Mines, Government of India, Delhi

APHA (2005) Standard methods for the examination of water and wastewater, 21st edn. American Public Health Association, Washington DC

Bayram A, Onsoy H (2015) Sand and gravel mining impact on the surface water quality: a case study from the city of Tirebolu (Giresun Province, NE Turkey). Environ Earth Sci 73:1997–2011

Bhumbla DR, Abrol IP (1972) Is your water suitable for irrigation. Indian Farm 22:15–17

Bishnoi SR, Brar SPS, Kumar D (1984) Underground water quality of Dhuri block, district Sangrur, Punjab. Indian J Ecol 11(2):220–228

Bureau of Indian Standards (BIS) (2012) Indian standard drinking water specifications (2nd Revision) BIS 10500: 2012, New Delhi

Central Ground Water Board (CGWB) (2013a) Groundwater Information Booklet, North Goa District, Goa, Ministry of Water Resources, Govt. of India, South West Region-Bengaluru

Central Ground Water Board (CGWB) (2013b) Groundwater Information Booklet District Mahendragarh, Haryana. Ministry of Water Resources. Government of India

Doneen LD (1961) In: Schiff L (ed) The influence of crop and soil on percolating waters. Proceedings of the biennial conference on ground water recharge

Doneen LD (1964) Water quality for agriculture. Department of Agriculture, University of California, Davis, p 48

Eaton EM (1950) Significance of carbonate in irrigation water. Soil Sci 69:123–133

Gaillardet J, Dupre B, Louvat P, Allegre CJ (1999) Global silicate weathering and CO_2 consumption rates deduced from the chemistry of large rivers. Chem Geol 59:3–30

Gibbs RJ (1970) Mechanism controlling world water chemistry. Science 17:1088–1090

Haritash AK, Baskar R, Sharma N, Paliwal S (2007) Impact of slate quarrying on soil properties in semi-arid Mahendragarh in India. Environ Goel 51:1439–1445

Haritash AK, Kaushik CP, Kaushik A, Kansal A, Yadav AK (2008) Suitability assessment of groundwater in some villages of Rewari district in Haryana. Environ Monit Assess 145(1–3):397–406

Haritash AK, Gaur S, Garg S (2016) Assessment of water quality and suitability analysis of River Ganga in Rishikesh, India. Appl Water Sci 6(4):383–392

Haritash AK, Mathur K, Priyanka S, Singh SK (2017) Hydrochemical characterization and suitability assessment of groundwater in Baga–Calangute stretch of Goa, India. Environ Earth Sci. https://doi.org/10.1007/s12665-017-6679-5

Jankowski J, Acworth RI (1997) Impact of debris-flow deposits on hydrogeochemical processes and the development of dryland salinity in the Yass River catchment. New South Wales, Australia. Hydrogeol J 5:71–88

Katz BG, Coplen TB, Bullen TD, Hal Davis J (1997) Use of chemical and isotopic tracer to characterize the interactions between groundwater and surface water in mantled karst. Groundwater 35(6):1014–1028

Kelly WP (1963) Use of saline irrigation water. Soil Sci 95:355–391

Matthess G (1982) The properties of ground water, 1st edn. Wiley, New York

Mayo AL, Loucks MD (1995) Solute and isotopic geochemistry and groundwater flow in the Central Wasatch Range, Utah. J Hydrol 172(1–4):31–59

Meybeck M (1986) Compositiondes ruisseau non pollutes de France. Sci Geo Bull 39:3–77

Meybeck M (1987) Global chemical weathering of surficial rocks estimated from river dissolved loads. Am J Sci 287:401–428

Moneim AAA (1988) Hydrogeology of the Nile Basin in Sohag Province. M.Sc. thesis, Geology Department, Faculty of Science, Assiut University, Assiut, Egypt

Nazzal Y, Ahmed I, Al-Arifi NSN, Ghrefat H, Zaidi FK, El-Waheidi MM, Batayneh A, Zumlot T (2014) A pragmatic approach to study the groundwater quality suitability for domestic and agriculture usage, Saq aquifer, northwest of Saudi Arabia. Environ Monit Assess 186:4655–4667

Paliwal KV (1972) Irrigation with saline water. IARI Monograph No. 2 (New Series), New Delhi, p 198

Piper AM (1953) A graphic procedure in geochemical interpretation of water analysis. USGS Groundw Note, No, p 12

Rajmohan N, Elango L (2004) Identification and evolution of hydrochemical process in the groundwater environment in an area of the Palar and Cheyyar River Basins, South India. Environ Geol 46:47–61

Richards LA (1954) Diagnosis and improvement of saline alkali soils. In: Agriculture handbook no 60. US Department of Agriculture, Washington, p 160

Saha DC, Padhy PK (2011) Effect of stone crushing industry on *Shorea robusta* and *Madhuca indica* foliage in Lalpahari forest. Atmos Pollut Res 2:463–476

Sami K (1992) Recharge mechanisms and geochemical processes in semi-arid sedimentary basin, Eastern Cape, South Africa. J Hydrol 139:27–48

Schoeller H (1977) Geochemistry of groundwater. In: Groundwater studies-an international guide for research and practice. UNESCO, Paris, vol 15, pp 1–18

Singh AK, Mahato MK, Neogi B, Tewary BK, Sinha A (2012) Environmental geochemistry and quality assessment of mine water of Jharia coalfield, India. Environ Earth Sci 65:49–65

Subramanian V (1987) Environmental geochemistry of Indian River basins-a review. J Geol Soc Ind 29:205–220

Wilcox LV (1955) Classification and use of irrigation water. USDA Circular 969, Washington DC, p 19

World Health Organization (WHO) (2006) Guidelines for drinking water quality. First addendum to 3rd edn, vol. 1, Geneva

Wu Q, Xing LT, He Ye C, Liu YZ (2011) The influences of coal mining on the large karst springs in North China. Environ Earth Sci 64:1513–1523

Zaczek J, Porowski A (2017) Hydrogeological settings and origin of groundwater composition in Southern part of Gorce Mts, Kowniec Maly catchment. Ann Soc Geol Pol 87:183–197

International Journal of Applied Engineering Research ISSN 0973-4562 Volume 13, Number 6 (2018) pp. 4053-4058
© Research India Publications. http://www.ripublication.com

Influence of Nano-particle on the Wear behaviour of Thin Film Coatings A Review

Shailesh Kumar Singh [*,1], Somnath Chattopadhyaya[1], A. Pramanik[2], Sanjeev Kumar[3], Navendu Gupta[4]

[1]Department of Mechanical engineering, Indian Institute of Technology (ISM), Dhanbad, Jharkhand, India.
[2]Department of Mechanical engineering, Curtin University, Bentley, WA, Australia.
[3]Department of Mechanical engineering, Krishna Engineering College, Ghaziabad, India.
[4]Department of Mechanical engineering, Delhi Technological University, Delhi, India.
Corresponding author

Abstract

The current study deals with the friction and wear behaviour of thin film coating used for automotive applications like piston rings, under the influence of nanoparticle like alumina-oxide, copper and many more. The study reports the influence of factors like load and speed under the presence of third body i.e. nano-particle and it has been found that the friction and wear of coatings are determined by adhesion at small load and dominated by adhesion and ploughing at higher load. The shape of particle also affects the wear properties during the test at Pin on disc tribometer. It is found that a small-sized particle can increase the wear of the coating by reducing the friction. These unique tribological mechanisms of the film can help to promote its wide applications in a sand-dust and presence of tiny particle environment.

Keywords: Nano particle; coating; wear; friction;

INTRODUCTION

Nanotechnology is a vibrant and developing area of science, engineering, and technology accomplished at the nanoscale level. In recent years, researchers have pointed out the numerous advantages of adding nanoparticles to lubricant oil. With its miniscule size, nanoparticles can easily mix with the lubricant oil to enhance its lubricating properties. The nanoparticles added to the lubricant oil help in preventing corrosion, reducing friction, and modifying the viscosity of the oil. Numerous articles have shown the effectiveness of adding nanoparticles to lubricants.

Influence of two kinds of nanoparticles as additives on GL-4 fully-formulated oil and poly-alpha olefin 8 base oil has been studied. Their experimental results showed that CuO additives had better effects on tribological behavior than Al_2O_3 nanoparticles in two types of synthetic oils. With 2 wt % CuO concentration dispersed in PAO8, the wear scar diameter reduced by 14% and the coefficient of friction reduced by 18%. Research studies [1-4] tested the tribological behavior of ZnO/ Al_2O_3 composite nanoparticles as additives to the lubricant. Their results showed that when added to lubricant the composite nanoparticles reduced friction and wear better than pure ZnO and Al_2O_3. Researcher synthesized and modified the surface of TiO2 nanoparticles with a double-coated agent. The concentration of nanoparticles ranged from 0.1 wt % to 1.6 wt % in a water-based medium. Their experimental results showed that the TiO_2-modified nanoparticles could increase the applicable load, reduce the friction force, and increase the anti-wear capacity of pure water. These excellent tribo-mechanical properties increase the research in nanoparticles that is also quite different relative to micro- particles and bulk materials. It also provides an effective way for surface modification of many devices that requires mechanical strength by improving the quality of nonmanufacturing/nanofabrication, etc. on the other hand nanoparticles with the lubricants also affect the tribological properties of mating parts in automobiles. In lubricated condition, the comparison in the hardness between nanoparticles and the mating parts determines whether particles are deformed into the surface when the contact pressure is sufficient [5-7].

This investigation aim is to review the important and recent trends in the tribo-mechanical properties of nanoparticles. The summarize work gives us a clear understanding to the Influence of nanoparticles on some of the mechanical properties of nanoparticles, such as wear, friction, hardness, elastic modulus and adhesion. and wide range of applications of nano-particles, include a lubricant with nano-particles as additives, nano-particles in nano manufacturing and nano-particle reinforced composite coating.

MATERIALS AND METHODS:

Table1give us a general classification and table 2 also clears the picture of the nanoparticles (NPs) application accordingly their weight, medium and effects in tribology. Some additive solutions contain the appropriate percentage of NPs have been used in the standard oil. Various mixing percentage and their effects are also shown in table2.

Table 1. General Classification of Nanomaterials

Engineered Nanomaterials	Carbon based	Fullerenes, C60 or C70 , Carbon nanotubes
	Metal based	Silver, nanometal oxide
	Dendrimers	Polymer with branched units
	Composites	Bioorganic complex

Table 2. Different materials (NPs) and their effects

S.No.	Name of NPs	Weight% and medium	Effects	Reference
1	Titanium oxide (TiO2)	0.1 to 1.6 wt % in a water-based medium	TiO_2-modified nanoparticles reduce the friction force, and increase the anti-wear capacity of pure water.	Gu et al. [7]
2	Titanium oxide (TiO2)	Added 25 nm TiO2 nanoparticles into a base oil with 0.01 wt %.	Significant reduction in coefficient of friction (COF) and wear rate has been observed in comparison to using a pure base oil lubricant with 0.01 wt %	Chang et al. [8]
3	Copper (Cu)	Tribology behavior of Pegasus 1005 oil with Cu additives as NPs.	Cu nanoparticles of 130 nm and engine oil was more effective than the engine oil itself containing 50 nm nanoparticles for the reduction in friction.	Zin et al. [9]
4	Copper (Cu)	Synthesized Cu NPs added into paraffin oil.	Their results showed that Cu nanoparticles of size 2–5 nm, reduced the COF of steel pair and displayed excellent thermal stability	Zhang et al. [10]
5	Alumina oxide (Al_2O_3)	Al_2O_3 NPs with different concentrations in engine oil has been used to evaluate their tribology. .	The analysis results showed that the minimum coefficient of friction was obtained with 0.8 wt % of medium nanoparticles size 60 nm.	Thakre et al. [11]

Synthesis of Nanoparticles

Nanomaterials attracts tremendous attention of the researchers due to its inherent properties in the preparation of nanoparticles. Some of the common methods are reported below.

Mechanical Attrition

Mechanical attrition produces its nanostructures by the structures decompositions of coarser gained structures as a result of plastic deformation. Some mechanical alloying process like rod milling and ball milling techniques received much attention as an advanced tool for the fabrication of several nanomaterials. These processes can be performed on both centrifugal type and high energy vibratory mills performed the experiments at room temperature. High energy ball mill includes [12,13]:

(a) Attrition Ball Mill (b) Planetary Ball Mill
(c) Vibrating Ball Mill (d) High energy Ball Mill
(e) Low energy Tumbling Mill

Chemical Precipitation

The basic method has been to synthesis and studies the nanomaterial in situ i.e. in the same liquid medium avoiding the physical changes and aggregation of tiny crystallites. The synthesis involved reaction between constituent material in suitable solvent. The dopent is added to the parent solution before precipitation reaction. Surfactant is used to maintain separation between the particles formed. Thermal coagulation and Oswald ripening were controlled by double layer repulsion of crystallites using non-aqueous solvents at lower temperatures for synthesis [12,13].

Gas Condensation

Gas condensation was the first technique used to synthesize Nano-crystalline metals and alloys. In this technique, a metallic or inorganic material is vaporized using thermal evaporation sources such as a Joule heated refractory crucibles, electron beam evaporation devices, in an atmosphere of 1-50 m bar. In gas evaporation, a high residual gas pressure causes the formation of ultra-fine particles (100 nm) by gas phase collision. The ultra-fine particles are formed by collision of evaporated atoms with residual gas molecules. Gas pressures greater than 3 mPa (10 torr) are required [14,15].

Vacuum Deposition and Vaporization

In vacuum deposition process, elements, alloys or compounds are vaporized and deposited in a vacuum. The vaporization source is the one that vaporizes materials by thermal processes. The process is carried out at pressure of less than 0.1 Pa (1 m Torr) and in vacuum levels of 10 to 0.1 MPa. The substrate temperature ranges from ambient to 500°C. The saturation or equilibrium vapor pressure of a material is defined as the vapor pressure of the material in equilibrium with the solid or liquid surface. For vacuum deposition, a reasonable deposition rate can be obtained if the vaporization rate is fairly high. A useful

deposition rate is obtained at a vapor pressure of 1.3 Pa (0.01 Torr) [16,17].

Electrodeposition

Nanostructured materials can also be produced by electrodeposition. These films are mechanically strong, uniform and strong. Substantial progress has been made in nanostructured coatings applied either by DVD or CVD. Many other non-conventional processes such as hypersonic plasma particle deposition (HPPD) have been used to synthesize and deposit nanoparticles. The significant potential of nanomaterial synthesis and their applications is virtually unexplored. They offer numerous challenges to overcome. Understanding more of synthesis would help in designing better materials. It has been shown that certain properties of nanostructured deposits such as hardness, wear resistance and electrical resistivity are strongly affected by grain size. A combination of increased hardness and wear resistance results in a superior coating performance [18,19].

EFFECT OF NANO-PARTICLES ON THE TRIBO-MECHANICAL PROPERTIES

Nanoparticles in lubrication

Nanoparticles play a major role in advance manufacturing due to its considerable impact at the mechanical properties. It may also influence the tribological properties of lubricated systems with nanoparticles. Various research reports about the wear behaviour of piston rings and liner with the lubricants. The effects of the mechanical properties of nanoparticles as lubricant additives on the tribological properties differ in various materials. From a general point of view, the combined effects of rolling, sliding and the formation of a third body layer and tribofilms are the main reasons for the increased lubricating behaviour after adding nanoparticles [20], as briefly described in the following parts. The lubricating properties of typical nanoparticle materials are summarized in table 3.

Spherical shaped nanoparticles which are mechanically stable without significant cluster are favourable for their rolling action contact area between tribopairs like piston rings and cylinder liner arrangement. This nature of nanoparticles with the lubricant (engine oil) provide a very low friction and wear. This reduction in coefficient of friction strongly reliant on the size, shape and concentration of nanoparticles in the lubricants. The sliding nature of nanoparticles also results in significant reduction in friction and wear. This behaviour came into existence due to particle non-spherical shape results low adhesion to the tribopairs. Besides, particle accumulation in the contact area is another factor that could lead to sliding friction during the shearing of tribopairs. Metal transfer and direct contact can be minimize by the nanoparticles play a role as a medium between the tribopairs. Another important aspect of the nanoparticle in the lubricant under a low applied pressure is that the viscosity of the lubricant could be enhanced and thereby the oil film formation properties in the lubricated contact could be improved. It is also pointed that nanoparticles as lubricant additives do not always give favourable tribological properties. Increases in friction and wear, as well as lubricant starvation, were also observed due to the abrasive effect of rigid nanoparticles under large pressures and heavy collections of oils with high particle concentrations in the inlet of the contact area [21-30].

Table-3 Different NPs and their favourable aspects with the lubrication mechanism

Material Category	**Example**	**Favourable aspects**	**Lubrication mechanism and regime**	**Unfavourable aspects**
Carbon-based nanoparticle	Graphite nanoparticle [29,30]	Friction reduction, anti-scuffing, surface polishing	(1) Ball-bearing effect (2) Viscosity-increasing effect (3) Increase in the surface hardness of tribopair	
	Diamond nanoparticle [31,32]	High temperature resistance, extreme pressure and self-lubrication ability	Ball-bearing spacers, reduce metal contact and increase the wettability of lubricant on surface	Water insoluble due to hydrophobicity
Silicon nanoparticle	SiO2 [33] Al2O3/SiO2 composite nanoparticles [34,35]	Cheap and easily available	Bear load, separate tribopair, prevent direct contact, and promote rolling, inhibit the expansion of the microcracks on the tribopair surface due to particle embedment	
Metal nanoparticles	Au [36], Ag [36, 37] Cu, Ni [38]	Friction and wear reduction, anti-contact fatigue, good extreme pressure	Friction and wear reduction, anti-contact fatigue, good extreme pressure.	Low dispersibility in organic solvent
	CuO, ZnO and ZrO_2 [39-40], TiO_2 Al_2O_3 [41,42]		Formation of the third body layer due to mechanical compaction	

NANOPARTICLES APPLICATION IN COATINGS

Incorporating diverse range of nanoparticles within a metal or polymer matrix to produce nanocomposites. Such nanocomposites can enhance the mechanical properties, wear resistance and self-lubricating properties [43].

Due to some of the integral assets of the matrix, for instance the high wear resistance, strength, modulus and high thermal and electrical conductivity, metal or metal alloy matrix composite coatings show distinct advantages over polymeric composites. In these coatings, ceramic (Al_2O_3, TiO_2, SiC and carbon-based graphite and CNTs nanoparticles are usually added. There are three reasons why ceramic particles are used as reinforcement to enhance the hardness and the wear resistance of composites. High strength and hardness of particles, migration and dislocation motion of grain boundaries can be prevented by the particles in the matrix. heterogeneous nucleation effect of particles in meta or metal alloys. The addition of graphite nanoparticles or CNTs in a metal matrix could, on the one hand, reduce the porosity of a pure metal coating, then the coating would be much denser and compact with fewer cracks. On the other hand, the crystalline size in the coating could be refined due to the presence of nanoparticles. In addition, the structural and chemical stability of CNTs, which have a higher stiffness and strength compared with the metal matrix are another important factor contributing to the strengthening effect. Some modification of the can be achieved by adding inorganic or organic nanoparticles, causing some new characteristics of polymers to be obtained in the physical properties [44-48].

CONCLUSIONS

Increasing demand of the tribological properties of many mechanical systems, new designs and improvements of surface modifications and manufacturing technologies. Nanoparticles exhibiting many unique mechanical properties have become one of the most attractive choices for meeting these needs in the past couple of years. The foregoing parts review basic physics and recent important results of nanoparticles from the perspectives of their mechanical properties and interfacial interactions, as well as related applications. Available fundamental research data regarding the mechanical properties of nanoparticles provide valuable guidance for their effective implementation in surface engineering, micro/Nano manufacturing and nanofabrication etc. Many of these applications with nanoparticles have already made impressive progress in practice and exhibited significant advantages in many fields. Despite these, further works are still needed to acquire information on the mechanical properties of more kinds of nanoparticles with the advances of convenient characterization techniques and mature nanoparticle production technologies. Quantitative descriptions of the mechanical properties of nanoparticles in relation to the size dependent and material effects etc. should be also made. Additionally, how to achieve a much clearer picture about the roles of nanoparticles in their specific applications is of great significance. Hence, direct visualizations of the interfacial behaviour of nanoparticles in applications on the micro-/nano- and even atomic scales would be very helpful.

REFERENCES

[1] Peña-Parás, L.; Taha-Tijerina, J.; Garza, L.; Maldonado-Cortés, D.; Michalczewski, R.; Lapray, C. Effect of CuO and Al2O3 nanoparticle additives on the tribological behavior of fully formulated oils. Wear 2015, 332–333, 1256–1261

[2] Mohanraj V and Chen Y 2006 Nanoparticles—a review Trop. J. Pharm. Res. **5** 561–73

[3] Manmode A S et al 2009 Nanoparticles-Tremendous therapeutic potential: a review Int. J. Pharm.Tech. Res. 1 1020–1027

[4] Bresme F and Oettel M 2007 Nanoparticles at fluid interfaces J. Phys.: Condens. Matter 19 413101

[5] Gu, Y.; Zhao, X.; Liu, Y.; Lv, Y. Preparation and tribological properties of dual-coated TiO2 nanoparticles as water-based lubricant additives. J. Nanomater. 2014, 2014, 8

[6] Akbulut M 2011 Nanoparticle-based lubrication systems J. Powder Metall. Min. 1 1

[7] Chang, H.; Li, Z.Y.; Kao, M.J.; Huang, K.D.; Wu, H.M. Tribological property of TiO2 nanolubricant on piston and cylinder surfaces. J. Alloys Compd. 2010, 495, 481–484.

[8] Zin, V.; Agresti, F.; Barison, S.; Colla, L.; Fabrizio, M. Influence of Cu, TiO2 nanoparticles and carbon nano-horns on tribological properties of engine oil. J. Nanosci. Nanotechnol. 2015, 15, 3590–3598.

[9] Zhang, Y.; Xu, Y.; Yang, Y.; Zhang, S.; Zhang, P.; Zhang, Z. Synthesis and tribological properties of oil-soluble copper nanoparticles as environmentally friendly lubricating oil additives. Ind. Lubr. Tribol. 2015, 67, 227–232.

[10] Thakre, A.A.; Thakur, A. Study of behaviour of aluminium oxide nanoparticles suspended in SAE20W40 oil under extreme pressure lubrication. Ind. Lubr. Tribol. 2015, 67, 328–335.

[11] Konrad,A., Herr, U., Tidecks, R. and Samwer, F.,(2001) " Luminescence of bulk and nanocrystalline cubic yttria" *J. of Appl. Phys.,* vol. 90(7) , pp3516-3523.

[12] Sharma, A.B., Sharma, M. and Pandey, R.K., (2009) " Synthesis, Properties and Potential Applications of Semiconductor Quantum Particles" *Asian Journal of Chemistry,* vol.21(10) , ppS033-038

[13] Hasany, S.F., Ahmad, I., Ranjan, J. & Rehman, A., (2012) "Systematic review of the preparation techniques of Iron oxide Magnetic Nanoparticles", Nanoscience & Nanotechnology, Vol. 2(6), pp148-158.

[14] Tissue, B.M. and Yuan H.B. , (2003) " Structure particle size and annealing gas phase-condensed Eu3+ : Y2O3 nanophosphors ", J. Solid State Chemistry, Vol. 171, pp12- 18.

[15] Chang, W., Skandan, G., Hahn, H., Danforth, S.C. and Kear, B.H., (1994)" Chemical vapor condensation of nanostructured ceramic powders", Nanostructured Materials, vol. 4(3), pp345- 351.

[16] Winterer, M. and Hahn, H., Metallkd, Z., (2003)" Chemical Vapor Synthesis of Nanocrystalline Powders ", Nanoceramics by Chemical Vapor Synthesis vol. 94, pp1084-1090.

[17] Dikusar**,** A.I., Globa**,** P.G., Belevskii**,** S.S. and Sidel'nikova**,** S.P., (2009) "On limiting rate of dimensional electrodeposition at meso- and nanomaterial manufacturing by template synthesis" Surface Engineering and Applied Electrochemistry, vol. 45(3), pp171-179.

[18] Silkin, S.A., Belevskii, S.S.**,** Gradinar'**,**A.S., Petrenko**,** V.I. and Yakovets, I.V., (2010) "Electrodeposition of nanocrystalline Co-W coatings from citrate electrolytes under controlled hydrodynamic conditions part 3: The micro- and macrodistribution of the deposition rates, the structure, and the mechanical properties" Surface Engineering and Applied Electrochemistry, vol. 46(3), pp206-214.

[19] Funehag J and Gustafson G 2008 Tunn. Undergr. Sp. Tech. 23 9

[20] Rapoport L et al 2003 Tribological properties of WS2 nanoparticles under mixed lubrication Wear 255 785–93

[21] Tevet O et al 2011 Friction mechanism of individual nanoparticles Proc. Natl Acad. Sci. USA 108 19901–6

[22] Xu T, Zhao J Z and Xu K 1996 The ball-bearing effect of diamond nanoparticles as an oil additive J. Phys. D: Appl. Phys. 29 2932

[23] Lee C G et al 2009 Study on the tribological characteristics of graphite nano lubricants Int. J. Precis. Eng. Manuf. 10 85–90

[24] Chen Q et al 2013 Preparation of water-soluble nanographite and its application in water-based cutting fluid Nanoscale Res. Lett. 8 52

[25] Chinas-Castillo F and Spikes H A 2003 Mechanism of action of colloidal solid dispersions Trans. ASME, J. Tribol. 125 552–7

[26] Song B Y et al 2003 Study of anti-contact fatigue performance of lubricant with nano silver particle Lubr. Eng. 5 23–6

[27] Yu H L et al 2008 Tribological properties and lubricating mechanisms of Cu nanoparticles in lubricant Trans. Nonferrous Met. Soc. China 18 636–41

[28] Zhang M et al Performance and anti-wear mechanism of Cu nanoparticles as lubricating oil additives Ind. Lubr. Tribol. 61 311–8

[29] Zhou J F et al 2000 Tribological behavior and lubricating mechanism of Cu nanoparticles in oil Tribol. Lett. 8 213–8

[30] Daeinabi K and Korayem M H 2011 Indentation analysis of nano-particle using nano-contact mechanics models during nano-manipulation based on atomic force microscopy J. Nanoparticle Res. 13 1075–91

[31] Kohonen M M et al 2004 On capillary bridges in wet granular materials Physica A 339 7–15.

[32] Li X H et al 2006 Surface-modification in situ of nano-SiO2 and its structure and tribological properties Appl. Surf. Sci. 252 7856–61.

[33] Kheireddin B A et al 2013 Inorganic nanoparticle-based ionic liquid lubricants Wear 303 185–90

[34] Jia D et al 2011 The tribology properties of alumina/silica composite nanoparticles as lubricant additives Appl. Surf. Sci. 257 5720–5

[35] Chinas-Castillo F and Spikes H A 2003 Mechanism of action of colloidal solid dispersions Trans. ASME, J. Tribol. 125 552–7.

[36] Song B Y et al 2003 Study of anti-contact fatigue performance of lubricant with nano silver particle Lubr.Eng. 5 23–6.

[37] Qiu S et al 2001 Preparation of Ni nanoparticles and evaluation of their tribological performance as potential additives in oils J. Tribol. 123 441–3.

[38] Battez A H et al 2008 CuO, ZrO2 and ZnO nanoparticles as antiwear additive in oil lubricants Wear 265 422–8

[39] Battez A H et al 2007 Wear prevention behaviour of nanoparticle suspension under extreme pressure conditions Wear 263 1568–74.

[40] Radice S and Mischler S 2005 Lubrication properties of Al_2O_3 nanoparticles in aqueous suspensions Tribol. Interface Eng. Ser. 48 101–5

[41] Radice S and Mischler S 2006 Effect of electrochemical and mechanical parameters on the lubrication behaviour of Al_2O_3 nanoparticles in aqueous suspensions Wear 261 1032–41.

[42] Lin J C et al 2006 Mechanical behavior of various nanoparticle filled composites at low-velocity impact Compos. Struct. 74 30–6.

[43] Shen J H et al 2013 Effect of ceramic nanoparticle reinforcements on the quasistatic and dynamic mechanical properties of magnesium-based metal matrix composites J. Mater. Res. **28** 1835–52

[44] Wang Z H et al 2010 SiC nanoparticles reinforced magnesium matrix composites fabricated by ultrasonic method Trans. Nonferrous. Met. Soc. China **20** s1029–32.

[45] Rohatgi P K and Schultz B 2007 Lightweight metal matrix nanocomposites-stretching the boundaries of metals Mater. Matters **2.4** 16

[46] Muralidhara H B et al 2012 Electrodeposition of Zn-Graphite nanoparticles composite and their characterization J. Chem. Pharm. Res. **4** 440–9

[47] Bakshi S R, Lahiri D and Agarwal A 2010 Carbon nanotube reinforced metal matrix composites—a review Int. Mater. Rev. **55** 41–64

Available online at www.sciencedirect.com

ScienceDirect

Materials Today: Proceedings 5 (2018) 4250–4257

materialstoday: PROCEEDINGS

www.materialstoday.com/proceedings

ICMPC 2017

Investigation of Chip-Tool Interface Temperature: Effect of Machining Parameters and Tool Material on Ferrous and Non-Ferrous Metal

Surabhi Lata[a,*], Ramakant Rana[b], Hitesh[c]

[a, c] *Maharaja Agrasen Institute of Technology, Rohini, Delhi 110086, India*
b Delhi Technological University, Bawana, Delhi 110042, India

Abstract

In the present context of sustainable manufacturing and eco-friendly scenario, investigation of cutting temperature generated during machining of various ferrous and non-ferrous metals is an act of concern to understand the metal cutting issues such as dimensional accuracy, surface finish, tool wear, material removal rate and tool life. In this investigation, average chip-tool interface temperature has been determined taking into account the effect of machining parameters and the tool material, namely, tungsten carbide and poly crystalline diamond (PCD) during turning of IS 733 Gr 63400 aluminium and IS 2062 steel. Mathematical model was developed based on experimental observations to predict the average chip-tool interface temperature. Experimental results concluded that the temperature showed a rise on increasing the machining parameters. It was also concluded that the temperature during machining of ferrous metals significantly depend on tool material while for non-ferrous metals (ductile) the tool material is less significant. Among the machining parameters cutting speed highly influence the average chip-tool interface temperature.
© 2017 Elsevier Ltd. All rights reserved.
Selection and/or Peer-review under responsibility of 7th International Conference of Materials Processing and Characterization.

Keywords: Chip-tool interface temperature; Tool-work thermocouple; Carbide, PCD

1. Introduction

In today's technological society, evaluation of the machining performance through predictive or simulation modelling to the progress of cutting technology has been extensively researched. The aim to maximize productivity

* Corresponding author. Tel.: +91 9210055994.
E-mail address: surabhilata_verma@yahoo.co.in

2214-7853© 2017 Elsevier Ltd. All rights reserved.
Selection and/or Peer-review under responsibility of 7th International Conference of Materials Processing and Characterization.

Nomenclature

ANN	Artificial Neural Network
DOC	Depth of Cut
Emf	Electromotive Force
FEM	Finite Element Modelling
GA	Genetic Algorithm
HAZ	Heat Affected Zone
IR	Infra-Red
PCD	Poly-crystalline Diamond
RSM	Response Surface Methodology

and obtain higher material removal rates has developed the curiosity to come up with new and more reliable predictive and simulation models for all machining and manufacturing processes. Heat generation in machining operations is an important factor as it greatly influences the dimensional accuracy, surface integrity, work surface structure, tool life etc. Therefore, evaluation and development of a mathematical model which can predict chip-tool interface temperature during machining has become vital. Previously, various techniques like tool-chip thermocouple, embedded thermocouple, thermo-colours and radiation have been developed to investigate the chip-tool interface temperature arising in the cutting zone during machining. Among all the most widely used technique, even today, is the tool-work thermocouple technique. Video analysis technique was developed by Cotterell et al. [1] to obtain shear strain and thermal model using high speed imaging and IR imaging for strain and temperature measurement during orthogonal cutting in a milling machine. Heigel et al. [2] estimated temperature distribution at the tool-chip interface in orthogonal machining of titanium alloys using YAG tools with the help of infrared technique for different cutting speeds. Tuğrul and Erol [3] introduced a methodology to predict cutting arrangement and friction attribute at tool-chip interface for material model of Johnson-Cook as an extended metal cutting analysis proposed by Oxley. Satish and Choudhury [4]and Abhang and Hameedullah [5] investigated the average temperature at chip-tool interface from a statistical model using tool-work thermocouple model accounting the effect of cutting parameters and coated tools for steel workpieces.GA based approach was developed by Guang et al. [6]for flow stress optimization of Johnson–Cook material model for titanium alloy manifested by finite element simulation model for diverse room temperatures and strain rates. Yogesh and Alan [7] simulated transient metal cutting operation for the estimation of cutting forces and interfacial tool-chip temperatures using advanced FEM. Using RSM technique Kannan et al. [8] optimized the cutting parameters for minimum cutting temperature and maximum surface finish in turning. Kun and Wenyu [9] ameliorated a thermal model of orthogonal cutting analytically for minimum residual stresses and HAZ on the machined workpiece. A numerical model to determine distribution of temperature in orthogonal cutting using FEM was established by Yahya et al. [10] and Pradip et al [11]. Amulya et al. [12] aimed to reduce the heat generation in turning using TLBO and GA by optimization of cutting parameters. Marcio and James [13] reviewed the analytical and experimental methods for temperature measurement in orthogonal cutting. Using GP modeling, equation for tool-chip contact length was proposed by Zadshakoyan and Pourmostaghimi [14]. Abdil et al. [15] showed the cutting speed as the most effectual parameter in tool-chip temperature assessment by K-type thermocouple and IRpyromete.Adnan et al. [16] reviewed the optimized selection of machining parameters including cutting temperature in turning operation using GA and aftermath the gaps in field of cutting temperature optimization. Tool-chip interface temperature in orthogonal cutting was determined and modelled by Pedro et al. [17], Julien et al. [18]and Daniel et al. [19] using infrared thermography for steel and titanium alloy jobs. Sutter and Ranc [20] experimentally determined the temperature distribution with the help of a ballistic device in orthogonal cutting by recording thermal cartographies for high speed machining of low and medium carbon steel. Fuat et al. [21] predicted cutting temperatures in orthogonal cutting of stainless steel with aid of ANN optimization technique. Abukhshim et al. [22] reviewed and compared heat generation, heat dissipation, and temperature measurement techniques for orthogonal high speed machining process. Sadeghifar et al. [23] optimized machining parameters using amalgamation of GA and SQP techniques for minimum cutting temperature and constant cutting force. Application Taguchi's method was employed by for Zoran

et al. [24] for optimization of the cutting variables based on minimum interfacial temperature of tool and chip, in turning steel with cemented carbide inserts using tool-work thermocouple method. Chikalthankar et al. [25] reviewed the effect of chip-tool contact temperature on turning performance on lathe with machining parameters such as speed, feed and depth of cut. Vishav and Rickramjeet [26] figured optimum machining parameters and turning be havior on workpiece for attaining minimum tool tip temperature by alleviating the temperature using vegetable oil. For economical dry and MQL machining, Mandal and Tanmoy [27] modelled and optimized the tool-chip temperature and surface roughness using GA and RSM techniques for steel work piece as shown in below Table 1.

2. Experimentation

The investigations were performed on IS 733 Gr 63400 aluminium and IS 2062 steel as work materials. The length and diameter of the workpiece used were 600 mm and 60 mm, respectively. Experimental tests were performed using the K10 carbide tool and KP500 Poly-crystalline Diamond tool conforming to Turning Applications Manual of Taegu Tec (Member IMC Group). This grade is usually used for turning, milling and hole making of cast iron, aluminium and non-ferrous alloys, steels and heat-resistant alloys. The optimum machining parameters were deduced in order to minimize the chip tool interface temperature and investigate various factors contributing as its cause. The details of tool geometries, tool materials and tool holders was extensively studied from the research work conducted in the past and the turning applications manuals of number of companies such as TaeguTec, Sandvik, etc. Dry orthogonal cutting was carried out on the conventional centre lathe from Hindustan Machine Tools. The machining parameters were set after conducting number of trial runs on different work diameters and available spindle speeds. The tool geometry, tool height, tool overhang and feed rate were kept constant throughout the conduction of experiments. A design matrix was generated considering the input parameters at three levels. This approach is the statistical technique which was used to conduct experimentation with all possible combinations. In this experiment, natural tool-work thermocouple method was used to measure the average chip-tool interface temperature during turning of IS 733 Gr 63400 aluminium and IS 2062 steel using tungsten carbide and PCD tools. The relation between the machining parameters and the average chip-tool interface temperature was developed by changing the cutting speed and the depth of cut in accordance to the designed matrix.



Fig. 1. Designed experimental set-up.

Response Surface Methodology (RSM) technique can authentically predict the responses within the low and high level only, hence additional experiments were performed to identify the temperature pattern for the work materials.

The relation between the electro-motive force (emf) and the average chip-tool interface temperature was established using a tool-work calibration set-up as shown in above Fig 1.

Table 1 Experimental Design Matrix showing Actual values of Machining Parameters

Run	Coded Levels		Cutting Speed (Rpm)	Depth Of Cut (Mm)
	Cutting Speed	Depth Of Cut		
1	-1	-1	233	0.5
2	-1	0	233	1.5
3	-1	+1	233	2.5
4	0	-1	340	0.5
5	0	0	340	1.5
6	0	+1	340	2.5
7	+1	-1	530	0.5
8	+1	0	530	1.5
9	+1	+1	530	2.5

3. Results and Discussion

3.1. Development of Predictive Model

Average chip-tool interface temperature was expressed in terms of cutting parameters, namely, cutting speed and depth of cut. In general, form the response function can be expressed as follows:

$$\gamma = \Phi(V, D) \quad (1)$$

where Y = Response (chip-tool interface temperature); V = Cutting speed (m/min); D = Depth of cut (mm)
Using the following regression equation

$$\gamma = \beta_o + \beta_1 V + \beta_2 D + \beta_{12} V * D \quad (2)$$

where β_0 is constant while β_1, β_2, and β_{12} are partial regression coefficients of the model
the response function was generated which is given below:

$$T = C * V^{*1} * D^{*2} \quad (3)$$

Where T = chip tool interface temperature (°C)
C = Constant
V = Cutting speed (m/min)
D = Depth of cut (mm)

The unknown coefficients, namely, exponents of cutting speed and depth of cut and constants involved in (3) were determined by minimizing the least squares error between experimental and predicted results obtained within the range of cutting conditions. The developed model of average chip-tool interface temperature for all combinations is further discussed in the following section.

3.2. Temperature Analysis

3.2.1. Ferrous Metal: IS 733 Gr 63400 Steel

- Tungsten Carbide

The governing response function is as follows:

$$T = 532.17*V^{0.213733}*D^{0.179545} \quad (4)$$

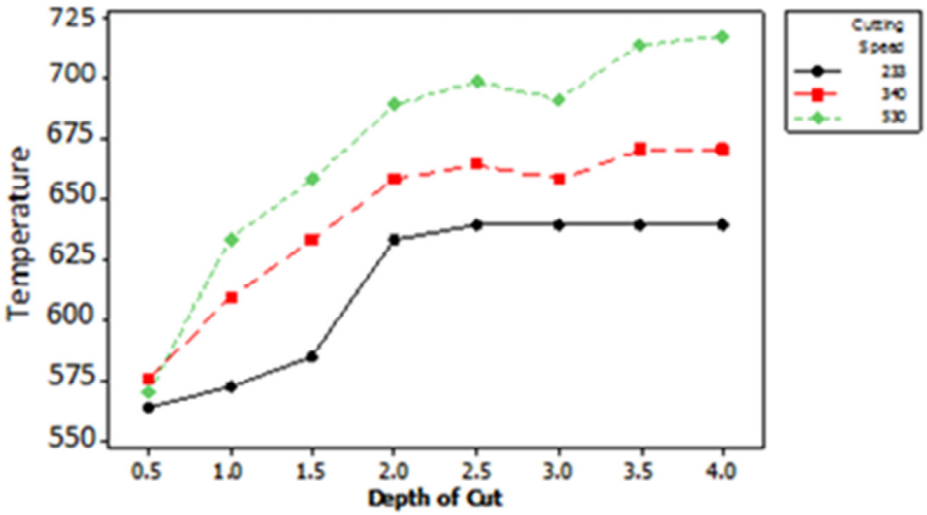


Fig. 2. Temperature-Depth of Cut Curvefor Tungsten Carbide – Steel Combination

From Fig 2 The plot of interaction effects for tungsten carbide tool and steel work shows that when cutting speed increases from 233 m/min to 340 m/min and further to 530 m/min, the chip tool interface temperature increases. While when depth of cut increases, the temperature reaches its maximum value at 2.5 mm of DOC and then decreases and further increases as DOC is increased.

- Poly Crystalline Diamond Insert

  The governing response function is as follows:

$$T = 614.1413*V^{0.177342}*D^{0.188984} \quad (5)$$

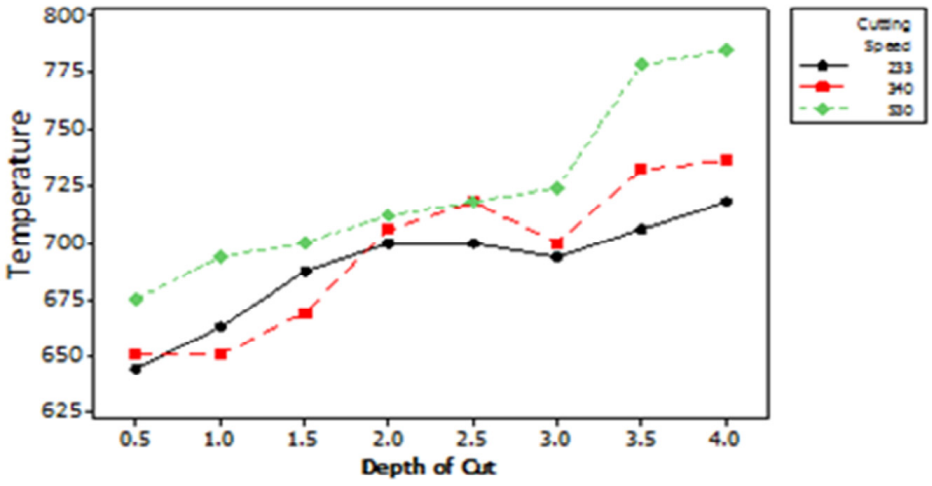


Fig. 3. Temperature-Depth of Cut Curve for PCD – Steel Combination

The plot of interaction effects for PCD tool and steel work shows that when cutting speed increases from 233 m/min to 340 m/min and further to 530 m/min the chip-tool interface temperature increases. While when depth of cut increases, the temperature increases to a maximum value at 2.5 mm DOC after which it decreases and further increase on increase in DOC values as shown in above Fig 3.

From the above two graphs, it can be inferred that the chip-tool interface temperature is also dependent on work and tool materials along with the machining parameters. When ferrous or hard metals are machined, the chip-tool interface temperature shows a steep rise when turned with the PCD tool while a gradual rise is exhibited with tungsten carbide tool. With the same work material, i.e. steel, the chip-tool interface temperature difference is high which clearly indicate the significance of tool material on the chip-tool interface temperature during turning operation.

3.2.2. Non-ferrous metal: IS 733 Gr 63400Aluminium

- Tungsten Carbide

  The governing response function is as follows:

$$T = 310.9611*V^{0.21971}*D^{0.0975696} \quad (6)$$

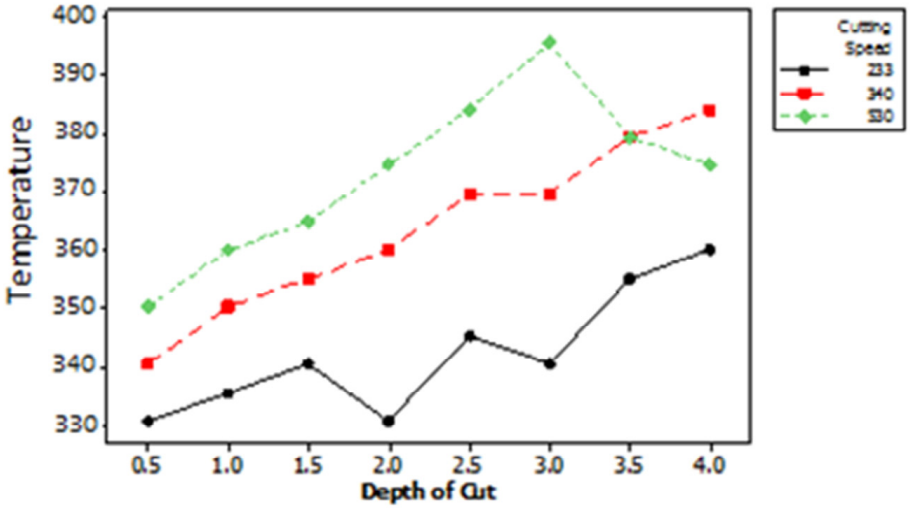


Fig. 4. Temperature-Depth of Cut Curve for Tungsten Carbide – Aluminium Combination

The plot of interaction effects for tungsten carbide tool and aluminum work shows that when cutting speed increases from 233 m/min to 340 m/min and further to 530 m/min, the chip tool interface temperature increases. As shown in Fig 4. While when depth of cut increases the temperature also increases. It shows how the chip-tool interface temperature varies at different cutting speeds between 0.5 to 4.0 mm DOC range. At 530 m/min cutting speed the temperature decreases when the DOC is increased from 3.0 mm to 3.5 mm and further while in other cases it increases.

- Poly Crystalline Diamond Insert

  The governing response function is as follows:

$$T = 338.79968*V^{0.196905}*D^{0.0718086} \quad (7)$$

The plot of interaction effects for PCD tool and aluminum work shows that when cutting speed increases from 233 m/min to 340 m/min the chip tool interface temperature increases and further increase of cutting speed to 530 m/min decreases the temperature. While when depth of cut increases, the temperature increases after initial dip at the value at 1.0 mm DOC.

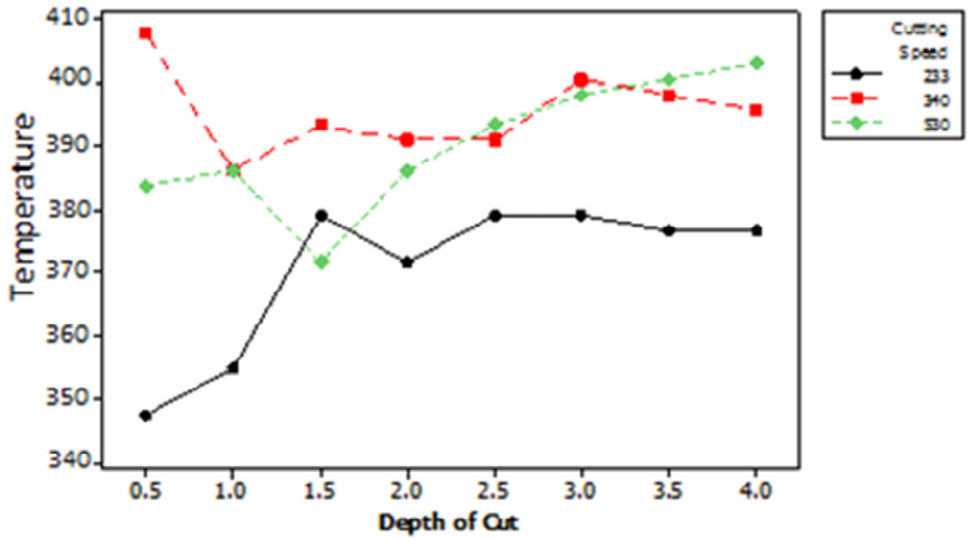


Fig. 5. Temperature-Depth of Cut Curve for PCD – Aluminium Combination

As seen from the above two graphs, the temperature generated at the chip-tool interface during machining of soft metals (usually non-ferrous) show very less dependency on tool materials. A close study of graphs reveal that when tungsten carbide and PCD tools are used, the chip-tool interface temperature difference is very minute. The most significant factor remains the cutting speed during the machining of soft and ductile metals.

The correlation coefficient (R-Squared value) found 0.9693 showed that the developed model is valid and could be used for predicting the average chip-tool interface temperature for the defined combination of tool and work material along with the domain of the cutting parameters. The graphical plot showing the predicted values of average chip-tool interface temperature (obtained using (2) along with the experimental values is shown in Fig. 5.

4. Conclusion

In this study, in view of probable effects of heat generated during machining on tool life, surface integrity and dimensional accuracy, a model can be formulated which could predict average chip-tool interface temperature during turning of IS 733 Gr 63400 aluminium and IS 2062 steel using K10 carbide tool and KP500 Poly-crystalline Diamond tools based on experimental observations. It can be concluded from the results that increase in machining parameters leads to increase in average chip-tool interface temperature. This is due to the frictional factors i.e. sticking and slipping frictions governing the shear zone plane in the cutting zone. The more is the heat generated more will be the structural changes on the surface of work materials. From the above results, it is inferred that tool material also plays a significant role in the heat generation. Not much significance is recorded in non-ferrous metals such as aluminium due to the tool material while the same parameter is highly significant in case of ferrous metals. The soft metals exhibit a variation of ± 10° - 20°C temperature difference on change of tool material whereas hard metals shows variation from ±100° - 150°C temperature. In general context, it can be concluded that poly crystalline diamond tool yields better results of machining at high speed and low depth of cut while machining with tungsten carbide tool best results are obtained at medium speed and medium depth of cut.

References

[1] M. Cotterell, E. Ares, J. Yanes, F. López, P. Hernandez, G. Peláez, Temperature and strain measurement during chip formation in orthogonal cutting conditions applied to Ti-6Al-4V, *Procedia Engineering*, 2013, Volume 63, pp. 922 – 930

[2] J. C. Heigel, E. Whitenton, B. Lane, M.A. Donmez, V. Madhavan, W. Moscoso-Kingsley, Infrared measurement of the temperature at thetool-chip interface while machining Ti-6Al-4V, *Journal of Materials Processing Technology*, 2016

[3] TuğrulÖzel and Erol Zeren, Estimation of work material flow stress and tool-chip interfacial friction by inverse computation of modified.

[4] Satish Chinchanikar and S. K. Choudhury, Evaluation of chip-tool interface temperature: Effect of tool coating and cutting parameters during turning hardened AISI 4340 steel, *Procedia Materials Science*, 2014, Volume 6, pp. 996 – 1005

[5] L. B. Abhang and M. Hameedullah, Chip-tool interface temperature prediction model for turning process, *International Journal of Engineering Science and Technology*, 2010, Volume 2, pp. 382 – 393

[6] Guang Chen, ChengzuRen,Wei Yu, Xiaoyong Yang and Lifeng Zhang, Application of genetic algorithms for optimizing the Johnson–Cook constitutive model parameters when simulating the titanium alloy Ti-6Al-4V machining process, *Journal of Engineering Manufacture*, 2012, Volume 226, pp. 1287– 1297

[7] Yogesh K. Potdar, Alan T. Zehnder, Measurements and simulations of temperature and deformation fields in transient metal cutting, *Journal of Manufacturing Science and Engineering*, 2003, Volume 125, pp. 645 – 655

[8] A. Kannan, K. Esakkiraja, Dr. M. Nataraj, Modeling and analysis for cutting temperature in turning of Aluminium 6063 using response surface methodology, *Journal of Mechanical and Civil Engineering*, 2013, Volume 9, pp. 59 – 64

[9] Kun Huang and Wenyu Yang, Analytical model of temperature field in workpiece machined surface layer in orthogonal cutting, *Journal of Materials Processing Technology*, 2015

[10] YahyaDogu, Ersan Aslan, NecipCamuscu, A numerical model to determine temperature distribution in orthogonal metal cutting, *Journal of Materials Processing Technology*, 2006, Volume 171, pp. 1 –9

[11] PradipMajumdar, R. Jayaramachandran, S. Ganesan, Finite element analysis of temperature rise in metal cutting processes, *Applied Thermal Engineering*, 2005, Volume 25, pp. 2152–2168

[12] N. Amulya, PVS Subhashini, K. Chinmayi, Naveen R., Parametric optimization of heat generation during turning operation, *Journal of Mechanical Engineering and Automation*, 2016, Volume 6, pp. 117–120

[13] MarcioBacci da Silva and James Wallbank, Cutting temperature: Prediction and measurement methods—A review, *Journal of Materials Processing Technology*, 1999, Volume 88, pp. 195–202

[14] M. Zadshakoyan, V. Pourmostaghimi, Genetic equation for the prediction of tool–chip contact length in orthogonal cutting, *Engineering Applications of Artificial Intelligence*, 2013, Volume 26, pp. 1725 –1730

[15] AbdilKus, YahyaIsik, M. CemalCakir, SalihCoşkun and KadirÖzdemir, Thermocouple and infrared sensor-based measurement of temperature distribution in metal cutting, *Sensors*, 2015, Volume 15, pp. 1274 – 1291

[16] Adnan Jameel, Mohamad Minhat, Md. Nizam, Using genetic algorithm to optimize machining parameters in turning operation: A review, *International Journal of Scientific and Research Publications*, 2013, Volume 3

[17] Pedro-J. Arrazola, PatxiAristimuno, Daniel Soler, Tom Childs, Metal cutting experiments and modelling for improved determination of chip/tool contact temperature by infrared thermography, *CIRP Annals - Manufacturing Technology*, 2015

[18] Julien Artozoul, Christophe Lescalier, Olivier Bomont, Daniel Dudzinski, Extended infrared thermography applied to orthogonal cutting: Mechanical and thermal aspects, *Applied Thermal Engineering*, 2014, Volume 64, pp. 441 – 452

[19] Daniel Soler, PatxiAristimuño, AinharaGaray, Pedro J. Arrazola, Uncertainty of temperature measurements in dry orthogonal cutting of titanium alloys, *Infrared Physics & Technology*, 2005, Volume 71, pp. 208 – 216

[20] G. Sutter and N. Ranc, Temperature fields in a chip during high-speed orthogonal cutting - An experimental investigation, *International Journal of Machine Tools & Manufacture*, 2007, Volume 47, pp. 1507 – 1517

[21] Fuat Kara, KubilayAslantaş, AdemÇiçek, Prediction of cutting temperature in orthogonal machining of AISI 316L using artificial neural network, *Applied Soft Computing*, 2015

[22] N. A. Abukhshim, P. T. Mativenga, M. A. Sheikh, Heat generation and temperature prediction in metal cutting:A review and implications for high speed machining, *International Journal of Machine Tools & Manufacture*, 2006, Volume 46, pp. 782–800

[23] M. Sadeghifar, R. Sedaghati , V. Songmene, FE modeling and optimization of cutting temperature in orthogonal turning,*International Congress of Theoretical and Applied Mechanics*, 2016, pp. 21 – 26

[24] Milenko Sekulić, Marin Gostimirović, Pavel Kovač, BorislavSavković, Optimization of cutting parameters based on toolchip interface temperature in turning process using Taguchi's method, *Journal of Trends in the Development of Machinery and Associated Technology*, 2011

[25] S. B. Chikalthankar, R. B. Kakade, V. M. Nandedkar, Investigation and Optimization of Tool Tip Temperature in Turning of OHNS, *International Journal of Engineering Research & Technology*, 2014, Volume 3, 1039 – 1044

[26] VishavKainth, Rickramjeet Singh, Optimization of machining parameters on tool tip temperature by using vegetable oil on EN8 material, *International Journal of Research in Engineering and Technology*, 2015, Volume 04, pp. 30 – 33

[27] N. K. Mandal and Tanmoy Roy, Modelling and optimization of tool chip interface temperature and surface roughness in CNC dry turning of EN 24 steel, *Advanced Engineering Forum*, 2016, Volume 16, pp. 7 – 15.

Long Term Load Forecasting with Hourly Predictions based on Long-Short-Term-Memory Networks

Rahul Kumar Agrawal[1], Frankle Muchahary[2],
[1]Dept. of Electrical Engineering,
[2]Dept. of Applied Chemistry, Delhi Technological University, New Delhi, India
[1]rahulagrawal0048@gmail.com,
[2]franklemuchahary@gmail.com

Madan Mohan Tripathi
Dept. of Electrical Engineering, Delhi Technological University,
New Delhi, India
mmmtripathi@gmail.com

***Abstract*— The conventional methodology for long term load forecasting is mostly restricted to electricity load data with monthly or annual granularity. This leads to forecasts with very low accuracy. In this paper, a novel method for long term load forecasting with hourly resolution is proposed. The model is fundamentally centered on Recurrent Neural Network consisting of Long-Short-Term-Memory (LSTM-RNN) cells. The long term relations in a time series data of electricity load demand are taken into account using LSTM-RNN and hence results in more accurate forecasts. The proposed model is implemented on real time data of ISO New England electricity market. Precisely, publicly available data of twelve years from 2004 to 2015 have been collected to train and validate the model. Electricity demand predictions have been made for a period of five years from 2011 to 2015 on a rolling basis. The proposed model is found to be highly accurate with a Mean Absolute Percentage Error (MAPE) of 6.54 within a confidence interval of 2.25%. Moreover, the model has a computation time of approximately 30 minutes which is favorable for offline training to forecast electricity load for a period of five years.**

Keywords—Long term load forecasting, Long-Short-Term-Memory, Recurrent Neural Network, Smart grid

I. INTRODUCTION

For efficient budget planning and profit analysis on investments, load forecasting of electricity load for a period of one year or more serves as an important tool for utility companies [1]. These utility companies use the load forecasts to decide the construction of new power plants, extension of transmission lines and determine the fuel sources of generation facilities. The accuracy of forecasting significantly affects the financial performance of participants in electricity market. Moreover, Energy Service Providers sign forward contracts on a yearly basis to maximize their profits and reduce the risks on investments [2]. This requires energy service providers to predict year-ahead load in order to make an informed decision and finalize their strategy. If the electricity load forecast is overestimated, it will result in higher investments than required while the customer load demand would be challenging to meet with an underestimation [3]. With a monthly or annual granularity, the limited number of observations cannot capture the features and dependencies of the parameters affecting electric loads and therefore lead to inaccurate predictions. As the modern smart grids offer high resolution hourly data of electricity load, prediction of hourly load demand on a long term basis can be advantageous for a more accurate forecast.

Long-term load forecasting refers to predicting electricity load demand in a particular area for durations pertaining longer than a year. Most of the work on load forecasting has been focused on short-term load forecasting where the forecast period does not exceed more than two weeks. Various statistical and deep learning based models have been proposed for short-term load forecasting including linear regression, Feed forward neural network, neuro-fuzzy models and support vector machines [4-6]. However, very limited work has been proposed for forecast of electric load demand of more than a year. Vlahovic et al. proposed a mathematical model based on regression for forecasting long term load demands back in the 1980s [7]. A model based on grey theory has also been suggested for accurate predictions [8]. Other models proposed were based on time series models like ARMA, fuzzy logic and hybrid neural model [9-11]. A spatial load forecasting method has been proposed for long term forecasting and is used by various utility companies [12]. However, majority of the mentioned works utilize annual resolution of either peak energy demand or total energy consumption to forecast load for a period of one to ten years. Attributed to the small number of observations, these forecasts are inadequate for making an informed decision of planning and investments for the utility companies.

This paper proposes a Long-Short-Term-Memory based Recurrent Neural Network (LSTM-RNN) model for forecasting electricity demand for a period of five years. The model is implemented on real time electricity data provided by the ISO New England. The predictions have hourly frequency and hence are highly beneficial for use by the utility companies. The hourly predictions provide a more accurate description of load demand in the forthcoming years and maximum load demand can also be computed on a monthly basis using the data obtained. For performing time series predictions, Recurrent Neural Networks (RNNs) are one of the most widely used models [13]. However, they suffer from an inherent problem of vanishing gradient descent. To overcome this problem and additionally formulate long term dependencies between training samples, LSTM-RNN is used which significantly increases the precision of the proposed model [14]. The model presented in the paper is found to be competently accurate with an overall Mean Absolute

978-1-5386-1006-0/18/$31.00 ©2018 IEEE

Percentage Error (MAPE) of 6.54 with a confidence interval of 2.25%. Training of the model requires a computational time of 30 minutes. A forecast of a period of five years requires offline training once a year and hence the mentioned computational time is favorable in the given scenario.

The rest of the paper is structured as follows: In Section II, Recurrent Neural Network model has been explained in mathematical terms. The benefits of Long-Short-Term-Memory cells to improve the performance of RNN are depicted in Section III. Section IV describes the complete methodology from feature engineering to training of the proposed model applied on ISO New England Market. Subsequently, the performance metrics have been included in Section V. This has been further illustrated with the use of plots. The paper has been recapitulated in Section VI and potential future works have also been discussed.

II. Recurrent Neural Network

For short term load forecasting, feed-forward neural networks have been able to forecast load with high accuracies. An implementation of feed-forward neural networks assumes that the training and test data are independent [15]. As the dataset of electricity load demand is a time series data, this assumption fails and hence feed-forward neural network is not suitable for long term forecasting. Conversely, Recurrent Neural Networks were introduced to work on time series data and allow the learning of time based dependencies from the data [13]. Feed forward neural networks also restrict the inputs and labels to be fixed length vectors and therefore are not suitable for prediction on time series electricity data.

In each subsequent cycle of training, the outputs of the previous cycle are used as inputs in RNN. There are internal connections among the hidden units and loops are introduced in the architecture. These internal connections help in using the historical data for forecasting. Each layer in an RNN has a recurrent link with a delay related to it. Hence the previous outputs are said to be stored in a kind of 'memory' and the part of the RNN that preserves a state over a specific temporal range is said to be a 'memory cell'. These memory cells can also be further modified to form other types of more complicated cells. Concretely, RNNs can be used to establish connections among data which are distant in time [16]. For long term load forecasting, as the electricity dataset is time series in nature and the load demand of the next year need to be forecasted, RNNs are found be an appropriate choice with high accuracy. However, in the case of longer term dependencies, RNNs tend to suffer from the very common problem of vanishing or exploding gradients.

Fig. 1 shows a layer of recurrent neurons consisting of four neurons labeled *N1*, *N2*, *N3* and *N4*. Each recurrent neuron receives two sets of inputs, the actual input vector $\boldsymbol{u}$ and also the output vector $\boldsymbol{y}$ from the previous step. It can be deduced from the figure that the weights for a recurrent neural network can be learned by training the network to learn the relation *[y(t), u(t)] → y(t + 1)* which can be denoted in terms of network parameters as

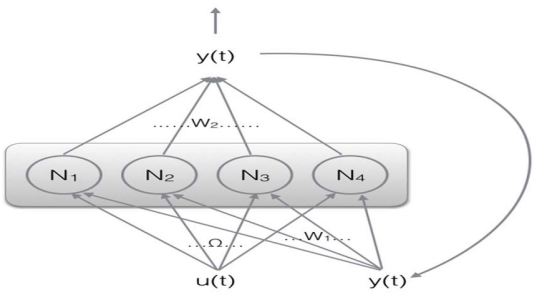


Fig.1. Recurrent Neural Network (RNN)

$$y(t+1) = W_2 g(W_1 y(t) + \Omega u(t) + b) \qquad (1)$$

where t is the discretized time index, u is the input vector of the current time index, y is the output vector which is also given as the input vector along with u for the next time index, Ω is the weight matrix for the input vector, W_1 is the weight matrix for the output vector, W_2 is the weight matrix from the hidden layer of neurons to the output layer of neurons, b is the bias vector consisting of bias terms for each neuron in the hidden layer and g(.) is the activation function [17].

III. Long-Short-Term-Memory

In 1997, LSTM was proposed by Hochreiter and Schmidhuber as a more efficient RNN architecture [14]. In a Recurrent neural network, the algorithm fails to converge to the optimum minima attributed to the problem of vanishing gradients. This was the primary motivation behind the development of LSTM which successfully incorporates long term dependencies and hence improves the overall accuracy of the model [18].

Contrary to an RNN model, the hidden layers of LSTM have a complex structure. In particular, each hidden layer in an LSTM is introduced to the concept of memory cells. Assuming each memory cell to be denoted by c_j, these memory cells encompass a central linear unit having a static self-connection. c_j receives inputs from input gate in_j, output gate out_j and *net* (c_j). We have

$$y\left(out_j(t)\right) = f\{out_j(net(out_j(t)))\} \qquad (2)$$

$$y\left(in_j(t)\right) = f\{in_j(net(in_j(t)))\} \qquad (3)$$

Here,

$$net\left(out_j(t)\right) = \sum_u w_{out_j u} y^u(t-1) \qquad (4)$$

$$net\left(in_j(t)\right) = \sum_u w_{in_j u} y^u(t-1) \qquad (5)$$

$$net\left(c_j(t)\right) = \sum_u w_{c_j u} y^u(t-1) \quad (6)$$

where $y(t)$ is the activation at time t of in_j or out_j, u may represent the input units, memory cells, gate units or hidden units. At any time t, the output of c_j is computed as

$$y^{c_j}(t) = y^{out_j}(t) h(s_{c_j}(t)) \quad (7)$$

Here $s_{c_j}(0) = 0$ and for t>0,

$$s_{c_j}(t) = s_{c_j}(t-1) + y^{in_j}(t) g(net\left(c_j(t)\right)) \quad (8)$$

In (7), $h()$ function scales memory cell outputs and in (8), $g()$ is a differential function that squashes $net(c_j(t))$ [14]. For long term load forecasting, long term dependencies between the samples of training data need to be taken into account. This is not necessary for short term and hence RNN forecasts day ahead load demand with a good accuracy [17], however for year ahead forecasting LSTM-RNN is a more appropriate choice of model and substantially improves the accuracy.

IV. Methodology

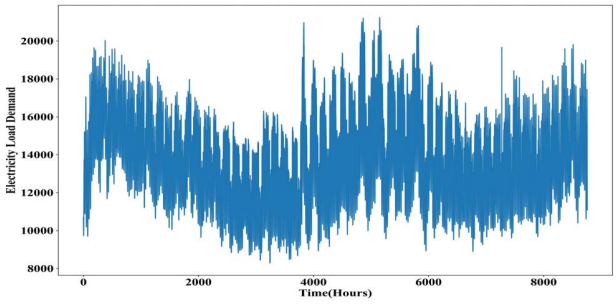


Fig. 2. Electricity load demand of ISO-New England

To evaluate the accuracy of the proposed model, it has been implemented on real time dataset on the ISO New England electricity market with hourly frequency. It should be mentioned here that the dataset is publicly available on the official website of the ISO New England Incorporation, USA [19]. The power generating and distribution system of the entire New England Area is managed and operated by the ISO New England. New England is a region comprising six states of USA: Connecticut, Maine, Rhone Island, Vermont, Massachusetts and New Hampshire. The dataset used includes electricity load demand of this region from 2004 to 2015 along with other features that may or may not affect the load demand. Fig. 2 illustrates the variation of hourly load demand of the year 2004. First, feature engineering is carried out on the data to finalize the set of features to be used for training the model. The data is divided into train and test sets. The proposed model is trained with optimized hyperparameters and used to forecast year-ahead load using the test set. To validate the performance of the model, a standard error metric Mean Absolute Percentage Error is used and 95% confidence interval is evaluated. The aforementioned process has been delineated in the forthcoming sections.

A. Dataset and Feature Engineering

The data obtained from ISO New England consists of load demand of the entire region, dry bulb temperature, dew point temperature and day ahead locational marginal price with its components. All these features are available with an hourly resolution. As mentioned before, data from the year 2004 to 2015 have been used. Hence the total number of observations in the dataset is 105120**.** Initially, this dataset is divided into training and test sets. Data of seven years from 2004 to 2009 was used in the train set and therefore consisted of 61320 samples. The electricity data of the year 2010 was used as the test set. In this implementation of long-term load forecasting, as the objective is to forecast electricity load for a period of five years, the load demand of 2011 is predicted with an hourly resolution. The data of 2010 is then included in the train set with the predicted values of 2011 as their target labels. The predicted load demand of 2011 now acts as the test set and is used to forecast the load demand of 2012. In a similar manner, the load demand of the entire period of five years from 2011 to 2015 is forecasted on a rolling basis. The whole forecast has an hourly frequency which provides substantial and meaningful information to the utility companies.

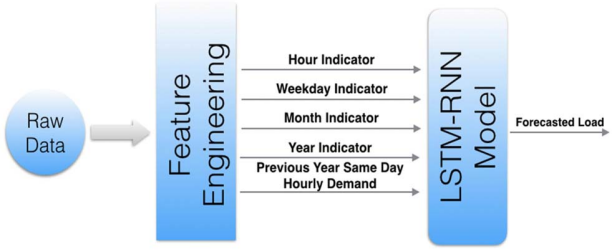


Fig. 3. Proposed Model for load forecasting

For optimum performance of the model, it is necessary to decide the features from the dataset which affect the load demand and also devise new features that might help in improving the performance of the model. This step of feature engineering is one of the most significant parts of any machine learning application and contributes greatly to the performance of the model. Concretely, on plotting the feature importance using Random Forest regressor which is a tree based ensemble model, it has been concluded that hour, month and year indicators are important features which help in deciding the load demand of any particular day. Here, day and month indicators were extracted from the date of any particular

observation and label encoded (1=Monday, 2=Tuesday... for weekdays and 1=January, 2=February... for months). The load demand of the same day and hour of the previous year is found to be the most important feature attributed to the routine lifestyle of human beings and similar climatic conditions during the same period of any two different years in a particular region. However, in the proposed model weather parameters like dry bulb temperature and dew point temperature have not been included. For forecasting electricity load for a period of five years on a rolling basis, this would require forecasting the weather parameters for the five years considered using a time series model and errors in these forecasts were found to significantly degrade the performance of the model overall. Hence the final set of features used for training the model is shown in Fig. 3.

B. Model

The final set of features concluded for training the proposed model was scaled using Standard scaler. This helps in faster convergence of the training algorithm as all the features are normalized to a magnitude in the range [-1, 1]. Moreover, this prevents features with relatively large magnitudes like previous year load demand to carry a larger weight during training.

The proposed model is a sequence model primarily based on RNN with LSTM cells. The said model was used because of the ability of the RNNs to perform well on time series datasets. However, simple RNNs do not perform very well on long term forecasts. LSTM-RNNs maintain both long-term and short term states, converge quicker and are also able to capture longer term dependencies, thus making them ideal for longer term forecasting of electricity load demands.

The model was trained and validated on the data on a rolling basis and the predictions were also made in a similar way. The predictions were made on a yearly basis and then appended to the training set which was further used to make predictions for the next year and so on. The model was tuned by an exhaustive search approach for hyper parameters. The model used had an input shape of 24 time steps and five features. Further, the proposed model had three LSTM layers with the output sequence of each layer as the input sequence of the next layer and consisted of 15 neurons each. The activation function used for each layer was Rectified Linear Unit (ReLU). The three layers were followed by an output layer which was a dense layer with no activation function. Nesterov Momentum applied Gradient Descent optimizer with a learning rate of 0.01 and momentum value of 0.9 was utilized to train the proposed model. The model was trained for 15 epochs with a batch size of 300.

C. Error Metrics

The performance of the models is also compared quantitatively using the performance metric MAPE. MAPE is defined by the formula:

$$MAPE = \frac{100}{n}\sum_{t=1}^{n}\left|\frac{A_t - F_t}{A_t}\right| \quad (9)$$

where A_t is the actual value and F_t is the forecast value, n is the number of observations in test set.

In order to provide a more precise metric of performance, 95% confidence interval of MAPE is calculated which contains true values of MAPE with varying degrees of confidence. The 95% confidence interval of a vector X containing the hourly point absolute percentage error values is calculated by following the given steps:

Step 1: The standard error (SE) is computed using the formula:

$$SE = \frac{std(X)}{\sqrt{n}} \quad (10)$$

where std(X) is the standard deviation of vector X and n is the number of elements in the vector X.

Step 2: Calculate the T-score which depends on the confidence interval needed. For 95% confidence interval, T-score is calculated as follow:

$$T = t * SE \quad (11)$$

where t=1.98 for 95% confidence interval and sample size 100.

Step 3: Finally calculate the 95% confidence interval (CI) using the formula:

$$CI = mean(X) + T \quad (12)$$

where mean(X) is the mean of vector X.

V. RESULTS

For application of long-term load forecasting, the presented model has been used to forecast load demand for a period of five years from 2011 to 2015 on the ISO New England dataset. It is important to note that the forecasts have been made with an hourly resolution which is one of the main characteristics of the proposed model. This has allowed the model to achieve high accuracy and the forecasted load data for a period of five years can serve several benefits to a utility company for long term planning and investments.

TABLE I. PERFORMANCE METRICS

Year	MAPE	Confidence Interval (%)	Confidence Band
2011	5.60	± 4.80	[5.4, 5.94]
2012	7.50	± 1.61	[7.4, 7.64]
2013	6.60	± 6.35	[6.26, 7.11]
2014	6.60	± 5.19	[6.31, 7.00]
2015	6.17	± 6.38	[5.77, 6.56]
Overall	**6.54**	**± 2.25**	**[6.39, 6.69]**

To analyze and validate the performance of the proposed model, MAPE values of each year from 2011 to 2015 for which load demands were forecasted have been tabulated in Table I. The overall MAPE of the entire period is found to be 6.54 with a confidence interval of ± 2.25 % which validates the competency of the proposed model. The resulting MAPE lies in the confidence band [6.39, 6.69].

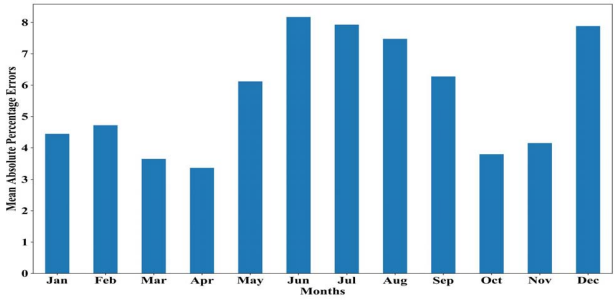
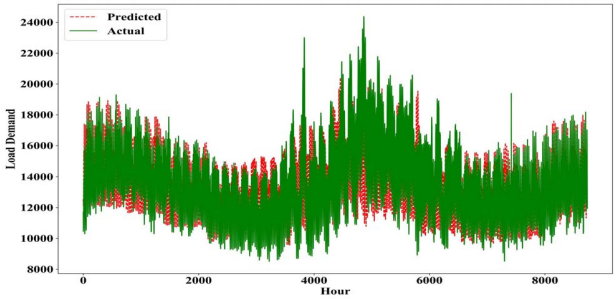


Fig. 4. Monthly error of year 2011

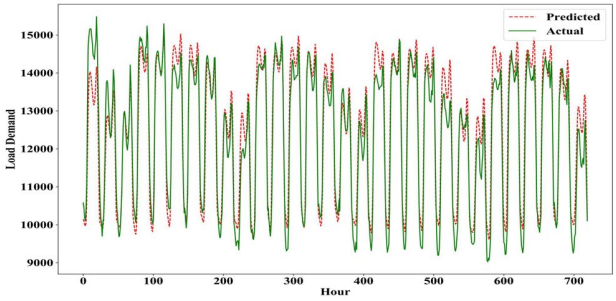
In order to further understand the significance of hourly predictions in long term forecasts, the monthly MAPE values of the year 2011 have been shown in Fig. 4. As depicted in the plot, for majority of the months the MAPE value is below 5% and the maximum value in the year under consideration does not exceed 8%. For the same year, season-wise error values have been listed in Table II. The observed error magnitudes demonstrate very high accuracy taking into account that load has been forecasted for a period of five years on an hourly basis.

TABLE II. SEASON-WISE MAPE

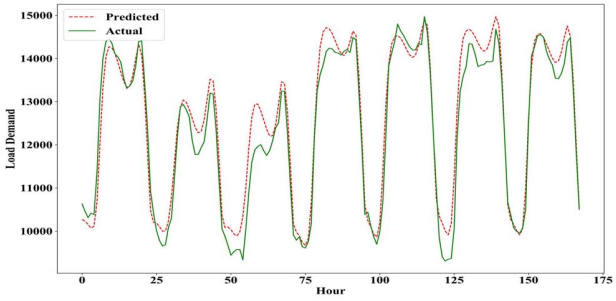
Season	**MAPE**
Summer	6.2
Fall	3.79
Winter	4.44
Spring	3.36



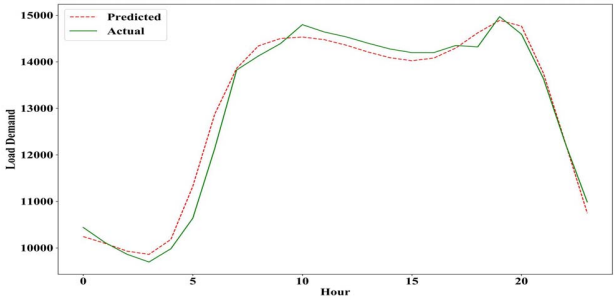
(a)



(b)



(c)



(d)

Fig. 5. Predicted vs. Actual Load Demand of (a) One year (b) One month (c) One Week (d) One day

To fully justify the performance of any machine learning model, a plot of predicted values vs. true values helps in providing a clear representation of the accuracy of a model. In this regard, the predicted vs. actual load curves for various periods of time have been plotted in Fig. 5. Specifically, Fig. 5(a) depicts the variations in the year 2011. From the period between 2011 and 2015, a month, a week and a day have been chosen at random and the performance plots have been illustrated. Overall, the plots demonstrate how the forecasted values closely follow the actual load demand and the high accuracy of the proposed model for long term load forecasting. It should be stated that the model was trained using a 12 GB NVIDIA Graphics Processing Unit (GPU) and required a computation time of approximately 30 minutes.

VI. Conclusion

This paper proposes LSTM-RNN model for long-term load forecasting with hourly resolution. Recurrent Neural Network model is extremely suitable for time series electricity data and

LSTM establishes long term dependencies in the data in order to increase the precision of long term electricity load forecasts. The proposed model has been implemented on real time data of the ISO New England electricity market. Long term load forecast with an hourly resolution can be used by energy service providers to plan investments with minimum risks and set up of new generation facilities. The high resolution of data helps in improving the accuracy as well as allows the companies to make a more informed decision and devise an effective strategy for investments. The model is found to be highly accurate with a Mean Absolute Percentage error of 6.54 and a confidence interval of 2.25%. The performance of the proposed model is comparable with previously suggested models for long term load forecasting, however the previously proposed models were implemented on data with annual or monthly resolution and failed to provide a clear representation of load forecast. Additionally, the computation time of the presented model is calculated to be approximately 30 minutes and is appropriate for offline training.

The performance of the model presented in this study can be further improved by incorporating weather parameters into the training dataset. However, in order to ensure beneficial contribution from such data, we need to perform highly accurate forecasts of the weather parameters on a rolling basis otherwise the drawbacks can outweigh the benefits. The presented LSTM-RNN model can also be recommended for predicting long-term locational marginal prices of the electricity market. As electricity prices are more volatile in nature than load demands, several other factors like economic conditions of the country and crude oil prices need to be incorporated in the dataset. This information along with the predictions of load demands can be of immense advantage to the energy service providers to maximize their profits as well as formulate better long term strategies.

REFERENCES

[1] C.-H. Wang, G. Grozev, and S. Seo, “Middle-long power load forecasting based on dynamic grey prediction and support vector machine,” vol. 41, pp. 313-325, Energy 2012.

[2] A. Safdarian, M. Fotuhi-Firuzabad, M. Lehtonen, M. Aghazadeh and A. Ozdemir, "A new approach for long-term electricity load forecasting," 8th International Conference on Electrical and Electronics Engineering (ELECO), Bursa, pp. 122-126, 2013.

[3] H. M. Al-Hamadi, "Long-term electric power load forecasting using fuzzy linear regression technique," 2011 IEEE Power Engineering and Automation Conference, Wuhan, pp. 96-99, 2011.

[4] D. Park, M. El-Sharkawi, R. J. Marks, L. Atlas, and M. Damborg, “Electric load forecasting using an artificial neural network,” IEEE Transactions on Power Systems, vol. 6, no. 2, pp. 442–449, May 1991.

[5] A. Khotanzad, E. Zhou, and H. Elragal, “A neuro-Fuzzy approach to short-term load forecasting in a price-sensitive environment,” IEEE Transactions on Power Systems, vol. 17, no. 4, pp. 1273–1282, Nov. 2002.

[6] B.-J. Chen, M.-W. Chang, and C.-J. Lin, “Load forecasting using support vector machines: A study on EUNITE competition 2001,” IEEE Transactions on Power Systems, vol. 19, no. 4, pp. 1821–1830, Nov. 2004.

[7] V.M. Vlahovic and I.M. Vujosevic, “Long-term forecasting a critical review of direct-trend extrapolation methods,” Electric Power Energy Syst, vol. 9, no. 1, pp 2-8, 1987.

[8] Z. Wenqing and N. Dongxiao, “A mid-long term load forecasting model based on improved grey theory,” The 2nd IEEE International Conference on Information Management and Engineering (ICIME), pp. 633 – 635, 2010.

[9] M.R. Gent, “Electric Supply and Demand in the US: Next 10 Years,” IEEE Power Engng Rev, pp. 8-13, 1992.

[10] Y. Lu, Z. Yao, X. Huifan, and Z. Qing, “The fuzzy logic clustering neural network approach for middle and long term load forecasting”, IEEE International Conference on Grey Systems and Intelligent Services, pp. 963-967, 2007.

[11] O.A.S. Carpinteiro, I. Lima, R.C. Leme, A.C.Z. de Souza, E.M. Moreira, and C.A.M. Pinheiro, “A hybrid neural model in long-term electrical load forecasting, ” 16th International Conference on Artificial Neural Networks (ICANN 2006), Athens, GREECE, pp. 717-725, 2006.

[12] D.J. Barger,“MGE experience with INSITE spatial load forecasting,” in Proc. 2011 Power Energy Soc. Gen. Meet., Detroit, MI, USA, Jul. 24–29, 2011.

[13] L. Medsker and L. Jain, “Recurrent neural networks,” Design and Applications, 2001.

[14] S. Hochreiter and J. Schmidhuber, “Long short-term memory,” Neural computation, vol. 9, no. 8, pp. 1735–1780, 1997.

[15] Z. C. Lipton, J. Berkowitz, and C. Elkan, “A critical review of recurrent neural networks for sequence learning,” arXiv preprint arXiv:1506.00019, 2015.

[16] R. Pascanu, T. Mikolov, and Y. Bengio, “On the difficulty of training recurrent neural networks.” ICML, vol. 28, no. 3, pp. 1310–1318, 2013.

[17] J. Vermaak, E. C. Botha, “Recurrent Neural Networks for Short-Term Load Forecasting”, IEEE Transactions on Power Systems, vol. 13, no. 1, pp. 126-132, February 1998.

[18] J. Zheng, C. Xu, Z. Zhang and X. Li, "Electric load forecasting in smart grids using Long-Short-Term-Memory based Recurrent Neural Network," 51st Annual Conference on Information Sciences and Systems (CISS), Baltimore, MD, pp 1-6, 2017.

[19] ISO New England Web Page of Pricing Reports. [Online]. Available: http://www.iso-ne.com/isoexpress/web/reports/ pricing, accessed October 28, 2017.

Ann Oper Res
https://doi.org/10.1007/s10479-018-2810-6

S.I.: GAME THEORY AND OPTIMIZATION

Matrix games with 2-tuple linguistic information

Anjali Singh[1] · **Anjana Gupta**[1] · **Aparna Mehra**[2]

© Springer Science+Business Media, LLC, part of Springer Nature 2018

Abstract In this contribution, a two-player constant-sum 2-tuple linguistic matrix game is described, and a linguistic linear programming (LLP) approach is proposed to solve this class of games. The proposed approach can be perceived as a unified mechanism in the sense that it can be adopted to solve linguistic matrix game problems, LLP problems, and linguistic multi-attribute decision-making (MADM) problems. The latter is exhibited by presenting examples of linguistic MADM problems modeled as two-player constant-sum linguistic matrix games with Nature as the second player.

Keywords 2-Tuple linguistic model · Linguistic linear programming problem · Linguistic matrix game · Multi-attribute decision-making problem

1 Introduction

Game theory is the study of cooperation and conflict between rational intelligent decision makers. Since the pioneering work of Neumann and Morgenstern (1944), game theory has successfully been applied in diverse fields (Bauso 2016; Mazalov 2014; Moura and Hutchison 2017; Nagurney et al. 2016; Saulo et al. 2013). Specifically, many real-life decision-making problems are modelled as games (Aliprantis and Chakrabarti 1998). In a decision process, when the decision makers do not cooperate, the situation falls into the realm of a non-

✉ Anjana Gupta
anjanagupta@dce.ac.in

Anjali Singh
anjilko1510@gmail.com

Aparna Mehra
apmehra@maths.iitd.ac.in

[1] Department of Applied Mathematics, Delhi Technological University, Bawana Road, Rohini, Delhi 110085, India

[2] Department of Mathematics, Indian Institute of Technology Delhi, Hauz Khas, New Delhi 110016, India

Published online: 19 March 2018

cooperative game. The classic non-cooperative game theory speculates that the underlying information pertaining to the game is precisely known to all players who can then fully describe their utility functions in terms of their strategies. This assumption is sometimes stringent to realize. To enhance the scope of game theory, imprecision and uncertainty have been incorporated into games using the framework of stochastic and fuzzy variables.

Butnariu (1978) use fuzzy sets to represent the belief of each player about the strategies of the other players in non-cooperative games. His ideas are further revised by Billot (1986). Campos (1989) apply fuzzy linear programming to study two-player zero-sum games with imprecise values in the payoff matrix. Since then, matrix games and bimatrix games with fuzzy payoffs and/or fuzzy goals have been the subject of many studies (Bector and Chandra 2005; Bector et al. 2004; Nishizaki and Sakawa 1997, 2001; Sakawa and Nishizaki 1994; Vijay et al. 2004, 2005). The fuzzy linear programming duality (Bector and Chandra 2005) lies at the foundation of several of these studies. The efforts are still ongoing, with several researchers contributing to enrichment of the literature of fuzzy game theory. Adding to these contributions, Arfi (2006a, b) develop a new game theory approach based on linguistic fuzzy logic, including the concepts of linguistic fuzzy domination and the linguistic Nash equilibrium. Our contribution in the present study is to introduce a non-cooperative two-player constant-sum matrix game problem in the 2-tuple linguistic framework.

Herrera and Martinez (2000) are the first to formalize and analyse 2-tuple linguistic variables. Among the various linguistic models, due to its veracity and interpretability, the 2-tuple linguistic model is extensively used in decision making and decision analysis (Balezentis and Balezentis 2011; Herrera and Martinez 2000; Wei 2010). The 2-tuple linguistic model has the ability to express the counting of information in the universe of discourse and is therefore a computationally beneficial model for computing with words (CW). For a detailed description of CW, one can refer to Cebi et al. (2010), Herrera and Martinez (2000).

This paper makes two contributions to the ongoing research in linguistic modelling. First, we formulate a linguistic linear programming (LLP) model and use it to solve a constant-sum matrix game with 2-tuple linguistic information, henceforth called a constant-sum linguistic matrix game. The LLP model is contrived as a modified linear programming problem (LPP) involving 2-tuple linguistic coefficients in the constraints. Second, we propose to apply this framework to the constant-sum linguistic matrix game formulation of linguistic multi-attribute decision-making (MADM) problems. An MADM problem is formulated as a two-player zero-sum game with an uncertain payoff matrix via $\alpha-$cuts and the max–min principle by Chen and Larbani (2006). The two players in the game are the actual decision maker (DM) and Nature. The DM intends to maximize his expected payoff while Nature chooses to play conflicting strategies to minimize its loss. The paper aims to extend this setup to the 2-tuple linguistic framework. In contrast to various existing methodologies, the one presented herein provides flexibility to the DM to choose the best alternative without a prior knowledge of the propensity of either the attributes or the alternatives.

The modelling approach presented in this paper is advantageous because it can be applied to solve LLP problems, linguistic game problems and linguistic MADM problems.

The remainder of this paper is organized as follows. Section 2 presents the 2-tuple linguistic model and the basic terminology of the conventional matrix game. Section 3 introduces the rudiments of 2-player constant-sum linguistic games. Section 4 explains the LLP formulation for solving such a game. Section 5 demonstrates the applicability of the proposed models and methodology to solve a linguistic MADM problem. Section 6 concludes the paper.

2 Preliminaries

This section reviews the notion of a 2-tuple linguistic variable and a two-player zero-sum matrix game.

2.1 2-tuple linguistic model

The following definitions are taken from the work of Herrera and Martinez (2000).

The generalized linguistic model consists of ℓ_i, where ℓ_i represents the linguistic label from a predefined linguistic terms set $LT = \{\ell_i : i = 0, 1, \ldots, g\}$ of cardinality $g + 1$. Generally, it is assumed that the index g of the granularity of uncertainty in information is an even positive integer. The value in $\{0, 1, \ldots, g\}$ indicates the index of the closest linguistic term in LT.

The set LT is totally ordered with the following characteristics.

1. $\ell_i \geq \ell_j$ if $i \geq j$ (the set LT is ordered);
2. $\max(\ell_i, \ell_j) = \ell_i$ if $\ell_i \geq \ell_j$ and $\min(\ell_i, \ell_j) = \ell_i$ if $\ell_i \leq \ell_j$;
3. $neg(\ell_i) = \ell_j$, $j = g - i$.

Definition 1 Let $\beta \in [0, g]$ be the result of an aggregation of the indices of a set of labels assessed in LT. Suppose $i = \text{round}(\beta)$, where round$(\cdot)$ is the usual rounding operation, and $\alpha = \beta - i$, $\alpha \in [-0.5, 0.5)$. Then, α is called the *symbolic translation*.

A 2-tuple linguistic variable is represented by (ℓ_i, α), which consists of a linguistic term ℓ_i and the symbolic translation α.

Herrera and Martinez (2000) proposed a 2-tuple linguistic model (ℓ_i, α_i) such that $\ell_i \in LT$ and $\alpha_i \in [-0.5, 0.5)$. They further defined the lexicographic ordering in the 2-tuple linguistic variables.

Definition 2 Let (ℓ_i, α_i) and (ℓ_j, α_j) be two 2-tuple linguistic variables.

(i) If $i < j$, then $(\ell_i, \alpha_i) < (\ell_j, \alpha_j)$.
(ii) If $i = j$, i. e., ℓ_i and ℓ_j are the same linguistics, then

- (a) if $\alpha_i = \alpha_j$, then $(\ell_i, \alpha_i) = (\ell_j, \alpha_j)$, that is, (ℓ_i, α_i) and (ℓ_j, α_j) represent the same information;
- (b) if $\alpha_i > \alpha_j$, then $(\ell_i, \alpha_i) > (\ell_j, \alpha_j)$;
- (c) if $\alpha_i < \alpha_j$, then $(\ell_i, \alpha_i) < (\ell_j, \alpha_j)$.

Definition 3 Let $\beta \in [0, g]$ be the value representing the result of a symbolic aggregation. An equivalent 2-tuple linguistic variable can be obtained using the function $\Delta : [0, g] \to LT \times [-0.5, 0.5)$, defined by

$$\Delta(\beta) = (\ell_i, \alpha_i) \text{ where } i = \text{round}(\beta) \text{ and } \alpha_i = \beta - i .$$

The function Δ is a bijection, and its inverse is given by

$$\Delta^{-1} : LT \times [-0.5, 0.5) \to [0, g] \text{ as } \Delta^{-1}(\ell_i, \alpha_i) = i + \alpha_i = \beta .$$

The literature defining various operators on the set of 2-tuple linguistic variables is vast and rich. We recall here only the weighted average operator because it is used in the following.

Definition 4 (Singh et al. 2015) Let $\{(\ell_{r_i}, \alpha_{r_i}),\ r_i \in \{0, 1, \ldots, g\},\ i = 1, \ldots, q\}$ be a set of 2-tuple linguistic variables and $w = (w_1, \ldots, w_q)^T$ be the weight vector satisfying

$0 \leq w_i \leq 1,\ i = 1, \ldots, q,\ \sum_{i=1}^{q} w_i = 1$. Then, the weighted average operator is defined as

$$LWA[(\ell_{r_i}, \alpha_{r_i}) : i = 1, \ldots, q] = (\ell_{r_1}, \alpha_{r_1})w_1 \oplus (\ell_{r_2}, \alpha_{r_2})w_2 \oplus \cdots \oplus (\ell_{r_q}, \alpha_{r_q})w_q$$
$$= \Delta\left(\sum_{i=1}^{q} w_i \Delta^{-1}(\ell_{r_i}, \alpha_{r_i})\right).$$

Consequently,

$$\Delta^{-1}\left(\bigoplus_{i=1}^{q}(\ell_{r_i}, \alpha_{r_i})w_i\right) = \sum_{i=1}^{q} w_i \Delta^{-1}(\ell_{r_i}, \alpha_{r_i}). \tag{1}$$

The negation operator for a 2-tuple linguistic variable $\widetilde{v} = (l_i, \alpha_i)$ is taken to be

$$neg\,(\widetilde{v}) = \Delta(g - \Delta^{-1}(\widetilde{v})).$$

Note that when $\widetilde{v}$ is a linguistic variable only (that is, $\widetilde{v} = (\ell_i, 0)$), then $neg(\widetilde{v}) = \ell_{g-i}$, which is the same as the standard negation $neg(\ell_i)$ of the linguistic variable.

For illustration of the above-described concepts, consider the predefined linguistic term set

$$LT = \{\ell_0 : \text{Very Bad}, \ell_1 : \text{Bad}, \ell_2 : \text{Medium}, \ell_3 : \text{Good}, \ell_4 : \text{Very Good}\}.$$

Let $S = \{(\ell_0, 0.4), (\ell_2, 0.432), (\ell_1, 0.432), (\ell_1, 0.259)\}$ be a set of 2-tuple linguistic variables.
If $\beta = 2.432$, then $i = \text{round}(\beta) = 2$ and $\alpha = \beta - i = 0.432$; hence, the corresponding 2-tuple linguistic variable is $(\ell_2, 0.432)$. By contrast, a 2-tuple linguistic variable $(\ell_1, 0.259)$ can be transformed into its numeric value using the Δ^{-1} operator as $\Delta^{-1}(\ell_1, 0.259) = 1.259$.

Using the lexicographic ordering, the elements of the set S are ordered as $(\ell_0, 0.4) < (\ell_1, 0.259) < (\ell_1, 0.432) < (\ell_2, 0.432)$. If the weight vector is $w = (0.2,\ 0.1,\ 0.3,\ 0.4)^T$, then the weighted average of S is

$$(\ell_0, 0.4)0.2 \oplus (\ell_2, 0.432)0.1 \oplus (\ell_1, 0.432)0.3 \oplus (\ell_1, 0.259)0.4$$
$$= \Delta[0.2 * 0.4 + 0.1 * 2.432 + 0.3 * 1.432 + 0.4 * 1.259] = \Delta[1.2564] = (\ell_1, 0.2564).$$

Remark 1 Using the linearity and the monotonic increasing property of the Δ operator, it is easy to observe that for the 2-tuple linguistic variables $\widetilde{v}_1 = (\ell_i, \alpha_i)$ and $\widetilde{v}_2 = (\ell_j, \alpha_j)$, the following hold:

(i) $neg\,(neg(\widetilde{v}_1)) = \widetilde{v}_1$;
(ii) $\min\{neg\,(\widetilde{v}_1),\ neg\,(\widetilde{v}_2)\} = neg\,(\max\{\widetilde{v}_1,\ \widetilde{v}_2\})$;
(iii) $\max\{neg\,(\widetilde{v}_1),\ neg\,(\widetilde{v}_2)\} = neg\,(\min\{\widetilde{v}_1,\ \widetilde{v}_2\})$;

where the max and min of two 2-tuple linguistic variables are taken in the spirit of Definition 2.

2.2 A zero-sum matrix game

We refresh some preliminaries from conventional non-cooperative matrix game theory. We refer to Barron (2011) for more details of this topic.

Definition 5 A two-player zero-sum matrix game G is a triplet (S^n, S^m, A), where

(i) S^n is a finite set of n strategies for player I;
(ii) S^m is a finite set of m strategies for player II;
(iii) A is a real $n \times m$ matrix representing the payoffs of player I against player II, and $-A$ is taken as the payoff matrix for player II.

Definition 6 A matrix game G with $A = [a_{ij}]_{n\times m}$ has the lower value and upper value defined, respectively, as

$$v^- = \max_{i=1,\ldots,n} \min_{j=1,\ldots,m} a_{ij}, \qquad v^+ = \min_{j=1,\ldots,m} \max_{i=1,\ldots,n} a_{ij}.$$

Here v^- (player I's gain floor) is the minimum payoff that player I is assured to receive and v^+ (player II's loss ceiling) is the maximum payoff that player II can loose. Game G has value if and only if $v^- = v^+$. The strategies i^* and j^*, yielding the payoffs $a_{i^*j^*} = v^- = v^+$, are optimal for player I and player II, respectively. Moreover, $a_{ij^*} \leq a_{i^*j^*} \leq a_{i^*j}, \quad \forall\, i = 1, \ldots, n,\ j = 1, \ldots, m$, and (i^*, j^*) is also called the saddle point of game G.

Definition 7 A mixed strategy is an ordered pair of vectors $(x, y) \in S^n \times S^m$, where

$$S^n = \left\{ (x_1, \ldots, x_n) \ : \ x_i \geq 0,\ i = 1 \ldots, n,\ \sum_{i=1}^{n} x_i = 1 \right\};$$

$$S^m = \left\{ (y_1, \ldots, y_m) \ : \ y_j \geq 0,\ j = 1, \ldots, m,\ \sum_{j=1}^{m} y_j = 1 \right\}.$$

Here, x_i is the probability of player I choosing strategy i and y_j is the probability of player II selecting strategy j.

Similarly, a two-player constant-sum game occurs when the sum of the payoffs for any given set of strategies is always constant (Barron 2011; Morris 1994). A zero-sum game is a particular case of a constant-sum game.

Zero-sum matrix games, both in the classic setup and in the fuzzy environment, are subject to numerous studies, such that quoting every contribution here is a daunting task. One can refer to the survey paper by Larbani (2009) and texts by Bector and Chandra (2005) and Li (2014) for the state of the art. However, game problems with linguistic payoff matrices are pristine and need to be explored as it may not always be plausible for DMs or players to precisely quantify the utility of choosing their strategies from their respective strategy spaces in terms of numeric values. Although the fuzzy set and its generalized variants have been used to overcome the difficulties in restricting payoffs to precision, they also require knowledge of membership or non-membership functions and their shapes. On the other hand, the linguistic variables enable an improved and more flexible framework to the players to express the granularity of the information and opinions of the payoffs by using the linguistic terms set LT. The study of linguistic matrix games will enrich game theory by adding an additional layer of finer granularity of information in the payoff matrix.

3 A constant-sum linguistic matrix game

Definition 8 A two-player constant-sum linguistic game $\widetilde{G}$ is defined by a quadruplet $(S^n, S^m, LT, \widetilde{A})$, where S^n and S^m are the strategy sets described above, $LT = \{\ell_0, \ell_1, \ldots, \ell_g\}$, with cardinality $g+1$, is a predefined linguistic term set for both the players,

$\widetilde{A}$ is the linguistic payoff matrix of player I against player II, and $neg(\widetilde{A})$ is the payoff matrix for player II.

The payoff matrix $\widetilde{A} = [\widetilde{a}_{ij}]_{n\times m}$ for player I is described in such a way that each $\widetilde{a}_{ij} \in LT$. If, in response to strategy i of player I, $i = 1, \ldots, n$, player II chooses strategy j, $j = 1, \ldots, m$, to play the game, then the payoff of player I is $\widetilde{a}_{ij} \in LT$ while the payoff of player II is $neg(\widetilde{a}_{ij}) = \Delta(g - \Delta^{-1}(\widetilde{a}_{ij}))$. In other words, the utility functions $u_1,\ u_2 : S^n \times S^m \to LT$ for player I and player II are described by $u_1(e_i, e_j) = \widetilde{a}_{ij},\ u_2(e_i, e_j) = neg(\widetilde{a}_{ij})$, and e_i is a unit vector with i-th component 1.

A linguistic payoff refers to how beneficial and advantageous it is for a player to play a strategy. which can be expressed on a linguistic scale in LT.

Note 1 The payoffs $\widetilde{a}_{ij},\ i = 1, \ldots, n,\ j = 1 \ldots, m$ can be linguistic variables or 2-tuple linguistic variables for any linguistic variable ℓ_i and can be expressed as a 2-tuple linguistic variable $(\ell_i,\ 0)$.

Since the lexicographic ordering is available in the 2-tuple linguistic variables, one can easily extend the notion of the value of the game to the linguistic matrix game $\widetilde{G}$.

Definition 9 Define the values $\widetilde{v}^{1-}$ and $\widetilde{v}^{2-}$ to represent the minimum (linguistic) benefit that player I and player II are, respectively, assured to receive.

$$\widetilde{v}^{1-} = \max_{i=1,\ldots,n} \min_{j=1,\ldots,m} \widetilde{a}_{ij}, \qquad \widetilde{v}^{2-} = \max_{j=1,\ldots,m} \min_{i=1,\ldots,n} neg(\widetilde{a}_{ij}).$$

Then, the lower value and the upper value of game $\widetilde{G}$ are defined, respectively, by $\widetilde{v}^{-} = \widetilde{v}^{1-}$ and $\widetilde{v}^{+} = neg\,(\widetilde{v}^{2-})$. The value $\widetilde{v}$ of game $\widetilde{G}$ is defined when $\widetilde{v}^{-} = \widetilde{v}^{+} = \widetilde{v}$.

The strategies i^* and j^*, giving the payoff $\widetilde{a}_{i^*j^*}$, such that $\widetilde{a}_{i^*j^*} = \widetilde{v}^{-} = \widetilde{v}^{+}$, are optimal pure strategies for player I and player II, respectively. In this case, the strategy pair (i^*, j^*) is termed as the saddle point of game $\widetilde{G}$.

In view of Remark 1, it is noteworthy that

$$\widetilde{v}^{+} = neg\,(\widetilde{v}^{2-}) = neg\,(\max_{j=1,\ldots,m} \min_{i=1,\ldots,n} neg\,(\widetilde{a}_{ij})) = \min_{j=1,\ldots,m} \max_{i=1,\ldots,n} (\widetilde{a}_{ij}).$$

We now present an example for illustration.

Example 1 Consider two insurance companies planning to introduce competing insurance schemes. They select the time to introduce the schemes, and their options are 1 month, 2 months and 3 months from now. The payoffs correspond to how much market share a company can expect to receive based on the month of the launch of the respective scheme. The payoffs are not quantified in numerics but rather given as linguistic labels from a predefined linguistic terms set LT = {Very Low: VL, Low: L, Average: Avg, High: H, Very High: VH}. Suppose the payoff matrix of company I is as follows.

$\widetilde{A} =$

I/II	1	2	3
1	Avg	H	VH
2	VL	L	Avg
3	VL	VH	VH

For instance, if company I and company II introduce their respective insurance schemes in the first and third months, respectively, then company I will receive Very High (i. e. $\widetilde{a}_{13}$)

market share. Additionally,

$$neg(\widetilde{A}) = \begin{array}{c|ccc} \text{I/II} & 1 & 2 & 3 \\ \hline 1 & \text{Avg} & \text{L} & \text{VL} \\ 2 & \text{VH} & \text{H} & \text{Avg} \\ 3 & \text{VH} & \text{VL} & \text{VL} \end{array}$$

is the payoff matrix of company II. The matrix suggests that if company I and company II introduce their respective insurance schemes in the first and third months, respectively, then company II will achieve Very Low market share.

The lower value of the player I (hence the lower value of the game) is given by

$$\begin{aligned} \widetilde{v}^{-} = \widetilde{v}^{1-} &= \max_{i=1,2,3} \min_{j=1,2,3} \widetilde{a}_{ij} \\ &= \max\{\min\{\text{Avg, H, VH}\}, \min\{\text{VL, L, Avg}\}, \min\{\text{VL, VH, VH}\}\} = \text{Avg}. \end{aligned}$$

Thus, company I is assured to receive at least an average market share by playing strategy 1. Similarly, the lower value of the player II is

$$\widetilde{v}^{2-} = \max_{j=1,2,3} \min_{i=1,2,3} neg(\widetilde{a}_{ij}) = \max\{\text{Avg, VL, VL}\} = \text{Avg}.$$

In other words, irrespective of when company I launches its scheme in the market, company II will receive at least an average market share by playing strategy 1.

The upper value of the game is $\widetilde{v}^{+} = neg\,(\widetilde{v}^{2-}) = \text{Avg}$. Thus, (1, 1) is the saddle point, and $\widetilde{v} = \text{Avg}$ is the value of this game.

Remark 2 In the above example, we have $\widetilde{v}^{1-} = \widetilde{v}^{2-}$, but that may not always be the case in a linguistic game. Suppose that entry $\widetilde{a}_{11}$ in the above payoff matrix, $\widetilde{A}$ is changed to L. Then, $\widetilde{v}^{1-} = \text{L}$ and $\widetilde{v}^{2-} = \text{H}$. However, (1, 1) remains the saddle point, and $\widetilde{v} = \text{L}$ is the value of the game.

The expected payoff of the traditional (crisp) two-player zero-sum matrix game is defined as the statistical expectation of information in the payoff matrix. In a linguistic matrix game, with ambiguous and uncertain assessment of the payoff entries of the payoff matrix, the accuracy of the expected value is inexplicable. It necessitates defining the linguistic expected payoffs of players as follows.

Definition 10 Let $x = (x_1, \ldots, x_n) \in S^n$ and $y = (y_1, \ldots, y_m) \in S^m$ be a pair of mixed strategies for player I and player II, respectively. The linguistic expected payoff of player I is defined by

$$\widetilde{E}_{\widetilde{A}}(x, y) = \bigoplus_{i=1}^{n} \left(x_i \left(\bigoplus_{j=1}^{m} \tilde{a}_{ij} y_j \right) \right).$$

The linguistic expected payoff of player II is $neg(\widetilde{E}_{\widetilde{A}}(x, y))$.

The linguistic expected payoff can be interpreted as the approximate gain (benefit) of the players in the uncertain environment of a real competitive system.

4 Linguistic linear programming formulation of a linguistic matrix game

This section introduces the LLP approach to solve the linguistic matrix game $\widetilde{G}$.

Let the linguistic terms set be $LT = \{\ell_0, \ell_1, \ldots, \ell_g\}$, where g is a positive even integer, and let the linguistic payoff matrix be

$$\widetilde{A} = \begin{bmatrix} \tilde{a}_{11} & \tilde{a}_{12} & \ldots & \tilde{a}_{1m} \\ \tilde{a}_{21} & \tilde{a}_{22} & \ldots & \tilde{a}_{2m} \\ \vdots & \ddots & \vdots & \\ \tilde{a}_{n1} & \tilde{a}_{n2} & \ldots & \tilde{a}_{nm} \end{bmatrix}$$

where $\tilde{a}_{ij} \in LT$ is the payoff of player I choosing the ith strategy when player II selects the jth strategy.

The mixed strategies of player I and player II are $x = (x_1, \ldots, x_n) \in S^n$ and $y = (y_1, \ldots, y_m) \in S^m$, respectively.

Player I's expected payoff for the jth strategy of player II is the weighted average of the linguistic variables $\widetilde{a}_{1j}, \widetilde{a}_{2j}, \ldots, \widetilde{a}_{nj}$, that is, $\widetilde{a}_{1j}x_1 \oplus \widetilde{a}_{2j}x_2 \oplus \cdots \oplus \widetilde{a}_{nj}x_n$. The problem for player I is to find the mixed strategy $x = (x_1, \ldots, x_n) \in S^n$ that achieves the maximum linguistic value of $\widetilde{v}^{1-}$. Consequently, player I has to consider the following system.

Player II pure strategy	Player I expected payoff
1	$\widetilde{a}_{11}x_1 \oplus \widetilde{a}_{21}x_2 \oplus \cdots \oplus \widetilde{a}_{n1}x_n \geq \widetilde{v}^{1-}$
2	$\widetilde{a}_{12}x_1 \oplus \widetilde{a}_{22}x_2 \oplus \cdots \oplus \widetilde{a}_{n2}x_n \geq \widetilde{v}^{1-}$
$\vdots$	$\vdots$
m	$\widetilde{a}_{1m}x_1 \oplus \widetilde{a}_{2m}x_2 \oplus \cdots \oplus \widetilde{a}_{nm}x_n \geq \widetilde{v}^{1-}$

The required LLP problem for player I is as follows:

$$\begin{aligned} &\max \quad \widetilde{v}^{1-} \\ &\text{subject to} \\ &\widetilde{a}_{11}x_1 \oplus \widetilde{a}_{21}x_2 \oplus \cdots \oplus \widetilde{a}_{n1}x_n \geq \widetilde{v}^{1-} \\ &\widetilde{a}_{12}x_1 \oplus \widetilde{a}_{22}x_2 \oplus \cdots \oplus \widetilde{a}_{n2}x_n \geq \widetilde{v}^{1-} \\ &\vdots \\ &\widetilde{a}_{1m}x_1 \oplus \widetilde{a}_{2m}x_2 \oplus \cdots \oplus \widetilde{a}_{nm}x_n \geq \widetilde{v}^{1-} \\ &x_1 + x_2 + \cdots + x_n = 1 \\ &x_1,\ x_2, \ldots, x_n \geq 0. \end{aligned} \tag{M1}$$

Since Δ^{-1} is monotonically increasing, by applying it to the constraints of model (M1) and using (1), the constraints become

$$\begin{aligned} &\Delta^{-1}(\widetilde{a}_{11})x_1 + \Delta^{-1}(\widetilde{a}_{21})x_2 + \cdots + \Delta^{-1}(\widetilde{a}_{n1})x_n \geq \Delta^{-1}(\widetilde{v}^{1-}) \\ &\Delta^{-1}(\widetilde{a}_{12})x_1 + \Delta^{-1}(\widetilde{a}_{22})x_2 + \cdots + \Delta^{-1}(\widetilde{a}_{n2})x_n \geq \Delta^{-1}(\widetilde{v}^{1-}) \\ &\vdots \\ &\Delta^{-1}(\widetilde{a}_{1m})x_1 + \Delta^{-1}(\widetilde{a}_{2m})x_2 + \cdots + \Delta^{-1}(\widetilde{a}_{nm})x_n \geq \Delta^{-1}(\widetilde{v}^{1-}), \end{aligned}$$

and the objective function max $\widetilde{v}^{1-}$ is equivalent to max $\Delta^{-1}(\widetilde{v}^{1-})$.

By setting $\Delta^{-1}(\widetilde{a}_{ij}) = a_{ij},\ i = 1, \ldots, n,\ j = 1, \ldots, m$, and $\Delta^{-1}(\widetilde{v}^{-}) = \Delta^{-1}(\widetilde{v}^{1-}) = v$, the constraints of model (M1) can be rewritten as follows:

$$
\begin{aligned}
& a_{11}x_1 + a_{21}x_2 + \cdots + a_{n1}x_n \geq v \\
& a_{12}x_1 + a_{22}x_2 + \cdots + a_{n2}x_n \geq v \\
& \vdots \\
& a_{1m}x_1 + a_{2m}x_2 + \cdots + a_{nm}x_n \geq v \\
& x_1 + x_2 + \cdots + x_n = 1 \\
& x_1,\ x_2, \ldots, x_n \geq 0.
\end{aligned}
$$

Here, we assume that $\Delta^{-1}(\widetilde{v}^{-}) = v > 0$.

We set $X_i = \dfrac{x_i}{v},\ i = 1, \ldots n$, and $V = \dfrac{1}{v}$. The transformed linear programming problem for player I is then as follows:

$$
\begin{aligned}
& \min\ V = \quad X_1 + X_2 + \cdots + X_n \qquad \text{(M2)} \\
& \text{subject to} \\
& a_{11}X_1 + a_{21}X_2 + \cdots + a_{n1}X_n \geq 1 \\
& a_{12}X_1 + a_{22}X_2 + \cdots + a_{n2}X_n \geq 1 \\
& \vdots \\
& a_{1m}X_1 + a_{2m}X_2 + \cdots + a_{nm}X_n \geq 1 \\
& X_1,\ X_2, \ldots, X_n \geq 0.
\end{aligned}
$$

Thus, the LLP model (M1) is transformed into the conventional linear programming model (M2).

The problem that player II must solve can be constructed in a similar manner.

$$
\begin{aligned}
& \max\ \widetilde{v}^{2-} \qquad \text{(M3)} \\
& \text{subject to} \\
& neg(\widetilde{a}_{11})\ y_1 \oplus\ neg(\widetilde{a}_{12})\ y_2 \oplus \cdots \oplus\ neg(\widetilde{a}_{1m})\ y_m \geq \widetilde{v}^{2-} \\
& neg(\widetilde{a}_{21})\ y_1 \oplus\ neg(\widetilde{a}_{22})\ y_2 \oplus \cdots \oplus\ neg(\widetilde{a}_{2m})\ y_m \geq \widetilde{v}^{2-} \\
& \vdots \\
& neg(\widetilde{a}_{n1})\ y_1 \oplus\ neg(\widetilde{a}_{n2})\ y_2 \oplus \cdots \oplus\ neg(\widetilde{a}_{nm})\ y_m \geq \widetilde{v}^{2-} \\
& y_1 + y_2 + \cdots + y_m = 1 \\
& y_1,\ y_2, \ldots, y_m \geq 0.
\end{aligned}
$$

Model (M3) is transformed into the following model using the definition of the negation operator, the properties of the Δ^{-1} operator and $neg\ (\widetilde{v}^{2-}) = \widetilde{v}^{+}$.

$$
\begin{aligned}
&\min\ \widetilde{v}^{+} \qquad\qquad\qquad\

$$
\begin{aligned}
&\max \quad \widetilde{v}^{-} \\
&\text{subject to} \\
&(\ell_4, 0)x_1 \oplus (\ell_4, 0)x_2 \oplus (\ell_3, 0.4)x_3 \geq \widetilde{v}^{-} \\
&(\ell_4, 0)x_1 \oplus (\ell_3, -0.4)x_2 \oplus (\ell_6, 0)x_3 \geq \widetilde{v}^{-} \\
&(\ell_3, 0)x_1 \oplus (\ell_6, -0.1)x_2 \oplus (\ell_4, 0)x_3 \geq \widetilde{v}^{-} \\
&(\ell_3, 0)x_1 \oplus (\ell_4, 0)x_2 \oplus (\ell_4, 0)x_3 \geq \widetilde{v}^{-} \\
&(\ell_4, 0.3)x_1 \oplus (\ell_0, 0)x_2 \oplus (\ell_4, 0)x_3 \geq \widetilde{v}^{-} \\
&x_1 + x_2 + x_3 = 1 \\
&x_1, x_2, x_3 \geq 0.
\end{aligned}
$$

Convert the above LLP into a linear programming problem using model (M2) as follows:

$$
\begin{aligned}
&\min V = \quad X_1 + X_2 + X_3 \\
&\text{subject to} \\
&4X_1 + 4X_2 + 3.4X_3 \geq 1 \\
&4X_1 + 2.6X_2 + 6X_3 \geq 1 \\
&3X_1 + 5.9X_2 + 4X_3 \geq 1 \\
&3X_1 + 4X_2 + 4X_3 \geq 1 \\
&4.3X_1 + 0X_2 + 4X_3 \geq 1 \\
&X_1, X_2, X_3 \geq 0.
\end{aligned}
$$

The optimal solution of the above problem is $(X_1^* = 0.0912,\ X_2^* = 0.0296,\ X_3^* = 0.1520)$ and $V^* = 0.2728$.

Hence, for player I, the optimal mixed strategy is $(x_1^* = 0.3343,\ x_2^* = 0.1085,\ x_3^* = 0.5572)$, and the optimal value is $\widetilde{v}^{-*} = (\ell_4,\ -0.3343)$.

The LLP problem for player II is obtained by using model (M4):

$$
\begin{aligned}
&\min \ \widetilde{v}^{+} \\
&\text{subject to} \\
&(\ell_4, 0)y_1 \oplus (\ell_4, 0)y_2 \oplus (\ell_3, 0)y_3 \oplus (\ell_3, 0)y_4 \oplus (\ell_4, 0.3)y_5 \leq \widetilde{v}^{+} \\
&(\ell_4, 0)y_1 \oplus (\ell_3, -0.4)y_2 \oplus (\ell_6, -0.1)y_3 \oplus (\ell_4, 0)y_4 \oplus (\ell_0, 0)y_5 \leq \widetilde{v}^{+} \\
&(\ell_3, 0.4)y_1 \oplus (\ell_6, 0)y_2 \oplus (\ell_4, 0)y_3 \oplus (\ell_4, 0)y_4 \oplus (\ell_4, 0)y_5 \leq \widetilde{v}^{+} \\
&y_1 + y_2 + y_3 + y_4 + y_5 = 1 \\
&y_1, y_2, y_3, y_4, y_5 \geq 0.
\end{aligned}
$$

The corresponding linear programming problem is given as follows:

$$
\begin{aligned}
&\max V = \quad Y_1 + Y_2 + Y_3 + Y_4 + Y_5 \\
&\text{subject to} \\
&4Y_1 + 4Y_2 + 3Y_3 + 3Y_4 + 4.3Y_5 \leq 1 \\
&4Y_1 + 2.6Y_2 + 5.9Y_3 + 4Y_4 + 0Y_5 \leq 1 \\
&3.4Y_1 + 6Y_2 + 4Y_3 + 4Y_4 + 4Y_5 \leq 1 \\
&Y_1, Y_2, Y_3, Y_4, Y_5 \geq 0.
\end{aligned}
$$

The optimal solution is $(Y_1^* = 0.152,\ Y_2^* = 0,\ Y_3^* = 0,\ Y_4^* = 0.098,\ Y_5^* = 0.0228)$ and $V^* = 0.2728$.

Hence, for player II, the optimal mixed strategy is $(y_1^* = 0.5572,\ y_2^* = 0,\ y_3^* = 0,\ y_4^* = 0.3592,\ y_5^* = 0.0836)$, and the optimal value is $\widetilde{v}^{2-*} = (\ell_2,\ 0.3343)$.
Note the optimal value of this game is $\widetilde{v}^* = \widetilde{v}^{-*} = \widetilde{v}^{+*} = (\ell_4,\ -0.3343)$.

By virtue of the linguistic game theory framework, in the following section, we propose a ranking scheme for alternatives in linguistic MADM problems. The scheme is demonstrated through illustrative examples.

5 Matrix game approach for linguistic MADM problems

Consider an MADM problem of ranking n homogeneous alternatives that are assessed on m attributes using linguistic labels from the predefined linguistic terms set $LT = \{\ell_0, \ell_1, \ldots, \ell_g\}$. Let the alternatives-attributes decision matrix be as follows:

$$\widetilde{A} = \begin{array}{c} \\ A_1 \\ A_2 \\ \vdots \\ A_n \end{array} \begin{array}{c} \begin{array}{cccc} C_1 & C_2 & \ldots & C_m \end{array} \\ \begin{bmatrix} \widetilde{a}_{11} & \widetilde{a}_{12} & \ldots & \widetilde{a}_{1m} \\ \widetilde{a}_{21} & \widetilde{a}_{22} & \ldots & \widetilde{a}_{2m} \\ \vdots & \vdots & \ddots & \vdots \\ \widetilde{a}_{n1} & \widetilde{a}_{n2} & \ldots & \widetilde{a}_{nm} \end{bmatrix} \end{array}.$$

The DM needs to select a criterion for decision making under uncertainty (Luce and Raiffa 1957). In this paper, we assume that the DM adopts Wald's criterion (Luce and Raiffa 1957), which assumes that the DM is reactionary and expects that Nature is competing against him to minimize his payoffs. In this sense, the above linguistic MADM problem can be cast as a two-player constant-sum linguistic game with player I being the DM and player II being Nature.

Since the DM is cautious about the strategy selection of Nature, he will choose his mixed strategy $x = (x_1, \ldots, x_n),\ x_i \geq 0,\ i = 1, \ldots, n,\ \sum_{i=1}^{n} x_i = 1$ over the set of alternatives $\{A_i : i = 1, \ldots, n\}$. The DM views Nature as a non-cooperative player, and to counter his mixed strategy choice, Nature will select the mixed strategy $y = (y_1, \ldots, y_m),\ y_j \geq 0,\ j = 1, \ldots, m,\ \sum_{j=1}^{m} y_j = 1$ over the set of attributes $\{C_j : j = 1, \ldots, m\}$. Thus, we obtain the corresponding two-player constant-sum linguistic game with payoff matrix $\widetilde{A}$, where $\tilde{a}_{ij} \in LT$ is the payoff of the DM when he chooses the ith strategy with probability x_i and Nature selects the jth strategy with probability y_j.

The LLP methodology in Sect. 4 can be adopted to solve the above linguistic game problem, and the optimal strategies $(x_1^*, \ldots, x_n^*)$ and $(y_1^*, \ldots, y_m^*)$ can be obtained for the DM and Nature, respectively. Analogous to Larbani and Chen (2014), here x_i^* can be interpreted as the proportion of times the DM selects alternative i as the best alternative if this MADM problem is repeated a certain number of times. The combined linguistic score of alternative A_i is computed as

$$\widetilde{S}_i = x_i^* \left(\bigoplus_{j=1}^{m} \tilde{a}_{ij} y_j^* \right), \quad i = 1, \ldots, n.$$

The value $(\bigoplus_{j=1}^{m} \tilde{a}_{ij} y_j^*)$ is the expected linguistic payoff to the DM when choosing alternative A_i. The linguistic score characterizing alternative A_i is the linguistic payoff with the highest probability (or the optimal proportion of times an alternative is chosen). The largest value

represents the alternative that achieves the maximum payoff with the highest probability for the DM. The alternatives are ranked in descending order of their scores.

The applicability and practicality of the proposed approach for solving the linguistic MADM is demonstrated through an example from Singh et al. (2015).

Example 3 The goal is to select the most appropriate air conditioning system for installation in a company based on specific attributes. The company created a committee to recommend the best among six distinct alternatives A_i, $i = 1, \ldots, 6$, offered by a civil contractor. The considered attributes are as follows:

C_1: Area (in units of 100 square feet) where the AC unit is to be installed
C_2: Seasonal energy efficiency ratio (SEER)
C_3: Refrigerant and global warming potential (GWP)
C_4: Maintenance and installation cost
C_5: Tonnage of the AC unit
C_6: Coefficient of performance (CoP)
C_7: Sound pressure level
C_8: Miscellaneous

The linguistic decision matrix given by the DM from the predetermined linguistic terms set $LT = \{\ell_0 : \text{Worst}\,(W), \ell_1 : \text{Extremely Poor}\,(EP), \ell_2 : \text{Very Poor}\,(VP), \ell_3 : \text{Poor}\,(P), \ell_4 : \text{Medium}\,(M), \ell_5 : \text{Good}\,(G), \ell_6 : \text{Very Good}\,(VG), \ell_7 : \text{Extremely Good}\,(EG)\}$ is as follows.

$$\widetilde{M} = \begin{array}{c} \\ A_1 \\ A_2 \\ A_3 \\ A_4 \\ A_5 \\ A_6 \end{array} \begin{array}{c} \begin{array}{cccccccc} C_1 & C_2 & C_3 & C_4 & C_5 & C_6 & C_7 & C_8 \end{array} \\ \begin{bmatrix} (\ell_4, 0) & (\ell_4, 0.4) & (\ell_2, 0.4) & (\ell_3, 0.4) & (\ell_4, -0.2) & (\ell_2, 0.2) & (\ell_4, -0.2) & (\ell_2, 0.4) \\ (\ell_2, 0.2) & (\ell_3, 0) & (\ell_4, 0.2) & (\ell_4, 0.2) & (\ell_2, 0.2) & (\ell_4, 0.2) & (\ell_2, 0.4) & (\ell_4, 0.2) \\ (\ell_5, 0) & (\ell_4, 0.2) & (\ell_4, 0.2) & (\ell_3, -0.2) & (\ell_5, -0.2) & (\ell_4, 0.2) & (\ell_5, -0.2) & (\ell_3, 0.4) \\ (\ell_5, 0.2) & (\ell_4, 0) & (\ell_4, -0.2) & (\ell_4, 0.4) & (\ell_3, 0.2) & (\ell_4, 0.2) & (\ell_4, -0.2) & (\ell_4, 0) \\ (\ell_5, -0.4) & (\ell_2, 0) & (\ell_3, 0.2) & (\ell_3, 0.4) & (\ell_5, -0.2) & (\ell_4, 0.2) & (\ell_5, -0.2) & (\ell_4, -0.4) \\ (\ell_4, 0) & (\ell_4, 0.4) & (\ell_2, 0.4) & (\ell_3, 0.4) & (\ell_4, -0.2) & (\ell_3, -0.4) & (\ell_4, 0) & (\ell_3, 0.2) \end{bmatrix} \end{array}$$

Using the linear programming model (M2), we solve the following problem for the DM.

$$\begin{aligned} \min V = \quad & X_1 + X_2 + X_3 + X_4 + X_5 + X_6 \\ \text{subject to} \quad & \\ & 4X_1 + 2.2X_2 + 5X_3 + 5.2X_4 + 4.6X_5 + 4X_6 \geq 1 \\ & 4.4X_1 + 3X_2 + 4.2X_3 + 4X_4 + 2X_5 + 4.4X_6 \geq 1 \\ & 2.4X_1 + 4.2X_2 + 4.2X_3 + 3.8X_4 + 3.2X_5 + 2.4X_6 \geq 1 \\ & 3.4X_1 + 4.2X_2 + 2.8X_3 + 4.4X_4 + 3.4X_5 + 3.4X_6 \geq 1 \\ & 3.8X_1 + 2.2X_2 + 4.8X_3 + 3.2X_4 + 4.8X_5 + 3.8X_6 \geq 1 \\ & 2.2X_1 + 4.2X_2 + 4.2X_3 + 4.2X_4 + 4.2X_5 + 2.6X_6 \geq 1 \\ & 3.8X_1 + 2.4X_2 + 4.8X_3 + 3.8X_4 + 4.8X_5 + 4X_6 \geq 1 \\ & 2.4X_1 + 4.2X_2 + 3.4X_3 + 4X_4 + 3.6X_5 + 3.2X_6 \geq 1 \\ & X_1, X_2, X_3, X_4, X_5, X_6 \geq 0. \end{aligned}$$

Here, $V = \dfrac{1}{\Delta^{-1}(\widetilde{v}^-)}$ and $X_i = \dfrac{x_i}{\Delta^{-1}(\widetilde{v}^-)}$, $i = 1, \ldots, 6$.

The optimal solution is $(0,\ 0,\ 0.0658,\ 0.1645,\ 0.0329,\ 0)$ and $V^* = 0.2632$. Thus, the optimal strategy for the DM is $(0,\ 0,\ 0.25,\ 0.625,\ 0.125,\ 0)$.

The problem for Nature to solve is as follows:

$$
\begin{aligned}
&\max V = \quad Y_1 + Y_2 + Y_3 + Y_4 + Y_5 + Y_6 + Y_7 + Y_8\\
&\text{subject to}\\
&4Y_1 + 4.4Y_2 + 2.4Y_3 + 3.4Y_4 + 3.8Y_5 + 2.2Y_6 + 3.8Y_7 + 2.4Y_8 \le 1\\
&2.2Y_1 + 3Y_2 + 4.2Y_3 + 4.2Y_4 + 2.2Y_5 + 4.2Y_6 + 2.4Y_7 + 4.2Y_8 \le 1\\
&5Y_1 + 4.2Y_2 + 4.2Y_3 + 2.8Y_4 + 4.8Y_5 + 4.2Y_6 + 4.8Y_7 + 3.4Y_8 \le 1\\
&5.2Y_1 + 4Y_2 + 3.8Y_3 + 4.4Y_4 + 3.2Y_5 + 4.2Y_6 + 3.8Y_7 + 4Y_8 \le 1\\
&4.6Y_1 + 2Y_2 + 3.2Y_3 + 3.4Y_4 + 4.8Y_5 + 4.2Y_6 + 4.8Y_7 + 3.6Y_8 \le 1\\
&4Y_1 + 4.4Y_2 + 2.4Y_3 + 3.4Y_4 + 3.8Y_5 + 2.6Y_6 + 4Y_7 + 3.2Y_8 \le 1\\
&Y_1, Y_2, Y_3, Y_4, Y_5, Y_6, Y_7, Y_8 \ge 0.
\end{aligned}
$$

The optimal solution is $(0,\ 0.0164,\ 0,\ 0,\ 0.0658,\ 0,\ 0,\ 0.1809)$ and $V^* = 0.2632$. Consequently, the optimal strategy for Nature is $(0,\ 0.0623,\ 0,\ 0,\ 0.25,\ 0,\ 0,\ 0.6873)$.

Here, for the DM, the attributes for which $y_j^* = 0$ are of least importance. Similarly, the alternatives with $x_i^* = 0$ are not relevant to the DM.

The combined scores of the alternatives are

$$
\widetilde{S}_1 = (\ell_0,\ 0),\ \widetilde{S}_2 = (\ell_0,\ 0),\ \widetilde{S}_3 = (\ell_1,\ 0.0722),\ \widetilde{S}_4 = (\ell_2,\ 0.3741),\\
\widetilde{S}_5 = (\ell_0,\ 0.4749),\ \widetilde{S}_6 = (\ell_0, 0).
$$

Therefore, the six alternatives are ranked as $A_4 > A_3 > A_5 > A_1 = A_2 = A_6$, and alternative A_4 is the recommended air conditioning system for installation in the company.

In the past decade, a few research works have reported on linguistic MADM problems wherein different techniques are proposed to solve this class of problems. Wei (2011) proposed a group decision-making method using different operators on the 2-tuple linguistic variables. We now present an example of an investment selection problem from Wei (2011) to demonstrate our proposed approach.

Example 4 An investment company is willing to invest a sum of money in one of five possible alternatives: A_1 a car company, A_2 a food company, A_3 a computer company, A_4 an arms company, and A_5 a TV company. The decision of the appointed panel is based on six attributes: C_1, financial risk; C_2, technical risk; C_3, production risk; C_4, market risk; C_5, management risk; and C_6, environment risk. The experts provide the assessment of each alternative under given attributes using predefined linguistic terms set $LT = \{\ell_1 : \text{Extremely Poor (EP)}, \ell_2 : \text{Very Poor (VP)}, \ell_3 : \text{Poor (P)}, \ell_4 : \text{Medium (M)}, \ell_5 : \text{Good (G)}, \ell_6 : \text{Very Good (VG)}, \ell_7 : \text{Extremely Good (EG)}\}$. We consider the alternatives-attributes decision matrix $\widetilde{R}$ (the same as in Table 4 of Wei (2011)) as follows:

$$
\widetilde{R} = \begin{array}{c} \\ A_1 \\ A_2 \\ A_3 \\ A_4 \\ A_5 \end{array}
\begin{array}{c}
\begin{array}{cccccc} C_1 & C_2 & C_3 & C_4 & C_5 & C_6 \end{array} \\
\begin{bmatrix}
(M,-0.3) & (P,0.2) & (VP,0.3) & (P,-0.3) & (VP,-0.1) & (VP,0.3) \\
(VP,0.3) & (VP,0.1) & (M,0.3) & (M,0.4) & (M,-0.4) & (M,0) \\
(VG,-0.3) & (VG,0) & (VG,-0.1) & (EG,0) & (G,-0.5) & (VG,0) \\
(VG,0.3) & (P,0.1) & (P,0.3) & (M,-0.1) & (VG,-0.4) & (G,-0.4) \\
(M,0.4) & (VP,-0.3) & (P,0.4) & (P,-0.4) & (P,0) & (M,-0.5)
\end{bmatrix}
\end{array}
$$

The above linguistic matrix is taken as the payoff matrix for the game problem between the DM and the combined risk of all forms taken together (which acts like Nature). The corresponding linear programming problems are formulated and solved. The optimal strategy

for the DM is obtained as (0, 0, 0.6248, 0.3747, 0) and the optimal weight for the risk is (0, 0.275, 0, 0, 0.725, 0). Based on the scores $\widetilde{S}_i$, the resulting ranking of the alternatives is $A_3 > A_4 > A_1 = A_2 = A_5$. The best two alternatives (A_3 and A_4) determined by the proposed method are the same as those reported in Wei (2011).

The game theory approach to solve an MADM problem is expedient and advantageous compared to the approach suggested by Wei (2011) in the sense that the latter requires prior knowledge of the weights of the attributes, whereas our proposed methodology evaluates the weights as an intermediate step. Additionally, the proposed approach adds a feature in the situation when there are multiple DMs involved in a group MADM problem. Each DM, based on his expertise, has a different payoff matrix for the same set of alternatives-attributes. The optimal weights of the attributes computed for each matrix represents the significance level (or importance) of these attributes to the respective DM. This approach appears to be reasonable because the DMs can have a different opinion about the set of attributes identified for a group MADM problem.

6 Conclusions

In this paper, a two-player constant-sum linguistic game is defined. The evaluation of the saddle point is discussed, and a linear programming approach is introduced to find the optimal mixed strategies for both players. Inspired by the approach discussed in Chen and Larbani (2006), we also proposed an innovative game theory approach for solving linguistic MADM problems. The expediency of the proposed method is that it naturally generates the optimal weights for the attributes in an intermediate step, in contrast to other existing methods where the weights are presumed to be known a priori.

The proposed approach presents a unified framework because it can be adopted to solve linguistic game problems, LLP problems and linguistic MADM problems. The wide application of our approach makes it promising. We envision that the present study can be extended to define linguistic bimatrix games. One can also explore the incorporation of interval-valued linguistic variables and hesitant linguistic variables in the payoff matrix of games.

Acknowledgements The authors are thankful to the esteemed referees for their valuable suggestions for improving the paper. The authors thank the editor for being supportive and considerate.

References

Aliprantis, C. D., & Chakrabarti, S. K. (1998). *Games and decision making*., Business and economics Oxford: Oxford University Press.

Arfi, B. (2006a). Linguistic fuzzy-logic game theory. *Journal of Conflict Resolution*, *50*(1), 28–57.

Arfi, B. (2006b). Linguistic fuzzy-logic social game of cooperation. *Rationality and Society*, *18*(4), 471–537.

Balezentis, A., & Balezentis, T. (2011). A novel method for group multi-attribute decision making with two-tuple linguistic computing: Supplier evaluation under uncertainty. *Economic Computation and Economic Cybernetics Studies and Research*, *45*(4), 5–30.

Barron, E. N. (2011). *Game theory: An introduction*. New Jersey: John Wiley and Sons.

Bauso, D. (2016). *Game theory with engineering applications*., Advances in design and control Philadelphia: SIAM.

Bector, C. R., & Chandra, S. (2005). *Fuzzy mathematical programming and Fuzzy matrix games*. Berlin: Springer.

Bector, C. R., Chandra, S., & Vijay, V. (2004). Duality in linear programming with fuzzy parameters and matrix games with fuzzy payoffs. *Fuzzy Sets and Systems*, *146*, 253–269.

Billot, A. (1986). A contribution to a mathematical theory of fuzzy games. In C. Ponsard & B. Fustier (Eds.), *Fuzzy economics and spatial analysis* (pp. 47–56). Dijon: Librairie del Universite.
Butnariu, D. (1978). Fuzzy games: A description of the concept. *Fuzzy Sets and Systems*, *1*, 1181–1192.
Campos, L. (1989). Fuzzy linear programming to solve fuzzy matrix games. *Fuzzy Sets and Systems*, *32*, 275–289.
Cebi, S., Kahraman, C., & Kaya, I. (2010). Renewable energy system selection based on computing with words. *International Journal of Computational Intelligence Systems*, *3*(4), 461–473.
Chen, Y. W., & Larbani, M. (2006). Two-person zero-sum game approach for fuzzy multiple attribute decision making problems. *Fuzzy Sets and Systems*, *157*, 34–51.
Herrera, F., & Martinez, L. (2000). A 2-tuple fuzzy linguistic representation model for computing with words. *IEEE Transactions on Fuzzy Systems*, *8*, 746–752.
Larbani, M. (2009). Non-cooperative fuzzy games in normal form: A survey. *Fuzzy Sets and Systems*, *160*, 3184–3210.
Larbani, M., & Chen, Y. W. (2014). Improving the game approach to fuzzy MADM. *Multiple Criteria Decision Making*, *9*, 58–71.
Li, D. F. (2014). *Decision and game theory in management with intuitionistic fuzzy sets*., Studies in fuzziness and soft computing Berlin, Heidelberg: Springer.
Luce, R. D., & Raiffa, H. (1957). *Games and decisions*. New Jersey: John Wiley & Sons.
Mazalov, V. (2014). *Mathematical game theory and applications*. New Jersey: John Wiley & Sons.
Morris, P. (1994). *Introduction to game theory*. Berlin: Springer.
Moura, J., & Hutchison, D. (2017). Survey of game theory and future trends for applications in emerging wireless data communication networks, Working Paper, https://arxiv.org/ftp/arxiv/papers/1704/1704.00323.pdf.
Nagurney, A., Daniele, P., & Shukla, S. (2016). A supply chain network game theory model of cybersecurity investments with nonlinear budget constraints. *Annals of Operations Research*, *248*(1–2), 405–427.
Neumann, J. V., & Morgenstern, O. (1944). *Theory of games and economic behavior*. New York: Princeton University Press.
Nishizaki, I., & Sakawa, M. (1997). Equilibrium solution in bimatrix games with fuzzy payoffs. *Japanese Journal of Fuzzy Theory Systems*, *9*(3), 307–324.
Nishizaki, I., & Sakawa, M. (2001). *Fuzzy and multiobjective games for conflict resolution*. Heidelberg: Physica.
Sakawa, M., & Nishizaki, I. (1994). Max-min solution for fuzzy multiobjective matrix games. *Fuzzy Sets and Systems*, *67*(1), 53–69.
Saulo, H., Rêgo, L. C., & Divino, J. A. (2013). Fiscal and monetary policy interactions: A game theory approach. *Annals of Operations Research*, *206*(1), 341–366.
Singh, A., Gupta, A., & Mehra, A. (2015). An AHP-PROMETHEE II method for 2-tuple linguistic multicriteria group decision making. https://doi.org/10.1109/ICRITO.2015.7359374
Vijay, V., Chandra, S., & Bector, C. R. (2004). Bi-matrix games with fuzzy goals and fuzzy payoffs. *Fuzzy Optimization & Decision Making*, *3*, 327–344.
Vijay, V., Chandra, S., & Bector, C. R. (2005). Matrix games with fuzzy goals and fuzzy payoffs. *Omega*, *33*, 425–429.
Wei, G. W. (2010). A method for multiple attribute group decision making based on the ET-WG and ET-OWG operators with 2-tuple linguistic information. *Expert Systems with Applications*, *37*(12), 7895–7900.
Wei, G. W. (2011). Some generalized aggregating operators with linguistic information and their application to multiple attribute group decision making. *Computers & Industrial Engineering*, *61*(1), 32–38.

Accepted Manuscript



Measure of entropy for past lifetime and k-record statistics

Ritu Goel, H.C. Taneja, Vikas Kumar

PII: S0378-4371(18)30286-3
DOI: https://doi.org/10.1016/j.physa.2018.02.200
Reference: PHYSA 19320

To appear in: *Physica A*

Received date : 14 September 2017
Revised date : 9 January 2018

Please cite this article as: R. Goel, H.C. Taneja, V. Kumar, Measure of entropy for past lifetime and k-record statistics, *Physica A* (2018), https://doi.org/10.1016/j.physa.2018.02.200

This is a PDF file of an unedited manuscript that has been accepted for publication. As a service to our customers we are providing this early version of the manuscript. The manuscript will undergo copyediting, typesetting, and review of the resulting proof before it is published in its final form. Please note that during the production process errors may be discovered which could affect the content, and all legal disclaimers that apply to the journal pertain.

ACCEPTED MANUSCRIPT

*Highlights (for review)

Highlights (for review)

- Extended the concept of measure of entropy for past lifetime to k-record values.
- Motivation and application of the proposed measure is given.
- The measure proposed characterizes the distribution function uniquely.
- Studied stochastic order properties and bounds to the proposed measure.

ACCEPTED MANUSCRIPT

ACCEPTED MANUSCRIPT

*Manuscript
Click here to view linked References

Measure of Entropy for Past Lifetime and k-Record Statistics

Ritu Goel[1], H.C. Taneja[2] and Vikas Kumar[3]

Abstract

In this paper we consider a measure of past entropy for n^{th} upper k-record value. A characterization result for the measure under consideration is given. We discuss some basic properties of the proposed measure. Also we construct bounds to the proposed past entropy measure for n^{th} k-records.

Keywords: Inactivity time; Past entropy; k-record value; Reverse hazard rate.

1 Introduction

If X is a random variable representing the lifetime of a system or a component with continuous cumulative distribution function (cdf) $F(x)$ and probability density function (pdf) $f(x)$, then the basic measure of uncertainty as given by Shannon (1948) is

$$H(f) = -\int_0^\infty f(x)\log f(x)dx. \tag{1.1}$$

It gives the average uncertainty contained in the probability density function $f(x)$ associated with the random variable X. But this measure is not suitable as a measure of uncertainty for the remaining lifetime of a system which has already survived up to time t. This time period $'t'$ has great importance in economics, reliability, business and survival analysis. For such type of systems Ebrahimi (1996) proposed the measure of uncertainty of the remaining lifetime $X_t = (X - t|X > t)$ as

$$H(f;t) = -\int_t^\infty \frac{f(x)}{\bar{F}(t)}\log\frac{f(x)}{\bar{F}(t)}dt, \quad t > 0. \tag{1.2}$$

[1]Department of Applied Mathematics, Delhi Technological University, Delhi-110042, India.
e-mail: ritujindalmahe@gmail.com
[2]Department of Applied Mathematics, Delhi Technological University, Delhi-110042, India.
e-mail: hctaneja@dce.ac.in
[3]Department of Applied Sciences, UIET, M. D. University, Rohtak-124001, India.
e-mail: vikas_iitr82@yahoo.co.in

ACCEPTED MANUSCRIPT

In many realistic situations, uncertainty is not related to future only, this may refer to past also. Suppose at time t, one has under gone a medical test to check for a certain disease. Let us assume that the test is positive. If we denote by X the age when the patient was infected, then it is known that $X < t$. Now the question is, how much time has elapsed since the patient had been infected by this disease. Such random time can be called *inactivity time or past lifetime* ${}_tX = [t - X|X < t]\,, \quad \text{for} \quad \text{fixed} \quad t > 0$. This gives the time elapsed from the failure of a component given that its lifetime is less than or equal to t. It is also called the reversed residual lifetime. Based on this idea Dicrescenzo and Longobardi (2002) defined the measure of uncertainty for past lifetime distribution over $(0, t)$ as

$$\bar{H}(f;t) = -\int_0^t \frac{f(x)}{F(t)} \log \frac{f(x)}{F(t)} dx. \tag{1.3}$$

The measure (1.3) can be considered as dual to the measure (1.2) proposed by Ebrahimi (1996). The above measure has applications in forensic science because in that a lifetime distribution truncated above is of vital importance. The measures of uncertainty for inactivity time, called past entropy, have been studied extensively in the literature, refer to Di Crescenzo and Longobardi (2004, 2009) and Kumar et al. (2010) and Kundu et al. (2010).

Let $\{X_i,\ i \geq 1\}$ be a sequence of independent and identically distributed continuous random variables with distribution function $F(x)$ and probability density function $f(x)$. An observation X_j is called an *upper record value* if its value exceeds that of all previous observations. Thus X_j is an upper record if $X_j > X_i$ for every $i < j$. *An analogous definition can be given for a lower record value.* Let $T(j)$ be the time (index) at which the j^{th} record value is observed. Records are closely connected with the occurrence times of a corresponding non-homogeneous Poisson process and reliability theory. But this record model becomes inadequate in several situations when the expected waiting time between two record values is very large. In those situations, second or third largest values are of great importance, insurance claims in some non-life insurance can be used as an example, see Kamps (1995). So, the concept of k-record values has been studied in the literature widely, refer to Berred (1995), Fashandi and Ahmadi (2012).

The definition of n^{th} upper k-record as given by Dziubdziela and Kopocinski (1976), is given as follows:
For a positive integer k, define $T_{1,k} = k$ and for $n \geq 2$,
$T_{n,k} = min\left\{j : j > T_{n-1,k};\ X_{j-k+1:j} > X_{T_{n-1,k}-k+1:T_{n-1,k}}\right\}$. Let $Y_{n,k} = X_{T_{n,k}-k+1:T_{n,k}}, n \geq 1$, where $X_{i:n}$ denotes the i^{th} order statistic in a sample of size n. The sequence $\{Y_{n,k}, n \geq 1\}$ are referred to as k-record values.
A lower k-record value can be defined analogously. If we put $k = 1$, the results for usual

ACCEPTED MANUSCRIPT

records can be obtained as special case.
The pdf of n^{th} upper k-record and the n^{th} lower k-record are given as

$$f_{n,k}(x) = \frac{k^n}{\Gamma n}[-\ln \bar{F}(x)]^{n-1}[\bar{F}(x)]^{k-1} f(x) \tag{1.4}$$

and

$$f^L_{n,k}(x) = \frac{k^n}{\Gamma n}[-\ln F(x)]^{n-1}[F(x)]^{k-1} f(x) \tag{1.5}$$

respectively, where $\Gamma.$ is the complete gamma function, see, Arnold et al. (1998).
These statistics have been used in a wide range of problems like estimation of parameters and prediction of future records, characterizations of probability distributions, refer to Balakrishnan and Chan (1998), Sultan et al. (2002), Balakrishnan and Stepanov (2004) and Su et al. (2008). Entropy properties of record values have been studied by several authors, refer to Zahedi and Shakil (2006), Baratpour et al. (2007, 2008), Madadi and Tata (2011), Razmkhan et al. (2012), Asha and Chacko (2015) and Kumar (2015, 2017).
In this paper we consider a measure of past entropy when the distribution is truncated above t in the context of k-record values; an extension of (1.3) to record values. The paper is organized as follows: In Section 2 we propose the measure of past entropy, derive bounds to the proposed measure and study its important properties like effect of linear transformation and stochastic ordering. In Section 3, we give the characterization result for the measure proposed. In Section 4, we find the past entropy for some specific distributions. Section 5 is devoted to conclusion.

2 Past Entropy for Upper k-Record

To elaborate the concept of k-record statistics, consider the following data giving the average temperature of a city during the month of July measured for twenty years, refer to Arnold et al. (1998):
19.0, 20.1, 18.4, 17.4, 19.7, 21.0, 21.4, 19.2, 19.9, 20.4, 20.9, 17.2, 20.2, 17.8, 18.1, 15.6, 19.4, 21.7, 16.2, 16.4
For $k = 3$, the upper and lower 3-record respectively denoted by $R^U_{n,3}$, $R^L_{n,3}$ and 3-record times respectively denoted by $T^U_{n,3}$ and $T^L_{n,3}$ are :

n	1	2	3	4	5	6	7
$T^U_{n,3}$	3	5	6	7	10	11	18
$R^U_{n,3}$	18.4	19.0	19.7	20.1	20.4	20.9	21.0
$T^L_{n,3}$	3	4	12	14	16	19	20
$R^L_{n,3}$	20.1	19.0	18.4	17.8	17.4	17.2	16.4

ACCEPTED MANUSCRIPT

In reliability theory, the $(n-k+1)^{th}$ order statistic in a sample of size n represents the life length of a $k-out\ of\ -n$ system. Therefore, the n^{th} k-record value is just the life length of a $k-out\ of\ -T_{n,k}$ system. Corresponding to measure (1.3) proposed by Dicrescenzo and Longobardi (2002), we define the measure of uncertainty for past life distribution over the interval $(0,t)$ for the distribution of n^{th} upper k-record value as follows:

$$\begin{aligned}\bar{H}(f_{n,k};t) &= -\int_0^t \frac{f_{n,k}(x)}{F_{n,k}(t)} \ln\left(\frac{f_{n,k}(x)}{F_{n,k}(t)}\right) dx \\ &= \ln F_{n,k}(t) - \frac{1}{F_{n,k}(t)} \int_0^t f_{n,k}(x) \ln f_{n,k}(x) dx \\ &= 1 - \frac{1}{F_{n,k}(t)} \int_0^t f_{n,k}(x) \ln r_{n,k}(x) dx, \end{aligned} \tag{2.1}$$

where $f_{n,k}(x)$ is the pdf of n^{th} upper k-record value given by (1.4) and $r_{n,k}(x) = \frac{f_{n,k}(x)}{F_{n,k}(x)}$ is the reversed hazard rate function or reversed failure rate of $X_{n,k}$.
Differentiating (2.1) with respect to t both sides, we get

$$\begin{aligned}\frac{d}{dt}(\bar{H}(f_{n,k};t)) &= -r_{n,k}(t)\ln r_{n,k}(t) + \frac{f_{n,k}(t)}{F_{n,k}^2(t)} \int_0^t f_{n,k}(x) \ln r_{n,k}(x) dx \\ &= -r_{n,k}(t)\ln r_{n,k}(t) + r_{n,k}(t) \int_0^t \frac{f_{n,k}(x)}{F_{n,k}(t)} \ln r_{n,k}(x) dx. \\ \frac{d}{dt}(\bar{H}(f_{n,k};t)) &= r_{n,k}(t)\left(1 - \bar{H}(f_{n,k};t) - \ln r_{n,k}(t)\right). \end{aligned} \tag{2.2}$$

Remark 2.1. *When we put $k=1$, (2.1) defines the past entropy measure for usual records. Further for $n=k=1$, the above equation reduces to (1.3). Also we can express Shannon differential entropy of n^{th} upper k-record value, in terms of the past entropy of n^{th} upper k-record value (2.1) and residual entropy of $X_{n,k}$*

$$H(f_{n,k};t) = -\int_t^\infty \frac{f_{n,k}(x)}{\bar{F}_{n,k}(t)} \ln\left(\frac{f_{n,k}(x)}{\bar{F}_{n,k}(t)}\right) dx, \tag{2.3}$$

given as

$$H(f_{n,k}) = F_{n,k}(t)\bar{H}(f_{n,k};t) + \bar{F}_{n,k}(t)H(f_{n,k};t) + B(F_{n,k}(t), \bar{F}_{n,k}(t)), \tag{2.4}$$

where $B(p,1-p) = -p\ln p - (1-p)\ln(1-p)$ is the Shannon entropy measure for a Bernoulli

ACCEPTED MANUSCRIPT

random variable. This follows as

$$\begin{aligned} H(f_{n,k}) &= -\int_0^\infty f_{n,k}(x)\ln f_{n,k}(x)dx \\ &= -\int_0^t f_{n,k}(x)\ln f_{n,k}(x)dx - \int_t^\infty f_{n,k}(x)\ln f_{n,k}(x)dx \\ &= -F_{n,k}(t)\int_0^t \frac{f_{n,k}(x)}{F_{n,k}(t)}\ln f_{n,k}(x)dx - \bar{F}_{n,k}(t)\int_t^\infty \frac{f_{n,k}(x)}{\bar{F}_{n,k}(t)}\ln f_{n,k}(x)dx \\ &= F_{n,k}(t)\bar{H}(f_{n,k};t) + \bar{F}_{n,k}(t)H(f_{n,k};t) - \bar{F}_{n,k}(t)\ln\bar{F}_{n,k}(t) - F_{n,k}(t)\ln F_{n,k}(t) \\ &= F_{n,k}(t)\bar{H}(f_{n,k};t) + \bar{F}_{n,k}(t)H(f_{n,k};t) + B(F_{n,k}(t),\bar{F}_{n,k}(t)). \end{aligned}$$

2.1 Some Results of Past Entropy for k-Record

I. An Upper Bound to Past entropy: *"If $\bar{H}(f_{n,k};t)$ is increasing function of $t>0$, then $r_{n,k}(t)\le\exp(1-\bar{H}(f_{n,k};t))$ and $\bar{H}(f_{n,k};t)\le 1-\ln r_{n,k}(t)$."*

Proof. From (2.1), we have

$$\bar{H}(f_{n,k};t) = 1 - \frac{1}{F_{n,k}(t)}\int_0^t f_{n,k}(x)\ln r_{n,k}(x)dx.$$

or

$$1-\bar{H}(f_{n,k};t) = \frac{1}{F_{n,k}(t)}\int_0^t f_{n,k}(x)\ln r_{n,k}(x)dx.$$

Now $1-\bar{H}(f_{n,k};t)$ is decreasing function of t as $\bar{H}(f_{n,k};t)$ is increasing, hence for $x\le t$,

$$\begin{aligned} 1-\bar{H}(f_{n,k};t) &\ge \frac{1}{F_{n,k}(t)}\int_0^t f_{n,k}(x)\ln r_{n,k}(t)dx \\ &= \ln r_{n,k}(t). \end{aligned}$$

or

$$r_{n,k}(t)\le\exp(1-\bar{H}(f_{n,k};t)). \tag{2.5}$$

Also from (2.5), it follows directly

$$r_{n,k}(t)\le\exp(1-\bar{H}(f_{n,k};t)). \tag{2.6}$$

Hence from (2.5) and (2.6), we get the result. □

II. Effect of Monotone Transform: *"For a strictly convex function ϕ with $\phi(0)=0$. Let $Y=\phi(X)$, then*

$$\bar{H}(g_{n,k};t) = \bar{H}(f_{n,k};\phi^{-1}(t)) + E_{f_{n,k}}[\ln\phi'(X)|X_{n,k}<\phi^{-1}(t)], \tag{2.7}$$

where $E_{f_{n,k}}$ denotes the expectation with respect to $f_{n,k}$ and other letters have usual meaning."

ACCEPTED MANUSCRIPT

Proof. From (2.1), the past measure of entropy associated with $Y_{n,k}$ is

$$\begin{aligned}
\bar{H}(g_{n,k};t) &= 1 - \frac{1}{G_{n,k}(t)} \int_0^t g_{n,k}(y) \ln r^G_{n,k}(y) dy, \quad t > 0 \\
&= 1 - \int_0^t \frac{k^n (-\ln \bar{G}(y))^{n-1} (\bar{G}(y))^{k-1} g(y)}{(\Gamma n) G_{n,k}(t)} \ln r^G_{n,k}(y) dy \\
&= 1 - \int_0^{\phi^{-1}(t)} \frac{k^n (-\ln \bar{F}(x))^{n-1} (\bar{F}(x))^{k-1} f(x)}{(\Gamma n) F_{n,k}(\phi^{-1}(t)) \phi'(x)} \ln \left(\frac{r^F_{n,k}(x)}{\phi'(x)} \right) \phi'(x) dx \\
&= 1 - \frac{1}{F_{n,k}(\phi^{-1}(t))} \int_0^{\phi^{-1}(t)} f_{n,k}(x) \ln r^F_{n,k}(x) dx + \frac{1}{F_{n,k}(\phi^{-1}(t))} \int_0^{\phi^{-1}(t)} f_{n,k}(x) \ln \phi'(x) dx \\
&= \bar{H}(f_{n,k}; \phi^{-1}(t)) + E_{f_{n,k}}[\ln \phi'(X) | X_{n,k} < \phi^{-1}(t)].
\end{aligned}$$

Here $r^F_{n,k}$ and $r^G_{n,k}$ denote the reversed hazard rates of the n^{th} k-record values corresponding to the distribution functions F and G respectively. □

III. Stochastic Ordering of Past Entropy:

Here we prove some order properties of the past entropy measure for k-record values. First, we give the following definitions from Nanda and Paul (2006).

Definition 2.1. *A random variable is said to have increasing uncertainty of life (IUL) if $\bar{H}(f;t)$ is increasing in $t \geq 0$.*

Definition 2.2. *Let X_1 and X_2 be two random variables denoting the lifetimes of two components with pdfs f_1 and f_2 respectively. Then X_1 is said to be greater than X_2 in past entropy order (written as $X_1 \overset{PE}{\geq} X_2$) if $\bar{H}(f_1;t) \leq \bar{H}(f_2;t), \quad \forall \ t \geq 0$.*

Example 2.1. *If X_1 and X_2 are two exponentially distributed random variable with means a_1 and $2a_1$, then for $n = k = 1$, we can easily see that $H(f_{n,k};t) \leq H(g_{n,k};t)$, where $f_{n,k}(x)$ and $g_{n,k}(x)$ represent the pdfs of n^{th} k-record values corresponding to X_1 and X_2 respectively. Therefore X_1 is greater than X_2 in past entropy order that is $X_1 \overset{PE}{\geq} X_2$.*

Next, Theorem 2.1 and Theorem 2.2 prove results on order properties of the past entropy measure (2.1).

Theorem 2.1. *Let X_1 and X_2 be two non-negative random variables such that $X^{(1)}_{n,k} \overset{PE}{\geq} X^{(2)}_{n,k}$ and ϕ be a strictly increasing convex function with $\phi(0) = 0$ and let $\phi'(x)$ exists and is continuous with $\phi'(0) \geq 1$. Then $\phi(X^{(1)}_{n,k}) \overset{PE}{\geq} \phi(X^{(2)}_{n,k})$, where $X^{(1)}_{n,k}$ and $X^{(2)}_{n,k}$ denote the n^{th} k-record values corresponding to X_1 and X_2 respectively.*

ACCEPTED MANUSCRIPT

Proof. From (2.7), we can write

$$\bar{H}(g_{n,k}^{(1)};t) - \bar{H}(g_{n,k}^{(2)};t) = \bar{H}(f_{n,k}^{(1)};\phi^{-1}(t)) - \bar{H}(f_{n,k}^{(2)};\phi^{-1}(t)) + E_{f_{n,k}^{(1)}}(\ln\phi'(X)|X_1 < \phi^{-1}(t)) - E_{f_{n,k}^{(2)}}(\ln\phi'(X)|X_2 < \phi^{-1}(t)). \quad (2.8)$$

Here $f_{n,k}^{(1)}$, $f_{n,k}^{(2)}$, $g_{n,k}^{(1)}$ and $g_{n,k}^{(2)}$ represent the pdfs of n^{th} k-record values corresponding to X_1, X_2, $\phi(X_1)$ and $\phi(X_2)$ respectively.

Now, $X_{n,k}^{(1)} \overset{PE}{\geq} X_{n,k}^{(2)}$ implies that $\bar{H}(f_{n,k}^{(1)};\phi^{-1}(t)) \leq \bar{H}(f_{n,k}^{(2)};\phi^{-1}(t))$, where as

$$\begin{aligned}
&E_{f_{n,k}^{(1)}}(\ln\phi'(X)|X_1 < \phi^{-1}(t)) - E_{f_{n,k}^{(2)}}(\ln\phi'(X)|X_2 < \phi^{-1}(t)) \\
&= \int_0^{\phi^{-1}(t)} \ln\phi'(x)\left(\frac{f_{n,k}^{(1)}(x)}{F_{n,k}^{(1)}(\phi^{-1}(t))} - \frac{f_{n,k}^{(2)}(x)}{F_{n,k}^{(2)}(\phi^{-1}(t))}\right)dx \\
&\leq \ln\phi'(\phi^{-1}(t)) \int_0^{\phi^{-1}(t)} \left(\frac{f_{n,k}^{(1)}(x)}{F_{n,k}^{(1)}(\phi^{-1}(t))} - \frac{f_{n,k}^{(2)}(x)}{F_{n,k}^{(2)}(\phi^{-1}(t))}\right)dx \\
&= 0.
\end{aligned}$$

The above inequality follows from the fact that $\phi'(x)$ is increasing function of x. Hence from (2.8), we get $\bar{H}(g_{n,k}^{(1)};t) \leq \bar{H}(g_{n,k}^{(2)};t)\ \forall\ t \geq 0$, which implies that $\phi(X_{n,k}^{(1)}) \overset{PE}{\geq} \phi(X_{n,k}^{(2)})$. □

Example 2.2. *From Example 2.1,* $X_1 \overset{PE}{\geq} X_2$. *Let us take* $\phi(x) = \lambda x$, *where* $\lambda \geq 1$. *Now* $\phi(x)$ *is strictly increasing convex function with* $\phi(0) = 0$ *and also* $\phi'(x)$ *exists and is continuous with* $\phi'(0) \geq 1$. *Therefore, by Theorem 2.1, for* $n = k = 1$, $\phi(X_{n,k}^{(1)}) \overset{PE}{\geq} \phi(X_{n,k}^{(2)})$.

Next, we show that past entropy order defined above is closed under increasing past entropy measure. First we prove the following lemma.

Lemma 2.1. *For any absolutely continuous random variable* X, *define* $Z = aX + b$, *where* a *and* b *are constants. Also* $a > 0$ *and* $b \geq 0$. *Then, for* $t > b$,

$$\bar{H}(g_{n,k};t) = \bar{H}(f_{n,k};\frac{t-b}{a}) + \ln a, \quad (2.9)$$

where $g_{n,k}$ *and* $f_{n,k}$ *are the pdf of* n^{th} *upper* k*-record values for* Z *and* X *respectively.*

Proof. We know that

$$\bar{H}(g_{n,k};t) = \ln G_{n,k}(t) - \frac{1}{G_{n,k}(t)}\int_0^t g_{n,k}(z)\ln g_{n,k}(z)dz.$$

After substituting (1.4) and using the transformation $Z = aX + b$ we get,

$$\begin{aligned}
\bar{H}(g_{n,k};t) &= \ln F_{n,k}(t) - \frac{1}{F_{n,k}(t)}\int_0^{\frac{t-b}{a}} f_{n,k}(x)\ln\left(\frac{f_{n,k}(x)}{a}\right)dx \\
&= \bar{H}(f_{n,k};\frac{t-b}{a}) + \ln a.
\end{aligned}$$

ACCEPTED MANUSCRIPT

Here $t > b,\ a > 0 \Rightarrow \frac{t-b}{a} > 0$. □

Theorem 2.2. *For any two absolutely continuous random variables X and Y, define $Z^x_{n,k} = a_1 X_{n,k} + b_1$ and $Z^y_{n,k} = a_2 Y_{n,k} + b_2$, where $a_1,\ a_2 > 0$ and $b_1,\ b_2 \geq 0$ are constants. Let (i) $X_{n,k} \overset{PE}{\geq} Y_{n,k}$, (ii) $a_1 \geq a_2$ and $b_1 \geq b_2$. Then, $Z^x_{n,k} \overset{PE}{\geq} Z^y_{n,k}$ if either $\bar{H}(f_{n,k};t)$ or $\bar{H}(g_{n,k};t)$ is increasing in $t > b_1$. Here $f_{n,k}(x)$ and $g_{n,k}(x)$ denote the p.d.f of n^{th} k-record values corresponding to X and Y respectively.*

Proof. Suppose $\bar{H}(f_{n,k};t)$ is increasing in t. Since $\frac{t-b_1}{a_1} \leq \frac{t-b_2}{a_2}$, we have

$$\bar{H}(f_{n,k};\frac{t-b_1}{a_1}) \leq \bar{H}(f_{n,k};\frac{t-b_2}{a_2}).$$

Also $X_{n,k} \overset{PE}{\geq} Y_{n,k}$

$$\Rightarrow \bar{H}(f_{n,k};\frac{t-b_2}{a_2}) \leq \bar{H}(g_{n,k};\frac{t-b_2}{a_2}).$$

Combining above two inequalities, we have

$$\bar{H}(f_{n,k};\frac{t-b_1}{a_1}) \leq \bar{H}(g_{n,k};\frac{t-b_2}{a_2}). \tag{2.10}$$

Using (2.9), we get

$$\bar{H}(z^x_{n,k};t) \leq \bar{H}(z^y_{n,k};t).$$

$$\Rightarrow Z^x_{n,k} \overset{PE}{\geq} Z^y_{n,k},$$

this proves the result. Also if $\bar{H}(g_{n,k};t)$ is increasing in t, then proof is similar and hence omitted. □

Corollary 2.1. *Let X and Y be two absolutely continuous random variables such that $X_{n,k} \overset{PE}{\geq} Y_{n,k}$. Define $Z^x_{n,k} = aX_{n,k} + b$ and $Z^y_{n,k} = aY_{n,k} + b$, where $a > 0$ and $b \geq 0$ are constants. Then, $Z^x_{n,k} \overset{PE}{\geq} Z^y_{n,k}$, if either $\bar{H}(f_{n,k};t)$ or $\bar{H}(g_{n,k};t)$ is increasing in $t > b$.*

Although this corollary can be derived directly from the above theorem by taking $a_1 = a_2 = a$ and $b_1 = b_2 = b$, a stronger result stated below as Theorem 2.3 can be proved in which condition of increasing entropy measure in the Theorem 2.2 has been droped.

Theorem 2.3. *Let X and Y be two absolutely continuous random variables. Define $Z^x_{n,k} = aX_{n,k} + b$ and $Z^y_{n,k} = aY_{n,k} + b$, where $a > 0$ and $b \geq 0$. Then, $Z^x_{n,k} \overset{PE}{\geq} Z^y_{n,k}$, if $X_{n,k} \overset{PE}{\geq} Y_{n,k}$.*

Proof. Proof can be done on the same lines as Theorem 2.2 and hence omitted. □

ACCEPTED MANUSCRIPT

3 Characterization Result

Since two different distributions may have equal Shannon information, so a distribution function can not be determined by its Shannon information. A natural question arises that whether the proposed past measure of entropy determines the lifetime distribution $F(.)$ uniquely. In this section we study the condition under which the proposed measure determines uniquely the parent distribution. For that we first state the following theorem and lemma (without proof) from Gupta and Kirmani (2008) which are useful in proving the characterization result.

Theorem 3.1. *Let the function f be a continuous function defined in a domain $D \subset R^2$ and let f satisfies Lipschitz condition (with respect to y) in D, that is*

$$|f(x, y_1) - f(x, y_2| \leq \ k\ |y_1 - y_2|, \ \ k > 0,$$

for every point (x, y_1) and (x, y_2) in D. Then the function $y = \phi(x)$ satisfying the initial value problem $y' = f(x, y)$ and $\phi(x_0) = y_0$, $x \epsilon I$, is unique.

The following lemma, refer to Gupta and Kirmani (2008), presents the sufficient condition which ensures that Lipschitz condition is satisfied in D.

Lemma 3.1. *Suppose that the function f is continuous in a convex region $D \subset R^2$. Suppose that $\frac{\partial f}{\partial y}$ exists and is continuous in D. Then, f satisfies Lipschitz condition in D.*

Theorem 3.2. *Let X be a non-negative continuous random variable with distribution function F(x). Let the past entropy measure of the corresponding n^{th} k-record value $\bar{H}(f_{n,k}; t)$ be finite for all $t \geq 0$. Then $\bar{H}(f_{n,k}; t)$ characterizes the distribution function uniquely.*

Proof. From (2.2), we have

$$\frac{d}{dt}(\bar{H}(f_{n,k}; t)) = r_{F_{n,k}}(t) - r_{F_{n,k}}(t)\bar{H}(f_{n,k}; t)) - r_{F_{n,k}}(t) \ln r_{F_{n,k}}(t),$$

where $r_{F_{n,k}}(t)$ is the reversed hazard rate function of $X_{n,k}$. Taking derivative with respect to t again, we obtain

$$r'_{F_{n,k}}(t) = \frac{\bar{H}'(f_{n,k}; t) r_{F_{n,k}}(t) + \bar{H}''(f_{n,k}; t)}{-\bar{H}(f_{n,k}; t) - \ln r_{F_{n,k}}(t)} \ . \tag{3.1}$$

Suppose there are two distribution functions F and F^* such that

$$\bar{H}(f_{n,k}; t) = \bar{H}(f^*_{n,k}; t) = \gamma(t), \ say.$$

Then $\forall\ t$, from (3.1) we get

$$r'_{F_{n,k}}(t) = \psi\left(t, r_{F_{n,k}}(t)\right), \ \ r'_{F^*_{n,k}}(t) = \psi\left(t, r_{F^*_{n,k}}(t)\right),$$

ACCEPTED MANUSCRIPT

where

$$\psi(t,y)=\left(-\frac{\gamma(t)y+\gamma''(t)}{\gamma(t)+\ln y}\right).$$

Using Theorem 3.1 and Lemma 3.1 we get, $r_{F_{n,k}}(t)=r_{F^*_{n,k}}(t)$, $\forall\, t$. This proves the uniqueness of reversed hazard rate function. As reversed hazard function characterizes the distribution function uniquely, therefore this characterizes the distribution function $F_{n,k}$ and hence parent distribution uniquely. So we get the desired result. □

Next, we derive the simplified expression for the computation of past entropy measure for specific distribution functions.

4 Past Entropy for some specific distributions

For this first we prove a lemma as given below.

Lemma 4.1. *Let $X_{n,k}$ denotes the n^{th} upper k-record value having pdf $f_{n,k}(x)$ from the distribution F(x) and with density function f(x). Then the past entropy measure can be expressed as*

$$\begin{aligned}\bar{H}(f_{n,k};t)=&\ln\left(F_{n,k}(t)\frac{\Gamma n}{k}\right)-\frac{1}{F_{n,k}(t)}\int_0^{-k\ln\bar{F}(t)}\frac{u^{n-1}e^{-u}}{\Gamma n}\ln\left(u^{n-1}f(F^{-1}(1-e^{-\frac{u}{k}}))\right)du\\&+\frac{n(k-1)}{k}\frac{F_{n+1,k}(t)}{F_{n,k}(t)}.\end{aligned}\tag{4.1}$$

Proof. We have

$$\bar{H}(f_{n,k};t)=\ln F_{n,k}(t)-\frac{1}{F_{n,k}(t)}\int_0^t f_{n,k}(x)\ln f_{n,k}(x)dx.$$

After substituting (1.4) and using substitution $-k\ln\bar{F}(x)=u$, we get

$$\begin{aligned}\bar{H}(f_{n,k};t)&=\ln F_{n,k}(t)-\frac{1}{F_{n,k}(t)\Gamma n}\int_0^{-k\ln\bar{F}(t)}u^{n-1}e^{-u}\ln\left(\frac{k}{\Gamma n}u^{n-1}e^{-(1-\frac{1}{k})u}f\left(F^{-1}(1-e^{-\frac{u}{k}})\right)\right)du\\&\quad+\frac{n(k-1)}{k}\frac{F_{n+1,k}(t)}{F_{n,k}(t)}\\&=\ln F_{n,k}(t)-\ln\frac{k}{\Gamma n}-\frac{1}{F_{n,k}(t)\Gamma n}\int_0^{-k\ln\bar{F}(t)}u^{n-1}e^{-u}\ln\left(u^{n-1}f\left(F^{-1}(1-e^{-\frac{u}{k}})\right)\right)du\\&\quad+\frac{n(k-1)}{k}\frac{F_{n+1,k}(t)}{F_{n,k}(t)}\\&=\ln\left(F_{n,k}(t)\frac{\Gamma n}{k}\right)-\frac{1}{F_{n,k}(t)}\int_0^{-k\ln\bar{F}(t)}\frac{u^{n-1}e^{-u}}{\Gamma n}\ln\left(u^{n-1}f\left(F^{-1}(1-e^{-\frac{u}{k}})\right)\right)du\\&\quad+\frac{n(k-1)}{k}\frac{F_{n+1,k}(t)}{F_{n,k}(t)}.\end{aligned}$$

□

ACCEPTED MANUSCRIPT

Now, the following example obtain the measure of past entropy for n^{th} upper k-record value from exponential distribution in terms of incomplete gamma function which is defined as

$$\Gamma(n;a) = \int_0^a u^{n-1}e^{-u}du \quad a > 0.$$

Example 4.1. *Let $f^*_{n,k}$ denotes the pdf of n^{th} upper k-record value from standard exponential distribution. Then $F_{n,k}(t) = \frac{\Gamma(n;kat)}{\Gamma(n)}$. Using (4.1), we get*

$$H(f^*_{n,k};t) = \ln\frac{\Gamma(n;kat)}{ak} - \frac{(n-1)\Gamma n}{\Gamma(n;kat)}E(\ln\nu^*) + \frac{\Gamma(n+1;kat)}{\Gamma(n;kat)}, \tag{4.2}$$

where ν^* follows the incomplete gamma distribution $\Gamma(n;kat)$.

Remark 4.1. *The entropy measure of n^{th} k-record value from distribution F(x) can be expressed in terms of past entropy measure from standard exponential distribution as*

$$\bar{H}(f_{n,k};t) = H(f^*_{n,k},t) + \ln a - \frac{1}{k}\frac{\Gamma(n+1;-k\ln\bar{F}(t))}{\Gamma(n;-k\ln\bar{F}(t))} - \frac{\Gamma n}{\Gamma(n;-\ln\bar{F}(t))}. \tag{4.3}$$

Proof. The proof follows directly using (4.1) and (4.2). □

Example 4.2. *If X follows the finite range distribution with pdf*

$$f(x) = \frac{a}{b}\left(1-\frac{x}{b}\right)^{a-1}, \quad a > 1, \ \ 0 \le x \le b.$$

and survival function

$$\bar{F}(x) = 1 - F(x) = \left(1-\frac{x}{b}\right)^a, \text{ then}$$

$$F_{n,k}(t) = \frac{\Gamma(n;-k\ln\bar{F}(t))}{\Gamma n} = \frac{\Gamma(n;-k\ln\left(1-\frac{t}{b}\right)^a)}{\Gamma n}.$$

Substituting $-k\ln\bar{F}(x) = u$, we observe that $x = F^{-1}(1-e^{-\frac{u}{k}}) = b(1-e^{-\frac{u}{ak}})$.
Using (4.1), we get

$$\begin{aligned}\bar{H}(f_{n,k};t) =& \ln\left(F_{n,k}(t)\frac{\Gamma n}{k}\right) - \frac{1}{F_{n,k}(t)}E\left(\ln\nu^{*n-1}\right) - \frac{1}{F_{n,k}(t)}\int_0^{-k\ln\bar{F}(t)}\frac{u^{n-1}e^{-u}}{\Gamma n}\ln\left(f\left(F^{-1}(1-e^{-\frac{u}{k}})\right)\right)d\\ &+ \frac{n(k-1)}{k}\frac{F_{n+1,k}(t)}{F_{n,k}(t)}\\ =& \ln\left(F_{n,k}(t)\frac{\Gamma n}{k}\right) - \frac{1}{F_{n,k}(t)}E(\ln\nu^{*n-1}) - \ln\frac{a}{b} + \frac{(a-1)nF_{n+1,k}(t)}{akF_{n,k}(t)}\\ &+ \frac{n(k-1)}{k}\frac{F_{n+1,k}(t)}{F_{n,k}(t)}.\end{aligned}$$

where ν^* follows the incomplete gamma distribution $\Gamma(n,-k\ln\left(1-\frac{t}{b}\right)^a)$.

ACCEPTED MANUSCRIPT

Example 4.3. *If X follows the Pareto distribution with pdf and cdf as*

$$f(x) = \frac{a}{x^{a+1}}, \;\; x \geq 1, \; a > 0 \;\; and \;\; F(x) = 1 - \frac{1}{x^a}, \; then$$

$$F_{n,k}(t) = \frac{\Gamma(n; ak \ln t)}{\Gamma n} \;\; and \;\; f\left(F^{-1}(1 - e^{-\frac{u}{k}})\right) = ae^{-\frac{u}{k}(1+\frac{1}{a})}.$$

Using (4.1) , we get

$$\bar{H}(f_{n,k}; t) = \ln\left(F_{n,k}(t)\frac{\Gamma n}{ak}\right) - \frac{(n-1)}{F_{n,k}(t)}E(\ln \nu^*) + \frac{nF_{n+1,k}(t)}{kF_{n,k}(t)}\left(2 + \frac{1}{a} - \frac{1}{k}\right),$$

where ν^* follows the incomplete gamma distribution $\Gamma(n; ak \ln t)$.

5 Conclusion

Past information measures have found applications in reliability and life testing. In this paper, we extend the concept given by Di Crescenzo and Longobardi (2002) regarding measure of uncertainty in past lifetime distribution for k-record values. We prove that the proposed measure of uncertainty for k-record values determines the underlying distribution uniquely. In addition to a few other properties it satisfies stochastic ordering property. Also we derive its expression for a few specific distributions.

Acknowledgements

Authors are thankful to learned referees for their valuable suggestions on the earlier version of the paper.

References

[1] Arnold, B. C., Balakrishnan, N. and Nagaraja, H. N. (1998). Records. Wiley, New York.

[2] Asha, P. S.,Chacko, M., (2015). Residual Renyi entropy of k-record values. Communications in Statistics - Theory and Methods, 45 (16), 4874-4885.

[3] Balakrishnan,N., Chan, P.S. (1998). On the normal record values and associated inference. Statistics and Probability Letters, 39, 73-80.

[4] Balakrishnan, N., Stepanov, A. (2004). Two characterizations based on order statistics and records. Journal of Statistical Planning and Inference, 124, 273-287.

ACCEPTED MANUSCRIPT

[5] Baratpour, S., Ahmadi, J. and Arghami, N. R. (2007). Entropy properties of record statistics. Statistical Papers, 48, 197-213.

[6] Baratpour, S., Ahmadi, J. and Arghami, N. R. (2008). Characterizations based on Renyi entropy of order statistics and record values. Journal of Statistical Planning and Inference, 138, 2544-2551.

[7] Berred, M. (1995). k-record values and the extreme-value index. Journal of Statistical Planning and Inference, 45, 49 - 63.

[8] Di Crescenzo, A., Longobardi, M. (2002). Entropy-based measure of uncertainty in past lifetime distributions. Journal of Applied Probability, 39, 434-440.

[9] Di Crescenzo, A., Longobardi, M. (2004). A measure of discrimination between past lifetime distributions. Statistics and Probability Letters, 67, 173-182.

[10] Di Crescenzo, A., Longobardi, M. (2009). On cumulative entropies. Journal of Statistical Planning and Inference, 139 (12), 4072-4087.

[11] Dziubdziela, W., Kopocinski, B. (1976). Limiting properties of the k^{th} record values. Applications of Mathematics, 15, 187-190.

[12] Ebrahimi, N. (1996). How to measure uncertainty in the residual lifetime distributions. Sankhya A, 58, 48-57.

[13] Fashandi, M., Ahmadi, J. (2012). Characterizations of symmatric distributions based on Renyi entropy. Statistics and Probability Letters, 82, 798-804.

[14] Gupta, R. C., Kirmani, S. N. U. A. (2008). Characterizations based on conditional mean function. Journal of Statistical Planning and Inference, 138, 964-970.

[15] Kamps, U. (1995). A concept of generalized order statistics. B. G. Teubner, Stuttgart.

[16] Kumar, V., Taneja, H. C. and Srivastava, R. (2010). A dynamic measure of inaccuracy between two past lifetime distributions. Metrika, 74(1) 1-10.

[17] Kumar, V. (2015). Generalized entropy measure in record values and its applications. Statistics and Probability Letters, 106, 46-51.

[18] Kumar, V. (2017). On Renyi's information measure and k-record values. Journal of Information and Optimization Sciences, Accepted.

[19] Kundu, C. Nanda, A. K. and Maiti, S. S. (2010). Some distributional results through past entropy. Journal of Statistical Planning and Inference, 140(5), 1280-1291.

ACCEPTED MANUSCRIPT

[20] Madadi, M., Tata M. (2011). Shannon information in record data. Metrika, 74, 11-31.

[21] Nanda, A. K., Paul, P. (2006). Some properties of past entropy and their applications. Metrika, 64, 47-61.

[22] Razmkhah, M., Morabbi, H. and Ahmadi, J. (2012). Comparing two sampling schemes based on entropy of record statistics. Statistical Papers, 53, 95-106.

[23] Shannon, C. E. (1948). A mathematical theory of communication, Bell System Technical Journal, 27, 379-432.

[24] Su, J.C., Su, N.C. and Huang, W.J. (2008). Characterizations based on record values and order statistics. Journal of Statistical Planning and Inference, 138, 1358-1367.

[25] Sultan, K. S., Moshref, M. E. and Childs, A. (2002). Record values from generalized Power function distribution and associated inference. Journal of Applied Statistical Science, 11, 143-156.

[26] Zahedi, H., Shakil, M. (2006). Properties of entropies of record values in reliability and life testing context. Communications in Statistics - Theory and Methods, 35, 997-1010.

ACCEPTED MANUSCRIPT

emeraldinsight

Journal of Advances in Management Research

Moderating effects of age, income and internet usage on Online Brand Community (OBC)-induced purchase intention

Anurag Tiruwa, Rajan Yadav, Pradeep Kumar Suri,

Article information:

To cite this document:
Anurag Tiruwa, Rajan Yadav, Pradeep Kumar Suri, (2018) "Moderating effects of age, income and internet usage on Online Brand Community (OBC)-induced purchase intention", Journal of Advances in Management Research, https://doi.org/10.1108/JAMR-04-2017-0043
Permanent link to this document:
https://doi.org/10.1108/JAMR-04-2017-0043

Downloaded on: 20 March 2018, At: 21:51 (PT)
References: this document contains references to 128 other documents.
To copy this document: permissions@emeraldinsight.com
The fulltext of this document has been downloaded 19 times since 2018*
Access to this document was granted through an Emerald subscription provided by emerald-srm:544911 []

For Authors

If you would like to write for this, or any other Emerald publication, then please use our Emerald for Authors service information about how to choose which publication to write for and submission guidelines are available for all. Please visit www.emeraldinsight.com/authors for more information.

About Emerald www.emeraldinsight.com

Emerald is a global publisher linking research and practice to the benefit of society. The company manages a portfolio of more than 290 journals and over 2,350 books and book series volumes, as well as providing an extensive range of online products and additional customer resources and services.

Emerald is both COUNTER 4 and TRANSFER compliant. The organization is a partner of the Committee on Publication Ethics (COPE) and also works with Portico and the LOCKSS initiative for digital archive preservation.

*Related content and download information correct at time of download.

Downloaded by Delhi Technological University At 21:51 20 March 2018 (PT)

The current issue and full text archive of this journal is available on Emerald Insight at:
www.emeraldinsight.com/0972-7981.htm

Moderating effects of age, income and internet usage on Online Brand Community (OBC)-induced purchase intention

Anurag Tiruwa, Rajan Yadav and Pradeep Kumar Suri
Delhi Technological University, Delhi, India

Downloaded by Delhi Technological University At 21:51 20 March 2018 (PT)

Abstract

Purpose – The purpose of this paper is to understand the customer attitude and perception towards the online brand communities (OBCs) and purchase intention (PI). The paper also analyses the moderating effects of age, income and internet usage on the relationship among the proposed variables.

Design/methodology/approach – The study employed a multi-analytical approach through the use of structural equation modelling and neural networks to test the proposed framework. The information was obtained from 236 respondents using a web-based questionnaire survey. Further, moderation analysis, with age, annual family income and weekly internet usage as moderating variables, was conducted on the structural model.

Findings – The results of the analysis demonstrate that the multi-group moderating effect for different groups within age, income and internet usage have significant differences for the relationships between the independent variables content perception, perceived usefulness, critical mass, brand attachment and attitude towards brand and the dependent variable, PI.

Originality/value – The study is one of its kind to understand and analyse the role of moderating variables (age, income and internet usage) on OBC-induced PI.

Keywords Network analysis, Structural equation modelling, Technology adoption, Social network analysis, Brand pages, Online brand community

Paper type Research paper

1. Introduction

The new millennium has ushered an era of remarkable growth in internet technology platforms. Over the years, the internet has evolved from being simple web pages to a consortium of web-based applications, which has led to an increase in internet users. In 2005, there were over one billion global internet users; this number has grown to 3.7 billion in 2017 (statista.com, 2015; Internet World Stats, 2017). The rapid expansion in internet penetration has been supported significantly by the advancements in mobile technologies which have changed the way people communicate with each other. The pace with which smartphone becoming a necessity in the day-to-day life, the internet has become mobile with faster personalised social interactions (Wei and Lo, 2006; Hooi Ting *et al.*, 2011).

Web 2.0 has opened new vistas for sharing user-generated contents like blogs, wikis, online brand communities (OBCs), etc. Social media sharing sites and social networking sites (SNSs) like Facebook, YouTube, Twitter, Pinterest, etc., have become quite a hit among the worldwide population (Constantinides *et al.*, 2008). Three effects are prominently seen with the introduction of Web 2.0. First, the web has become a platform where a large number of activities are now centred (Berthon *et al.*, 2012). Second, value creation is now shifted from the marketers to the consumers (Kietzmann *et al.*, 2011; Hanna *et al.*, 2011; Araujo and Neijens, 2012; Berthon *et al.*, 2012; Rathore *et al.*, 2016). Third, consumer has more power than the marketers (Hanna *et al.*, 2011; Berthon *et al.*, 2012). The three effects of Web 2.0 had given the consumer a stronger stand when compared to earlier times when the consumer was more on receiving end and played a passive part in the marketing activities.

Journal of Advances in Management Research
© Emerald Publishing Limited
0972-7981
DOI 10.1108/JAMR-04-2017-0043

Downloaded by Delhi Technological University At 21:51 20 March 2018 (PT)

Social media has evolved as an important communication platform which has to be explored in depth by marketers and academicians to understand its dynamics and their implications (Kietzmann *et al.*, 2011). SNSs provide a plethora of opportunities to the user to create and share content as well as information by creating OBCs. With the rise in SNSs, the communication which was once controlled and initiated by the corporate has now been transferred to the customers who engage and create content on these sites (Kietzmann *et al.*, 2011, France *et al.*, 2015).

SNS-based OBCs are capable of two-way communication, helping marketers in communicating with their customers with frequent engagements (Thackeray *et al.*, 2008; Sashi, 2012; Tiruwa *et al.*, 2016). While discussing OBCs the term "engage" and "engagement" is used to describe the nature of the participation of the user with the community (Schau *et al.*, 2009; Brodie *et al.*, 2011). The SNSs and the internet tools enable and facilitate new and extended forms of interactive consumer experiences, which may contribute to the development of customer and/or consumer engagement with specific brands (Vivek *et al.*, 2012). By analysing this communication, marketers can identify the customer's perception and attitude towards the brand or its products, which can help them to develop appropriate interaction in brand management.

There is an abundance of literature which focusses on the customer's inclinations or intentions to join the SNSs and their attitude towards the engagements that happen on these online portals. The literature lacks on research works which connect the customer engagement through the SNSs and the influences that it has with the intention of the customer to purchase. This study focuses on the factors: content perception (CP), perceived usefulness (PU), critical mass (CM), brand attachment (BA) and attitude towards brand (ATB) that influence the customers and create the purchase intention (PI). Further, the effects of moderating variables – age, income and internet usage – were observed on the relationships between the dependent and the independent variables. In the academic literature, there are very few studies which explore the moderating effects of age, income and internet usage per week, in the area of online customer engagement and PI. The findings of this study could provide significant insights into the nature of OBCs' engagement and intention to purchase mechanism, and also help practitioners to formulate a suitable strategic framework to promote intention to purchase.

This study is organised into three sections. Section 2 consists of an overview of the literature and the proposed framework. Section 3 focusses on the detailed research methodology used in the study. Section 4 presents the data analysis and results. Section 5 presents findings and discussion, while Section 6 presents conclusion, managerial implications and the limitations of the study.

2. Literature review and conceptual framework

2.1 OBCs

For creating the close and interactive relationship utilising social media, internet technologies have developed into different platforms. These platforms have various properties and functions in the form of social media sites and SNSs which have become the origin of OBCs (Calder *et al.*, 2009; Brodie *et al.*, 2011; Wirtz *et al.*, 2013). The wikis blogs and forums were the early forms of such OBCs where the users discussed, exchanged information and opinions. With OBCs in the digital scene, they have attracted both marketers and customers towards them. While the users of OBC contribute within the community to generate and share content regarding a brand or its products, it is possible that they might become advocates for the brand and add value to it (Sashi, 2012; Jahn and Kunz, 2012; Yadav, 2015). Customers who become advocates, by virtue of their knowledge, are capable of influencing the decision made by users within the community; attitude being one such decision (Sashi, 2012).

Previous studies provide a structured understanding of social media, encompassing the related elements about both traditional and digital media. Critical insights, as well as lessons relating to integration strategies for successfully integrating social media in firms marketing communication, has also been discussed in these studies (Hanna *et al.*, 2011; Gamboa and Gonçalves, 2014). Marketers are trying to use and exploit the engagement aspect of these OBCs to build relationships with their customers. SNSs has attracted the attention of the marketers as well as academicians; and these tools and technologies which incorporate the contemporary internet have become a part of strategic planning to utilise the internet as a commercial platform (Constantinides *et al.*, 2008; Hanna *et al.*, 2011; Kietzmann *et al.*, 2011; Acker *et al.*, 2011; Berthon *et al.*, 2012; Shi *et al.*, 2016). Customers, being creator and multiplier of brand messages, have taken a more active position when it comes to a marketer-customer relationship (Sashi, 2012; Jahn and Kunz, 2012; Kaur *et al.*, 2016).

Marketers have to understand the different experiences that the customers have while engaging with an OBC so that they can relate and effectively employ advertising strategy implementation in the context of online media (Calder *et al.*, 2009; Baldus *et al.*, 2015). As discussed before, OBCs are the latest evolutionary step for the communities that supported marketing activities. Firms cannot ignore the development of OBCs as it is noted that customers tend to create their communities without involving the firms. The emergence of mobile technology has further made the creation of an OBC, and engagement with it, much easy. The low cost of creating an OBC and the penetration it has within the masses provides a strategic opportunity to the marketers to establish their brand, by developing a brand community. This brand community is pivotal in enlarging the brand identity that already exists with the masses (Wirtz *et al.*, 2013, Gao and Feng, 2016). Facebook has emerged as a platform which gives users a friendly environment with capabilities to interact, connects and shares information and media, and can be considered a reliable tool (Nie, 2001, Servia-Rodriguez *et al.*, 2013, Nguyen *et al.*, 2015).

Literature emphasises on two decisions that are critical to consider when using the social media brand community for customer engagement (Araujo and Neijens, 2012). The first decision question is if the brand is ready to make itself present in the social network sphere. The second decision reflects on the level and the extent to which a marketer or brand is willing to engage with the customer, i.e. the different methods of interactions, how they will communicate, the scope and the most important factor, the content and the value generated by the same. It has been noted that the brand pages have a significant influence on the customer-brand relationship and also has positive effects on brand fans, which affects their behaviour to participate as well as manage the OBCs (McAlexander *et al.*, 2002; Jahn and Kunz, 2012; Kang *et al.*, 2014).

2.2 Customer engagement

In last decade, the term "engagement" has been increasingly used in the marketing literature. The term has been addressed and defined in the literature (Patterson *et al.*, 2006; Bowden, 2009; Mollen and Wilson, 2010; Van Doorn *et al.*, 2010; Hollebeek, 2011; Vivek *et al.*, 2012). However, a working definition of engagement in context to OBCs is:

> Consumer engagement in a virtual brand community involves specific interactive experiences between consumers and the brand, and/or other members of the community. Consumer engagement is a context-dependent, psychological state characterized by fluctuating intensity levels that occur within dynamic, iterative engagement processes. Consumer engagement is a multidimensional concept comprising cognitive, emotional, and/or behavioural dimensions, and plays a central role in the process of relational exchange where other relational concepts are engagement antecedents and/or consequences in iterative engagement processes within the brand community (Brodie *et al.*, 2011).

Downloaded by Delhi Technological University At 21:51 20 March 2018 (PT)

A number of researchers have explored engagement in the field of customer relationship and retention. Few of them elaborated the engagement as the "expanded domain of relationship marketing," where the marketers focus on prospective customers along with the existing customers (Vargo and Lusch 2004, 2008; Prahalad and Ramaswamy, 2004a, b; Vivek *et al.*, 2012). They also have an interest in the customer communities, and the value co-created by the networks by/within these customers made communities. Literature suggests and conceptualises the perspective of "who engages with whom", elaborating on the subject, i.e. consumer/customer and the engagement object, brand product or organisation (Hollebeek, 2011). The engagement objective needs to have an interactive relationship with the customer, and requires the individuals to experience value from the brand interactions (Mollen and Wilson, 2010). For creating such a kind of close interaction with the social media, sophisticated information and communication technologies have been developed within the SNSs and the other internet platforms. It is important to understand how engagement is related to the effectiveness of connecting to the customer in the context of online media. To understand engagement, one needs to understand the different experiences that the customers have while browsing/connecting to the site (Calder *et al.*, 2009).

The contemporary internet and mobile technologies have provided a new platform where communities can be built at a low cost. Also, it helps in establishing a relationship between providers, customers and users who are unified by these OBCs. The interactivity which is promoted by these OBCs is mutually beneficial, as the brand gets to know customer's perception of the brand and its product and the customers gets to learn more about the brand by information issued by the brand or from the user-generated content (Wirtz *et al.*, 2013). Amazon India© elaborates as a good example of customer engagement on social media website (Facebook) and the benefits it holds. E-Commerce platform Amazon India© owns a Facebook brand page which currently has more than 60 million followers. This Facebook page provides important information regarding new products, upcoming sales, etc. They also share images and video from other Facebook pages which are linked to their products or any festive occasion for which Amazon India© is offering the sale of relevant products. These posts containing images, videos and information about sales or promotion of product are viewed by a large number of people and gets shared; thus, progressing the word of mouth about Amazon India©. This platform also acts as a customer grievances portal as most of the customers' comment on these posts are regarding some issue they have faced for the services provided by Amazon India©. All such comments get a reply from Amazon India© customer representative for further investigation. The replies are personal in nature and directly address the customer. Amazon India's© digital marketing strategy is beneficial in many ways, as they are able to connect to the customers, promote itself, take of the customer grievances and create a dialogue using the interactive nature of the Facebook page by the online engagement of customer through Facebook pages. Similar strategies can be made by other organisations based on their requirements thus making it easy for them to connect control and communicate with the customers.

2.3 Moderating variables: age, income and internet usage

Literature has considered the socioeconomic and demographic characteristics like age, income and internet usage of individuals to be key factors in the analysis of their behaviour towards the technology (Venkatesh and Morris, 2000; Venkatesh *et al.*, 2003). Age as one of these socioeconomic characteristics has been underlined by the traditional literature (Harrison and Rainer, 1992; Hubona and Kennick, 1996). It is suggested that the younger individuals are more receptive and have greater experience with the internet and aspects such as usefulness and attitude acquire greater importance for them. Previous studies have discussed the older users' lack of experience with the medium prevents them from evaluating the advantages that the internet offers in the context of shopping channel

Downloaded by Delhi Technological University At 21:51 20 March 2018 (PT)

(Trocchia and Janda, 2000). Some studies have included age as a relevant variable in the explanation of online shopping behaviour (Zhang, 2009). It has also been observed that age influences the initial decision regarding whether to purchase on the internet Thus, it might be a relevant moderating factor while observing the OBC-induced PI.

Income is another characteristic that has attracted considerable research attention in the field of technology acceptance (Serenko *et al.*, 2006; Allard *et al.*, 2009; Shin, 2009). Usually, income is reflected in terms of the professional status or social class of the individual – different professional categories are accompanied by different incomes. Studies on online purchase behaviours suggest that higher income causes users to perceive lower implicit risks in undertaking online purchases. However, low income might discourage the user for online purchases, due to possible financial losses that might occur if their decision backfires (Hernández *et al.*, 2011). This makes income to be an important factor which moderates the purchase intents and decisions of the customer.

It is noted that the frequent visits to online portals and brand communities have a significant effect on decisions made during the pre-purchase stage (Frambach *et al.*, 2007). Using these channels for gathering information and continual usage is a precursor to purchase intent. Therefore, internet usage is important while discussing online customer engagement and the duration for with a user engages itself with a brand or OBC might influence the perception and the attitude they hold for the brand. There is a dearth of literature in academic research, which focusses on the internet usage and its effects on PI, online or otherwise. Users who engage with the OBC more on a weekly basis, have more information and involvement with the brand; whereas, users with low internet usage may not be so involved with the brand. This considerable difference in internet usage acts as a moderating effect, and it might be an important factor to impact PI of the customer.

2.4 Conceptual framework

Using SNSs for marketing purposes is being adopted by firms and organisations, but there is much exploration which can be done to understand the marketing models. Previous studies on technology adoption model (TAM) and unified theory of acceptance and use of technology (UTAUT) have identified constructs to understand the adoption of various technologies in different context. In the backdrop of these themes, this study uses an integrated framework to understand the way such variables influence the PI and analyse how gender age and income moderate this effect. However, to understand and identify the influencing factors, it is necessary to seek contemporary variables apart from the traditionally suggested. This study identifies the constructs that are influential towards steering the behavioural intents of the customers engaged with the OBCs. Figure 1 shows the proposed framework.

2.5 Hypotheses development

2.5.1 CP. Marketers and brand are using social media to connect with their customers to create meaningful dialogue. For the purpose of this interaction, creating and managing the media content is an important task (Evans, 2012; Tuten and Solomon, 2013). Recent research works have studied and analysed the corporate Facebook pages to create and understanding regarding the different social media content and the response that it generates (McCorkindale, 2010; Cvijikj and Michahelles, 2011, 2013; De Vries *et al.*, 2012; Swani *et al.*, 2013). For OBCs and SNSs, it is important to have constant involvement when it comes to engaging customers. Most of the OBCs and SNSs have moderators to oversee the posting activity to engage customers. A higher level of customer engagement can be achieved if the content posted on the Facebook brand page provides relevant information related to the brand; also, the interactiveness of the content act as a motivator for customers to engage with the brand page (Pletikosa Cvijikj and Michahelles, 2013). The content and the

Downloaded by Delhi Technological University At 21:51 20 March 2018 (PT)

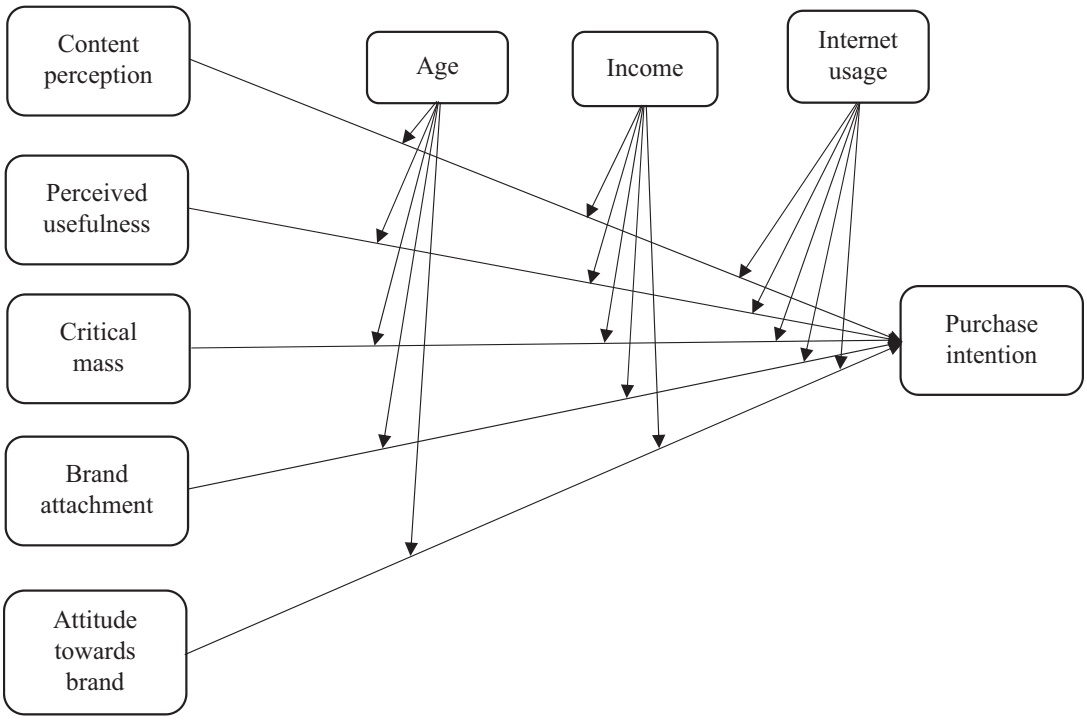


Figure 1.
Conceptual framework for the study

information create customers' perception about the brand and motivates him/her to move past the engagement stage to the intent stage for purchase or acquisition. This leads to the following hypothesis:

H1. CP has a significant influence on PI.

2.5.2 PU. PU has been defined as the extent to which a user finds a system/technology to be helpful in enhancing his/her job performance (Taylor and Todd, 1995; Davis, 1989). Social media is a dynamic web-based application which can readily be used for customer communications. This communication includes disseminating information to the masses about product or service, responding to the customer suggestions, queries and grievances (Mangold and Faulds, 2009; Kaplan and Haenlein, 2010; Kozinets *et al.*, 2010; Kumar and Bhagwat, 2010; Larson and Watson, 2011). Previous studies and models like TRA (Fishbein and Ajzen, 1975) and TPB (Ajzen, 1985) suggest that the PU leads to behavioural intentions and recent studies also support that PU of the social media has an effect on offline behavioural intentions (Paris *et al.*, 2010). This leads to the following hypothesis:

H2. Perceived usefulness has a significant influence on PI.

2.5.3 CM. Previous studies suggest that CM is a major factor in determining the adoption of technology by users (Glass and Li, 2010; Lou *et al.*, 2000; Cheng *et al.*, 2012). CM is defined as a close-knit network of the user with whom the user engages on SNSs and for whom the user access these SNSs (Sweeney *et al.*, 2008; Chu and Kim, 2011; Rauniar *et al.*, 2012; Coulter and Roggeveen, 2012). Regarding social media, it is the number of people that matter the most in a user's social network. Since, OBCs involve sharing of information, from which a large part is that of user-generated content, users often rely on the suggestions and opinions given to them by their peer network on the SNSs. Most of the time they try to adhere to the expectations of the CM and to acquire, purchase and use products or services that CM views as acceptable (Madan and Yadav, 2016). The users want to seek approval from the peers and the CM influence their decision making or influencing their behavioural intentions.

Downloaded by Delhi Technological University At 21:51 20 March 2018 (PT)

Therefore, CM is an important factor, and it should be considered since the study focusses on behavioural intentions, and in this case the intention to purchase (Hsu and Lu, 2004; Yu *et al.*, 2005; Cheng *et al.*, 2012). This leads to the following hypothesis:

H3. CM has a significant influence on PI.

2.5.4 BA. In the last couple of years, the BA has emerged as a new concept that plays a major role in identifying and understanding the factors or variables that affect the relationship between the customer and the brand (Louis and Lombart, 2010; Belaid and Temessek Behi, 2011). BA has been found to be a multi-faceted subject, with definitions varying with the varying perspective of the studies. Attachment theory provides a simpler definition which suggests BA be an emotional bond or link between an individual and a brand (Thomson *et al.*, 2005; Didier and Lombart, 2010). This emotional link supports the individual's capacity to identify oneself with the brand and establishes a close relationship between the individual and the brand. Literature suggests that bond and connection a customer feels with the brand strongly predicts the past and future purchase behaviour (McAlexander *et al.*, 2003; Thomson *et al.*, 2005; Esch *et al.*, 2006; Assiouras *et al.*, 2015). Therefore, suggesting that BA is a strong determinant of both current purchase behaviour and future intentions to purchase. This leads to the following hypothesis:

H4. BA has a significant influence on PI.

2.5.5 ATB. Customer's attitude has always been linked to behavioural intention, where an individual's attitude has a positive influence on his/her behavioural intents (Ajzen and Fishbein, 1980). Literature further states that when brands are involved, the attitude of individuals towards a brand can lead to behavioural intention, dictating the customer to buy it or not. Previous studies and models show that customers' attitude towards a brand directly affects the intention to purchase (Ajzen and Fishbein, 2005; Jin and Suh, 2005; Leonidou *et al.*, 2010; Limbu *et al.*, 2012; Punyatoya, 2015; Tiruwa *et al.*, 2016). This leads to following hypothesis:

H5. ATB has a significant influence on PI.

2.5.6 Moderating variables. Apart from identifying the important factors that may affect the PI, this study observed the effects of moderating variables on the relationship proposed in previous sections. For the purpose of this study, moderating effects of age, income and internet usage has been taken into consideration and analysis is done to find out whether these variables affect the relationships among the independent and dependent variables.

Age. Previous studies have observed and suggested that age is an important demographical variable, which has a significant effect on the behavioural intentions (PI in the context of this study) (Harrison and Rainer, 1992; Hubona and Kennick, 1996; Venkatesh *et al.*, 2003; Porter and Donthu, 2006; King and He, 2006; Wang *et al.*, 2009; Chung *et al.*, 2010). It is also observed that the inclusion of age as a moderator has helped in incrementing the explanatory power of classic technology acceptance models (Venkatesh *et al.*, 2003; Chung *et al.*, 2010). Some studies have considered age to be a relevant variable to affect the shopping behaviours of the customers (Zhang, 2009). Hence, it is hypothesized that:

H6. The influence of independent variables (CP, PU, CM, BA, ATB) towards PI is moderated by age.

Income. Income is another variable that has been given attention in previous studies (Serenko *et al.*, 2006; Allard *et al.*, 2009; Shin, 2009, Hernández *et al.*, 2011). Even though the results from the previous studies have been contradictory, they do support that income acts as an explanatory variable to shopping behaviour (Miyazaki and Fernández, 2001; Raijas and Tuunainen, 2001; Lu *et al.*, 2003; Al-Somali *et al.*, 2009). It has been noted that

Downloaded by Delhi Technological University At 21:51 20 March 2018 (PT)

different income groups hold different perceptions and exhibit different user behaviours (Hubona and Kennick, 1996; Chau and Hu, 2002). Hence, it is hypothesized that:

H7. The influence of independent variables (CP, PU, CM, BA, ATB) towards PI is moderated by income.

Internet usage. The amount of time an individual spends on browsing through the internet leads to a higher engagement; therefore, is pivotal in creating an intent to purchase. The literature suggests internet usage as an important factor for varying fields and research works, but there is a dearth of literature where internet usage is seen as a moderating factor to relations affecting the PI. This study explores internet usage as a moderating variable and its influence on PI. Hence, it is hypothesized that:

H8. The influence of independent variables (CP, PU, CM, BA, ATB) towards PI is moderated by internet usage per week.

Downloaded by Delhi Technological University At 21:51 20 March 2018 (PT)

3. Research methodology

3.1 Participants

The survey is based on the primary data collected from the postgraduate students of the two state universities located in national capital – Delhi. As the national capital of India, Delhi has a huge inflow of students for various postgraduate programmes, from all parts of India. Therefore, this region is considered a good representation of the population under study. Table I summarises the demographic profile of the respondents.

Among the 236 respondents, 136 (57.6 per cent) are men and 100 (42.2 per cent) women. The majority or respondents were under the age of 25 years, accounting for 52.5 per cent of the total sample, followed by the respondents aged 26-30 years (37.7 per cent) and those aged 31-35 years and older (8.5 per cent). Regarding the respondents' highest educational level, 36.4 per cent of the respondents had a postgraduate degree, and 36.4 per cent were undergraduate students. In total, 104 (44.1 per cent) respondents cited their occupation as a student, followed by 96 (40.7 per cent) government and private sector employees combined.

3.2 Construct measurement

The scales were adapted from previous studies discussed in the literature review, which showed satisfactory internal reliability and convergent validity. Out of six constructs, five are independent, and one is dependent. Collectively, 15 items were used to measure the predictors, and 3 were used to measure the intention to purchase. A seven-point Likert scale was used: 1 suggesting (strongly disagree) and 7 suggesting (strongly agree). The construct reliability (Cronbach's α) of the questionnaire is above the recommended value of 0.7 (Hair *et al.*, 2010). Table II shows the value of Cronbach's α for each construct.

3.3 Research instrument

Given the nature of the study, online survey method was used, and it was helpful in providing a wider coverage along with helping with the problem of incomplete form submission. A pilot study was conducted on a sample of 30 respondents, selected through non-probabilistic sampling for the purpose of testing the reliability of the questionnaire. These respondents were those people who were active on the SNS – Facebook. The survey instrument was modified and redesigned with minor amendments based on the feedback obtained during the pilot testing phase. The data collected for the purpose of pilot study were not included in the main analysis. The survey was also conducted offline for the purpose of understanding the true feeling and the nature of their perception towards the questionnaire.

Characteristics	Frequency	Percentage
Gender		
Female	100	42.4
Male	136	57.6
Age		
Below 20	3	1.3
21-25	124	52.5
26-30	89	37.7
31-35	6	2.5
36-40	7	3
Above 40	7	3
Annual family income		
Below 5,00,000	46	19.5
5,00,000-7,50,000	67	28.4
7,50,000-10,00,000	56	23.7
Above 10,00,000	67	28.4
Education		
Up to 12th	6	2.5
Graduation or equivalent	86	36.4
Post-graduation or equivalent	142	60.2
Others	2	0.8
Occupation		
Student	104	44.1
Govt./private sector employee	96	40.7
Self-employed professional	15	6.4
Entrepreneur/trader	3	1.3
Other	18	7.6
Internet usage		
Less than 5 hours/week	121	51.3
About 10 hours/week	61	25.8
About 15 hours/week	25	10.6
More than 15 hours/week	29	12.3

Table I.
Demographic details

Downloaded by Delhi Technological University At 21:51 20 March 2018 (PT)

3.4 Data collection and sampling

The online survey was sent to the respondents as a link through message delivery service provided by Facebook. This method was found to be convenient, as the respondents were already using Facebook and expected to have knowledge of Facebook brand pages. The online survey was administered in such a manner that it addressed the problems of incomplete survey forms.

The main survey consisted of six constructs comprised of 18 items and was administered to a sample of 272 respondents belonging to the Delhi and National Capital Region. Due to the absence of a sampling frame, a non-random sampling technique was employed. The online survey link was opened from March to April 2016, for a window of 30 days. From the 272 responses collected, 26 were rejected due to the biased responses; thus, concluding with a response rate of 86.8 per cent. The sample size of 236 was considered fit for the study, which is above the recommended value for a SEM model (Hair *et al.*, 2010).

4. Data analysis and results

A multi-analytical approach using structural equation modelling-neural network (SEM-NN) was followed for analysing the data collected from the 236 respondents. SEM is utilised for

Downloaded by Delhi Technological University At 21:51 20 March 2018 (PT)

Table II.
Reliability and factor analysis results

S. No.	Name of dimension	Factor loadings[a]						Cronbach α[b]	KMO[c]
D1	*Content perception*							0.865	0.730
1	Posts/Images/videos posted on the Facebook brand page are exciting	0.766							
2	Posts/images/videos posted on the Facebook brand page are refreshing.	0.862							
3	Content of the post/images/videos posted on the Facebook brand page gives adequate information about the existing product/brand	0.849							
D2	*Perceived usefulness*							0.891	0.711
4	Facebook brand page is useful in my daily life		0.737						
5	Facebook brand page enables me to get connected and stay in touch with brand		0.942						
6	Facebook brand page makes it easier for me to stay informed about the brand and its product		0.891						
D3	*Critical mass*							0.877	0.742
7	Facebook brand page is popular among my family and friends			0.836					
8	Most of the people who are important for me are engaged with this Facebook brand page			0.863					
9	Most of the people who are important for me would appreciate if I would engage with this Facebook brand page			0.818					
D4	*Attachment with brand*							0.866	0.721
10	I have lot of affection for this brand				0.747				
11	I am attracted to this brand				0.899				
12	Thinking about this brand brings a lot of joy, pleasure				0.836				
D5	*Attitude towards brand*							0.908	0.744
13	Bad ……. Good					0.848			
14	Unfavourable …….. Favourable					0.933			
15	Unlikable ……. Likable					0.849			
D6	*Purchase intention*							0.894	0.746
16	I will definitely purchase product in the future, belonging to brand associated with the Facebook brand page						0.842		
17	I will continue to buy the products of the brand in future belonging to brand associated with the Facebook brand page						0.898		
18	I will refer the products of the brand, associated with the Facebook brand page to my friends/ family/colleagues						0.839		

Notes: [a]Factor loadings greater than 0.5 is acceptable (Hair *et al.* 1995); [b]α values of 70 per cent or higher are considered acceptable (Nunnally, 1978); [c]KMO static values above 0.6 are acceptable (Tabachnick and Fidell, 2001)

the validation of a proposed theory, and it is a covariance-based analytical technique, which only detects the linear relationships. Use of SEM might lead to simplification of probable complexities of PIs. Therefore, to deal with this shortcoming, an integrated approach using both SEM and NN was employed since NN is capable of assessing both linear and non-linear relationship. NN is also capable of performing predictions which are more accurate when compared to the traditional regression techniques (Morris *et al.*, 2004). Despite the fact that NN can detect both linear and non-linear relations, it is not suitable for theory testing because of its "black-box" operation (Hew *et al.*, 2016). Examination of the model becomes difficult for the researchers, as this "black-box" operation does not allow them to understand how NN arrive at the results (Garson, 1998). Thus, a multi-analytical approach for data analysis was used to seek the benefits offered by both SEM and NN to examine the proposed model and the hypotheses. Following subsections discuss the results obtained from the analysis of the data.

4.1 Testing the assumptions of multivariate analysis

There are several assumptions that are to be satisfied to perform SEM (Hair *et al.*, 2010). These assumptions include normality, multicollinearity, linearity, adequate sample size, the absence of outliers, construct reliability and convergent and discriminant validity. This study considered a sample size of 236 respondents which exceeds the threshold of 200 required to implement SEM. Analysis for skewness and kurtosis showed that normality was achieved through skewness $< \pm 0.56$ and kurtosis $< \pm 0.55$, which is well under the criteria (skewness $< \pm 3$ and kurtosis $< \pm 10$) (Hair *et al.*, 2010). Table III depicts the results of the same. Homoscedasticity was verified by the scatter plot of standard predicted and residual values as shown in Figure 2. Matrix scatter plot was used to prove the linearity between the dependent and the independent variables; Figure 3 illustrates the output for the same. Multicollinearity was examined through the collinearity statistic, variance inflation factor (VIF) using regression analysis. All the factors had VIF < 3, i.e. well under the stipulated value along with the tolerance values greater than 0.1 as shows in Table IV (Hair *et al.*, 2010). From the initial 272 respondents 7 were rejected as outliers based on the Mahalanobis distance ($d2 > 22.74$, $\mathrm{df} = 3$, $p = 0.001$). Therefore, there were no violations of the basic assumptions of a multivariate model.

4.2 Exploratory factor analysis

Kaiser-Meyer-Olkin (KMO) was used to measure the appropriateness of EFA along with Bartlett's test of sphericity to confirm the adequacy of sample size. KMO values greater than 0.6 are considered adequate for the analysis (Tabachnick and Fidell, 2001). Factor analysis extracted six factors distinctly, and the output from the same is reported in Table II along with the values for respective factor loadings for the constructs.

	Valid	Missing	Mean	SD	Skewness	SE of skewness	Kurtosis	SE of kurtosis	Minimum	Maximum
CP	236	0	4.28	0.078	−0.205	0.158	−0.555	0.316	1	7
PU	236	0	4.33	0.091	−0.371	0.158	−0.531	0.316	1	7
CM	236	0	5.06	0.083	−0.551	0.158	−0.12	0.316	1	7
AWB	236	0	4.13	0.082	−0.147	0.158	−0.547	0.316	1	7
ATB	236	0	4.17	0.086	−0.373	0.158	−0.555	0.316	1	7
PI	236	0	4.69	0.085	−0.563	0.158	−0.285	0.316	1	7

Table III. Skewness and kurtosis statistics

Downloaded by Delhi Technological University At 21:51 20 March 2018 (PT)

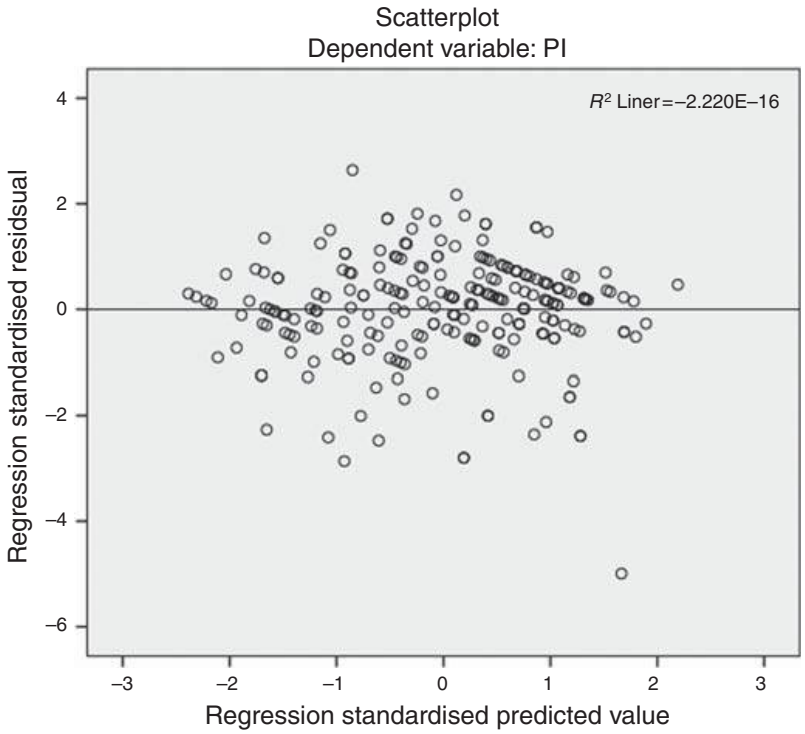


Figure 2.
Homoscedasticity

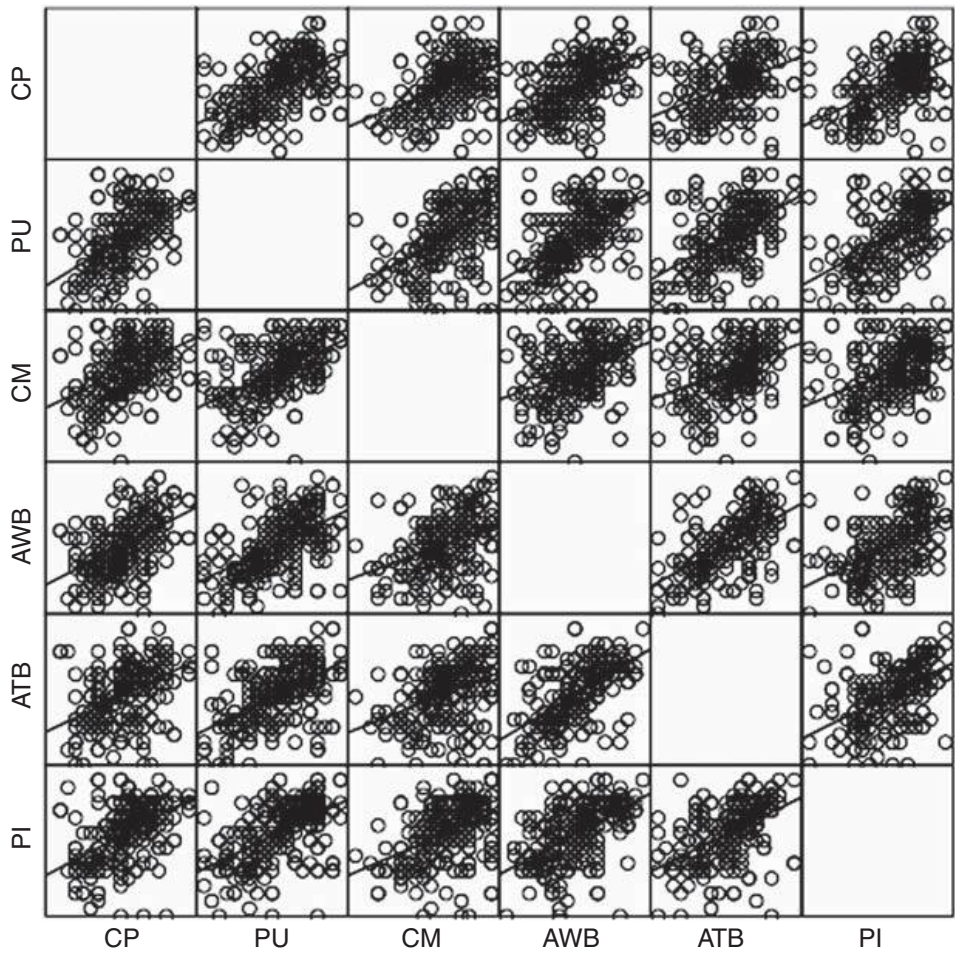


Figure 3.
Matrix scatter plot

Downloaded by Delhi Technological University At 21:51 20 March 2018 (PT)

Downloaded by Delhi Technological University At 21:51 20 March 2018 (PT)

4.3 Confirmatory factor analysis

Composite reliability (CR) along with average variance extracted (AVE) were also calculated to measure the convergent validity. The literature suggests that to confirm the convergent validity (correlation among the items within a factor), $CR > 0.70$, $AVE > 0.50$, where $CR > AVE$ (Hair *et al.*, 2010; Liébana-Cabanillas *et al.*, 2014; Mohamed *et al.*, 2014; Xu *et al.*, 2014). The values obtained after the calculations were found to be well within the acceptable ranges which are represented in Table V.

Discriminant validity was measured by calculating the values for AVE, maximum shared squared variance (MSV) and average shared squared variance (ASV). The values for MSV, ASV and AVE were well within the acceptable ranges as suggested by the literature, i.e. $MSV > AVE$ and $ASV > AVE$ (Hair *et al.*, 2010; Wong *et al.*, 2014; Zhou, 2014). Table V represents the values for MSV, ASV and AVE demonstrating discriminant validity, as the items do not correlate highly with each other.

4.4 Measurement and structural results

Measurement model was assessed first followed by the examination of hypotheses using the structural model. For measurement model, six indices for the goodness-of-fit were chosen as recommended by previous studies i.e. χ^2/df ($\leqslant 3.00$), goodness-of-fit index (GFI $\geqslant 0.90$), normed fit index (NFI $\geqslant 0.90$), Tucker-Lewis index (TLI $\geqslant 0.90$), comparative fit index (CFI $\geqslant 0.90$) and root mean square error of approximation (RMSEA $\leqslant 0.08$) (Arbuckle and Wothke, 1999; Browne and Cudeck, 1993; Hair *et al.*, 2010, Leong *et al.*, 2011). These indices were found to be within the acceptable ranges and are represented in Table VI, indicating that the measurement model is well fitted to the data collected. Measurement model was further tested for common method bias (CMB) using a common latent factor. CMB was calculated to be having a value of 14 per cent; thus, showing that there was no significant CMB present in the study (Podsakoff *et al.*, 2003).

The structural model analysis was conducted without any changes in the items within the proposed constructs. The analysis tested the five proposed hypotheses, and the results showed

Model	Unstandardised coefficients		Standardized coefficients			Collinearity statistics	
	B	SE	*β*	*t*	Sig.	Tolerance	VIF
(Constant)	1.037	0.316		3.276	0.001		
CP	0.187	0.07	0.173	2.687	0.008	0.618	1.619
PU	0.151	0.065	0.161	2.305	0.022	0.526	1.902
CM	0.125	0.063	0.122	1.993	0.047	0.692	1.446
AWB	0.204	0.07	0.197	2.903	0.004	0.561	1.781
ATB	0.174	0.066	0.176	2.661	0.008	0.589	1.698

Table IV. Coefficients

	CR	AVE	MSV	ASV	ATB	CP	PU	CM	AWB	PI
ATB	0.910	0.770	0.412	0.297	0.878					
CP	0.866	0.684	0.373	0.301	0.500	0.827				
PU	0.895	0.741	0.373	0.341	0.574	0.611	0.861			
CM	0.877	0.703	0.347	0.237	0.430	0.496	0.589	0.839		
AWB	0.869	0.689	0.412	0.316	0.642	0.579	0.571	0.421	0.830	
PI	0.895	0.740	0.329	0.300	0.555	0.549	0.574	0.479	0.574	0.860

Notes: CR, composite reliability; AVE, average variance extracted; MSV, maximum shared squared variance; ASV, average shared squared variance

Table V. Reliability and validity of constructs

that two out the five hypotheses, i.e. *H4* and *H5* were supported by data at $p < 0.001$ significance level. Three proposed hypotheses out of five, i.e. *H1*, *H2* and *H3* were supported by data at the significance level of $p < 0.05$. Table VII shows the different p-values of the different constructs.

4.5 NN results

This study employed the NN capabilities of IBM SPSS v.22 for building NN model. For NN model training, Multilayer perceptron training algorithm was used. The NN model was tested by incrementing the number of nodes from one to ten in the hidden layer, using the hyperbolic activation function (Wang and Elhag, 2008; Chong, 2013; Yadav *et al.*, 2016). While cross-validation is applied to only those variables that have been deemed significant by SEM analysis, i.e. CP, ATB, PU, ATB and CM. Since SEM analysis suggested all the variables to be significant, therefore all the five variables are taken as the independent variables for the input layer. PI being the dependent variable was contained in the output layer. The complexity of NN model was incremented by use of ten nodes in the hidden layer, starting from 1. Incremental nodes in hidden nodes check that no additional error incurs to the model.

In total, 90 per cent of the data were used to train the NN model and rest of the 10 per cent was used to measure the predicting accuracy of the network, as tenfold cross-validation. The tenfold cross-validations used in the study overcome the problem of over-fitting of the NN model which arises due to a large number of hidden neurons. By taking the incrementing number of neurons in the hidden layers, the model is able to generalise the training examples and not simply memorise them. The results of the validation of the training and testing models are represented as a root means square error (RMSE) in Table VIII; with 0.4865 and 0.4965 being the average cross-validated RMSE for training and testing, respectively. The RMSE values for the testing and training models for each NN model show low variations, therefore it can be concluded from the results that the model is robust and shows consistency throughout.

For sensitivity analysis, the average importance of the input variables was calculated for all the ten networks. Sensitive analysis is represented in Table IX. CP about the Facebook brand page was found to be the most significant predictor of PI, followed by the ATB, PU, attachment with the brand and CM.

4.6 Moderating effects

Once the proposed model was tested and the hypotheses validated by both SEM and NN, the effects of the moderating variables on the relationship between the independent

χ^2/df	GFI	NFI	TLI	CFI	RMSEA
1.776	0.913	0.932	0.960	0.969	0.057

Table VI. Model fit indices

Notes: GFI, goodness-of-fit index; NFI, normed fit index; TLI, Tucker-Lewis index; CFI, comparative fit index; RMSEA, root mean square error of approximation

Hypotheses	Estimate	SE	CR	p-values	Remarks
H1	0.218	0.070	3.105	0.002	Supported
H2	0.209	0.064	3.261	0.001	Supported
H3	0.145	0.059	2.477	0.013	Supported
H4	0.255	0.071	3.609	***	Supported
H5	0.215	0.059	3.630	***	Supported

Table VII. Structural results

Note: ***Significant at $p < 0.05$

Downloaded by Delhi Technological University At 21:51 20 March 2018 (PT)

Network	Training	Testing
ANN1	0.603	0.429
ANN2	0.602	0.425
ANN3	0.558	0.418
ANN4	0.455	0.497
ANN5	0.488	0.58
ANN6	0.390	0.603
ANN7	0.447	0.526
ANN8	0.541	0.455
ANN9	0.387	0.501
ANN10	0.394	0.531
Mean	0.4865	0.4965
SD	0.080819861	0.061602354

Table VIII. Results of neural network model

Constructs	Relative importance
Content perception	0.225
Perceived usefulness	0.217
Critical mass	0.146
Attachment with brand	0.193
Attitude towards brand	0.220

Table IX. Sensitivity analysis

constructs (CP, PU, CM, BA, ATB) and the dependent constructs (PI) were also analysed. This study utilised the multi-group analysis capabilities of the SEM technique to investigate the moderating effects of age, income and internet usage on the relations between the dependent and the independent variables. The data sample was divided into smaller sub-groups (such as age sub-group, income sub-group and internet usage per week sub-group), followed by the structural model being run for each sub-group. The pairwise comparison of path coefficients across sub-groups considering the critical ratios for the differences among the groups for establishing reliability and validity. Table IX represents the results of the multi-group analysis, with the moderating effects of the variables that hold for the relations established in the SEM analysis.

4.6.1 Age. The sample was divided into two age groups, one being respondent with age less than 25 years and other belonging to an age greater than 25 years. The results show that the age moderates two of the relationships out of the five, i.e. there is a significant difference between the relations existing between PU and ATB with PI ($z = 1.893$* and $z = -2.693$***, significant at $p < 0.1$ and $p < 0.05$ shown in Table X) suggesting moderating effects of different age groups.

4.6.2 Income. After evaluating the demographic data collected from the survey, the respondents were divided into two groups based on annual family income per annum. One group comprised of respondents that have a family income less than INR700,000 pa, and the other where the family income was greater than INR700,000 pa. The results of the analysis indicated that the relations existing between CP, PU and PI has a significant difference ($z = -1.65$* and $z = -2.88$***, significant at $p < 0.1$ and $p < 0.05$ shown in Table X) between them suggesting moderating effects of Income.

4.6.3 Internet usage. By usage, the respondents were put in two different groups. One where the respondents use internet for less than ten hours in a week and the other, where the respondents use internet for more than ten hours in a week. The results showed that there is

Downloaded by Delhi Technological University At 21:51 20 March 2018 (PT)

	Estimate	*p*	Estimate	*p*	*z*-score	Results
Age	< 25 years		> 25 years			
CP → PI	0.202	0.057	0.338	***	0.953	Not supported
PU → PI	0.032	0.726	0.273	0.002	1.893*	Supported
CM → PI	0.082	0.371	0.165	0.023	0.713	Not supported
AWB → PI	0.034	0.727	0.213	0.012	1.385	Not supported
ATB → PI	0.581	***	0.208	0.004	−2.693***	Supported
Family Income	< INR700,000 pa		> INR700,000 pa			
CP → PI	0.186	***	0.428	0.031	−1.65*	Supported
PU → PI	0.256	***	−0.166	0.19	−2.88***	Supported
CM → PI	0.131	0.108	0.244	0.002	0.985	Not supported
AWB → PI	0.292	***	0.076	0.49	−1.532	Not supported
ATB → PI	0.183	0.011	0.274	0.005	0.751	Not supported
Internet usage	< 10 hours/week		> 10 hours/week			
CP → PI	0.011	0.887	0.487	***	3.293***	Supported
PU → PI	0.295	***	0.071	0.427	−1.826*	Supported
CM → PI	0.128	0.051	0.166	0.102	0.308	Not supported
AWB → PI	0.421	***	0.091	0.348	−2.397**	Supported
ATB → PI	0.16	0.02	0.291	0.003	1.11	Not supported

Notes: *$p < 0.10$; **$p < 0.05$; ***$p < 0.01$
Source: Tarhini *et al.* (2014)

Table X.
Moderating effect of individual differences

a significant difference between the relations existing between CU, PU and BA and PI ($z = 3.2.93$***, $z = -1.826$* and $z = -2.397$**, significant at $p < 0.1$, $p < 0.05$ and $p < 0.001$ shown in Table X) suggesting the moderating effects of different internet usage per week.

5. Findings and discussion

In recent years, the importance of digital media and its use as a channel to establish a dialogue with the customers has become apparent to the marketers and brands. SNSs and their increasing influence on people, especially of the younger generation are supported by previous studies. The OBCs that have evolved within these SNSs has become a phenomenon in the recent past. Previous studies focussed on the importance and need of integrating OBCs in business, along with the benefits they provided; such as understanding the behavioural intention of the customers, their inclination towards the brand and their attitudes. Now, marketers include the digital platforms for interaction and communication into their business strategies, and it has become a vital part of marketing, customer engagement and relations. They have understood the vital benefits that these OBCs offered and the normative and subjective information that can be collected from the interactions among the peers, within the group as well as the interaction between the marketer and the customers and vice versa. Due to the widespread popularity of the SNS – Facebook, the study was focussed on the online brand pages present on Facebook. It tries to establish a relation between using and engaging with the Facebook page that has been created by the brand and the intention to purchase the brand in future.

Previous studies were focussed on the acceptance of SNSs and OBCs as a medium of communication by the customers, and there are models likes TAM, TAM2 and UTAUT that encompass and touch significant factors that were pivotal in engagement and thus influencing the behavioural intentions. This study focussed on the factors that might play a major role for a marketer or a brand to create a stronger influence on the customers for creating a behavioural intent towards purchasing. This study presents the causal relationships that exist between the independent factors CP, PU, CM, attachment with the brand, attitude towards the brand, with the dependent factor PI.

Downloaded by Delhi Technological University At 21:51 20 March 2018 (PT)

The structural results obtained from the SEM implementation of the proposed model and the cross-validation through neural networks, CP was the most important factor that influences the purchasing intention of the customers engaged with the brand page. When it comes to engagement through the different internet tools such as blogs and OBCs, the quality and essence of the content put forward to the customers on the OBCs is a must. The prime objective of OBCs is the exchange of information among and between the peers and marketer. This information can be in the form of text, audio or video and thus it is important for marketers/brands to keep this informative media to host high-quality content. If the content posted on an OBC is of less relevance and contains media which focusses on lesser number of customers connected to the OBC, then the level of engagement between the customers, and the marketers will diminish as time proceeds. Similarly, the OBCs are to be moderated carefully to keep the user-generated content relevant, informative and useful for other users. The majority of the posts on a OBC are related to the products or services offered by the marketer or the brand. Therefore, the information helps the customers in decision making and the supporting media in the form of informational audio or videos further engages the customer in creating a positive intent towards purchase.

ATB was found to be the second most important factor to influence the PI. Customers tend to develop an attitude towards the brand they either use or admire. This attitude can be either positive or negative based on the perceptions and experiences of the customer with that brand. Most of the times, the attitude towards the brand is developed based on the brand images and the brand influence due to the marketing and promotions conducted by the said brand. The OBCs help in developing customers' attitude towards any brand by virtue of relevant, informative posts. The promotional information and the user-generated content (which is a part of word-of-mouth communication) help in building a positive attitude; thus, helping marketers in using OBCs for positive brand image building. The customers' intent to purchase or the decision to purchase is affected by the attitude that they hold towards the brand.

This study also observed PU be an important factor which influences PI. The usefulness of a OBC can mean different for different users. For some, it might be the informational capabilities; for others, it might be the enjoyment of engaging with the official brand page. In a broad way, the usefulness of the OBC, as perceived by customers, is that of the source of information which is useful. Brands nowadays are using OBCs to posts that are relevant and hold some significant importance for the customers. The content, therefore, has to be vivid and informative to keep the customers engaged with the OBC and for them to return again and again to the brand page.

Furthermore, BA and CM were also found to have a significant influence on the PI of the customers. Customers that are regular users/purchasers of a brand tend to have affinity or attachment towards the brand which affects their decision to purchase to a great extent. CM also has a significant effect on the PI. A customer is influenced by the social circle that surrounds him/her and with whom he/she interacts on a regular basis. OBCs are mostly joined by users when they find their peers in the same community, or they are referred to the said OBC by someone belonging to the CM. Since the OBCs are built on a social networking platform, therefore the effects of the CM come into play while considering its effect on the behavioural intents.

Apart from hypotheses testing and finding the relevant factors that affect PI, this study also focussed on analysing the moderating effects of age, annual family income and the internet usage per week to see how they affected the results obtained from the SEM analysis. Age showed significance difference for two relations, i.e. ATB and PU on PI. The fact, that the younger generation is more attuned to the current trends and the brand that are emerging. They are more technologically active as compared to the older age group, which might be the major reasons for the lower age group (< 25) to show more significant

Downloaded by Delhi Technological University At 21:51 20 March 2018 (PT)

relation as compared to the older age group (> 25) for ATB and PI. The younger age group has a tendency to have wider perceptions and thus, they hold a certain ATBs. They tend to incline more towards different brands that are very popular and visible in the cyber-sphere. The older age group mostly consists of working people who have become attached to particular brand depending on their needs and necessities. They do have attitudes towards their desired brands, but they are more judgmental based on the quality, services and other attributes of the different brand present in the market. Contrary to ATB, for PU and PI, older age group showed a more significant relation with PI. The respondents belonging to this group are more experienced compared to the younger age group, and they tend to seek information before making a purchase. If they find the OBC to divulge useful and detailed information about the products and services of the brands, this usefulness might play a role in their decision making in a positive manner; whereas the respondents belonging to the younger group tends to overlook the details, and the usefulness of the OBC plays a lesser role in their purchase decisions.

Annual income of the family also showed a significant difference between two relations, i.e. PU and CP on PI. The respondents from lower income group (< INR700,000 pa) showed more significant relation than higher income group (> INR700,000 pa) for PU and PI. The respondents from lower income group are more sensitive to price, and therefore, they tend to seek more details and information about the product, which they get from the information obtained by engagements and interactions on the OBCs. Thus, the usefulness that these respondents see in the OBCs becomes essential for their decisions to purchase. The higher income group, on the other hand, does not care much about the details as they have the purchasing power and are more interested in the product rather than the details. This predicament might be supported by the fact they are a staunch supporter of the brand they purchase and trust the brand for its quality and service. For CP and PI, the lower income group showed a more significant relation. Since they have less purchasing power, they might be inclined to a higher quality of content in the form the text, audio or video to get more information about the product or service; whereas, the higher income group focusses more on the brand image and value, and might not consider the content posted by users or brand on the OBCs.

Internet usage per week was another moderating factor, whose effects were observed in this study, which showed significant differences for three relations, i.e. CP, BA and PU on PI. The respondents belonging to the higher usage group (> ten hours/week) showed a more significant relation than the respondents from lower usage group (< ten hours/week) for CP and PI. Previous studies have reported that when an individual spends a large amount of time on the internet, they may be presented with too much information or content exceeding his/her processing capabilities, and information overload occurs (Karr-Wisniewski and Lu, 2010). However, the findings of the study say otherwise since customers who are more active online are familiar with the concepts of OBCs. Therefore, they focus more on the content published by these OBCs to seek more information and also base their decision on the quality of user-generated content on such OBCs as well; therefore, influencing their intent to purchase. Since the respondents from lower usage group are not that active online, they might not be affected by CP as compared to the respondents from higher usage group. For BA and PI, the lower usage group showed more significant relation as compared to the higher usage group. The lower usage group might be more active in physically browsing through the brand products in shops and stores instead of searching for information for the same online. This close encounter with the product might lead to more affinity and attachment to the brand. The higher usage group, on the other hand, uses the internet to find information and judges the brand based on the information and opinions found online on different community platforms, therefore lesser influence on their purchase decisions by BA. For lower usage group, OBCs are the source of useful and relevant information if they

Downloaded by Delhi Technological University At 21:51 20 March 2018 (PT)

are seeking the said information for making a purchase decision. Due to their lesser active status online, the usefulness of these OBC becomes pertinent and important to them; thus, helping them in their decision making. The higher group, on the other hand, seeks information from many sources and limiting only to OBCs for information seek redundant to them. Thus, their decision making may not be affected by the usefulness of the OBCs in totality, for they might be consulting the other sources of information as well.

6. Conclusion, limitations and managerial implications

With the progressing millennia, the innovations in internet technologies have resulted in a new application to interact and communicate. Web 2.0 or the social media has changed the way people communicate and exchange information. Using this ability of the SNSs, brands can utilise the platform to connect and collaborate with the users to understand their perception of the brand and from the interactions and the SNS-based OBCs they can find more about the customers' inclinations towards the brand. Marketers and brands are using such OBCs for business purposes for the various capabilities. The premise of this research was to explore the factors of OBC engagement that have not been linked with PI in previous studies. Through the multi-analytical approach of SEM-NN, this research was able to demonstrate that the identified factors, i.e. CP, PU, CM, BA and ATB have a significant influence on PI of the customer succeeded by observing the moderating effects of age, annual family income and internet usage per week.

OBCs are being included increasingly in the business strategies nowadays, with brands creating brand pages on popular SNSs. The primary uses of SNS-based OBCs are to maintain and engage the existing customers, increase brand awareness and purchase and attract new ones. This paper focussed on identifying the factors that play an important role in influencing the PI of customers who engage with such OBCs. The findings of this paper suggest that factors and the relationships proposed are significant, and brands should consider these factors while creating a brand page. The study further observed the effects of the moderating variables on the proposed model to strengthen the understanding of the customer behaviour when it comes to the factors identified and the intention to purchase.

There were four major limitations to this study, thus requiring caution while interpreting the results. First, the sample considered for this study has a size of 236, which might not be large enough. Second, only one predictor was involved, i.e. purchase intention. Predictors like lifestyle, personality and culture can be included in future such research works. Third, the study was focussed and limited to Facebook. Thus, leaving scope to conduct a similar study on other such SNSs. Fourth, the study was structured and designed considering the population residing within India. This study can be replicated in other countries to validate the socio-cultural impact on the model proposed as well as the effects of the moderating variables.

Marketers and brands can benefit from this study by changing their content and promotion strategies based on the results discussed in previous sections. The empirical results show that customer is inclined towards the type and quality of the content of the posts on OBCs. The marketers and brands need to create and co-create meaningful, enjoyable and informational content. Similarly, the nature of information disseminated within the OBC to the users also plays an important part. The majority of focus should be given to the content generation, and systematic content strategy should be made to exploit the capabilities of the OBCs to the maximum. Previous sections also discussed the moderating effects of age, annual income and internet usage per week, which can easily help the marketers and brands to identify the demographics as per their need, making segmentation of the population and targeting potential customers much easy. Especially the small and medium enterprises in India which do not have adequate resources to undertake extensive promotional campaigns may take advantage of the findings of this study.

Downloaded by Delhi Technological University At 21:51 20 March 2018 (PT)

They can formulate appropriate strategic interventions, specifically targeting the age, income groups which are more susceptible to the nature of online engagements based on their internet usage. These enterprises also get to understand what factors to keep in mind while creating an online brand engagement strategy to maximise the effect of the engagements with the customers. There have been a lot of studies which have discussed the moderating effects of age, income and internet usage; separately not in conjoint. But, none of them has studied the effects of these variables in the context of the OBC-induced PI. With this study, marketers would be able to understand the differences among the moderating variable groups and thus target the most appropriate group within the moderating variables. Brand pages if moderated properly can steer the emotional aspect of the customer's behaviour and can lead to a positive brand image as well as a sense of affection and affinity within the target market, towards the brand. If properly studied and implemented in the digital strategy; these factors can help, engage the customers successfully and creating an intent within the mass towards the brand.

Downloaded by Delhi Technological University At 21:51 20 March 2018 (PT)

References

Acker, O., Gröne, F., Akkad, F., Pötscher, F. and Yazbek, R. (2011), "Social CRM: how companies can link into the social web of consumers", *Journal of Direct, Data and Digital Marketing Practice*, Vol. 13 No. 1, pp. 3-10.

Ajzen, I. (1985), *From Intentions to Actions: A Theory of Planned Behavior*, Springer, Berlin and Heidelberg.

Ajzen, I. and Fishbein, M. (1980), *Understanding Attitudes and Predicting Social Behaviour*, Prentice-Hall, Englewood Cliffs, NJ.

Ajzen, I. and Fishbein, M. (2005), "The influence of attitudes on behavior", in Albarracín, D., Johnson, B.T. and Zanna, M.P. (Eds), *The Handbook of Attitudes*, Lawrence Erlbaum Associates Publishers, Mahwah, NJ, pp. 173-221.

Allard, T., Banin, B. and Chebat, J. (2009), "When income matters: customers' evaluation of shopping malls' hedonic and utilitarian orientations", *Journal of Retailing and Consumer Services*, Vol. 16 No. 1, pp. 40-49.

Al-Somali, S., Gholami, R. and Clegg, B. (2009), "An investigation into the acceptance of online banking in Saudi Arabia", *Technovation*, Vol. 29 No. 2, pp. 130-141.

Araujo, T. and Neijens, P. (2012), "Friend me: which factors influence top global brands participation in social network sites", *Internet Research*, Vol. 22 No. 5, pp. 626-640.

Arbuckle, J.L. and Wothke, W. (1999), *Amos 4.0 User's Guide*, SPSS, Chicago, IL.

Assiouras, I., Liapati, G., Kouletsis, G. and Koniordos, M. (2015), "The impact of brand authenticity on brand attachment in the food industry", *British Food Journal*, Vol. 117 No. 2, pp. 538-552.

Baldus, B.J., Voorhees, C. and Calantone, R. (2015), "Online brand community engagement: scale development and validation", *Journal of Business Research*, Vol. 68 No. 5, pp. 978-985.

Belaid, S. and Temessek Behi, A. (2011), "The role of attachment in building customer-brand relationships: an empirical investigation in the utilitarian consumption context", *Journal of Product & Brand Management*, Vol. 20 No. 1, pp. 37-47.

Berthon, P.R., Pitt, L.F., Plangger, K. and Shapiro, D. (2012), "Marketing meets Web 2.0, social media, and creative customers: implications for international marketing strategy", *Business Horizons*, Vol. 55 No. 3, pp. 261-271.

Bowden, J.L.H. (2009), "The process of customer engagement: a conceptual framework", *Journal of Marketing Theory and Practice*, Vol. 17 No. 1, pp. 63-74.

Brodie, R.J., Ilic, A., Biljana, J. and Hollebeek, L. (2011), "Customer engagement in a virtual brand community: an exploratory analysis", *Journal of Business Research*, Vol. 66 No. 1, pp. 314-329.

Browne, M.W. and Cudeck, R. (1993), *Alternative Ways of Assessing Model Fit*, Sage Publications, Newbury Park, CA.

Calder, B.J., Malthouse, E.C. and Schaedel, U. (2009), "An experimental study of the relationship between online engagement and advertising effectiveness", *Journal of Interactive Marketing*, Vol. 23 No. 4, pp. 321-331.

Chau, P.Y.K. and Hu, J.H. (2002), "Investigating healthcare professionals' decisions to accept telemedicine technology: an empirical test of competing theories", *Information & Management*, Vol. 39 No. 4, pp. 297-311.

Cheng, S.Y., Tsai, M.T., Cheng, N.C. and Chen, K.S. (2012), "Predicting intention to purchase on group buying website in Taiwan: virtual community, critical mass, and risk", *Online Information Review*, Vol. 36 No. 5, pp. 698-712.

Cheng, X., Liu, J., Wang, H. and Wang, C. (2012), "Coordinate live streaming and storage sharing for social media content distribution", *IEEE Transactions on Multimedia*, Vol. 14 No. 6, pp. 1558-1565.

Chong, A.Y.L. (2013), "A two-staged SEM-neural network approach for understanding and predicting the determinants of m-commerce adoption", *Expert Systems with Applications*, Vol. 40 No. 4, pp. 1240-1247.

Chu, S.C. and Kim, Y. (2011), "Determinants of consumer engagement in electronic word-of-mouth (eWOM) in social networking sites", *International Journal of Advertising*, Vol. 30 No. 1, pp. 47-75.

Chung, J.E., Park, N., Wang, H., Fulk, J. and McLaughlin, M. (2010), "Age differences in perceptions of online community participation among non-users: an extension of the technology acceptance model", *Computers in Human Behavior*, Vol. 26 No. 6, pp. 1674-1684.

Constantinides, E., Romero, C.L. and Boria, M.A.G. (2008), "Social media: a new frontier for retailers?", in Swoboda, B., Morschett, D., Rudolph, T., Schnedlitz, P. and Schramm-Klein, H. (Eds), *European Retail Research. European Retail Research*, Gabler Verlag, Wiesbaden.

Coulter, K.S. and Roggeveen, A. (2012), "'Like it or not' consumer responses to word-of-mouth communication in on-line social networks", *Management Research Review*, Vol. 35 No. 9, pp. 878-899.

Cvijikj, I.P. and Michahelles, F. (2011), "A case study of the effects of moderator posts within a Facebook brand page", in Datta, A., Shulman, S., Zheng, B., Lin, S.D., Sun, A. and Lim, E.P. (Eds), *Social Informatics. SocInfo 2011. Lecture Notes in Computer Science*, Vol. 6984, Springer, Berlin and Heidelberg.

Cvijikj, I.P. and Michahelles, F. (2013), "Online engagement factors on Facebook brand pages", *Social Network Analysis and Mining*, Vol. 3 No. 4, pp. 843-861.

Davis, F.D. (1989), "Perceived usefulness, perceived ease of use, and user acceptance of information technology", *MIS Quarterly*, Vol. 13 No. 3, pp. 319-340.

De Vries, L., Gensler, S. and Leeflang, P.S.H. (2012), "Popularity of brand posts on brand fan pages: an investigation of the effects of social media marketing", *Journal of Interactive Marketing*, Vol. 26 No. 1, pp. 83-91.

Didier, L. and Lombart, C. (2010), "Impact of brand personality on three major relational consequences (trust, attachment, and commitment to the brand)", *Journal of Product and Brand Management*, Vol. 19 No. 2, pp. 114-130.

Esch, F.R., Langner, T., Schmitt, B.H. and Geus, P. (2006), "Are brands forever? How brand knowledge and relationships affect current and future purchases", *Journal of Product & Brand Management*, Vol. 5 No. 2, pp. 98-105.

Evans, D. (2012), *Social Media Marketing: An Hour a Day*, 2nd ed., John Wiley & Sons, Indianapolis, IN.

Fishbein, M. and Ajzen, I. (1975), "Belief, attitude, intention and behavior: An introduction to theory and research".

Frambach, R.T., Roest, H.C.A. and Krishnan, T.V. (2007), "The impact of consumer internet experience on channel preference and usage intentions across the different stages of the buying process", *Journal of Interactive Marketing*, Vol. 21 No. 2, pp. 26-41.

France, C., Merrilees, B. and Miller, D. (2015), "Customer brand co-creation: a conceptual model", *Marketing Intelligence & Planning*, Vol. 33 No. 6, pp. 848-864.

Downloaded by Delhi Technological University At 21:51 20 March 2018 (PT)

Gamboa, A.M. and Gonçalves, H.M. (2014), "Customer loyalty through social networks: lessons from Zara on Facebook", *Business Horizon*, Vol. 57 No. 6, pp. 709-717.

Gao, Q. and Feng, C. (2016), "Branding with social media: user gratifications, usage patterns, and brand message content strategies", *Computers in Human Behavior*, Vol. 63, pp. 868-890.

Garson, G.D. (1998), *Neural Networks: An Introductory Guide for Social Scientists*, Sage, Thousand Oaks, CA.

Glass, R. and Li, S. (2010), "Social influence and instant messaging adoption", *Journal of Computer Information Systems*, Vol. 51 No. 2, pp. 24-30.

Hair, J.F. Jr, Anderson, R.E., Tatham, R.L. and William, C. (1995), *Multivariate Data Analysis with Readings*, Prentice Hall, NJ.

Hair, J.F., Black, W.C., Babin, B.J. and Anderson, R.E. (2010), *Multivariate Data Analysis: A Global Perspective*, 7th ed., Prentice Hall, NJ.

Hanna, R., Rohm, A. and Crittenden, V.L. (2011), "We're all connected: the power of the social media ecosystem", *Business Horizons*, Vol. 54 No. 3, pp. 265-273.

Harrison, A.W. and Rainer, R.K. (1992), "The influence of individual differences on skill in end-user computing", *Journal of Management Information Systems*, Vol. 9 No. 1, pp. 93-111.

Hernández, B., Jiménez, J. and José Martín, M. (2011), "Age, gender and income: do they really moderate online shopping behaviour?", *Online Information Review*, Vol. 35 No. 1, pp. 113-133.

Hew, T.S., Leong, L.Y., Ooi, K.B. and Chong, A.Y.L. (2016), "Predicting drivers of mobile entertainment adoption: a two-stage SEM-artificial-neural-network analysis", *Journal of Computer Information Systems*, Vol. 56 No. 4, pp. 352-370.

Hollebeek, L.D. (2011), "Demystifying customer brand engagement: exploring the loyalty nexus", *Journal of Marketing Management*, Vol. 27 Nos 7/8, pp. 785-807.

Hooi Ting, D., Fong Lim, S., Siuly Patanmacia, T., Gie Low, C. and Chuan Ker, G. (2011), "Dependency on smartphone and the impact on purchase behaviour", *Young Consumers*, Vol. 12 No. 3, pp. 193-203.

Hsu, C.L. and Lu, H.P. (2004), "Why do people play on-line games? An extended TAM with social influences and flow experience", *Information & Management*, Vol. 41 No. 7, pp. 853-868.

Hubona, G.S. and Kennick, E. (1996), "The impact of external variables on information technology usage behavior", *IEEE Proceedings of the Hawaii International Conference on System Sciences*, Vol. 4, IEEE Press, Los Alamitos, CA, pp. 166-175.

Internet World Stats (2017), "World internet users and 2017 population stats", available at: www.internetworldstats.com/stats.htm (accessed 3 April 2017).

Jahn, B. and Kunz, W. (2012), "How to transform customers into fans of your brand", *Journal of Service Management*, Vol. 23 No. 3, pp. 344-361.

Jin, B. and Suh, Y.G. (2005), "Integrating effect of consumer perception factors in predicting private brand purchase in a Korean discount store context", *Journal of Consumer Marketing*, Vol. 22 No. 2, pp. 62-71.

Kang, J., Tang, L. and Fiore, A.M. (2014), "Enhancing consumer-brand relationships on restaurant Facebook fan pages: maximizing consumer benefits and increasing active participation", *International Journal of Hospitality Management*, Vol. 36, pp. 145-155.

Kaplan, A.M. and Haenlein, M. (2010), "Users of the world, unite! The challenges and opportunities of Social Media", *Business Horizons*, Vol. 53 No. 1, pp. 59-68.

Karr-Wisniewski, P. and Lu, Y. (2010), "When more is too much: operationalizing technology overload and exploring its impact on knowledge worker productivity", *Computers in Human Behavior*, Vol. 26 No. 5, pp. 1061-1072.

Kaur, P., Dhir, A. and Rajala, R. (2016), "Assessing flow experience in social networking site based brand communities", *Computers in Human Behavior*, Vol. 64, pp. 217-225.

Downloaded by Delhi Technological University At 21:51 20 March 2018 (PT)

Kietzmann, J.H., Hermkens, K., McCarthy, I.P. and Silvestre, B.S. (2011), "Social media? Get serious! Understanding the functional building blocks of social media", *Business Horizons*, Vol. 54, pp. 241-251.

King, W.R. and He, J. (2006), "A meta-analysis of the technology acceptance model", *Information & Management*, Vol. 43 No. 6, pp. 740-755.

Kozinets, R.V., de Valck, K., Wognicki, A.C. and Wilner, S.J.S. (2010), "Networked narratives: understanding word-of-mouth marketing in online communities", *Journal of Marketing*, Vol. 74 No. 1, pp. 71-89.

Kumar, V. and Bhagwat, Y. (2010), "Listen to the customer", *Marketing Research*, Vol. 22 No. 2, pp. 14-19.

Larson, K. and Watson, R.T. (2011), "The value of social media: toward measuring social media strategies", *Proceedings of the Thirty-Second International Conference on Information Systems (ICIS), Shanghai*, pp. 3262-3279.

Leong, L.Y., Hew, T.S., Ooi, K.B. and Lin, B. (2011), "Influence of gender and English proficiency on Facebook mobile adoption", *International Journal of Mobile Communication*, Vol. 9 No. 5, pp. 495-521.

Leonidou, L.C., Leonidou, C.N. and Kvasova, O. (2010), "Antecedents and outcomes of consumer environmentally friendly attitudes and behavior", *Journal of Marketing Management*, Vol. 26 Nos 13/14, pp. 1319-1344.

Liébana-Cabanillas, F.J., Sánchez-Fernández, J. and Muñoz-Leiva, F. (2014), "Role of gender on acceptance of mobile payment", *Industrial Management & Data Systems*, Vol. 114 No. 2, pp. 220-240.

Limbu, Y.B., Wolf, M. and Lunsford, D. (2012), "Perceived ethics of online retailers and consumer behavioral intentions: the mediating roles of trust and attitude", *Journal of Research in Interactive Marketing*, Vol. 6 No. 2, pp. 133-154.

Lou, H., Luo, W. and Strong, D. (2000), "Perceived critical mass effect on groupware acceptance", *European Journal of Information Systems*, Vol. 9 No. 2, pp. 91-103.

Louis, D. and Lombart, C. (2010), "Impact of brand personality on three major relational consequences (trust, attachment, and commitment to the brand)", *Journal of Product & Brand Management*, Vol. 19 No. 2, pp. 114-130.

Lu, J., Yu, C.S., Liu, C. and Yao, J. (2003), "Technology acceptance model for wireless Internet", *Internet Research: Electronic Networking Applications and Policy*, Vol. 13 No. 3, pp. 206-222.

McAlexander, J.H., Kim, S.K. and Roberts, S.D. (2003), "Loyalty: the influences of satisfaction and brand community integration", *Journal of Marketing Theory and Practice*, Vol. 11 No. 4, pp. 1-11.

McAlexander, J.H., Schouten, J.W. and Koenig, H.F. (2002), "Building brand community", *Journal of Marketing*, Vol. 66 No. 1, pp. 38-54.

McCorkindale, T. (2010), "Can you see the writing on my wall?: a content analysis of the Fortune 50's Facebook social networking sites", *Public Relations Journal*, Vol. 4 No. 3, pp. 1-13.

Madan, K. and Yadav, R. (2016), "Behavioural intention to adopt mobile wallet: a developing country perspective", *Journal of Indian Business Research*, Vol. 8 No. 3, pp. 227-244.

Mangold, W.G. and Faulds, D.J. (2009), "Social media: the new hybrid element of the promotion mix", *Business Horizons*, Vol. 52 No. 4, pp. 357-365.

Miyazaki, A.D. and Fernández, A. (2001), "Consumer perceptions of privacy and security risks for online shopping", *The Journal of Consumer Affairs*, Vol. 35 No. 1, pp. 27-44.

Mohamed, N., Hussein, R., Ahmad Zamzuri, N.H. and Haghshenas, H. (2014), "Insights into individual's online shopping continuance intention", *Industrial Management & Data Systems*, Vol. 114 No. 9, pp. 1453-1476.

Downloaded by Delhi Technological University At 21:51 20 March 2018 (PT)

Mollen, A. and Wilson, H. (2010), "Engagement, telepresence and interactivity in online consumer experience: reconciling scholastic and managerial perspectives", *Journal of Business Research*, Vol. 63 Nos 9-10, pp. 919-925.

Morris, S.A., Greer, T.H., Hughes, C. and Clark, W.J. (2004), "Prediction of CASE adoption: a neural network approach", *Industrial Management & Data Systems*, Vol. 104 No. 2, pp. 129-135.

Nguyen, B., Yu, X., Melewar, T.C. and Chen, J. (2015), "Brand innovation and social media: knowledge acquisition from social media, market orientation, and the moderating role of social media strategic capability", *Industrial Marketing Management*, Vol. 51, pp. 11-25.

Nie, N.H. (2001), "Sociability, interpersonal relations, and the internet reconciling conflicting findings", *American Behavioural Scientist*, Vol. 45 No. 3, pp. 420-435.

Nunnally, J.C. (1978), *Psychometric Theory*, McGraw-Hill, New York, NY.

Paris, C.M., Lee, W. and Seery, P. (2010), "The role of social media in promoting special events: acceptance of Facebook 'events'", in Gretzel, U., Law, R. and Fuchs, M. (Eds), *Information and Communication Technologies in Tourism*, Springer, Vienna.

Patterson, P., Yu, T. and De Ruyter, K. (2006), "Understanding customer engagement in services", *Advancing Theory, Maintaining Relevance, Proceedings of ANZMAC Conference, Brisbane*, pp. 4-6.

Podsakoff, P.M., MacKenzie, S.B., Lee, J.Y. and Podsakoff, N.P. (2003), "Common method biases in behavioral research: a critical review of the literature and recommended remedies", *Journal of Applied Psychology*, Vol. 88 No. 5, pp. 879-903.

Porter, C.E. and Donthu, N. (2006), "Using the technology acceptance model to explain how attitudes determine internet usage: the role of perceived access barriers and demographics", *Journal of Business Research*, Vol. 59 No. 9, pp. 999-1007.

Prahalad, C.K. and Ramaswamy, V. (2004a), "Co-creating unique value with customers", *Strategy & Leadership*, Vol. 32 No. 3, pp. 4-9.

Prahalad, C.K. and Ramaswamy, V. (2004b), "Co-creation experiences: the next practice in value creation", *Journal of Interactive Marketing*, Vol. 18 No. 3, pp. 5-14.

Punyatoya, P. (2015), "Effect of perceived brand environment-friendliness on Indian consumer attitude and purchase intention: an integrated model", *Marketing Intelligence & Planning*, Vol. 33 No. 3, pp. 258-275.

Raijas, A. and Tuunainen, V.K. (2001), "Critical factors in electronic grocery shopping", *International Journal of Retail, Distribution and Consumer Research*, Vol. 11 No. 3, pp. 255-265.

Rathore, A.K., Ilavarasan, P.V. and Dwivedi, Y.K. (2016), "Social media content and product co-creation: an emerging paradigm", *Journal of Enterprise Information Management*, Vol. 29 No. 1, pp. 7-18.

Rauniar, R., Rawski, G., Yang, J. and Johnson, B. (2012), "Technology acceptance model (TAM) and social media usage: an empirical study on Facebook", *Journal of Enterprise Information Management*, Vol. 27 No. 1, pp. 6-30.

Sashi, C. (2012), "Customer engagement, buyer-seller relationships, and social media", *Management Decision*, Vol. 50 No. 2, pp. 253-272.

Schau, H.J., Muñiz, A.M. Jr and Arnould, E.J. (2009), "How brand community practices create value", *Journal of Marketing*, Vol. 73 No. 5, pp. 30-51.

Serenko, K., Turel, O. and Yol, S. (2006), "Moderating roles of user demographics in the American customer satisfaction model within the context of mobile services", *Journal of Information Technology Management*, Vol. 17 No. 4, pp. 20-32.

Servia-Rodriguez, S., Fernandez-Vilas, A., Diaz-Redondo, R.P. and Pazos-Arias, J.J. (2013), "Inferring contexts from Facebook interactions: a social publicity scenario", *IEEE Transactions on Multimedia*, Vol. 15 No. 6, pp. 1296-1303.

Shi, S., Chen, Y. and Chow, W.S. (2016), "Key values driving continued interaction on brand pages in social media: an examination across genders", *Computers in Human Behavior*, Vol. 62, pp. 578-589.

Downloaded by Delhi Technological University At 21:51 20 March 2018 (PT)

Shin, D.-H. (2009), "Towards an understanding of the consumer acceptance of mobile wallet", *Computers in Human Behavior*, Vol. 25 No. 6, pp. 1343-1354.

statista.com (2015), "Number of worldwide Internet users from 2000 to 2015", available at: www.statista.com/statistics/273018/number-of-Internet-users-worldwide/ (accessed 1 March 2016).

Swani, K., Milne, G.R. and Brown, B.P. (2013), "Spreading the word through likes on Facebook: evaluating the message strategy effectiveness of Fortune 500 companies", *Journal of Research in Interactive Marketing*, Vol. 7 No. 4, pp. 269-294.

Sweeney, J.C., Soutar, G.N. and Mazzarol, T. (2008), "Factors influencing word of mouth effectiveness: receiver perspectives", *European Journal of Marketing*, Vol. 42 Nos 3/4, pp. 344-364.

Tabachnick, B.G. and Fidell, L.S. (2001), *Using Multivariate Statistics*, Allyn & Bacon, Needham Heights, MA.

Tarhini, A., Hone, K. and Liu, X. (2014), "Measuring the moderating effect of gender and age on e-learning acceptance in England: a structural equation modeling approach for an extended technology acceptance model", *Journal of Educational Computing Research*, Vol. 51 No. 2, pp. 163-184.

Taylor, S. and Todd, P. (1995), "Understanding information technology usage: a test of competing models", *Information Systems Research*, Vol. 6 No. 2, pp. 144-176.

Thackeray, R., Neiger, B.I., Hanson, C.L. and McKenzie, J.F. (2008), "Enhancing promotional strategies within social marketing programs: use of Web 2.0 social media", *Health Promotion Practice*, Vol. 9 No. 4, pp. 338-343.

Thomson, M., MacInnis, D.J. and Park, W.C. (2005), "The ties that bind: measuring the strength of consumers' emotional attachments to brands", *Journal of Personality and Social Psychology*, Vol. 15 No. 1, pp. 77-91.

Tiruwa, A., Yadav, R. and Suri, P.K. (2016), "An exploration of online brand community (OBC) engagement and customer's intention to purchase", *Journal of Indian Business Research*, Vol. 8 No. 4, pp. 295-314.

Trocchia, P.J. and Janda, S. (2000), "A phenomenological investigation of internet usage among older individuals", *Journal of Consumer Marketing*, Vol. 17 No. 7, pp. 605-616.

Tuten, T.L. and Solomon, M.R. (2013), *Social Media Marketing*, Pearson Education, Upper Saddle River, NJ.

Van Doorn, J., Lemon, K.N., Mittal, V., Nass, S., Pick, D., Pirner, P. and Verhoef, P.C. (2010), "Customer engagement behavior: theoretical foundations and research directions", *Journal of Service Research*, Vol. 13 No. 3, pp. 253-266.

Vargo, S.L. and Lusch, R.F. (2004), "Evolving to a new dominant logic for marketing", *Journal of Marketing*, Vol. 68 No. 1, pp. 1-17.

Vargo, S.L. and Lusch, R.F. (2008), "Service-dominant logic: continuing the evolution", *Journal of the Academy of marketing Science*, Vol. 36 No. 1, pp. 1-10.

Venkatesh, V. and Morris, M.G. (2000), "Why don't men ever stop to ask for directions? Gender, social influence, and their role in technology acceptance and usage behaviour", *MIS Quarterly*, Vol. 24 No. 1, pp. 115-139.

Venkatesh, V., Morris, M.G., Davis, G.B. and Davis, F.D. (2003), "User acceptance of information technology: toward a unified view", *MIS Quarterly*, Vol. 27 No. 3, pp. 425-478.

Vivek, S.D., Beatty, S.E. and Morgan, R.M. (2012), "Customer engagement: exploring customer relationships beyond purchase", *Journal of Marketing Theory and Practice*, Vol. 20 No. 2, pp. 122-146.

Wang, Y.M. and Elhag, T.M. (2008), "An adaptive neuro-fuzzy inference system for bridge risk assessment", *Expert Systems with Applications*, Vol. 34 No. 4, pp. 3099-3106.

Wang, Y.S., Wu, M.C. and Wang, H.Y. (2009), "Investigating the determinants and age and gender differences in the acceptance of mobile learning", *British Journal of Educational Technology*, Vol. 40 No. 1, pp. 92-118.

Downloaded by Delhi Technological University At 21:51 20 March 2018 (PT)

Wei, R. and Lo, V.-H. (2006), "Staying connected while on move: cell phone use and social connectedness", *New Media Society*, Vol. 8 No. 1, pp. 53-72.

Wirtz, J., Den Ambtman, A., Bloemer, J., Horváth, C., Ramaseshan, B., Van De Klundert, J., Gurhan Canli, Z. and Kandampully, J. (2013), "Managing brands and customer engagement in online brand communities", *Journal of Service Management*, Vol. 24 No. 3, pp. 223-244.

Wong, C.H., Tan, G.W.H., Loke, S.P. and Ooi, K.B. (2014), "Mobile TV: a new form of entertainment?", *Industrial Management & Data Systems*, Vol. 114 No. 7, pp. 1050-1067.

Xu, D.H., Huo, B.F. and Sun, L.Y. (2014), "Relationships between intra-organizational resources, supply chain integration and business performance", *Industrial Management & Data Systems*, Vol. 114 No. 8, pp. 1186-1206.

Yadav, R. (2015), "An exploration into the nature of comments on Facebook (page of large Indian organizations)", in Chatterjee, S., Singh, N., Goyal, D. and Gupta, N. (Eds), *Managing in Recovering Markets. Springer Proceedings in Business and Economics*, Springer, New Delhi.

Yadav, R., Sharma, S.K. and Tarhini, A. (2016), "A multi-analytical approach to understand and predict the mobile commerce adoption", *Journal of Enterprise Information Management*, Vol. 29 No. 2, pp. 222-237.

Yu, J., Ha, I., Choi, M. and Rho, J. (2005), "Extending the TAM for a t-commerce", *Information & Management*, Vol. 42 No. 7, pp. 965-976.

Zhang, J. (2009), "Exploring drivers in the adoption of mobile commerce in China", *The Journal of the American Academy of Business*, Vol. 15 No. 1, pp. 64-69.

Zhou, T. (2014), "Understanding the determinants of mobile payment continuance usage", *Industrial Management & Data Systems*, Vol. 114 No. 6, pp. 936-948.

Further reading

Hernandez, B., Jimenez, J. and Martin, M.J. (2009), "The impact of self-efficacy, ease of use and usefulness on e-purchasing: an analysis of experienced e-shoppers", *Interacting with Computers*, Vol. 21 Nos 1/2, pp. 146-156.

Hollebeek, L.D. (2011b), "Exploring customer brand engagement: definition & themes", *Journal of Strategic Marketing*, Vol. 19 No. 7, pp. 555-573.

Revels, J., Tojib, D. and Tsarenko, Y. (2010), "Understanding consumer intention to use mobile services", *Australasian Marketing Journal*, Vol. 18 No. 2, pp. 74-80.

Rouibah, K., Abbas, H. and Rouibah, S. (2011), "Factors affecting camera mobile phone adoption before e-shopping in the Arab world", *Technology in Society*, Vol. 33 Nos 3/4, pp. 271-283.

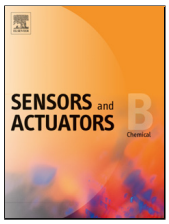
Vargo, S.L. (2009), "Toward a transcending conceptualization of relationship: a service-dominant logic perspective", *The Journal of Business and Industrial Marketing*, Vol. 24 Nos 5/6, pp. 373-379.

Corresponding author
Anurag Tiruwa can be contacted at: anuraag.dsm13@gmail.com

For instructions on how to order reprints of this article, please visit our website:
www.emeraldgrouppublishing.com/licensing/reprints.htm
Or contact us for further details: **permissions@emeraldinsight.com**

Downloaded by Delhi Technological University At 21:51 20 March 2018 (PT)

Accepted Manuscript



Title: Multiwalled Carbon Nanotube Modified Microfluidic-Based Biosensor Chip for Nucleic Acid Detection

Authors: Aditya Sharma Ghrera, Chandra Mouli Pandey, Bansi Dhar Malhotra

PII: S0925-4005(18)30616-6
DOI: https://doi.org/10.1016/j.snb.2018.03.118
Reference: SNB 24403

To appear in: *Sensors and Actuators B*

Received date: 17-1-2018
Revised date: 15-3-2018
Accepted date: 19-3-2018

Please cite this article as: Aditya Sharma Ghrera, Chandra Mouli Pandey, Bansi Dhar Malhotra, Multiwalled Carbon Nanotube Modified Microfluidic-Based Biosensor Chip for Nucleic Acid Detection, Sensors and Actuators B: Chemical https://doi.org/10.1016/j.snb.2018.03.118

This is a PDF file of an unedited manuscript that has been accepted for publication. As a service to our customers we are providing this early version of the manuscript. The manuscript will undergo copyediting, typesetting, and review of the resulting proof before it is published in its final form. Please note that during the production process errors may be discovered which could affect the content, and all legal disclaimers that apply to the journal pertain.

ACCEPTED MANUSCRIPT

Multiwalled Carbon Nanotube Modified Microfluidic-Based Biosensor Chip for Nucleic Acid Detection

Aditya Sharma Ghrera[1,*], Chandra Mouli Pandey[2] and Bansi Dhar Malhotra[3,*]

[1]Applied Science Department, The NorthCap University, Gurugram–122017, India
[2]Department of Applied Chemistry, Delhi Technological University, Delhi–110042, India
[3]Department of Biotechnology, Delhi Technological University, Delhi–110042, India

[*]**Corresponding author:** adityasharmaghrera@gmail.com, bansi.malhotra@gmail.com

Research Highlights

- Fabrication of microfluidics-based chip for electrochemical sensing.
- Electrophoretic deposition of MWCNT onto patterned ITO coated glass substrate.
- Fabricated MWCNT based chip can detect complementary DNA upto femtomolar concentration range.
- This platform is self–contained, easy–to–operate and has the potential to achieve rapid, simple, and specific detection of DNA.

Abstract

An impedimetric microfluidic–based biosensor was fabricated and investigated for quantification of the DNA sequence specific to chronic myelogenous leukemia (CML). The sensor chip was constructed by electrophoretic deposition of carboxyl-modified multiwalled carbon nanotubes (MWCNT) on the patterned (via wet chemical etching method) indium–tin–oxide (ITO) coated glass substrate. The MWCNT surface was immobilized with CML specific deoxyribonucleic acid probe, followed by sealing of the biochip with poly (dimethylsiloxane) microchannel for fluid control. This integrated miniaturized system was used to monitor complementary target DNA concentration by measuring the interfacial charge transfer resistance via hybridization. The presence of complementary DNA in buffer solution resulted in significant decrease in electrical conductivity of the interface thereby presenting a barrier for transport of the redox probe ions. Under optimal conditions, this microfluidic biochip exhibited good calibration range from 1 μM to 1 fM and a response time of 60 s.

ACCEPTED MANUSCRIPT

Keywords: Carbon nanotube, Microfluidic device, Electrophoretic deposition, Nucleic acid hybridization, Chronic myelogenous leukemia, Electrochemical impedance spectroscopy.

1. Introduction

There is a rapid growth towards the development of sensitive, cost-effective, hand held, on–chip biosensing devices that may be directly used to indicate the presence of desired bioanalytes via detection of an electronic signal. In this context, it has been predicted that biosensors can perhaps be used to estimate the target concentration in a given sample using a transducer [1]. Such a device should, however, have the ability to distinguish the biomolecules and its analogues so as to provide specific information about the presence of the desired target in a test sample [1].

The past decade has seen significant advances in micro– and nano–fabrication resulting in emergence of several analytical methods. There is, thus, a growing demand to integrate the desired biosensors with microfluidics (MF) to provide miniaturized platforms with favourable properties, such as reduced sample volume, low reagent consumption, decreased processing time, low cost analysis, portability and versatility in design [2-3]. Integrating a biosensor with a MF chip may perhaps yield enhanced analytical capability by bringing together several unit operations (e.g. sample extraction, purification, sensing, etc.) on a single platform and allow parallel detection of multiple samples thereby widening the possibilities of applications in clinical diagnostics [2-4]. Microfluidic biosensors can be fabricated using fluorescent and electrochemical technique, respectively [5-6]. Compared to fluorescent technique, MF based electrochemical biosensors utilize the electroactive molecules [1, 6] and are known to offer better sensitivity and lower detection limit [5]. Additionally, electrochemical sensors have been found to be resistant towards the presence of ambient impurities making them suitable for use for point–of–care diagnostics [1, 5, 7].

Carbon based materials have recently been found to play an important role in the development of electrochemical biosensors [8-10]. Carbon nanotubes (CNT) are promising materials for sensing applications owing to their electrical, chemical, mechanical and structural properties [8, 10]. CNT have been found to display metallic, semiconducting and superconducting chracteristics, possess a hollow core that is suitable for storing guest molecules and have the largest elastic modulus and exhibit high surface–to–volume ratio [11]. Furthermore, for a wide range of electroactive species, CNT can be used as mediators for improved electron–transfer kinetics [8]. Recent studies have demonstrated that electrochemical activity of biomolecules can be enhanced using CNT [8, 10, 12-13]. Even for

ACCEPTED MANUSCRIPT

proteins having deeply embedded redox centres within a glycoprotein shell, CNT have been found to result in enhanced electron–transfer [12-14]. For sensing application, the CNT can be suitably functionalized for immobilization of desired biomolecules. The functionalization of CNT may lead to biocompatibility and improved dispersibility in the solution phase of biomolecules [15-16]. CNT can be obtained as single–walled (SW) and multi–walled (MW) depending on if a single or multiple layers of graphene sheets are rolled into tubes.

Nucleic acids–based biosensors, are known to provide simple and cost-effective testing and monitoring tool for genetic and infectious diseases [1, 7]. An electrochemical hybridization biosensor can be used to monitor the change in electrochemical behaviour of an electrode on duplex formation. The application of CNT may perhaps result in improved performance of a sensor [1, 5, 17] since the adsorptive accumulation and thus oxidation signal intensity of the guanine nucleobase is facilitated via CNT [3, 15, 17]. Erdem and co–workers reported direct (label–free) electrochemical detection of the guanine oxidation signal using pencil graphite electrode modified with MWCNT [18]. Similarly, enhancement of the guanine response was reported at electrodes containing MWCNT paste [19] and single walled CNT [20].

Many techniques (arc discharge, laser ablation, flame pyrolysis, chemical vapour deposition, spray coating, dip coating, vacuum filtration and electrodeposition techniques) have been employed for thin film deposition of CNT [21]. Among these techniques, electrophoretic deposition (EPD) method is known to be the simplest. For EPD, charged particles dispersed in a polar solvent when subjected to an electric field, migrate and are adsorbed on the surface of oppositely charged electrode via coagulation [22-23]. By varying deposition time and the applied potential, the thickness and morphology of the deposited film can be easily controlled [22, 24]. Thus, in a low processing time, it can produce uniform, dense and a porous film of the desired conducting material. The EPD deposited CNT films have been found to have the improved adherence to the electrode surface due to formation of the metal hydroxides that form a hydrogen bond with the oxidized nanotubes [23].

This manuscript contains results of the studies relating to the development of an electrochemical MF device for detection of chronic myelogenous leukemia (CML) specific DNA sequence. CML is a blood-related disorder that is identified by increased proliferation of the granulocytic cell–line without loss of their capability to differentiate [25-27]. In more than 95% cases, the cytogenetic aberration known as the Philadelphia chromosome arises due to reciprocal translocation of breakpoint cluster region (BCR) and Abelson murine leukemia viral genes (ABL) [28]. This translocation produces oncogene (BCR–ABL), which codes for

ACCEPTED MANUSCRIPT

the chimeric tyrosine kinase. The device features MF channels made from poly(dimethylsiloxane) (PDMS) coupled to a fixed volume injector, and incorporates a biocatalytic sensing electrode, silver wire with silver chloride coating (Ag/AgCl) as the reference electrode, and patterned indium–tin–oxide (ITO) substrate as the counter electrode. The MF chip has been designed via wet chemical etching technique. The sensing electrode in the chip is prepared via EPD of carboxyl functionalized MWCNT followed by immobilization of CML-specific DNA probe (pDNA) sequence. The integration of CNT film with MF assembly has been found to result in improved sensing performance of the biochip.

2. MATERIALS AND METHODS

2.1. Preparation of MWCNT

The MWCNT were prepared via catalytic chemical vapor deposition technique [29] followed by purification and functionalization using boiling acid treatment [30]. The functionalization of MWCNT was carried out by refluxing with concentrated boiling nitric acid for 12 h, and then washing with distilled water followed by rinsing with ethanol and drying at 60ºC [30].

2.2. Dispersion of MWCNT

The stable suspension of the material in a suitable solvent is a prerequisite for its successful EPD. For dispersing CNT, quaternary ammonium salt tetraoctylammonium bromide (TOAB) was employed [23]. The optimized quantities (1:13 w/w) of MWCNT and TOAB were mixed. 130 mg of TOAB was added to the MWCNT solution in tetrahydrofuran (THF) (10 mg MWCNT in 25 ml THF) and the solution was sonicated **(Figure 1A)**. After 30 min of sonication, a stable black suspension was obtained, indicating that the MWCNT, which were agglomerated and settled down initially, got exfoliated on sonication. The n–octyl chains of TOAB are reported to bind with the CNT surface via hydrophobic interactions and the charged ammonium groups prevent their aggregation [23]. The suspension was centrifuged for 10 min at 10,000 rpm. The supernatant was discarded and the centrifugate was dried. The TOAB–bound MWCNT centrifugate was re–suspended in 25 ml of tetrahydrofuran (THF) after 10 min of sonication.

2.3. Fabrication of PDMS microchannels

The soft lithography technique was used for the fabrication of PDMS microchannels having dimension of 200 µm × 200 µm × 2 cm (width×height×length) [31]. Using the photoresist spinner, the 200 mm thick coating of the negative SU–8 photoresist over a silicon

ACCEPTED MANUSCRIPT

wafer was performed. The wafer was heated at 100ºC to evaporate solvent and the UV radiation was passed through it using a desired photomask. It was again heated at 110ºC to bring about the selective cross–links in the uncovered part of SU–8. Using the developer, the covered SU–8 was thereafter removed to obtain the master. Prior to use, the wafer was subjected to cleaning with acetone and exposure to fuming nitric acid. The mixing of PDMS prepolymer and curing agent (Sylgard 184, Dow Corning) was done in 10:1 ratio (v/v) followed by pouring of the degassed mixture over the master. The mixture was allowed to cure for about 30 min at 80ºC and then PDMS replica was peeled off from the master. In the PDMS slab, the holes were punched at desired positions to form reservoirs. Thereafter, the slab was sealed with the patterned ITO substrate containing working and counter electrode [31]. In the inlet reservoir the syringe pump was introduced, while in the outlet reservoir of the microchannel, Ag/AgCl wire (0.4 mm diameter) was introduced as the reference electrode (RE) **(Figure 1B)**.

2.4. Patterning of ITO substrate

The ITO coated (thickness ~150 Å) glass substrate having sheet resistance ~30 Ω was patterned to obtain the working and counter electrodes at the chip. Using wet chemical etching method, ITO coating was patterned into a desired dimension (2 mm × 2.0 cm) on the glass substrate [31-32]. For etching process, the ITO (3.0 × 2.0 cm^2) was selectively masked (2 mm × 2.0 cm) at two positions (0.5 cm apart) using a masking tape followed by dipping in the etchant solution [HNO_3:HCl:H_2O (1:10:10)] for about 15 min [31]. The solution etched the exposed ITO layer, whereas, the masked ITO was left un–etched. The obtained pattern was cleaned with acetone and washed with water. One of the electrodes on the chip was modified with MWCNT using EPD technique to serve as the working electrode (WE) and the other one was used as counter electrode (CE) **(Figure 1B)**.

2.5. Electrophoretic deposition of MWCNT

Prior to the EPD, the ITO chip was hydrolyzed with H_2O_2/NH_4OH/H_2O solution (1:1:5, v/v) for 30 min at 80ºC. A uniform film of the MWCNT was electrophoretically deposited on hydrolyzed ITO electrode over the chip **(Figure 1C)**. For EPD, 15 ml of the MWCNT–TOAB suspension in THF was transferred to an electrophoretic cell having WE of the chip and the platinum electrode connected to the negative and positive terminals of a direct current (DC) battery, respectively (Bio Rad, Model 200/2.0). Since the etched part of the chip was non–conducting, the deposition did not occur there. The cathode and anode were positioned 20 mm apart in the electrophoretic cell. On application of the DC voltage (50 V),

ACCEPTED MANUSCRIPT

the movement of MWCNT was observed. Since the MWCNT–TOAB exhibited positive charge, owing to the presence of ammonium groups on the TOAB, the MWCNT chains were attracted towards cathode and were deposited over the hydrolyzed ITO electrode on the chip. After deposition, the electrode was disconnected from the power supply, removed from the solution, rinsed with Milli–Q water, and stored in a desiccator.

2.6. Fabrication of pDNA/MWCNT/ITO biochip

The amine terminated pDNA was covalently immobilized on the WE of the chip (details of chemicals and oligonucleotides are provided in the Supplementary Section). For this purpose, the MWCNT were activated via N–ethyl–N'–(3–dimethylaminopropyl) carbodiimide (EDC; 0.2 M) and N–hydroxy succinimide (NHS; 0.05 M). The pDNA (20 µL of 1 µM) molecules were spread over the activated MWCNT and were incubated for 6 h in a humid chamber at 25ºC **(Figure 1D)**. This allowed the bonding of carboxyl functionalities of MWCNT with that of amine terminal of the DNA probe [33]. The biochip was repeatedly rinsed with Tris–ethylenediaminetetraacetic acid buffer (TE; pH 8.0) to remove the unbound pDNA molecules, and stored in refrigerator at 4°C after drying.

2.7. Characterization

The Fourier transform infrared (FT–IR) spectra were recorded using Perkin–Elmer, Spectrum BX–II spectrophotometer. The zeta potential was determined with a Zetasizer Nano–ZS–90 (Malvern Instruments) at a scattering angle of 90° at 25°C. The morphological characterization was carried out using scanning electron microscope (SEM, VP–EVO MA10, Carl Zeiss). The electrochemical studies were conducted on an Autolab Potentiostat/Galvanostat (Eco Chemie, Netherlands) using a three–electrode system in phosphate buffer saline (PBS, 100 mM, pH 7.4, 0.9% NaCl) containing 5 mM $[Fe(CN)_6]^{3-/4-}$.

3. Results and discussion

3.1. Characterization of the TOAB stabilized MWCNT

The zeta potential (ZP) of the TOAB stabilized MWCNT (TOAB–MWCNT) was determined via dynamic light scattering using Smoluchowski method and the results are presented in **Figure S1**. The ZP of MWCNT recorded soon after sonication was found to be –53 mV (Figure S1, Panel A) and it gradually increased with respect to increase in the TOAB quantity. This could perhaps be attributed to the adsorption of cations over the MWCNT. At 1:13 (w/w) ratio of MWCNT–TOAB, the ZP increased to 36 mV **(Figure S1, Panel B)**. The

ACCEPTED MANUSCRIPT

high value of zeta potential (>30 mV) for TOAB–MWCNT indicated stability of the MWCNT after its capping with the TOAB [34].

3.2. Characterization of the biochip

The results of morphological studies carried out on MWCNT/ITO chip, and pDNA/MWCNT/ITO biochip surface are shown in **Figure 2**. The electro–deposition of MWCNT over the WE of MF chip was confirmed via SEM **(Figure 2A)**. Since MWCNT agglomerates were not observed at any site of the electrode, this revealed that at the applied potential, MWCNT chains migrated and were deposited at the ITO electrode and did not coagulate in solution. After incubation of the MWCNT/ITO chip with DNA probe, the observed variation in morphology could be attributed to the immobilization of the pDNA **(Figure 2B)**.

The FT–IR spectrum of MWCNT/ITO chip was recorded in the specular reflection mode and compared with that of pDNA/MWCNT/ITO biochip to confirm the immobilization of the DNA probe **(Figure 3)**. In case of the MWCNT/ITO modified chip, the peaks observed at 1706 and 1556 cm^{-1} in the IR spectrum of MWCNT corresponded to the presence of carboxyl and carboxylate groups, respectively, while the peak at 1182 cm^{-1} related to the C–O bond **(Figure 3A)** [35]. The peak at 3300 cm^{-1} was assigned to the O–H stretch from carboxyl groups while the peak at 2346 cm^{-1} was associated with the O−H stretch from strong hydrogen–bonded –COOH and it became less intense after immobilization of the pDNA. The appearance of these characteristic peaks confirmed the deposition of carboxyl functionalized MWCNT on the ITO surface of the chip. After immobilization of the pDNA onto the MWCNT/ITO chip, a significant change in the FTIR spectrum was observed **(Figure 3B)**. The appearance of the medium intensity peak at 1088 cm^{-1} ascribed to symmetric stretch vibration of phosphate functional groups (PO_2–O–CH_2) was correlated to the presence of phosphodiester backbone. The peak at 1748 cm^{-1} and 1446 cm^{-1}, indicated the presence of ketones in the nucleobases and the C–C stretch (in–ring) in aromatic nucleobases, respectively. The observed shift of the peak from 1706 to 1668 cm^{-1} for C=O stretch was attributed to the formation of 2° amide (amide I band) and the peak at 1550 cm^{-1} was assigned to either carboxylate groups on MWCNT or CN stretching (Amide II). The peak at 3066 cm^{-1} was due to aromatic C–H stretch of nucleobases. The high-intensity peak at 3303 cm^{-1} was assigned to NH stretching (amide A) along with O–H stretch from carboxyl groups. The presence of these additional peaks indicated the successful immobilization of the

ACCEPTED MANUSCRIPT

probe onto the MWCNT/ITO electrode surface of the chip. The results have been summarized in supplementary information file **(Table ST1)**.

3.3. Electrochemical evaluation of the chip and biochip

In order to investigate the biosensing characteristics of the fabricated MF biochip, electrochemical impedance spectroscopic (EIS) technique was employed. The observed dominant effect of the EIS based biosensor was due to the change in electrode/electrolyte interfacial properties in response to the application of a small alternating current signal as a function of frequency [36-37]. The Faradic impedance signal obtained for the chip and biochip was investigated at 25°C in the frequency range, 10^{5}–10^{-5} Hz using $[Fe(CN)_6]^{3-/4-}$ as the redox mediator [38]. Since MF devices are known to utilize low sample volumes and provide fast reaction rates due to the smaller diffusion distances, we, therefore, applied a diffusion restriction model [39]. The Nyquist plot for the Faradic impedance spectrum is presented in **Figure 4 (A and B)**. The semicircle region in the plot at higher frequencies is attributed to the electron–transfer limited process, whereas, the linear part in the lower frequency range indicates diffusion–limited electron–transfer process [37, 40].

The modification over the chip surface causes a change in its interfacial property, which is reflected by the change in charge transfer resistance (R_{ct}) value, calculated from the semi–circular diameter of EIS spectrum, that presents the charge transfer kinetics of the redox mediator across the interface [37]. In case of the DNA biosensor, the change in R_{ct} value was perhaps induced either by hybridization or conformational changes of the DNA probe over the electrode surface. **Figure 4A** shows the EIS spectra obtained for MWCNT/ITO chip and (3–aminopropyl)tri methoxy silane (AS) modified ITO chip (AS/ITO) before and after immobilization of pDNA molecules at the buffer flow rate of 1.2 µL min^{-1}. This flow was selected as the value of R_{ct} was found maximum among all other studied flow rates **(Figure S2)** for the MWCNT/ITO chip. The R_{ct} for the MWCNT modified ITO chip was recorded to be 1.10 kΩ **(Figure 4A, curve i)**. The decreased R_{ct} for MWCNT/ITO chip compared to bare ITO was observed **(**1.31 kΩ**; Figure 4A, curve ii)**. This was perhaps because of the highly conducting nature of the carbon nanotubes, which in spite of its electron rich nature; enhanced the electron transfer across the chip/electrolyte interface. The modification of working electrode of the chip with DNA probe resulted in significant increase in the R_{ct} value to 1.42 kΩ **(Figure 4A, curve iii)**. This could be attributed to perturbation of the interfacial electron–transfer rate across the chip/electrolyte interface due to non–conducting nature of

ACCEPTED MANUSCRIPT

DNA molecules. Furthermore, the enhanced negative charges at the chip surface, arising from phosphate ions of DNA molecules, electrostatically repelled the marker $[Fe(CN)_6]^{3-/4-}$ ions and resulted in increased R_{ct} [38]. The control experiments were carried out by immobilizing pDNA directly over the silanized ITO chip. For silanization of the WE of the chip, the hydrolyzed WE was immersed in 0.2% (v/v) aqueous solution of AS for about 2 h for SAM formation. The chip was then washed with deionized water to remove unbound silane molecules. Subsequently, the amine terminated probe DNA molecules were covalently immobilized onto AS/ITO chip using glutaraldehyde as a cross–linker. For this purpose, AS/ITO chip was activated by incubation in an aqueous glutaraldehyde solution (0.1% v/v) for about 4 h followed by washing with deionized water. For the biochip preparation, the pDNA was incubated with the chip using the above-mentioned protocol. It was found that the R_{ct} value for AS/ITO chip was very high (1.59 kΩ; **Figure 4A**, **curve iv**) as compared to that of MWCNT/ITO chip, which was due to increased resistance offered by AS/ITO chip for interfacial electron–transfer owing to the insulating nature of the silane. On immobilization of the pDNA on AS/ITO chip, an increased R_{ct} value was obtained (1.68 kΩ**; Figure 4A, curve v**). Nevertheless, the observed change was not significant. This indicated that pDNA molecules were immobilized on the AS/ITO chip. Eight sets of experiments were performed under similar conditions for different electrodes, and the corresponding R_{ct} value has been presented in the supplementary information **(Figure S3)**. For each of the electrode, <6.5% deviation was obtained indicating reproducibility of the electrode under provided experimental conditions.

3.4. Selectivity studies of the bioelectrode

Prior to performing the specificity studies, 20 µL of the target DNA solution in TE buffer (pH 8.0) was introduced into the microchannel through the inlet. This solution was then allowed to incubate with biochip for 30 min, after which it was removed, and the channels were evacuated. The 30 min incubation period was provided to complete the hybridization event between complementary base–pairs of target DNA and probe DNA immobilized on the biochip surface. After that, the biochip and microchannels were washed thrice, by repeated insertion and evacuation of TE buffer, so as to remove the non–hybridized DNA. The response characteristics of the pDNA/MWCNT/ITO biochip towards various DNA sequences were monitored via EIS, and the spectra are presented in **Figure 4B**. Incubation of pDNA/MWCNT/ITO biochip **(**1.42 kΩ; **Figure 4B, curve i)** with the complementary DNA (1 µM) resulted in about 3.3–fold enhancement in its R_{ct} **(**4.77 kΩ;

ACCEPTED MANUSCRIPT

Figure 4B, curve v). This significant enhancement revealed the accumulation of more negative charged moieties at biochip surface and were due to DNA probe hybridization with the complementary DNA strands [38-39, 41]. When pDNA/MWCNT/ITO biochip was incubated with the same concentration of the non–complementary DNA, its R_{ct} value did not change significantly **(**1.57 kΩ; **Figure 4B, curve ii)**. The negligible change in R_{ct} value of the biochip clearly ruled out the possibility of hybridization event at the biochip surface. Further, as the pDNA/MWCNT/ITO biochip was incubated with one–base mismatch DNA sequence (1 µM), about a two-fold increase in the R_{ct} value (2.41 kΩ) was observed. The increased R_{ct} value was a clear indication of the pairing of bases of one–base mismatch DNA with the complementary counterparts of the probe DNA **(Figure 4B, curve iii)**. However, the increase in R_{ct} was not as much as in the case when biochip was incubated with complementary DNA (3.5 fold). This could be due to the fact that a single base mismatch perhaps inhibited the hybridization process to occur, because of which, accumulation of the negative charge was less at the biochip surface. Having studied the EIS behavior of biochip with various designed synthetic DNA sequences, these oligonucleotides were introduced into the microchannels. The EIS signal obtained was found to be similar to that obtained for the pDNA/MWCNT/ITO biochip when it was incubated with complementary target DNA sequence **(**4.72 kΩ; **Figure 4B, curve iv)** and the R_{ct} value was also found to be the same. The experiments with mixed DNA samples were repeated with all the eight biochips prepared, and the results are summarized in the supplementary information file **(Figure S4)**. The results of these studies carried out with the synthetic DNA samples suggested that the prepared pDNA/MWCNT/ITO biochip could selectively identify its complementary target (3.5% deviation) among a pool of oligonucleotide sequences.

The results of the specificity studies performed with pDNA/AS/ITO biochip and its comparison with the pDNA/MWCNT/ITO biochip are shown in **Figure 4C**. Eight different sets of experiments were performed, and the variation in R_{ct} values obtained for the biochips during specificity studies are shown by error bars in **Figure 4C**. On incubation with the non–complementary DNA, the signal for pDNA/AS/ITO biochip remained unchanged (1.68 kΩ). However, a comparable increase in R_{ct} value was observed when pDNA/AS/ITO biochip was incubated with complementary (2.58 kΩ) and the one–base mismatch DNA sequences (2.25 kΩ). This revealed that the pDNA/AS/ITO biochip presented poor signal resolution for discrimination of target DNA sequences.

ACCEPTED MANUSCRIPT

3.5. Monitoring of the target DNA detection

The sensitivity of the pDNA/MWCNT/ITO MF biochip was investigated as a function of complementary DNA concentration **(Figure 5A)**. For each concentration, the biochips were incubated with 20 µL of complementary DNA solution. As the complementary DNA concentration was increased, the R_{ct} value of each of the biochip also increased. This could be assigned to the progressive charge accumulation by complementary DNA that was hybridized with the probe DNA, producing a packed layer that effectively decreased the electron transfer rate for the redox probe [38]. The response time of the microfluidics electrode was 60 s, after which the R_{ct} value of the biochip for all the concentrations of complementary DNA did not considerably change. Eight sets of experiments were performed for pDNA/MWCNT/ITO biochip with 1fM, 1nM and 1µM concentrations of complementary DNA and the results are presented in supplementary information **(Figure S5)**. The variation among all the biochips for different concentration was found to be <5.5% indicating reproducibility of the assay for synthetic complementary DNA sequence.

For both the biochips, a linear relationship between the R_{ct} values and the logarithm of the complementary DNA concentrations was obtained. For pDNA/MWCNT/ITO biochip, three–fold rise in R_{ct} value was observed in ten–decade concentration range from 1 fM to 1 µM **(Figure 5B, curve i)**. The regression equation for pDNA/MWCNT/ITO biochip is presented in equation 1 and the regression coefficient for linearity was calculated to be 0.9952.

$$R_{ct}\,[\text{biochip}]\ (k\Omega) = 4.82\ (k\Omega) + 0.31\ (k\Omega)\ [\log\ (\text{complementary DNA concentration})] \quad \textbf{(1)}$$

The results of sensing studies performed with pDNA/AS/ITO biochip revealed that it could be used to detect complementary DNA from 10 pM to 1 µM concentration range which was 4 orders of magnitudes less than the detection made by pDNA/MWCNT/ITO biochip. The regression equation for pDNA/AS/ITO biochip is presented in equation 2 and the regression coefficient for linearity was calculated to be 0.97088.

$$R_{ct}\,[\text{biochip}]\ (k\Omega) = 0.29\ (k\Omega) + 0.14\ (k\Omega)\ [\log\ (\text{complementary DNA concentration})] \quad \textbf{(2)}$$

With pDNA/AS/ITO biochip, a large deviation was observed **(Figure 5B, curve ii)**, indicating its lesser suitability for the sensing of complementary target DNA. The observed poor resolution could be assigned to the signal overlap. As a result, the intermediate concentrations could not be accurately estimated. On the other hand, the pDNA/MWCNT/ITO biochip presented significantly better and uniform resolution of the

ACCEPTED MANUSCRIPT

signal at different concentrations when used for complementary DNA detection **(Figure 5B, curve i)**. This was attributed to the excellent electrical conductivity and electrocatalytic action of CNT that helped in enhancing the electron transfer reactions and improving the sensitivity of the biosensor. The results of the sensing studies revealed that the fabricated MWCNT–based biochip presented wide (ten decades) detection range and improved detection capability of CML-related DNA sequences with low sample consumption compared to other reported electrochemical biosensors **(Table ST2)**.

3.6. Reproducibility of the assay

The reproducibility of the biosensor was calculated using the intra– and inter–assay coefficient of variation (CoV). To carry out the precision studies of the biosensor, two different concentrations of the complementary target DNA (10^{-15} M and 10^{-8} M) were used. The intra–assay CoV was calculated by detecting each sample for five times using five parallel prepared biosensors and was found to be 4.2% and 4.8% for 10^{-15} M and 10^{-8} M of target DNA specific to CML, respectively. Similarly, the inter–assay CoV calculated for 10^{-15} M and 10^{-8} M concentration of target DNA were found to be 5.1% and 3.9%, respectively (data not shown). The stability of MF based DNA sensor was studied with eight different electrodes and all the electrodes were found to retain 90% of its original R_{ct} response after 30 days of storage in 100 mM PBS at 4 °C **(Figure S6)**.

4. Conclusions

We have fabricated an electrochemical microfluidic DNA sensor based on the carboxyl functionalized MWCNT as the transducer surface. The ITO substrate has been patterned via wet chemical etching technique to develop working and counter electrodes. The working electrode has been modified by electrophoretic deposition of MWCNT and subsequent immobilization of DNA probe. The covalently immobilized aminated capture probe has been found to specifically hybridize with its complementary DNA allowing the biosensor to readily detect target oligonucleotide at a concentration as low as 1 fM with a response time of 1 min. The improved linear range and sensitivity of the device has been attributed to the improved loading of DNA due to enhanced surface area of the electrode through modification by MWCNT. The selectivity of the biosensor has been demonstrated by discrimination of single–nucleotide mismatch and non–complementary DNA sequence. The fabricated impedimetric biochip is self–contained, easy–to–operate and hence can be used for

ACCEPTED MANUSCRIPT

POC applications. The efforts should be made to utilize this MF biochip for detection of blood cancer in clinical samples.

Acknowledgements

Authors thank Professor A.K. Mulchandani for providing the microfluidic channels and Dr. Gajjala Sumana (CSIR–NPL, India), Dr. Azahar Ali for interesting discussions relating to the microchip fabrication. A.S. Ghrera acknowledges financial support received from SERB (DST), India under Young Scientist project (Grant No. YSS/2015/001330) and C.M. Pandey acknowledges the financial support received from DST, India under DST-INSPIRE Faculty project (Grant No. DST/INSPIRE/04/2015/000932).

ACCEPTED MANUSCRIPT

ACCEPTED MANUSCRIPT

References

1. J. Zhang, Y. Wan, L. Wang, S. Song, C. Fan, The electrochemical DNA biosensor, Prog. Chem. 19 (2007) 1576-1584.
2. F.S. Ligler, K.E. Sapsford, J.P. Golden, L.C. Shriver-Lake, C.R. Taitt, M.A. Dyer, S. Barone, C.J. Myatt, The array biosensor: Portable, automated systems, Anal. Sci. 23 (2007) 5-10.
3. C. M. Pandey, S. Augustine, S. Kumar, S. Kumar, S. Nara, S. Srivastava, B. D. Malhotra, Microfluidics based point-of-care diagnostics. Biotechnol. J. 13 (2018) 1-11.
4. G. Lee, J. Lee, J. Kim, H. S. Choi, J. Kim, S. Lee, H. Lee, Single microfluidic electrochemical sensor system for simultaneous multi-pulmonary hypertension biomarker analyses. Sci. Rep. 7 (2017) 1-8.
5. Y. Zhao, H. Zhang, X. Wu, Z. Liu, J. Wang, Progress of the study on DNA electrochemical biosensor, J. Biomed. Eng. 30 (2013) 208-212.
6. H.J. Lee, S.W. Han, U.S. Chung, W.G. Koh, Application of cellular micropatterns to miniaturized cell-based biosensor, Biomed. Eng. Lett. 3 (2013) 117-130.
7. A.S. Ghrera, M.K. Pandey, B.D. Malhotra, Quantum dot monolayer for surface plasmon resonance signal enhancement and DNA hybridization detection, Biosens. Bioelectron. 80 (2016) 477-482.
8. A. Harper, M.R. Anderson, Electrochemical glucose sensors-developments using electrostatic assembly and carbon nanotubes for biosensor construction, Sensors 10 (2010) 8248-8274.
9. Z. Yan, H. Li, DNA electrochemical biosensor based on graphene-functionalized composite materials, Chemistry Bulletin/ Huaxue Tongbao 77 (2014) 839-847.
10. S.H. Yeom, B.H. Kang, K.J. Kim, S.W. Kang, Nanostructures in biosensor-a review, Front. Bioscience 16 (2011) 997-1023.
11. V.N. Popov, Carbon nanotubes: Properties and application, Mat. Sci. Eng. R-Rep. 43 (2004) 61-102.
12. M. Das, P. Goswami, Direct electrochemistry of alcohol oxidase using multiwalled carbon nanotube as electroactive matrix for biosensor application, Bioelectrochemistry 89 (2013) 19-25.
13. M. Liu, G. Zhao, Y. Tang, H. Shi, N. Yang, Direct electrochemistry of hemoglobin on vertically aligned carbon hybrid TiO2 nanotubes and its highly sensitive biosensor performance, Chinese J. Chem. 31 (2013) 215-220.
14. M.V. Jose, S. Marx, H. Murata, R.R. Koepsel, A.J. Russell, Direct electron transfer in a mediator-free glucose oxidase-based carbon nanotube-coated biosensor, Carbon 50 (2012) 4010-4020.
15. W. Zheng, Q. Li, Y. Yan, L. Su, L. Mao, Functionalization of carbon nanotubes for direct electrochemistry of horseradish peroxidase, Indian J. Chem. A 44 (2005) 950-955.
16. T. Coccini, E. Roda, D.A. Sarigiannis, P. Mustarelli, E. Quartarone, A. Profumo, L. Manzo, Effects of water-soluble functionalized multi-walled carbon nanotubes examined by different cytotoxicity methods in human astrocyte D384 and lung A549 cells, Toxicology 269 (2010) 41-53.
17. A. Kumar, C.H. Lee, Synthesis and Biomedical Applications of Graphene: Present and Future Trends, Chapter 3, Advances in Graphene Science, 2013.
18. A. Erdem, P. Papakonstantinou, H. Murphy, M. McMullan, H. Karadeniz, S. Sharma, Streptavidin modified carbon nanotube based graphite electrode for label-free sequence specific DNA detection, Electroanal. 22 (2010) 611-617.

ACCEPTED MANUSCRIPT

19. M. Pedano, amp, x, L. a, G.A. Rivas, Adsorption and electrooxidation of nucleic acids at carbon nanotubes paste electrodes, Electrochem. Commun. 6 (2004) 10-16.
20. J. Wang, M. Li, Z. Shi, N. Li, Z. Gu, Electrochemistry of DNA at Single-Wall Carbon Nanotubes, Electroanal. 16 (2004) 140-144.
21. L. Fu, A.M. Yu, Carbon nanotubes based thin films: Fabrication, characterization and applications, Rev. Adv. Mater. Sci. 36 (2014) 40-61.
22. A.R. Boccaccini, S. Keim, R. Ma, Y. Li, I. Zhitomirsky, Electrophoretic deposition of biomaterials, J. R. Soc. Interface 7 (2010) S581-S613.
23. A.R. Boccaccini, J. Cho, J.A. Roether, B.J.C. Thomas, E. Jane Minay, M.S.P. Shaffer, Electrophoretic deposition of carbon nanotubes, Carbon 44 (2006) 3149-3160.
24. A. Sharma, C.M. Pandey, G. Sumana, U. Soni, S. Sapra, A.K. Srivastava, T. Chatterjee, B.D. Malhotra, Chitosan encapsulated quantum dots platform for leukemia detection, Biosens. Bioelectron. 38 (2012) 107-113.
25. A. Sharma, G. Sumana, S. Sapra, B.D. Malhotra, Quantum Dots Self Assembly Based Interface for Blood Cancer Detection, Langmuir 29 (2013) 8753-8762.
26. J.M. Goldman, J.V. Melo, BCR-ABL in chronic myelogenous leukemia - How does it work?, Acta Haematol. 119 (2008) 212-217.
27. A. Sharma, C.M. Pandey, Z. Matharu, U. Soni, S. Sapra, G. Sumana, M.K. Pandey, T. Chatterjee, B.D. Malhotra, Nanopatterned Cadmium Selenide Langmuir–Blodgett Platform for Leukemia Detection, Anal. Chem. 84 (2012) 3082-3089.
28. W. Al Achkar, A. Wafa, H. Mkrtchyan, F. Moassass, L. Thomas, A rare case of philadelphia chromosome-positive chronic myelogenous leukemia with inversion in chromosome 9 and t(10;17), Oncol. Lett. 1 (2010) 793-795.
29. R.B. Mathur, B.P. Singh, P.K. Tiwari, T.K. Gupta, V. Choudhary, Enhancement in the thermomechanical properties of carbon fibre–carbon nanotubes–epoxy hybrid composites, Int. J. Nanotechnol. 9 (2012) 1040-1049.
30. D. Chunsheng, P. Ning, High power density supercapacitor electrodes of carbon nanotube films by electrophoretic deposition, Nanotechnology 17 (2006) 5314.
31. A.S. Ghrera, C.M. Pandey, M.A. Ali, B.D. Malhotra, Quantum dot-based microfluidic biosensor for cancer detection, Appl. Phys. Lett. 106 (2015) 193703.
32. S. Srivastava, M.A. Ali, P.R. Solanki, P.M. Chavhan, M.K. Pandey, A. Mulchandani, A. Srivastava, B.D. Malhotra, Mediator-free microfluidics biosensor based on titania-zirconia nanocomposite for urea detection, RSC Adv. 3 (2013) 228-235.
33. M.J. Fischer, Amine Coupling Through EDC/NHS: A Practical Approach, Methods Mol. Biol. 627 (2010) 55-73.
34. S. Verma, G. Bhanjana, N. Dilbaghi, S. Kumar, A. Umar, Urea biosensor based on zinc oxide/multi-walled carbon nanotubes/chitosan nanocomposite thin films, Sensor Lett. 12 (2014) 50-55.
35. H.Z. Zhao, Q. Du, Z.S. Li, Q.Z. Yang, Mechanisms for the Direct Electron Transfer of Cytochrome c Induced by Multi-Walled Carbon Nanotubes, Sensors 12 (2012) 10450-10462.
36. B.Y. Chang, S.M. Park, Electrochemical Impedance Spectroscopy, Annu. Rev. Anal. Chem. 3 (2010) 207-229.
37. M. Moisel, M.A.F.L.de Mele, W.D. Müller, Biomaterial Interface Investigated by Electrochemical Impedance Spectroscopy, Adv. Eng. Mater. 10 (2008).
38. C.M. Pandey, G. Sumana, B.D. Malhotra, Microstructured Cystine Dendrites-Based Impedimetric Sensor for Nucleic Acid Detection, Biomacromolecules 12 (2011) 2925-2932.

ACCEPTED MANUSCRIPT

39. H. Ben-Yoav, P.H. Dykstra, W.E. Bentley, R. Ghodssi, A microfluidic-based electrochemical biochip for label-free diffusion-restricted DNA hybridization analysis, Biosens. Bioelectron. 38 (2012) 114-120.
40. J. Bisquert, A. Compte, Theory of the electrochemical impedance of anomalous diffusion, J. Electroanal.Chem. 499 (2001) 112-120.
41. L. Santiago-Rodríguez, G. Sánchez-Pomales, C.R. Cabrera, Single-Walled Carbon Nanotubes Modified Gold Electrodes as an Impedimetric DNA Sensor, Electroanal. 22 (2010) 399-405.

ACCEPTED MANUSCRIPT

ACCEPTED MANUSCRIPT

Author Biographies

Aditya Sharma Ghrera completed her Ph.D. in Chemistry (2015) from Indian Institute of Technology Delhi, India, in collaboration with National Physical Laboratory, Delhi, as a CSIR- Junior and Senior research fellow. She is the recipient of the prestigious fellowship from Council of Scientific and Industrial Research, India, for pursuing doctoral studies and has been awarded the young scientist project (2016) from Science and Engineering Research Board (DST) to pursue her post-PhD research. She has published 7 research papers, all in SCI-indexed, peer reviewed journals. Her areas of research interest include Biosensor development, Lateral flow assay, Cancer and Urinary tract infection diagnostics, Langmuir–Blodgett monolayers, and Microfluidics devices. Presently, she is placed at The Northcap University, India as Assistant Professor.

Chandra Mouli Pandey received his PhD (Chemistry; 2015) from Banaras Hindu University, Varanasi, India, in collaboration with National Physical Laboratory, New Delhi, India. He is presently working as DST-INSPIRE Faculty in Department of Chemistry, Delhi Technological University, Delhi, on the development of microfludics based biosensors for cancer biomarker detection. He has published more than 20 research papers in international journals and has recently authored a book entitled 'Biosensors: Fundamentals and Applications'. His main interest of research is development of biosensor for health care based on nano-materials, conducting polymers, self-assembled monolayers and bio-nanocomposites.

Bansi Dhar Malhotra received his PhD from the University of Delhi, Delhi in 1980. He has published more than 300 papers in refereed international journals, has filed 13 patents, and has recently co-authored text books on 'Nanomaterials for Biosensors: Fundamentals and Applications' and 'Biosensors: Fundamentals and Applications'. He is a recipient of the National Research Development Corporation Award 2005 for invention on 'Blood Glucose Biochemical Analyzer' and is a Fellow of the Indian National Science Academy, the National Academy of Sciences, India and Academician of Asia Pacific Academy of Materials. His current research activities include Nanobiomaterials, Biosensors, Bio-fuel cells, Ordered Molecular Assemblies, Conducting Polymers, Langmuir-Blodgett Films, Self-assembled Monolayers, Nano-Biotechnology, Biomedical Engineering and Biomolecular Electronics.

ACCEPTED MANUSCRIPT

He is currently a Professor at the Department of Biotechnology, Delhi Technological University, Delhi, India.

ACCEPTED MANUSCRIPT

ACCEPTED MANUSCRIPT

Figure Captions

Figure 1: Stepwise illustration of microfluidic biochip fabrication for electrochemical detection of DNA hybridization. **(A)** Exfoliation of MWCNT via sonication with TOAB, **(B)** micropatterning of the ITO substrate and fabrication of microchannels, **(C)** EPD of MWCNT over the working electrode of the chip and **(D)** immobilization of DNA probe on the surface of MWCNT/ITO chip.

Figure 2: SEM image for **(A)** MWCNT/ITO chip and **(B)** pDNA/MWCNT/ITO biochip.

Figure 3: FTIR spectra of **(A)** MWCNT/ITO chip and **(B)** pDNA/MWCNT/ITO biochip.

Figure 4: (A) Nyquist diagram for the Faradic impedance of **(i)** MWCNT/ITO chip, **(ii)** ITO chip **(iii)** pDNA/MWCNT/ITO biochip, **(iv)** AS/ITO chip and **(v)** pDNA/AS/ITO biochip

(B) EIS response of **(i)** pDNA/MWCNT/ITO biochip with respect to 1 µM concentration of **(ii)** non–complementary DNA, **(iii)** one–base mismatch DNA, **(iv)** synthetic DNA mixture and **(v)** complementary DNA.

(C) Bar diagram showing comparison of EIS response for pDNA/MWCNT/ITO and pDNA/AS/ITO biochips towards designed synthetic DNA sequences. Error bar represents variation in R_{ct} values obtained for eight independent sets of experiments.

Figure 5: (A) EIS response of the pDNA/MWCNT/ITO biochip as a function of complementary DNA concentrations (1 fM to 1 µM).

(B) Plot of the variation in R_{ct} of **(i)** pDNA/MWCNT/ITO and **(ii)** pDNA/AS/ITO biochips as a function of target DNA concentrations on logarithm scale. Error bars represent deviation of data points from linearity.

ACCEPTED MANUSCRIPT

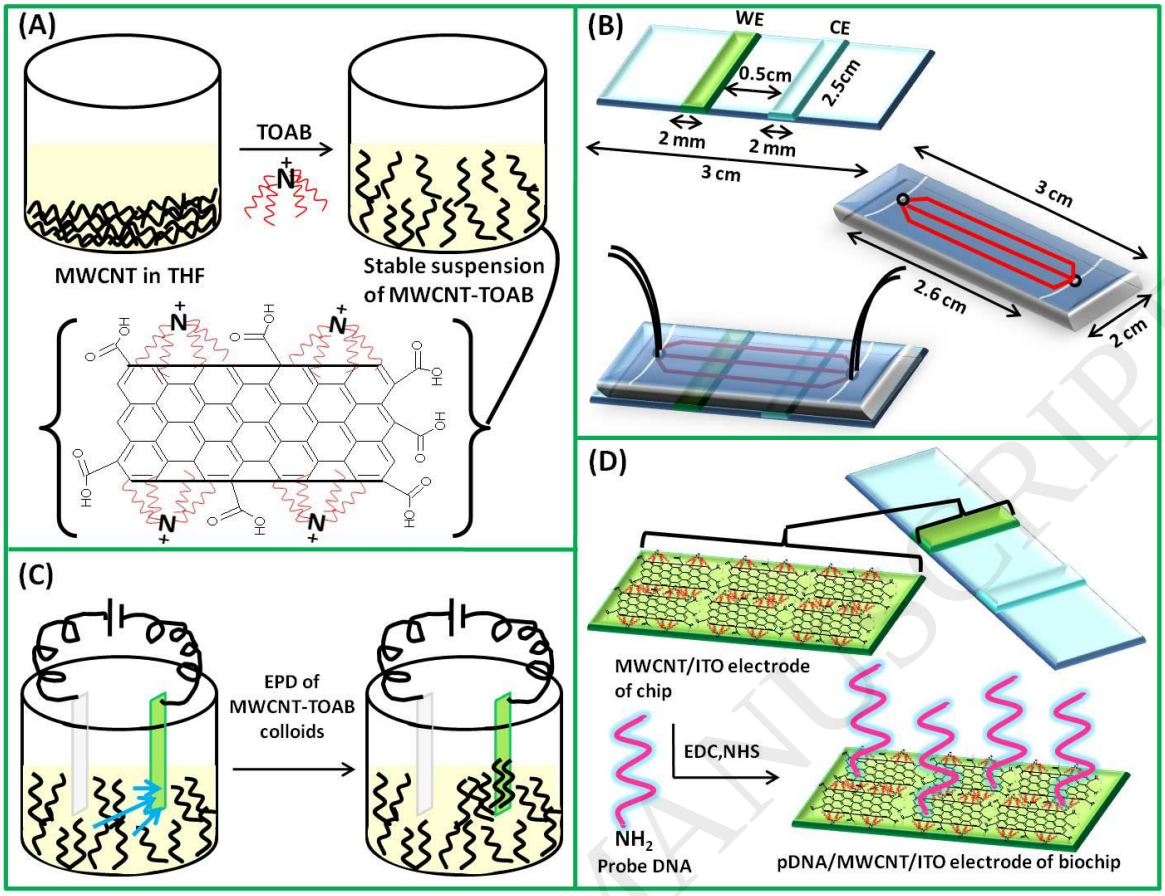


FIG 1

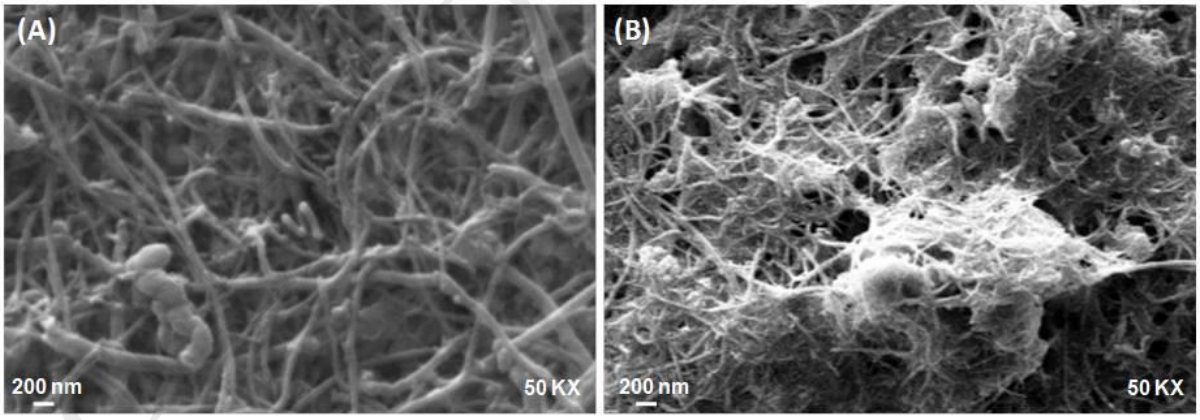


FIG 2

ACCEPTED MANUSCRIPT

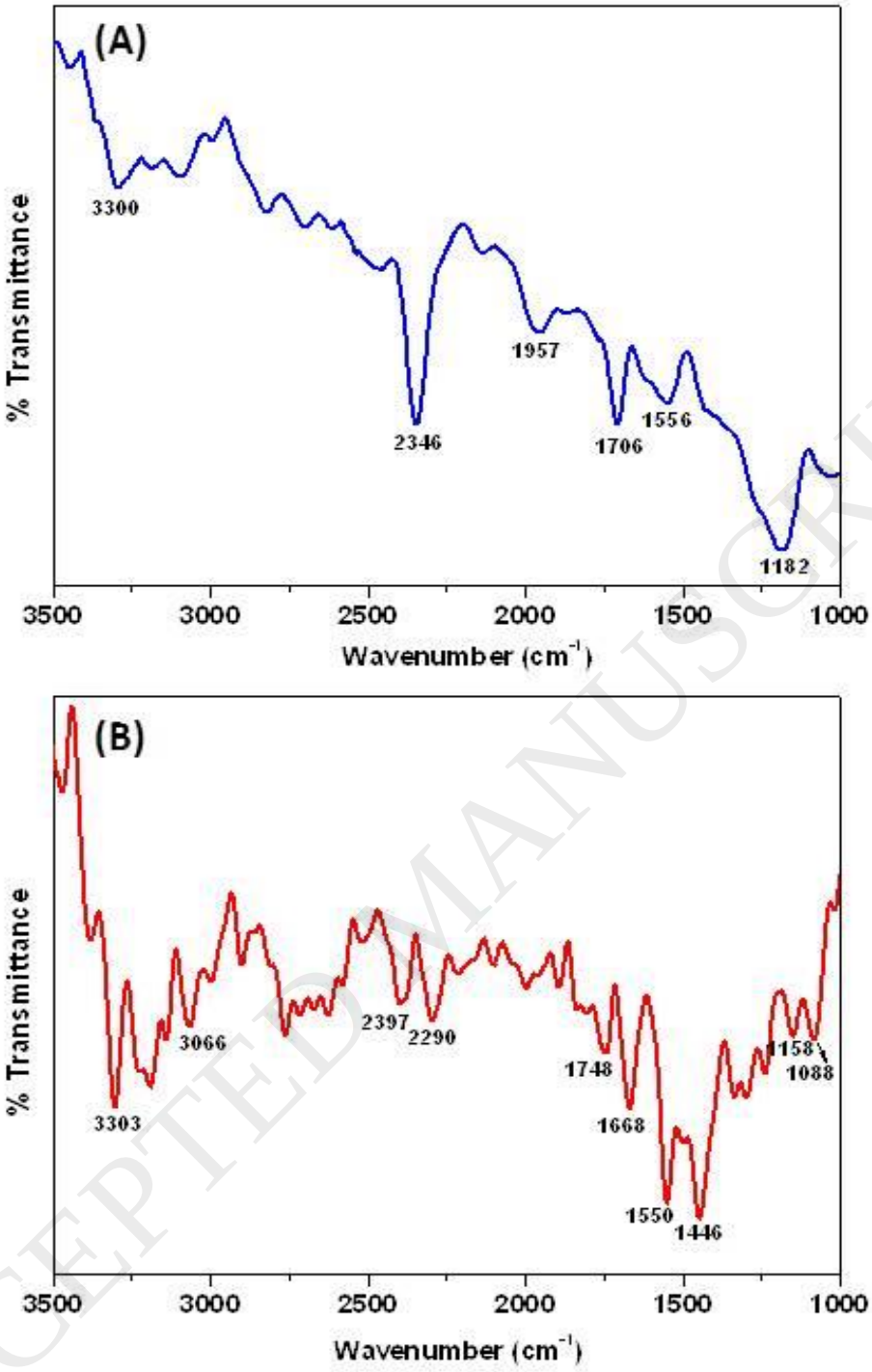
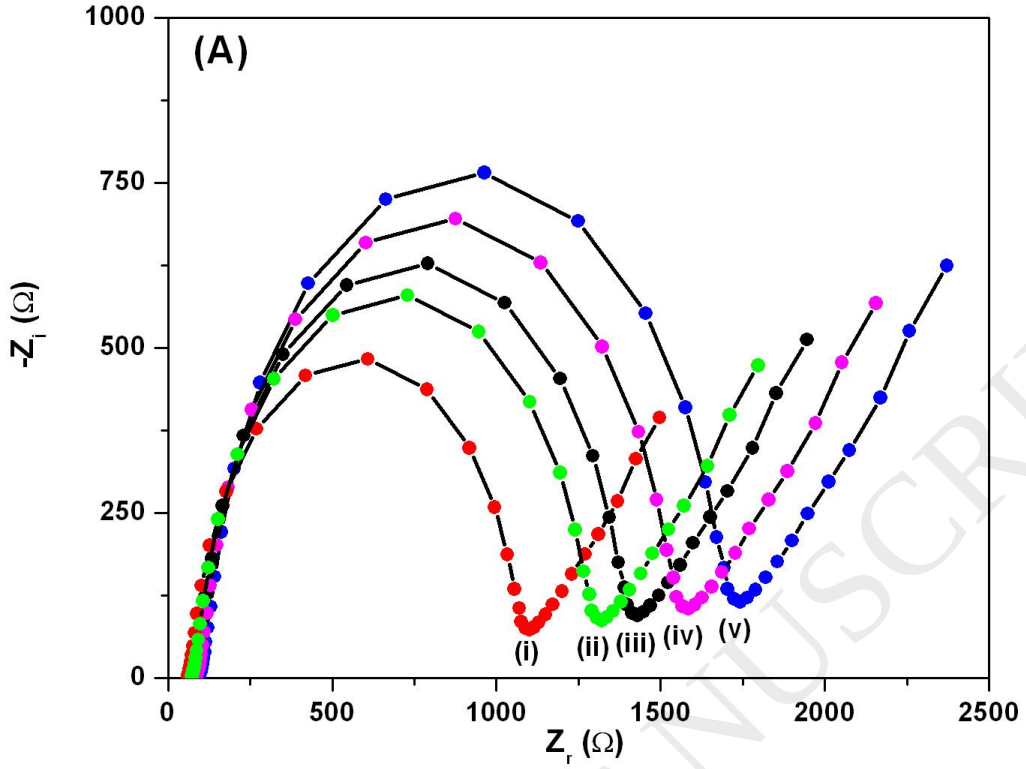
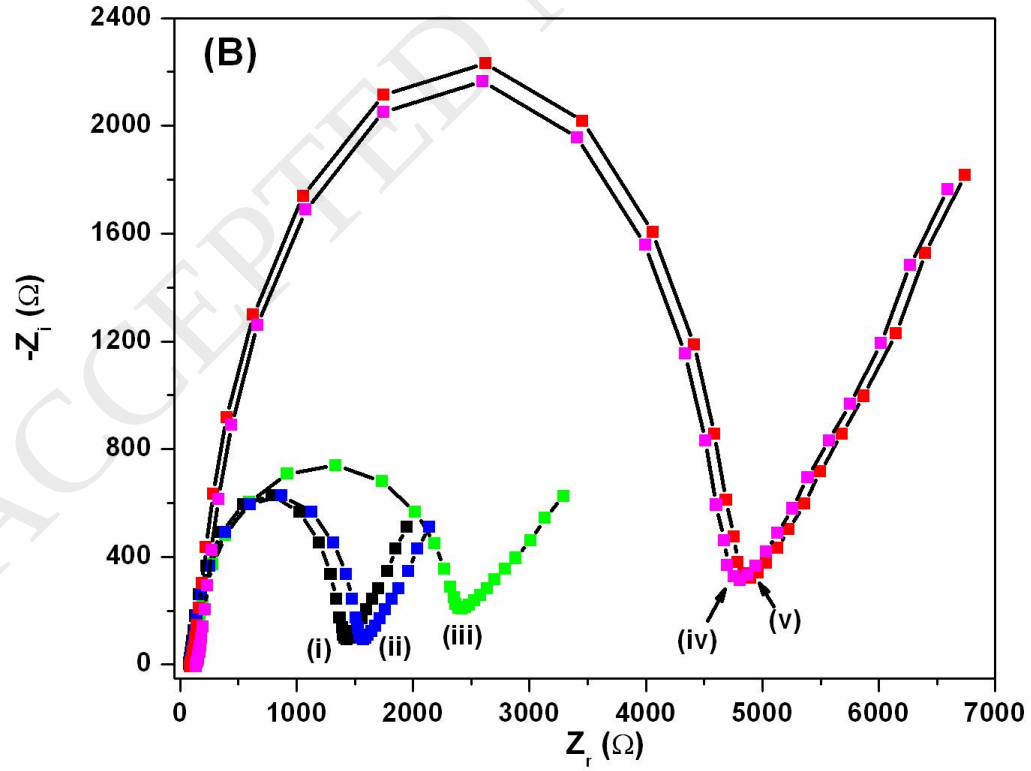


FIG 3

ACCEPTED MANUSCRIPT





ACCEPTED MANUSCRIPT

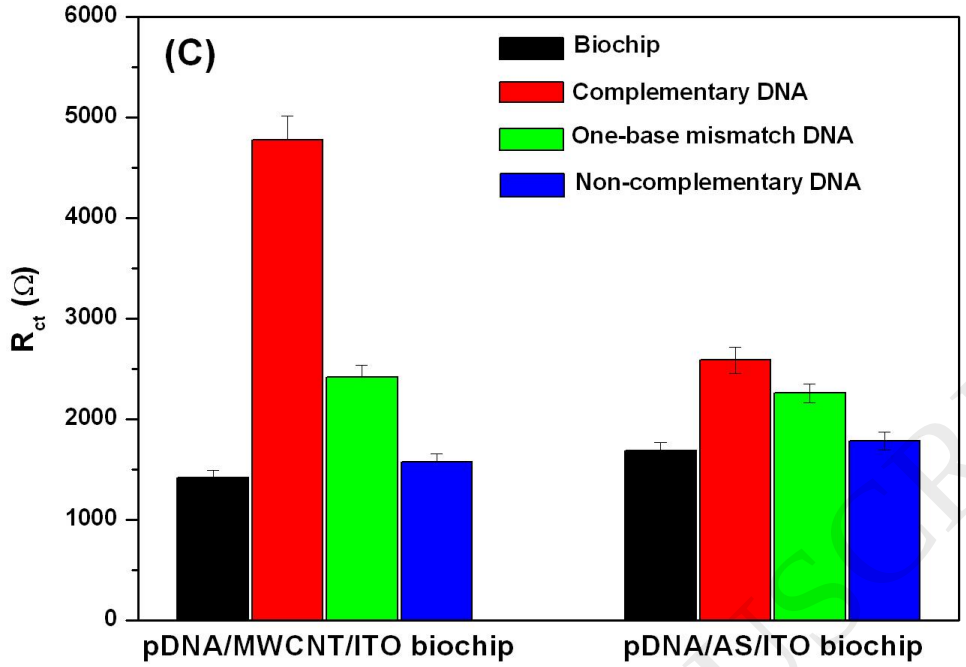
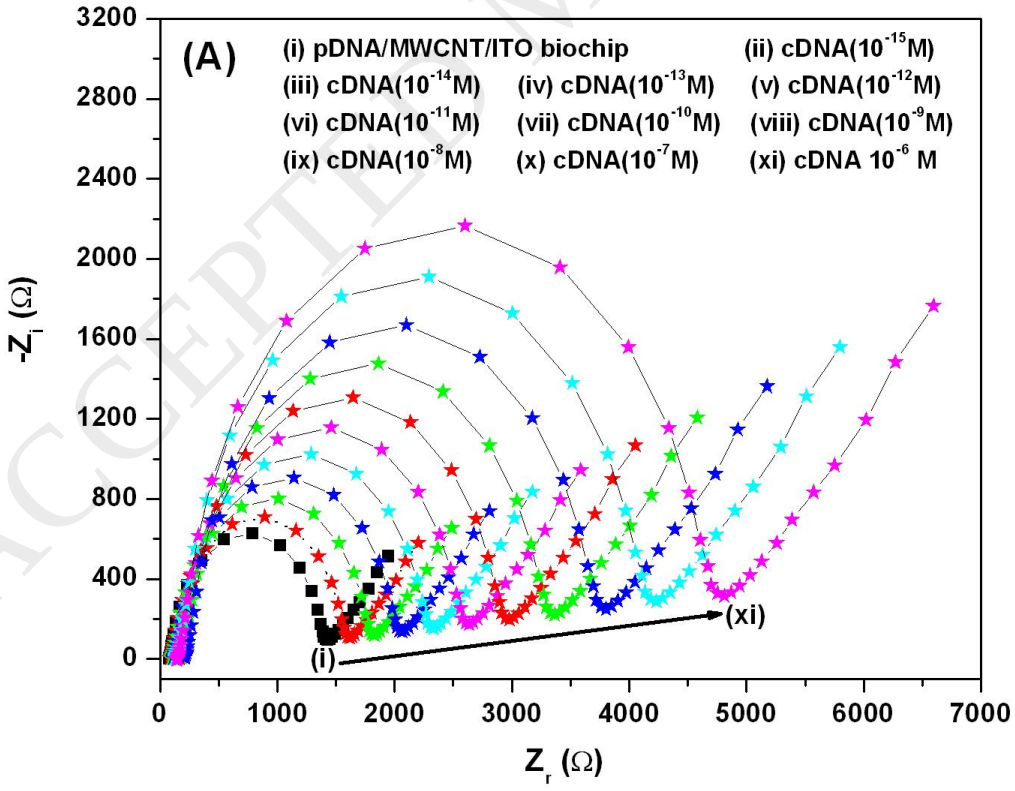


FIG 4



ACCEPTED MANUSCRIPT

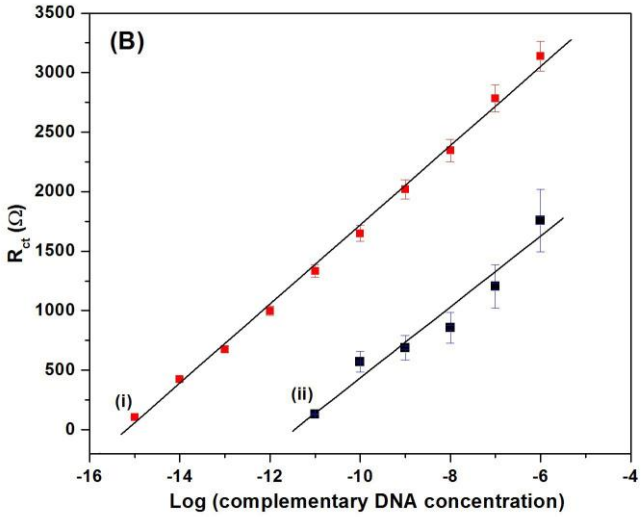


FIG 5

ACCEPTED MANUSCRIPT

Novel High speed Vedic Multiplier proposal incorporating Adder based on Quaternary Signed Digit number system

Preyesh Dalmia, Vikas, Abhinav Parashar, Akshi Tomar and Dr. Neeta Pandey
Dept. of Electronics and Communication Engineering
Delhi Technological University (formerly Delhi College of Engineering)
New Delhi, India
{preyeshdalmia, vikas.dce2016, abhinavparashar.1810, akshitomar274}@gmail.com, neetapandey@dce.ac.in

***Abstract*— This paper presents a high-speed Vedic multiplier based on the Urdhva Tiryagbhyam sutra of Vedic mathematics that incorporates a novel adder based on Quaternary Signed digit number system. Three operations are inherent in multiplication: partial products generation, partial products reduction and addition. A fast adder architecture therefore greatly enhances the speed of the overall process. A Quaternary logic adder architecture is proposed that works on a hybrid of binary and quaternary number systems. A given binary string is first divided into quaternary digits of 2 bits each followed by parallel addition reducing the carry propagation delay. The design doesn't require a radix conversion module as the sum is directly generated in binary using the novel concept of an adjusting bit. The proposed multiplier design is compared with a Vedic multiplier based on multi voltage or multi value logic [MVL], Vedic Multiplier that incorporates a QSD adder with a conversion module for quaternary to binary conversion, Vedic multiplier that uses Carry Select Adder and a commonly used fast multiplication mechanism such as Booth multiplier. All these designs have been developed using Verilog HDL and synthesized by Synopsys Design Compiler. They have been realized using the open source NAN gate 15nm technology library. The proposal shows a maximum of 88.75% speed improvement with respect to Multi Value logic based 128x128 Vedic multiplier while the minimum is 17.47%.**

Keywords-Multiplier; Quaternary Signed Digit adder [QSD]; Urdhva Tiryagbhyam; Vedic Mathematics

I. INTRODUCTION

One of the primary features that help us determine the computational power of a processor is the speed of its arithmetic unit. An important function of an arithmetic block is multiplication because, in most mathematical computations, it forms the bulk of the execution time. Thus, the development of a fast multiplier has been a key research area for a long time.

Some of the important algorithms proposed for fast multiplication in literature are Array, Booth and Wallace multipliers [1]-[5]. Vedic Mathematics [6, 7] is a methodology of arithmetic rules that allows for more efficient implementations regarding speed. Multiplication in this methodology consists of three steps: generation of partial products, reduction of partial products, and finally carry-propagate addition. Multiplier design based on Vedic mathematics has many advantages as the partial products and sums are generated in one step, which reduces the carry propagation from LSB to MSB. This feature helps in scaling the design for larger inputs without proportionally increasing the propagation delay as all smaller blocks of the design work concurrently. References [8], [9] and [11] compared Vedic Multiplier with other multiplier architectures namely Booth, Array and Wallace on the basis of delay and power consumption. Vedic multiplier showed improvements in both the parameters over other architectures. Thus, many implementations of multiplication algorithms based on Vedic sutras have been reported in literature [10]-[12]. Vedic multiplier schemes proposed in literature are based on Urdhva Tiryagbhyam and Nikhilam sutras of Vedic Mathematics. As Nikhilam sutra is only efficient for inputs that are close to the power of 10, in this paper a design to perform high-speed multiplication based on the Urdhva Tiryagbhyam sutra of Vedic Mathematics which is generalized method for all numbers, has been presented.

The final step, carry-propagate addition, requires a fast adder scheme because it forms a part of the critical path. A variety of adder schemes have been proposed in literature to optimize the performance of Vedic multiplier [13]. Adder based on QSD shows an improvement in speed over other state of the art adders [14, 15]. Earlier implementations of QSD adder were based on Multi Voltage or Multi Value Logic (MVL) [16]. The difficulty in application of quaternary addition outside MVL (Multi Voltage logic) is that, the adder is only a small unit of the design whose outputs will needed to be converted back to binary for further processing. However, use of a conversion module undermines the advantages gained in speed by using QSD. In this paper, a novel implementation of an adder based on QSD is proposed, which reduces the carry propagation delay in the design by making use of carry free arithmetic. The proposed adder design works on a hybrid of binary and quaternary number systems wherein the sum is directly generated in binary using the concept of an adjusting bit, eliminating the conversion module. The design can be scaled to larger bit implementations such as 32, 64, 128 or more with minimal increase in propagation delay owing to the parallelism prevalent in the design. We have compared our design with a Vedic multiplier based on MVL logic that uses a ripple carry adder [16], Vedic Multiplier that incorporates a QSD adder and a conversion module for quaternary to binary conversion, Vedic multiplier that uses state of the art fast adder scheme such as Carry select adder [17] and a commonly used fast multiplication mechanism such as Booth multiplier [18], to prove the feasibility of our design across important comparison points.

This paper is organized as follows. Section II describes the Basic Terminology associated with our design. Section III describes the Proposed Multiplier architecture based on Vedic

multiplication and Quaternary addition. Section IV comprises of Result in which device utilization summary and computational path delay obtained for the proposed Vedic multiplier (after synthesis) is discussed and Section V consists of Conclusion.

II. Basic Terminology

A. Urdhva Tiryagbhyam (UT) Sutra

The UT sutra is an ancient Vedic Mathematics sutra that can be used for multiplication of two numbers in any number system. It is based on "Vertical and Crosswise" multiplication. A 2x2 multiplier based on UT sutra is depicted in Fig. 1 and Fig. 2, where X and Y represent inputs while Z corresponds to output. Stepwise procedure is outlined below.

Step1: Vertical Multiplication: The least significant digits of the multiplicand and the multiplier are multiplied, as in (1).

$$Z0=X0.Y0 \quad (1)$$

Step2: Crosswise Multiplication and Addition: Z1, in (2), is obtained by cross multiplying X1 and Y0, and Y1 and X0 and subsequently adding the two products. In this stage a carry C1, as in (3), might be generated, that is propagated to the next step.

$$Z1= (X0.Y1) \oplus (X1.Y0) \quad (2)$$

$$C1=X0.X1.Y0.Y1 \quad (3)$$

Step3: Vertical Multiplication and Addition: The most significant digits of the multiplicand and the multiplier are multiplied, and the product is added with the carry of the previous step to obtain Z3 and Z2, as in (4) and (5) respectively.

$$Z2= (X1.Y1) \oplus C1 \quad (4)$$

$$Z3= X0.X1.Y0.Y1 \quad (5)$$

The final result is concatenation of Z3, Z2, Z1 and Z0.

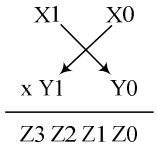


Fig. 1. Vertical and Crosswise multiplication

The logic circuit for 2x2 UT multiplier is shown Fig. 2.

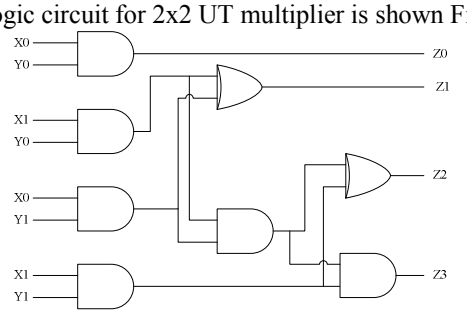


Fig. 2. 2x2 UT multiplier

B. Quaternary Signed Digit (QSD number system)

The QSD is a radix-4 number system that provides the benefit of faster arithmetic calculations over binary computation, as it eliminates rippling of carry during addition. Every number in QSD can be represented using digits from the set {-3,-2,-1, 0, 1, 2, 3}. Being a higher radix number system it utilizes less number of gates and hence saves on time and reduces circuit complexity. The stages involved in addition of two numbers in QSD are:

Stage1: Generation of intermediate carry and sum: When two digits are added in QSD number system, the resulting sum ranges between -6 to +6. Numbers with magnitude higher than 3 are represented by multiple digits with least significant digit representing sum and the next digit corresponds to carry. Also, every number in QSD can have multiple representations [14, 15]. The representation is chosen such that the magnitude of sum digit is 2 or less than 2 and the magnitude of carry digit is 1 or less than 1, the reason for which is explained in the next stage.

Stage2: The intermediate sum and carry have a limit fixed on their magnitude because this allows carry free addition in the second step. The result can be obtained directly by adding the sum digit with the carry of the lower significant digit [14, 15].

III. Proposed Design

A. 4x4 Multiplier

Block diagram of a 4x4 multiplier is shown in Fig. 3. In this multiplier, four 2x2 multipliers are arranged systematically. Each multiplier accepts four input bits; two bits from multiplicand and other two bits from multiplier. Addition of partial products is done using two four bit Quaternary adders, a two-bit adder and a half adder. The final result is obtained by concatenating the least significant two bits of the first multiplier, four sum bits of the second four-bit Quaternary adder and the sum bits of two-bit adder.

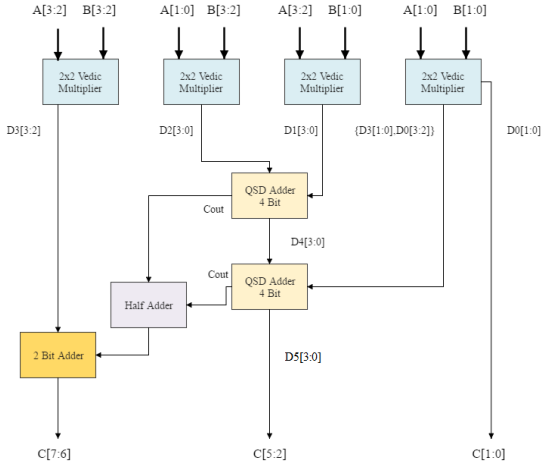


Fig. 3. Proposed 4x4 Multiplier

Table I shows all intermediate and final results involved in the multiplication process of two binary numbers, A = $(1111)_2$ and B = $(1001)_2$.

The data flow in the proposed 4x4 multiplier is given below:

1) A[1:0] and B[1:0], A[3:2] and B[1:0], A[1:0] and B[3:2], and A[3:2] and B[3:2] are multiplied by 2x2 Vedic multipliers, giving output D0[3:0], D1[3:0], D2[3:0] and D3[3:0] respectively.

2) D1 [3:0] and D2[3:0] are added by the proposed 4 bit QSD adder, giving D4[3:0] and a carry out as the outputs.

3) D4[3:0] and {D3[1:0], D0[3:2]} are added by the second 4 bit QSD adder, giving D5[3:0] and a carry out as the outputs.

4) The half adder is used to add the carry outs of the QSD adders. The output obtained is fed to the 2 Bit Adder along with D3[3:2].

5) The result, C, in binary is obtained by concatenation of output of 2 Bit Adder, D5[3:0] and D0[1:0].

The proposed design can be extended to multiply both negative and positive integers by an addition of a sign bit in both inputs. An XOR logic can then be used to compute the sign bit of the final output. The multiplication of the magnitudes will proceed simultaneously in a similar manner to the example described above.

TABLE I. MULTIPLICATION RESULT OF TWO 4 BIT BINARY NUMBERS USING THE PROPOSED DESIGN

	Binary equivalent	**Decimal equivalent**	**Explanation**
A	$(1111)_2$	15	Input 1
B	$(1001)_2$	9	Input 2
D0	$(0011)_2$	3	Output of 2x2 Vedic Multiplier 1
D1	$(0011)_2$	3	Output of 2x2 Vedic Multiplier 2
D2	$(0110)_2$	6	Output of 2x2 Vedic Multiplier 3
D3	$(0110)_2$	6	Output of 2x2 Vedic Multiplier 4
D4	$(01001)_2$	9	Output of 4 bit QSD adder 1 (D1+D2)
D5	$(10001)_2$	17	Output of 4 bit QSD adder 2 (D4 +{D3[1:0],D0[3:2]})
C[1:0]	$(11)_2$	3	D0[1:0]
C[5:2]	$(0001)_2$	1	D5[3:0]
C[7:6]	$(10)_2$	2	Output of 2 Bit Adder (D3[3:2]+D4[4]+D5[4])
C[7:0]	$(10000111)_2$	135	Final Result

B. 32x32 multiplier

The 4x4 multiplier design can be scaled to multiply larger numbers as shown in Fig. 4, where the design is scaled up for a 32 bit multiplier.

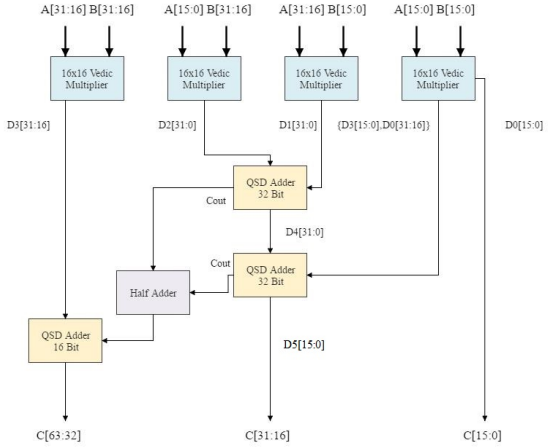


Fig. 4. Proposed 32x32 Multiplier

C. Proposed adder design based on QSD

In this paper, a novel idea of an adder, based on QSD (Quaternary Signed Digit) is proposed. The algorithm for the proposed adder uses a hybrid of quaternary and binary number systems. The outputs from smaller multipliers are obtained as binary strings. Inside the addition module, this string is broken into quaternary digits of two bits each. Addition using QSD allows us to reduce the carry propagation delay by making use of carry free arithmetic i.e. the carry doesn't ripple past the subsequent quaternary digit. Especially for higher bit input strings this method is extremely efficient.

The difficulty in application of quaternary addition outside MVL (Multi Voltage logic) is that the least significant 2 bits of the binary representation of the quaternary digits can't be directly concatenated to form an output binary string for every case as depicted in Table II. Each string would have to be read individually and a conversion module that converts quaternary to binary would have to be employed. To overcome this limitation, the concept of an adjusting bit has been introduced.

TABLE II. CONVERSION OF A QUATERNARY NUMBER TO BINARY NUMBER SYSTEM

Quaternary number A	2 1 → 010_001	Quaternary number B	2 $\bar{1}$ → 010_111
Binary equivalent of A	1001	Incorrect Binary equivalent of B	1011
Decimal equivalent of A	9	Incorrect Decimal equivalent of B	11

The Intermediate sum lies in the range [0, 6], as the operands are unsigned numbers. From [16], for quaternary addition to be carry free beyond the first stage, the intermediate sum can't be greater than 2. To ensure this stipulation holds true, the $(1\bar{1})_4$ representation of 3 needs to be chosen while adding. However, this represents a blocking case when converting the final output string back into binary as it prohibits us from simply concatenating the lower two bits of quaternary output strings to get the binary equivalent.

For addition of unsigned numbers, if the $(03)_4$ representation would have been used, direct concatenation of results could have been possible. But, then that wouldn't have always been carry free after the initial stage. Thus, the concept of an adjusting bit has been devised to solve the dilemma of which representation of 3 to use, such that both carry free addition and concatenation of output string bits to get the final output can be realized in the same design.

The solution to the problem described above, is that the $(03)_4$ representation of 3 is required to be taken instead of the $(1\bar{1})_4$ representation in some cases. But, determining when such a change is required before proceeding with the addition will increase the delay of the design and be counter-productive. Thus, the $(1\bar{1})_4$ representation of 3 is always selected in stage 1, to satisfy necessary conditions for carry free arithmetic. While necessary adjustments are made in stage 2 if $(03)_4$ representation was to be taken, the need for such an adjustment is determined via an adjusting bit.

OBSERVATION 1: In both quaternary representations of 3, $(03)_4$ or $(1\bar{1})_4$, the two least significant bits of the least

significant digit are 11. Thus, regardless of which representation was supposed to be taken, the lower two bits of the intermediate sum will remain same and these are the two-bit positions that would be concatenated in the end.

The problem of incorrect representation would come under certain cases. To better understand these cases an example is described. The example uses two numbers as inputs represented using three quaternary digits each:

Input A= $(X_3X_2X_1)_4 = (A_8A_7A_6A_5A_4A_3A_2A_1A_0)_2 = (030)_4$

Input B = $(Y_3Y_2Y_1)_4 = (B_8B_7B_6B_5B_4B_3B_2B_1B_0)_2 = (001)_4$

The Base case: For addition of X_2 and Y_2, if the intermediate sum comes out to be 3, as stated above $(1\bar{1})_4$ representation will be chosen in stage 1. The Intermediate sum for this digit addition becomes $\bar{1}$ or $(111)_2$. If then the intermediate carry from the addition of X_1 and Y_1 is 0, the final output after stage 2 for this addition would be $\bar{1}$. The intermediate carry that will be added to addition of X_3 and Y_3 would be 1. The binary output thus received after the concatenation of lower two bits will be wrong, as shown in Table III.

As established above, this problem wouldn't have been there if the $(03)_4$ representation of 3 would have been used. According to the findings of observation 1, the intermediate carry from addition of X_2 and Y_2 needs to be negated for the correct result because for $(03)_4$ there would have been no carry. This negation will be done by the adjusting bit.

TABLE III. EXAMPLE OF QUATERNARY ADDITION USING ORIGINAL LOGIC

$X_3X_2X_1$	0 3 0 → 000_011_000	Input A
$Y_3Y_2Y_1$	0 0 1 → 000_000_001	Input B
U1	$0\,\bar{1}\,1$ → 000_111_111	Stage 1 output (Intermediate sum)
U2	0 1 0	Stage 1 output (Intermediate carry)
R	$1\,\bar{1}\,1$ → 001_111_001	Result (Before concatenation)
R'	$(01\ 11\ 01)_2$	Incorrect Result (After concatenation)

Mathematically this can be written as:

Final output = Intermediate sum + Intermediate carry – Adjusting bit.

Thus, adjusting bit can be said to be 1 when $(S_{n-1}.\bar{c})$ is true where S_{n-1} and $\bar{c}$ are defined as:

S_{n-1}: True if n-1th intermediate sum digit is 3.

$\bar{c}$: True if there is no carry from n-2th digits sum.

Secondly, another special case could arise when the intermediate sum for addition of X_2 and Y_2 and X_1 and Y_1 are both 3. For example if A = $(030)_4$ and B = $(003)_4$. Now as per previously devised logic the addition would have proceeded as in Table IV.

Thus, the final result as shown in Table IV, would have been $(01\ 11\ 11)_2$ which is incorrect. The intermediate carry from the addition of X_2 and Y_2 hasn't been negated while carry from addition of X_1 and Y_1 has. This is because intermediate carry from X_1 and Y_1 is taken as 1 while calculating the adjusting bit for X_3 and Y_3 While an adjustment is made to it later to negate it to 0. This adjustment hasn't been factored into the formula. Thus, the modified and complete formula for adjusting bit becomes as in (10).

TABLE IV. EXAMPLE OF QUATERNARY ADDITION USING INITIAL MODIFIED LOGIC

$X_3X_2X_1$	0 3 0 → 000_011_000	Input A
$Y_3Y_2Y_1$	0 0 3 → 000_000_011	Input B
U1	$0\,\bar{1}\,\bar{1}$ → 000_111_111	Stage 1 output (Intermediate sum)
U2	0 1 1	Stage 1 output (Intermediate carry)
A	0 1 0	Adjusting Bit
R	$1\,\bar{1}\,\bar{1}$ → 001_111_111	Result (Before concatenation)
R'	$(01\ 11\ 11)_2$	Incorrect Result (After concatenation)

$$\text{Adjusting bit} = S_{n-1}.(S_{n-2}+\bar{c}) \quad (10)$$

Where S_{n-2} is true if n-2th intermediate sum digit is 3. This formula can cover the problem of n consecutive 3's in a similar manner.

The adjusting bit can be predicted based on the initial inputs to the adders itself. It can be computed in parallel with Stage 1. Thus, effect on delay of the adder is minimal. The above example is revaluated with the modified formula:

Input A= $(X_3X_2X_1)_4 = (A_8A_7A_6A_5A_4A_3A_2A_1A_0)_2 = (030)_4$

Input B = $(Y_3Y_2Y_1)_4 = (B_8B_7B_6B_5B_4B_3B_2B_1B_0)_2 = (003)_4$

Adjusting Bit for addition of X_n and Y_n is $S_{n-1}.(S_{n-2}+\bar{c})$. As can be seen from the flow of data shown in Table V. The modified formula gives the correct binary output after concatenation.

The proposed adder works in two stages, as shown in Fig. 5.

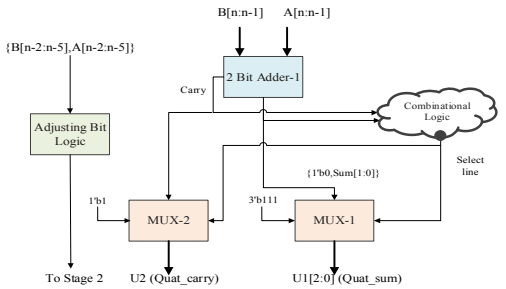
1) In the first stage, as in Fig. 5(a), every individual digit at the same position in the quaternary representation of two n-bit numbers A and B is added using a 2 Bit Adder to generate a sum. This sum lies in the range [0, 6]. From the sum obtained from the adder, the intermediate sum and intermediate carry for the next stage are calculated in parallel using 2x1 multiplexers. The logic for the selection of the representation of sum and carry has been explained in [16]. The adjusting bit is also computed in parallel with the addition process. The input to the adjusting bit calculation block for every quaternary digit addition are the previous two quaternary digits of A and B signified by [n-2: n-5].

2) Second stage has two modules as shown in Fig. 5(b). One is a one-bit module that performs the computation (A+B-C). In this case A would be LSB of intermediate sum, B would be carry from the previous quaternary digit addition and C would be the adjusting bit. The other module will be a half adder which will add the carry from the (A+B-C) module and the bit to the left of the least significant bit of the intermediate sum. As for the final concatenation, the sign bit would not be

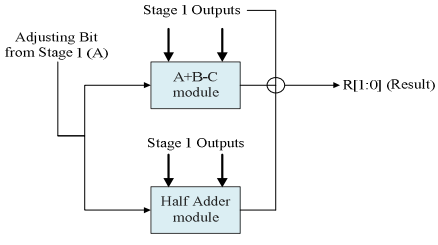
used owing to the adjustments proposed in the design. Thus, its final value is not computed.

TABLE V. EXAMPLE OF QUATERNARY ADDITION USING PROPOSED LOGIC

A	$(1100)_2$	Input 1
B	$(0011)_2$	Input 2
Q1	11_00 → 3 0	Quaternary representation of Binary number A
Q2	00_11 → 0 3	Quaternary representation of Binary number B
X_2X_1	3 0 → 011_000	Input A
Y_2Y_1	0 3 → 000_011	Input B
U1	$\overline{1}\,\overline{1}$ → 111_111	Stage 1 output (Intermediate sum)
U2	1 1	Stage 1 output (Intermediate carry)
S2	1	2nd intermediate sum digit is 3
S1	1	1st intermediate sum digit is 3
S0	0	0th digits do not exist
C1	1	Carry from sum of 2nd digits is 1
C0	1	Carry from sum of 1st digits is 1
A2	S2.(S1+ $\overline{C1}$) = 1	2nd Adjusting Bit
A1	S1.(S0 + $\overline{C0}$) = 0	1st Adjusting Bit
A	1 0	Stage 1 output (Adjusting Bit)
U3	001_111_111	Stage 2 output (Before Adjusting Bit logic)
U4	000_111_111	Stage 2 output (After Adjusting Bit logic)
R	$(1111)_2$	Result after concatenation



(a) Stage 1



(b) Stage 2

Fig. 5. Proposed Adder

IV. RESULTS

In this section, we present a comparison between proposed design of multiplier and existing architectures namely Vedic multiplier based on MVL logic that uses a ripple carry adder [16], Vedic Multiplier that incorporates a QSD adder with a conversion module for quaternary to binary conversion, Vedic multiplier based on a different fast adder scheme such as Carry select adder [17] and a known fast multiplication scheme such as Booth multiplier [18]. These four architectures were chosen and implemented to verify the viability of proposed design across all domains it's pertinent to. All architectures are described using Verilog HDL and all the possible states including corner cases for digit by digit multiplication blocks are verified using simulation with Xilinx ISim simulator. The design synthesis has been carried out using Synopsys Design Compiler, using the open-source NAN gate 15nm technology library[19]. Table VI shows that proposed design has made substantial improvements in terms of speed over the existing designs. The total delay of 128x128 Multiplier based on Proposed Design comes out to be 578.85 ps which is 88.75% faster than booth multiplier,71.35% faster than MVL multiplier based Multiplier, 17.47% faster than Carry select adder based Multiplier and 51.69% faster when compared with QSD Adder based Vedic Multiplier using conversion module.

Proposed 128x128 design has 7.7% lower implementation area then CSA based Vedic multiplier but shows an increase in area over other three designs, as shown in Table VII, it can be considered as a tradeoff for the substantial improvement in speed over those designs. As shown in Table VIII, for 16 input bit value the proposed design consumes the lowest power amongst the designs compared. Whereas, for the larger input sizes, the power consumed by proposed designs is 25.14% and 20.64% more than the lowest recorded power amongst the designs compared for 64 bit and 128 bit respectively.

TABLE VI. COMPARISON OF PROPOSED DESIGN WITH OTHER MULTIPLIER ARCHITECTURES ON THE BASIS OF TOTAL DELAY

Type Of Multiplier	**Delay (ps)**			
	16 bit	***32 bit***	***64 bit***	***128 bit***
Proposed Design	266.13	422.65	501.68	578.85
QSD Adder based Vedic Multiplier with conversion module	308.27	506.96	878.25	1198.21
CSA based Binary Vedic Multiplier	362.61	484.88	595.11	701.43
MVL Multiplier	431.18	949.25	1763.98	2020.71
Booth Multiplier	637.57	1259	2604	5148.56

TABLE VII. COMPARISON OF PROPOSED DESIGN WITH OTHER MULTIPLIER ARCHITECTURES ON THE BASIS OF AREA

Type Of Multiplier	**Area (No. of Cells)**			
	16 bit	***32 bit***	***64 bit***	***128 bit***
Proposed Design	768	3475	14440.6	58842.6
QSD Adder based Vedic Multiplier with conversion module	678.9	2660.8	12303	50181.9
CSA based Binary Vedic Multiplier	938	3884.2	15801	63767
MVL Multiplier	432	1765.1	7212	29464.2
Booth Multiplier	605	2332	8977	35987

TABLE VIII. COMPARISON OF PROPOSED DESIGN WITH OTHER MULTIPLIER ARCHITECTURES ON THE BASIS OF POWER

Type Of Multiplier	Power (mW)			
	16 bit	*32 bit*	*64 bit*	*128 bit*
Proposed Design	737.72	4446.7	24132	99630
QSDA based Vedic Multiplier with conversion module	774.35	4066.3	20958	87176
CSA based Binary Vedic Multiplier	1024.4	4558.7	19284	82580
MVL Multiplier	912.5	4722.2	21189	96478
Booth Multiplier	800.62	4627.1	19659	86556

V. CONCLUSION

It can be concluded that the design when scaled to higher bits only shows a marginal rise in delay due to its core strengths. Firstly, the parallelism involved in its partial product generation. Secondly, reduction of carry propagation delay in the novel adder it incorporates. Due to the use of QSD, the design is able to incorporate carry free arithmetic while eliminating radix conversion module speed overhead by integrating concept of adjusting bit logic in its architecture.

The proposed design showed an increase in implementation area over some designs due to increased parallelism even in finer nuances of the architecture. The proposed design is targeted towards digital systems requiring high throughput and low latency at the cost of area overhead. For example, in a DSP system, operations such as Fast Fourier Transform, Convolution, Filtering and Discrete Wavelet transform etc. Multipliers play a key role in determining the speed of the system. Similarly, this architecture would be a good candidate to be implemented as a large part of systems like DCT, Central Processing Unit (CPU), MAC (Multiply and Accumulate) Unit, Image Processors where high-speed multiplications are critical to the performance of the system.

It can also be observed that despite the objective of decreasing the delay, the proposed design performs better than most designs compared in terms of power for lower input bit sizes [16 and 32 bit]. Although it consumes more power than other designs higher input bit sizes [64 and 128 bit], it is justifiable when factored in with advantages gained in speed for higher input bits.

REFERENCES

[1] M. Rabaey, A. Chandrakasan, and B. Nikolic, "Digital Integrated Circuits A Design Perspective," PHI, 2003.

[2] B. Pahrami, "Computer Arithmetic and Hardware Design," New York, Oxford University Press, 2000.

[3] M. Ercegovac, and T. Lang, "Digital Arithmetic, San Francisco, Morgan Kaufmann," 2004.

[4] C S Wallace, "A Suggestion for a Fast multiplier", IEEE Transactions on Electronic Computers, Vol. EC-13, Issue 1, pp. 14-17, 1964.

[5] K. Choi and M. Song, "Design of a high performance 32x32-bit multiplier with a novel sign select booth Encoder," in IEEE International Symposium on Circuits and Systems, Volume 2, 2001, pp. 701-704.

[6] J. Swami S. B. K.Tirthaji Maharaja, "Vedic Mathematics: Sixteen Simple Mathematical Formulae from the Veda," Delhi, 1965.

[7] S. N. A and K. N, "Implementation of Power Efficient Vedic Multiplier," International Journal of Computer Applications (0975 – 8887), Vol. 43– No.16, 2012, pp. 21-24.

[8] S. Vaidya and D. Dandekar, "Delay-Power Performance Comparison of Multipliers In VLSI Circuit Design," International Journal of Computer Networks & Communications (IJCNC), Vol.2, No.4, July 2-010.

[9] H. Thapliyal and M. B. Srinivas, "High Speed Efficient N X N Bit Parallel Hierarchical Overlay Multiplier Architecture Based On Ancient Indian Vedic Mathematics", Enformatika (Transactions on Engineering, Computing and Technology),Vol. 2, Dec 2004, pp. 225-228.

[10] H. D. Tiwari, G. Gankhuyag, C. M. Kim and Y. B. Cho, "Multiplier design based on ancient Indian Vedic Mathematics," International SoC Design Conference, 2008, pp. 65-68.

[11] D. Jaina, K. Sethi and R. Panda, "Vedic Mathematics based multiply accumulate Unit," IEEE International Conference on Computational Intelligence and Communication Systems.2011, pp. 754-757.

[12] S. Jinesh, P. Ramesh and J. Thomas, "Implementation of 64 bit high speed multiplier for DSP application- based on Vedic mathematics," in IEEE TENCON,2015, pp. 1-5.

[13] J. Thomas, R Pushpangadan, S Jinesh, "Comparative study of performance of vedic multiplier on the basis of adders used," IEEE-WIECON, 2015, pp. 325-328.

[14] R. Rani, L. K. Singh and N. Sharma, "FPGA Implementation of Fast Adders using Quaternary Signed Digit Number System," 2009 International Conference on Emerging Trends in Electronic and Photonic Devices & Systems (ELECTRO-2009), pp. 132 - 135.

[15] Nagamani A. N, Nishchai S, "Quaternary High Performance Arithmetic Logic Unit Design", 14th Euromicro Conference on Digital System Design 2011 IEEE.

[16] A. S. Shende, M. A. Gaikwad and D. R. Dandekar, "Design of efficient 4X4 Quaternary Vedic Multiplier Using Current Mode Multi Valued Logic," Int. J. on recent Trends in Engineering and Technology,Vol 10, No 2, Jan. 2014, pp. 59-69.

[17] G. R. Gokhale, S. R. Gokhale, "Design of area and delay efficient Vedic multiplier using Carry Select Adder," International Conference on Information Processing (ICIP), 2015, pp. 295 – 300.

[18] S. Kim and K. Cho, "Design of High-speed Modified Booth Multipliers Operating at GHz Ranges," World Academy of Science, Engineering and Technology 61, 2010, pp. 1-4.

[19] M. Martins, J. M. Matos, R. P. Ribas, A. Reis, G. Schlinker, L. Rech and J. Michelsen, "Open Cell Library in 15nm FreePDK Technology", In Proceedings of the International Symposium on Physical Design (ISPD), 2015.

Available online at www.sciencedirect.com

ScienceDirect

Materials Today: Proceedings 5 (2018) 4720–4729

materialstoday: PROCEEDINGS

www.materialstoday.com/proceedings

ICMPC 2017

Optimization to the parameters of abrasive flow machining by Taguchi method

Ravi Butola[a], Rishabh Jain[b*], Priyesh Bhangadia[c] ,Ashwani Bandhu[d],R.S Walia[e] , Qasim Murtaza[f]

[abcde]*Department of Mechanical Engineering, Delhi Technological University, New Delhi-110042, India*
[f] *Department of Mechanical Engineering, Aligarh Muslim University, Aligarh, 202002, INDIA*

Abstract

This project summarizes the study of the parameters (Number of process cycles, Extrusion pressure and Abrasive concentration) and experimented variation used in Abrasive flow machining (AFM) for the surface finishing process and its optimization using Taguchi method. Abrasive flow machining (AFM) process is a most suitable non-conventional finishing process of internal passages of IC engine vehicles .Workpiece were machined by making all possible arrangements of these parameters on 3 levels which resulted into total of 27 workpiece which were machined to find the optimum value of parameters. Finally the results were verified using Taguchi method to find the optimum value of parameters. It has been found through the experiment that the optimum result is obtained when 'Number of cycles is equal to 6, Extrusion pressure is 15 bars and Abrasive concentration is 100gm', which shows that the percentage difference in surface roughness after machining is 26.42%. The result obtained shows that Taguchi designs recognize that not all the factors that causes variability can be controlled. These non-controllable factors are called noise factors. Taguchi designs try to identify controllable factors that can minimize the effects of noise factors.

© 2017 Elsevier Ltd. All rights reserved.
Selection and/or Peer-review under responsibility of 7th International Conference of Materials Processing and Characterization.

*Keywords:*Extrusion pressure; Abrasive;Optimization

1. Introduction

Finishing of a part improves its aesthetics and functional performance i.e. the fine finished parts have better dimensional controls, endurance strength and thus more life. In the recent times, there are requirements of fine finished products with close dimensional controls along with increasing complexity in their shapes. For such finishing requirements, Abrasive flow machining (AFM) process is a most suitable non-conventional finishing process. It is a nontraditional polishing process to polish metallic components using a semi-liquid paste, and with which complicated or miniaturized parts requiring high surface finish can be economically produced [1].

* Corresponding author.
E-mail address: ashwani021994@gmail.com

2214-7853© 2017 Elsevier Ltd. All rights reserved.
Selection and/or Peer-review under responsibility of 7th International Conference of Materials Processing and Characterization.

Extrusion of abrasives laden media (made up of a liquid polymer with abrasive particles) through a controlled passage results in abrasion of the required surface due the cutting action of a number of randomly oriented cutting points of abrasives. This process is mainly suitable for the complex shaped internal cavities or for the fine finishing of micro size holes/slots (even for the simultaneous polishing of different cavities).

*1.1*AFM Process

Abrasive flow machining (AFM) was invented by U.S.A based Extrudes Hones Corporation in 1960. Abrasive Flow Machining (AFM) is widely used in the fine finishing of complex inaccessible shapes, miniaturized parts, and for simultaneous finishing of many areas of a part or many parts itself [2]. Abrasives laden media (made up of a liquid polymer with abrasive particles) is forced through a controlled passage for the simultaneous finishing of the required external/internal surface with a large number of randomly oriented cutting points. The medium made by abrasives and polymer has low viscosity and good abrading capability. This media is also known as abrasive laden medium, not-so-silly putty [3]. Layer thickness of material being removed is of the order of about 1 to 10 μm. It can produce best surface finish achieved up to 50nm [4].

2. Literature review

Abrasive flow machining (AFM) is a purely mechanical process. A chemically inactive and noncorrosive media, similar to soft clay, is used to improve surface finish and edge conditions. The abrasive particles in the media grind away, rather than shear off, the material. The same type of media can be used on different metals. In many cases, the same batch of media can be used on different metals without transferring removed material between work pieces. AFM is used for surface or edge conditioning of internal, external, and otherwise inaccessible holes, slots, and edges. It is highly efficient and accurate, and can be used in one-way or two-way applications. The most abrasive action occurs during AFM, if a hole changes size or direction. In any industry the final finishing of complex and precision components is the most time consuming and labour intensive part .This considers about 15 % expenditure on the overall manufacturing process. The complex finishing process requires manual handling which is very slow and detrimental to the health of the workers. AFM process replaces a lot of manual finishing processes leading to more standardization of manufactured parts, hence their interchangeability, mass production and reduced costs.

2.1 Effect of AFM process parameters

The material removed from the surface and surface quality depends on the following: (1) No. of Cycle (2) Extrusion Pressure (3) Temperature (4) Media Flow rate (5) Viscosity (6) Abrasive particle size (7) Abrasive concentration (8) Particle density (9) Particle Hardness A lot of work has been done to study the effects of important AFM process parameters. Some of the works have been reported as under:

- Number of Process Cycles: The travel of media from lower cylinder to upper cylinder and then back to lower cylinder is termed as a cycle. Several cycles are required to get a particular amount of material removal and final surface finish on a component. Various researchers have reported that the improvement in surface finish and required amount of material removal occurs in some of the initial cycles and then it stabilizes. Jain V.K. [5] concluded that initially the material removal is higher at the 20 starting of cycle and after increasing no. of cycles the material removal decreases. Jain[6] reported from the experimental observations that on increasing the no. of cycles the value of surface roughness decreases.
- Extrusion pressure: It has been seen from the experiment that for better surface finish extrusion pressure should be high. If low extrusion pressure is used with low abrasive concentration and small grain size the surface finish will decrease. If low extrusion pressure is used with larger grains, it causes uneven distribution and that results the variation in the surface finish of two work pieces. So for better surface finish optimum combination of extrusion pressure, grain mesh size and abrasive concentration is required [7]. Jain et al. [8] mentioned according to their experimental observation that large extrusion pressure decreases the surface roughness up to certain value. It was reported that cutting is faster at high pressure

when all other parameters are kept constant. Jain [9] reported that at higher pressure the improvement in material removal just tends to stabilize probably due to localized rolling of abrasion particles.

- Media Temperature: Temperature is a very important parameter in AFM because it tells about the effectiveness of the AFM process. Liang Fang et al. [10] investigated that as the no. of cycle increases the temperature continuously increases. It causes less material removal.
- Media Flow Rate: When the media flow rate is higher it causes more abrasion. Media flow rate depends upon the parameters such as viscosity of media, pressure that affects the uniformity of the material removal.
- Media viscosity: Viscosity of media is the significant parameter affecting the quality of surface finish and amount of material removal in AFM process. The media with high viscosity causes more material removal in comparison to low viscosity media. High viscosity media also causes the improvement in surface roughness. Viscosity of highly viscous medium reduces very fast with a small increase in temperature between 2 to 10 °C. Material removal capacity of the low and high viscous media is different from each other [11].

3. Analysis of experiment

3.1 Workpiece cutting

Twenty seven workpiece were used for varying different parameters of experiment. The dimensions of all the workpiece were same and are as follows:
Length of workpiece- 16mm
Inner diameter- 8mm
Outer diameter- 10mm (i.e. thickness of workpiece is 1mm)

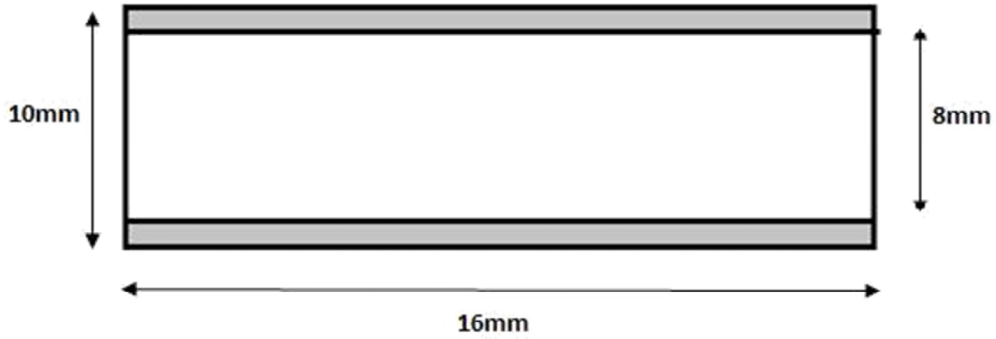


Fig.1. workpiece dimension

3.2 Calculation of surface roughness and weight measurements

Surface roughness and weight measurements were also done before and after the experiment for calculation purpose. Surface roughness was calculated using Taylor Hobson's "TALYSURF" as shown in below table (1) (2) and (3) .

The TALYSURF is an electronic instrument working on carrier modulating principle. The measuring head of this instrument consists of a diamond stylus of about 0.002 mm tip radius and skid or shoe which is drawn across the surface by means of a motorized driving unit (gearbox), which provides three motorized speeds giving respectively x 20, and x 100 horizontal magnification and a speed suitable for average reading. A neutral position in which the pick-up can be traversed manually is also provided. In this case the arm carrying the stylus forms an armature which pivots about the Centre piece of E-shaped stamping. On two legs of (outer pole pieces) the J5-shaped stamping there are coils carrying an a.c current. These two coils with other two resistances form an oscillator. As the armature is pivoted about the central leg, any movement of the stylus causes the air gap to vary and thus the amplitude of the original a.c current flowing in the coils is modulated. The output of the bridge thus consists of modulation only.

Table 1: Value or amount of parameter used for machining different workpiece

Parameter	Level 1	Level 2	Level 3
No. of cycles	2	4	6
Pressure	10	15	20
Amount of abrasive	100	200	300

Table 2: Parameter value used for machining on different workpiece

Workpiece	No. of cycles	Pressure	Amount of abrasive
1	2	10	100
2	2	10	100
3	2	10	100
4	2	15	200
5	2	15	200
6	2	15	200
7	2	20	300
8	2	20	300
9	2	20	300
10	4	10	200
11	4	10	200
12	4	10	200
13	4	15	300
14	4	15	300
15	4	15	300
16	4	20	100
17	4	20	100
18	4	20	100
19	6	10	300
20	6	10	300
21	6	10	300
22	6	15	100
23	6	15	100
24	6	15	100
25	6	20	200
26	6	20	200
27	6	20	200

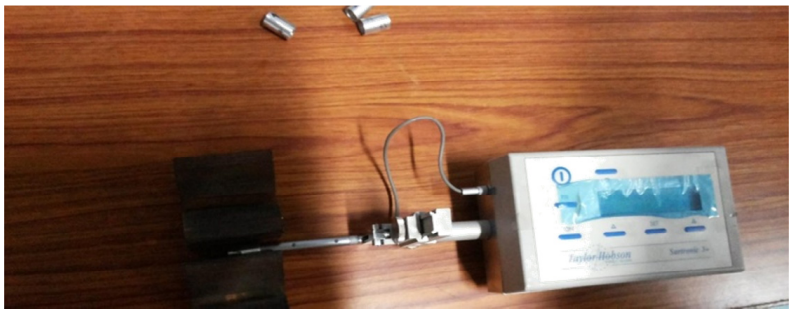


Fig.2.Talysurf and surface roughness calculation

The value obtained using "TALYSURF" is in micrometers (μm) and it's called as Ra value. Ra is the average value of roughness profile. Also during surface finishing abrasives tend to break chips so that there is an expected change in weight of the workpiece. To note this change workpiece weight is measured upto 4 decimal places on a digital weighing machine before and after machining. Change in weight is calculated as shown in above Fig 1 and Fig 2.

3.3 Preparation of media

AFM uses a non-Newtonian liquid polymer containing abrasives particles of Aluminium oxide, Silicone carbide, Boron carbide or diamond as the grinding medium and additives [9]. The additives are used to modify the base polymer to get the desired flowability and rheological characteristics of media. The amount of media used in different cycles was 100gm, 200gm and 300gm as shown in below Fig (3) (4) (5) and Fig (6) (7) (8).



Fig .3. Media used for machining

3.4 Machining

The material removed from the surface and surface quality depends on the following:

- No. of cycles - The travel of media from lower cylinder to upper cylinder and then back to lower cylinder is termed as a cycle. Several cycles are required to get a particular amount of material removal and final surface finish on a component.

- Extrusion Pressure - for better surface finish extrusion pressure should be high. If low extrusion pressure is used with low abrasive concentration and small grain size the surface finish will decrease. If low extrusion pressure is used with larger grains, it causes uneven distribution and that results the variation in the surface finish of two work pieces. So for better surface finish optimum combination of extrusion pressure, grain mesh size and abrasive concentration is required.

- Abrasive Concentration – It is the ratio of weight of abrasive particles to the weight of carrier compound multiplied by 100. Jain V.K. [8] concluded that as the abrasive concentration of abrasive in medium increases the material removal increases while surface roughness value decreases because number of active grains increases.

3.4 Machining

The material removed from the surface and surface quality depends on the following:

- No. of cycles - The travel of media from lower cylinder to upper cylinder and then back to lower cylinder is termed as a cycle. Several cycles are required to get a particular amount of material removal and final surface finish on a component.

- Extrusion Pressure - for better surface finish extrusion pressure should be high. If low extrusion pressure is used with low abrasive concentration and small grain size the surface finish will decrease. If low extrusion pressure is used with larger grains, it causes uneven distribution and that results the variation in the surface finish of two work pieces. So for better surface finish optimum combination of extrusion pressure, grain mesh size and abrasive concentration is required.

- Abrasive Concentration – It is the ratio of weight of abrasive particles to the weight of carrier compound multiplied by 100. Jain V.K. [8] concluded that as the abrasive concentration of abrasive in medium increases the material removal increases while surface roughness value decreases because number of active grains increases.

3.5. Calculations

Table: 3 Surface roughness calculations (before & after machining) and % change

Workpiece No.	Value of roughness (Ra value)		% change in roughness value
	Before machining	After machining	
1	3.70	2.69	27.35
2	4.00	3.09	22.67
3	4.40	3.58	18.58
4	3.60	2.91	19.07
5	3.00	2.53	15.83
6	3.80	2.67	29.76
7	2.50	2.17	13.34
8	2.90	1.89	34.83
9	2.90	1.90	34.53
10	2.60	2.30	11.65
11	3.40	2.31	32.11
12	3.70	2.95	20.25
13	4.70	2.57	45.34
14	1.30	1.03	20.94
15	0.70	0.55	22.01
16	2.80	2.14	23.71
17	3.10	2.18	29.66
18	2.70	1.97	27.14
19	2.40	1.73	28.00
20	1.60	1.21	24.08
21	2.10	1.69	19.67
22	3.34	2.74	17.83
23	3.31	2.44	26.42
24	3.28	2.50	23.63
25	3.31	2.42	26.90
26	3.08	2.43	21.26
27	2.85	2.40	15.79

3.6. Design of experiment

The design of experiments (DOE) also known as DOX or experimental design is the design of any task that aims to describe or explain the variation of information under conditions that are hypothesized to reflect the variation. It is a systematic method to determine the relationship between factors affecting a process and the output of that process. In other words, it is used to find cause-and-effect relationships. This information is needed to manage process inputs in order to optimize the output. DOE gives the optimized result of given experimental values or outcome of the experiment performed. Here in the experiment, we are going to plot the effect of various parameters with the help of surface roughness value (Ra value) calculated before and after the machining. The results were obtained using Minitab software and been illustrated below Table 4.

Table: 4 Results of experiments by Taguchi method using Minitab software

S.no.	No. of process cycles	Extrusion pressure	Abrasive concentration	Result 1	Result 2	Result 3
1	2	10	100	27.35	22.67	18.58
2	2	15	200	19.07	15.83	29.76
3	2	20	300	13.34	34.83	34.53
4	4	10	200	11.65	32.11	20.25
5	4	15	300	45.34	20.94	22.01
6	4	20	100	23.71	29.66	27.14
7	6	10	300	28.00	24.08	19.67
8	6	15	100	17.83	26.42	23.63
9	6	20	200	26.90	21.26	15.79

4.8 Results and discussion

The material removed from the surface and surface quality depends on a number of factors. Out of these parameters, three different parameters were used –

- No. of cycles - The travel of media from lower cylinder to upper cylinder and then back to lower cylinder is termed as a cycle. Several cycles are required to get a particular amount of material removal and final surface finish on a component.

- Extrusion Pressure - for better surface finish extrusion pressure should be high. If low extrusion pressure is used with low abrasive concentration and small grain size the surface finish will decrease.

- Abrasive Concentration – It is the ratio of weight of abrasive particles to the weight of carrier compound multiplied by 100.

The optimized condition for AFM using the three parameters (No. of working cycle, Extrusion pressure, Abrasive concentration) is obtained when –
Number of working cycles are 6, Extrusion pressure is 15 bars and Abrasive concentration is 100gm. During experimentation, we manipulate control factors to evaluate variability that occurs and then determine optimal control setting factors that minimizes the process variability. A process designed with this goal will produce more consistent and better output and performance regardless of the environment in which it is used.

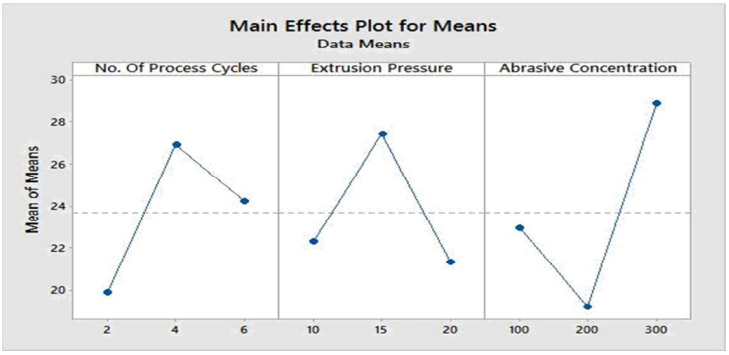


Fig.5. Graphs for Result 1

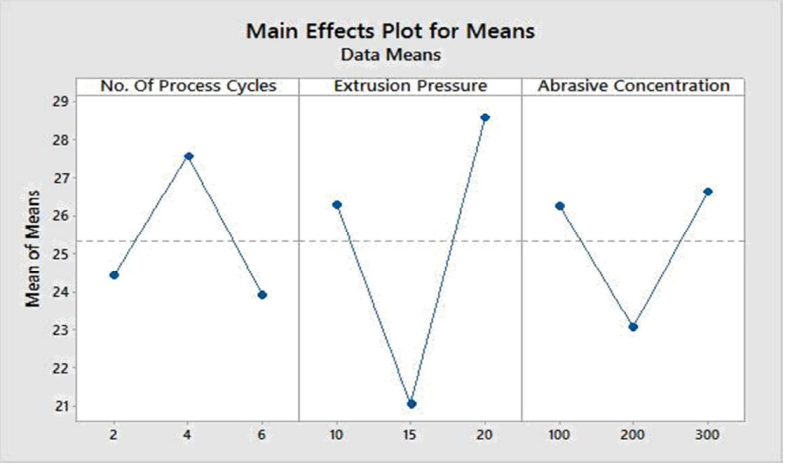


Fig.6. Graphs for Result 2

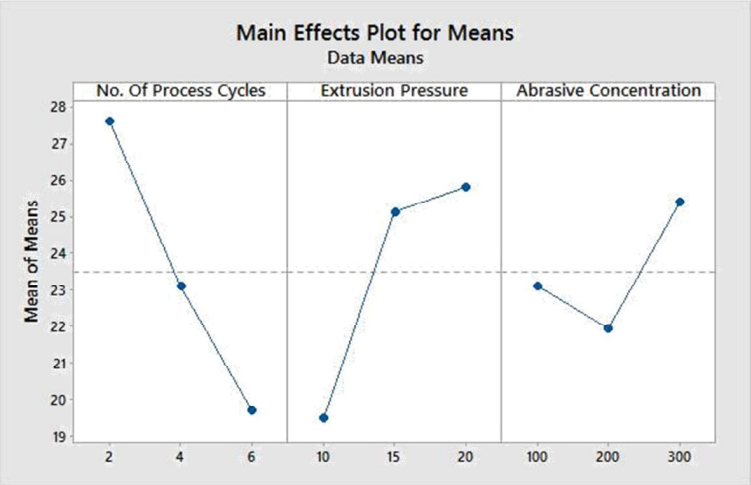


Fig.7. Graphs for Result 3

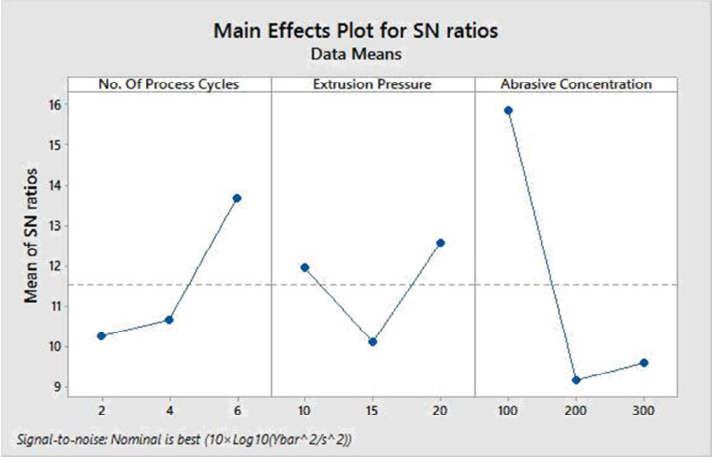


Fig.8. SN Ratio for all the factors together

4. Conclusion

In the experiment performed on 'Optimization to the Parameters of Abrasive Flow Machining by Taguchi Method' the parameters 'Number of process cycles', 'Extrusion pressure', 'Abrasive concentration' were studied. It has been found that-

- For first nine workpiece the optimized output is obtained when the number of cycles should be 4, parameter 2 (Extrusion pressure) should be 15bars and parameter 3 (Abrasive concentration) should be 200gm.
- For workpiece numbered 10 to 18 shows that for optimized output, the number of cycles should be 4, parameter 2 (Extrusion pressure) should be 20bars and parameter 3 (Abrasive concentration) should be 300gm.
- In case of last nine workpiece shows that for optimized output, the number of cycles should be 2, parameter 2 (Extrusion pressure) should be 20bars and parameter 3 (Abrasive concentration) should be 300gm.
- The SN ratio curve shows Signal to Noise ratio for all the workpiece by varying the three parameters. For parameter 1 (No. of cycles), the SN ratio is highest when the number of cycles are 6. For parameter 2 (Extrusion pressure), the SN ratio is highest when the pressure is 15 bars and for parameter 3 (Abrasive concentration), the SN ratio is highest when concentration is 100gm.

Thus the optimum condition is achieved when –
Number of cycles is equal to 6, Extrusion pressure is 15 bars and Abrasive concentration is 100gm.

The above result is obtained because Taguchi designs recognize that not all the factors that causes variability can be controlled. These non-controllable factors are called noise factors. Taguchi designs try to identify controllable factors that can minimize the effects of noise factors.

Further the optimized results can be calculated for other parameters also. It also in clude the change of workpiece material and use of other abrasive materials for increasing the overall efficiency which is obtained about 20% to 30% in the experiment performed above.

References

[1] V.K. Goranaa, V.K. Jainb, G.K. Lal; Experimental investigation into cutting forces and active grain density during abrasive flow machining; International Journal of Machine Tools & Manufacture, Vol 44,2004, pp 201–211.

[2] A.C. Wang, S.H. Weng; developing the polymer abrasive gels in AFM processs; Journal of Materials Processing Technology, Vol 192–193, 2007, pp 486–490.

[3] Sehijpal Singh, H.S. Shan; Development of magneto abrasive flow machining process; International Journal of Machine Tools & Manufacture, Vol 42, 2002, pp 953–959.

[4] Manas Das, V.K. Jain, P.S. Ghoshdastidar; Fluid flow analysis of magnetorheological abrasive flow finishing (MRAFF) process; International Journal of Machine Tools & Manufacture, Vol 48, 2008, pp 415–426.

[5] M. Ravi Sankar, V. K. Jain, J. Ramkumar; Abrasive flow machining (AFM): An Overview.

[6] Hitomi Yamaguchi, Anil K. Srivastava, Michael A. Tan, Raul E. Riveros, Fukuo Hashimoto; Magnetic abrasive finishing of cutting tools for machining of titanium alloys; CIRP Annals - Manufacturing Technology Vol 61, 2012, pp 311–314.

[7] Rajendra K. Jain, Vijay K. Jain, P.M. Dixit; Modeling of material removal and surface roughness in abrasive flow machining process; International Journal of Machine Tools & Manufacture, Vol 39, 1999, pp 1903–1923.

[8] R.K. Jain, V.K. Jain, P.K. Kalra; Modelling of abrasive flow machining process: a neural network approach;Wear Vol 231, 1999, pp242–248.

[9] Rajendra Kumar Jain, Vijay Kumar Jain; Optimum selection of machining conditions in abrasive flow machining using neural network; Journal of Materials Processing Technology, Vol 108, 2000, pp 62-67.

[10] Liang Fang, Jia Zhao, Kun Sun, Degang Zheng, Dexin Ma; Temperature as sensitive monitor for efficiency of work in abrasive flow machining; Wear Vol 266, 2009, pp 678– 687.

[11] Rajendra K. Jain, V.K. Jain; Stochastic simulation of active grain density in abrasive flow machining;

Journal of Non-Crystalline Solids xxx (xxxx) xxx–xxx

Contents lists available at ScienceDirect

Journal of Non-Crystalline Solids

journal homepage: www.elsevier.com/locate/jnoncrysol

Pr^{3+} ions doped single alkali and mixed alkali fluoro tungsten tellurite glasses for visible red luminescent devices

Ch.B Annapurna Devi[a], Sk. Mahamuda[a], K. Swapna[a], M. Venkateswarlu[a], A. Srinivasa Rao[a,b,*], G. Vijaya Prakash[c]

[a] Department of Physics, Koneru Lakshmaiah Education Foundation, Green Fields, Vaddeswaram, 522 502 Guntur (Dt), Andhra Pradesh, India
[b] Department of Applied Physics, Delhi Technological University, Bawana Road, New Delhi 110 042, India
[c] Department of Physics, Indian Institute of Technology-Delhi, Hauz Khas, New Delhi 110 016, India

ARTICLE INFO

Keywords:
Glasses
Praseodymium
J-O parameters
Optical properties
Photoluminescence
Radiative properties

ABSTRACT

The present work illustrates the optical absorption and fluorescence properties of Pr^{3+} ions doped single alkali and mixed alkali fluoro tungsten tellurite glasses prepared by using melt quenching technique. The prepared glasses were characterized by using absorption, excitation and photoluminescence (PL) spectral measurements. The energies of the absorption spectral features called oscillator strengths were calculated using area method and in turn used to evaluate the Judd-Ofelt (J-O) intensity parameters (Ω_2, Ω_4, Ω_6). Such J-O parameters are used to estimate various radiative parameters such as radiative transition probabilities (A_R), branching ratios (β_R), and radiative lifetimes (τ_R) for the prominent fluorescent levels of Pr^{3+} ions in these glasses. The PL spectra of the as prepared glasses show three prominent peaks at wavelengths 488, 646 and 670 nm related to the transitions $^3P_0 \rightarrow {}^3H_4$, $^3P_0 \rightarrow {}^3F_2$ and $^1D_2 \rightarrow {}^3H_5$ respectively for which emission cross-sections and branching ratios were evaluated. The variations in the spectral parameters with the variation of glass matrix composition have been examined in detailed. The decay profiles of the prepared glasses have been recorded to evaluate quantum efficiency of present series of glasses. From the measured branching ratios, emission cross-sections and quantum efficiency, it was concluded that the tungsten tellurite glasses added with potassium fluoride and doped with 1 mol% of Pr^{3+} ions (TeWK glass) are quite suitable to produce visible red emission at 670 nm suitable to fabricate red luminescent devices.

1. Introduction

Recently Rare Earth (RE) ions doped oxide glasses are playing vital role in diversified fields such as photonics, optoelectronic devices, wavelength conversion devices, optical fiber amplifiers, fiber lasers and compact microchip lasers [1–4]. Glassy materials have got so much of attention when compared with crystalline materials for the aforementioned applications because of their low cost and simple manufacturing procedure. Over and above the bulk samples of glassy materials can be prepared easily when compared with single crystalline materials [5]. Many researchers have investigated the lasing potentialities of RE ions doped fluoride, borate, fluoroborate and tellurite glasses to understand the effect of the host material and doped RE ion concentration [6–10]. Among the various types of oxide glasses, tellurite based oxide glasses have gained so much of attention in recent years because of their unique properties such as low phonon energy and low melting point (800^0 ± C); which are in fact the key points to get relatively higher quantum efficiency [11,12]. Tellurite glasses doped with RE ions have dragged so much attention for spectroscopic investigations, due to their potential applications in diversified areas like biochemical studies, telecommunications and optical sensors etc. [13–16]. Tellurite host matrices have several interesting features like low phonon energy ($< 800\ cm^{-1}$), high refractive index, large dielectric constant, broad transmission window (~0.4–5 μm), large RE ion solubility and higher stability among various other oxides hosts [17–26]. The above characteristics prompted us to choose tellurites as host matrix for the present investigation. On the other hand tellurite based glasses are conditional glass formers; i.e., independently they can't form a glass without the support of intermediates/modifiers such as WO_3, Ti_2O, Bi_2O_3, Li, Na and K [21]. Addition of tungsten oxide to tellurite's makes them non-hygroscopic and transparent in the visible and NIR regions. One of the special features of tungsten ions is that they show strong influence on luminescence properties of RE ions in the tellurite glasses because of their various valency states (W^{6+}, W^{5+} and W^{4+}). The

* Corresponding author at: Department of Applied Physics, Delhi Technological University, Bawana Road, New Delhi 110 042, India.
E-mail address: drsrallam@gmail.com (A. Srinivasa Rao).

https://doi.org/10.1016/j.jnoncrysol.2018.03.034
Received 23 November 2017; Received in revised form 24 January 2018; Accepted 12 March 2018
0022-3093/ © 2018 Elsevier B.V. All rights reserved.

thermo-reversible disproportionate reaction of these ions is represented as $W^{5+} + W^{6+} \leftrightarrow W^{4+} + W^{6+}$ [27–29]. Each valency state of tungsten ion has a unique importance depending upon the formation of bonds with tellurium oxide. Tungsten ions with 5+ valence state (W^{5+}) form the complexes of $W^{5+}O^{3-}$. Due to these complexes, structural changes happen in tellurite network because TeO_4 structural units changes to TeO_{3+1} structural units [30,31]. The 6+ valence state of tungsten ions entered into the network of glasses as WO_4 and WO_6. Due to these units, new networks/linkages formed between Te ions and tungsten ions such as Te-O-W with TeO_4 and TeO_3 structural units [30,31]. In addition to the above, addition of WO_3 to a tellurite glass enhances the chemical stability and devitrification resistance. This loosens the glass network and increases the solubility of RE ions in the host glass [32–34].

The present series of tungsten tellurite glasses have been prepared in combination with different alkali fluorides (RF; where R stands for Li, Na and K metals) which act as network modifiers (NWM) and increase the stability of the glasses [35]. Moreover alkali fluorides can avert the moisture in glasses more effectively than alkali oxides and iodides [36]. The fluoride ions in alkali fluorides act as co-activators and replace the activators in the lattice. Due to the addition of these alkali fluorides, the mixed alkali effect (MAE) raised which can change various physical properties such as dielectric loss, ionic conductivity and alkali diffusion coefficient due to cation movements [37–40]. In addition to the above, fluorides addition to the glasses can lower the phonon energy (300-600 cm^{-1}) which in turn reduces non-radiative decay losses due to multiphonon relaxations. If non-radiative losses are reduced, the quantum efficiency of RE ion doped glass will increase. Due to these low non-radiative decay rates near maximum infrared (IR) cut-off edge will occur, which can lowers the non-linear refractive index. Hence transmission ability enhances from UV to IR. Addition of alkali fluorides to these glasses decreases OH absorption because fluoride ions reacting with OH group will form HF [41–43]. Fluoride content added to these glasses can also decrease the phonon energy and enhance the emission cross-section and quantum efficiency. This has been reported by many researchers in Pr^{3+} ions doped host glasses [44,45].

Among different RE ions, Pr^{3+} ion is one of the optical activator which gives luminescence in blue, green, red and IR regions with numerous applications such as optical devices, up-conversion lasers and fiber amplifiers [46–53]. The Pr^{3+} ions have a number of metastable states which are able to provide the efficient luminescence from visible to infrared region. Recent studies have been focused on 1.3 μm ($^1G_4 \rightarrow {}^3H_4$) emission from Pr^{3+} ions doped glasses which are very useful in telecommunication window [10,11,69]. Pr^{3+} ions also acts as an active luminescent centre, to give red luminescence in 600-720 nm wavelength region [11–25], which locates in the maximum absorption region of the Photo sensitizing currently used in photodynamic therapy or clinical trials [54,55]. Favourable red luminescence from Pr^{3+} ions doped glass fibers with sufficient intensity and suitable directivity are quite suitable for PDT treatment [54,55]. On the other hand, the studies on $^3P_0 \rightarrow {}^3H_6$ (orange-red emission) are not as much focused even though this luminescence is very useful as signal light source in astronomical telescope, in medical therapies (ophthalmology for the treatment of retinal disorders, removal of tissues, tumours and in the treatment of acne and in skin restoration). Various scientific patronages offered by the chemical constituents such as TeO_2, WO_3 and alkali fluorides have prompted us to take up a systematic investigation on Pr^{3+} ions doped different compositions of single and mixed alkali fluoro tungsten tellurite glasses for orange-red luminescent device applications.

2. Experimental

2.1. Synthesis and characterization of glasses

In the present work, the glass samples have been prepared by conventional melt quenching method with the following compositions.

TeWLi: $59TeO_2$ - $20WO_3$ - 20LiF - $1Pr_6O_{11}$
TeWNa: $59TeO_2$ - $20WO_3$ - 20NaF - 1 Pr_6O_{11}
TeWK: $59TeO_2$ - $20WO_3$ - 20 KF - 1 Pr_6O_{11}
TeWLiNa: 59 TeO_2 - $20WO_3$ - 10LiF - 10NaF - 1 Pr_6O_{11}.
TeWLiK: $59TeO_2$ - $20WO_3$ - 10LiF - 10KF - 1 Pr_6O_{11}.
TeWNaK: $59TeO_2$ - $20WO_3$ - 10NaF - 10KF - 1 Pr_6O_{11}.

The analar grade chemicals of TeO_2, WO_3, LiF, NaF, KF & Pr_6O_{11} were used as raw materials to prepare the glass materials. Approximately 10 g of each batch composition was weighed in an electrical balance and crushed in an agate mortar for 2 h to obtain uniform mixture. Then the mixture was collected in a silica crucible and it is sintered at 750 °C for ½ h and kept in a temperature controlled furnace and swirled inside the furnace to obtain homogeneous melt. The bubble free melt was then quenched in between a couple of pre-heated brass plates to get the glass samples with a uniform thickness. Later, these glass samples were annealed at 400 °C for 4 h to avoid the internal stresses generated by rapid cooling and to improve structural stability. The prepared samples are polished with emery paper before using them for absorption and luminescence spectral characterizations. For the prepared samples, densities are measured using standard Archimede's principle, using water as buoyant liquid. Refractive indices of the prepared glass samples were measured using the Brewster's angle method (He-Ne laser at λ = 650 nm) with an accuracy ± 0.01. The optical absorption spectra of the as prepared glasses have been recorded by using a double beam JASCO V-670 UV–vis-NIR spectrophotometer at room temperature with a spectral resolution of 0.1 nm. This is to be noted that the host glass matrix optical band gap is typically about 3 eV (i.e., absorption edge at 400 nm). While calculating the oscillator strengths (from areas under the absorption curve) and corresponding Judd-Ofelt parameters, appropriate background corrections have been made. The PL spectra of these glasses were recorded using RF-5301 PC Spectrofluorophotometer at room temperature. The decay profiles for the present series of glasses have been recorded using Edinburgh FLSP900 with a spectral resolution of 0.1 nm.

3. Results and discussions

3.1. Analysis of optical absorption spectra-measurement of oscillator strengths& J-O parameters

In order to understand the radiative properties possessed by Pr^{3+} ions doped in the as prepared glasses, absorption spectra have been recorded from 400 to 2200 nm. Fig. 1 shows the absorption spectra of Pr^{3+} ions doped alkali and mixed alkali fluoro tungsten tellurite

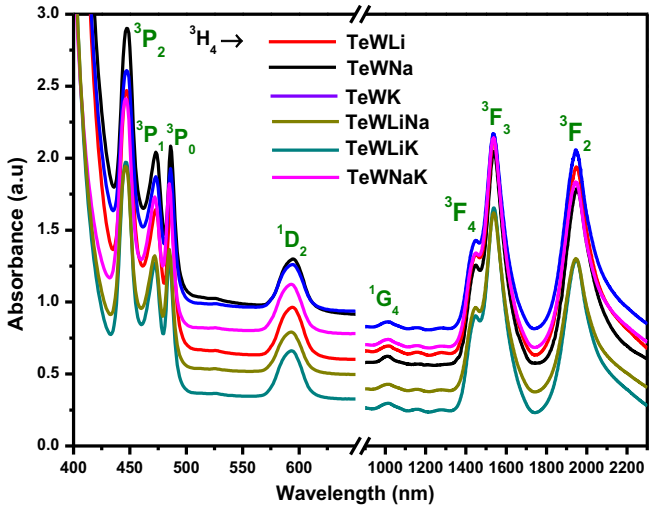


Fig. 1. Absorption spectra of Pr^{3+} ions doped single alkali and mixed alkali fluoro tungsten tellurite glasses.

glasses. As shown in Fig. 1, the absorption spectra show eight absorption peaks related to the transitions $^3H_4 \rightarrow {}^3P_2$, $^3P_1$, $^3P_0$, $^1D_2$, $^1G_4$, $^3F_4$, $^3F_3$ and $^3F_2$ belonging to $4f^2$ configuration at 447 nm, 472 nm, 485 nm, 599 nm, 1019 nm, 1451 nm, 1539 nm and 1944 nm respectively. All these transitions are assigned according to Carnall et al. [56] and assumed to be electric dipole transitions. The assignment of these absorption bands are in good agreement with the literature [21,56]. Among all the transitions, $^3H_4 \rightarrow {}^3P_2$ (447 nm) transition is known as hypersensitive transition. This transition strongly depends upon the local environment around the RE ions. This hypersensitive transition is represented by the selection rule $\Delta S = 0$, $|\Delta L| \leq 2$ and $|\Delta J| \leq 2$ [57]. By using the absorption spectral data, the nature of bonding in the prepared glasses can be estimated in terms of nephelauxetic ratio ($\bar{\beta}$) and bonding parameter (δ). Depending upon the ligands, the value of bonding parameter is positive or negative which indicates covalent or ionic nature between the ligands. For the present series of glasses, the nephelauxetic ratio and bonding parameters are TeWNa – 0.9933 & 0.6671, TeWLi – 0.9931 & 0.6891, TeWK – 0.9924 & 0.7649, TeWLiK – 0.9956 & 0.4419, TeWNaK – 0.9942 & 0.5819 and TeWLiNa – 0.9938 & 0.6141. From the obtained bonding parameters values it is concluded that TeWK glass is more covalent when compared with other single alkali and mixed alkali glasses. These values are also comparable to the values reported to the other alkali and mixed alkali glasses like LiCdBS (1.2146), NaCdBS (1.0918), KCdBS (0.8573) [58].

The electric dipole oscillator strengths for all the peaks in the optical absorption spectra (f_{exp}) have been evaluated using the expression given in the literature [21].Using these oscillator strengths and J-O theory, the calculated oscillator strengths have been evaluated using the equations available in the literature [21] with and without including the hypersensitive transition. As the deviations observed in calculated oscillator strengths with and without including oscillator strengths are very less, in Table 1 we gave only oscillator strengths with the inclusion of hypersensitive transition along with the experimental oscillator strengths and rms deviation values. From Table 1 it is observed that among all the glasses (single and mixed alkali) the TeWK glass possesses the maximum values of oscillator strengths and the magnitude of hypersensitive transition is also high for this glass.

The required conditions for good lasing materials are higher magnitudes of branching ratios and stimulated emission cross-sections of particular luminescent level. Evaluation of these crucial parameters is possible using J-O theory. This theory was explained based on the following four assumptions [60].

1. An average energy is assumed for excited configurations above the $4f^N$
2. The energy difference between two states J and J' is small when compared to the difference between the energy of the $4f^N$ configuration and the energy of the $4f^N5d^1$configuration.
3. All stark levels are equally populated.
4. The material is optically isotropic

For most of the RE ions, the first two assumptions are satisfied moderately which need to be simplified greatly. In Pr^{3+} ions, the 4f $^N5d^1$ band is very low and very close to $^3P_2$, $^3P_1$, $^1I_6$, and $^3P_0$ levels, so that they perturb noticeably for the J-O calculation. The J-O parameters (Ω_λ, $\lambda = 2$, 4 and 6) have been measured using least square fitting method by considering the hypersensitive transition $^3H_4 \rightarrow {}^3P_2$ and are given in Table 2 along with the other reported values [21,59,61–66]. From Table 2, it is observed that the J-O intensity parameters are following two different trends for single alkali and mixed alkali tungsten tellurite glasses. Single alkali tellurite glasses follow the trend $\Omega_2 > \Omega_4 > \Omega_6$ whereas mixed alkali glasses follows a different trend $\Omega_4 > \Omega_2 > \Omega_6$. The J-O parameter Ω_2 is a representation of covalency of metal ligand bond and other two parameters Ω_4 and Ω_6 represents the viscosity and rigidity of the host glass matrix. Among all the glasses (single and mixed alkali) the TeWK glass possesses higher values for the J-O parameters. Among the alkali ions, K^+ has less ionization energy when compared with Li^+ and Na^+ ions. This helps potassium ions to act as a relatively good network modifier when compared with lithium and sodium ions. Consequently, the presence of potassium in a glass can produce more number of non-bridging oxygen's when compared with the lithium and sodium ions. This makes the glasses containing potassium (a good network modifier) to give relatively higher values for J-O parameters when compared with other alkali ions [67–69].

These values are found to be high when compared with other reported glasses such as oxy-fluoride, mixed halide, phosphate, MgTP, LBTAF, ZBP_3, Glass A and tellurite [21,59,61–66] glasses. The larger values of Ω_2 parameter of TeWK glass suggests that, the bonding

Table 2
J-O Intensity Parameters ($\Omega_\lambda = 10^{-20}\,cm^2$; $\lambda = 2,4,6$) of Pr^{3+} ions doped single alkali and mixed alkali fluoro tungsten tellurite glasses.

Glass System	Ω_2	Ω_4	Ω_6	Trend	Reference
TeWLi	8.37	7.43	2.07	$\Omega_2 > \Omega_4 > \Omega_6$	Present work
TeWNa	7.20	6.72	2.04	$\Omega_2 > \Omega_4 > \Omega_6$	Present work
TeWK	12.75	11.18	3.37	$\Omega_2 > \Omega_4 > \Omega_6$	Present work
TeWLiNa	10.08	10.59	3.26	$\Omega_4 > \Omega_2 > \Omega_6$	Present work
TeWLiK	8.56	9.55	2.80	$\Omega_4 > \Omega_2 > \Omega_6$	Present work
TeWNaK	9.39	9.64	2.81	$\Omega_4 > \Omega_2 > \Omega_6$	Present work
Glass A	4.78	6.15	2.21	$\Omega_4 > \Omega_2 > \Omega_6$	[21]
Oxy-fluoride	0.13	4.09	6.33	$\Omega_6 > \Omega_4 > \Omega_2$	[59]
Mixed halide	2.70	4.40	5.40	$\Omega_6 > \Omega_4 > \Omega_2$	[61]
Phosphate	4.19	4.29	6.40	$\Omega_6 > \Omega_4 > \Omega_2$	[62]
MgTP	2.69	11.8	8.39	$\Omega_4 > \Omega_6 > \Omega_2$	[63]
LBTAF	2.42	2.54	4.23	$\Omega_6 > \Omega_4 > \Omega_2$	[64]
ZBP_3	2.89	2.04	1.99	$\Omega_2 > \Omega_6 > \Omega_4$	[65]
Tellurite	3.81	5.81	4.10	$\Omega_4 > \Omega_6 > \Omega_2$	[66]

Table 1
Experimental (f_{exp}) and calculated (f_{cal}) oscillator strengths ($\times 10^{-6}$), r.m.s deviations (δ_{rms}), refractive indices and density (g/cm^3) of Pr^{3+} ions doped single alkali and mixed alkali fluoro tungsten tellurite glasses.

Transition from $^3H_4 \rightarrow$	TeWLi		TeWNa		TeWK		TeWLiNa		TeWLiK		TeWNaK	
	f_{exp}	f_{cal}	f_{exp}	f_{cal}	f_{exp}	f_{cal}	f_{exp}	f_{cal}	f_{exp}	f_{cal}	f_{exp}	f_{cal}
$^3P_2$	13.5	0.41	10.0	0.36	22.1	0.61	18.55	0.57	15.73	0.51	16.26	0.52
$^3P_1$	5.64	9.49	4.18	8.31	9.75	14.1	8.50	13.15	6.75	11.80	7.45	11.99
$^3P_0$	5.49	9.35	4.82	8.18	8.16	13.9	7.45	12.95	6.28	11.65	6.29	11.83
$^1D_2$	8.78	1.52	8.55	1.38	13.0	2.36	11.74	2.17	11.52	1.91	11.60	1.96
$^1G_4$	1.98	0.42	1.32	0.38	3.31	0.65	2.48	0.59	11.52	1.91	2.21	0.54
$^3F_4$	1.21	3.74	0.96	3.45	2.52	5.90	2.12	5.45	2.54	0.52	1.54	4.87
$^3F_3$	11.9	10.53	10.8	9.40	18.0	16.1	16.59	14.72	1.27	4.71	15.38	13.49
$^3F_2$	13.5	13.59	11.5	11.6	20.4	20.5	17.19	17.31	14.97	13.00	15.92	17.04
$\delta_{rms}(\times 10^{-6})$	± 5.77		± 4.77		± 4.77		± 7.78		± 7.04		± 7.15	
n	2.463		2.423		2.423		2.426		2.423		2.436	
d	5.518		5.546		5.546		5.532		5.502		5.516	

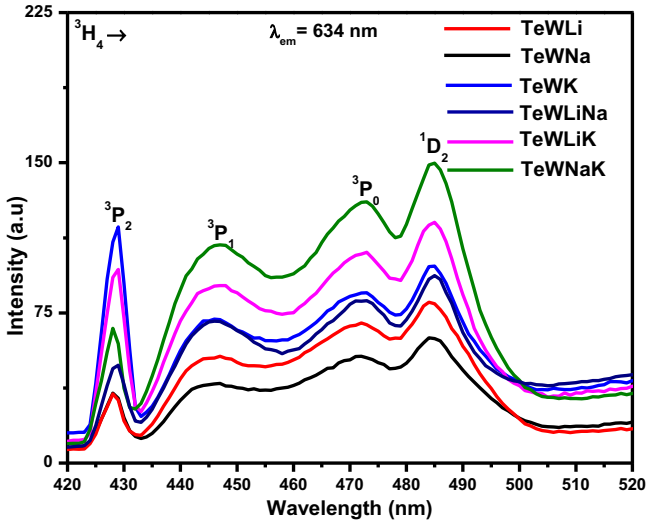


Fig. 2. Excitation spectra of Pr^{3+} ions doped single alkali and mixed alkali fluoro tungsten tellurite glasses.

between Pr^{3+} ions and the ligands is highly covalent in nature and the RE ion sites are having lower asymmetry [59] in these base glasses than the other reported glasses in literature [21,59–66]. This result is also in consistent with the result obtained from nephelauxetic ratio and bonding parameter.

3.2. Analysis of photoluminescence spectra and evaluation of radiative properties

Fig.2 represents the excitation spectra of TeWK glass at an emission wavelength 634 nm in the range 420–520 nm. It has four excitation bands corresponding to the transitions $^3H_4 \rightarrow {}^3P_2$, $^3H_4 \rightarrow {}^3P_1$, $^3H_4 \rightarrow {}^3P_0$ & $^3H_4 \rightarrow {}^1D_2$ at wavelengths 429 nm, 446 nm, 472 nm and 485 nm respectively. Among all the excitation bands, the band at 429 nm corresponding to the transition $^3H_4 \rightarrow {}^3P_2$ is more intense and is used as an excitation wavelength to record emission spectra. Fig.3 shows the PL spectra recorded for all the glasses under 429 nm excitation in the wavelength range 475–750 nm. The PL spectra of all the glasses show six luminescence bands at wavelengths 488, 529, 616, 646, 670 and 730 nm corresponding to the transitions $^3P_0 \rightarrow {}^3H_4$, $^3P_0 \rightarrow {}^3H_5$, $^3P_0 \rightarrow$

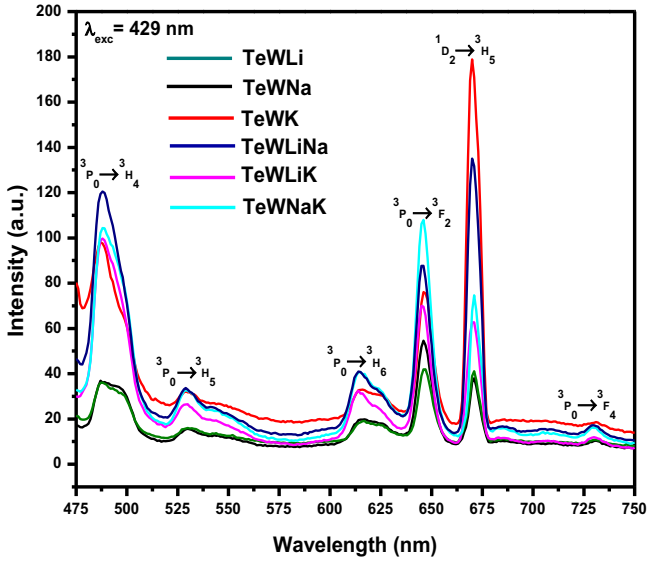


Fig. 3. Photoluminescence spectra of Pr^{3+} ions doped single alkali and mixed alkali fluoro tungsten tellurite glasses.

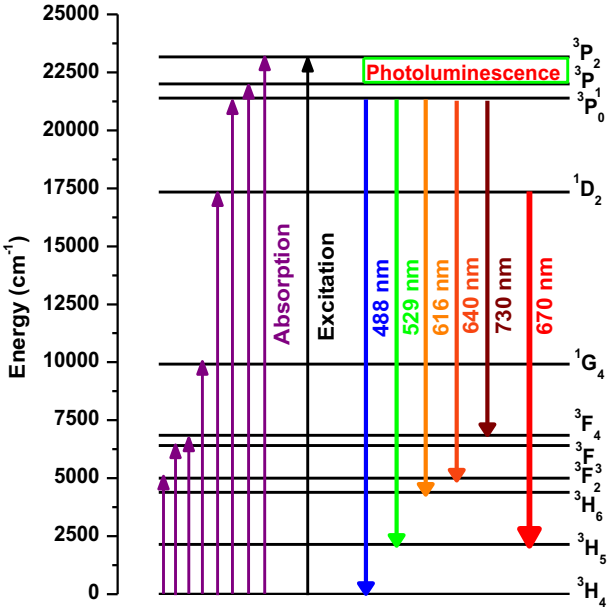


Fig. 4. Energy level diagram of Pr^{3+} ions doped single alkali and mixed alkali fluoro tungsten tellurite glasses.

$^3H_6$, $^3P_0 \rightarrow {}^3F_2$, $^1D_2 \rightarrow {}^3H_5$ and $^3P_0 \rightarrow {}^3F_4$ respectively. Among all these transitions, two transitions are highly intense in bluish-green and bright red regions at 488 nm and 670 nm corresponding to the transitions $^3P_0 \rightarrow {}^3H_4$ and $^1D_2 \rightarrow {}^3H_5$ for TeWK glass. These two transitions are originating from $^3P_0$ and $^1D_2$ and they are well resolved. The bluish-green emission from Pr^{3+} ions doped glasses can be explained on the basis of its energy level structure. The energy gap between $^3P_0$ and $^1D_2$ is 4042 cm^{-1}. In the present series of glasses, red luminescence dominates bluish-green luminescence because of non-radiative relaxation that took place from $^3P_0$ to $^1D_2$. In some cases bluish-green luminescence dominates the red luminescence because of increased radiative transition from $^3P_0$ to ground state instead of non-radiative relaxation of $^3P_0$ to $^1D_2$ state. The PL mechanism involved in the present work can be understood from Fig.4. In order to understand the PL performance of Pr^{3+} ions doped single alkali and mixed alkali fluoro tungsten tellurite glasses, the various radiative parameters have to be evaluated. For the present series of glasses radiative transition probability (A_R), radiative and experimental branching ratios (β_R & β_{exp}) were measured for the observed emission transitions by coupling the J-O parameters with PL data and are given in Table 3 along with the emission peak wavelength (λ_P), effective band widths ($\Delta\lambda_P$), stimulated emission cross-section (σ_{se}), gain band width ($\sigma_{se} \times \Delta\lambda_P$) and optical gain parameters ($\sigma_{se} \times \tau_R$). The necessary mathematical expressions required to evaluate the above mentioned radiative parameters were collected from literature [56]. The most essential condition for a particular transition to act as an efficient laser transition is having higher values for branching ratio and stimulated emission cross-sections [70]. From the Table 3, it is observed that, the transitions $^3P_0 \rightarrow {}^3H_4$ and $^1D_2 \rightarrow {}^3H_5$ possess higher values of branching ratio, stimulated emission cross-sections for TeWK glass. Hence, in the present series of glasses (Single and Mixed Alkali), TeWK glass is more suitable as lasing material to give bright red luminescence at 670 nm.

3.3. PL decay spectral analysis

To identify the better luminescent material, another important parameter is quantum efficiency which can be evaluated from the radiative and experimental lifetimes. Radiative lifetime can be measured from the J-O analysis and the experimental lifetime can be measured from decay spectra. Hence the PL decay spectra for all the glasses have

Table 3
Emission peak wavelength (λ_P) (nm), effective band widths ($\Delta\lambda_P$) (nm), transition probability (A_R), Branching ratios (β_R&β_{exp}) stimulated emission cross-sections (σ_{se}) (cm^2), gain band width ($\sigma_{se} \times \Delta\lambda_P$) ($cm^3$) and optical gain ($\sigma_{se} \times \tau_R$) ($cm^2$ s) for the emission transitions of Pr^{3+} ions in single alkali and mixed alkali fluoro tungsten tellurite glasses.

Spectral parameters	TeWLi	TeWNa	TeWK	TeWLiNa	TeWLiK	TeWNaK
$^3P_0 \rightarrow {}^3H_4$, λ_P = 488 nm						
$\Delta\lambda_P$	16.4	17.9	8.82	15.2	15.7	16.2
A_R	146,240	124,021	217,371	196,810	175,850	182,101
β_R	0.476	0.482	0.472	0.493	0.516	0.500
β_{exp}	0.286	0.291	0.323	0.361	0.415	0.369
$\sigma_{se}(\times 10^{-18})$	11.11	8.88	30.8	16.56	25.50	14.28
$\sigma_{se} \times \Delta\lambda_P$ $(\times 10^{-25})$	1.81	1.59	2.72	2.52	2.25	2.31
$\sigma_{se} \times \tau_R(\times 10^{-20})$	3.31	2.66	6.16	3.30	5.10	2.84
$^3P_0 \rightarrow {}^3F_2$, λ_P = 646 nm						
$\Delta\lambda_P$	9.65	9.98	9.75	9.98	9.35	9.35
A_R	118,536	96,314	179,146	143,841	113,704	128,319
β_R	0.385	0.374	0.389	0.360	0.333	0.352
β_{exp}	0.216	0.238	0.159	0.168	0.177	0.214
$\sigma_{se}(\times 10^{-18})$	46.8	38.9	93.6	53.4	70.5	47.8
$\sigma_{se} \times \Delta\lambda_P$ $(\times 10^{-25})$	4.51	3.79	6.88	5.65	4.47	4.99
$\sigma_{se} \times \tau_R(\times 10^{-20})$	14.0	11.4	14.1	11.3	9.57	10.7
$^1D_2 \rightarrow {}^3H_5$, λ_P = 670 nm						
$\Delta\lambda_P$	5.96	6.08	7.35	6.84	7.45	5.15
A_R	84,475	69,343	127,175	105,130	85,852	94,671
β_R	0.301	0.295	0.302	0.288	0.275	0.284
β_{exp}	0.145	0.125	0.231	0.182	0.125	0.109
$\sigma_{se}(\times 10^{-18})$	62.4	51.9	76.9	69.8	53.2	82.8
$\sigma_{se} \times \Delta\lambda_P$ $(\times 10^{-25})$	3.72	3.16	5.65	4.77	3.91	4.26
$\sigma_{se} \times \tau_R(\times 10^{-20})$	18.7	15.5	15.3	13.9	10.6	16.5

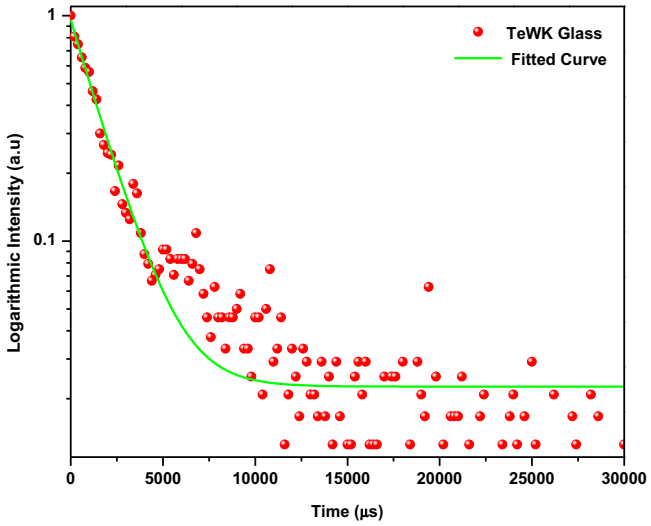


Fig. 5. The photoluminescence decay spectrum of Pr^{3+} ions doped TeWK glass for $^5D_0 \rightarrow {}^3H_5$ (670 nm) emission transition.

Table 4
The Experimental (τ_{exp}) (μs), radiative (τ_R) (μs) lifetimes, quantum efficiencies (η) and non-radiative decay rates (W_{NR}) ($\times 10^6\ s^{-1}$) for $^1D_2 \rightarrow {}^3H_5$ transition of Pr^{3+} ions doped single alkali and mixed alkali fluoro tungsten tellurite glasses under 429 nm excitation.

Glass	τ_{exp}	τ_R	η	W_{NR}	Reference
TeWLi	0.491	3	16.3	1.703	Present glasses
TeWNa	0.705	3	23.5	1.085	Present glasses
TeWK	1.450	2	72.5	0.269	Present glasses
TeWLiNa	0.896	2	44.8	0.616	Present glasses
TeWLiK	0.976	2	48.8	0.524	Present glasses
TeWNaK	1.014	2	50.7	0.486	Present glasses
Li	0.120	–	–	–	[71]
Na	0.231	–	–	–	
K	0.305	–	–	–	
LiK	0.160	–	–	–	
NaK	0.251	–	–	–	
2.5Pr NaF	0.206	–	–	–	[72]

been recorded for the luminescent level $^1D_2 \rightarrow {}^3H_5$ of Pr^{3+} ions doped single alkali and mixed alkali fluoro tungsten tellurite glasses at an excitation wavelength of 429 nm. All the decay profiles are fitted in single exponential and Fig.5 shows the decay profile of TeWK glass. The experimental lifetimes (τ_{exp}) for the luminescent level $^1D_2 \rightarrow {}^3H_5$ for all the glasses under investigation are tabulated in Table 4 along with the radiative lifetimes (τ_R). From the Table 4, it is observed that the experimental lifetimes (τ_{exp}) are smaller than the radiative lifetimes (τ_R). The experimental lifetimes are also compared with other reported values [71,72]. The variations between experimental and radiative lifetimes may be due to the non-radiative relaxation rates (W_{NR}) of excited state which includes multi-phonon relaxation (MPR), energy transfer through cross-relaxation (CR) and several other non-radiative processes. The non-radiative relaxation rates (W_{NR}) of present series of glasses also given in Table 4. The ratio of number of photons emitted to the number of photons absorbed is known as luminescence quantum efficiency (η). For RE doped materials it is equal to the ratio of the experimental lifetime to the predicted radiative lifetime for respective levels. The quantum efficiency values measured for all the glasses under investigation are given in Table 4. From the evaluated quantum efficiency values, it has been observed that, TeWK glass possesses maximum value of quantum efficiency. Hence, in the present series of Pr^{3+} ions doped single alkali and mixed alkali glasses, TeWK glass is quite suitable for the emission of laser in bright red region (670 nm).

4. Conclusions

Good optical quality single alkali and mixed alkali fluoro tungsten tellurite glasses doped with Pr^{3+} ions have been fabricated using conventional melt quenching technique. From the absorption spectra the J-O intensity parameters have been evaluated. In the present series of glasses, the single alkali based glasses follows the trend $\Omega_2 > \Omega_4 > \Omega_6$ whereas mixed alkali based glasses follows the trend $\Omega_4 > \Omega_2 > \Omega_6$. Among all the glasses, TeWK glasses have highest values of J-O parameters which confirm that the bonding between RE ions and the surrounding ligands is highly covalent in nature. Under 429 nm excitation, the PL spectra show two sharp peaks at 488 nm and 670 nm in bluish-green and bright red region corresponding to the transitions $^3P_0 \rightarrow {}^3H_4$ and $^1D_2 \rightarrow {}^3H_5$ respectively. Among these transitions, red color

emission predominates corresponding to the transition $^1D_2 \rightarrow {}^3H_5$ (670 nm) for the TeWK glass. The radiative properties evaluated such as branching ratio, stimulated emission cross-section are also high for these two transitions in particular for TeWK glass. From the PL decay spectra, the experimental lifetimes have been measured and in turn used to evaluate the quantum efficiency of glasses. Among all the glasses, TeWK glass possesses highest values of quantum efficiency for the transition $^1D_2 \rightarrow {}^3H_5$ at 670 nm. The emission cross-section, branching ratios and quantum efficiency measured for all these glasses allowed us to conclude that Tungsten tellurite glass with potassium fluoride as network modifier (TeWK glass) is aptly suitable to generate bright red laser at 670 nm.

Acknowledgements

This work is partly supported by High-impact Research initiative of IIT-Delhi, UK-India Education Research Initiative (UKIERI) and Department of Science and Technology (DST), Govt. of India, New Delhi. The authors, Prof. A. S. Rao (File Number: EMR/2016/007766), Dr. Sk. Mahamuda (File Number: ECR/2016/000376) and Dr. K. Swapna (File Number: ECR/2015/000335) are thankful to DST, Govt. of India, New Delhi for the award of a major research project to them.

References

[1] A. Jha, B. Richards, G. Jose, T. Teddy-Fernandez, P. Joshi, X. Jiang, J. Lousteau, Rare-earth ion doped TeO_2 and GeO_2 glasses as laser materials, Prog. Mater. Sci. 57 (2012) 1426–1491.
[2] A. Jha, B.D.O. Richards, G. Jose, T.T. Fernandez, C.J. Hill, J. Lousteau, P. Joshi, Review on structural, thermal, optical and spectroscopic properties of tellurium oxide based glasses for fibre optic and waveguide applications, Int. Mater. Rev. 57 (2012) 357–382.
[3] Bozena Burtan, Jan Cisowski, Zbigniew Mazurak, Bozena Jarzabek, Maria Czaja, Manuela Reben, Iwona Grelowska, Concentration-dependent spectroscopic properties of Pr^{3+} ions in TeO_2–WO_3–PbO–La_2O_3 glass, J. Non-Cryst. Solids 400 (2014) 21–26.
[4] M. Naftaly, A. Jha, Nd^{3+} doped fluoroaluminate glasses for a 1.3 μm amplifier, J. Appl. Physiol. 87 (2000) 2098–2104.
[5] J. Suresh Kumar, K. Pavani, A. Mohan Babu, N.K. Giri, S.B. Rai, L. Rama Moorthy, Fluorescence characteristics of Dy^{3+} ions in calcium fluoroborate glasses, J. Lumin. 130 (2010) 1916–1923.
[6] G. Sharma, R. Bagga, A. Cemmi, M. Falconieri, S. Baccaro, Spectroscopic investigations on γ-irradiated Eu^{3+} and Dy^{3+} doped oxyfluoride glasses, Radiat. Phys. Chem. 108 (2015) 48–53.
[7] S. Arunkumar, G. Venkataiah, K. Marimuthu, Spectroscopic and energy transfer behaviour of Dy^{3+} ions in B_2O_3- TeO_2 – PbO-PbF_2 - Bi_2O_3 - CdO glasses for laser and WLED applications, Spectrochim. Acta A Mol. Biomol. Spectrosc. 136 (2015) 1684–1697.
[8] R. Vijaya kumar, K. Maheshvaran, V. Sudarsan, K. Marimuthu, Concentration dependent luminescence studies on Eu^{3+} doped telluro fluoro borate glasses, J. Lumin. 154 (2014) 160–167.
[9] G. Venkataiah, C.K. Jayasankar, K. Venkata Krishnaiah, P. Dharmaiah, N. Vijaya, Concentration dependent luminescence properties of Sm^{3+} ions in tellurite–tungsten–zirconium glasses, Opt. Mater. 40 (2015) 26–35.
[10] M. Venkateswarlu, Sk. Mahamuda, K. Swapna, M.V.V.K.S. Prasad, A. SrinivasaRao, A. MohanBabu, Suman Shakya, G. VijayaPrakash, Spectroscopic studies of Nd^{3+} doped lead tungsten tellurite glasses for the NIR emission at 1062 nm, Opt. Mater. 39 (2015) 8–15.
[11] K. Kumar, S.B. Rai, D.K. Rai, Upconversion studies in Er^{3+} doped TeO_2–M_2O (M = Li, Na and K) binary glasses, Solid State Commun. 139 (2006) 363–369.
[12] H.T. Amorim, M.V.D. Vermelho, A.S. Gouveia-Neto, F.C. Cassanjes, S.J.L. Ribeiro, Y. Messaddeq, Red–green–blue upconversion emission and energy-transfer between Tm^{3+} and Er^{3+} ions in tellurite glasses excited at 1.064 μm, Sol. State Chem. 171 (2003) 278–281.
[13] E. Downing, L. Hesselink, J. Ralston, R. Macfarlane, A three-color, solid-state, three-dimensional display, Science 273 (1996) 1185–1189.
[14] M.J. Dejneka, A. Streltsov, S. Pal, A.G. Frutos, C.L. Powell, K. Yost, Po Ki Yuen, U. Muller, J. Lahiri, Rare earth-doped glass microbarcodes, Proc. Natl. Acad. Sci. U. S. A. 100 (2003) 389–393.
[15] S.A. Wade, S.F. Collins, G.W. Baxter, The fluorescence intensity ratio technique for optical fiber point temperature sensing, J. Appl. Phys. 94 (2003) 4743–4756.
[16] P. Xie, T.R. Gosnell, Room-temperature upconversion fiber laser tunable in the red, orange, green, and blue spectral regions, Opt. Lett. 20 (1995) 1014–1016.
[17] M. Tsuda, K. Sousa, H. Inoue, S. Inoue, A. Makishima, Upconversion mechanism in Er^{3+}-doped fluorozirconate glasses under 800 nm excitation, J. Appl. Phys. 85 (1999) 29–37.
[18] M. Venkateswarlu, Sk. Mahamuda, K. Swapna, A. Srinivasa Rao, A. Mohan Babu, Suman Shakya, D. Haranath, G. Vijaya Prakash, Luminescence spectral studies of Tm^{3+} ions doped lead tungsten tellurite glasses for visible red and NIR applications, J. Lumin. 175 (2016) 225–231.
[19] H. Ebendorff-Heidepriem, D. Ehrt, M. Bettinelli, A. Speghini, Rare-earth-doped materials and devices III, SPIE Proc. 3622 (1999) 19–30.
[20] J.S. Wang, E.M. Vogel, E. Snitzer, J.L. Jackel, V.L. da Silva, Y. Silberberg, 1.3 μm emission of neodymium and praseodymium in tellurite-based glasses, J. Non-Cryst. Solids 178 (1994) 109–113.
[21] M. Venkateswarlu, M.V.V.K.S. Prasad, K. Swapna, Sk. Mahamuda, A. Srinivasa Rao, A. MohanBabu, D. Haranath, Pr^{3+} doped lead tungsten tellurite glasses for visible red lasers. Ceramics International, Ceram. Int. 40 (2014) 6261–6269.
[22] A.K. Yakhkind, Tellurite glasses, J. Am. Ceram. Soc. 49 (1966) 670–675.
[23] V. Kozhukharov, M. Marinov, G. Grigorova, Glass-formation range in binary tellurite systems containing transition metal oxides, J. Non-Cryst. Solids 28 (1978) 429–430.
[24] R. El-Mallawany, The optical properties of tellurite glasses, J. Appl. Phys. 72 (1992) 1774–1777.
[25] A. Berthereau, Y. Le Luyer, R. Olazcuaga, G. Le Flem, M. Couzi, L. Canioni, P. Segonds, L. Sarger, A. Ducasse, Nonlinear optical properties of some tellurium (IV) oxide glasses, Mater. Res. Bull. 29 (1994) 933–941.
[26] S.H. Kim, T. Yoko, Nonlinear optical properties of TeO_2-based glasses: MO_x-TeO_2 (M = Sc, Ti, V, Nb, Mo, Ta, and W) binary glasses, J. Am. Ceram. Soc. 78 (1995) 1061–1065.
[27] M.A. Newhouse, R.F. Bartholomev, B.G. Aitken, L.J. Button, N.F. Borrelli, Pr-doped mixed-halide glasses for 1300 nm amplification, IEEE Photon. Technol. Lett. 6 (1994) 189–191.
[28] P. Subbalakshmi, N. Veeraiah, Study of CaO–WO_3 – P_2O_5 glass system by dielectric properties, IR spectra and differential thermal analysis, J. Non-Cryst. Solids 298 (2002) 89–98.
[29] A.E. Ersundu, M. Celikbilek, S. Aydin, Characterization of B_2O_3 and/or WO_3 containing tellurite glasses, J. Non-Cryst. Solids 358 (2012) 641–647.
[30] J. Ozdanova, H. Ticha, L. Tichy, Optical band gap and Raman spectra in some $(Bi_2O_3)_x$ $(WO_3)_y$ $(TeO_2)_{100-x-y}$ and $(PbO)_x$ (WO3)y$(TeO2)_{100-x-y}$ glasses, J. Non-Cryst. Solids 355 (2009) 2318–2322.
[31] D. Munoz-Martin, M.A. Villegas, J. Gonzalo, J.M. Fernandez-Navarro, Characterisation of glasses in the TeO_2 – WO_3 - PbO. System, J. Eur. Ceram. Soc. 29 (2009) 2903–2913.
[32] M. Celikbilek, A.E. Ersundu, N. Solak, S. Aydın, Investigation on thermal and microstructural characterization of the TeO_2–WO_3 system, J. Alloys Compd. 509 (2011) 5646–5654.
[33] M. Celikbilek, A.E. Ersundu, N. Solak, S. Aydın, Crystallization kinetics of the tungsten–tellurite glasses, J. Non-Cryst. Solids 357 (2011) 88–95.
[34] A.E. Ersundu, M. Celikbilek, N. Solak, S. Aydın, Glass formation area and characterization studies in the CdO–TeO_2–WO_3 ternary system, J. Eur. Ceram. Soc. 31 (2011) 2775–2781.
[35] M.R. Sahor, A.K. Jehnu, M.M. Karim, TeO_2 – ZnO – $ZnCl_2$ glasses for IR transmission, J. Non-Cryst. Solids 213 (1997) 164–167.
[36] P. Nageswara Rao, G. Naga Raju, D. Krishna Rao, N. Veeraiah, Optical absorption and thermoluminescence studies on LiF–Sb_2O_3–B_2O_3 glasses doped with Ni^{2+} ions, J. Lumin. 117 (2006) 53–60.
[37] J.O. Isard, The mixed alkali effect in glass, J. Non-Cryst. Solids 1 (1969) 235–261.
[38] D.E. Day, Mixed alkali glasses — their properties and uses, J. Non-Cryst. Solids 21 (1976) 343–372.
[39] J.F. Stebbins, Cation sites in mixed-alkali oxide glasses: correlations of NMR chemical shift data with site size and bond distance, Solid State Ionics 112 (1998) 137–141.
[40] T. Uchino, T. Yoko, Sodium and lithium environments in single- and mixed-alkali silicate glasses. An ab initio molecular orbital study, J. Phys. Chem. B 103 (1999) 1854–1858.
[41] Adam J. Stevenson, Helene Serier-Brault, Patrick Gredin, Michel Mortier, Fluoride materials for optical applications: single crystals, ceramics, glasses, and glass–-ceramics, J. Fluor. Chem. 132 (2011) 1165–1173.
[42] Ying Tian, Junjie Zhang, Yifan Zhu Xufeng, Shiqing Xu, Intense mid-infrared emissions and energy transfer dynamics in Ho^{3+}/Er^{3+} codoped fluoride glass, J. Lumin. 138 (2013) 94–97.
[43] Barbara Klimesz, Grazyna Dominiak-Dzik, Witold Ryba-Romanowski, Thermal and radiative characteristics of oxyfluoride glass singly doped with lanthanide ions, J. Rare Earths 28 (2010) 893–898.
[44] L. Zhang, L. Wen, J. zhang, L. Hu, Influence of TeO_2, PbF_2, ZnF_2 on the spectroscopic and lasing properties of Yb^{3+} doped fluorophosphate glass, J. Alloys Compd. 391 (2005) 156–161.
[45] K. Binnemans, D. Verboven, C. Görller-Walrand, J. Lucas, N. Duhamel-Henny, J.L. Adam, Absorption and magnetic circular dichroism spectra of praseodymium doped fluorozirconate (ZBLAN) glass, J. Alloys Compd. 250 (1997) 321–325.
[46] A.A. Kaminskii, Achievements of modern crystal-laser physics, Ann. Phys. Fr. 16 (1991) 639–706.
[47] Y.K. Sharma, S.P. Tondon, S.S.L. Surana, Laser action in praseodymium doped zinc chloride borophosphate glasses, Mater. Sci. Eng. B 77 (2000) 167–171.
[48] L. Bokatial, S. Rai, Optical properties and upconversion of Pr^{3+} doped CdS nanoparticles in sol-gel glasses, J. Lumin. 130 (2010) 1857–1862.
[49] Y.C. Ratnakaram, A.V. Kumar, D.T. Naidu, N.O. Gopal, Compositional dependencies of optical absorption and emission properties of Pr^{3+} in mixed alkali borate glasses, Mater. Lett. 58 (2004) 3908–3914.
[50] L. Del Longo, M. Ferrari, E. Zanghellini, M. Bettinelli, J.A. Capobiaanco, M. Montagna, F. Rossi, Optical spectroscopy of zinc borate glass activated by Pr^{3+} ions, J. Non-Cryst. Solids 231 (1998) 178–188.
[51] L. Zhang, G. Dong, M. Peng, J. Qiu, Comparative investigation on the spectroscopic

properties of Pr^{3+}-doped boro-phosphate, boro-germo-silicate and tellurite glasses, Spectrochim. Acta A 93 (2012) 223–227.
[52] V. Nazabal, M. Poulain, M. Olivier, P. Pirasteh, P. Camy, J.L. Doualan, S. Guy, T. Djouama, A. Boutarfaia, J.L. Adam, Fluoride and oxyfluoride glasses for optical applications, J. Fluor. Chem. 134 (2012) 18–23.
[53] L. Bokatial, S. Rai, Optical properties and up-conversion of Pr^{3+} doped CdS nanoparticles in sol–gel glasses, J. Lumin. 130 (2010) 1857–1862.
[54] M.E. Rodriguez, V.E. Diz, J. Awruch, L.E. Dicelio, Photophysics of zinc (II) phthalocyanine polymer and gel formulation, Photochem. Photobiol. 86 (2010) 513–519.
[55] J.T.F. Lau, P.C. Lo, Y.M. Tsang, W.P. Fong, D.K.P. Ng, Unsymmetrical β-cyclodextrin-conjugated silicon(IV) phthalocyanines as highly potent photo sensitisers for photodynamic therapy, Chem. Commun. 47 (2011) 9657–9659.
[56] W.T. Carnall, P.R. Fields, K. Rajnek, Electronic energy levels in the trivalent lanthanide aquo ions. I. Pr^{3+}, Nd^{3+}, Pm^{3+}, Sm^{3+}, Dy^{3+}, Ho^{3+}, Er^{3+}, and Tm^{3+}, J. Chem. Phys. 49 (1968) 4424–4442.
[57] Sk. Mahamuda, K. Swapna, A. SrinivasaRao, T. Sasikala, L. RamaMoorthy, Reddish-orange emission from Pr^{3+} doped zinc alumino bismuth borate glasses, Physica B 428 (2013) 36–42.
[58] V.V. Ravi Kanth Kumar, C.K. Jayasankar, Spectroscopic investigations of Pr(III) ions in alkali cadmium borosulphate glasses, J. Non-Cryst. Solids 163 (1993) 249–260.
[59] Sk. Mahamuda, K. Swapna, M. Venkateswarlu, A. Srinivasa Rao, Suman Shakya, G. Vijaya Prakash, Spectral characterisation of Sm^{3+} ions doped oxy-fluoroborate glasses for visible orange luminescent applications, J. Lumin. 154 (2014) 410–424.
[60] Melinda Olivier, Jean-Louis Doualan, Virginie Nazabal, Patrice Camy, Jean-Luc Adam, Spectroscopic study and Judd–Ofelt analysis of Pr^{3+}-doped Zr–Ba–La–Al glasses in visible spectral range, J. Opt. Soc. Am. B 30 (2013) 2032–2042.
[61] M.A. Newhouse, R.F. Bartholomew, B.G. Aitken, L.J. Button, N.F. Borrelli, Pr-doped mixed-halide glasses for 1300 nm amplification, IEEE Photon. Technol. Lett. 6 (1994) 189–191.
[62] Z. Mazurak, S. Bodyl, R. Lisiecki, J. Gabrys-Pisarska, M. Czaja, Optical properties of Pr^{3+}, Sm^{3+} and Er^{3+} doped P_2O_5–CaO–SrO–BaO phosphate glass, Opt. Mater. 32 (2010) 547–553.
[63] D.V.R. Murthy, B.C. Jamalaiah, T. Sasi Kala, L. Rama Moorthy, M. Jayasimhadri, Kiwan Jang, HoSueb Lee, Soung Soo Yi, Jung Hyun Jeong, Optical absorption and emission characteristics of Pr^{3+}-doped RTP glasses, Physica B 405 (2010) 1095–1100.
[64] B.C. Jamalaiah, J. Suresh Kumar, A. Mohan Babu, L. Rama Moorthy, Kiwan Jang, HoSueb Lee, M. Jaya Simhadri, Jung Hyun Jeong, Hyukjoon Choi, Optical absorption, fluorescence and decay properties of Pr^{3+}-doped PbO–H_3BO_3–TiO_2–AlF_3 glasses, J. Lumin. 129 (2009) 1023–1028.
[65] I. Pal, A. Agarwal, S. Sanghi, M.P. Aggarwal, Structural, absorption and fluorescence spectral analysis of Pr^{3+} ions doped zinc bismuth borate glasses, J. Alloys Compd. 509 (2011) 7625–7631.
[66] V.K. Rai, S.B. Rai, D.K. Rai, Spectroscopic properties of Pr^{3+} doped in tellurite glass, Spectrochim. Acta A 62 (2005) 302–306.
[67] J.E. Shelby, Introduction to Glass Science and Technology, 2nd ed., (2005), pp. 72–95 (Chapter 5).
[68] Fuxi Gan, Optical properties of fluoride glasses: a review, J. Non-Cryst. Solids 184 (1995) 9–20.
[69] T. Nakajima, B. Zemva, A. Tressaud, Advanced Inorganic Fluorides: Synthesis, Characterization and Applications, 1st ed., Elsevier, 2000.
[70] N.Q. Wang, X. Zhao, C.M. Li, E.Y.B. Pun, H. Lin, Upconversion and color tunability in Tm^{3+}/Ho^{3+}/Yb^{3+} doped low phonon energy bismuth tellurite glasses, J. Lumin. 130 (2010) 1044–1047.
[71] G. Amarnath, S. Buddhudu, Spectroscopic properties of Pr^{3+} doped multi component fluoride glasses, Mater. Res. Bull. 25 (1990) 1317–1323.
[72] Fenz Zhang, Zhuanfang Bi, Anping Huang, Zhisong Xiao, J. Lumin. 160 (2015) 85–89.

Predicting Crowdfunding Success with Optimally Weighted Random Forests

Fahad Sarfaraz Ahmad[1], Devank Tyagi[2], Simran Kaur[3]

[1]*Electronics & Communication Engineering Delhi Technological University New Delhi, India fahad bt2k14@dtu.ac.in*
[2]*Dept. of Computer Engineering Delhi Technological University New Delhi, India ank@gmail.com*
[3]*Dept. of Computer Engineering Delhi Technological University New Delhi, India simrankaur1509@gmail.com*

Abstract: ***The social media version of fundraising, crowdfund- ing has, within a very short time, become an important and often critical element of the process that allows budding entrepreneurs to grow in todays market. While the underlying principle behind crowdfunding - to get multiple people to financially back an idea and collectively amass enough resources to make it happen - is simple enough in theory, it is much harder to actually implement. Kickstarter, the largest and most well-known crowdfunding website internationally, sees more than half of the uploaded projects rejected due to inadequate funds gathered. In this study, we take a closer look at the reasons for success and failure of these projects from the project description pages, where the creators attempt to persuade potential backers into supporting their respective creations. A dataset of over 26 thousand Kickstarter projects was created and used to understand the factors that most affect the chances of acquiring successful funding. In this study, we propose a novel algorithm for the RandomForests learning model in which we assign optimal weights to the individual classifiers and perform weighted majority voting on them using the 13 predictors that were found to be most suitable through implementation logic. These predictors will serve to be useful to both, a project creator as well as a potential backer, in order to devote their energy and resources judiciously. Finally, we tested our optimized learning model on the freshly acquired dataset and observed 94.289% accuracy, 94.5% precision, 94.3% recall and 94.3% F-measure value in success prediction. This research achieved the best accuracy and greatest amount of success in this field.***

Keywords: Crowdfunding, Kickstarter, learning models, Decision Trees, RandomForests

I. INTRODUCTION

Crowdfunding has been around as a useful concept since 2007, but was able to gain traction only after the advent of websites such as Kickstarter, which allowed everyone from experienced creators to novice experimenters to put up their ideas in front of a large group of people and allow them to decide the viability of the ideas. However, while experienced creators may know how to acquire the required funding for the fruitful completion of their projects, the novice creators usually struggle to become successful, even if their ideas are viable as well as productive.

Online crowdfunding websites such as Kickstarter work in an all-or-nothing manner - if the funds collected for the project in the stipulated time match or exceed the creator-defined goal, the project creator gets the funding and his/her project is successful. However, if the funds collected fall short of the goal, even by a dollar, the creator will get nothing and the project is declared to be a failure. This strategy means that novice creators usually end up on the wrong side of successful funding [9], since it is difficult to know what 'works' for the large pool of potential backers out over the World Wide Web. According to Kickstarter, as of July 2017, there have been 367,763 projects uploaded, out of which only 130,209 projects have received successful funding - a success rate of merely 35.83% excluding live projects.

TABLE I: Project Statistics On Kickstarter.

Total projects	367,763
Successful projects	130,209
Unsuccessful projects	233,207
Live projects	4,347
Total money pledged	$3.23B
Money pledged successfully	$2.84B
Money pledged unsuccessfully	$356M

Hence, an urgent need for a guideline is apparent, one that supports novices and experts alike in seeing whether their project description and presentation are conducive to receiving successful funding or not. This research is thus motivated to provide this guideline in the form of a machine learning tool, which identifies the individual traits of a crowdfunding project and shows them to the creator, giving him/her the time and opportunity to make revisions to their projects before

978-1-5386-0514-1/17/$31.00 ©2017 IEEE

launching them on the online crowdfunding platform. This tool is prepared and tested for efficiency using the very large amount of data that is present from past projects, both successful and unsuccessful.

II. DATASETS

The website *kicktraq.com* contains the URLs of all the project description pages that have been uploaded on Kickstarter's servers. These URLs were used to automate the process of web scraping the data on the project description pages. The final dataset created contained the details of 26,191 Kickstarter projects. All these projects had their creation dates lie from 01/12/2009 to 20/03/2017. The dataset contains details of projects over 15 categories, with 12,911 of these projects having proven successful. While this is in contrast to the actual success rate of projects on Kickstarter, a higher number of successful projects were required by the learning model since success is the driving force behind the model's functioning. The web scraping process is illustrated in Figure 1.

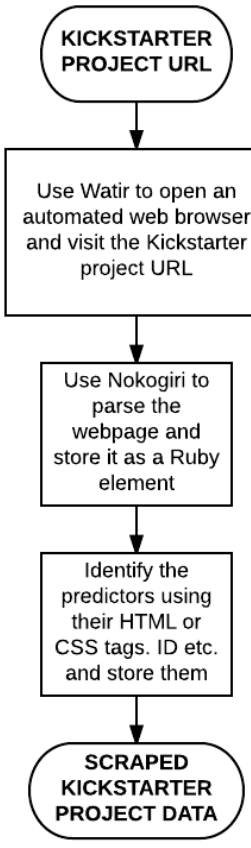


Fig. 1. The web scraping process to create the data

TABLE III: Learning Model Predictors.

Project Category	The field in which the idea/product falls
Goal	The creator-defined goal for accumulated funding received
SmogMain	The readability index of the project description given
SentMain	Number of sentences in the project description given
SentReward	Number of sentences in the reward description given
#Images	Number of images on project description page
#Videos	Number of videos on project description page
#Rewards	Number of rewards given by user
#Websites	Number of webpages related to the project
#Collaborators	Number of project collaborators
#FbFriends	Number of Facebook friends the creator has
#CreatedProjects	Number of projects created by project creator
#BackedProjects	Number of projects backed by project creator

TABLE II: Dataset Description Statistics.

Total projects scraped	26,191
Successful projects scraped	12,911
Unsuccessful projects scraped	13,280
Ratio of successful projects scraped	0.493
Creation time of first project scraped	01/12/2009
Creation time of last project scraped	20/03/2017
Number of predictors in dataset	13

The dataset consists of 13 predictors, attributes of data obtained from the project description page. Some of the predictors have been tested in past literature such as Greenberg [1] and Chung [2]. However, a large part of this research has been coming up with newer, better predictors that have hitherto been untapped for the purpose of learning. For example, one of our predictors is the SMOG Index of the project description [4] [6], which allows us to calculate the readability of a piece of text. Mitra and Gilbert [10] illustrate how the phrases used in the project description go a long way in determining the

success of a project due to its comprehensibility and tone. The 13 predictors are given in Table III.

III. EXPERIMENTAL DESIGN

A. Proposed Approach

The problem posed in front of us is twofold. Firstly, we must attempt to create a predictive model that can accurately classify the data points into the classes of success and failure. Secondly, we must find the factors that most affect the chances of success of the project, in order to allow the project creator to focus on those aspects of the project description page. Keeping these requirements in mind, the Decision Tree [11] learning algorithm was decided upon as a suitable solution. The Decision Tree algorithm is a simple inductive algorithm which is visualized in the form of a top-down tree, wherein each node except the root node is formed as a result of the parent node splitting, on the basis of some irregularity or disorder in the data. The leaf nodes of the Decision Tree are the results obtained, and each path in the Decision Tree corresponds to an independent decision-making logic. This ensures that not only do we get a class as an answer (in this case, the classification into success or failure), we also obtain the decision-making logic and the importance of each decision (in this case, the predictors most important in achieving the accuracy in prediction).

The accuracy obtained by the Decision Tree classifier, however, can be improved. Chandra et al. [14] and Soares et al. [15] discuss how ensembles of classifiers tend to give better results for classification accuracy than standalone classifiers.

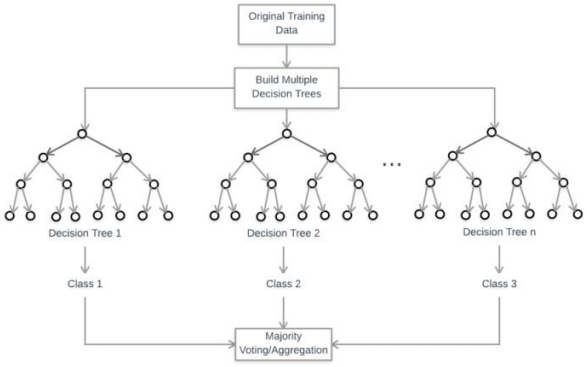


Fig. 2. The Conventional RandomForests Learning Model [5].

Hence, a randomly distributed ensemble of Decision Trees was decided upon as the learning model which would work upon our dataset. This is known as the RandomForests learning model [12], as shown in Figure 2.

The RandomForests learning model creates a number of independent Decision Trees with low correlation between the classifiers, with different combinations of predictors. These combinations of m predictors, where m<M (the total number of predictors to be used) is defined manually, are generated randomly by a meta-algorithm known as *random subspace method*. New training sets are generated by randomly sampling data from the original training set with replacement and using them to train the model. This is known as *bootstrap aggregating*, and it reduces the variance that Decision Trees, Neural Networks and other complex algorithms generally suffer from.

The RandomForests learning model evaluates the class of

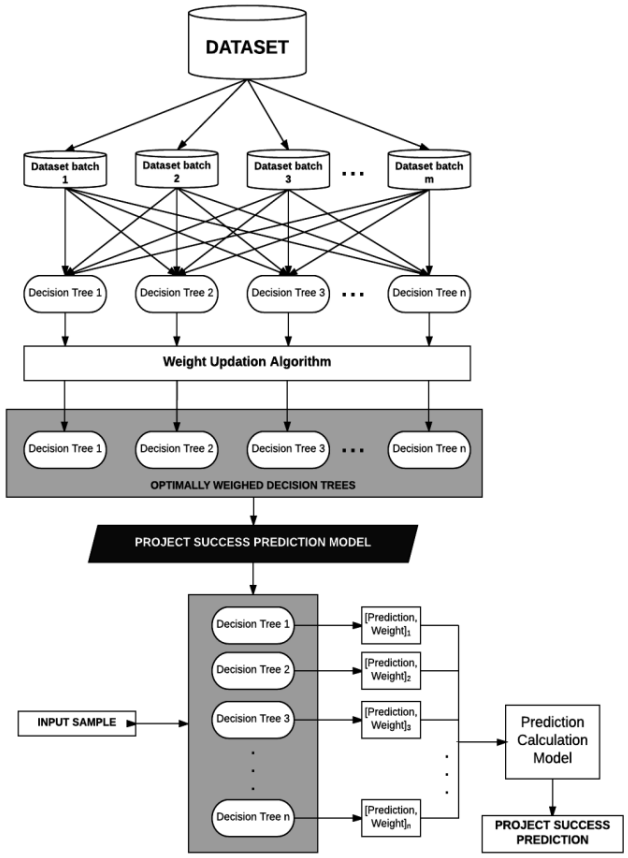


Fig. 3. Proposed Architecture of Optimally Weighted RandomForests Model, with *m* batches of data and *n* Decision Trees in the ensemble.

the data by taking the results of all the Decision Trees and conducting majority voting. It is easy to reason that some Decision Trees will return successful predictions with a higher accuracy than other trees, due to the random set of predictors bagged by them. It logically follows that the decisions taken by these trees should be considered with more importance than the decisions taken by trees with lower rates of accurate predictions. Winham et al. [7] and Lee et al. [8] used the out-of-bag (OOB) error rates to predict accuracy and assigned these accuracies as the weights of the Decision Trees. Our proposed model for the RandomForests learning model on this dataset uses a unique approach to assign greater weights to

the decisions made by high-accuracy Decision Trees in the ensemble.

Figure 3 shows the architecture of the proposed model. The Kickstarter projects training set is divided into *m* batches of projects, whcih are given batchwise to the conventional RandomForests learning model for training. Every Decision Tree performs the classification procedure and obtains an accuracy measure, A_c. This value of accuracy is compared against the accuracy of the ensemble, A_e to give a decision parameter, θ.

$$\theta = \frac{A_c}{A_e}$$

The decision parameter θ was used to decide the magnitude of weight updation required. If $\theta > 1$, the ensemble is working at a lower accuracy than the classifier itself, and that particular Decision Tree must be considered with a much greater weight than other trees. Similarly, if $\theta < 0.33$ (empirically determined value), the weight of this Decision Tree's predictions must be drastically reduced in order to increase the ensemble's overall accuracy. In this manner, all the trees are given updated weights on the basis of their individual accuracy rates. The decision parameter θ is scaled upto the weights of the trees by a weighing factor, β, which we take as the running average of the weights of trees till that point.

$$\theta = \theta * \beta$$

Once all the Decision Trees in the ensemble have been trained in this manner, the test set is passed to the ensemble learning model, where each Decision Tree classifies the data given into the class of either success or failure. These decisions, D_i, are multiplied by the weight of their respective Decision Tree to give the weighted vote, V_i. Weighted majority voting is then performed to decide the final class of the project.

$$V = \sum_{i=1}^{n} V_i$$

Algorithm 1: Weight Updation

Input: treeForest: ensemble of Decision Trees used for classification, the weight of each of which is initialized as 1, n: number of Decision Trees, m: number of batches of data from dataset

Output: treeForest: ensemble of Decision Trees with weights appropriately updated

1. obtain m batches of data from original dataset
2. $\beta \leftarrow 1$ (average weight of all Decision Trees)
3) for i ← 1 to m (for each batch) do:
4) numData ← number of project descriptions in batch
5) for j ← 1 to numData (for each project) do:
6) for k ← 1 to n (for each Decision Tree) do:
7. $\theta \leftarrow A_c/A_e$
8. $\theta_1 \leftarrow \theta * \beta$
9. if $\theta > 1$ weight[k] ← weight[k] + $(\theta_1 * n)$
10. else if $\theta > 0.66$ weight[k] ← weight[k] + θ_1
11. else if $\theta > 0.33$ weight[k] ← weight[k] - θ_1
12. else weight[k] ← weight[k] - $(\theta_1 * n)$
13. $\beta \leftarrow$ update running average with new weight
14) return treeForest with newly weighted Decision Trees

Algorithm 2: Prediction Calculation

Input: treeForest: ensemble of Decision Trees used for classification, with optimally weighted Decision Trees, n: number of Decision Trees, testSet: the test set of data on which accuracy is derived

Output: Success: binary variable denoting 1 for success and 0 for failure

1) numData ← number of projects in testSet
2) for i ← 1 to numData (for each project) do:
3) initialize zeroc and onec as 0
4) for j ← 1 to n (for each Decision Tree) do:
5) pass testSet[i] to treeForest[j]
6) c ← result of classification by treeForest[i]
7) if c is 0, zeroc ← zeroc + weight[j]
8) else onec ← onec + weight[j]
9) if zeroc > onec success ← 0
10) else success ← 1
11) output success

The web scraping and classification were performed on Intel Dual Core i7-7500U (upto 3.5GHz), with 12GB DDR4-2133 SDRAM and Ubuntu 16.04 operating system. The classification was performed over the dataset described above, with a 66-34 train-to-test split after resampling the data to avoid sampling bias.

The classification process was divided into two phases.

- The first phase involved the classification of the entire dataset. In this phase, we retained "Project Category" as a predictor.
- The second phase involved classification over 15 different datasets, partitioned on the basis of their project categories,to test whether projects of different categories could be predicted with more accuracy by different pre-

dictive models for each category separately. In this phase, "Project Category" was not retained as a predictor.

B. Evaluation Metrics

- ***Accuracy:*** Accuracy is one of the most popular evaluation metrics, used for predictive models in most literatures. In terms of the confusion matrix, accuracy is defined as the sum of the true positives and false negatives (number of correct predictions) over the total number of predictions.

$$\text{Accuracy} = \frac{tp + tn}{tp + tn + fp + fn}$$

- Precision: Precision is an evaluation metric that gives a measure of the number of relevant predictions from amongst the total predictions made. In terms of the confusion matrix, precision is defined as the number of true positive predictions over the total number of positive predictions made.

$$\text{Precision} = \frac{tp}{tp + fp}$$

- ***Recall:*** Recall is an evaluation metric that gives a measure of the number of relevant predictions made from amongst the actual relevant instances. In terms of the confusion matrix, recall is defined as the number of true positive predictions made over the total number of positive instances.

$$\text{Recall} = \frac{tp}{tp + fn}$$

- ***F-Measure:*** F-Measure or F-score is also one of the most popular evaluation metrics used for predictive models. The F-Measure is calculated by first calculating the precision and recall values of the model and then finding the harmonic mean of these values.

$$\text{F-Measure} = \frac{2 \cdot Precision \cdot Recall}{Precision + Recall}$$

IV. EXPERIMENTAL RESULT ANALYSIS

Upon empirically testing our optimally weighted RandomForests learning model, we were able to arrive at the following values for the aforementioned evaluation metrics:

TABLE IV: Result Evaluation Metrics.

Accuracy	94.29%
Precision	94.5%
Recall	94.3%
F-Measure	94.3%

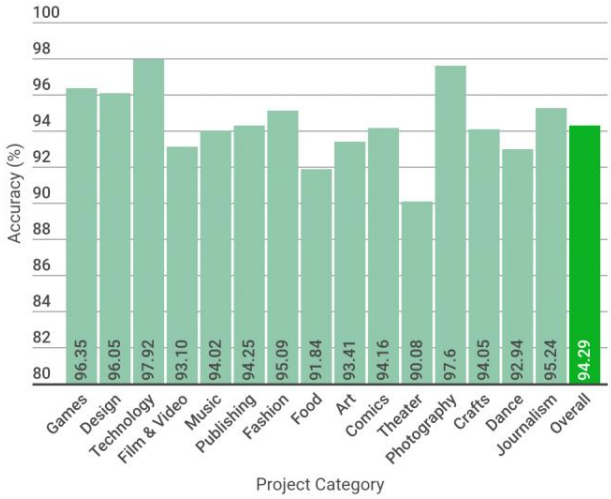


Fig. 4. Category-Wise Accuracies Using Random Forests

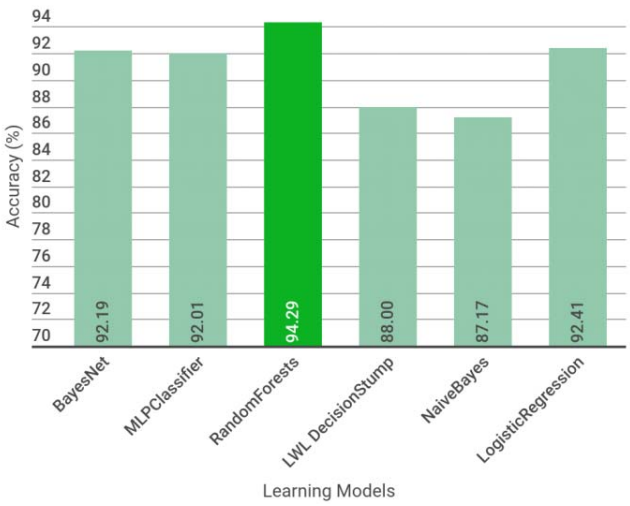


Fig. 5. Comparison of Accuracies of Different Learning Models.

We then partitioned the dataset on the basis of project category and performed the classification process on these 15 datasets, with 12 parameters. The findings of this process are illustrated in Figure 4, which shows the performance of our learning model over each of the categories. It is easy to observe that the accuracy obtained on the entire dataset is almost equal to the accuracies obtained on each dataset with a different category.

The optimally weighted RandomForests learning model eclipsed the performance of other, more conventional algorithms by at least 1 percent in all cases. Figure 5 shows the accuracies of success prediction by some well-known algorithms on the dataset, in comparison to the accuracy produced by our RandomForests learning model. It is interesting to note that even the learning models that are either commonly used or have been implemented in past literature, gave greatly improved results over the data.

We were also able to compare the importance of various predictors with respect to each other, based upon the average impurity decrease (Gini-index) and the number of nodes using that predictor. It was found that *#Websites*, which is the number of webpage links given about the project, and *SmogMain*, which is the Smog Index (readability measure) of the project description, proved to be amongst the most important predictors from amongst the 13 predictors. This was experimentally verified by attempting to perform success prediction on the dataset without the *#Websites* and *SmogMain* predictors. This time, the learning model yielded an accuracy measure of only 78.62%.

It also came to our notice that the *#created* predictor, which is the number of projects created in the past by the current project creator, had the least importance. In fact, it was not used even once to classify success in this dataset. This result conflicted with our intuition that an experienced project creator would have a better grasp of the platform and hence, find it easier

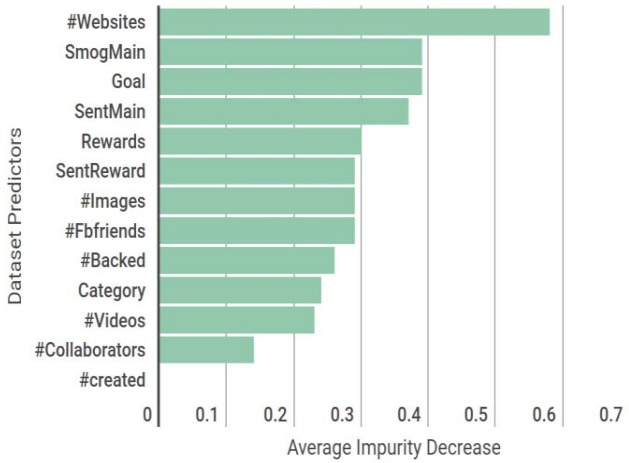


Fig. 6. Comparison of Predictor Importances.

to receive the appropriate funding for their project. Figure 6 shows the different predictors in order of their importance, as decided by their average impurity decrease in the learning model.

The limitations of our model are brought into light when trying to predict project success at various instances of its duration using temporal features. Chung and Lee [2] incorporated temporal features into their study. Our proposed model only predicts success at the inception of the project.

V. RELATED WORKS

There have been previous attempts to use a predictive model to forecast the success of a project from an online crowdfunding website such as Kickstarter, considering the popularity of crowndfunding ventures. Greenberg et al [1] in 2013 used a variety of machine learning techniques and ran classification algorithms such as SVMs, decision trees, REPTree, logistic regression etc. in order to try and classify projects as either bound to be successful or otherwise. They reached Decision Trees as their optimal learning model, with 68% accuracy in prediction of success.

Etter [3] attempted to put the time series of pledged money per project to use, to classify live projects as probable success and failures. This research also tied social features with the success prediction model and showed significant improvement in the predictive power of the model. Their learning model of choice was the Support Vector Machine (SVM).

Chung and Lee [2] improved the predictors that were existent in the model present at that time and also attempted to add temporal features and Twitter analytics, which allowed them to achieve 76.4% accuracy with static features and 78.9% accuracy with Twitter features, using the AdaBoost M1 classifier. They also created a pledged money range indicator which could predict the total funds collected per project with 86.5% accuracy.

Compared with the previous research work, we obtained the highest accuracy for the success prediction process using our modified RandomForests algorithms using optimally weighted Decision Trees, on static data. Our next step with this line of thinking would be to complement this research with real-time data, which would allow for the success prediction of live projects as well, at the time of their inception or at any point during their fundraising period.

Another comparison lies in the selection of predictors for the learning model. We are the first to use the parameters of number of websites related to the project on the page, and the readability index of the project description, together in the same dataset. Empirical testing has already shown that the absence of these predictors brings the results of the evaluation metrics down to the results obtained in past literature.

TABLE V: Comparison With Previous Works.

Decision Trees, 2013	68% (static)
SVM, 2013	76% after 4 hours from launch (real-time)
AdaBoostM1, 2015	76.4% (static), 78.9% (Twitter-augmented)
RandomForests, 2017	94.29% (static)

VI. CONCLUSION

The problem of being able to predict the success of a project on an online crowdfunding website such as Kickstarter was effectively tackled in this research, where a dataset of over 26 thousand projects trained and tested experimentally using our novel proposed approach in comparison to pre-existing learning models and algorithms. The Optimally Weighed RandomForests learning model proved to be the most effective at

success prediction, with a 94.29% accuracy rate. This research suggests that the same learning model can be used over the entire dataset, or over each category of projects. We also proposed the use of predictors that have not been used together before, such as *#websites* and *SmogMain*. Finally, we showed how the number of projects created by the creator in the past has little or no effect on the success of the current project,contrary to intuition, which serves as good news for novice creators with no experience in crowdfunding. We believe that this research serves two purposes in one shot, since it allows the project creator to make the necessary changes in their presentation of their project online, as well as allowing the project backer to determine whether a given project is worth the investment he can offer. Our future work shall be to include real-time factors to allow the success prediction of live projects as well.

REFERENCES

[1] M. D. Greenberg et al., "Crowdfunding Support Tools: Predicting Success and Failure" CHI'13, Paris, France: April 27 - May 2, 2013.

[2] J.Chung and K. Lee, "A Long-Term Study of a Crowdfunding Platform: Predicting Project Success and Fundraising Amount", HT '15, Guze- lyurt, Northern Cyprus: September 1-4, 2015.

[3] V. Etter et al.,"Launch Hard or Go Home!-Predicting the Success of Kickstarter Campaigns" COSN'13, Boston, Massachusetts, USA: October 7-8, 2013.

[4] M. Zhou et al., "Project description and crowdfunding success: an exploratory study" Information Systems Frontiers, Springer, December 7, 2016, pp. 1-16.

[5] T.K. Ho, "Random Decision Forest", Proceedings of the 3rd International Conference of Document Analysis and Recognition, Montreal, QC: 14- 16 August 1995.

[6] G. H. McLaughlin, "SMOG Grading a New Readability Formula", Journal of Reading, May 1969.

[7] S.J. Winham et al., "A Weighted Random Forests Approach to Improve Predictive Performance", Statistical Analysis and Data Mining: The ASA Data Science Journal, 2013, Volume 6, Issue 6, pp. 496-505

[8] H.B. Lee et al., "Trees Weighting Random Forests Method for Classify- ing High-Dimensional Noisy Data", IEEE 7th International Conference on e-Business Engineering (ICEBE), 2010.

[9] M. D. Greenberg, E. M. Gerber, "Learning to Fail: Experiencing Public Failure Online Through Crowdfunding", CHI 2014, Toronto, Ontario, Canada: April 26-May 1, 2014.

[10] T. Mitra, E. Gilbert "The Language that Gets People to Give: Phrases that Predict Success on Kickstarter", CSCW14, Baltimore, Maryland, USA: February 15-19, 2014.

[11] Q. Dai et al., "Research of Decision Tree Classification Algorithm in Data Mining", International Journal of Database Theory and Application Vol.9, No.5, 2016, pp.1-8

[12] L. Breiman, "Random Forests", Statistics Department, University of California Berkeley, CA 94720: January 2001

[13] Q. Ren et al., "Research on Machine Learning Framework Based on Random Forest Algorithm", Advances in Materials, Machinery, Electronics I AIP Conf. Proc. 1820, DOI: 10.1063/1.4977376

[14] A. Chandra and X. Yao "Ensemble Learning Using Multi-Objective Evolutionary Algorithms", Journal of Mathematical and Algorithms, 2006, Volume 5, Issue 4, pp. 417-445.

[15] S.G. Soares et al., "A Genetic Algorithm for Designing Neural Network Ensembles", GECCO12, Philadelphia, Pennsylvania: July 7-11, 2012.

Optical Materials 78 (2018) 457–464

Contents lists available at ScienceDirect

Optical Materials

journal homepage: www.elsevier.com/locate/optmat

Spectroscopic study of Pr^{3+} ions doped Zinc Lead Tungsten Tellurite glasses for visible photonic device applications

Ritu Sharma [a], A.S. Rao [a, *], Nisha Deopa [a], M. Venkateswarlu [b], M. Jayasimhadri [a], D. Haranath [c], G. Vijaya Prakash [d]

[a] Department of Applied Physics, Delhi Technological University, Bawana Road, New Delhi, 110 042, India
[b] Department of Physics, K L University, Vaddeswaram, 522 502, Guntur (Dt), Andhra Pradesh, India
[c] CSIR-National Physical Laboratory, Dr.K.S. Krishnan Marg, Pusa Road, New Delhi, 110 012, India
[d] Nanophotonic Lab, Department of Physics, IIT-Delhi, Hauz Khas, New Delhi, 110 016, India

ARTICLE INFO

Article history:
Received 21 November 2017
Received in revised form
24 February 2018
Accepted 25 February 2018

Keywords:
Glasses
Luminescence
Optical materials
Oxides
Optical properties

ABSTRACT

Zinc Lead Tungsten Tellurite (ZnPbWTe) glasses doped with different Pr^{3+} ion concentrations having the composition 5ZnO + 15PbO + 20WO_3 + (60-x)TeO_2 + xPr_6O_{11} (where $x = 0.5$, 1, 1.5, 2.0 and 2.5 mol%) were prepared by using sudden quenching technique and characterized to understand their visible emission characteristic features using spectroscopic techniques such as absorption, excitation and emission. The Judd-Ofelt (J-O) theory has been applied to the absorption spectral features with an aim to evaluate various radiative properties for the prominent fluorescent levels of Pr^{3+}ions in the as-prepared glasses. The emission spectra recorded for the as-prepared glasses under 468 nm excitation show three prominent emission transitions $^3P_0 \rightarrow {}^3H_6$, $^3P_0 \rightarrow {}^3F_2$ and $^3P_1 \rightarrow {}^3F_4$, of which $^3P_0 \rightarrow {}^3F_2$ observed in visible red region (648 nm), is relatively more intense. The intensity of $^3P_0 \rightarrow {}^3F_2$ emission transition in the titled glasses increases up to 1mol% of Pr^{3+} ions and beyond concentration quenching is observed. Branching ratios (β_R) and emission cross-sections (σ_{se}) were estimated for $^3P_0 \rightarrow {}^3F_2$ transition to understand the luminescence efficiency in visible red region (648 nm). The CIE chromaticity coordinates were also evaluated in order to understand the suitability of these glasses for visible red luminescence devices. From the emission cross-sections, quantum efficiency and CIE coordinates, it was concluded that 1mol% of Pr^{3+} ions in ZnPbWTe glasses are quite suitable for preparing visible reddish orange luminescent devices.

© 2018 Elsevier B.V. All rights reserved.

1. Introduction

Recently, Rare Earth (RE) doped crystalline and non-crystalline materials are playing a vital role in the field of science and technology because of their applications in diversified fields [1–4]. Quite recently, studies on non-crystalline materials (glasses) doped with RE ions have attracted great deal of attention by researchers because of their potential applications in designing lasers, fiber communication, color display devices, sensors and hole burning memories, etc. [5,6]. Further, RE doped glassy matrices are considered as luminescence material due to their higher emission efficiencies corresponding to 4f-4f and 4f-5d electronic transitions [7]. The sharp fluorescence pattern observed from 4f-4f electronic transitions in UV to NIR regions owing to shielding effect of 5s, 5p orbital on 4f orbitals. Furthermore, intensity, effective bandwidths of emission transitions and thereby quantum efficiency depends much on the structure of the host matrix. Therefore selecting a good host matrix with relatively higher luminescence efficiency is very much essential for the design and development of a good photonic device [8].

It is reported in literature that, heavy metal oxide glasses are quite suitable for the development of non-linear optical devices, electro-optic modulators, electro-optic switches, solid state laser materials and IR technologies because of their high density, refractive index and low phonon energy [9–12]. In general, the host glass with relatively low phonon energies can give high quantum efficiency and therefore useful for the designing of a good photonic device [13]. Tellurite glasses are one such kind of materials having lowest phonon energy [~800 cm^{-1}] and high refractive index [14,15]. Further, tellurite glasses have recently gained wide

* Corresponding author.
E-mail address: drsrallam@gmail.com (A.S. Rao).

https://doi.org/10.1016/j.optmat.2018.02.054
0925-3467/© 2018 Elsevier B.V. All rights reserved.

attention due to their physical and chemical properties. They also exhibit excellent chemical stability, good mechanical strength, slow crystallization rate, high homogeneity and good transparency in the spectral region from visible to NIR region [16,17].

Addition of WO_3 to tellurite glasses has potential applications in the field of IR technologies, nonlinear optics and fiber optics because of their high linear refractive index. Presence of ZnO in the host glass is having unique characteristics owing to its dual nature as glass former (ZnO_4) as well as network modifier [18,19]. Also ZnO containing glasses are thermally stable, sublime and appreciably covalent in character [20]. Addition of PbO to a ternary glassy network (TeO_2-WO_3-ZnO) can reduce the rate of crystallization by acting as a network modifier and enhances the radiative emissive property of the host glass. Among the two network modifier oxides, i.e., ZnO and PbO, it is expected that ZnO can shorten the time taken for solidification of glasses during the quenching process [21,22]. Pondering on the aforementioned scientific patronages offered by various chemical constituents, for the present work we prepared a germane optical glassy system namely Zinc Lead Tungsten Tellurite (ZnPbWTe) glass doped with Pr^{3+} ions. The prime aim of the present work is to find out a visible photonic device with relatively good quantum efficiency. Among the RE ions, Praseodymium is one of the interesting ion because of its significant importance in visible luminescent devices under blue excitation. Pr^{3+} is a significant optical activator with its several meta stable states ($^3P_0$, $^1D_2$, $^1G_4$) that can offer stimulated emissions in blue, green, orange, red and infrared regions [23,24]. Further, Pr^{3+}doped glasses are very good candidates to develop 1.3 μm optical amplifier for telecommunication applications [25,26]. It is also reported that Pr^{3+} doped glasses possess lasing action from $^1D_2 \rightarrow {}^3H_4$ transition around 600 nm [27]. Because of the aforementioned various scientific applications, the glasses doped with Pr^{3+} ions having low phonon energies are quit suitable for the design and development of solid state lasers and optical fiber amplifiers in visible region.

In the present work, preparation and characterization of ZnPbWTe glasses were done by varying Pr^{3+}ions concentration using melt quenching technique to study their physical, optical and luminescent properties with an aim to identify a better glass for visible photonic applications.

2. Experimental

2.1. Glass preparation

ZnPbWTe glasses doped with different concentrations of Pr^{3+} ions were prepared by conventional melt quenching technique with the following composition 5ZnO + 15PbO + 20WO_3+ (60-x) TeO_2+ xPr_6O_{11}(where $x = 0.5$, 1, 1.5, 2.0 and 2.5 mol%). For our convenience these glasses are designated as glass A-E depending on the '*x*' value from 0.5 to 2.5 mol% respectively. All the chemicals used to prepare ZnPbWTe glasses were of analar grade with 99.9% purity. The chemical constituents taken as per the aforementioned stoichiometric ratio were thoroughly mixed in an agate mortar for about 3 h to get homogeneous mixing and then melted using a silica crucible at 830 °C in a programmable electrical furnace (Indfur made) for about 55 min. The resultant melts were stirred 4–6 times before quenching to get homogeneous mixture. Such melts were then poured on a preheated brass plate and pressed quickly with another pre heated brass plate. The prepared samples were annealed in another furnace for about 1 h at 250°C to remove thermal strains that were produced due to sudden quenching. The glasses thus obtained were highly polished to achieve a uniform thickness of 0.159 cm.

2.2. Physical and optical measurements

Archimedes's principle is used to measure densities of the as prepared glasses with distilled water as an immersion liquid. The refractive indices of all the as-prepared glasses were measured by using Brewster's angle method with He-Ne laser operating at 632 nm. The XRD spectrum was monitored by using high resolution X-ray diffractometer Bruker; Model D8 advance which operates at 40 KV and 40 mA. Perkin-Elmer's Frontier spectrometer was used to record FT-IR spectrum of the un-doped ZnPbWTe glass. The optical absorption spectra were recorded for all the prepared glass samples from 400 to 2400 nm at room temperature with a spectral resolution of 0.1 nm using a Jasco V-670 UV–vis–NIR spectrometer. Schimadzu RF-5301PC spectrophotometer is used to record Photoluminescence (PL) spectra. The PL decay spectral measurements were taken from Edinburg FLSP900 fluorescence spectrometer having 0.1 nm spectral resolution.

3. Results and discussion

3.1. XRD spectral analysis

Fig. 1 shows the XRD spectrum of an un-doped ZnPbWTe glass. Absence of sharp peaks and instead a broad hump observed in the XRD spectrum, clearly confirms the amorphous nature of the as prepared ZnPbWTe glass.

3.2. FT-IR spectral analysis

Fig. 2 shows the FT-IR spectrum of an un-doped ZnPbWTe glass in the range 500–4000 cm^{-1}. The shoulder observed at 664 cm^{-1} is due to the stretching vibrations of Te-O bonds in TeO_4 trigonal bi pyramid unit [28]. It is well known that addition of glass modifiers into tellurite glass results in the opening of glass network which leads to the formation of non-bridging oxygen by allowing TeO_{3+1} and TeO_3 structural units. The band observed at 944 cm^{-1} is due to the stretching vibrations of W-O^- and W-O bond in WO_4 or WO_6 unit as well as ϑ_1 vibrations of WO_4 group [29]. The shoulders observed in the region 1600-3000 cm^{-1} are attributed to the presence of hydrogen bonding. The characteristic band observed at 3437 cm^{-1} is due to the fundamental vibrations of OH group [30]. In order to obtain high quantum efficiency for the glassy material, the

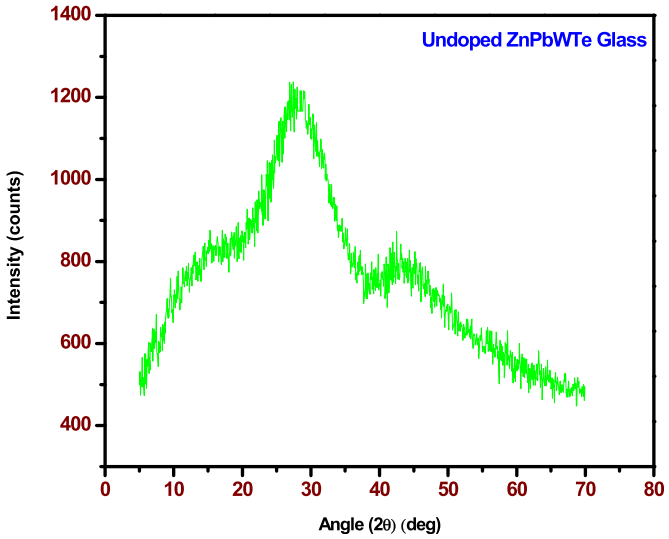


Fig. 1. XRD spectrum of an un-doped ZnPbWTe glass.

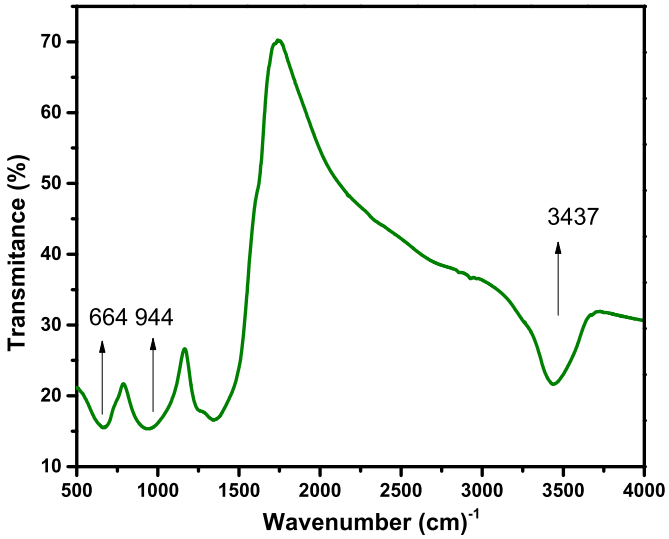


Fig. 2. FT-IR spectrum of an un-doped ZnPbWTe glass.

amount of OH content present in the glass must be low. Higher value of OH content in the glass leads to increase in radiative losses resulting decrease in quantum efficiency. From Fig. 2 it is clear that the intensity of OH band observed for as-prepared glasses is low which confirms presence of less OH content in the titled glasses. Thus synthesized glasses are suitable for better luminescence efficiency with less radiative losses.

3.3. Optical absorption spectra and Judd-Ofelt analysis

In order to understand the radiative properties possessed by Pr^{3+} ions doped ZnPbWTe glasses, absorption spectra have been recorded from 400 to 2400 nm. The absorption spectrum of 1.0mol % Pr^{3+} ions in ZnPbWTe glass (Glass B) is shown in Fig. 3 along with assignment of the absorption bands as a representative. While the absorption spectra for the remaining glasses quite similar in their band positions and their respective absorption intensities and absorption band edges shows systematic variation with concentration, which will be discussed in the forthcoming sections. The absorption bands are assigned to different transitions according to Carnall report [31] and the corresponding peak wavelength are given in Table 1. The band assignments are in good agreement with earlier reports [23,32]. Pr^{3+} ion doped ZnPbWTe glasses contain seven absorption bands corresponding to the transitions between the $^3H_4$ground level and the excited states$^3P_2$, $^1I_6$, $^3P_0$, $^1D_2$, (vis region)$^3F_4$,$^3F_3$ and$^3F_2$ (NIR region). The experimental oscillator strength (f_{exp}) for the electric dipole transitions were calculated from following equation [33].

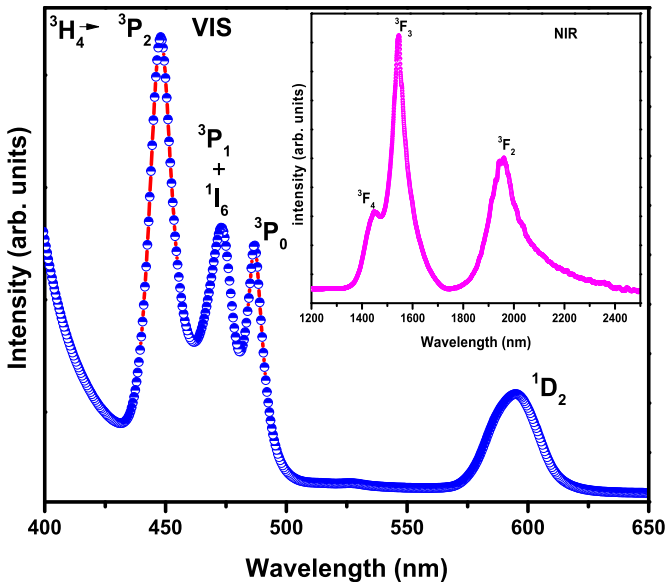


Fig. 3. Absorption spectrum of 1mol% Pr^{3+} ions (glass B) in ZnPbWTe glass.

$$f_{exp} = 4.32 \times 10^{-6} \int \varepsilon(\vartheta) d\vartheta \quad (1)$$

here, $\varepsilon(\vartheta)$ is the molar extinction coefficient corresponding to the energy (ϑcm^{-1}) and $d\vartheta$ is the half band width of the absorption band. In the present work, for all the absorption bands, the intensities were measured by the area under the curve method. Judd and Ofelt (J-O) independently derived expressions for the oscillator strengths of induced electric dipole transitions for the f^N configurations [34,35]. The calculated oscillator strengths (f_{cal}) are determined by least square fit procedure and are given in Table 1 along with f_{exp} values. The doubly reduced matrix elements were taken from the literature as they are insensitive to the environment of RE ions. The specific features of J-O parameters may be distributed by the contributions of the phonon subsystem [36]. The quality of fit is determined by root mean square deviation (δ_{rms}) between the experimental and calculated oscillator strengths by using the following expression and is given in Table 1.

$$\delta_{rms} = \sqrt{\sum \left(f_{exp} - f_{cal}\right)^2 / N} \quad (2)$$

where, N is the total number of energy levels included in the fitting procedure.

The J-O intensity parameters (Ω_2, Ω_4, Ω_6) obtained through least square fit method for all the as-prepared glasses are tabulated in Table 2, along with some reported values [32,37–44]. The magnitude of the J-O intensity parameters is related to the physical and chemical properties such as viscosity and covalent character of the chemical bonds. From Table 2, it is observed that the J-O intensity parameters are following the same order (Ω_2> Ω_6> Ω_4) in all the glasses under investigation. For all the as-prepared glasses, the magnitude of Ω_2 is larger than Ω_4 and Ω_6. The large Ω_2 parameter values are indicators of the covalent character of the chemical bonds among the glass matrix and RE ions. The intensity parameters Ω_4 and Ω_6 are related to the bulk properties such as viscosity and dielectric of the media. In glasses, the RE ions are randomly distributed over non-equivalent sites with a wide distribution of crystal fields. From Table 2, it is observed that, the J-O intensity parameters (Ω_4 and Ω_6) are found to be high for glass B, indicating that it is more asymmetric, more covalent and more rigid than the other Pr^{3+} ions doped ZnPbWTe glasses. The variation of hypersensitive transition ($^3P_2$) oscillator strength and ($\Sigma\Omega_\lambda$) with Pr^{3+} ions can be seen from Fig. 4. It is clear from Fig. 4 that both parameters are varying in the same manner with Pr^{3+} ions concentration except intensity.

3.4. Emission spectra and radiative properties analysis

To understand the emission spectral properties of the as-prepared glasses, it is necessary to know about the apt excitation wavelength for getting proper population inversion to occur. For this reason we have recorded the excitation spectrum of Pr^{3+} doped ZnPbWTe glass (glass B) by fixing the emission at 648 nm and is

Table 1
Assignment of absorption bands, experimental (f_{exp}) (10^{-6}), calculated oscillator strengths (f_{cal}) (10^{-6}) and r.m.s deviation (δ_{rms}) (10^{-6}) (with and without hypersensitive transition) of Pr^{3+} ions doped ZnPbWTe glasses.

Transition $^3H_4\rightarrow$	λ(nm)	Glass A		Glass B		Glass C		Glass D		Glass E	
		f_{exp}	f_{cal}	f_{exp}	f_{cal}	f_{exp}	f_{cal}	f_{exp}	f_{cal}	f_{exp}	f_{cal}
$^3P_2$	448	6.92	1.81	8.50	3.98	7.79	3.39	6.65	2.95	6.02	1.99
$^3P_1+^1I_6$	473	1.81	1.35	2.04	2.32	1.80	2.70	1.00	3.67	0.86	3.02
$^3P_0$	487	2.72	1.32	3.78	2.28	3.21	2.66	2.99	2.32	2.54	1.97
$^1D_2$	595	3.92	0.62	3.18	1.27	2.40	1.08	2.04	1.54	1.65	1.07
$^3F_4$	1446	2.35	1.99	4.54	4.34	3.25	3.55	2.99	2.97	2.56	2.68
$^3F_3$	1541	3.09	3.71	7.12	7.57	6.45	6.54	5.45	5.48	5.02	4.87
$^3F_2$	1955	4.87	4.82	7.85	7.81	6.29	6.27	5.74	5.73	5.34	5.38
δ_{rms}		±2.38		±1.95		±1.78		±1.56		±1.32	
		±0.69		±0.68		±0.48		±0.31		±0.28	

Table 2
Judd-Ofelt intensity parameters Ω_2, Ω_4 and Ω_6 (10^{-20} m^2) of Pr^{3+} ions in ZnPbWTe glass along with various reported hosts.

Samples	Ω_2	Ω_4	Ω_6	Trend	Reference
Glass A	4.29	1.16	1.28	$\Omega_2>\Omega_6>\Omega_4$	Present work
Glass B	6.27	2.07	3.05	$\Omega_2>\Omega_6>\Omega_4$	Present work
Glass C	4.32	2.23	2.36	$\Omega_2>\Omega_6>\Omega_4$	Present work
Glass D	3.92	2.29	2.44	$\Omega_2>\Omega_6>\Omega_4$	Present work
Glass E	3.84	2.36	2.68	$\Omega_2>\Omega_6>\Omega_4$	Present work
ZnAlBiB	3.73	1.17	3.23	$\Omega_2>\Omega_6>\Omega_4$	[37]
ZBP3	2.89	2.04	1.99	$\Omega_2>\Omega_6>\Omega_4$	[38]
ZBP4	3.23	1.88	2.03	$\Omega_2>\Omega_6>\Omega_4$	[38]
ZBP5	3.94	1.34	1.99	$\Omega_2>\Omega_6>\Omega_4$	[38]
Phosphate	4.19	4.29	6.40	$\Omega_6>\Omega_4>\Omega_2$	[39]
MgTP	2.69	11.8	8.39	$\Omega_4>\Omega_6>\Omega_2$	[32]
LBTAF	2.42	2.54	4.23	$\Omega_6>\Omega_4>\Omega_2$	[40]
Oxy -Fluoride	0.13	4.09	6.33	$\Omega_6>\Omega_4>\Omega_2$	[41]
ZBLAN	2.9	6.40	5.50	$\Omega_4>\Omega_6>\Omega_2$	[42]
Mixed hallide	2.70	4.40	5.40	$\Omega_6>\Omega_4>\Omega_2$	[43]
SASP	12	2.1	8.5	$\Omega_2>\Omega_6>\Omega_4$	[44]

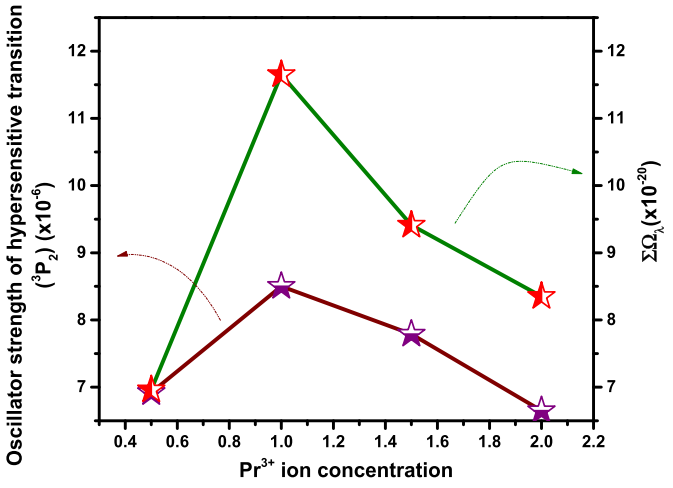


Fig. 4. Variation of intensity of hypersensitive transition and $\Sigma\Omega_\lambda$ with Pr^{3+} ions concentration in ZnPbWTe glass.

shown in Fig. 5. The excitation spectra recorded from 400-520 nm gives three emission bands at wavelengths approximately 450,468 and 485 nm corresponding to the transitions $^3H_4\rightarrow{}^3P_2$, $^3H_4\rightarrow{}^3P_1+{}^1I_6$, $^3H_4\rightarrow{}^3P_0$ respectively. It is well known that the wavelength corresponding to the intense excitation band can give intense emissions. Among all the excitation bands, a band corresponding to the transition $^3H_4\rightarrow{}^1I_6$ (468 nm) is more intense and is used as an excitation wavelength to record the emission spectra for

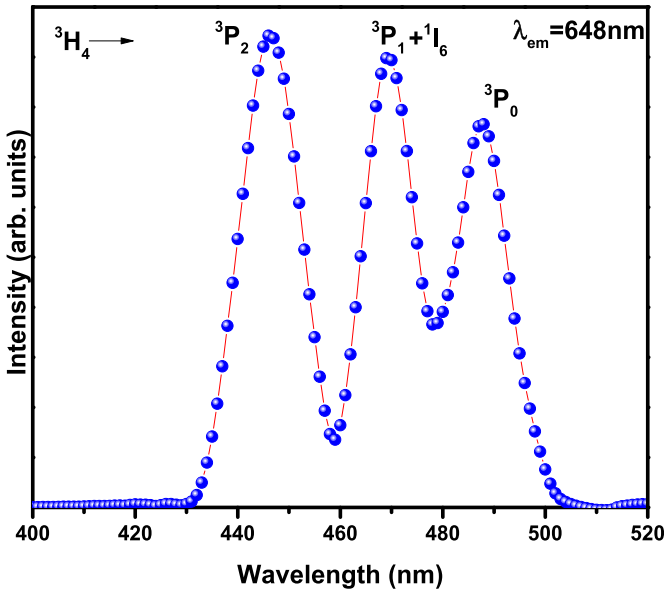


Fig. 5. Excitation spectrum of 1mol% of Pr^{3+} ions in ZnPbWTe glass.

all the glasses under investigation. Emission spectra of Pr^{3+} doped ZnPbWTe glasses are shown in Fig. 6. From Fig. 6 it is observed that, the emission spectra of titled glasses show three emission peaks at 616, 648, 705 nm corresponding to $^3P_0\rightarrow{}^3H_6$, $^3P_0\rightarrow{}^3F_2$, $^3P_1\rightarrow{}^3F_4$

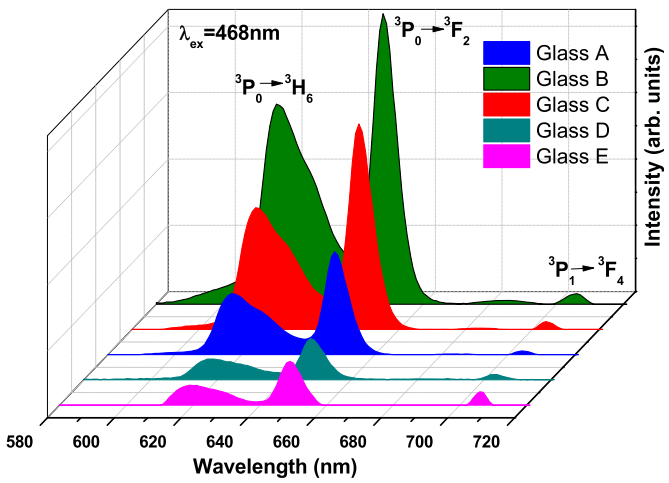


Fig. 6. Emission spectra of Pr^{3+} ions in ZnPbWTe glasses.

transitions respectively. Among all these transitions $^3P_0 \rightarrow {}^3F_2$ exhibits bright reddish-orange emission at 648 nm and other two transitions are feeble. From Fig. 6, it can be observed that the emission quenching has been occurred at 1mol% of Pr^{3+}ion in ZnPbWTe glass which may be due to energy transfer via cross relaxation between Pr^{3+}-Pr^{3+} ions. Fig. 7 shows the energy level diagram of 1mol% of Pr^{3+}ion in ZnPbWTe glass showing absorption, emission and cross-relaxation channels. The possible cross-relaxation channels responsible for concentration quenching are shown below

$$CR1\text{-}\ {}^3P_0 + {}^3H_4 \rightarrow {}^1D_2 + {}^3H_6$$

$$CR2\text{-}\ {}^3P_0 + {}^3H_4 \rightarrow {}^1G_4 + {}^1G_4$$

$$CR3\text{-}\ {}^3P_0 + {}^3H_4 \rightarrow {}^3H_6 + {}^1D_2$$

In order to understand the PL performance of Pr^{3+}ions doped ZnPbWTe glasses, the radiative parameters such as spontaneous transition probabilities (A_R), total transition probabilities (A_T), radiative lifetime (τ_R) and luminescence branching ratios (β_R) for all the emission transitions have been evaluated by using the J-O parameters obtained from the absorption spectral measurements and are presented in Table 3. In treating the fluorescence process, the radiative parameters such as A_R, A_T, τ_R and β_R for the observed emission transitions are evaluated by using the expressions given in literature [1,32].

The stimulated emission cross-section (σ_{se}) is an important parameter for glassy material to act as a good luminescent host material and its value signifies the rate of energy extraction from the optical material. From the observed emission bands σ_{se} can be estimated by using the following expression [1,32].

$$\sigma_{se} = \frac{\lambda_p^4}{8\pi c n^2 \Delta\lambda_{eff}} A_R \qquad (3)$$

λ_p is the emission peak wavelength, n is refractive index, $\Delta\lambda_p$ is the full width at half maximum which can be calculated by integrating the intensity at the peak wavelength [45].

The radiative parameters thus evaluated are given in Tables 3 and 4. In addition to these parameters, the other radiative parameters like gain band width (σ_{se} x $\Delta\lambda_p$) and optical gain parameters (σ_{se} x τ_R), which are also important to identify a laser active medium, were evaluated and included in Table 4. Among all the glasses investigated, glass B has got highest transition probability for $^3P_0 \rightarrow {}^3F_2$ transition. For a glassy material to act as a good lasing material, the branching ratio (β_R) must be high. From Table 3 it is observed that the β_R value for all the glasses is highest for transition $^3P_0 \rightarrow {}^3F_2$. This indicates that this energy transition can give laser emission at 648 nm in the prepared ZnPbWTe glasses. Further, σ_{se} is another significant parameter to estimate laser performance of a material. From Table 4, it is found that among all the emission transitions, a transition $^3P_0 \rightarrow {}^3F_2$ observed at 648 nm possesses highest σ_{se} value for glass B. Thus ZnPbWTe glass doped with 1mol % Pr^{3+} ions show the potentiality to emit bright red laser at 648 nm. The values of σ_{se} x $\Delta\lambda_p$ and σ_{se}x τ_R are higher for glass B for transition $^3P_0 \rightarrow {}^3F_2$. The measured radiative parameters indicate that, ZnPbWTe glass doped with 1mol% of Pr^{3+} ions can be used for red laser emission at 648 nm corresponding to the transition $^3P_0 \rightarrow {}^3F_2$.

Table 3
Transition probabilities (A_R) (s^{-1}), total transition probability (A_T) (s^{-1}), branching ratio (β_R) and radiative lifetimes (τ_R) (μs) for the observed emission transitions of Pr^{3+} doped ZnPbWTe glasses.

Name	Transition	A_R	A_T	β_R	τ_R
Glass A	$^3P_1 \rightarrow {}^3F_4$	18246	77140	0.24	12
	$^3P_0 \rightarrow {}^3F_2$	54456	84343	0.61	11
	$^3P_0 \rightarrow {}^3H_6$	20382	84343	0.24	11
Glass B	$^3P_1 \rightarrow {}^3F_4$	28468	134239	0.21	7
	$^3P_0 \rightarrow {}^3F_2$	84963	144909	0.62	6
	$^3P_0 \rightarrow {}^3H_6$	38812	144909	0.26	6
Glass C	$^3P_1 \rightarrow {}^3F_4$	19951	118883	0.16	8
	$^3P_0 \rightarrow {}^3F_2$	59545	128201	0.46	7
	$^3P_0 \rightarrow {}^3H_6$	48019	128201	0.37	7
Glass D	$^3P_1 \rightarrow {}^3F_4$	15342	108136	0.13	9
	$^3P_0 \rightarrow {}^3F_2$	54321	119321	0.43	8
	$^3P_0 \rightarrow {}^3H_6$	49203	119321	0.39	8
Glass E	$^3P_1 \rightarrow {}^3F_4$	13385	102013	0.13	10
	$^3P_0 \rightarrow {}^3F_2$	52632	108826	0.47	9
	$^3P_0 \rightarrow {}^3H_6$	49871	108826	0.44	9

Table 4
Emission peak wavelength (λ_P) (nm), effective band widths ($\Delta\lambda_P$) (nm), stimulated emission cross-sections (σ_{se}) ($\times 10^{-20}$) (cm^2), gain band width (σ_{se} x $\Delta\lambda_p$) (10^{-26}) (cm^3) and optical gain parameters (σ_{se} x τ_R) (10^{-25}) (cm^2 s) for the emission transitions of Pr^{3+} doped ZnPbWTe glasses.

Spectral parameters	Glass A	Glass B	Glass C	Glass D	Glass E
$^3P_0 \rightarrow {}^3H_6$					
λp	616	616	616	616	616
Δλp	17.3	19.4	19.4	25.9	26.4
σ_{se}	3.94	8.92	6.63	5.01	4.88
σ_{se} x Δλp	6.81	17.3	12.9	13.0	12.0
σ_{se} x τ_R	4.33	5.35	4.64	4.01	4.39
$^3P_0 \rightarrow {}^3F_2$					
λp	648	648	648	648	648
Δλp	8.64	9.72	8.64	9.18	8.13
σ_{se}	25.8	47.8	22.6	19.1	20.5
σ_{se} x Δλp	22.3	46.4	19.5	17.6	16.6
σ_{se} x τ_R	28.4	28.7	15.8	15.3	18.4
$^3P_1 \rightarrow {}^3F_4$					
λp	705	705	705	705	705
Δλp	5.4	4.86	5.94	5.4	5.4
σ_{se}	19.4	44.8	15.4	12.9	11.0
σ_{se} x Δλp	10.6	21.8	9.17	6.95	5.93
σ_{se} x τ_R	23.3	31.4	12.3	11.6	11.0

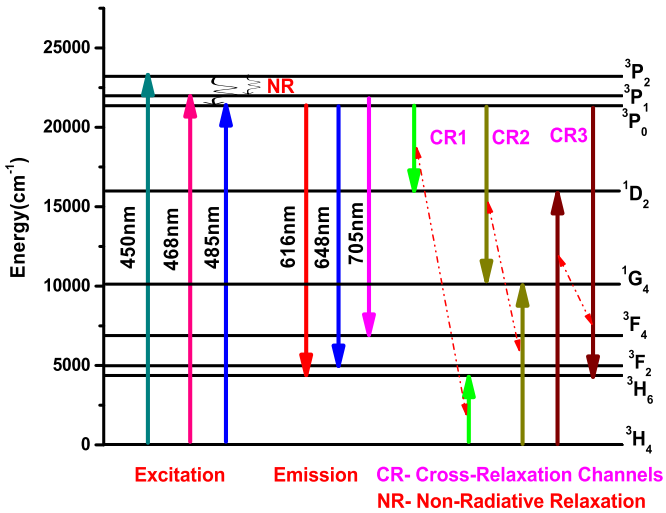


Fig. 7. Energy level diagram of 1 mol% of Pr^{3+} ions in ZnPbWTe glass.

3.5. CIE chromaticity co-ordinates

The evaluation and quantification of color emitted by a substance is referred to as the "science of color or colorimetry". The CIE coordinates are more helpful to find the color of the light emitted

by the prepared substance under excitation. Such CIE co-ordinates are measured from the emission spectra of ZnPbWTe glasses doped with Pr^{3+} ions using the procedures given in literature [46] and such CIE coordinates are given in Table 5. The emission spectra consist of three regions, the first region is orange to red, second is red and the third region is NIR. The CIE color co-ordinates for all the samples were found to be in the bright red region. Among all the glass samples, particularly glass B color co-ordinates (x = 0.60, y = 0.38) are nearby to the bright red region corresponding to $^3P_0 \rightarrow {}^3F_2$ (648 nm) transition. Fig. 8, shows the CIE diagram for color co-ordinates of 1mol% of Pr^{3+}doped ZnPbWTe glass (glass B) excited at 468 nm wavelength. Hence ZnPbWTe with 1 mol% of Pr^{3+}ions is quite suitable to give bright red color laser at 648 nm.

3.6. Photoluminescence decay spectral analysis

Fig. 9 represents the PL decay profiles of Pr^{3+} doped ZnPbWTe glasses under 468 nm excitation and 648 nm emission. All the decay curves are originating from $^3P_0$ energy level to $^3F_2$ observed at 648 nm. The decay profile are showing exponential nature for lower Pr^{3+}concentration and non-exponential for higher concentration. The non-exponential nature may be due to energy transfer between nearby Pr^{3+}-Pr^{3+}ions through cross-relaxation. The experimental lifetime (τ_{exp}) values were evaluated by using the bi-exponential equation expressed as follows

$$I = I_0 + A_1\tau_{exp}\left(-\frac{t}{\tau_1}\right) + A_2\tau_{exp}\left(-\frac{t}{\tau_2}\right) \quad (4)$$

here, I_0 and I are the luminescence intensities at time t and t_0 respectively. A_1 and A_2 are the decay constants while τ_1 and τ_2 are the lifetimes of the two components contributing to the decay processes. The average values of experimental lifetime (τ_{avg}) of the titled glasses can be obtained from the following expression.

$$\tau_{avg} = \frac{A_1\tau_1^2 + A_1\tau_1^2}{A_1\tau_1 + A_2\tau_2} \quad (5)$$

The quantum efficiency (η) is another important parameter and can be evaluated by taking the ratio of τ_{exp} to τ_R. The non-radiative (W_{NR}) decay rates can be estimated by using the formula

$$\frac{1}{\tau_{exp}} = \frac{1}{\tau_R} + W_{NR} \quad (6)$$

The τ_{exp}, η and W_{NR} values are presented in Table 6. It is observed from Table 6 that τ_{exp} values are decreasing with Pr^{3+} ion concentration while η is maximum for glass B and W_{NR} is having minimum value for glass B.

3.7. Inokuti-Hiryama (I-H) model analysis

It is well-known that an ion reaching to an excited state can relax to the lower energy state via two different mechanisms. In first mechanism the donor ions can migrate the energy between the donor ions prior to the energy reaches to the un-excited acceptor ions. In second mechanism the donor ions can transfer energy directly to the acceptor ions. When donor and acceptor ions are distributed homogeneously in the host matrix, and if the energy migration between donor ions are negligible, then the energy

Table 5
CIE chromaticity co-ordinates of Pr^{3+} ions doped ZnPbWTe glasses.

Name of the glass	Color Co-ordinates	
	X-Co-ordinates	Y-Co-ordinates
Glass A	0.59	0.39
Glass B	0.60	0.38
Glass C	0.57	0.40
Glass D	0.53	0.44
Glass E	0.50	0.42

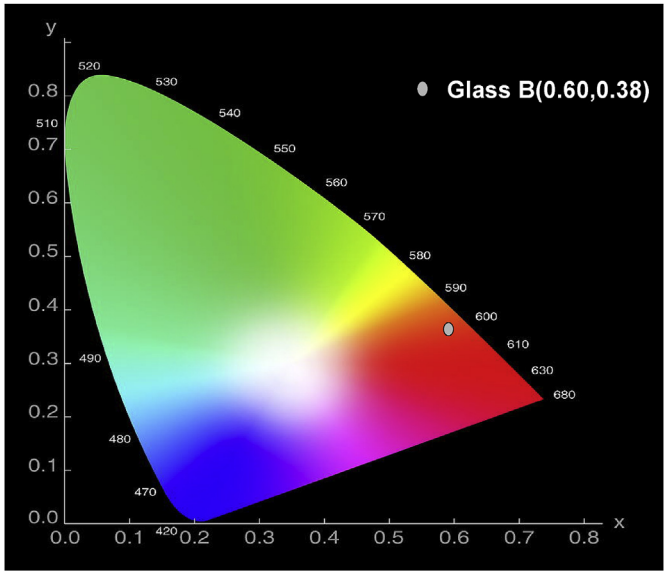


Fig. 8. CIE chromaticity coordinates of Pr^{3+} ions in ZnPbWTe glasses.

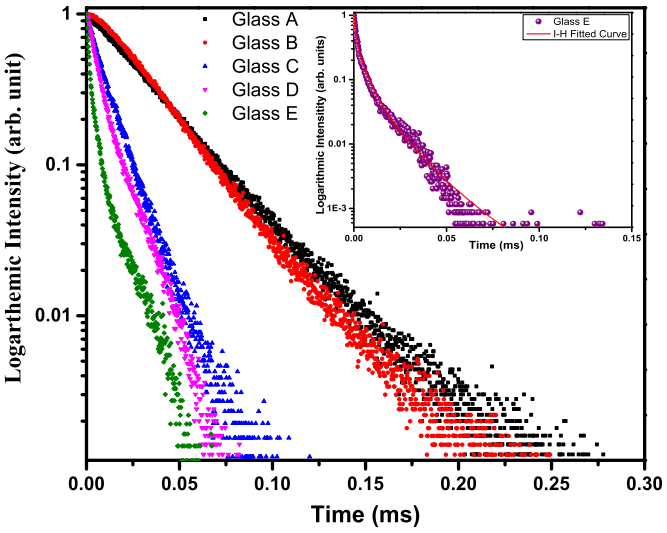


Fig. 9. Decay profiles of Pr^{3+} ions in ZnPbWTe glasses for $^3P_0 \rightarrow {}^3F_2$ transition along with I-H fitted curve for Glass E.

Table 6
Experimental lifetime (τ_{exp}) (μs), energy transfer parameter (Q), and critical transfer distance (R_0) (Å), donor acceptor interaction parameter (C_{DA}, 10^{-42} cm^6 s^{-1}) quantum efficiency (η) and non-radiative decay rates (W_{NR}) for $^3P_0 \rightarrow {}^3F_2$ transition of Pr^{3+} in ZnPbWTe glasses.

Name of sample	τ_{exp}	Q	R_0	C_{DA}	η (%)	W_{NR}
Glass A	`4.18	–	–	–	38.7	14832
Glass B	4.52	–	–	–	75.3	5457
Glass C	2.06	0.37	1.37	0.02	29.4	34257
Glass D	1.78	1.61	2.03	0.25	22.2	43679
Glass E	1.31	4.87	2.72	1.43	14.5	65224

transfer which took place between the donor and acceptor ions is responsible for the fast decay. In such cases, the I-H model is quite suitable to understand the predominant energy transfer mechanism [47]. The luminescence intensity in such a case is given by

$$I_t = I_0 \exp\left\{ -\frac{t}{\tau_0} - Q\left(\frac{t}{\tau_0}\right)^{\frac{3}{S}} \right\} \quad (7)$$

here, 't' is the time after excitation, 'τ_0' is the intrinsic decay time of the donors (absence of acceptors). 'Q' is the energy transfer parameter can be evaluated by the following expression

$$Q = \frac{4\pi}{3}\Gamma\left(1-\frac{3}{S}\right)N_0 R_0^3 \quad (8)$$

here, N_0 is concentration of acceptor ions, R_0 is critical energy transfer distance. Based on the values of S and gamma function $\Gamma(x)$, interactions involved in the mechanism can be classified as dipole-dipole ($S = 6$, $\Gamma(x) = 1.77$), dipole-quadrupole ($S = 8$, $\Gamma(x) = 1.43$) and quadrupole-quadrupole ($S = 10$, $\Gamma(x) = 1.43$). Following expressions are employed to evaluate the donor-acceptor interaction parameter C_{DA} and the energy transfer probability W_{ET}

$$C_{DA} = R_0^{(S)} {\tau_0}^{-1} \text{ and } W_{ET} = C_{DA} R_0^{(S)} \quad (9)$$

In the present study, the decay profiles are fitted by taking $S = 6$ which further confirms dipole-dipole interaction between Pr^{3+} ions. The inset in Fig. 9 shows the I-H fitted curve for glass E, taking $S = 6$. The various parameters Q, R_0 and C_{DA} are evaluated with the help of aforementioned formulae and placed in Table 6. It is observed that Q, R_0 and C_{DA} values increase with increase in Pr^{3+}ions concentration due to the enhanced energy transfer between Pr^{3+}- Pr^{3+}ions via cross relaxation. Fig. 10 shows the variation of energy transfer parameter (Q) and τ_{exp} with increase in Pr^{3+} ion concentration. From Fig. 10, it is conspicuous that as the Pr^{3+} ion content increases in the titled glasses, the τ_{exp} decreases while Q increases.

4. Conclusions

Zinc Lead Tungsten Tellurite glasses doped with varying concentrations of Pr^{3+}ions were productively prepared by using melt quenching technique. A broad hump in the XRD spectrum observed for an un-doped ZnPbWTe glass confirms the amorphous nature of the as-prepared glass. From the measured absorption spectral features, the energies of bands called oscillator strengths were measured to predict Judd-Ofelt (J-O) parameters and subsequently used to calculate various radiative properties for the prominent fluorescent levels. The emission spectra of Pr^{3+} doped ZnPbWTe glasses show three emission bands at 616, 648 and 705 nm wavelengths. Among them an emission band at 648 nm corresponding to transition $^3P_0 \rightarrow {}^3F_2$ is highly intense and is falling in red region. Decay profiles recorded for the titled glasses shows predominant exponential nature for lower Pr^{3+} ions concentration and non-exponential nature for higher concentration. The decay profiles for higher RE content are well fitted to Inokuti-Hiryama (I-H) model which confirms the dipole-dipole interaction between Pr^{3+}-Pr^{3+} ions. The CIE co-ordinates measured for optimized sample lie in visible red region. From the measured emission cross-sections, quantum efficiency and CIE chromaticity coordinates, it is concluded that 1mol% of Pr^{3+} ions in ZnPbWTe glass is quite suitable for producing visible red photonic devices in principle.

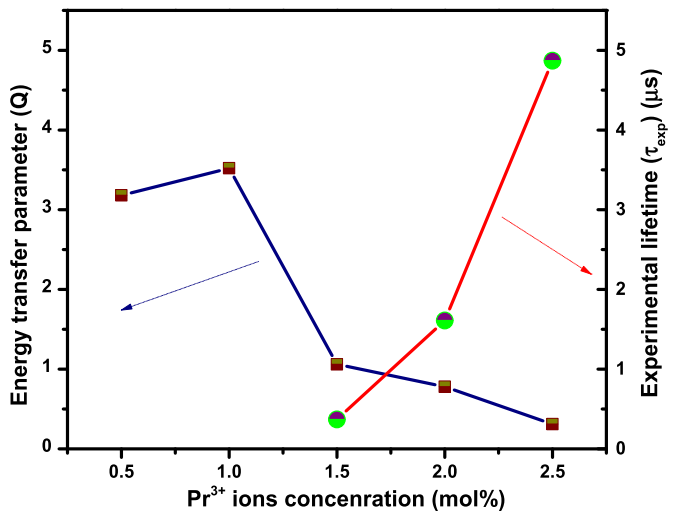


Fig. 10. Variation of energy transfer parameter (Q) and experimental lifetime (τ_{exp}) with Pr^{3+} ions in ZnPbWTe glasses.

Acknowledgement

Two of the authors Prof. A.S. Rao and Prof. G.V. Prakash are thankful to Department of Science and Technology (DST), Govt. of India, New Delhi for award of a Major Research Project (EMR/2016/007766) to them.

References

[1] N. Deopa, A.S. Rao, Sk. Mahamuda, M. Gupta, M. Jayasimhadri, D. Haranath, G.V. Prakash, J. Alloys Compd. 708 (2017) 911–921.
[2] K. Jha, M. Jayasimhadri, J. Am. Ceram. Soc. 100 (2017) 1402–1411.
[3] Z. Wang, H. Guo, X. Xiao, Y. Xu, X. Cui, M. Lu, B. Peng, A. Yang, Z. Yang, S. Gu, J. Alloys Compd. 692 (2017) 1010–1017.
[4] C.B. Annapurna Devi, Sk. Mahamuda, M. Venkateswarlu, K. Swapna, A. Srinivasa Rao, G. Vijaya Prakash, Opt. Mater. (Amst) 62 (2016) 569–577.
[5] K.S.V. Sudhakar, M.S. Reddy, L.S. Rao, N. Veeraiah, J. Lumin. 128 (2008) 1791–1798.
[6] S. Shanmuga Sundari, K. Marimuthu, M. Sivraman, S.S. Babu, J. Lumin. 130 (2010) 1313–1319.
[7] K. Swapna, Sk. Mahamuda, A.S. Rao, T. Sasikala, D. Haranath, G. VijayaPrakash, Spectrochim. Acta Part A 125 (2014) 53–60.
[8] Sk. Mahamuda, K. Swapna, M. Venkateswarlu, A.S. Rao, S. Shakya, G.V. Prakash, J. Lumin. 154 (2014) 410–424.
[9] M. Venkateswarlu, M.V.V.K.S. Prasad, K. Swapna, S. Mahamuda, A. Rao, A.M. Babu, D. Haranath, Ceram. Int. 40 (2014) 6261–6269.
[10] T. Kosuge, Y. Benino, V. Dimitrov, R. Sato, T. Komatsu, J. Non Cryst. Solids 242 (1998) 154–164.
[11] I. Shaltout, Y. Tang, R. Braunstein, E.E. Shaisha, J. Phys. Chem. Solids 57 (1996) 1223–1230.
[12] J. Yang, S. Dai, Y. Zhou, L. Wen, L. Hu, Z.H. Jiang, J. Appl. Phys. 93 (2) (2003) 977–983.
[13] Y.G. Choi, J. Heo, J. Non Cryst. Solids 217 (1997) 199–207.
[14] M. Venkateswarlu, Sk. Mahamuda, K. Swapna, A. Srinivasa Rao, A.M. Babu, S. Shakya, D. Haranath, G.V. Prakash, J. Lumin. 175 (2016) 225–231.
[15] A. Mori, Y. Ohishi, S. Sudo, Electron. Lett. Online 33 (1997) 863–864.
[16] D. Rajesh, R.J. Amjad, M. Reza Dousti, A.S.S. de Camargo, J. Alloys Compd. 695 (2017) 607–612.
[17] H. Nii, K. Ozaki, M. Herren, M. Morita, J. Lumin. 76 (1998) 116–119.
[18] M. Szumera, I. Waclawska, J. Sulowska, J. Mol. Struct. 1114 (2016) 78–83.
[19] K. Swapna, Sk. Mahamuda, A.S. Rao, T. Sasikala, P. Packiyaraj, L.R. Moorthy, G.V. Prakash, J. Lumin. 156 (2014) 80–86.
[20] J.D. Lee, Concise Inorganic Chemistry, Blackwell Science, Oxford, 1996.
[21] M.R. Reddy, S.B. Raju, N. Veeraiah, J. Non Cryst. Solids 61 (2000) 1567–1571.
[22] P. Pascuta, G. Borodi, N. Jumate, I. Vida-Simiti, D. Viorel, E. Culea, J. Alloys Compd. 504 (2010) 479–483.
[23] R. Balda, A. Mendioroz, J. Fernández, M.A. Arriandiaga, L.S. Griscom, J.L. Adam, Opt. Mater. (Amst) 16 (2001) 249–254.
[24] A.A. Kaminskii, Laser Crystal, second ed., Springer-Verlag, Berlin, 1990.
[25] K. Wei, D.P. Machewirth, J. Wenzel, E. Snitzer, G.H. Siger Jr., J. Non Cryst. Solids 182 (1995) 257–261.
[26] J. Hegarty, D.L. Huber, W.M. Yen, Phys. Rev. B 25 (1982) 5638–5645.
[27] F. Varsanyi, Surface lasers, Appl. Phys. Lett. 19 (1971) 169–171.
[28] Y. Dimitriev, V. Dimitrov, M. Arnau dov, J. Mater. Sci. 18 (1983) 1353–1358.

[29] Ch, Srinivasa Rao, V. Ravikumar, T. Srikumar, Y. Gandhi, N. Veeraiah, J. Non Cryst. Solids 357 (2011) 3094–3102.
[30] M. Venkateswarlu, Sk. Mahamuda, K. Swapna, M.V.V.K.S. Prasad, A.S. Rao, S. Shakya, A. MohanBabu, G. VijayaPrakash, J. Lumin. 163 (2015) 64–71.
[31] W.T. Carnall, P.R. Fields, K. Rajnak, J. Chem. Phys. 49 (1968) 4424–4442.
[32] D.V.R. Murthy, B.C. Jamalaiah, T. Sasikala, L. Rama Moorthy, M. Jayasimhadri, K. Jang, H.S. Lee, S.S. Yi, J.H. Jeong, Phys. B Condens. Matter 405 (2010) 1095–1100.
[33] W.T. Carnall, J.P. Hesseler, F. Wagner Jr., J. Phys. Chem. 82 (1978) 2152–2158.
[34] B.R. Judd, Phys. Rev. 127 (1962) 750–761.
[35] G.S. Ofelt, J. Chem. Phys. 37 (1962) 511–520.
[36] A. Brenier, I.V. Kityk, Appl. Phys. 90 (2001) 232–236.
[37] Sk. Mahamuda, K. Swapna, A. Srinivasa Rao, T. Sasikala, L. Rama Moorthy, Phys. B Condens. Matter 428 (2013) 36–42.
[38] I. Pal, A. Agarwal, S. Sanghi, M.P. Aggarwal, J. Alloys Compd. 509 (2011) 7625–7631.
[39] Z. Mazurak, S. Bodyi, R. Lisiecki, Gabrys-Pisarska, M. Czaja, Opt. Mater. (Amst) 32 (2010) 547–553.
[40] B.C. Jamalaiah, J. Suresh Kumar, A. Mohan Babu, L. Rama Moorthy, K. Jang, H.S. Lee, M. Jayasimhadri, J.H. Jeong, H. Choi, J. Lumin. 129 (2009) 1023–1028.
[41] R.T. Génova, I.R. Martín, Rodríguez-Mendoza, F. Lahoz, A. Lozano-Gorrín, P. Núñez, J. González-Platas, V. Lavín, J. Alloys Compd. 380 (2004) 167–172.
[42] D.R. Simons, A.J. Faber, H. De Wall, Opt. Lett. 20 (1995) 468–470.
[43] M.A. Newhouse, R.F. Bartholomew, B.G. Aitken, L.J. Button, N.F. Borrelli, IEEE Photon. Technol. Lett. 6 (1994) 189–191.
[44] S.V.J. Lakshman, A.S. Kumar, J. Phys. Chem. Solids 49 (1988) 807–811.
[45] B. Karthikeyan, S. Mohan, M.L. Baesso, Phys. B Condens. Matter 337 (2003) 249–254.
[46] W.M. Yen, S. Shionoya, Phosphor Hand Book, CRC Press, New York, 1999, p. 805.
[47] M. Inokuti, F. Hirayama, J. Chem. Phys. 43 (1965) 1978–1988.

This article has been accepted for publication in a future issue of this journal, but has not been fully edited. Content may change prior to final publication. Citation information: DOI 10.1109/TASC.2018.2805170, IEEE Transactions on Applied Superconductivity

STRESS INDUCED MAGNETIC FIELD INHOMOGENEITY IN A 1.5 T SUPERCONDUCTING MRI MAGNET

S. R. Thekkethil, S. Kar, M. Kumar, V. Soni, N. K. Suman, R.G. Sharma, V. Rastogi and T. S. Datta

***Abstract*—**The heart of the present-day MRI scanners is a superconducting magnet producing the required central field. A 1.5 T multi-coil magnet with ±5.5 ppm field homogeneity in 45 cm field of view (FOV) is designed. These coils will operate at an average current density of 130 A/mm^2. The magnet bobbin will be made of 5083 aluminium alloy, while the winding pack of the magnet will be a composite structure which will consist of Nb-Ti, copper, epoxy and insulations. The winding pre-tension, thermal strains; due to cooling and Lorentz forces contributes to the overall stress, which during operation can cause deformation of the magnet. To design a structurally sound and stable magnet system it is critical to evaluate the stresses that are generated in the magnet during winding, cool down and operation. The paper discusses the stresses generated on the magnet and deformations produced due to the forces acting on the coils. The effect of deformation on the field homogeneity and the influence of winding tension on the overall operational stress are also studied. The von-Mises stress during the operation is found to be 40 MPa along the median line. The deformations of the magnet due to operational stresses increased the field homogeneity to ±85 ppm in the FOV.

***Index Terms*—Electromagnetic modelling, Numerical simulation, Magnetic resonance imaging, Stress measurement, Superconducting devices**

I. INTRODUCTION

The heart of the present-day MRI scanners is a superconducting magnet. The magnet provides the required magnetic field with very high homogeneity in the Field of View (FOV) in the range of 45-50 cm. High homogeneity is needed in the desired FOV for getting quality images [1]. To minimise the amount of superconductor thus the cost, while maintaining the desired size of the clear bore, MRI magnets are built in an axisymmetric multi-coil configuration with 6-12 individual coils instead of a single coil solenoid [1]. The coils are designed and arranged in axially symmetric position in such a way that they produce a high homogeneity at the desired field in the FOV region. The field homogeneity has to be of the order of 10 ppm. This multi-coil configuration, however, leads to higher peak field so the Lorentz forces and thereby large stresses on the coils, both in radial as well as in axial directions [2]. Besides, the winding pre-tension and thermal contraction during its cool-down to 4.2 K also lead to additional mechanical stresses. These stresses will eventually deform the coil structure, and consequently, there will be a degradation of homogeneity in the FOV. This paper discusses the calculation of these stresses and shows how they can degrade the homogeneity of the MRI magnet and how the winding pre-tension can be chosen to neutralise the effect of other stresses.

This work is supported by Ministry of Electronics and Information Technology (MeitY), Govt. of India.

Sankar Ram Thekkethil is with Inter-University Accelerator Centre (IUAC), New Delhi, India (e-mail: sankarram90@gmail.com)

Soumen Kar is with Inter-University Accelerator Centre (IUAC), New Delhi, India (email: kar.soumen@gmail.com)

Vikas Rastogi is with Delhi Technological University, New Delhi, India

Other authors are with Inter-University Accelerator Centre (IUAC), IN

Color versions of one or more of the figures in this paper are available online at http://ieeexplore.ieee.org.

Digital Object Identifier will be inserted here upon acceptance.

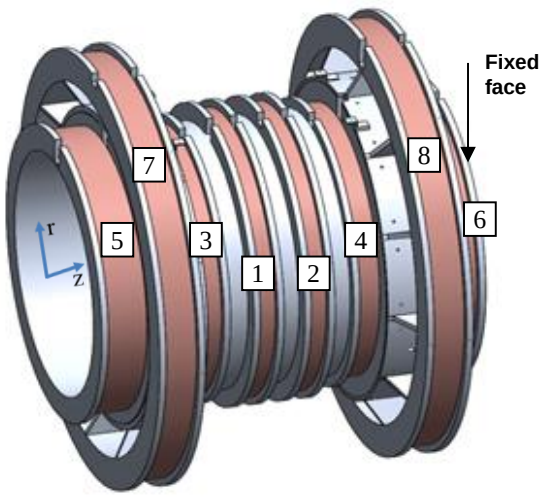


Fig. 1. The six primary coils (1-6) and two shield coils (7, 8) mounted on an aluminium 5083 alloy bobbin.

II. MAGNET PARAMETERS

We have designed an MRI magnet which will produce a central field of 1.5 T with a peak-to-peak field homogeneity of 10 ppm in a 45 cm FOV. The magnet has four pairs of coils positioned symmetrically on either side of the mid-plane. The coils will operate at an average current density of 130 A/mm^2. The magnet will have a clear bore of 0.9 m over a length of 1.5 m. The coils are designed to operate at 60% of conductor's critical current. The magnet coils will be wound over an aluminium 5083 alloy bobbin and will be mechanically fixed on to the inner helium vessel to prevent any movement during the operation. The magnet coils along with its bobbin are shown in Fig. 1.

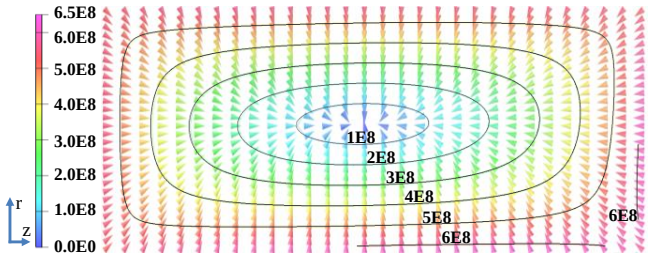


Fig. 2. The Lorentz force vectors and contours inside the coil-6 as calculated from the magnetic field profile. The colour scale is the magnitude, in N/m^3.

Template version 8.0, 27 July 2017. IEEE will put copyright information in this area
See http://www.ieee.org/publications_standards/publications/rights/indes.html for more information.

1051-8223 (c) 2018 IEEE. Personal use is permitted, but republication/redistribution requires IEEE permission. See http://www.ieee.org/publications_standards/publications/rights/index.html for more information.

This article has been accepted for publication in a future issue of this journal, but has not been fully edited. Content may change prior to final publication. Citation information: DOI 10.1109/TASC.2018.2805170, IEEE Transactions on Applied Superconductivity

III. Estimation of Operational Stresses

A. Lorentz Forces

The coils of the MRI magnet will experience outward radial forces due to the axial field of the magnet. These coils will also experience higher axial forces due to their off-centre positions relative to the overall magnetic field. The Lorentz force (***F***) is calculated as the cross product of magnetic field profile (***B***) and current density (***J***) as

$$\boldsymbol{F}=\boldsymbol{J}\times\boldsymbol{B} \tag{1}$$

The magnetic field is calculated for a 1 mm grid using integration method in OPERA 3D software. The Lorentz forces in each coil are calculated using the magnetic field and the current density values. In our calculations, we assumed that there is no force in the azimuthal direction and the current density is constant over the entire coil cross-section. The Lorentz force vectors in coil-6 are shown in Fig 2.

B. Thermal Stresses

The calculation of the thermal stresses in the magnet is primarily dependent on the proper evaluation of thermal expansion coefficient of the coil [3]. The winding pack of each coil is a composite consisting of copper, niobium-titanium, polyester insulation, epoxy etc. There is insufficient data available on the material properties of epoxy and polyester insulation at cryogenic temperature range. Therefore we had to use the existing data that is available in the literature with some extrapolation or interpolation for our calculations [4]. Composite mixture rules are employed for the material to estimate their physical properties such as thermal expansion coefficient, Young's modulus etc.

C. Winding stress

The pre-tension applied during winding will act to compensate for the effects of Lorentz forces and cool down. In this configuration, the coil is designed to act as a floating coil [5], [6]. This method of coil design reduces shear stresses between bobbin and coil at the corners thus minimizing the chances of quench. The condition used for the estimation of winding pre-tension is that during the operation of the magnet there is no gap between the bobbin and the coil [7]. Thus, the winding tension has to compensate for the effects of thermal cool down and the Lorentz forces. The winding pressure and the resultant hoop stress can be calculated by using the combined homogeneous cylinder method (CHCM) which is explained below [8].

If we consider the first layer being wound, it can be regarded as the thin wall cylinder resisting the inner pressure from the bobbin. In turn, the bobbin bears an equivalent outer pressure from the first layer. From the equation of the thin wall cylinder under inner pressure, the pressure p_1 applied by winding of the first layer is

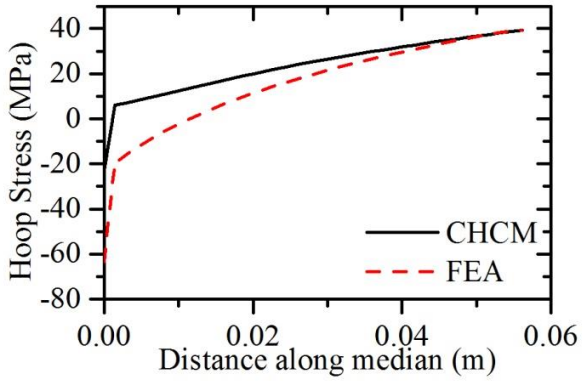


Fig. 3. The calculation of hoop stress in the coil 6 using CHCM method (solid line) and FEA simulations (dotted line).

$$p_1 = \frac{\sigma_w \,.\, t}{R_{ID}} \tag{2}$$

where σ_w is the winding pre-tension applied on the first layer of conductor, R_{ID} is the inner radius of the coil, and t is the thickness of a layer. While winding the ith layer, the layer resists an inner pressure from a cylinder composed of (i-1) number of layers and the bobbin. The pressure p_i applied by winding the ith layer is

$$p_i = \frac{\sigma_w . t}{R_{ID} + (i-1).t} \tag{3}$$

If a single length conductor of uniform thickness is used and the pre-tension applied on the conductor is constant, the pressure p_i goes down as the layer moves from inner diameter to outer diameter of the coil. The circumferential or hoop stress ($\sigma_{\theta i}$) developed on the ith layer due to all the layers below is given by

$$\sigma_{\theta i} = \frac{p_i.(R_{ID} + (i-1).t)}{t_{bobbin} + (i-1).t} \tag{4}$$

where t_{bobbin} is the thickness of the bobbin. The hoop stress on the kth layer ($\sigma_{\theta k}$) due to its winding pre-tension and compression from layers above it till outer most layer n is given as

$$\sigma_{\theta k} = \sigma_w + \sum_{i=k+1}^{n} \sigma_{\theta i} \tag{5}$$

This method, however, has its limitations, such as only one homogenous material is assumed for the bobbin and the effect of boundary conditions cannot be studied. To get a more accurate result, finite element analysis (FEA) is used to study the winding stress along with other forces acting on each coil. The winding pre-tension is modelled using Element Death and Birth method in ANSYS [9], [10]. The comparison between the CHCM method and the FEA method can be seen in Fig. 3. The FEA calculations consider different materials for bobbin and coil and also accounts for the slip plane between the bobbin and the coil.

1051-8223 (c) 2018 IEEE. Personal use is permitted, but republication/redistribution requires IEEE permission. See http://www.ieee.org/publications_standards/publications/rights/index.html for more information.

This article has been accepted for publication in a future issue of this journal, but has not been fully edited. Content may change prior to final publication. Citation information: DOI 10.1109/TASC.2018.2805170, IEEE Transactions on Applied Superconductivity

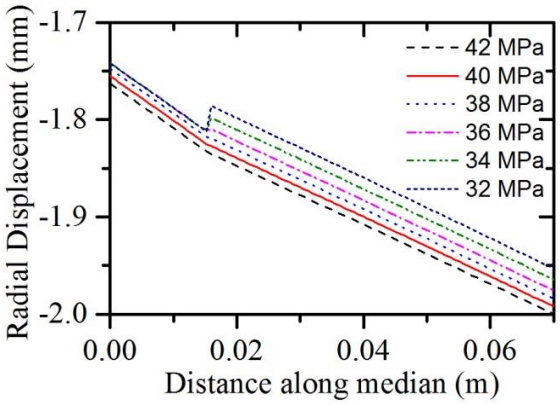


Fig. 4. The radial displacement of coil-6 and the bobbin during operation for various values of winding pre-tensions. At 40 MPa winding pre-tension, the coil and bobbin move together without any gap appearing between them.

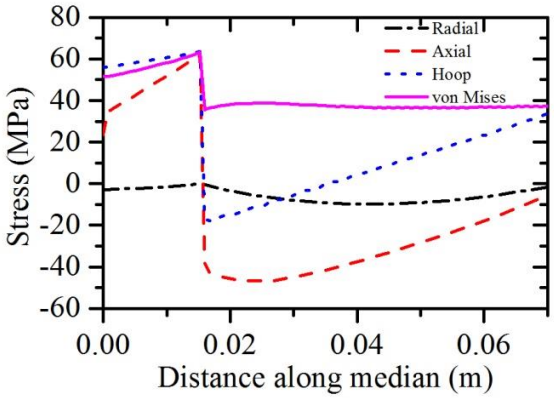


Fig. 6. The various stresses in the coil-6 during operation, plotted along a median line passing from the inner diameter of bobbin to the outer diameter of the coil.

IV. Operational Stresses in Coils

The stresses in the coils are calculated using ANSYS and OPERA FEA. The criteria for selecting the winding pre-tension during the result analysis are:

- There is no gap between the coil and bobbin after charging, so that delamination of individual turns and shifting of magnetic iso-centre is avoided [7].
- The peak stress in the coil needs to be well below the failure stress value of the weakest material in the coil, i.e. the epoxy.
- The variation in the central field homogeneity due to displacements should be small enough to be easily manageable by shimming [11][12].

Since the stresses due to the Lorentz forces and the thermal contraction are fixed parameters for a given geometry, the winding pre-tension is considered to be the variable parameter. The FEA simulation is done over a range of winding pre-tensions, and the corresponding relative displacements between the coil and bobbin is shown in Fig. 4. The final value of 40 MPa is selected such that there is no gap between the coil and the bobbin.

The combined operational stresses are calculated based on the calculations above, and the corresponding displacements are calculated. The result of one of the primary coils, coil-6 is discussed here, since those coils are exposed to the highest magnetic field, thus to highest Lorentz forces. Figure 5 shows the von-Mises stress contour of the bobbin cross-section during coil operation. Various stresses acting in coil 6 during operation, plotted along a median line passing from the inner radius of the bobbin to the outer radius of the coil are shown in Fig. 6. It shows the radial force in the coil is completely compressive, which can keep the individual wires bundled together in the coil. The peak radial stress is 9 MPa at the middle of the coil and is smaller compared to other components of the stress. At the inner diameter of the coil, the hoop stress is 17 MPa which is compressive in nature. It changes to tensile stress at the outer diameter. Unlike conventional solenoid magnets where the magnetic centre and geometric centre of coils coincide, these coils also experience high axial stresses. The axial stresses, like the radial stresses, are also fully compressive in nature with a maximum value of 47 MPa.

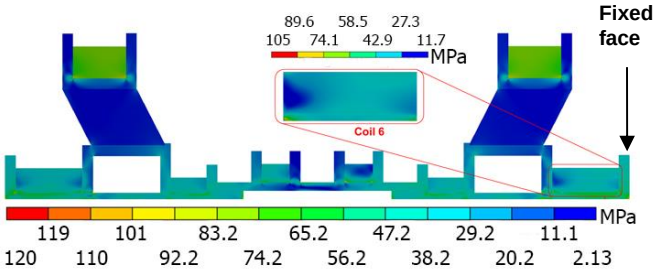


Fig. 5. The von-Mises stress contour of the bobbin cross-section during coil operation. The enlarged view of coil-6 is also shown in the inset. The colour scale is shown in MPa.

A. Coil deformation during operation

During the assembly of the MRI cryostat, the bobbin is fixed to the bore of the helium vessel at one of the ends, so that the bobbin will axially shrink towards an end rather than towards the axial centre. The bobbin is fixed at only one end to reduce thermal stress during cooldown. The radial contraction of the bobbin is also restricted by the helium vessel which will contract less compared to the aluminium bobbin. These boundary conditions are incorporated into the FEA simulation model, and the corresponding deformation of the coil is calculated.

TABLE I
THE MOVEMENT OF COIL CENTRES DUE TO OPERATIONAL STRESSES. THE AXIAL MOVEMENT IS TOWARDS THE FIXED END OF THE BOBBIN, WHILE THE RADIAL MOVEMENT IS TOWARDS THE CENTRE OF THE BOBBIN.

Coil Number	Axial Movement (Δz, mm)	Radial Movement (Δr, mm)
1	3.393	1.911
2	2.496	2.097
3	4.188	1.806
4	1.694	1.804
5	5.512	1.909
6	0.372	1.913
7	4.965	2.542
8	0.899	2.541

1051-8223 (c) 2018 IEEE. Personal use is permitted, but republication/redistribution requires IEEE permission. See http://www.ieee.org/publications_standards/publications/rights/index.html for more information.

This article has been accepted for publication in a future issue of this journal, but has not been fully edited. Content may change prior to final publication. Citation information: DOI 10.1109/TASC.2018.2805170, IEEE Transactions on Applied Superconductivity

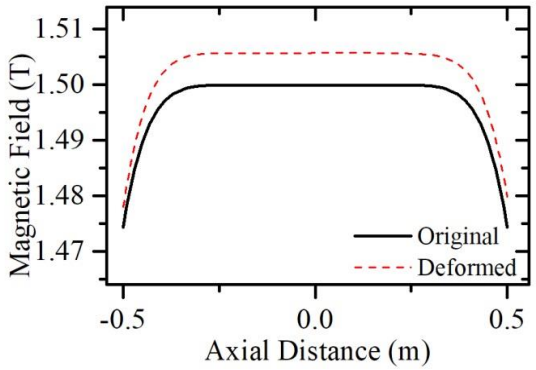


Fig 7. The variation of magnetic field in the central axis of the magnet due the movement of coil centres and reduction of coil dimensions.

During operation, the iso-centre is shifted by 2.94 mm towards the fixed face. The variation in the position of the mid-planes of individual coil pairs is within ±6.3 μm with respect to new iso-centre. Based on the final coordinates of the deformed coil, the magnetic field is recalculated to see the effects of various forces on the coils. The movement of coil centres is summarised in Table I.

B. *Variation of magnetic field*

The variation of the magnetic field (B) in the central axis of the magnet due to change in axial position and shape of the coils is shown in Fig. 7. The central field at the iso-centre is increased by 57.6 G, while an asymmetry is also introduced in the field profile. The increase of magnetic field is due to the reduction in the diameter and the area of cross-section of the coils. This change will have to be compensated during operation by adjusting the operating current to appropriate values.

The field homogeneity in the FOV is calculated to find out the effect of deviation in coil position and shape. The FOV is positioned at the new iso-centre. The field homogeneity (ΔB) at a point in the FOV is calculated by (6)

$$\Delta B = \frac{B - B_0}{B_0} \times 10^6 \qquad (6)$$

where B is the field at a point, and B_0 is the central field. The maximum inhomogeneity increased from 5.5 ppm to 85 ppm. The plots of homogeneity in a 45 cm FOV are shown in Fig 8.

The deviation in the field homogeneity can also be analysed in terms of their corresponding coefficients of Legendre polynomial expansion. The major contributing components of Legendre polynomial expansion for the design value and the coil

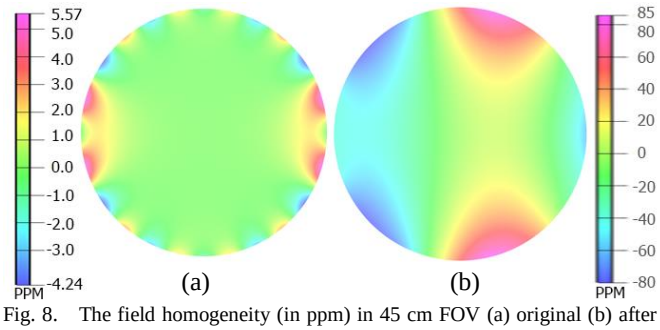


Fig. 8. The field homogeneity (in ppm) in 45 cm FOV (a) original (b) after deformation.

TABLE II
THE COEFFICIENT OF LEGENDRE EXPANSION ($a_{n,m}$) OF THE CENTRAL MAGNETIC FIELD FOR THE DESIGN CONDITION AND AFTER DEFORMATION [1]. ODD ORDER TERMS ARE INTRODUCED TO THE SERIES DUE TO THE DEFORMATION

Polynomial Order (n,m)	Coefficient of Legendre expansion ($a_{n,m}$)	
	Design Value	Deformed Value
0,0	1.499964	1.505726
1,0	2.85E-17	8.99E-05
2,0	8.21E-07	-1.09E-04
3,0	-7.84E-16	-1.26E-04
4,0	4.70E-06	5.45E-05
5,0	7.24E-16	2.55E-05
6,0	-1.32E-07	-1.25E-05
7,0	-2.29E-16	-3.24E-06
8,0	1.05E-05	1.09E-05
9,0	-1.77E-15	3.63E-07
10,0	-3.54E-06	-3.42E-06
11,0	-1.87E-15	4.13E-07
12,0	-4.58E-04	-4.64E-04

after deformation are given in Table II. The deformations in coil configuration introduced odd order of harmonic components which are absent in axisymmetric solenoid designs [13]. These components will have to be compensated using passive shimming. The corresponding 5G fringe field of this magnet is well within the safety limits of 5 m axial x 3 m radial, as dictated by ISO-IEC 60601-2-33 standard [14].

V. CONCLUSION

Multi-coil configuration used in solenoid magnet in the MRI scanners imposes higher stresses which lead to movement of coils and distortion of the required field homogeneity. A numerical model is developed to study the stresses and deformations in a 1.5 T MRI magnet. The effect of fixing the bobbin only at one end is presented here. The stresses and corresponding deformations are quantified, and the deviation in the magnetic field is calculated. The final field is analysed in terms of field homogeneity and Legendre polynomials. The von-Mises stress is found to be 40 MPa over the coil geometry with stress concentration points at the corners of the coils. Due to the deformations, the central field is increased by 57.6 G with an increase of field inhomogeneity to 85 ppm from 5.5 ppm. The asymmetry in geometry also introduced odd order terms into the Legendre polynomials expansion.

ACKNOWLEDGMENT

Authors would like to thank Mr. Abdullah Al Amin, Case Western Reserve University, USA for his valuable guidance in using ANSYS APDL. Authors would also like to thank Mr. Venkatesu Samala, ICON Design Automation, IN for his assistance in using OPERA 3D software.

1051-8223 (c) 2018 IEEE. Personal use is permitted, but republication/redistribution requires IEEE permission. See http://www.ieee.org/publications_standards/publications/rights/index.html for more information.

This article has been accepted for publication in a future issue of this journal, but has not been fully edited. Content may change prior to final publication. Citation information: DOI 10.1109/TASC.2018.2805170, IEEE Transactions on Applied Superconductivity

REFERENCE

[1] Y. Lvovsky, E. W. Stautner, and T. Zhang, "Novel technologies and configurations of superconducting magnets for MRI," *Supercond. Sci. Technol.*, vol. 26, no. 9, p. 93001, Sep. 2013.

[2] H. Miyazaki *et al.*, "Design of a conduction-cooled 9.4 T REBCO magnet for whole-body MRI systems," *Supercond. Sci. Technol.*, vol. 29, no. 10, p. 104001, Oct. 2016.

[3] NIST, "NIST Material Database." [Online]. Available: http://www.cryogenics.nist.gov/MPropsMAY/material properties.htm. [Accessed: 27-Jun-2017].

[4] N. Bagrets, S. Otten, K.-P. Weiss, A. Kario, and W. Goldacker, "Thermal and mechanical properties of advanced impregnation materials for HTS cables and coils," *IOP Conf. Ser. Mater. Sci. Eng.*, vol. 102, no. 1, p. 12021, Dec. 2015.

[5] E. S. Bobrov, J. E. C. Williams, and Y. Iwasa, "Experimental and theoretical investigation of mechanical disturbances in epoxy-impregnated superconducting coils. 2. Shear-stress-induced epoxy fracture as the principal source of premature quenches and training theoretical analysis," *Cryogenics (Guildf).*, vol. 25, no. 6, pp. 307–316, Jun. 1985.

[6] L. Wang, H. Pan, H. Wu, X. L. Guo, Y. Cheng, and M. A. Green, "Effects of Slip Planes on Stresses in MICE Coupling Solenoid Coil Assembly," *IEEE Trans. Appl. Supercond.*, vol. 20, no. 3, pp. 1940–1943, Jun. 2010.

[7] R. D. Kephart, "CDF Coil Engineering Design Note #24 CDF Winding Tension and banding," 1981.

[8] Lankai Li, Zhipeng Ni, Junsheng Cheng, Housheng Wang, Qiuliang Wang, and Baozhi Zhao, "Effect of Pretension, Support Condition, and Cool Down on Mechanical Disturbance of Superconducting Coils," *IEEE Trans. Appl. Supercond.*, vol. 22, no. 2, pp. 3800104–3800104, Apr. 2012.

[9] A. Al Amin *et al.*, "A multiscale and multiphysics model of strain development in a 1.5 T MRI magnet designed with 36 filament composite MgB 2 superconducting wire," *Supercond. Sci. Technol.*, vol. 29, no. 5, p. 55008, May 2016.

[10] Ansys Inc., *ANSYS Advanced Analysis Techniques Guide*, 10.0. Ansys inc., 2005.

[11] Jiangbo Chen and Xiaohua Jiang, "Stress Analysis of a 7 T Actively Shielded Superconducting Magnet for Animal MRI," *IEEE Trans. Appl. Supercond.*, vol. 22, no. 3, pp. 4903104–4903104, Jun. 2012.

[12] Y. Lvovsky and P. Jarvis, "Superconducting Systems for MRI—Present Solutions and New Trends," *IEEE Trans. Appiled Supercond.*, vol. 15, no. 2, pp. 1317–1325, Jun. 2005.

[13] A. K. Kalafala, "A design approach for actively shielded magnetic resonance imaging magnets," *IEEE Trans. Magn.*, vol. 26, no. 3, pp. 1181–1188, May 1990.

[14] British Standards Institute, "IEC 60601-2-33 Particular requirements for the basic safety and essential performance of magnetic resonance equipment for medical diagnosis," in *Medical electrical equipment*, 3.1., INTERNATIONAL STANDARD, 2010.

1051-8223 (c) 2018 IEEE. Personal use is permitted, but republication/redistribution requires IEEE permission. See http://www.ieee.org/publications_standards/publications/rights/index.html for more information.

Optical Materials 79 (2018) 21–32

Contents lists available at ScienceDirect

Optical Materials

journal homepage: www.elsevier.com/locate/optmat

Structural, optical absorption and photoluminescence spectral studies of Sm^{3+} ions in Alkaline-Earth Boro Tellurite glasses

K. Siva Rama Krishna Reddy [a], K. Swapna [a, *], Sk. Mahamuda [a], M. Venkateswarlu [a], M.V.V.K. Srinivas Prasad [a], A.S. Rao [b], G. Vijaya Prakash [c]

[a] Department of Physics, Koneru Lakshmaiah Education foundation, Green Fields, Vaddeswaram, Guntur, Andhra Pradesh 522502, India
[b] Department of Applied Physics, Delhi Technological University, Bawana Road, New Delhi, 110042, India
[c] Nanophotonics Laboratory, Department of Physics, Indian Institute of Technology-Delhi, Hauz Khas, New Delhi, 110016, India

ARTICLE INFO

Article history:
Received 29 December 2017
Received in revised form
9 February 2018
Accepted 5 March 2018

Keywords:
Glasses
FT-IR
J-O theory
Radiative properties
Quantum efficiency
CIE chromaticity coordinates
Optoelectronic devices

ABSTRACT

Sm^{3+} ions doped Alkaline-Earth Boro Tellurite (AEBT) glasses were prepared by using conventional melt quenching technique and characterized using the spectroscopic techniques such as FT-IR, optical absorption, emission and decay spectral measurements to understand their utility in optoelectronic devices. From absorption spectra, the bonding parameters, nephelauxetic ratios were determined to know the nature of bonding between Sm^{3+} ions and its surrounding ligands. From the measured oscillator strengths, the Judd-Ofelt (J-O) intensity parameters were evaluated and in turn used to estimate various radiative parameters for the fluorescent levels of Sm^{3+} ions in AEBT glasses. The PL spectra of Sm^{3+} ions exhibit three emission bands corresponding to the transitions $^4G_{5/2} \rightarrow {}^6H_{5/2}$, $^6H_{7/2}$ and $^6H_{9/2}$ in the visible region for which the emission cross-sections and branching ratios were evaluated. The decay spectral profiles measured for $^4G_{5/2} \rightarrow {}^6H_{7/2}$ transition showed single exponential for lower concentration and non-exponential for higher concentration of doped rare earth ion in the as prepared glasses. Conversion of decay spectral profiles from single to non-exponential have been analyzed using Inokuti–Hirayama (I–H) model to understand the energy transfer mechanism involved in the decay process. CIE Chromaticity coordinates were measured using emission spectral data to identify the exact region of emission from the as-prepared glasses. From the evaluated radiative parameters, emission cross-sections and quantum efficiencies, it was observed that AEBT glass with 1 mol% of Sm^{3+} ions is more suitable for designing optoelectronic devices.

© 2018 Elsevier B.V. All rights reserved.

1. Introduction

Glassy materials are playing a starring role in designing the photonics and optoelectronics devices due to their advantages over crystalline materials. The crystalline materials have huge optical losses resulting from light scattering produced the grain boundaries. Moreover, the compositional/concentration variation facility of glassy materials provides ample scope for researchers to work on various alloys to produce relatively good optoelectronic devices. Glass materials possess short-range order and random network structure; they have stronger ability to provide accommodation for foreign atoms in their interstitial positions. Due to this, glass materials easily accept various dopants like nano particles, transition metal ions and Rare Earth (RE) ions [1]. Especially glassy materials doped with RE ions have the utmost importance because of their advantages such as insensitiveness of the spectral transitions of RE ions to the host glass materials, the stable intense narrow emissions of RE ions which are originated from the 4f-4f and 4f-5d electronic transitions and the long lifetimes of RE's meta stable states [2]. Due to these advantages, glass network incorporated with the RE ions attains the feasibility of employing them in the designing of optoelectronic devices like light converters, sensors, lasers, color displays, optical amplifiers and solid-state lightening devices depending on the emission regions of the RE ions [3,4].

Among the RE ions, samarium (Sm^{3+}) ion has strong emission transitions with $4f^5$ configuration in the orange-red visible region. Especially, the excited level $^4G_{5/2}$ of Sm^{3+} ion has strong luminescence and high quantum efficiency. Due to these reasons, Sm^{3+} ions doped glasses have numerous applications in the development of photonic devices like color displays, high-density optical memory

* Corresponding author.
E-mail address: kswapna80@gmail.com (K. Swapna).

https://doi.org/10.1016/j.optmat.2018.03.005
0925-3467/© 2018 Elsevier B.V. All rights reserved.

storage devices, lasers in the visible region etc. [5,6]. Few factors that influence the luminescence intensities of Sm^{3+} ions in the glass network are concentration of Sm^{3+} ions, multiphonon relaxation associated with phonon energy of host matrices, energy back transfer through non-radiative cross-relaxation and ligand environment of host glass network [7]. Choice of host glass materials and their compositions play a crucial role in getting efficient luminescence from the RE ions. Moreover, the host glass must have desired optical characteristics like good optical transparency, low phonon energies; and physical properties like low melting point, high chemical stability, and good RE ion solubility to get efficient luminescence from RE ions. Unfortunately, still there exist too many problems to get the desired efficiency from RE ions in the host glass. To overcome this, a new glass system was prepared to get efficient luminescence and to design optoelectronic devices with technological relevance.

Among the oxide-based glasses, borate (B_2O_3) glasses have so many advantages over other oxide glasses because of their large dielectric constant, good RE ion solubility, mechanical strength, low cost, low melting point and high chemical durability etc. But the foremost disadvantage of borate glass is higher phonon energy (~1300 cm^{-1}) which in turn springs up the non-radiative losses through multiphonon relaxation process and lowers the effective radiative transition rate [4]. To reduce the redundant phonon energies and to enhance the luminescence efficiency, we have added TeO_2 to the borate glass network [8]. Borate glasses containing TeO_2 and doped with RE ions have potential applications in the development of non-linear optical devices because of their efficient non-linear optical properties [9]. Ordinarily, boron atoms in the borate glasses coordinate with either three or four oxygen atoms by forming two fundamental groups BO_3 and BO_4. These two fundamental groups lead to the formation of various B_xO_y structural units like boroxol rings, diborate groups, tetraborate groups and Penta borate groups [10], and in TeO_2 the basic structural units are TeO_4 and TeO_3. According to S. Rada et al. [11] excess content of B_2O_3 in binary B_2O_3-TeO_2 glasses causes the transformation of TeO_3 structural units to TeO_4 and BO_4 structural units to BO_3. These transformations of TeO_3 structural units to TeO_4 and BO_4 structural units to BO_3 create non-bridging oxygens (NBOs) and decrease the rigidity of glass network [12]. Further addition of modifier oxide such as CaO to the binary B_2O_3- TeO_2 system leads to the conversion of BO_3 structural units into BO_4 and TeO_3 into TeO_4 [13]. As BO_4 units possess lower phonon energy over BO_3 units, the enhancement in the number of BO_4 units over BO_3 units improves the luminescence properties of the glasses under investigation [14]. The transformation of BO_3 structural units into BO_4 leads to the formation of bridging oxygens (BOs) and increases the rigidity of glass network [11]. The remaining NBOs formed due to the transformation of TeO_3 structural units into TeO_4 can participate in the formation of bonds with RE ions and help to stabilize the glass network and increase the rigidity. Also, the addition of alkaline earth metal oxides like CaO & MgO to the binary B_2O_3-TeO_2 glass network can decrease the crystallinity growth and enhances the amorphous nature [15]. Further addition of post-transition metal oxides like Al_2O_3 & TiO_2 to the glass network can increase the mechanical strength of the glass [16]. Additionally, the glass systems based on modifiers such as MgO and CaO possess low melting temperature, high thermal stability, non-hygroscopic nature and are very attractive to evaluate the effects of the chemical environment on the optical properties of RE ions [17]. Further, these glass modifiers influence emission spectra of RE doped glasses. The impact of oxide glass modifiers on absorption, luminescence properties and decay measurements of RE ions doped to different borate and fluoroborate glass matrices have been studied by many researchers [18–20].

In the backdrop of the above discussion and considering various scientific patronages offered by the aforementioned chemical constituents, we prepared a glassy system namely Alkaline-Earth Boro Tellurite (AEBT) glasses. We have employed various spectroscopic techniques such as FT-IR, absorption, emission and decay spectral studies to understand the practical utility of the AEBT glasses doped with Sm^{3+} ions in optoelectronic devices.

2. Experimental

2.1. Synthesis

A series of AEBT glasses with the chemical compositions $60B_2O_3$ -$15TeO_2$ - (10-x) CaO - 5MgO - $5Al_2O_3$ - $5TiO_2$ - xSm_2O_3 (Where x = 0.1, 0.5, 1.0, 1.5, 2.0, 2.5 mol%) were prepared by using conventional melt quenching technique. The appropriate amounts of all chemical compositions are mixed well in an agate mortar to get homogeneous mixture. The homogeneous powders were then collected in high purity alumina crucibles and heated at 1150 °C for 20 min in an electric furnace until the uniform melts were obtained. The melts were then quenched on a preheated brass plate and pressed quickly with another brass plate to get uniform thickness. To get rid of internal stress of the prepared glasses, the glasses were annealed for 2 h at 200^0 C. Finally, the Sm^{3+} ions doped AEBT glasses were polished before going for experimental measurements. For our convenience, these glass samples are named as AEBTSm0.1, AEBTSm0.5, AEBTSm1.0, AEBTSm1.5, AEBTSm2.0, AEBTSm2.5 for x = 0.1, 0.5, 1.0, 15, 2.0, 2.5 mol% respectively.

2.2. Characterization

The densities of the prepared glass samples were measured by using Archimedes' method with water as an immersion liquid. Brewster's angle method (He-Ne laser with a wavelength 650 nm line) was used to measure refractive indices of the as prepared glasses. A Thermo scientific make Nicolet-380 spectrometer was used to record the FT-IR spectrum of an undoped AEBT glass. By using a JASCO model V-670 UV–vis–NIR spectrometer, the absorption spectra of samples were recorded at room temperature. Photoluminescence (PL) spectra and PL decay spectral measurements were recorded at room temperature by using a JASCO model FP-8300 spectrofluorometer.

3. Results and discussion

3.1. Structural analysis

Fig. 1 shows the Fourier Transform Infrared spectrum (FT-IR) of an undoped AEBT glass recorded in the wavelength range 3500-500 cm^{-1}. In general, FT-IR is used to identify the functional groups and local structure of the glass network by means of change in the dipole moment of the molecules [21]. The spectrum exhibits seven transmission bands around 676 cm^{-1}, 902 cm^{-1}, 1244 cm^{-1}, 1424 cm^{-1}, 2352 cm^{-1}, 2721 cm^{-1} and 3279 cm^{-1}. Generally, the functional group region i.e., from 4000 to 1500 cm^{-1} represents the bands which are produced due to the presence of fundamental groups like OH bond, Hydrogen bond, and H-O-H bending. The transmission band centered around 3279 cm^{-1} is due to stretching and bending vibrational modes of O-H molecules in the present AEBT glass [22,23]. The band observed around 2721 cm^{-1} is due to hydrogen bonding [24]. The transmission peak observed at 2352 cm^{-1} is because of vibrations of O-H bonds formed at non-bridging oxygen (NBO) sites [25]. In the fingerprint region, i.e., from 1500 cm^{-1} to 400 cm^{-1}, the band located at 1424 cm^{-1} is the characteristic of the stretching vibrations of BO_3 groups. At 1244 cm^{-1} the band is due to asymmetric stretching vibrations of

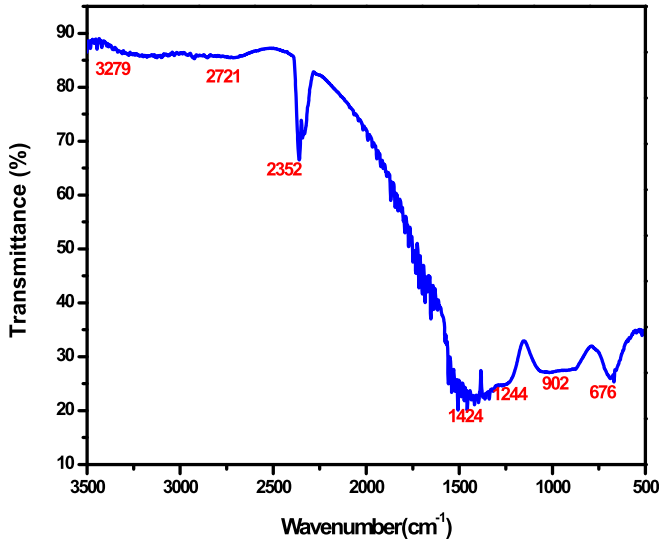


Fig. 1. FT-IR spectrum of an undoped AEBT glass.

B-O bonds from orthoborate groups [26]. The wide band at 902 cm^{-1} is the indication for the progressive change of boron coordination number from BO_3 to BO_4 units [27]. This enhancement in BO_4 structural units over BO_3 units is due to the addition of network modifiers like CaO and MgO. Transformation of BO_3 structural units into BO_4 leads to the formation of Bridging Oxygens (BOs) and increases the rigidity of glass network [11]. The transmission peak at 676 cm^{-1} represents the stretching vibrations of TeO_4 trigonal bipyramidal units [28]. Table 1 gives all the assigned bands from the FT-IR spectrum of an un-doped AEBT glass.

3.2. Physical properties

Densities, refractive indices and nominal Sm-Sm inter atomic distance of titled glasses are presented in Table 2. Using densities and refractive indices, physical properties like average molecular weight ($\overline{M}$), molar refractivity (R_m), mean atomic volume (V), molar electronic polarizability (α_e), inter ionic distance (r_i), rare-earth ion concentration (N), Dielectric constant (ε), Optical dielectric constant (ε-1), Reflection losses (R), Polaron radius (r_p), Field strength and Theoretical optical basicity ($\wedge_{th}$) were calculated with the help of relevant expressions given in literature [29] and are given in Table 2. From the data given in Table 2 it is observed that the physical properties like refractive index, interionic distance, molecular electronic polarizability, polaron radius, reflection losses and dielectric constant are decreasing with increase in Sm^{3+} ion content. This could be attributed to the reduction in NBOs. The Sm^{3+} ions in the as prepared glasses forms bonds with NBOs by acting as network modifier and reduces the number of NBOs in the as prepared glass [30]. The other physical properties like density, average molecular weight, mean atomic volume, and field strength are increasing with the increase in Sm^{3+} ion concentration due to the similar effect. Decrease in inter atomic distances also enhances the density of the glasses at higher Sm^{3+} ions concentration. The field strength values are also increasing from AEBTSm0.1 to AEBTSm2.5 glass which indicates the good RE ion solubility.

3.3. Optical studies

3.3.1. Absorption spectral analysis

Fig. 2 represents optical absorption spectra of different concentrations of Sm^{3+} ions doped AEBT glasses in the region 350–1700 nm. All the prepared glass samples hold absorption bands in nearly similar wavelength regions with uneven intensities. In general, absorption bands are divided into the high energy group (350–800 nm) and the low energy group (900–2200 nm) [6]. It was observed that the absorption bands located in high energy group are weak in intensity due to spin forbidden [6]. Hence the prepared glass samples are transparent in that region. Absorption spectra of the titled glasses at low energy group contains seven absorption bands located at 10582, 9255, 8142, 7282, 6774, 6565, 6310 cm^{-1} related to the transitions $^6H_{5/2} \rightarrow {}^6F_{11/2}$, $^6H_{5/2} \rightarrow {}^6F_{9/2}$, $^6H_{5/2} \rightarrow {}^6F_{7/2}$, $^6H_{5/2} \rightarrow {}^6F_{5/2}$, $^6H_{5/2} \rightarrow {}^6F_{3/2}$, $^6H_{5/2} \rightarrow {}^6H_{15/2}$, $^6H_{5/2} \rightarrow {}^6F_{1/2}$ respectively. The absorption band positions and their assignments for all Sm^{3+} ions doped AEBT glasses are done as per the Carnell paper [31] and are given in Table 3. In the present work, the intensity of absorption bands are increasing relatively from AEBTSm0.1 to AEBTSm2.5 glass. These bands are inhomogeneously broadened due to the disorderness and distribution of crystal fields in the as prepared glass [32]. This happens because of overlap of the oxygen orbitals with the 4f orbitals of RE ions. The nature of the bonding between sm^{3+} ions and oxygen orbitals can be estimated using nephelauxetic ratios (β) and bonding parameters (δ). The covalent or ionic nature of bonding depends upon the positive and negative values of bonding parameter. For the present series of glasses, nephelauxetic ratios (β) and bonding parameters (δ) were estimated using the equations available in the literature [7] and are given in Table 3. From Table 3, it is observed that the bonding parameter (δ) values are found to be negative for all the Sm^{3+} ions doped AEBT glasses. Hence in the present series of Sm^{3+} ions doped AEBT glasses, the nature of Sm-O bond is ionic and the ionic nature decreases with the increase in the concentration of Sm^{3+} ions in AEBT glasses.

3.3.2. Oscillator strengths

In the present series of glasses, the intensities of absorption bands are increasing with the increase in Sm^{3+} ions concentration. The strength of these absorption bands was measured with the help of area under absorption bands by using the formula given in literature [31,33].

Table 1
Band positions (in cm^{-1}) and their assignments of FT-IR spectrum of an undoped AEBT glass.

Band positions (cm^{-1})	Assignment
3279	Stretching and bending vibrational modes of O-H molecules
2721	Hydrogen bonding
2352	Vibrations of O-H bonds formed at non-bridging oxygen sites
1424	Stretching vibrations of BO_3 groups
1244	Asymmetric stretching vibrations of B-O bonds from ortho borate groups
902	Progressive change of boron coordination number from BO_3 to BO_4 units
676	Stretching vibrations of TeO_4 trigonal bi pyramidal units

Table 2
Physical properties of Sm^{3+} ions doped AEBT glasses.

Physical properties	AEBTSm0.1	AEBTSm0.5	AEBTSm1.0	AEBTSm1.5	AEBTSm2.0	AEBTSm2.5
Refractive index (n_d)	2.507	2.462	2.423	2.400	2.384	2.379
Density (d) (g/cc)	3.254	3.274	3.299	3.324	3.349	3.374
Average molecular weight ($\overline{M}$) (g)	82.71	83.88	85.35	86.81	88.27	89.74
Sm^{3+} ion concentration (N) ($x10^{22}$ ions/cm^3)	0.236	1.175	2.327	3.459	4.569	5.661
Mean atomic Volume (V) (g/cm^3/atom)	6.120	6.168	6.228	6.287	6.346	6.403
Dielectric Constant (ε)	6.288	6.065	5.871	5.763	5.685	5.377
Optical Dielectric constant ($\varepsilon - 1$)	5.288	5.065	4.871	4.763	4.685	4.377
Reflection losses (R)	0.184	0.178	0.172	0.169	0.167	0.157
Molar Refraction (R_m) (cm^{-3})	16.21	16.08	16.00	16.02	16.06	16.17
Polaron radius (r_p) (Å)	3.072	1.803	1.435	1.258	1.147	1.068
Interionic distance (r_i) (Å)	7.624	4.473	3.562	3.122	2.846	2.650
Molar electronic polarizability (α_e) ($x10^{-23}cm^3$)	6.430	1.276	0.634	0.423	0.318	0.250
Field Strength (x $10^{15}cm^{-2}$)	3.177	9.230	14.55	18.94	22.80	26.29
Optical basicity (Λ_{th})	0.454	0.455	0.456	0.457	0.458	0.459

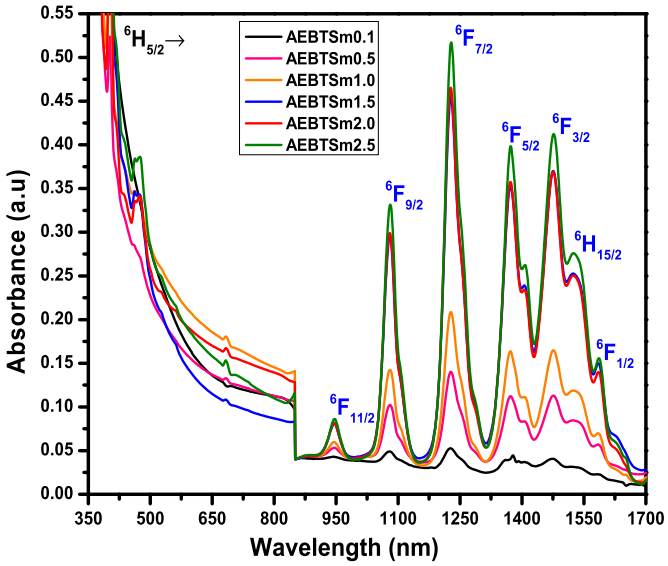


Fig. 2. Absorption Spectra of Sm^{3+} ions doped AEBT glasses.

$$f_{exp} = 4.32\ X\ 10^{-9} \int \varepsilon(\nu) d\nu \quad (1)$$

where $\varepsilon(\nu)$ is the molar absorptivity of a band at a wave number (ν) in cm^{-1}. These measured strengths of absorption bands are known as experimental oscillator strengths (f_{exp}). The calculated oscillator strengths (f_{cal}) of absorption transitions were obtained using J-O theory. According to J-O theory, the calculated oscillator strengths of an absorption transitions from the ground state ψJ to an excited state $\psi' J'$ are determined using the following expression [34,35].

$$f_{cal} = \left(\frac{8\pi^2 mc\nu}{3h(2J+1)}\right)\left(\frac{(n^2+2)^2}{9n}\right)\sum_{\lambda=2;4;6}\Omega_\lambda\left(\psi J\left|\left|U^\lambda\right|\right|\psi' J'\right)^2 \quad (2)$$

where ν is the wave number in cm^{-1} of a particular transition from the ground state (ψJ) to the excited state ($\psi' J'$) m is the mass of the electron, c is the velocity of light in vacuum, h is the Planck's constant, n is refractive index, $(n^2+2)^2/9n$ is the Lorentz local field correction for the absorption band, Ω_λ ($\lambda = 2, 4, 6$) are the host dependent J-O intensity parameters and $||U^\lambda||^2$ are the doubly reduced matrix elements of the unit tensor operator which are considered to be independent of the host. The quality of the fit between the experimental and calculated oscillator strengths was measured by root mean square deviation (δ_{rms}) [7] using the following formula

$$\delta_{rms} = \left(\frac{\sum\left(f_{exp} - f_{cal}\right)^2}{n}\right)^{\frac{1}{2}} \quad (3)$$

where 'n' is the total number of transitions involved in the fitting procedure. The experimental oscillator strengths (f_{exp}), calculated oscillator strengths (f_{cal}) and root mean square deviation (δ_{rms}) values are presented in Table 4. From Table 4, it can be observed that, the variation in the oscillator strengths (f_{exp}, f_{cal}) illustrates the modification in the local environment around Sm^{3+} ions due to the small change in Sm^{3+} ion concentration. The small values of root mean square deviation (δ_{rms}) represent the good fit between experimental and calculated oscillator strengths. The values of J-O intensity parameters Ω_λ ($\lambda = 2,4,6$) of different concentrations of

Table 3
Nephelauxetic ratios (β) and bonding parameters (δ) of Sm^{3+} ions doped AEBT glasses.

Transition from $^6H_{5/2}\rightarrow$	AEBTSm0.1	AEBTSm0.5	AEBTSm1.0	AEBTSm1.5	AEBTSm2.0	AEBTSm2.5
	β	β	β	β	β	β
$^6F_{11/2}$	1.0110	1.0078	1.0078	1.0078	1.0067	1.0056
$^6F_{9/2}$	1.0064	1.0064	1.0064	1.0064	1.0055	1.0045
$^6F_{7/2}$	1.0187	1.0179	1.0179	1.0179	1.0170	1.0170
$^6F_{5/2}$	1.0220	1.0265	1.0265	1.0265	1.0258	1.0258
$^6F_{3/2}$	1.0225	1.0218	1.0218	1.0218	1.0211	1.0204
$^6H_{15/2}$	1.0102	1.0089	1.0082	1.0082	1.0082	1.0082
$^6F_{1/2}$	0.9876	0.9864	0.9864	0.9858	0.9851	0.9845
$\bar{\beta}$	1.0112	1.0108	1.0107	1.0106	1.0099	1.0094
δ	−0.0111	−0.0107	−0.0106	−0.0105	−0.0098	−0.0094

Sm^{3+} ions doped AEBT glasses are compared with other reported values in Table 5 [36–39]. The J-O parameters are host dependent and give the information about influence of host on the emission characteristics of RE ions because they consist of intra configurational radial integrals and interaction of central ions and crystal parameters with the nearest neighbouring environment. Due to this reason, the J-O Parameters are important to know the local structure and bonding vicinity of RE ions. The variation of the J-O parameters Ω_λ ($\lambda = 2, 4, 6$) with Sm^{3+} ion concentration is shown in Fig. 3. In general, Ω_2 parameter is found to be associated with the covalancy, structural change and symmetry of the ligand field around RE ion sites [40]. The remaining two parameters Ω_4 and Ω_6 are the characteristics of viscosity and rigidity of the glass matrix [41]. From Fig. 3, it can be observed that in the present series of Sm^{3+} ions doped AEBT glasses, the Ω_2 values are low and increase up to 1 mol% Sm^{3+} ion concentration and then decrease due to concentration quenching. From Table 5, it is observed that the Ω_2 parameter has the relatively least values for all the as prepared glasses indicating lower ligand field symmetry around Sm^{3+} ion sites. This lower asymmetry around the Sm^{3+} ion sites is due to the higher mixing of opposite parity electronic configurations that are responsible for the large spectral intensities. The lower values of Ω_2 indicate high centro symmetric, coordination environment and strong ionic nature between the Sm^{3+}- and oxygen ligand. This is also in consistent with negative values of bonding parameters (δ) reported in Table 3. The high magnitude of Ω_6 indicates the high rigidity of the glass matrices, obtained with the addition of Sm^{3+} ions [42].

3.4. Optical band gap and urbach's energy

The investigation of energy band gap of amorphous materials is possible with the study of optical absorption near the absorption edge. The relatively less sharpness of the optical absorption edge of amorphous materials is credited to the localization of some states in the energy gap. These localized states in the energy gap are evidences for the existence of vacancies, broken bonds, impurities and dangling bonds. The density of these localized states increases with increase in disorder in the amorphous materials [43]. So, the study of optical absorption of a glass material in UV–vis–NIR regions provides the information about short range structure of glasses and surroundings of the absorbing atom [44]. According to Mott and Davis [45] the relation between the absorption coefficient $\alpha(\nu)$ and the optical band gap E_{opt} can be expressed as follows,

$$(\alpha h\nu)^{n} = B\,(h\nu - E_{opt}) \tag{4}$$

where n is an index used to denote the nature of transition causing the absorption. With the help of the above equation (for $n = \frac{1}{2}$) and the absorption spectral data, the relation between $(\alpha h\nu)^{\frac{1}{2}}$ and the photon energy $h\nu$ (eV) was obtained and shown in Fig. 4. From Fig. 4, by extrapolating the linear portion of the curve to $(\alpha h\nu)^{\frac{1}{2}} = 0$, the optical band gap ($E_{opt}$) values for the present series of Sm^{3+} ions doped AEBT glasses were obtained. The obtained band gap values are 2.620 eV for AEBTSm0.1, 2.767 eV for AEBTSm0.5, 2.905 eV for AEBTSm-1.0, 2.986 eV for AEBTSm1.5, 3.047 eV for AEBTSm2.0 and 3.095 eV for AEBTSm2.5. Clearly, the optical band gap values are increasing with increase in the concentration of Sm^{3+} ions from AEBTSm0.1 to AEBTSm2.5 glasses. The variation of band gap values with Sm^{3+} ion concentration for the present series of glasses are shown in Fig. 5. The optical band gap values for Sm^{3+} ions doped AEBT glasses along with other reported values are presented in Table 6 [46–48]. Urbach's energy can be calculated using the following urbach's empirical formula [49].

$$\alpha(\nu) = C\,\exp\left(\frac{h\nu}{\Delta E}\right) \tag{5}$$

where $\alpha(\nu)$ is the absorption coefficient, C is constant and ΔE is Urbach's energy. Urbach's energy provides the information about exponential behaviour of the absorption coefficient $\alpha(\nu)$ and it is used to estimate the degree of disorderness in non-crystalline materials. Urbach's energy (ΔE) values were obtained by taking the reciprocal of slope of the linear portion of the curve plotted between $\ln(\alpha)$ and $h\nu$, i.e., $\Delta E = \frac{h\nu}{\ln(\alpha)}$. The Urbach's energy values for present series of glasses are 0.872 eV for AEBTSm0.1, 0.890 eV for AEBTSm0.5, 0.894 eV for AEBTSm1.0, 0.901 eV for AEBTSm1.5, 0.903 eV for AEBTSm2.0 and 0.904 eV for AEBTSm2.5. The range of Urbach's energy values for the present glasses are between 0.872 eV and 0.904 eV. This variation in Urbach's energies is due to the presence of defects within the localized states. In oxide glasses the shift of energy gap to higher energies could be related to the decrease in the concentration of NBOs, which bind excited electrons less tightly than BOs. In glasses, negative charges on BOs have lesser magnitude than that on NBOs; so, decrease in the concentration of NBOs decreases the magnitude of negative charges and then leads to the increase in band gap values. Here addition of Sm^{3+} ions to the base glass AEBT leads to the formation of bonds between NBOs and Sm^{3+} ions and reduces the concentration of NBOs. This reduction in the concentration of NBOs leads to the shrink in the magnitude of negative charges of oxygen ions as well as the top of the valance band and then causes the raise in energy Band Gap (E_{opt}) and Urbach's energy (ΔE) values [50,51].

3.5. Emission spectra analysis and radiative properties

In order to know the suitable excitation wavelength to record the emission spectra, the excitation spectrum of AEBTSm0.1 glass was recorded under 602 nm emission and is shown in Fig. 6. Fig. 6 shows, ten different excitation bands associated with the transitions $^6H_{5/2} \rightarrow (^4F_{3/2}, {}^4I_{13/2})$, $^4P_{1/2}$, $(^4H_{9/2}, {}^4D_{7/2})$, $^4D_{3/2}$, $^6P_{7/2}$, $^4F_{7/2}$, $(^6P, {}^4P)_{5/2}$, $^4G_{9/2}$, $^4I_{13/2}$, $^4I_{11/2}$ at the wavelengths 273 nm, 323 nm,

Table 4
Measured (f_{exp} x 10^{-6}) and calculated (f_{cal} x 10^{-6}) oscillator strengths along with rms deviations of Sm^{3+} ions doped AEBT glasses.

Transition from $^6H_{5/2}$ →	AEBTSm0.1		AEBTSm0.5		AEBTSm1.0		AEBTSm1.5		AEBTSm2.0		AEBTSm2.5	
	f_{exp}	f_{cal}	f_{exp}	f_{cal}	f_{exp}	f_{cal}	f_{exp}	f_{cal}	f_{exp}	f_{cal}	f_{exp}	f_{cal}
$^6F_{11/2}$	0.445 ± 0.046	0.506	0.480 ± 0.018	0.561	0.585 ± 0.028	0.754	0.533 ± 0.032	0.625	0.425 ± 0.031	0.476	0.324 ± 0.020	0.464
$^6F_{9/2}$	2.911 ± 0.165	3.058	3.521 ± 0.121	3.383	4.101 ± 0.107	4.526	3.347 ± 0.110	3.764	2.771 ± 0.100	2.860	2.604 ± 0.117	2.778
$^6F_{7/2}$	4.261 ± 0.091	4.154	4.471 ± 0.139	4.561	6.271 ± 0.151	5.959	5.312 ± 0.167	5.013	3.843 ± 0.155	3.776	3.753 ± 0.084	3.619
$^6F_{5/2}$	1.636 ± 0.085	1.656	1.817 ± 0.166	1.759	1.937 ± 0.086	2.045	1.719 ± 0.100	1.822	1.307 ± 0.159	1.313	1.125 ± 0.081	1.167
$^6F_{3/2}$	0.705 ± 0.026	0.744	0.750 ± 0.015	0.798	0.919 ± 0.014	0.932	0.812 ± 0.027	0.825	0.559 ± 0.013	0.594	0.508 ± 0.010	0.523
$^6H_{15/2}$	0.122 ± 0.022	0.025	0.137 ± 0.011	0.028	0.155 ± 0.019	0.038	0.121 ± 0.033	0.032	0.109 ± 0.015	0.024	0.098 ± 0.001	0.023
$^6F_{1/2}$	0.035 ± 0.002	0.006	0.044 ± 0.002	0.018	0.049 ± 0.002	0.026	0.040 ± 0.003	0.017	0.036 ± 0.002	0.011	0.020 ± 0.001	0.003
δ_{rms} (**x10**$^{-6}$)	±0.084		±0.086		±0.218		±0.204		±0.059		±0.104	

Table 5
Judd-Ofelt Parameters (Ω_λ x10^{-22} cm^2, where $\lambda = 2,4,6$) and trends for Sm^{3+} ions doped AEBT glasses along with other reported glasses.

Glass Composition	J O Parameters			Trend	References
	Ω_2	Ω_4	Ω_6		
AEBTSm0.1	1.066 ± 0.343	150.400 ± 5.890	173.100 ± 5.590	$\Omega_6>\Omega_4>\Omega_2$	Present Work
AEBTSm0.5	3.054 ± 0.004	168.690 ± 13.760	202.890 ± 4.710	$\Omega_6>\Omega_4>\Omega_2$	Present Work
AEBTSm1.0	4.331 ± 1.131	198.010 ± 7.670	275.880 ± 6.260	$\Omega_6>\Omega_4>\Omega_2$	Present Work
AEBTSm1.5	2.901 ± 0.581	179.140 ± 9.320	232.150 ± 6.700	$\Omega_6>\Omega_4>\Omega_2$	Present Work
AEBTSm2.0	1.870 ± 1.919	130.100 ± 1.750	178.150 ± 3.190	$\Omega_6>\Omega_4>\Omega_2$	Present Work
AEBTSm2.5	0.670 ± 0.340	117.530 ± 5.120	176.440 ± 11.390	$\Omega_6>\Omega_4>\Omega_2$	Present Work
PbF_2-TeO_2-B_2O_3	21	142	187	$\Omega_6>\Omega_4>\Omega_2$	[36]
LTTSm10	130	308	154	$\Omega_4>\Omega_6>\Omega_2$	[37]
NaZnBS	55	968	977	$\Omega_6>\Omega_4>\Omega_2$	[38]
KZnBS (Set A)	18	1137	1145	$\Omega_6>\Omega_4>\Omega_2$	[38]
KZnBS (Set B)	93	1097	1141	$\Omega_6>\Omega_4>\Omega_2$	[38]
LCN borate	84	400	502	$\Omega_6>\Omega_4>\Omega_2$	[39]

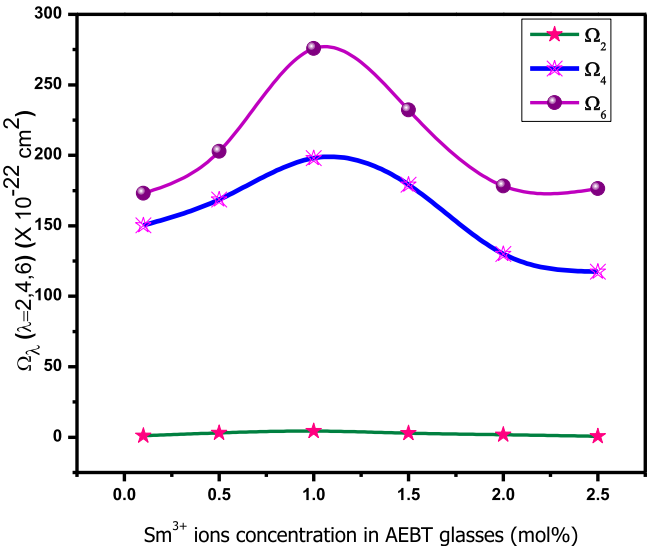


Fig. 3. Variation of J-O parameters (Ω_λ; $\lambda = 2, 4, 6$) with Sm^{3+} ions concentration in AEBT glasses.

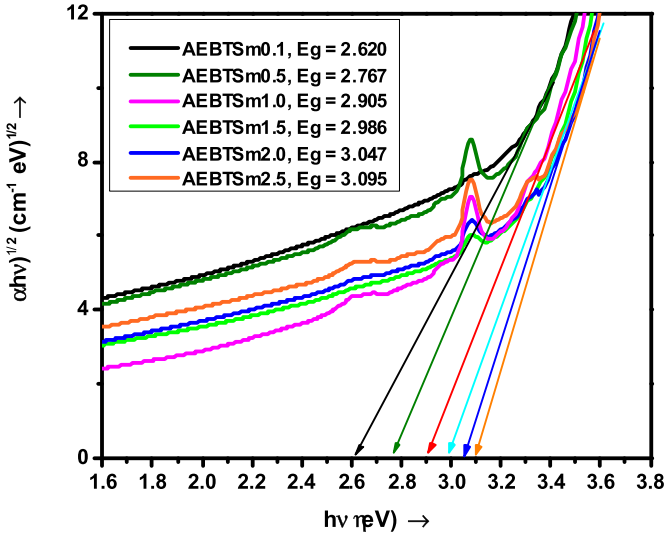


Fig. 4. Optical band gap evaluation for Sm^{3+} ions doped AEBT glasses.

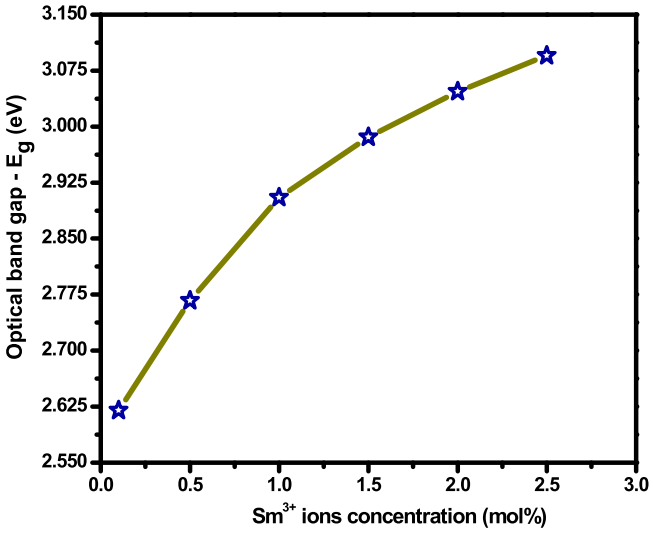


Fig. 5. Variation of Optical band gap with Sm^{3+} ion concentration in AEBT glasses.

344 nm, 361 nm, 374 nm, 402 nm, 417 nm, 441 nm, 463 nm, 485 nm respectively. Among all the excited transitions, the transition $^6H_{5/2} \rightarrow {}^4F_{7/2}$ at 402 nm is very intense, and is used as an excitation wavelength to record the emission spectra of the titled glasses. The emission spectra of Sm^{3+} doped AEBT glasses recorded from 525 to 675 nm under 402 nm excitation wavelength is shown in Fig. 7. As shown in Fig. 7 the emission spectra of Sm^{3+} ions doped AEBT glasses show three intense emission peaks at the wavelengths 565 nm (green), 601 nm (orange) and 648 nm (red) with corresponding transitions $^4G_{5/2} \rightarrow {}^6H_{5/2}$, $^4G_{5/2} \rightarrow {}^6H_{7/2}$ and $^4G_{5/2} \rightarrow {}^6H_{9/2}$ respectively. Among the three observed bands, the transition $^4G_{5/2} \rightarrow {}^6H_{7/2}$ at 601 nm (orange) shows relatively highest intensity than the other transitions. Fig. 8 shows the intensity variation of the magnetic dipole allowed transition $^4G_{5/2} \rightarrow {}^6H_{7/2}$ (601 nm) in the titled glasses with Sm^{3+} ion concentration. This region is used to develop new device applications like color display devices, high density optical storage devices and medical devices. Relatively more intensity shown by the magnetic allowed transition ($^4G_{5/2} \rightarrow {}^6H_{7/2}$) than the electric dipole transition ($^4G_{5/2} \rightarrow {}^6H_{9/2}$) indicates ionic nature and symmetry. The intensity of the emission peaks increases up to 1.0 mol% of Sm^{3+} ions and beyond that concentration quenching is observed. In general, the concentration quenching originated from the non-radiative process consists of multiphonon relaxation and non-radiative cross-relaxation between the Sm^{3+} ions through dipole-quadrupole or dipole-dipole

Table 6
Optical band gap values of Sm^{3+} ions doped AEBT glasses along with other reported glasses.

Glass Sample	Optical band gap (eV)	Reference
AEBTSm0.1	2.620 ± 0.256	Present Work
AEBTSm0.5	2.767 ± 0.335	Present Work
AEBTSm1.0	2.905 ± 0.265	Present Work
AEBTSm1.5	2.986 ± 0.212	Present Work
AEBTSm2.0	3.047 ± 0.225	Present Work
AEBTSm2.5	3.095 ± 0.192	Present Work
2.0 LBTPS	2.860	[46]
0.05 LBTPS	2.990	[46]
TBL1	3.340	[47]
TBL6	3.240	[47]
0.05SmPbFB	2.636	[48]
3SmPbFB	2.551	[48]

or quadrupole-quadrupole interactions [52–55]. When the glass system is closely packed with Sm^{3+} ions, the decrease in inter ionic distance (r_i) between Sm^{3+}- Sm^{3+} ions with the further addition of Sm_2O_3 content may leads to the strong interaction between two Sm^{3+} ions. Therefore, the strong interaction between two Sm^{3+} ions is able to transfer the excitation energy from one Sm^{3+} ion to the other [56]. This effective energy transfer between Sm^{3+}-Sm^{3+} ion sites result in emission quenching as shown in Fig. 8. From the calculated J-O parameters, the radiative properties like radiative transition probability (A_R), radiative branching ratio (β_R) and total radiative transition probability (A_T) were calculated and are compared with other reported values [13,40,49,57] in Table 7. The experimental branching ratios (β_{exp}) which were calculated from the emission spectral data are also presented in Table 7. The emission peak wavelength (λ_P), effective band width (FWHM) ($\Delta\lambda_P$) and stimulated emission cross-section (σ_{se}) calculated from the emission spectral data for the glasses under investigation are presented in Table 8 along with other reported values [40,53,58–60]. Table 9 represents gain band width ($\sigma_{se} \times \Delta\lambda_P$) and optical gain ($\sigma_{se} \times \tau_R$) of the emission transitions. For a particular transition, the stimulated emission cross-section (σ_{se}) can be calculated by using the following formula [61].

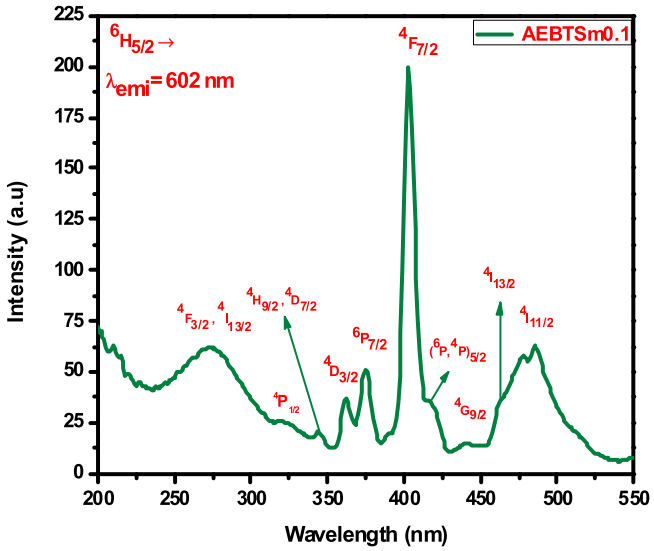


Fig. 6. Excitation Spectrum of 0.1 mol% Sm^{3+} ions doped AEBT glass.

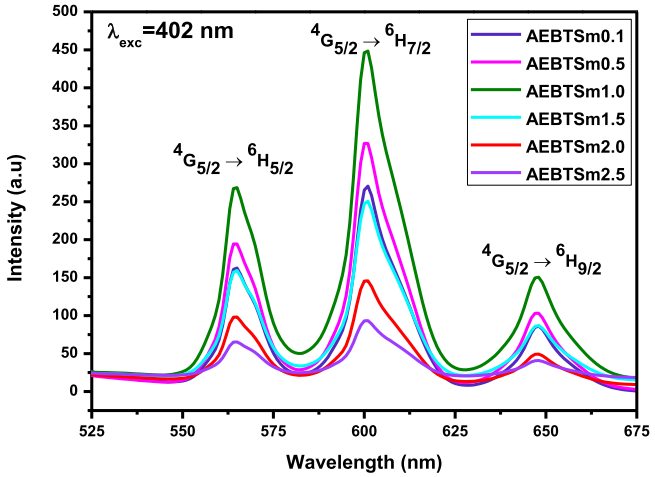


Fig. 7. Emission Spectra of Sm^{3+} ions doped AEBT glasses.

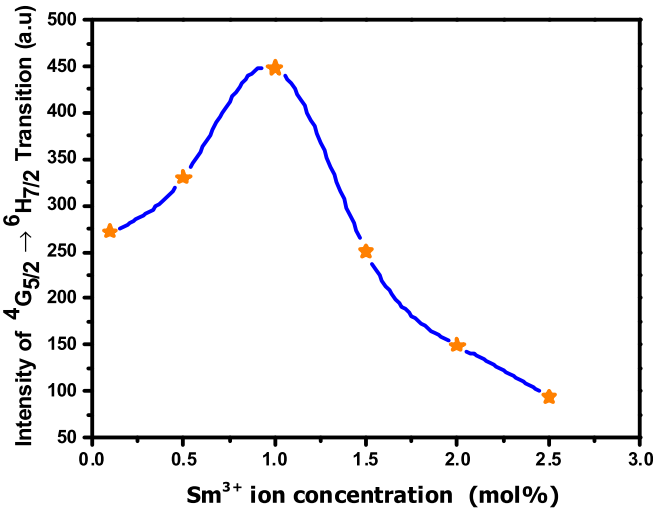


Fig. 8. Variation of intensity of $^4G_{5/2} \rightarrow {}^6H_{7/2}$ transition with Sm^{3+} ion concentration in AEBT glasses.

$$\sigma_{se} = \frac{\lambda_p^4}{8\pi c n^2 \Delta\lambda_p} A_R \quad (6)$$

where λ_p is the emission peak wavelength, $\Delta\lambda_p$ is the effective band width, n is the refractive index, and A_R is the radiative transition probability. The σ_{se} signifies rate of energy extracted from the lasing materials and gives the detailed information about the potential laser performance of the materials. From Tables 8 and 7, it is observed that among the all prepared glass samples, AEBTSm1.0 glass has the highest σ_{se} and branching ratios (β_{cal} and β_{exp}) for the emission transition $^4G_{5/2} \rightarrow {}^6H_{7/2}$ at the wavelength 601 nm. The higher values of stimulated emission cross-section and other radiative properties observed for the transitions $^4G_{5/2} \rightarrow {}^6H_{7/2}$ of Sm^{3+} doped AEBT glasses indicates the superiority of the as prepared glasses for visible orange lasing action.

3.6. Inokuti–Hirayama (I–H) model analysis of decay curves and quantum efficiencies

Fig. 9 represents the decay curves recorded under 402 nm excitation for the $^4G_{5/2}$ emission level (601 nm) of Sm^{3+} ions doped

Table 7
Radiative transition probability (A_R) (s^{-1}), radiative branching ratio (β_R), experimental branching ratio (β_{exp}) and total radiative transition probability (A_T) (s^{-1}) for Sm^{3+} ions doped AEBT glasses along with other reported glasses.

Transition	parameter	AEBTSm0.1	AEBTSm0.5	AEBTSm1.0	AEBTSm1.5	AEBTSm2.0	AEBTSm2.5	Sm20CTFB [13]	TSZNB [40]	0.5SmPbFB [49]	LCZSFB [57]
$^4G_{5/2} \rightarrow {}^6H_{5/2}$	A_R	69.080 ± 0.420	64.460 ± 0.860	65.290 ± 0.440	62.560 ± 0.550	58.890 ± 0.040	56.680 ± 0.280	40.140	26.030	31.190	31.020
	β_R	0.107 ± 0.002	0.099 ± 0.002	0.085 ± 0.001	0.094 ± 0.002	0.113 ± 0.001	0.117 ± 0.003	0.133	6.150	0.304	0.050
	β_{exp}	0.261	0.256	0.258	0.266	0.272	0.268	0.193	–	0.119	0.210
$^4G_{5/2} \rightarrow {}^6H_{7/2}$	A_R	329.900 ± 9.980	333.820 ± 14.240	405.950 ± 10.600	347.660 ± 11.840	267.460 ± 1.190	249.500 ± 11.720	286.620	216.580	186.640	264.880
	β_R	0.512 ± 0.001	0.517 ± 0.001	0.531 ± 0.001	0.524 ± 0.001	0.514 ± 0.001	0.517 ± 0.003	0.256	51.080	0.542	0.590
	β_{exp}	0.580	0.574	0.578	0.570	0.561	0.571	0.579	–	0.489	0.440
$^4G_{5/2} \rightarrow {}^6H_{9/2}$	A_R	108.010 ± 4.310	111.060 ± 7.190	133.610 ± 3.570	114.180 ± 4.690	82.750 ± 1.110	73.710 ± 3.430	166.310	120.290	83.380	173.500
	β_R	0.167 ± 0.002	0.172 ± 0.004	0.175 ± 0.001	0.172 ± 0.002	0.159 ± 0.001	0.152 ± 0.001	0.475	–	0.144	0.190
	β_{exp}	0.157	0.168	0.162	0.163	0.165	0.160	0.219	28.370	0.214	0.290
A_T		501.900 ± 160.395	545.620 ± 128.177	563.220 ± 218.259	586.440 ± 98.393	619.500 ± 97.296	682.440 ± 180.951	–	–	–	–

AEBT glasses. From Fig. 9, it is conspicuous that, the decay curves are single exponential for lower concentration (0.1–1 mol%) and non-exponential for the higher concentration (1.5–2.5 mol%). The non-exponential nature of decay curves is well fitted through Inokuti–Hirayama (I–H) model analysis [62] to understand the energy transfer mechanism involved between the doped RE ions. The experimental lifetimes (τ_{exp}) along with the radiative lifetimes (τ_R) measured from J-O theory are compared with other reported values in Table 10. From Table 10 it is observed that the experimental lifetimes are relatively less than the radiative lifetimes. The reason for this difference may be due to non-radiative decay of the excited RE ions and concentration quenching observed in the emission transitions of the present series of glasses. The non-radiative decay may be possible in two ways. One is multi-phonon relaxation and the other one is cross relaxation i.e., energy transfer between the RE ions. Here in the case of Sm^{3+} ions the multi-phonon relaxation is almost impossible to occur because the energy difference between the adjacent levels $^4G_{5/2}$ and $^6F_{11/2}$ is huge (7351 cm^{-1}). So, the possible non-radiative decay process is cross-relaxation only. The mechanism behind the cross-relaxation process can be found through I-H model analysis. As stated by I-H model, if the dopant RE ions are in lower concentrations then the interaction between the RE ions is negligible and their decay curves are almost single exponential. But, when the concentration is large enough, the interaction between the RE ions becomes so prominent and energy transfer between an excited RE ion (donor) and a non-excited RE ion (acceptor) takes place and this leads to a non-exponential shape of the decay curve. The I-H model is applicable when the energy transfer between the donor and the accepter is faster than the energy transfer between the donor and the donor. In such a situation, the luminescence decay intensity is given by

$$I(t) = I_o \ \exp\left(\frac{-t}{\tau_0} - Q\left(\frac{t}{\tau_0}\right)^{\frac{3}{s}}\right) \tag{7}$$

where t is time after excitation, I_o is the initial intensity at $t = 0$, τ_o is intrinsic decay time of donors in absence of acceptors, Q is Energy transfer parameter defined as

$$Q = \frac{4\pi}{3}\Gamma\left[1 - \frac{3}{s}\right]N_o R^3{}_o \tag{8}$$

where N_0 is acceptor concentration, R_0 is donor-acceptor separation or critical energy transfer distance and s is the multi polar interaction parameter. The Γ is Euler's Function with the values 1.77 for dipole-dipole interaction ($s = 6$), 1.43 for dipole-quadrupole interaction ($s = 8$) and 1.30 for quadrupole-quadrupole interaction ($s = 10$). The decay curves observed for the higher concentrations (1.5–2.5 mol% of Sm^{3+}) were well fitted to Eq. (7) for $s = 6$ declaring that the energy transfer mechanism between the donor and acceptor ions is predominantly dipole-dipole in nature. It is also possible to measure the energy transfer parameter (Q) by fitting the decay curves with I-H model. By using the Q value and Eq. (8) it is possible to calculate critical energy transfer distance (R_0). Donor–acceptor or dipole-dipole interaction parameter (C_{DA}) can be calculated using the expression,

$$C_{DA} = R_0^S \ \tau_0^{-1} \tag{9}$$

The measured values of energy transfer parameter (Q), critical energy transfer distance (R_0), and donor–acceptor interaction parameter (C_{DA}) for the present series of glasses are given in Table 11. From Table 11 it can be observe that the magnitude of energy transfer parameter (Q) increases whereas the critical energy

Table 8
Emission peak wavelength (λ_P) (nm), effective band widths (FWHM) ($\Delta\lambda_P$) (nm), stimulated emission cross-section (σ_{se}) ($\times 10^{-22}$) (cm^2) for Sm^{3+} ions in AEBT glasses along with other reported glasses.

Sample	$^4G_{5/2} \rightarrow {}^6H_{5/2}$			$^4G_{5/2} \rightarrow {}^6H_{7/2}$			$^4G_{5/2} \rightarrow {}^6H_{9/2}$		
	λ_P	$\Delta\lambda_p$	σ_{se}	λ_P	$\Delta\lambda_p$	σ_{se}	λ_P	$\Delta\lambda_p$	σ_{se}
AEBTSm0.1	565	10.595	1.400 ± 0.008	601	13.301	6.821 ± 0.206	648	11.152	3.600 ± 0.143
AEBTSm0.5	565	10.682	1.414 ± 0.018	601	13.567	7.383 ± 0.314	648	12.051	3.737 ± 0.241
AEBTSm1.0	565	10.626	1.459 ± 0.009	601	13.522	9.132 ± 0.238	648	11.766	4.668 ± 0.124
AEBTSm1.5	565	10.604	1.357 ± 0.011	601	13.488	7.592 ± 0.258	648	12.041	3.774 ± 0.155
AEBTSm2.0	565	10.581	1.239 ± 0.001	601	13.388	5.696 ± 0.025	648	12.349	2.582 ± 0.034
AEBTSm2.5	565	10.694	1.272 ± 0.006	601	13.717	5.591 ± 0.262	648	12.223	2.505 ± 0.116
TSZNB [40]	564	14.000	1.010	599	26.000	5.730	643	23.000	4.780
PKFBASM10 [53]	563	3.640	5.500	599	6.040	6.760	644	16.920	2.570
PPNSm10 [58]	563	10.400	1.210	598	10.400	6.760	645	13.900	7.060
L5FBS [59]	562	20.000	0.703	598	27.000	5.744	645	32.000	3.814
Sm^{3+}: tellurite [60]	561	11.000	0.990	597	12.000	5.920	644	14.000	4.490

Table 9
Gain band width ($\sigma_{se} \times \Delta\lambda_P$) ($\times 10^{-28}$) (cm^3) and optical gain ($\sigma_{se} \times \tau_R$) ($\times 10^{-25}$) (cm^2 s) parameters evaluated from the visible emission spectra of Sm^{3+} ions in AEBT glasses.

Sample	$^4G_{5/2} \rightarrow {}^6H_{5/2}$		$^4G_{5/2} \rightarrow {}^6H_{7/2}$		$^4G_{5/2} \rightarrow {}^6H_{9/2}$	
	$\sigma_{se}x\Delta\lambda_p$	$\sigma_{se}x\tau_R$	$\sigma_{se}x\Delta\lambda_p$	$\sigma_{se}x\tau_R$	$\sigma_{se}x\Delta\lambda_p$	$\sigma_{se}x\tau_R$
AEBTSm0.1	1.484	2.175	9.073	10.593	4.014	5.590
AEBTSm0.5	1.510	2.189	10.017	11.428	4.503	5.785
AEBTSm1.0	1.551	1.912	12.348	11.963	5.492	6.115
AEBTSm1.5	1.439	2.045	10.241	11.442	4.545	5.688
AEBTSm2.0	1.311	2.384	7.627	10.960	3.189	4.968
AEBTSm2.5	1.361	2.637	7.670	11.586	3.062	5.191

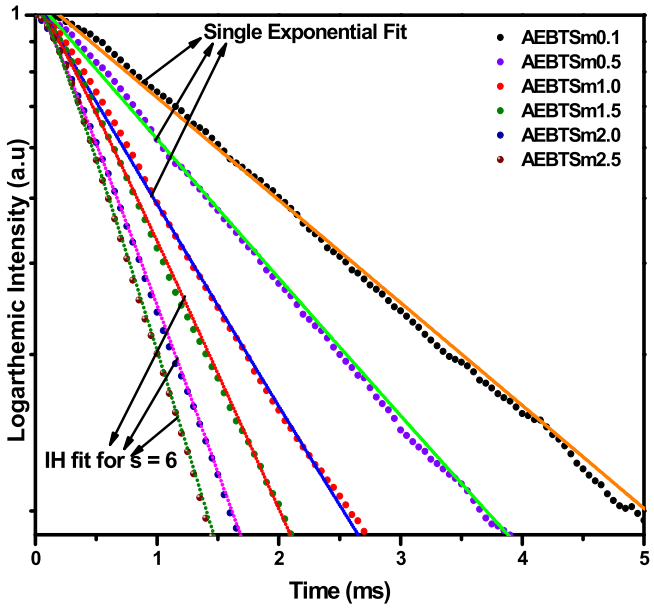


Fig. 9. Fluorescence decay curves with I-H fitting for $^4G_{5/2}$ level of Sm^{3+} ions doped AEBT glasses.

transfer distance (R_0) and donor–acceptor interaction parameter (C_{DA}) decreases with increase in Sm^{3+} ion concentration. Thus, the increase in energy transfer parameter (Q) along with decrease in critical energy transfer distance (R_0) make the energy transfer between the RE ions and lead to the shrink in the experimental lifetimes. The partial energy level diagram and the cross-relaxation channels of energy transfer observed between the Sm^{3+} ions in present glasses are illustrated in Fig. 10 [a] and Fig. 10 [b]

Table 10
Radiative lifetime (τ_R) (ms), experimental lifetimes (τ_{exp}) (ms) and quantum efficiencies (η) for $^4G_{5/2} \rightarrow {}^6H_{7/2}$ transition of Sm^{3+} ions in AEBT glasses along with other reported glasses.

Sample	τ_R	τ_{exp}	η (%)	References
AEBTSm0.1	1.996 ± 0.048	1.339 ± 0.015	67 ± 2	Present Work
AEBTSm0.5	1.548 ± 0.064	1.232 ± 0.008	79 ± 3	Present Work
AEBTSm1.0	1.310 ± 0.031	1.093 ± 0.006	83 ± 2	Present Work
AEBTSm1.5	1.507 ± 0.047	0.760 ± 0.005	50 ± 2	Present Work
AEBTSm2.0	1.924 ± 0.010	0.611 ± 0.002	31 ± 1	Present Work
AEBTSm2.5	2.072 ± 0.078	0.506 ± 0.002	24 ± 1	Present Work
OFBSm01	2.970	2.467	83	[7]
PPNSm10	2.820	1.896	58	[58]
PKACaLFSm10	1.660	1.520	92	[65]
SFB	3.040	1.490	49	[66]

respectively. From Fig. 10 [a] we can observe that the energy levels positioned on top of the level $^4G_{5/2}$ are closely spaced. This closeness leads to the non-radiative decay of the excited Sm^{3+} ions from higher energy levels to the meta-stable state $^4G_{5/2}$. From Fig. 10 [b] the huge energy gap (7351 cm^{-1}) present between meta-stable state $^4G_{5/2}$ and its lower level $^6F_{11/2}$ is a great hurdle for the multi phonon relaxation to occur. So, the only possible way for non-radiative decay is cross-relaxation. The channels which are responsible for the cross-relaxation of Sm^{3+} ions are presented in Fig. 10 [b]. Those channels are represented by CR_1: ($^4G_{5/2}$, $^6H_{5/2}$) → ($^6F_{5/2}$, $^6F_{11/2}$), CR_2: ($^4G_{5/2}$, $^6H_{5/2}$) → ($^6F_{7/2}$, $^6F_{9/2}$), CR_3: ($^4G_{5/2}$, $^6H_{5/2}$) → ($^6F_{9/2}$, $^6F_{7/2}$). The leading energy transfer channel among all the above mentioned cross-relaxation channels is CR_1: ($^4G_{5/2}$, $^6H_{5/2}$) → ($^6F_{5/2}$, $^6F_{11/2}$) because the emission band ($^4G_{5/2} \rightarrow {}^6F_{5/2}$) and the absorption band ($^6H_{5/2} \rightarrow {}^6F_{11/2}$) of these channels have nearly equal energy when compared to other two channels. By using experimental and radiative lifetimes we can find the Non- Radiative relaxation rate (W_{NR}) and quantum efficiencies (η) using the following relations,

Table 11
Energy transfer parameter (Q), critical transfer distance (R_0) (A^0), donor-acceptor interaction parameter (C_{DA}, 10^{-45} cm^{-6} s^{-1}), Non- Radiative relaxation rate (W_{NR}) (s^{-1}) of Sm^{3+} ions doped AEBT glasses.

Sample	Q	R_0	C_{DA}	W_{NR}
AEBTSm0.1	–	–	–	246
AEBTSm0.5	–	–	–	166
AEBTSm1.0	–	–	–	152
AEBTSm1.5	0.256	1.259	2.983	652
AEBTSm2.0	0.278	1.180	2.019	1116
AEBTSm2.5	0.301	1.128	1.541	1493

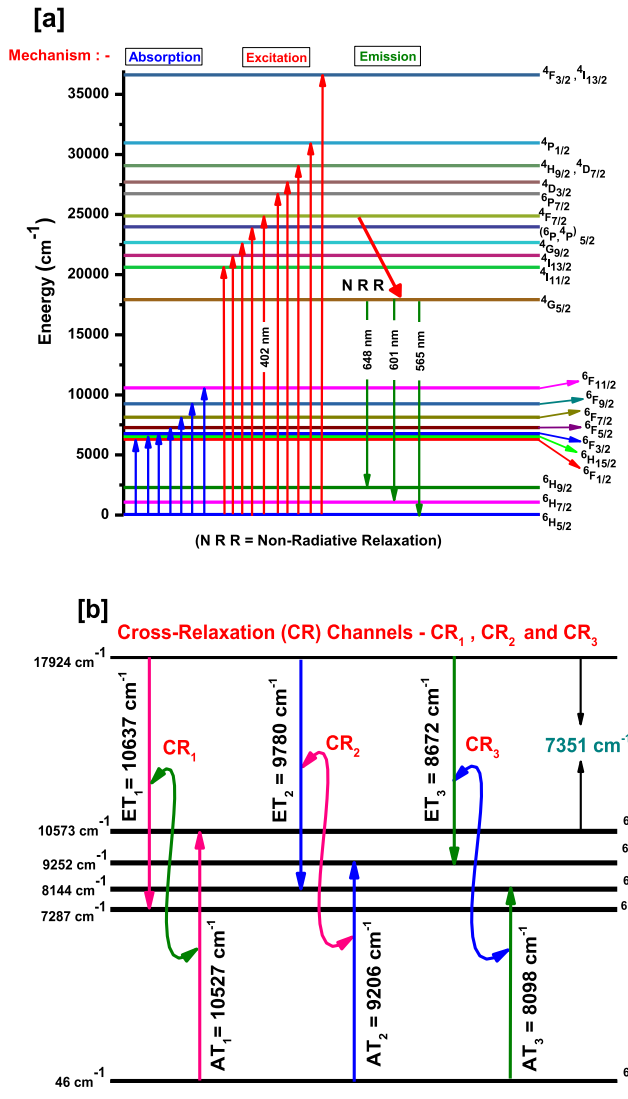


Fig. 10. [a]: Partial energy level diagram of Sm^{3+} ions in AEBT glasses, [b]: Possible cross-relaxation channels of Sm^{3+} ions in AEBT glasses.

$$W_{NR} = \frac{1}{\tau_{exp}} - \frac{1}{\tau_R} \tag{10}$$

$$\eta = \frac{\tau_{exp}}{\tau_R} X\ 100 \tag{11}$$

The Non- Radiative relaxation rate (W_{NR}) are presented in Table 11. The quantum efficiency plays an important role in predicting the suitable material for the lasing action. Various parameters like emission cross-section, radiative transition probability, concentration of RE ion can affect the quantum efficiency (η) of the material [63,64]. Table 10 represents the values of quantum efficiencies of all Sm^{3+} doped AEBT glasses. It can be clearly observed from Table 10 that the glass sample AEBTSm1.0 has the greater quantum efficiency compared to other glasses and some of the other reported glasses [7,58,65,66].

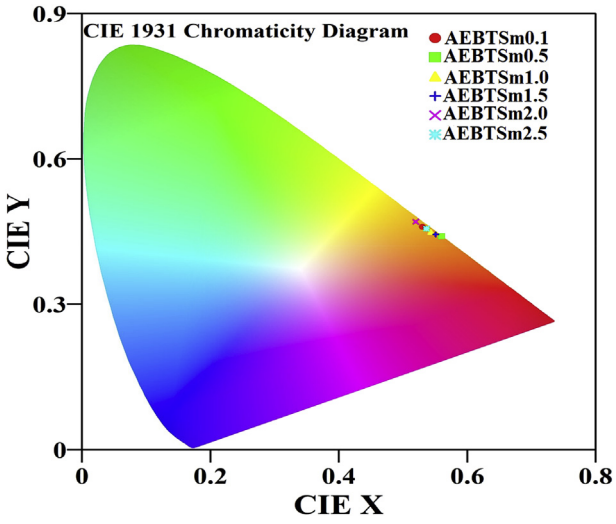


Fig. 11. CIE chromaticity co-ordinates for Sm^{3+} ions in AEBT glasses.

3.7. CIE chromaticity co-ordinates

With the help of the procedure existing in Commission International de l'Eclaiage France CIE system [67], the chromaticity co-ordinates for the Sm^{3+} doped AEBT glasses were evaluated using emission spectral data. The evaluated chromaticity coordinates for the as-prepared glasses are presented in Table 12. Fig. 11 represents the sites of chromaticity coordinates of the as-prepared glasses. For all the glass samples under investigation the chromaticity co-ordinates are falling in orange red region. Among all the AEBT glasses, AEBTSm1.0 glass has its coordinates falling exactly in bright orange red region.

4. Conclusion

A new family of different concentrations of Sm^{3+} ions doped AEBT glasses were prepared by using melt quenching technique. The FT-IR study indicates the presence of O-H stretching vibrations. Studies on bonding parameters through the absorption spectra confirm that the Sm – oxygen ligand is of ionic nature and it decreases with increase in Sm^{3+} ions concentrations. The nephelauxetic effect on the absorption transitions were used to reveal the metal-ligand bonding nature and the results suggests that Sm^{3+} ions possess dominant ionic bonding with the host matrix. This nature was re-confirmed by the J-O analysis also. The emission spectra of all the titled glasses show three emission bands in the visible region ranging from 525 to 675 nm. Among the three emissions transitions a transition $^4G_{5/2} \rightarrow {}^6H_{7/2}$ observed at 601 nm for AEBTSm1.0 glass possesses large stimulated emission cross-section and high branching ratios. The quantum efficiency is higher for the AEBTSm1.0 glass. Decay curves were obtained for

Table 12
CIE Chromaticity coordinates for the Sm^{3+} ions doped AEBT glasses.

Color Coordinates	AEBTSm 0.1	AEBTSm 0.5	AEBTSm 1.0	AEBTSm 1.5	AEBTSm 2.0	AEBTSm 2.5
X	0.527	0.562	0.543	0.550	0.523	0.535
Y	0.462	0.434	0.449	0.444	0.465	0.456

AEBT glasses show single and non-exponential for lower and higher RE ion concentrations respectively. The non-exponential nature of decay spectral features are well fitted to Inokuti–Hirayama (I–H) to understand the energy transfer mechanism involved in concentration quenching as well as conversion of decay from single to non-exponential with increase in RE ion concentrations. The intensity of orange emission is found to be maximum for AEBTSm1.0 glass. Based on the studied structural and optical properties, it is concluded that AEBTSm1.0 glass might be potentially useful in laser active medium for laser applications at 601 nm emission wavelength.

Acknowledgements

The authors, Dr. K. Swapna (File Number: ECR/2015/000335), Dr. Sk. Mahamuda (File Number: ECR/2016/000376), Prof. A.S.Rao and Prof. G. V. Prakash (File Number: EMR/2016/007766) are thankful to Department of Science and Technology (DST), Govt. of India, New Delhi for the award of major research projects to them under DST-SERB.

References

[1] S.O. Kasap, P. Capper, Springer Handbook of Electronic and Photonic Materials, Springer Science & Business Media, 2007.
[2] W.J. Miniscalco, Rare-earth-doped fiber lasers and amplifiers, Opt. Sci. Eng 71 (2001) 17–112.
[3] K.S.V. Sudhakar, M. Srinivasa Reddy, L. Srinivasa Rao, N. Veeraiah, Influence of modifier oxide on spectroscopic and thermoluminescence characteristics of Sm^{3+}ion in antimony borate glass system, J. Lumin. 128 (2008) 1791–1798.
[4] S. Shanmuga Sundari, K. Marimuthu, M. Sivraman, S.S. Babu, Composition dependent structural and optical properties of Sm^{3+}-doped sodium borate and sodium fluoroborate glasses, J. Lumin. 130 (2010) 1313–1319.
[5] C.K. Jayasankar, K. Upendra Kumar, V. Venkatramu, P. Babu, T. Tröster, W. Sievers, G. Wortmann, Effect of pressure on luminescence properties of Sm^{3+} ions in potassium niobate tellurite glass, J. Lumin. 128 (2008) 718–720.
[6] K.K. Mahato, D.K. Rai, S.B. Rai, Optical studies of Sm^{3+} doped oxyfluoroborate glass, Solid State Commun. 108 (1998) 671–676.
[7] Sk Mahamuda, K. Swapna, M. Venkateswarlu, A. Srinivasa Rao, S. Shakya, G. Vijaya Prakash, Spectral characterisation of Sm^{3+}ions doped Oxy-fluoroborate glasses for visible orange luminescent applications, J. Lumin. 154 (2014) 410–424.
[8] P. Babu, H.J. Seo, C.R. Kesavulu, K.H. Jang, C.K. Jayasankar, Thermal and optical properties of Er^{3+}-doped oxyfluorotellurite glasses, J. Lumin. 129 (2009) 444–448.
[9] M. Udovic, P. Thomas, A. Mirgorodsky, O. Durand, M. Soulis, O. Masson, T. Merle-Méjean, J.C. Champarnaud-Mesjard, Thermal characteristics, Raman spectra and structural properties of new tellurite glasses within the Bi_2O_3-TiO_2-TeO_2 system, J. Solid State Chem. 179 (2006) 3252–3259.
[10] R.A. Narayanan, J.W. Zwanziger, The glass forming ability of tellurites: a rigid polytope approach, J. Non-Cryst. Solids 316 (2003) 273–280.
[11] S. Rada, M. Culea, E. Culea, Structure of TeO_2-B_2O_3 glasses inferred from infrared spectroscopy and DFT calculations, J. Non-Cryst. Solids 354 (2008) 5491–5495.
[12] M. Halimah, H. Sidek, W. Daud, H. Zainul, Z. Talib, A. Zaidan, A. Zainal, H. Mansor, Ultrasonic study and physical properties of borotellurite glasses, Am. J. Appl. Sci. 2 (2005) 1541–1546.
[13] P. Karthikeyan, S. Arunkumar, C. Basavapoornima, K. Marimuthu, Modifier effect on the spectroscopic properties of tellurofluoroborate glasses containing Sm^{3+} ions, J. Lumin. 178 (2016) 43–53.
[14] H.A. Othman, H.S. Elkholy, I.Z. Hager, Structural and optical investigation of undoped and Sm^{3+} doped lead oxyfluoroborate glasses, Mater. Res. Bull. 89 (2017) 210–216.
[15] S. Li, H. Liu, F. Wu, Z. Chang, Y. Yue, Effects of alkaline-earth metal oxides on structure and properties of iron phosphate glasses, J. Non-Cryst. Solids 434 (2016) 108–114.
[16] D. Möncke, E.I. Kamitsos, D. Palles, R. Limbach, T. Honma, Z. Yao, T. Rouxel, L. Wondraczek, Transition and post-transition metal ions in borate glasses : borate ligand speciation, cluster formation and their effect on glass transition and mechanical properties Revised manuscript JCP July 2016, J. Chem. Phys. 145 (2016), 124501.
[17] S.S. Rojas, J.E. De Souza, K. Yukimitu, A.C. Hernandes, Structural, thermal and optical properties of CaBO and CaLiBO glasses doped with Eu3 +, J. Non-Cryst. Solids 398–399 (2014) 57–61.
[18] P.R. Rao, N. Venkatramaiah, Y. Gandhi, V.R. Kumar, I.V. Kityk, N. Veeraiah, Role of modifier oxide in emission spectra and kinetics of Er–Ho codoped Na_2SO_4–MO–P_2O_5 glasses, Spectrochim. Acta Part A Mol. Biomol. Spectrosc 86 (2012) 472–480.
[19] Y.C. Ratnakaram, A. Balakrishna, D. Rajesh, Effect of modifier oxides on absorption and emission properties of Eu^{3+} doped different lithium fluoroborate glass matrices, Phys. B Condens. Matter 407 (2012) 4303–4307.
[20] J. Anjaiah, C. Laxmikanth, N. Veeraiah, Spectroscopic properties and luminescence behaviour of europium doped lithium borate glasses, Phys. B Condens. Matter 454 (2014) 148–156.
[21] J. Wong, C. Angell, Glass: Structure by Spectroscopy, M. Dekker New York, 1976.
[22] B.K. Sharma, D.C. Dube, A. Mansingh, Preparation and characterisation of V_2O_5-B_2O_3 glasses, J. Non-Cryst. Solids 65 (1984) 39–51.
[23] P. Muralidharan, M. Venkateswarlu, N. Satyanarayana, Sol-gel synthesis, structural and ion transport studies of lithium borosilicate glasses, Solid State Ionics 166 (2004) 27–38.
[24] S.G. Motke, S.P. Yawale, S.S. Yawale, Infrared spectra of zinc doped lead borate glasses, Bull. Mater. Sci. 25 (2002) 75–78.
[25] A.K. Yadav, C.R. Gautam, A. Gautam, V.K. Mishra, Structural and crystallization behavior of (Ba,Sr)TiO_3 borosilicate glasses, Phase Transitions 86 (2013) 1000–1016.
[26] R. Ciceo-Lucacel, I. Ardelean, FT-IR and Raman study of silver lead borate-based glasses, J. Non-Cryst. Solids 353 (2007) 2020–2024.
[27] Sk Mahamuda, K. Swapna, P. Packiyaraj, A. Srinivasa Rao, G. Vijaya Prakash, Visible red, NIR and mid-IR emission studies of Ho^{3+} doped zinc alumino bismuth borate glasses, Opt. Mater. 36 (2013) 362–371.
[28] Y. Dimitriev, V. Dimitrov, M. Arnaudov, IR spectra and structures of tellurite glasses, J. Mater. Sci. 18 (1983) 1353–1358.
[29] A. Rao, Y. Ahammed, R. Reddy, T.V. Rao, Spectroscopic studies of Nd^{3+} - doped alkali fluoroborophosphate glasses, Opt. Mater. 10 (1998) 245–252.
[30] M. Vijayakumar, K. Marimuthu, V. Sudarsan, Concentration dependent spectroscopic behavior of Sm^{3+} doped leadfluoro-borophosphate glasses for laser and LED applications, J. Alloys. Compd. 647 (2015) 209–220.
[31] W.T. Carnall, P.R. Fields, K. Rajnak, Electronic energy levels in the trivalent lanthanide aquo ions. I. Pr^{3+}, Nd^{3+}, Pm^{3+}, Sm^{3+}, Dy^{3+}, Ho^{3+}, Er^{3+}, and Tm^{3+}, J. Chem. Phys. 49 (1968) 4424–4442.
[32] T. Srihari, C.K. Jayasankar, Spectral investigations of Sm^{3+} -doped niobium phosphate glasses, Opt. Mater. 66 (2017) 35–42.
[33] C. Görller-Walrand, K. Binnemans, Spectral intesities of f-f transitions, Handb. Phys. Chem. Rare Earths 25 (1998) 101–264.
[34] B.R. Judd, Optical absorption intensities of RE ions, Phys. Rev. 127 (1962) 750–761.
[35] G.S. Ofelt, Intensities of crystal spectra of rare-earth ions, J. Chem. Phys. 37 (1962) 511–520.
[36] B.C. Jamalaiah, M.V. Vijaya Kumar, K. Rama Gopal, Fluorescence properties and energy transfer mechanism of Sm^{3+} ion in lead telluroborate glasses, Opt. Mater. 33 (2011) 1643–1647.
[37] A. Mohan Babu, B.C. Jamalaiah, T. Sasikala, S.A. Saleem, L. Rama Moorthy, Absorption and emission spectral studies of Sm^{3+}-doped lead tungstate tellurite glasses, J. Alloys. Compd. 509 (2011) 4743–4747.
[38] C.K. Jayasankar, E. Rukmini, Optical properties of Sm^{3+} ions in zinc and alkali zinc borosulphate glasses, Opt. Mater. 8 (1997) 193–205.
[39] M.B. Saisudha, J. Ramakrishna, Optical absorption of Nd^{3+}, Sm^{3+} and Dy^{3+} in bismuth borate glasses with large radiative transition probabilities, Opt. Mater. 18 (2002) 403–417.
[40] O. Ravi, C. Madhukar Reddy, L. Manoj, B. Deva Prasad Raju, Structural and optical studies of Sm^{3+} ions doped niobium borotellurite glasses, J. Mol. Struct. 1029 (2012) 53–59.
[41] M. Jayasimhadri, E.-J. Cho, K.-W. Jang, H.S. Lee, S. Il Kim, Spectroscopic properties and Judd–Ofelt analysis of Sm^{3+} doped lead–germanate–tellurite glasses, J. Phys. D Appl. Phys. 41 (2008), 175101.
[42] C. Venkateswarlu, M. Seshadri, Y.C. Ratnakaram, Influence of mixed alkalis on spectroscopic parameters of Sm^{3+}, Dy^{3+} doped chloroborate glasses, Opt. Mater. 33 (2011) 799–806.
[43] I.Z. Hager, Optical properties of lithium barium haloborate glasses, J. Phys. Chem. Solid. 70 (2009) 210–217.
[44] X. Zou, T. Izumitani, Spectroscopic properties and mechanisms of excited state absorption and energy transfer upconversion for Er^{3+}-doped glasses, J. Non-Cryst. Solids 162 (1993) 68–80.
[45] A. Lösche, N.F. Mott, E.A. Davis, Electronic Processes in Non-crystalline Materials, vol. 7, Clarendon-Press, Oxford 1971 437 Seiten., Krist. Und Tech, 1972, pp. K55–K56.
[46] S. Selvi, K. Marimuthu, G. Muralidharan, Structural and luminescence behavior of Sm^{3+} ions doped lead boro-telluro-phosphate glasses, J. Lumin. 159 (2015) 207–218.
[47] N. Elkhoshkhany, R. El-Mallawany, Optical and kinetics parameters of lithium boro-tellurite glasses, Ceram. Int. 41 (2015) 3561–3567.
[48] S. Arunkumar, K. Marimuthu, Concentration effect of Sm^{3+} ions in B_2O_3–PbO–PbF_2–Bi_2O_3–ZnO glasses – structural and luminescence investigations, J. Alloys. Compd. 565 (2013) 104–114.
[49] M. Vijayakumar, K. Marimuthu, Structural and luminescence properties of Dy^{3+} doped oxyfluoro-borophosphate glasses for lasing materials and white LEDs, J. Alloys. Compd. 629 (2015) 230–241.
[50] V.I. Arbuzov, Fundamental absorption spectra and elementary electronic excitations in oxide glasses, Glass Phys. Chem. 22 (1996) 477–489.
[51] B.H. Venkataraman, K.B.R. Varma, Structural and optical properties of (100-x) ($Li_2B_4O_7$) – x (SrO - Bi_2O_3 - 0.7Nb_2O_5 - 0.3V_2O_5) glasses and glass nanocrystal composites, Opt. Mater. 28 (2006) 1423–1431.

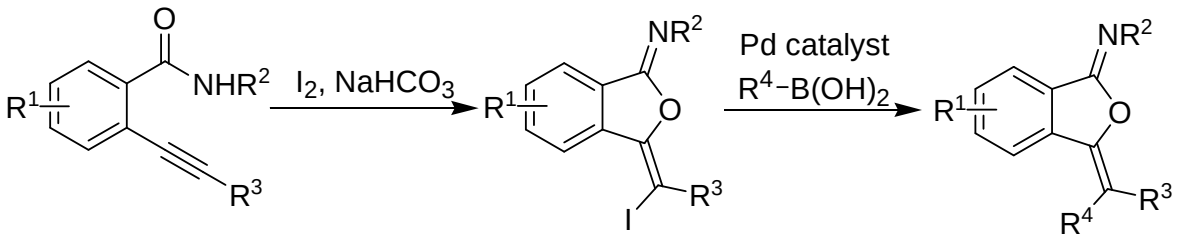
[52] S. Thomas, R. George, S. Nayab Rasool, M. Rathaiah, V. Venkatramu, C. Joseph, N.V. Unnikrishnan, Optical properties of Sm^{3+} ions in zinc potassium fluorophosphate glasses, Opt. Mater. 36 (2013) 242–250.
[53] T. Suhasini, J. Suresh Kumar, T. Sasikala, K. Jang, H.S. Lee, M. Jayasimhadri, J.H. Jeong, S.S. Yi, L. Rama Moorthy, Absorption and fluorescence properties of Sm^{3+} ions in fluoride containing phosphate glasses, Opt. Mater. 31 (2009) 1167–1172.
[54] P. Solarz, W. Ryba-Romanowski, Luminescence and energy transfer processes of Sm^{3+} in $K_5Li_2LaF_{10}$:Sm^{3+} - $K_5Li_2SmF_{10}$ single crystals, Phys. Rev. B 72 (2005) 75105.
[55] V. Lavín, I.R. Martín, C.K. Jayasankar, T. Tröster, Pressure-induced energy transfer processes between Sm^{3+} ions in lithium fluoroborate glasses, Phys. Rev. B Condens. Matter. 66 (2002) 642071–642077.
[56] D.D. Ramteke, V.Y. Ganvir, S.R. Munishwar, R.S. Gedam, Concentration effect of Sm^{3+} ions on structural and luminescence properties of lithium borate glasses, Phys. Procedia 76 (2015) 25–30.
[57] C. Madhukar Reddy, G.R. Dillip, K. Mallikarjuna, S. Zulifiqar Ali Ahamed, B. Sudhakar Reddy, B. Deva Prasad Raju, Absorption and fluorescence studies of Sm3 ions in lead containing sodium fluoroborate glasses, J. Lumin. 131 (2011) 1368–1375.
[58] R. Praveena, V. Venkatramu, P. Babu, C.K. Jayasankar, Fluorescence spectroscopy of Sm^{3+} ions in P_2O_5–PbO–Nb_2O_5 glasses, Phys. B Condens. Matter. 403 (2008) 3527–3534.
[59] C. Jayasankar, P. Babu, Optical properties of Sm^{3+} ions in lithium borate and lithium fluoroborate glasses, J. Alloys. Compd. 307 (2000) 82–95.
[60] A. Kumar, D. Rai, S. Rai, Optical properties of Sm^{3+} ions doped in tellurite glass, Spectrochim. Acta Part A Mol. Biomol. Spectrosc 59 (2003) 917–925.
[61] K. Swapna, Sk Mahamuda, A. Srinivasa Rao, S. Shakya, T. Sasikala, D. Haranath, G. Vijaya Prakash, Optical studies of Sm^{3+} ions doped zinc alumino bismuth borate glasses, Spectrochim. Acta Part A Mol. Biomol. Spectrosc 125 (2014) 53–60.
[62] M. Inokuti, F. Hirayama, Influence of energy transfer by the exchange mechanism on donor luminescence, J. Chem. Phys. 43 (1965) 1978–1989.
[63] F. Lahoz, I.R. Martín, J. Méndez-Ramos, P. Núñez, Dopant distribution in a Tm^{3+}-Yb^{3+} codoped silica based glass ceramic: an infrared-laser induced upconversion study, J. Chem. Phys. 120 (2004) 6180–6190.
[64] S. Babu, C.K. Jayasankar, P. Babu, T. Troester, W. Sievers, G. Wortmann, Luminescence and energy transfer properties of Sm^{3+}: borate glasses, Phys. Chem. Glas. J. Glas. Sci. Technol. Part B 47 (2006) 548–552.
[65] K. Kiran Kumar, C.K. Jayasankar, Visible luminescence of Sm^{3+}:K - Ca - Li fluorophosphate glasses, J. Mol. Struct. 1074 (2014) 496–502.
[66] D. Umamaheswari, B.C. Jamalaiah, T. Sasikala, I.G. Kim, L.R. Moorthy, Photoluminescence properties of Sm^{3+}-doped SFB glasses for efficient visible lasers, J. Non-Cryst. Solids 358 (2012) 782–787.
[67] W.M. Yen, S. Shionoya, H. Yamamoto, Phosphor Handbook, CRC press, 2007.

International Journal of Engineering Technology Science and Research
IJETSR
www.ijetsr.com
ISSN 2394 – 3386
Volume 5, Issue 2
February 2018

Synthesis of Iminolactones through Iodocyclization of Functionally Substituted Alkynes

Saurabh Mehta*
Department of Applied Chemistry,
Delhi Technological University,
Bawana Road, Delhi, India

ABSTRACT



R^1 = H, OMe
R^2 = Me, Bn, aryl
R^3= alkyl, alkenyl, aryl, TMS, *etc.*
R^4 = aryl, heteroaryl, *etc.*

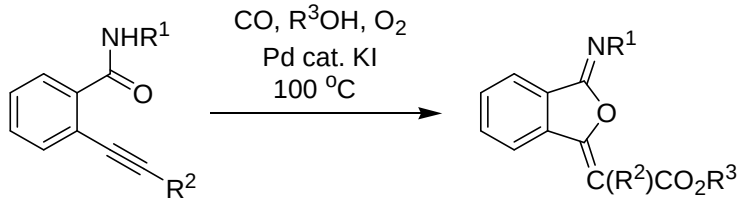
The efforts for the iodocyclization of amide or nitrone-functionalized alkynes have been briefly reviewed in this paper. It has been shown that the iodine as the electrophile generally works well and the reaction results in the formation of iminolactones in high yields. The cyclization happens through through the oxygen of the functional group and the reaction is very regio- and stereoselective. The iminolactones obtained through iodocyclization may be further functionalized using various metal catalyzed coupling reactions and a reasonable amount of chemical diversity may be introduced.

INTRODUCTION

Iminolactones, also known as cyclic imidates or iminoethers are important heterocyclic compounds. With respect to the synthesis and applications, there have been many reports on this heterocyclic scaffold in the literature. Many research groups have published several synthetic strategies for 5- and 6-membered rings containing cyclic imidates/iminolactones.[1-3] For example, Mancuso *et al.* have reported a Pd-catalyzed annulations reaction for the synthesis of this scaffold (Scheme 1).[4] The biological profile of this scaffold has been investigated in a few cases and important biological activities have been noticed. Examples include GIL (Gossylic Iminolactone) derived from the natural compound Gossypol that has been found to show anti-HIV property.[5]

International Journal of Engineering Technology Science and Research
IJETSR
www.ijetsr.com
ISSN 2394 – 3386
Volume 5, Issue 2
February 2018

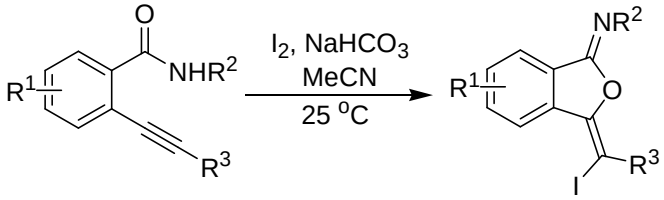
Scheme 1. Palladium catalyzed synthesis of Iminolactones



DISCUSSION

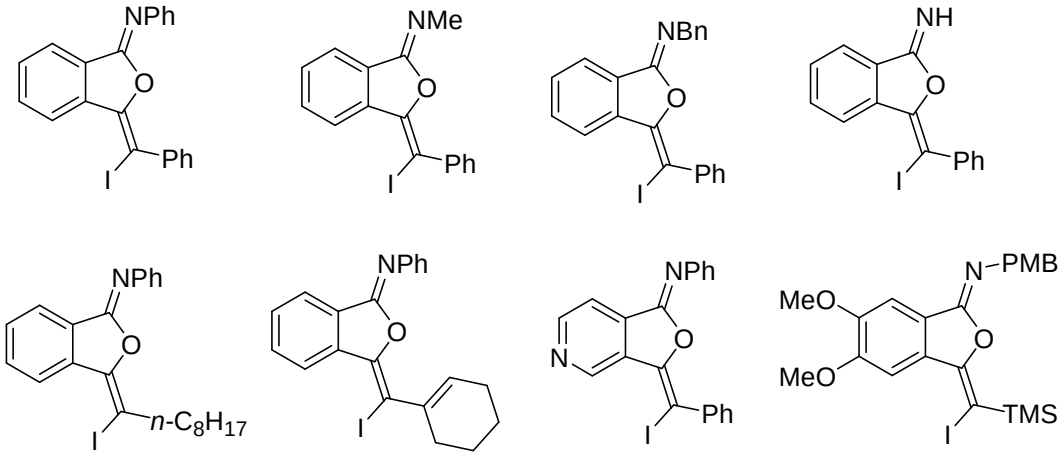
The electrophilic cyclization of alkynes is known to be a very efficient method for the synthesis of a wide variety of interesting as well as useful heterocycles and carbocycles.[6] We as well as other scientists have used this methodology and have reported the synthesis of many important heterocyclic compounds such as benzofurans,[7] benzothiophenes,[8] indoles,[9] quinolines,[10] isocoumarins,[11] isoxazoles,[12] pyrroles,[13] pyrazoles,[14] polyheterocyclic compounds,[15] *etc*. We also studied the electrophilic cyclization of 2-(1-alkynyl)benzamides and found that it can lead to the formation of interesting iminolactone derivatives (Scheme 2).[16]

Scheme 2. Iodocyclization of Alkynylbenzamides



Several derivatives of *o*-(1-alkynyl)carboxamides with varying substitution patterns were iodocyclized and the products were identified by the analytical and spectral data. The results are shown in Figure 1.

Figure 1. Representative Iminolactones Prepared through Iodocyclization.

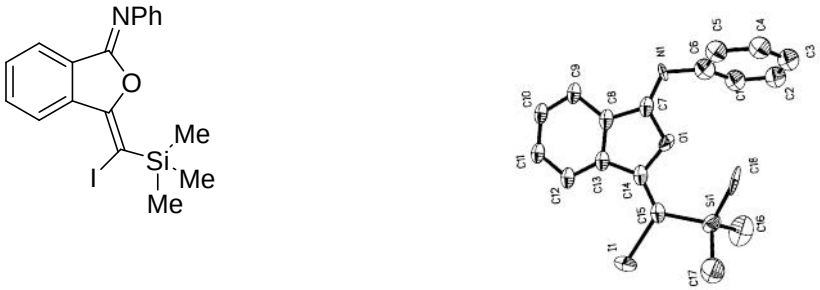


It appears that several factors may affect the regiochemistry of the products, and those include the stability of the carbocation intermediate, the relative rates of the competing reactions, the stability of the product, *etc*. As far as the nature of the electrophile is of concern, use of I_2 resulted in better regioselectivity. Mostly the 5-membered iminolactones were obtained as the major products.

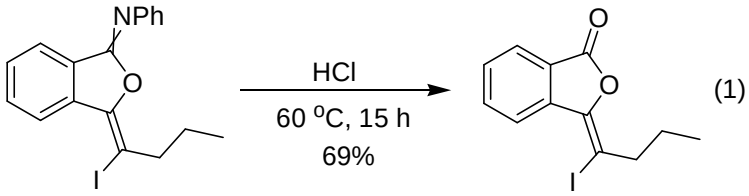
To confirm the stereochemistry of the products, one of the cyclized iminolactones was characterized using NMR spectroscopic as well as single crystal X-ray crystallographic experiments. (Figure 2). It confirmed that an iminolactone was formed due to the *O*-cyclization.

International Journal of Engineering Technology Science and Research
IJETSR
www.ijetsr.com
ISSN 2394 – 3386
Volume 5, Issue 2
February 2018

Figure 2. X-ray confirmatory evidence for the Iminolactone structure[16]

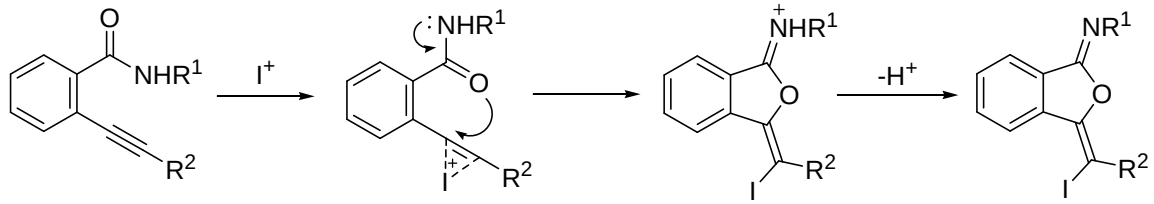


The hydrolysis of the iminolactones was also examined. The iminolactone derivative was prepared using the optimized iodocyclization reaction and it was hydrolyzed in presence of acid. It resulted in the formation of the lactone derivative (eq 1). This additional evidence also confirmed that iminolactones are formed through the iodocyclization under these conditions.



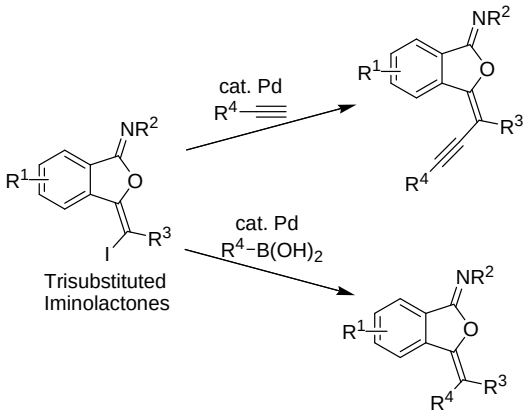
The possible mechanism of the iodocyclization reaction is shown below (Scheme 3). It is known that that amide group is an ambident nucleophile, and also the fact that use of various reagents leads to the formation of different products.[17-18] Under these iodocyclization reactions the nucleophilic attack happens through the oxygen of the $–CONH_2$ group, followed by the loss of proton, affording the iminolactones.

Scheme 3. Mechanism for the iodocyclization of 2-(1-Alkynyl)benzamides leading to Iminolactones



The iminolactone derivatives that are obtained by the iodocyclization reaction, can be further modified using known metal-catalyzed processes. We demonstrated this by constructing a library of 71-member iminolactones using this methodology (Scheme 4).[19]

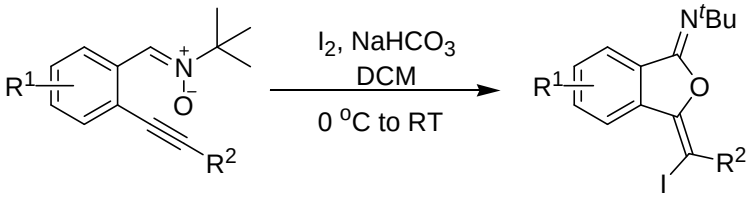
Scheme 4. Library Synthesis



International Journal of Engineering Technology Science and Research
IJETSR
www.ijetsr.com
ISSN 2394 – 3386
Volume 5, Issue 2
February 2018

Similarly, Li *et al.* reported the cyclization of Nitrone- Functionalized Alkynes (Scheme 5). It seems that the authors also obtained the iminolactones instead of the isoindolones.[20]

Scheme 5: Cyclization of Alkynyl Nitrones



CONCLUSIONS

Thus, o-(1-alkynyl)benzamides or the nitrone derivatives undergo *O*-cyclization yielding the corresponding iminolactones under mild iodocyclization reactions, and the excellent regio- and stereoselectivity is observed. The iodine-bearing iminolactones were elaborated using known metal-catalyzed reactions. This synthetic strategy may be very useful for the preparation of medicinally important iminolactones.

REFERENCES

[1] Liu, G.; Zhou, Y.; Ye, D.; Zhang, D.; Ding, X.; Jiang, H.; Liu, H. 2009. Silver-Catalyzed Intramolecular Cyclization of *o*-(1-Alkynyl)benzamides: Efficient Synthesis of (1*H*)-Isochromen-1-imines. *Adv. Synth. Catal. 351*, 2605-2610.

[2] Xiong, T.; Zhang, Q.; Zhang, Z.; Liu, Q. 2007. A Divergent Synthesis of *γ*-Iminolactones, Dihydroquinolin-2-ones, and *γ*-Lactames from *β*-Hydroxymethylcyclopropanylamides *J. Org. Chem. 72*, 8005-8009.

[3] Ma, S.; Gu, Z.; Yu, Z. *J.* 2005. $Pd(CH_3CN)_2Cl_2$-Catalyzed Oxidative Heterodimerization Reaction of 2,3-Allenamides and 1,2-Allenyl Ketones: An Efficient Synthesis of 4-(Furan-3-yl)-2(5*H*)-furanimines. *J. Org. Chem. 70*, 6291-6294.

[4] Mancuso, R.; Ziccarelli, I.; Armentano, D.; Marino, N.; Giofrè, S. V.; Gabriele, B. 2014. Divergent Palladium Iodide Catalyzed Multicomponent Carbonylative Approaches to Functionalized Isoindolinone and Isobenzofuranimine Derivatives. *J. Org. Chem. 79* (8), 3506–3518.

[5] (a) Yu, Y.; Deck, J. A.; Hunsaker, L. A.; Deck, L. M.; Royer, R. E.; Goldberg, E.; Jagt, D. L. V. 2001. Selective active site inhibitors of human lactate dehydrogenases A_4, B_4, and C_4. *Biochem. Pharmacol., 62*, 81. (b) Royer, R. E.; Deck, L. M.; Jagt, T. J. V.; Martinez, F. J.; Mills, R. G.; Young, S. A.; Jagt, D. L. V. 1995. Synthesis and Anti-HIV Activity of 1,1'-Dideoxygossypol and Related Compounds. *J. Med. Chem., 38*, 2427-2432.

[6] Godoi, B.; Schumacher, R. F.; Zeni, G. 2011. Synthesis of Heterocycles via Electrophilic Cyclization of Alkynes Containing Heteroatom. *Chem. Rev. 111*, 2937-2980.

[7] Manarin, F.; Roehrs, J. A.; Gay, R. M.; Brandão, R.; Menezes, P. H.; Nogueira, C. W.; Zeni, G. 2009. Electrophilic Cyclization of 2-Chalcogenealkynylanisoles: Versatile Access to 2-Chalcogen-benzo[*b*]furans. *J. Org. Chem. 74*, 2153-2162.

[8] Cho, C.-H.; Jung, D.-I.; Neuenswander, B.; Larock, R. C. 2011. Parallel Synthesis of a Desketoraloxifene Analogue Library *via* Iodocyclization/Palladium-Catalyzed Coupling. *ACS Comb. Sci., 13*, 501-510.

[9] Barluenga, J.; Trincado, M.; Rubio, E.; González, J. M. 2003. IPy_2BF_4-Promoted Intramolecular Addition of Masked and Unmasked Anilines to Alkynes: Direct Assembly of 3-Iodoindole Cores. *Angew. Chem., Int. Ed., 42*, 2406-2409.

[10] Verma, A. K.; Shukla, S. P.; Singh, J.; Rustagi, V. 2011. Synthesis of 5-Iodopyrrolo[1,2-*a*]quinolines and Indolo[1,2-*a*]quinolines via Iodine-Mediated Electrophilic and Regioselective 6-endo-dig Ring Closure. *J. Org. Chem. 76*, 5670-5684.

[11] Verma, A. K.; Rustagi, V.; Aggarwal, T.; Singh, A. P. 2010. Iodine-Mediated Solvent-Controlled Selective Electrophilic Cyclization and Oxidative Esterification of o-Alkynyl Aldehydes: An Easy Access to Pyranoquinolines, Pyranoquinolinones, and Isocumarins. *J. Org. Chem. 75*, 7691.

[12] Okitsu, T.; Sato, K.; Potewar, T. M.; Wada, A. 2011. Iodocyclization of Hydroxylamine Derivatives Based on the Control of Oxidative Aromatization Leading to 2,5-Dihydroisoxazoles and Isoxazoles. *J. Org. Chem., 76*, 3438-3449.

[13] Knight, D. W.; Redfern, A. L.; Gilmore, J. 1998. 5-endo-dig Cyclisations of homopropargylic sulfonamides: a new route to 2,3-dihydropyrroles and *β*-iodopyrroles. *Chem. Commun.* 2207.

[14] Zora, M.; Kivrak, A.; Yazici, C. 2011. Synthesis of Pyrazoles via Electrophilic Cyclization. *J. Org. Chem. 76*, 6726-6742.

[15] Mehta, S.; Larock, R. C. 2010. Iodine/Palladium Approaches to the Synthesis of Polyheterocyclic Compounds. *J. Org. Chem.*, *75*, 1652-1658.

[16] Mehta, S.; Yao, T.; Larock, R. C. 2012. Regio- and Stereoselective Synthesis of Cyclic Imidates via Electrophilic Cyclization of 2-(1-Alkynyl)benzamides. A Correction. *J. Org. Chem. 77*, 10938-10944.

[17] Bianchi, G.; Chiarini, M.; Marinelli, F.; Rossi, L.; Arcadi, A. 2010. Product Selectivity Control in the Heteroannulation of *o*-(1-Alkynyl)benzamides. *Adv. Synth. Catal*. *352*, 136-142.

[18] Hu, T.; Liu, K.; Shen, M.; Yuan, X.; Tang, Y.; Li, C. 2007. *O*-Attack versus *N*-Attack: Electrophilic Halocyclization of Unsaturated Amides with Vinylic Halogen Substitution. *J. Org. Chem. 72*, 8555-8558.

[19] Mehta, S.; Waldo, J. P.; Neuenswander, B.; Lushington, G. H; Larock, R. C. 2013. Solution-Phase Parallel Synthesis of a Multisubstituted Cyclic Imidate Library. *ACS Comb. Sci. 15*, 247−254.

[20] Chen, D.; Song, G.; Jia, A.; Li, X. 2011. Gold- and Iodine-Mediated Internal Oxygen Transfer of Nitrone- and Sulfoxide-Functionalized Alkynes. *J. Org. Chem. 76*, 8488–8494.

International Journal of Research in Engineering and Innovation (IJREI)
journal home page: http://www.ijrei.com
ISSN (Online): 2456-6934



Thermodynamic (energy-exergy) analysis of combined cycle power plant for improving thermal energetic and exergetic efficiencies by integration of organic Rankine cycle (ORC)

Yunis Khan, R.S. Mishra

Department of Mechanical Engineering, Delhi Technological University, Delhi, India

Abstract

The exergy analysis (second law analysis) is used for providing information about the losses qualitatively as well as quantitatively along with their locations. Exergetic (thermodynamic) optimization improves the performance of a system by reducing the exergetic inefficiencies (exergy destruction and exergy losses) and increasing exergetic efficiency. The primary objective of this work is to utilize the waste heat from the stack which is coming from HRSG by integration of ORC plant with combined cycle. Then thermodynamic analysis is done .After comparison it is found that the system overall thermodynamic efficiencies (thermal and exergetic) are improved by integration of ORC system to existing combined cycle. Thermal efficiencies are improved by 3.32% and 4.09% first law and second law (exergetic efficiency) respectively. There is also separately calculation is done for each component. A program code is established to perform the calculations required for the exergy plant analysis considering real variation ranges of the main operating parameters such as pressure ratio, air fuel ratio. The effects of theses parameters on the system performances are presented in this paper.
© 2018 ijrei.com. All rights reserved
Key words: combined cycle, ORC, heat recovery steam generator, exergy, efficiency improvement, gas turbine

1. Introduction

Energy systems contain a colossal number and a few types of coordinated efforts with the world outside their physical limitations. Thus, architects must address numerous wide issues, particularly energy, economy and the environment. Combined cycle power plants (CCPPs) have as of late gotten significant consideration because of their nearly high energy efficiencies, low poisonous waste and ozone depleting substance releases, and operational suppleness. A typical combined cycle power plant is the cycle, which is comprised of a gas cycle (topping cycle) and a steam turbine cycle (bottoming cycle) coupled through a Heat recovery steam generator (HRSG).

To streamline the efficiency, cost viability and ecological effect of such plants, it is critical to decide the areas, sorts and genuine extents of wasteful aspects (irreversibility's). Exergy investigation is a helpful tool for such examinations, and allows measurement of the thermodynamic wasteful aspects of the procedure. Advancement of energy change frameworks turns out to be more vital because of impediments of non-renewable energy sources and the ecological effect amid their utilization. The utilization of energy is discovered wherever in an assortment of uses from warming and cooling to atomic power plants. For a considerable length of time, the reaction to the constantly developing requirement for electric era limit was to manufacture another steam power plant, one not altogether different from the past one. The energy transformation engineer is confronted with an assortment of issues today: rising advances, changing the social and technological climate in which a differing qualities of methodologies is probably going to be acknowledged.

Some critical qualities of new power activities are low capital and working costs, capacity to work with an assortment of energizes and with high resistance to fuel fluctuation, short development time, low emanation of toxins, attractive or possibly dormant and effortlessly expendable waste items, and high efficiency, maintainability, finance ability, and reliability. Ordinarily, first law analysis gives just energy usage situation regarding preservation of energy. In any case, it can't give the

Corresponding author: R.S. Mishra
Email Id: hod.mechanical.rsm@dtu.ac.in

data with respect to the losses both subjectively and quantitatively, and can't discover the area of these losses. These constraints compel 3 Another main problem faced by the energy conversion engineer is the finiteness of natural resources critically important for human beings (such as natural gas and oil) in 2 the world and ever-increasing energy demands by developing countries. Maybe future power plants ought to use coal and nuclear energy to spare the flammable gas and oil for mechanical sustain stocks and other more basic Established thermodynamics gives the idea of energy, energy transfer by heat and work, energy balance, entropy and entropy adjust and estimations of thermodynamic properties at balance. The second law of thermodynamics upgrades an energy balance by ascertaining the genuine thermodynamic estimation of an energy balance and genuine thermodynamic inefficiencies and losses from the procedure and framework. Exergy is the greatest valuable work achievable from an energy carrier under the given natural conditions. The exergy of an energy carrier is a thermodynamic property that relies on upon both the condition of the carrier being considered and the condition of nature. It communicates the greatest ability of the energy balance to bring about changes. Along these lines, energy is firmly identified with the financial estimation of the balance since clients pay the capability of energy to bring about changes. At the point when expenses are doled out to energy balance, exergy ought to fill in as a premise in the costing procedure. us to perform exergy examination in view of second law of thermodynamics. Exergy is not a conserved property but rather some of it is demolished in the genuine process. Exergy investigation gives a uniform base for correlation of different thermodynamic procedures. This analysis demonstrates the data with respect to losses that incorporate their area subjectively and quantitatively. This data can be utilized for further change in the outline and operation of the framework. By finding the exergy destruction, the system performance can be enhanced by enhancing the exergetic proficiency of the component and the system.

The scope and purpose of this research is to develop effective methodology to achieve exergetic optimizations of CCGT power plants. Therefore, the aim of the work is to improve the performance of the power plant by means of integration of ORC and exergy optimization method. With the help of this method, it would be possible to:

(a) Provide information about the exergy destruction and exergy losses along with their location.
(b) Predict the highest exergy destructor components of the system.
(c) Suggest ways of improving the exergetic efficiency.
(d) Find the optimal realistic values of operating parameters, which gives the maximum possible power output and efficiency. Additionally, is would be possible to calculate minimum possible exergy destructions.

2. Literature Review

In order to have an idea of the present methodology development in the area of performance and optimization of combined cycle gas turbine power plant, a brief survey of available literature was made. However, this chapter is concerned with a review of literature on optimization performed on various thermal systems. In general, some authors focus on the gas turbine operating parameters (topping cycle), others optimize the steam plant (bottoming cycle) on the basis of a given gas turbine, whereas others propose appropriate optimization methods for the whole combined cycle power plant without integration of ORC. Furthermore, the optimization can be analysed from a thermodynamic point of view, according to the first and/or second law analysis, or using a thermo economic or environmental-economic strategy Kaviri et al [1], Ahmadi and Dincer [2], Boyano et al [3] and Petrakopoulou et al [4]. From the point of view of optimization methodology, there are many types of analyses. In this work, the review will highlight most common methodology: the exergy destruction method, and the efficiency improvement method.

3. Analysis and Optimization of Topping Cycle

3.1 Thermodynamic Analysis and Optimization

The gas turbine operating parameters which influence the combined cycle gas turbine performance are; ambient conditions, compressor pressure ratio, and turbine inlet temperature.

3.2 The Effect of Ambient Conditions

One of the factors that affect gas turbine performance is the ambient conditions, mainly ambient temperature, atmospheric pressure, and the relative humidity of air. These parameters affect the generated electric power and the heat-rate during operation. The location of power plant plays a major role on its performance. The atmospheric air, which enters the compressor, becomes hotter after compression and it is directed to a combustion chamber. Several authors reported the effect of ambient temperature: Ibrahim et al [5], Ameri and Hejazi [6], Boonnasa et al [7] and Hosseini et al [8]. The properties of air entering combustion chamber depend upon the compressor pressure ratio studied. Ibrahim and Rahman [9], and Khaliq and Kaushik et al [10] performed a parametric thermodynamic analysis of a combined cycle gas turbine. They investigated the effect of operating parameters, compression ratio, gas-turbine peak temperature ratio, isentropic compressor and efficiency and air fuel ratio on the overall plant performance. Their results show that the compression ratios, air to fuel ratio as well as the isentropic efficiencies are strongly influenced by the overall thermal efficiency of the combined cycle gas turbine power plant. The overall thermal efficiency increases with compression ratio as well as isentropic compressor and turbine efficiency. However, the variation of overall thermal efficiency is minor at the lower compression ratio while it is very significant at the higher

compression ratio for both isentropic compressor and turbine efficiency. The overall efficiencies for combined cycle gas turbine are much higher than the efficiencies of gas turbine plants power output decreases linearly with the increase temperature.

3.3 Analysis and Optimization of Bottoming Cycle

The efficiency of steam power plants can be improved by increasing the live steam and reheat-steam parameters, and by introducing high-efficiency, low-loss turbine blade geometries. The first goal, to increase the steam parameters, is primarily achieved by choosing appropriate materials for the components operating under live-steam and reheat-steam conditions while retaining the proven designs. Collaborative European programs have led to the development and qualification of steels with much improved creep properties at temperatures of up to 600 °C, appropriate for the manufacture of key components. At the same time, optimization of the blade profiles and geometries allowed further major improvements in operating efficiency. The achievable improvements in efficiency is about 0.5% per 10 °C live steam and reheat (RH) temperature increase, and 0.2 % per 10 bar pressure increase. Second important part of the bottoming cycle is the heat recovery steam turbine (HRSG), its design and optimization affects to a large extent influence the efficiency and the cost of the whole plant. Mohagheghi and Shayegan et al [13] performed the thermodynamic optimization of design variables and properties of air entering combustion chamber depend upon the compressor pressure ratio. heat exchangers layout in a heat recovery steam generator HRSG for combined cycle gas turbine CCGT using a genetic algorithm. Their method was introduced for modelling the steam cycle in advanced combined cycles by organizing the non-linear equations and their simultaneous used solutions with numerical methods. 8 In addition to the optimization of design variables of the recovery boiler, they performed the distribution of heat exchangers among different sections and optimized their layouts in HRSGs. A standard gas turbine was assumed, and then outlet gas stream conditions (mass flow rate, temperature, and chemical composition of gas stream) were considered as the inlet parameters for the recovery boiler model. From the optimization process maximum output power from a steam cycle for different HRSGs was then analysed. Bracco and Silvia [14] studied a combined cycle power plant with a single level heat recovery steam generator HRSG. They developed a mathematical model to determine the optimal steam pressure values in the HRSG according to different objective functions (in the HRSG for a given gas turbine). Their work reports numerical results for the combined cycle power plant considering four different gas turbines. The optimization approach was focused on the study of the heat transfer between the steam and the exhaust gas in the HRSG, based on an exergetic analysis. They present the comparison among different objective functions that refer to the HRSG specifically or to the whole bottoming cycle. In their mathematical model, they considered the presence of specific constraints for the operating parameters of the power plant, the most important constraints that were considered refer to the steam quality at the turbine outlet, the HRSG outlet exhaust gas temperature and the steam turbine blade height. In their work, a parametric analysis was also performed to evaluate the influence of the gas temperature at the HRSG inlet and the pinch point temperature difference on the considered objective functions. Woudstra et al [15**]** performed the thermodynamic evaluation of combined cycle plants with the same gas turbine and different steam bottoming cycles. The evaluation showed that the increasing the number of pressure levels of steam generation will reduce the losses due to heat transfer in the HRSG, but also the exergy loss due to the exhaust of flue gas to the stack. Among the investigated configurations for bottoming cycle, triple pressure reheat was the best option from exergy point of view. Mansouri et al [16] investigated the effect of pressure levels of steam generation at heat recovery steam generator HRSG on the energetic and exergetic efficiency of HRSG, bottoming cycle and combined cycle power plants, as well as the effect of Xiang and Chen [17] considered a combined cycle with three-pressure HRSG, equipped with the GE PG9351FA gas turbine. They maximized the combined cycle efficiency through the optimization of the HRSG operating parameters by minimizing exergy losses. Moreover, they highlighted the influence of the HRSG inlet gas temperature on the bottoming cycle efficiency. They studied the influence of HRSG inlet gas temperature on the steam bottoming cycle efficiency. Their result shows that increasing the HRSG inlet temperature has less improvement to steam cycle efficiency when it is over 590ºC. Kelly et al [18] demonstrated that the most efficient way for converting solar thermal energy into electricity is to withdraw feed water from the heat recovery steam generator (HRSG) downstream of the last economizer, to produce high pressure saturated steam and to return the steam to the HRSG for superheating and reheating. The integrated solar plant concept offers an effective means for the continued development of parabolic trough technology. In a careful plant design, solar thermal to electric conversion efficiencies will exceed, often by a significant amount, those of a solar-only parabolic trough project. An integrated plant bears only the incremental capital cost of a larger Rankine cycle which provides further reductions in the levelized cost of solar energy.He Ya Ling et al [19] proposed a model for a typical parabolic trough solar thermal power generation system with Organic Rankine Cycle (PT-SEGS–ORC) was built within the transient energy simulation package TRNSYS. They found that the heat loss of the solar collector (qloss) increases sharply with the increase in Pinter at beginning and then reaches to an approximately constant value. The variation of heat collecting efficiency with v is quite similar to the variation of gloss with Pinter. However θ exhibit opposite effect on η_{hc}. In addition, it is found that the optimal volume of the thermal storage system is sensitively dependent on the solar radiation intensity. The optimal volumes are 100, 150, 50, and 0 m3forspring equinox, summer solstice,

autumnal equinox an proposed d winter solstice, respectively Gang et al [20] the innovative configuration of low temperature solar thermal electricity generation with regenerative Organic Rankine Cycle (ORC) mainly consisting of small concentration ratio compound parabolic concentrators (CPC) and the regenerative ORC. The effects of regenerative cycle on the collector, ORC, and overall electricity efficiency are then analyzed. The results indicate that the regenerative cycle has positive effects on the ORC efficiency but negative ones on the collector efficiency due to increment of the average working temperature of the first-stage collectors. And found that there generative cycle optimization of the solar thermal electric generation differs from that of a solo ORC. The system electricity efficiency with regenerative ORC is about 8.6% for irradiance 750 W/m^2 and is relatively higher than that without the regenerative cycle by4.9%.Manolakos D et al [21] proposed co-generation system producing electricity and fresh water by a solar field driven supercritical organic Rankine cycle (SORC) coupled with desalination. The proposed system can use parabolic trough solar collectors (among other options) to produce 700 kW thermal energy with temperatures up to 400°C at peak conditions. Thermal energy is delivered to the SORC which uses hexamethyldisiloxane (MM) as the working organic fluid and could achieve cycle efficiency close to 21%. The SORC condensation process is undertaken by the feed seawater to reduce thermal pollution. Due to the elevated temperature of the preheated seawater, the RO unit specific energy consumption decreases. Although , lot of literature it is found that the efficiency of the combined cycle is more than the simple individual cycle. Other important conclusion found that the more and more energy going to waste from stack with exhaust flue gases even after passing through HGRC. Almost flue gas around 150-180 ^{0}C is going to waste from stack.

After reading literature review it is concluded that no researcher use the energy at temperature 150-180^{0}C from the flue gases.

In this research integration of the ORC (organic Rankine cycle) in the pre existing cycle is done for recovery of the low temperature heat from the exhaust gases which are coming from the HRSG after generation of the steam for simple Rankine cycle. It is proposed to examine the effect of the various parameters on the performance of the combined cycle and comparison is done with or without integration of the ORC. These parameters are following

- Effect of the pressure ratio
- Effect of the air fuel(A/F) ratio

4. Thermodynamic Analysis

For thermodynamic analysis (exergetic and energetic) a model is proposed in this model there are following components

- Compressor
- Combustor
- Gas turbine
- HRSG
- Steam turbine
- Condenser
- Heat recovery boiler
- Organic pump
- Water pump
- Organic surface condenser

4.1 System Description

Systems have the different components which are described above following ways it is works through following points

At stage 1. There is ambient conditions are defined this is the entry of the compressor and point 2 is the entry of the combustion chamber where heat is given and then combustion of fuel takes place. After the combustion is over the hot flue gases goes to the gas turbine at stage 3 where work is taken by rotation of the shaft .After expansion flue gases goes to the HRSG at stage 4 at pressure above the slightly above the atmospheric pressure where heat is given to the water for generation of the steam and remaining hot gases from stack goes to the heat recovery boiler at stage 9.stage 5 is entry to steam turbine and stage 6 exit to the steam turbine and entry to the surface condenser. In heat recovery boiler the heat is given to the organic fluid (R410A) which is circulates in ORC plant. At stage 10 organic fluid vapor goes to the organic expander where small amount of work is recovered. At stage 14 the remaining gases goes to atmosphere almost at atmospheric temperature and pressure. Then there is no potential remains. This is shown in figure 1.

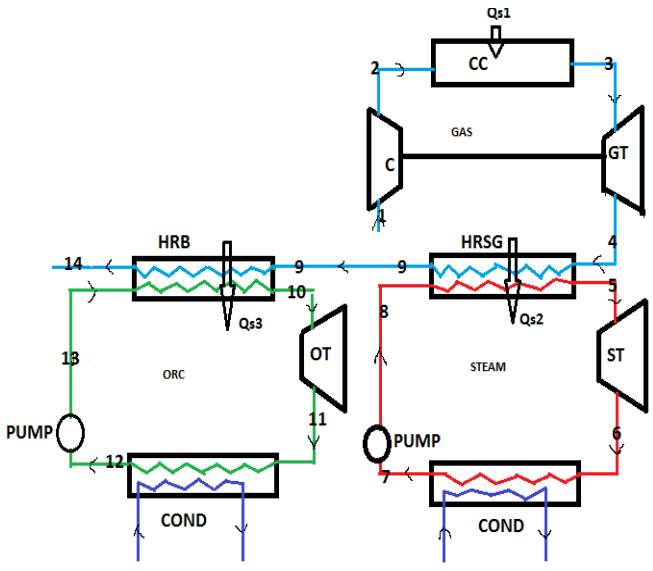


Figure 1: Thermodynamic model of combined cycle with Organic Rankine cycle (ORC)

Following assumptions are made in the study of this model:

1. All components are in steady state.
2. No pressure loss in any component.
3. There is no heat and pressure loss in pipes connecting in each components.
4. After steam turbine and organic expander fluids are

saturated vapor.

5. No pressure loss in HRSG and heat recovery boiler.

4.2 Energy Analysis

In this system I consider the whole system is control volume. Each component of the whole system is separately considered as control volume. The equations are given as
Mass balance

$$\sum m_{in} = \sum m_{out}$$

Energy balance

$$Q - W + \sum m_{in} - \sum m_{out} = 0$$

Overall thermal efficiency of plant without ORC

$$\dot{\eta}_{without\ ORC} = (W_{GT} + W_{ST} - W_C - W_P)/Q_{s1}$$

Overall thermal efficiency of plant with ORC

$$\dot{\eta}_{with\ ORC} = (W_{GT} + W_{ST} + W_{OT} - W_C - W_P - W_{OP})/Q_{s1}$$

4.3 Exergy Analysis

Exergy destruction or loss is given by

$$\dot{E}D_i = \sum(\dot{m}e)_{in} - \sum(\dot{m}e)_{out} + \left[\sum\left(\dot{Q}(1-\frac{T_0}{T})\right)_{in} + \sum\left(\dot{Q}(1-\frac{T_0}{T})\right)_{out}\right] \pm \sum \dot{W}$$

Exergy destruction for each component is also calculated from above question
Exergy transfer in combustion chamber from fuel is given as
$ET = Q_{S1}*[1-T_0/T_C]$
Overall exergetic efficiency of plant without ORC

$$\dot{\eta}_{exergetic\ without\ ORC} = (W_{GT} + W_{ST} - W_C - W_P)/ET$$

Overall exergetic efficiency of plant with ORC

$$\dot{\eta}_{exergetic\ with\ ORC} = (W_{GT} + W_{ST} + W_{OT} - W_C - W_P - W_{OP})/ET$$

5. Results and Discussion

This thermodynamic model developed by engineering question solver (EES commercial version).The calculation of efficiencies is done by this software and results have been calculated. Comparison is done in figures .From figure 2 to figure 3 the exergetic efficiency vs pressure ratio and air fuel given respectively and compare with and without ORC .It is shown that exergetic efficiency is increasing continuously with pressure ratio but decreasing with air fuel ratio. This is because increasing pressure ratio compressor outlet temperature is increase responding exergy transfer decrease having same work out put hence exergetic efficiency increases. On other hand decrease in efficiency with increase in air fuel ratio because increase in air fuel ratio decreases the inlet temperature of the gas turbine and also flue gases .so exergy transfer in combustor have to be increase .Figure 4 and 5 shown the variation of thermal efficiency with respect to the pressure ratio and air fuel ratio respectively and compared efficiency with and without ORC. Same effects are calculated as well as exergetic efficiency. Here also same reason for increase and decrease of thermal efficiency with pressure ratio and air fuel ratio as exergetic efficiency. Input parameters taken for study are given below these parameters are taken from different running power plants. These are following

Ambient temperature	T_0=298K
Flue gases temperature from HRSG	T_9=423K
Constant pressure in HRSG	P_5=10bar
Temperature inlet to steam turbine	T_5=813K
Temperature inlet to organic turbine	T_{10}=403K
Pressure inlet to organic turbine	P_{10}=25bar
Pressure outlet to organic turbine	P_{11}=2bar
Pressure outlet to steam turbine	P_6=0.07bar
Outlet temperature of gases from HRB	T_{14}=300K
Organic fluid for ORC	R410A

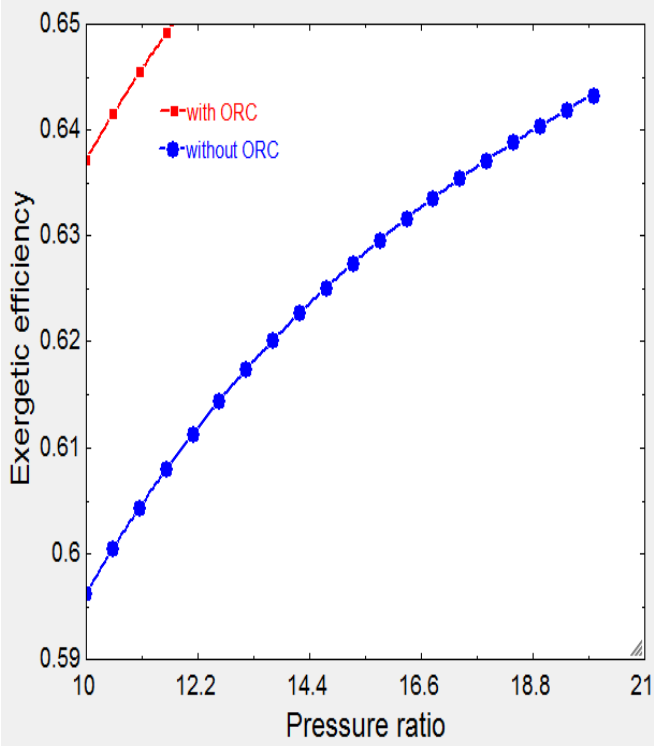


Figure 2: Exergetic efficiency vs pressure ratio

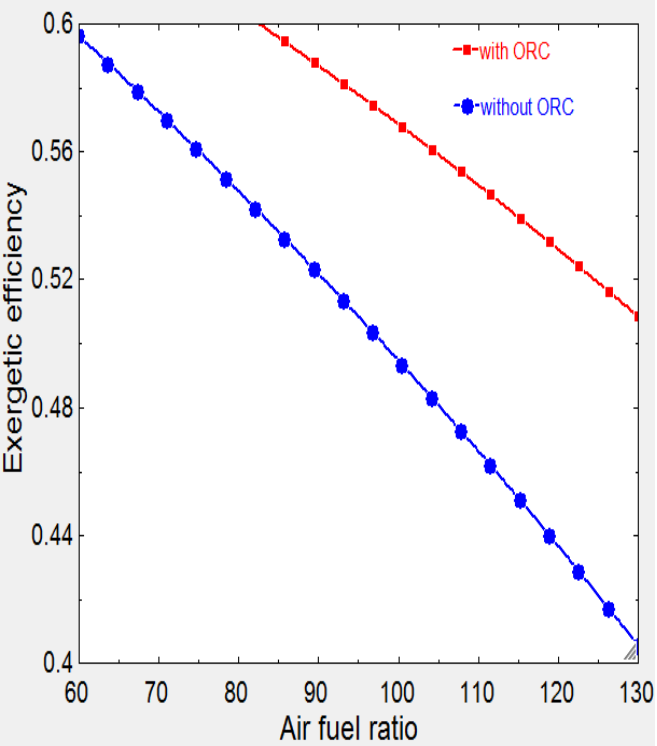


Figure 3: Exergetic efficiency vs air fuel ratio

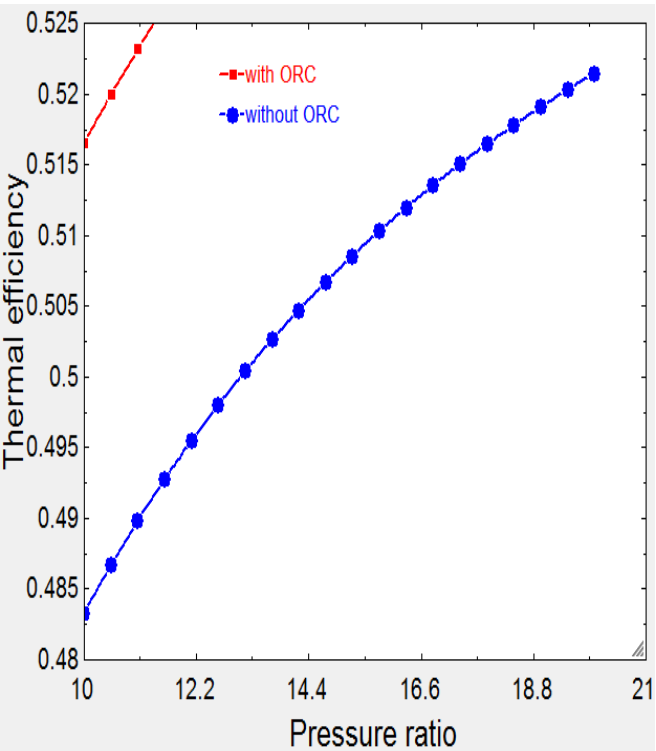


Figure 4: Thermal efficiency vs pressure ratio

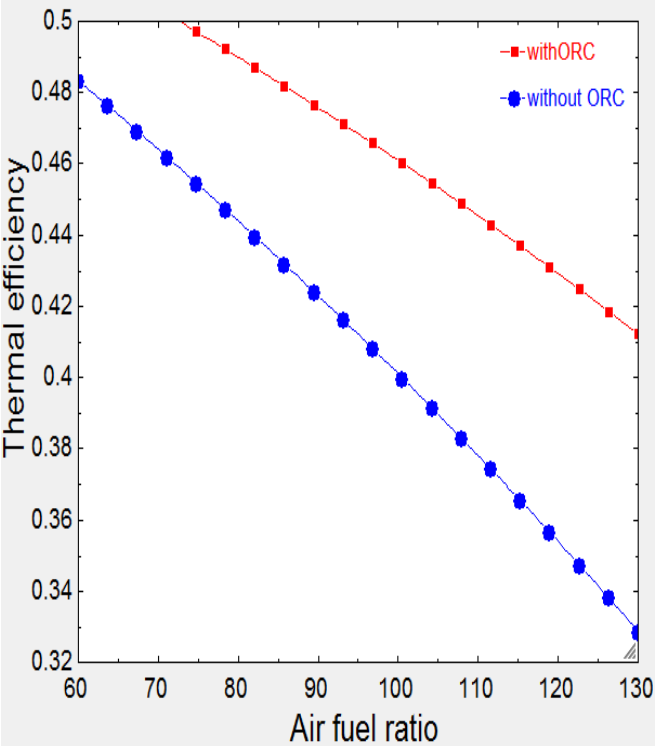


Figure 5: Thermal efficiency vs air fuel ratio

6. Conclusions

The numerical computations have been carried out for R 410a using thermodynamic (energy) analysis of combined cycle power plant by integrating of organic Rankine cycle the following conclusions are made

1. With ORC exergetic efficiency is more than without ORC.
2. With ORC thermal efficiency is more than without ORC.
3. So integration of ORC with the existing combined cycle is effective.
4. So heat from the exhaust gases is fully utilized by integration of ORC.

References

[1] Kaviri A. G., Jaafar M. N., Lazim T. M., ikoij\Barzegaravval, H., Exergy environmental optimization of Heat Recovery Steam Generators in combined cycle power plant through energy and exergy analysis. Energy Conversion and Management, 6(2013), pp.27–33.

[2] Ahmadi P., Dincer I., Exergo environmental Analysis and Optimization of a Cogeneration Plant System using Multimodal Genetic Algorithm (MGA). Energy, 35(2010), pp. 5161-72.

[3] Boyano A., Blanco-Marigorta A. M., Morosuk T., Tsatsaronis G., Exergoenvironmental Analysis of a Steam Methane Reforming Process for Hydrogen Production. Energy, 36(2011), pp. 2202-2214.

[4] Petrakopoulou F., Boyano A., Cabrera M., Tsatsaronis G., Exergo economic and Exergo environmental Analyses of a Combined Cycle Power Plant with Chemical Looping Technology. International Journal of Greenhouse Gas Control, 5(2011), pp. 475-482.

[5] Ibrahim K. T., Rahman M. M., Abdalla N. A., Optimum Gas Turbine Configuration for Improving the Performance of Combined Cycle Power Plant. Procedia Engineering,15(2011), pp.4216-4223.

[6] Ameri M., Hejazi H. S., The Study of Capacity Enhancement of the Chabahar Gas Turbine Installation using an Absorption Chiller. Applied Thermal Engineering, 24(2004), pp.59–68.
[7] Boonnasa S., Namprakai P., Muangnapoh T., Performance Improvement of the Combined Cycle Power Plant by Intake Air Cooling using an Absorption Chiller, Energy,31(2006), pp. 2036–2046.
[8] Hosseini R., BeshkanI. A., Soltani M., Performance Improvement of Gas Turbines of Fars (Iran) Combined Cycle Power Plant by Intake Air Cooling using a Media Evaporative Cooler. Energy Conversion and Management, 48(2007), pp. 1055–1064.
[9] Ibrahim T. K., Rahman M. M., Effect of Compression Ratio on Performance of Combined Cycle Gas Turbine. International Journal of Energy Engineering,2(2012)1, pp. 9-14.63.
[10] Khaliq A., Kaushik S., Thermodynamic Performance Evaluation of Combustion Gas Turbine Cogeneration System with Reheat. Applied Thermal Engineering, 24(2004), pp. 1785–1795.
[11] Mohagheghi M., Shayegan J., Thermodynamic Optimization of Design Variables and Heat Exchangers Layout in HRSGs for CCGT, using Genetic Algorithm. Applied Thermal Engineering, 29(2009), pp. 290–299.
[12] Bracco S., Silvia S., Exergetic Optimization of Single Level Combined Gas Steam Power Plants Considering Different Objective Functions. Energy, 35(2010), pp. 5365-5373.
[13] Woudstra N., Woudstra T., Pirone A., Van der Stelt T., Thermodynamic Evaluation of Combined Cycle Plants. Energy Conversion and Management, 51(2010)5, pp. 1099–1110.
[14] Mansouri M. T., Ahmadi P., Kaviri A. G., Exergetic and Economic Evaluation of the Effect of HRSG Configurations on the Performance of Combined Cycle Power Plants. Energy Conversion and Management, 58(2012), pp. 47–58.
[15] Xiang W., Chen Y., Performance Improvement of Combined Cycle Power Plant Based on the Optimization of the Bottom Cycle and Heat, Recuperation, Thermal science,16(2007), pp. 84-89.
[16] Kelly B, Herrmann U, Hale MJ. "Optimization studies for integrated solar combined cycle systems" In: Proceedings of solar forum 2001, solar energy: the power to choose; 2001April 21–25, Washington DC, USA.
[17] He Ya-Ling, Mei Dan-Hua, Tao Wen-Quan, Yang Wei-Wei, Liu Huai-Liang. "Simulation of Parabolic trough solar energy generation system with organic Rankine cycle" Applied Energy2012;97 :630–41.
[18] Gang Pei, Li Jing, JieJi. "Analysis of low temperature solar thermal electric generation using regenerative organic Rankine cycle" Applied Thermal Eng 2010; 30:998–1004.
[19] Li C, Kosmadakis G, Manolakos D, Stefanakos E, Papadakis G, Goswami DY., performance investigation of concentrating solar collectors coupled with a transcritical organic Rankine cycle for power and seawater desalination cogeneration Desalination"2013;318:107–17.

Nomenclature

Symbols/Subscript

ED	Exergy destruction
Qs1	Heat addition to combustion chamber
Qs2	Heat addition to HRSG
Qs3	Heat transfer to HRB
HRB	Heat recovery boiler
GT	Gas turbine
ST	Steam turbine
OT	Organic turbine
W	work
C	compressor
P	pump
m	mass flow rate
CC	combustion chamber
ṅ	Efficiency
HRSG	Heat recovery steam generator
ORC	Organic Rankine cycle
a	Air
COND	Condenser

ResearchGate

See discussions, stats, and author profiles for this publication at: https://www.researchgate.net/publication/323827103

Thermodynamic Analysis of Irreversible Regenerative Gas Turbine Cycle

Conference Paper · March 2018

DOI: 10.29126/23951303/NFEEES2018-108

CITATIONS
0

READS
20

2 authors:



Shabir Grover
Delhi Technological University
3 PUBLICATIONS **0** CITATIONS
SEE PROFILE



s.s. Bhatti
Indian Institute of Technology Delhi
2 PUBLICATIONS **0** CITATIONS
SEE PROFILE

All content following this page was uploaded by Shabir Grover on 17 March 2018.

The user has requested enhancement of the downloaded file.

New Frontier in Energy, Engineering, Environment & Science (NFEES-2018) Feb - 2018

RESEARCH ARTICLE OPEN ACCESS

Thermodynamic Analysis of Irreversible Regenerative Gas Turbine Cycle

Shabir Grover[1], S.S.Bhatti[2]

1(Mechanical Engineering Department, Delhi Technological University, Delhi)

2 (Mechanical Engineering Department, DTTE Govt. of NCT of Delhi)

Abstract:

The present paper describes the energy analysis of an irreversible regenerative gas turbine power cycle. Gas turbine cycle model is simulated in MATLAB environment considering a real Brayton cycle having irreversibility and regeneration. The effect of thermodynamic parameters such as pressure ratio, regeneration effectiveness and turbine/compressor isentropic efficiency on specific power output and thermal efficiencies are examined. It was found that incorporating regeneration in gas turbine cycle results in an increase in the output power of the cycle and a subsequent decrease in the exhaust gas temperature. The results also show a significant increase in the thermal efficiency of the cycle when regeneration is included in cycle by utilizing turbine exhaust to heat the compressed working fluid. A 67.9% increase in efficiency was observed for the optimum pressure ratio value of 6 for the regenerative case compared to non-regenerative one. The above heat engine model represents a real case scenario which when juxtaposed with the ideal cycle without regeneration helps us to discern the differences between the two.

Keywords — **Irreversibility, Regeneration, Brayton cycle.**

I. INTRODUCTION

Rising energy consumption, opening of electricity markets and environmental issues are the main concerns for researchers and scientists. Increasing the thermal efficiency results in reduction in fuel consumption and also reduces the emissions. Numerous research activates are going on to increase the thermal efficiency of power generation Such as increasing pressure ratio, reheating, regeneration, combined cycle power plants etc.

Gas turbine power plants works on the basis of Brayton cycle. Thermodynamic analysis based on first law analysis was applied for designing power plants at first stage. Also regeneration process has significant effect on cycle efficiency. The aim of this study is to examine the effect of regeneration and different parameters on gas turbine cycle to increase the thermal efficiency. Further, all the fluid friction losses in the compressor and turbine are incorporated by an isentropic efficiency term.

II. LITERATURE REVIEW

Ibrahim and Rahman [2] investigated the effects of isentropic efficiency and reheat on performance of Gas Turbines. Patil, Pawase and Deore [3] went one step further to include the effect of intercooling on the SFC and specific work output of a regenerative, reheated Gas Turbine cycle. The effect of ambient air temperature is also included in their analysis. Wu and Chen [4] analysed the performance of an endoreversible regenerative system with a keen focus on reducing the irreversibility losses in the hot and cold heat exchangers. Al-Sood and Matrawy [5] studied the effects of 1st and 2nd law efficiency, ecological coefficient of performance and exergy loses based on a range of operating

parameters such as inlet conditions to first stage and second stage turbine and heat transfer coefficient-area product of the complete heat exchanger. Mahmood and Tariq [6] performed multi criteria optimization in which turbine inlet temperature, ambient air temperature, compression ratio and effectiveness were used to select the optimum configuration. They observed that regeneration with low compression ratio lead to high efficiency values. Kumar and Kaushik [7] discussed the power optimization of irreversible regenerative Brayton cycle with isothermal heat addition. They proved that the introduction of two heat additions significantly enhanced model efficiency by 20 percent compared to conventional cycle. Their analysis considered isothermal pressure drop ratio, pressure drop recovery coefficients and heat capacitance rate of working fluid among other parameters. Chen, Sun and Kiang [8] assessed the performance of a closed regenerative Brayton cycle using the technique of finite time thermodynamics (FTT). Kaushik and Tyagi [9] also used the FTT technique to maximize the power output with respect to the working fluid temperatures. They observed that the effect of cold side effectiveness is more pronounced for the power output while the effect of regenerative effectiveness is more pronounced for the thermal efficiency. Other researchers [10-12] have also worked on the same domain to improve their understanding of power analysis and efficiency of the regenerative Gas Turbine cycle. The present study is undertaken with an aim to provide an in depth analysis of the same.

III. THERMODYNAMIC ANALYSIS

A. System Configuration

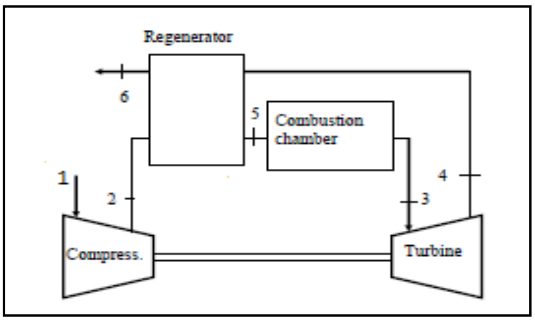


Fig. 1(a) Schematic diagram of the system layout

Figure 1(a)shows the regenerative gas turbine cycle, and Figure 1(b) shows the T-S diagram of the cycle. Regeneration is a thermodynamic processthat utilizes the heat energy in the exhaust gases from the gas turbine toheat the air entering to the gas turbine. Heat exchange process takes placebetween the exhaust gases and compressed air by utilizing shell and tube type heat exchanger.

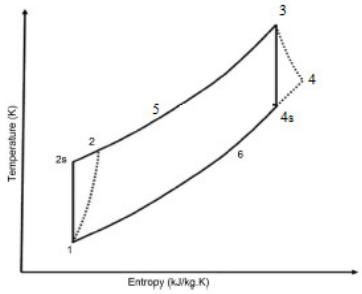


Fig. 1(b) T-s diagram of the cycle

B. Assumptions used in present analysis:

1. No pressure and heat losses
2. Inlet temperature and pressure(T1=303K,P1=1 bar, Isentropic Turbine & Compressor efficiency=0.85, Effectiveness=0.85)
3. Isentropic compressor and turbine efficiencies
4. Effectiveness of heat exchanger

IV. ENERGY ANALYSIS

Energy analysis based on first law of thermodynamics is performed to find the thermodynamic performance of irreversible regenerative gas turbine cycle

The compressor pressure ratio (r_p) can be defined as below:

$$r_p = P_2 / P_1 \quad (1)$$

The isentropic efficiency of the compressor expressed as

$$\eta_c = \frac{(T_{2s} - T_1)}{(T_2 - T_1)} \quad (2)$$

The work of the compressor (W_C)

$$W_C = \dot{m} c_p (T_2 - T_1) \quad (3)$$

The effectiveness of regenerator (ε) are considered in this study.

$$\varepsilon_{reg} = \frac{(T_5 - T_2)}{(T_4 - T_2)} \quad (4)$$

The isentropic efficiency of the turbine expressed as

$$\eta_e = \frac{(T_3 - T_4)}{(T_3 - T_{4S})} \quad (5)$$

The work produced from the turbine is determined by the following equation.

$$W_T = \dot{m} c_p (T_3 - T_4) \quad (6)$$

The network of the Gas Turbine (W_{net}) is calculated by Equation

$$W_{net} = W_T - W_C \quad (7)$$

Thermal efficiency of Gas Turbine cycle is given by:

$$\eta_{th} = \frac{(W_T - W_C)}{\dot{m} c_p (T_3 - T_2)} \text{ without regeneration} \quad (8)$$

$$\eta_{th} = \frac{(W_T - W_C)}{\dot{m} c_p (T_3 - T_5)} \text{ with regeneration} \quad (9)$$

V. RESULTS AND GRAPHS

1) ***Effect of pressure ratio on work output:***Fig.3 shows the effect of pressure ratio on the net power output of irreversible regenerative brayton cycle.

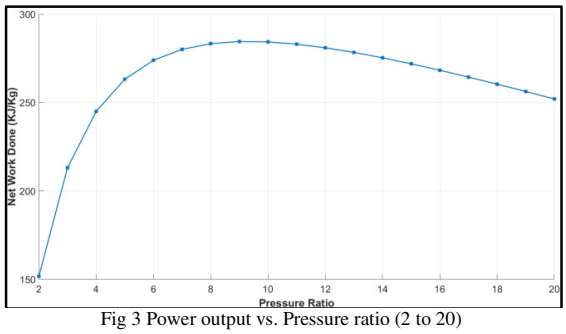


Fig 3 Power output vs. Pressure ratio (2 to 20)

Fig.4 shows the effect of pressure ratio on the thermal efficiency of irreversible regenerative brayton cycle for both cases with and without regeneration.

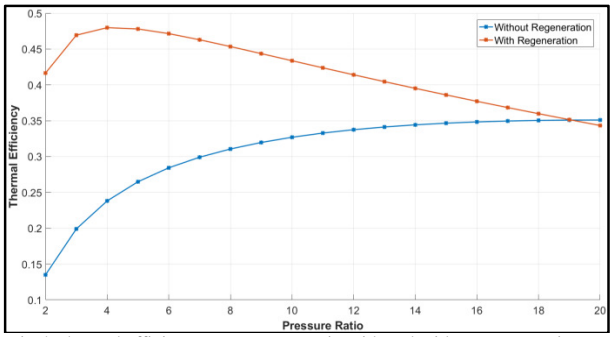


Fig 4 Thermal efficiency vs. Pressure ratio with and without regeneration

2) ***Effect of regeneration on thermal efficiency:***Fig.5 shows the effect of effectiveness of regenerator on the thermal efficiency of irreversible regenerative brayton cycle for both cases with and without regeneration.

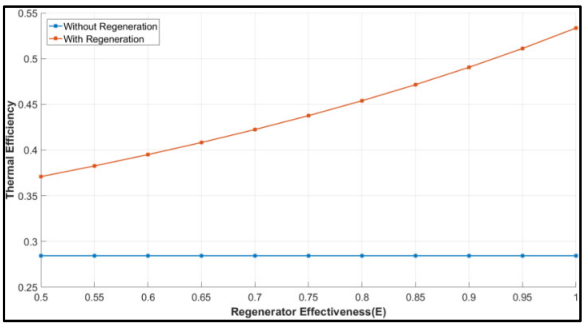


Fig 5 Thermal efficiency vs. Effectiveness for the 2 cases

3) *Effect of compressor efficiency on thermal efficiency for different turbine efficiencies:* Fig.6 shows the effect of compressor efficiency on the thermal efficiency of irreversible regenerative brayton cycle for efficiencies of turbine.

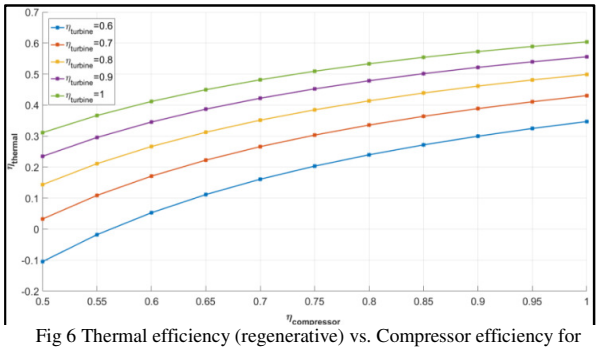


Fig 6 Thermal efficiency (regenerative) vs. Compressor efficiency for different turbine efficiencies

V1. CONCLUSIONS

The conclusion from this study leads to following important points. There certainly is a jump in the thermal efficiency of the system due to regeneration. However, with an increase in the pressure ratio, this increase gradually starts decreasing until at a certain value (Rp=19 in this case) when both the efficiency values for regenerative and non-regenerative case become equal. Also note that the net work output is independent of the cycle is independent of the regeneration effect. Further, it is observed that the efficiency value is strongly dependent on the compressor and turbine isentropic efficiency. As these loses in turbine and compressor decrease, the efficiency enhances as can be seen in figure 6. Lastly, the net work is not linearly related to pressure ratio. It claims its highest value around Rp value 8 and then starts to descend. This goes to show that work output and efficiency do not attain optimum values at a single point only.

REFERENCES

1. *S.C. Kaushik, S.K. Tyagi, M.K. Singhal, Parametric study of an irreversible regenerative Brayton cycle with isothermal heat addition, Energy Convers. Manage. 44 (12) (2003) 2013–2025.*

2. *Thamir K. Ibrahim, M.M. Rahman, Effects of Isentropic Efficiency and Enhancing Strategies on Gas Turbine Performance, Journal of Mechanical Engineering and Sciences (JMES), Volume 4, pp. 383-396, June 2013.*

3. *Milind S. Patil, Datta B. Pawase, Eknath R. Deore, Thermal Performance of Reheat, Regenerative, Inter Cooled Gas Turbine Cycle, International Journal of Research in Mechanical Engineering & Technology, IJRMET Vol. 5, Issue 2, May - Oct 2015.*

4. *Chih Wu, Lingen Chen, Fengrui Sun, Performance of a Regenerative Brayton Heat Engine, Elsevier Science Ltd., Energy Vol. 21 No. 2, pp. 71-76, 1996.*

5. *Maher M. Abou Al-Sood, Kassem. K. Matrawy, Yousef M. Abdel-Rahim, OPTIMUM Operating Parameters of an Irreversible Gas Turbine Cycle, Journal of Engineering Sciences, Assiut University, Vol. 40 No 6 pp.1695-1714 - November 2012.*

6. *Omar ShakirMahmood, Dr. Mohammed Tariq, Analysis of a Regenerative Gas Turbine Cycle for Power Plant, International Journal of Scientific Engineering and Technology Research, ISSN 2319-8885 Vol.03, Issue.04, April-2014, Pages: 0611-0616.*

7. *Rajesh Kumar, S.C Kaushik, Raj Kumar, Power Optimization of an Irreversible Regenerative Brayton Cycle with Isothermal Heat Addition, Journal of Thermal Engineering, Vol. 1, Issue No. 4, pp. 279-286, October, 2015.*

8. *Lingen Chen, Fengrui Sun, Chih Wu, R.L. Kiang, Theoretical Analysis of the Performance of a Regenerative Closed Brayton with Internal Irreversibilities, Energy Convers. Manage. , Vol. 38 No. 9 pp.871-877, 1997.*

9. *S. C. Kaushik and S. K. Tyagi, Finite time thermodynamic analysis of an irreversible regenerative closed cycle brayton heat engine, International Journal of Solar Energy, 2002, Vol. 22(3–4), pp. 141–151.*

10. *A Calvo Hernandez, A Medina and J.M. M Roco, Power and efficiency in a regenerative gas turbine, J. Phys. D: Appl. Phys. 28 (1995) 2020-2023.*

11. *Aram Mohammed Ahmed, Dr. Mohammad Tariq, Thermal Analysis of a Gas Turbine Power Plant to Improve Performance Efficiency, International Journal of Mechanical Engineering and Technology (IJMET), ISSN 0976 – 6359(Online) Volume 4, Issue 6, November - December (2013).*

12. *Ashok Kumar, SS Kachhwaha, RS Mishra, Thermodynamic analysis of a regenerative gas turbine cogeneration plant, Journal of Scientific and Industrial Research, Vol. 69, March 2010, pp. 235*

View publication stats

International Journal of Research in Engineering and Innovation (IJREI)
journal home page: http://www.ijrei.com
ISSN (Online): 2456-6934

Validation of various cryogenics systems using exergy analysis

R.S. Mishra, Devender Kumar

Department of Mechanical Engineering, Delhi Technological University, Delhi, India

Abstract

The exergy analysis (second law analysis) is used for providing information about the losses qualitatively as well as quantitatively along with their locations. Exergetic (thermodynamic) optimization improves the performance of a system. This paper present, the validation of Linde,Dual compressor Linde system , Pre-cooled Linde system, simple Claude Katiza Claude Haylent Claude, Collin system Hydrogen liquefaction system, Modified Helium liquefaction systemin terms of system performances.

© 2018 ijrei.com. All rights reserved

Key words: Cryogenicsystems, Thermodynamic Analysis, Energy-exergy Optimization, Low temperature system Validation

1. Introduction

Cryogenics has been an important area of refrigeration because of its application in industrial and commercial utilization, and many scientific and engineering researches are going on by using low temperature liquefied gases. Cryogenics isa branch of physics which deals with the achieving very low temperatures (below the 173 K.) and study their effects on matter .Cryogenic study presents broad goals for cryogenic support for various gas liquefaction systems. Due to industrial revolution, various issues like cost, efficiency and reliability are the challenges factors in employment of cryogenic support technology. In field of mechanical engineering we try to refine or improve the ability or quality of material to get in maximum use at maximum level at a reduce cost. In past many fantasticclaimhave been made as to the degree of improve performance achieved by employing cryogenics technology.

2. Literature Review

Second law efficiency are very low in all above said cryogenic systems like hydrogen ,helium liquefaction etc. and its value ranging from 3% to 23 % for most of systems. Effect of different input gas also studies carefully and behavior of different gases in different system is concluded i.e. first law efficiency (COP) and second law efficiency (exergetic efficiency) of Claude system decrease with increase in pressure ratio. For Methane gas COP decreases [1].
It was observed that in all gases methane gas show highest performance in most of systems while argon show lowest thermodynamic performance. Improved Collin system show high efficiency as compared to Collin system, the nitrogen chamber and extra expander gives extra refrigerant effect which enhance liquefaction rate in the system and increasing the performance parameters of systems. (xii) The improved Collin system at PR 11 bars show highest exergtic efficiency of 54.19% keeping the expander ratio of all three expander is 70%,10%,10% respectively while simple Collin helium liquefaction system show 3.54% exergtic efficiency keeping the both expander flow ratio 35% and 50% respectively [2].
Argon has the highest value of second law efficiency (i.e. exergetic efficiency = 41.32%) and fluorine has the maximum value of first law efficiency (i.e. COP=0.9595) among the other gases. Methane has the highest value of liquefaction value of mass flow rate, which is around 0.3167 at cycle pressure ratio of 40. Fluorine has the highest value of exergy destruction rate in separator and it first decreasing up to 400K and then it starts increasing order [3]. It was observed that the outlet temperature of compressor affect the performance parameters of system. The second law efficiency decreasing with increasing compressor outlet temperature Similarly liquefaction rate is decreasing with increase outlet temperature of compressor and optimum expander flow fraction 0.55 flow ratio and optimum second law efficiency is 3.5 %, while first heat exchanger (HX1) shows highest rate of exergy destruction ranging from 36 % to 24 % with increase in temperature from 200 K to 400 K [4-5]. COP and second law efficiency decrease with increase

Corresponding author: R.S. Mishra
Email Id: hod.mechanical.rsm@dtu.ac.in

in pressure ratio. For Methane gas COP decreases. Second law efficiency of system is highest for fluorine gas followed by nitrogen, air oxygen respectively which has 80-83% and methane gas shows lowest second law efficiency is which continuously decreases [6].

3. Result and Discussion

3.1 Validation of Linde system

Linde system and its T-S diagram in current study is shown in fig-1(a)-1(b) respectively.

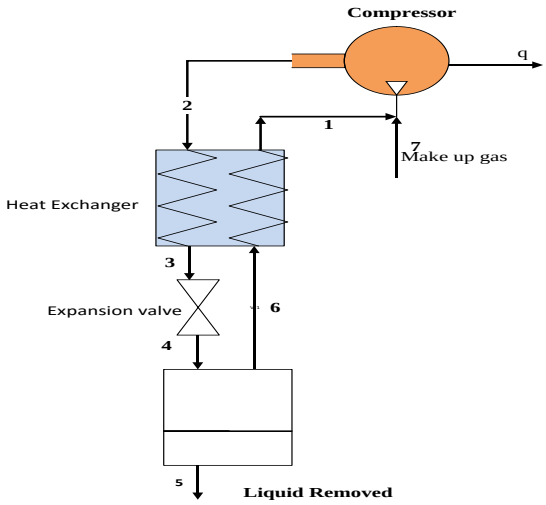


Fig: 1(a) Schematics Linde Hampson System [7]

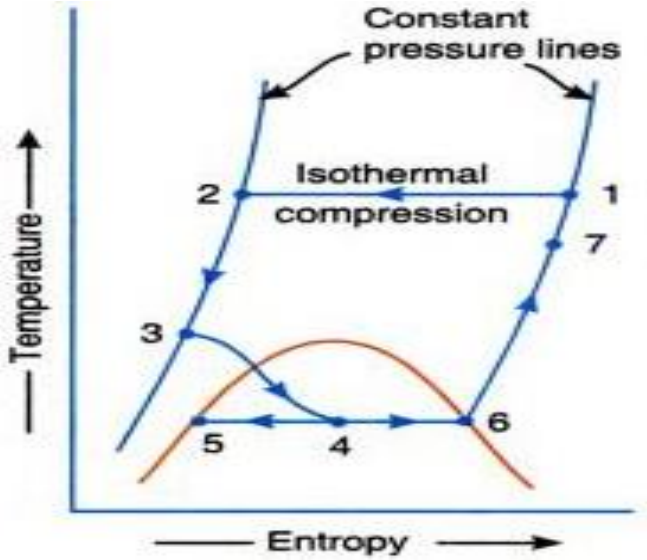


Fig: 1(b) Schematics Linde Hampson System T-S diagram [7]

The results of Linde system in current study has been validated with previous model, i.e. The COP and second law efficiency of the Linde cycle matched with the results of Kanoglu et al. [7] as shown in Fig.1(c). It has been observed that results related to efficiency and COP of the current model properly follows the results of COP and efficiency was concluded by Kanoglu et al [7]

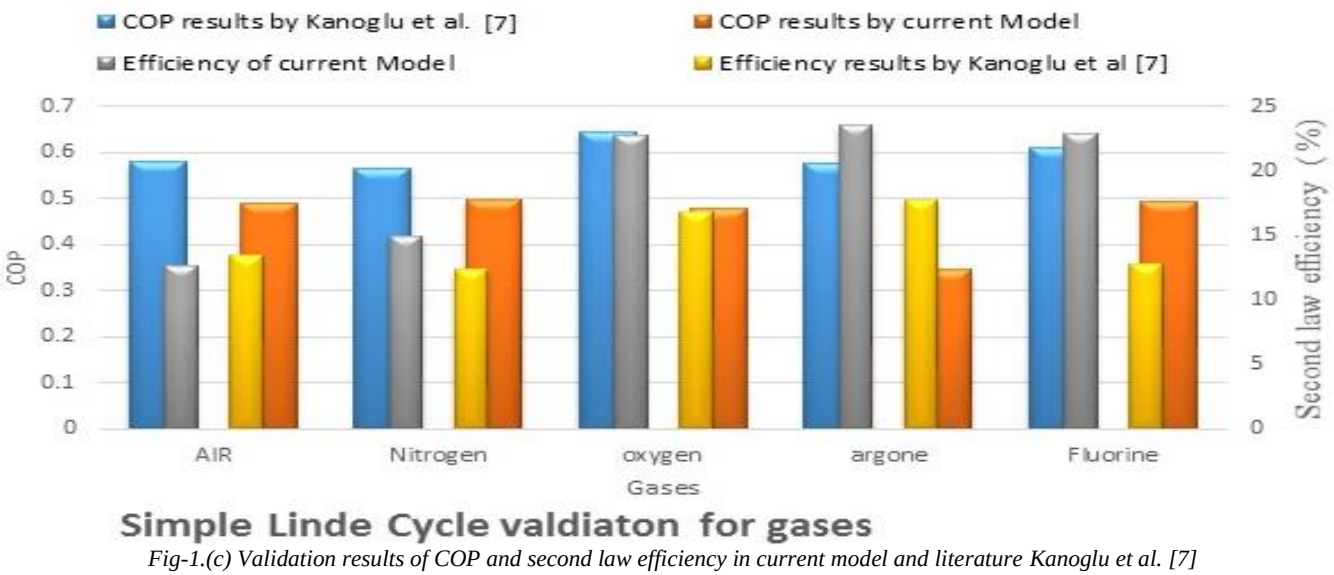


Fig-1.(c) Validation results of COP and second law efficiency in current model and literature Kanoglu et al. [7]

It has been also concluded that both the model shows the highest value of second law efficiency in case of argon gas, i.e. 23.49% for current model and 17.8% for the previous model results. Moreover, the results of work done of simple Linde cycle in the current study has been validated with the results of previous model results, (i.e. Kanoglu et al. [7] as illustrated in Fig.1.(d).

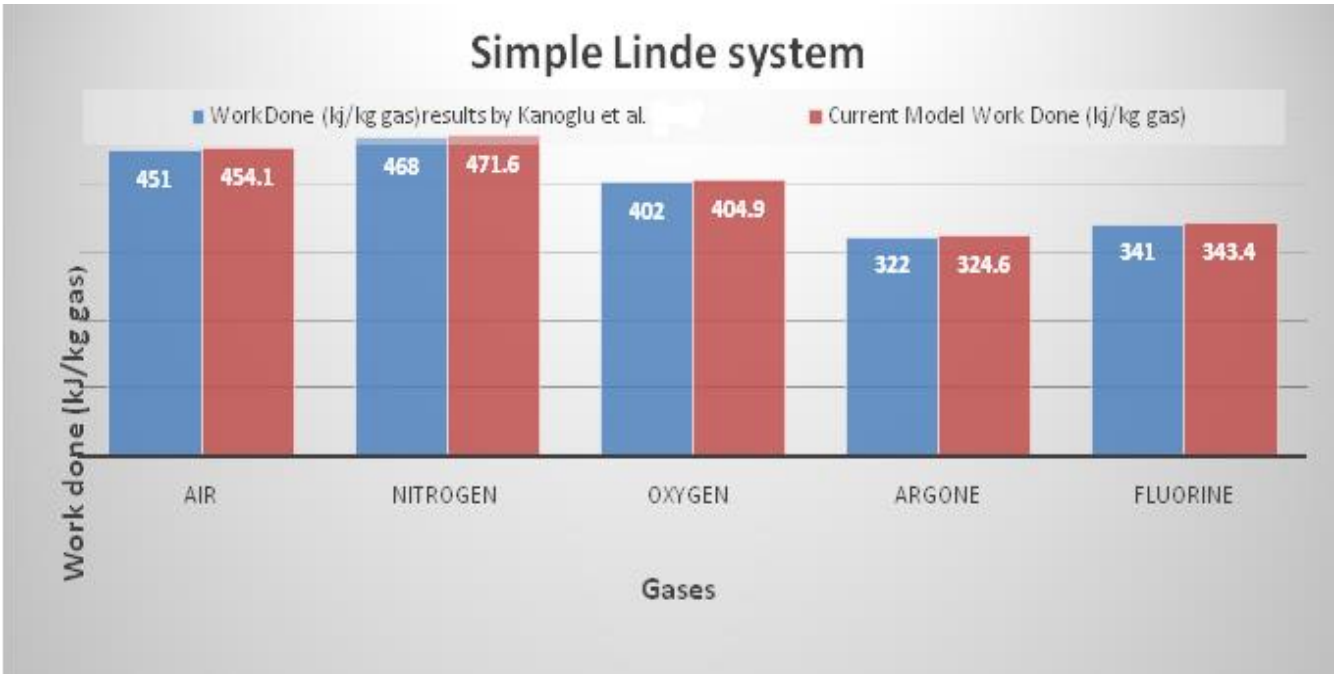


Fig. 1(d) Validation results of work done in current model and literature[7]

It has been concluded that work done by all gases follows the same trend of work done concluded in past research work. It has been found that nitrogen has the highest value of work done, i.e. 471.6kJ/kg. While in case of previous research, the work done by nitrogen is found to be 468kJ/kg. On the other hand, work done concluded by Linde, Dual compressor Linde, Pre-cooled Linde in the current model has been validated with previous results of Kanoglu et al. [7] .It has been concluded that all the systems in the current study shows good results and in the order as compared to previous model result. Lastly, it has been observed that pre-cooled Linde model has the highest work done, i.e. 784.7kJ/kg among the other listed systems as shown in Fig.2

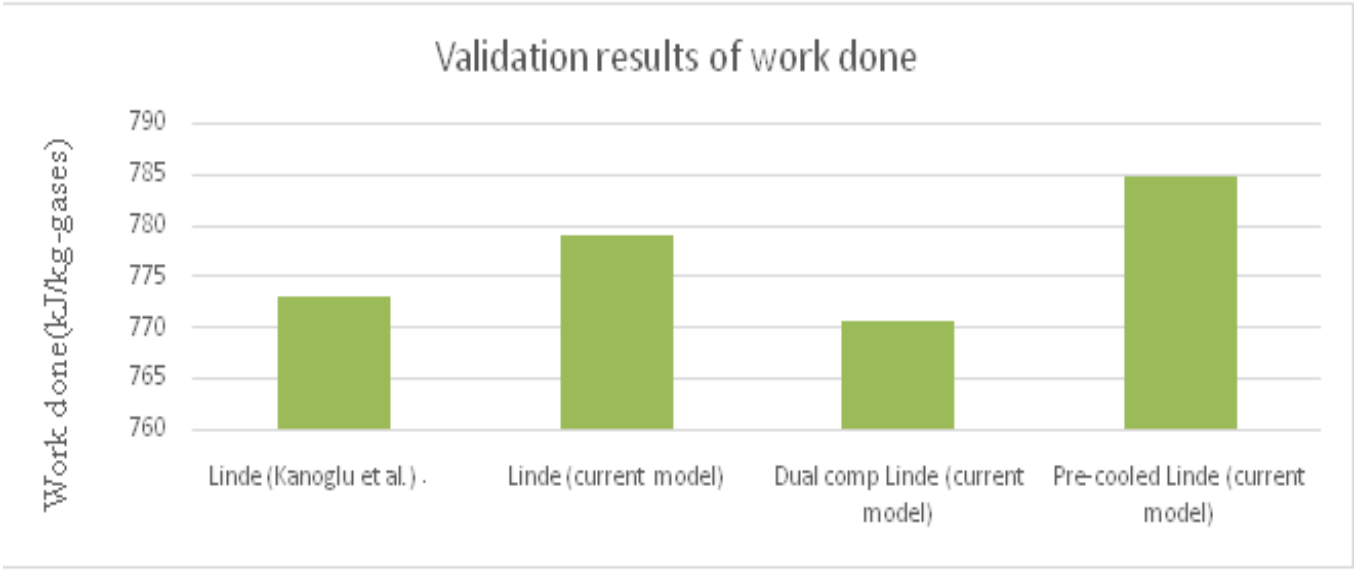


Fig.2. Validation results of work done in current model and literature for different systems

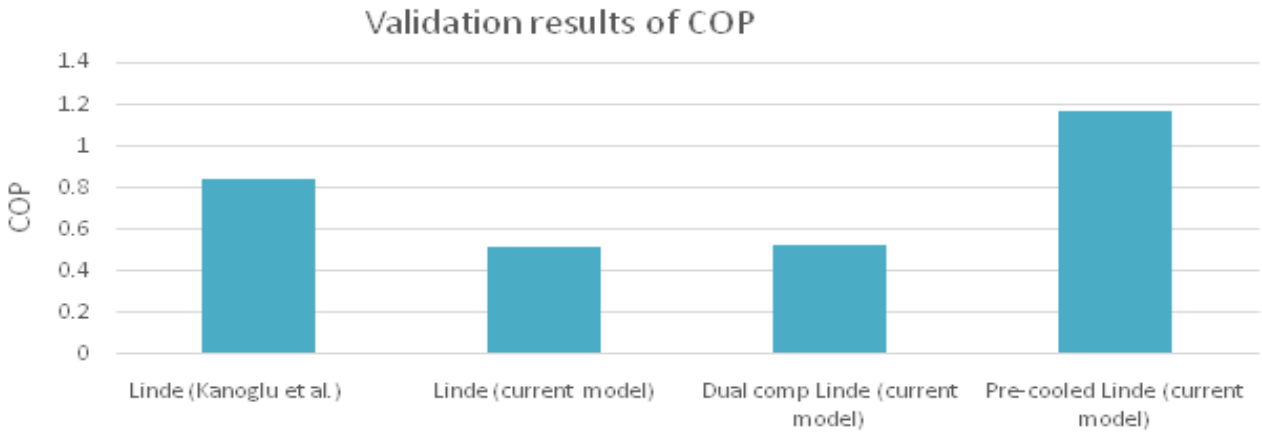


Fig.3. Validation results of COP in current model and literature for different systems

In addition, the second law efficiency results of Linde, Dual compressor Linde, and pre-cooled Linde system has been validated with the literature. Table 1

Simple Claude (AirLiquefaction)	P2	r _Exp ratio (%)	EHX effectiveness (%)	Compressor_ Efficiency _ (%)	Liquid yield y-m/mf	Work done (Btu/lb)	Work done kJ/kg gas
Timmerhaus[9]	40	0.7	100	100	0.260	382	-
Timmerhaus [9]	40	0.7	95	70	0.189	867	-
Ruhemann et al.	-	-	-	-	-	1540	-
Simple Claude	40	0.7	0.85	100	0.2828	-	396
Katizaclaude	40	0.7	0.85	100	0.1409	-	486.8
Haylentclaude	40	0.7	0.85	100	0.00599	-	309.8

Validation of simple Claude (air liquefaction) system It has been found that pre-cooled Linde has the highest second law efficiency, i.e. 46.73% among the other considered system as well as previous model as shown in Fig4

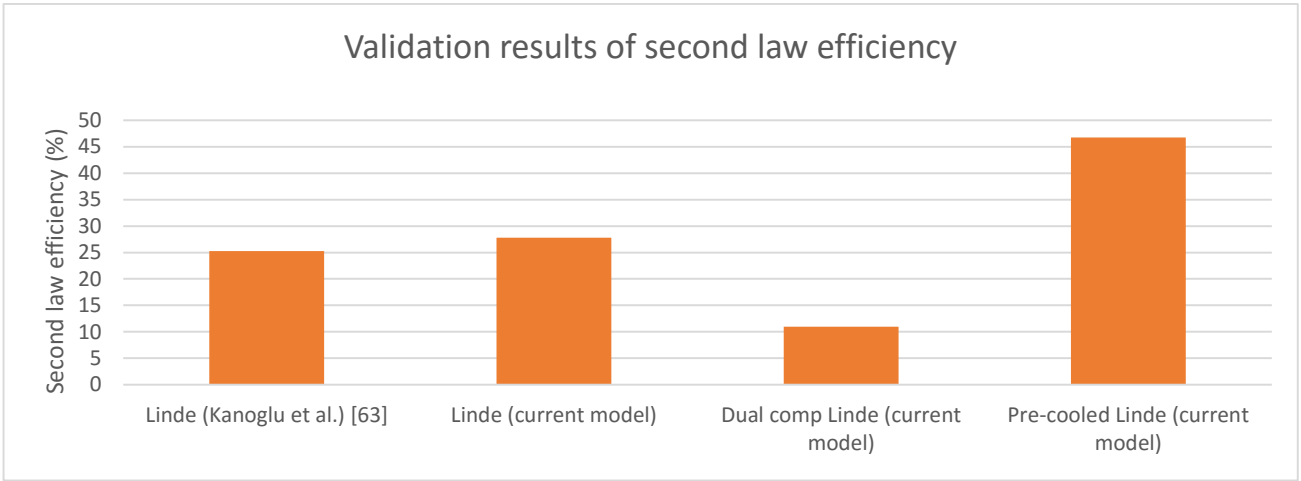


Fig.4: Validation results of second law efficiency in current mode and literature of differentLinde,Dual compressor Linde, Pre-cooled Linde system

3.2 Validation of Claude systems

Table 1 validation results of current study as well as previous model. It has been observed that at the same simulated conditions, i.e. pressure (P2), expander flow ratio, and effectiveness, the efficiency, liquid yields and work done of the current model are in good order with the previous study of Timmerhaus [9]. In this study, the concluded results of liquid yield ofsimple Claude, Katizaclaude, and Haylentclaude system is found to be0.2828, 0.1409, and 0.00599 y-m/mf, respectively. On the other hand, the concluded results of work done by these systems in current study is found to be 396, 486.8, and 309.8kJ/kg.

3.3 Validation of Hydrogen system

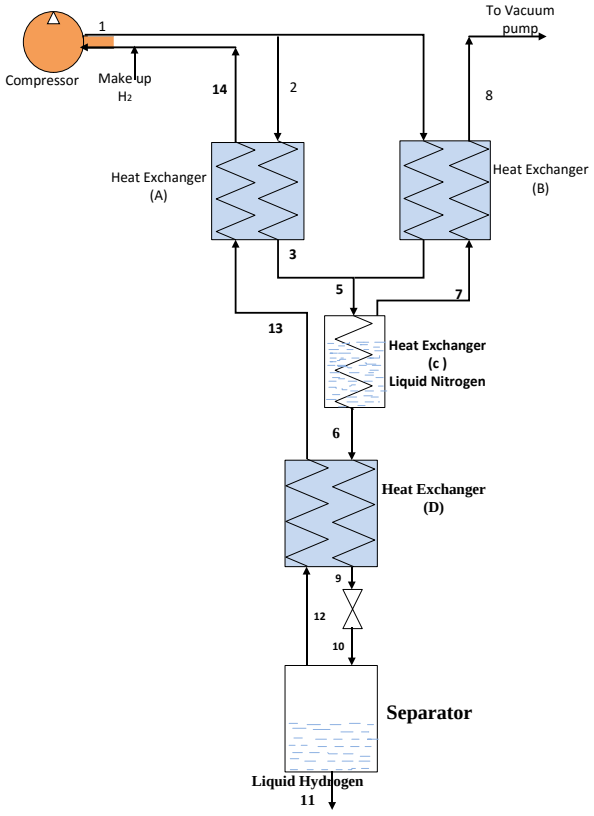


Fig: 5. Block diagram of hydrogen liquefaction system

The results of current model of hydrogen liquefaction system has been validated with the results concluded by Sargolzaei et al. [10]. The results of work done and mass flow of liquid nitrogen has been compared with the previous study results as shown in fig.3**.** It has been observed that current model shows better results relative to the results concluded in past results. It has been found that work done and mass flow of liquid nitrogen in current model was found to be 4593kJ/s and 0.5237kg/s, respectively as compared to the results of previous study, i.e. 4815kJ/s and 0.516kg/s

3.4 Validation of collin system

The collin system shown in Fig-6(a) & 6(b) is validated against the theoritical study of Sargolzaei et al. [10].

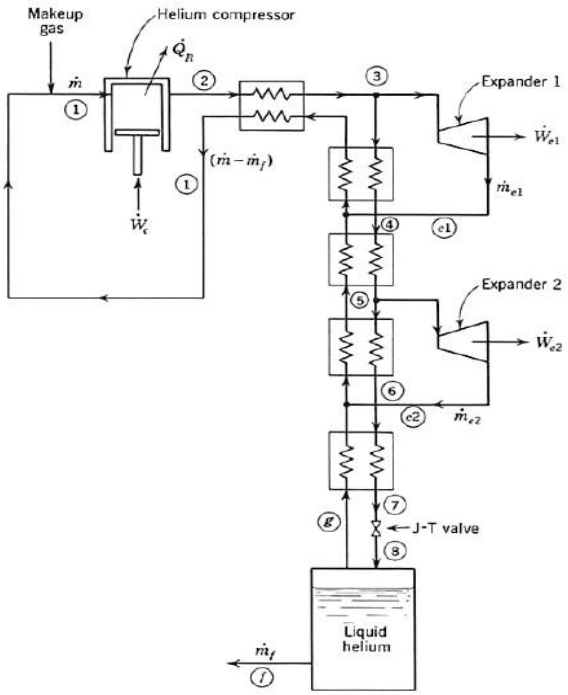


Fig: 6. (a) Schematic of Collin system

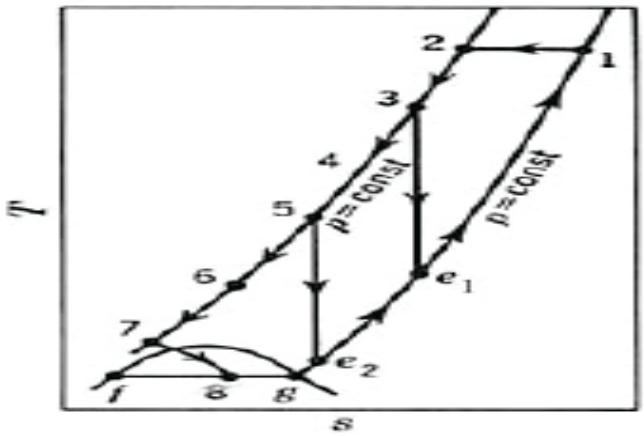


Fig: 6(b) T-S Diagram of Collin system

In the system, calculated values of second law efficiency of helium system (Collin system) found to be maximum i.e. 3.269 % at cycle pressure ratio of 11 bar. While in previous study, the maximum second law efficiency of the helium liquefaction system was approx. 7.1 % at cycle pressure ratio of 14 bar. There is marginal difference between the results of current study and previous one. Moreover, the trend of second law efficiency of current study follows the same trend as that of previous study results

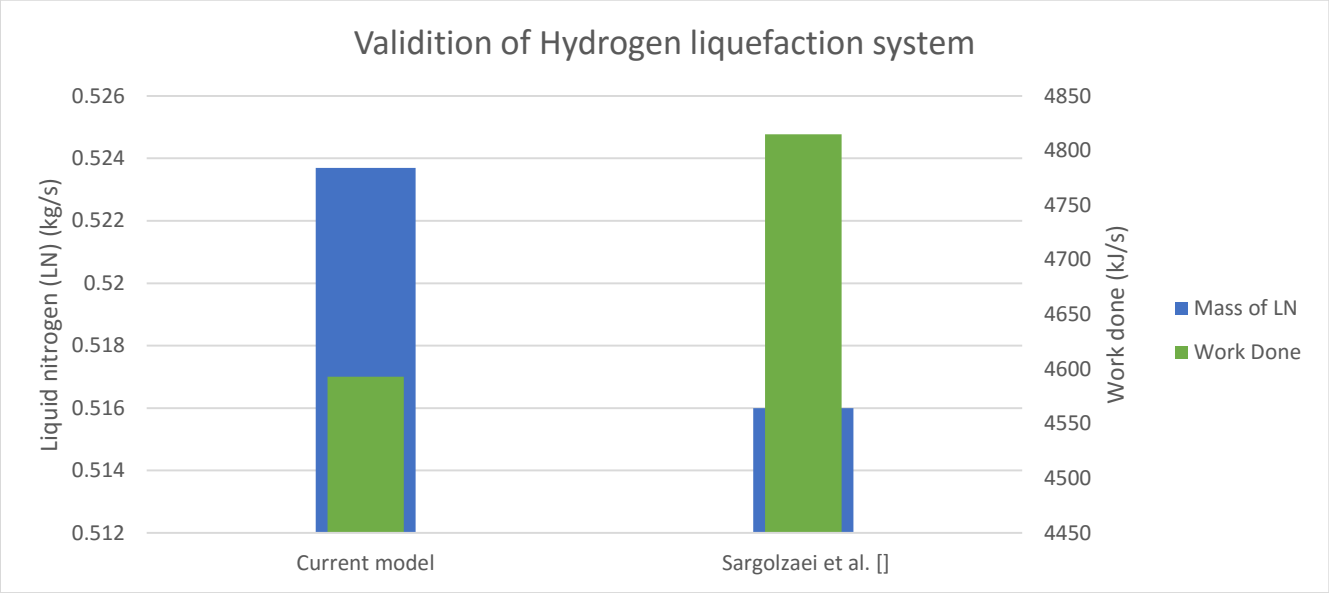


Fig.7 Validation results of liquid nitrogen and work done in current model and literature

The collin system shown in Fig-6(a) & 6(b) and Fig-7 respectively is validated. In the system, calculated values of second law efficiency of helium system (Collin system) found to be maximum i.e. 3.269 % at cycle pressure ratio of 11 bar. While in previous study, the maximum second law efficiency of the helium liquefaction system was approx. 7.1 % at cycle pressure ratio of 14 bar. There is marginal difference between the results of current study and previous one. Moreover, the trend of second law efficiency of current study follows the same trend as that of previous study results. Moreover, liquefaction rate of improved Collin system fig-6(a) & 6(b), with respect to expander flow ratio of first expander (r1) compared with the results of previous study results related to liquefaction rate. It has been observed that calculated liquefaction rate in current study was found to be 0.04 at expander flow ratio (r1) of 0.4. While as comparison with the past literature, it has depicted that the liquefaction rate was almost same for as that of currentmodel.In addition, results of exergy destruction of heat exchangers i.e. HX1, HX2, HX3, HX4, and HX5 of Collin system are compared with exergy destruction of all the same heat exchangers in the same type of helium liquefaction system. The comparative analysis shows that exergy destruction graph of HX3 and HX5 gradually decreasing in the current study between the cycle pressure ratio of 5 to 29 as same as that of previous study results of HX3 and HX5 between the cycle pressure ratio of 12 to 24 shown in Fig-9 & Fig-10 respectively .

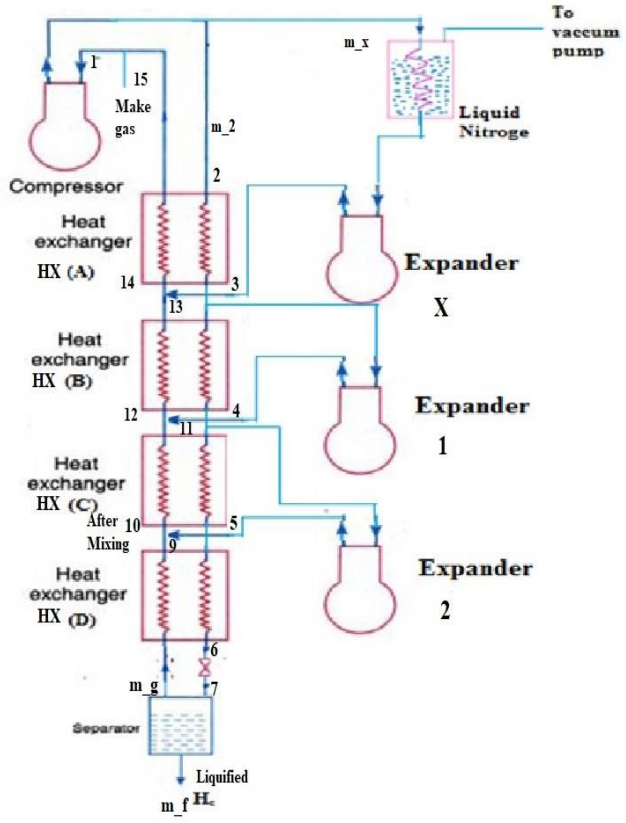


Fig: 8 Block diagram of modified Helium liquefaction system

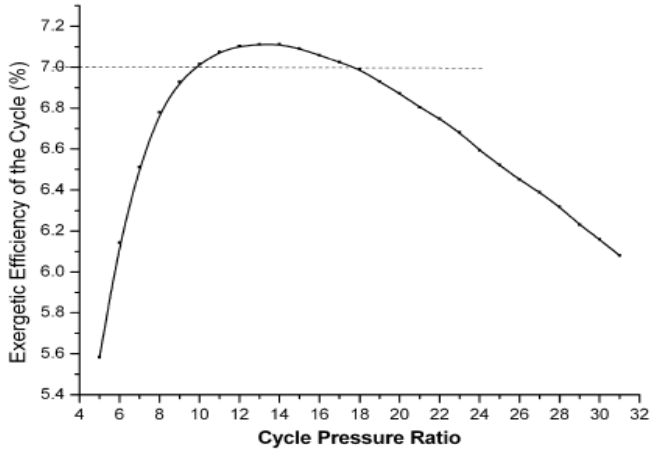


Fig.9 Validation results of exergy efficiency by R.J. Thomas et al. [11]

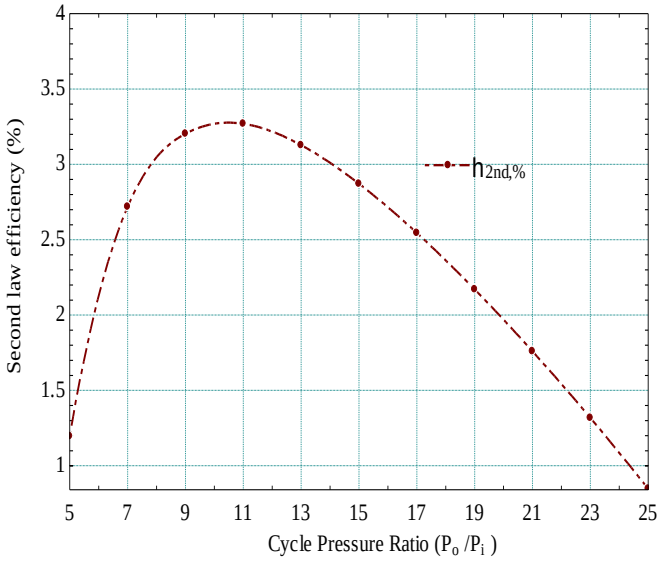


Fig.10 Validation results of exergy efficiency in current model

On the other hand, the exergy destruction rate of HX1 and HX3 does not vary so much or almost constant according to current study as same as results of HX1 and HX3 as observed from literature work [10].

4. Conclusions

Exergy analysis of cryogenics systems in which first six system with different gases and rest systems such as hydrogen, Collin, improved Collin system are evaluated on the basis of pressure ratio, compressor outlet temperature, and expander mass flow ratio. Experiment has been done on the vapor compression system to give valuable suggestion for increasing efficiency of cryogenics systems. Following results are concluded from study.

(1) During off design condition, performance of cycle does not hamper within the specific range of cyclic pressure ratio, for considered system there is always appropriate operating pressure ratio range for each working gas on which system work better

(2) All six system are compared on the basis of performance parameters at different pressure ratio, form the data observation it observed that simple Claude cycle is most suitable system because the three heat exchanger help in achieving more refrigerant effect which is in turn optimize the performance of the system.

(3) During PR increase, there is an imbalance in mass flow of forward and return stream of heat exchanger HX. Second law efficiency with the help of increasing pressure ratio which variate and create specific heat imbalance to overcome the mass imbalance.

(4) Variation in expander mass flow has highly influence the refrigeration effect of expander and overall performance of system. Optimum range of expender flow fraction (r) producing refrigeration effect is 0.55 to 0.7. Liquid production rate is highly influenced by refrigeration effect of expander.

(5) Inlet temperature of expander also plays an important factor to determine the refrigeration effect while other parameters in the system are constant. As the mass flow fraction increases through EXP, the output temperature of expander T_e also decreases which in turn lower the inlet temperature of input temperature of $T_{in\ EXP}$.

(6) In all gases methane gas show highest performance parameters in most of system while argon show lowest.

(7) The performance of hydrogen liquefaction cycle does not much deteriorate during off design condition when it is operated in selected operated range of PR 20-52 bar (the compressor suction pressure is atmospheric).

(8) Exergetic efficiency of the heat exchanger (HXD) at the lowest temperature of a hydrogen liquefier can be improved by increasing the pressure ratio because the mass imbalance gets compensated by the specific heat imbalance.

(9) While designing the hydrogen liquefaction cycle, owing to their lower exergetic efficiencies, additional care should be taken for ensuring superior heat transfer performance by the high temperature heat exchanger HXA and the lowest temperature heat exchanger HXD.

(10) Initial feasible range of pressure ratio in hydrogen liquefaction system is 20 to 87 bar, COP of the system decrease at very rapid rate but after that the rate of reduction in COP with increase PR start becoming constant with very less change while the second law efficiency show a constant reduction with increase in PR.

(11) Design parameter NTU for HX is carefully study for best performance of system. NTU term continuously decrease in hydrogen liquefaction system upto 70 bar for the J-T heat exchanger HXD and minimum at 70 bar while the variation in NTU term for HXA and HXB is quite different due to the different cold stream temperature of exchangers.

(12) Improved Collin system show high efficiency as compared to Collin system, the nitrogen chamber and extra expander gives extra refrigerant effect.

References

[1] R.S Mishra, Devendra Kumar, Utility of thermodynamic (exergy-exergy) analysis in cryogenic systems for liquefaction of gases: A Review, International Journal of Research in Engineering and Innovation, Vol-1, Issue-4, 30-42, 2017.

[2] R.S Mishra, Devendra Kumar, Thermodynamic performance comparison of six cryogenic systems, International Journal of Research in Engineering and Innovation, Vol-1, Issue-4, 95-103, 2017.

[3] R.S Mishra, Devendra Kumar, Thermodynamic analysis of kaptiza cryogetic system, International Journal of Research in Engineering and Innovation, Vol-1, Issue-4, 95-148-159, 2017.

[4] R.S Mishra, Devendra Kumar, Thermodynamic performance of modified collin cryonic system using energy-exergy analysis for liquefaction of helium gas, Vol-1, Issue-4, 95-167-178, 2017.

[5] R.S Mishra, Devendra Kumar, Thermodynamic (energy-exergy) analysis of pre-cooled linde system, , Vol-1, Issue-5, 1-6, 2017.

[6] R.S Mishra, Devendra Kumar, Thermodynamic performance analysis of claude cryogenic system, Vol-1, Issue-5, 7-20, 2017.

[7] Mehmet Kanoglu, Melda Ozdinc,Carpınlıoglu and MurtazaYıldırım, (2004) "Energy and exergy analyses of an experimental open-cycle desiccant cooling system", Applied Thermal Engineering 24, Pages 919–932.

[8] Mehmet Kanoglu, Ibrahim Dincery and Marc A. Rosen (2008)"Performance analysis of gas liquefaction cycles" International journal of energy research ,32:35–43.

[9] Timmerhaus K.D. (1989) "Cryogenic Process Engineering" "International Cryogenics Monograph Series": International Cryogenics Monograph Series, ISBN 978-1-4684-8758-9.

[10] Sargolzaei et al.,(2009)"Design of cryogenic system for liquefaction of hydrogen" The sixth international chemical engineering congree and exhibition ,ICHEC..

[11] Rijo Jacob Thomas, Parthasarathi Ghosh and Kanchan Chowdhury, (2013)"Optimum number of stages and intermediate pressure level for highest exergy efficiency in large helium liquefiers" International Journal of Refrigeration, June 2013.

[12] Rijo Jacob Thomas, Parthasarathi Ghosh, Kanchan Chowdhury, (2011)Exergy analysis of helium liquefaction systems based on modified Claude cycle with two-expanders, Cryogenics, Vol-51, Issue- 6, June 2011, Pages 287-294.

[13] Rijo Jacob Thomas, Parthasarathi Ghosh and Kanchan Chowdhury, " Exergy based analysis on different expander arrangements in helium liquefiers" international journal of refrigeration ,35 (2012).

[14] Rijo Jacob Thomas, Parthasarathi Ghosh and Kanchan Chowdhury,(2012) "Application of exergy analysis in designing helium liquefiers" 7th Biennial International Workshop "Advances in Energy Studies" Volume 37, Issue 1, January 2012, Pages 207–21.

[15] Rijo Jacob Thomas, Parthasarathi Ghosh and Kanchan Chowdhury,(2013) "Optimum number of stages and intermediate pressure level for highest exergy efficiency in large helium liquefiers" International Journal of Refrigeration, June 2013.

[16] Rijo Jacob Thomas, Parthasarathi Ghosh and Kanchan Chowdhury,(2012) " Applicability of equations of state for modelling helium systems" Cryogenics 52 , pages 375–38.

[17] G. Cammarata, A. Fichera and D. Guglielmino,(2001),"Optimization of a liquefaction plant using genetic algorithms", Applied Energy 68 ,Pages 19-29.

Eur. Phys. J. C (2018) 78:190
https://doi.org/10.1140/epjc/s10052-018-5683-6

THE EUROPEAN PHYSICAL JOURNAL C

Regular Article - Theoretical Physics

Viscous cosmology in new holographic dark energy model and the cosmic acceleration

C. P. Singh[a], **Milan Srivastava**[b]

Department of Applied Mathematics, Delhi Technological University, Bawana Road, Delhi 110 042, India

Received: 19 January 2018 / Accepted: 27 February 2018
© The Author(s) 2018. This article is an open access publication

Abstract In this work, we study a flat Friedmann–Robertson–Walker universe filled with dark matter and viscous new holographic dark energy. We present four possible solutions of the model depending on the choice of the viscous term. We obtain the evolution of the cosmological quantities such as scale factor, deceleration parameter and transition redshift to observe the effect of viscosity in the evolution. We also emphasis upon the two independent geometrical diagnostics for our model, namely the statefinder and the Om diagnostics. In the first case we study new holographic dark energy model without viscous and obtain power-law expansion of the universe which gives constant deceleration parameter and statefinder parameters. In the limit of the parameter, the model approaches to ΛCDM model. In new holographic dark energy model with viscous, the bulk viscous coefficient is assumed as $\zeta = \zeta_0 + \zeta_1 H$, where ζ_0 and ζ_1 are constants, and H is the Hubble parameter. In this model, we obtain all possible solutions with viscous term and analyze the expansion history of the universe. We draw the evolution graphs of the scale factor and deceleration parameter. It is observed that the universe transits from deceleration to acceleration for small values of ζ in late time. However, it accelerates very fast from the beginning for large values of ζ. By illustrating the evolutionary trajectories in $r-s$ and $r-q$ planes, we find that our model behaves as an quintessence like for small values of viscous coefficient and a Chaplygin gas like for large values of bulk viscous coefficient at early stage. However, model has close resemblance to that of the ΛCDM cosmology in late time. The Om has positive and negative curvatures for phantom and quintessence models, respectively depending on ζ. Our study shows that the bulk viscosity plays very important role in the expansion history of the universe.

1 Introduction

The astrophysical data obtained from high redshift surveys of supernovae [1–3], Wilkinson Microwave Anisotropy Probe (WMAP) [4,5] and the large scale structure from Slogan Digital Sky Survey (SDSS) [6,7] support the existence of dark energy (DE). The DE is considered as an exotic energy component with negative pressure. The cosmological analysis of these observations suggest that the universe consists of about 70% DE, 30% dust matter (cold dark matter plus baryons), and negligible radiation. It is the most accepted idea that DE leads to the late-time accelerated expansion of the universe. Nevertheless, the nature of such a DE is still the source of debate. Many theoretical models have been proposed to describe this late-time acceleration of the universe. The most obvious theoretical candidate for DE is the cosmological constant [8], which has the equation of state (EoS) $\omega_\Lambda = -1$. However, it suffers the so-called cosmological constant (CC) problem (the fine-tuning problem) and the cosmic coincidence problem [9–11]. Both of these problems are related to the DE density.

In order to solve the cosmological constant problems, many candidates such as quintessence [12,13], phantom [14], tachyon field [15], quintom [16], holographic dark energy [17,18], agegraphic dark energy [19,20] have been proposed to explain the nature of DE phenomenon. Starobinsky [21] and Kerner et al. [22] proposed an another way to explain the accelerated expansion of the universe by modifying the geometrical part of Einstein field equations which is known as modified gravity theory.

In recent years, the considerable interest has been noticed in the study of holographic dark energy (HDE) model to explain the recent phase transition of the universe. The idea of HDE is basically based on the holographic principle [23–25]. According to holographic principle a short distance (ultraviolet) cut-off Λ is related to the long distance (infrared) cut-off L due to the limit set by the formation of a black hole [26]. Li

[a] e-mail: cpsphd@rediffmail.com
[b] e-mail: milandtu@gmail.com

Published online: 06 March 2018

[18] argued that the total energy in a region of size L should not exceed the mass of a black hole of same size for a system with ultraviolet (UV) cut-off Λ, thus $L^3\rho_\Lambda \leq LM_{pl}^2$, where ρ_Λ is the quantum zero-point energy density caused by UV cot-off Λ and M_{pl} is the reduced Planck mass $M_{pl}^{-2} = 8\pi G$. The largest L allowed is the one saturating this inequality, thus the HDE density is defined as $\rho_\Lambda = 3c^2M_{pl}^2L^{-2}$, where c is a numerical constant. The UV cut-off is related to the vacuum energy, and the infrared (IR) cut-off is related to the large scale structure of the universe, i.e., Hubble horizon, particle horizon, event horizon, Ricci scalar, etc. The HDE model suffers the choice of IR cut-off problem. In the Ref. [17], it has been discussed that the HDE model with Hubble horizon or particle horizon can not drive the accelerated expansion of the universe. However, HDE model with event horizon can drive the accelerated expansion of the universe [18]. The drawback with event horizon is that it is a global concept of spacetime and existence of universe, depends on the future evolution of the universe. The HDE with event horizon is also not compatible with the age of some old high redshift objects [27]. Gao et al. [28] proposed IR cut-off as a function of Ricci scalar. So, the length L is given by the average radius of Ricci scalar curvature.

As the origin of the HDE is still unknown, Granda and Oliveros [29] proposed a new IR cut-off for HDE, known as new holographic dark energy (NHDE), which besides the square of the Hubble scale also contains the time derivative of the Hubble scale. The advantage is that this NHDE model depends on local quantities and avoids the causality problem appearing with event horizon IR cut-off. The authors, in their other paper [30], reconstructed the scalar field models for HDE by using this new IR cut-off in flat Friedmann–Robertson–Walker (FRW) universe with only DE content. Karami and Fehri [31] generated the results of Ref. [29] for non-flat FRW universe. Malekjani et al. [32] have studied the statefinder diagnostic with new IR cut-off proposed in [29] in a non-flat model. Sharif and Jawad [33] have investigated interacting NHDE model in non-flat universe. Debnath and Chattopadhyay [34] have considered flat FRW model filled with mixture of dark matter and NHDE, and have studied the statefinder and Om diagnostics. Wang and Xu [35] have obtained the constraints on HDE model with new IR cut-off via the Markov Chain Monte Carlo method with the combined constraints of current cosmological observations. Oliveros and Acero [36] have studied NHDE model with a non-linear interaction between the DE and dark matter (DM) in flat FRW universe.

A large number of models within modified theories can explain the DE phenomenon. It is therefore important to find the ways to discriminate among various competing models. For this purpose, Sahni et al. [37] and Alam et al. [38] introduced an important geometrical diagnostic, known as statefinder pair $\{r, s\}$ to remove the degeneracy of H_0 and q_0 of different DE models. The statefinder diagnostic has been extensively used in the literature to distinguish among various models of DE and modified theories of gravity. The various DE models have different evolutionary trajectories in (r, s) plane.

In order to complement the statefinder [37,38], a new diagnostic called Om was proposed by Sahni et al. [39] in 2008, which is used to distinguish among the energy densities of various DE models. The advantage of Om over the statefinder parameters is that, Om involves only the first order derivative of scale factor. For the ΛCDM model Om diagnostic turns out to be constant. We provide the mathematical expressions of statefinder and Om diagnostic in the appropriate section.

Evolution of the universe involves a sequence of dissipative processes. These processes include bulk viscosity, shear viscosity and heat transport. The theory of dissipation was proposed by Eckart [40] and the full causal theory was developed by Israel and Stewart [41]. In the case of isotropic and homogeneous model, the dissipative process is modeled as a bulk viscosity, see Refs. [42–50]. Brevik et al. [51] discussed the general account about viscous cosmology for early and late time universe. Norman and Brevik [52] analyze characteristic properties of two different viscous cosmology models for the future universe. In other paper, Norman and Brevik [53] derived a general formalism for bulk viscous and estimated the bulk viscosity in the cosmic fluid. The HDE model has been studied in some recent literatures [54,55] under the influence of bulk viscosity. Feng and Li [56] have investigated the viscous Ricci dark energy (RDE) model by assuming that there is bulk viscosity in the linear barotropic fluid and RDE. Singh and Kumar [57] have discussed the statefinder diagnosis of the viscous HDE cosmology. The main motive of this work is to explain the acceleration with the help of bulk viscosity for new holographic dark energy (NHDE) in GR which has not been studied sofar.

The bulk viscosity introduces dissipation by only redefining the effective pressure, p_{eff}, according as $p_{eff} = p - 3\zeta H$, where ζ is the bulk viscosity coefficient and H is the Hubble parameter. In this paper, we are interested when the universe is dominated by viscous HDE and dark matter with Granda–Oliveros IR cut-off to study the influence of bulk viscosity to the cosmic evolution. We consider the general form of bulk viscosity $\zeta = \zeta_0 + \zeta_1 H$, where ζ_0 and ζ_1 are the constants and H is the Hubble's parameter, see Refs. [42,43]. First, we discuss the non-viscous NHDE model to find out the exact solution of the field equations. In the second case, we find out the exact solutions of the field equations with constant and varying bulk viscous term. We find the exact forms of scale factor, deceleration parameter and transition redshift and discuss the evolution through the graphs. We also discuss the geometrical diagnostics like statefinder parameter and Om diagnostic to discriminate our model with ΛCDM. We plot the trajectories

of these parameters and observe the effect of bulk viscous coefficient.

The paper is organised as follows. In Sect. 2, we discuss the non-viscous HDE model with new IR cut-off. Section 3 presents the viscous NHDE model and is divided into Sects. 3.1 and 3.2. In Sects. 3.1 and 3.2 we present the solutions with constant and time varying bulk viscous term. Section 4 presents the summary of the results.

2 Non-viscous NHDE model

We consider a spatially homogeneous and isotropic flat Friedmann–Robertson–Walker (FRW) space-time, specified by the line element

$$ds^2 = dt^2 - a^2(t)\left[dr^2 + r^2(d\theta^2 + sin^2\theta d\phi^2)\right], \tag{1}$$

where $a(t)$ is the scale factor, t is the cosmic time and (r, θ, ϕ) are the comoving coordinates.

We consider that the Universe is filled with NHDE plus pressureless dark matter (DM) (ignoring the contribution of the baryonic matter here for simplicity). For Einstein field equations $R_{\mu\nu} - g_{\mu\nu}R/2 = T_{\mu\nu}$ in the units where $8\pi G = c = 1$, we obtain the Friedmann equations for the metric (1) as

$$3H^2 = \rho_m + \rho_d, \tag{2}$$

$$2\dot{H} + 3H^2 = -p_d, \tag{3}$$

where ρ_m and ρ_d are the energy density of DM and NHDE, respectively, and p_d is the pressure of the NHDE. A relation between ρ_d and p_d is given by equation of state (EoS) parameter $\omega_d = p_d/\rho_d$. Here, $H = \dot{a}/a$ is the Hubble parameter. A dot denotes a derivative with respect to the cosmic time t.

As suggested by Granda and Oliveros in paper [29], the energy density of HDE with the new IR cut-off is given by

$$\rho_d = 3(\alpha H^2 + \beta\dot{H}), \tag{4}$$

where α and β are the dimensionless parameters, which must satisfy the restrictions imposed by the current observational data.

Using (4), Eqs. (2) and (3) give

$$\dot{H} + \frac{3(1+\alpha\ \omega_d)}{(2+3\beta\ \omega_d)}H^2 = 0. \tag{5}$$

The solution of (5) is given by

$$H = \frac{1}{c_0 + \frac{3(1+\alpha\ \omega_d)}{(2+3\beta\ \omega_d)}t}, \tag{6}$$

where c_0 is an integration constant. Equation (6) can be rewritten as

$$H = \frac{H_0}{\left\{1 + \frac{3H_0(1+\alpha\ \omega_d)}{(2+3\beta\ \omega_d)}(t - t_0)\right\}}, \tag{7}$$

where H_0 is the present value of the Hubble parameter at $t = t_0$, where NHDE starts to dominate. As we know $H = \dot{a}/a$, Eq. (7) gives the solution for the scale factor which is given by

$$a = a_0\left\{1 + \frac{3(1+\alpha\ \omega_d)H_0}{(2+3\beta\ \omega_d)}(t - t_0)\right\}^{\frac{(2+3\beta\ \omega_d)}{3(1+\alpha\ \omega_d)}}, \quad \text{for } \alpha \neq -1/\omega_d,\ \beta \neq -2/3\omega_d, \tag{8}$$

where a_0 is the present value of the scale factor at a cosmic time $t = t_0$. Equation (8) shows the power-law $a \propto t^m$, where m is a constant, type expansion of the scale factor. As we know that the universe will undergo with decelerated expansion for $m < 1$, i.e., $(2 + 3\beta\omega_d) < (3 + 3\alpha\omega_d)$ in our case whereas it accelerates for $m > 1$, i.e., $(2 + 3\beta\omega_d) > (3 + 3\alpha\omega_d)$. For $m = 1$, i.e., $(2 + 3\beta\omega_d) = (3 + 3\alpha\omega_d)$, the universe will show marginal inflation. In the absence of NHDE, i.e., for $\alpha = \beta = 0$, we get the dark matter dominated scale factor, $a = a_0(1 + \frac{3}{2}H_0(t - t_0))^{2/3}$.

Let us consider the deceleration parameter (DP) which is very useful parameter to discuss the behaviour of the universe. The sign (positive or negative) of DP explains whether the universe decelerates or accelerates. It is defined as $q = -\frac{a\ddot{a}}{\dot{a}^2}$. From (8), we get

$$q = \frac{3(1+\alpha\omega_d)}{(2+3\beta\omega_d)} - 1, \tag{9}$$

which is a constant value throughout the evolution of the universe. The universe will expand with decelerated rate for $q > 0$, i.e., $(2 + 3\beta\omega_d) < (3 + 3\alpha\omega_d)$, accelerated rate for $q < 0$, i.e., $(2+3\beta\omega_d) > (3+3\alpha\omega_d)$ and marginal inflation for $q = 0$, i.e., $(2+3\beta\omega_d) = (3+3\alpha\omega_d)$. One can explicitly observe the dependence of DP q on the model parameters α, β and EoS parameter ω_d under above constraints. Thus, we can obtain a decelerated or accelerated expansion of the universe depending on the suitable choices of these parameters. In this case, the model does not show the phase transition due to power-law expansion or constant DP. The model shows marginal inflation, $q = 0$ when $\omega_d = 1/3(\beta - \alpha)$. Using Markov chain Monte Carlo method on latest observational data, Wang and Xu [35] have constrained the NHDE model and obtained the best fit values of the parameters $\alpha = 0.8502^{+0.0984+0.1299}_{-0.0875-0.1064}$ and $\beta = 0.4817^{+0.0842+0.1176}_{-0.0773-0.0955}$ with 1σ and 2σ errors in flat model. In the best fit NHDE models, they have obtained the EoS parameter $\omega_d = -1.1414 \pm 0.0608$. Putting these values of parameters (excluding the errors) in Eq.(9), we get $q = -0.7468$, which shows that our NHDE model is consistent with current observation data given in [35].

In order to discriminate among the various DE models, Sahni et al. [37] and Alam et al. [38] introduced a new geometrical diagnostic pair for DE, which is known as statefinder pair and is denoted as $\{r, s\}$. The statefinder probes the expan-

sion dynamics of the universe through higher derivatives of the scale factor and is a geometrical diagnosis in the sense that it depends on the scale factor and hence describes the spacetime. The statefinder pair is defined as

$$r = \frac{\dddot{a}}{aH^3} \quad \text{and} \quad s = \frac{r-1}{3(q-1/2)}. \tag{10}$$

Substituting the required values from (8) and (9) into (10), we get

$$r = 1 - \frac{9(1+\alpha\omega_d)}{(2+3\beta\omega_d)} + \frac{18(1+\alpha\omega_d)^2}{(2+3\beta\omega_d)^2}, \tag{11}$$

and

$$s = \frac{2(1+\alpha\omega_d)}{2+3\beta\omega_d}. \tag{12}$$

From (11) and (12), we can observe that these statefinder parameters are constant whose values depend on α, β and ω_d. As Sahni et al. [37] and Alam et al. [38] have observed that Lambda cold dark matter (ΛCDM) model and standard cold dark matter (SCDM) model have fixed point values of statefinder parameter $\{r, s\} = \{1, 0\}$ and $\{r, s\} = \{1, 1\}$, respectively. Putting the values of parameters [35] as mentioned above, we observe that this set of data do not favor the NHDE model over the ΛCDM as well as $SCDM$ model. However, NHDE model behaves like $SCDM$ model for $\alpha = 3\beta/2$. We can also observe that this model approaches to $\{r, s\} \to \{1, 0\}$ in the limit of $\alpha \to -1/\omega_d$ but there is no such value of parameters which would clearly show the ΛCDM.

3 Viscous NHDE model

In the previous section, we have observed that the non-viscous NHDE model gives constant DP which is unable to represent the phase transition. However, the observations show that the phase transition plays a vital role in describing the evolution of the universe. Therefore, it will be interesting to study the NHDE model with viscous to investigate whether a viscous NHDE model with Granda-Oliveros IR cut-off would be able to find the phase transition.

In an isotropic and homogeneous FRW universe, the dissipative effects arise due to the presence of bulk viscosity in cosmic fluids as shear viscosity plays no role. DE with bulk viscosity has a peculiar property to cause accelerated expansion of phantom type in the late time evolution of the universe [58–60]. It can also alleviate the problem like age problem and coincidence problem.

Let us assume that the effective pressure of NHDE is a sum of pressure of NHDE and bulk viscosity, i.e., the universe is filled with bulk viscous NHDE plus pressureless dark matter (DM) (ignoring the contribution of the baryonic matter here for simplicity). Then, the field equations (2) and (3) modify to

$$3H^2 = \rho_m + \rho_d, \tag{13}$$

$$2\dot{H} + 3H^2 = -\tilde{p_d}, \tag{14}$$

where $\tilde{p_d} = p_d - 3H\zeta$ is the effective pressure of NHDE. This form of effective pressure was originally proposed by Eckart [40] in the context of relativistic dissipative process occurring in thermodynamic systems went out of local thermal equilibrium. The term ζ is the bulk viscosity coefficient [61–63]. On the thermodynamical grounds, ζ is conventionally chosen to be a positive quantity and generically depends on the cosmic time t, or redshift z, or the scale factor a, or the energy density ρ_d, or a more complicated combination form. Maartens [64] assumed the bulk viscous coefficient as $\zeta \propto \rho^n$, where n is a constant. In the Refs. [42–44], the most general form of bulk viscosity has been considered with generalized equation of state. Following [42–44,65], we take the bulk viscosity coefficient in the following form.

$$\zeta = \zeta_0 + \zeta_1 H, \tag{15}$$

where ζ_0 and ζ_1 are positive constants. The motivation for considering this bulk viscosity has been discussed in Refs. [42–44].

From the dynamical equations (13) and (14), we can formulate a first order differential equation for the Hubble parameter by using Eqs. (4) and (15) as,

$$\dot{H} + \frac{3(1+\alpha\omega_d)}{(2+3\beta\omega_d)}H^2 - \frac{3\zeta}{(2+3\beta\omega_d)}H = 0. \tag{16}$$

It can be observed that Eq. (16) reduces to the non-viscous equation (5) for $\zeta = 0$ as discussed in previous section.

In the following subsections, we classify different viscous NHDE models arises due to the constant and variable bulk viscous coefficient. We analyze the behavior of the scale factor, DP, statefinder parameter and Om diagnostic of these different cases.

3.1 NHDE Model with constant bulk viscosity

The simplest case of viscous NHDE model is to be taken with constant bulk viscous coefficient. Therefore, assuming $\zeta_1 = 0$ in Eq. (15), the bulk viscous coefficient reduces to

$$\zeta = \zeta_0 = \text{const.} \tag{17}$$

Using (17) into (16), we get

$$\dot{H} + \frac{3(1+\alpha\omega_d)}{(2+3\beta\omega_d)}H^2 - \frac{3\zeta_0}{(2+3\beta\omega_d)}H = 0. \tag{18}$$

The solution of (18) in terms of cosmic time t can be given by

$$H = e^{\frac{3\zeta_0 t}{(2+3\beta\omega_d)}}\left[c_1 + \frac{(1+\alpha\omega_d)}{\zeta_0}\, e^{\frac{3\zeta_0 t}{(2+3\beta\omega_d)}}\right]^{-1}, \tag{19}$$

where c_1 is the constant of integration. From (19), we get the evolution of the scale factor as

$$a = c_2\left[c_1 + \frac{(1+\alpha\omega_d)}{\zeta_0}\, e^{\frac{3\zeta_0 t}{(2+3\beta\omega_d)}}\right]^{\frac{(2+3\beta\omega_d)}{3(1+\alpha\omega_d)}}, \tag{20}$$

where c_2 is an integration constant. The above scale factor can be rewritten as

$$a = \left[1 + \frac{H_0(1+\alpha\omega_d)}{\zeta_0}\left\{e^{\frac{3\zeta_0(t-t_0)}{(2+3\beta\omega_d)}} - 1\right\}\right]^{\frac{(2+3\beta\omega_d)}{3(1+\alpha\omega_d)}}, \quad \text{for } \alpha \neq -1/\omega_d,\ \zeta_0 \neq 0 \tag{21}$$

where t_0 is the present cosmic time. Here, we get exponential form of the scale factor which shows non-singular solution. Equation (21) shows that in early stages of the evolution, the scale factor can be approximated as $a(t) \sim \left[1 + \frac{3H_0(1+\alpha\omega_d)}{(2+3\beta\omega_d)}(t-t_0)\right]^{\frac{(2+3\beta\omega_d)}{3(1+\alpha\omega_d)}}$, and as $(t-t_0) \to \infty$, the scale factor approaches to a form like that of the de Sitter universe, i.e., $a(t) \to \exp\left[\frac{3\zeta_0(t-t_0)}{(2+3\beta\omega_d)}\right]$. Thus, we observe that the universe starts with a finite volume followed by an early decelerated epoch, then making a transition into the accelerated epoch in the late time of the evolution.

From (21), we can obtain the Hubble parameter in terms of scale factor a as

$$H(a) = \frac{H_0}{(1+\alpha\omega_d)} \times\left[\frac{\zeta_0}{H_0} + \{(1+\alpha\omega_d) - \frac{\zeta_0}{H_0}\}\, a^{-\frac{(3+3\alpha\omega_d)}{(2+3\beta\omega_d)}}\right], \tag{22}$$

where H_0 is the present value of the Hubble parameter and we have made the assumption that the present value of scale factor is $a_0 = 1$. The derivative of $\dot{a}$ with respect to a can be obtained as [65]

$$\frac{d\dot{a}}{da} = \frac{H_0}{(1+\alpha w_d)}\left[\frac{\zeta_0}{H_0} - \left\{(1+\alpha w_d) - \frac{\zeta_0}{H_0}\right\} \times\left(\frac{(1+3(\alpha-\beta)w_d)}{2+3\beta w_d}\right) a^{-\frac{3(1+\alpha w_d)}{(2+3\beta w_d)}}\right]. \tag{23}$$

Equation (23) to zero, the transition scale factor a_T can be obtained as

$$a_T = \left[\frac{(1+3(\alpha-\beta)w_d)\,\{(1+\alpha w_d)H_0 - \zeta_0\}}{(2+3\beta w_d)\zeta_0}\right]^{\frac{(2+3\beta w_d)}{3(1+\alpha w_d)}}. \tag{24}$$

The corresponding transition redshift z_T, where $a = (1+z)^{-1}$, is

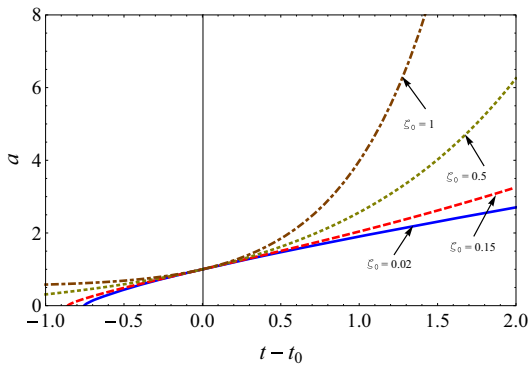


Fig. 1 The scale factor evolution for different values of $\zeta_0 > 0$ with $H_0 = 1$, $\omega_d = -0.5$, $\alpha = 0.8502$ and $\beta = 0.4817$

$$z_T = \left[\frac{(1+3(\alpha-\beta)w_d)\,\{(1+\alpha w_d)H_0 - \zeta_0\}}{(2+3\beta w_d)\zeta_0}\right]^{-\frac{(2+3\beta w_d)}{3(1+\alpha w_d)}} - 1. \tag{25}$$

From (24) or (25), we observe that for $\zeta_0 = \frac{\{1+3(\alpha-\beta)w_d\}H_0}{3}$, the transition from decelerated phase to accelerated phase occurs at $a_T = 1$ or $z_T = 0$, which corresponds to the present time of the universe. On taking the observed values of $\alpha = 0.8502$ and $\beta = 0.4817$ [35], $H_0 = 1$ and $\omega_d = -0.5$ in this expression of ζ_0, we get $\zeta_0 = 0.15$. Figure 1 represents the evolution of the scale factor $a(t)$ with respect to time $(t - t_0)$ for different values of $\zeta_0 > 0$. It is observed that the transition from decelerated to accelerated phase takes place in late time for small values of ζ_0, i.e., in $0 < \zeta_0 < 0.15$. The transition from decelerated phase to accelerated one occurs at $a_T = 1$ for $\zeta_0 = 0.15$ which corresponds to the present time of the universe. However, the transition takes place in early stages of the evolution for large values of ζ_0, i.e., $\zeta_0 > 0.15$. Thus, as the value of ζ_0 increases, the scale factor expands more rapidly with exponential rate.

The result regarding the transition of the universe into the accelerated epoch discussed above can be further verified by studying the evolution of DP q. In this case, DP is given by

$$q = \frac{3\left\{(1+\alpha\omega_d) - \frac{\zeta_0}{H_0}\right\}}{(2+3\beta\omega_d)}\, e^{-\frac{3\zeta_0(t-t_0)}{(2+3\beta\omega_d)}} - 1. \tag{26}$$

Thus, we find a time-varying DP in the case of constant viscous NHDE, which describes the phase transition of the evolution of the universe. DP must change its sign at $t = t_0$, i.e., the time at which the viscous NHDE begins to dominate. This time can be achieved if $[1+3(\alpha-\beta)\omega_d]H_0 = 3\zeta_0$. The universe must decelerate for $t < t_0$ and accelerate for $t > t_0$ for any parametric values of α, β and ω_d.

From (26), DP can be written in terms of scale factor as

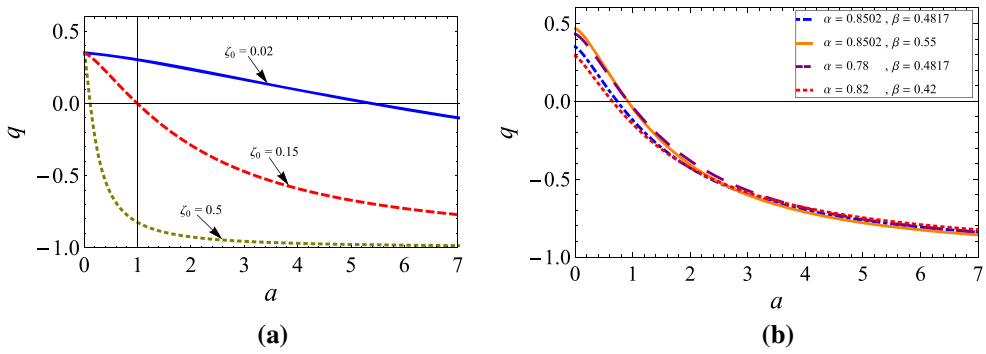


Fig. 2 **a** The variation of q with a for different values of ζ_0 with fixed $\omega_d = -0.5$, $\alpha = 0.8502$ and $\beta = 0.4817$. **b** The variation of q with a for different values of α and β with fixed $\zeta_0 = 0.2$ and $\omega_d = -0.5$

$$q = \frac{\{3(1+\alpha\omega_d) - 3\zeta_0\}}{(2+3\beta\omega_d)} \times \left[\frac{(1+\alpha\omega_d)}{\left(a^{\frac{3+3\alpha\omega_d}{2+3\beta\omega_d}} - 1\right)\zeta_0 + (1+\alpha\omega_d)}\right] - 1. \tag{27}$$

In terms of red shift z, the above equation becomes

$$q = \frac{\{3(1+\alpha\omega_d) - 3\zeta_0\}}{(2+3\beta\omega_d)} \times \left[\frac{(1+\alpha\omega_d)}{\left((1+z)^{-\frac{3+3\alpha\omega_d}{2+3\beta\omega_d}} - 1\right)\zeta_0 + (1+\alpha\omega_d)}\right] - 1. \tag{28}$$

When the bulk viscous parameter and all other parameters are zero, the deceleration parameter $q = 1/2$, which corresponds to a decelerating matter-dominated universe with null bulk viscosity. However, when only the bulk viscous term $\zeta_0 = 0$, the value of q is same as obtained in Eq. (9) for non-viscous NHDE model.

The present value of q corresponds to $z = 0$ or $a = 1$ is,

$$q_0 = q(a=1) = \frac{3(1+\alpha\omega_d) - 3\zeta_0}{(2+3\beta\omega_d)} - 1. \tag{29}$$

This equation shows that if $3\zeta_0 = [1 + 3(\alpha - \beta)\omega_d]$, the deceleration parameter $q_0 = 0$. This implies that the transition into the accelerating phase would occur at the present time. The current DP $q_0 < 0$ if $3\zeta_0 > [1 + 3(\alpha - \beta)\omega_d]$, implying that the present universe is in the accelerating epoch and it entered this epoch at an early stage. But $q_0 > 0$ if $3\zeta_0 < [1 + 3(\alpha - \beta)\omega_d]$ implying that the present universe is decelerating and it will be entering the accelerating phase at a future time. The evolution of q with a is shown in Fig. 2 by taking fixed constant α and β (or ζ_0), from which we can see that the evolution of the universe is from deceleration to acceleration. Figure 2a illustrates the evolutionary history of DP for different value of ζ_0 with $\omega_d = -0.5$, $\alpha = 0.8502$ and $\beta = 0.4817$. On considering $\alpha = 0.8502$, $\beta = 0.4817$ [35] and $\omega_d = -0.5$ in Eq. (29), we get $\zeta_0 = 0.15$ which gives $q_0 = 0$. Thus, the transition into accelerating phase would occur at present time. If $\zeta_0 > 0.15$, $q_0 < 0$, i.e., the universe is in accelerating epoch and it entered this epoch at an early stage. If $\zeta_0 < 0.15$, $q_0 > 0$, i.e., the universe is in decelerating epoch and it enters in an accelerating phase in future. Thus, the larger the value ζ_0 is, the earlier acceleration occurs. The similar results for a fixed ζ_0 also appear in Fig. 2b. The larger the values α and β is, the earlier q changes it sign from $q > 0$ to $q < 0$ for a fixed ζ_0. In both Fig. 2a, b, we observe that $q \to -1$ in late time of evolution.

Statefinder diagnostic

From above discussion we conclude that there is a transition from decelerated phase to accelerated one in future for small bulk viscous coefficient, $0 < \zeta_0 < 0.15$. It takes place to the present time for $\zeta = 0.15$. However, the transition takes place in past for $\zeta > 0.15$. The behavior of scale factor and deceleration parameter shows that the constant bulk viscous coefficient plays the role of DE. In what follows, we will present the statefinder diagnostic of the viscous NHDE model . In this model, the statefinder parameters defined in (10) can be obtained as

$$r = 1 + \frac{9\left(\frac{\zeta_0}{H_0} - (1+\alpha\omega_d)\right)\left(1 - \frac{1+\alpha\omega_d}{(2+3\beta\omega_d)}\right)}{(2+3\beta\omega_d)} e^{-\frac{3\zeta_0(t-t_0)}{(2+3\beta\omega_d)}} + \frac{9\left(\frac{\zeta_0}{H_0} - (1+\alpha\omega_d)\right)^2}{(2+3\beta\omega_d)^2} e^{-\frac{6\zeta_0(t-t_0)}{(2+3\beta\omega_d)}}, \tag{30}$$

and

$$s = \frac{\frac{2\left(\frac{\zeta_0}{H_0} - (1+\alpha\omega_d)\right)\left(1 - \frac{1+\alpha\omega_d}{(2+3\beta\omega_d)}\right)}{(2+3\beta\omega_d)} e^{-\frac{3\zeta_0(t-t_0)}{(2+3\beta\omega_d)}} + \frac{2\left(\frac{\zeta_0}{H_0} - (1+\alpha\omega_d)\right)^2}{(2+3\beta\omega_d)^2} e^{-\frac{6\zeta_0(t-t_0)}{(2+3\beta\omega_d)}}}{\frac{2\left((1+\alpha\omega_d) - \frac{\zeta_0}{H_0}\right)}{(2+3\beta\omega_d)} e^{-\frac{3\zeta_0(t-t_0)}{(2+3\beta\omega_d)}} - 1}. \tag{31}$$

Here, these values of statefinder parameter are time-dependent and this is due to the bulk viscous coefficient ζ_0.

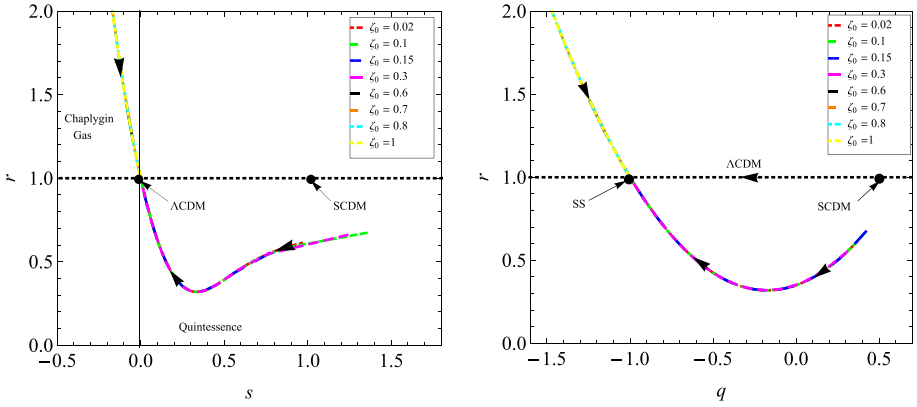


Fig. 3 **a** The $r-s$ trajectories are plotted in $r-s$ plane for different values of $\zeta_0 > 0$ with $\omega_d = -0.5$, $\alpha = 0.8502$ and $\beta = 0.4817$. The arrows represent the directions of the evolutions of statefinder diagnostic pair with time. The curves are coinciding with each other for smaller and larger values of ζ_0. **b** The $r-q$ trajectories are plotted in $r-q$ plane for different values of $\zeta_0 > 0$ with $\omega_d = -0.5$, $\alpha = 0.8502$ and $\beta = 0.4817$. The arrows represent the directions of the time evolution pair $\{r, q\}$ with time. The curves are coinciding with each other for smaller and larger values of ζ_0

In previous Sect. 2, we see that the diagnostic pair is constant in the absence of viscous term. As we can observe from the above two equations that in the limit of $(t - t_0) \to \infty$, the model approaches to $\{r, s\} \to \{1, 0\}$ and for this limit we get $q \to -1$. We draw the trajectories of the statefinder pair $\{r, s\}$ in $r - s$ plane for different values of constant ζ_0 with $\omega_d = -0.5$, $H_0 = t_0 = 1$, $\alpha = 0.8502$ and $\beta = 0.4817$ as shown in Fig. 3a. Here, we observe that the model approaches to $\{r, s\} \to \{1, 0\}$ for all positive values of ζ_0. In Fig. 3a, the fixed points $\{r, s\} = \{1, 1\}$ and $\{r, s\} = \{1, 0\}$ are shown as $SCDM$ and ΛCDM models, respectively.

It is observed from figures that the statefinder diagnostic of our model can discriminate from other DE models. For example, in quiessence with constant EoS parameter [37,38] and the Ricci dark energy (RDE) model [66], the trajectory in $r - s$ plane is a vertical segment, i.e. s is constant during the evolution of the universe whereas the trajectories for the Chaplygin gas (CG) [67] and the quintessence (inverse power-law) models (Q) [37,38] are similar to arcs of a parabola (downward and upward) lying in the regions $s < 0, r > 1$ and $s > 0, r < 1$, respectively. In modified NHDE model [68], the trajectory in $r-s$ is from left to right. In holographic dark energy model with future event horizon [69,70] its evolution starts from the point $s = 2/3$, $r = 1$ and ends at ΛCDM model fixed point in future.

In Fig. 3a, the plot reveals that the $r - s$ plane can be divided into two regions $r < 1, s > 0$ and $r > 1, s < 0$ which are showing the similar characteristics to Q and CG models, respectively. The present model starts in both regions $r < 1, s > 0$ and $r > 1, s < 0$, and end on the ΛCDM point in the $r - s$ plane in far future. The trajectories in the right side of the vertical line correspond to the different values of ζ_0, i.e., $\zeta_0 = 0.02$, $\zeta_0 = 0.10$, $\zeta_0 = 0.15$ and $\zeta_0 = 0.30$ lying in the range $0 < \zeta_0 \leq 0.57$ whereas the trajectories to the left side of the vertical line correspond to $\zeta_0 > 0.57$, i.e., $\zeta_0 = 0.60$, $\zeta_0 = 0.70$, $\zeta_0 = 0.80$ and $\zeta_0 = 1.00$. This reveals that smaller values of ζ_0 give the model similar to Q model and larger values correspond to the CG model. We find that the evolutions are coinciding each other for all different values of ζ_0 in both regions.

We also study the evolutionary behaviour of constant viscous NHDE model in $r - q$ plane. For different values of ζ_0, as taken in $\{r, s\}$, the trajectories are shown in Fig. 3b for $w_d = -0.5$, $H_0 = t_0 = 1$, $\alpha = 0.8502$ and $\beta = 0.4817$. The $SCDM$ model and steady state (SS) model corresponds to fixed point $\{r, q\} = \{1, 0.5\}$ and $\{r, q\} = \{1, -1\}$, respectively. It can be seen that there is a sign change of q from positive to negative which explain the recent phase transition. The trajectories show that viscous NHDE models commence evolving from different points for different values of ζ_0 with respect to ΛCDM which starts from $SCDM$ fixed point. The viscous NHDE model always converges to SS model as ΛCDM, Q and CG models in late-time evolution of the universe. Thus, the constant viscous NHDE model is compatible with Q and CG models.

The above discussion concludes the effect of viscous term in NHDE model. Let us discuss the model in view point of model parameters α and β. Figure 4a, b show the trajectories in $r-s$ and $r-q$ planes, respectively, for the different values of α and β with constant $\omega_d = -0.5$, $H_0 = t_0 = 1$ and $\zeta_0 = 0.02$. The arrows in the diagram denote the evolution directions of the statefinder trajectories and $r-q$ trajectories. From Fig. 4a, we observe that for this fixed value of ζ_0 the constant viscous NHDE model always correspond to the Q

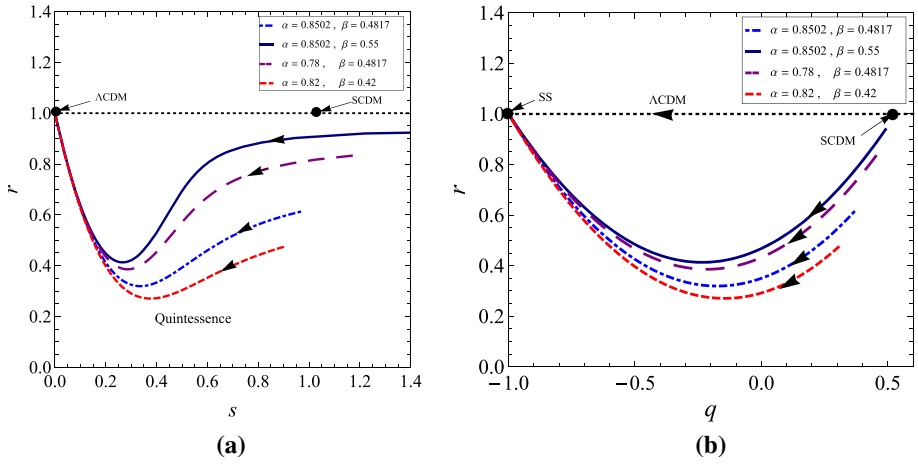


Fig. 4 **a** The $r-s$ trajectories are plotted in $r-s$ plane for different values of α and β with $\omega_d = -0.5$ and $\zeta_0 = 0.02$. The arrows represent the directions of the evolutions of statefinder diagnostic pair with time. **b** The $r-q$ trajectories are plotted in $r-q$ plane for different values of α and β with $\omega_d = -0.5$ and $\zeta_0 = 0.02$. The arrows represent the directions of the time evolution pair $\{r, q\}$ with time

model. It may start from the vicinity of $SCDM$ model in early time of evolution for some values of α and β, e.g., $(\alpha, \beta) = (0.8502, 0.55)$. In late-time of evolution the model always converges to ΛCDM model for any values of (α, β).

The panel (b) of Fig. 4 shows the time evolution of the $r-q$ trajectories in $r-q$ plane. The horizontal line at $r = 1$ corresponds to the time evolution of the ΛCDM model. The signature change from positive to negative in q clearly explain the phase transition of the universe. The constant viscous NHDE model may start from the vicinity of the $SCDM$ model ($\{r, q\} = \{1, 0.5\}$) for some values of α and β (e.g., $\alpha = 0.8502$, $\beta = 0.55$). However, the constant viscous NHDE model approaches to the SS model as the ΛCDM and Q models in future . Thus, the viscous NHDE model is compatible with the ΛCDM and Q models with variables model parameters and constant value of ζ_0.

Thus, we conclude that our model corresponds to both Q and CG models for the different values of viscous coefficient ζ_0 whereas for the different values of model parameters α and β with respect to the fixed value of ζ_0, our model only corresponds to Q model. Hence, we can conclude that due to the viscosity NHDE model is compatible with the Q and CG models. By above analysis, we can say that the bulk viscous coefficient and model parameters play the important roles in the evolution of the universe, i.e., they both determine the evolutionary behavior as well as the ultimate fate of the universe.

Om diagnostic

In addition to statefinder $\{r, s\}$, another diagnostic model, *Om(z)* is widely used to discriminate DE models. It is a new geometrical diagnostic which combines Hubble parameter H and redshift z. The *Om(z)* diagnostic [39] has been proposed to differentiate ΛCDM to other DE models. Many authors [71–73] have studied the DE models based on *Om(z)* diagnostic. Its constant behaviour with respect to z represents that DE is a cosmological constant (ΛCDM). The positive slope of *Om(z)* with respect to z shows that the DE behaves as phantom and negative slope shows that DE behaves like quintessence. According to Ref. [39], *Om(z)* parameter for spatially flat universe is defined as

$$Om(z) = \frac{\frac{H^2(z)}{H_0^2} - 1}{(1+z)^3 - 1}, \tag{32}$$

where H_0 is the present value of the Hubble parameter. Since the *Om(z)* involves only the first derivative of scale factor, so it is easier to reconstruct it as compare to statefinder parameters. It has been shown that the slope of *Om(z)* can distinguish dynamical dark energy from the cosmological constant in a robust manner, both with and without reference to the value of the matter density.

On substituting the required value of $H(z)$ from (22) in (32), we get the value of *Om(z)* as

$$Om(z) = \frac{\left[\frac{\zeta_0}{H_0} + \left\{1 + \alpha\omega_d - \frac{\zeta_0}{H_0}\right\}(1+z)^{\frac{3(1+\alpha\omega_d)}{2+3\beta\omega_d}}\right]^2 - (1+\alpha\omega_d)^2}{(1+\alpha\omega_d)^2[(1+z)^3 - 1]}. \tag{33}$$

For comparison, we plot *Om(z)* trajectory with respect to z for different values of $\zeta_0 > 0$ (or α and β) with fixed α and β (or ζ_0), with $H_0 = 1$ and $\omega_d = -0.5$ as shown in Fig. 5. From Fig. 5a, we observe that for $0 < \zeta_0 \leq 0.57$, the trajectory shows the negative slope, i.e., the DE behaves like quintessence and for $\zeta_0 > 0.57$, the positive slope of the *Om* trajectory is observed, i.e., the DE behaves as phantom. For the late future stage of evolution when $z = -1$, we get $Om(z) = 1 - \frac{\zeta_0^2}{H_0^2(1+\alpha\omega_d)^2}$, which is the constant value of *Om(z)*. Thus for $z = -1$, the DE will correspond to ΛCDM.

The Fig. 5b shows the *Om(z)* trajectory for different values of model parameters α and β with fixed $\zeta_0 = 0.02$, $\omega_d = -0.5$ and $H_0 = 1$. This trajectory only shows the negative curvature which imply that the DE behaves like quintessence.

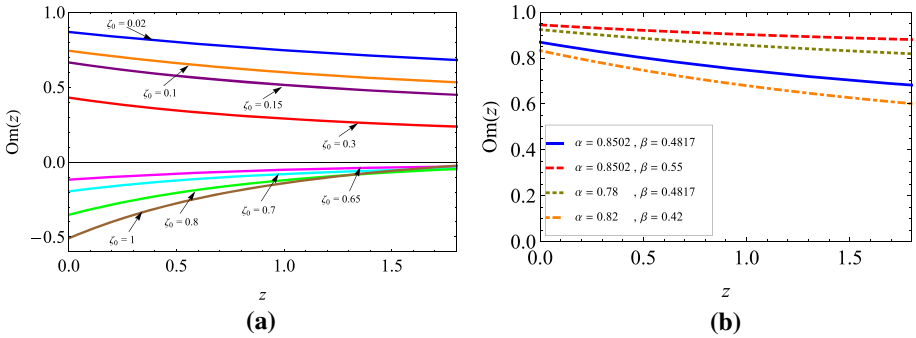


Fig. 5 **a** The *Om(z)* evolutionary diagram of viscous NHDE for different values of $\zeta_0 > 0$ with fixed $\omega_d = -0.5$, $\alpha = 0.8502$ and $\beta = 0.4817$. **b** The *Om(z)* evolutionary diagram of viscous NHDE for different values of α and β with fixed $\zeta_0 = 0.02$ with $\omega_d = -0.5$

From the above discussion with constant bulk viscous coefficient, we find that the constant ζ_0 (or cosmological parameters α and β) play important roles in the evolution of the universe, i.e., they both determine the evolutionary behavior as well as the ultimate fate of the universe.

3.2 Solution for variable bulk viscosity coefficient

In this section, we consider two cases: **(i)** $\zeta_0 = 0$ and $\zeta_1 \neq 0$, and **(ii)** $\zeta_0 \neq 0$ and $\zeta_1 \neq 0$.

Case (i) $\zeta_0 = 0$ and $\zeta_1 \neq 0$:

In this case, the bulk viscosity coefficient given in (15) reduces to

$$\zeta = \zeta_1 H, \tag{34}$$

which shows that the bulk viscous coefficient is directly proportional to Hubble parameter.

Using (34) into (16), we get

$$\dot{H} + \frac{3(1-\zeta_1+\alpha\omega_d)}{(2+3\beta\omega_d)} H^2 = 0. \tag{35}$$

The above equation is similar to the Eq.(5) obtained in the case of non-viscous NHDE model in Sect. 2. The solution of (35) for H in terms of t is given by

$$H = \frac{1}{c_3 + \frac{3(1-\zeta_1+\alpha\omega_d)}{(2+3\beta\omega_d)} t}, \tag{36}$$

where c_3 represents the constant of integration. The scale factor can be obtained as

$$a = a_0 \left[1 + \frac{3(1-\zeta_1+\alpha\omega_d)H_0}{(2+3\beta\omega_d)}(t-t_0)\right]^{\frac{(2+3\beta\omega_d)}{3(1-\zeta_1+\alpha\omega_d)}}, \quad \text{for } \zeta_1 \neq (1+\alpha\omega_d), \quad \beta \neq -\frac{2}{3\omega_d} \tag{37}$$

The scale factor varies as power-law expansion. Now, the DP is

$$q = \frac{3(1-\zeta_1+\alpha\omega_d)}{(2+3\beta\omega_d)} - 1. \tag{38}$$

which is a constant value. Such form of ζ gives no transition phase. The positive or negative sign of q depends on whether $3\zeta_1 < (1+3(\alpha-\beta)\omega_d)$ or $3\zeta_1 > (1+3(\alpha-\beta)\omega_d)$, respectively.

Now, the statefinder parameter can be given as

$$r = 1 - \frac{9(1+\alpha\omega_d-\zeta_1)}{(2+3\beta\omega_d)} + \frac{18(1+\alpha\omega_d-\zeta_1)^2}{(2+3\beta\omega_d)^2}, \tag{39}$$

and

$$s = \frac{2(1+\alpha\omega_d-\zeta_1)}{(2+3\beta\omega_d)}. \tag{40}$$

In this case the statefinder pair is constant. In the limit of $\zeta_1 \to (1+\alpha\omega_d)$, the statefinder pair $\{r, s\} \to \{1, 0\}$ and for $\zeta_1 = \frac{(2\alpha-3\beta)\omega_d}{2}$, this model behaves as SCDM, i.e., $\{r, s\} = \{1, 1\}$.

Case (ii) $\zeta_0 \neq 0$ and $\zeta_1 \neq 0$:

Let us consider the more general form of the bulk viscous coefficient, i.e., $\zeta = \zeta_0 + \zeta_1 H$. Using (15) into (16), we get

$$\dot{H} + \frac{3(1-\zeta_1+\alpha\omega_d)}{(2+3\beta\omega_d)} H^2 - \frac{3\zeta_0}{(2+3\beta\omega_d)} H = 0. \tag{41}$$

Solving the above equation, we get the Hubble parameter in terms of t as

$$H = H_0 e^{\frac{3\zeta_0(t-t_0)}{(2+3\beta\omega_d)}} \times \left[1 + \frac{H_0(1-\zeta_1+\alpha\omega_d)}{\zeta_0}\left\{e^{\frac{3\zeta_0(t-t_0)}{(2+3\beta\omega_d)}} - 1\right\}\right]^{-1}, \tag{42}$$

where H_0 is the present value of the Hubble parameter and we have made the assumption that the present value of scale factor is $a_0 = 1$. The solution of (42) for the scale factor a in terms of t is given by

$$a = \left[1 + \frac{H_0(1-\zeta_1+\alpha\omega_d)}{\zeta_0}\left\{e^{\frac{3\zeta_0(t-t_0)}{(2+3\beta\omega_d)}} - 1\right\}\right]^{\frac{(2+3\beta\omega_d)}{3(1-\zeta_1+\alpha\omega_d)}}, \quad \text{for } \zeta_0 \neq 0, \quad \zeta_1 \neq (1+\alpha\omega_d) \tag{43}$$

Here, we get an exponential type scale factor with the viscous terms. As $(t-t_0) \to 0$, the scale factor behaves as

$$a \to \left[1 + \frac{3H_0(1-\zeta_1+\alpha\omega_d)(t-t_0)}{(2+3\beta\omega_d)}\right]^{\frac{(2+3\beta\omega_d)}{3(1-\zeta_1+\alpha\omega_d)}}, \tag{44}$$

which shows power-law expansion in early time. On the other hand, if $\zeta_0 = H_0(1-\zeta_1+\alpha\omega_d)$ or $(t-t_0)\to\infty$, we obtain

$$a(t) = \exp\left(\frac{3\zeta_0(t-t_0)}{(2+3\beta\omega_d)}\right). \tag{45}$$

This case corresponds the de Sitter universe which shows accelerated expansion in the later time of evolution.

Now, with the help of (43), the Hubble parameter in terms of scale factor can be written as

$$H(a) = \frac{H_0}{(1-\zeta_1+\alpha\omega_d)} \times\left[\frac{\zeta_0}{H_0}+\left\{(1-\zeta_1+\alpha\omega_d)-\frac{\zeta_0}{H_0}\right\}a^{-\frac{3(1-\zeta_1+\alpha\omega_d)}{(2+3\beta\omega_d)}}\right]. \tag{46}$$

This equations shows that if both ζ_0 and ζ_1 are zero, the Hubble parameter, $H = H_0 a^{\frac{-3(1+\alpha\omega_d)}{(2+3\alpha\omega_d)}}$, which corresponds to non-viscous NHDE model. When $\zeta_1 = 0$, H reduces to Eq. (22) which is the case of constant viscosity.

The derivative of $\dot{a}$ with respect to a can be obtained from (46), which is given by

$$\frac{d\dot{a}}{da} = \frac{H_0}{(1-\zeta_1+\alpha w_d)}\left[\frac{\zeta_0}{H_0}-\left\{(1-\zeta_1+\alpha w_d)-\frac{\zeta_0}{H_0}\right\} \times\left(\frac{(1+3(\alpha-\beta)w_d-3\zeta_1)}{2+3\beta w_d}\right)a^{-\frac{3(1-\zeta_1+\alpha w_d)}{(2+3\beta w_d)}}\right]. \tag{47}$$

Equating (47) to zero to get the transition scale factor a_T as

$$a_T = \left[\frac{(1+3(\alpha-\beta)w_d-3\zeta_1)\{(1-\zeta_1+\alpha w_d)H_0-\zeta_0\}}{(2+3\beta w_d)\zeta_0}\right]^{\frac{(2+3\beta w_d)}{3(1-\zeta_1+\alpha w_d)}}. \tag{48}$$

The corresponding transition redshift z_T is

$$z_T = \left[\frac{(1+(\alpha-\beta)w_d-3\zeta_1)\{(1-\zeta_1+\alpha w_d)H_0-\zeta_0\}}{(2+3\beta w_d)\zeta_0}\right]^{-\frac{(2+3\beta w_d)}{3(1-\zeta_1+\alpha w_d)}}-1. \tag{49}$$

It can be observed that for $(\zeta_0+\zeta_1 H_0) = \frac{\{1+3(\alpha-\beta)w_d\}H_0}{3}$, the transition from decelerated phase to accelerated phase occurs at $a_T = 1$ or $z_T = 0$, which corresponds to the present time of the universe. By considering the observational value $\alpha = 0.8502$ and $\beta = 0.4817$ along with $\omega_d = -0.5$, $H_0 = 1$, we get $(\zeta_0+\zeta_1) = 0.15$. A plot of the evolution of the scale factor is given in Fig. 6. Thus, for $0 < (\zeta_0+\zeta_1) \le 0.15$ the scale factor has earlier deceleration phase followed by an acceleration phase in later stage of the evolution. The transition from the decelerated to accelerated expansion depends on the viscosity ζ_0 and ζ_1 as shown above. For $(\zeta_0+\zeta_1) > 0.15$, the transition takes place in past of the universe and the scale factor increases with accelerated rate forever.

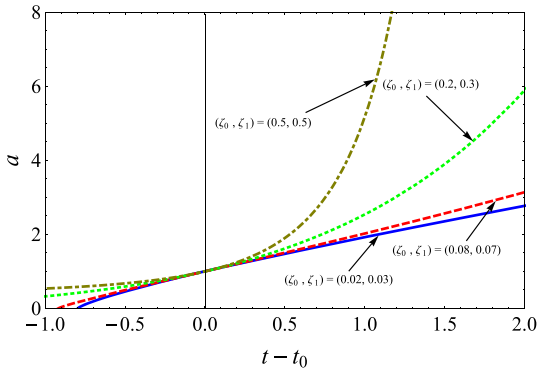


Fig. 6 The plot of the scale factor with respect to $t-t_0$ for different values of ζ_0, ζ_1 when $\zeta_0 > 0$ and $\zeta_1 > 0$ with $\omega_d = -0.5$, $\alpha = 0.8502$ and $\beta = 0.4817$

The transition may also be discussed through the evolution of DP. In this case, we get

$$q = \frac{3\left\{(1-\zeta_1+\alpha\omega_d)-\frac{\zeta_0}{H_0}\right\}}{(2+3\beta\omega_d)}e^{-\frac{3\zeta_0(t-t_0)}{(2+3\beta\omega_d)}}-1, \tag{50}$$

which is a time-dependent value of DP, which may describe the transition phase of the universe. It can be observed that DP must change its sign at $t = t_0$. This time can be achieved if $3(\zeta_0+\zeta_1 H_0) = \{1+3(\alpha-\beta)w_d\}H_0$. The sign of q is positive for $t < t_0$ and it is negative for $t > t_0$. The values of ζ_0 and ζ_1 can be obtained for a given values of ω_d, α and β, which may be obtained from observation, or vice-versa.

From (50), DP can be written in terms of scale factor as

$$q(a) = \frac{\{3(1-\zeta_1+\alpha\omega_d)-3\zeta_0\}}{(2+3\beta\omega_d)} \times\left[\frac{(1-\zeta_1+\alpha\omega_d)}{(a^{\frac{3(1-\zeta_1+\alpha\omega_d)}{2+3\beta\omega_d}}-1)\zeta_0+(1-\zeta_1+\alpha\omega_d)}\right]-1. \tag{51}$$

In terms of red shift z, the above equation becomes

$$q(z) = \frac{\{3(1-\zeta_1+\alpha\omega_d)-3\zeta_0\}}{(2+3\beta\omega_d)} \times\left[\frac{(1-\zeta_1+\alpha\omega_d)}{\left((1+z)^{-\frac{3(1-\zeta_1+\alpha\omega_d)}{2+3\beta\omega_d}}-1\right)\zeta_0+(1-\zeta_1+\alpha\omega_d)}\right]-1. \tag{52}$$

When the bulk viscous parameter and all other parameter are zero, the deceleration parameter $q = 1/2$, which corresponds to a decelerating matter dominated universe with null bulk viscosity. However, when only the bulk viscous term $\zeta_0 = 0$ and $\zeta_1 \neq 0$, the value of q is same as obtained in Eq. (38) for

case (i) of variable viscous NHDE model, and when $\zeta_0 \neq 0$ and $\zeta_1 = 0$, Eq. (51) reduces to Eq. (27) of constant viscous coefficient.

The present value of q corresponds to $z = 0$ or $a = 1$ is,

$$q_0 = q(a=1) = \frac{3(1-\zeta_1+\alpha\omega_d) - 3\zeta_0}{(2+3\beta\omega_d)} - 1. \tag{53}$$

This equation shows that if $3(\zeta_0+\zeta_1) = [1+3(\alpha-\beta)\omega_d]$, the deceleration parameter $q = 0$. This implies that the transition into the accelerating phase would occur at the present time. The current DP $q_0 < 0$ if $3(\zeta_0+\zeta_1) > [1+3(\alpha-\beta)\omega_d]$, implying that the present universe is in the accelerating epoch and it entered this epoch at an early stage. But $q_0 > 0$ if $3(\zeta_0+\zeta_1) < [1+3(\alpha-\beta)\omega_d]$ implying that the present universe is decelerating and it will be entering the accelerating phase at a future time. For the observational value $\alpha = 0.8502$ and $\beta = 0.4817$ with $\omega_d = -0.5$ and $H_0 = 1$, we get $(\zeta_0+\zeta_1) = 0.15$ which gives $q_0 = 0$. Thus for this value set, the transition into accelerating phase would occur at present time. If $(\zeta_0+\zeta_1) > 0.15$, $q_0 < 0$, i.e., the universe is in accelerating phase and it entered this epoch at an early stage. If $(\zeta_0+\zeta_1) < 0.15$, $q_0 > 0$, i.e., the universe is in decelerating epoch and it will be entered into the accelerated phase in future. This result is verified graphically which is represented by Fig. 7a. The Fig. 7b shows the $q-a$ graph in $q-a$ plane to discuss the evolution of the universe with respect to model parameters α and β. Here, the signature change in the value of DP can be seen by the figure. From above discussion we say that both viscous coefficient and model parameter have their own role in the evolution of the universe. Some values of bulk viscous term gives the accelerated phase from the beginning and continues to be accelerated in late time.

Statefinder diagnostic

As we have mentioned above , the scale factor and deceleration parameter have been discussed to explain the accelerating universe with viscous term or model parameters. So it is necessary to distinguished these models in a model-independent manner. In what follows we will apply two geometrical approaches to viscous NHDE model, i.e., the statefinder and *Om* diagnostic from which we can compute the evolutionary trajectories with ones of the ΛCDM model to show the difference among them.

In this case, the statefinder parameters defined in Eq. (10) can be evaluated as

$$r = 1 + \frac{9\left(\frac{\zeta_0}{H_0} - (1-\zeta_1+\alpha\omega_d)\right)\left(1-\frac{(1-\zeta_1+\alpha\omega_d)}{(2+3\beta\omega_d)}\right)e^{-\frac{3\zeta_0(t-t_0)}{(2+3\beta\omega_d)}}}{(2+3\beta\omega_d)} + \frac{9\left(\frac{\zeta_0}{H_0} - (1-\zeta_1+\alpha\omega_d)\right)^2 e^{-\frac{6\zeta_0(t-t_0)}{(2+3\beta\omega_d)}}}{(2+3\beta\omega_d)^2}, \tag{54}$$

and

$$s = \frac{\frac{2\left(\frac{\zeta_0}{H_0}-(1-\zeta_1+\alpha\omega_d)\right)\left(1-\frac{1-\zeta_1+\alpha\omega_d}{(2+3\beta\omega_d)}\right)}{(2+3\beta\omega_d)}e^{-\frac{3\zeta_0(t-t_0)}{(2+3\beta\omega_d)}} + \frac{2\left(\frac{\zeta_0}{H_0}-(1-\zeta_1+\alpha\omega_d)\right)^2}{(2+3\beta\omega_d)^2}e^{-\frac{6\zeta_0(t-t_0)}{(2+3\beta\omega_d)}}}{\frac{2\left((1-\zeta_1+\alpha\omega_d)-\frac{\zeta_0}{H_0}\right)}{(2+3\beta\omega_d)}e^{-\frac{3\zeta_0(t-t_0)}{(2+3\beta\omega_d)}} - 1}. \tag{55}$$

From (54) and (55) it can be observed that the viscous NHDE model converges to $\{r,s\} \to \{1,0\}$ in the limit of $(t-t_0) \to \infty$. This can also be achieved at $(\zeta_0 + H_0\zeta_1) = H_0(1+\alpha\omega_d)$ but this is a very fixed point. Thus, the statefinder diagnostic fails to discriminate between ΛCDM and the NHDE model. Here, we obtain time-dependent statefinder pair which needs to study the general behavior. Let us see the effect of viscosity coefficients ζ_0, ζ_1 and model parameters α, β for the general form of variable viscous NHDE model. Figure 8a shows the $r-s$ trajectory in $r-s$ plane for different values of ζ_0 and ζ_1 with $H_0 = t_0 = 1$, $\alpha = 0.8502$ and $\beta = 0.4817$. The model behaviors to Q models for $0 < (\zeta_0+\zeta_1) \leq 0.57$ and CG models for $(\zeta_0+\zeta_1) > 0.57$. The trajectories in Q-model and CG-model both converge to the ΛCDM model in late time of evolution.

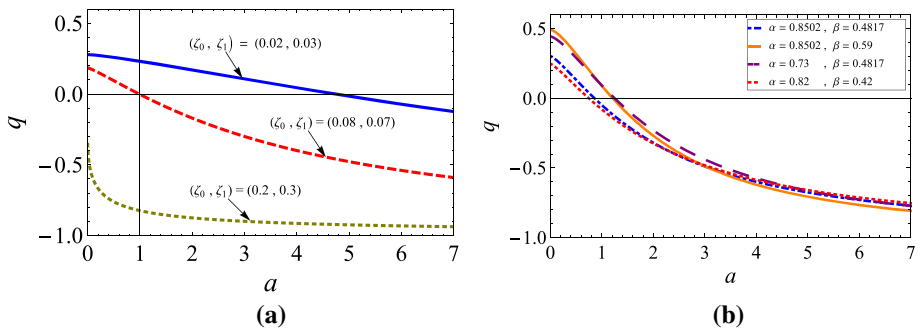


Fig. 7 **a** The $q-a$ graph in $q-a$ plane for different values of $\zeta_0 > 0$ and $\zeta_1 > 0$ with $\omega_d = -0.5$, $\alpha = 0.8502$ and $\beta = 0.4817$. **b** The $q-a$ graph in $q-a$ plane for different values of α and β with $\zeta_0 = 0.2$, $\zeta_1 = 0.3$ and $\omega_d = -0.5$

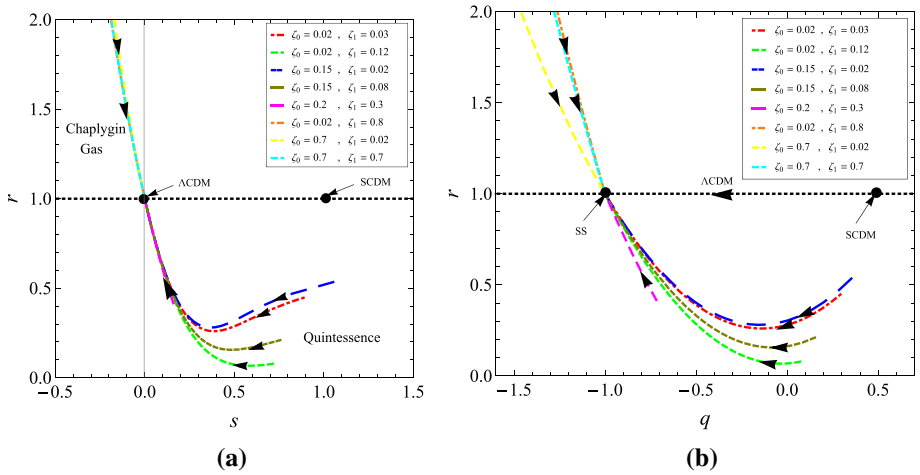


Fig. 8 **a** The $r-s$ trajectories are plotted in $r-s$ plane for different values of $\zeta_0 > 0$ and $\zeta_1 > 0$ with $\omega_d = -0.5$, $\alpha = 0.8502$ and $\beta = 0.4817$. The arrows represent the directions of the evolutions of statefinder diagnostic pair with time. **b** The $r-q$ trajectories are plotted in $r-q$ plane for different values of $\zeta_0 > 0$ and $\zeta_1 > 0$ with $\omega_d = -0.5$, $\alpha = 0.8502$ and $\beta = 0.4817$. The arrows represent the directions of the time evolution pair $\{r, q\}$ with time

Figure 8b shows the time evolution of $\{r, q\}$ pair in $r-q$ plane for different combinations of the values of ζ_0 and ζ_1 with $H_0 = t_0 = 1$, $\alpha = 0.8502$ and $\beta = 0.4817$. The fixed points $\{r, q\} = \{1, 0.5\}$ and $\{r, q\} = \{1, -1\}$ represents the $SCDM$ and SS models, respectively. Since q changes its sign from positive to negative with respect to time which shows the phase transition of the universe from deceleration to acceleration. In beginning this model behaves different from the ΛCDM but in future it behaves same as ΛCDM which converges to SS model in late-time. Hence the variable viscous NHDE model always converges to SS model as ΛCDM, Q and CG models in late-time evolution of the universe. For all the ranges of $(\zeta_0 + \zeta_1)$ the trajectories correspond to Q and CG models as in Fig. 8a. Thus the variable viscous NHDE model is compatible with both Q and CG models.

Thus, the viscosity coefficients are able to correspond to both Q and CG models for different combinations of ζ_0, ζ_1 and also explain the phase transition of the universe.

Now, we are curious to know the behaviour of variable viscous NHDE model with respect to the model parameters α and β. Here, Fig. 9a, b represents the $r-s$ and $r-q$ trajectories in $r-s$ and $r-q$ plane, respectively, for the different values of α and β close to it's observational value with $\omega_d = -0.5$, $H_0 = t_0 = 1$, $\zeta_0 = 0.02$ and $\zeta_1 = 0.03$. The evolutionary directions of both the trajectories are shown in the figures by the arrows. In Fig. 9a, we analysed that for this fixed value of ζ_0 and ζ_1 the (r, s) trajectories are lying in the region corresponds to $r < 1$, $s > 0$ which shows that our model is similar to the Q model. It also starts from the vicinity of $SCDM$ model in early time of evolution for some values of α and β, e.g., $(\alpha, \beta) = (0.8502, 0.59)$. It is different from RDE model and quiessence model as it produces the curved trajectories for any values of (α, β) close to observational value which approach to ΛCDM in late-time of evolution as the Q model tends to ΛCDM model in late-time of evolution.

The $r-q$ trajectories in $r-q$ plane are shown by the Fig. 9b. This model is also able to explain the phase transition of the universe. It also starts from the neighbourhood of the $SCDM$ model for some values of α and β (e.g., $\alpha = 0.8502$, $\beta = 0.55$) and approaches to SS model in late-time for any value of α and β close to the observational value. In future the variable viscous NHDE model approaches to the SS model same as the ΛCDM and Q models. Thus the viscous NHDE model is compatible with the ΛCDM and Q models.

Thus, we observed from Figs. 8 and 9 that viscous NHDE model is compatible to Q and CG models for different ranges of viscosity coefficients in the presence of the fixed observational value of model parameters whereas the model parameter in the presence of fixed value of viscosity coefficients approaches only to Q model.

Om diagnostic

Let us discuss the another geometrical parameter, i.e., *Om(z)* diagnostic in viscous NHDE model. By substituting the required values in Eq. (32), we get the *Om(z)* diagnostic for $\zeta = \zeta_0 + \zeta_1 H$ as

$$Om(z) = \frac{\left[\frac{\zeta_0}{H_0} + \left\{(1-\zeta_1+\alpha\omega_d) - \frac{\zeta_0}{H_0}\right\}(1+z)^{\frac{3(1-\zeta_1+\alpha\omega_d)}{2+3\beta\omega_d}}\right]^2 - (1-\zeta_1+\alpha\omega_d)^2}{(1-\zeta_1+\alpha\omega_d)^2[(1+z)^3-1]}. \tag{56}$$

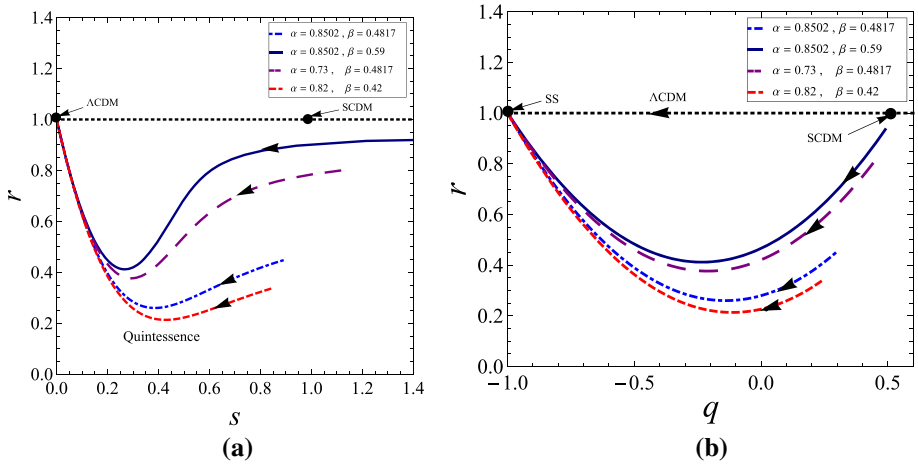


Fig. 9 **a** The $r-s$ trajectories are plotted in $r-s$ plane for different values of α and β with $\omega_d = -0.5$, $\zeta_0 = 0.02$ and $\zeta_1 = 0.03$. The arrows represent the directions of the evolutions of statefinder diagnostic pair with time. **b** The $r-q$ trajectories are plotted in $r-q$ plane for different values of α and β with $\omega_d = -0.5$, $\zeta_0 = 0.02$ and $\zeta_1 = 0.03$. The arrows represent the directions of the time evolution pair $\{r, q\}$ with time

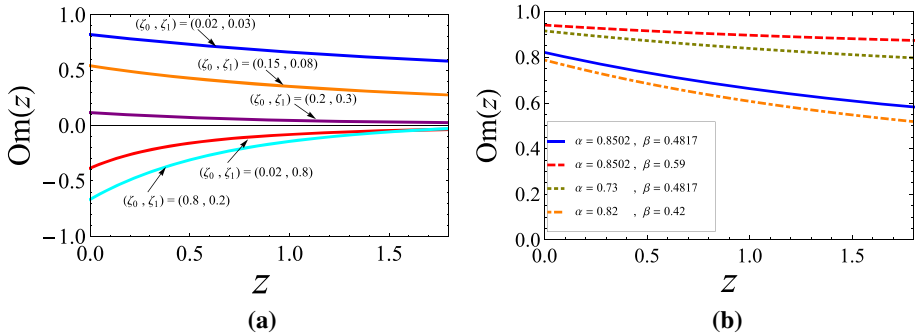


Fig. 10 **a** The evolution of $Om(z)$ versus the redshift z for different values of $\zeta_0 > 0$ and $\zeta_1 > 0$ with $\omega_d = -0.5$, $\alpha = 0.8502$ and $\beta = 0.4817$. **b** The evolution of $Om(z)$ versus the redshift z for different values of α and β with $\zeta_0 = 0.02$, $\zeta_1 = 0.03$ and $\omega_d = -0.5$

Figure 10a shows the $Om(z)$ trajectory with respect to z for different values of $\zeta_0 > 0$ and $\zeta_1 > 0$ corresponding to $\alpha = 0.8502$, $\beta = 0.4817$, $H_0 = 1$ and $\omega_d = -0.5$. Here, the trajectory represents the negative curvature, i.e., the viscous NHDE behaves as quintessence for the limit $0 < (\zeta_0 + \zeta_1) \leq 0.57$ and it shows the positive curvature, i.e., the viscous DE behaves as phantom, for $(\zeta_0 + \zeta_1) > 0.57$ whereas for $z = -1$, i.e., in future time we get $Om(z) = 1 - \frac{\zeta_0^2}{H_0^2(1-\zeta_1+\alpha\omega_d)^2}$, which is the constant value of $Om(z)$. Thus for $z = -1$, the viscous NHDE will correspond to ΛCDM.

Figure 10b plot the $Om(z)$ versus z for different model parameters α and β correspond to fixed ζ_0 and ζ_1. The graph shows that there is always negative curvature for any values of model parameters. This shows that the model behaviors similar to quintessence model.

4 Conclusion

We have studied some viscous cosmological NHDE models on the evolution of the universe, where the IR cutoff is given by the modified Ricci scalar, proposed by Granda and Oliveros [29,30]. It has been tried to demonstrate that the bulk viscosity can also play the role as a possible candidate of DE. We have performed a detailed study of both non-viscous and viscous NHDE models. The component of this model is DE and pressureless DM. We have obtained the solutions for scale factor and deceleration parameter. We have also studied these models from two independent geometrical point of view, namely the statefinder parameter and Om diagnostic. We have studied the different possible scenarios of viscous NHDE and analyzed the evolution of the universe according to the assumption of bulk viscous coefficient ζ. In the following we summarize the results obtained in different sections for non-viscous and viscous NHDE models.

In Sect. 2, we have investigated non-viscous NHDE in flat FRW universe. We have calculated the relevant cosmological parameters and their evolution. The evolution of scale factor has been studied. We have obtained power-law form of scale factor for which the model may decelerate or accelerate depending on the constraint of model parameters. The deceleration parameter is constant in this case. Therefore, the model can not describe the transition phase of the universe. The statefinder parameters are also constant. We have observed that the observed set of data of model parameters do not favor the NHDE model over the ΛCDM as well as $SCDM$ model. However, NHDE model behaves like $SCDM$ model for $\alpha \to 3\beta/2$. It has been observed that this model approaches to $\{r, s\} \to \{1, 0\}$ in the limit of $\alpha \to -1/\omega_d$ but there is no such value of parameters which would clearly show the ΛCDM.

In viscous NHDE model as discussed in Sect. 3, we have considered that the matter consists of viscous holographic dark energy and pressureless DM. We have assumed a most

general form $\zeta = \zeta_0 + \zeta_1 H$ to observe the effect of bulk viscous coefficient in the evolution of the universe during early and late time. We have studied three cases: $(\zeta_0 \neq 0,\ \zeta_1 = 0)$; $(\zeta_0 = 0,\ \zeta_1 \neq 0)$ and $(\zeta_0 \neq 0,\ \zeta_1 \neq 0)$.

In the first case where we have constant bulk viscous coefficient, i.e., $\zeta = \zeta_0$, an exponential form of the scale factor is obtained. Therefore, the universe starts from a finite volume followed by an early decelerated phase and then transits into an accelerated phase in late time of evolution. As $(t - t_0) \rightarrow 0$, the scale factor reduces to the power-law form which corresponds to an early decelerated expansion. As $(t - t_0) \rightarrow \infty$, the scale factor tends to the exponential form which corresponds to acceleration similar to the de Sitter phase. The scale factor and red shift corresponding to the transition from decelerated to accelerated expansion has been obtained. The evolution of scale factor has been shown is Fig. 1. It is clear from Fig. 1 that if $\zeta_0 = 0.15$, transition from decelerated phase to accelerated phase occurs at $a_T = 1$ and $z_T = 0$, which corresponds to the present time of the universe. The transition would takes place in past if $\zeta_0 > 0.15$ and in future if $0 < \zeta_0 < 0.15$.

The result regarding the transition of the universe into accelerated epoch discussed above have been further verified by studying the evolution of DP. The viscous NHDE model gives time-dependent DP which would describe the phase transition. We have obtained q in terms of a and z. The variation of q with a has been shown in Fig. 2a, b with varying ζ_0 and constant model parameters, and varying model parameters and constant ζ_0, respectively. The evolution of DP shows that the transition from decelerated to accelerated epoch occurs at the present time, corresponding to $q = 0$ if $\zeta_0 = 0.15$. The transition would be in recent past, corresponds to $q < 0$ at present $\zeta_0 > 0.15$ and the transition into accelerating epoch will be in the future, corresponds to $q > 0$ at present if $0 < \zeta_0 < 0.15$.

As the model predicts the late time acceleration, we have analyzed the model using statefinder parameter and *Om* diagnostic to distinguished it from other DE models especially from ΛCDM model. The evolution of the viscous NHDE model in the $\{r, s\}$ plane is shown in Fig. 3a with different values of ζ_0 with constant α and β. It shows that the evolution of $\{r, s\}$ parameter is in such a way that $r < 1, s > 0$, a feature of quintessence model where as $r > 1$, $s < 0$ corresponds to the Chaplygin gas model. In both models, the trajectories are coinciding with each other for any value of ζ_0. The viscous NHDE model behaving quintessence and Chaplygin gas models in early time for different ζ_0 untimely approaches to ΛCDM model in late time. We have also discussed the evolutionary behavior of $\{r, q\}$ to discriminate the viscous NHDE model. The trajectory of $\{r, q\}$ has been plotted in Fig. 3b which shows the phase transition from decelerated to accelerated phase. If $0 < \zeta_0 \leq 0.57$, the transition takes place from quintessence region and approaches to SS model in late time as ΛCDM model approaches from SCDM. However, if $\zeta_0 > 0.57$, the transition starts from Chaplygin gas model and approaches to SS model in late time. Both the trajectories in Q model and CG model are coinciding on each other for any value of ζ_0.

A study of *Om* diagnostic of viscous NHDE model has been carried out in Fig. 5a for different values of ζ_0 and fixed α and β. The trajectory shows that if $0 < \zeta_0 \leq 0.57$, the *Om(z)* trajectory shows the negative slope which means viscous NHDE behaves like quintessence and if $\zeta_0 > 0.57$, the positive slope of the *Om(z)* trajectory is observed, i.e., the viscous NHDE behaves like phantom. In future as $z \rightarrow -1$, the *Om(z)* becomes constant, i.e, it may approach to ΛCDM model.

The above discussion shows that effect of bulk viscous coefficient on NHDE model with different values of ζ_0. We have also discussed the viscous NHDE model with varying model parameters α and β taking fixed ζ_0. The trajectory for q versus a as shown in Fig. 2b shows that the transition takes place from decelerated to accelerated phase in future for any values of α and β and approaches to $q = -1$ in late-time. The trajectory for $\{r, s\}$ and $\{r, q\}$ have also been plotted respectively in Fig. 4a, b for different values of α and β with fixed value of ζ_0. The $\{r, s\}$ trajectory as shown in Fig. 4a shows that the trajectory starts from the quintessence region, even though some starts from the vicinity of $SCDM$ and approaches to ΛCDM in late-time. The signature change of q from positive to negative has been observed in $r - q$ plane as shown in Fig. 4b. The viscous NHDE model approaches to SS model in late-time as ΛCDM does. The *Om* trajectory has been plotted in Fig. 5b for different values of α and β for fixed ζ_0. This trajectory only shows the negative curvature which imply that the viscous NHDE behaves like quintessence.

From the above discussion with constant bulk viscous coefficient, we find that the constant ζ_0 (or cosmological parameters α and β) play important roles in the evolution of the universe i.e., they both determine the evolutionary behavior as well as the ultimate fate of the universe.

In second viscous NHDE model we have assumed $\zeta = \zeta_1 H$. The solution of this model is similar to the non-viscous NHDE one. We have obtained power-law form of scale factor which gives constant values of DP and statefinder pairs.

In last case we have taken the most general form of bulk viscous coefficient $\zeta = \zeta_0 + \zeta_1 H$. The solution of this model is similar to the constant bulk viscous coefficient ζ_0. The effect of both non-zero values of ζ_0 and ζ_1 have been discussed. We have obtained exponential scale factor which gives time-dependent DP and statefinder pairs. The transition from decelerated to accelerated epoch has been discussed. As $(t - t_0) \rightarrow 0$, the scale factor asymptotically gives the power-law which shows that the model decelerates in early time and accelerates in late-time. As $(t - t_0) \rightarrow \infty$, the model corresponds to de Sitter like. The transition scale factor and

hence corresponding transition redshift has been calculated. If $(\zeta_0 + \zeta_1) = 0.15$, the transition from decelerated to accelerated phase occurs at $a_T = 1$ or $z_T = 0$, i.e., at present time of the universe. Figure 6 shows that evolution of the scale factor with $(t - t_0)$. If $0 < (\zeta_0 + \zeta_1) < 0.15$, the scale factor has earlier deceleration phase followed by an acceleration phase in later stage of the evolution. For $(\zeta_0 + \zeta_1) > 0.15$, the transition takes place in past of the universe and the scale factor increases with accelerated rate forever.

The DP is time-dependent which shows phase transition from decelerated to accelerated phase. The DP has been written in terms of scale factor or redshift. We have calculated the present value q_0 which gives $\zeta_0 + \zeta_1 = 0.15$. This shows that the transition into acceleration phase occurs at present time. If $(\zeta_0 + \zeta_1) > 0.15$, $q_0 < 0$, i.e., the universe is in accelerating phase and it entered this epoch at an early stage. If $(\zeta_0 + \zeta_1) < 0.15$, $q_0 > 0$, i.e., the universe is in decelerating epoch and it will be entered into the accelerated phase in future. We have plotted q versus a for different values of (ζ_0, ζ_1) with fixed model parameters and others as shown in Fig. 7a. The Fig. 7b plots the $q - a$ for different models parameters α, β with fixed ζ_0, ζ_1 and others.

Figure 8a shows the $r - s$ trajectory in $r - s$ plane for different values of ζ_0 and ζ_1 with constant model parameters and others. The model behaviors to Q models for $0 < (\zeta_0 + \zeta_1) \leq 0.57$ and CG models for $(\zeta_0 + \zeta_1) > 0.57$. The trajectories in Q-model and CG model both converge to the ΛCDM model in late time of evolution. Figure 8b plots the trajectory of $q - r$ for different values of (ζ_0, ζ_1) with constant model parameters and others. The DP changes its sign from positive to negative with respect to time which shows the phase transition of the universe from deceleration to acceleration. In beginning this model behaves different from the ΛCDM but in future it behaves same as ΛCDM which converges to SS model in late-time. Thus, the variable viscous NHDE model is compatible with both Q and CG model. Figure 9a, b plot the trajectories of $r - s$ and $r - q$ for different model parameters (α, β) with fixed ζ_0, ζ_1 and others. In Fig. 9a, we have analysed that for this fixed value of ζ_0 and ζ_1 the $\{r, s\}$ trajectories are lying in the region corresponds to $r < 1$, $s > 0$ which shows that our model is similar to the Q model. Figure 9b shows that this model is also able to explain the phase transition of the universe. It also starts from the neighbourhood of the $SCDM$ model for some values of α and β. In future the variable viscous NHDE model approaches to the SS model same as the ΛCDM and Q models. Thus the viscous NHDE model is compatible with the ΛCDM and Q models.

We conclude that the trajectory of $s - r$ and $q - r$ suggest a different behavior as compare to Ricci dark energy done by Feng [16] where it was found that the $s - r$ trajectory is a vertical segment, i.e., s is constant during the evolution of the universe. The trajectory in our viscous NHDE model is mostly confined a parabolic curve and approaches to $\{r, s\} = \{1, 0\}$ in $s - r$ plane and $\{r, q\} = \{1, -1\}$ in $q - r$ plane.

From Om diagnostic we find that the trajectory represents the negative curvature, i.e, viscous NHDE behaves as a quintessence for $0 < (\zeta_0 + \zeta_1) \leq 0.57$ and it shows the positive curvature, i.e., the viscous DE behaves as phantom, for $(\zeta_0 + \zeta_1) > 0.57$, which is graphically represented by Fig. 10a. We have also concluded that as $z \to -1$, we get the constant value of Om, which corresponds to ΛCDM model. However, plot of Om as shown in Fig. 10b for different model parameters with constant ζ_o and ζ_1 reveal that there is always negative curvature for any values of model parameters. This shows that the viscous NHDE behaviors similar to quintessence.

In concluding remarks, let us compare our work with respect to the earlier studied in this direction. Feng and Li [56] who investigated the viscous Ricci DE model by assuming bulk viscous coefficient proportional to the velocity vector of the fluid. Chattopadhyay [55] reported a study on modified Chaplygin gas based reconstructed scheme for extended HDE in the presence of bulk viscosity. In comparison to the said work, the present work lies not only in its choice of different bulk viscous coefficient but also in its different approach to discuss the evolution of the universe. The present viscous NHDE model successfully describes the present accelerated epoch. The ΛCDM model is attainable by present model. The NHDE model behaves quintessence model and Chaplygin gas model inn early time due to viscous effect. However, it behaves only quintessence if we consider the model parameters with fixed viscous coefficient. Our work implies the theoretical basis for future observations to constraint the viscous NHDE.

Acknowledgements The authors express their sincere thank to the referee for his suggestions to improve the manuscript. One of the author MS sincerely acknowledges the University Grant Commission, which provided the Senior Research Fellowship under UGC-NET Scholarship.

Open Access This article is distributed under the terms of the Creative Commons Attribution 4.0 International License (http://creativecommons.org/licenses/by/4.0/), which permits unrestricted use, distribution, and reproduction in any medium, provided you give appropriate credit to the original author(s) and the source, provide a link to the Creative Commons license, and indicate if changes were made.
Funded by SCOAP[3].

References

1. A.G. Riess et al., Astron. J. **116**, 1009 (1998)
2. S. Perlmutter et al., Nature **391**, 51 (1998)
3. S. Perlmutter et al., Astrophys. J. **517**, 565 (1999)
4. D.N. Spergel et al., Astrophys. J. Suppl. Ser. **148**, 175 (2003)
5. D.N. Spergel et al., Astrophys. J. Suppl. Ser. **170**, 377 (2007)
6. M. Tegmark et al., Phys. Rev. D **69**, 103501 (2004)
7. M. Tegmark et al., Astrophys. J. **606**, 702 (2004)
8. S.M. Carroll, Living Rev. Relativ. **4**, 1 (2001)

9. S. Weinberg, Rev. Mod. Phys. **61**, 1 (1989)
10. P.J.E. Peebles, Rev. Mod. Phys. **75**, 559 (2003)
11. E.J. Copeland, M. Sami, S. Tsujikawa, Int. J. Mod. Phys. D **15**, 1753 (2006)
12. P.J.E. Peebles, B. Ratra, Astrophys. J. **325**, L17 (1988)
13. M.S. Turner, Int. J. Mod. Phys. A **17**, 180 (2002)
14. R.R. Caldwell, M. Kamionkowski, N.N. Weinberg, Phys. Rev. Lett. **91**, 071301 (2003)
15. T. Padmanabhan, T.R. Chaudhary, Phys. Rev. D **66**, 081301 (2002)
16. B. Feng et al., Phys. Lett. B **607**, 35 (2005)
17. S.D. Hsu, Phys. Lett. B **594**, 13 (2004)
18. M. Li, Phys. Lett. B **603**, 1 (2004)
19. R.G. Cai, Phys. Lett. B **657**, 228 (2007)
20. H. Wei, R.G. Cai, Phys. Lett. B **660**, 113 (2008)
21. A.A. Starobinsky, Phys. Lett. B **91**, 99 (1980)
22. R. Kerner, Gen. Relativ. Gravit. **14**, 453 (1982)
23. G. t'Hooft, arXiv:gr-qc/9310026
24. L. Susskind, J. Math. Phys. **36**, 6377 (1995)
25. R. Bousso, Class. Quantum Gravity **17**, 997 (2000)
26. A.G. Cohen, D.B. Kaplan, A.E. Nelson, Phys. Rev. Lett. **82**, 4971 (1999)
27. H. Wei, S.N. Zhang, arXiv:0707.2129
28. C. Gao, F. Wu, X. Chen, Phys. Rev. D **79**, 043511 (2009)
29. L.N. Granda, A. Oliveros, Phys. Lett. B **669**, 275 (2008)
30. L.N. Granda, A. Oliveros, Phys. Lett. B **671**, 199 (2009)
31. K. Karami, J. Fehri, Phy. Lett. B **684**, 61 (2010)
32. M. Malekjani, A. Khodam-Mohammadi, N. Nazari-Pooya, arXiv:1011.4805 [gr-qc]
33. M. Sharif, A. Jawad, arXiv:1212.0129 [gr-qc]
34. U. Debnath, S. Chattopadhyay, arXiv:1102.0091 [physics.gen-ph]
35. Y. Wang, L. Xu, Phys. Rev. D **81**, 083523 (2010)
36. A. Oliveros, M.A. Acero, Astrophys. Space Sci. **357**, 12 (2015)
37. V. Sahni et al., JETP Lett. **77**, 201 (2003)
38. U. Alam et al., Mon. Not. R. Astron. Soc. **344**, 1057 (2003)
39. V. Sahni, A. Shafieloo, A.A. Starobinsky, Phys. Rev. D **78**, 103502 (2008)
40. C. Eckart, Phys. Rev. D **58**, 919 (1940)
41. W. Israel, J.M. Stewart, Phys. Lett. A **58**, 213 (1976)
42. X.H. Meng, J. Ren, M.G. Hu, Commun. Theor. Phys. **47**, 379 (2007)
43. X.H. Meng, X. Duo, Commun. Theor. Phys. **52**, 377 (2009)
44. J. Ren, X.H. Meng, Phys. Lett. B **633**, 1 (2006)
45. M.G. Hu, X.H. Meng, Phys. Lett. B 635, (2006).
46. C.P. Singh, S. Kumar, A. Pradhan, Class. Quantum Gravity **24**, 455 (2007)
47. C.P. Singh, Pramana J. Phys. **71**, 33 (2009)
48. C.P. Singh, Mod. Phys. Lett. A **27**, 1250070 (2012)
49. C.P. Singh, P. Kumar, Eur. Phys. J. C **74**, 3070 (2014)
50. P. Kumar, C.P. Singh, Astrophys. Space Sci. **357**, 120 (2015)
51. I. Brevik et al., Int. J. Mod. Phys. D **26**, 1730024 (2017)
52. B.D. Normann, I. Brevik, Mod. Phys. Lett. A **32**, 1750026 (2017)
53. B.D. Normann, I. Brevik, Entropy **18**, 215 (2016)
54. M. Jamil, M.U. Farooq, Int. J. Theor. Phys. **49**, 42 (2010)
55. S. Chattopadhyay, Int. J. Mod. Phys. D **26**, 1750042 (2017)
56. C.-J. Feng, X.-Z. Li, Phys. Lett. B **680**, 355 (2009)
57. C.P. Singh, P. Kumar, Astrophys. Space Sci. **361**, 157 (2016)
58. I. Brevik, O. Gorbunova, Y.A. Shaido, Int. J. Mod. Phys. D **14**, 1899 (2005)
59. I. Brevik, O. Gorbunova, Eur. Phys. J. C **56**, 425 (2008)
60. I. Brevik, O. Gorbunova, D.S. Gomez, Gen. Relativ. Gravit. **42**, 1513 (2010)
61. W. Zimdahl, D. Pavon, Phys. Lett. B **521**, 133 (2001)
62. W. Zimdahl, D. Pavon, Gen. Relativ. Gravit. **35**, 413 (2003)
63. L.P. Chimento, A.S. Jakubi, D. Pavon, W. Zimdahl, Phys. Rev. D **67**, 083513 (2003)
64. R. Maartens, Class. Quantum Gravity **12**, 1455 (1995)
65. A. Avelino, U. Nucamendi, J. Cosmol. Astropart. Phys. **08**, 009 (2010)
66. C.J. Feng, Phys. Lett. B **670**, 231 (2008)
67. B. Wu, S. Li, M.H. Fu, J. He, Gen. Relativ. Grav. **39**, 653 (2007)
68. T.K. Mathew, J. Suresh, D. Divakaran, Int. J. Mod. Phys. D **22**, 1350056 (2013)
69. Z.G. Haung, X.M. Song, H.Q. Lu, W. Fang, Astrophys. Space Sci. **315**, 175 (2008)
70. B. Wang, Y. Gong, E. Abdalla, Phys. Rev. D **74**, 083520 (2006)
71. M.L. Tong, Y. Zhang, Phys. Rev. D **80**, 023503 (2009)
72. J.B. Lu, L.X. Xu, Int. J. Mod. Phys. D **18**, 1741 (2009)
73. Z.G. Huang, H.Q. Lu, K. Zhang, Astrophys. Space Sci. **331**, 331 (2011)